Designed Synthesis and Catalytic Applications of Azo-Based Ligands in Transition Metal Complexes

THESIS SUBMITTED FOR THE DEGREE OF

DOCTOR OF PHILOSOPHY (SCIENCE)

JADAVPUR UNIVERSITY

By

Srijita Naskar

Index No.: 61/19/Chem./26

Registration No.: SCHEM1106119

DEPARTMENT OF CHEMISTRY

JADAVPUR UNIVERSITY

KOLKATA-700032

September, 2025

Prof. (Dr.) K. Pramanik
Professor
Department of Chemistry
Inorganic Chemistry Section

JADAVPUR UNIVERSITY
KOLKATA700032, INDIA
Tel: +91 33 2457 2781
Mob: +91-8910935661
email: kausikis.pramanik@jadavpuruniversity.in

CERTIFICATE FROM THE SUPERVISOR

This is to certify that the thesis titled "***Designed Synthesis and Catalytic Applications of Azo-Based Ligands in Transition Metal Complexes***" submitted by **Ms. Srijita Naskar**, who enrolled on September 2, 2019 (Registration No.: SCHEM1106119) for the Ph.D. (Science) degree at the Jadavpur University, is an account of original research conducted by her under my supervision. I further declare that no portion of this thesis has been submitted earlier for the award of any degree, diploma, or academic award at any other university or institution.

It is further confirmed that she has satisfied all the regulatory criteria concerning both the conduct and duration of the research.

29/2025
Dr. Kausikisankar Pramanik
Professor of Chemistry
Jadavpur University
Kolkata-700032

(Dr. Kausikisankar Pramanik)
Professor
Department of Chemistry
Jadavpur University
Kolkata – 700 032

Declaration

I hereby affirm that this submission is the result of my own original work and creative effort, articulated in my own words. Any ideas, data, or contributions from other sources have been duly acknowledged and cited using credible and authentic references. I have adhered to the principles of academic integrity and honesty, and have neither misrepresented nor fabricated or falsified any data, methodology, or source. I fully understand that any violation of these principles may result in disciplinary action by the University, as well as potential legal or academic consequences from original sources that were improperly cited or used without due permission.

Srijita Naskar

Date: 2/9/2025

Srijita Naskar

Registration no.: **SCHEM1106119**

Index no.: **61/19/Chem./26**


Dedicated
to my parents, brother
&
my teachers

Acknowledgements

"Chemistry is necessarily an experimental science: its conclusions are drawn from data, and its principles supported by evidence from facts" — Michael Faraday

I express my profound gratitude to the **Almighty**, whose boundless grace and guidance have illuminated every step of this journey. **His** divine presence has been an unfailing source of strength, resilience, and perseverance, without which the successful completion of this work would not have been possible.

With a deep sense of accomplishment and scholarly pride, I present this dissertation, the culmination of years of rigorous research, intellectual pursuit and personal growth. This academic journey has been deeply influenced by the enduring legacy of the scientific community and especially by the pioneering contributions of chemists whose foundational work has illuminated and inspired the path of my own research.

I take this opportunity to express my earnest gratitude and heartfelt appreciation to my esteemed supervisor, ***Prof. (Dr.) Kausikisankar Pramanik***, Professor, Department of Chemistry, Jadavpur University, Kolkata. His exceptional guidance, steadfast support and constant encouragement have been the cornerstone of my research journey. I am truly thankful for his profound knowledge, meticulous attention to detail and the unwavering mentorship he has extended throughout every phase of this work. His visionary insights and pragmatic approach have consistently guided and elevated the direction of this dissertation.

I extend my sincere gratitude and utmost respect to ***Dr. Sanjib Ganguly*** of St. Xavier's College, Kolkata, for his invaluable mentorship and unwavering support. His insightful guidance, along with his generous provision of laboratory resources, played a pivotal role in the successful execution of my research work.

I am extremely indebted to the esteemed members of my Research Advisory Committee (RAC), **Prof. Sasankasekhar Mohanta** (University of Calcutta) and **Prof. Kajal Krishna Rajak** (Head, Department of Chemistry, Jadavpur University, Kolkata), for their valuable suggestions, insightful guidance and continuous support throughout the annual RAC meetings. Their constructive feedback has been instrumental in shaping the progress and direction of my research.

I am pleased to acknowledge **Prof. Samaresh Bhattacharyya**, **Prof. Subrata Mukherjee**, **Prof. S. K. Baitalik**, **Prof. J. P. Naskar**, and **Dr. Bibhuti Bhushan Shaw** of the Department of Chemistry, Jadavpur University, for their ceaseless academic support and inspiration.

I would like to express my profound gratitude to **Dr. Koushik Sarkar**, Assistant Professor, Department of Chemistry, St. Xavier's College, Kolkata, for his expert guidance and valuable suggestions, which offered both intellectual direction and emotional support during crucial phases of my research. I am also sincerely thankful to **Dr. Rahul Sharma**, Associate Professor in the same department, for his consistent encouragement and thoughtful input, which significantly contributed to the advancement of this work.

I wish to convey my deepest gratitude to my esteemed research collaborators **Prof. Soumyajit Roy** (IISER Kolkata), **Dr. Subhadip Roy** (The ICFAI University, Tripura), **Dr. Shyama Charan Mandal** (Stanford University, USA), **Ms. Nischal Bharadwaj** (IIT Indore) and **Ms. Bidisha Chatterjee** (St**.** Xavier's College, Kolkata). Their unwavering support, insightful collaboration and shared enthusiasm have played a significant role in advancing and successfully completing this research.

It has been a privilege to work alongside **Mr. Debashis Jana**, **Mr. Gopal Kanrar**, **Mr. Sampad Malik** and **Ms. Aritra Das**. Their commitment, enthusiasm, collaborative spirit and

positivity greatly enriched this journey, fostering a research environment that was both productive and enjoyable.

I take this opportunity to acknowledge my former esteemed senior lab members: **Dr. Sarat Chandra Patra**, **Dr. Shuvam Pramanik**, **Dr. Tapas Ghorui**, for their steadfast cooperation and encouragement throughout this academic journey.

I am truly grateful to **Dr. Soumitra Dinda** for being a constant source of inspiration and support throughout my research. His thoughtful guidance, especially during challenging times, provided both confidence and clarity. I owe much of this thesis's completion to his meaningful involvement and invaluable mentorship.

It is with heartfelt appreciation that I recognize the encouragement and assistance of my contemporaries **Dr. Debopam Sinha**, **Dr. Mitali Majumdar**, **Dr. Tapashi Das**, **Dr. Roumi Patra**, **Mr. Uday Shee**, **Dr. Rakesh Debnath**, **Mr. Supriya Debnath**, **Ms. Sneha Ray**, **Mr. Biswajit Khutia**, **Dr. Ashoke Patra** (RKMRC, Narendrapur), **Mr. Anik Roy** (RKMRC, Narendrapur), **Mr. Sourav Ghosh** (RKMRC, Narendrapur), **Dr. Ujjwal Maji** (IACS, Kolkata), and **Mr. Arindam Basak** (IACS) whose support and assistance in various capacities have been invaluable throughout the course of my research. Their camaraderie, encouragement, and generous help at different stages of this journey are deeply appreciated and fondly remembered.

I remain truly thankful to all the staff members of my department for their steady support and tireless efforts behind the scenes. Their commitment and helpfulness, often extended without expectation of acknowledgment, greatly contributed to creating a positive and efficient atmosphere for my research.

I feel immense gratitude toward my parents, **Dr. Nityananda Naskar** and **Mrs. Malabika Naskar**, as well as my brother, **Dr. Kaushik Naskar** (Jadavpur University) and sister-in-law,

Mrs. Sajani Pal, whose unwavering faith in me, along with their endless love and silent sacrifices, have been the true pillars of strength of my journey. Their encouragement and constant support gave me the courage to overcome every challenge along the way. I am equally thankful to my parents-in-law, **Mr. Sujit Kumar Halder** and **Mrs. Pratima Halder**, for their heartfelt blessings, and kindness, which brought immense strength and comfort throughout this endeavour.

Above all, I extend my deepest gratitude to my husband, **Mr. Supriyo Halder**, whose unwavering support has been both a pillar of emotional strength and a source of professional encouragement throughout my research journey. His patience, understanding, and steadfast presence have made an immeasurable difference, and this achievement would not have been possible without him.

I deeply appreciate to all my teachers, friends, family members, and well-wishers whose encouragement and kindness have supported me throughout this journey. Even if not named individually, your contributions have been deeply felt and truly appreciate.

I am sincerely thankful to **Swami Vivekananda Merit-Cum-Means Scholarship (SVMCM), West Bengal** for awarding me the scholarship that provided crucial financial assistance throughout the course of my research. I also wish to express my deep appreciation to **Jadavpur University**, **St. Xavier's College (Autonomous), Kolkata**, **IISER Kolkata**, and **IACS Kolkata** for offering vital infrastructure and access to research facilities that significantly advanced my work. To everyone not named individually, I extend my deepest thanks. Your support whether through kind words, timely help, or quiet encouragement has made a lasting impact and is deeply valued.

Srijita Naskar

September, 2025

Preface

This dissertation, entitled *"**Designed Synthesis and Catalytic Applications of Azo-Based Ligands in Transition Metal Complexes**"*, presents the outcomes of my doctoral research initiated in March 2019. The central theme of this study revolves around the rational design and synthesis of azo-based ligands and their coordination to transition metals in order to explore their structural, electronic and functional versatility. Azo ligands are known for their redox non-innocence, π-acidic properties and ability to stabilize unusual electronic states, thereby serving as ideal candidates for constructing transition metal complexes with enhanced reactivity and potential bioactivity.

The overarching objective of this work has been to develop novel azo-derived frameworks namely diaryl-azo-oxime, amino-azo-quinoline, and pyridyl-azo-amine and to investigate their roles in dictating redox properties, optoelectronic behaviour, radical stabilization, catalytic transformations and biological responses. The thesis is organized into five chapters, each addressing a distinct aspect of this research.

Chapter 1 provides a comprehensive introduction to azo-based redox-active ligands, their coordination chemistry and their significance in modern inorganic and organometallic research. This chapter outlines the motivation for selecting azo-oxime and aryl-azo-amine scaffolds, summarizes the major objectives of the work and highlights the strategies employed for ligand design and metal incorporation. It also details the spectroscopic, electrochemical, and computational tools used throughout the thesis, ensuring a clear methodological foundation for the studies that follow.

Chapter 2 focuses on the redox behaviour of phenyl-azo-oxime ligands (HL) in complexes with rhodium(III), a redox-innocent center. It explores how ligand orientation governs electron-accepting properties, comparing the *cis*- and *trans*-isomers of $[Rh^{III}(L)_2Cl(PPh_3)]$. Structural

and spectroscopic analyses demonstrate that only the *trans* isomer stabilizes an unpaired electron *via* intramolecular hydrogen bonding and π–π stacking interactions. This chapter highlights the subtle but crucial role of geometry in regulating ligand non-innocence, with experimental observations supported by DFT and TD-DFT studies.

Chapter 3 presents the synthesis, structure, and electrochemistry of a novel amino-azo-quinoline ligand and its nickel(II) complexes. Detailed structural analysis reveals extensive hydrogen bonding and π–π interactions in the crystalline state. Electrochemical studies indicate ligand-centered reductions and combined metal-ligand oxidations. Beyond structural chemistry, this chapter expands into biological relevance by evaluating anti-cancer activity. Both ligand and complexes display significant cytotoxic potential, with the square-planar complexes showing superior efficacy, attributed to their enhanced rigidity and DNA binding, as confirmed by molecular docking with B-DNA.

Chapter 4 moves into the catalytic applications of azo-oxime ligands with ruthenium. A ruthenium(II) complex of *p*-chloro-aryl-azo-oxime is synthesized and shown to possess remarkable air and moisture stability. Extensive characterization demonstrates its function as a ligand-based catalyst for alcohol dehydrogenation and selective C–H activation of fluorene under aerobic conditions. This chapter underscores how the coordinated azo moiety, rather than the metal center, drives catalytic redox events, offering an efficient, lower catalyst loading with broad substrate scope and operational simplicity.

Chapter 5 further explores catalysis by introducing a ruthenium(II)-hydride complex with 2-(pyridylazo)aniline ligand. This system facilitates direct dehydrogenative synthesis of biologically important bis(indolyl)methanes (BIMs) using both aromatic and aliphatic alcohols as starting materials. Mechanistic investigations reveal a cooperative process: hydrogen atom transfer from alcohols to the azo group initiates aldehyde formation, followed by condensation

with indoles and base induced nucleophilic addition step. This ligand-metal synergy highlights the sustainable potential of azo-based frameworks in designing efficient routes to heterocyclic scaffolds of pharmaceutical importance.

Taken together, the work presented in this dissertation demonstrates how azo-based ligands can act as more than passive spectators: they are electronic regulators, redox-active and even catalytic participants. By bridging structural chemistry, radical stabilization, catalysis and bioactivity, this study contributes to the growing recognition of ligand non-innocence as a powerful concept in coordination chemistry. It is my hope that these findings will inspire further exploration into azo-derived systems for the development of next-generation catalysts and biologically relevant metal complexes.

INDEX

Chapter 1

Introduction, Experimental Methodology and Research Summary

1.1 General introduction

The development of highly efficient and selective catalysts remains a central goal of modern chemistry, a discipline fundamentally concerned with understanding matter and its transformations. In the context of building a sustainable society, the demand for catalytic systems that promote greener, more selective and energy-efficient synthetic methodologies continues to grow. Homogeneous catalysis, in particular, has gained prominence owing to its tunability, allowing for the rational design of ligand environments that can direct the reactivity of the coordinated metal center toward specific transformations. Traditionally, ligands have been designed to modulate the steric and electronic properties of the metal, while themselves remaining passive "spectators." In this classical framework, catalytic activity is localized at the metal site, and the role of the ligand is limited to fine-tuning the metal's reactivity. However, recent advances in catalyst design have shifted this paradigm, bringing forward the concept of "actor" ligands, the ligands which are able to actively participate in bond activation processes rather than serving as mere stabilizing units.[1] By directly engaging in elementary steps of the catalytic cycle, such ligands exert a decisive influence on overall reactivity and selectivity. Within this context, the exploitation of redox-active and chemically non-innocent ligands has emerged as a transformative strategy in catalysis. Unlike conventional ligands, these frameworks possess the intrinsic ability to reversibly accept and donate electrons, thereby accessing multiple oxidation states in a controlled manner. This dual capacity for electronic adaptability and structural robustness ensures that they can undergo redox events without compromising the stability of the overall framework, which is an essential feature for sustaining long-term catalytic efficiency. The distinctive reactivity of redox-active ligands is rooted in their frontier orbital characteristics. Many of these ligands possess either accessible filled π-bonding orbitals or low-lying π* antibonding orbitals, enabling electron transfer at potentials comparable to, or milder than, those associated with metal-centered transformations.

Consequently, such ligands can act as electron reservoirs, directly engaging in redox events while sparing the metal center from energetically demanding changes in oxidation state. This cooperative interplay between the ligand and the metal center provides alternative mechanistic pathways that can lower activation barriers, broaden the range of accessible transformations, and enhance the overall efficiency of catalytic processes. By decoupling electron transfer from the metal and distributing redox responsibility across the metal-ligand ensemble, complexes incorporating redox non-innocent ligands expand the mechanistic versatility of homogeneous catalysis. These systems thus hold significant promise for advancing sustainable, energy-efficient chemical transformations and uncovering entirely new modes of reactivity.

The concept of redox non-innocence can be traced back to the pioneering work of Prof. Christian Klixbüll Jørgensen in 1966, who first introduced a formalism to classify ligands as either "*innocent*" or "*non-innocent*".[2] This distinction was motivated by the persistent ambiguity surrounding the assignment of oxidation states in metal complexes. In cases where the electronic structure of a coordination compound could be described unambiguously, with the oxidation state of the central metal clearly defined and the ligands behaving as electronically passive entities, the ligand was considered *innocent*. Conversely, when the electronic structure could not be described in such a straightforward manner because the ligand itself participated in redox processes or shared electron density with the metal in a way that obscured the metal's formal oxidation state, the ligand was designated as *non-innocent*. Over time, this concept has become central to modern coordination chemistry, especially in understanding catalytic mechanisms where electron delocalization between the metal and the ligand plays a pivotal role.[3] Redox non-innocent ligands are now generally regarded as a specific subclass of the broader family of redox-active ligands. While all non-innocent ligands are redox-active by definition, not all redox-active ligands necessarily create ambiguity in oxidation state assignments. The term *redox-active ligand* is often used in a broader context to

describe any ligand capable of undergoing reversible electron transfer, whereas the *non-innocent* classification emphasizes the resulting difficulty in formally ascribing oxidation states to the metal center due to the strong metal-ligand electronic interplay. Prototypical examples of redox-active ligands include donor-appended diarylamines,[4] dithiolene frameworks,[5] salen ligands and their derivatives,[6] dipyrrins along with their extended porphyrin analogues,[7] 1,4-diimines and related 2-iminopyridines,[8] bis(imino)pyridines,[9] 1,2-catechols and *o*-phenylenediamines,[10] formazanates.[11] Redox non-innocent ligands play fundamental roles in numerous natural processes mediated by metalloenzymes.[12] Advances in synthetic catalytic design have increasingly drawn inspiration from these biological systems, particularly due to the widespread occurrence of metal-radical motifs within their active sites. Prominent examples include hydrogenases,[13] galactose oxidase,[14] and cytochrome P-450 and cytochrome c oxidase,[15] where ligand non-innocence is regarded as a crucial factor underlying their exceptional reactivity. A central advantage of ligand non-innocence in such enzymatic systems is its capacity to reduce the reorganization energy required for electron transfer, a consequence of effective delocalization of redox equivalents across the metal-ligand framework. In addition, the cooperative action of multiple non-innocent ligands, often distributed at spatially distinct sites, enables long-range electronic communication between remote reaction centers through electron transfer. These intrinsic features of metalloenzymes provide a powerful conceptual foundation for the rational design of synthetic catalysts that exploit similar principles of metal-ligand cooperativity to accomplish demanding chemical transformations.

1.2 Azo-oximes: A potential ligand exhibiting redox non-innocence

Oxime derivatives represent a well-established class of compounds in both organic and inorganic chemistry, owing to their broad applicability across diverse areas such as synthetic methodology, medicinal chemistry and coordination chemistry.[16] The oxime functional group, characterized by a –C=N–OH moiety, is widely encountered in organic molecules as well as in

metal complexes, where it plays a crucial role in dictating reactivity and stability. Based on their precursors, oximes are commonly classified into three major categories: aldoximes, obtained from aldehydes; ketoximes, derived from ketones; and amidoximes, originating from amides.[17] Structurally, the general formula for oximes is expressed as $R_1R_2C{=}NOH$, where R_1 and R_2 represent organic substituents. In aldoximes, R_2 corresponds to hydrogen, whereas in ketoximes it is typically an alkyl or aryl substituent. Amidoximes, by contrast, follow the formula $R_1C(=NOH)NR_2R_3$, in which an additional amino substituent is present, further enriching their chemical diversity. Stereochemically, oximes exhibit geometrical isomerism due to restricted rotation about the C=N double bond. Depending on the relative orientation of the substituent and the hydroxyl group, oximes generally exist in either the *syn* or *anti* form. This isomerism is particularly well-documented for both aldoximes and ketoximes, with the notable exception of aromatic aldoximes, which are typically restricted to a single stable configuration due to conjugation effects. The coexistence of these isomers not only adds to the structural complexity of oximes but also significantly influences their chemical reactivity and coordination behaviour, thereby broadening their scope in advanced chemical research.

Organic scaffolds that integrate both azo (–N=N–) and oxime (–C=NOH) functionalities have attracted considerable attention due to their ability to engage in complex redox processes upon coordination to transition metal centers. Unlike conventional spectator ligands, azo-oxime frameworks frequently display redox non-innocent behaviour, wherein the ligand itself actively participates in electron-transfer events.[18] The azo unit, in particular, can undergo stepwise one-electron reductions into its low-lying π^* orbitals, a property that is often influenced and further stabilized by the adjacent oxime functionality. Beyond serving as an electronic modulator, the oxime group has also been implicated in enhancing photophysical responses, in some cases functioning as a photosensitizer, thereby expanding the scope of reactivity accessible to metal–ligand assemblies based on these frameworks.

From a synthetic perspective, azo-oxime ligands are readily accessible through classical methods that remain in use today. A well-documented approach, originally reported by Bamberger and Pemsel in 1903, involves the reaction of aryl hydrazone precursors with isoamyl nitrite under mild conditions.[19] This transformation is believed to proceed *via* the formation of a transient C-nitroso intermediate, which subsequently undergoes rapid isomerization to afford an aryl azo-oximate species. Treatment with dilute aqueous acid induces protonation of the oximate intermediate, thereby facilitating its transformation into the corresponding aryl-azo-oxime with excellent yield. Mechanistically straightforward yet conceptually elegant, this synthetic route provides reliable access to azo-oxime ligands, which serve as versatile platforms for exploring rich coordination chemistry, redox activity and photophysical behaviour.

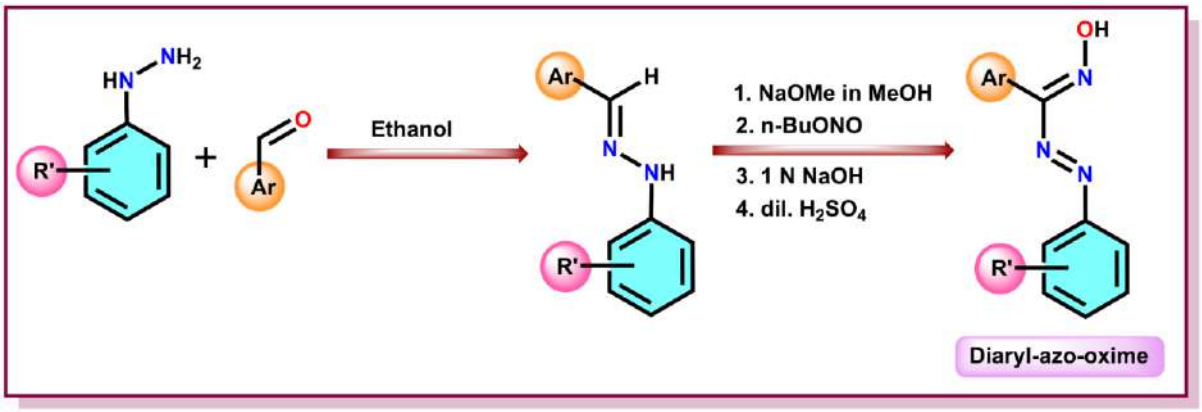

Scheme 1.1: Stepwise synthesis of diaryl-azo-oxime ligands from aryl aldehyde precursors

Aryl-azo-oximes established itself an important class of multifunctional ligands, widely recognized for their ability to generate stable coordination complexes with a broad range of transition metal ions. The combined presence of azo (–N=N–) and oxime (–C=NOH) functionalities endows these ligands with rich electronic properties and flexible coordination behaviour, rendering them particularly attractive for the design of novel coordination architectures and functional materials. The coordination chemistry of this ligand family can be

traced back to 1941, when L. Hunter and C. B. Roberts reported the first cobalt complexes derived from azo-oxime ligands. This pioneering contribution established the foundation for subsequent investigations into the coordination potential of azo-oximes.

Building upon this early work, extensive studies were carried out by Prof. Animesh Chakravorty and co-workers, who systematically explored the chemistry of azo-oxime ligands with a diverse range of transition metals. Their pioneering investigations substantially expanded the scope of azo-oxime coordination chemistry by establishing the successful synthesis and detailed characterization of metal complexes across the periodic table. In particular, these studies encompassed a wide range of first-row transition metals, including vanadium, manganese, nickel and cobalt as well as heavier congeners from the second and third transition series such as rhenium, ruthenium, osmium, rhodium, iridium, palladium and platinum.[20] This broad coverage not only highlighted the adaptability of azo-oxime ligands toward diverse metal centers but also emphasized their ability to stabilize a variety of oxidation states and coordination environments, thereby opening avenues for both structural and functional explorations in coordination chemistry. These studies revealed that the dual donor character and flexidentate nature of aryl-azo-oximes allow for a wide spectrum of coordination modes. Depending on the choice of metal center and reaction conditions, such ligands can adopt variable binding geometries, often leading to structurally robust complexes with tunable electronic properties. Collectively, these findings highlight the versatility of aryl-azo-oximes as redox-active scaffolds in transition metal coordination chemistry.

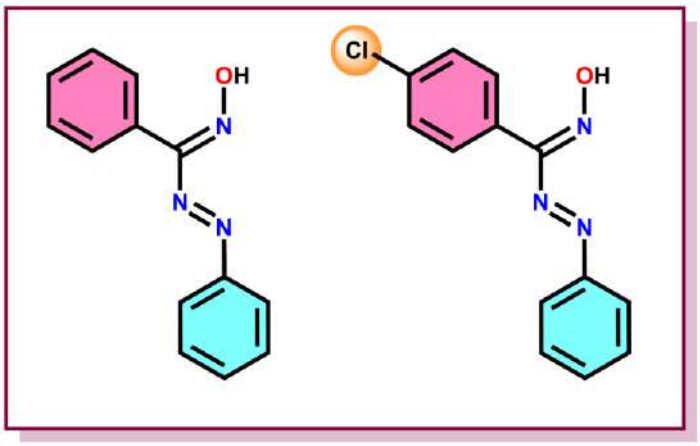

Scheme 1.2: Diaryl-azo-oxime ligands employed in this thesis

The presence of azo functionality within aryl-azo-oxime scaffold plays a decisive role in shaping their electronic behaviour. The azo group enhances electron density through extended π-conjugation, thereby imparting distinctive photophysical characteristics to these systems. Consequently, aryl-azo-oxime ligands often display intrinsic photoluminescence, functioning as efficient chromophores with measurable emissive properties. Notably, this luminescent character is not confined to the uncoordinated ligands; in many instances, coordination to transition metal centers sustains or even amplifies the emissive response. Such ligand-to-metal or metal-to-ligand charge-transfer interactions frequently give rise to complexes with pronounced luminescence, positioning them as attractive candidates for applications in light-emitting devices, optical sensors and fundamental photophysical investigations.

Overall, the coordination chemistry of aryl-azo-oximes represent a versatile platform that integrates redox activity, structural diversity, and photophysical responsiveness. This unique combination highlights their potential in diverse application domains, ranging from catalysis and materials science to molecular electronics and photochemistry.

1.3 Aryl-azo-amine ligands

Azoaromatic compounds have attracted growing attention in materials chemistry due to their distinctive combination of geometric and electronic features. The presence of a low-lying azo-centered π* molecular orbital accounts for their strong long-wavelength absorption (dye properties) as well as their nonlinear optical behaviour (information storage applications). Furthermore, this chromophore undergoes photoinduced Z/E isomerization and can be readily modified to generate mesogenic films or polymers.[20] Chemical tailoring of azo compounds has facilitated their incorporation into mesogenic systems and liquid-crystalline polymers, thereby expanding their applications in advanced material development. From an electrochemical perspective, The low-lying azo-centered π* orbital can accept one or two electrons, either through chemical reduction or electrochemical pathways. This process establishes a distinct two-step redox mechanism, proceeding via a persistent radical anion intermediate and culminating in the fully reduced 1,2-disubstituted hydrazides (2^{-}) species (Scheme 1.3). Such reversible redox activity forms the basis of their relevance in molecular electronics and in the design of redox-active coordination complexes.[21]

Beyond their photo responsive nature, the arylazo framework possesses a low-lying vacant π* orbital that, particularly upon coordination to transition metals, imparts strong redox-acceptor character. This property places azo ligands within the family of redox non-innocent systems .[22] Effective orbital overlap between the azo functionality and metal centers enables intramolecular electron transfer across the metal-ligand interface, thereby stimulating continued interest in their electronic communication and bonding interactions within coordination chemistry.[23]

The reduction pathway of azo groups ($[–N=N–]^0 \rightarrow [–NN–]^{\bullet–} \rightarrow [–N–N–]^{2–} \rightarrow 2[=N–]^{2–}$) exhibits striking parallels with the multistep redox processes of biologically significant oxygen species ($O_2 \rightarrow O^{2\bullet–} \rightarrow O_2^{2–} \rightarrow 2O^{2–}$)[24] as well as nitrosoarenes ($Ar–NO \rightarrow Ar–NO^{\bullet–} \rightarrow Ar–NO^{2–} \rightarrow [Ar–N^{2–}][O^{2–}]$).[25] Such analogies provide valuable insights into nitrogen reduction pathways, which hold significance in both biological and industrial nitrogen fixation cycles.[26] The reversible redox transformations of the azo moiety ($[–N=N–]^{0/\bullet–/2–}$) reinforce its function as a redox equivalent in a variety of catalytic processes.[27] Furthermore, complete reduction of azo ligands often generates metal-imido (M=NR) intermediates, which are key species in a range of bond-forming reactions, including metathesis, cycloaddition, nitrene transfer and hydroamination.[28] In addition to their catalytic relevance, azo-heteroarenes and their coordination complexes have emerged as promising building blocks for molecular electronic devices, owing to their tunable photochromism and redox-induced bis-stability, which together provide an attractive platform for the design of memory storage systems and switchable molecular architectures.[29] The coordination of azo-arene ligands with transition metals was first reported in 1969 by Baldwin, Lever and Parish, who demonstrated that such systems exhibit distinctive features including multiple accessible oxidation states, intense long-wavelength charge-transfer transitions, short metal-metal separations, structural isomerism, and remarkable stability of radical intermediates as well as mixed-valent species.[30] In the early 1980s, the coordination chemistry of the 2-(arylazo)pyridine ligand was independently pioneered by Prof. A. Chakravorty, R. A. Krause and co-workers.[31] Building on these foundational contributions, the research group led by Prof. S. Goswami along with Prof G. K. Lahiri and others have undertaken a systematic exploration of transition-metal complexes incorporating azo-aromatic ligands. This endeavor has been driven by the recognition that azo-based systems uniquely combine geometric flexibility with electronic versatility, features that have greatly enhanced their relevance in modern materials chemistry.[32] When coordinated to

metal centers, azo ligands act as versatile acceptors, giving rise to complexes with distinctive electronic and structural characteristics. In particular, reductive population of the azo-centered orbital, achieved either chemically or electrochemically, can introduce one or two electrons into the system, thereby stabilizing open-shell or closed-shell configurations with markedly different reactivity and stability profiles.

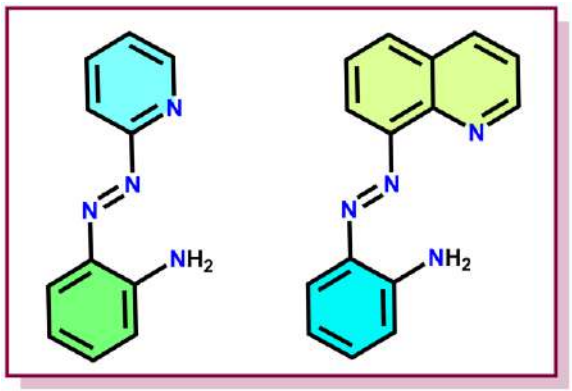

Scheme 1.3: The aryl-azo-amine ligands incorporated in this thesis

A wide variety of synthetic strategies have been developed for the preparation of azo derivatives,[33] and the choice of method largely depends on the type of azoarene of interest– whether symmetric or unsymmetric and whether aromatic or heteroaromatic substituents are attached to the azo (–N=N–) core. Symmetric azo-benzenes are generally straightforward to access, most commonly through reductive homodimerization of nitrobenzenes or oxidative homodimerization of aromatic amines.[34] In contrast, the synthesis of unsymmetric aromatic azo compounds remains more challenging. These are typically obtained either by the coupling of aryl diazonium salts with electron-rich aromatics or *via* the Baeyer-Mills reaction, which involves the condensation of aromatic amines with nitrosobenzenes.[35] However, both methods require complementary electronic properties in the amine partners (electron-rich and electron-deficient), thereby limiting their broad applicability. To address these challenges, several catalytic oxidative dimerization approaches employing oxygen as the oxidant have been reported. Corma, García and co-workers demonstrated the aerial oxidation of anilines using

gold nanoparticles as the catalyst,[36] while He and Li employed silver nanoparticles as a heterogeneous catalyst for this transformation.[37] Zhang and Jiao later showed that copper(I) catalysts combined with dioxygen could promote this oxidative dimerization under mild conditions.[38] More recently, Takeda, Minakata and co-workers introduced a metal-free protocol using *tert*-butyl hypoiodite (t-BuOI) as the oxidant, which operates *via* an umpolung reactivity pathway. This approach provides a sustainable route to both symmetric and unsymmetric aromatic as well as heteroaromatic azo compounds.[39]

An alternative route involves the reductive coupling of aromatic nitro compounds to furnish the corresponding azo derivatives. Examples include reduction with a combination of indium(III) salts and hydrosilanes,[26c] Pd nanoparticles under H_2/KOH,[26d] or Au nanoparticles with H_2, followed by oxidative dimerization with O_2. While these methods are effective, they often generate undesired side products such as azoxyarenes, diarylhydrazines, and anilines. Within the present study, ligands of the 2-(pyridylazo)aniline and azo-amino-quinoline ligands were synthesized primarily through the modified Baeyer-Mills reaction.

1.4 Summary of the research work

Chapter 2

This chapter describes the redox behaviour of the phenyl-azo-oxime ligand (HL) when coordinated to rhodium(III). Particular emphasis is placed on the influence of the spatial arrangement of electron-deficient azo-oxime units in bis-complexes, which governs their redox non-innocent character. The presence of two ligands enables stabilization of an odd electron, mediated by hydrogen-bonding interactions. The reaction of Wilkinson's catalyst with HL proceeds through oxidative coordination, affording two isomeric complexes, *cis*-$[Rh^{III}(L)_2Cl(PPh_3)]$ and *trans*-$[Rh^{III}(L)_2Cl(PPh_3)]$, both structurally confirmed by single-crystal X-ray diffraction (SCXRD). In the *trans* isomer, pronounced π–π stacking interactions enhance

its electron-accepting properties, rendering it superior to the *cis* analogue. Treatment of the *trans* complex with $NaBH_4$ generates a radical species, *trans*-$[Rh^{III}(HL^{\bullet-})(L^{-I})Cl(PPh_3)]$, *via* a proton-coupled electron transfer (PCET) process. The unpaired electron is further stabilized through intramolecular oxime…oximato hydrogen bonding. In contrast, the *cis* isomer, owing to the non-coplanar orientation of the ligands, does not exhibit significant electron-accepting ability. Complementary DFT and TD-DFT calculations corroborate these observations, providing theoretical validation of the electronic structures and absorption spectra.

Chapter 3

This chapter presents the design, synthesis, structural features, electrochemical properties and biological evaluation of a novel azo-quinoline ligand (H_2L) incorporating an electron-deficient azo unit and a biologically significant quinoline moiety, together with its cost-effective nickel(II) complexes, $[Ni(HL)(OAc)]\cdot H_2O$ and [Ni(HL)Cl]. Single-crystal X-ray diffraction (SCXRD) analysis of $[Ni(HL)(OAc)]\cdot H_2O$ reveals a well-defined hydrogen-bonding network facilitated by lattice water molecules, while π–π stacking interactions are observed in both complexes, contributing to overall lattice stability. Electrochemical data and theoretical calculations demonstrate that the ligand-centered π* orbital dominates the reduction pathway, whereas oxidation is jointly influenced by the nickel center and the ligand. Biological assays highlight that both the free ligand and its nickel(II) complexes exhibit promising anti-cancer activity, with significantly enhanced efficacy in the complexes. This superior activity is attributed to the rigid, square-planar geometry of the complexes, which likely promotes stronger DNA binding compared to the more conformationally flexible free ligand. Molecular docking studies further support these findings, employing nine conformers of H_2L and both complexes, and reveal favourable interactions with B-DNA (PDB ID: 1BNA).

Chapter 4

In this chapter, we report the synthesis of the ruthenium(II) complex *trans*-[Ru(*p*-Cl-aaO)(PPh_3)$_2$Cl(CO)], derived from the redox-active bidentate ligand *p*-chloro-aryl-azo-oxime (*p*-Cl-aaOH). The complex exhibits exceptional stability under ambient conditions, maintaining integrity in the presence of air and moisture. Comprehensive characterization was achieved through spectroscopic, electrochemical and single-crystal X-ray diffraction (SCXRD) analyses, further supported by theoretical studies to assess its redox-catalytic potential. Catalytic investigations reveal that the complex efficiently promotes ligand-centered dehydrogenation of diverse aromatic and aliphatic primary alcohols, followed by selective sp^3 C–H activation of 9*H*-fluorene under aerobic conditions *via* a tandem pathway. Mechanistic insights suggest that the coordinated azo group governs both dehydrogenation and borrowing hydrogenation processes, while the Ru(II) center acts primarily as a redox-innocent spectator. Notably, this catalyst offers several practical advantages, including facile synthesis, minimal loading (0.1 mol%), broad substrate scope, shorter reaction times and lower operational temperatures, emphasizing its promise for sustainable catalytic transformations.

Chapter 5

This chapter explores a ruthenium(II)-hydride complex bearing a pyridyl-azo amine ligand and its catalytic application in the direct dehydrogenative synthesis of biologically relevant bis(indolyl)methane (BIM) derivatives. The catalyst efficiently mediates the transformation of both aromatic and aliphatic primary alcohols, offering high selectivity and functional group tolerance. Mechanistic studies establish that the azo functionality within the ligand framework is central to the dehydrogenation process, whereas the ruthenium center remains redox-innocent. The catalytic cycle proceeds *via* a hydrogen atom transfer (HAT) from the alcohol to the azo group, leading to aldehyde formation. The in situ generated aldehyde subsequently undergoes condensation with indole derivatives, followed by base promoted 1,4-Michael type nucleophilic addition, affording

the desired BIM products. This work emphasizes the cooperative role of the ligand and metal center, enabling a streamlined and sustainable strategy for the synthesis of pharmaceutically important bis(indolyl)methanes.

1.5 Experimental details

1.5.1 Physical Measurements

The properties of the synthesized compounds were characterized using multiple physical techniques. These methods are summarized below and discussed in detail in the following chapters.

Elemental Analysis

Elemental analyses (C, H, N) of the ligands and their corresponding ruthenium complexes were performed using a Perkin–Elmer 2400 Series II elemental analyzer. The instrument quantifies carbon, hydrogen and nitrogen contents *via* thermal conductivity detection of the combustion products (CO_2, H_2O and N_2). Accurately weighed samples (1.5–2.5 mg) were introduced into a high-temperature combustion chamber maintained at 900–980 °C. Combustion was carried out under a pure oxygen atmosphere and the resulting gases were transported through the detection system using high-purity helium as the carrier gas.

Infrared Spectra

The FT-IR spectra for all ligands and their complexes were acquired using a PerkinElmer L-0100 spectrometer with a diamond ATR module.

NMR Spectra

^{1}H, ^{13}C, ^{19}F and ^{31}P nuclear magnetic resonance (NMR) spectra were recorded on Bruker AVANCE III spectrometers operating at 400 MHz and 300 MHz frequencies, depending on the nuclei under investigation, using deuterated solvents as the medium. All chemical shifts (δ)

are reported in parts per million (ppm). For ^{1}H NMR spectra, chemical shifts were referenced against tetramethylsilane (TMS, $\delta = 0.00$ ppm) as an external standard, with residual solvent resonances employed as internal standards (for $CDCl_3$: $\delta_H = 7.26$ ppm). The ^{1}H NMR data are systematically described in the following format: chemical shift (δ), multiplicity, coupling constant(s) (J, in Hz), and signal integration. The multiplicities are denoted as: s = singlet, d = doublet, dd = doublet of doublets, t = triplet, q = quartet, m = multiplet, and br = broad signal. For ^{13}C NMR spectra, chemical shifts are also reported relative to TMS ($\delta = 0.00$ ppm), with the central resonance of the deuterated solvent used as the internal reference (for $CDCl_3$: $\delta_C = 77.16$ ppm). ^{19}F and ^{31}P NMR spectra were similarly referenced relative to their respective standards, and chemical shifts are expressed in ppm.

Electronic Spectra

Electronic absorption spectra were recorded using a Perkin-Elmer LAMBDA EZ-301 and a Shimadzu UV-1800 UV–Vis spectrophotometer, covering the wavelength range of 190-1100 nm. All measurements were carried out in a matched pair of quartz cuvettes with a path length of 1 cm.

Mass spectrometric data

Mass spectrometric analyses were performed on a Micromass Quadrupole Time-of-Flight (Q-TOF) micro mass spectrometer equipped with an electrospray ionization (ESI) source. High-resolution mass spectra (HRMS) were acquired on the same instrument, operating at a resolution of 5,000-7,000 (FWHM). Polyethylene glycol (PEG) was employed as an internal reference standard for accurate mass calibration.

Electrochemical Measurements

Cyclic voltammetry (CV) measurements were carried out on a BASi Epsilon-EC electrochemical workstation at a controlled temperature of 298 K. All experiments involving

the ligands and their corresponding metal complexes were performed in dry, degassed dichloromethane/acetonitrile mixtures (1:9 v/v), employing 0.2 M tetrabutylammonium hexafluorophosphate (TBAP) as the supporting electrolyte. A conventional three-electrode configuration was used, comprising a platinum disc working electrode, a platinum wire auxiliary electrode and a saturated Ag/AgCl electrode as the reference. Prior to each measurement, the electrolyte solutions were rigorously degassed by purging with high-purity argon gas to remove dissolved oxygen and traces of moisture. All electrochemical potentials are reported with respect to the Ag/AgCl reference electrode, unless stated otherwise.

X-Ray Crystallographic studies

Single-crystal X-ray diffraction (SCXRD) data were collected on a Bruker D8 QUEST diffractometer equipped with a Mo Kα radiation source (λ = 0.71073 Å), operated at 50 kV and 1 mA. A suitable single crystal was carefully mounted on a loop, and data acquisition was performed at a controlled temperature of 273(2) K. Data collection, indexing, integration, scaling, and absorption corrections were carried out using the standard Bruker software suite. The crystal structures were solved using the ShelXT program *via* intrinsic phasing methods,[40,41] and subsequently refined by full-matrix least-squares minimization on F^2 with ShelXL,[42] implemented within the Olex2[43] graphical user interface. All non-hydrogen atoms were located from successive Fourier difference maps and refined with anisotropic displacement parameters, whereas hydrogen atoms were introduced at calculated positions and refined using a riding model with isotropic displacement parameters. Comprehensive crystallographic refinement details are provided in the corresponding CIF files. The crystallographic data have been deposited with the Cambridge Crystallographic Data Centre (CCDC) and are available free of charge at www.ccdc.cam.ac.uk/data_request/cif

Computational Studies

All computational investigations were carried out using the Gaussian 09 software package.[44] Geometry optimizations of the ligands and their corresponding transition metal complexes were initiated from the experimentally determined crystallographic coordinates, with no simplification of the ligand framework. The optimizations were performed at the (R/U)B3LYP level of density functional theory (DFT) in the solution phase, employing an implicit solvent model.[45] The optimized molecular geometries exhibited overall good agreement with the solid-state crystallographic data, with minor deviations attributed to lattice effects present in the crystal environment. To verify the reliability of the optimized geometries, vibrational frequency analyses were conducted. All stationary points were confirmed to be true minima on the potential energy surface, as evidenced by the absence of imaginary frequencies ($N_{Imag} = 0$). On the basis of the optimized structures, electronic absorption and emission spectra in dichloromethane (CH_2Cl_2) were computed using time-dependent density functional theory (TD-DFT).[46] Solvent effects were incorporated through the conductor-like polarizable continuum model (CPCM).[47] TD-DFT is widely regarded as a reliable method for predicting electronic excitation energies of transition metal complexes,[48] thereby providing valuable insight into their photophysical properties. To further elucidate the nature of the electronic transitions, natural transition orbital (NTO) analyses were carried out using the transition density matrices obtained from TD-DFT calculations.[49] This approach affords a compact and intuitive representation of excited states in terms of single-particle “hole” (occupied) and “electron” (unoccupied) orbitals, enabling a clear interpretation of the dominant orbital contributions to each excitation. For all calculations, the ruthenium centers were modelled using the LANL2DZ[50] effective core potential with a double-ζ basis set, while a 6-311+G(d,p) basis set was applied to all other non-hydrogen atoms. Hydrogen atoms were described using a 6-311G basis set.[51] Frontier molecular orbital (FMO) energy diagrams and electronic density

plots were generated with GaussView 6.0, and the contributions of individual atoms or ligand fragments to the molecular orbitals were analyzed using the GaussSum 3.0 program.[52]

1.6 References

[1] (a) H. Grützmacher, *Angew. Chem., Int. Ed.*, **2008**, *47*, 1814−1818. (b) J. I. van der Vlugt, J. N. H. Reek, *Angew. Chem., Int. Ed.*, **2009**, *48*, 8832−8846. (c) P. J. Chirik, K. Wieghardt, *Science*, **2010**, *327*, 794−795. (d) V. Lyaskovskyy, B. de Bruin, *ACS Catal.*, **2012**, *2*, 270−279.

[2] C. K. Jørgensen, *Coord. Chem. Rev.*, **1966**, *1*, 164−178. (b) P. J. Chirik, *Inorg. Chem.*, **2011**, *50*, 9737−9740.

[3] (a) R. Eisenberg, H. B. Gray, *Inorg. Chem.*, **2011**, *50*, 9741–9751. (b) O. R. Luca, R. H. Crabtree, *Chem. Soc. Rev.*, **2013**, *42*, 1440−1459. (c) D. L. J. Broere, R. Plessius, J. I. van der Vlugt, *Chem. Soc. Rev.*, **2015**, *44*, 6886−6915.

[4] (a) S. B. Harkins, N. P. Mankad, A. J. M. Miller, R. K. Szilagyi, J. C. Peters, *J. Am. Chem. Soc.*, **2008**, *130*, 3478−3485. (b) D. Adhikari, S. Mossin, F. Basuli, J. C. Huffman, R. K. Szilagyi, K. Meyer, D. J. Mindiola, *J. Am. Chem. Soc.*, **2008**, *130*, 3676−3682. (c) D. Wang, S. V. Lindeman, A. T. Fiedler, *Inorg. Chem.*, **2015**, *54*, 8744−8754.

[5] A. Vlcek, *Coord. Chem. Rev.*, **2010**, *254*, 1357.

[6] (a) D. de Bellefeuille, M. Orio, A.- L. Barra, A. Aukauloo, Y. Journaux, C. Philouze, X. Ottenwaelder, F. Thomas, *Inorg. Chem.*, **2015**, *54*, 9013−9026. (b) R. M. Clarke, K. Hazin, J. R. Thompson, D. Savard, K. E. Prosser, T. Storr, *Inorg. Chem.*, **2016**, *55*, 762−774.

[7] (a) R. Gautam, T. M. Chang, A. V. Astashkin, K. M. Lincoln, E. Tomat, *Chem. Commun.*, **2016**, *52*, 6585−6588. (b) J. R. Pankhurst, N. L. Bell, M. Zegke, L. N. Platts, C. A. Lamfsus, L. Maron, L. S. Natrajan, S. Sproules, P. L. Arnold, J. B. Love, *Chem. Sci.*, **2017**, *8*, 108−116.

[8] (a) T. W. Myers, L. A. Berben, *Inorg. Chem.*, **2012**, *51*, 1480−1488. (b) V. A. Williams, E. B. Hulley, P. T. Wolczanski, K. M. Lancaster, E. B. Lobkovsky, *Chem. Sci.*, **2013**, *4*, 3636−3648. (c) P. J. Chirik, *Acc. Chem. Res.*, **2015**, *48*, 1687−1695.

[9] (a) D. Sieh, M. Schlimm, L. Andernach, F. Angersbach, S. Nückel, J. Schoffel, N. Susnjar, P. Burger, *Eur. J. Inorg. Chem.*, **2012**, *2012*, 444−462. (b) C. Romelt, T. Weyhermuller, K. Wieghardt, *Coord. Chem. Rev.*, **2019**, *380*, 287−317.

[10] (a) C. G. Pierpont, *Inorg. Chem.*, **2011***, 50,* 9766−9772. (b) S. Bera, S. Mondal, S. Maity, T. Weyhermüller, P. Ghosh, *Inorg. Chem.*, **2016**, *55*, 4746−4756.

[11] (a) A. Mandal, B. Schwederski, J. Fiedler, W. Kaim, G. K. Lahiri, *Inorg. Chem.*, **2015**, *54*, 8126−8135. (b) J. B. Gilroy, E. Otten, *Chem. Soc. Rev.*, **2020**, *49*, 85−113.

[12] (b) J. H. Dawson, *Science*, **1988**, *240*, 433–439. (c) E. I. Solomon, P. Chen, M. Metz, S. -K. Lee, A. E. Palmer, *Angew. Chem. Int. Edn Engl.*, **2001**, *40*, 4570–4590. (a) L. Que, W.B. Tolman, *Nature*, **2008**, *455*, 333–340.

[13] (a) Hydrogen as a Fuel: Learning from Nature; R. Cammack, M. Frey, R. Robson, Eds.; Taylor & Francis: London, **2001**. (b) R. Robson, In Hydrogen as a Fuel: Learning from Nature; R. Cammack, M. Frey, R. Robson, Eds.; Taylor & Francis: London, **2001**. (c) P. M. Vignais, B. Billoud, J. Meyer, *FEMS Microbiol. Rev.*, **2001**, *25*, 455−501. (d) P. M. Vignais, B. Billoud, *Chem. Rev.*, **2007**, *107*, 4206−4272. (e) W. Lubitz, H. Ogata, O. Rü diger, E. Reijerse, *Chem. Rev.*, **2014**, *114*, 4081−4148.

[14] (a) P. F. Knowles, R. D. Brown III, S. H. Koenig, S. Wang, R. A. Scott, M. A. McGuirl, D. E. Brown, D. M. Dooley, *Inorg. Chem.*, **1995**, *34*, 3895-3902. (b) M. M. Whittaker, W. R. Duncan, J. W. Whittaker, *Inorg. Chem.*, **1996**, *35*, 382−386. (c) S. Itoh, M. Taki, S. Fukuzumi, *Coord. Chem. Rev.*, **2000**, *198*, 3–20.

[15] (a) I. G. Denisov, T. M. Makris, S. G. Sligar, I. Schlichting, *Chem. Rev.*, **2005**, *105*, 2253−2277. (b) J. Rittle, M. T. Green, *Science*, **2010**, *330*, 933−937. (c) S. Yoshikawa, A. Shimada, *Chem. Rev.*, **2015**, *115*, 1936−1989.

[16] (a) A. W. Marsman, E. D. Leussink, J. W. Zwikker, L. W. Jenneskens, W. J. J. Smeets, N. Veldman, A. L. Spek, *Chem. Mater.*, **1999**, *11*, 1484–1491. (b) Z. Rappoport, J. F. Liebman, The Chemistry of Hydroxylamines, Oximes and Hydroxamic Acids, **2009**, vol. 1.

[17] (a) Christer B. Aakeroy, A. S. Sinha, K. N. Epa, C. L. Spartz, J. Desper, *Chem. Commun.*, **2012**, *48*, 11289–11291. (b) C. B. Aakeroy, A. S. Sinha, *RSC Adv.*, **2013**, *3*, 8168–8171.

[18] (a) A. Chakravorty, K. C. Kalia, *Inorg. Nucl. Chem. Lett.*, **1967**, *3*, 319−321. (b) K. C. Kalia, A. Chakravorty, *Inorg. Chem.*, **1968**, *7*, 2016−2020. (c) K. C. Kalia, A. Chakravorty, *Inorg. Chem.*, **1969**, *8*, 2586−2590. (d) S. Karmakar, A. Chakravorty, *Inorg. Chem.*, **1996**, *35*, 1935–1939. (e) V. Manivannan, B. K. Dirghangi, C. K. Pal, A. Chakravorty, *Inorg. Chem.*, **1997**, *36*, 1526–1528. (f) S. Ganguly, S. Karmakar, C. K. Pal, A. Chakravorty, *Inorg. Chem.*,

1999, *38*, 5984–5987. (g) S. Ganguly, *J. Ind. Chem. Soc.*, **2004**, *81*, 327–329. (h) I. Chakraborty, B. K. Panda, J. Gangopadhyay, A. Chakravorty, *Inorg. Chem.*, **2005**, *44*, 1054–1060. (i) S. Ganguly, S. Mukherjee, *J. Ind. Chem. Soc.*, **2005**, *82*, 898–902. (j) S. Dinda, S. Pramanik, J. Basu, S. C. Patra, K. Pramanik, S. Ganguly, *Dalton Trans.*, **2022**, *51*, 10121–10135. (k) S. Naskar, S. Halder, G. Kanrar, D. Jana, S. Dinda, K. Pramanik, S. Ganguly, *Polyhedron*, **2023**, *235*, 116342.

[19] E. Bamberger, W. Pemsel, *Ber.*, **1903**, *36*, 85−89.

[20] (a) M. Eich, J. H. Wendorff, B. Reck, H. Ringsdorf, *Makromol. Chem. Rapid Commun.*, **1987**, *8*, 59−63. (b) U. Wiesner, M. Antonietti, C. Boeffel, H. W. Spiess, *Makromol. Chem.*, **1990**, *191*, 2133−2149. (c) A. Natansohn, P. Rochon, J. Gosselin, S. Xie, *Macromolecules*, **1992**, *25*, 2268−2273. (d) S. Hvilsted, F. Andruzzi, P. S. Ramanujam, *Optics Lett.*, **1992**, *17*, 1234. (e) S. Hvilsted, F. Andruzzi, C. Kulinna, H. W. Siesler, P. S. Ramanujam, *Macromolecules*, **1995**, *28*, 2172−2183. (f) R. H. Berg, S. Hvilsted, P. S. Ramanujam, Nature, **1996**, *383*, 505− 508. (g) R. Hildebrandt, M. Hegelich, H. -M. Keller, G. Marowsky, S. Hvilsted, N. C. R. Holme, P. S. Ramanujam, *Phys. ReV. Lett.*, **1998**, *81*, 5548. (h) C. Kulinna, S. Hvilsted, C. Hendann, H. W. Siesler, P. S. Ramanujam, *Macromolecules*, **1998**, *31*, 2141. (i) A. Natansohn (Ed.), Azobenzene-Containing Materials, Wiley-VCH, Weinheim, **1999**. (j) L. Andruzzi, A. Altomare, F. Ciardelli, R. Solaro, S. Hvilsted, P. S. Ramanujam, *Macromolecules*, **1999**, *32*, 448. (k) P. -O. Astrand, P.S. Ramanujam, S. Hvilsted, K.L. Bak, S.P.A. Sauer, *J. Am. Chem. Soc.*, **2000**, *122*, 3482−3487. (l) K. Harada, M. Itoh, T. Yatagai, S. Kamemaru, *Opt. Rev.*, **2005**, *12*, 130–134. (m) H. M. D. Bandara, S. C. Burdette, *Chem. Soc. Rev.*, **2012**, *41*, 1809–1825. (n) S. Fu, Y. Zhao, *Macromolecules*, **2015**, *48*, 5088–5098. (o) Y. -B. Wei, Q. Tang, C. -B. Gong, M. H. -W. Lam, *Anal. Chim. Acta*, **2015**, *900*, 10–20.

[21] (a) S. Pal, D. Bandyopadhyay, D. Datta, A. Chakravorty, *J. Chem. Soc., Dalton Trans.*, **1985**, 159–162. (b) B. K. Ghosh, R. Mukherjee, A. Chakravorty, *Inorg. Chem.*, **1987**, *26*, 1946–1950. (c) S. Karmakar, S. B. Choudhury, A. Chakravorty, *Inorg. Chem.*, **1994**, *33*, 6148–6153. (d S. Karmakar, A. Chakravorty, *Inorg. Chem.*, **1996**, *35*, 1935–1939. (e) K. Pramanik, S. Karmakar, S. B. Choudhury, A. Chakravorty, *Inorg. Chem.*, **1997**, *36*, 3562–3564. (f) V. Manivannan, B. K. Dirghangi, C. K. Pal, A. Chakravorty, *Inorg. Chem.*, **1997**, *36*, 1526–1528. (g) S. Ganguly, S. Karmakar, C. K. Pal, A. Chakravorty, *Inorg. Chem.*, **1999**, *38*, 5984–5987. (h) W. Kaim, *Coord. Chem. Rev.*, **2001**, *219*, 463–488. (i) S. Pramanik, S. Roy, T. Ghorui, S.

Ganguly, K. Pramanik, *Dalton Trans.*, **2014**, *43*, 5317–5334. (j) S. Pramanik, S. Roy, T. Ghorui, S. Ganguly, K. Pramanik, *Inorg. Chem.*, **2016**, *55*, 1461−1468.

[22] (a) B. Sarkar, S. Patra, J. Fiedler, R. B. Sunoj, D. Janardanan, S. K. Mobin, M. Niemeyer, G. K. Lahiri, *Angew. Chem. Int. Ed.*, **2005**, *44*, 5655–5658. (b) B. Sarkar, S. Patra, J. Fiedler, R. B. Sunoj, D. Janardanan, G. K. Lahiri, W. Kaim, *J. Am. Chem. Soc.*, **2008**, *130*, 3532–3542. (c) M. Chakraborty, D. Sengupta, T. Saha, S. Goswami, *J. Org. Chem.*, **2018**, *83*, 7771–7778. (d) S. Chandra, O. Kelm, U. Albold, A. S. Hazari, D. Urankar, J. Košmrlj, B. Sarkar, *Organometallics*, **2021**, *40*, 3907–3916.

[23] (a) F. F. Khan, J. Klein, J. Priego, B. Sarkar, R. Jimenez-Aparicio, G.K. Lahiri, *Inorg. Chem.*, **2018**, *57*, 12800–12810. (b) A. Singh, S. Panda, S. Dey, G. K. Lahiri, *Angew. Chem. Int. Ed.*, **2021**, *60*, 11206–11210. (c) S. Panda, A. Singh, S. Dey, K. -W. Huang, G. K. Lahiri, *Dalton Trans.*, **2022**, *51*, 2547–2559.

[24] (a) H. -C. Liang, C. X. Zhang, M. J. Henson, R. D. Sommer, K. R. Hatwell, S. Kaderli, A. D. Zuberbühler, A. L. Rheingold, E. I. Solomon, K. D. Karlin, *J. Am. Chem. Soc.*, **2002**, *124*, 4170–4171. (b) C. Würtele, E. Gaoutchenova, K. Harms, M.C. Holthausen, J. Sundermeyer, S. Schin dle, *Angew. Chem. Int. Ed.*, **2006**, *45* 3867–3869. (c) C. Würtele, O. Sander, V. Lutz, T. Waitz, F. Tuczek, S. Schindler, J. Am. Chem. Soc. **2009**, *131*, 7544–7545. (d) C. E. Elwell, N. L. Gagnon, B. D. Neisen, D. Dhar, A. D. Spaeth, G. M. Yee, W. B. Tolman, *Chem. Rev.*, **2017**, *117*, 2059–2107. (e) S. Panda, S. K. Bera, P. Goel, A. K. Dutta, G. K. Lahiri, *Inorg. Chem.*, **2019**, *58*, 11458–11469. (f) A. Brinkmeier, R.A. Schulz, M. Buchhorn, C. -J. Spyra, S. Dechert, S. Demeshko, V. Krewald, F. Meyer, *J. Am. Chem. Soc.*, **2021**, *143*, 10361–10366.

[25] (a) X. Dai, P. Kapoor, T. H. Warren, *J. Am. Chem. Soc.*, **2004**, *126*, 4798–4799. (b) N. C. Tomson, L. A. Labios, T. Weyhermüller, J. S. Figueroa, K. Wieghardt, *Inorg. Chem.*, **2011**, *50*, 5763–5776. (c) S. Kundu, S. C. E. Stieber, M. G. Ferrier, S. A. Kozimor, J. A. Bertke, T. H. Warren, *Angew. Chem. Int. Ed.*, **2016**, *55*, 10321–10325. (d) S. Xu, D. Yang, B. Wang, Y. Chen, S. Ye, J. Qu, *J. Am. Chem. Soc.*, **2021**, *143*, 17374–17387.

[26] (a) W.B. Tollman, *Activation of small molecules: Organometallic and bioinorganic perspectives*, Wiley-VCH (**2006**). (b) Y. Nishibayashi, *Transition metal-dinitrogen complexes: Preparation and reactivity*, Wiley-VCH (**2019**). (c) M. J. Chalkley, M. W. Drover, J. C. Peters, *Chem. Rev.*, **2020**, *120*, 5582–5636.

[27] (a) I. E. Marko, P. R. Giles, M. Tsukazaki, S. M. Brown, C. J. Urch, *Science*, **1996**, *274*, 2044–2046. (b) L. Que Jr, W. B. Tolman, *Nature*, **2008**, *445*, 333–340. (c) S. D. McCann, S. S. Stahl, *J. Am. Chem. Soc.*, 2016, *138*, 199–206. (d) H. Li, M. B. Hall, *J. Am. Chem. Soc.*, **2015**, *137*, 12330−12342. (e) K. Kawakita, E. P. Beaumier, Y. Kakiuchi, H. Tsurugi, I.A. Tonks, K. Mashima, *J. Am. Chem. Soc.*, **2019**, *141*, 4194–4198.

[28] (a) T. E. Müller, K. C. Hultzsch, M. Yus, F. Foubelo, M. Tada, *Chem. Rev.*, **2008**, *108*, 3795–3892. (b) A. D. Schofield, A. Nova, J. D. Selby, C. D. Manley, A. D. Schwarz, E. Clot, P. Mountford, *J. Am. Chem. Soc.*, **2010**, *132*, 10484–10497. (c) P. A. Zhizhko, A. A. Zhizhin, O. A. Belyakova, Y. V. Zubavichus, Y. G. Kolyagin, D. N. Zarubin, N. A. Ustynyuk, *Organometallics*, **2013**, 32, 3611–3617. (d) B. M. Kriegel, R. G. Bergman, J. Arnold, *J. Am. Chem. Soc.*, **2016**, *138*, 52–55. (e) H. -C. Chiu, X. Y. See, I. A. Tonks, *ACS Catal.*, **2019**, *9*, 216–223. (f) A. R. Martínez, L. P. Morales, E. D. Ojeda, M. C. Rodríguez, I. Rodríguez-García, *J. Org. Chem.*, **2021**, *86*, 1311–1329.

[29] (a) Y. Takashima, S. Hatanaka, M. Otsubo, M. Nakahata, T. Kakuta, A. Hashidzume, H. Yamaguchi, A. Harada, *Nat.Commun.*, **2012**, *3*, 1270. (b) S. Goswami, A. J. Matula, S. P. Rath, S. Hedström, S. Saha, M. Annamalai, D. Sengupta, A. Patra, S. Ghosh, H. Jani, S. Sarkar, M.R. Motapothula, C. A. Nijhuis, J. Martin, S. Goswami, V. S. Batista, T. Venkatesan, *Nat. Mater.*, **2017**, *16*, 1216–1224. (c) Z. -B. Wen, D. Liu, X. -Y. Li, C. -H. Zhu, R. -F. Shao, R. Visvanathan, N. A. Clark, K. -K. Yang, Y. -Z. Wang, *ACS Appl. Mater. Interfaces*, **2017**, *9*, 24947–24954. (d) H. Nie, J. L. Self, A. S. Kuenstler, R. C. Hayward, J. R. de Alaniz, *Adv. Opt. Mater.*, **2019**, *7*, 1900224.

[30] (a) D.A. Baldwin, A.B.P. Lever, R.V. Parish, *Inorg. Chem.*, **1969**, *8*, 107–115. (b) S. Panda, S. Dhara, A. Singh, S. Dey, G. K. Lahiri, *Coord. Chem. Rev.*, **2023**, *475*, 214895.

[31] (a) B. K. Ghosh, A. Chakravorty, *Coord. Chem. Rev.*, 1989, **95**, 239. (b) V. Ferreira, R. A. Krause and S. Larsen, *Inorg. Chim. Acta*, **1988**, *145*, 29–38. (c) R. A. Krause, K. Krause, *Inorg. Chem.*, **1984**, *23*, 2195–2198. (d) R. A. Krause, K. Krause, *Inorg. Chem.*, 1980, **19**, 2600–2603. (e) R. A. Krause and K. Krause, *Inorg. Chem.*, 1982, **21**, 1714–1720.

[32] (a) S. Goswami, A. R. Chakravarty, A. Chakravorty, *Inorg. Chem.*, **1981**, *20*, 2246–2250. (b) S. Goswami, A. R. Chakravarty, A. Chakravorty, *Inorg. Chem.*, **1982**, *21*, 2737–2742. (c) S. Goswami, A. R. Chakravarty, A. Chakravorty, *Inorg. Chem.*, **1983**, *22*, 602–609. (d) S. Goswami, R. N. Mukherjee, A. Chakravorty, *Inorg. Chem.*, **1983**, *22*, 2825–2832. (e) B. K. Ghosh, S. Goswami, A. Chakravorty, *Inorg. Chem.*, **1983**, *22*, 3358–3360. (f) B. K. Ghosh, A.

Mukhopadhyay, S. Goswami, S. Ray, A. Chakravorty, *Inorg. Chem.*, **1984**, *23*, 4633–4639. (g) G. K. Lahiri, S. Goswami, L. R. Falvello, A. Chakravorty, *Inorg. Chem.*, **1987**, *26*, 3365–3370. (h) A. K. Deb, P. C. Paul, S. Goswami, *J. Chem. Soc., Dalton Trans.*, **1988**, 2051–2054. (i) A. K. Deb, S. Goswami, *J. Chem. Soc., Dalton Trans.*, **1989**, 1635–1637. (j) G. K. Lahiri, S. Bhattacharya, S. Goswami, A. Chakravorty, *J. Chem. Soc.*, *Dalton Trans.*, **1990**, 561–565. (k) A. K. Deb, S. Choudhury, S. Goswami, *Polyhedron*, **1990**, *9*, 2251–2255. (l) A. K. Deb, M. Kakoti, S. Goswami, *J. Chem. Soc., Dalton Trans.*, **1991**, 3249–3251. (m) M. Kakoti, A. K. Deb, S. Goswami, *Inorg. Chem.*, **1992**, *31*, 1302–1304. (n) M. Kakoti, S. Chaudhury, A. K. Deb, S. Goswami, *Polyhedron*, **1993**, *12*, 783–789. (o) W. Kharmawphlang, S. Choudhury, A. K. Deb, S. Goswami, *Inorg. Chem.*, **1995**, *34*, 3826–3828. (p) P. Majumdar, A. K. Ghosh, L. R. Falvello, S. -M. Peng, S. Goswami, *Inorg. Chem.*, **1998**, *37*, 1651–1654. (q) P. Majumdar, S. -M. Peng, S. Goswami, *J. Chem. Soc., Dalton Trans.*, **1998**, 1569–1574. (r) S. Mandal, N. D. Paul, P. Banerjee, T. K. Mondal, S. Goswami, *Dalton Trans.*, **2010**, *39*, 2717–2726.

[33] (a) F. Hamon, F. Djedaini-Pilard, F. Barbot, C. Len, Tetrahedron **2009**, *65*, 10105–10123. (b) E. Merino, *Chem. Soc. Rev.*, **2011**, *40*, 3835–3853.

[34] (a) E. Baer, A. L. Tosoni, *J. Am. Chem. Soc.*, **1956**, 78, 2857–2858. (b) A. Corma, P. Concepción, P. Serna, *Angew. Chem. Int. Ed.*, **2007**, 46, 7266–7769. (c) N. Sakai, K. Fujii, S. Nabeshima, R. Ikeda, T. Konakahara, *Chem. Commun.*, **2010**, *46* 3173–3175. (d) L. Hu, X. Cao, L. Shi, F. Qi, Z. Guo, J. Lu, H. Gu, *Org. Lett.*, **2011**, *13*, 5640–5643. (e) Y. Zhu, Y. Shi, *Org. Lett.*, **2013**, 15, 1942–1945.

[35] (a) W. H. Nutting, R.A. Jewell, H. Rapoport, *J. Org. Chem.*, **1970**, *35*, 505–508. (b) K. Krageloh, G.H. Anderson, P.J. Stang, *J. Am. Chem. Soc.*, **1984**, *106*, 6015–6021. (c) T.K. Misra, D. Das, C. Sinha, P. Ghosh, C. K. Pal, *Inorg. Chem.*, **1998**, *37*, 1672–1678. (d) M. Barbero, I. Degani, S. Dughera, R. Fochi, P. Perracino, *Synthesis*, **1998**, 1235–1237. (e) P. K. Santra, D. Das, T. K. Misra, R. Roy, C. Sinha, S. -M. Peng, Polyhedron, **1999**, *18*, 1909–1915. (f) M. Barbero, S. Cadamuro, S. Dughera, C. Giaveno, *Eur. J. Org. Chem.*, **2006**, 4884–4890. (g) H. A. Dabbagh, A. Teimouri, A. N. Chermahini, *Dyes Pigm.*, **2007**, 73, 239–244.

[36] A. Grirrane, A. Corma, H. García, *Science*, **2008**, *322*, 1661–1664.

[37] S. Cai, H. Rong, X. Yu, X. Liu, D. Wang, W. He, Y. Li, *ACS Catal.*, **2013**, *3*, 478–486.

[38] C. Zhang, N. Jiao, *Angew. Chem. Int. Ed.*, **2010**, *122*, 6310–6313.

[39] (a) Y. Takeda, S. Okumura, S. Minakata, *Angew. Chem. Int. Ed.*, **2012**, *124*, 1–6. (b) S. Okumura, C. -H. Lin, Y. Takeda, S. Minakata, *J. Org. Chem.*, **2013**, *78*, 12090–12105.

[40] (a) G. M. Sheldrick, SADABS, Program for Area Detector Adsorption Correction, Institute for Inorganic Chemistry, University of Gőttingen, Germany, **1996**. (b) SAINT, Data Reduction and Frame Integration Program for the CCD Area-Detector System, Bruker Analytical X-ray Systems, Madison, Wisconsin, USA, 1997–2006.

[41] G. M. Sheldrick, *Acta Crystallogr., Sect. C: Struct. Chem.*, **2015**, *71*, 3–8.

[42] G. M. Sheldrick, SHELXTL, v. 6.14; Bruker AXS Inc.: Madison, WI, **2003**.

[43] O. V. Dolomanov, L. J. Bourhis, R. J. Gildea, J. A. K. Howard, H. Puschmann, *J. Appl. Crystallogr.*, **2009**, *42*, 339–341.

[44] M. J. Frisch, G. W. Trucks, H. B. Schlegel, G. E. Scuseria, M. A. Robb, J. R. Cheeseman, G. Scalmani, V. Barone, B. Mennucci, G. A. Petersson, H. Nakatsuji, M. Caricato, X. Li, H. P. Hratchian, A. F. Izmaylov, J. Bloino, G. Zheng, J. L. Sonnenberg, M. Hada, M. Ehara, K. Toyota, R. Fukuda, J. Hasegawa, M. Ishida, T. Nakajima, Y. Honda, O. Kitao, H. Nakai, T. Vreven, J. A. Montgomery, Jr., J. E. Peralta, F. Ogliaro, M. Bearpark, J. J. Heyd, E. Brothers, K. N. Kudin, V. N. Staroverov, R. Kobayashi, J. Normand, K. Raghavachari, A. Rendell, J. C. Burant, S. S. Iyengar, J. Tomasi, M. Cossi, N. Rega, J. M. Millam, M. Klene, J. E. Knox, J. B. Cross, V. Bakken, C. Adamo, J. Jaramillo, R. Gomperts, R. E. Stratmann, O. Yazyev, A. J. Austin, R. Cammi, C. Pomelli, J. W. Ochterski, R. L. Martin, K. Morokuma, V. G. Zakrzewski, G. A. Voth, P. Salvador, J. J. Dannenberg, S. Dapprich, A. D. Daniels, O. Farkas, J. B. Foresman, J. V. Ortiz, J. Cioslowski and D. J. Fox, Gaussian 09 (Revision A.01), Gaussian, Inc., Wallingford CT, **2009**.

[45] C. Lee, W. Yang, R.G. Parr, *Phys. Rev. B*, **1998**, *37*, 785−789.

[46] (a) E. K. U. Gross, W. Kohn, *Adv. Quantum Chem.*, **1990**, *21*, 255−291. (b) T. Helgaker, P. Jørgensen, *J. Chem. Phys.*, **1991**, *95*, 2595−2601. (c) K. L. Bak, P. Jørgensen, T. Helgaker, K. Rund, H. J. A. Jenson, *J. Chem. Phys.*, **1993**, *98*, 8873−8887. (d) J. Autschbach, T. Ziegler, S. J. A. Gisbergen, E. J. Baerends, *J. Chem. Phys.*, **2002**, *116*, 6930−6940.

[47] (a) V. Barone, M. Cossi, *J. Phys. Chem. A*, **1998**, *102*, 1995−2001. (b) M. Cossi, V. Barone, *J. Chem. Phys.*, **2001**, *115*, 4708−4717. (c) M. Cossi, N. Rega, G. Scalmani, V. Barone, *J. Comput. Chem.*, **2003**, *24*, 669−681.

[48] (a) X. Zhou, H. X. Zhang, Q. J. Pan, B. H. Xia, A. C. Tang, *J. Phys. Chem. A*, **2005**, *109*, 8809−8818. (b) A. Albertino, C. Garino, S. Ghiani, R. Gobetto, C. Nervi, L. Salassa, E. Rosenverg, A. Sharmin, G. Viscardi, R. Buscaino, G. Cross, M. Milanesio, *J. Organomet. Chem.*, **2007**, *692*, 1377–1391.

[49] R. L. Martin, *J. Chem. Phys.*, **2003**, *118*, 4775–4777.

[50] (a) P. J. Hay, W. R. Wadt, *J. Chem. Phys.*, **1985**, *82*, 299−310. (b) P. J. Hay, W. R. Wadt, *J. Chem. Phys.*, **1985**, *82*, 270−283.

[51] (a) J. S. Binkley, J. A. Pople, W. J. Hehre, *J. Am. Chem. Soc.*, **1980**, *102*, 939–947. (b) M. S. Gordon, J. S. Binkley, J. A. Pople, W. J. Pietro, W. J. Hehre, *J. Am. Chem. Soc.*, **1982**, *104*, 2797–2803.

[52] N. M. O'Boyle, A. L. Tenderholt, K. M. Langner, *J. Comp. Chem.*, **2008**, *29*, 839–845.

Chapter 2

Role of Ligand Disposition and Oxime…Oximato Hydrogen Bonding upon Redox Non-innocent Character of Rhodium(III) Phenyl-Azo-Oximates

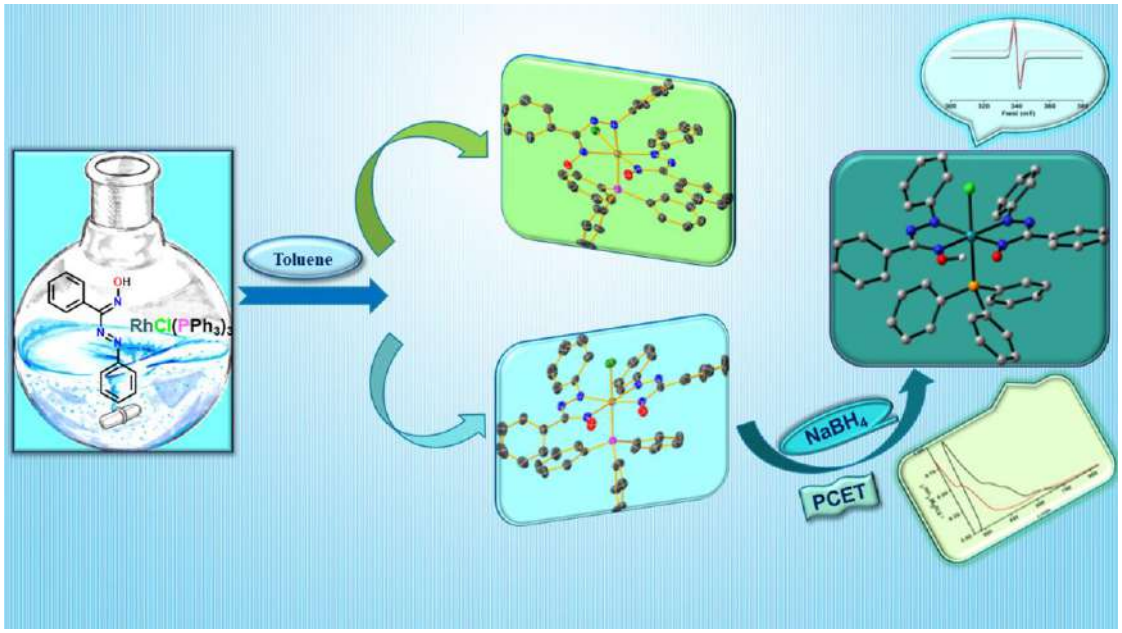

2.1 Introduction

Redox non-innocent ligands are interesting owing to their inherent capacity to exhibit various ligand redox levels upon coordination[1-23] and such systems have the aptitude to embrace and reject electron(s) during the course of catalytic processes,[24-30] in chemical and biochemical reactions.[31-33] Coordinated azo-aromatic systems have been found to act as apposite precursors for stabilizing ligand centered anion radical complexes since they possess low-lying azo-π* orbital.[34-47] It has been well understood that structure of the ligand skeleton and redox character of the metal centre has a significant role for controlling the stabilisation of these type of complexes and ligand-metal π-interaction can further adjust the electronic structural features for maximum stabilization.[48-50] Moreover, ligand environment around the metal centre may also influence the aptitude of these chelated azo-ligands in conjunction with other moieties to receive or donate odd electron(s) and this may be attributed to electronic or steric factors. The impact of electronic environment of auxiliary ligands in supporting extra electron(s) within π* LUMO of these ligands have been much less reported.[51,52] As a continuation of our study on stabilization of odd electron in coordinated azooximes,[52-54] we have tried to investigate the competence of these ligand to retain an unpaired electron over azo-oxime framework in presence of rhodium(III) and to stabilize the corresponding open shell complexes. In this regard, we have started with the diaryl-azo-oxime HL, **1** which possesses low lying π∗ LUMO, thereby having the aptitude to perform as an electron-sink upon ligation, and have successfully isolated two isomeric complexes of type *cis*-[$Rh^{III}L_2Cl(PPh_3)$] (**2a**), where Cl and PPh_3 are in *cis* positions and *trans*-[$Rh^{III}L_2Cl(PPh_3)$] (**2b**), where they are *trans* with respect to each other. The complex **2b** can be reduced to the azo-oxime radical anion complex of type *trans*-[$Rh^{III}(HL^{\bullet})(L^{-})Cl(PPh_3)$] (**3**) and the reaction appears to progress *via* PCET but the corresponding anion radical analogue of the *cis* isomer could not be isolated. Thus, the *trans* isomer behaves as a superior electron carrier and this has been attributed to stereochemical

control around the rhodium centre. In fact, in the *trans* isomer **2b**, there is scope for unpaired electron to be delocalized on both the ligands much more efficiently since they are practically coplanar (Scheme 2.1). Furthermore, the stabilization of **3** may also be attributed to formation of oxime...oximato intramolecular hydrogen bonding during the course of electron acceptance in presence of protons and this is also consistent with theoretical scrutiny.

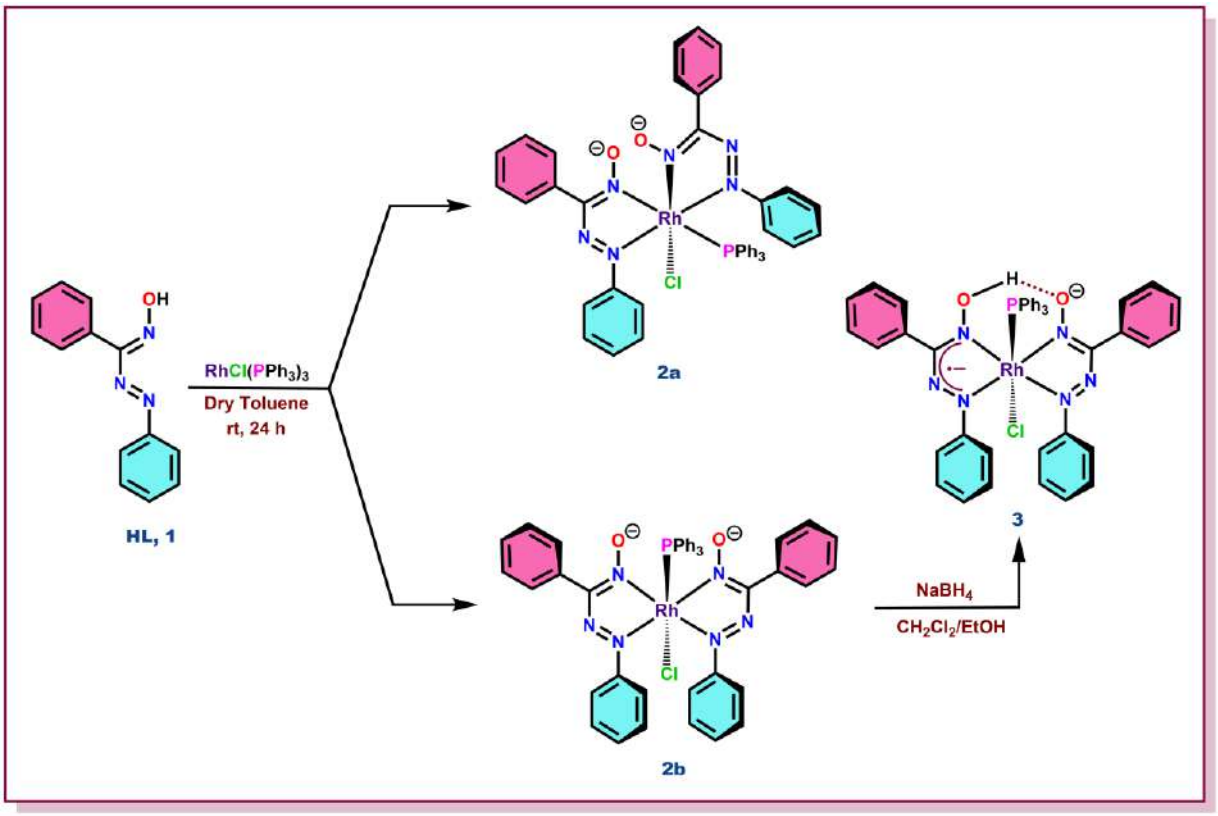

Scheme 2.1: Schematic representation of designed synthesis of *cis*-[$Rh^{III}L_2Cl(PPh_3)$] (**2a**), *trans*-[$Rh^{III}L_2Cl(PPh_3)$] (**2b**) and *trans*-[$Rh^{III}(HL^{\bullet})(L^{-})Cl(PPh_3)$] (**3**)

2.2 Results and discussion

2.2.1 Synthesis of rhodium complexes and X-ray crystal structure

The ligand utilized in this study *viz.* HL, **1** was generated by literature procedure starting from phenyl hydrazine.[56,57] It behaves as typically bidentate monoanionic and can bind to the metal centres *via* two N-donor atoms, *viz*. $N_{oximato}$ and N_{azo}. Upon stirring **1** with [$Rh^{I}Cl(PPh_3)_3$] for 24 h in molar ratio of 2:1 in anhydrous toluene as solvent, the resulting solution turned purple

red. It was then evaporated to dryness and chromatographed to isolate complexes *cis*-[$Rh^{III}L_2Cl(PPh_3)$] **2a** and *trans*-[$Rh^{III}L_2Cl(PPh_3)$] **2b** in good yields. The reaction must have progressed *via* oxidative coordination[58] and the d^6 Low Spin complexes having t_2^6 configuration are stabilized. When **2b** is treated with sodium borohydride, the colour changes from dark pink to intense blue to form the radical anion *trans*-[$Rh^{III}(HL^{\bullet})(L^{-})Cl(PPh_3)$], **3** and this reaction has possibly proceeded through a PCET[35,59-61] pathway. Probably, $NaBH_4$ provides both the electron and proton ($H^- \rightarrow H^+ + 2e$) during the progress of the reaction. The PMR of **2a** and **2b** are shown in Figure 2.6.A1 and 2.6.A4 and the $^{31}P\{1H\}$ NMR spectra authenticate the trans disposition of Cl and PPh_3 in molecules **2a** and **2b** (Figure 2.6.A3 and 2.6.A6). The structures of **2a** and **2b** were found out by SCXRD technique and they crystallized in $P\bar{1}$ and $P2_1/c$ space groups respectively. **2a** crystallized with a molecule of benzene as the solvate unlike the case of **2b**. The geometry of both complexes is distorted octahedral and their mode of ligation is bidentate *via* the softer N_{azo} and $N_{oximato}$ forming five-membered chelate rings while the anionic $O_{oximato}$ is not engaged in coordination with softer rhodium(III). In the *cis* isomer **2a**, the PPh_3 and Cl are in cis position, with P–Rh–Cl bond angle of 97.97(6)° while in the *trans* isomer **2b**, they are in trans disposition [P–Rh–Cl bond angle of 177.63(3)°]. In **2b**, the two ligand frameworks are practically in same plane. ORTEP view for **2a** as well as **2b** are represented in Figure 2.1 and 2.2 respectively with their metric parameters (selected) and details of crystallographic information are tabulated in (Table 2.1). The syn form is observed in **2b**, in spite of the fact that there is no oxime-oximato hydrogen bonding and its stability can be ascribed to robust intramolecular non-covalent face-to-face Ph_π–Ph_π stacking[62-70] amongst the two hanging phenyls of the ligands. The centroids of two phenyl moieties are separated by a distance of 3.887(18) Å in **2b** having dihedral angles 24.54 (15) ° and inter- planar separations (average), 3.345(3) Å (Table 2.3, Fig 2.3). We could not grow X-ray quality crystal of *trans*-[$Rh^{III}(HL^{\bullet})(L^{-})Cl(PPh_3)$], **3** even after repeated attempts but the geometrically optimized

structure has been reported (Figure 2.4). It has been found that the mode of coordination is alike that of **2b** but N2−N3 (azo) length over the protonated ligand framework is 1.320 Å and this is longer than that in the deprotonated ligand (N5−N6, 1.276 Å). The lengthening of azo bond in the protonated ligand moiety of **3** is a clear indicator that the odd electron must be present within this skeleton and this may be attributed to lesser electron cloud over it in comparison to the deprotonated form. The oxime-oximato O…O distance in the complex is 2.652Å, suggesting the occurrence of moderately strong oxime…oximato intramolecular hydrogen bonding.[35]

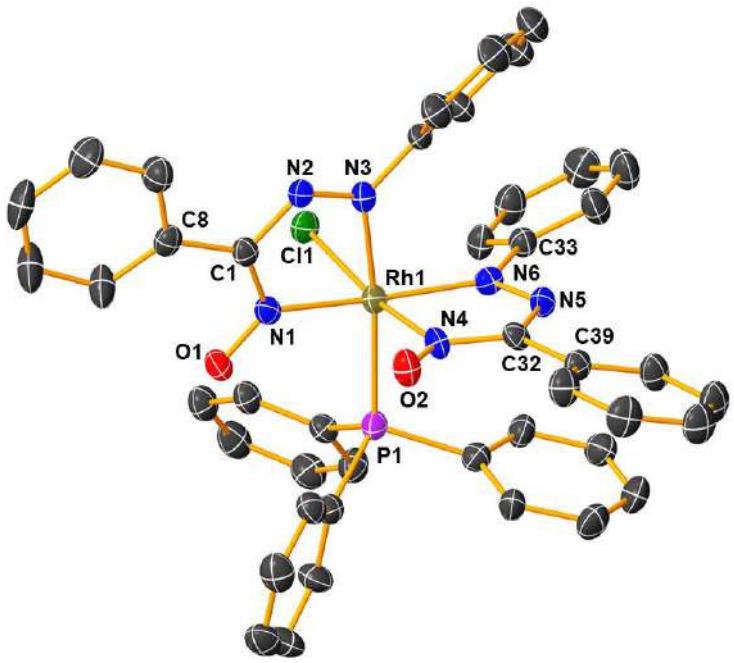

Figure 2.1: ORTEP diagram of **2a.C_6H_6** (Solvent molecule and H-atoms are discarded for simplicity and thermal ellipsoids are set at 50% probability); **CCDC No: 2215353;** Selected bond lengths (Å) and bond angles (º) Rh1–N1 1.990(5), Rh1–N3 2.073(5), Rh1–N4 2.002(5), Rh1–N6 2.060(5), Rh1–Cl1 2.380(15), Rh1–P1 2.391(17), N2–N3 1.278(6), N5–N6 1.298(6), N1–O1 1.272(5), N4–O2 1.260(5), C1–N1 1.359(7); N1–Rh1–N3 77.03(19), N4–Rh1–N6 78.16(18), N3–Rh1–Cl1 84.85(13), N6–Rh1–P1 89.69(13)

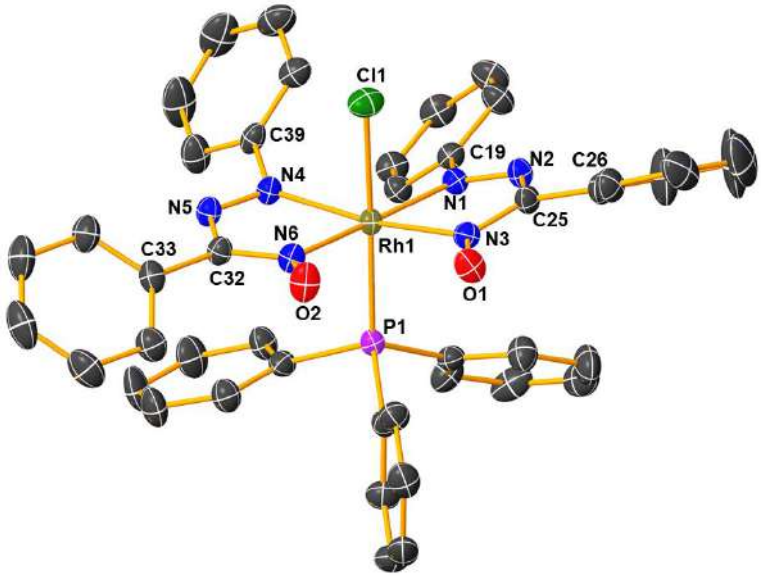

Figure 2.2: ORTEP diagram of **2b** (Solvent molecule and H-atoms are discarded for simplicity and thermal ellipsoids are set at 50% probability); **CCDC No: 2215354;** Selected bond lengths (Å) and bond angles (^{0}): Rh1–N1 2.063(2), Rh1–N3 2.036(2), Rh1–N4 2.073(2), Rh1–N6 2.031(2), Rh1–Cl1 2.358(7), Rh1–P1 2.345(7), N1–N2 1.284(3), N4–N5 1.287(3) N3–O1 1.262(3), N6–O2 1.253(3); N1–Rh1–N3 76.12(8), N4–Rh1–N6 76.51(8), N1–Rh1–Cl1 89.03(6), N1–Rh1–P1 93.27(6)

Table 2.1: Crystallographic details of complexes **2a** and **2b**

	2a.C_6H_6	**2b**
Empirical formula	$C_{50}H_{41}N_6ClO_2PRh$	C_{44} $H_{41}N_6O_2ClPRh$
T/K	298K	298K
fw	927.22	855.16
Crystal system	Triclinic	Monoclinic
Space Group	$P\bar{1}$	P 21/c
a/Å	10.4965(11)	19.4533(7)
b/*Å*	11.1525(12)	9.2318(4)
c/ *Å*	19.706(2)	21.7251(8)
α/deg	103.438(7)	90
β/deg	101.837(7)	102.584
γ/deg	95.326(7)	90
V/ $Å^3$	2171.9(4)	3807.9(3)
Z	2	4
D_c/Mgm^{-3}	1.418	1.492
μ/mm^{-1}	0.540	0.608
F(000)	952	1760
cryst size/mm^3	0.5×0.4×0.2	0.4×0.3×0.2
θ/deg	1.898- 27.702	1.072-27.536
Measured reflns	34395	63990
Unique reflns	9917	17273
[a]GOF on F^2	0.975	1.036
R1[b], wR2[c][$I>2\sigma(I)$]	0.0694, 0.1528	0.0372, 0.0875
R1, wR2	0.1997	0.0569

[a]GOF = $\{\Sigma[w(F_o{}^2-F_c{}^2)2]/(n-p)\}^{1/2}$. [b]R1 = Σ [$|F_o|-|F_c|$]/ Σ $|F_o|$.
[c]wR2 = $[\Sigma\ [w(F_o{}^2-F_c{}^2)^2]/\ \Sigma\ [w(F_o{}^2)^2]]^{1/2}$ where w = 1/[
$\sigma^2(F_o{}^2)+(aP)^2+bP]$, P = $(F_o{}^2+2F_c{}^2)/3$.

Table 2.2: Selected bond length (Å) and bond angle (º)

2a			2b			3
	Expt.	**Theo.**		**Expt.**	**Theo.**	**Theo.**
Rh1–N1	1.990(5)	2.054	Rh1–N1	2.063(2)	2.140	2.100
Rh1–N3	2.073(5)	2.104	Rh1–N3	2.036(2)	2.067	2.038
Rh1–N4	2.002(5)	2.039	Rh1–N4	2.073(2)	2.144	2.134
Rh1–N6	2.060(5)	2.125	Rh1–N6	2.031(2)	2.075	2.043
Rh1–Cll	2.380(15)	2.471	Rh1–Cl1	2.358(7)	2.464	2.425
Rh1–P1	2.391(17)	2.501	Rh1–P1	2.345(7)	2.453	2.485
N1–O1	1.272(5)	1.241	N3–O1	1.262(3)	1.236	1.261
N4–O2	1.260(5)	1.247	N6–O2	1.253(3)	1.243	1.375
N2–N3	1.278(6)	1.270	N1–N2	1.284(3)	1.273	1.276
N5–N6	1.298(6)	1.273	N4–N5	1.287(3)	1.269	1.320
N1–C1	1.359(7)	1.358	N5–C32	1.357(3)	1.357	1.345
N2–C1	1.371(7)	1.354	N4–C39	1.445(3)	1.436	1.419
N4–C32	1.349(7)	1.352	N3–C25	1.345(3)	1.356	1.343
N5–C32	1.374(7)	1.359	N1–C19	1.428(3)	1.430	1.427
N3–C2	1.412(7)	1.425	N6–C32	1.351(3)	1.351	1.329
N6–C33	1.439(7)	1.427	N2–C25	1.362(3)	1.354	1.362
N1–Rh1–N3	77.03(19)	76.40	N1–Rh1–N3	76.12(8)	75.68	74.99
N1–Rh1–N4	97.48(18)	96.66	N1–Rh1–N4	106.17(8)	108.68	111.72
N3–Rh1–N6	97.24(18)	97.19	N3–Rh1–N6	100.65(9)	99.73	97.19
N4–Rh1–N6	78.16(18)	76.64	N4–Rh1–N6	76.51(8)	75.16	74.50
N1–Rh1–Cl1	83.77(13)	83.98	N1–Rh1–Cl1	89.03(6)	87.85	87.23
N3–Rh1–Cl1	84.85(13)	86.54	N3–Rh1–Cl1	84.09(6)	84.59	84.32
N4–Rh1–Cl1	171.05(14)	171.01	N4–Rh1–Cl1	85.29(6)	85.55	86.52
N6–Rh1–Cl1	99.71(13)	101.73	N6–Rh1–Cl1	88.04(6)	88.02	89.16
N1–Rh1–P1	95.78(15)	94.73	N1–Rh1–P1	93.27(6)	94.89	94.14
N3–Rh1–P1	172.00(14)	169.65	N3–Rh1–P1	95.91(6)	92.00	92.13
N4–Rh1–P1	90.74(14)	90.93	N4–Rh1–P1	94.60(6)	97.50	96.64
N6–Rh1–P1	89.69(13)	91.03	N6–Rh1–P1	89.63(6)	88.91	89.00
Cl1–Rh1–P1	97.97(6)	97.95	Cl1–Rh1–P1	177.63(3)	174.98	175.78

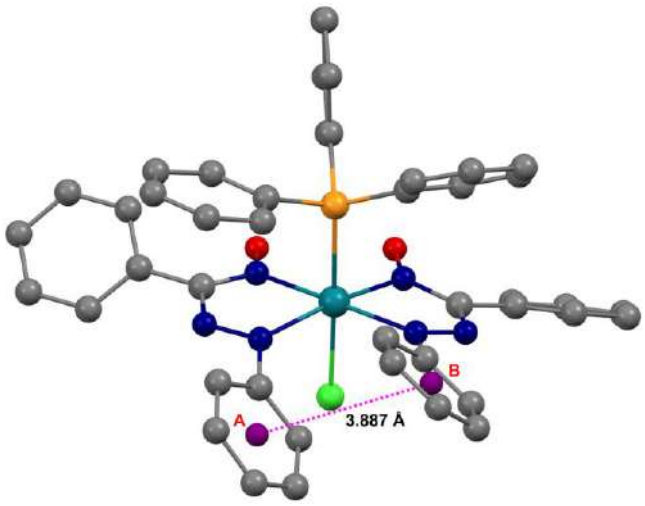

Figure 2.3: Intramolecular non-covalent **π–π** stacking interaction in **2b**

Table 2.3: Intramolecular **π- π** stacking parameter[a] for complex **2b**

Stacking parameter	Ring A–B
$d(c_i–c_j)$ Å/α°	3.887(18)/24.54(15)
$d(\perp c_i–P_j)$ Å/β°	3.345(12)/30.6
$d(\perp c_i–P_j)$ Å/γ°	3.309(13)/31.6

[a]c = ring centroid, α = dihedral angle between rings, β and γ (slip angle) = angle between the vector $c_i–c_j$ and the normal to plane P_i or P_j from c_i and c_j respectively, $d(c_i–c_j)$ = centroid-centroid distance, $d(\perp c_i–P_j)$ = ⊥ distance from c_i of P_i on ring P_i.

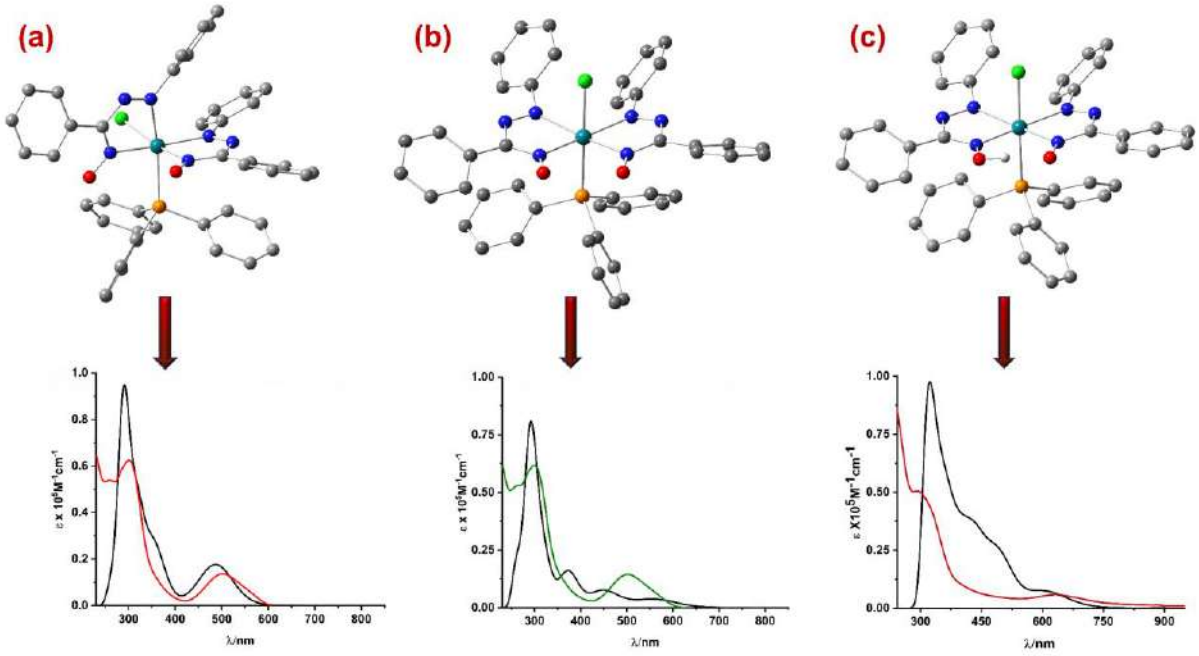

Figure 2.4: Solution phase optimized geometry of complexes (a) *cis*-[$Rh^{III}L_2Cl(PPh_3)$] **2a**, (b) *trans*-[$Rh^{III}L_2Cl(PPh_3)$] **2b** & (c) *trans*-[$Rh^{III}(HL^{\bullet})(L^{-})Cl(PPh_3)$], **3** (only oximato-H included) along with their experimental and calculated absorption spectra respectively

2.2.2 Electrochemistry and EPR spectrum

The rhodium(III) complexes **2a** and **2b** display single electron reductive couple in the region −0.22 to −0.72 V in addition to irreversible oxidative (anodic) signal in the region +1.37 to +1.52 V vs. Ag/AgCl (Table 2.4, Figure 2.4). Computational studies (*vide infra*) were carried out for **2a** and **2b** (by using their coordinates of X-ray) by optimization of their geometries in CH_2Cl_2 and concentrating on the type of FMOs, in an effort to have a knowledge about the

type of redox orbitals. It was found that reductive responses are majorly accredited to that of chelating ligands (*vide infra*) as the LUMO, LUMO+1 for these both the chelates are almost ligand-centric with appreciable involvement from the π* orbital of azo-oximato nature (Tables 2.5 and 2.6) but the rhodium centre is not redox active. The HOMO of **2a**/**2b** are of π–symmetry and is practically centred over the ligand scaffold along with significant contributions from oxime, phenyl and azo moieties. Therefore, irreversible oxidative response for both the complexes may be attributed to that of coordinated ligand.

The first reductive response of **2b** at around -0.22 V clearly suggest that the LUMO is extensively stabilized and this prompted us to explore its ability to behave as an electron sink or electron carrier to generate the single-electron reduced radical anion complex. Upon treatment of **2b** with sodium borohydride, a dark blue solution was formed, which upon rapid evaporation yielded a dark solid of composition [Rh(HL)L(PPh_3)Cl], **3**. The magnetic moment of the complex **3** (μ_{eff} = 1.91 μ_B) corresponds to one unpaired electron and it display a sharp EPR signal with band width ΔH = 3.04 mT (X-band EPR spectrum Figure 2.6) in dichloromethane solution at 298 K with g ≈ 1.996, thereby signifying the existence of a free electron. The absence of any hyperfine in the EPR signal further demonstrates that there is virtually no participation of metal to the orbital bearing the spin.[37,38,52-54] This clearly suggests that **3** must contain an odd electron and it is practically delocalized on the ligand skeleton, having no participation from metal centre. The CV of **2b** (initial cathodic scan) is nearly similar to that of **3** (anodic scan initially). **3** has been found to be stable in the solid phase in anhydrous environment, but in solution it is oxidized quickly to more stable precursor **2b**. Although, the X-ray quality single crystals of **3** could not be generated, its characterization has been performed by theoretical studies and spectral techniques. The most realistic description of **3** is *trans*-[$Rh^{III}(HL^{\bullet})(L^{-})Cl(PPh_3)$] as evident from EPR and DFT studies, with the unpaired spin delocalized over π* orbital of one of the chelated phenyl-azo-oxime. The presence of a

protonated ligand in **3** has been further substantiated from IR spectroscopy where a broad stretch at around 3450 cm^{-1} is observed (Figure 2.6.A9) and this is absent in the non-radical congener **2b**. The net spin density of **3** as portrayed in Figure 2.6, signifies that reduction is virtually ligand-centric. The electrochemical data and stability of the radical complex unambiguously indicates the redox non-innocent nature of phenyl-azo-oxime. Notably, the *cis*-isomer does not exhibit the aptitude to accept an electron, perhaps due to the fact that since the two ligands in the chelate are not coplanar.

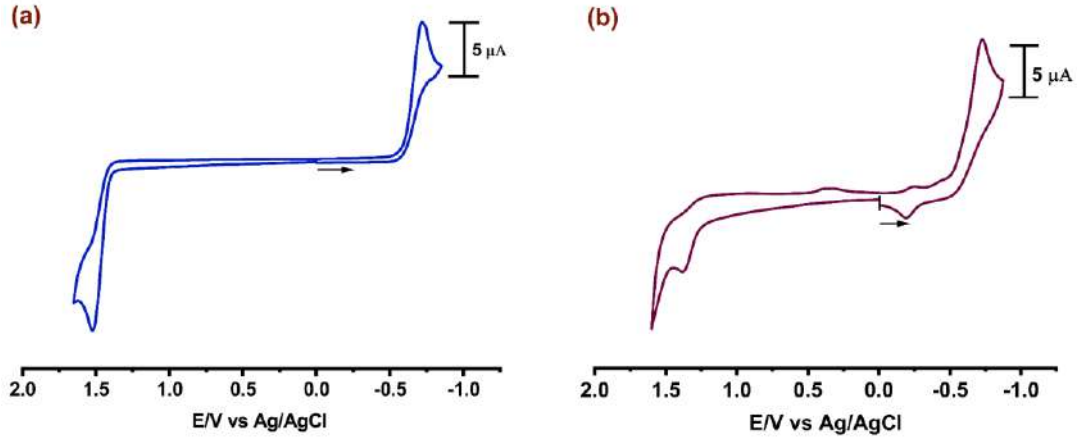

Figure 2.5: Cyclic voltammogram of **2a** (left) and **2b** (right) (scan rate: 100 mV) in CH_2Cl_2/CH_3CN (1:9 v/v) at 298K

Table 2.4: Cyclic Voltametric data for **2a, 2b** & **3** with respect to Ag/AgCl

Complex	$E_{1/2}$**/V (**ΔE**/mV)**	
	Oxidation	**Reduction**
2a	+1.52(E_{pa}/V)	–0.71(E_{pc}/V)
2b	+1.37(E_{pa}/V)	–0.22(90), –0.72(E_{pc}/V)
3	+1.32(E_{pa}/V), –0.20(90)	–0.68(E_{pc}/V)
$E_{1/2}$ = ½(E_{pa} + E_{pc}), E_{pa} = anodic peak potential; E_{pc} = cathodic peak potential, ΔE = peak-to-peak separation		

Table 2.5: Frontier Molecular Orbital Composition (%) in the Ground State for complex **2a**

Orbital	MO	Energy (eV)	Contribution (%)						Contribution
			Rh	Cl	Azo	Oxime	PPh_3	Ph	
209	L+5	-1.26	0	0	5	11	43	41	π*(Oxime + PPh_3 +Ph)
208	L+4	-1.40	1	0	7	19	8	65	π*(Oxime + Ph)
207	L+3	-2.07	50	7	11	25	3	4	d_z^2+π*(Azo + Oxime)
206	L+2	-2.51	39	6	13	12	28	3	d_z^2 + π* (Azo + Oxime + PPh_3)
205	L+1	-3.18	4	1	40	43	1	11	π* (Azo + Oxime + Ph)
204	LUMO	-3.35	5	0	40	38	1	16	π* (Azo + Oxime + Ph)
203	HOMO	-6.15	3	0	12	41	1	43	π (Azo + Oxime + Ph)
202	H–1	-6.23	4	1	9	40	1	45	π (Oxime + Ph)
201	H–2	-6.75	3	7	10	49	20	10	π (Azo + Oxime + PPh_3 + Ph)
200	H–3	-6.95	7	29	7	22	21	14	π (Cl + Oxime + PPh_3 + Ph)
199	H–4	-7.05	5	18	3	3	62	9	π (Cl + PPh_3)
198	H–5	-7.13	9	47	2	12	11	19	π (Cl + Oxime + PPh_3 + Ph)

Table 2.6: Frontier Molecular Orbital Composition (%) in the ground state for complex **2b**

Orbital	MO	Energy (eV)	Contribution (%)						Contribution
			Rh	Cl	Azo	Oxime	PPh_3	Ph	
209	L+5	-1.35	1	0	0	0	95	4	π* (Oxime + PPh_3 + Ph)
208	L+4	-1.39	0	0	2	2	90	6	π* (Oxime + Ph)
207	L+3	-1.89	48	0	16	26	1	9	d_z^2 + π* (Azo + Oxime)
206	L+2	-2.77	41	13	4	9	31	2	d_z^2 + π* (Cl+PPh_3)
205	L+1	-2.93	6	0	41	41	1	11	π* (Azo + Oxime + Ph)
204	LUMO	-3.33	2	3	41	42	1	11	π* (Azo + Oxime + Ph)
203	HOMO	-6.06	4	0	11	43	1	41	π (Azo + Oxime + Ph)
202	H–1	-6.23	1	0	13	43	1	42	π (Azo + Oxime + Ph)
201	H–2	-6.75	1	5	16	67	1	10	π (Azo + Oxime + Ph)
200	H–3	-7.00	1	8	9	27	1	54	π (Oxime + Ph)
199	H–4	-7.14	5	5	3	5	25	58	π (PPh_3 + Ph)
198	H–5	-7.19	3	2	1	1	24	69	π (PPh_3 + Ph)

Table 2.7: Frontier **α**-Molecular Orbital Composition (%) in the ground state for complex **3**

Orbital	α-MO	Energy (eV)	Contribution (%)						Contribution
			Rh	Cl	Azo	Oxime	PPh_3	Ph	
210	L+5	-1.25	2	0	1	3	89	5	π*(PPh_3)
209	L+4	-1.36	8	0	3	4	82	4	π*(PPh_3)
208	L+3	-1.45	3	0	1	0	93	3	π*(PPh_3)
207	L+2	-1.47	40	0	14	19	20	8	$d_{x^2-z^2}$ + π*(Azo + Oxime + PPh_3)
206	L+1	-2.46	38	18	5	8	32	1	d_z^2 + π* (Cl + PPh_3)
205	LUMO	-3.06	7	1	41	36	1	15	π*(Azo + Oxime + Ph)

204	HOMO	-4.52	2	2	46	29	2	19	π (Azo + Oxime + Ph)
203	H–1	6.02	5	1	9	41	1	43	π (Azo + Oxime + Ph)
202	H–2	-6.33	6	9	7	30	1	45	π (Azo + Oxime + Ph)
201	H–3	-6.54	4	48	13	14	0	22	π (Cl + Azo + Oxime + Ph)
200	H–4	-6.65	9	74	5	3	1	9	d_{xz} + π (Cl + Ph)
199	H–5	-6.78	0	1	4	1	0	94	π (Ph)

Table 2.8: Frontier β-Molecular Orbital Composition (%) in the ground state for complex **3**

Orbital	β-MO	Energy (eV)	Contribution (%)						Contribution
			Rh	Cl	Azo	Oxime	PPh_3	Ph	
209	L+5	-1.34	17	0	6	8	64	6	$d_{x^2-z^2}$ + π*(Azo + Oxime + PPh_3)
208	L+4	-1.42	31	0	12	15	36	6	$d_{x^2-z^2}$ + π*(Azo + Oxime + PPh_3)
207	L+3	-1.45	1	0	0	0	97	3	π*(PPh_3)
206	L+2	-2.33	7	3	38	32	2	18	π*(Azo + Oxime + Ph)
205	L+1	-2.45	34	15	7	10	31	3	d_{z^2} + π* (Cl + Oxime + PPh_3)
204	LUMO	-3.07	3	1	42	38	2	15	π*(Azo + Oxime + Ph)
203	HOMO	-5.82	6	1	14	41	1	38	π (Azo + Oxime + Ph)
202	H–1	-6.05	1	1	10	42	1	46	π (Azo + Oxime + Ph)
201	H–2	-6.45	2	41	16	15	0	26	π (Cl + Azo + Oxime + Ph)
200	H–3	-6.62	11	66	5	1	1	17	d_{xz} + π (Cl + Ph)
199	H–4	-6.69	1	16	7	1	1	74	π (Cl + Ph)
198	H–5	-6.74	3	19	3	0	1	74	π (Cl + Ph)

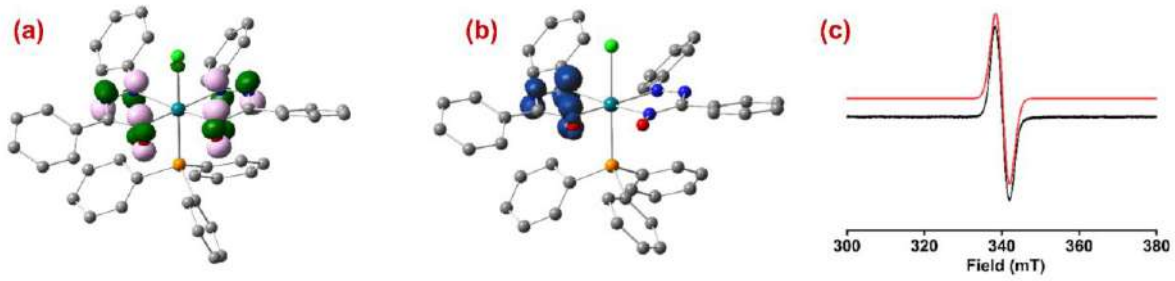

Figure 2.6: (a) LUMO of **2b** (b) Spin Density in **3** (c) EPR spectrum (X-band) of **3** in CH_2Cl_2 at 298 K: Simulated (red), Experimental (black)

2.2.3 Absorption spectra

All complexes exhibit multiple absorption bands in their respective UV-Vis spectrum which are attributed primarily to the CT within the phenyl-azo-oxime unit with some involvement of d-orbitals of rhodium. TD-DFT in CH_2Cl_2 was done using CPCM model to predict the nature

of the bands. (Table 2.9, 2.10 and 2.11). NTO[71] Analysis was performed to scrutinized the source of electronic transitions (Table 2.12, 2.13 and 2.14).

For Complex **2a,** electronic transition at 502 nm is computed to be around 498 nm (f = 0.1294, 2.4886 eV) and is primarily [π (oxime + azo) → π* (oxime + azo)] ILCT character. The absorption at 490 nm (2.5622 eV, f = 0.0886) is calculated at near 483 nm and can be described as primarily [π (Oxime + Ph + Azo) → π* (Oxime + Azo)] ILCT character. The 300 nm band is calculated at near 289 nm (f = 0.0963, 4.2560 eV) which again may be ascribed as [π (Oxime + Azo) → π* (Oxime + Azo)] ILCT type. The 281 nm band is calculated at 281.63 nm which can assigned as [π (Ph + PPh_3) → π* (Ph + PPh_3)] ILCT type.

Complex **2b** displays similar type of spectrum with lowest energy band at 488 nm which is assessed at near 568 nm (f = 0.0533, 2.1812 eV). This optical transition can be assigned as ILCT along with significant contribution from d-d [π (Oxime + Azo) → π* (Oxime +Azo) & $d_{x^2-y^2} \rightarrow d_{z^2}$]. The 370 nm band which is calculated at near 378 nm (f = 0.0200, 3.2775 eV) and may be attributed to ILCT type [π (Oxime + Ph + Azo) → π* (PPh_3)]. The 298 nm band at is calculated at 301 nm which is again described as ILCT [π (Azo + Oxime) → π* (Azo + Oxime)] type. The band at 256 nm is computed at 287 nm and it involves both ILCT [π (Oxime +Cl) → π* (Ph)] as well as MLCT [d_{yz}→ π* (Ph)]. The solid-state absorption spectra have been included in Figure 2.7.

The radical complex **3** exhibits transition at 636 nm which is computed near to 606 nm (2.0439 eV, f = 0.0298) with a band of lowest energy. This optical transition is allocated as mostly [π (Oxime + Azo + Ph) → π* (Oxime + Azo + Ph)] ILCT character. The band at 314 nm is evaluated at near 320 nm (3.8716 eV, f = 0.0293) can be designated as ILCT & d–d [π (Oxime + Azo) → π* (Oxime + Azo) & $d_{xy} \rightarrow d_{x^2-y^2}$]. The subtle differences in theoretical absorption

spectra of the complexes from the experimental ones may be ascribed to the restrictions of theoretical approach that we have adopted for the complicated geometry of 4d complexes.[72]

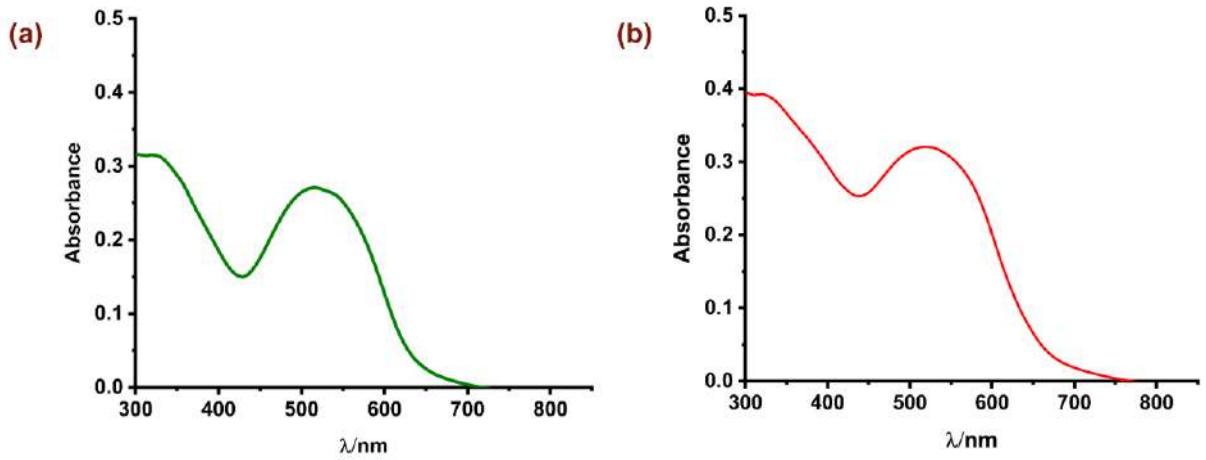

Figure 2.7: Solid state absorption of spectra of **2a** and **2b**

Table 2.9: Main Optical Transitions at the TD-DFT/B3LYP/6-311+G(d,p) Level for the complex **2a** with composition in terms of Molecular Orbital Contribution of the Transition, Computed Vertical Excitation Energies and Oscillator Strength in Dichloromethane

Transition	CI	Composition	E (eV)	Oscillator strength (*f*)	λ_{theo} (nm)
$S_0 \rightarrow S_5$	0.64152	H–1 → LUMO (82%)	2.4886	0.1294	498.20
$S_0 \rightarrow S_6$	0.61056	HOMO → L+1 (75%)	2.5622	0.0886	483.89
$S_0 \rightarrow S_{63}$	0.34215	H–1 → L+4 (23%)	4.2860	0.0963	289.28
$S_0 \rightarrow S_{70}$	0.51220	HOMO → L+6 (52%)	4.4022	0.0224	281.64

Table 2.10: Main Optical Transitions at the TD-DFT/B3LYP/6-311+g(d,p) Level for the complex **2b** with composition in terms of Molecular Orbital Contribution of the Transition, Computed Vertical Excitation Energies and Oscillator Strength in Dichloromethane

Transition	CI	Composition	Energy (eV)	Oscillator Strength (*f*)	λ_{theo} (nm)
$S_0 \rightarrow S_1$	0.66915	HOMO → LUMO (90%)	2.1812	0.0533	568.43
$S_0 \rightarrow S_{16}$	0.50763	H–5 → LUMO (52%)	3.2775	0.0200	378.29
$S_0 \rightarrow S_{55}$	0.44283	HOMO → L+4 (39%)	4.1186	0.0634	301.03
$S_0 \rightarrow S_{69}$	0.57395	H–1 → L+4 (66%)	4.3174	0.1173	287.18

Table 2.11: Main Optical Transitions at the TD-DFT/B3LYP/6-311++g(d,p) Level for the complex **3** with composition in terms of Molecular Orbital Contribution of the Transition, Computed Vertical Excitation Energies and Oscillator Strength in Dichloromethane

Transition	CI	Composition	Energy (eV)	Oscillator Strength (*f*)	λ_{theo} (nm)
$S_0 \rightarrow S_5$	0.77609	HOMO-β→LUMO-β (57%)	2.0439	0.0286	606.61
$S_0 \rightarrow S_{90}$	0.47378	H–5-β → L+2-β (22%)	3.8716	0.0293	320.24
$S_0 \rightarrow S_{98}$	0.54612	H–6-β → L+1-β (30%)	3.9480	0.0359	314.05

Table 2.12: Natural transition orbitals (NTOs) for complex **2a**, illustrating the nature of singlet excited states in the absorption bands spanning 200–900 nm. For each state, the state number, transition energy (eV), and oscillator strength (in parentheses) are provided. Only the occupied (hole) and unoccupied (electron) NTO pairs contributing more than 15% to each excited state are shown

		Hole	Electron
502 nm	S_5 w = 0.8230 2.4886 (0.1294) 498.20 nm ILCT π (Azo + Oxime) → π* (Az + Oxime)	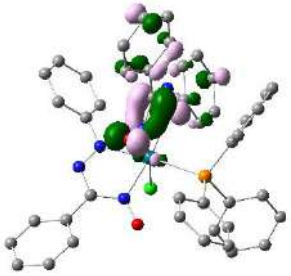	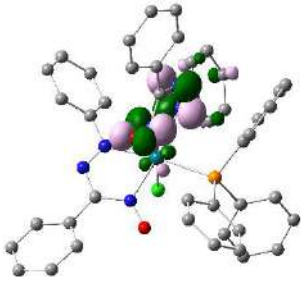
490 nm	S_6 w = 0.7455 2.5622 (0.0886) 483.89 nm ILCT π (Azo + Oxime + Ph) → π* (Azo + Oxime)	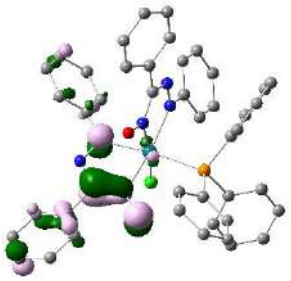	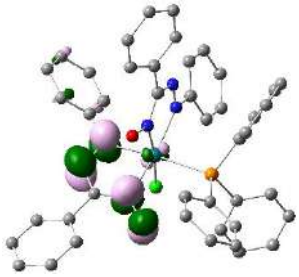
300 nm	S_{63} w = 0.2341 4.2860 (0.0963) 289.28 nm ILCT π (Azo + Oxime) → π* (Azo + Oxime)	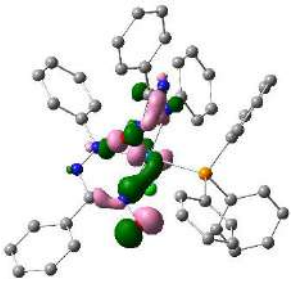	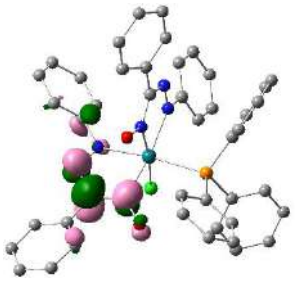
281 nm	S_{70} w = 0.5246 4.4022 (0.0221) 281.63 ILCT π (Ph + PPh_3) → π* (Ph + PPh_3)	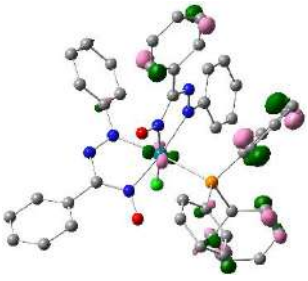	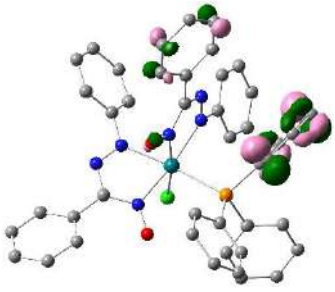

Table 2.13: Natural transition orbitals (NTOs) for complex **2b**, illustrating the nature of singlet excited states in the absorption bands spanning 200–900 nm. For each state, the state number, transition energy (eV), and oscillator strength (in parentheses) are provided. Only the occupied (hole) and unoccupied (electron) NTO pairs contributing more than 15% to each excited state are shown

		Hole	Electron
488 nm	S_7 w = 0.8955 2.1812 (0.0533) 568.43 nm ILCT & d–d π (Azo + Oxime) → π* (Azo + Oxime) & $d_{x^2-y^2} \rightarrow d_{z^2}$	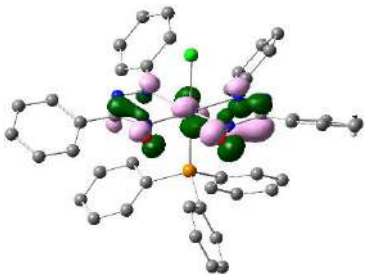	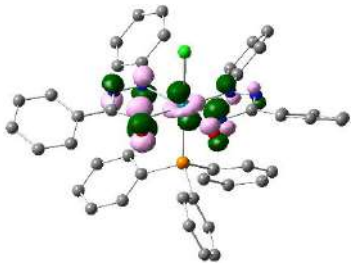
370 nm	S_{16} w = 0.5153 3.2775 (0.0200) 378.29 nm ILCT π (Azo + Oxime + Ph) → π* (PPh_3)	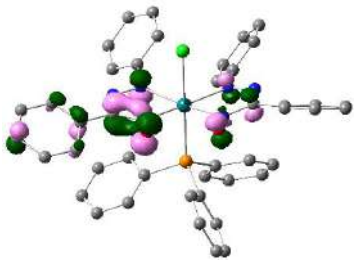	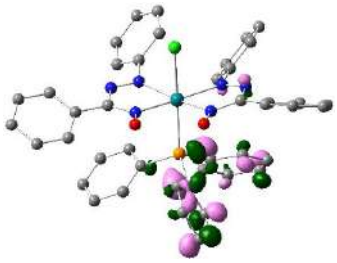
298 nm	S_{55} w = 0.3921 4.1186 (0.0634) 301.03 nm ILCT π (Azo + Oxime) → π* (Azo + Oxime)	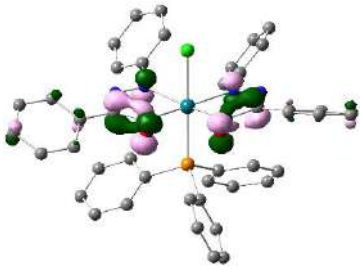	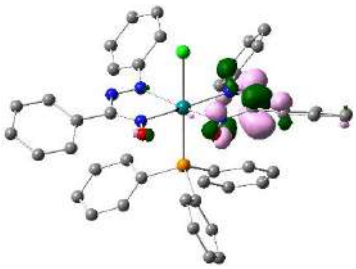
256 nm	S_{69} w = 0.6588 4.3174 (0.1173) 287.18 nm ILCT & MLCT π (Oxime +Cl) → π* (Ph) & $d_{yz} \rightarrow$ π* (Ph)	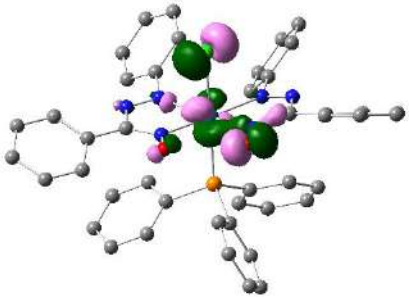	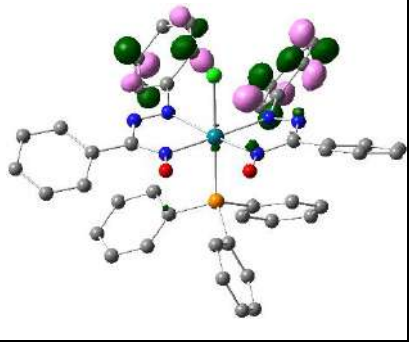

Table 2.14: Natural transition orbitals (NTOs) for complex **3**, illustrating the nature of singlet excited states in the absorption bands spanning 200–900 nm. For each state, the state number, transition energy (eV), and oscillator strength (in parentheses) are provided. Only the occupied (hole) and unoccupied (electron) NTO pairs contributing more than 15% to each excited state are shown

		Hole	Electron
636 nm	S_5 w =1.2046 2.0439 (0.0286) 606.01 nm ILCT & d–d π (Azo + Oxime + Ph) →π*(Azo + Oxime + Ph)	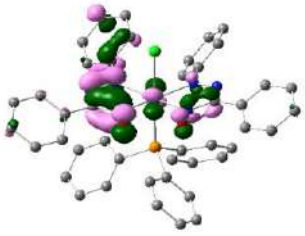	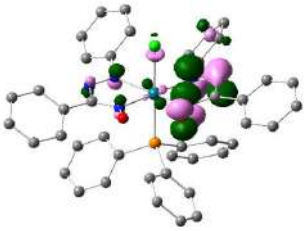
314 nm	S_{90} w = 0.4489 3.8716 (0.0293) 320.24 nm ILCT & d–d π (Azo + Oxime) → π* (Azo + Oxime) & d_{xy}→ $d_{x^2-y^2}$	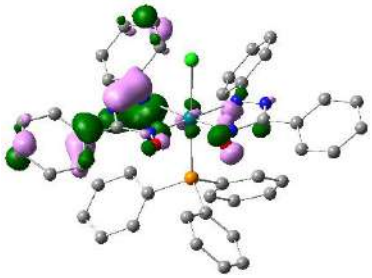	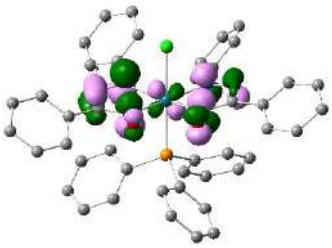
290 nm	S_{98} w =0.5964 3.9480 (0.0359) 314.05 nm ILCT π (Ph) → π*(Azo + Ph)	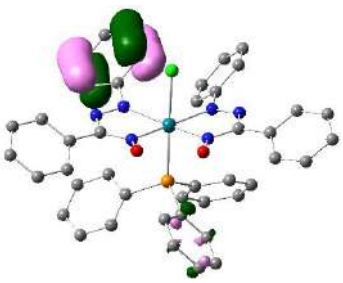	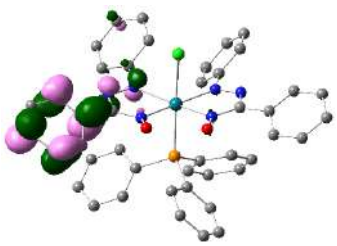

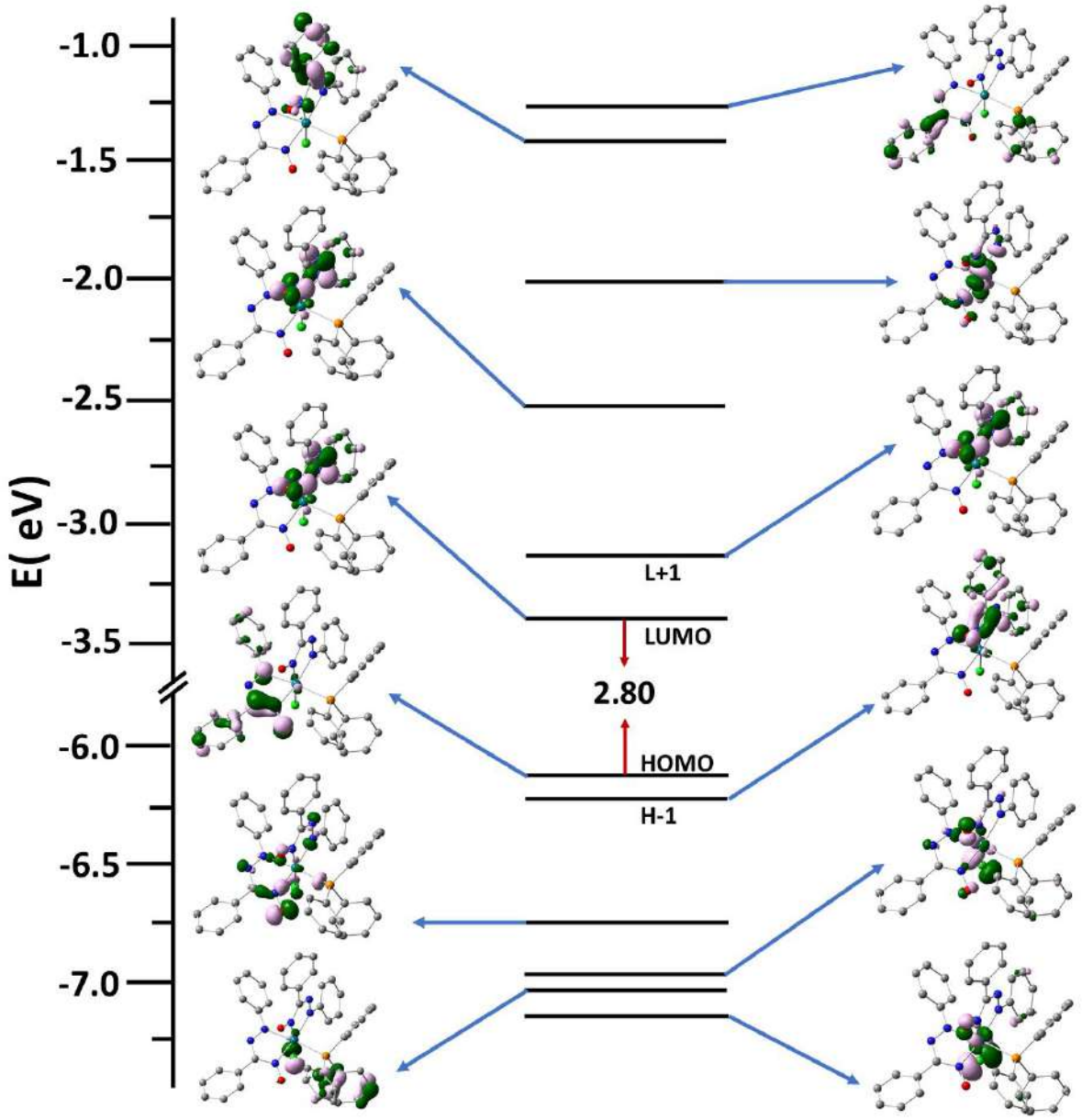

Figure 2.8: Partial MO diagram and isodensity surface plots (isovalue = 0.06) for selected FMOs of the complex **2a**. The arrows are used to highlight the HOMO–LUMO energy gaps. All the DFT energy values are given in eV

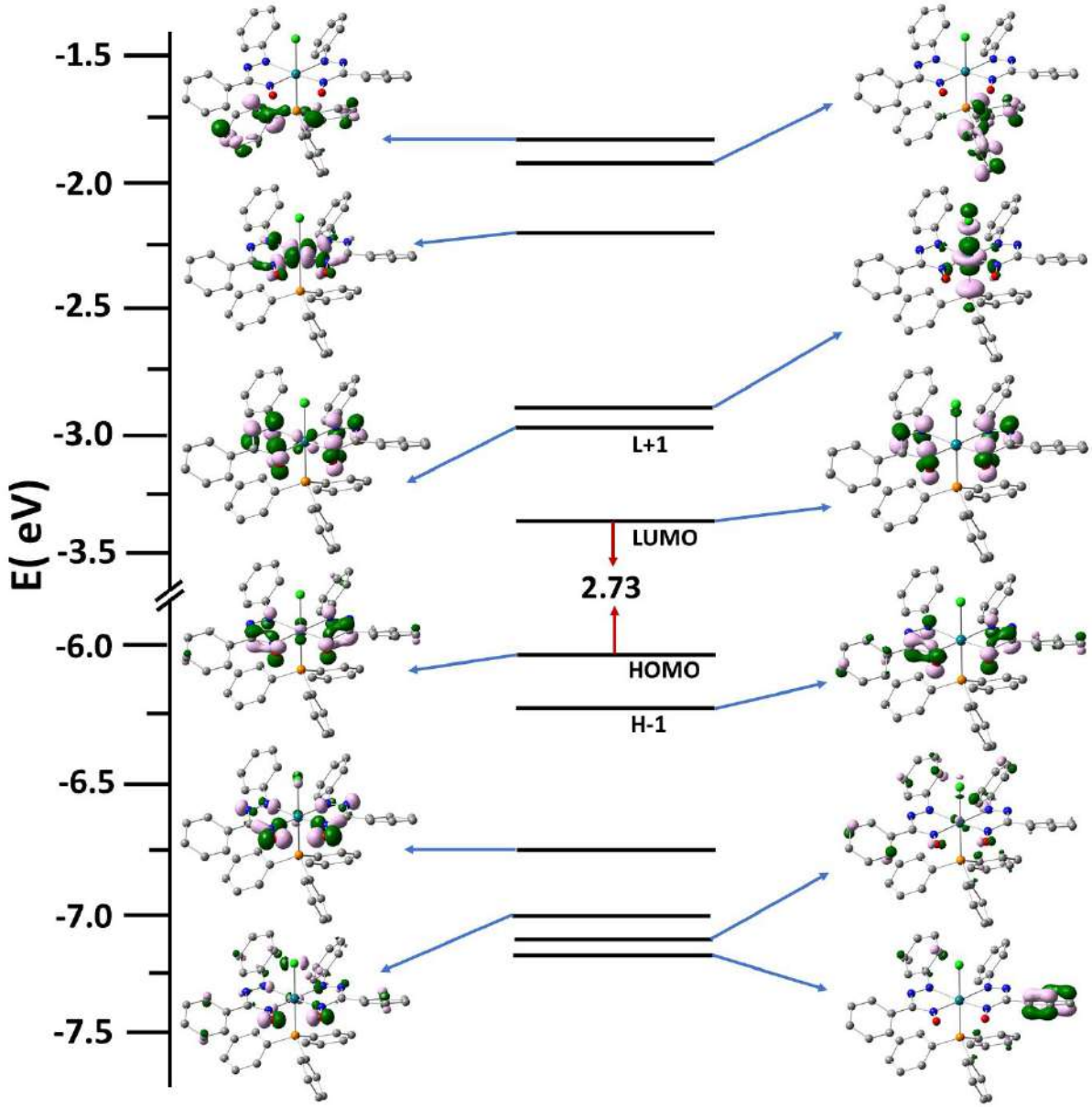

Figure 2.9: Partial MO diagram and isodensity surface plots (isovalue = 0.06) for selected FMOs of the complex **2b**. The arrows are used to highlight the HOMO–LUMO energy gaps. All the DFT energy values are given in eV

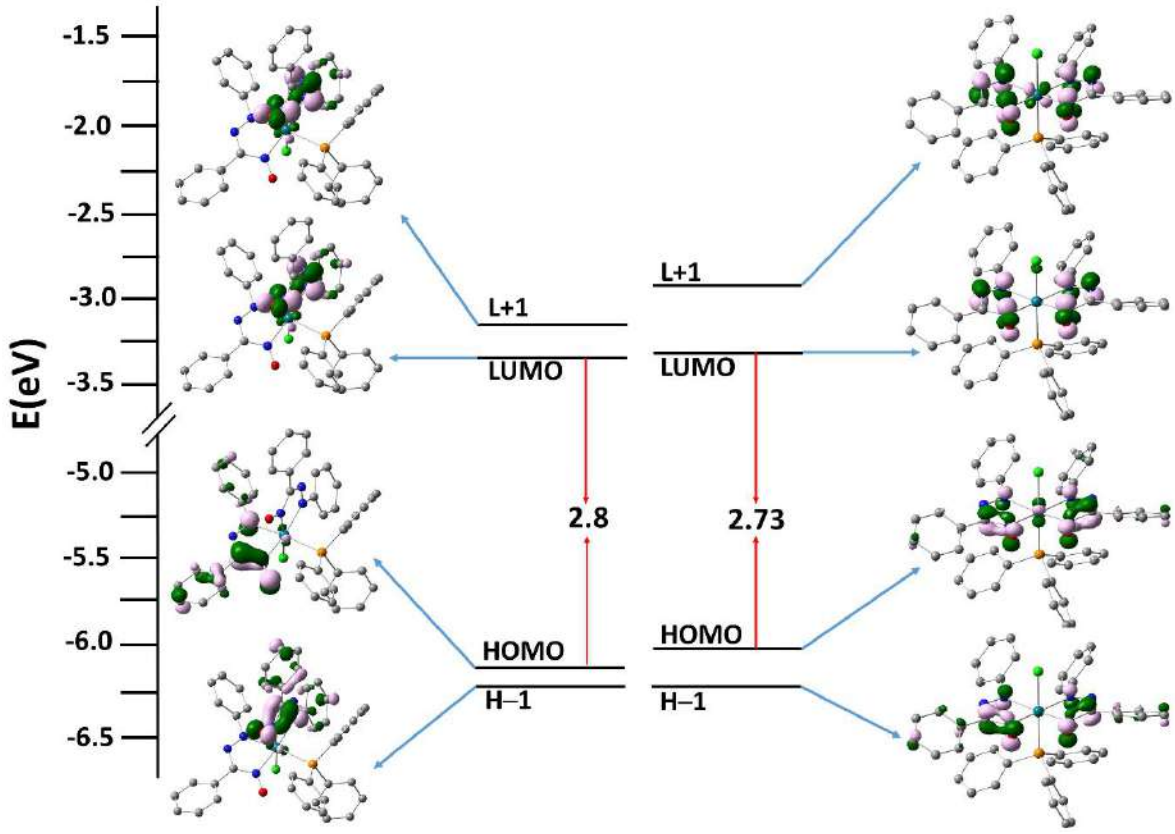

Figure 2.10: Combined MO diagram and isodensity surface plots (isovalue = 0.06) for selected FMOs of complex **2a** (left) and **2b** (right). The arrows are used to highlight the HOMO–LUMO energy gaps. All the DFT energy values are given in eV

2.3 Conclusion

This work demonstrates the ability of phenyl-azo-oxime ligand HL, **1** to perform as a sink for electron upon being ligated to rhodium(III). It further exemplifies that suitable spatial disposition of electron poor azo-oxime moiety around metal centre in bis-complex is crucial to exhibit its propensity towards redox non-innocence of coordinated phenyl-azo-oxime. The composite of dual ligands provides further scope of retaining an odd electron so as to be controlled *via* the formation of hydrogen bond. Reaction of Wilkinson's catalyst with the ligand have progressed *via* oxidative coordination, leading to formation of two isomeric complexes *cis*-[$Rh^{III}L_2Cl(PPh_3)$], **2a** (Cl and PPh_3 disposed cis orientation) and *trans*-[$Rh^{III}L_2Cl(PPh_3)$], **2b** (Cl and PPh_3 are mutually trans to each other). Both chelates have been structurally characterized by SCXRD. Significant interactions in the form of π-π stacking among pendant

phenyl rings is apparent in the *trans* form. Electrochemical studies reveal that the trans isomer **2b** acts as a superior electron acceptor and upon reaction with sodium borohydride, complex **3** is formed, possibly *via* a PCET. Theoretical and spectral studies reveal that the plausible description of **3** would be *trans*-[$Rh^{III}(HL^{\bullet})(L^{-})Cl(PPh_3)$] and stability of the unpaired electron within the ligand is further enhanced *via* oxime…oximato intramolecular hydrogen bonding. Notably, the absence of electron acceptor ability in *cis*-isomer can be attributed to mutual non-coplanar orientation of two ligand skeletons. Experimental findings are corroborated by DFT and TD-DFT, which substantiate the anticipated electronic structures along with absorption spectra.

2.4 Experimental section

2.4.1 Synthesis of ligand

The ligand was synthesised according to literature procedure.[55]

2.4.2 Synthesis of complex 2a and 2b

An oven dried 50 mL round-bottom flask was charged with HL, **1** (44 mg, 0.2 mmol, 2.0 equiv.) and [$RhCl(PPh_3)_3$] (92 mg, 0.1 mmol, 1.0 equiv.) in 25 mL of dry and degassed toluene. The reaction mixture was stirred at room temperature for 24 h, during which the solution developed a dark purple-red colour. Upon completion, the solvent was removed under reduced pressure. The residue was purified by column chromatography using toluene as the eluent, affording compound **2a**. Subsequent elution of the column with a toluene/acetonitrile mixture (20:1 v/v) furnished compound **2b**. Crystals suitable for single crystal X-ray diffraction were obtained for both complexes by slow diffusion of a dichloromethane solution into n-hexane.

2.4.3 Synthesis of complex 3

A solution of compound **2b** (42.76 mg, 0.05 mmol) in dichloromethane (CH_2Cl_2, 5 ml) was prepared in a clean, oven dried 50 ml round bottom flask under an inert argon atmosphere. To this stirred solution, a freshly prepared alcoholic solution of sodium borohydride ($NaBH_4$, 7.57 mg, 0.2 mmol) was added dropwise over a few minutes while maintaining the temperature at -5 °C using an ice-salt cooling bath. The reaction mixture was stirred for an additional 20 minutes at this temperature under a continuous flow of argon to ensure an oxygen-free environment. Following completion of the reduction, the solvent was rapidly removed under reduced pressure using a rotary evaporator. This furnishes a bluish-green solid, designated as compound **3**, which was collected for further analysis.

2.4.4 Analytical data of complex 2a

2a: Purple red coloured solid, Yield: 30 mg (35%). Anal. Calcd (%) for **2a** $C_{44}H_{35}N_6O_2ClPRh$: C, 62.24; H, 4.15; N, 9.90. Found: C, 62.11; H, 4.10; N, 9.95. **FT-IR (cm^{-1}):** 1483 (m, $\nu_{N=N}$), 1456 (m, $\nu_{N=N}$), 1090 (m, ν_{N-O}), 687 (vs $\nu_{Rh-P(sym)}$), 523 (vs $\nu_{Rh-P\,(asym)}$); **^{1}H NMR (400 MHz, $CDCl_3$):** δ 8.13 (d, *J* = 6.4 Hz, 2H), 7.66 – 7.61 (m, 4H), 7.60 – 7.56 (m, 4H), 7.53 (d, *J* = 7.7 Hz, 2H), 7.37 (d, *J* = 7.4 Hz, 3H), 7.31 – 7.26 (m, 6H), 7.23 (d, *J* = 8.6 Hz, 4H), 7.12 (dd, *J* = 10.6, 7.6 Hz, 8H), 7.07 – 7.01 (m, 2H). **^{13}C{^{1}H} NMR (101 MHz, $CDCl_3$):** δ 162.94, 162.55, 152.49, 134.78, 134.69, 130.71, 130.68, 129.53, 129.35, 129.20, 129.18, 129.14, 129.03, 128.98, 128.74, 128.57, 128.37, 128.22, 128.16, 128.11, 128.05, 128.00, 127.49, 124.67, 123.27. **^{31}P{^{1}H} NMR (162 MHz, $CDCl_3$):** δ 18.19 (d, $^1J_{Rh-P}$ = 121.0 Hz).

2.4.5 Analytical data of complex 2b

2b: Yield: 20 mg (23%) Anal. Calcd (%) for **2b** $C_{44}H_{35}N_6O_2ClPRh$: C, 62.24; H, 4.15; N, 9.90. Found: C, 62.13; H, 4.11; N, 9.97. **FT-IR (cm^{-1}):** 1482 (m, $\nu_{N=N}$), 1090 (m, ν_{N-O}) 690 (vs $\nu_{Rh-P(\,sym)}$), 512 (vs $\nu_{Rh-P(\,asym)}$); **^{1}H NMR (400 MHz, $CDCl_3$):** δ 7.89 (d, *J* = 9.0 Hz, 1H), 7.79 (d,

J = 9.8 Hz, 1H), 7.70 (dd, *J* = 11.1, 7.1 Hz, 3H), 7.54 (d, *J* = 7.6 Hz, 2H), 7.50 – 7.43 (m, 3H), 7.42 – 7.37 (m, 2H), 7.34 (dd, *J* = 7.6, 2.9 Hz, 8H), 7.29 – 7.22 (m, 6H), 7.21 – 7.17 (m, 3H), 7.15 (d, *J* = 5.8 Hz, 3H), 7.06 (t, *J* = 7.4 Hz, 1H), 6.92 (t, *J* = 7.7 Hz, 1H), 6.55 (d, *J* = 8.0 Hz, 1H). **^{13}C{^{1}H} NMR (101 MHz, CDCl$_3$):** δ 135.27, 135.18, 134.28, 134.18, 131.70, 130.94, 130.91, 129.75, 129.48, 129.18, 129.07, 129.01, 128.88, 128.78, 128.66, 128.37, 128.32, 128.22, 128.11, 128.01, 127.97, 127.91, 127.85, 127.62, 127.36, 125.76, 125.45, 122.82, 122.73. **^{31}P{^{1}H} NMR (162 MHz, CDCl$_3$):** δ 19.67 (d, $^{1}J_{Rh-P}$ = 119.4 Hz).

2.5 References

[1] T. Storr, R. Mukherjee, *Inorg. Chem.*, **2018**, *57*, 9577– 9579.

[2] W. I. Dzik, X. P. Zhang, B. de Bruin, *Inorg. Chem.*, **2011**, *50*, 9896–9903.

[3] P. J. Chirik, *Inorg. Chem.*, **2011**, *50*, 9737−9740.

[4] S. Samanta, P. Ghosh, S. Goswami, *Dalton Trans.*, **2012**, *41*, 2213−2226.

[5] N. D. Paul, U. Rana, S. Goswami, T. K. Mondal, S. Goswami, *J. Am. Chem. Soc.*, **2012**, *134*, 6520−6523.

[6] J. I. Van der Vlugt, J. N. H. Reek, *Angew. Chem. Int. Ed.*, **2009**, *48*, 8832−8846.

[7] P. Ghosh, E. Bill, T. Weyhermuller, F. Neese, K. Wieghardt, *J. Am. Chem. Soc.*, **2003**, *125*, 1293−1308.

[8] W. Kaim, B. Schwederski, *Coord. Chem. Rev.*, **2010**, *254*, 1580−1588.

[9] W. Kaim, *Dalton Trans.*, **2019**, *48*, 8521−8529.

[10] B. Butschke, K. L. Fillman, T. Bendikov, L. J. W. Shimon, Y. Diskin-Posner, G. Leitus, S. I. Gorelsky, M. L. Neidig, D. Milstein, *Inorg. Chem.*, **2015**, *54*, 4909−4926.

[11] P. Daw, A Kumar, D, Oren, N. A. Espinosa-Jalapa, D. Srimani, Y. Diskin-Posner, G. Leitus, L. J. W. Shimon, R. Carmieli, Y. BenDavid, D. Milstein, *Organometallics*, **2020**, *39*, 279−285.

[12] W. Kaim, A. Das, J. Fiedler, S. Záliš, B. Sarkar, *Coord. Chem. Rev.*, **2020**, *404*, 213114.

[13] A. M. Tondreau, C. Milsmann, A. D. Patrick, H. M. Hoyt, E. Lobkovsky, K. Wieghardt, P. J. Chirik, *J. Am. Chem. Soc.*, **2010**, *132*, 15046−15059.

[14] S. Kundu, S. Maity, T. Weyhermuller, P. Ghosh, *Inorg. Chem.*, **2013**, *52*, 7417−7430.

[15] J. Jacquet, S. Blanchard, E. Derat, M. D. Murr, L. Fensterbank, *Chem. Sci.*, **2016**, *7*, 2030–2036.

[16] S Blanchard, E, Derat, M. Desage-El Murr, L. Fensterbank, M. Malacria, V.Mouriès-Mansuy, *Eur. J. Inorg. Chem.*, **2012**, 376–389.

[17] P. J. Chirik, K. Wieghardt, Science, **2010**, *327*, 794−795.

[18] C. Mukherjee, T. Weyhermuller, E. Bothe, P. Chaudhuri, *Inorg. Chem.*, **2008**, *47*, 11620−11632.

[19] R. Rakshit, S. Ghorai, S. Biswas, C. Mukherjee, *Inorg. Chem.*, **2014**, *53*, 3333−3337.

[20] J. Sun, J. Abbenseth, H. Verplancke, M. Diefenbach, B. de Bruin, D. Hunger, C. Würtele, J. van Slageren, M. C. Holthausen, S. Schneide, *Nature Chemistry*, **2020**, *12*, 1054–1059.

[21] R. E. Rodríguez-Lugo, B. de Bruin, M. Trincadoand, H. Grutzmacher, *Chem. Eur. J.*, **2017**, *23*, 6795–6802.

[22] V. Lyaskovskyy, B.de Bruin, *ACS Catal.*, **2012**, *2*, 270−279.

[23] T. Tezgerevska, K. G. Alley, C. Boskovic, *Coord. Chem. Rev.*, **2014**, *268*, 23−40.

[24] O. R. Luca, R. H.Crabtree, *Chem. Soc. Rev.*, **2013**, 42, 1440−1459.

[25] D. L. J. Broere, R. Plessius, J. I.van der Vlugt, *Chem. Soc. Rev.*, **2015**, *44*, 7010−7010.

[26] G. Zhang, J. Wu, S. Zheng, M. C. Neary, J. Mao, M. Flores, R. J. Trovitch, P. A. Dub, *J. Am. Chem. Soc.*, **2019**, *141*, 15230−15239.

[27] N. P. van Leest, M. A. Tepaske, J. H. Oudsen, B. Venderbosch, N. R. Rietdijk, M. A. Siegler, M. Tromp, J. I. van der Vlugt, B. de Bruin, *J. Am. Chem. Soc.*, **2020**, *142*, 552−563.

[28] G. Chakraborty, R. Sikari, S. Das, R. Mondal, S. Sinha, S. Banerjee, N. D. Paul, *J. Org. Chem.*, **2019**, *84*, 2626–2641.

[29] S. Sinha, S. Das, R. Sikari, S. Parua, P. Brandao, S. Demeshko, F. Meyer, N. D. Paul, *Inorg. Chem.*, **2017**, *56*, 14084–14100.

[30] R. Sikari, S. Sinha, G. Chakraborty, S. Das, N. P. van Leest, N. D. Paul, *Adv. Synth. Catal.*, **2019**, *361*, 4342−4353.

[31] M. Orio, O. Jarjayes, H. Kanso, C. Philouze, F. Neese, F. Thomas, *Angew. Chem. Int. Ed.*, **2010**, *49*, 4989−4992.

[32] W. Kaim, B. Schwederski, *Coord. Chem. Rev.*, **2010**, *254*, 1580−1588.

[33] K. M. Miranda, *J. Inorg. Biochem.*, **2019**, *24*, 315–316.

[34] W. Kaim, G. K. Lahiri, *Coord. Chem. Rev.*, **2019**, *393*, 1−8.

[35] S. Pramanik, S. Roy, T. Ghorui, S. Ganguly, K. Pramanik, *Inorg. Chem.*, **2016**, *55*, 1461−1468.

[36] S. Roy, S. Pramanik, T. Ghorui, *RSC Adv.*, **2015**, *5*, 22544–22559.

[37] S. Roy, S. Pramanik, S. C. Patra, B. Adhikari, A. Mondal, S. Ganguly, K. Pramanik, *Inorg. Chem.*, **2017**, *56*, 12764−12774.

[38] S. Roy, S. Pramanik, T. Ghorui, S. Dinda, S. C. Patra, K. Pramanik, *New J. Chem.*, **2018**, *42*, 5548−5555.

[39] T. Ghorui, S. Roy, S. Pramanik, K. Pramanik, *Dalton Trans.*, **2016**, *45*, 5720–5729.

[40] S. Das, S. Sinha, U. Jash, R. Sikari, A. Saha, S. K. Barman, P. Brandao, N. D. Paul, *Inorg. Chem.*, **2018**, *57*, 5830−5841.

[41] M. Shivakumar, K. Pramanik, I. Bhattacharyya, A. Chakravorty, *Inorg. Chem.*, **2000**, *39*, 4332−4338.

[42] F. F. Khan, J. Klein, J. L. Priego, B. Sarkar, R. Jimenez-Aparicio, G. K. Lahiri, *Inorg. Chem.*, **2018**, *57*, 12800−12810.

[43] B. Sarkar, S. Patra, J. Fiedler, R. B. Sunoj, D. Janardanan, G. K. Lahiri, W. Kaim, *J. Am. Chem. Soc.*, **2008**, *130*, 3532−3542.

[44] F. F. Khan, A. D. Chowdhury, G. K. Lahiri, *Eur. J. Inorg. Chem.*, **2020**, 1138−1146.

[45] S. Panda, S. K. Bera, P. Goel, A. K. Dutta, G. K. Lahiri, *Inorg. Chem.*, **2019**, *58*, 11458–11469.

[46] D. Sengupta, R. Bhattacharjee, R. Pramanick, S. P. Rath, N. S. Chowdhury, A. Datta, S. Goswami, *Inorg. Chem.*, **2016**, *55*, 9602–9610.

[47] I. Chatterjee, N. S. Chowdhury, P. Ghosh, S. Goswami, *Inorg. Chem.*, **2015**, *54*, 5257–5265.

[48] S. P. Rath, D. Sengupta, P. Ghosh, R. Bhattacharjee, M. Chakraborty, S. Samanta, A. Datta, S. Goswami, *Inorg. Chem.*, **2018**, *57*, 11995−12009.

[49] G. C. Paul, K. Das, S. Maity, S. Begum, H. K. Srivastava, C. Mukherjee, *Inorg. Chem.*, **2019**, *58*, 1782–1793.

[50] P. Sarkar, A. Sarmah, C. Mukherjee, *Chem. Commun*., **2021**, *57*, 1352−1355.

[51] S. P. Rath, D. Sengupta, P. Ghosh, R. Bhattacharjee, M. Chakraborty, S. Samanta, A. Datta, S. Goswami, *Inorg*. Chem., **2018**, *57*, 11995−12009.

[52] S. Dinda, S. Pramanik, J. Basu, S. C. Patra, K. Pramanik, S. Ganguly, *Dalton Trans.*, **2022**, *51*, 10121−10135.

[53] S. Pramanik, S. Roy, T. Ghorui, S. Ganguly, K. Pramanik, *Dalton Trans.*, **2014**, *43*, 5317–5334.

[54] S. Pramanik, S. Dutta, S. Roy, S. Dinda, T. Ghorui, A. K. Mitra, K. Pramanik, S. Ganguly, *New J. Chem.*, **2017**, *41*, 4157−4164.

[55] S. Dinda, K. Sarkar, B. K. Panda, K. Pramanik, S. Ganguly, *Trans. Met. Chem.*, **2022**, *47*, 31–38.

[56] S. Dinda, S. Roy, S. C Patra, S Bhandary, K. Pramanik, S. Ganguly, *New J. Chem.*, **2020**, *44***,** 3737–3744.

[57] I. Bhattacharyya, S. Ganguly, B. K. Panda, A. Chakravorty, *J. Chem. Sci.*, **2008**, *120*, 87–93.

[58] S. Dinda, S. Naskar, S. Roy, K. Pramanik, S. Ganguly, *Polyhedron*, **2021**, *205*,115318–115324.

[59] M. H. V. Huynh, T. J. Meyer, *Chem. Rev.*, **2007**, *107*, 5004–5064.

[60] S. Hammes-Schiffer, *Chem. Rev.*, **2010**, *110*, 6937–6938.

[61] E. C. Gentry. R. R. Knowles, *Acc. Chem. Res.*, **2016**, *49*, 1546–1556.

[62] C. Janiak, *J. Chem. Soc., Dalton Trans.*, **2000**, 3885−3896.

[63] S. Pradhan, D. Ghosh, L. Xu, S. Chen, *J. Am. Chem. Soc.*, **2007**, *129*, 10622−10623.

[64] X. Yang, F. Drepper, B. Wu, W. H. Sun, W. Haehnel, C. Janiak, *Dalton Trans.*, **2005**, 256−267.

[65] C. A. Hunter, J. K. M. Sanders, *J. Am. Chem. Soc.*, **1990**, *112*, 5525−5534.

[66] S. Y. Son, J. Kim, E. Song, K. Choi, J. Lee, K. Cho, T. Kim, T. Park, *Macromolecules*, **2018**, *51*, 2572−2579.

[67] Z. Yao, J. Wang J. Pei, *Cryst. Growth Des.*, **2018**, *18*, 7−15.

[68] M. D. DeFuria, M. Zeller, D. T. Genna, *Cryst. Growth Des.*, **2016**, *16*, 3530−3534.

[69] U. Das, T. Ghorui, B. Adhikari, S. Roy, S. Pramanik, K. Pramanik, *Dalton Trans.*, **2015**, *44*, 8625–8639.

[70] C. R. Martinez, B. L. Iverson, *Chem. Sci.*, **2012**, *3*, 2191−2201.

[71] R.L. Martin, *J. Chem. Phys.*, **2003**, *118*, 4775−4777.

[72] S. Dinda, T. Sultana, S. Sultana, S. C. Patra, A. K. Mitra, S. Roy, K. Pramanik, S. Ganguly, *New J. Chem.*, **2020**, *44*,11022−11034.

2.6 Appendix:

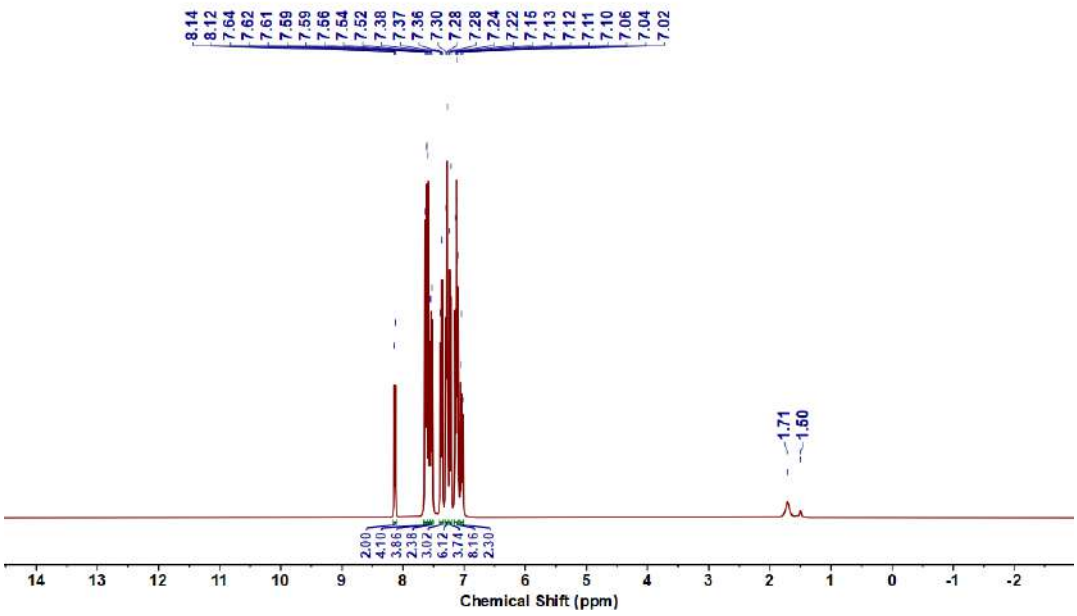

Figure 2.6.A1: ^{1}H NMR spectrum of **2a**

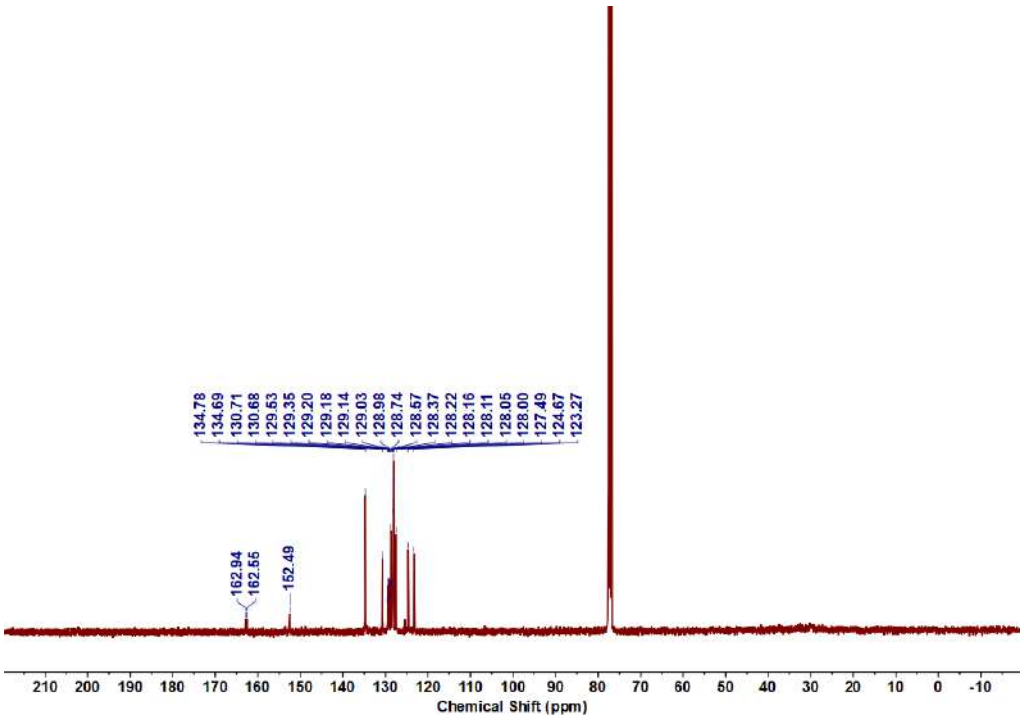

Figure 2.6.A2: $^{13}C\{^{1}H\}$ NMR spectrum of **2a**

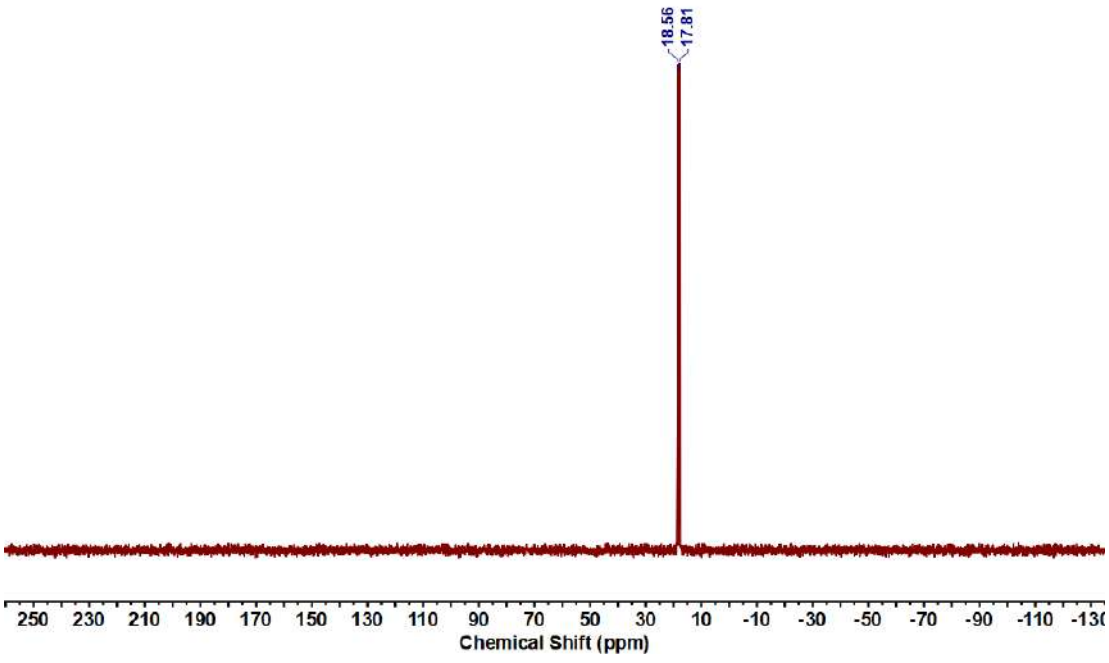

Figure 2.6.A3: $^{31}P\{^{1}H\}$ NMR spectrum of **2a**

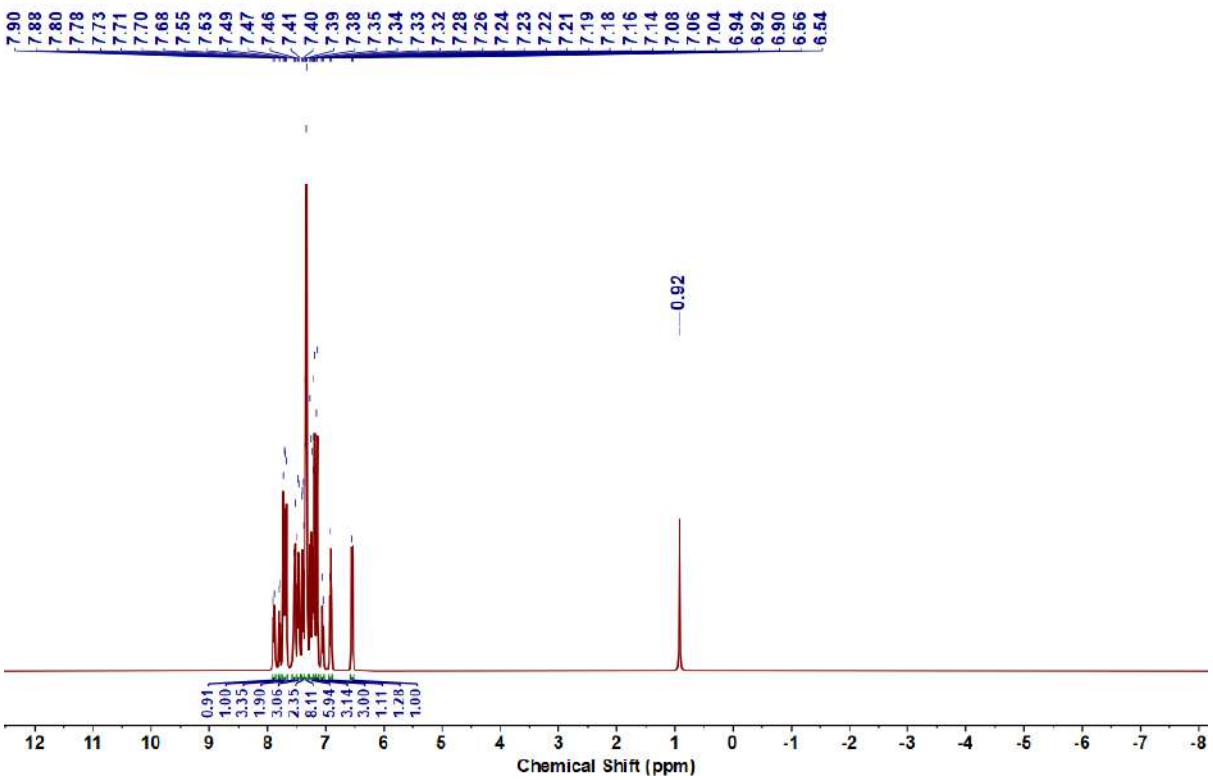

Figure 2.6.A4: ^{1}H NMR spectrum of **2b**

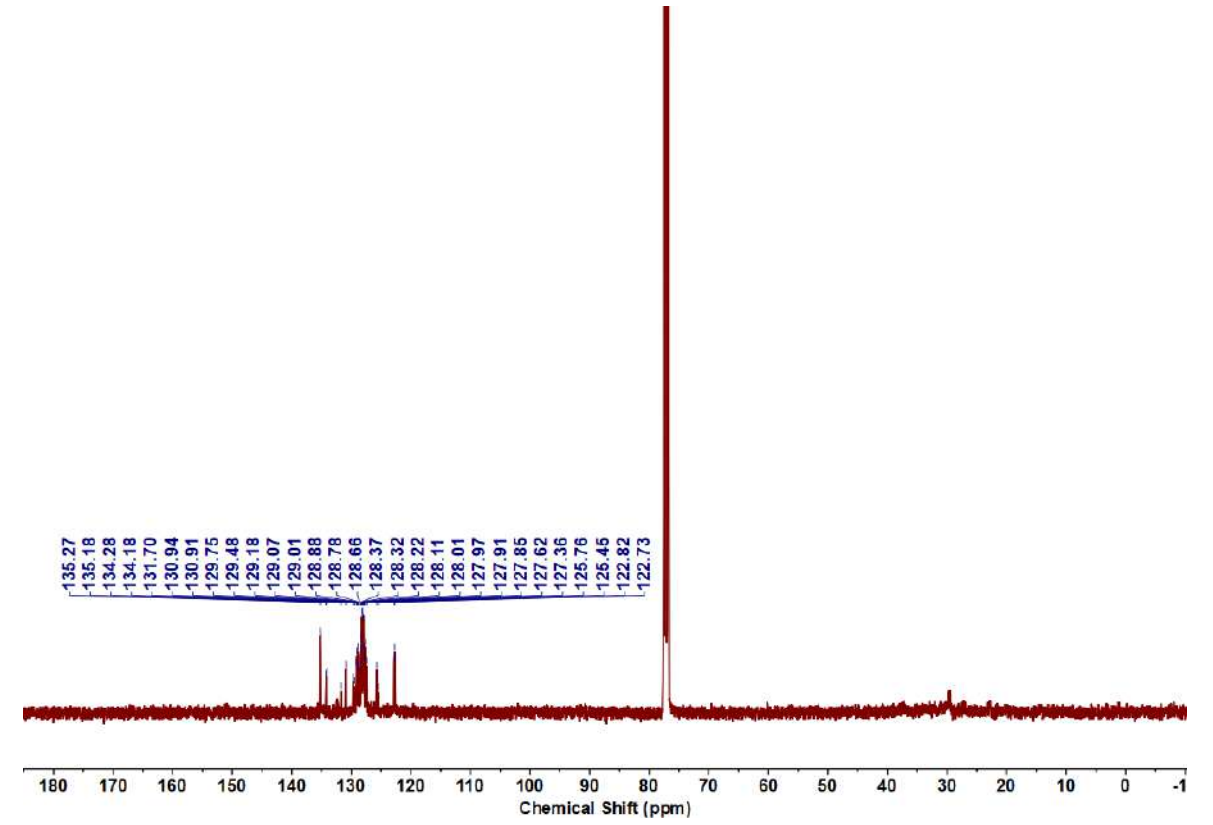

Figure 2.6.A5: $^{13}C\{^{1}H\}$ NMR spectrum of **2b**

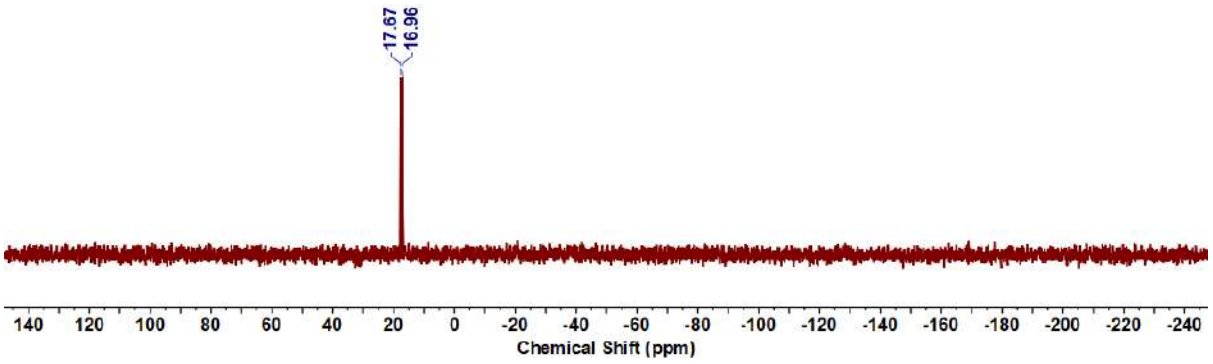

Figure 2.6.A6: $^{31}P\{1H\}$ NMR spectrum of **2b**

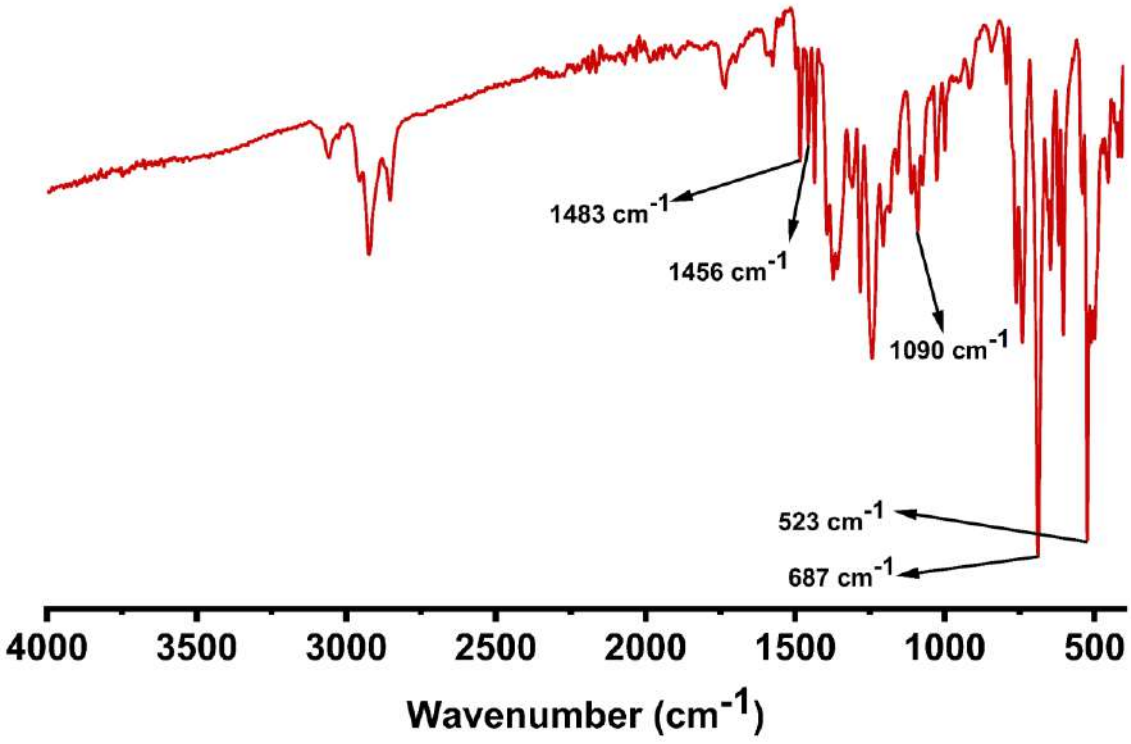

Figure 2.6.A7: IR spectrum of complex **2a**

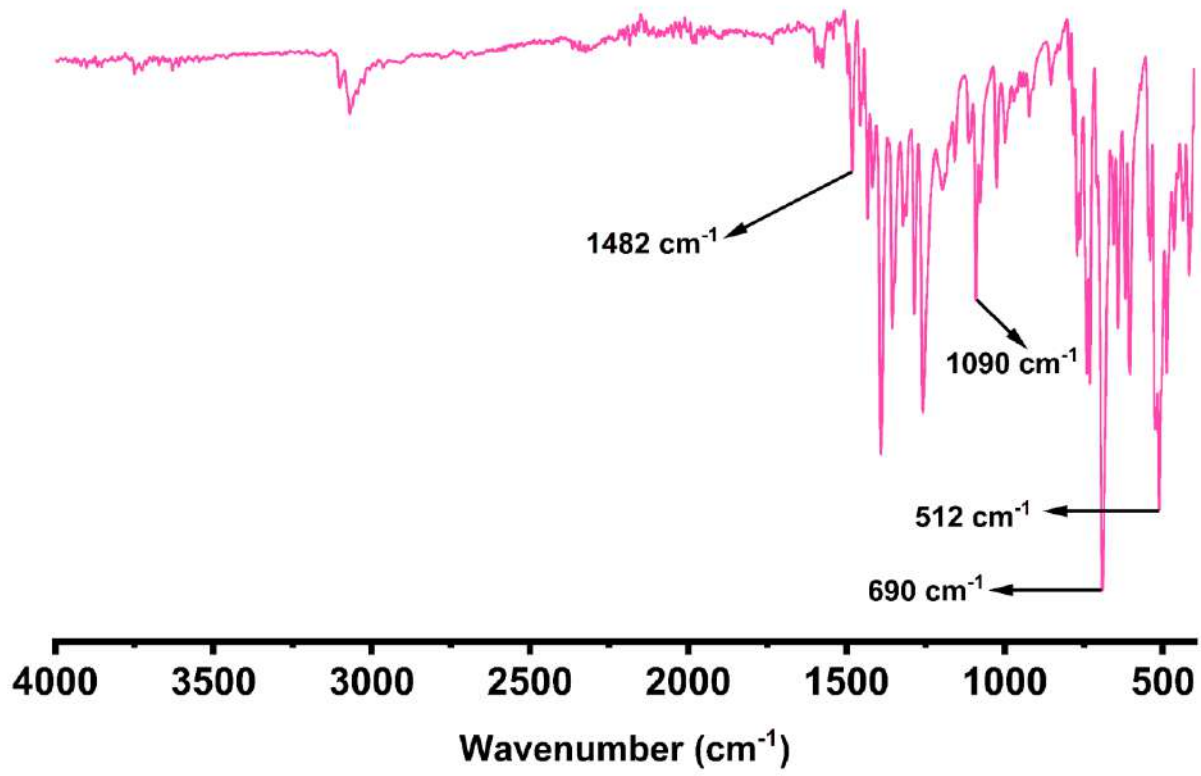

Figure 2.6.A8: IR spectrum of complex **2b**

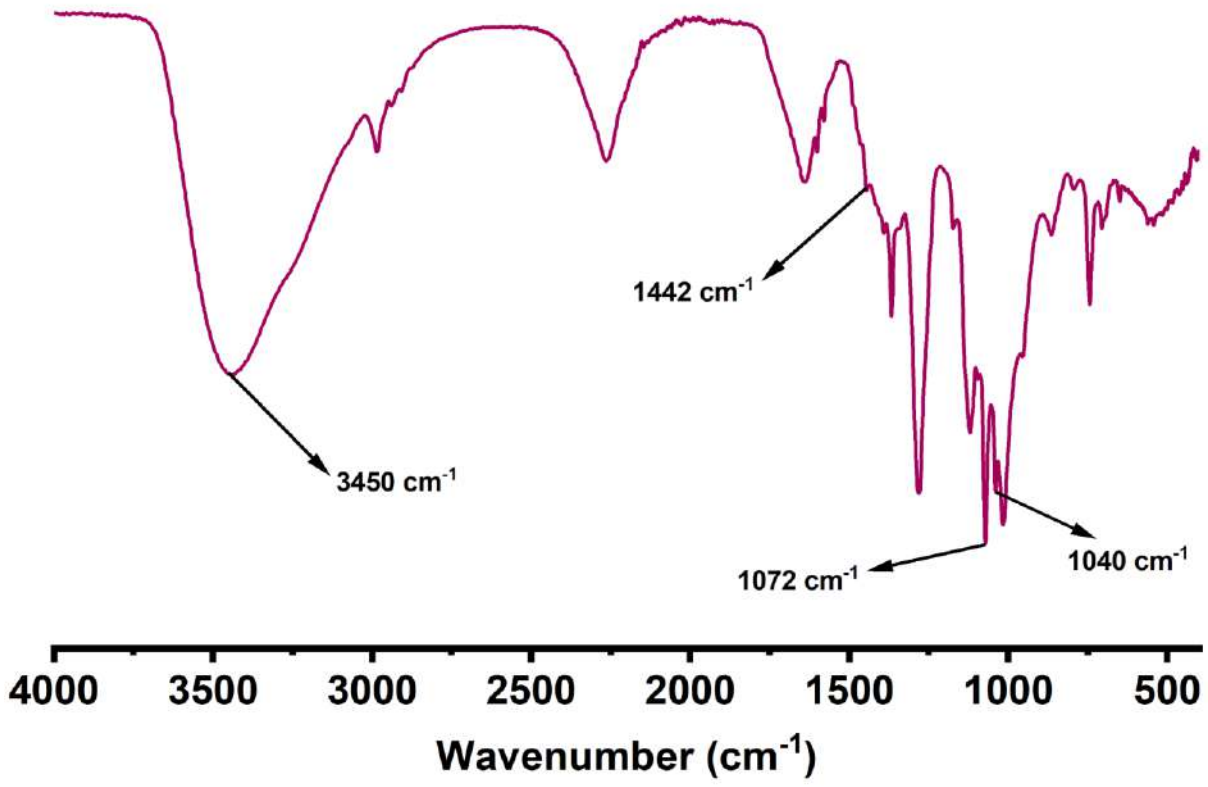

Figure 2.6.A9: IR spectrum of complex **3**

Table A.1: Cartesian Coordinates of Optimized Geometry of **2a**

Tag	Symbol	X	Y	Z
1	Rh	0.536	2.480	4.622
2	Cl	-1.173	2.464	2.877
3	O	-0.546	0.300	5.640
4	O	1.710	2.941	7.286
5	N	-0.610	1.536	5.720
6	N	-1.604	3.501	6.414
7	N	-0.876	4.049	5.556
8	N	1.773	3.406	6.414
9	N	2.534	4.911	4.563
10	N	1.715	4.377	3.748
11	C	-1.512	2.154	6.526
12	C	-1.005	5.507	5.502
13	C	-1.004	6.141	4.257
14	H	-0.915	5.551	3.354
15	C	-1.164	7.522	4.192
16	H	-1.181	8.013	3.225
17	C	-1.309	8.272	5.360
18	H	-1.425	9.349	5.304
19	C	-1.299	7.633	6.602
20	H	-1.402	8.211	7.513
21	C	-1.151	6.252	6.679
22	H	-1.137	5.747	7.637
23	C	-2.432	1.469	7.454
24	C	-3.654	2.084	7.779
25	H	-3.912	3.031	7.320
26	H	-4.532	41.491	8.681
27	H	-5.472	1.980	8.913
28	C	-4.207	0.274	9.282
29	H	-4.891	-0.189	9.985
30	C	-2.996	-0.342	8.969
31	H	-2.731	-1.287	9.434
32	C	-2.116	0.242	8.061
33	H	-1.184	-0.253	7.827
34	C	3.885	1.766	3.666
35	C	4.190	2.262	2.600
36	H	3.434	2.896	1.874
37	C	5.475	3.141	2.488
38	H	5.691	3.796	1.610
39	C	6.474	2.819	3.365
40	H	7.747	3.222	3.246
41	C	6.180	1.975	4.433
42	H	6.949	1.718	5.154
43	C	4.987	1.450	4.583
44	H	4.696	0.788	5.416
45	C	1.736	0.254	2.306

46	C	0.474	-0.354	2.231
47	H	-0.221	-0.261	3.056
48	C	0.110	-1.079	1.100
49	H	-0.868	-1.547	1.056
50	C	0.995	-1.201	0.028
51	H	0.707	-1.764	-0.854
52	C	2.251	-0.603	0.098
53	H	2.950	-0.702	-0.726
54	C	2.625	0.117	1.233
55	H	3.616	0.549	1.276
56	C	2.419	-0.313	5.047
57	C	2.366	-0.126	6.434
58	H	2.110	0.839	6.852
59	C	2.638	-1.185	7.298
60	H	2.593	-1.024	8.370
61	C	2.960	-2.444	6.791
62	H	3.167	-3.268	7.466
63	C	3.012	-2.637	5.412
64	H	3.261	-3.612	5.005
65	C	2.745	-1.580	4.544
66	H	2.793	-1.753	3.476
67	C	2.597	4.433	5.833
68	C	1.675	4.988	2.459
69	C	2.105	6.313	2.277
70	H	2.441	6.888	3.130
71	C	2.080	6.878	1.009
72	H	1.616	6.586	-1.076
73	C	1.632	6.138	-0.088
74	H	1.612	6.586	-1.076
75	C	1.200	4.826	0.096
76	H	0.848	4.243	-0.748
77	C	1.214	4.250	1.364
78	H	0.865	3.238	1.504
79	C	3.557	5.070	6.757
80	C	4.630	5.798	6.207
81	H	4.737	5.858	5.132
82	C	5.552	6.436	7.029
83	H	6.375	6.985	6.582
84	C	5.424	6.371	8.817
85	H	6.143	6.870	9.057
86	C	4.362	5.660	8.972
87	H	4.248	5.606	10.049
88	C	3.438	5.009	8.156
89	H	2.624	4.460	8.606
90	P	2.174	1.101	3.882

Table A.2: Cartesian Coordinates of Optimized Geometry of **2b**

Tag	Symbol	X	Y	Z
1	Rh	3.374	3.943	9.712
2	Cl	5.165	2.672	10.830
3	P	1.502	5.019	8.547
4	O	3.091	1.576	7.995
5	O	1.561	1.731	10.441
6	N	4.890	4.897	8.543
7	N	5.337	4.176	7.594
8	N	3.700	2.642	8.139
9	N	3.182	4.988	11.575
10	N	2.003	2.833	10.806
11	N	2.003	2.833	10.806
12	C	1.987	6.429	7.462
13	C	2.849	6.164	6.387
14	H	3.231	5.164	6.221
15	C	3.205	7.175	5.501
16	H	3.871	6.952	4.674
17	C	2.707	8.467	5.674
18	H	2.986	9.255	4.984
19	C	1.842	8.736	6.732
20	H	1.439	9.734	6.868
21	C	1.479	9.723	7.621
22	H	0.790	7.953	8.423
23	C	0.241	5.681	9.714
24	C	-1.063	5.170	9.729
25	H	-1.349	4.373	9.055
26	C	-2.012	5.688	10.609
27	H	-3.017	5.281	10.610
28	C	-1.674	6.725	11.477
29	H	-2.416	7.131	12.156
30	C	-0.377	7.238	11.468
31	H	-0.107	8.048	12.137
32	C	0.577	3.953	7.391
33	H	1.580	7.122	10.617
34	C	0.533	3.953	7.391
35	C	0.305	2.599	7.688
36	H	0.761	2.127	8.526
37	C	-0.505	1.839	6.824
38	H	-0.669	0.790	7.047
39	C	-1.097	2.417	5.704
40	H	-1.726	1.822	5.050
41	C	-0.879	3.767	5.426
42	H	-1.338	4.229	4.559
43	C	-0.070	4.532	6.263
44	H	0.081	5.578	6.031
45	C	5.640	6.098	8.744

46	C	7.033	6.087	8.744
47	H	7.534	5.155	8.353
48	C	7.757	7.264	8.353
49	H	8.835	7.247	8.862
50	C	7.102	8.460	9.041
51	H	7.668	9.378	9.156
52	C	5.717	8.465	9.206
53	H	5.200	9.989	9.441
54	C	4.987	7.288	9.073
55	H	3.914	7.307	9.191
56	C	4.739	2.988	7.340
57	C	5.254	2.183	6.213
58	C	5.137	0.784	6.157
59	H	4.631	0.251	6.949
60	C	5.676	0.073	5.087
61	H	5.582	-1.007	5.066
62	C	6.331	0.737	4.051
63	H	6.744	0.179	3.217
64	C	6.451	2.127	4.096
65	H	6.958	2.657	3.296
66	C	5.922	2.842	5.165
67	H	6.026	3.920	5.195
68	C	1.660	3.373	11.996
69	C	0.695	2.794	12.952
70	C	0.819	3.107	14.318
71	H	1.635	3.739	14.646
72	C	-0.089	2.611	15.248
73	H	0.032	2.859	16.297
74	C	-1.147	1.799	14.386
75	H	-1.854	1.421	15.561
76	C	-1.283	1.488	13.484
77	H	-2.102	0.859	13.151
78	C	-0.372	1.973	12.548
79	H	-0.490	1.713	11.506
80	C	3.950	6.051	12.159
81	C	5.339	6.051	12.159
82	H	5.820	5.263	11.457
83	C	6.095	7.032	12.656
84	H	7.175	7.014	12.652
85	C	5.473	8.025	13.411
86	H	6.066	8.792	13.898
87	C	4.083	8.025	13.543
88	H	3.591	8.792	14.132
89	C	3.321	7.036	12.931
90	H	2.246	7.014	13.054

Table A.3: Cartesian Coordinates of Optimized Geometry of **3**

Tag	Symbol	X	Y	Z
1	C	2.1061	6.1328	7.1748
2	C	2.6806	5.4625	6.1043
3	H	2.7706	4.5374	6.1374
4	C	3.122	6.152	4.9871
5	H	3.4953	5.6876	4.273
6	C	3.0102	7.5124	4.9313
7	H	3.3193	7.976	4.1867
8	C	2.4451	8.1862	5.9688
9	H	2.3733	9.1127	5.9321
10	C	1.9754	7.5045	7.08
11	H	1.5675	7.9761	7.77
12	C	0.6266	6.0358	9.7878
13	C	–0.4214	5.3871	10.4237
14	H	–0.657	4.5277	10.1575
15	C	–1.1197	5.9971	11.4451
16	H	–1.8094	5.539	11.8685
17	C	–0.8085	7.2684	11.8417
18	H	–1.2872	7.678	12.5258
19	C	0.2184	7.9332	11.2185
20	H	0.423	8.8039	11.4734
21	C	0.9501	7.3272	10.2201
22	H	1.6636	7.7793	9.8309
23	C	0.2726	4.081	7.7464
24	C	0.3039	2.7026	7.6728
25	H	1.0071	2.2312	8.0577
26	C	–0.7183	2.021	7.0219
27	H	–0.6947	1.0925	6.9754
28	C	–1.7629	2.7036	6.4466
29	H	–2.4385	2.2409	6.0058
30	C	–1.8025	4.082	6.5275
31	H	–2.5133	4.551	6.1539
32	C	–0.7843	4.7606	7.1643
33	H	–0.808	5.6895	7.2034
34	C	5.3155	6.248	8.8146
35	C	6.6442	6.5693	8.5384
36	H	7.2204	5.9342	8.1784
37	C	7.0867	7.8445	8.809
38	H	7.9733	8.0675	8.6383
39	C	6.2376	8.7937	9.3278
40	H	6.5509	9.6533	9.4942
41	C	4.9288	8.4786	9.6015
42	H	4.3521	9.1218	9.946
43	C	4.4811	7.2	9.36
44	H	3.603	6.9749	9.5678
45	C	4.8684	3.0796	7.3384

46	C	5.5519	2.3084	6.2851
47	C	5.5104	0.9308	6.2032
48	H	4.992	0.4477	6.8056
49	C	6.2341	0.2647	5.232
50	H	6.2016	–0.6638	5.1889
51	C	6.9902	0.9519	4.3423
52	H	7.4695	0.4971	3.6879
53	C	7.0458	2.3042	4.4093
54	H	7.5662	2.7739	3.7982
55	C	6.3375	2.9933	5.3758
56	H	6.3894	3.921	5.4149
57	C	1.5536	3.2703	11.7471
58	C	0.5196	2.6729	12.6092
59	C	0.6669	2.7343	13.9941
60	H	1.4284	3.1221	14.361
61	C	–0.3093	2.2237	14.8236
62	H	–0.2079	2.2744	15.7467
63	C	–1.4356	1.6382	14.2856
64	H	–2.0819	1.278	14.849
65	C	–1.6108	1.5825	12.9259
66	H	–2.3823	1.2041	12.5701
67	C	–0.6324	2.0929	12.0824
68	H	–0.7469	2.0473	11.1606
69	C	3.9222	5.8529	12.0782
70	C	5.298	5.7799	11.9531
71	H	5.6906	5.1302	11.4157
72	C	6.0809	6.6925	12.6431
73	H	7.0075	6.6435	12.5817
74	C	5.5055	7.6615	13.4109
75	H	6.0391	8.2622	13.8791
76	C	4.129	7.7501	13.4927
77	H	3.7377	8.4275	13.9956
78	C	3.3285	6.8332	12.8283
79	H	2.4019	6.8831	12.8912
80	Cl	5.0239	2.6571	10.6695
81	N	4.7879	4.9435	8.578
82	N	5.3794	4.3046	7.6345
83	N	3.7576	2.709	8.0033
84	N	3.1097	4.8516	11.4271
85	N	2.2182	4.3555	12.2122
86	N	1.967	2.7483	10.5704
87	O	3.1727	1.6242	7.7363
88	O	1.5614	1.6254	10.194
89	P	1.5784	5.0693	8.5645
90	Rh	3.3285	3.8992	9.5983
91	H	2.31399	1.06031	10.00458

Chapter 3

Designed Synthesis of Amino-Azo-Quinoline and their Nickel(II) Complexes: Molecular Structure, Electrochemistry and an Insight into their in vitro Anti-Cancer Activities

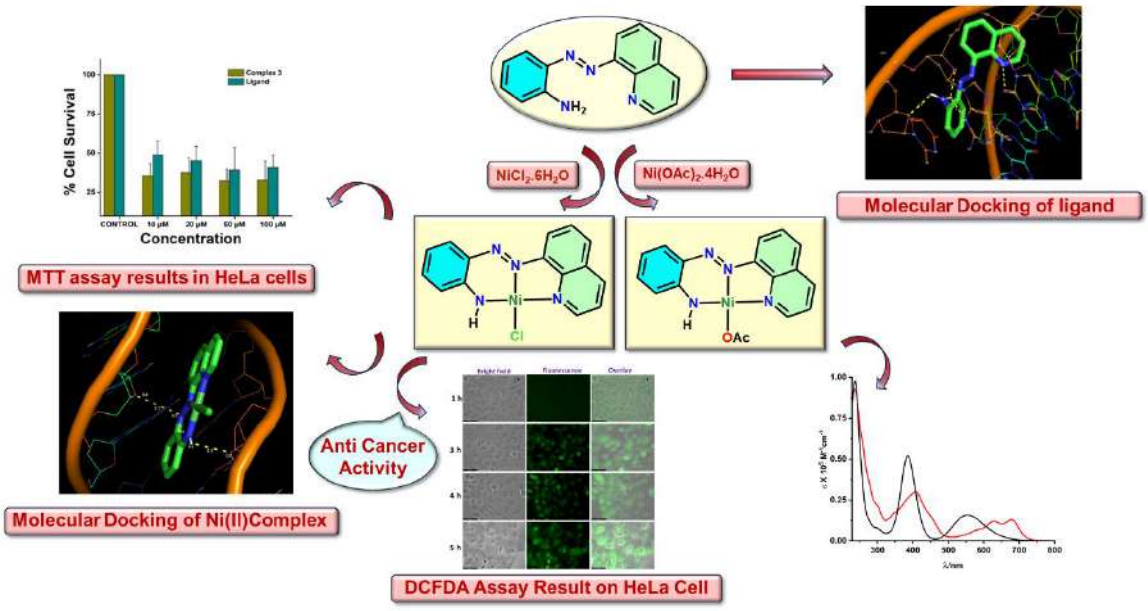

3.1 Introduction

The fabrication of *cis*-platin as a chemotherapeutic for a wide range of cancer treatment including solid cancers such as bladder, cervical, head and neck, lung cancer, testicular, ovarian, gastric cancer etc.,[1-4] has triggered the research on anti-blastoma activity of several other platinum complexes.[5,6] Over the years, combination-chemotherapy with *cis*-DDP has proven to be the basis for treatment of various cancers with relatively good efficacy but the major issue with them includes low selectivity and unwanted side effects including renal damage, neurological disorder, ototoxicity and so on.[7-17] Furthermore, platinum-based drugs are highly expensive and the extent of heavy metal toxicity is very high. Therefore, the pursuit of apposite less toxic and inexpensive 3d complexes as anti-cancer drugs have gained significant attention in modern cancer research.[18-22] Certain complexes of iron,[23-25] cobalt[26-28] as well as nickel[29-35] have been shown to exhibit ant-cancer activity. In addition to this, recent scientific developments have also revealed that nitrogenous heterocycles, particularly those incorporating quinoline moiety in presence of amino or amide groups[36-39] has the potential to exhibit appreciable anti-neoplastic activity and hence quest for such species as chemotherapeutic drug is imperative for advancement of cancer research. Another major benefit of using quinoline-based anti-cancer agent is that these frameworks have already proven to display significant anti-microbial activity,[40-46] and therefore they may have the aptitude to provide an additional protection to immunocompromised cancer patients during chemotherapy.

With this perception of the role of metal ions as well as ligand frameworks as anti-cancer agents, we have devised and synthesized a π–acidic tridentate amino-azo-quinoline ligand, H_2L **1**, and the corresponding nickel(II) complexes to have an understanding of their role as anti-cancer agents. It is well understood that in presence of electron-poor ligands, nickel(II) may exhibit similar square planar geometry like that of platinum(II) complexes and they can possess

certain comparable physical and chemical properties. Therefore, we were inquisitive towards exploration of anti-blastoma activity of the above ligand and their nickel(II) complexes since they can provide some insight for development of new and inexpensive anti-cancer drug. The ligand was synthesized starting from *o*-nitrosoacetanilide and 8-aminoquinoline and upon treatment with of H_2L separately with $Ni(OAc)_2.4H_2O$ and $NiCl_2.6H_2O$ in ethanolic solution, the square planar complexes [Ni(HL)(OAc)] **2** and [Ni(HL)Cl] **3** are formed respectively (Scheme 3.1). The complexes have been characterized by different spectral, electrochemical as well as X-ray diffractometric techniques and theoretical explorations have also been performed to give credence to the experimental results. Thereafter, anticancer properties of the ligand and complex were assessed by MTT assay using HeLa cells grown in Dulbecco's Modified Eagle Medium (DMEM) and it revealed significant damage of the cancer cells. Scratch assay has also been carried out to further investigate their ability to impede the orchestrated growth of cancer cell line. The data supported well with the MTT assay and the results authenticates that they inhibit proliferation of cancer cell to a much higher extent than the starting nickel(II) metal salts, although the activity is somewhat higher for the Ni(II) complexes with respect to the free ligand. One of the major rationales behind their anticancer activities may be attributed to generation of oxidative stress owing to excess accumulation of reactive oxygen species (ROS) within the cells. This is possibly owing to the defence mechanism against the applied drug, leading to the programmed cell death. The generation of ROS has been assessed by treating the cells with one of the nickel(II) complexes, incubated further with 2,7-dichlorofluorescene diacetate (DCFDA) in various time frames. The data revealed an incremental generation of green fluorescence after 3 h, indicative of generation of ROS after 3 h of treatment with the complex. Molecular docking with the free ligand and complexes further recommends that they possibly interact with the DNA strands during the course of their anticancer activity. Notably,

the DNA binding affinity for the complexes is higher than that of the free ligand and this may be attributed to the structural rigidity of the square planar nickel(II) complexes.

3.2 Results and Discussion

3.2.1 Synthesis, structure and spectral properties

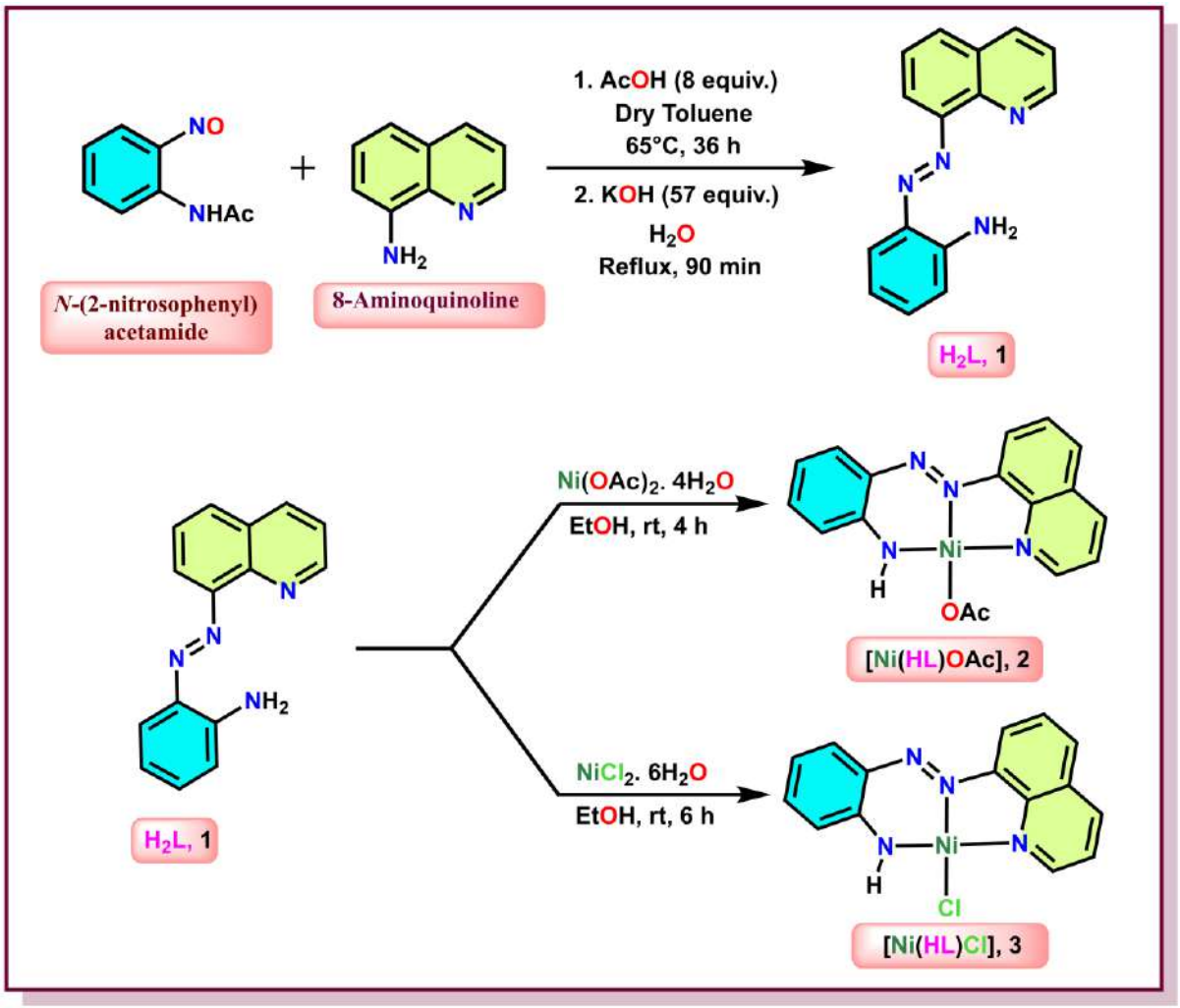

Scheme 3.1: Schematic illustration of synthesis of ligand **1** and its Ni(II)-complexes **2** and **3**

The novel amino-azo-quinoline ligand H_2L, **1** was synthesized by a two-step method *via* condensation of 2-nitrosoacetanilide with 8-aminoquinoline (Scheme 3.1) and the spectral characterizations are provided in Figure 3.6.A10–3.6.A13. It has been utilized to synthesize complexes of type [Ni(HL)(OAc)] **2** and [Ni(HL)Cl] **3** upon stirring **1** with $Ni(OAc)_2.4H_2O$ and $NiCl_2.6H_2O$ respectively in ethanol with subsequent evaporation to dryness and

purification. The structures of both the complexes were solved by SCXRD and their ORTEPs along with selected bond parameters are provided in Figure 3.1 and 3.2, while the crystallographic information and metric parameters are provided in Table 3.1 and 3.2. In both cases, the ligand behaves as tridentate $N_{quinoline}$, N_{azo}, N_{amino} monoanionic, thereby forming abutting five and six membered rings. The complexes are square planar as expected for nickel(II) with ligands having electron-poor centres and hence these are diamagnetic. The order of bond lengths in both cases: Ni–N1 (quinolinyl) > Ni–N2 (azo) > Ni–N4 (amino) and it points towards the fact that there occurs extensive delocalization of electron density from the amino-N towards the azo-N, thereby leading to the greater π-acceptor ability of the former with respect to that of latter. The pyridyl-N on the other hand possibly behaves as weakly π-acidic and this explanation is also supported from bond lengths within the coordinated ligand skeleton where N4 (amino)–C11 and N2–N3 (azo) lengths are much shorter than that of N1 (quinolinyl)–C1. Theoretically optimized geometries of **2** and **3** are provided in Figure 3.6 and selected experimental as well as theoretical bond lengths (Å) and angles (°) are tabularized in Table 3.2. It has been observed that [Ni(HL)(OAc)] **2**, crystallizes with a molecule of water as solvent and the latter is involved in inter-connecting the different molecular units *via* hydrogen bonding through the acetate-O atoms as well as the amino-Ns (Figure 3.3, Table 3.3). In fact, the solvent water molecules act both as electron donor as well as electron acceptor in stabilizing lattice. In addition, the lattice is further stabilized by inter-molecular π–π stacking interactions and such non-bonded interactions are also observed in **3** (Figure 3.4, Table 3.4 and Table 3.5).

The ^{1}H-NMR spectrum of the ligand **1** displays two types of signals: aromatic protons and also for protons from aromatic primary amine group (–NH_2). The aromatic proton signals are observed in the range of 6.77–9.07 ppm, while the signal corresponds to the protons of –NH_2 group lie within the chemical shift range of 6.77–6.88 ppm as evident from integration value. (Figure 3.6.A10). A similar pattern is observed for both complexes **2** and **3**. In complex **2**,

aromatic proton signals appear in the range of 6.57–8.47 ppm, whereas the amido proton (–N–H) appears as a characteristic broad singlet at 7.94 ppm, shifted downfield compared to that of free ligand. The signal for methyl protons of the coordinated acetate appears as a sharp singlet at 2.11 ppm (Figure 3.6.A14). For **3**, the signal for amido proton is observed as a characteristic broad singlet at 6.03 ppm, slightly downfield compared to the free ligand (Figure 3.6.A18). $^{13}C\{^{1}H\}$ NMR spectra (Figure 3.6.A11, 3.6.A15 and 3.6.A19) of all synthesised compounds are consistent with their ^{1}H NMR spectra. For complex **2**, the signal for methyl and carbonyl carbon appears at 25.49 and 180.18 ppm respectively.

IR analysis of ligand and complexes (See Figure 3.6.A12, 3.6.A16 and 3.6.A20) is in keeping with the observed structures. In the free ligand, bands at 3470 cm^{-1} and 3387 cm^{-1} correspond to N–H stretching, while N–H bending stretch is recorded at 1610 cm^{-1}. Additionally, the stretching frequency for the azo moiety is observed at 1488 cm^{-1}. For **2**, the N–H stretching band (secondary amine) appears at 3171 cm^{-1}, while the N–H band for bending mode is observed at 1600 cm^{-1}. The N=N stretching appears as a weak band at 1461 cm^{-1}. Similarly, in **3**, the N–H stretching and bending modes are observed at 3338 cm^{-1} and 1614 cm^{-1}, respectively, while the N=N stretching band appears at 1455 cm^{-1}.

The mass spectrometric data (Figure 3.6.A13, 3.6.A17 and 3.6.A21) of all synthesized compounds were consistent with their proposed structures. For ligand **1**, the molecular ion peak (M+H) was observed at *m/z* 249.1141, closely matching the calculated value of 249.1142. In case of Ni(II) complexes, ionization resulted in the dissociation of both co-ligands (acetate for **2** and chloride for **3**), yielding a molecular ion peak at *m/z* 305.0332, which closely corresponds to the calculated value of 305.0337.

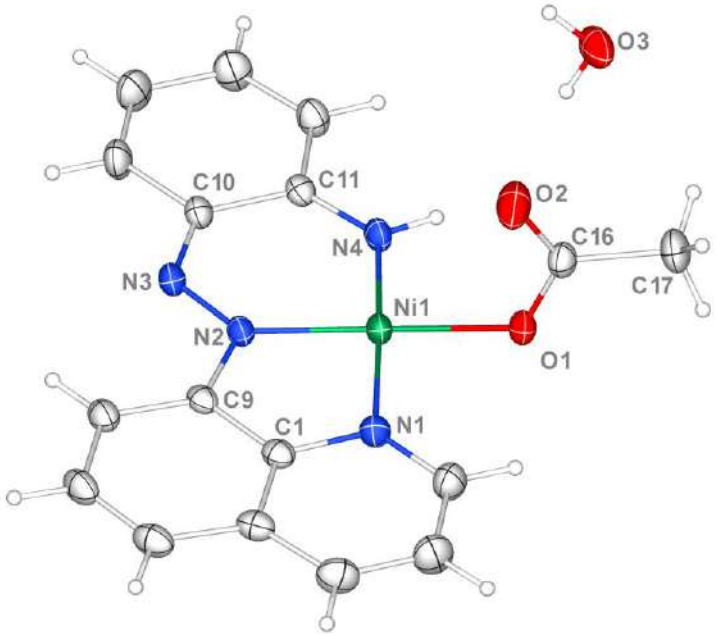

Figure 3.1: ORTEP view of **2** with atom numbering scheme (Thermal ellipsoids are set at 40% probability). **CCDC No.: 2377738**; Selected bond lengths (Å) and bond angles (°): Ni–N1 1.9046(18), Ni–N2 1.8414(16), Ni–N4 1.8123(17), N2–N3 1.301(2), Ni–O1 1.9057(14), N1–Ni1–N2 85.70(7), N2–Ni1–N4 92.34(7), N1–Ni1–O1 92.27(7), N4–Ni1–O1 89.74(7)

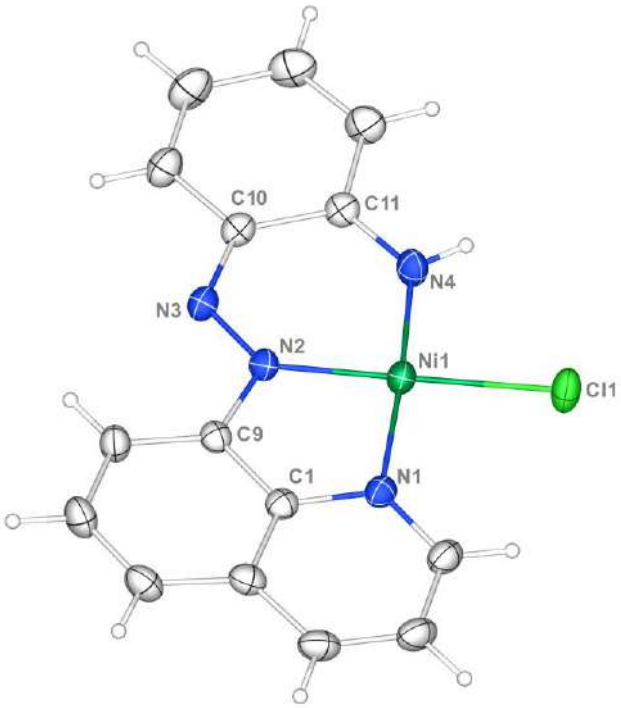

Figure 3.2: ORTEP view of **3** with atom numbering scheme (Thermal ellipsoids are set at 40% probability). **CCDC No.: 2377739**; Selected bond lengths (Å) and bond angles (°): Ni–N1 1.9168(19), Ni–N2 1.8493(17), Ni–N4 1.811(2), N2–N3 1.291(2), Ni–Cl1 2.2085(6), N1–Ni1–N2 85.53(8), N2–Ni1–N4 90.68(9), N4–Ni1–Cl1 89.85(7)

Table 3.1: Crystallographic Details of complex **2** and **3**

	2. H_2O	**3**
Empirical formula	$C_{17}H_{14}N_4O_2Ni$	$C_{15}H_{11}N_4ClNi$
T/K	273.15	273.15
fw	383.05	341.44
Crystal system	Monoclinic	Monoclinic
Space Group	$P2_1/n$	$C2/c$
a/Å	6.8134(2)	17.0429(7)
b/*Å*	12.3902(4)	13.6869(5)
c/ *Å*	19.5828(7)	14.0833(5)
α/deg	90	90
β/deg	94.9430(10)	124.8000(10)
γ/deg	90	90
V/ $Å^3$	1647.02(9)	2697.58(18)
Z	4	8
D_c/Mgm^{-3}	1.545	1.681
μ/mm^{-1}	1.203	1.633
F(000)	792	1392
cryst size/mm^3	0.37 × 0.26 × 0.12	0.31×0.27×0.12
θ/deg	3.091–25.711	2.123–27.171
Measured reflns	28965	44233
Unique reflns	3124	2994
[a]GOF on F^2	1.108	1.155
R_1[b], wR_2[c][$I>2\sigma(I)$]	0.0300, 0.0703	0.0343, 0.0749
R_1, wR_2	0.0362, 0.0734	0.0396, 0.0775
Largest diff. peak/hole / e $Å^{-3}$	0.26/-0.22	0.328/-0.305
[a]GOF = $\{\Sigma[w(F_o{}^2-F_c{}^2)2]/(n-p)\}^{1/2}$. [b]$R_1 = \Sigma\,[\lvert F_o\rvert-\lvert F_c\rvert]/\,\Sigma\,\lvert F_o\rvert$. [c]$wR_2 = [\Sigma\,[w(F_o{}^2-F_c{}^2)^2]/\,\Sigma\,[w(F_o{}^2)^2]]^{1/2}$ where $w = 1/[\,\sigma^2(F_o{}^2)+(aP)^2+bP]$, $P = (F_o{}^2+2F_c{}^2)/3$.		

Table 3.2: Selected Experimental and Theoretical Bond Lengths (Å) and Angles (°) of **2** and **3**

Metrical Parameters	2		Metrical Parameters	3	
	Expt.	Theo.		Expt.	Theo.
Ni–N1	1.9046(18)	1.940	Ni–N1	1.9168(19)	1.955
Ni–N2	1.8414(16)	1.885	Ni–N2	1.8493(17)	1.888
Ni–N4	1.8123(17)	1.843	Ni–N4	1.811(2)	1.845
Ni–O1	1.9057(14)	1.914	Ni–Cl1	2.2085(6)	2.278
N2–N3	1.301(2)	1.285	N2–N3	1.291(2)	1.284
C1–N1	1.371(3)	1.366	C1–N1	1.371(3)	1.368
C9–N2	1.418(3)	1.413	C9–N2	1.421(3)	1.413
C10–N3	1.339(3)	1.343	C10–N3	1.344(3)	1.341
C11–N4	1.313(3)	1.321	C11–N4	1.322(3)	1.321
N1–Ni1–N2	85.70(7)	85.15	N1–Ni1–N2	85.53(8)	85.00
N2–Ni1–N4	92.34(7)	91.35	N2–Ni1–N4	90.68(9)	90.79
N1–Ni1–O1	92.27(7)	93.51	N1–Ni1–Cl1	93.92(6)	94.86
N4–Ni1–O1	89.74(7)	89.93	N4–Ni1–Cl1	89.85(7)	89.34
N2–Ni1–O1	177.46(7)	177.76	N2–Ni1–Cl1	177.90(6)	179.86

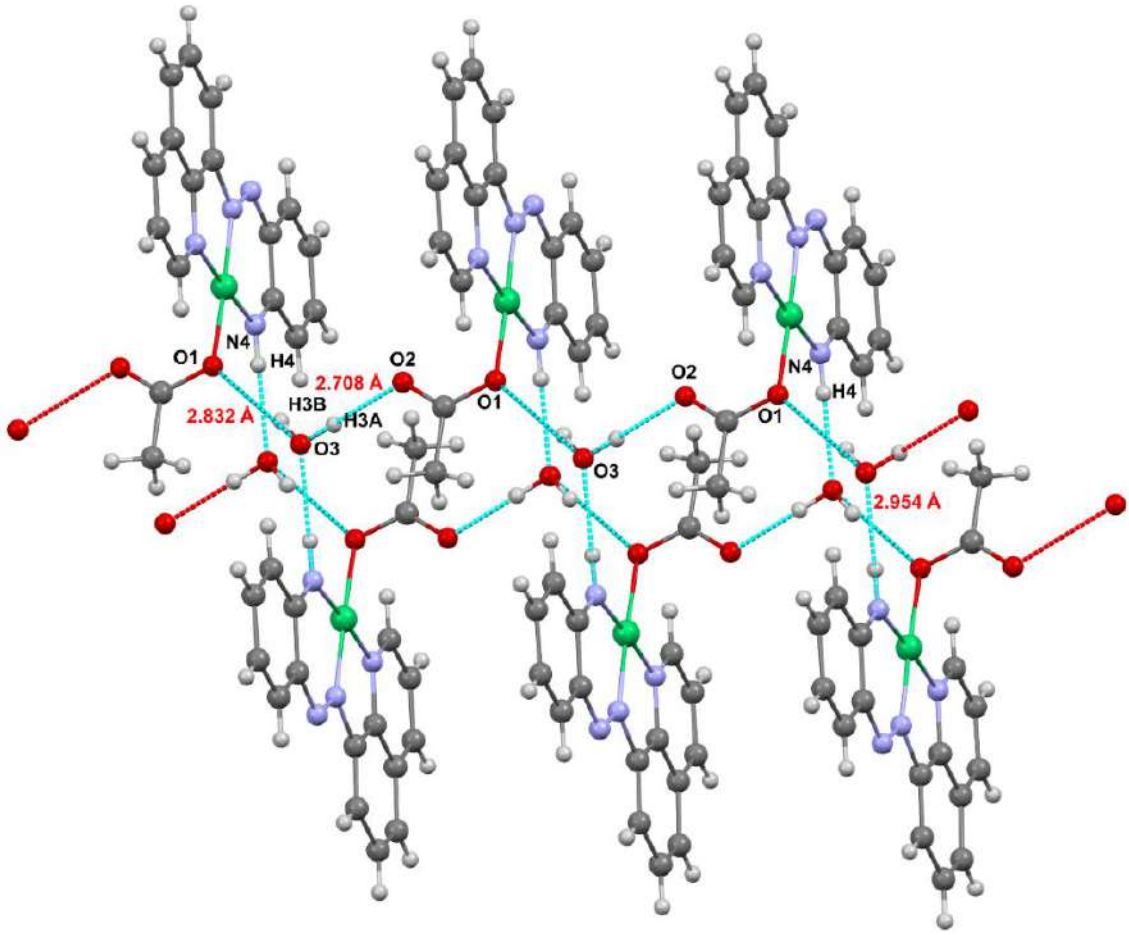

Figure 3.3: Representation of Intermolecular H-Bonding network along with Donor–Acceptor distances of complex **2**

Table 3.3: Intermolecular H-Bonding of complex **2**

Donor……H	Acceptor	D……A (Å)	D–H……A (degree)
O3……H3A	O2	2.708(3)	169
O3……H3B	O1	2.832(2)	160
N4……H4	O3	2.954(2)	170

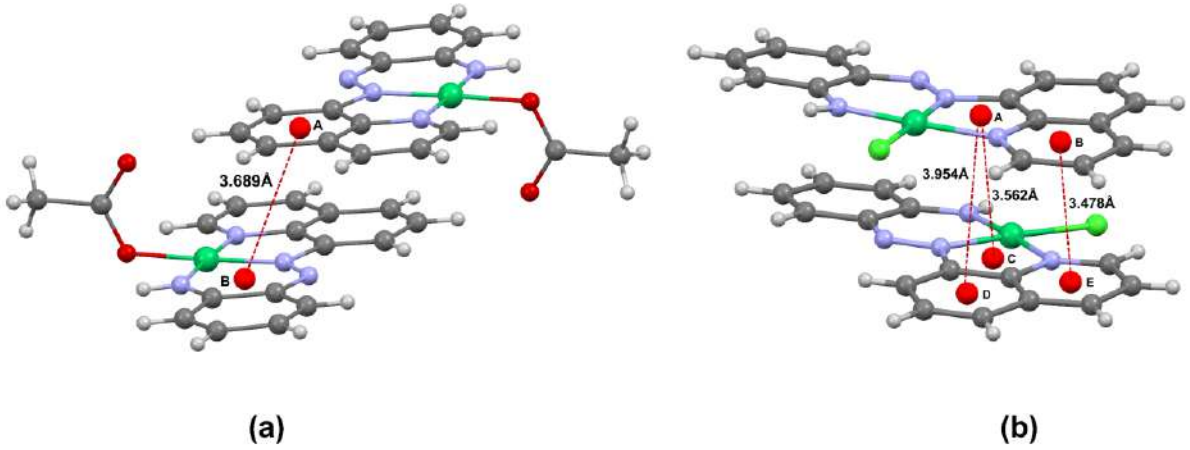

Figure 3.4: Intermolecular pi–pi stacking of complex **2** (left) and **3** (right)

Table 3.4: Different stacking parameters of complex **2**

Stacking Parameters	Ring A–B
d[$C_g(I) - C_g(J)$] Å/α°	3.6897(12)/1.26(9)
d[Cg(*I*) – R(*J*)] Å/β°	3.3245(7)/25.0
d[Cg(*J*) – R(*I*)] Å/γ°	3.3429(9)/25.7

Table 3.5: Intermolecular π–π stacking of complex **3**

Stacking Parameters	Ring A–C	Ring A–D	Ring B–E
d[$C_g(I) - C_g(J)$] Å/α°	3.5621(12)/1.51(11)	3.9537(16)/2.52(12)	3.4777(15)/2.16(13)
d[Cg(*I*) – R(*J*)] Å/β°	3.5126(9)/9.6	3.5528(9)/42.1	3.4591(11)/5.9
d[Cg(*J*) – R(*I*)] Å/γ°	3.5127(9)/9.6	3.4224(11)/39.6	3.4593(11)/5.9

3.2.2 Electrochemistry and computational studies

The electrochemical data of **2** and **3** are provided in Figure 3.5 and Table 3.6 where the irreversible oxidative responses are attributed primarily to ligand oxidation with some contribution from the metal centre (Table 3.8 and 3.9). From theoretical calculations of FMOs it has been observed that HOMO of **2** has very high participation of π (Azo + NH_2 + Ph) from the coordinated ligand while for **3**, the contributions are primarily from π (Cl + Azo + NH_2 +Quino+ Ph). In both the complexes, the metal ion participation of HOMO is extremely weak. Therefore, the oxidation process is attributed to ligand oxidation with very slight contribution from nickel(II). Also, LUMO and (LUMO + 1) for both complexes have very high contribution from π* (Azo + Quino + Ph) primarily thereby signifying that reductive responses are chiefly due to ligand reduction (Figure 3.5, Table 3.6).

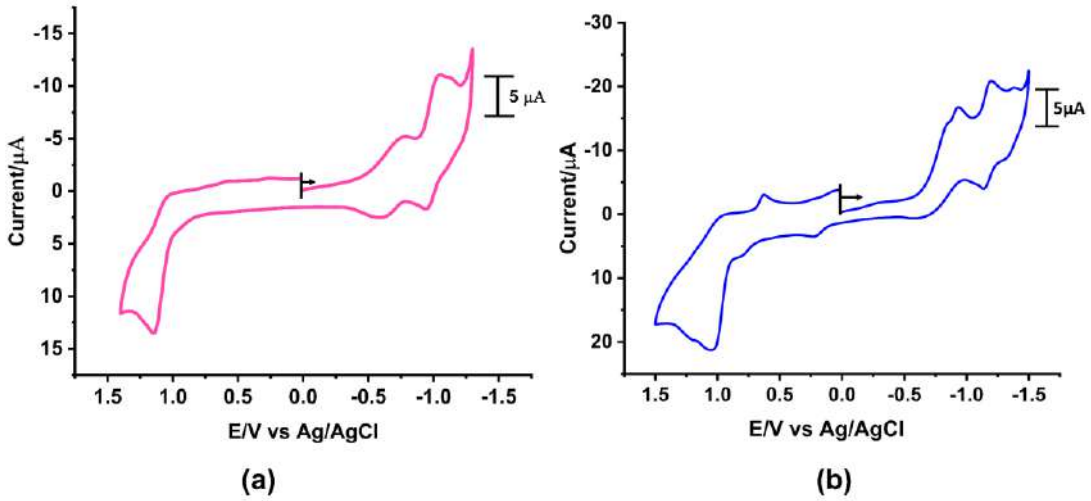

Figure 3.5: Cyclic Voltammogram of complex **2** (left) and **3** (right)

Table 3.6: Electrochemical data of Ni(II)-complexes with respect to Ag/AgCl

Complex	$E_{1/2}$/V (ΔE /mV)	
	Oxidation	Reduction
2	+1.14 (E_{pa}/V)	-0.77(E_{pc}/V), -0.99 (97 mV) V
3	+1.05 (E_{pa}/V)	-0.93(E_{pc}/V), -1.16 (50 mV) V
$E_{1/2}$ = ½(E_{pa} + E_{pc}), E_{pa} = anodic peak potential; E_{pc} = cathodic peak potential, ΔE = peak-to-peak separation		

Table 3.7: Frontier Molecular Orbital Composition (%) in the Ground State for ligand **1**

MO No.	MO	E (eV)	Contribution (%)				Contribution
			Azo	NH_2	Quino	Ph	
70	L+4	0.51	2	4	44	50	π* (Quino + Ph)
69	L+3	0.19	3	3	7	87	π* (Quino + Ph)
68	L+2	-0.69	0	0	99	1	π* (Quino)
67	L+1	-1.23	16	1	71	12	π* (Azo + Quino + Ph)
66	LUMO	-2.32	29	4	48	19	π* (Azo + Quino + Ph)
65	HOMO	-5.38	8	24	17	51	π (Azo + NH_2 + Quino + Ph)
64	H–1	-5.96	73	3	16	9	π (Azo + Quino + Ph)
63	H–2	-6.23	7	5	43	45	π (Azo + Quino + Ph)
62	H–3	-7.09	0	0	100	0	π (Quino)
61	H–4	-7.19	8	0	43	49	π (Azo + Quino + Ph)

Table 3.8: Frontier Molecular Orbital Composition (%) in the Ground State for complex **2**

MO No.	MO	E (eV)	Contribution (%)						Contribution
			Ni	Azo	NH_2	Quino	Ph	Ac	
94	L+4	-0.10	1	3	0	54	43	0	π* (Quino + Ph)
93	L+3	-1.25	0	0	0	99	1	0	π* (Quino)
92	L+2	-1.3	60	9	9	9	2	10	$d_{x^2-y^2}$ + π* (Azo + NH_2 +Quino + Ph)
91	L+1	-1.99	4	18	5	57	16	0	π* (Azo + Quino + Ph)
90	LUMO	-2.82	1	18	6	55	20	0	π* (Azo + Quino + Ph)
89	HOMO	-5.45	12	13	21	11	42	1	d_{xz} + π (Azo + NH_2 + Ph)
88	H–1	-5.95	24	0	1	1	0	74	d_{z^2}+ π (Acetate)
87	H–2	-6.49	20	9	2	33	35	1	d_{yz}+ π (Quino + Ph)
86	H–3	-6.67	71	0	1	0	0	28	d_{z^2}+ π (Acetate)
85	H–4	-6.83	10	0	1	2	0	87	π (Acetate)

The optimised geometries of **1** at (R)B3LYP/6-311G(d,p) while for **2** and **3** at (R)B3LYP/6-311+G(d,p) level of theory, are shown in Figure 3.6 along with their theoretical and experimental electronic spectra. The solution phase absorption spectra of ligand **1** and complex **2** & **3** were recorded in dichloromethane solution at room temperature. Multiple low-energy absorption bands are characteristic of all compounds and are believed to be charge-transfer transitions between ligand skeleton with slight contribution from metal in complexes. The experimentally observed spectra of complexes **2** and **3** are practically identical with a slight

difference at around 600 nm (Figure 3.6e and 3.6f). In order to comprehend the optoelectronic properties of these compounds, we performed time dependent density functional theory (TD-DFT) using CPCM model and DCM as solvent.

Table 3.9: Frontier Molecular Orbital Composition (%) in the Ground State for complex **3**

MO No.	MO	E (eV)	Contribution (%)						Contribution
			Ni	Cl	Azo	NH_2	Quino	Ph	
87	L+4	-0.20	1	0	3	0	55	42	π* (Quino + Ph)
86	L+3	-1.33	0	0	0	0	99	1	π* (Quino)
85	L+2	-1.78	58	11	10	10	9	2	$d_{x^2-y^2}$ + π* (Cl + Azo + NH_2 +Quino)
84	L+1	-2.11	4	0	18	5	58	16	d_{xy} + π* (Azo + NH_2 +Quino + Ph)
83	LUMO	-2.93	1	0	19	6	54	20	π* (Azo + NH_2 +Quino + Ph)
82	HOMO	-5.54	12	6	12	19	11	39	d_{xy} + π (Cl + Azo + NH_2 +Quino+ Ph)
81	H–1	-6.51	25	32	5	3	9	26	d_{xz}+ π (Cl + Azo + NH_2 +Quino+ Ph)
80	H–2	-6.74	71	24	2	2	0	0	d_{z^2}+ π (Cl)
79	H–3	-6.77	11	32	5	0	36	16	d_{yz} π (Cl + Quino+ Ph)
78	H–4	-6.83	29	67	0	0	2	0	d_{xy} + π (Cl)

The calculated vertical transitions were estimated from the equilibrium geometry of the singlet ground state (S_0) and can be defined as one-electron excitations of the molecular orbitals of the corresponding S_0 geometry. The suitable transitions along with their corresponding energies, oscillator strengths (*f*) and characters are tabulated in Table 3.10–3.15.

For ligand **1**, absorption band at 431 nm is calculated to around 463 nm (f = 0.4157, 2.6749 eV) and is mostly [π (Azo + Quino + NH_2 + Ph) & d_{xz} → π* (Azo + Quino + NH_2 + Ph)] π→ π* character. The next absorption at 336 nm (3.4432 eV, f = 0.4171) is computed at 360 nm and it can be ascribed as π→ π* [π (Azo + Quino + NH_2 + Ph) & d_{yz} → π* (Azo + Quino + NH_2 + Ph)] transition. The 251 nm band is calculated at 284 nm (4.3626 eV, f = 0.0647) which can be assigned as [π (Azo + Quino + Ph) & π (Azo + Quino + NH_2 + Ph) → π* (Azo + Quino

+ Ph)]. The 281 nm band is calculated at 281.63 nm which can assigned as [π (Ph + PPh_3) → π* (Ph + PPh_3)] π→ π* character. The last band at 230 nm is comprised of two transitions at about 227 nm (4.3626 eV, *f* = 0.0647) which are assigned as [π (Azo + Quino + Ph) & π (Azo + Quino + NH_2 + Ph) → π* (Azo + Quino + Ph), π (Azo + Quino + Ph) & π (Azo + Quino + NH_2 + Ph) → π* (Azo + Quino + Ph)] π→ π* type transition (Table 3.10 and 3.13).

In complex **2**, the lowest energy band in the higher part of visible region at 628 nm is computationally obtained near 540 nm (2.2926 eV, *f* = 0.0985) which is composed of two transitions. Both transitions are assigned as LLCT, MLCT and d-d character [π (Azo + Quino + NH_2 + Ph) & d_{xz} → π* (Azo + Quino + NH_2 + Ph) & π (Ac) & d_z^2 → π* (Ac + NH_2) & d_z^2 → $d_{x^2-y^2}$]. The next higher energy absorption band is attributed to LLCT & MLCT type [π (Azo + Quino + NH_2 + Ph) & d_{yz} → π* (Azo + Quino + NH_2 + Ph)] which is computed at 383 nm (3.2299 eV, *f* = 0.4211). The highest energy band around 236 nm is computed at 226 nm (5.4777 eV, *f* = 0.2781), and this is primarily assigned as MLCT & LLCT [d_{xy} → π* (Azo + Quino + Ph) & π (Azo + Quino + NH_2 + Ph) → π* (Azo + Quino + Ph)] transition (Table 3.11 and 3.14).

In case of complex **3**, the band with lowest energy at 630 nm is computed at 552 nm (2.2451 eV, *f* = 0.1513) which is a combination LLCT & MLCT [π (Azo + NH_2 + Ph) & d_{xz} → π* (Azo + Quino + NH_2 + Ph)] character. The very next band appears at 404 nm and calculated near 388 nm (3.1895 eV, *f* = 0.3135) having mostly ILCT & MLCT [π (Azo + Quino + NH_2 + Ph) & d_{yz} → π* (Azo + Quino + NH_2 + Ph)] character. Finally, the highest energy band is observed at 237 nm which is theoretically computed at near 231 nm (5.3563 eV, *f* = 0.5780) is mainly composed of MLCT & LLCT [π (Cl) & $d_{x^2-y^2}$ → π* (Quino)] type transition (Table 3.12 and 3.15). Although the calculated and experimental spectra of ligand and complexes are more or less similar, there are slight differences that may be attributed to limitations of theoretical approach that we have taken into consideration for the complexes.

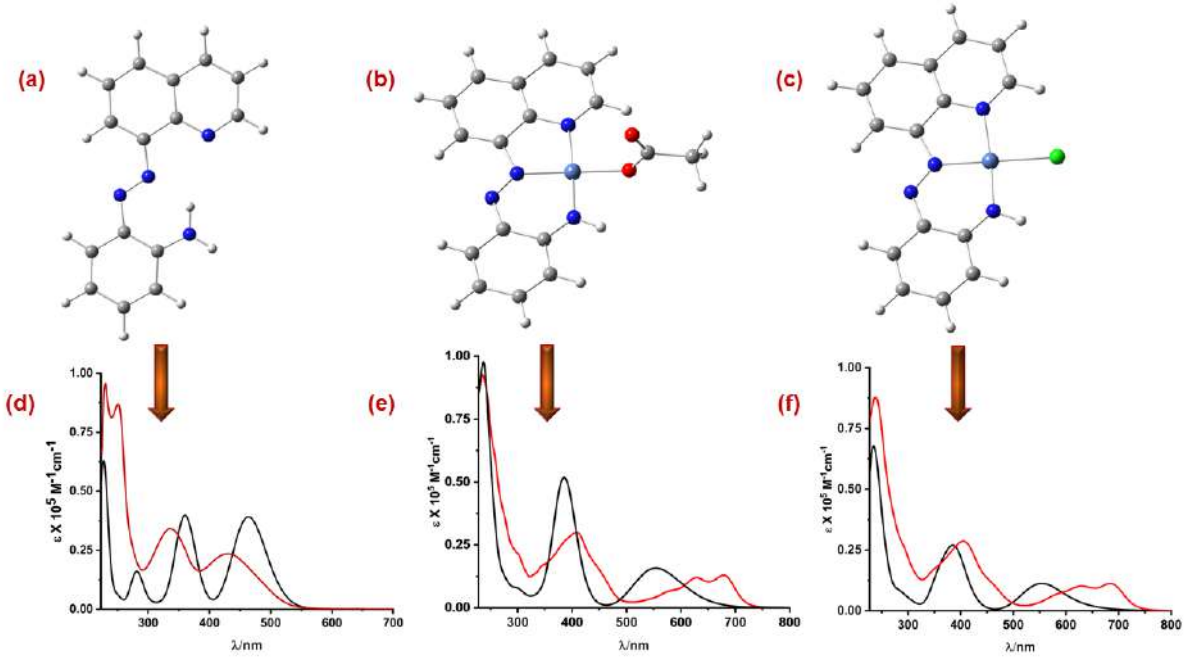

Figure 3.6: (a) Optimised geometry of ligand **1** at (R)B3LYP/6-311G(d,p) level of theory. **(b)** & **(c)** optimised geometry of complex **2** & **3** at (R)B3LYP/6-311+G(d,p) level of theory. **(d)**, **(e)** & **(f)** Experimental (red) and calculated absorption spectra (black) of ligand **1**, complex **2** & **3** respectively

Table 3.10: Main Optical Transition at the TD-DFT/B3LYP/6-311G(d,p) Level for the ligand **1** with composition in terms of Molecular Orbital Contribution of the Transition, Computed Vertical Excitation Energies and Oscillator Strength in Dichloromethane

Transition	CI	Composition	E(eV)	Oscillator Strength (*f*)	λ_{theo}(nm)
$S_0 \rightarrow S_2$	0.70319	HOMO → LUMO (99%)	2.6749	0.4157	463.50
$S_0 \rightarrow S_3$	0.69632	H–2→ LUMO (97%)	3.4432	0.4171	360.08
$S_0 \rightarrow S_8$	0.59697	H–4→ LUMO (71%)	4.3626	0.0647	284.20
$S_0 \rightarrow S_{17}$	0.35326 0.34483	H–2→ L+2 (25%) HOMO→ L+4 (24%)	5.4450	0.4342	227.70

Table 3.11: Main Optical Transition at the TD-DFT/B3LYP/6-311+G(d,p) Level for the complex **2** with composition in terms of Molecular Orbital Contribution of the Transition, Computed Vertical Excitation Energies and Oscillator Strength in Dichloromethane

Transition	CI	Composition	E(eV)	Oscillator Strength (*f*)	λ_{theo}(nm)
$S_0 \rightarrow S_3$	0.56371 0.34281	HOMO → LUMO (64%) H–1→ L+2 (24%)	2.2926	0.0985	540.81
$S_0 \rightarrow S_8$	0.66477	H–2→ LUMO (88%)	3.2299	0.4211	383.86
$S_0 \rightarrow S_{40}$	0.47611	H–4→ L+3 (45%)	5.4777	0.2781	226.34

Table 3.12: Main Optical Transition at the TD-DFT/B3LYP/6-311+G(d,p) Level for the complex **3** with composition in terms of Molecular Orbital Contribution of the Transition, Computed Vertical Excitation Energies and Oscillator Strength in Dichloromethane

Transition	CI	Composition	E(eV)	Oscillator Strength (*f*)	λ_{theo}(nm)
$S_0 \rightarrow S_3$	0.67265	HOMO → LUMO (90%)	2.2451	0.1513	552.24
$S_0 \rightarrow S_8$	0.67084	H–1→ LUMO (90%)	3.1895	0.3135	388.72
$S_0 \rightarrow S_{41}$	0.50871	H–3→ L+3 (52%)	5.3563	0.5780	231.47

Table 3.13: Natural transition orbitals (NTOs) for ligand **1** illustrating the nature of singlet excited states in the absorption bands in the range 200-800 nm. For each state, the respective number of the state, transition energy (eV), and the oscillator strength (in parentheses) are listed. Shown are only occupied (holes) and unoccupied (electrons) NTO pairs that contribute more than 20% to each excited state.

Expt. λ_{max}		Hole	Electron
431 nm	S_2 w = 0.9889 2.6749 (0.4157) 463.50 nm π (Azo + Quino + NH_2 + Ph) & d_{xz} → π* (Azo + Quino + NH_2 + Ph)	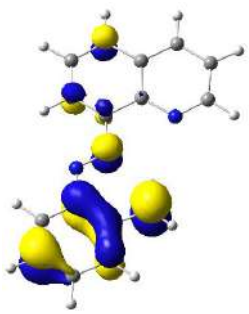	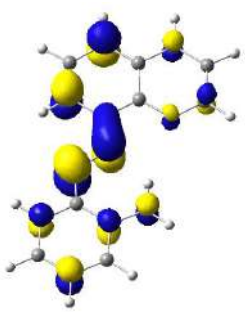

336 nm	*S_3* w = 0.9697 3.4432 (0.4171) 360.08 nm π (Azo + Quino + NH_2 + Ph) & d_{yz} → π* (Azo + Quino + NH_2 + Ph)	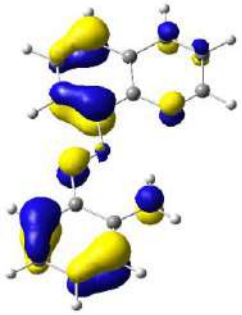	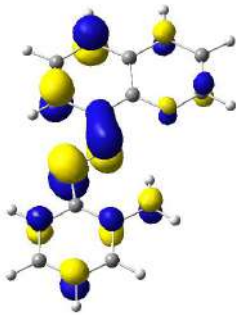
251 nm	*S_8* w = 0.7127 4.3626 (0.0647) 284.20 nm π (Azo + Quino + Ph) & π (Azo + Quino + NH_2 + Ph) → π* (Azo + Quino + Ph)	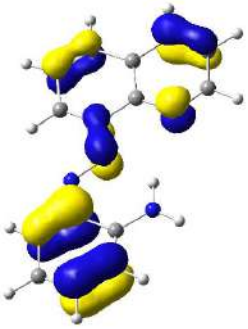	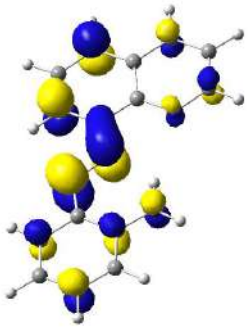
230 nm	*S_{17}* w = 0.2495 5.4450 (0.4342) 227.70 nm π (Azo + Quino + Ph) & π (Azo + Quino + NH_2 + Ph) → π* (Azo + Quino + Ph)	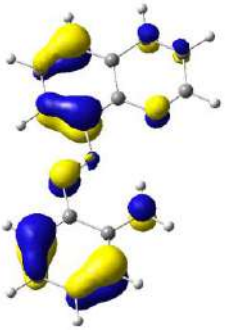	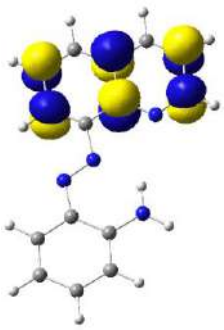
	S_{17} w = 0.2378 5.4450 (0.4342) 227.70 nm π (Azo + Quino + Ph) & π (Azo + Quino + NH_2 + Ph) → π* (Azo + Quino + Ph)	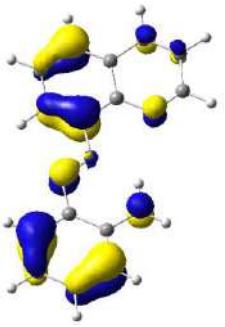	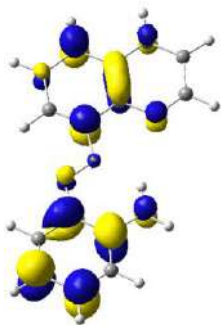

Table 3.14: Natural transition orbitals (NTOs) for complex **2** illustrating the nature of singlet excited states in the absorption bands in the range 200-800 nm. For each state, the respective number of the state, transition energy (eV), and the oscillator strength (in parentheses) are listed. Shown are only occupied (holes) and unoccupied (electrons) NTO pairs that contribute more than 20% to each excited state

Expt λ_{max}		**Hole**	**Electron**
628 nm	*S*3 w = 0.6355 2.2926 (0.0985) 540.81 nm LLCT & MLCT π (Azo + Quino + NH_2 + Ph) & d_{xz} → π* (Azo + Quino + NH_2 + Ph)	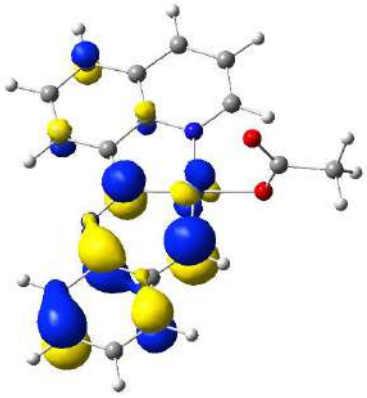	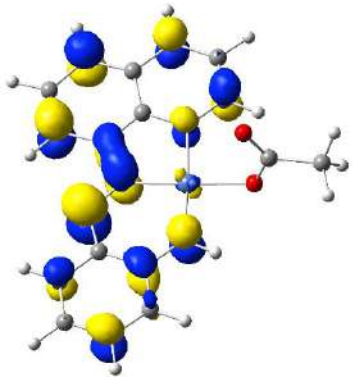
	*S*3 w = 0.2350 2.2926 (0.0985) 540.81 nm LLCT, MLCT & d-d π (Ac) & d_{z^2} → π* (Ac + NH_2) & d_{z^2} → $d_{x^2-y^2}$	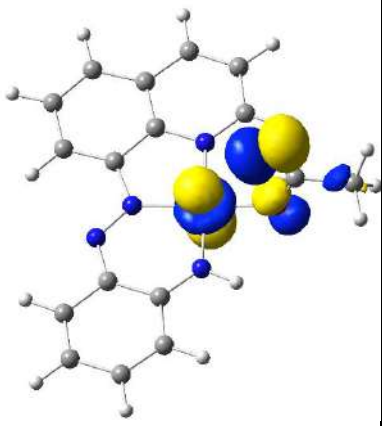	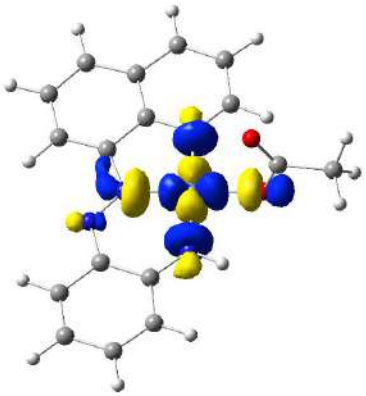
405 nm	*S*8 w = 0.8838 3.2299 (0.4211) 383.86 nm LLCT & MLCT π (Azo + Quino + NH_2 + Ph) & d_{yz} → π* (Azo + Quino + NH_2 + Ph)	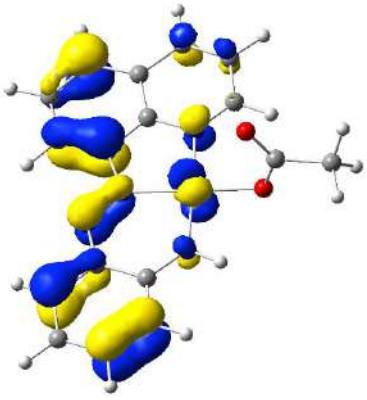	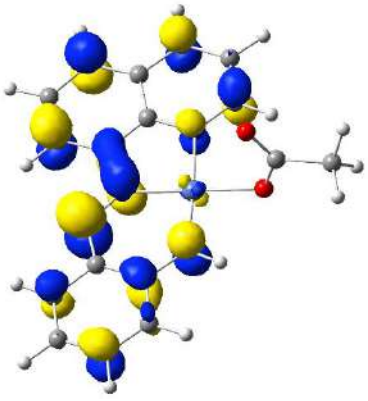

236 nm	S_{41} w = 0.4533 5.4777 (0.2781) 226.34 nm MLCT & LLCT $d_{xy} \rightarrow \pi^*$ (Azo + Quino + Ph) & π (Azo + Quino + NH_2 + Ph) $\rightarrow \pi^*$ (Azo + Quino + Ph)	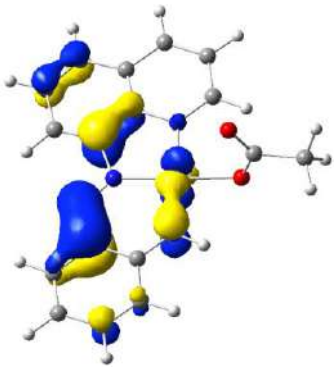	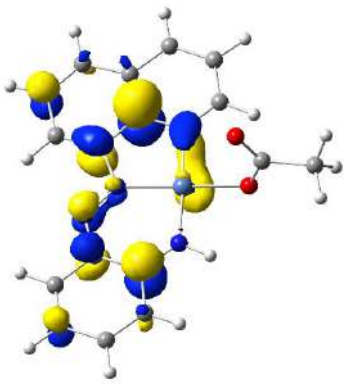

Table 3.15: Natural transition orbitals (NTOs) for complex **3** illustrating the nature of singlet excited states in the absorption bands in the range 200-800 nm. For each state, the respective number of the state, transition energy (eV), and the oscillator strength (in parentheses) are listed. Shown are only occupied (holes) and unoccupied (electrons) NTO pairs that contribute more than 20% to each excited state

Expt. λ_{max}		**Hole**	**Electron**
630 nm	S_3 w = 0.9049 2.2451 (0.1513) 552.24 nm LLCT & MLCT π (Azo + NH_2 + Ph) & $d_{xz} \rightarrow \pi^*$ (Azo + Quino + NH_2 + Ph)	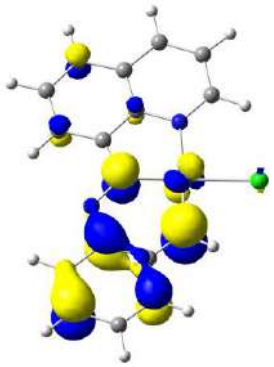	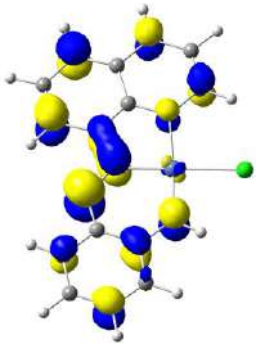
404 nm	S_8 w = 0.9000 3.1895 (0. 3135) 388.72 nm ILCT & MLCT π (Azo + Quino + NH_2 + Ph) & $d_{yz} \rightarrow \pi^*$ (Azo + Quino + NH_2 + Ph)	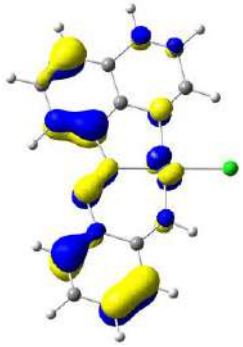	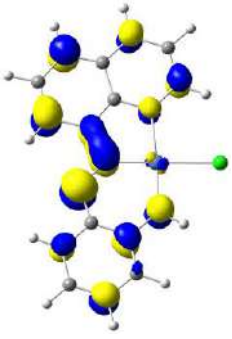

237 nm	S_{41} w = 0.5175 5.3563 (0.5780) 231.47 nm MLCT & LLCT π (Cl) & $d_{x^2-y^2}$ → π* (Quino)	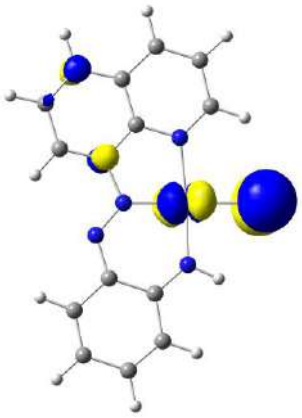	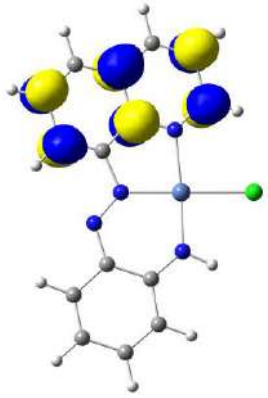

3.2.3 Anticancer studies with ligand and complex

The quinoline moiety that is present in the ligand skeleton has been recorded to exhibit anticancer activities.[45] Therefore, to probe the anticancer property of **1**, we have performed MTT assay on human epithelial cancer cell line (HeLa cells) which is widely used for anticancer research. For this purpose, HeLa cells are grown in DMEM media and subsequently treated with various concentration of the ligand. The data revealed that~49 ± 8% cells survived at a concentration of 10 μM (IC_{50}), thereby pointing towards conspicuous anticancer activity of the ligand. However, the anticancer activity remains virtually analogous upon increasing the concentration further up to100 μM. A prime reason for such anticancer activity of the ligand may be owing to intercalation and binding of it with nucleic acids and this is common for quinoline based anticancer drugs such as doxorubicin, streptonigrin, mitoxantrone.[46] The complex **3** is square planar with a labile chloride like that of *cis*-platin and this led us to believe that it may have the potential to exhibit good anti-cancer activity. Thereafter, we embarked to assess the anticancer property with **3** using MTT assay and it revealed that ~65 ± 7% cell death at a concentration of 10 μM, thereby signifying more pronounced anticancer effect in **3** than simple ligand, **1**. (Figure 3.7c)

Cell migration plays a crucial role in growth and maintenance of cellular organisms in the form of wound healing, immune response and so on. Nevertheless, metastatic nature of cancer cells leads to unrestrained growth and movement which is often uncontrolled. Thus, assessing migration speed *in vitro* in presence of potential anticancer agent is an additional method of evaluating anticancer activity of the agent; lesser the migration speed higher will be the ability of the agent to show anticancer properties. Accordingly, cell migration assay has been performed using same cell line using 1% DMSO in DMEM media as control. The ligand **1** and complex **3** showed significant arrest in migration speed- for the complex **3** it is 2.155 µm/h and for ligand (4.363 µm/h) while for the control it is 5.148 µm/h. Quantification of cell migration speed has been tabulated in Table 3.16. The data further supports that anticancer behavior of complex **3** is more effective than that of ligand (Figure 3.7a and 3.7b)

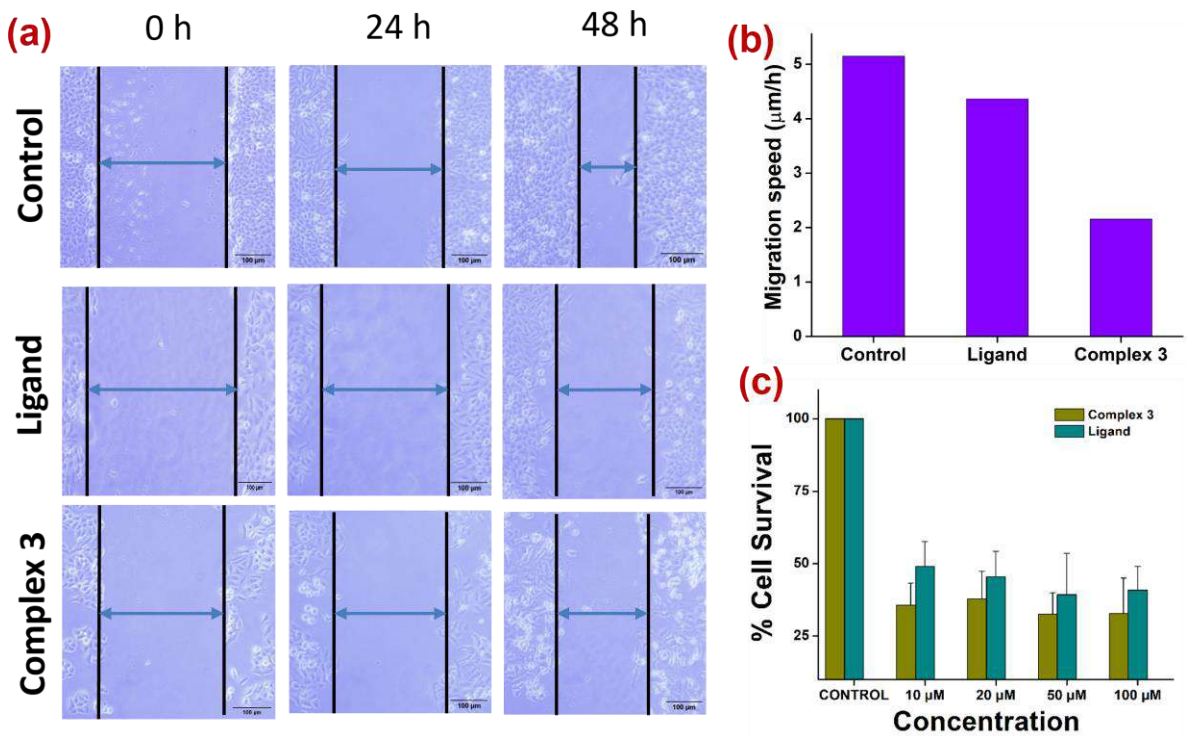

Figure 3.7: a) Cell migration (Scale Bar: 100µm), b) migration speed comparison, and c) MTT assay of complex **3** and ligand in HeLa cells

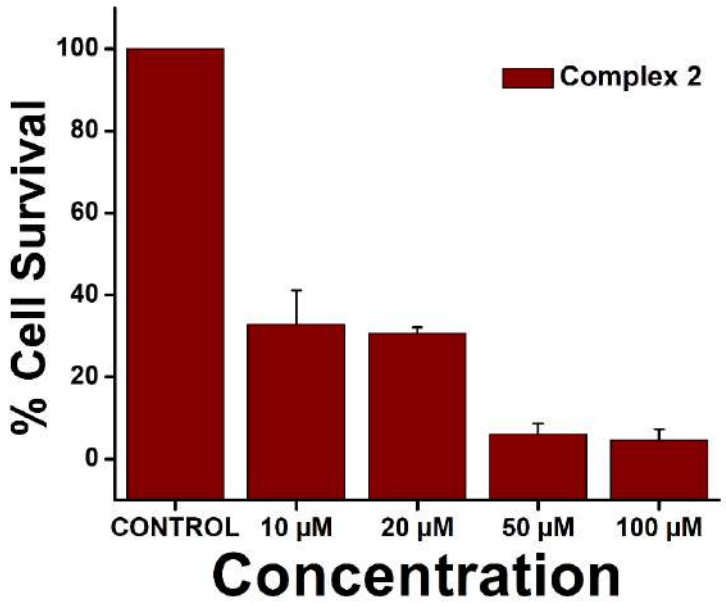

Figure 3.8: MTT assay of complex **2** in HeLa cells

Enhanced concentration of reactive oxygen species (ROS) is one of the markers of cancer and this may be attributed to genetic aberrations or gene mutation, relative hypoxia as well as due to increased metabolic rate.[49,50] In fact, elevated ROS levels can further stimulate tumour growth and they can invade aggressively.[51] However, increase in the concentration of ROS above a cytotoxic threshold can damage proteins, nucleic acids, organelles and therefore is detrimental for cancer cells as well, resulting in cancer cell apoptosis.[52] Thus, several anticancer therapeutics have been designed to abruptly increase the levels of ROS within the cancer cells leading to cell death.[53-55] Since complex **3** exhibits superior anti-cancer activity than that of free ligand **1**, we have tried to rationalize the effect of treatment of **3** in ROS level within the cell. The cells were incubated with **3** in presence of 2′,7′-Dichlorofluorescein diacetate (DCFDA), a non-fluorescent dye, that dissociates in presence of the ROS to give green fluorescence.[56] The data discloses that after 1 h of incubation with **3**, the green fluorescence (proportional to the ROS level) is not so prominent which increases significantly with increase in the time of incubation of 3 h, 4 h and 5 h (Figure 3.9). The data clearly point towards the increase ROS levels in cancer cells that promotes cellular damage, thereby leading

to cancer cell death. The MTT assay and molecular docking studies of **2** have also been performed and these are provided in (Figure 3.8 & 3.6.A9 and Table 3.6.A1).

Table 3.16: Quantification of Cell Migration Speed

	Control	Ligand	Complex 3
0 h	371.13 mm	445.644 mm	305.398 mm
48 h	124.02 mm	236.2 mm	201.92 mm
Gap covered after 48 h	247.11 mm	209.444 mm	103.478 mm
Migration speed	5.148125 mm/h	4.363417 mm/h	2.155792 mm/h

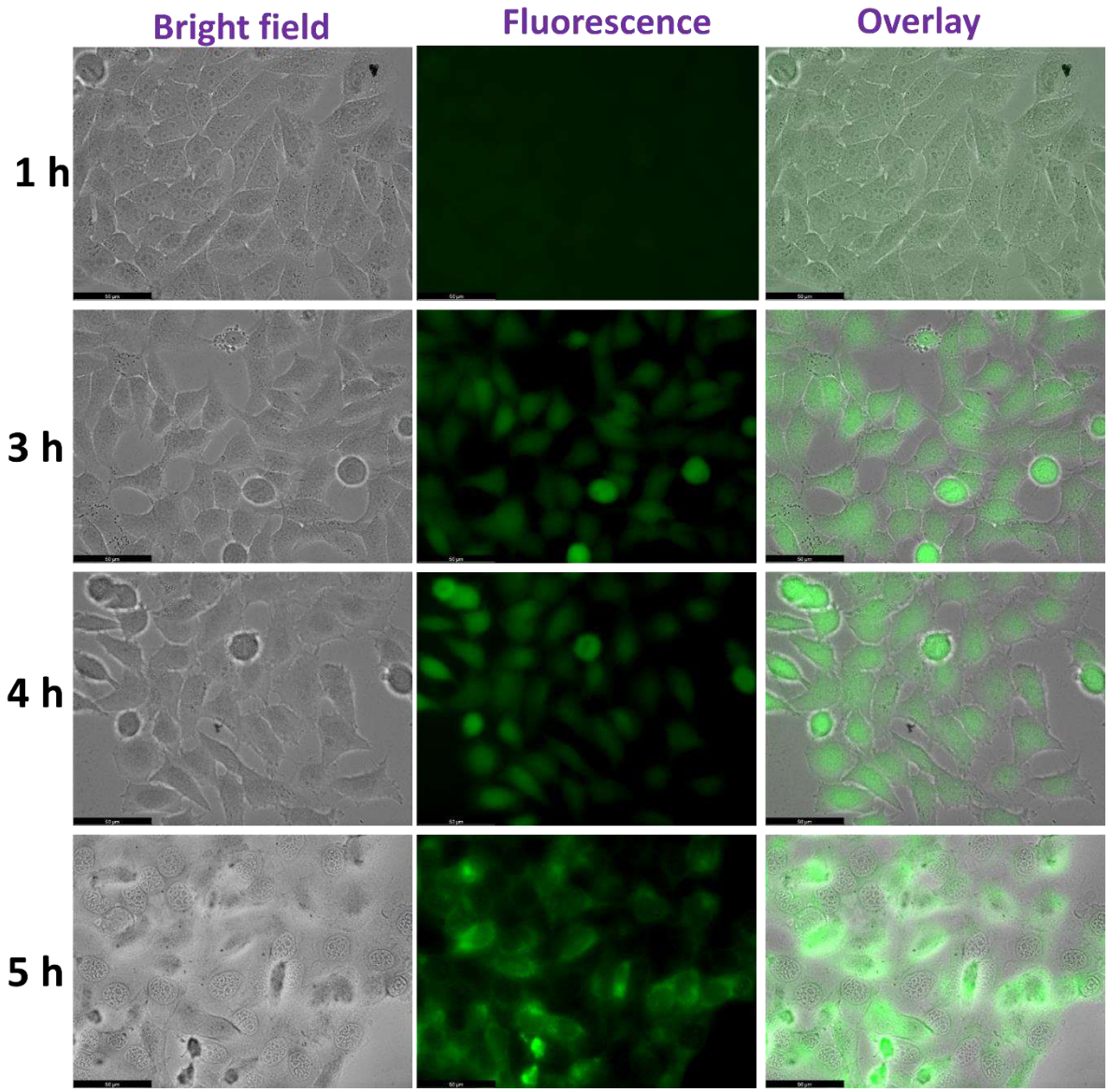

Figure 3.9: Generation of ROS in HeLa cells on the treatment of complex **3** under various incubation times (Scale Bar 50 µm)

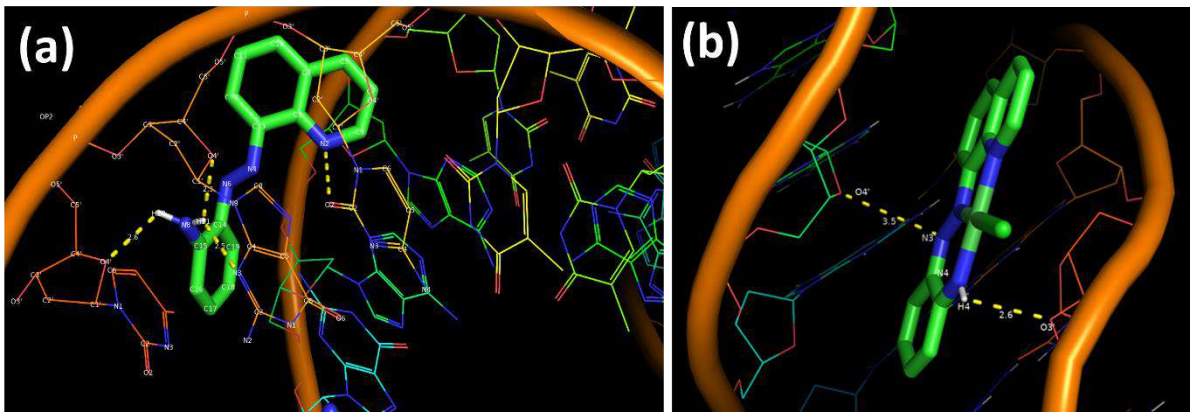

Figure 3.10: Molecular docking results of a) ligand **1** (conformer 4 having highest binding affinity) and b) complex **3** with B-DNA (PDB ID: 1BNA)

It has been well understood that generation of ROS may lead to DNA damage and double strand break (DSB) during cancer.[57-60] With this intuition, we have performed molecular docking analysis using **1** and **3** to comparatively assess the affinity of DNA binding that may increase the oxidative stress within the cells leading to cancer cell death. It is due to flexibility of the ligand skeleton that we have been able to generate nine conformers which lie within 1 eV of the putative global minimum by using Adaptive Mutation Simulated Annealing (Table 3.6.A7).[61] Optimization of nine different molecular conformations of **1** have been performed (Figure 3.6.A1–3.6.A8) and molecular docking with all the nine conformers was carried out to assess their binding affinity with B-DNA (PDB ID: 1BNA). It was found that the binding affinity ranges from ~ -5.5 to -7.5 kcal/mol and this is ascribed to bond rotation within the ligand skeleton that leads to structural deformation from planarity (Figure 3.10, Figure 3.6.A1–3.6.A8 and Table 3.6.A3). Molecular docking with **3** in a similar way revealed higher binding affinity (~ -8.4 kcal/mol) [Figure 3.7b and Table 3.6.A2] and it is presumably due to much higher rigidity of square planar geometry of nickel(II) complex. Conceivably, this allows the formation of stronger H-bonds with nucleotides of the DNA thereby leading to superior anticancer activity of **3** with respect to **1**.

3.3 Conclusion

The current report provides an insight into the synthesis, structure, electrochemistry and anti-blastoma activity of a novel ligand H_2L **1**, containing electron poor azo moiety along with biologically relevant quinoline group and its cost-efficient nickel(II) complexes [Ni(HL)(OAc)] **2** and [Ni(HL)Cl] **3**. The structure of both complexes has been found out by SCXRD and **2** exhibits extensive hydrogen bonding in the crystalline phase, where the solvent water molecules are involved in linking acetate-O and coordinated amino-N of the ligand framework. In both complexes, π–π stacking interactions are involved in further stabilizing the lattices. The novel ligand as well as the complexes have been scrutinized by IR, electronic and NMR spectral techniques. Theoretical investigation of redox orbitals reveals that reduction process for both complexes are attributed to the coordinated ligand since π*-LUMO is practically of ligand character. On the other hand, there is some contribution of the nickel centre along with ligand during the oxidative events. We have assessed the anti-cancer properties of the ligand and nickel (II) complexes in the form of MTT assay. Cell migration as well as generation of ROS by using HeLa cells for the ligand and one of the complexes have been carried out. Both the ligand and complexes have been found to exhibit efficacious anti-cancer activity but it is more encouraging in the case of latter. This may be attributed to rigid and robust nature of square planar geometry of complexes, which possibly accounts for stronger binding with DNA with respect to that of the more flexible free ligand. These results have been further corroborated by molecular docking by using nine conformers of the ligand as well as with both complexes *via* interaction with B-DNA (PDB ID: 1BNA).

3.4 Experimental Section

3.4.1 General Information

All the reactions revealed in this work were performed under aerobic conditions. The necessary reagents and solvents were used as soon as they received. 8-Aminoquinoline & *o*-Phenylenediamine were purchased from BLD Pharmatech Ltd. Nickel(II) acetate tetrahydrate, Nickel(II) Chloride hexahydrate were purchased from Sigma Aldrich. *o*-nitroso acetanilide was synthesized according to literature method.[62] Cell lines were purchased and maintained using the guidelines of the American Type Culture Collection (ATCC). MTT (3-(4,5-Dimethylthiazol-2-yl)-2,5-diphenyltetrazolium bromide) dye was purchased from Sigma Aldrich India and DCFDA (2′,7′-Dichlorofluorescin Diacetate) dye was purchased from TCI India Pvt. Ltd. and used without further purification.

3.4.2 Synthesis of ligand 1

8-Aminoquinoline (1 g, 6.93 mmol, 1.0 equiv.) was dissolved in dry toluene and degassed with a gentle stream of nitrogen for about 15 min. To this solution, *o*-nitrosoacetanilide (1.137 g, 6.93 mmol, 1.0 equiv.) was added followed by addition of acetic acid (3ml) and the reaction mixture was stirred at 65°C for 36 h. After completion of the reaction, dark red coloured solution was evaporated under reduced pressure to remove volatile organic impurities. The pure compound was isolated as red solid after column chromatography using silica gel (100-200 mesh) and hexane/EtOAc mixture (2:1 v/v) as eluent (Yield: 74%, 1.5 g). The solid was then dissolved in 60 ml EtOH and an aqueous solution of KOH (30% w/v) in EtOH (30 ml) was added to it. The dark red coloured solution was then refluxed for about 90 min. Thereafter, the reaction mixture was cooled to room temperature, poured into crushed ice (300 g) and extracted with CH_2Cl_2. The desired compound was obtained as dark red solid and recrystallised from warm heptane solution. Yield: 95%, 1.25 g.

3.4.3 Analytical data of ligand 1

***(E)-2-(quinolin-8-yldiazenyl)aniline*: HRMS:** [M+H] *m/z* = 249.1141 (calcd. 249.1140); **^{1}H NMR (400 MHz, $CDCl_3$):** δ 9.07 (d, *J* = 7.6 Hz, 1H), 8.24 (d, *J* = 9.3 Hz, 1H), 7.99 (dd, *J* = 7.6, 3.8 Hz, 2H), 7.90 (dd, *J* = 8.1, 2.9 Hz, 1H), 7.69 – 7.63 (m, 1H), 7.51 (dt, *J* = 8.0, 3.6 Hz, 1H), 7.21 (d, *J* = 7.0 Hz, 1H), 6.88 – 6.77 (m, 4H). **^{13}C{^{1}H} NMR (75 MHz, $CDCl_3$):** δ 151.14, 148.61, 144.56, 142.02, 138.35, 136.19, 132.22, 132.04, 129.74, 129.27, 126.81, 121.73, 117.33, 116.98, 114.71. **IR (cm^{-1}):** 3470 (ν_{N-H}, stretch), 3387 (ν_{N-H}, stretch), 1610 (ν_{N-H}, bend) and 1488 ($\nu_{N=N}$, stretch).

3.4.4 Synthesis of complex 2 and 3

The azo amine ligand, **1** (25 mg, 0.1 mmol, 1.0 equiv.) was dissolved in reagent grade EtOH in a 50 ml round bottom flask equipped with magnetic stirring bar. The corresponding solid nickel salt (0.15 mmol, 1.5 equiv.) was added to the above solution and stirred for about 4-6 h. After completion of reaction the solution was evaporated to dryness and washed with cold hexane to remove the unreacted ligand (if any). It was further dissolved in dichloromethane, the supernatant liquid decanted off (to discard the excess metal salt) and further evaporated to dryness to obtain a green residue. Suitable single crystals for SCXRD study were obtained by solvent diffusion method (where residue was dissolved in dichloromethane solution and taken in a test tube with glass stopper; *n*-hexane was then added carefully to the above the DCM solution and allowed to diffuse slowly).

3.4.5 Analytical data of complex 2 and 3

2: The complex was synthesized according to the above-mentioned procedure. Yield: 70%, 25 mg; **HRMS:** [M–OAc] *m/z* = 305.0332 (calcd. 305.0337); **^{1}H NMR (300 MHz, $CDCl_3$):** δ 8.47 (dd, *J* = 5.1, 1.4 Hz, 1H), 8.31 (ddd, *J* = 13.4, 7.0, 2.3 Hz, 2H), 7.94 (br s, 1H), 7.64 – 7.52 (m, 3H), 7.43 (d, *J* = 8.8 Hz, 1H), 7.00 (ddd, *J* = 8.2, 6.4, 1.5 Hz, 1H), 6.81 (d, *J* = 8.3 Hz, 1H),

6.57 (ddd, *J* = 8.8, 6.4, 1.2 Hz, 1H), 2.11 (s, 3H). **$^{13}C\{^{1}H\}$ NMR (75 MHz, $CDCl_3$):** δ 180.18, 150.81, 149.00, 141.41, 140.27, 138.63, 131.80, 130.90, 129.18, 127.78, 124.23, 122.27, 120.96, 118.26, 117.32, 100.14, 25.49. **IR (cm^{-1}):** 3436 (ν_{O-H}, stretch), 3173 (ν_{N-H}, stretch), 1600 (ν_{N-H}, bend) and 1505 ($\nu_{N=N}$, stretch).

3: The complex was synthesised according to above mentioned procedure. Yield: 67%, 23 mg; **HRMS:** [M–Cl] *m/z* = 305.0332 (calcd. 305.0337); **^{1}H NMR (300 MHz, $CDCl_3$):** δ 9.19 (s, 1H), 8.36 – 8.22 (m, 2H), 7.65 – 7.52 (m, 2H), 7.51 – 7.35 (m, 2H), 6.99 (ddd, *J* = 8.4, 6.4, 1.5 Hz, 1H), 6.66 (d, *J* = 8.8 Hz, 1H), 6.60 – 6.49 (m, 1H), 6.03 (br s, 1H). **$^{13}C\{^{1}H\}$ NMR (101 MHz, $CDCl_3$):** δ 152.99, 150.93, 140.61, 140.59, 138.67, 137.72, 132.35, 131.06, 129.15, 127.88, 124.85, 122.52, 120.89, 118.38, 117.62. **IR (cm^{-1}):** 3338 (ν_{N-H}, stretch), 3056 (ν_{N-H}, stretch), 1614 (ν_{N-H}, bend) and 1504 ($\nu_{N=N}$, stretch).

3.4.6 Biological Studies

MTT Assay: Anticancer activity of the ligand and complex **3** was analyzed using standard protocol for MTT assay in HeLa cell lines. Briefly, culture media was prepared by adding 1% penicillin-streptomycin and 10% Fetal Bovine Serum as supplement in the Dulbecco's Modified Eagle's Medium (DMEM). The cells were then cultured in the DMEM media in a humidified CO_2-incubator maintaining the condition at 37 °C and 5% CO_2. Moreover,~ 10^4 cells (counted using hemocytometer) were seeded in a 96 well plate maintaining similar conditions. After 24 h, different concentrations of ligands and complex 3 in 1% DMSO in DMEM were added separately and further incubated for 72 h inside the incubator. For control experiment, only 1% DMSO in DMEM media was used. MTT dye was then dissolved in DMEM media maintaining concentration of 1mg/ml and added to the each well after discarding the culture media and further incubated for 2 h. The formazan produced was then dissolved by

adding 100 ml DMSO per well and further incubated for 1 h. Absorbance data for each well was determined using BIO-RAD iMark ELISA reader at 590 nm.

Cell migration assay:

HeLa cells were cultured in 6-well plate and scratch was introduced using a 200 µL sterile tip. After discarding the culture media, solutions of the ligand 1 and complex 3 were added maintaining the final concentration of 5 µM in 1% DMSO in DMEM media. For control experiment, only 1% DMSO in DMEM media was used. Images at different time frames were taken using Magnus INVI optical microscope at 20x optical zoom.

Intracellular ROS determination:

Formation of reactive oxygen species (ROS) inside the HeLa cells after treatment of complex **3** was determined by using DCFDA (2′,7′-Dichlorofluorescin Diacetate) dye. Cells were treated with complex **3** at a concentration of 5 µM in 1% DMSO in DMEM media. Development of intracellular ROS after different time frame was monitored by incubating the cells with 5 µM DCFDA dye for 15 min followed by washing thrice with PBS. Images were taken in a LEICA Microscope DM4B With Leica DFC3000DIGITAL Camera LED1 Fluroscent Light and LAIX MULTI CHANNEL.

3.5 References

[1] Y. Yang, O. Adebali, W. Gang, C. P. Selby, Y. Chiou, N. Rashid, H. Jinchuan, J. B. Hogenesch, A. Sancar, *Proc. Nat. Acad. Sci.*, **2018**, *115*, E4777–E4785.

[2] G. Y. Ho, N. Woodward, J. I. G. Coward, *Crit. Rev. Oncol. Hematol.*, **2016**, *102*, 37–46.

[3] S. Dasari, P. B. Tchounwou, *Eur. J. Pharmacol*., **2014**, *5*, 364–378.

[4] E. E. Trimmer, John M. Essigmann, Cisplatin, *Essays Biochem.*, **1999**, *34*, 191–211.

[5] A. Upadhyay, S. Gautam, V. Ramu, P. Kondaiah, A. R. Chakravarty, *Dalton Trans.*, **2019**, *48*, 17556–17565.

[6] A. Bera, A. Nepalia, A. Upadhyay, D. K. Saini, A. R. Chakravarty, *Dalton Trans.*, **2023**, *52*, 13339–13350.

[7] N. P. Farrell, *Chem. Soc. Rev.*, **2015**, *44*, 8773–8785.

[8] C. Disler, P. Perego, *Nature Reviews Cancer*, **2021**, *21*, 37–50.

[9] N. J. Wheate, J. G. Collins, *Coord. Chem. Rev.*, **2003**, *241*, 133–145.

[10] S. Su, Y. Chen, P, Zhang, R. Ma, W. Zhang, J. Liu, T. Li, H. Niu, Y. Cao, B. Hu, J. Gao, H. Sun, D. Fang, J. Wang, P. G. Wang, S. Xie, C. Wang, J. Ma, *European Journal of Medicinal Chemistry*, **2022**, *243*, 114680–114699.

[11] B. Michalke, *Journal of Trace Elements in Medicine and Biology*, **2010**, *24*, 69–77.

[12] G. Giaccone, R. S. Herbst, C. Manegold, G. Scagliotti, R. Rosell, V. Miller, R.B. Natale, J. H. Schiller, J. von Pawel, A. Pluzanska, U. Gatzemeier, J. Grous, J. S. Ochs, S. D. Averbuch, M. K. Wolf, P. Rennie, A. Fandi, D.H. Johnson, *J. Clin. Oncol*. **2004**, *22*, 777–784.

[13] C. Zhang, C. Xu, X. Gao, Q. Yao, *Theranostics*, **2022**, *12*, 2115–2132.

[14] R. Sharma, V. J. Singh, P. A. Chawla, *Anti-Cancer Agents in Medicinal Chemistry*, **2022**, *22*, 821–835.

[15] J. Jeon, S. Lee, H. Kim, H. Kang, H. S. Youn, S. Jo, B. H. Youn, H. Y. Kim, *Int. J. Mol. Sci.*, **2021**, *22*, 5111–5130.

[16] T. S. Prathima, B, Choudhury, Md. G. Ahmad, K. Chanda, M. M. Balamurali, *Coord. Chem. Rev.*, **2023**, 490, 215231–215278.

[17] M. Shahlaei, S. M. Asl, A. Derakhshani, L. Kurek, J. Karges, R. Macgregor, M. Saeidifar, I. Kostova, A. A. Saboury, *J. Mol. Struct.*, **2024**, *1301*, 137366–137383.

[18] P. Biswas, P. Dastidar, *Inorg. Chem.*, **2021**, *60*, 3218–3231.

[19] T. Q. Manhee, A. J. Alabdali, *Vietnam Journal of Chemistry*, **2024**, *62*, 201–210.

[20] Z. M. Abdnoor, A.J. Alabdali, *Journal of the Chinese Chemical Society*, **2019**, *66*, 1474–1483.

[21] S. Bera, H. K. Datta, P. Dastidar, *ACS Appl. Mater. Interfaces*, **2023**, *15*, 25098–25109.

[22] S. Karim, S. Halder, S. Mukherjee, U. Debnath, A. K. Misra, K. Jana, D. Das, *ACS Appl. Mater. Interfaces*, **2023**, *15*, 26442–26456.

[23] W. A. Wani, U. Baig, S. Shreaz, R. A. Shiekh, Prince F. Iqbal, E. Jameel, A. Ahmad, S. H. Mohd-Setapar, M. Mushtaqueh, L. T. Hun, *New J. Chem.*, **2016**, *40*, 1063–1090.

[24] G. Jaouen, A. Vessières, S. Top, *Chem. Soc. Rev.*, **2015**, *44*, 8802–8817.

[25] P. Graván, S. Rojas, D. F. Picchi, F. Galisteo-González, P. Horcajada, J. A. Marchal, *Nanomaterials*, **2024**, *14*, 784–794.

[26] C. R. Munteanu, K. Suntharalingam, *Dalton Trans.*, **2015**, *44*, 13796–13808.

[27] K. Kar, D. Ghosh, B. Kabi, A. Chandra, *Polyhedron*, **2022**, *222*, 115890–115919.

[28] D. Lison, S. van den Brule, G. Van Maele-Fabry, *Critical Reviews in Toxicology*, **2018**, *48*, 522–539.

[29] B. Ay, İ. Gönül, B. S. Demir, Y. Saygıdeğer, İ. Kani, *Inorg. Chem. Commun*., **2020**, *114*, 107824–107831.

[30] L. Masaryk, B. Tesarova, D. Choquesillo-Lazarte, V. Milosavljevic, Z. Heger, P. Kopel, *J. Inorg. Biochem.*, **2021**, *217*, 111395–111404.

[31] Md. A. Arafath, F. Adam, M. R. Razali, L. E. A. Hassan, M. B. K. Ahamed, A. Malik, S. A. Majid, *Journal of Molecular Structure*, **2017**, *1130*, 791–798.

[32] B. Ay, O. Şahin, B. S. Demir, Y. Saygideğer, J. M. López de Luzuriaga Fernández, G. Mahmoudi, D. A. Safin, *New J. Chem.*, **2020**, *44*, 9064–9072.

[33] T. Damena, M. B. Alem, D. Zeleke, T. Desalegn, R. Eswaramoorthy, T. B. Demissie, *Front. Chem.*, **2022**, *10*, 1053532–1053552.

[34] Q. Yang, Q. Cao, Q. Qin, C. Deng, H. Liang, Z. Chen, *Int. J. Mol. Sci.,* **2018**, *19*, 1874–1890.

[35] U. M. Rafi, D. M. A. K. Haleel, R. P. Nankar, M. Dobleb, A. K. Rahiman, *New J. Chem.*, **2016**, *40*, 2451–2465.

[36] J. Roy, A. Kyani, M. Hanafi, Y. Xu, J. Takyi-Williams, D. Sun, E. E. A. Osman, N. Neamat, *J. Med. Chem.*, **2023**, *66*, 1990–2019.

[37] O. O. Ajani, K. T. Iyaye, O. T. Ademosun, *RSC Adv*., **2022**, *12*, 18594–18614.

[38] K. Marciniec, Z. Rzepka, E. Chrobak, S. Boryczka, M. Latocha, D. Wrze´sniok, A. Beberok, *Molecules*, **2023**, *28*, 2509–2526.

[39] L. Ravindar, S. A. Hasbullah, K. P. Rakesh, S. Raheem, H. K. Agustar, N. Ismail, L. Y. Ling, N. I. Hassan, *European Journal of Medicinal Chemistry*, **2024**, *264*, 116043–116069.

[40] A. R. Bhat, Tazeem, A. Azam, I. Choi, F. Athar, *European Journal of Medicinal Chemistry*, **2011**, *46*, 3158–3166.

[41] S. M. Nkosi, K. Anand, S. Anandakumar, S. Singh, A. A. Chuturgoon, R. M. Gengan, *Journal of Photochemistry and Photobiology B: Biology*, **2016**, *165*, 266–276.

[42] H. R. Sonawane, B. T. Vibhute, B. D. Aghav, J. V. Deore, S. K. Patil, *European Journal of Medicinal Chemistry*, **2023**, *258*, 115549–15274.

[43] Md. S. Hossain, C. M. Zakaria, Md. Kudrat-E-Zahan, *American Journal of Heterocyclic Chemistry*, **2018**, *4*, 1–21.

[44] N. S. H. H. Damit, M. H. S. A. Hamid, N. S. R. H. A. Rahman, S. N. H. H. Ilias, N. A. Keasberry, *Inorg. Chim. Acta*, **2021**, *527*, 120557–120565.

[45] K. P. Chennam, M. Ravi, B. Ushaiah, V. Srinu, R. K. Eslavath, C. S. Devi, *J Fluoresc*., **2016**, *26*, 189–205.

[46] A. Keivanloo, M. Fakharian, S. Sepehri, *Journal of Molecular Structure*, **2020**, *1202*, 127262–127271.

[47] S. Jain, V. Chandra, P. K. Jain, K. Pathak, D. Pathak, A. Vaidya, *Arabian Journal of Chemistry*, **2019**, *12*, 4920–4946.

[48] A. Ryckebusch, D. Garcin, A. Lansiaux, J. -F. Goossens, B Baldeyrou, R. Houssin, C. Bailly, J.-P. Hénichart, *J. Med. Chem.*, **2008**, *51*, 3617–3629.

[49] M Schieber, N. S. Chandel, *Curr Biol*, **2014**, *24*, R453–R462.

[50] B. Perillo, M. Di Donato, A. Pezone, E. Di Zazzo, P. Giovannelli, G. Galasso, G. Castoria, A. Migliaccio, *Exp Mol Med.*, **2020**, *52*, 192–203.

[51] M. A. Shah, H. A. Rogoff, *Seminars in Oncology*, **2021**, *48*, 238–245.

[52] A. Q. Khan, K. Rashid, A. A. AlAmodi, M. V. Agha, S. Akhtar, I. Hakeem, S. S. Raza, S. Uddin, *Biomedicine & Pharmacotherapy*, **2021**, *143*, 112142–112156.

[53] A. Siomek, J. Tujakowski, D. Gackowski1, R. Rozalski, M. Foksinski, T. Dziaman, K. Roszkowski, R. Olinski, *Int. J. Cancer*, **2006**, *119*, 2228–2230.

[54] S. J. Dougan, A. Habtemariam, S. E. McHale, S. Parsons, P. J. Sadler, *Proc. Natl. Acad. Sci. USA*, **2008**, *105*, 11628–11633.

[55] H. Nakamura, K. Takada, *Cancer Science.*, **2021**, *112*, 3945–3952.

[56] D. Figueroa, M. Asaduzzaman, F. Young, *Journal of Pharmacological and Toxicological Methods,* **2018**, *94*, 26–33.

[57] A. Maya-Mendozaa, J. Ostrakovaa , M. Kosara, A. Halla, P. Duskovac , M. Mistrikc, J. Maria Merchut-Mayaa, Z. Hodny, J. Bartkovaa, C. Christensena, J. Barteka, *Molecular Oncology*, **2015**, *9*, 601–616.

[58] D. I. Moin, A. K. Mittal, I. Verma, S. Chakraborti, B. K. Ray, S. Roychoudhury, (eds) *Handbook of Oxidative Stress in Cancer: Mechanistic Aspects. Springer, Singapore,* **2022**.

[59] J. Pan, M. She; Z. -Xiang Xu, L. Sun; S. -Ching J. Yeung, *Cancer Res.,* **2005**, *65*, 3671–3681.

[60] U. Sai Srinivasa, B. W.Q. Tana, B. A. Vellayappanb , A. D. Jeyasekharana, *Redox Biology*, **2019**, *25*, 101084–101092.

[61] S. K. Biring, R. Sharma, P. Chaudhury, *Journal of Mathematical Chemistry*, **2014**, *52*, 368–397.

[62] N. Kumari, S. Halder, S. Naskar, S. Ganguly, K. Pramanik, F. Yari, A. Dorniak, W. Schofberger, S. Roy, *Materials Today Catalysis*, **2024**, *5*,100049–100058.

[63] J. Eberhardt, D. Santos-Martins, A. F. Tillack, S. Forli. *J. Chem. Inf. Model.*, **2021**, *61*, 3891−3898.

[64] H. R. Drew, R. M. Wing, T. Takano, C. Broka, S. Tanaka, K. Itakura, R. E. Dickerson, *Proc. Nati. Acad. Sci.*, **1981**, *78*, 2179–2183.

[65] O. Trott, A. J. Olson, *Journal of Computational Chemistry*, **2010**, *31*, 455–461.

[66] W. L. DeLano, The PyMOL Molecular Graphics System (2002) DeLano Scientific, San Carlos, CA, USA.

3.6 Appendix

3.6.1 Molecular Docking Studies

Molecular docking was conducted using AutoDock Tools 1.5.7 and AutoDock Vina software.[63] The crystallographic structures of nickel complexes were used as ligands, converted into PDBQT format for docking. The receptor was taken as B-DNA (PDB ID: 1BNA)[64] with the sequence 5'-D(*CP*GP*CP*GP*AP*AP*TP*TP*CP*GP*CP*G)-3'. A rectangular grid box of 64x58x118 Å was generated for both complexes encompassing the sugar-phosphate backbone as well as the nucleotides. The receptor was prepped by removing water molecules surrounding the DNA and adding Gasteiger charges. The polar Hydrogen bonds and Kollman charges were assigned to the DNA and converted into ".pdbqt" format for AutoDock Vina. The conformers of the ligand were also converted to ".pdbqt" format followed by adjusting the number of torsional bonds present, which for both the ligands was 0. A configuration file was then generated containing the Ligand and the Receptor information as well as the size and location of the rectangular grid box in 3-dimensional space. The global search exhaustiveness was set to 16, and the maximum number of binding modes was set to 10.[65] The best optimized docking pose with minimum energy and RMSD 0.0 was chosen and analysed. The docking images were then generated using PyMOL (TM) Molecular Graphics System, Version 2.5.0.[66]

3.6.2 Results

The binding affinities for the both the complexes were added in the Table 3.6.A1 and 3.6.A2. The binding affinity with the lowest RMSD (= 0.0) value was taken.

Table 3.6.A1: Docking interaction and binding affinities

Compound	Binding energy (kcal/mol)	Docking interactions (Nucleic acid-Ligand)	Length of bond Å	Number of H bonds
Complex **2**	-8.0	O of acetate of ligand to DA-17	2.2 for DA 17 to lig O	2
		O of acetate of ligand to DA-16	2.4 for DG 16 lig to O	

Table 3.6.A2: Docking interaction and binding affinities

Compound	Binding affinity (kcal/mol) RMSD = 0	Docking interactions (Complex 3 – DNA)	Distance in Å	Number of H bonds
Complex **3**	-8.4	N3 to dA-17	3.5	1
		H4 to dC-11	2.6	

Table 3.6.A3: Molecular docking result of ligand **1**

Conformers	Binding affinity(kcal/mol) RMSD = 0	Docking interactions (Ligand to DNA)	Distance in Å	Number of H bonds
1	-5.9	H20 to O4 of Ribose sugar of dA	2.8	1
		H21 to N3 of dG	2.3	
2	-7.3	N7 to O2 of dC	3.1	2
		H20 to O4 ribose sugar of dC	2.6	
		H21 to N3 of dG	2.5	
		H21 to O4 of ribose sugar of dG	2.3	

3	-5.5	H21 to O4 of dG	1.8	1
4	-7.5	H20 to O4 of ribose sugar of dG	2.6	2
		H20 to N3 of dG	2.4	
		H21 to O4 of dC	2.3	
		N2 to O2 of dC	3.1	
5	-5.9	N4 to O4 of Ribose sugar of dC	3.1	2
		N4 to O2 of dG	3.4	
		N2 to O2 of dG	3.2	
6	-5.8	H20 to O4 of ribose sugar of dA	2.6	2
		H21 to N3 of dG	2.8	
7	-5.7	H20 to O4 of ribose sugar dA	2.7	2
		H21 to N3 of dC	2.8	
8	-7.4	N2 to O2 of dC	3.1	2
		H20 to O of dG	2.4	
		H21 to O4 of ribose sugar of dC	2.1	
9	-7.4	N2 to O2 of dC	3.0	2
		H20 to O of ribose of dG	2.5	
		H20 to N3 of dG	2.4	
		H21 to O4 of ribose of dC	2.2	

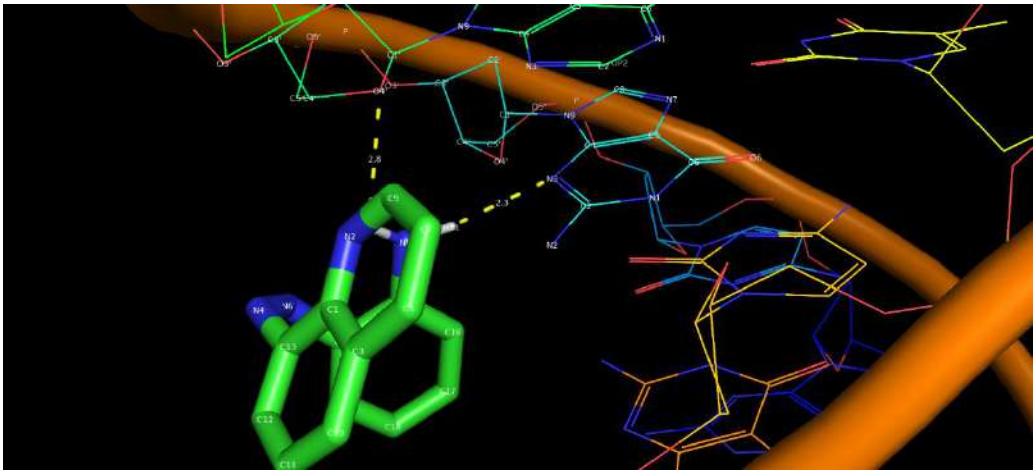

Figure 3.6.A1: Molecular docking results of ligand **1** (conformer 1)

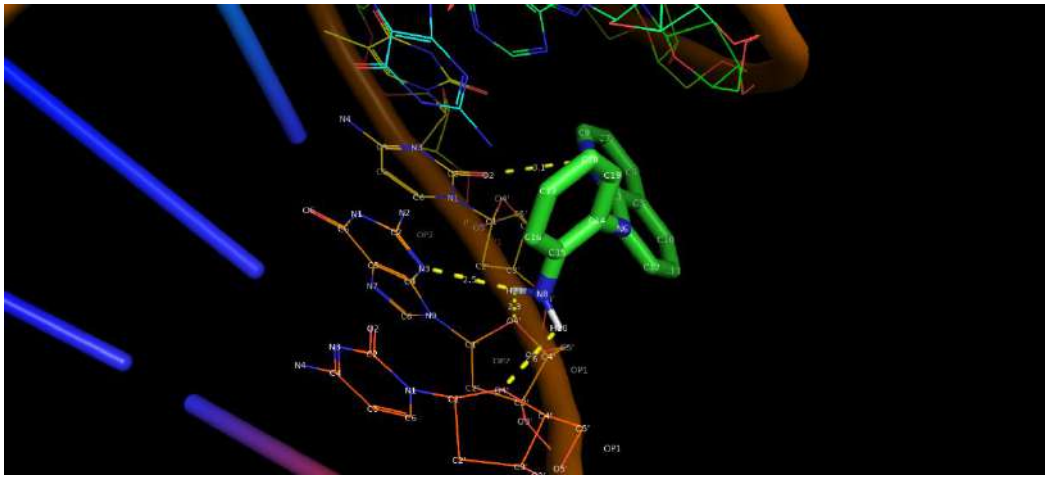

Figure 3.6.A2: Molecular docking results of ligand **1** (conformer 2)

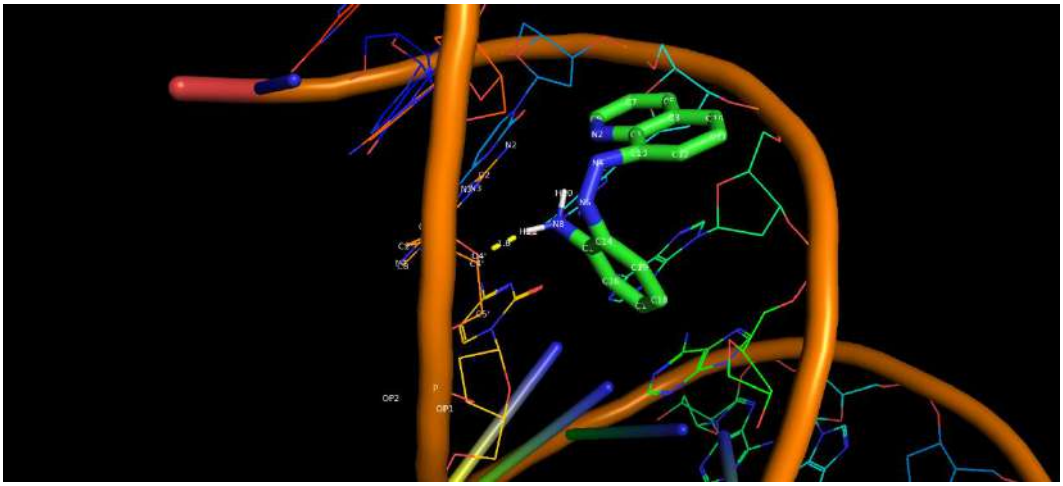

Figure 3.6.A3: Molecular docking results of ligand **1** (conformer 3)

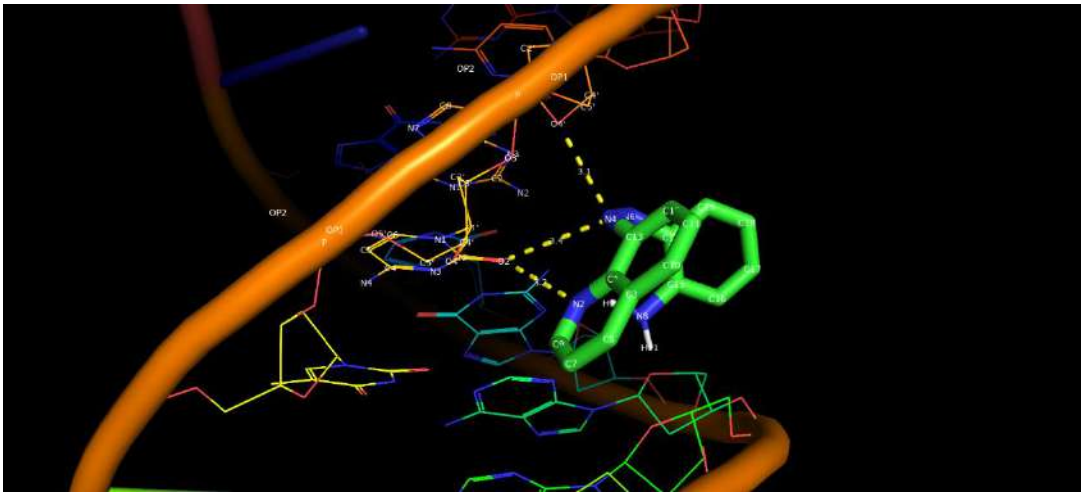

Figure 3.6.A4: Molecular docking results of ligand **1** (conformer 5)

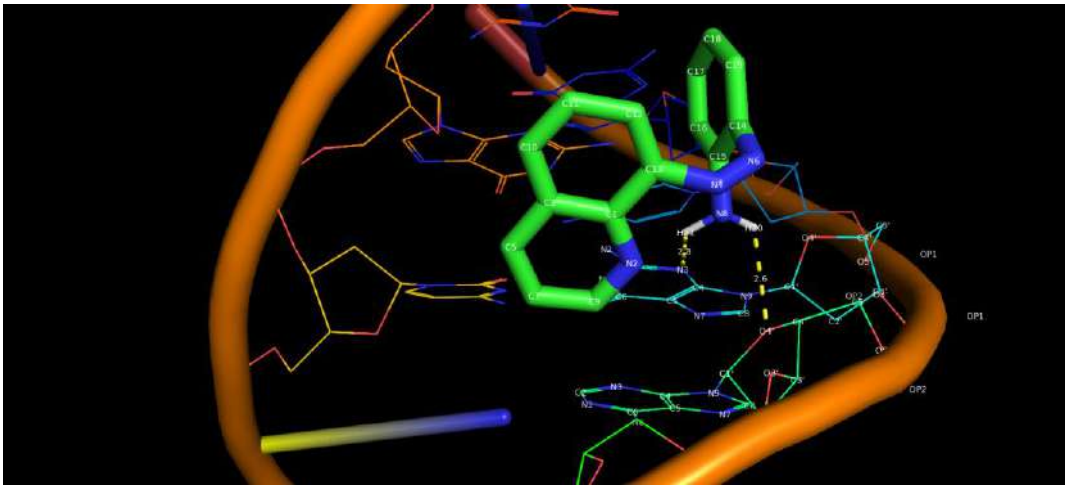

Figure 3.6.A5: Molecular docking results of ligand **1** (conformer 6)

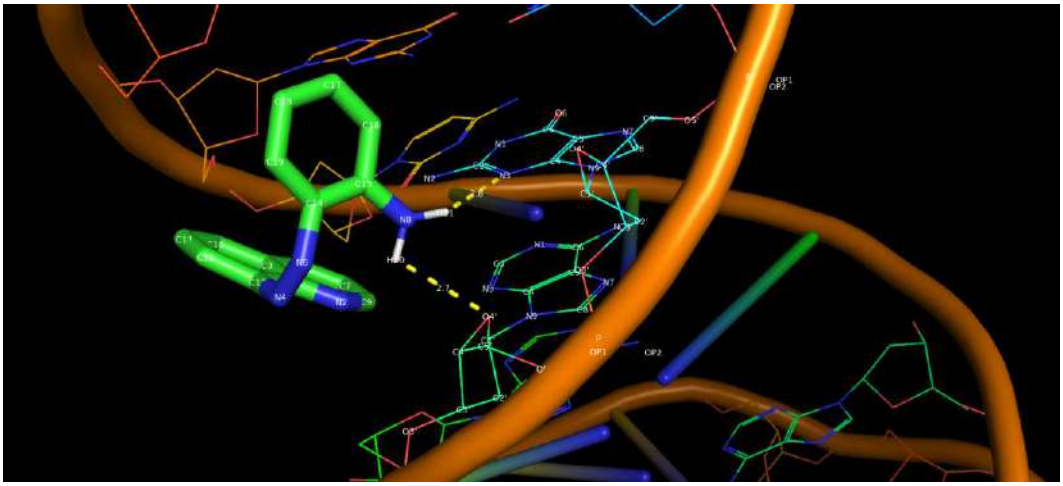

Figure 3.6.A6: Molecular docking results of ligand **1** (conformer 7)

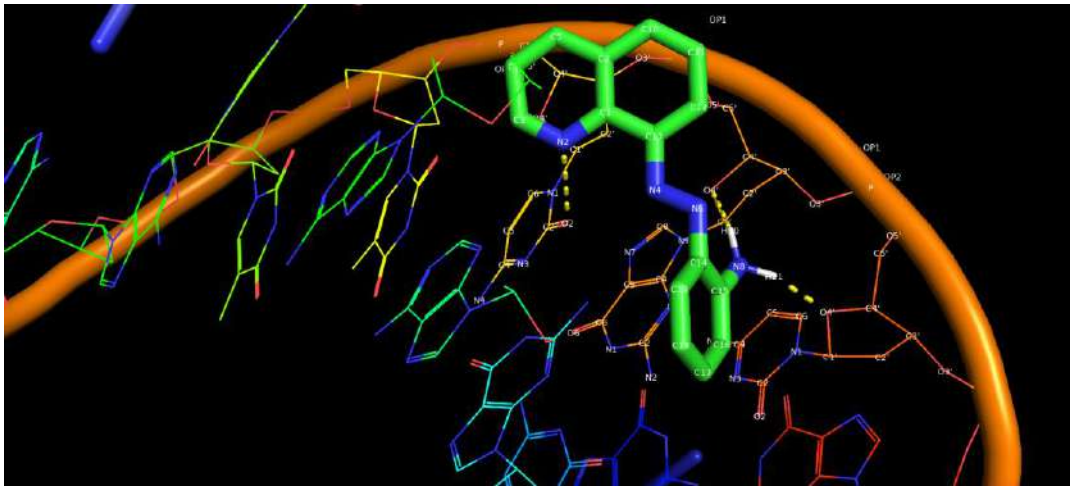

Figure 3.6.A7: Molecular docking results of ligand **1** (conformer 8)

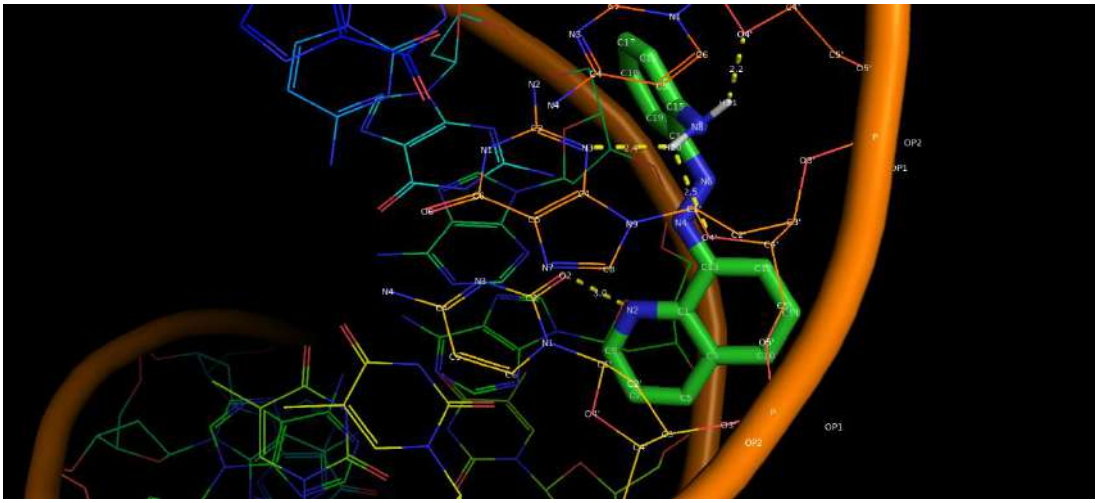

Figure 3.6.A8: Molecular docking results of ligand **1** (conformer 9)

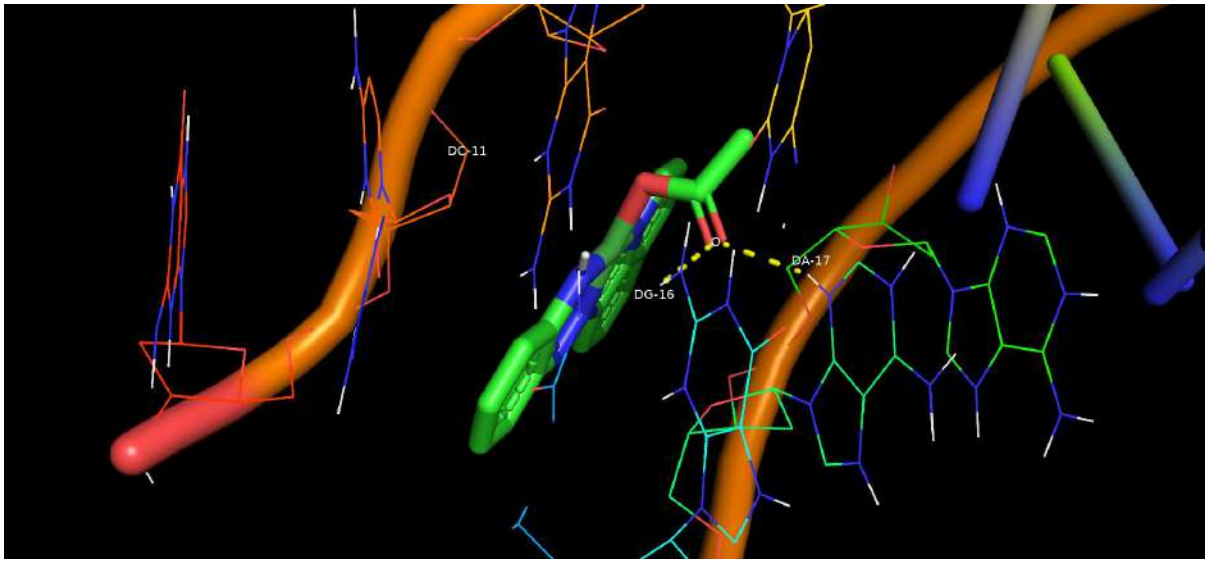

Figure 3.6.A9: Docking poses for complex **2** with B-DNA (PDB ID: 1BNA) generated in Pymol

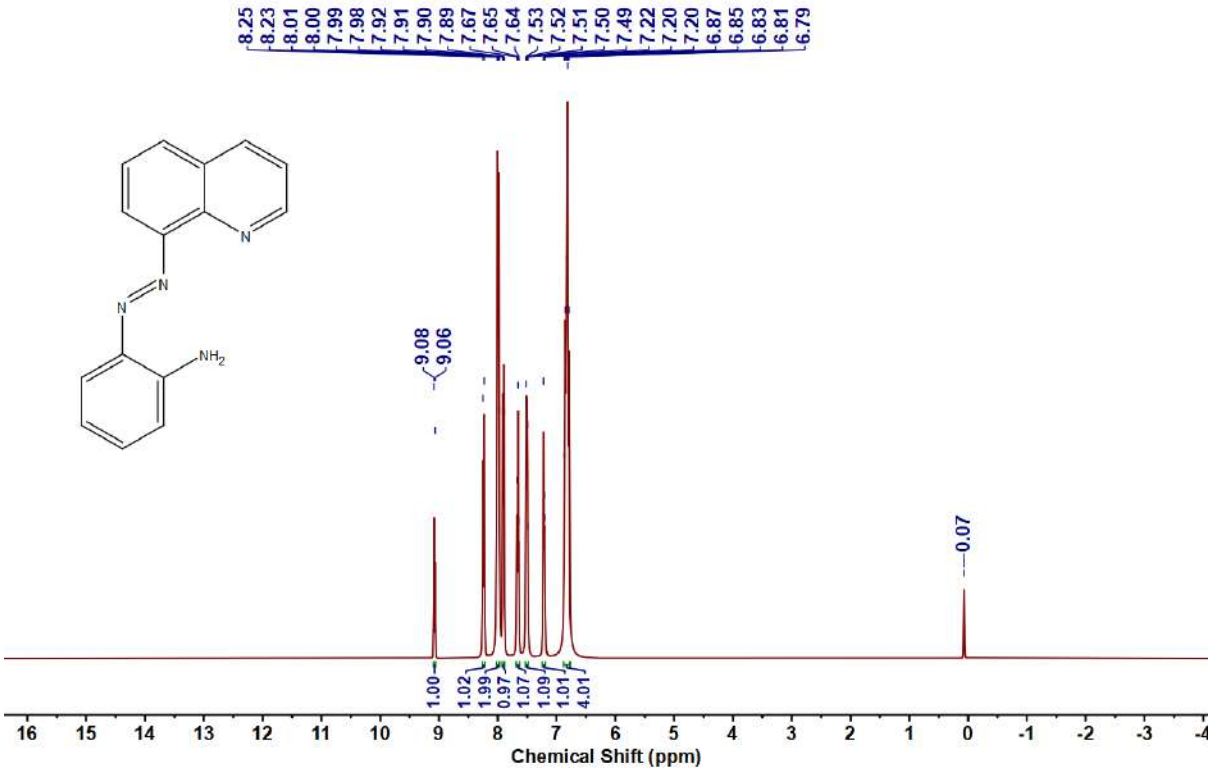

Figure 3.6.A10: ^{1}H NMR spectrum of ligand **1**

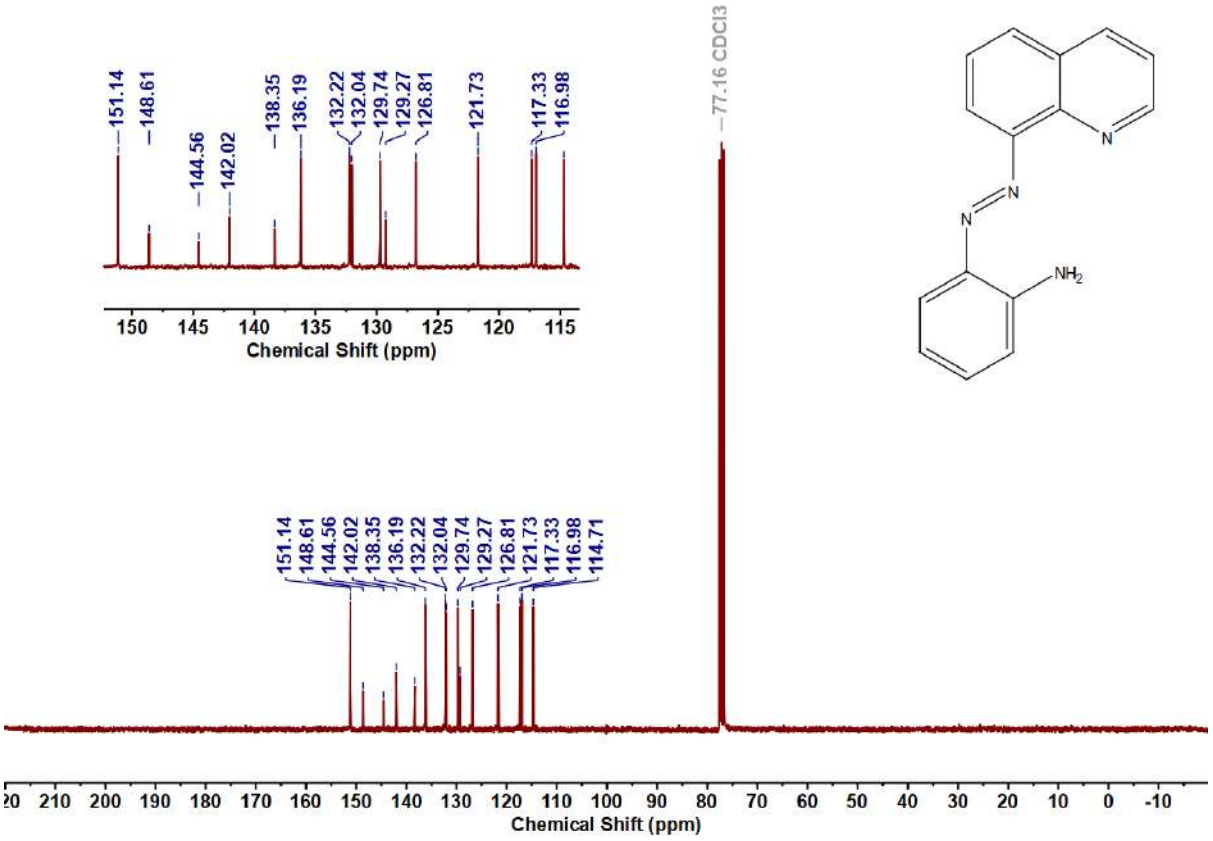

Figure 3.6.A11: $^{13}C\{^{1}H\}$ NMR spectrum of ligand **1**

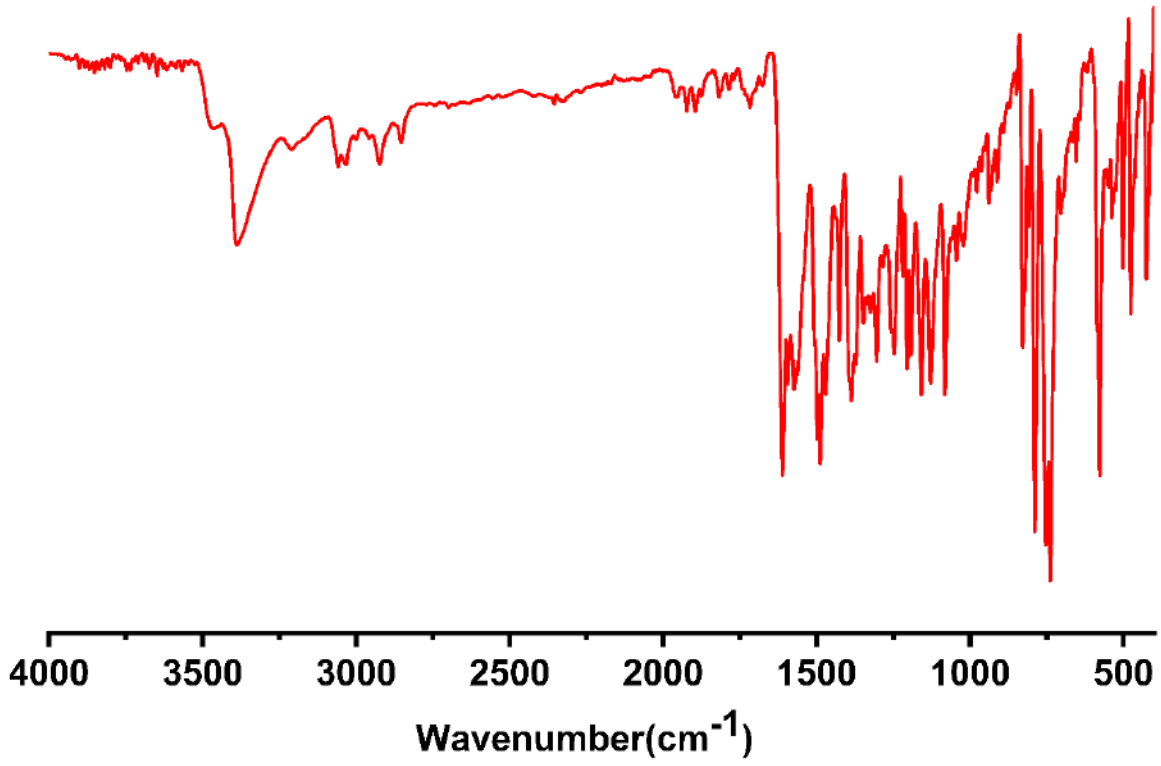

Figure 3.6.A12: IR spectrum of ligand **1**

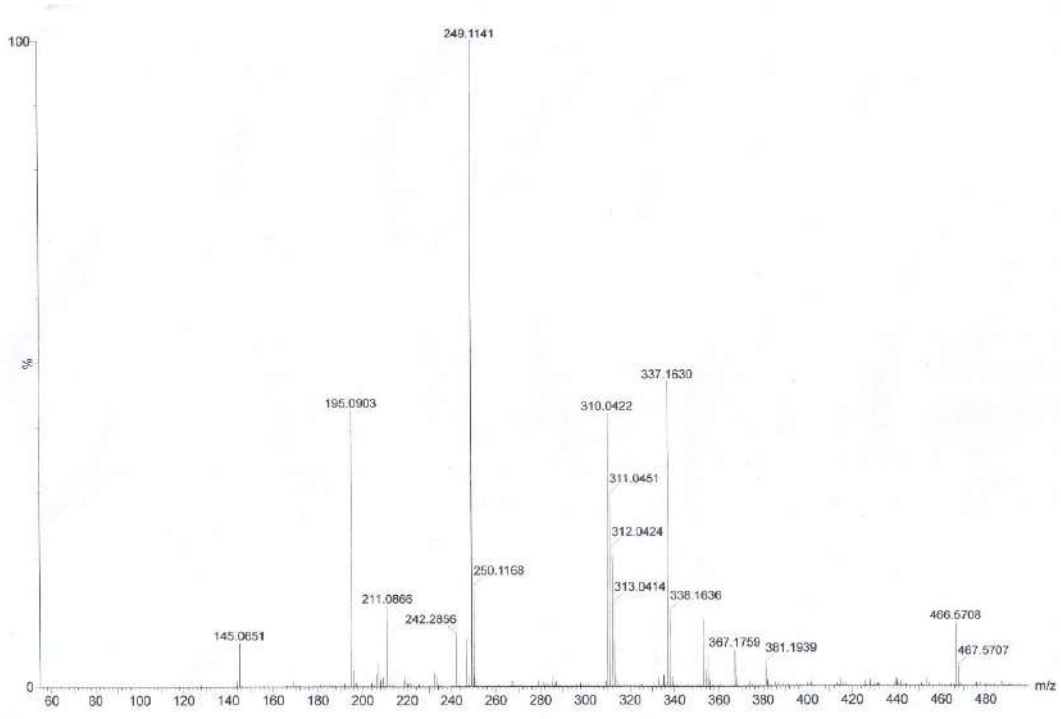

Figure 3.6.A13: HRMS spectrum of ligand **1**

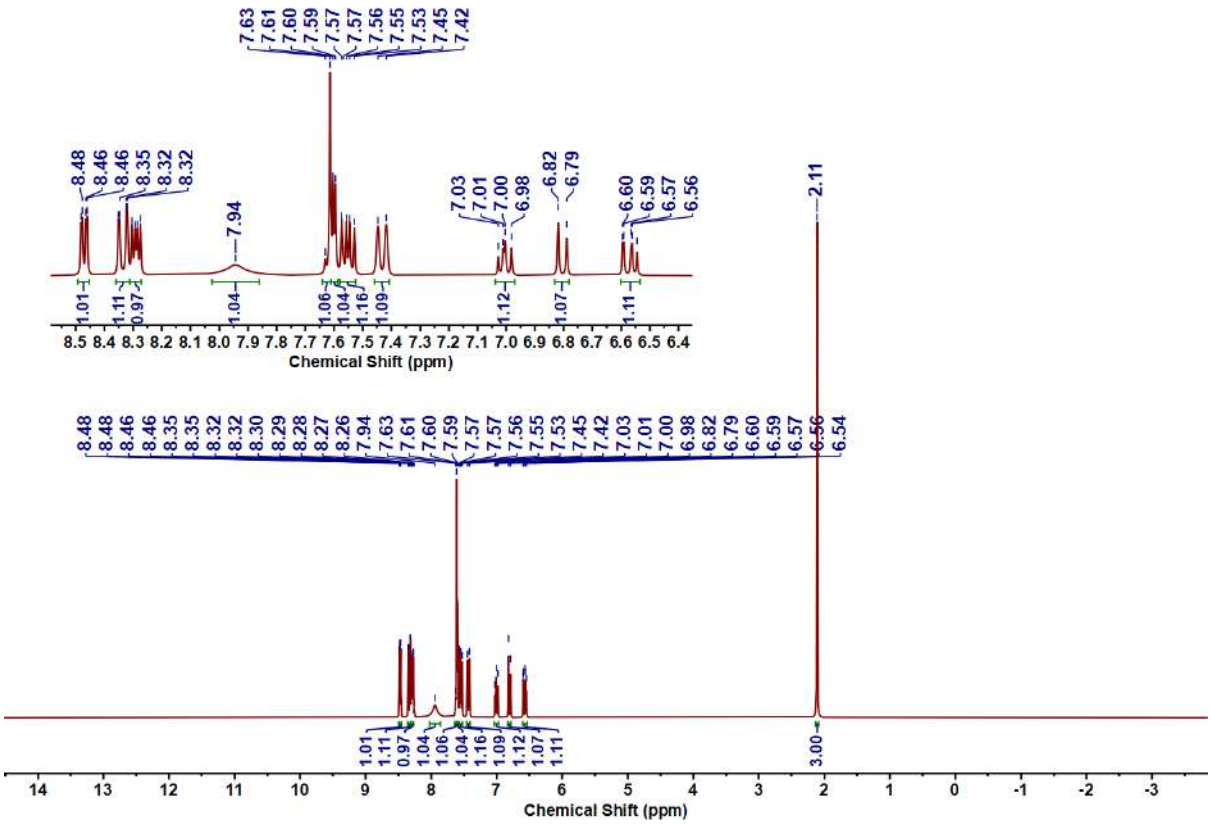

Figure 3.6.A14: ^{1}H NMR spectrum of complex **2**

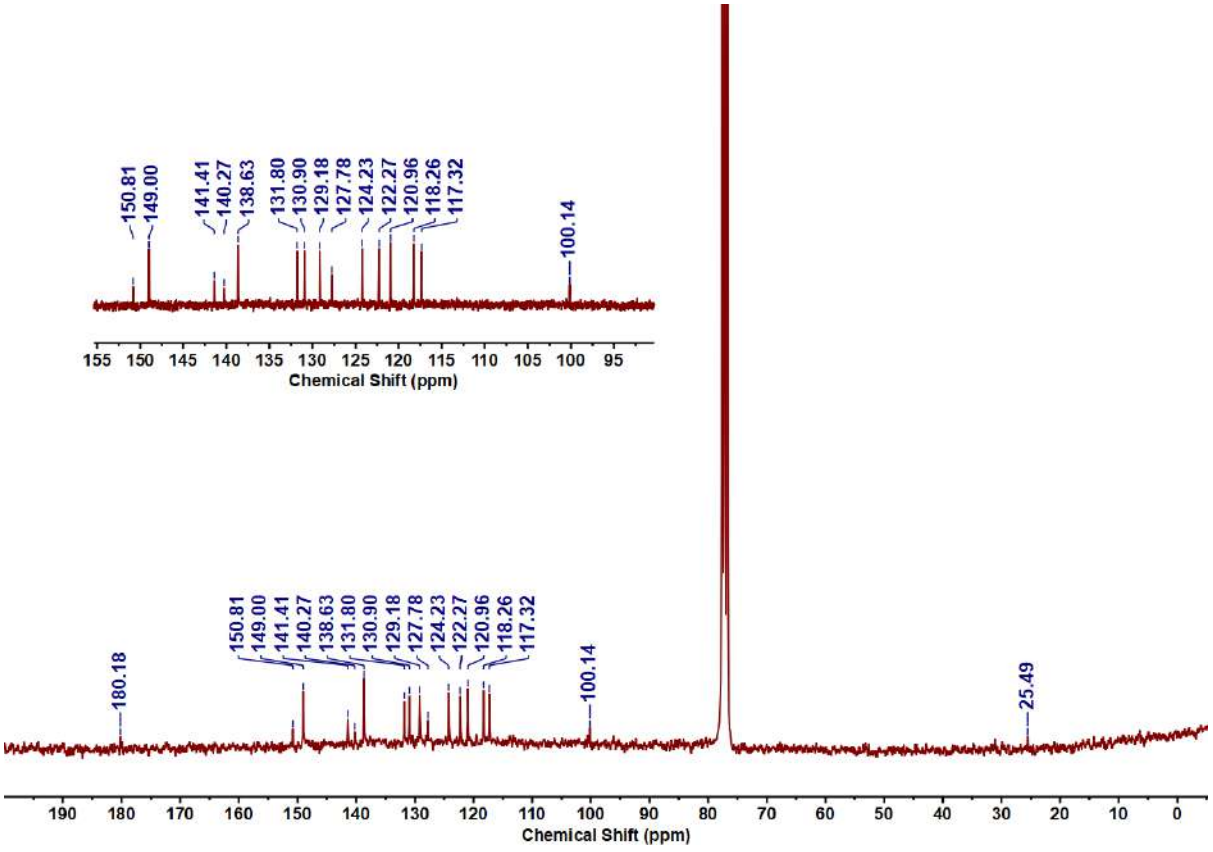

Figure 3.6.A15: $^{13}C\{^{1}H\}$ NMR spectrum of complex **2**

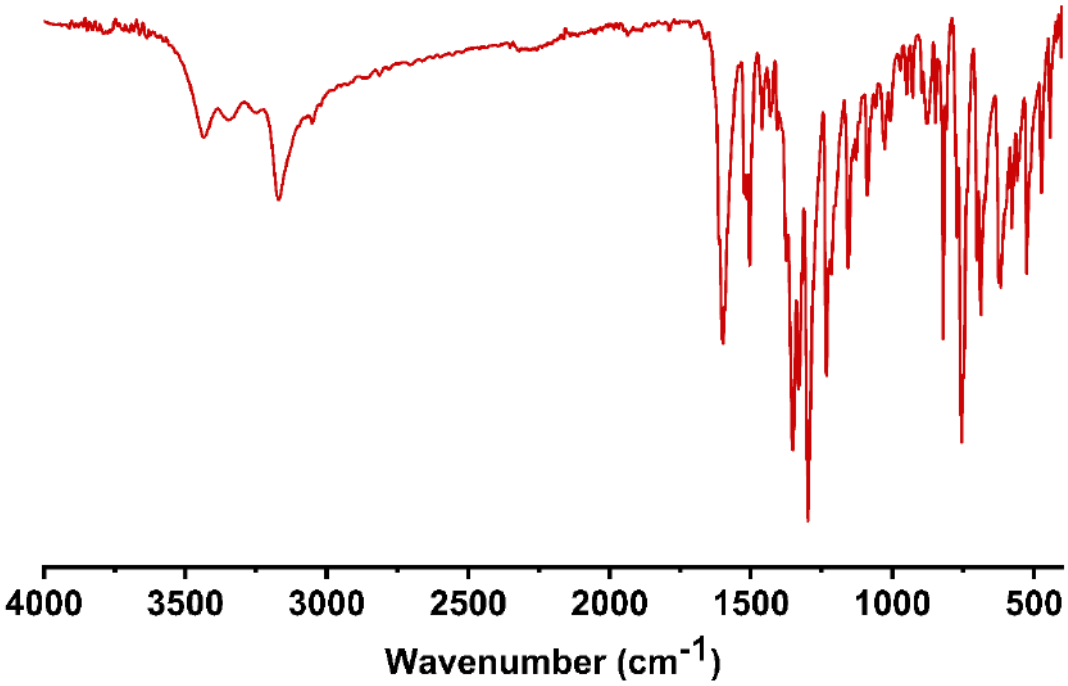

Figure 3.6.A16: IR spectrum of complex **2**

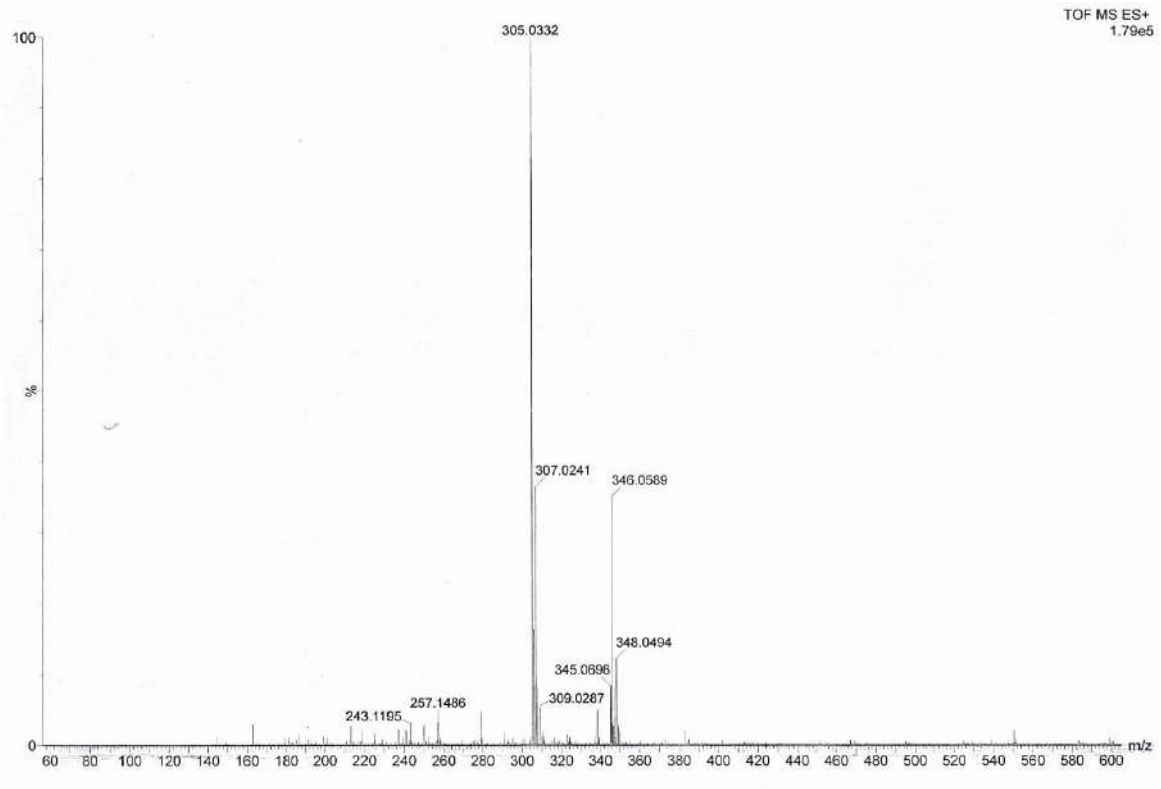

Figure 3.6.A17: HRMS spectrum of complex **2**

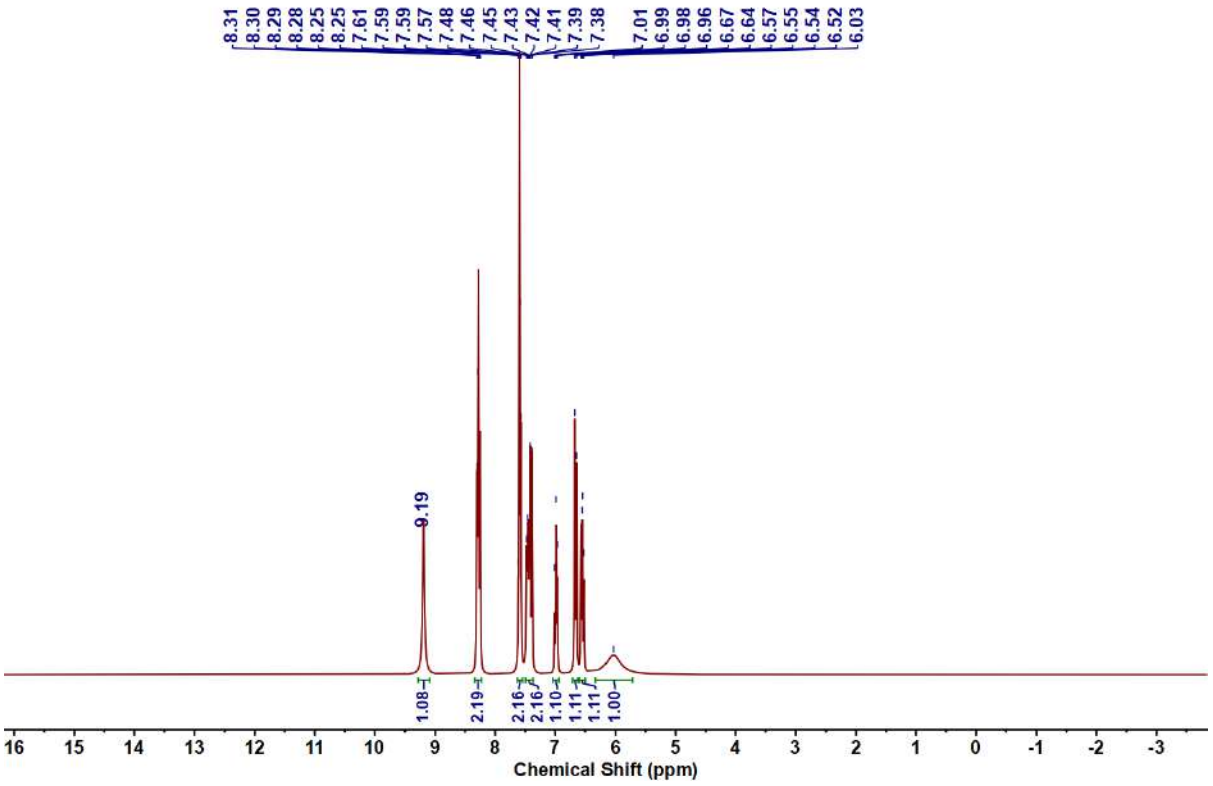

Figure 3.6.A18: ^{1}H NMR spectrum of complex **3**

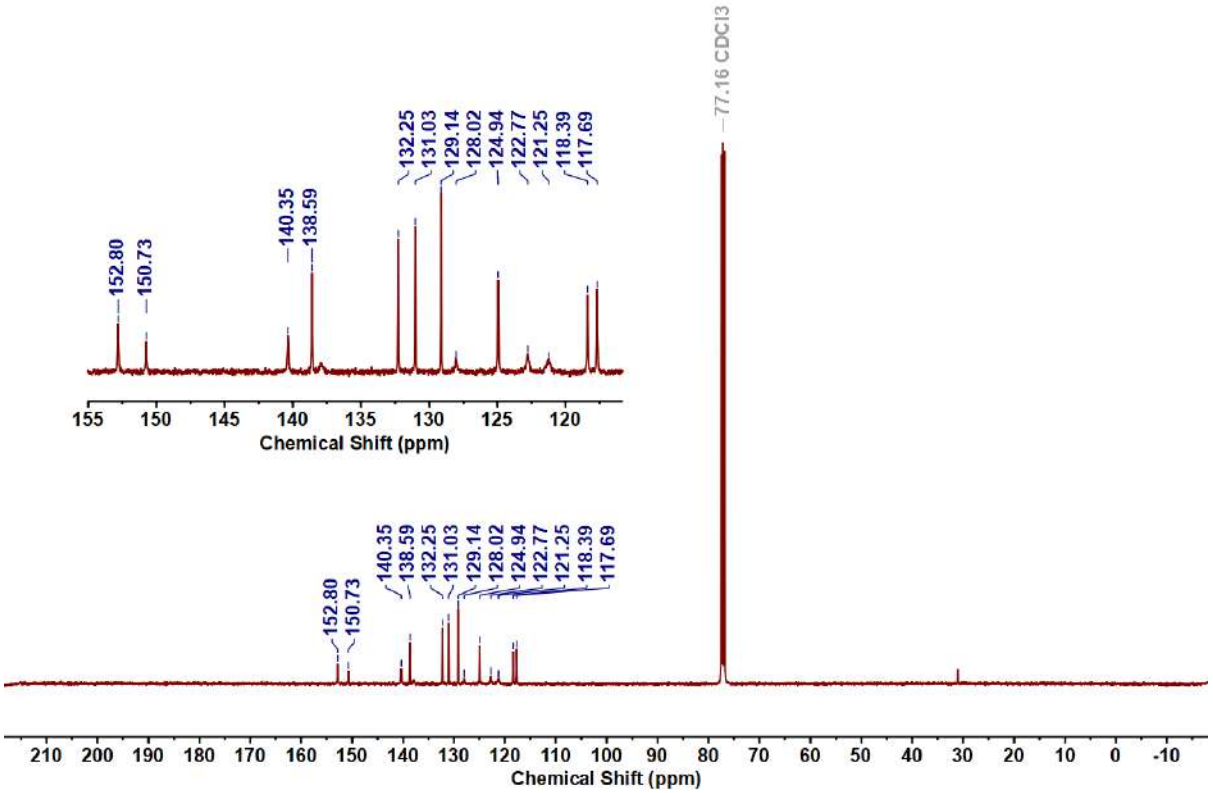

Figure 3.6.A19: $^{13}C\{^{1}H\}$ NMR spectrum of complex **3**

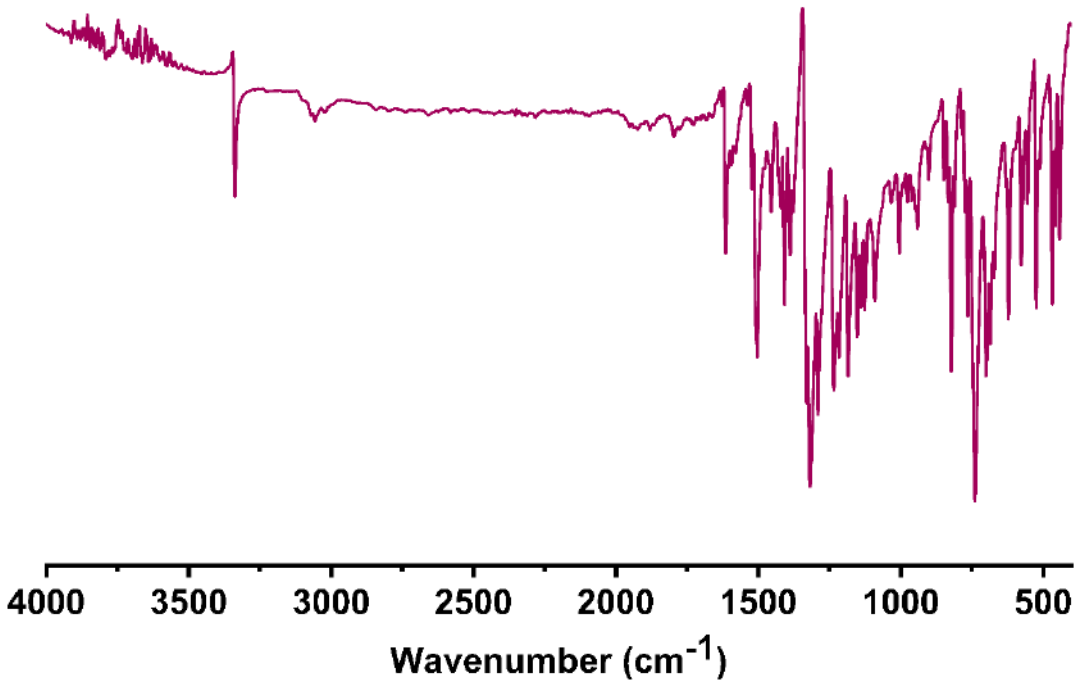

Figure 3.6.A20: IR spectrum of complex **3**

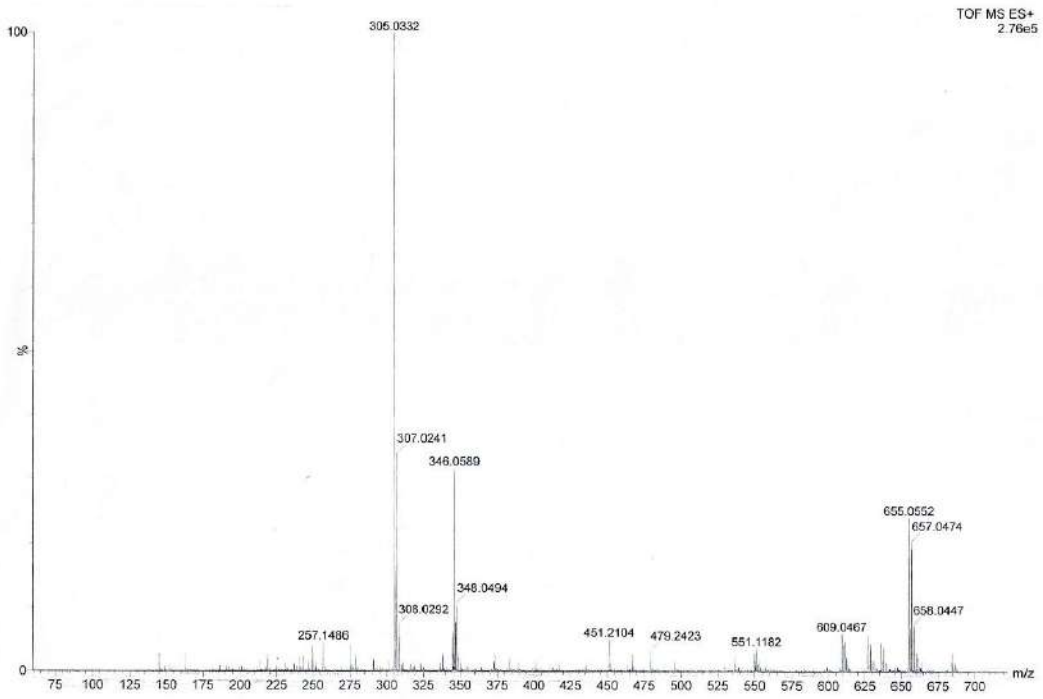

Figure 3.6.A21: HRMS spectrum of complex **3**

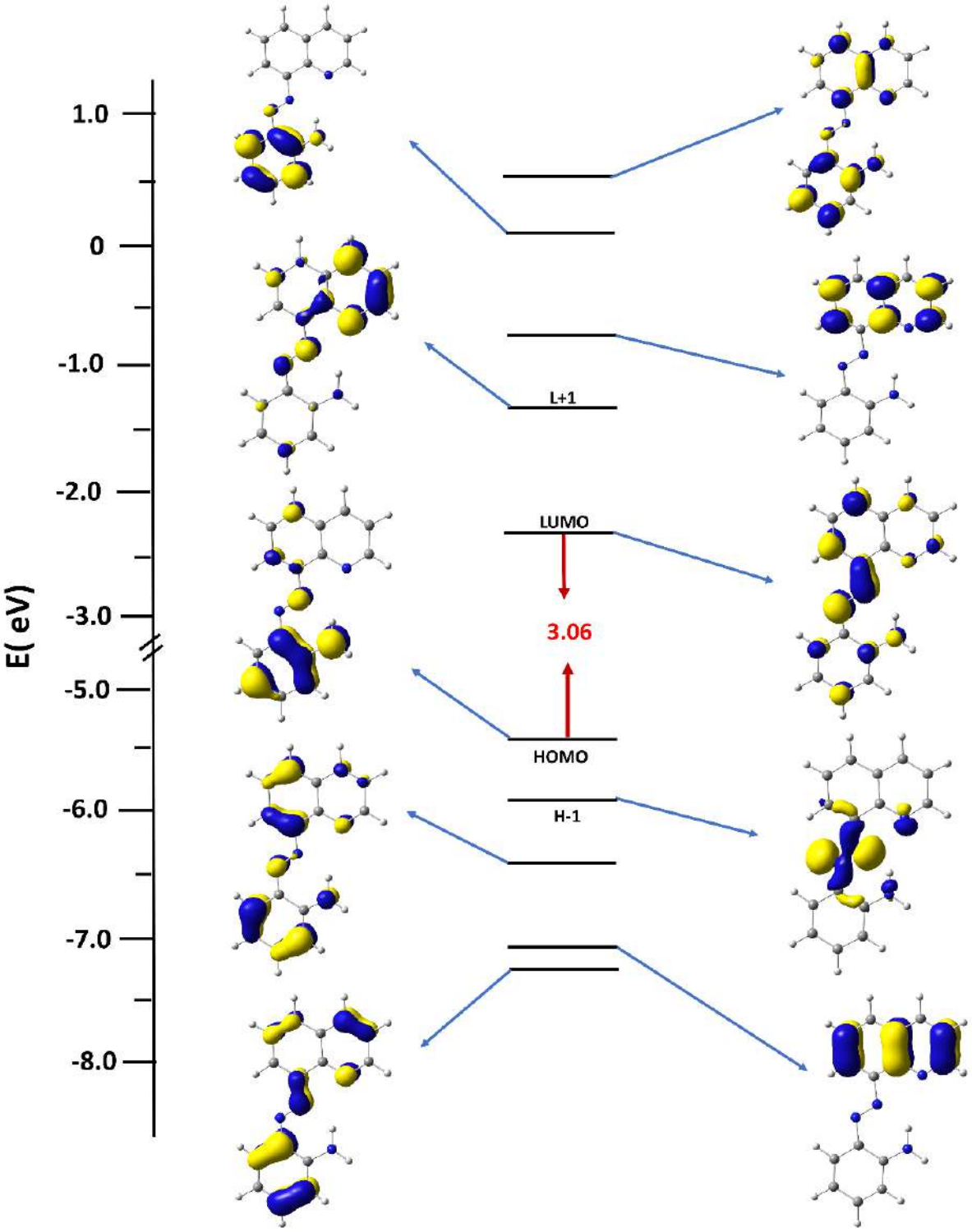

Figure 3.6.A22: Partial MO Energy diagram of ligand **1** (iso values are set at 0.05)

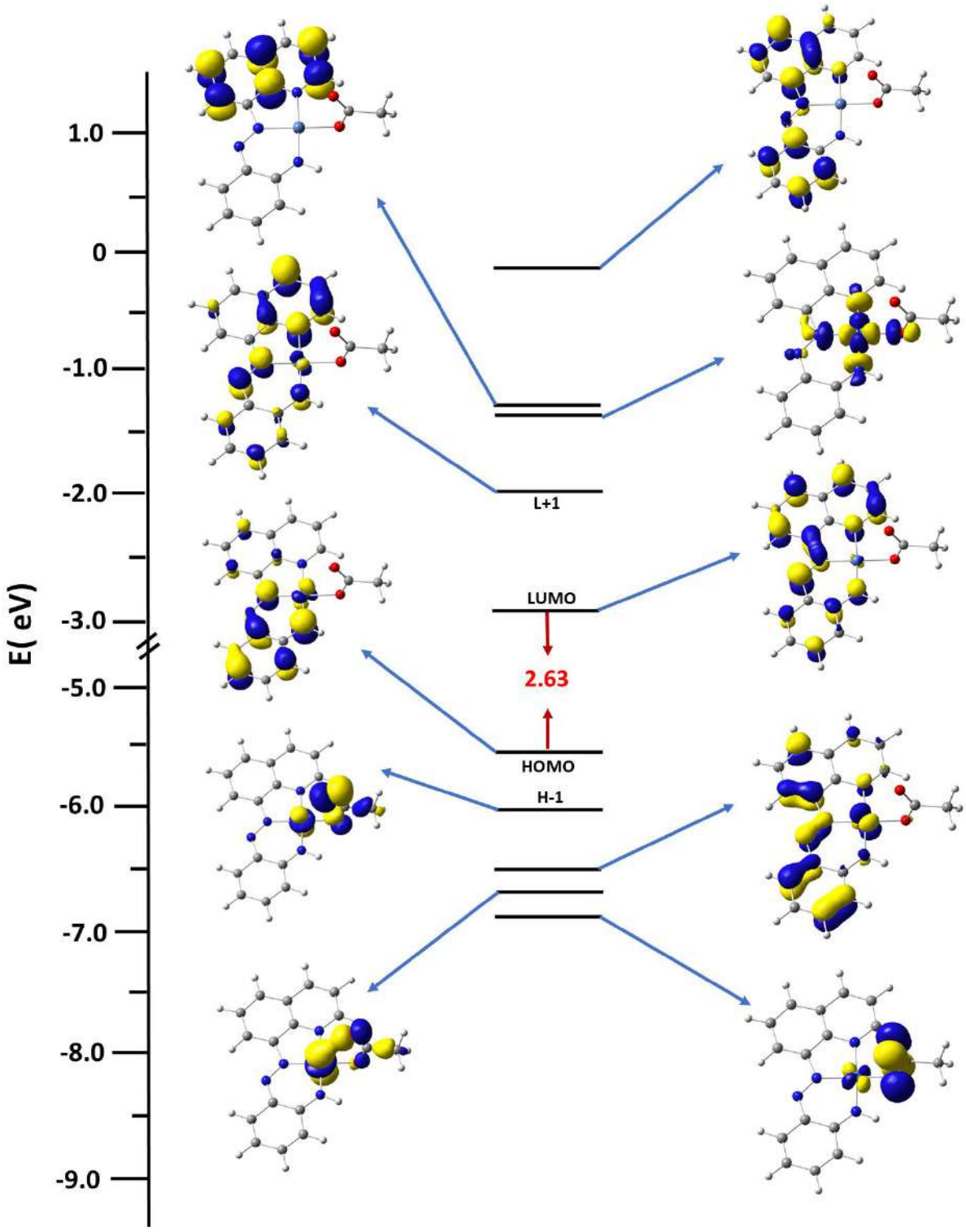

Figure 3.6.A23: Partial MO Energy diagram of Complex **2** (iso values are set at 0.05)

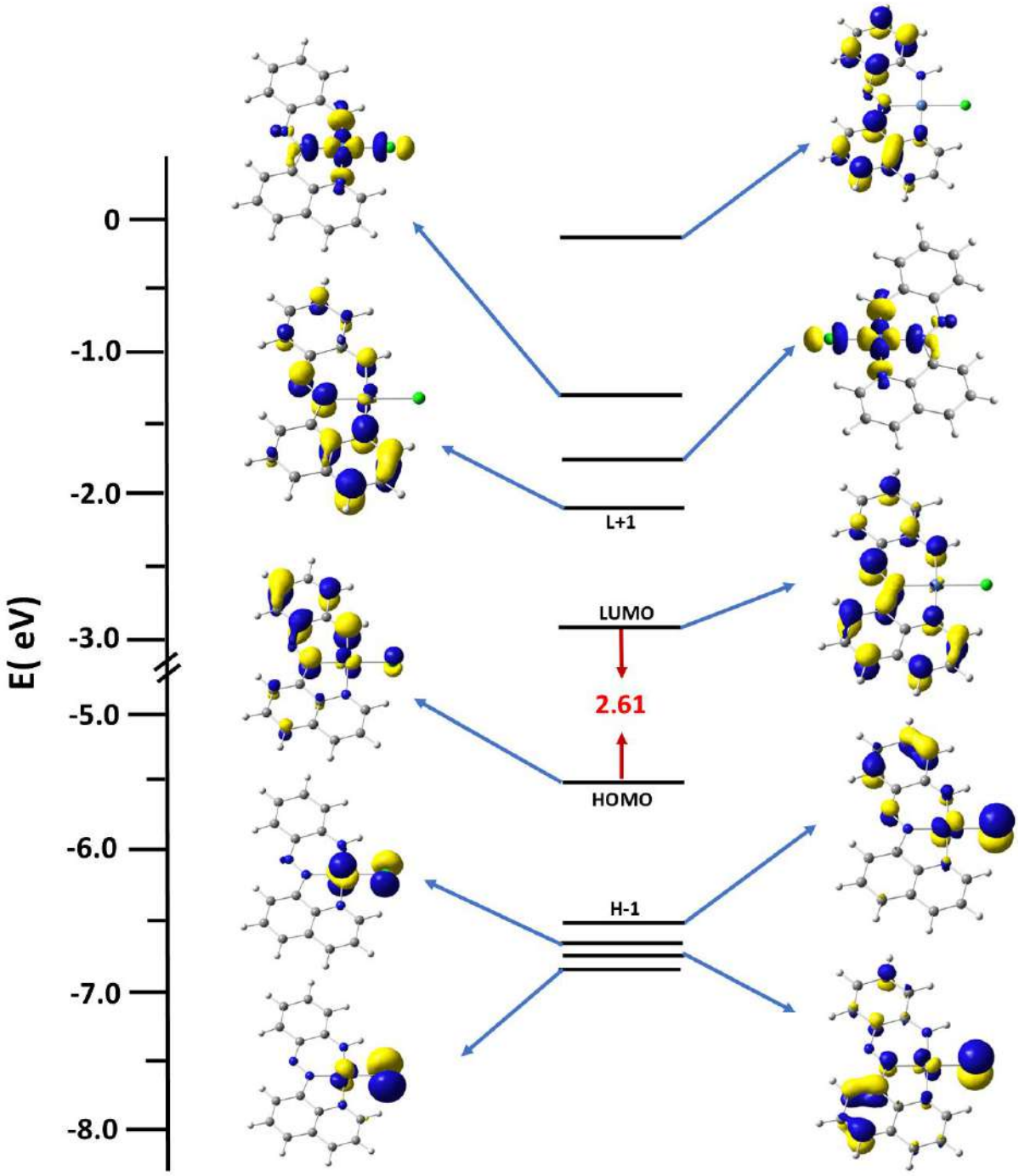

Figure 3.6.A24: Partial MO Energy diagram of Complex **3** (iso values are set at 0.05)

Table 3.6.A4: Coordinates of Optimized Geometry of ligand **1**

Tag	Symbol	X	Y	Z
1	C	-4.1159	0.28194	0.051641
2	C	-2.74535	0.257679	0.021855
3	C	-2.02514	1.479043	0.007918
4	C	-2.78081	2.693652	0.025893
5	C	-4.76751	1.537384	0.067583
6	H	-0.04748	0.59812	-0.03601
7	H	-4.70156	-0.63302	0.063074
8	H	-2.19995	-0.6837	0.008682
9	C	-0.60984	1.529149	-0.02285
10	C	-2.07458	3.944439	0.011516
11	H	-5.85731	1.575605	0.091415
12	C	-0.68818	3.94579	-0.01829
13	C	0.040326	2.743301	-0.03538
14	H	-0.17055	4.900317	-0.02775
15	H	1.126777	2.779281	-0.05821
16	N	-2.87588	5.100179	0.032707
17	N	-2.25531	6.207599	0.001963
18	C	-3.03314	7.356576	0.024252
19	C	-4.46918	7.411198	0.076353
20	C	-2.29928	8.563301	-0.01017
21	C	-5.07416	8.69259	0.090026
22	C	-2.91444	9.797036	0.004656
23	H	-1.21629	8.473915	-0.04914
24	C	-4.31955	9.847981	0.055442
25	H	-6.16036	8.750657	0.128571
26	H	-2.32846	10.71127	-0.02243
27	H	-4.82599	10.81075	0.06768
28	N	-5.23412	6.295681	0.11179
29	H	-4.77882	5.384594	0.096747
30	H	-6.24058	6.3781	0.140803
31	N	-4.1435	2.696645	0.055517

Table 3.6.A5: Coordinates of Optimized Geometry of Complex **2**

Tag	Symbol	X	Y	Z
1	Ni	0.339381	8.907436	9.737139
2	O	0.074334	10.5499	10.64373
3	O	2.259547	10.53458	11.17223
4	N	0.167218	7.833414	11.33767
5	N	0.787427	6.976205	7.61147
6	N	0.600138	7.254349	8.855497
7	N	0.433216	9.821345	8.145186
8	H	0.319315	10.82782	8.227269
9	C	0.600156	6.154419	9.734437
10	C	1.026531	7.483991	5.338479
11	H	1.154602	6.413561	5.201509
12	C	0.80328	4.826165	9.410309
13	H	0.989393	4.554129	8.376845
14	C	1.160756	11.07136	11.15858
15	C	0.313749	5.522688	12.10473
16	C	0.894412	9.744342	4.526665
17	H	0.928979	10.43715	3.688273
18	C	0.767443	3.844438	10.42302
19	H	0.932644	2.805581	10.14792
20	C	1.069239	8.35034	4.286373
21	H	1.234829	7.990108	3.27511
22	C	0.358845	6.505676	11.08609
23	C	0.810931	7.937458	6.677255
24	C	0.941968	12.46187	11.7458
25	H	-0.03543	12.53915	12.23255
26	H	0.963366	13.20059	10.93455
27	H	1.742025	12.7003	12.45132
28	C	0.528386	4.169434	11.74088
29	H	0.502469	3.399425	12.50796
30	C	0.686454	10.23011	5.784906
31	H	0.557091	11.29791	5.951544
32	C	0.633973	9.360335	6.927749
33	C	0.050317	5.979687	13.41913
34	H	0.007788	5.263735	14.23725
35	C	-0.08624	8.228757	12.57176
36	H	-0.24704	9.293659	12.70288
37	C	-0.15183	7.320224	13.64773
38	H	-0.35967	7.696891	14.64464

Table 3.6.A6: Coordinates of Optimized Geometry of Complex **3**

Tag	Symbol	X	Y	Z
1	Ni	2.286432	6.879342	6.162955
2	Cl	0.652513	6.171307	4.794536
3	N	2.857086	5.086865	6.674625
4	N	3.666863	7.466624	7.321105
5	N	4.063647	8.649004	7.642611
6	N	1.847959	8.619348	5.759337
7	H	1.077864	8.718912	5.103434
8	C	2.38179	3.912056	6.29308
9	H	1.551054	3.941303	5.594751
10	C	2.919719	2.696738	6.763338
11	H	2.487795	1.7634	6.415098
12	C	3.972147	2.712016	7.646044
13	H	4.400908	1.784425	8.01958
14	C	4.506303	3.950668	8.075584
15	C	5.588369	4.092815	8.979911
16	H	6.06142	3.203424	9.388822
17	C	6.028361	5.350699	9.329879
18	H	6.859138	5.456847	10.02315
19	C	5.427106	6.514947	8.809442
20	H	5.782786	7.499825	9.092161
21	C	4.369551	6.407268	7.925468
22	C	3.904445	5.122864	7.553701
23	C	3.484876	9.744988	7.137781
24	C	2.378295	9.742998	6.195072
25	C	1.892702	11.02526	5.762987
26	H	1.064637	11.04526	5.05724
27	C	2.445576	12.1861	6.219102
28	H	2.049354	13.1369	5.868469
29	C	3.53049	12.18256	7.144783
30	H	3.95134	13.12214	7.491053
31	C	4.026682	10.99133	7.583544
32	H	4.852803	10.94109	8.287773

Table 3.6.A7: Energies of nine possible conformers of the ligand which lie within 1 eV of the putative global minimum by using Adaptive Mutation Simulated Annealing

Conformer	Energy (Hartree)	
1	-797.981446	
2	-798.008123	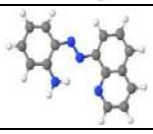
3	-797.981010	
4	-798.000147	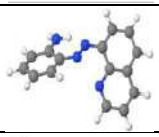
5	-797.976474	
6	-797.981011	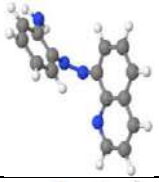
7	-797.971834	
8	-798.001200	
9	-798.001014	

Chapter 4

Alcohol Dehydrogenation Catalyzed by Azo-Oxime Coordinated Ruthenium(II): A Strategic and Sustainable Route Towards Site-Selective C(sp³)–H Functionalization of 9H-Fluorene

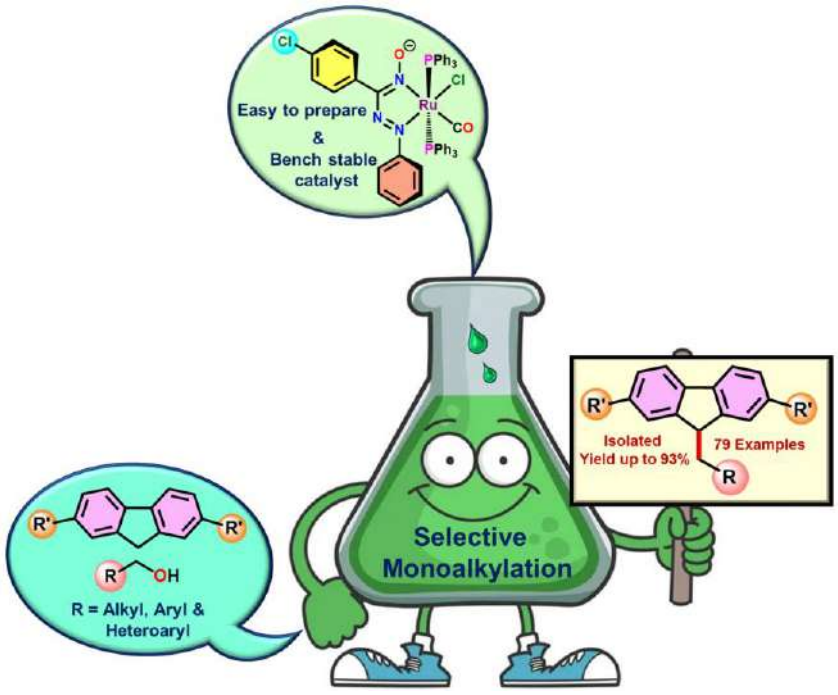

4.1 Introduction

Fluorene and its derivatives are important group of compounds having a biphenyl skeleton along with a rigid plane, thereby facilitating π–cloud delocalization.[1] These remarkable structural features accounts for their varied properties and they can be further modulated *via* introducing suitable functional groups into the fluorene ring.[2] The sustainable synthetic strategies of fluorene derivatives is gaining importance in current research owing to their potential applications in electronic and photochromic materials, particularly OLED[3] and solar cells.[4] This is majorly attributed to the rich photophysical and photoelectric properties of fluorene.[5] These features have also been smartly exploited over the years to formulate and synthesize a wide range of polymers[6] and dyes.[7] This polyaromatic hydrocarbon (PAH) framework has been found to exhibit anti-cancer and antimicrobial properties.[8] It also finds utility for exploration of two-photon fluorescence bioimaging[9] (Scheme 4.1). As a crucial component of coal tar, this PAH framework enables the C−H functionalization of fluorene derivatives at the 9-position, offering a transformative strategy for advancing environmental sustainability and converting coal tar into valuable, high-impact products.

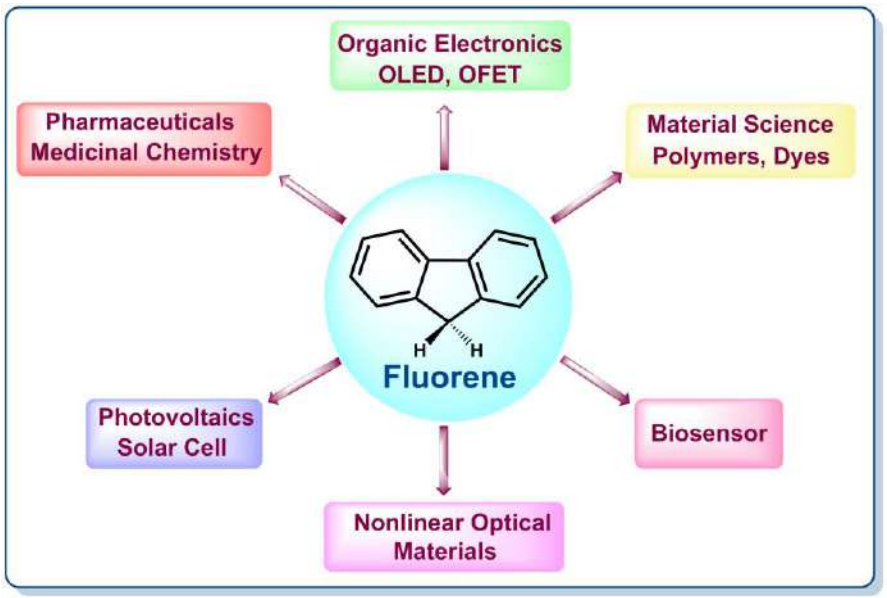

Scheme 4.1: Application area of fluorene and its derivatives in current research

Conventional approaches for 9-alkylation of fluorene involve condensation of aldehydes with fluorene, followed by hydrogenation or an S_N2 reaction of fluorenes with excess alkylating agents like haloalkanes in presence of strong and highly reactive bases *e.g.*, KOH or t-BuLi. The earliest report, published in 1955 by Becker and co-workers, defined the base-promoted alkylation of fluorene using several aliphatic alcohols conducted under rigorous conditions that involved the use of excess base and elevated temperatures ranging from 210-220°C. In 1965, Atkin's group at Union Carbide Corporation revealed a method for base-catalysed alkylation of fluorene and indene with aliphatic alcohols.[10] The process, however, demanded excessive amount of base and harsh reaction conditions such as high temperature (250°C) and pressure (500 psi). The major shortcoming of these strategies is formation of certain undesirable byproducts and poly-alkylated compounds.[11] These methods lack sufficient control, often leading to a higher degree of dialkylation rather than selective monoalkylation. A greener and more selective approach for synthesis is the dehydrogenation of alcohols using appropriate transition metal complexes as catalyst *via* dehydrogenation and borrowing hydrogenation (BH) or hydrogen auto-transfer (HAT).[12] Owing to its operational simplicity and capacity to form a wide range of carbon–carbon bonds, this strategy has gain increasing interest as an atom-economical method. This emerging focus mirrors the increasing demand for sustainable, green, and atom-efficient approaches in modern synthetic chemistry. In addition, alcohols offer a highly attractive class of renewable feedstocks due to their wide availability from lignocellulosic biomass, low environmental burden, and economic viability. Alcohol-based catalytic transformations have thus emerged as a sustainable route to access value added chemicals.

In recent years, significant progress has been made in the catalytic dehydrogenative functionalization of fluorene, particularly at the 9-position, using alcohols as alkylating agents. The research groups of Gnanaprakasam[13a] and Tu[13b] have independently developed

methodologies involving ruthenium- and iridium-based catalysts, respectively, for the direct alkylation of fluorene. These transition-metal-catalysed transformations proceed under relatively mild conditions and offer an efficient strategy for C–H bond activation and subsequent C–C bond formation, using readily available alcohols. Their effectiveness is attributed to strong metal–ligand cooperativity and the thermal and chemical stability of these catalytic systems.[14] Building on this foundation, the research groups of Adhikari[15a] and Srimani[15b] have reported the synthesis of monoalkylated fluorenes through a 3d-metal-catalyzed alcohol dehydrogenation approach. More recently, a similar catalytic method has also been explored by the research group of Balaraman,[16a] Paul[16b] and Samanta[16c] further demonstrating the versatility and applicability of this approach in the selective monoalkylation of fluorene derivatives.

For the past few years, we have been exploring the potential of redox non-innocent behaviour of azo-oxime coordinated transition metal complexes[17] and this has further motivated us to exploit them as redox catalyst[18] to carry out the dehydrogenative functionalization of aliphatic and aromatic alcohols, along with the tandem catalytic synthesis of value-added products.[19-21] In the present work we represent a comprehensive study of *N,N*-bidentate ligand-based ruthenium(II) catalyst, *trans*-[Ru(*p*-Cl-aaO)Cl(CO)(PPh_3)$_2$] (**2**), for functionalization of fluorene at 9-position using alcohol as an alkylating agent. Its electrochemical properties were subsequently investigated to evaluate its potential as a ligand-centered redox catalyst, supported by computational studies. Finally, we demonstrated its catalytic potential in one-pot synthesis of selective 9-monoalkylated fluorene derivatives. A probable mechanism for the catalytic dehydrogenative functionalization has been provided based on certain control experiments. This ruthenium catalyst offers straightforward synthesis, robustness, operational simplicity, low catalyst loading, broad substrate scope and the ability to promote transformations efficiently at reduced reaction time and temperature.

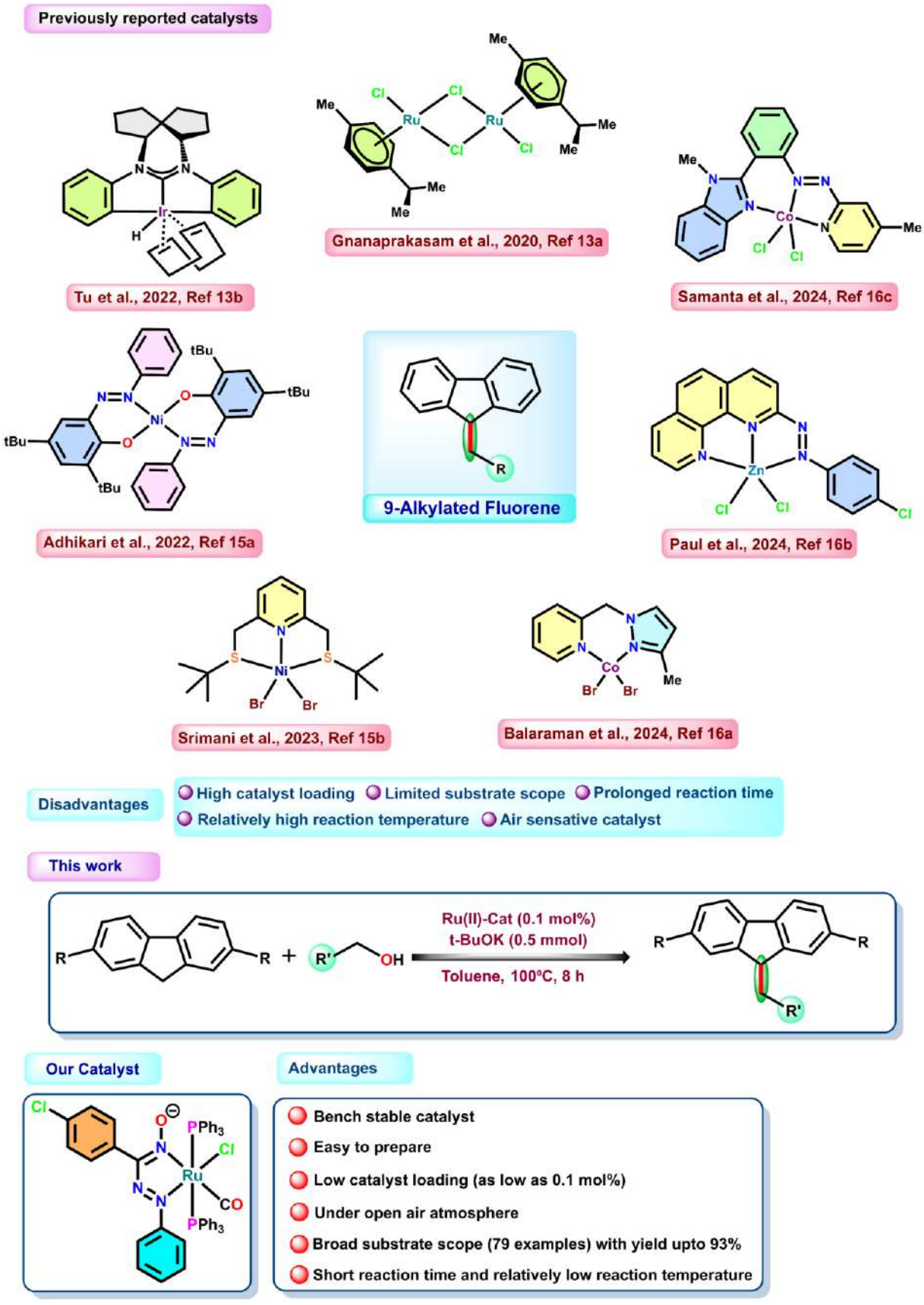

Scheme 4.2: Overview of earlier and present approaches to transition metal catalysed dehydrogenative alkylation of fluorene with alcohols as alkylating agents

4.2 Results and Discussion

4.2.1 Synthesis and characterization of ligand and catalyst

The ligand *p*-chloro-aryl-azo-oxime, *p*-Cl-aaOH (**1**), has been prepared starting from *p*-chlorobenzaldehyde and phenyl hydrazine[15] (Scheme 4.3) and characterized using different analytical methods (High Resolution Mass Spectrometry) and spectroscopic techniques (IR, NMR and UV-Vis) (Figure 4.6.A1– 4.6.A 6). It has the potential to act as a bidentate, electron-poor, monoanionic N(oximato), N(azo) donor during coordination. Upon stirring $[RuH(CO)Cl(PPh_3)_3]$ with the ligand in toluene (in an equimolar ratio) at room temperature for about 6 h, a dark pinkish red colored solution is formed, from which *trans*-[Ru(*p*-Cl-aaO)Cl(CO)$(PPh_3)_2$] (**2**), is isolated in excellent yields after chromatographic separation (See the Experimental Section). The Single-Crystal X-Ray Diffraction (SCXRD) study reveals that the complex crystallizes in monoclinic $P2_1/n$ space group, the molecular structure is shown in Figure 1 while crystallographic details and comprehensive metrical parameters are summarised in Table 1 and 2 respectively. The study further confirms that the ruthenium(II) centre adopts a distorted octahedral geometry, coordinated by the nitrogen atoms of both the oximato ($N_{oximato}$) and azo (N_{azo}) groups from the ligand framework. The two triphenylphosphine (PPh_3) co-ligands are positioned in a *trans* arrangement. The complex is highly robust and this may be attributed to the fact that more π–acidic azo group is oriented *trans* with respect to the strong σ–donor chloride while CO is also *trans* to oximato-N as expected from *trans* influence. The ^{1}H-NMR of **2** display signals within the region 6.83–7.48 (Figure 4.6.A7). The trans orientation of the two magnetically equivalent PPh_3 moieties is confirmed by proton-decoupled $^{31}P\{^1H\}$-NMR spectroscopy (Figure 4.6.A10). Additionally, complex **2** is stabilised by an intramolecular non-covalent π–π stacking interaction between pendent phenyl rings of azo-oxime moiety and PPh_3 with a centroid-to-centroid separation is 3.7351(16) Å and corresponding dihedral angle is 16.29(13)˚(Figure 4.2, Table 4.3).

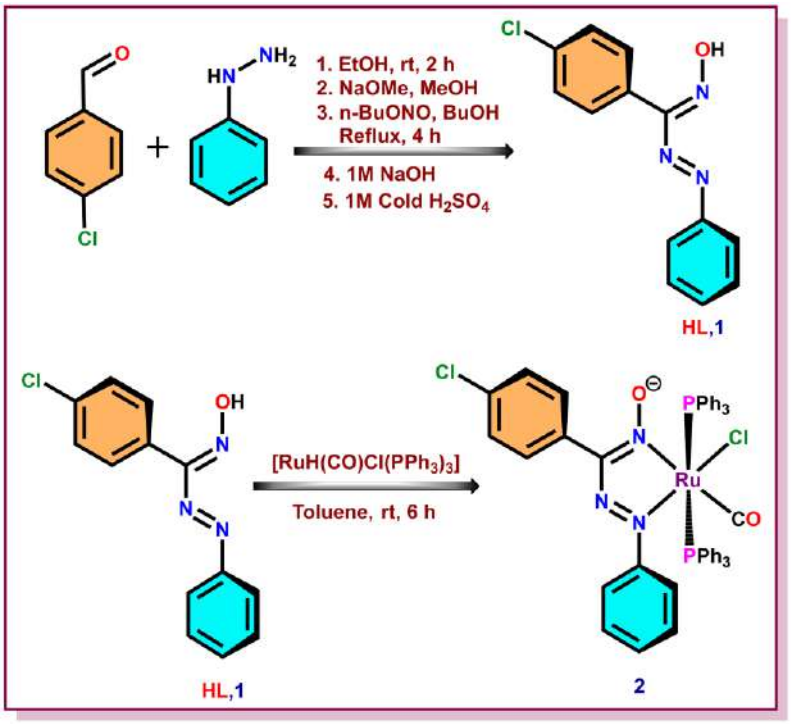

Scheme 4.3: Schematic representation of the synthetic strategy for ligand **1** and its subsequent synthesis into ruthenium(II) complex **2**

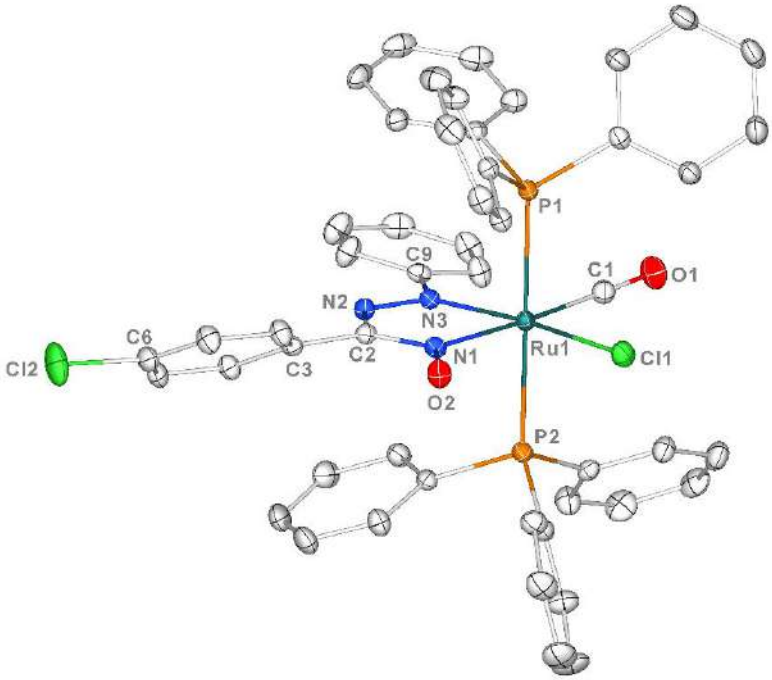

Figure 4.1: ORTEP diagram of *trans*-[Ru(*p*-Cl-aaOCl(CO)(PPh_3)$_2$] (**2**) with thermal ellipsoids are set at 50% (Hydrogen atoms are omitted for clarity); **CCDC No.: 2426769**. Selected bond lengths (Å) and bond angles (degrees): Ru1–N1 2.0883(19), Ru1–N3 2.0558(18), Ru1– Cl1 2.4212(6), Ru1–P1 2.4046(6), Ru1–P2 2.4284(6), N2–N3 1.298(2), N1–O2 1.258(2), N1–Ru1–N3 76.56(7), C1–Ru1–Cl1 88.63(8), N1–Ru1–Cl1 93.70(5), and P1–Ru1–P2 179.45(2)

Table 4.1: Crystallographic details of complex **2**

	2
Empirical formula	$C_{50}H_{39}N_3O_2Cl_2P_2Ru$
T/K	298.00
f_w	947.75
Crystal system	Monoclinic
Space Group	$P2_1/n$
a/Å	10.5600(6)
b/Å	21.2959(12)
c/Å	19.0927(11)
α/deg	90
β/deg	94.255(2)
γ/deg	90
V/ $Å^3$	4281.8(4)
Z	4
D_c/Mgm^{-3}	1.470
μ/mm^{-1}	0.611
F(000)	1936.0
cryst size/mm^3	0.31 × 0.25 × 0.14
θ/deg	1.913 – 25.741
Measured reflns	161682
Unique reflns	8141
[a]GOF on F^2	1.064
R_1[b], $wR2$[c][$I>2\sigma(I)$]	R_1= 0.0313, wR_2= 0.0676
R_1, wR_2	R_1= 0.0503, wR_2= 0.0719
[a]GOF = $\{\Sigma[w(F_o^2-F_c^2)^2]/(n-p)\}1/2$. [b]$R1 = \Sigma [\|F_o\|-\|F_c\|]/ \Sigma \|F_o\|$. [c]$wR2 = [\Sigma [w(F_o^2-F_c^2)^2]/ \Sigma [w(F_o^2)^2]]^{1/2}$ where $w = 1/[\sigma^2(F_o^2)+(aP)^2+bP]$, $P = (F_o^2+2F_c^2)/3$.	

Table 4.2: Selected Experimental and Theoretical Bond Lengths (Å) and Angles (°) of **2**

Metrical Parameter of 2					
Bond lengths			**Bond Angles**		
	Expt.	**Theo.**		**Expt.**	**Theo.**
Ru1–N1	2.0883(19)	2.134	N1–Ru1–N3	76.56(7)	75.33
Ru1–N3	2.0558(18)	2.080	Cl1–Ru1–C1	88.63(8)	87.30
Ru1–P1	2.4046(6)	2.516	N1–Ru1–Cl1	93.70(5)	97.96
Ru1–P2	2.4284(6)	2.511	N3–Ru1–C1	101.13(9)	99.47
Ru1–C1	1.882(3)	1.902	N1–Ru1–P2	88.32(5)	88.61
Ru1–Cl1	2.4212(6)	2.527	N3–Ru1–P1	90.52(5)	91.85
N2–N3	1.298(2)	1.281	N3–Ru1–P2	89.04(5)	91.61
N1–O2	1.258(2)	1.256	Cl1–Ru1–P1	90.47(2)	86.10
C1–O1	1.149(3)	1.147	Cl1–Ru1–P2	90.02(2)	90.00
N2–C2	1.345(3)	1.352	C1–Ru1–P1	85.96(8)	88.68
N3–C9	1.440(3)	1.435	C1–Ru1–P2	93.80(8)	94.53
C2–C3	1.472(3)	1.476	P1–Ru1–P2	179.45(2)	174.81

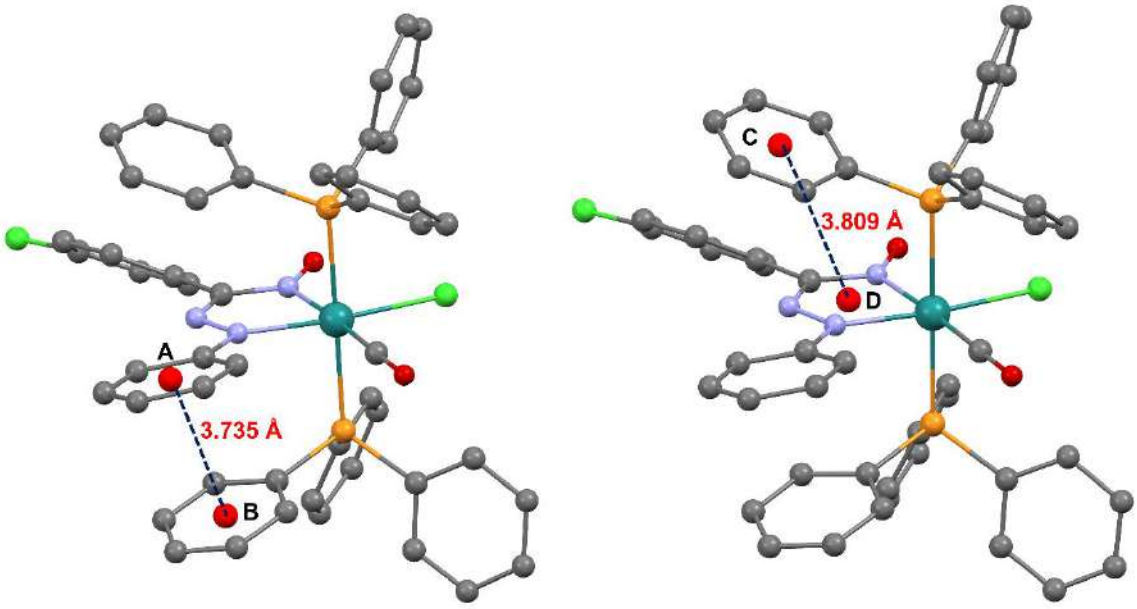

Figure 4.2: Intramolecular pi-pi stacking diagram of complex **2**

Table 4.3: Different stacking parameters* of complex **2**

Stacking Parameters	Ring A–B	Ring C–D
d[C_g(*I*) – C_g(*J*)] Å/α°	3.7351(16)/16.29(13)	3.8094(14)/22.12(12)
d[Cg(*I*) – R(*J*)] Å/β°	3.6968(12)/24.4	2.9285(8)/21.9
d[Cg(*J*) – R(*I*)] Å/γ°	3.4012(11)/8.2	3.5357(11)/39.8

*Cg(I) = Centroid of ring I, Cg(J) = Centroid of ring J, d[Cg(I) – Cg(J)] = Separation between two ring centroids, d[Cg(I) – R(J)] = Perpendicular distance of Cg(I) on ring J, d[Cg(J) – R(I)] = Perpendicular distance of Cg(J) on ring I, α = Dihedral angle between Planes I of ring I and plane J of ring J, β and γ = Angle between the vector Cg(I) – Cg(J) and the normal to plane P(I) or P(J) from Cg(I) and Cg(J) respectively

4.2.2 Electrochemistry and computational study

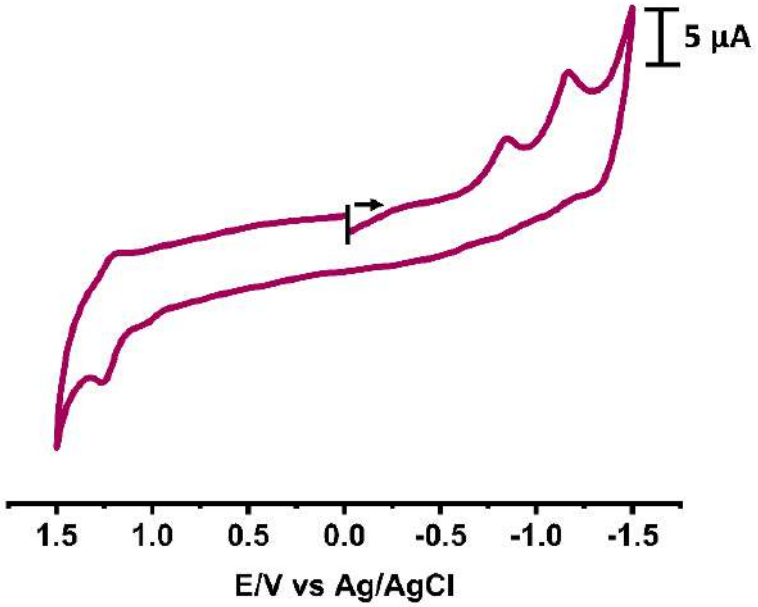

Figure 4.3: Cyclic voltammogram of complex *trans*-[Ru(*p*-Cl-aaO)(PPh_3)$_2$Cl(CO)]

The electrochemical study of *trans*-[Ru(*p*-Cl-aaO)Cl(CO)(PPh_3)$_2$] (**2**) is carried out in acetonitrile/dichloromethane (9:1 v/v) solution, 0.2 M tetrabutyl ammonium hexafluorophosphate (TBAF) as supporting electrolyte, using platinum as the working electrode, and saturated Ag/AgCl as the reference electrode. It displays two single electron irreversible reductive couple at −0.84 V and −1.16 V along with a reversible oxidative response

at +1.22 V with peak-to-peak separation of 53 mV (Figure 4.3, Table 4.4). Theoretical exploration of redox orbitals points towards the fact that first reduction process is majorly due to coordinated azo-oxime reduction while the subsequent reduction has contributions from both

Table 4.4: Electrochemical data of complex **2** with respect to Ag/AgCl

Complex	$E_{1/2}$/V (ΔE^a/mV)	
	Oxidation	**Reduction**
2	+1.22(53[a])	−0.84 (E_p^2/V), −1.16 (E_p^2/V)
E_P^1 = anodic peak potential; E_p^2 = cathodic peak potential, peak-to-peak separation		

the metal and ligand (Table 4.6.A2). The irreversible character of these responses may be attributed to dissociation of Ru–Cl bond[18a, 22a] during the reduction process. This is an indicator that azo-oxime skeleton of the complex may be suitably exploited to bring about ligand-centric electron transfer catalysis and it may be initiated *via* cleavage of Ru–Cl bond. Also, oxidation process may be ascribed to ligand oxidation along with some metal contribution. The optimized geometry of the complex is depicted in Figure 4.4(a) while the calculated and experimental absorption spectrum in Figure 4.4(b).

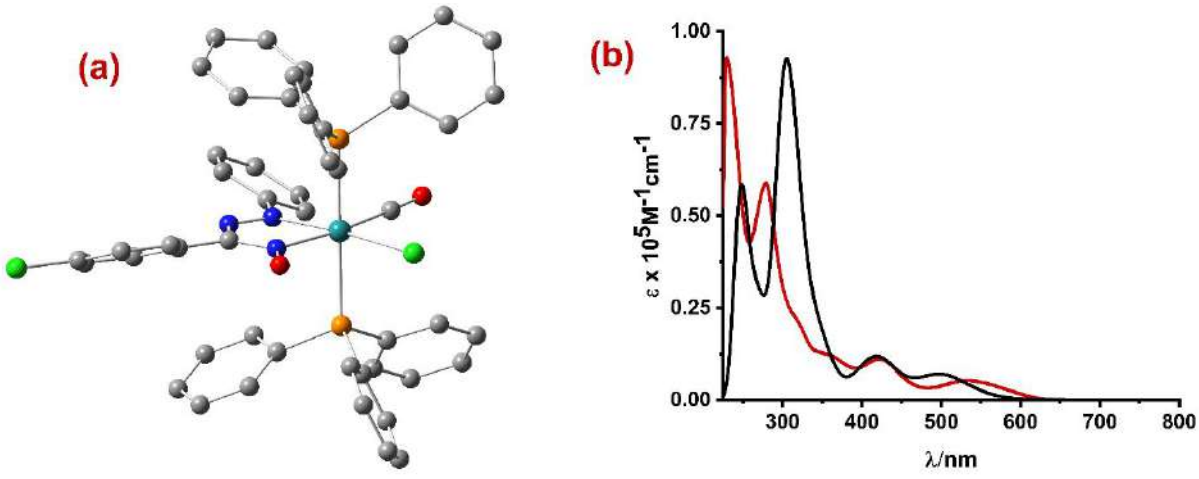

Figure 4.4: (a) The optimized geometry of complex *trans*-[Ru(*p*-Cl-aaO)Cl(CO)(PPh_3)$_2$] (**2**) at (R)B3LYP/6-311+G(d,p) level of theory & (b) Experimental (red) and Calculated (black) absorption spectrum of **2**

4.2.3 Absorption spectra

Time-dependent density functional theory (TD-DFT) calculations were performed at the (R)B3LYP level of theory using the 6-311+G(d,p) basis set for all non-hydrogen atoms and the LANL2DZ basis set for Ru, together with the conductor-like polarizable continuum model (CPCM) in dichloromethane (CH_2Cl_2) to simulate the absorption spectra. For complex **2**, the lowest 100 singlet–singlet transitions were systematically evaluated for both absorption and emission processes. The computational results obtained from TD-DFT were found to be in good qualitative agreement with the experimental data. At present, TD-DFT is well recognized as a rigorous formalism within the DFT framework for describing electronic excitation energies and it has been extensively applied to investigate the spectral properties of transition metal complexes.

To gain deeper insight into the electronic nature of the absorption and emission processes, natural transition orbital (NTO) analysis was performed (Table 4.6.A3). This approach provides an accurate representation of the transition density between the ground and excited states, expressed in terms of single-particle transitions involving paired 'hole' and 'electron' states. In this context, the occupied and unoccupied NTOs are referred to as 'hole' and 'electron' orbitals, respectively (Table 4.6.A4).

The vertical excitation energies were computed at the equilibrium geometry of the ground state (S_0) and described in terms of one-electron excitations from the molecular orbitals of the corresponding S_0 geometry. The calculated electronic transitions with appreciable oscillator strengths ($f \geq 0.02$) were distributed across both the lower and higher wavelength regions of the spectrum, thereby reproducing the key features observed experimentally.

In complex **2**, the absorption band at 532 nm is calculated to around 498 nm ($f = 0.0609$, 2.4866 eV) and is primarily composed of ILCT [π (Azo + Oxime +Ph) → π* (Azo + Oxime + Ph) &

d-d [$d_{xz} \rightarrow d_{yz}$] transition. The next absorption at 420 nm (2.9470 eV, f = 0.0722) is computed at rightly 420.72 nm and it can be ascribed as the combination of LLCT, ILCT & d-d [π (Cl + Oxime) → π* (Azo + Oxime + Ph) & $d_{xz} \rightarrow d_{yz}$]. The 362 nm band is calculated at around 352 nm (3.5221 eV, f = 0.0125) which can be ascribed again as the accumulation of ILCT, LLCT & d-d [π (Cl + Oxime) → π* (Cl + PPh_3) & $d_{xz} \rightarrow d_z^2$]. The 279 nm band is calculated at 300 nm (4.1299 eV, f = 0.1788) is consist of two transitions. First one can be described as combination of ILCT, LLCT & d-d [π (PPh_3) → π* (Cl + PPh_3) & $d_{xz} \rightarrow d_z^2$] transition. The second one is comprised of LLCT and MLCT [π (Azo + Oxime + Ph) → π* (PPh_3) & d_{yz} → π* (PPh_3)] character. The lowest energy band at 230 nm is calculated at 246 nm (5.0343 eV, f = 0.0525) which can be designated ILCT & LLCT [π (PPh_3) → π* (PPh_3) & π (PPh_3) → π* (Azo + Ph)] character.

4.2.4 Catalytic Activity

Based on our previous report on Ru(II)-catalyst,[18] we have successfully employed the current ruthenium complex *trans*-[Ru(*p*-Cl-aaO)Cl(CO)(PPh_3)$_2$] (**2**) for the selective C-alkylation of fluorene. To assess the optimal reaction conditions, we initially used *9H*-fluorene (**3**) and benzyl alcohol (**7a**) as model substrates. The details of optimized conditions are summarized in Table 4.5. Initially, 1.0 mmol of 9H-fluorene and 2.0 mmol of benzyl alcohol were treated with 0.5 equiv. of K_2CO_3 and 0.1 mol% of pre-catalyst **2**, they were yielding 9-benzyl-*9H*-fluorene (**8a**) with 55% yield after 8 h in toluene at 100 °C (Table 4.5, Entry 1). The yield of **8a** remained largely unaffected by further variations in the amount of base (Table 4.5, Entry 2). Substituting the base with Cs_2CO_3 also unable to improve the yield of **8a** (Table 4.5, Entries 3–5). However, switching from an alkaline metal carbonate to an alkoxide base, such as t-BuOK, without altering other reaction parameters, led to a dramatic improvement in the yield, achieving 93% (Table 4.5, Entry 6). Notably, organic amine bases such as i-Pr_2NEt, Et_3N (Table 4.5, Entry 20, 21) fail to produce any meaningful result. The reduced yield of compound **8a**

observed with alkaline earth metal carbonates can likely be attributed to their comparatively lower basicity, which may limit their effectiveness in facilitating the reaction. In our search for a suitable solvent beyond toluene, we carried the same reaction in different solvents such as tetrahydrofuran (THF), *N, N*-dimethylformamide (DMF), ethanol, xylene, acetonitrile, however, we found that their performance was not as impressive as compared to toluene (Table 4.5, Entry 22, 23, 24 & 25). The reduced efficiency in forming **8a** when using polar solvents (e.g., THF, ethanol, DMF, acetonitrile) can be explained through their competitive coordination with the transition metal centre, thereby interfering with the catalytic cycle. The reduction of reaction temperature from 100 °C to 75 °C led to a significant reduction in yield. (Table 4.5, Entry 26). No substantial improvement in yield was observed when the alkylation reaction was performed at an elevated temperature (120 °C) (Table 4.5, Entry 27). Thus, t-BuOK was chosen as the preferred base, and toluene was selected as the optimal solvent for the aforementioned catalytic reaction. After achieving the optimal reaction condition for the alkylation of fluorene, we tried to explore the reactivity of fluorene and primary alcohol under solvent-free condition. Since both the catalyst and substrate have very high melting points, the amount of the intended product was drastically reduced (Table 4.5, Entry 28). Thus, the standardized reaction condition is as follows: 1.0 mmol of fluorene, 2.0 mmol of alcohol, 0.5 equiv. of t-BuOK, and 0.1 mol% of ruthenium catalyst (**2**) in toluene solvent at 100 ºC for 8 h.

Based on our standardized reaction conditions, initially we began assessing the scope of various alcohol derivatives. Several aromatic and heteroaromatic as well as aliphatic alcohols, including substituted benzyl alcohols featuring both electron-donating and electron-withdrawing substituents at the ortho, meta, and para positions were successfully employed to alkylate the 9-position of fluorene, resulting in good to excellent yield (Table 4.6, **8a**-**8z**).

Table 4.5: Optimization of the reaction conditions for 9-substituted monoalkylated fluorene *via* catalytic dehydrogenation using catalyst **2**[a,b,c]

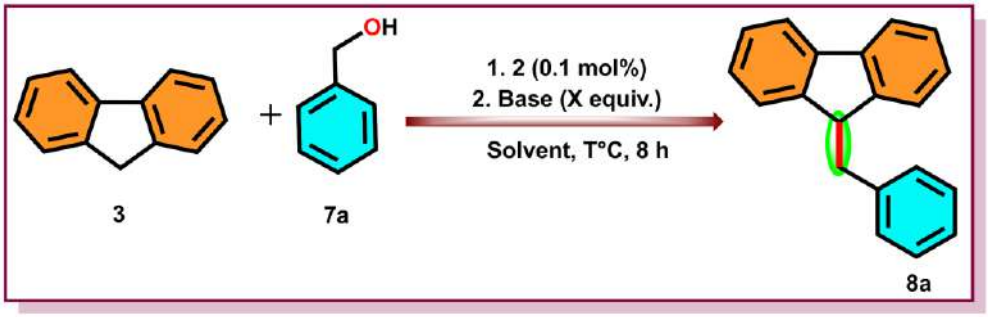

Entry	Catalyst (0.1 mol%)	Base	x (equiv.)	Solvent	T°C	Yield[b] (%)
1	2	K_2CO_3	0.5	Toluene	100	55
2	2	K_2CO_3	1.0	Toluene	100	57
3	2	Cs_2CO_3	0.5	Toluene	100	52
4	2	Cs_2CO_3	1.0	Toluene	100	54
5	2	Cs_2CO_3	1.5	Toluene	100	45
6	**2**	**t-BuOK**	**0.5**	**Toluene**	**100**	**93**
7	2	t-BuOK	1.0	Toluene	100	85
8	2	t-BuOK	1.5	Toluene	100	78
9	2	KOH	0.5	Toluene	100	70
10	2	KOH	1.0	Toluene	100	72
11	2	NaOH	1	DMF	100	Trace
12	2	NaOH	1	THF	100	39
13	2	t-BuOK	0.5	THF	100	50
14	2	Cs_2CO_3	0.5	Xylene	100	40
15	2	Cs_2CO_3	1.0	Xylene	100	45
16	2	K_2CO_3	0.5	CH_3CN	82	10
17	2	K_2CO_3	1.0	CH_3CN	82	14
18	2	K_3PO_4	0.5	Toluene	100	5
19	2	K_3PO_4	1.0	Toluene	100	8
20	2	i-Pr_2NEt	1.0	Toluene	100	NR
21	2	Et_3N	1.0	Toluene	100	NR
22	2	t-BuOK	0.5	DMF	100	Trace
23	2	t-BuOK	0.5	EtOH	78	Trace
24	2	t-BuOK	0.5	Xylene	100	65
25	2	t-BuOK	0.5	CH_3CN	100	20

26	2	t-BuOK	0.5	Toluene	75	55
27	2	t-BuOK	0.5	Toluene	120	94
28	2	t-BuOK	0.5	–	100	20
29	–	t-BuOK	0.5	Toluene	100	Trace
30	–	t-BuOK	1.0	Toluene	100	Trace
31	2	–	–	Toluene	100	NR

[a]*Standardized Reaction conditions:* **3** (1 mmol), **7a** (2.0 mmol), Catalyst **2** (0.1 mol %), base (x equiv.), solvent (3 ml), 100 ºC (oil bath), 8 h. [b]Isolated yield after column chromatography, [c]Under air

Benzyl alcohols with electron-donating functionalities produced the corresponding C-alkylated products in excellent yields (Table 4.6, **8b**: 87%, **8f**: 92%, **8g**: 82%, **8h**: 87%, **8i**: 89%, **8j**: 88%). Benzyl alcohols with moderate to strong electron-withdrawing groups at *meta* and *para* position were also effectively utilized in C(sp^3)–H alkylation of fluorene yielding up to 89% (Table 4.6, **8d**: 86%, **8e**: 82%, **8k**: 89%, **8i**: 88%, **8m**: 85%, **8n**: 80%). We are also able to alkylate the fluorene with aromatic polycyclic benzyl alcohols, achieving excellent yield (Table 4.6, **8u**: 80%, **8y**: 85%). These results demonstrate the effectiveness of this homogeneous ligand-based Ru(II) catalyst in alkylating the C(sp^3)–H of fluorene. The alcohols with heteroaromatic functionality such as thiophene and furan were also successfully engaged in alkylation protocol with good yields (Table 4.6, **8w**: 79%, **8x**: 78%). Thereafter, we focused on utilizing aliphatic alcohols as alkylating agents for the aforesaid reaction. Aliphatic alcohols are usually less reactive and are difficult to dehydrogenate but it is worth mentioning that in this catalytic protocol 1-propanol, 1-butanol, 1-hexanol, 1-heptanol, 1-octanol and 1-nonanol were effectively employed to alkylate the fluorene, achieving yields up to 87% (Table 4.6, **8o**: 74%, **8p**: 76%, **8q**: **77**%, **8r**: 80%, **8s**: 83%, **8t**: 87%). The yield improves progressively from lower to higher alcohols. Despite our repeated attempts, the present catalytic protocol has failed to activate methanol and ethanol to alkylate the fluorene. To further demonstrate the versatility and general applicability of the developed catalytic protocol, we extended our investigation to a range of structurally diverse 2,7-disubstituted fluorenes.

Table 4.6: Substrate scope of various alcohols with fluorene

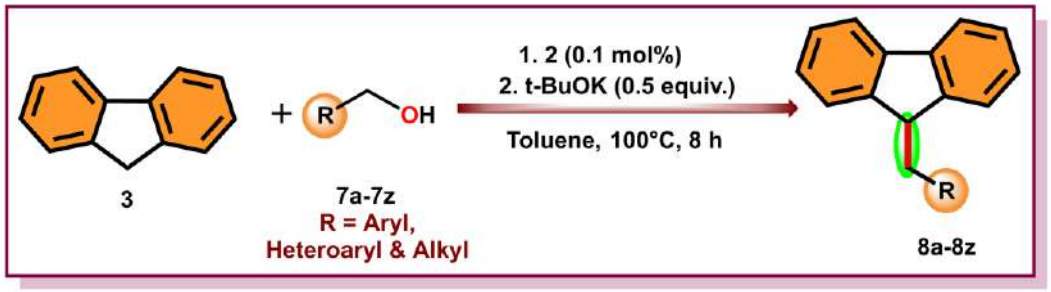

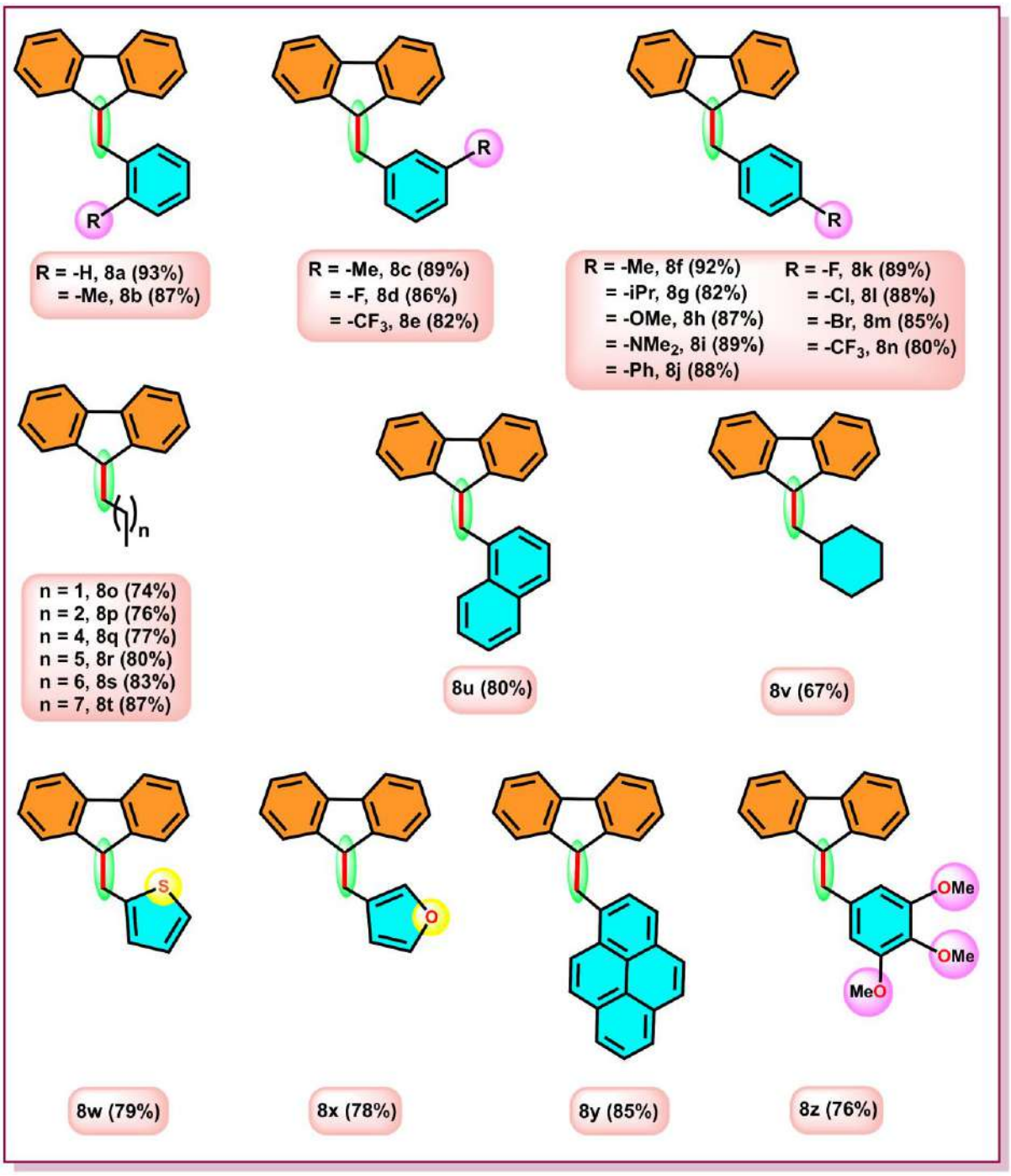

Different 2,7-disubstituted fluorenes, such as 2,7-dichloro-*9H*-fluorene, 2,7-dibromo-*9H*-fluorene, and 2,7-di-tert-butyl-*9H*-fluorene, were efficiently monoalkylated using this established catalytic protocol. Both 2,7-dichloro-*9H*-fluorene and 2,7-dibromo-*9H*-fluorene were successfully coupled with diverse array of alcohols. Benzyl alcohols with both electron-donating and withdrawing groups at ortho, meta, and para position proved to be highly effective alkylating agents, yielding the corresponding C9-alkylated products in excellent yields (Table 4.7, **9b**: 80%, **9c**: 82%, **9d**: 84%, **9e**: 80%, **9f**: 86%, **9g**: 78%, **9h**: 81%, **9i**: 84%, **9m**: 82%, **9n**: 81%). A similar reactivity is exhibited by 2,7-dibromo-*9H*-fluorene with various alcohols, resulting in good to excellent yields (Table 4.7, **10a**: 84%, **10b**: 78%, **10c**: 75%, **10d**: 79%, **10e**: 80%). Polyaromatic alcohols such as naphthalen-1-ylmethanol (Table 4.7, **9w**: 80%, **10m**: 78%), naphthalen-2-ylmethanol (Table 4.7, **9x**: 82%), pyren-1-ylmethanol (Table 4.7, **9y**: 78%) were also successfully utilized in sp^3 C-alkylation of fluorene with good yield. The previously mentioned fluorenes are also highly reactive toward aliphatic alcohols, albeit with somewhat lower yields (Table 4.7, **9o**: 68%, **9p**: 70%, **9q**: 71%, **9r**: 76%, **10f**: 78%, **10g**: 81%, **10h**: 84%, **10i**: 85%). Cyclohexylmethanol also afforded the corresponding alkylated product in good yield (Table 4.7, **9t**: 60%). As previously observed, the product yield increases with the length of the alcohol chain. Pleasingly, 2,7-di-tert-butyl-*9H*-fluorene was as reactive as other substituted fluorenes and alkylated with a wide variety of benzyl alcohols to afford the C9-alkylated products in good to excellent yield. Both electron-donating groups, such as alkyl, –NMe_2, and methoxy, and electron-withdrawing groups including fluoride, chloride, and trifluoromethyl (–CF_3), afforded the respective alkylated products with excellent yields (Table 4.7). Among these, electron-withdrawing groups are particularly very effective in coupling with 2,7-di-tert-butyl-*9H*-fluorene, producing 9-alkylated fluorenes with yields of up to 88% (Table 4.7; **11g**: 87%, **11h**: 88%, **11i**: 84%).

Table 4.7: Scope of different fluorene derivatives with various alcohols

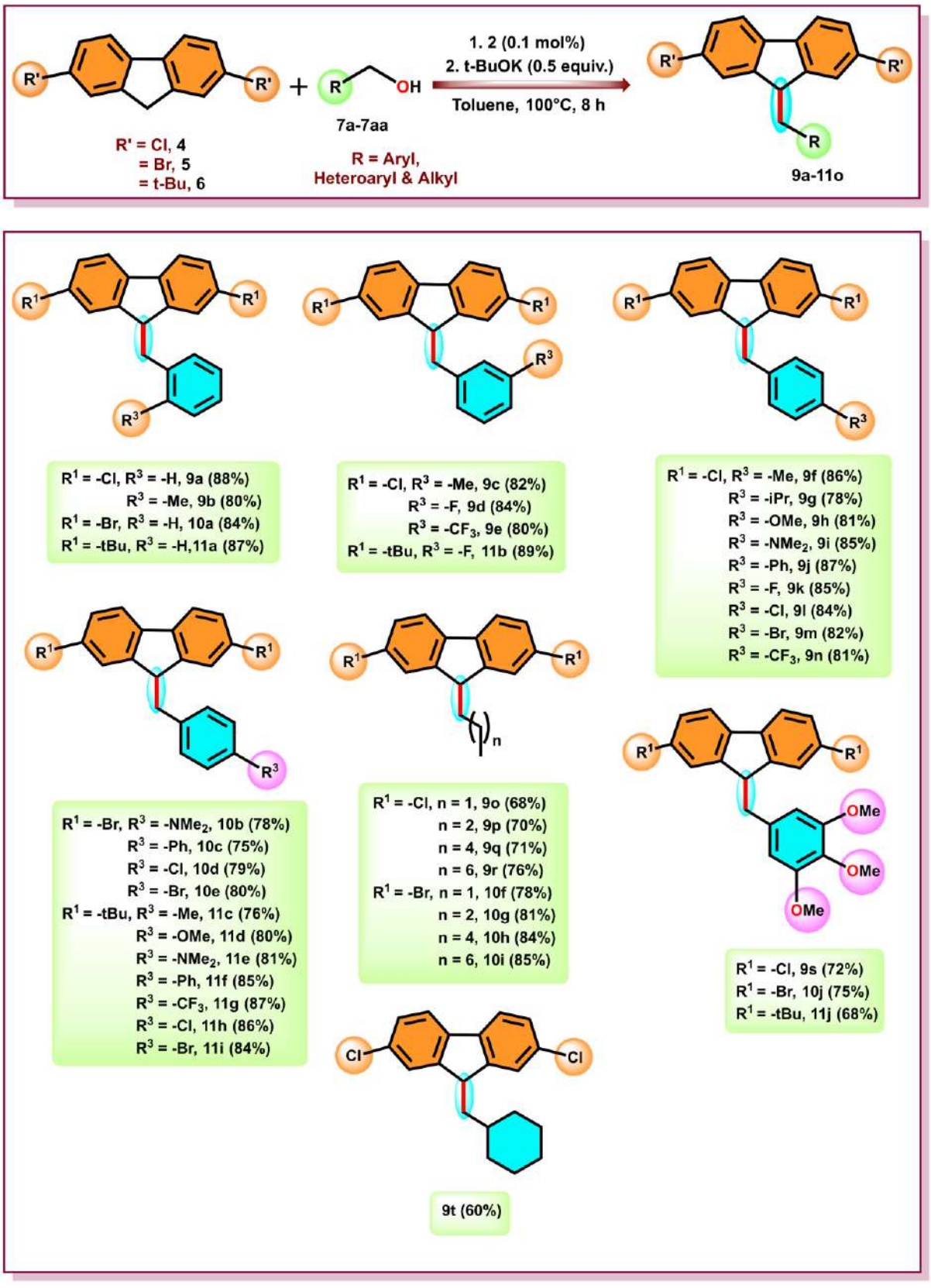

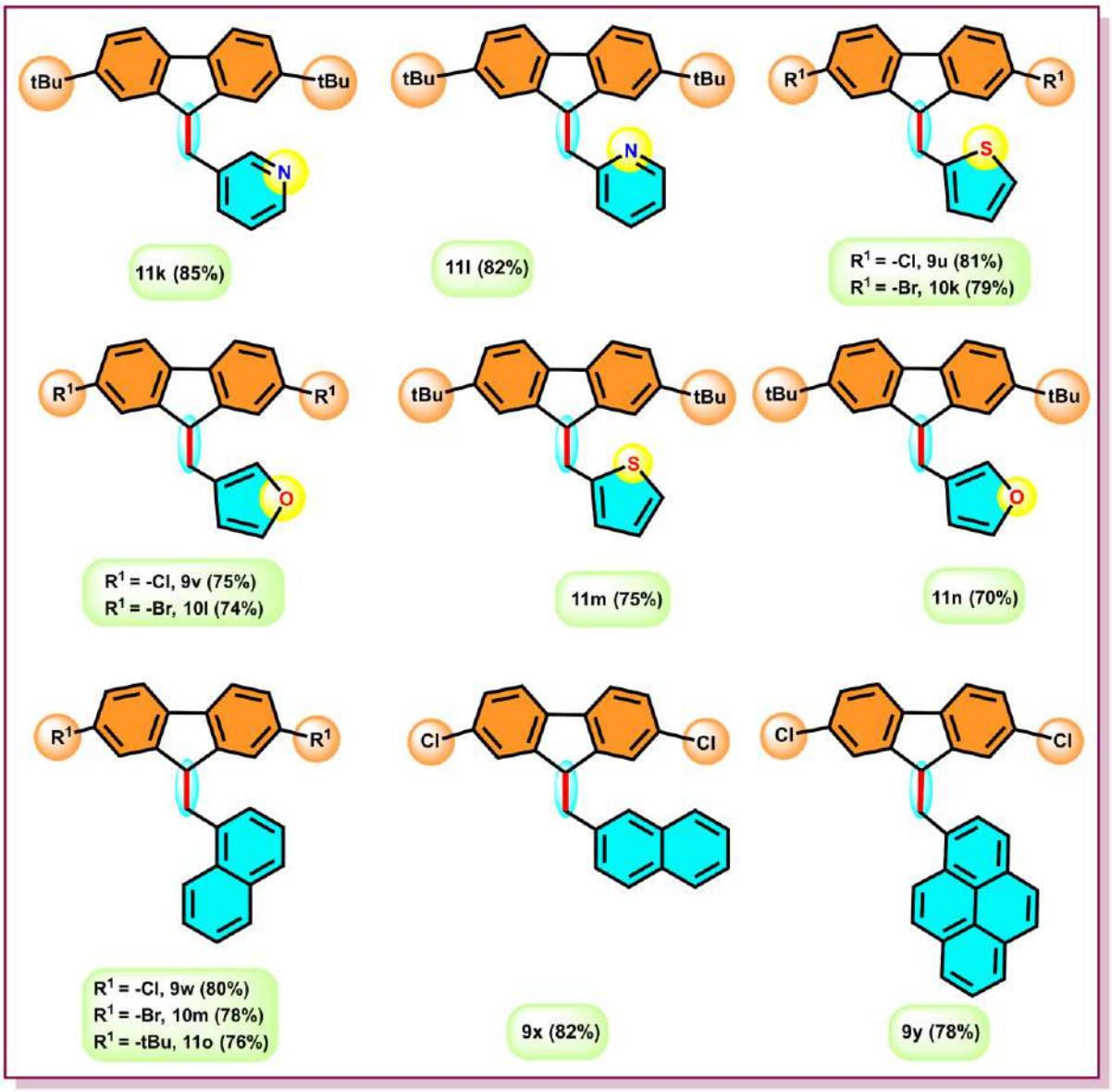

Alcohols with heteroaryl groups, such as pyridin-2-ylmethanol, pyridin-3-ylmethanol, furan-3-ylmethanol, and thiophene-2-ylmethanol, were also utilized to alkylate 2,7-di-tert-butyl-9H-fluorene, yielding the corresponding products in reasonable yields (Table 4.7; **11k**: 85%, **11l**: 82%, **11m**: 75%, **11n**: 70%). We also obtained solid state crystal structures of some synthesized 9-alkylated fluorenes, as shown in Figure 4.5.

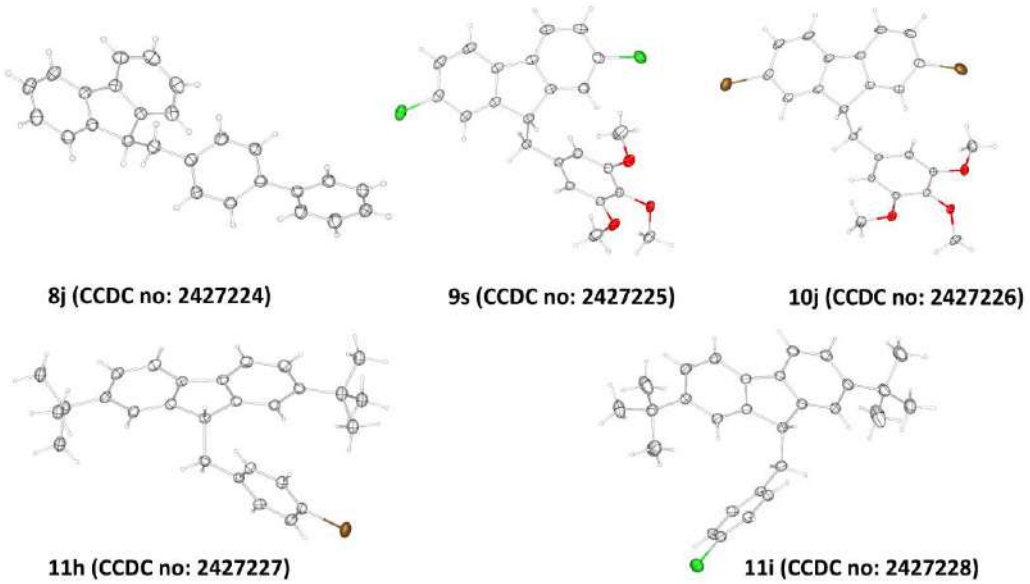

Figure 4.5: ORTEP diagram of some synthesised 9-monoalkylated fluorene derivatives determined by single-crystal X-ray diffraction (SCXRD). Thermal ellipsoids are drawn at the 50% probability level

4.2.5: Mechanistic investigation

To unveil the plausible reaction pathway for the synthesis of 9-alkylated fluorene, we conducted a series of control experiments. Since the alkylation reaction was carried out at a relatively high temperature (100°C) we initially assessed the stability of the catalyst. When the catalyst was heated in different organic solvents at elevated temperatures, we observed that the catalyst remained intact even at 130°C in solvents like toluene and xylene under both aerobic and isolated conditions. Next, we evaluated the homogeneity of the catalysis. Upon conducting the oxidation of primary alcohol as well as the alkylation of fluorene (**3**) with benzyl alcohol (**7a**) in presence of elemental mercury, both reactions proceeded very smoothly under the previously mentioned conditions (Scheme 4.4a, See experimental section for details). These experimental results confirmed that ruthenium nanoparticles did not involve in the catalysis and the molecular ruthenium catalyst **2** remained as active species throughout the catalytic process. To determine whether the dehydrogenative functionalization of alcohols proceeds *via* an "acceptorless dehydrogenation" (ADC) pathway, we converted benzyl alcohol to

benzaldehyde under standard reaction conditions. Instead of detecting dihydrogen, we observed the formation of hydrogen peroxide, which was confirmed spectrophotometrically (Scheme 4.4b & 4.5, for details see the experimental section). The condensation reaction between 1-napthaldehyde (**7s**) and fluorene (**3**) in the presence of catalyst **2** yielded the alkenylated product **8s'** with excellent yield (87%) (Scheme 4.4c). The similar observation was observed in absence of catalyst **2** (with 80% yield). Practically no reaction was found to occur without base. The intermediate **8s'** was then hydrogenated *via* a metal-bound "borrowing hydrogenation" pathway leading to the observed alkylated fluorene as the final product. To validate the above hypothesis, we performed the catalytic hydrogenation of alkenylated fluorene **8s'** with benzyl alcohol **7a** under the standard reaction condition. The reaction successfully yielded the C9-alkylated product **8s** with an 80% yield and 56% of benzaldehyde (Scheme 4.4d). This is an indicator that benzyl alcohol assists the hydrogenation process and acts as the source of hydrogen. In order to confirm that the alkylation reaction proceeds *via* alkenylated intermediate as mentioned above, we conducted the reaction between **3** and **7s** (Scheme 4.4e) for only 3 h. After usual chromatographic separation (See experimental section for details), we were able to isolate alkenylated product **8s'** (20% isolated yield) along with alkylated product **8s** (10% isolated yield). We also investigated whether the alkylation reaction proceeds *via* the formation of any organic radical species and for this, we have performed the alkylation reaction between fluorene (**3**) and benzyl alcohol (**7a**) in the presence of radical scavengers like **TEMPO** (2,2,6,6- tetramethylpiperidin-1-yl)oxyl) and **BHT**(2,6-di-tert-butyl-4-methylphenol) (Scheme 4.4f). The reaction proceeded smoothly, yielding C9-alkylated products with yields of 80% and 85%, respectively. These experimental results indicate that the reaction doesn't involve any ketyl type radical which is typically associated with a one-electron hydrogen atom transfer process (HAT). Instead, the evidence supports that the

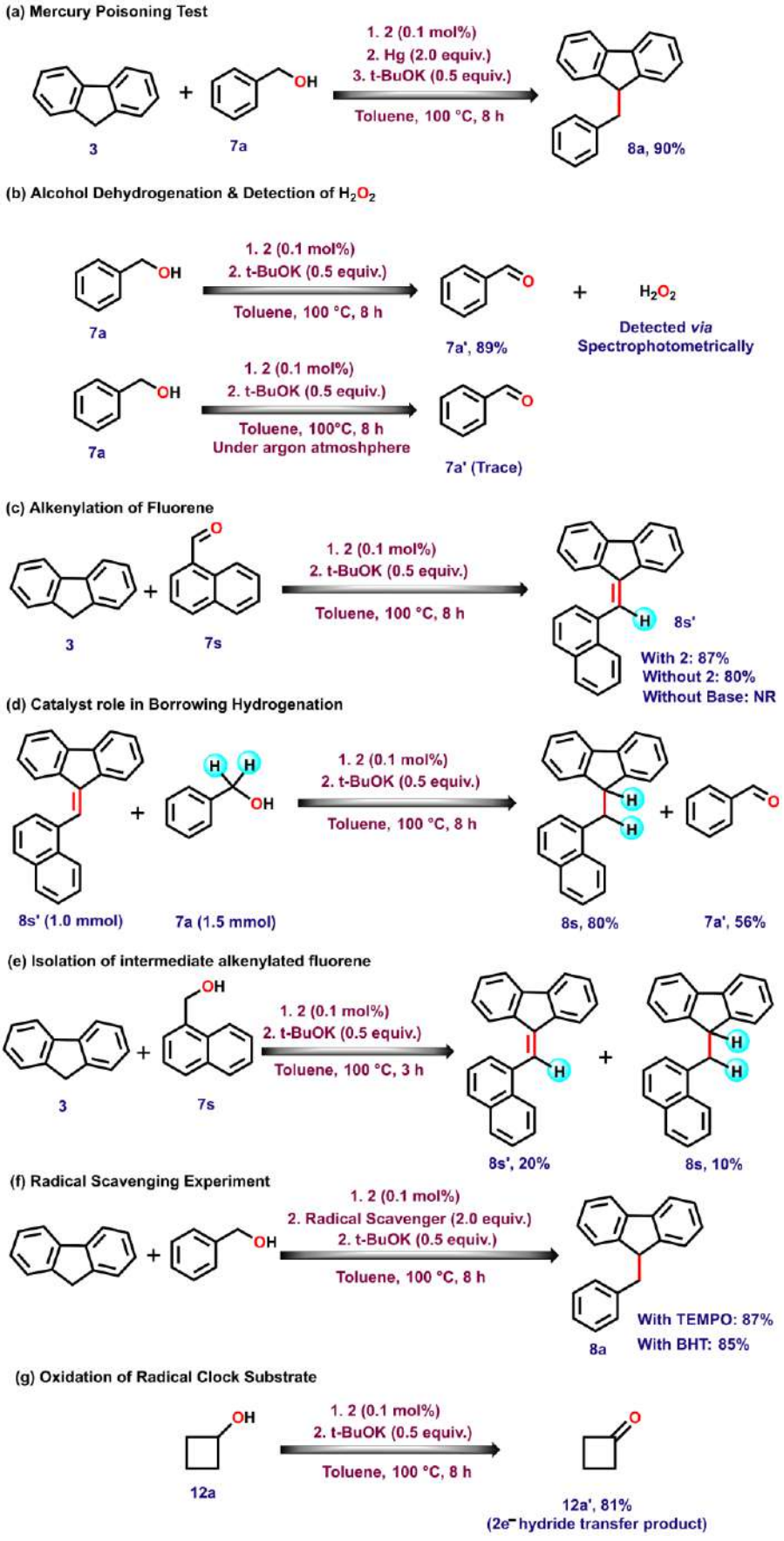

Scheme 4.4: Control Experiments

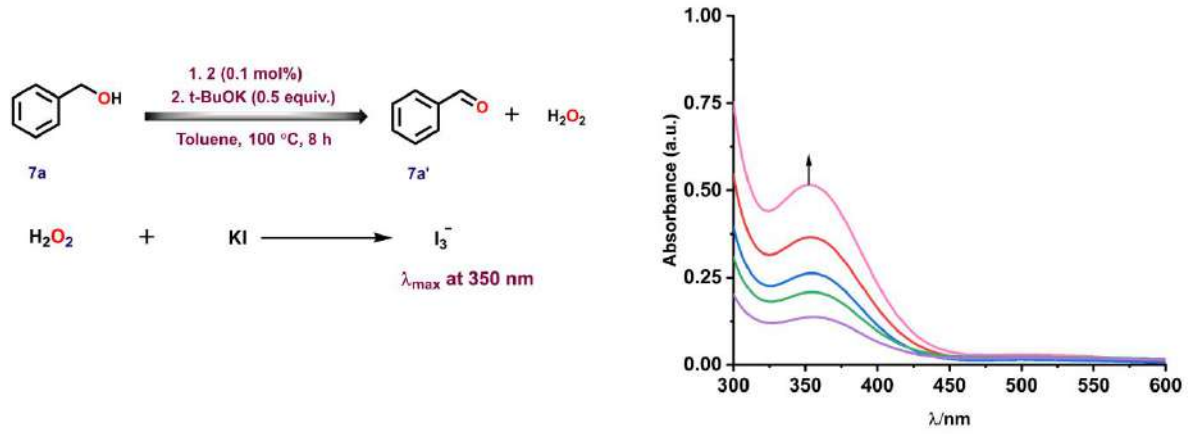

Scheme 4.5: Detection of H_2O_2 and determination of λ_{max} of triiodide (I_3^-) anion at 350 nm

mechanism should involve a two-electron hydride transfer pathway where hydrogen donor simultaneously transfers both proton and a pair of electrons. In pursuit of more conclusive evidence, we have further conducted the oxidation of a radical clock substrate *viz.* cyclobutanol (**12a**), under identical reaction conditions (Scheme 4.4g). The formation of cyclobutanone in 81% yield rather than multiple ring-opening products directly pointed towards the two-electron hydride transfer pathway for dehydrogenation of alcohol. [22]

To get a more comprehensive insights of mechanistic pathway we further carried out the sub-stoichiometric oxidation of 1-phenylethanol (**13a**) under argon atmosphere in the presence of 0.5 equiv. of t-BuOK and 0.5 mol% of catalyst **2** and the reaction mixture was analysed by IR spectroscopy. New stretches were observed at 3025 cm^{-1} and 3068 cm^{-1}corresponding to N–H groups while the one at around 1433 cm^{-1} (N=N stretches) was missing. It implies that coordinated azo to hydrazido conversion must have taken place *via* two-electron reduction process during the catalytic reaction (Figure 4.6.A16).[18b] Similarly, when we conducted the same reaction using deuterated 1-phenylethanol (**14a**), the corresponding N–D stretching frequencies were observed at 2327 cm^{-1} and 2353 cm^{-1} (Figure 4.6.A17). These observations are consistent with the probable participation of the azo/hydrazo redox couple during the dehydrogenation of alcohol.

Based upon the above control experiments as well as from our previous report, [18b] we have proposed a plausible mechanism for ruthenium-catalysed C-alkylation of fluorene, as illustrated in Scheme 4.6. In the initial step, the pre-catalyst **2** is activated in presence of t-BuOK under hot reaction condition to generate active catalyst **I**, the latter is coordinatively unsaturated due to removal of chloride. The alcohol (RCH_2OH) is now attacks the Ru(II) and gets coordinated *via* the O, leading to the formation of cationic hydroxo species **II**. Thereafter, the activated hydrogen atom of hydroxyl group (–OH) is transferred to the non-coordinated N_{Azo} atom of the ligand sphere to generate complex **III**.[18b] The coordinated N_{azo} atom of ligand framework in intermediate **III** is then activated and removes one of active methylene hydrogens ($–CH_2$) of RCH_2OH to generate intermediate **IV**, during the course of which the coordinated RCH_2O^- is transformed to RCHO. Subsequently, the coordinated RCHO is released from intermediate **IV** to form the coordinated hydrazido intermediate **V**. The active catalyst **I** is regenerated through oxidation of intermediate **V** in presence of dioxygen, the latter is simultaneously reduced to H_2O_2 (detected spectrophotometrically). Regeneration of active catalyst **I** enables the reaction to proceed to the next cycle of catalytic process.

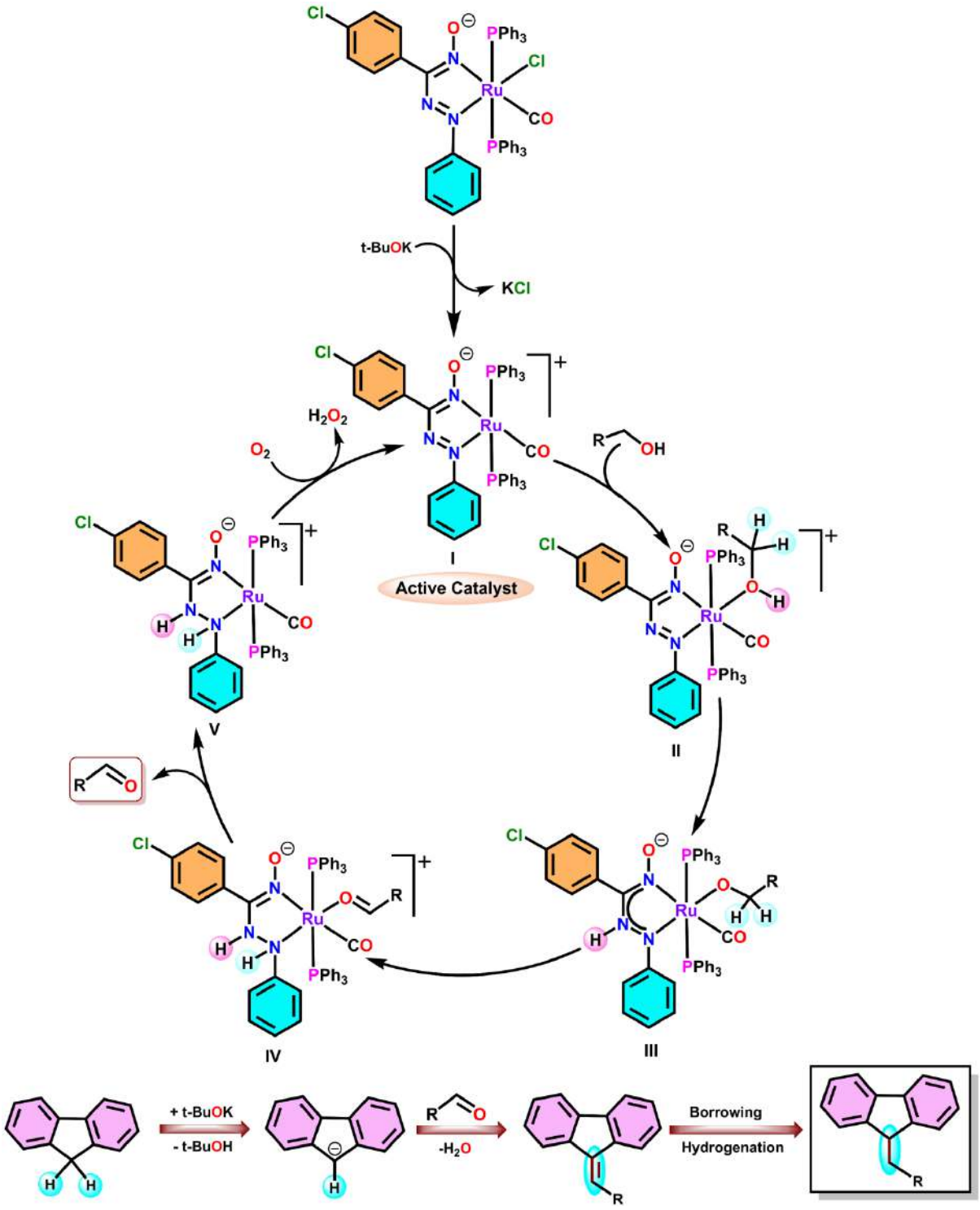

Scheme 4.6: Plausible mechanistic pathway of formation 9-alkylated fluorene

The aldehyde (RCHO) formed *via* the catalytic dehydrogenation process, possibly undergoes a condensation reaction with carbanion generated *via* the deprotonation of fluorene in presence of t-BuOK at C9-position to form alkenyl fluorene. This intermediate is then expected to

undergo reduction *via* metal-bound "borrowing hydrogenation" pathway to yield 9-alkylated fluorene as the final product.

4.3 Conclusion

In the present work, a ruthenium(II) complex, *trans*-[Ru(*p*-Cl-aaO)Cl(CO)(PPh_3)$_2$], has been synthesized using a bidentate redox-active azo-oxime ligand, *p*-chloro-aryl-azo-oxime (*p*-Cl-aaOH), and [RuHCl(CO)(PPh_3)$_3$] as the metal precursor. The complex is robust and stable in aerobic (air and moisture) condition. It has been thoroughly characterized by analytical, spectroscopic, SCXRD, and electrochemical techniques. The observed reductive redox responses are complemented with theoretical scrutiny of redox orbitals and this provided us with a perception of the ability of *trans*-[Ru(*p*-Cl-aaO)Cl(CO)(PPh_3)$_2$] to act as ligand-centric electron transfer catalyst. The complex was subsequently employed as an efficient redox catalyst for dehydrogenation of diverse array of aromatic and aliphatic primary alcohols, followed by single-pot selective C(sp^3)–H activation of 9H-fluorene under aerobic conditions (79 examples). A plausible mechanism for alcohol dehydrogenation has been proposed based upon several control experiments, thereby demonstrating that coordinated azo group actively participates in both dehydrogenation and borrowing hydrogen processes, whereas the metal centre acts as a redox-inactive spectator throughout the catalytic cycle. Significant advantages of this catalyst include its straightforward synthesis, low catalyst loading (0.1 mol%), broad substrate compatibility, and the ability to carry out transformations efficiently under relatively mild conditions with reduced reaction times.

4.4 Experimental Section

4.4.1 General Information

In this work all the reactions were carried out under aerobic condition. Required reagents and solvents were used as received without further chemical manipulation. Phenyl hydrazine, *p*-

chlorobenzaldehyde were acquired from TCI Chemical (India) Pvt. Ltd. Triphenylphosphine (PPh_3) was purchased from Sigma-Aldrich. Silica gel (60-120 mesh) brought from Merck was used for column chromatographic separation of the products. Ruthenium trichloride ($RuCl_3.xH_2O$) was received from Arora-Matthey (India) Ltd.

4.4.2 Synthesis of ligand

The ligand was prepared according to earlier published report.[18a]

4.4.3 Analytical data of ligand 1

***(E)-(4-chlorophenyl)((E)-phenyldiazenyl)methanone oxime (1)*:** Orange crystalline solid, Yield: 806 mg, 72%. HRMS: [M+H] *m/z* = 260.0590 (calcd. 260.0591); **FT-IR/cm^{-1}** υ = 3162 (υ_{O-H}), 1448 ($\upsilon_{N=N}$), 1052 (υ_{N-O})**;** **^{1}H NMR (300 MHz, DMSO-d^6):** δ 12.73 (s, 1H), 7.57 – 7.52 (m, 4H), 7.50 (d, *J* = 6.9 Hz, 3H), 7.33 (d, *J* = 8.5 Hz, 2H). **^{13}C{^{1}H} NMR (101 MHz, $CDCl_3$):** δ 165.88, 152.23, 134.28, 132.56, 131.69, 130.11, 129.97, 128.50, 122.96.

4.4.4 Synthesis of complex 2

The *p*-chlorobenzaldoxime (**1**) (0.1 mmol, 26 mg, 1 equiv.) was dissolved in 25 ml of reagent-grade toluene in a 50 ml round-bottom flask equipped with a magnetic stir bar. To this solution, the precursor ruthenium complex, $RuH(CO)Cl(PPh_3)_3$ (0.1 mmol, 95 mg, 1 equiv.) was added and stirred for 6 h. The obtained reddish-brown coloured solution was evaporated to dryness and subjected to column chromatography. The desired ruthenium complex was obtained after elution with a mixture toluene/acetonitrile (35:1 v/v). The deep purple red coloured solution was then evaporated under reduced pressure and crystallized from dichloromethane/hexane solvent mixture.

4.4.5 Analytical data of complex 2

***trans*-[Ru(*p*-Cl-aaO)Cl(CO)(PPh_3)$_2$] (2):** Purple red coloured solid, Yield: 56 mg, 60%. HRMS: [M+H] m/z = 948.0789 (calcd for $C_{50}H_{40}Cl_2N_3O_2P_2Ru$ 948.1022); FT-IR/cm^{-1} υ = 1973 ($\upsilon_{C=O}$), 1433 ($\upsilon_{N=N}$), 1090 (υ_{N-O}); **^{1}H NMR (400 MHz, $CDCl_3$):** δ 7.44 (dq, *J* = 15.7, 7.5 Hz, 12H), 7.28 (s, 12H), 7.19 (t, *J* = 7.4 Hz, 11H), 6.96 (t, *J* = 7.8 Hz, 2H), 6.84 (d, *J* = 8.1 Hz, 2H). **^{13}C{^{1}H} NMR (101 MHz, $CDCl_3$):** δ 166.31, 155.42, 134.33, 134.28, 134.22, 133.34, 130.72, 130.49, 130.26, 130.18, 128.97, 128.89, 128.10, 128.05, 128.00, 127.82, 122.98. **^{31}P{^{1}H} NMR (162 MHz, $CDCl_3$):** δ 21.78.

4.4.6 General procedure for the synthesis of 9-alkylated fluorenes

An oven dried 20 ml round bottom flask equipped with magnetic stir bar was charged with fluorene/substituted fluorenes (**3-6)** (1.0 mmol, 1 equiv.), primary alcohols (**7a-7aa)** (2.0 mmol, 2 equiv.), t-BuOK (0.5 mmol, 0.5 equiv.) and ruthenium catalyst **2** (0.1 mol%, 0.9 mg). To this mixture, 3 ml of toluene was added and the resulting solution was heated in an oil bath at 100°C for 8 h under open air atmosphere. After the reaction was complete, as monitored by thin layer chromatography (TLC), the mixture was cooled to room temperature and solvent was subsequently removed under reduced pressure using rotary evaporator. The obtained crude mass was subjected to purification by column chromatography on silica gel (60-120 mesh/100-200 mesh) and the desired product was eluted with hexane or hexane/Ethyl Acetate (40:1 v/v).

4.4.7 Isolation of intermediate alkenyl fluorene (8s')

To a mixture of fluorene (**3**) (332 mg, 2.0 mmol, 1 equiv.), naphthalen-1-ylmethanol (**7s**) (632 mg, 4.0 mmol, 2 equiv.), t-BuOK (112 mg, 1.0 mmol, 0.5 equiv.) catalyst **2** (1.8 mg, 0.1 mol%) in a 50 ml round bottom flask equipped with a magnetic stir bar, 15 mL of dry toluene was added and mixture was heated at 100°C in an preheated oil bath for 3 h under open air atmosphere. Thereafter the solvent was removed under reduced pressure and crude mass was

purified through column chromatography using silica gel (100-200 mesh). **8s** (white solid) and **8s'** (bright yellow solid) were isolated with hexane and hexane/EtOAc mixture (60:1 v/v) as eluent respectively.

NMR Data of *9-(naphthalen-1-ylmethylene)-9H-fluorene* (8s'): ^{1}H NMR (400 MHz, $CDCl_3$): δ 8.11 (d, *J* = 7.9 Hz, 2H), 7.98 (dt, *J* = 8.6, 4.9 Hz, 3H), 7.84 – 7.72 (m, 3H), 7.64 – 7.55 (m, 2H), 7.51 (dd, *J* = 13.3, 5.9 Hz, 1H), 7.45 (dd, *J* = 9.0, 7.1 Hz, 2H), 7.30 (t, *J* = 7.5 Hz, 1H), 7.12 (d, *J* = 7.8 Hz, 1H), 6.94 (t, *J* = 7.6 Hz, 1H).**^{13}C{^{1}H} NMR (75 MHz, $CDCl_3$):** δ 141.31, 139.53, 139.31, 138.12, 136.85, 134.43, 133.81, 131.81, 128.67, 128.64, 128.61, 128.52, 127.29, 127.19, 126.84, 126.52, 126.40, 125.61, 125.43, 125.31, 124.85, 120.60, 119.81, 119.77.

4.4.8 Alcohol Dehydrogenation and Detection of H_2O_2

During the dehydrogenation of benzyl alcohol, the formation of H_2O_2 was detected spectrophotometrically by monitoring the steady increase in the characteristic absorption band of I_3^- at 350 nm. The reaction between benzyl alcohol (**7a**) and catalyst **2** was conducted under open-air conditions in a 25 mL oven-dried round-bottomed flask containing 1 mmol of **4a**, 0.01 mol% (0.9 mg) of catalyst **2**, and 0.5 mmol (56 mg) of t-BuOK in 5 mL of dry toluene. The reaction mixture was stirred and heated at 100°C for 8 h. After completion, 15 mL of water was added to the mixture, which was then extracted twice with CH_2Cl_2. The aqueous layer was acidified to pH 2 with dilute H_2SO_4 to prevent further oxidation. Subsequently, 1 mL of a 10% KI solution and a few drops of a 3% $(NH_4)_2MoO_4$ solution were added. In this process, H_2O_2 oxidized I^- to I_2, which then reacted with excess I^- to form I_3^-, as described by the following chemical steps.

1. $H_2O_2 + 2I^- + 2H^+ \rightarrow 2H_2O + I_2$
2. $I_2(aq) + I^- \rightarrow I_3^-$

4.4.9 Mercury Poisoning Test

To a 20 ml round-bottomed flask charged with fluorene (**3**) (166 mg, 1.0 mmol, 1 equiv.), benzyl alcohol (**7a**) (216 mg, 0.2 ml, 2.0 mmol, 2 equiv.), t-BuOK (112 mg, 1.0 mmol, 0.5 equiv.), 5 ml of toluene with a magnetic stir bar, catalyst **2** (1.8 mg, 0.01 mol%) and 50 equivalents of mercury (738 mg) were added under an open-air atmosphere. The reaction mixture was stirred and heated at 100°C for 8 h. Upon completion (checked by TLC), the reaction mixture was extracted with dichloromethane (CH_2Cl_2) twice and purified by column chromatography using hexane as the eluent, affording the desired product (**8a**) in 90% isolated yield.

4.4.10 Radical Scavenging Experiment

In an oven dried 20 ml round-bottomed flask, fluorene (**3**) (166 mg, 1.0 mmol), benzyl alcohol (**7a**) (216 mg, 2.0 mmol), t-BuOK (112 mg, 1.0 mmol), catalyst **2** (0.2 mg, 0.1 mol%), and (2,2,6,6-Tetramethylpiperidin-1-yl)oxyl (**TEMPO**) (312 mg, 2.0 mmol, 2 equiv.) were combined in 5 ml toluene under an open-air atmosphere. The mixture was stirred at 100°C for 8 h and monitored by TLC. After completion, the reaction mixture was extracted with ethyl acetate (EtOAc) and purified by column chromatography (hexane), yielding the product (**8a**) with 87%.

4.5 References

[1] G. Rieveschl, F. E. Ray, *Chem. Rev.*, **1938**, *23*, 287–389.

[2] K. Morimoto, M. Itoh, K. Hirano, T. Satoh, Y. Shibata, K. Tanaka, M. Miura, *Angew. Chem. Int. Ed*., **2012**, *51*, 5359–5362.

[3] (a) K. M. Schelkle, M. Bender, K. Jeltsch, T. Buckup, K. Müllen, M. Hamburger, U. H. F. Bunz, *Angew. Chem*., **2015**, *54*, 14545–14548. (b) G. Li, J. Zheng, K. Klimes, Z. -Q. Zhu, J. Wu, H. Zhu, J. Li, *ACS Appl. Mater. Interfaces*, **2019**, *11*, 40320–40331. (c) D. K. Dubey, G. Krucaite, S. S. Swayamprabha, R. A. K. Yadav, D. Blazevicius, J. Tagare, S. Chavhan, T. -C. Hsueh, S. Vaidyanathan, S. Grigalevicius, J. -H. Jou, *Organic Electronics*, **2020**, *79*, 105633.

[4] (a) Suman, A. Bagui, R. Datt, V. Gupta, S. P. Singh, *Chem. Commun.*, **2017**, *53*, 12790–12793. (b) N. J. Jeon, H. Na, E. H. Jung, T. -Y. Yang, Y. G. Lee, G. Kim, H. -W. Shin, S. I. Seok, J. Lee, J. Seo, *Nat Energy*, **2018**, *3*, 682–689. (c) Y. -J. Xue, F. -Y. Cao, P. -K. Huang, Y. -C. Sua, Y. -J. Cheng, *J. Mater. Chem. A*, **2020**, *8*, 5315–5322. (d) G. Z. Wubie, M. -N. Lu, M. A. Desta, H. D. Weldekirstos, M. M. Lee, W. -T. Wu, S. -R. Li, T. -C. Wei, S. -S. Sun, *ACS Appl. Mater. Interfaces*, **2021**, *13*, 23513–23522. (e) R. D. Gayathri, T. Gokulnath, H. -Y. Park, Z. Xie, S. -H. Jin, S. C. Han, J. W. Lee, *Macromol. Res.*, **2022**, *30*, 745–750.

[5] (a) J. Shaya, P. R. Corridon, B. Al-Omari, A. Aoudi, A. Shunnar, M. I. H. Mohideen, A. Qurashi, B.Y. Michel, A. Burger, *Journal of Photochemistry and Photobiology C: Photochemistry Reviews*, **2022**, *52*, 100529. (b) H. Shao, X. Chen, Z. Wang, P. Lu, *Journal of Luminescence*, **2007**, *127*, 349–354. (c) M. Belletête, S. Beaupré, J. Bouchard, P. Blondin, M. Leclerc, G. Durocher, *J. Phys. Chem. B,* **2000**, *104*, 9118–9125.

[6] (a) A. Donat-Bouillud, I. Le´vesque, Y. Tao, M. D'Iorio, *Chem. Mater.*, **2000**, *12*, 1931–1936 (b) G. Zeng, W. -L. Yu, S. -J. Chua, W. Huang, *Macromolecules*, **2002**, *35*, 6907–6914. (c) F. Chen, B. Wang,Y. Chen, L. -J. Li, *Nano Lett.*, **2007**, *7*, 3013–3017. (d) F. Montilla, R. Mallavia, *Adv. Funct. Mater.*, **2007**, *17*, 71–78. (e) C. Kulkarni, M. H. C. van Son, D. Di Nuzzo, S. C. J. Meskers, A. R. A. Palmans, E. W. Meijer, *Chem. Mater.*, **2019**, *31*, 6633–6641. (f) S. Semin, X. Li, Y. Duan, T. Rasing, *Adv. Optical Mater*., **2021**, *9*, 2100327. (g) R. Batool, N. Riaz, H. M. Junaid, M. T. Waseem, Z. A. Khan, S. Nawazish, U. Farooq, C. Yu, S. A. Shahzad, *ACS Omega*, **2022**, *7*, 1057−1070. (h) M. Ni, X. An, L. Bai, K. Wang, J. Cai, S. Wang, L. He, M. Xu, H. Liu, J. Lin, X. Ding, C. Yin, W. Huang, *Adv. Funct. Mater.*, **2022**, *32*, 2106564. (i) B. B. Carbas, *Polymer,* **2022**, *254*, 125040. (j) H. Li, M. Yu,J. Gu, Q. Bao, Y. Wang, Y. Li, Y. Ma, L. Bai, Z. Zhuo, Y. Zhang, J. Zhang, Y. Wang, M. Luo, Y. Liu, C. Li, J. Lin, X. Zhang, Q. Feng,L. Xie, *Adv. Funct. Mater.*, **2023**, *33*, 2303947.

[7] (a) A. M. Breul, M. D. Hager, U. S. Schubert, *Chem. Soc. Rev.*, **2013**, *42*, 5366–5407. (b) H. Yeo, K. Tanaka, Y. Chujo, *Polymer*, **2015**, *60*, 228–233. (c) G. Noirbent, F. Dumur, *Materials*, **2018**, *11*, 2425.

[8] (a) M. M. Haghdoost, G. Golbaghi, J. Guard, S. Sielanczyk, S. A. Patten, A. Castonguay, *Dalton Trans.*, **2019**, *48*, 13396–13405. (b) E. M. Husseina, M. S. Malika, R. I. Alsantali, B. H. Asghar, M. Morada, M. A. Ansari, Q. M. S. Jamal, A. A. Alsimareef, A. N. Abdalla, A. S. Algarni, R. S. Jassas, H. M. Altass, S. A. Ahmeda, *J. Mol. Struct*., **2021**, *1246*, 131232. (c) R.

Urade, W. -T. Chang, C. -C. Ko, R. -N. Li, H. -M. Yang, H. -Y. Chen, L. -Y. Huang, M. -Y. Chang, C. -Y. Wu, C. -C. Chiu, *Life Sciences*, **2023**, *329*, 121835.

[9] (a) H. Zhang, J. Fan, H. Dong, S. Zhang, W. Xu, J. Wang, P. Gaob, X. Peng, *J. Mater. Chem. B*, **2013**, *1*, 5450–5455. (b) C. A. Amritha, D. Punn Ag Ai, K. ArAvelu, *J. Clin. diagnostic Res. JCDR*, **2015**, *9*, FC14−FC16. (c) T. Yang, Y. Zuo, Y. Zhang, Z. Gou, X. Wang,W. Lin, *J. Mater. Chem. B*, **2019**, *7*, 4649−4654.

[10] (a) K. L. Schoen, E. I. Becker, *J. Am. Chem. Soc.*, **1955**, *77*, 6030−6031. (b) H. E. Fritz, D. W. Peck, M. A. Eccles, K. E. Atkins, *J. Org. Chem.* **1965**, *30*, 2540–2542. (c) Q. Pei, Y. Yang, *J. Am. Chem. Soc*., **1996**, *118*, 7416−7417. (d) M. Ranger, M. Leclerc, *Chem. Commun*., **1997**, 1597−1598. (e) S. Setayesh, A. C. Grimsdale, T. Weil, V. Enkelmann, K. Müllen, F. Meghdadi, E. J. W. List, G. Leising, *J. Am. Chem. Soc.*, **2001**, *123*, 946−953. (f) G. Saikia, P. K. Iyer, *J. Org. Chem.*, **2010**, *75*, 2714–2717.

[11] C. S. Yeung, V. M. Dong, *Chem. Rev.*, **2011**, *111*, 1215−1292.

[12] D. Jana, S. Roy, S. Naskar, S. Halder, G. Kanrar, K. Pramanik, *Org. Biomol. Chem.*, **2024**, *22*, 6393−6408.

[13] (a) M. A. Shaikh, S. G. Agalave, A. S. Ubale, B. Gnanaprakasam, *J. Org. Chem.*, **2020**, *85*, 2277−2290. (b) K.-L. Dai, Q.-L. Chen, W.-P. Xie, K. Lu, Z.-B. Yan, M. Peng, C.-K. Li, Y.-Q. Tu, T.-M. Ding, *Angew. Chem. Int. Ed.*, **2022**, *61*, e202206446.

[14] (a) C. Gunanathan, D. Milstein, *Chem. Rev.*, **2014**, *114*, 12024−12087. (b) M. K. Awasthi, S. K. Singh, *Inorg. Chem.*, **2019**, *58*, 14912−14923. (c) S. Shahane, C. Fischmeister, C. Bruneau, *Catal. Sci. Technol.*, **2012**, *2*, 1425–1428. (d) V. Brabec, J. Kasparkova, Coordination Chemistry Reviews 376 (2018) 75–94. (e) G. Veeranna, V. R. R. Chittireddy, V. Ravinder, *Results in Chemistry*, **2024**, 9 101618–101626. (f) A. K. Guin, S. Chakraborty, S. Khanra, A. S. Mohapatra, N. D. Paul *Catal. Sci. Technol.*, **2024**, *14*, 3540–3549. (g) R. Sharma, A. Samanta, B. Sardar, M. Roy, D, Srimani, *Org. Biomol. Chem.*, **2022**, 20, 7998–8030.

[15] (a) A. Biswas, A. K. Bains, D. Adhikari, *Catal. Sci. Technol.*, **2022**, *12*, 4211–4216. (b) R. Sharma, A. Mondal, A. Samanta, D. Srimani, *Catal. Sci. Technol.*, **2023**, *13*, 611–617.

[16] (a) Kamal, S. Samanta, *J. Org. Chem.*, **2024**, *89*, 1910−1926. (b) S. Pal, A. K. Guin, S. Chakraborty, N. D. Paul, *ChemCatChem*, **2024**, *16*, e202400026. (c) R. Kumar, S. R. Padhy, E. Balaraman, *J. Org. Chem.*, **2024**, *89*, 15103−15116.

[17] (a) S. Pramanik, S. Roy, T. Ghorui, S. Ganguly, K. Pramanik, *Inorg. Chem.*, **2016**, *55*, 1461–1468. (b) S. Roy, S. Pramanik, S. C. Patra, B. Adhikari, A. Mondal, S. Ganguly, K. Pramanik, *Inorg. Chem.*, **2017**, *56*, 12764–12774. (c) S. Pramanik, S. Dutta, S. Roy, S. Dinda, T. Ghorui, A. K. Mitra, K. Pramanik, S. Ganguly, *New J. Chem.*, **2017**,*41*, 4157–4164. (d) S. Dinda, S. Roy, S. C. Patra, S. Bhandary, K. Pramanik, S. Ganguly, *New J. Chem.*, **2020**, *44*, 3737–3747. (e) S. Dinda, S. Pramanik, J. Basu, S. C. Patra, K. Pramanik, S. Ganguly, *Dalton Trans.*, **2022**, *51*, 10121–10135.

[18] (a) S. Halder, S. Naskar, D. Jana, G. Kanrar, K. Pramanik, S. Ganguly, *New J. Chem.*, **2024**, *48*, 8181–8194. (b) S. Halder, S. Naskar, D. Jana, G. Kanrar, S. C. Mandal, S. Roy, N. Bharadwaj, K. Pramanik, S. Ganguly, *Chem Asian J.*, **2024**, *20*, e202401278.

[19] (a) M. G. Edwards, R. F. R. Jazzar, B. M. Paine, D. J. Shermer, M. K. Whittlesey, J. M. J. Williams, D. D. Edney, *Chem. Commun.*, **2004**, *4*, 90–91. (b) K. Polidano, B. D. W. Allen, J. M. J. Williams, L. C. Morrill, *ACS Catal.*, **2018**, *8*, 6440−6445. (c) T. Mori, C. Ishii, M. Kimura, *Org. Process Res. Dev.*,**2019**, *23*, 1709–1717. (d) P. Chandra, T. Ghosh, N. Choudhary, A. Mohammad, S. M. Mobin, *Coord. Chem. Rev.*, **2020**, *411*, 213241–213299. (e) H. Fuse, H. Mitsunuma, M. Kanai, *J. Am. Chem. Soc.*, **2020**, *142*, 4493–4499. (f) L. M. Kabadwal, S. Bera, D. Banerjee, *Org. Chem. Front.*, **2021**, *8*, 7077–7096. (g) A. K. Guin, R. Mondal, G. Chakraborty, S. Pal, N. D. Paul, *J. Org. Chem.*, **2022**, *87*, 7106–7123. (h) G. Sivakumar, R. Kumar, V. Yadav, V. Gupta, E. Balaraman, *ACS Catal.*, **2023**, *13*, 15013–15053. (i) A. A. Swatiputra, D. Mukherjee, S. Dinda, S. Roy, K. Pramanik, S. Ganguly, *Dalton Trans.*, **2023**, *52*, 15627–15646 and *references therein*. (j) M. Khatua, B. Goswami, A. Devi, Kamal, S. Hans, S. Samanta, *Inorg. Chem.*, **2024**, *63*, 9786–9800. (k) S. Bera, L. M. Kabadwal, D. Banerjee, *Chem. Soc. Rev.*, **2024**, *53*, 4607–4647.

[20] (a) S. Muthaiah, S. H. Hong, *Adv. Synth. Catal.*, **2012**, *354*, 3045–3053. (b) S. Shahane, C. Fischmeister, C. Bruneau, *Catal. Sci. Technol.*, **2012**, *2*, 1425–1428. (c) Q. Yang, Q. Wanga, Z. Yu, *Chem. Soc. Rev.*, **2015**, *44*, 2305–2329. (d) I. Dutta, A. Sarbajna, P. Pandey, S. M. W. Rahaman, K. Singh, J. K. Bera, *Organometallics*, **2016**, *35*, 1505−1513. (e) Z. Shao, Y. Wang, Y. Liu, Q. Wang, X. Fub, Q. Li, *Org. Chem. Front.*, **2018**, *5*, 1248–1256. (f) T. Irrgang, R. Kempe, *Chem. Rev.*, **2019**, *119*, 2524–2549. (g) B. G. Reed-Berendt, K. Polidano, L. C. Morrill, *Org. Biomol. Chem.*, **2019**, *17*, 1595–1607. (h) M. Kannan, P. Barteja, P. Devi, S. Muthaiah, *Journal of Catalysis*, **2020**, *386*, 1–11. (i) M. Maji, D. Panja, I. Borthakur, S. Kundu, *Org. Chem. Front.*, **2021**, *8*, 2673–2709. (j) M. Trincado, J. Bösken, H. Grützmacher, *Coord. Chem.*

Rev., **2021**, *443*, 213967–214000. (k) A. M. Pandey, N. K. Digrawal, N. Mohanta, A. B. Jamdade, M. B. Chaudhari, G. S. Bisht, B. Gnanaprakasam, *J. Org. Chem.*, **2021**, *86*, 8805–8828. (l) S. Nandi, I. Borthakur, K. Ganguli, S. Kundu, *Organometallics*, **2023**, *42*, 1793−1802. (m) S. Bansal, B. Punji, *ChemCatChem*, **2024**, *16*, 1–11.

[21] (a) J. Zhang, M. Gandelman, L. J. W. Shimon, H. Rozenberg, D. Milstein, *Organometallics*, **2004**, *23*, 4026–4033. (b) D. Shen, D. L. Poole, C. C. Shotton, A. F. Kornahrens, M. P. Healy, T. J. Donohoe, *Angew. Chem. Int. Ed.*, **2015**, *54*, 1642 –1645. (b) S. Chakraborty, P. Daw, Y. B. David, D. Milstein, *ACS Catal.*, **2018**, *8*, 10300−10305. (c) J. Rana, R. Babu, M. Subaramaniana, E. Balaraman, *Org. Chem. Front.*, **2018**, *5*, 3250–3255. (d) B. Paul, M. Maji, K. Chakrabarti, S. Kundu, *Org. Biomol. Chem.*, **2020**, *18*, 2193–2214. (e) B. C. Roy, K. Ganguli, S. A. Samim, S. Kundu, *Asian J. Org. Chem.*, **2021**, *10*, 1218–1232. (f) B. G. Reed-Berendt, D. E. Latham, M. B. Dambatta, Louis C. Morrill, *ACS Cent. Sci.*, **2021**, *7*, 570−585. (g) I. Borthakur, A. Sau, S. Kundu, *Coord. Chem. Rev.*, **2022**, *451*, 214257–214292. (h) I. Borthakur, S. Kumari, S. Kundu, *Dalton Trans.*, **2022**, *51*, 11987–12020. (i) S. Yin, Q. Zheng, J. Chen, T. Tu, *Journal of Catalysis*, **2022**, *408*, 165–172.

[22] (a) R. Ray, S. Chandra, D. Maiti, G. K. Lahiri, *Chem. Eur. J.*, **2016**, *22*, 8814–8822 (b) S. P. Rath, D. Sengupta, P. Ghosh, R. Bhattacharjee, M. Chakraborty, S. Samanta, A. Datta, S. Goswami, *Inorg. Chem.*, **2018**, *57*, 11995−12009. (c) S. Sinha, S. Das, R. Mondal, S. Mandal, N. D. Paul, *Dalton Trans.*, **2020**, *49*, 8448–8478. (d) B. Goswami, M. Khatua, S. Samanta, *Dalton Trans.*, **2022**, *51*, 1454–1463. (e) D. Jana, S. Malik, G. Kanrar, S. Halder, S. Naskar, K. Pramanik, *ChemCatChem*, **2025**, e202401851.

4.6 Appendix

Table 4.6.A1: Crystallographic details of some synthesized 9-alkylated fluorene derivatives

	8j	9s	10j	11h	11i
Empirical formula	$C_{26}H_{20}$	$C_{23}H_{20}Cl_2O_3$	$C_{23}H_{20}Br_2O_3$	$C_{28}H_{31}Br$	$C_{28}H_{31}Cl$
T/K	273.15	273.15	273.15	273.15	273.15
f_w	332.42	415.29	504.21	447.44	402.98
Crystal system	Monoclinic	Monoclinic	Monoclinic	Monoclinic	Monoclinic
Space Group	*P*121/*n*1	*P*121/*c*1	*P*121/*c*1	*P*121/*n*1	*P*121/*n*1
a/Å	9.8692(7)	17.9981(5)	18.0628(11)	18.358(3)	18.0745(14)
b/Å	18.8657(13)	8.1701(2)	8.2745(5)	6.2588(11)	6.2864(4)
c/Å	10.8267(8)	13.9676(4)	13.9986(9)	20.912(4)	20.8673(14)
α/deg	90	90	90	90	90
β/deg	112.921(2)	91.3010(10)	90.468(2)	90.336(7)	91.019(2)
γ/deg	90	90	90	90	90
V/ Å^3	1856.7(2)	2053.35(10)	2092.2(2)	2402.8(7)	2370.6(3)
Z	4	4	4	4	4
D_c/Mgm^{-3}	1.189	1.343	1.601	1.237	1.129
μ/mm^{-1}	0.067	0.337	3.895	1.722	0.172
F(000)	704	864	1008	936	864
cryst size/mm^3	0.22 × 0.19 × 0.14	0.28 × 0.20 × 0.14	0.26 × 0.16 × 0.12	0.25 × 0.17 × 0.10	0.28 × 0.20 × 0.15
θ/deg	2.31 – 23.91	2.74 – 25.35	2.86 – 25.81	2.94 – 21.61	2.25 – 23.68
Measured reflns	31804	63176	54024	62151	48315
Unique reflns	3378	3869	4004	4581	4369
[a]GOF on F^2	1.060	1.074	1.052	1.024	1.087
R_1[b], wR_2[c][$I>2\sigma(I)$]	0.0611, 0.1644	0.0459, 0.1177	0.0398, 0.0967	0.0669, 0.1787	0.0737, 0.2056
R_1, wR_2	0.0869, 0.1794	0.0603, 0.1393	0.0607, 0.1113	0.1049, 0.2078	0.1080, 0.2579

[a]GOF = $\{\Sigma[w(F_o^2-F_c^2)^2]/(n-p)\}1/2$. [b]$R_1 = \Sigma\,[|F_o|-|F_c|]/\,\Sigma\,|F_o|$. [c]$wR_2 = [\Sigma\,[w(F_o^2-F_c^2)^2]/\,\Sigma\,[w(F_o^2)^2]]^{1/2}$ where $w = 1/[\sigma^2(F_o^2)+(aP)^2+bP]$, $P = (F_o^2+2F_c^2)/3$.

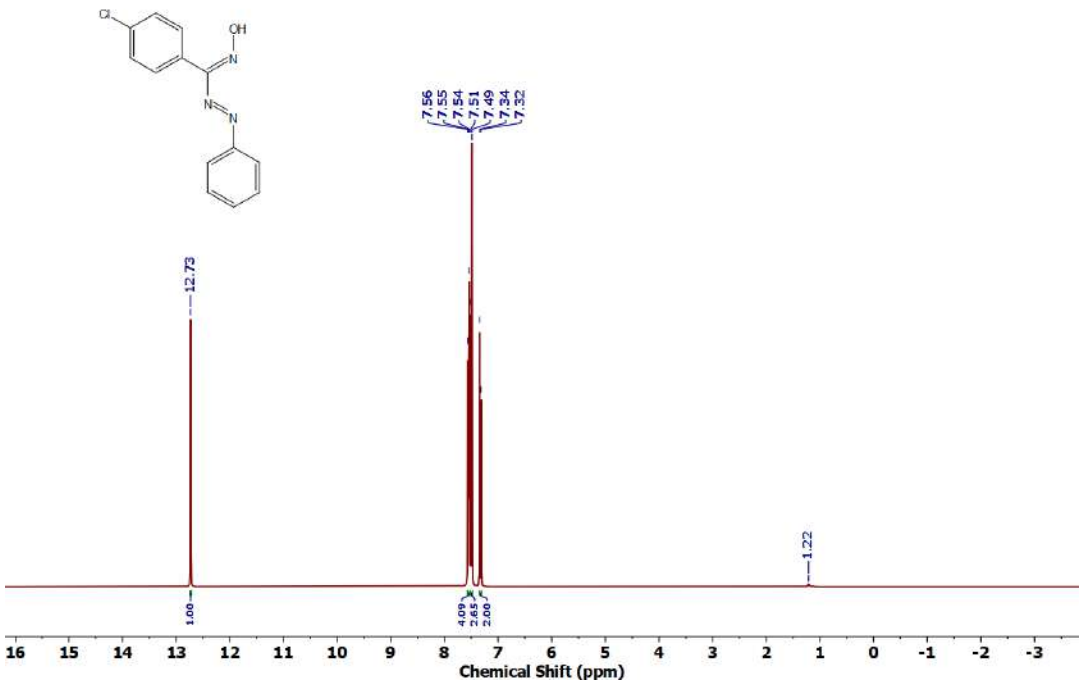

Figure 4.6.A1: ^{1}H NMR spectrum of **1**

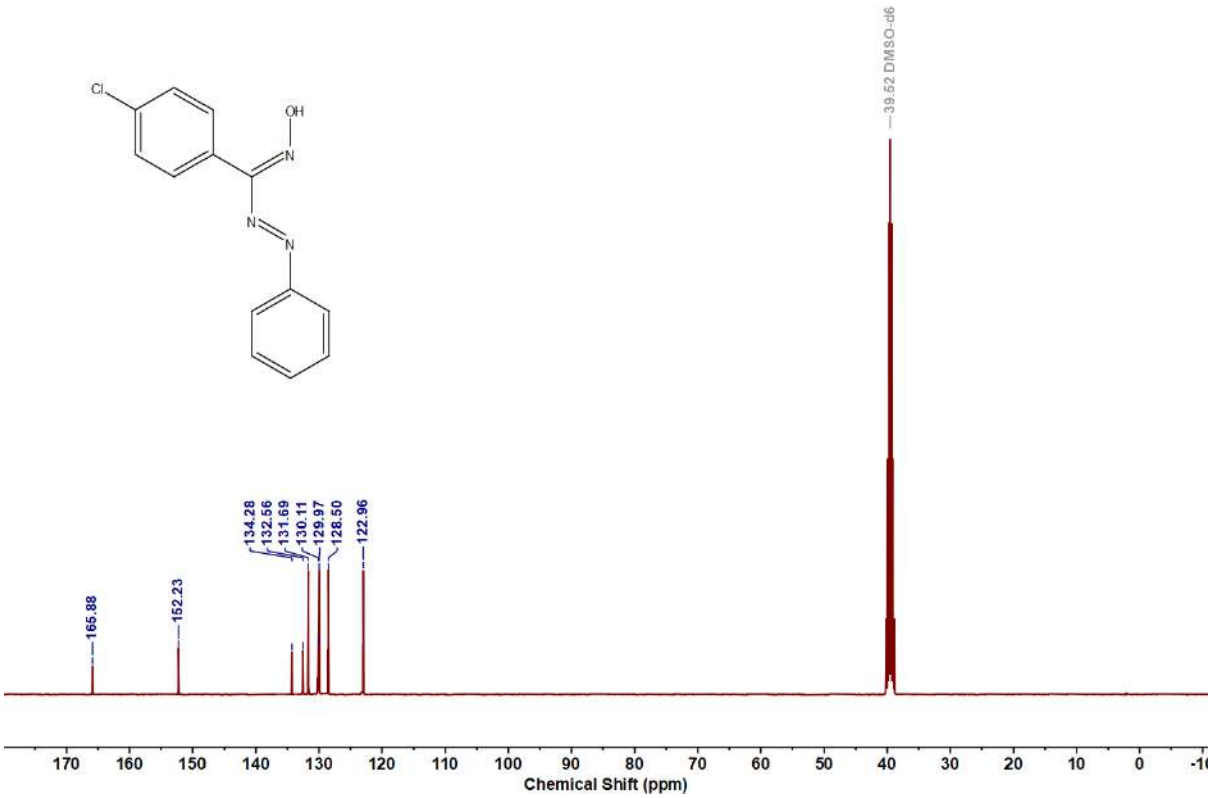

Figure 4.6.A2: $^{13}C\{^{1}H\}$ NMR spectrum of **1**

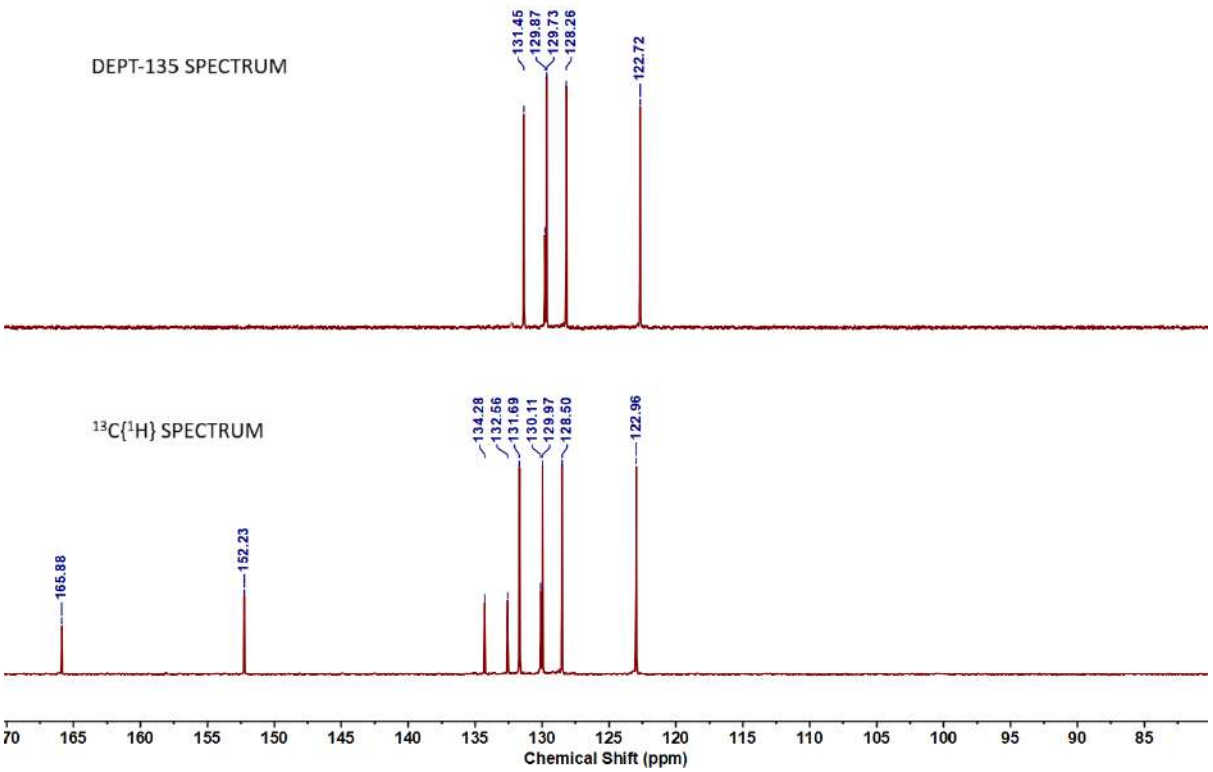

Figure 4.6.A3: $^{13}C\{^{1}H\}$ and DEPT-135 NMR spectrum of **1**

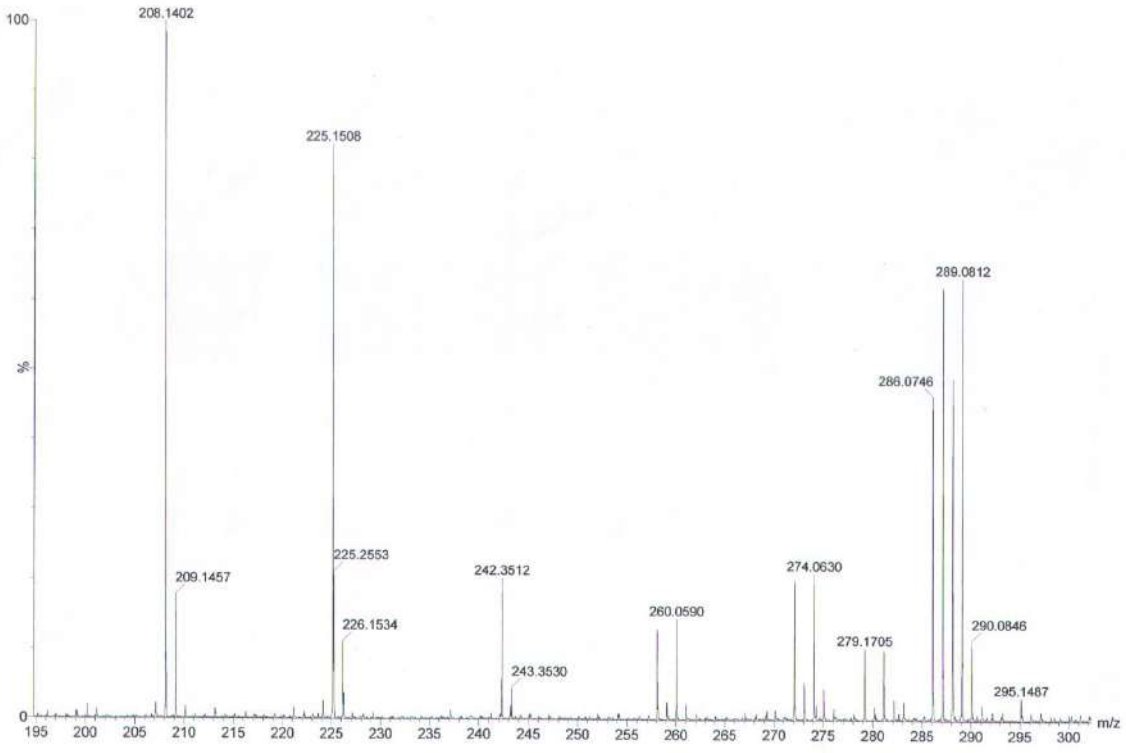

Figure 4.6.A4: HRMS spectrum of **1**

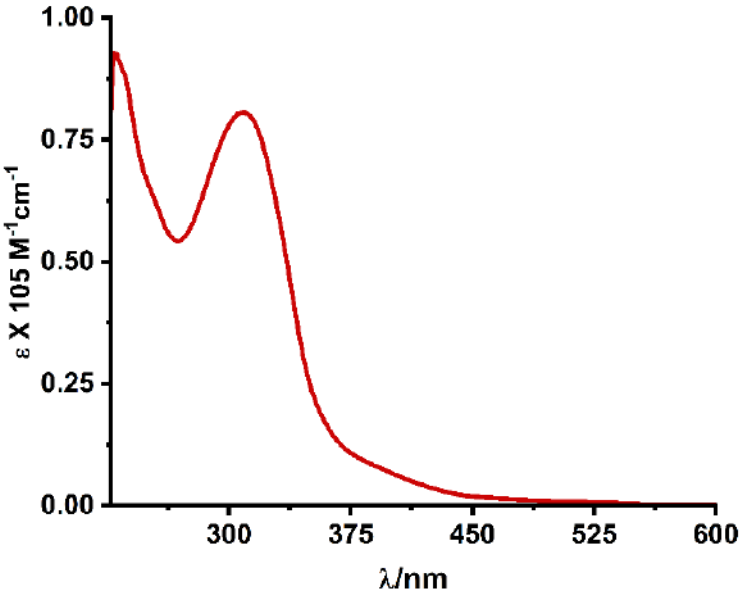

Figure 4.6.A5: UV-Vis spectrum of ligand **1**

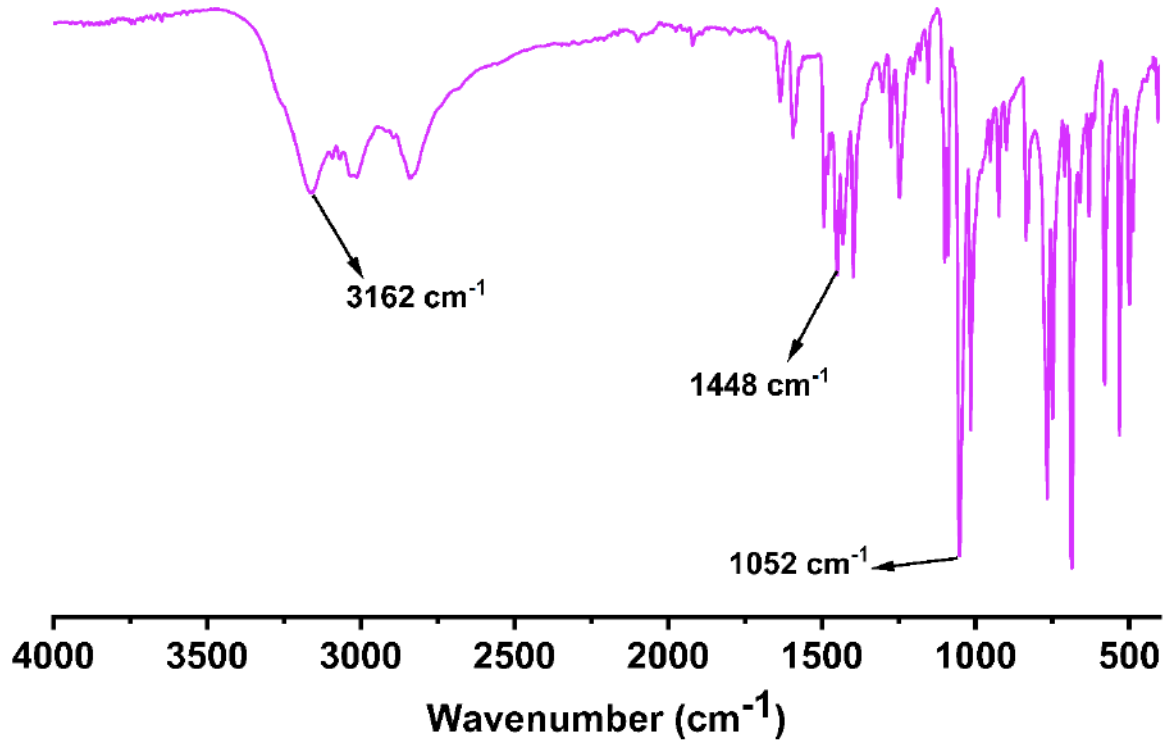

Figure 4.6.A6: IR spectrum of ligand **1**

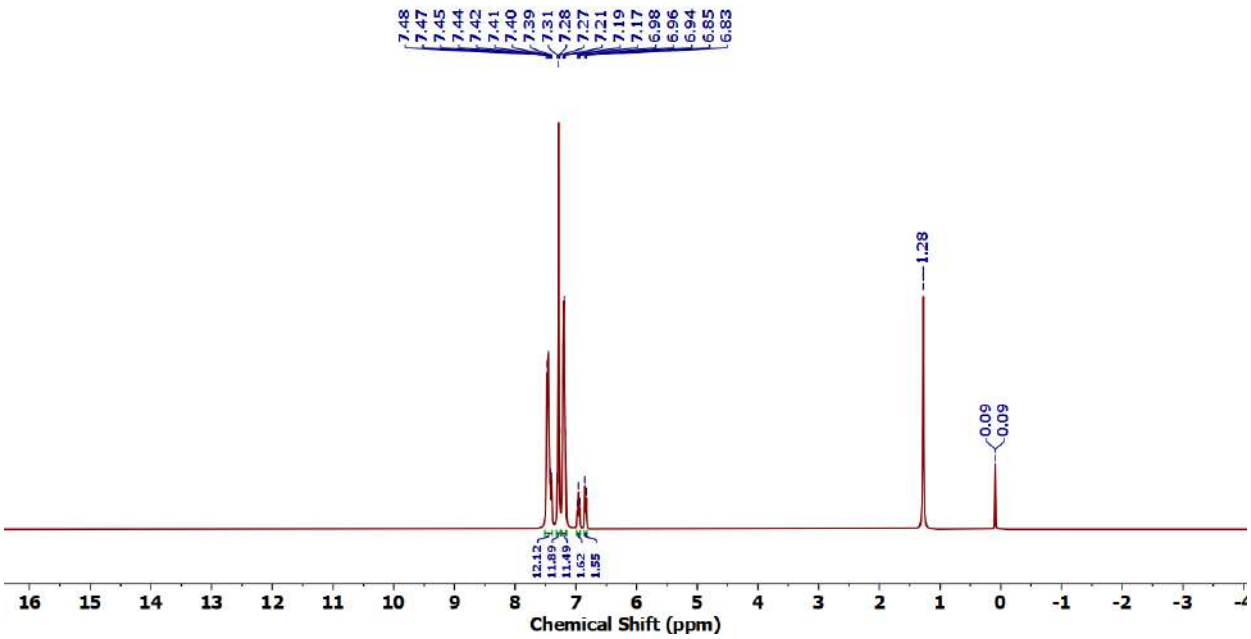

Figure 4.6.A7: ^{1}H NMR spectrum of **2**

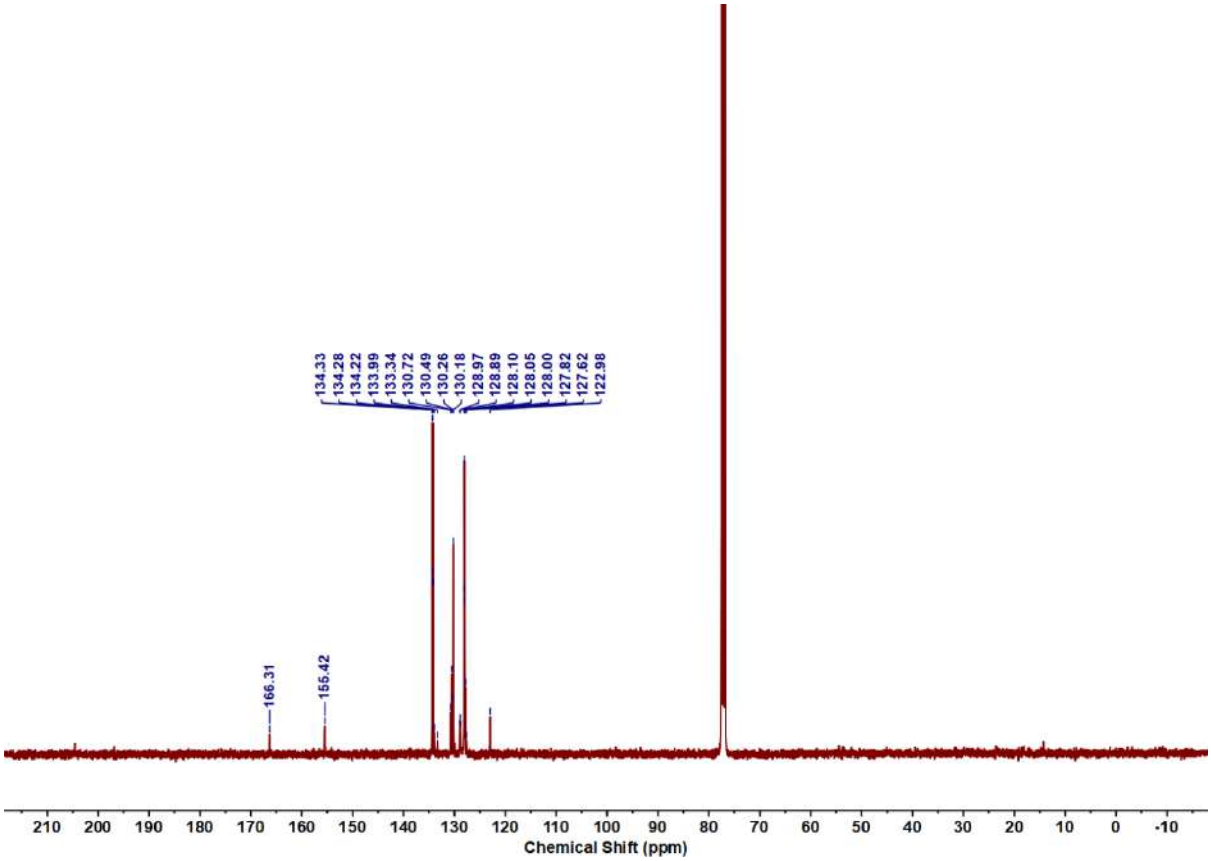

Figure 4.6.A8: $^{13}C\{^{1}H\}$ NMR spectrum of **2**

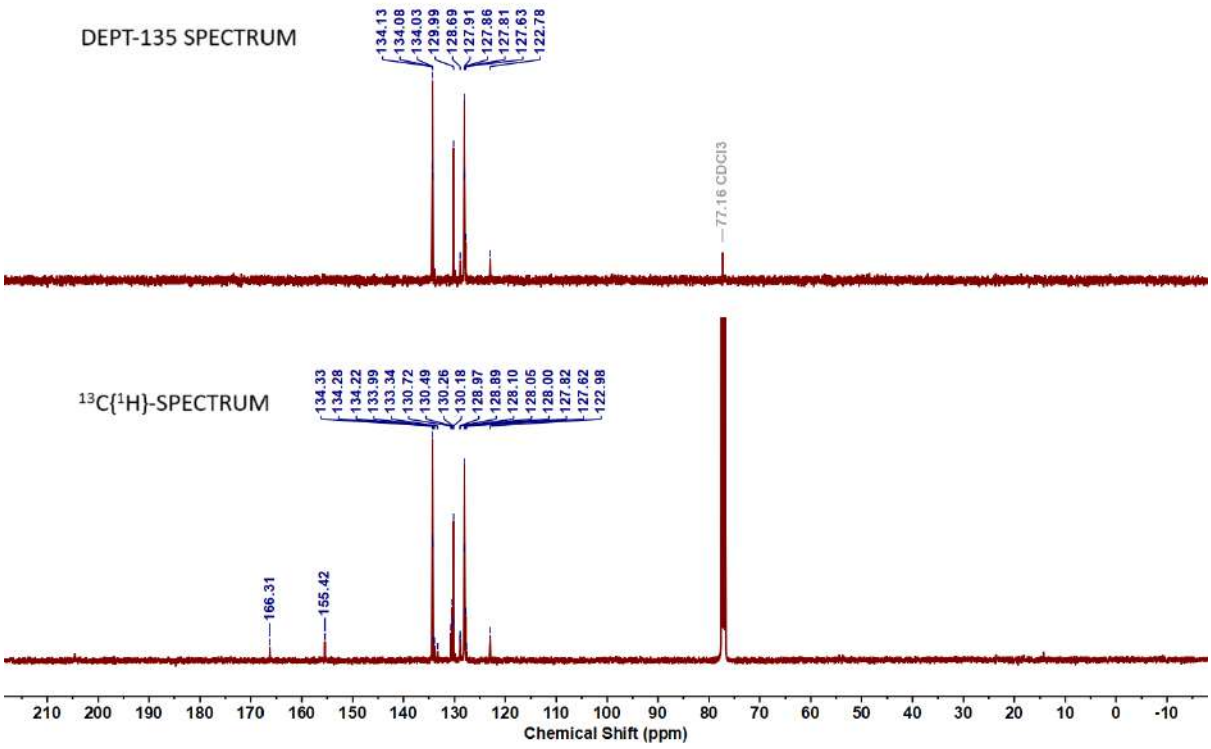

Figure 4.6.A9: $^{13}C\{^{1}H\}$ and DEPT-135 NMR spectrum of **2**

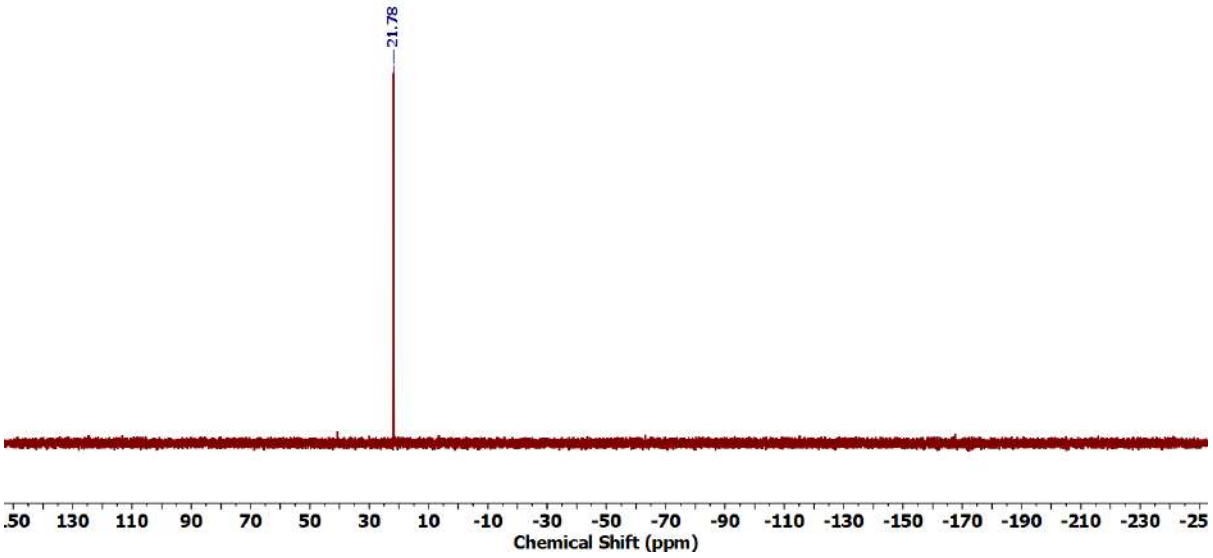

Figure 4.6.A10: $^{31}P\{^{1}H\}$ NMR spectrum of **2**

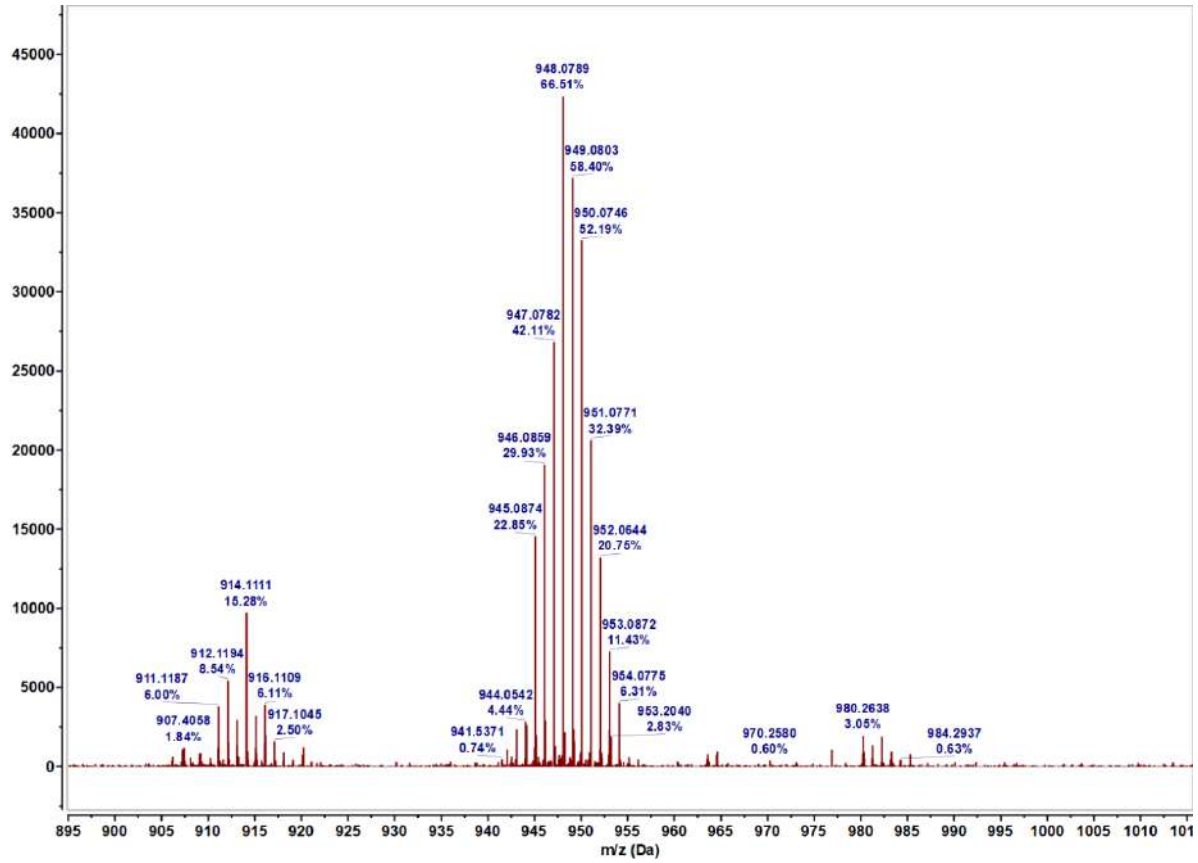

Figure 4.6.A11: HRMS spectrum of **2**

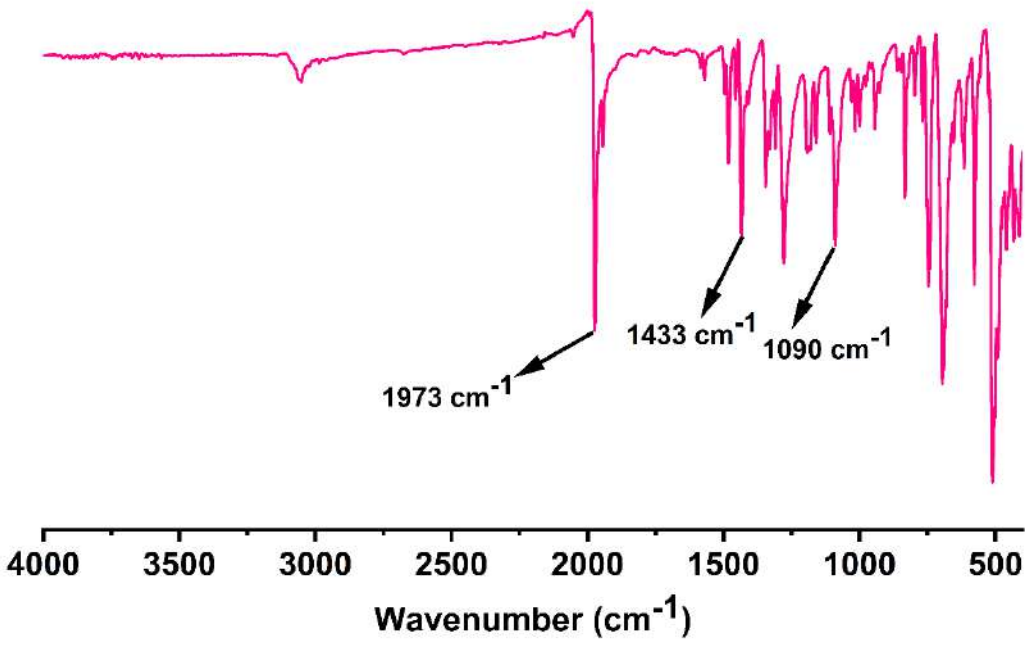

Figure 4.6.A12: IR spectrum of **2**

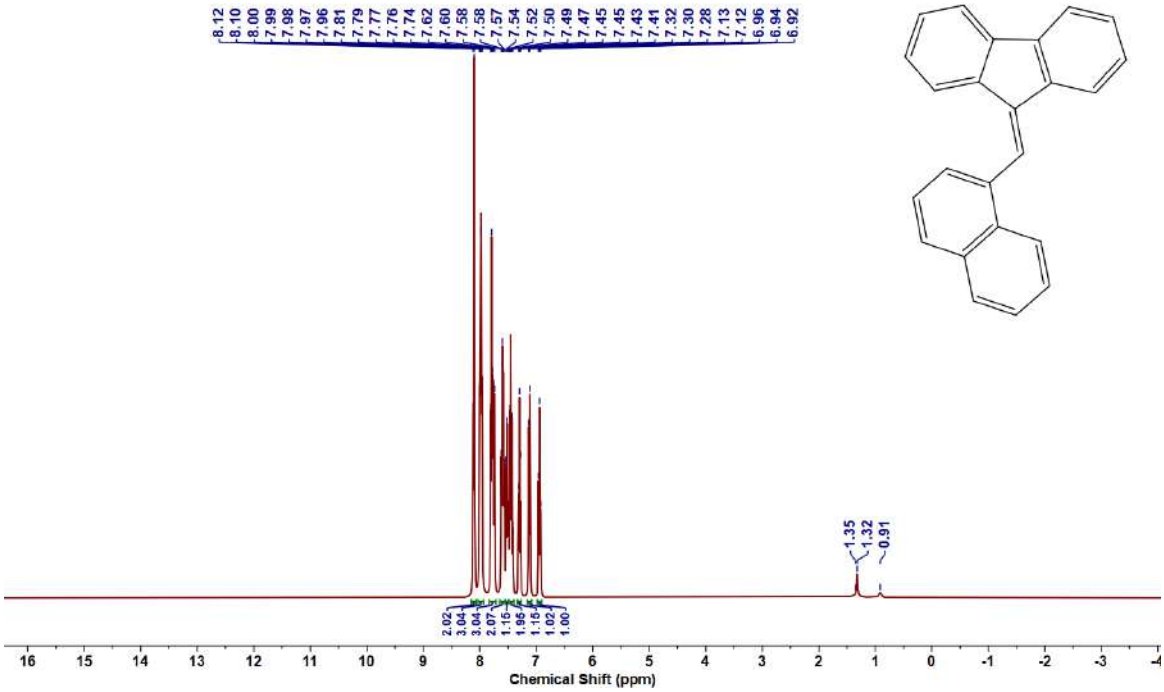

Figure 4.6.A13: ^{1}H NMR spectrum of **8s′**

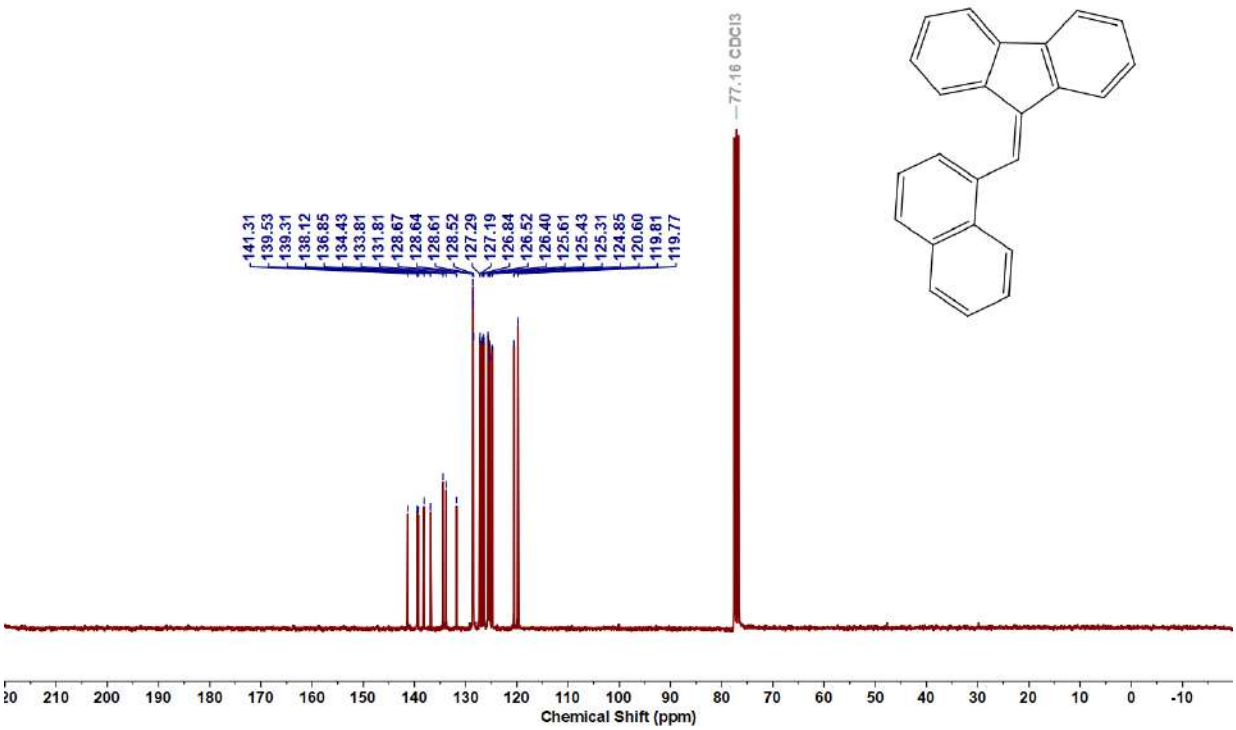

Figure 4.6.A14: $^{13}C\{^{1}H\}$ NMR spectrum of **8s′**

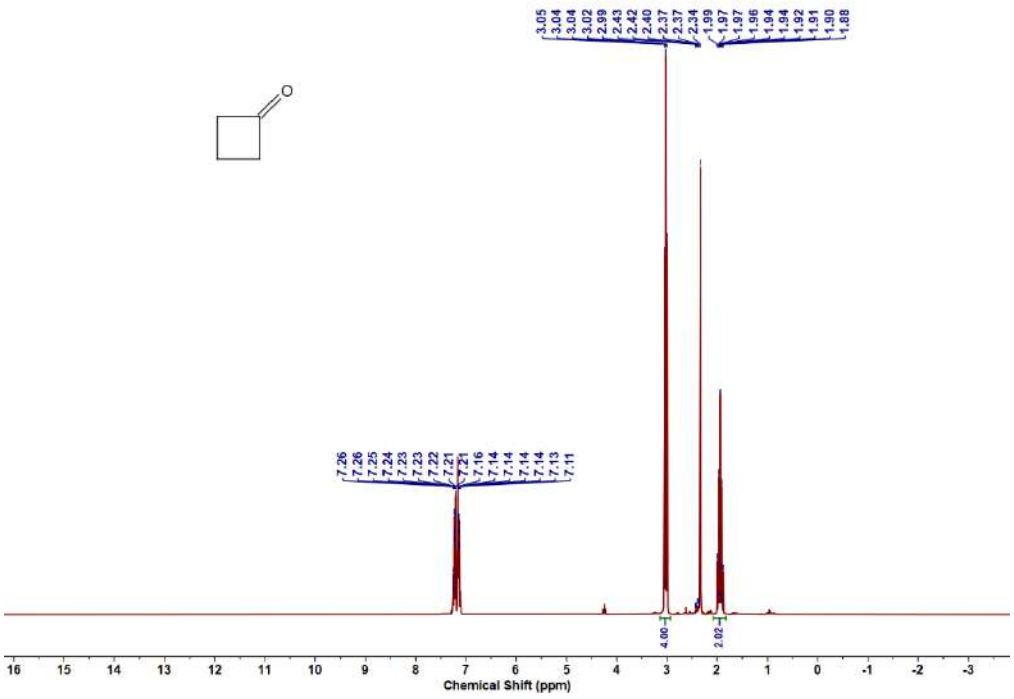

Figure 4.6.A15: ^{1}H NMR spectrum of cyclobutanone (**12a′**)

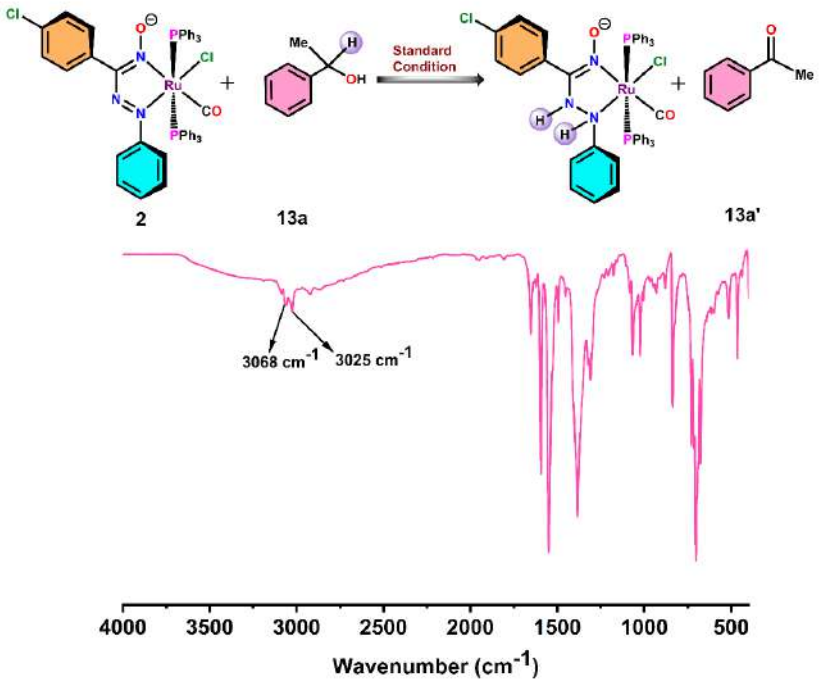

Figure 4.6.A16: IR spectrum recorded with the reaction mixture taken from sub-stoichiometric alcohol dehydrogenation of 1-phenylethanol (**13a**) under argon atmosphere suggesting the involvement of azo/hydrazo redox couple within catalyst **2**

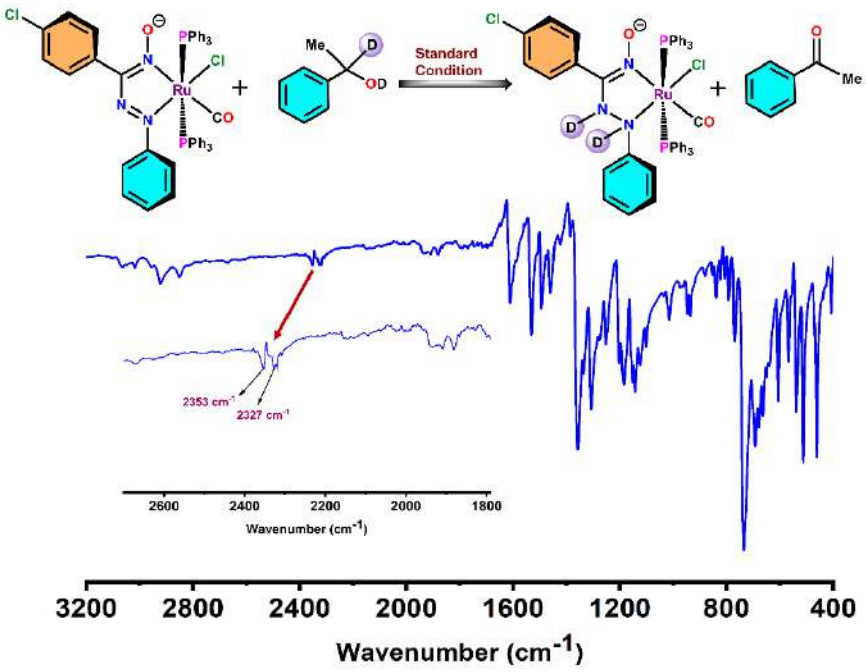

Figure 4.6.A17: IR spectrum recorded with the reaction mixture taken from sub-stoichiometric alcohol dehydrogenation of 1-phenylethanol (**14a**) under argon atmosphere suggesting the involvement of azo/hydrazo redox couple within catalyst **2**

Table 4.6.A2: Molecular orbital contribution table of the complex *trans*-[Ru(*p*-Cl-aaO)(PPh_3)$_2$Cl(CO)], **2**

Orbital	MO	Energy (eV)	Contribution (%)							Contribution
			Ru	Cl	CO	Azo	Oxime	Ph	PPh3	
234	L+5	-1.02	3	0	1	0	0	2	94	π*(PPh_3)
233	L+4	-1.11	2	0	3	5	12	56	22	π*(Oxime + Ph + PPh_3)
232	L+3	-1.15	2	0	2	0	1	5	90	π*(PPh_3)
231	L+2	-1.28	0	0	2	2	2	5	89	π*(PPh_3)
230	L+1	-1.73	32	2	2	3	1	0	60	d_z^2 + π* (PPh_3)
229	LUMO	-2.72	6	0	2	35	39	14	4	π*(Azo + Oxime + Ph)
228	HOMO	-5.62	14	5	0	10	37	31	3	d_{xz} + π (Azo + Oxime + Ph)
227	H–1	-6.11	24	43	3	2	17	4	7	d_{xy} + π (Cl + Oxime)
226	H–2	-6.15	20	43	2	3	15	7	10	d_{yz} + π (Cl + Oxime)
225	H–3	-6.49	7	28	6	3	52	2	2	π (Cl + Oxime)
224	H–4	-6.63	13	0	0	3	1	10	73	d_{xz} + π (Ph + PPh_3)
223	H–5	-6.90	1	1	0	1	0	7	90	π (PPh_3)

Table 4.6.A3: Main Optical Transition at the TD-DFT/B3LYP/6-311G+(d,p) level of theory for the complex **2** with composition in terms of Molecular Orbital Contribution of the Transition, Computed Vertical Excitation Energies, and Oscillator Strength in Dichloromethane

Transition	CI	Composition	E(eV)	Oscillator Strength (*f*)	λ_{theo}(nm)
$S_0 \rightarrow S_2$	0.62186	HOMO → LUMO (77%)	2.4866	0.0609	498.62
$S_0 \rightarrow S_5$	0.60004	H–2→ LUMO (72%)	2.9470	0.0722	420.72
$S_0 \rightarrow S_8$	0.38081	H–2→ L+1 (29%)	3.5221	0.0125	352.02
$S_0 \rightarrow S_{28}$	-0.33377 0.42554	H–3→ L+1 (22%) HOMO→ L+4 (36%)	4.1299	0.1788	300.21
$S_0 \rightarrow S_{84}$	0.39500	H–5→ L+2 (31%)	5.0343	0.0525	246.28

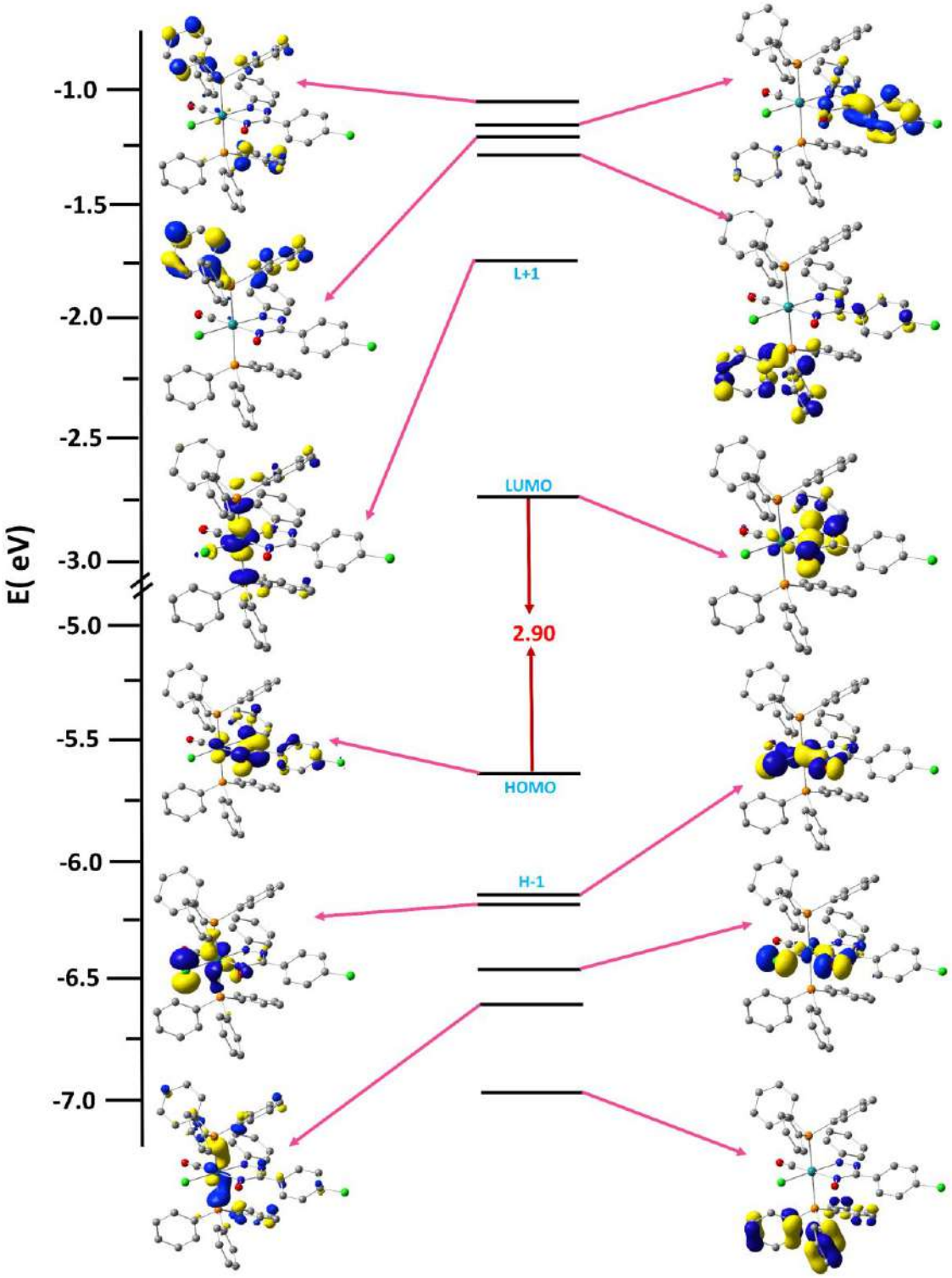

Figure 4.6.A18: Partial Frontier Molecular Orbital Energy Diagram of complex **2** (Iso values are set at 0.05)

Table 4.6.A4: Natural transition orbitals (NTOs) for **2** illustrating the nature of singlet excited states in the absorption bands in the range 200–800 nm. For each state, the respective number of the state, transition energy (eV), and the oscillator strength (in parentheses) are listed. Shown are only occupied (holes) and unoccupied (electrons) NTO pairs that contribute more than 20% to each excited state.

Expt. λ_{max}		**Hole**	**Electron**
532 nm	*S_2* w = 0.7734 2.4866 (0.0609) 498.62 nm ILCT & d-d π (Azo + Oxime +Ph) → π* (Azo + Oxime + Ph) & d_{xz} → d_{yz}	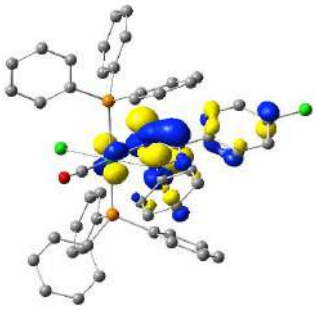	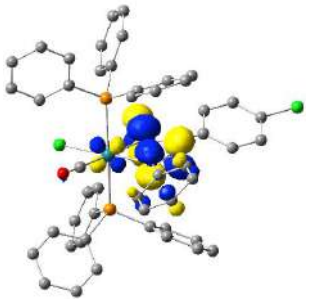
420 nm	*S_5* w = 0.7200 2.9470 (0.0722) 420.72 nm LLCT, ILCT & d-d π (Cl + Oxime) → π* (Azo + Oxime + Ph) & d_{xz} → d_{yz}	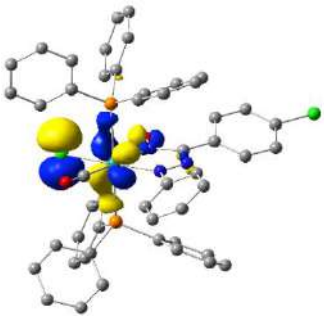	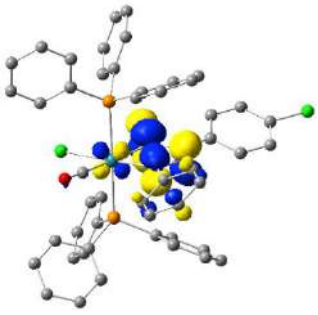
362 nm	*S_8* w = 0.2900 3.5221 (0.0125) 352.02 nm ILCT, LLCT & d-d π (Cl + Oxime) → π* (Cl + PPh_3) & d_{xz} → d_z^2	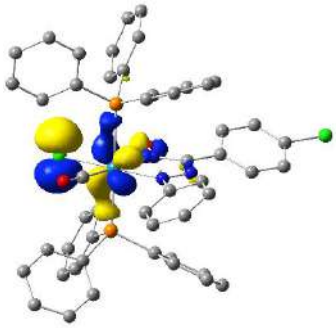	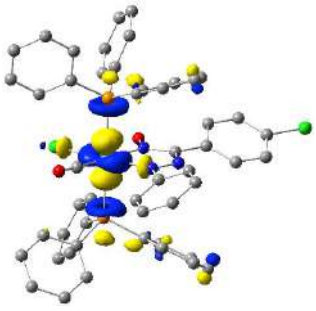
279 nm	*S_{28}* w = 0.2228 4.1299 (0.1788) 300.21nm ILCT, LLCT & d-d π (PPh_3) → π* (Cl + PPh_3) & d_{xz} → d_z^2	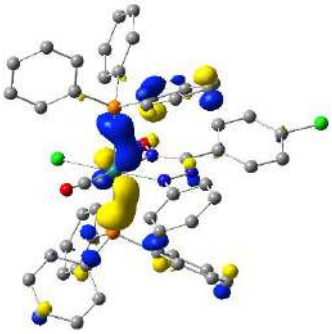	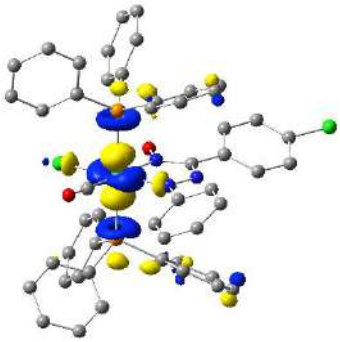

	S_{28} w = 0.3621 4.1299 (0.1788) 300.21nm LLCT & MLCT π (Azo + Oxime + Ph) → π* (PPh_3) & d_{yz} → π* (PPh_3)	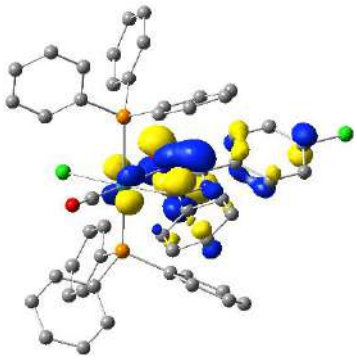	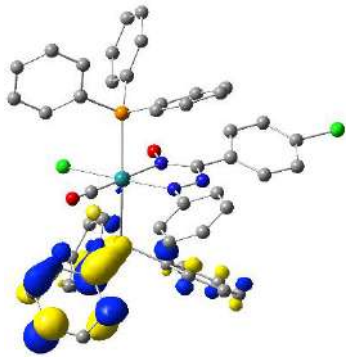
230 nm	S_{84} w = 0.3120 5.0343 (0.0525) 246.28 nm ILCT & LLCT π (PPh_3) → π* (PPh_3) & π (PPh_3) → π* (Azo + Ph)	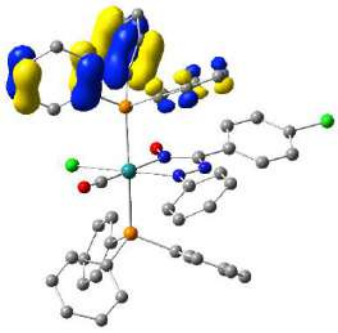	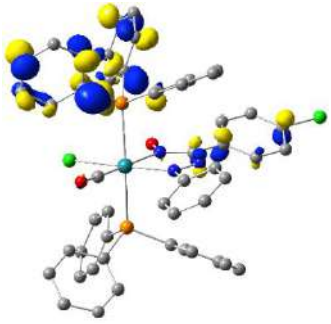

Table 4.6.A5: Coordinates of optimized geometry of **2**

Tag	Symbol	X	Y	Z
1	Ru	4.978774	6.977425	13.67047
2	P	4.105479	8.305218	15.62172
3	P	6.040423	5.615826	11.84725
4	Cl	5.818087	5.326774	15.39074
5	Cl	10.5221	13.65507	11.48926
6	O	7.735751	8.139025	14.30888
7	N	4.472392	8.485568	12.33046
8	N	6.683865	8.261859	13.63275
9	N	5.360493	9.382656	12.11072
10	O	2.510339	5.20821	13.39682
11	C	6.541943	9.294502	12.76323
12	C	5.690371	6.33139	10.1819
13	C	4.050285	10.13215	15.32111
14	C	7.886801	5.440069	11.89532
15	C	7.544678	10.34385	12.49135

16	C	2.39831	7.818135	16.14293
17	C	3.424314	5.890552	13.51865
18	C	3.275326	8.679528	11.5629
19	C	8.547094	5.431161	13.12911
20	H	7.99249	5.612266	14.04216
21	C	5.03044	8.197266	17.22278
22	C	5.534126	3.835506	11.67239
23	C	7.111027	11.58145	11.98212
24	H	6.050768	11.75312	11.82591
25	C	8.924302	10.15489	12.6807
26	H	9.294713	9.215558	13.07039
27	C	6.518634	7.325441	9.643344
28	H	7.39862	7.661749	10.18446
29	C	8.011549	12.59439	11.67536
30	H	7.65672	13.54593	11.2895
31	C	3.132331	10.6832	14.41497
32	H	2.416297	10.05088	13.90038
33	C	4.962077	10.98892	15.95367
34	H	5.686984	10.596	16.6596
35	C	2.186426	6.462703	16.4392
36	H	2.999155	5.747625	16.33182
37	C	9.834946	11.16227	12.36927
38	H	10.89888	10.99804	12.51501
39	C	9.371567	12.3744	11.87274
40	C	8.625078	5.188459	10.72776
41	H	8.141356	5.181265	9.75577
42	C	1.346299	8.722885	16.32371
43	H	1.487828	9.781705	16.13298
44	C	6.421565	8.041711	17.23699
45	H	6.967864	7.906943	16.30941
46	C	2.04364	8.225628	12.04348
47	H	1.975699	7.739196	13.00825
48	C	9.919083	5.183389	13.19234
49	H	10.41753	5.180969	14.15948

50	C	5.026938	3.123118	12.76407
51	H	4.886405	3.616517	13.71939
52	C	0.926493	9.109	10.08957
53	H	0.016951	9.27155	9.516042
54	C	3.320997	9.357468	10.33574
55	H	4.274406	9.701726	9.952209
56	C	4.552624	5.939342	9.462557
57	H	3.881565	5.184219	9.86342
58	C	6.239948	7.880789	8.395579
59	H	6.902142	8.641479	7.987758
60	C	5.757344	3.152986	10.46593
61	H	6.159436	3.673825	9.602096
62	C	10.64674	4.944058	12.02943
63	H	11.71654	4.753109	12.08123
64	C	0.101168	8.277209	16.77078
65	H	-0.70705	8.993115	16.90344
66	C	4.943239	1.098165	11.4438
67	H	4.711129	0.039198	11.35407
68	C	4.948336	12.35881	15.69272
69	H	5.66535	13.00518	16.19421
70	C	0.877993	8.441359	11.31153
71	H	-0.07176	8.090028	11.7081
72	C	-0.10299	6.929078	17.05457
73	H	-1.07326	6.584757	17.40554
74	C	0.946636	6.023414	16.89415
75	H	0.800653	4.970095	17.12314
76	C	9.994741	4.94702	10.7956
77	H	10.552	4.758096	9.88053
78	C	7.116771	8.054074	18.44602
79	H	8.19799	7.932262	18.44239
80	C	2.155076	9.566432	9.609301
81	H	2.208649	10.08292	8.653356
82	C	4.732611	1.763612	12.64846
83	H	4.338492	1.227067	13.50885

84	C	4.278097	6.493899	8.214422
85	H	3.398304	6.166834	7.664651
86	C	5.125371	7.459131	7.672772
87	H	4.914124	7.886075	6.694839
88	C	5.460096	1.797702	10.35247
89	H	5.634565	1.287559	9.407596
90	C	4.350023	8.358487	18.43797
91	H	3.271006	8.480409	18.45475
92	C	3.112292	12.05338	14.16527
93	H	2.383232	12.46019	13.46783
94	C	4.021688	12.89666	14.80245
95	H	4.007856	13.96626	14.60497
96	C	6.435018	8.212643	19.6513
97	H	6.980315	8.216891	20.59273
98	C	5.048921	8.364422	19.64395
99	H	4.505718	8.488046	20.57839

4.6.1 NMR data of synthesized products

***9-benzyl-9H-fluorene (8a)*[7]:** White solid; Eluent: Hexane; Yield: 238 mg, 93%. **^{1}H NMR**

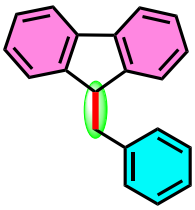

(300 MHz, $CDCl_3$): δ 7.82 (d, *J* = 7.4 Hz, 2H), 7.48 – 7.16 (m, 11H), 4.31 (t, *J* = 7.4 Hz, 1H), 3.19 (d, *J* = 7.7 Hz, 2H). **^{13}C{^{1}H} NMR (101 MHz, $CDCl_3$):** δ 146.94, 140.94, 139.93, 129.64, 128.39, 127.22, 126.76, 126.47, 124.95, 119.93, 48.82, 40.19.

***9-(2-methylbenzyl)-9H-fluorene (8b)*[7]:** White solid; Eluent: Hexane; Yield: 235 mg, 87%. **^{1}H**

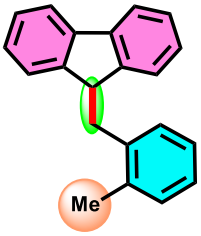

NMR (300 MHz, $CDCl_3$): δ 7.88 (d, *J* = 7.5 Hz, 2H), 7.47 (t, *J* = 7.3 Hz, 2H), 7.37 – 7.29 (m, 6H), 7.23 (d, *J* = 7.5 Hz, 2H), 4.31 (t, *J* = 8.0 Hz, 1H), 3.17 (d, *J* = 8.1 Hz, 2H), 2.39 (s, 3H). **^{13}C{^{1}H} NMR (101 MHz, $CDCl_3$):** δ 147.25, 140.89, 138.55, 136.91, 130.61, 130.56, 127.29, 126.87, 126.82, 126.09, 125.03, 120.00, 47.78, 37.87, 19.91.

9-(3-methylbenzyl)-9H-fluorene (8c) [7]**:** White crystalline solid; Eluent: Hexane; Yield: 240

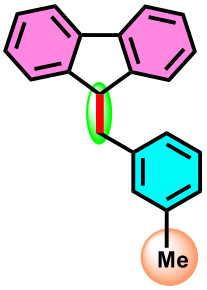

mg, 89%. **^{1}H NMR (300 MHz, $CDCl_3$):** δ 7.82 (d, *J* = 7.5 Hz, 2H), 7.46 – 7.36 (m, 2H), 7.36 – 7.22 (m, 5H), 7.20 – 7.07 (m, 3H), 4.31 (t, *J* = 7.6 Hz, 1H), 3.14 (d, *J* = 7.7 Hz, 2H), 2.43 (s, 3H). **^{13}C{^{1}H} NMR (75 MHz, $CDCl_3$):** δ 147.08, 140.91, 139.97, 137.97, 130.42, 128.30, 127.20, 126.74, 126.68, 125.00, 119.91, 48.82, 40.20, 21.58.

9-(3-fluorobenzyl)-9H-fluorene (8d) [7]**:** Off white coloured solid; Eluent: Hexane; Yield: 236

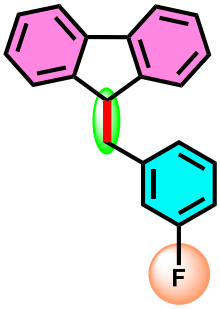

mg, 86%. **^{1}H NMR (300 MHz, $CDCl_3$):** δ 7.83 – 7.76 (m, 2H), 7.41 (tt, *J* = 7.3, 2.0 Hz, 2H), 7.33 – 7.21 (m, 5H), 7.06 – 6.94 (m, 3H), 4.26 (t, *J* = 7.4 Hz, 1H), 3.17 (d, *J* = 7.4 Hz, 2H). **^{13}C{^{1}H} NMR (75 MHz, $CDCl_3$):** δ 162.87 (d, *J* = 245.5 Hz), 146.51, 142.39 (d, *J* = 7.2 Hz), 140.96, 129.74 (d, *J* = 8.3 Hz), 127.37, 126.87, 125.32 (d, *J* = 2.7 Hz), 124.83, 120.01, 116.41 (d, *J* = 21.0 Hz), 113.39 (d, *J* = 21.0 Hz), 48.49, 39.81 (d, *J* = 1.8 Hz). **^{19}F NMR (282 MHz, $CDCl_3$):** δ -113.51.

9-(3-(trifluoromethyl)benzyl)-9H-fluorene (8e) [7]**:** Pale yellow solid; Eluent: Hexane; Yield:

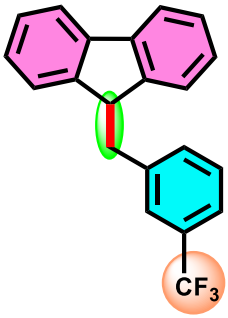

266 mg, 82%. **^{1}H NMR (400 MHz, $CDCl_3$):** δ 7.78 (d, *J* = 7.7 Hz, 2H), 7.58 – 7.47 (m, 2H), 7.41 (q, *J* = 6.8 Hz, 3H), 7.37 – 7.28 (m, 3H), 7.25 (d, *J* = 8.1 Hz, 2H), 4.29 (t, *J* = 6.3 Hz, 1H), 3.25 (d, *J* = 7.3 Hz, 2H). **^{13}C{^{1}H} NMR (101 MHz, $CDCl_3$):** δ 146.23, 141.03, 140.45, 133.02, 130.54 (q, $^2J_{C–F}$ = 32.0 Hz), 128.63, 127.46, 126.89, 126.39 (q, $^3J_{C–F}$ = 3.6 Hz), 124.81, 124.66 (q, $^1J_{C–F}$ = 271 Hz), 123.31 (q, $^3J_{C–F}$ = 3.7 Hz), 120.07. 48.48, 39.83. **^{19}F NMR (377 MHz, $CDCl_3$):** δ -62.49.

9-(4-methylbenzyl)-9H-fluorene (8f) [8]**:** White crystalline solid; Eluent: Hexane; Yield: 248

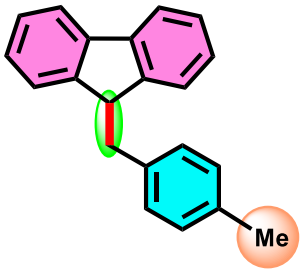

mg, 92%. **^{1}H NMR (300 MHz, $CDCl_3$):** δ 7.79 (d, *J* = 7.6 Hz, 2H), 7.39 (ddd, *J* = 7.6, 6.7, 1.9 Hz, 2H), 7.31 – 7.20 (m, 4H), 7.17 (s, 4H), 4.26 (t, *J* = 7.6 Hz, 1H), 3.12 (d, *J* = 7.6 Hz, 2H), 2.41 (s, 3H). **^{13}C{^{1}H} NMR (101 MHz, $CDCl_3$):** δ 147.09, 140.94, 136.85, 135.92, 129.50, 129.11, 127.18, 126.75, 125.00, 119.91, 48.91, 39.77, 21.25.

9-(4-isopropylbenzyl)-9H-fluorene (8g)**:** White crystalline solid; Eluent: Hexane; Yield: 245

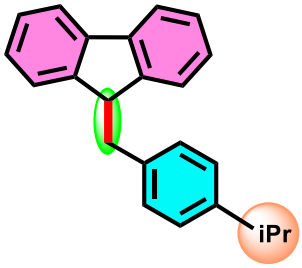

mg, 82%. **^{1}H NMR (300 MHz, $CDCl_3$):** δ 7.85 (d, *J* = 7.6 Hz, 2H), 7.45 (td, *J* = 7.3, 1.7 Hz, 2H), 7.33 – 7.22 (m, 8H), 4.31 (t, *J* = 7.7 Hz, 1H), 3.17 (d, *J* = 7.6 Hz, 2H), 3.03 (h, *J* = 6.9 Hz, 1H), 1.40 (d, *J* = 6.9 Hz, 6H). **^{13}C{^{1}H} NMR (75 MHz, $CDCl_3$):** δ 147.12, 147.03, 140.88, 137.32, 129.49, 127.14, 126.72, 126.43, 124.97, 119.86, 48.89, 39.82, 33.83, 24.21.

9-(4-methoxybenzyl)-9H-fluorene (8h) [8]**:** White solid; Eluent: Hexane/EtOAc (40:1v/v);

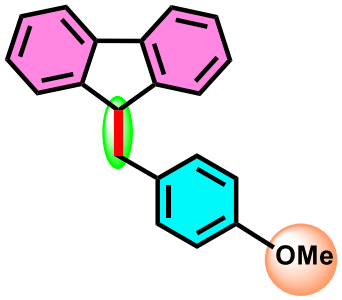

Yield: 249 mg, 87%. **^{1}H NMR (300 MHz, $CDCl_3$):** δ 7.80 (dd, *J* = 8.0, 2.2 Hz, 2H), 7.41 (td, *J* = 7.1, 1.9 Hz, 2H), 7.35 – 7.14 (m, 6H), 6.97 – 6.86 (m, 2H), 4.25 (t, *J* = 7.4 Hz, 1H), 3.87 (d, *J* = 1.3 Hz, 3H), 3.13 (dd, *J* = 7.6, 2.2 Hz, 2H). **^{13}C{^{1}H} NMR (101 MHz, $CDCl_3$):** δ 158.24, 147.00, 140.95, 131.94, 130.53, 127.16, 126.73, 124.97, 119.90, 113.74, 55.31, 49.02, 39.26.

4-((9H-fluoren-9-yl)methyl)-N,N-dimethylaniline (8i) [8]**:** Yellow solid; Eluent:

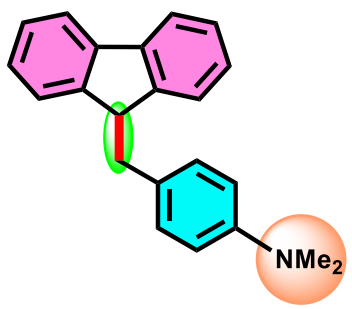

Hexane/EtOAc (40:1 v/v); Yield: 266 mg, 89%. **^{1}H NMR (300 MHz, $CDCl_3$):** δ 7.80 (d, *J* = 7.6 Hz, 2H), 7.45 – 7.36 (m, 2H), 7.30 – 7.24 (m, 4H), 7.17 (d, *J* = 8.5 Hz, 2H), 6.83 – 6.76 (m, 2H), 4.24 (t, *J* = 7.7 Hz, 1H), 3.07 (d, *J* = 7.7 Hz, 2H), 3.01 (s, 6H).

$^{13}C\{^{1}H\}$ NMR (101 MHz, $CDCl_3$): δ 149.19, 147.30, 140.93, 130.26, 128.52, 127.08, 126.71, 125.07, 119.86, 113.11, 49.18, 41.12, 39.28.

9-([1,1'-biphenyl]-4-ylmethyl)-9H-fluorene (8j) [8]**:** White crystalline solid; Eluent: Hexane;

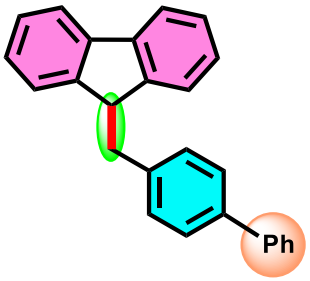

Yield: 292 mg, 88%. **^{1}H NMR (300 MHz, $CDCl_3$):** δ 7.80 (d, *J* = 7.3 Hz, 2H), 7.71 – 7.65 (m, 2H), 7.63 – 7.58 (m, 2H), 7.49 (t, *J* = 7.5 Hz, 2H), 7.44 – 7.32 (m, 5H), 7.28 (d, *J* = 3.9 Hz, 4H), 4.31 (t, *J* = 7.5 Hz, 1H), 3.20 (d, *J* = 7.6 Hz, 2H). **$^{13}C\{^{1}H\}$ NMR (75 MHz, $CDCl_3$):** δ 146.92, 141.01, 140.97, 139.26, 139.08, 130.07, 128.94, 128.90, 127.28, 127.09, 127.05, 126.82, 124.99, 119.98, 48.79, 39.85.

9-(4-fluorobenzyl)-9H-fluorene (8k) [8]**:** White crystalline solid; Eluent: Hexane; Yield: 244

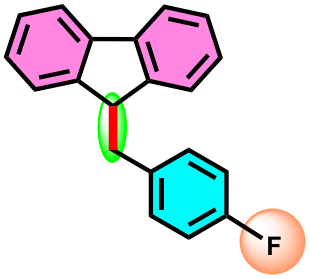

mg, 89%. **^{1}H NMR (300 MHz, $CDCl_3$):** δ 7.80 (dd, *J* = 7.5, 0.9 Hz, 2H), 7.43 (td, *J* = 7.3, 1.6 Hz, 2H), 7.33 (dd, *J* = 7.5, 1.2 Hz, 1H), 7.30 – 7.23 (m, 3H), 7.23 – 7.14 (m, 2H), 7.07 – 6.99 (m, 2H), 4.25 (t, *J* = 7.3 Hz, 1H), 3.17 (d, *J* = 7.4 Hz, 2H). **$^{13}C\{^{1}H\}$ NMR (75 MHz, $CDCl_3$):** δ 161.67 (d, $^{1}J_{C\text{-}F}$ = 244.1 Hz), 146.60, 140.99, 135.31 (d, $^{4}J_{C\text{-}F}$ = 3.2 Hz), 130.97 (d, $^{3}J_{C\text{-}F}$ = 7.7 Hz), 127.30, 126.79, 124.86, 119.99, 115.07 (d, *J* = 21.1 Hz), 48.80, 39.19. **^{19}F NMR (282 MHz, $CDCl_3$):** δ -116.68.

9-(4-chlorobenzyl)-9H-fluorene (8l) [8]**:** White crystalline solid; Eluent: Hexane; Yield: 256

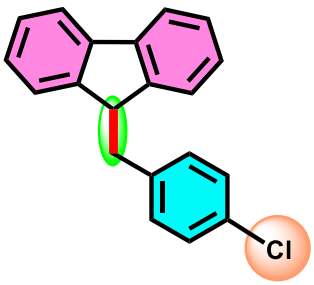

mg, 88%. **^{1}H NMR (300 MHz, $CDCl_3$):** δ 7.81 – 7.74 (m, 2H), 7.40 (tt, *J* = 7.4, 1.9 Hz, 2H), 7.32 – 7.22 (m, 6H), 7.13 (d, *J* = 8.2 Hz, 2H), 4.24 (t, *J* = 7.3 Hz, 1H), 3.15 (d, *J* = 7.3 Hz, 2H). **$^{13}C\{^{1}H\}$ NMR (75 MHz, $CDCl_3$):** δ 146.48, 141.00, 138.12, 132.20, 130.96, 128.43, 127.36, 126.84, 124.84, 120.03, 48.59, 39.37.

9-(4-bromobenzyl)-9H-fluorene (8m) [8]**:** White crystalline solid; Eluent: Hexane; Yield: 285 mg, 85%. **^{1}H NMR (300 MHz, $CDCl_3$):** δ 7.76 (dt, *J* = 7.6, 1.0 Hz, 2H), 7.45 – 7.34 (m, 4H), 7.31 – 7.21 (m, 4H), 7.11 – 7.03 (m, 2H), 4.23 (t, *J* = 7.3 Hz, 1H), 3.13 (d, *J* = 7.3 Hz, 2H). **^{13}C{^{1}H} NMR (101 MHz, $CDCl_3$):** δ 146.46, 141.01, 138.65, 131.39, 131.37, 127.38, 126.85, 124.85, 120.30, 120.05, 48.54, 39.44.

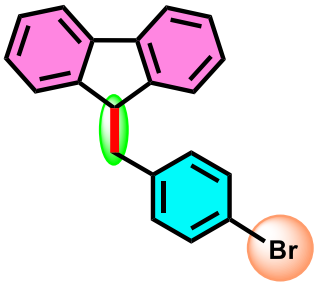

9-(4-(trifluoromethyl)benzyl)-9H-fluorene (8n) [7]**:** White crystalline solid; Eluent: Hexane; Yield: 259 mg, 80%. **^{1}H NMR (400 MHz, $CDCl_3$):** δ 7.76 (t, *J* = 6.8 Hz, 3H), 7.56 (d, *J* = 8.0 Hz, 2H), 7.40 (t, *J* = 7.8 Hz, 2H), 7.33 – 7.27 (m, 3H), 7.23 (d, *J* = 7.5 Hz, 2H), 4.28 (t, *J* = 7.3 Hz, 1H), 3.23 (d, *J* = 7.3 Hz, 2H). **^{13}C{^{1}H} NMR (101 MHz, $CDCl_3$):** δ 146.30, 143.79, 141.01, 129.93, 127.47, 126.92, 125.64 (q, $^3J_{C–F}$ = 3.8 Hz), 125.23 (q, $^3J_{C–F}$ = 3.7 Hz), 124.79, 124.52 (q, $^1J_{C–F}$ = 218 Hz), 120.10, 48.40, 39.82. **^{19}F NMR (282 MHz, $CDCl_3$):** δ -62.19.

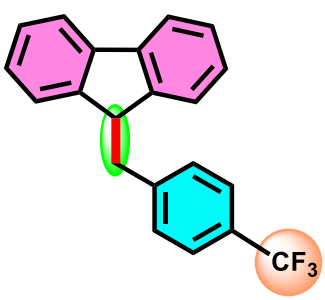

***9-propyl-9H-fluorene (8o)*:** Colourless oil; Eluent: Hexane; Yield: 154 mg, 74%. **^{1}H NMR (400 MHz, $CDCl_3$):** δ 7.92 (dd, *J* = 7.7, 2.6 Hz, 2H), 7.68 (dd, *J* = 7.5, 2.5 Hz, 2H), 7.52 (td, *J* = 7.3, 2.3 Hz, 2H), 7.50 – 7.43 (m, 2H), 4.14 (t, *J* = 5.9 Hz, 1H), 2.25 – 2.07 (m, 2H), 1.42 (ddt, *J* = 15.1, 11.0, 7.4 Hz, 2H), 1.05 (t, *J* = 7.4 Hz, 3H). **^{13}C{^{1}H} NMR (101 MHz, $CDCl_3$):** δ 147.73, 141.21, 126.93, 126.87, 124.45, 119.87, 47.50, 35.51, 19.14, 14.51.

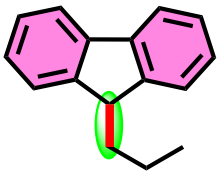

9-butyl-9H-fluorene (8p) [8]**:** Colourless oil; Eluent: Hexane; Yield: 169 mg, 76%. **^{1}H NMR (400 MHz, $CDCl_3$):** δ 7.90 (d, *J* = 7.4 Hz, 2H), 7.66 (d, *J* = 7.4 Hz, 2H), 7.54 – 7.42 (m, 4H), 4.12 (t, *J* = 5.9 Hz, 1H), 2.16 (dd, *J* = 16.1, 5.8 Hz, 2H), 1.44 (h, *J* = 6.6 Hz, 2H), 1.39 – 1.29 (m, 2H), 0.99 (t, *J* = 7.3 Hz, 3H).

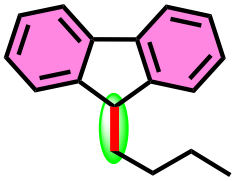

$^{13}C\{^{1}H\}$ NMR (75 MHz, $CDCl_3$): δ 147.72, 141.24, 126.93, 126.88, 124.44, 119.88, 47.57, 32.91, 27.91, 23.14, 14.04.

9-hexyl-9H-fluorene (8q) [8]**:** Colourless oil; Eluent: Hexane; Yield: 193 mg, 77%. **^{1}H NMR (300 MHz, $CDCl_3$):** δ 7.85 (d, *J* = 8.3 Hz, 2H), 7.62 (d, *J* = 7.3 Hz, 2H), 7.50 – 7.39 (m, 4H), 4.07 (t, *J* = 6.0 Hz, 1H), 2.10 (dt, *J* = 9.1, 5.8 Hz, 2H), 1.44 – 1.28 (m, 8H), 0.95 (t, *J* = 6.7 Hz, 3H). **$^{13}C\{^{1}H\}$ NMR (101 MHz, $CDCl_3$):** δ 147.74, 141.22, 126.93, 126.88, 124.45, 119.88, 47.62, 33.24, 31.78, 29.77, 25.79, 22.77, 14.19.

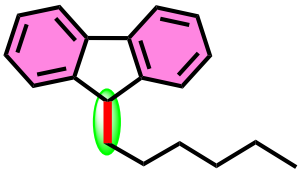

9-heptyl-9H-fluorene (8r) [8]**:** Colourless oil; Eluent: Hexane; Yield: 211 mg, 80%. **^{1}H NMR (300 MHz, $CDCl_3$):** δ 7.82 – 7.76 (m, 2H), 7.55 (dq, *J* = 7.1, 1.0 Hz, 2H), 7.45 – 7.28 (m, 4H), 4.01 (t, *J* = 5.9 Hz, 1H), 2.03 (dt, *J* = 9.5, 5.7 Hz, 2H), 1.25 (pd, *J* = 7.8, 5.2 Hz, 10H), 0.89 (t, *J* = 6.8 Hz, 3H). **$^{13}C\{^{1}H\}$ NMR (75 MHz, $CDCl_3$):** δ 147.76, 141.24, 126.93, 126.89, 124.46, 119.88, 47.63, 33.25, 31.98, 30.09, 29.25, 25.86, 22.77, 14.22.

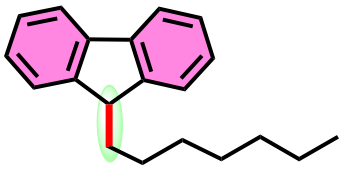

9-octyl-9H-fluorene (8s) [8]**:** Colourless sticky oil; Eluent: Hexane; Yield: 231 mg, 83%. **^{1}H NMR (300 MHz, $CDCl_3$):** δ 7.96 – 7.87 (m, 2H), 7.68 (d, *J* = 7.2 Hz, 2H), 7.57 – 7.43 (m, 4H), 4.14 (t, *J* = 5.8 Hz, 1H), 2.18 (dt, *J* = 10.3, 5.6 Hz, 2H), 1.46 (d, *J* = 16.0 Hz, 12H), 1.08 (t, *J* = 7.1 Hz, 3H). **$^{13}C\{^{1}H\}$ NMR (101 MHz, $CDCl_3$):** δ 147.73, 141.23, 126.92, 126.87, 124.43, 119.86, 47.61, 33.23, 31.99, 30.11, 29.53, 29.44, 25.84, 22.79, 14.25.

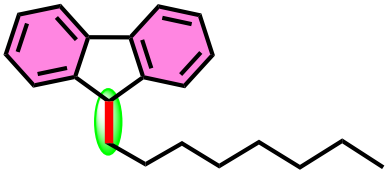

***9-nonyl-9H-fluorene (8t)*:** Colourless oil; Eluent: Hexane; Yield: 254 mg, 87%. **^{1}H NMR (300 MHz, $CDCl_3$):** δ 7.82 (d, *J* = 8.0 Hz, 2H), 7.59 (d, *J* = 7.4 Hz, 2H), 7.46 – 7.34 (m, 4H), 4.04 (t, *J* = 5.9 Hz, 1H), 2.07 (dt, *J* = 14.1, 4.9 Hz, 2H), 1.40 – 1.25 (m, 14H), 0.95 (td, *J* = 6.8, 1.9 Hz, 3H). **$^{13}C\{^{1}H\}$ NMR**

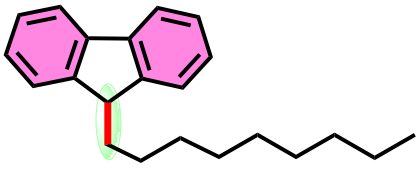

(75 MHz, $CDCl_3$): δ 147.75, 141.24, 126.93, 126.88, 124.45, 119.88, 47.63, 33.24, 32.02, 30.12, 29.73, 29.58, 29.44, 25.85, 22.83, 14.26.

***9-(naphthalen-1-ylmethyl)-9H-fluorene (8u)*:** Pale yellow solid; Eluent: Hexane; Yield: 245

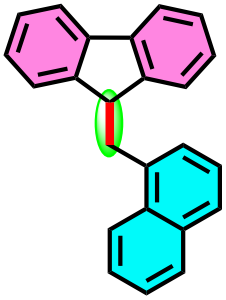

mg, 80%. **^{1}H NMR (300 MHz, $CDCl_3$):** δ 8.39 (d, *J* = 8.3 Hz, 1H), 8.04 (dd, *J* = 7.3, 2.3 Hz, 1H), 7.94 (d, *J* = 8.2 Hz, 1H), 7.87 (d, *J* = 7.4 Hz, 2H), 7.70 – 7.59 (m, 2H), 7.57 – 7.50 (m, 1H), 7.44 (t, *J* = 7.5 Hz, 2H), 7.36 (d, *J* = 6.9 Hz, 1H), 7.28 (t, *J* = 7.4 Hz, 2H), 7.17 (d, *J* = 7.7 Hz, 2H), 4.50 (t, *J* = 7.8 Hz, 1H), 3.56 (d, *J* = 7.9 Hz, 2H). **^{13}C{^{1}H} NMR (75 MHz, $CDCl_3$):** δ 147.17, 140.86, 136.10, 134.17, 132.15, 129.19, 128.36, 127.61, 127.27, 126.76, 126.19, 125.80, 125.44, 125.26, 123.86, 119.95, 47.70, 38.13.

***9-(cyclohexylmethyl)-9H-fluorene (8v)*:** White solid; Eluent: Hexane; Yield: 176 mg, 67%. **^{1}H**

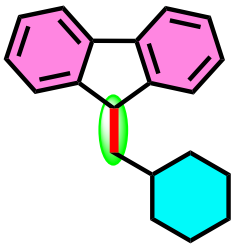

NMR (300 MHz, $CDCl_3$): δ 7.81 (dd, *J* = 7.6, 4.9 Hz, 2H), 7.50 – 7.30 (m, 6H), 7.23 – 7.17 (m, 1H), 6.97 (td, *J* = 5.2, 3.2 Hz, 1H), 6.79 (t, *J* = 4.2 Hz, 1H), 4.31 (t, *J* = 6.3 Hz, 1H), 3.47 (d, *J* = 7.0 Hz, 2H). **^{13}C{^{1}H} NMR (75 MHz, $CDCl_3$):** δ 148.40, 140.94, 126.91, 126.83, 124.75, 119.94, 44.93, 41.94, 35.76, 33.84, 26.78, 26.42.

***2-((9H-fluoren-9-yl)methyl)thiophene (8w)* [8]:** Yellow crystalline solid; Eluent:

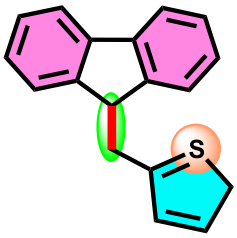

Hexane/EtOAc (40:1 v/v); Yield: 207 mg, 79%. **^{1}H NMR (400 MHz, $CDCl_3$):** δ 7.80 (dd, *J* = 7.6, 2.9 Hz, 2H), 7.43 (t, *J* = 7.2 Hz, 2H), 7.35 (dd, *J* = 12.3, 6.6 Hz, 4H), 7.18 (d, *J* = 5.2 Hz, 1H), 7.00 – 6.91 (m, 1H), 6.78 (s, 1H), 4.30 (t, *J* = 7.0 Hz, 1H), 3.46 (d, *J* = 7.1 Hz, 2H). **^{13}C{^{1}H} NMR (75 MHz, $CDCl_3$):** δ 146.28, 142.18, 141.12, 127.42, 126.93, 126.65, 126.10, 124.77, 123.86, 119.96, 49.11, 34.07.

***3-((9H-fluoren-9-yl)methyl)furan (8x)[8]*:** Yellow solid; Eluent: Hexane/EtOAc (40:1 v/v);

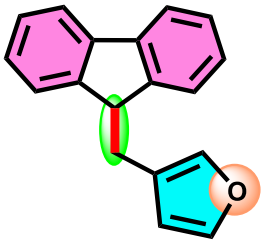

Yield: 192 mg, 78%. **^{1}H NMR (400 MHz, $CDCl_3$):** δ 7.77 (d, *J* = 7.2 Hz, 2H), 7.46 – 7.36 (m, 4H), 7.35 – 7.29 (m, 3H), 7.07 (s, 1H), 6.19 (d, *J* = 2.4 Hz, 1H), 4.18 (t, *J* = 6.7 Hz, 1H), 3.09 (d, *J* = 6.7 Hz, 2H). **^{13}C{^{1}H} NMR (101 MHz, $CDCl_3$):** δ 146.83, 142.71, 141.18, 140.15, 127.29, 126.89, 124.66, 122.17, 119.95, 111.40, 47.56, 28.80.

***1-((9H-fluoren-9-yl)methyl)pyrene (8y)*:** Pale yellow coloured solid; Eluent: Hexane/EtOAc

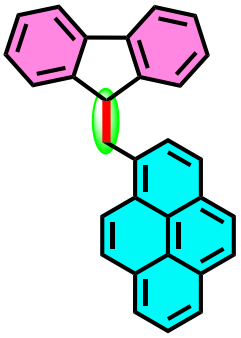

(40:1 v/v); Yield: 323 mg, 85%. **^{1}H NMR (400 MHz, $CDCl_3$)**: δ 8.47 (d, *J* = 9.2 Hz, 1H), 8.30 – 8.17 (m, 6H), 8.07 (dd, *J* = 15.5, 8.1 Hz, 3H), 7.90 (d, *J* = 7.8 Hz, 1H), 7.86 – 7.81 (m, 2H), 7.40 (td, *J* = 8.7, 3.1 Hz, 2H), 7.04 (d, *J* = 7.6 Hz, 2H), 4.57 (t, *J* = 8.0 Hz, 1H), 3.79 (d, *J* = 8.0 Hz, 2H). **^{13}C{^{1}H} NMR (75 MHz, $CDCl_3$):** δ 147.05, 140.92, 134.31, 131.60, 131.07, 130.53, 129.10, 128.71, 128.56, 127.76, 127.66, 127.34, 127.10, 126.82, 126.28, 126.08, 125.29, 125.12, 124.72, 123.52, 120.69, 120.00, 48.85, 38.39.

***9-(3,4,5-trimethoxybenzyl)-9H-fluorene (8z)[8]*:** White coloured solid; Eluent: Hexane/EtOAc

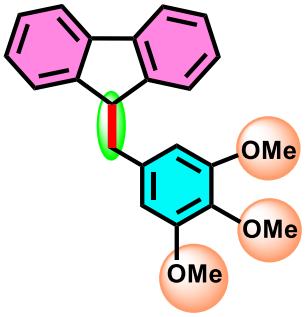

(30:1 v/v); Yield: 263 mg, 76%. **^{1}H NMR (400 MHz, $CDCl_3$):** δ 7.76 (d, *J* = 7.6 Hz, 2H), 7.38 (t, *J* = 6.2 Hz, 2H), 7.29 (q, *J* = 7.7 Hz, 4H), 6.39 (s, 2H), 4.26 (t, *J* = 7.2 Hz, 1H), 3.89 (s, 3H), 3.78 (s, 6H), 3.13 (d, *J* = 7.2 Hz, 2H). **^{13}C{^{1}H} NMR (101 MHz, $CDCl_3$):** δ 152.84, 146.57, 140.96, 136.48, 135.06, 127.17, 126.62, 124.89, 119.88, 106.49, 60.94, 56.03, 48.65, 40.20.

9-benzyl-2,7-dichloro-9H-fluorene (9a) [7]**:** White solid; Eluent: Hexane; Yield: 286 mg, 88%.

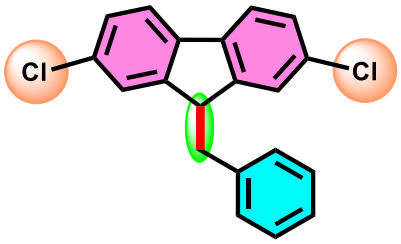

^{1}H NMR (300 MHz, $CDCl_3$): δ 7.59 (d, *J* = 8.1 Hz, 2H), 7.34 (ddd, *J* = 6.9, 5.2, 2.7 Hz, 5H), 7.23 – 7.16 (m, 2H), 7.13 (d, *J* = 1.9 Hz, 2H), 4.15 (t, *J* = 7.5 Hz, 1H), 3.09 (d, *J* = 7.6 Hz, 2H). **^{13}C{^{1}H} NMR (101 MHz, $CDCl_3$):** δ 148.32, 138.73, 138.45, 132.76, 129.50, 128.58, 127.71, 126.91, 125.39, 120.84, 48.74, 39.74.

***2,7-dichloro-9-(2-methylbenzyl)-9H-fluorene (9b)*:** White solid; Eluent: Hexane; Yield: 271 mg, 80%.

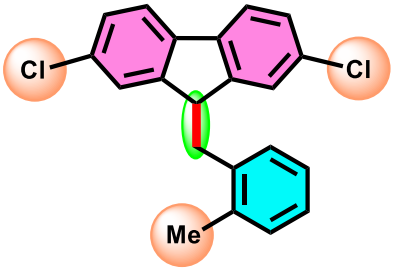

^{1}H NMR (300 MHz, $CDCl_3$): δ 7.63 (d, *J* = 8.1 Hz, 2H), 7.42 – 7.30 (m, 5H), 7.25 – 7.20 (m, 1H), 7.08 (d, *J* = 1.9 Hz, 2H), 4.09 (t, *J* = 8.1 Hz, 1H), 3.03 (d, *J* = 8.1 Hz, 2H), 2.33 (s, 3H). **^{13}C{^{1}H} NMR (101 MHz, $CDCl_3$):** δ 148.50, 138.25, 137.28, 136.62, 132.74, 130.70, 130.35, 127.64, 127.18, 126.16, 125.38, 120.80, 47.53, 37.37, 19.65.

***2,7-dichloro-9-(3-methylbenzyl)-9H-fluorene (9c)*:** White solid; Eluent: Hexane; Yield: 278 mg, 82%.

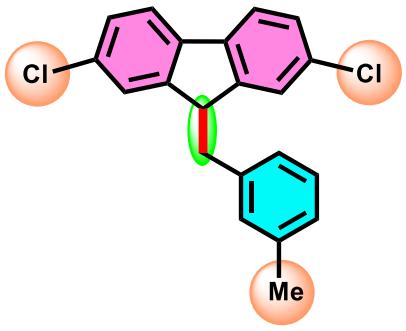

^{1}H NMR (300 MHz, $CDCl_3$): δ 7.59 (d, *J* = 8.1 Hz, 2H), 7.35 (dd, *J* = 8.1, 2.0 Hz, 2H), 7.28 (t, *J* = 7.5 Hz, 1H), 7.20 – 7.09 (m, 3H), 7.08 – 6.98 (m, 2H), 4.13 (t, *J* = 7.7 Hz, 1H), 3.03 (d, *J* = 7.7 Hz, 2H), 2.41 (s, 3H). **^{13}C{^{1}H} NMR (101 MHz, $CDCl_3$):** δ 148.44, 138.77, 138.40, 138.20, 132.72, 130.37, 128.49, 127.66, 127.64, 126.50, 125.47, 120.80, 48.81, 39.79, 21.51.

***2,7-dichloro-9-(3-fluorobenzyl)-9H-fluorene (9d)*:** White crystalline solid; Eluent: Hexane;

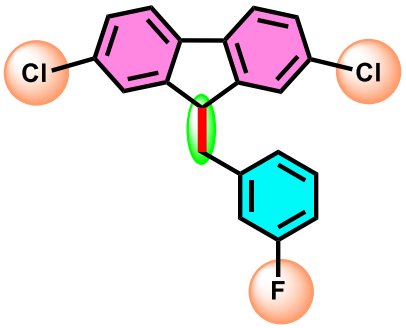

Yield: 288 mg, 84%. **^{1}H NMR (300 MHz, $CDCl_3$):** δ 7.58 (d, *J* = 8.1 Hz, 2H), 7.42 – 7.23 (m, 3H), 7.14 (s, 2H), 7.07 – 6.94 (m, 1H), 6.94 – 6.84 (m, 2H), 4.12 (t, *J* = 7.4 Hz, 1H), 3.08 (d, *J* = 7.4 Hz, 2H). **^{13}C{^{1}H} NMR (101 MHz, $CDCl_3$):** δ 162.90 (d, *J* = 246.3 Hz), 147.90, 141.18 (d, *J* = 7.1 Hz), 138.45, 132.86, 129.99 (d, *J* = 8.2 Hz), 127.86, 125.24, 120.93, 116.32, 116.11, 113.86 (d, *J* = 20.9 Hz), 48.34, 39.32. **^{19}F NMR (282 MHz, $CDCl_3$):** δ -112.88.

2,7-dichloro-9-(3-(trifluoromethyl)benzyl)-9H-fluorene (9e) [7]**:** White solid; Eluent: Hexane;

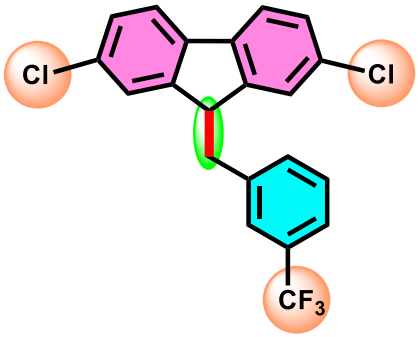

Yield: 314 mg, 80%. **^{1}H NMR (400 MHz, $CDCl_3$):** δ 7.58 (d, *J* = 8.1 Hz, 2H), 7.54 (d, *J* = 7.8 Hz, 1H), 7.44 – 7.37 (m, 2H), 7.35 (dd, *J* = 8.2, 2.0 Hz, 2H), 7.30 (d, *J* = 7.4 Hz, 1H), 7.16 (s, 2H), 4.18 (t, *J* = 7.2 Hz, 1H), 3.18 (d, *J* = 7.2 Hz, 2H). **^{13}C{^{1}H} NMR (101 MHz, $CDCl_3$):** δ 147.64, 139.37, 138.51, 132.95, 132.86, 130.80 (q, $^{2}J_{C–F}$ = 32.1 Hz), 128.90, 127.96, 126.34 (q, $^{3}J_{C–F}$ = 3.8 Hz), 125.26, 124.16 (q, $^{3}J_{C–F}$ = 219 Hz) 123.72 (q, $^{3}J_{C–F}$ = 3.8 Hz), 121.00, 48.42, 39.48. **^{19}F NMR (377 MHz, $CDCl_3$):** δ -62.65.

***2,7-dichloro-9-(4-methylbenzyl)-9H-fluorene (9f)*:** White solid; Eluent: Hexane; Yield: 292

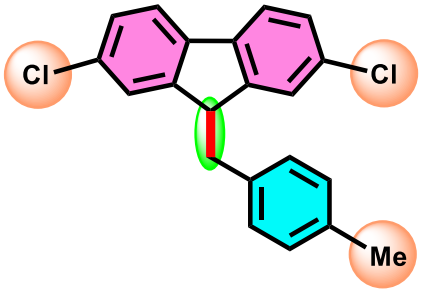

mg, 86%. **^{1}H NMR (300 MHz, $CDCl_3$):** δ 7.59 (d, *J* = 8.1 Hz, 2H), 7.34 (dd, *J* = 8.2, 1.9 Hz, 2H), 7.21 – 7.12 (m, 4H), 7.09 (d, *J* = 8.1 Hz, 2H), 4.14 (t, *J* = 7.5 Hz, 1H), 3.06 (d, *J* = 7.5 Hz, 2H), 2.40 (s, 3H). **^{13}C{^{1}H} NMR (101 MHz, $CDCl_3$):** δ 148.48, 138.46, 136.39, 135.62, 132.75, 129.35, 129.26, 127.67, 125.41, 120.82, 48.85, 39.31, 21.23.

***2,7-dichloro-9-(4-isopropylbenzyl)-9H-fluorene (9g)*:** White crystalline solid; Eluent: Hexane; Yield: 286 mg, 78%. **^{1}H NMR (300 MHz, $CDCl_3$):** δ 7.59 (d, *J* = 8.1 Hz, 2H), 7.38 – 7.32 (m, 2H), 7.25 (d, *J* = 8.1 Hz, 2H), 7.18 – 7.12 (m, 2H), 7.09 (s, 2H), 4.13 (t, *J* = 7.7 Hz, 1H), 3.05 (d, *J* = 7.7 Hz, 2H), 3.01– 2.94 (m, 1H), 1.34 (d, *J* = 6.9 Hz, 6H). **^{13}C{^{1}H} NMR (101 MHz, $CDCl_3$):** δ 148.47, 147.64, 138.41, 136.20, 132.72, 129.44, 127.63, 126.62, 125.46, 120.79, 48.89, 39.38, 33.91, 24.21.

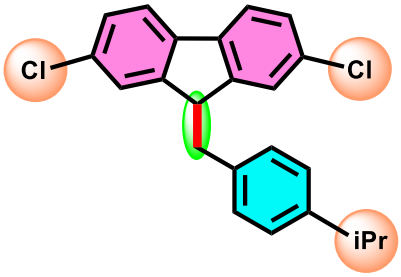

***2,7-dichloro-9-(4-methoxybenzyl)-9H-fluorene (9h)*:** White crystalline solid; Eluent: Hexane/EtOAc (40:1 v/v); Yield: 288 mg, 81%. **^{1}H NMR (300 MHz, $CDCl_3$):** δ 7.58 (d, *J* = 8.1 Hz, 2H), 7.34 (dd, *J* = 8.2, 2.0 Hz, 2H), 7.16 (d, *J* = 2.0 Hz, 2H), 7.12 – 7.02 (m, 2H), 6.93 – 6.80 (m, 2H), 4.11 (t, *J* = 7.4 Hz, 1H), 3.84 (s, 3H), 3.04 (d, *J* = 7.4 Hz, 2H). **^{13}C{^{1}H} NMR (101 MHz, $CDCl_3$):** δ 158.52, 148.41, 138.49, 132.74, 130.69, 130.44, 127.66, 125.39, 120.84, 113.93, 55.38, 48.98, 38.85.

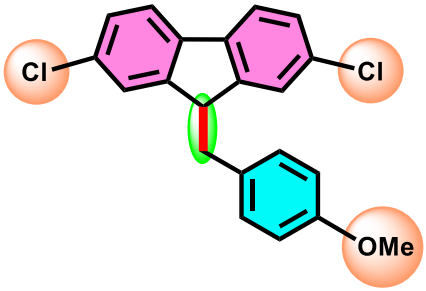

***4-((2,7-dichloro-9H-fluoren-9-yl)methyl)-N,N-dimethylaniline (9i)*:** Yellow crystalline solid; Eluent: Hexane/EtOAc (40:1 v/v); Yield: 313 mg, 85%. **^{1}H NMR (300 MHz, $CDCl_3$):** δ 7.59 (d, *J* = 8.1 Hz, 2H), 7.40 – 7.26 (m, 2H), 7.19 (s, 2H), 7.12 – 7.00 (m, 2H), 6.75 (d, *J* = 8.6 Hz, 2H), 4.12 (t, *J* = 7.5 Hz, 1H), 3.02–2.98 (m, 8H, Both –CH_2 and NMe_2 protons appear in same region). **^{13}C{^{1}H} NMR (101 MHz, $CDCl_3$):** δ 149.42, 148.69, 138.47, 132.68, 130.14, 127.55, 127.10, 125.47, 120.78, 113.15, 49.17, 41.06, 38.83.

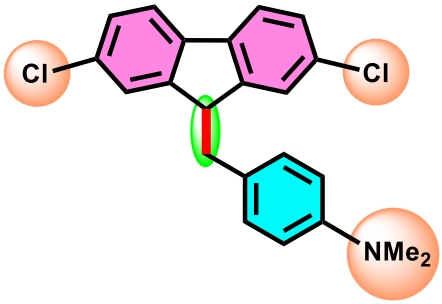

***9-([1,1'-biphenyl]-4-ylmethyl)-2,7-dichloro-9H-fluorene (9j)*:** White crystalline solid; Eluent: Hexane; Yield: 349 mg, 87%. **^{1}H NMR (300 MHz, $CDCl_3$):** δ 7.68 – 7.62 (m, 3H), 7.61 – 7.56 (m, 3H), 7.48 (t, *J* = 7.5 Hz, 2H), 7.38 (td, *J* = 8.8, 1.7 Hz, 3H), 7.29 – 7.20 (m, 4H), 4.22 (t, *J* = 7.4 Hz, 1H), 3.15 (d, *J* = 7.4 Hz, 2H). **^{13}C{^{1}H} NMR (101 MHz, $CDCl_3$):** δ 148.32, 140.88, 139.73, 138.53, 137.80, 132.84, 129.95, 128.91, 127.79, 127.37, 127.23, 127.15, 125.44, 120.93, 48.74, 39.39.

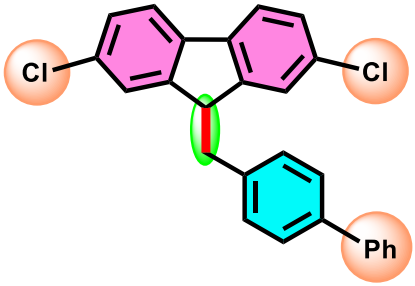

***2,7-dichloro-9-(4-fluorobenzyl)-9H-fluorene (9k)*:** White crystalline solid; Eluent: Hexane; Yield: 292 mg, 85%. **^{1}H NMR (300 MHz, $CDCl_3$):** δ 7.57 (d, *J* = 8.1 Hz, 2H), 7.34 (dd, *J* = 8.1, 1.9 Hz, 2H), 7.16 (d, *J* = 1.9 Hz, 2H), 7.08 (ddd, *J* = 8.3, 5.4, 2.5 Hz, 2H), 7.04 – 6.96 (m, 2H), 4.10 (t, *J* = 7.3 Hz, 1H), 3.08 (d, *J* = 7.3 Hz, 2H). **^{13}C{^{1}H} NMR (101 MHz, $CDCl_3$):** δ 161.85 (d, *J* = 245.0 Hz), 148.01, 138.52, 134.16 (d, *J* = 3.3 Hz), 130.90 (d, *J* = 7.8 Hz), 127.81, 125.29, 120.93, 115.33 (d, *J* = 21.3 Hz), 48.70, 38.79. **^{19}F NMR (282 MHz, $CDCl_3$):** δ -115.91.

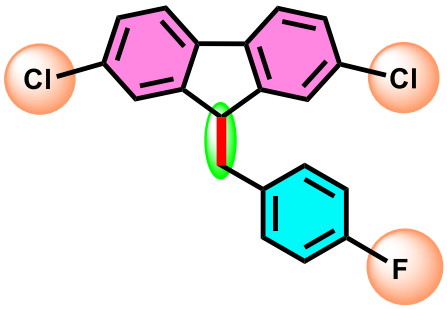

***2,7-dichloro-9-(4-chlorobenzyl)-9H-fluorene (9l)*:** White crystalline solid; Eluent: Hexane; Yield: 84%. **^{1}H NMR (300 MHz, $CDCl_3$):** δ 7.56 (d, *J* = 8.2 Hz, 2H), 7.34 (dd, *J* = 8.1, 1.9 Hz, 2H), 7.31 – 7.22 (m, 2H), 7.19 (d, *J* = 1.9 Hz, 2H), 7.10 – 6.99 (m, 2H), 4.11 (t, *J* = 7.1 Hz, 1H), 3.08 (d, *J* = 7.1 Hz, 2H). **^{13}C{^{1}H} NMR (75 MHz, $CDCl_3$):** δ 147.88, 138.51, 136.87, 132.86, 132.64, 130.78, 128.60, 127.85, 125.22, 120.96, 48.44, 38.86.

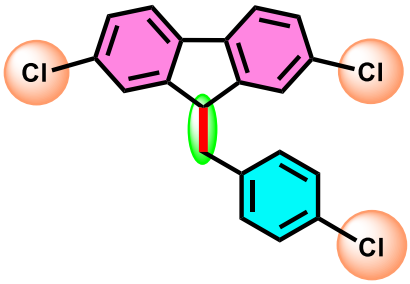

***9-(4-bromobenzyl)-2,7-dichloro-9H-fluorene (9m)*:** White solid; Eluent: Hexane; Yield: 295

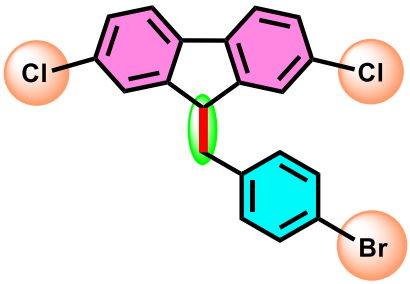

mg, 82%. **^{1}H NMR (300 MHz, $CDCl_3$):** δ 7.57 (d, *J* = 8.1 Hz, 2H), 7.45 – 7.37 (m, 2H), 7.34 (dd, *J* = 8.1, 1.9 Hz, 2H), 7.20 (s, 2H), 7.04 – 6.94 (m, 2H), 4.12 (t, *J* = 7.2 Hz, 1H), 3.07 (d, *J* = 7.1 Hz, 2H). **^{13}C{^{1}H} NMR (75 MHz, $CDCl_3$):** δ 147.85, 138.52, 137.36, 132.86, 131.54, 131.16, 127.87, 125.22, 120.97, 120.72, 48.37, 38.91.

***2,7-dichloro-9-(4-(trifluoromethyl)benzyl)-9H-fluorene (9n)*[7]:** White solid; Eluent: Hexane;

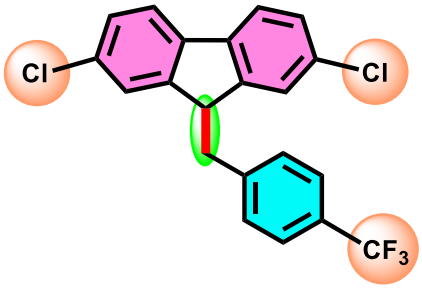

Yield: 318 mg, 81%. **^{1}H NMR (400 MHz, $CDCl_3$):** δ 7.58 (d, *J* = 8.1 Hz, 2H), 7.54 (d, *J* = 7.8 Hz, 1H), 7.44 – 7.37 (m, 2H), 7.35 (dd, *J* = 8.2, 2.0 Hz, 2H), 7.30 (d, *J* = 7.4 Hz, 1H), 7.16 (s, 2H), 4.18 (t, *J* = 7.2 Hz, 1H), 3.18 (d, *J* = 7.2 Hz, 2H). **^{13}C{^{1}H} NMR (75 MHz, $CDCl_3$):** δ 147.68, 142.53, 138.55, 132.96, 129.82, 129.41, 127.99, 125.40 (q, $^3J_{C-F}$ = 3.8 Hz), 125.21, 124.02 (q, $^1J_{C-F}$ = 272.6 Hz), 121.05, 48.25, 39.29. **^{19}F NMR (377 MHz, $CDCl_3$):** δ -62.65.

***2,7-dichloro-9-propyl-9H-fluorene (9o)*:** Colourless sticky oil; Eluent: Hexane; Yield: 188 mg,

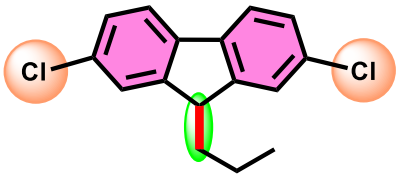

68%. **^{1}H NMR (400 MHz, $CDCl_3$):** δ 7.60 (d, *J* = 8.1 Hz, 2H), 7.48 (d, *J* = 2.0 Hz, 2H), 7.38 – 7.33 (m, 2H), 3.93 (t, *J* = 5.9 Hz, 1H), 2.00 – 1.92 (m, 2H), 1.25 – 1.17 (m, 2H), 0.91 (t, *J* = 7.4 Hz, 3H). **^{13}C{^{1}H} NMR (101 MHz, $CDCl_3$):** δ 149.21, 138.72, 132.97, 127.45, 124.84, 120.81, 47.48, 35.09, 18.91, 14.38.

***9-butyl-2,7-dichloro-9H-fluorene (9p)*:** Colourless sticky oil; Eluent: Hexane; Yield: 204 mg,

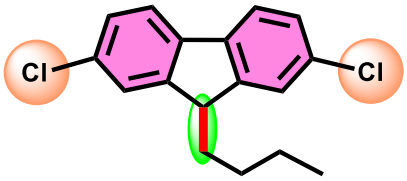

70%. **^{1}H NMR (400 MHz, $CDCl_3$):** δ 7.61 (d, *J* = 8.1 Hz, 2H), 7.49 (d, *J* = 2.1 Hz, 2H), 7.36 (dd, *J* = 8.3, 2.0 Hz, 2H),

3.95 (t, *J* = 5.8 Hz, 1H), 2.06 – 1.94 (m, 2H), 1.32 (h, *J* = 7.4 Hz, 2H), 1.21 – 1.09 (m, 2H), 0.88 (t, *J* = 7.4 Hz, 3H). **$^{13}C\{^{1}H\}$ NMR (101 MHz, $CDCl_3$):** δ 149.19, 138.75, 132.98, 127.46, 124.83, 120.82, 47.55, 32.54, 27.62, 23.02, 13.97.

***2,7-dichloro-9-hexyl-9H-fluorene (9q)*:** Colourless sticky oil; Eluent: Hexane; Yield: 227 mg, 71%. **^{1}H NMR (300 MHz, $CDCl_3$):** δ 7.61 (d, *J* = 8.1 Hz, 2H), 7.49 (d, *J* = 1.3 Hz, 2H), 7.36 (dd, *J* = 8.2, 1.7 Hz, 2H), 3.94 (t, *J* = 5.8 Hz, 1H), 2.05 – 1.94 (m, 2H), 1.35 – 1.16 (m, 8H), 0.95 – 0.85 (m, 3H). **$^{13}C\{^{1}H\}$ NMR (101 MHz, $CDCl_3$):** δ 149.21, 138.74, 132.99, 127.46, 124.83, 120.82, 47.59, 32.84, 31.70, 29.64, 25.54, 22.76, 14.16.

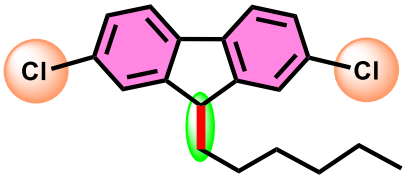

***2,7-dichloro-9-octyl-9H-fluorene (9r)*:** Colourless sticky oil; Eluent: Hexane; Yield: 264 mg, 76%. **^{1}H NMR (400 MHz, $CDCl_3$):** δ 7.60 (d, *J* = 8.2 Hz, 2H), 7.51 (d, *J* = 2.1 Hz, 2H), 7.37 (d, *J* = 8.2 Hz, 2H), 3.93 (t, *J* = 5.9 Hz, 1H), 2.00 (dt, *J* = 10.6, 6.1 Hz, 2H), 1.45 – 1.23 (m, 10H), 1.19 (dq, *J* = 12.1, 5.4 Hz, 2H), 0.95 (t, *J* = 7.0 Hz, 3H). **$^{13}C\{^{1}H\}$ NMR (75 MHz, $CDCl_3$):** δ 149.20, 138.72, 132.99, 127.44, 124.82, 120.78, 47.58, 32.80, 31.94, 29.43, 29.40, 25.56, 22.77, 14.22.

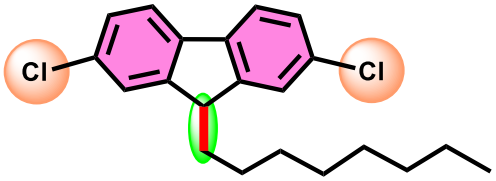

***2,7-dichloro-9-(3,4,5-trimethoxybenzyl)-9H-fluorene (9s)*[8]:** White solid; Eluent: Hexane/EtOAc (20:1 v/v); Yield: 299 mg, 72%. **^{1}H NMR (400 MHz, $CDCl_3$):** δ 7.59 (dd, *J* = 8.1, 2.1 Hz, 2H), 7.34 (dd, *J* = 8.1, 1.9 Hz, 2H), 7.26 (d, *J* = 2.0 Hz, 2H), 6.31 (s, 2H), 4.16 (t, *J* = 7.1 Hz, 1H), 3.86 (s, 3H), 3.79 (s, 6H), 3.06 (d, *J* = 7.1 Hz, 2H). **$^{13}C\{^{1}H\}$ NMR (75 MHz, $CDCl_3$):** δ 153.08, 148.12, 138.63, 136.93, 133.96, 132.77, 127.75, 125.55, 120.97, 106.66, 61.11, 56.21, 48.89, 40.10.

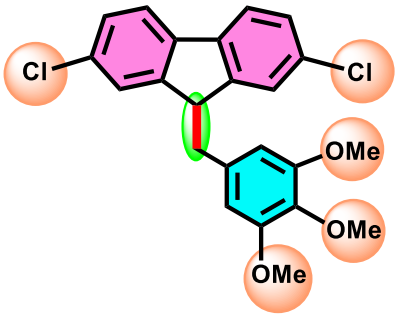

***2,7-dichloro-9-(cyclohexylmethyl)-9H-fluorene (9t)*:** White solid; Eluent: Hexane; Yield: 199

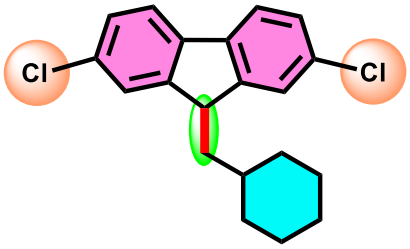

mg, 60%. **^{1}H NMR (400 MHz, $CDCl_3$):** δ 7.60 (d, *J* = 8.1 Hz, 2H), 7.46 (s, 2H), 7.35 (dd, *J* = 8.2, 1.9 Hz, 2H), 3.95 (t, *J* = 6.9 Hz, 1H), 1.75 (ddd, *J* = 20.7, 12.2, 5.2 Hz, 8H), 1.37 – 1.25 (m, 3H), 1.09 – 0.98 (m, 2H). **^{13}C{^{1}H} NMR (101 MHz, $CDCl_3$):** δ 149.86, 138.41, 132.87, 127.39, 125.08, 120.84, 44.94, 41.40, 35.59, 33.71, 26.63, 26.25.

***2-((2,7-dichloro-9H-fluoren-9-yl)methyl)thiophene (9u)*:** Yellow solid; Eluent:

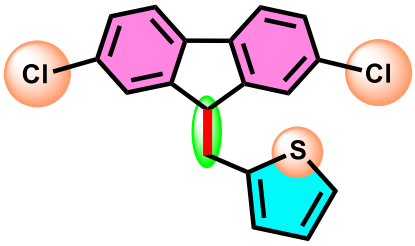

Hexane/EtOAc (30:1 v/v); Yield: 238 mg, 72%. **^{1}H NMR (300 MHz, $CDCl_3$):** δ 7.58 (d, *J* = 8.1 Hz, 2H), 7.36 (dd, *J* = 8.2, 1.7 Hz, 2H), 7.26 (d, *J* = 1.9 Hz, 2H), 7.17 (d, *J* = 5.1 Hz, 1H), 6.96 – 6.90 (m, 1H), 6.73 (d, *J* = 3.4 Hz, 1H), 4.17 (t, *J* = 6.9 Hz, 1H), 3.38 (d, *J* = 6.9 Hz, 2H). **^{13}C{^{1}H} NMR (101 MHz, $CDCl_3$):** δ 147.69, 140.78, 138.63, 132.93, 127.90, 126.79, 126.43, 125.19, 124.27, 120.87, 48.94, 33.61.

***3-((2,7-dichloro-9H-fluoren-9-yl)methyl)furan (9v)*:** White solid; Eluent: Hexane/EtOAc

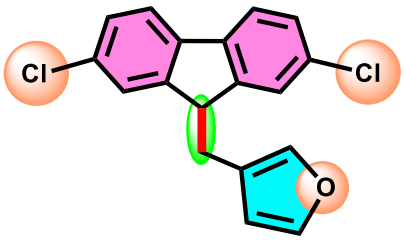

(30:1 v/v); Yield: 236 mg, 75%. **^{1}H NMR (400 MHz, $CDCl_3$):** δ 7.97 (s, 1H), 7.77 (s, 1H), 7.67 (s, 1H), 7.56 (d, *J* = 7.1 Hz, 3H), 7.39 (s, 1H), 7.05 (s, 1H), 6.73 (s, 1H), 4.10 (t, *J* = 6.6 Hz, 1H), 3.03 (d, *J* = 6.6 Hz, 2H). **^{13}C{^{1}H} NMR (101 MHz, $CDCl_3$):** δ 148.27, 143.94, 140.22, 138.70, 132.94, 128.62, 127.80, 125.05, 120.90, 111.15, 47.50, 36.71.

***2,7-dichloro-9-(naphthalen-1-ylmethyl)-9H-fluorene (9w)*:** Pale yellow solid; Eluent: Hexane/EtOAc (40:1 v/v); Yield: 300 mg, 80%. **^{1}H NMR (300 MHz, $CDCl_3$):** δ 8.24 (d, *J* = 9.4 Hz, 1H), 8.04 – 7.97 (m, 1H), 7.92 (d, *J* = 8.2 Hz, 1H), 7.68 – 7.58 (m, 4H), 7.55 – 7.47 (m, 1H), 7.36 (dd, *J* = 8.1, 1.4 Hz, 2H), 7.24 (d, *J* = 5.8 Hz, 1H), 7.02 (d, *J* = 1.7 Hz, 2H), 4.34 (t, *J* = 7.9 Hz, 1H), 3.44 (d, *J* = 7.9 Hz, 2H). **^{13}C{^{1}H} NMR (101 MHz, $CDCl_3$):** δ 148.52, 138.36, 134.88, 134.19, 132.74, 131.84, 129.36, 128.45, 128.11, 127.73, 126.41, 125.97, 125.74, 125.36, 123.46, 120.85, 47.53, 37.80.

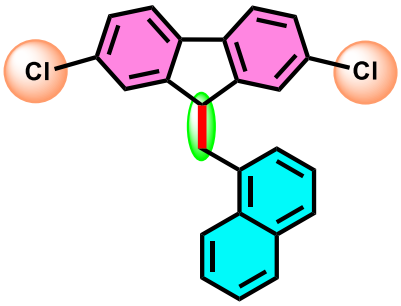

***2,7-dichloro-9-(naphthalen-2-ylmethyl)-9H-fluorene (9x)*:** White solid; Eluent: Hexane/EtOAc (40:1 v/v); Yield: 308 mg, 82%. **^{1}H NMR (300 MHz, $CDCl_3$):** δ 7.95 – 7.76 (m, 3H), 7.64 – 7.47 (m, 5H), 7.35 (dd, *J* = 8.2, 1.9 Hz, 3H), 7.20 (d, *J* = 1.9 Hz, 2H), 4.25 (t, *J* = 7.3 Hz, 1H), 3.24 (d, *J* = 7.4 Hz, 2H). **^{13}C{^{1}H} NMR (101 MHz, $CDCl_3$):** δ 148.35, 138.48, 136.20, 133.52, 132.82, 132.45, 128.24, 128.11, 127.80, 127.76, 127.73, 127.65, 126.27, 125.74, 125.39, 120.89, 48.62, 39.89.

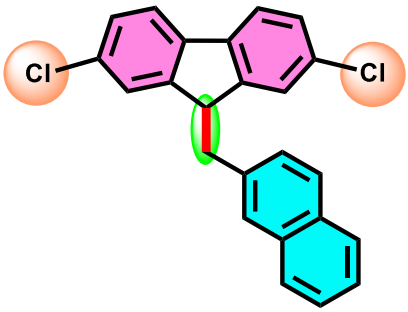

***1-((2,7-dichloro-9H-fluoren-9-yl)methyl)pyrene (9y)*:** Yellow solid; Eluent: Hexane/EtOAc (40:1 v/v); Yield: 350 mg, 78%. **^{1}H NMR (300 MHz, $CDCl_3$):** δ 8.41 (d, *J* = 9.2 Hz, 1H), 8.29 – 8.01 (m, 7H), 7.78 (d, *J* = 7.8 Hz, 1H), 7.66 (d, *J* = 8.1 Hz, 2H), 7.36 (dd, *J* = 8.1, 2.0 Hz, 2H), 6.98 (d, *J* = 1.9 Hz, 2H), 4.46 (t, *J* = 7.9 Hz, 1H), 3.72 (d, *J* = 7.9 Hz, 2H). **^{13}C{^{1}H} NMR (101 MHz, $CDCl_3$):** δ 148.48, 138.44, 132.87, 132.83, 131.58, 130.99,

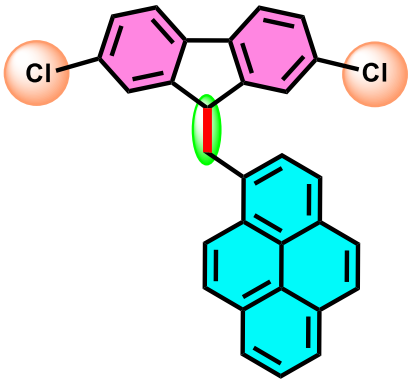

130.86, 129.11, 129.04, 128.00, 127.83, 127.76, 127.31, 126.20, 125.77, 125.47, 125.37, 125.30, 125.14, 124.67, 122.99, 120.94, 48.59, 38.21.

9-benzyl-2,7-dibromo-9H-fluorene (10a)[7]**:** White solid; Eluent: Hexane; Yield: 348 mg, 84%. **^{1}H NMR (300 MHz, $CDCl_3$):** δ 7.52 (q, *J* = 8.1 Hz, 4H), 7.38 – 7.27 (m, 5H), 7.19 (d, *J* = 7.7 Hz, 2H), 4.17 (t, *J* = 7.5 Hz, 1H), 3.09 (d, *J* = 7.6 Hz, 2H). **^{13}C{^{1}H} NMR (101 MHz, $CDCl_3$):** δ 148.52, 138.92, 138.72, 130.59, 129.54, 128.59, 128.36, 126.94, 121.28, 121.00, 48.81, 39.78.

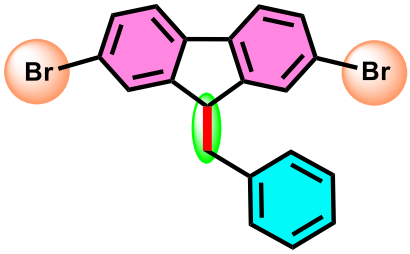

***4-((2,7-dibromo-9H-fluoren-9-yl)methyl)-N,N-dimethylaniline (10b)*:** Yellow solid; Eluent: Hexane; Yield: 357 mg, 78%. **^{1}H NMR (400 MHz, $CDCl_3$):** δ 7.56 (d, *J* = 8.1 Hz, 2H), 7.48 (dd, *J* = 8.2, 1.8 Hz, 2H), 7.33 (d, *J* = 1.7 Hz, 2H), 7.05 (d, *J* = 8.3 Hz, 2H), 6.73 (d, *J* = 8.6 Hz, 2H), 4.12 (t, *J* = 7.6 Hz, 1H), 3.00 (d, *J* = 7.4 Hz, 2H), 2.97 (s, 6H). **^{13}C{^{1}H} NMR (75 MHz, $CDCl_3$):** δ 149.76, 148.94, 138.95, 130.43, 130.15, 128.47, 126.71, 121.22, 120.95, 112.98, 49.34, 40.96, 38.89.

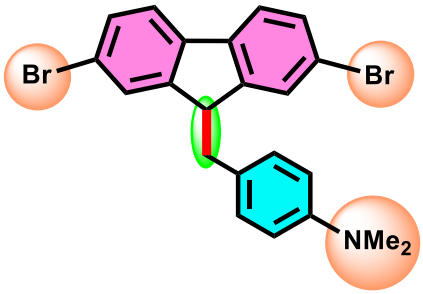

***9-([1,1'-biphenyl]-4-ylmethyl)-2,7-dibromo-9H-fluorene (10c)*:** White solid; Eluent: Hexane; Yield: 368 mg, 75%. **^{1}H NMR (300 MHz, $CDCl_3$):** δ 7.71 – 7.61 (m, 2H), 7.62 – 7.54 (m, 4H), 7.53 – 7.45 (m, 4H), 7.42 – 7.34 (m, 3H), 7.25 (d, *J* = 8.2 Hz, 2H), 4.20 (t, *J* = 7.4 Hz, 1H), 3.14 (d, *J* = 7.5 Hz, 2H). **^{13}C{^{1}H} NMR (101 MHz, $CDCl_3$):** δ 148.48, 140.91, 139.77, 138.96, 137.77, 130.63, 129.96, 128.90, 128.38, 127.36, 127.23, 127.16, 121.33, 121.05, 48.78, 39.39.

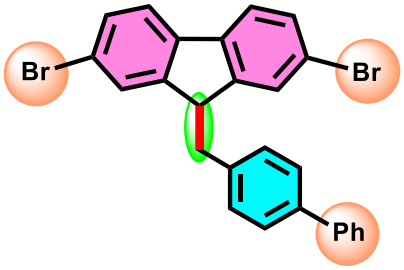

***2,7-dibromo-9-(4-chlorobenzyl)-9H-fluorene (10d)*:** White solid; Eluent: Hexane; Yield: 354

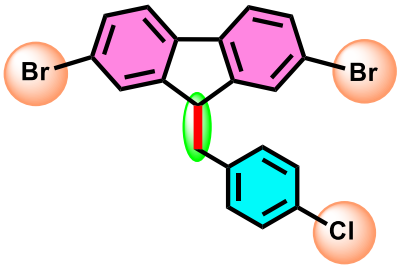

mg, 79%. **^{1}H NMR (400 MHz, $CDCl_3$):** δ 7.61 – 7.44 (m, 4H), 7.35 (s, 2H), 7.26 (d, *J* = 8.1 Hz, 2H), 7.04 (d, *J* = 8.1 Hz, 2H), 4.14 (t, *J* = 7.1 Hz, 1H), 3.10 (d, *J* = 7.2 Hz, 2H). **^{13}C{^{1}H} NMR (75 MHz, $CDCl_3$):** δ 148.08, 139.00, 136.85, 132.68, 130.82, 130.75, 128.62, 128.20, 121.40, 121.08, 48.51, 38.91.

***2,7-dibromo-9-(4-bromobenzyl)-9H-fluorene (10e)*:** White solid; Eluent: Hexane; Yield: 394

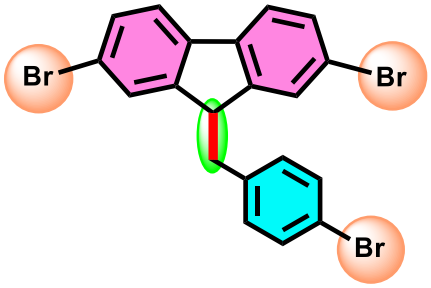

mg, 80%. **^{1}H NMR (400 MHz, $CDCl_3$):** δ 7.55 – 7.48 (m, 4H), 7.43 – 7.40 (m, 2H), 7.35 (d, *J* = 1.7 Hz, 2H), 7.00 – 6.96 (m, 2H), 4.14 (t, *J* = 7.1 Hz, 1H), 3.08 (d, *J* = 7.1 Hz, 2H). **^{13}C{^{1}H} NMR (101 MHz, $CDCl_3$):** δ 148.06, 139.01, 137.35, 131.56, 131.21, 130.76, 128.20, 121.42, 121.09, 120.75, 48.44, 38.96.

***2,7-dibromo-9-propyl-9H-fluorene (10f)*:** Colourless sticky oil; Eluent: Hexane; Yield: 285

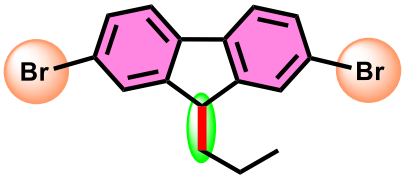

mg, 78%. **^{1}H NMR (400 MHz, $CDCl_3$):** δ 7.65 (s, 2H), 7.54 (d, *J* = 8.2 Hz, 2H), 7.50 (dd, *J* = 8.1, 1.8 Hz, 2H), 3.91 (t, *J* = 6.1 Hz, 1H), 1.95 (dt, *J* = 11.0, 5.7 Hz, 2H), 1.23 (dq, *J* = 15.1, 7.3 Hz, 2H), 0.92 (t, *J* = 7.4 Hz, 3H). **^{13}C{^{1}H} NMR (75 MHz, $CDCl_3$):** δ 149.30, 139.05, 130.24, 127.66, 121.18, 121.15, 47.41, 35.01, 18.94, 14.35.

***2,7-dibromo-9-butyl-9H-fluorene (10g)*:** Colourless sticky oil; Eluent: Hexane; Yield: 308 mg,

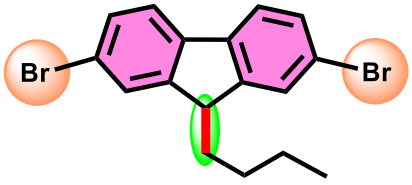

81%. **^{1}H NMR (400 MHz, $CDCl_3$):** δ 7.65 (s, 2H), 7.56 (d, *J* = 8.0 Hz, 2H), 7.50 (d, *J* = 8.1 Hz, 2H), 3.93 (t, *J* = 6.0 Hz, 1H), 2.05 – 1.93 (m, 2H), 1.31 (q, *J* = 7.5 Hz, 2H), 1.20 – 1.09 (m, 2H), 0.87 (t, *J* = 7.4 Hz, 3H). **^{13}C{^{1}H} NMR (101 MHz, $CDCl_3$):** δ 149.33, 139.13, 130.29, 127.69, 127.65, 121.21, 47.52, 32.49, 27.61, 23.00, 13.97.

***2,7-dibromo-9-hexyl-9H-fluorene (10h)*:** Colourless sticky oil; Eluent: Hexane; Yield: 343 mg, 84%. **^{1}H NMR (400 MHz, $CDCl_3$):** δ 7.65 (s, 2H), 7.57 – 7.55 (m, 2H), 7.50 (d, *J* = 8.3 Hz, 2H), 3.94 (t, *J* = 6.0 Hz, 1H), 1.99 (dd, *J* = 10.6, 5.4 Hz, 2H), 1.32 – 1.19 (m, 8H), 0.89 (t, *J* = 6.8 Hz, 3H). **^{13}C{^{1}H} NMR (101 MHz, $CDCl_3$):** δ 149.35, 139.14, 130.29, 127.71, 121.22, 47.57, 32.77, 31.66, 29.62, 25.51, 22.74, 14.18.

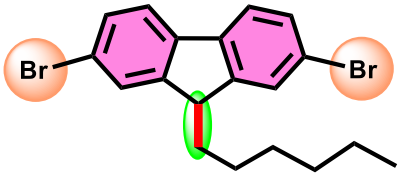

***2,7-dibromo-9-octyl-9H-fluorene (10i)*:** Colourless sticky oil; Eluent: Hexane; Yield: 371 mg, 85%. **^{1}H NMR (400 MHz, $CDCl_3$):** δ 7.64 (s, 2H), 7.57 – 7.49 (m, 4H), 3.94 (t, *J* = 5.8 Hz, 1H), 1.98 (dt, *J* = 10.2, 6.1 Hz, 2H), 1.34 – 1.26 (m, 4H), 1.24 (s, 6H), 1.20 – 1.11 (m, 2H), 0.89 (t, *J* = 6.9 Hz, 3H). **^{13}C{^{1}H} NMR (101 MHz, $CDCl_3$):** δ 149.36, 139.15, 130.30, 127.71, 121.22, 47.57, 32.75, 31.93, 29.93, 29.41, 29.38, 25.53, 22.77, 14.25.

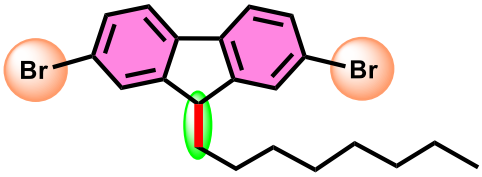

***2,7-dibromo-9-(3,4,5-trimethoxybenzyl)-9H-fluorene (10j)*:** White crystalline solid; Eluent: Hexane/EtOAc (20:1 v/v); Yield: 377 mg, 75%. **^{1}H NMR (400 MHz, $CDCl_3$):** δ 7.55 (d, *J* = 8.1 Hz, 2H), 7.49 (dd, *J* = 8.1, 1.7 Hz, 2H), 7.41 (s, 2H), 6.30 (s, 2H), 4.16 (t, *J* = 7.2 Hz, 1H), 3.86 (s, 3H), 3.79 (s, 6H), 3.06 (d, *J* = 7.1 Hz, 2H). **^{13}C{^{1}H} NMR (75 MHz, $CDCl_3$):** δ 153.09, 148.31, 139.10, 136.97, 133.92, 130.62, 128.52, 121.40, 120.95, 106.71, 61.12, 56.25, 48.98, 40.12.

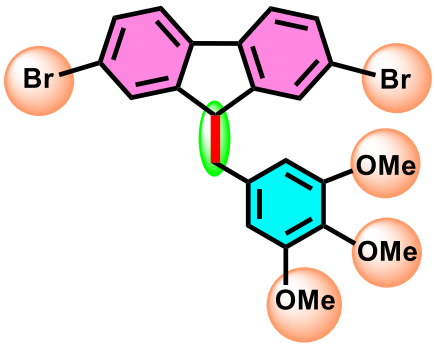

***2-((2,7-dibromo-9H-fluoren-9-yl)methyl)thiophene (10k)*:** Yellow crystalline solid; Eluent: Hexane/EtOAc (35:1 v/v); Yield: 332 mg, 79%. **^{1}H NMR (400 MHz, $CDCl_3$):** δ 7.52 (t, *J* = 5.8 Hz, 4H), 7.40 (s, 2H), 7.16 (d, *J* = 5.1 Hz, 1H), 6.92 (ddd, *J* = 5.0, 3.3, 1.2 Hz, 1H), 6.71 (d, *J* = 3.5 Hz, 1H), 4.16 (t, *J* = 7.0 Hz, 1H), 3.36 (d, *J*

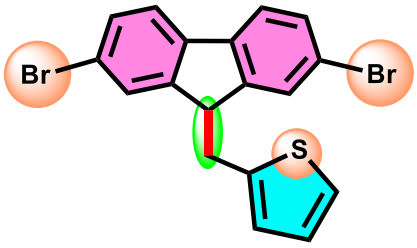

= 7.0 Hz, 2H). **$^{13}C\{^{1}H\}$ NMR (75 MHz, $CDCl_3$):** δ 147.80, 140.70, 139.00, 130.70, 128.06, 126.75, 126.41, 124.25, 121.24, 121.12, 48.91, 33.53.

***3-((2,7-dibromo-9H-fluoren-9-yl)methyl)furan (10l)*:** Light yellow crystalline solid; Eluent: Hexane/EtOAc (35:1 v/v); Yield: 299 mg, 74%. **^{1}H NMR (300 MHz, $CDCl_3$):** δ 7.50 (q, *J* = 1.9 Hz, 6H), 7.32 (s, 1H), 7.05 (s, 1H), 6.11 (d, *J* = 1.8 Hz, 1H), 4.07 (t, *J* = 6.5 Hz, 1H), 3.02 (d, *J* = 6.8 Hz, 2H). **$^{13}C\{^{1}H\}$ NMR (101 MHz, $CDCl_3$):** δ 148.38, 142.95, 140.15, 139.05, 130.59, 127.89, 121.26, 121.12, 121.09, 111.11, 47.42, 28.36.

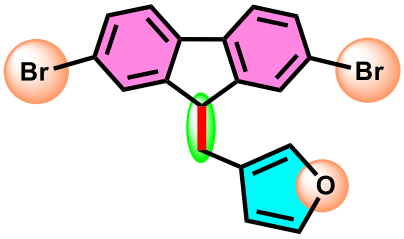

***2,7-dibromo-9-(naphthalen-1-ylmethyl)-9H-fluorene (10m)*:** Light yellow crystalline solid; Eluent: Hexane/EtOAc (40:1 v/v); Yield: 362 mg, 78%. **^{1}H NMR (300 MHz, $CDCl_3$):** δ 8.24 (d, *J* = 8.4 Hz, 1H), 8.04 – 7.97 (m, 1H), 7.92 (d, *J* = 8.4 Hz, 1H), 7.65 – 7.58 (m, 4H), 7.54 – 7.47 (m, 3H), 7.25 (d, *J* = 6.5 Hz, 1H), 7.17 (d, *J* = 1.8 Hz, 2H), 4.37 (t, *J* = 7.9 Hz, 1H), 3.46 (d, *J* = 7.9 Hz, 2H). **$^{13}C\{^{1}H\}$ NMR (75 MHz, $CDCl_3$):** δ 148.73, 138.88, 134.89, 134.23, 131.87, 130.64, 129.39, 128.74, 128.54, 128.16, 126.45, 126.02, 125.37, 123.50, 121.32, 120.99, 47.62, 37.88.

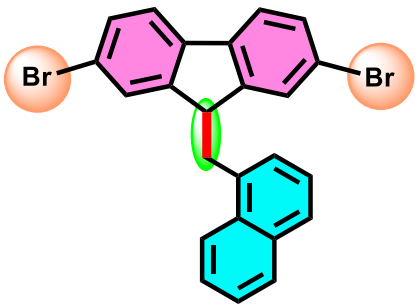

***9-benzyl-2,7-di-tert-butyl-9H-fluorene (11a)*[8]:** White solid; Eluent: Hexane; Yield: 321 mg, 87%. **^{1}H NMR (300 MHz, $CDCl_3$):** δ 7.68 (d, *J* = 8.0 Hz, 2H), 7.45 – 7.37 (m, 4H), 7.37 – 7.30 (m, 3H), 7.18 (d, *J* = 1.9 Hz, 2H), 4.21 (t, *J* = 7.9 Hz, 1H), 3.13 (d, *J* = 7.9 Hz, 2H), 1.35 (s, 18H). **$^{13}C\{^{1}H\}$ NMR (75 MHz, $CDCl_3$):** δ 149.42, 146.97, 140.48, 138.30, 129.89, 128.43, 126.44, 124.17, 122.02, 119.11, 49.13, 40.81, 34.92, 31.66.

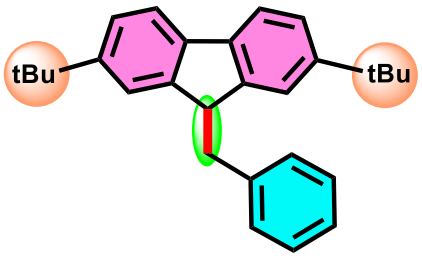

***2,7-di-tert-butyl-9-(3-fluorobenzyl)-9H-fluorene (11b)*:** White crystalline solid; Eluent: Hexane; Yield: 344 mg, 89%. **^{1}H NMR (400 MHz, $CDCl_3$):** δ 7.71 (d, *J* = 8.0 Hz, 2H), 7.47 (dd, *J* = 8.0, 1.7 Hz, 2H), 7.41 – 7.33 (m, 1H), 7.25 (s, 2H), 7.12 (d, *J* = 7.6 Hz, 1H), 7.06 (t, *J* = 8.0 Hz, 2H), 4.23 (t, *J* = 7.8 Hz, 1H), 3.17 (d, *J* = 7.8 Hz, 2H), 1.41 (s, 18H). **^{13}C{^{1}H} NMR (75 MHz, $CDCl_3$):** δ 162.95 (d, *J* = 245.5 Hz), 149.53, 146.55, 142.99 (d, *J* = 7.2 Hz), 138.33, 129.77 (d, *J* = 8.3 Hz), 125.52 (d, *J* = 2.8 Hz), 124.34, 121.89, 119.24, 116.76 (d, *J* = 20.9 Hz), 113.31 (d, *J* = 20.9 Hz), 48.88, 40.51, 34.93, 31.67. **^{19}F NMR (377 MHz, $CDCl_3$):** δ -113.65.

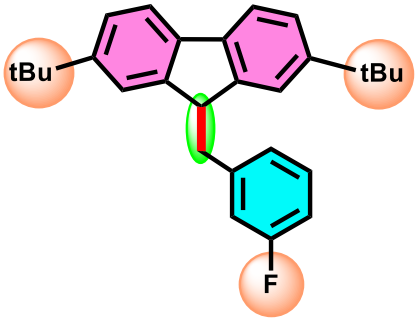

***2,7-di-tert-butyl-9-(4-methylbenzyl)-9H-fluorene (11c)*:** White crystalline solid; Eluent: Hexane; Yield: 291 mg, 76%. **^{1}H NMR (400 MHz, $CDCl_3$):** δ 7.78 – 7.64 (m, 5H), 7.61 (d, *J* = 7.8 Hz, 1H), 7.48 (d, *J* = 8.0 Hz, 1H), 7.44 (d, *J* = 6.1 Hz, 2H), 7.35 (d, *J* = 7.8 Hz, 1H), 4.21 (t, *J* = 7.9 Hz, 1H), 3.13 (d, *J* = 7.9 Hz, 2H), 2.46 (s, 3H), 1.39 (s, 18H). **^{13}C{^{1}H} NMR (101 MHz, $CDCl_3$):** δ 149.34, 147.07, 138.30, 135.82, 129.77, 129.45, 129.06, 124.11, 122.04, 119.08, 49.25, 40.33, 34.91, 31.65, 21.20.

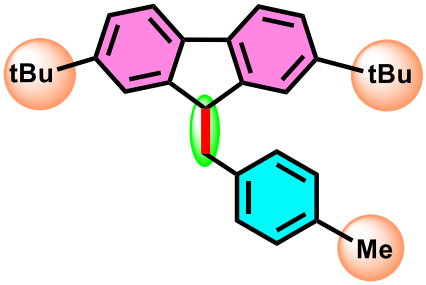

***2,7-di-tert-butyl-9-(4-methoxybenzyl)-9H-fluorene (11d)*:** White solid; Eluent: Hexane; Yield: 319 mg, 80%. **^{1}H NMR (400 MHz, $CDCl_3$):** δ 7.64 (d, *J* = 8.0 Hz, 2H), 7.42 – 7.35 (m, 2H), 7.23 – 7.14 (m, 4H), 6.94 – 6.87 (m, 2H), 4.12 (t, *J* = 7.8 Hz, 1H), 3.86 (s, 3H), 3.05 (d, *J* = 7.9 Hz, 2H), 1.33 (s, 18H). **^{13}C{^{1}H} NMR (101 MHz, $CDCl_3$):** δ 158.31, 149.39, 147.03, 138.31, 132.58, 130.78, 124.11, 122.04, 119.08, 113.86, 55.52, 49.35, 39.88, 34.93, 31.68.

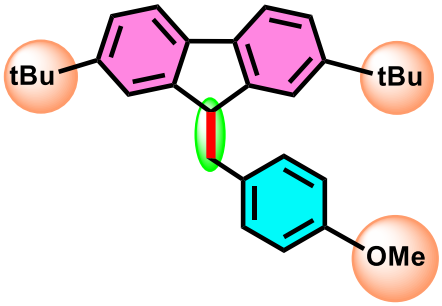

***4-((2,7-di-tert-butyl-9H-fluoren-9-yl)methyl)-N,N-dimethylaniline (11e)*:** White solid; Eluent: Hexane/EtOAc (35:1 v/v); Yield: 333 mg, 81%. **^{1}H NMR (300 MHz, $CDCl_3$):** δ 7.69 – 7.63 (m, 2H), 7.43 – 7.35 (m, 2H), 7.23 – 7.13 (m, 4H), 6.82 (d, *J* = 8.6 Hz, 2H), 4.13 (t, *J* = 7.9 Hz, 1H), 3.03 (d, *J* = 7.9 Hz, 2H), 3.00 (s, 6H), 1.35 (s, 18H). **^{13}C{^{1}H} NMR (101 MHz, $CDCl_3$):** δ 149.30, 147.27, 138.30, 130.49, 124.00, 122.14, 119.01, 113.48, 49.53, 41.35, 39.84, 34.94, 31.70.

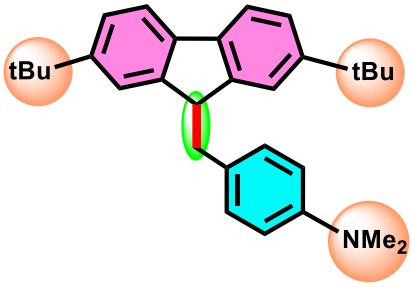

***9-([1,1'-biphenyl]-4-ylmethyl)-2,7-di-tert-butyl-9H-fluorene (11f)*:** White solid; Eluent: Hexane; Yield: 378 mg, 85%. **^{1}H NMR (300 MHz, $CDCl_3$):** δ 7.74 – 7.67 (m, 4H), 7.64 (d, *J* = 2.2 Hz, 2H), 7.58 – 7.50 (m, 2H), 7.48 – 7.38 (m, 5H), 7.22 (d, *J* = 5.3 Hz, 2H), 4.26 (t, *J* = 7.9 Hz, 1H), 3.19 (d, *J* = 8.2 Hz, 2H), 1.38 (s, 18H). **^{13}C{^{1}H} NMR (101 MHz, $CDCl_3$):** δ 149.42, 146.90, 141.36, 139.65, 139.42, 138.30, 130.32, 128.90, 127.22, 127.20, 124.22, 122.03, 119.16, 49.10, 40.43, 34.92, 31.66.

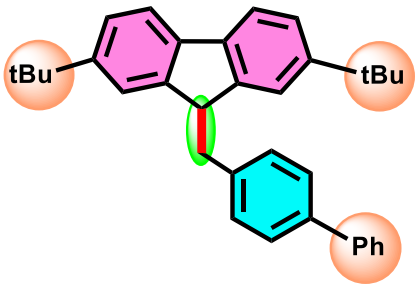

***2,7-di-tert-butyl-9-(4-(trifluoromethyl)benzyl)-9H-fluorene (11g)*:** White solid; Eluent: Hexane; Yield: 380 mg, 87%. **^{1}H NMR (300 MHz, $CDCl_3$):** δ 7.69 – 7.66 (m, 2H), 7.62 (s, 2H), 7.43 (d, *J* = 8.3 Hz, 2H), 7.39 (d, *J* = 8.4 Hz, 2H), 7.15 (d, *J* = 2.3 Hz, 2H), 4.22 (t, *J* = 7.8 Hz, 1H), 3.21 (d, *J* = 8.1 Hz, 2H), 1.36 (s, 18H). **^{13}C{^{1}H} NMR (101 MHz, $CDCl_3$):** δ 149.64, 146.33, 144.51, 138.34, 130.20, 128.83 (q, $^{2}J_{C–F}$ = 32.4 Hz), 125.26 (q, $^{3}J_{C–F}$ = 3.7 Hz), 124.44, 121.81, 120.54 (q, $^{3}J_{C–F}$ = 218 Hz), 119.29, 48.74, 40.49, 34.91, 31.61. **^{19}F NMR (377 MHz, $CDCl_3$):** δ -62.28.

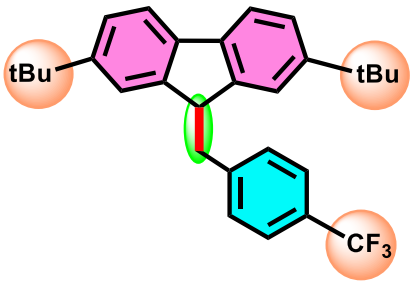

***2,7-di-tert-butyl-9-(4-chlorobenzyl)-9H-fluorene (11h)*:** White crystalline solid; Eluent: Hexane; Yield: 346 mg, 86%. **^{1}H NMR (300 MHz, $CDCl_3$):** δ 7.68 (d, *J* = 8.0 Hz, 2H), 7.44 (dd, *J* = 8.1, 1.8 Hz, 2H), 7.34 (d, *J* = 8.3 Hz, 2H), 7.26 – 7.15 (m, 4H), 4.19 (t, *J* = 7.6 Hz, 1H), 3.14 (d, *J* = 7.7 Hz, 2H), 1.40 (s, 18H). **^{13}C{^{1}H} NMR (101 MHz, $CDCl_3$):** δ 149.50, 146.52, 138.72, 138.33, 132.15, 131.18, 128.39, 124.30, 121.86, 119.22, 48.90, 39.96, 34.92, 31.66.

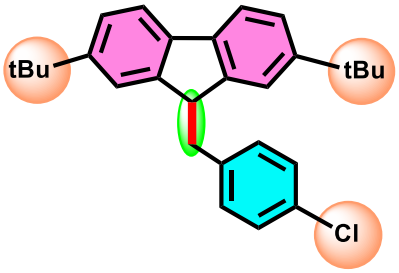

***9-(4-bromobenzyl)-2,7-di-tert-butyl-9H-fluorene (11i)*:** White crystalline solid; Eluent: Hexane; Yield: 376 mg, 84%. **^{1}H NMR (300 MHz, $CDCl_3$):** δ 7.65 (d, *J* = 8.0 Hz, 2H), 7.47 (d, *J* = 8.3 Hz, 2H), 7.43 – 7.38 (m, 2H), 7.19 (d, *J* = 0.9 Hz, 2H), 7.12 (d, *J* = 8.3 Hz, 2H), 4.16 (t, *J* = 7.6 Hz, 1H), 3.10 (d, *J* = 7.6 Hz, 2H), 1.36 (s, 18H). **^{13}C{^{1}H} NMR (101 MHz, $CDCl_3$):** δ 149.52, 146.48, 139.23, 138.32, 131.59, 131.35, 124.31, 121.86, 120.20, 119.22, 48.84, 40.01, 34.92, 31.65.

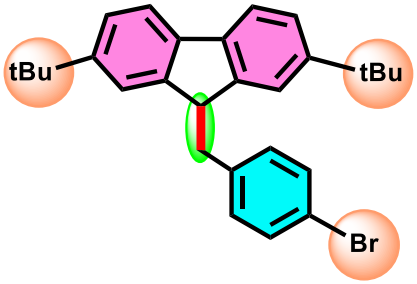

***2,7-di-tert-butyl-9-(3,4,5-trimethoxybenzyl)-9H-fluorene (11j)*:** White solid; Eluent: Hexane/EtOAc (20:1 v/v); Yield: 312 mg, 68%. **^{1}H NMR (300 MHz, $CDCl_3$):** δ 7.65 (d, *J* = 8.0 Hz, 2H), 7.46 – 7.34 (m, 2H), 7.23 (s, 2H), 6.45 (s, 2H), 4.20 (t, *J* = 7.6 Hz, 1H), 3.89 (s, 3H), 3.81 (s, 6H), 3.11 (d, *J* = 7.6 Hz, 2H), 1.36 (s, 18H). **^{13}C{^{1}H} NMR (101 MHz, $CDCl_3$):** δ 153.00, 149.40, 146.61, 138.39, 136.52, 135.86, 124.23, 121.81, 119.15, 106.58, 60.97, 56.07, 49.05, 40.73, 34.89, 31.68.

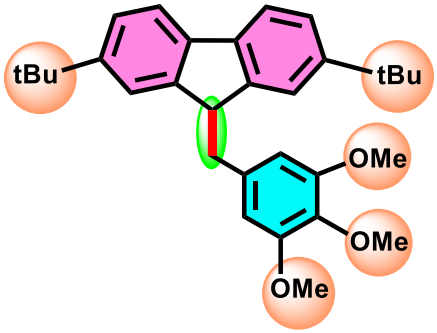

***3-((2,7-di-tert-butyl-9H-fluoren-9-yl)methyl)pyridine (11k)*:** Pale yellow solid; Eluent: Hexane/EtOAc (40:1 v/v); Yield: 314 mg, 85%. **^{1}H NMR (300 MHz, $CDCl_3$):** δ 8.78 (d, *J* = 4.9 Hz, 1H), 7.71 – 7.63 (m, 3H), 7.39 (dd, *J* = 8.0, 1.8 Hz, 2H), 7.32 – 7.26 (m, 1H), 7.13 – 7.03 (m, 3H), 4.56 (t, *J* = 7.9 Hz, 1H), 3.23 (d, *J* = 8.0 Hz, 2H), 1.30 (s, 18H). **^{13}C{^{1}H} NMR (101 MHz, $CDCl_3$):** δ 160.59, 149.82, 149.50, 147.14, 138.25, 136.31, 124.83, 124.19, 121.81, 121.73, 119.16, 47.72, 43.27, 34.89, 31.62.

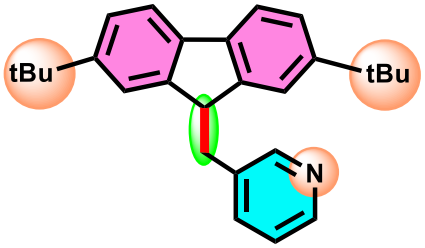

***2-((2,7-di-tert-butyl-9H-fluoren-9-yl)methyl)pyridine (11l)*:** Pale yellow solid; Eluent: Hexane/EtOAc (35:1 v/v); Yield: 303 mg, 82%. **^{1}H NMR (300 MHz, $CDCl_3$):** δ 8.79 (d, *J* = 3.9 Hz, 1H), 7.75 – 7.59 (m, 3H), 7.40 (dd, *J* = 8.0, 1.8 Hz, 2H), 7.32 – 7.26 (m, 1H), 7.12 – 7.05 (m, 3H), 4.58 (t, *J* = 7.9 Hz, 1H), 3.25 (d, *J* = 8.0 Hz, 2H), 1.32 (s, 18H). **^{13}C{^{1}H} NMR (101 MHz, $CDCl_3$):** δ 160.53, 149.71, 149.50, 147.11, 138.24, 136.34, 124.82, 124.19, 121.80, 121.72, 119.15, 47.69, 43.20, 34.88, 31.62.

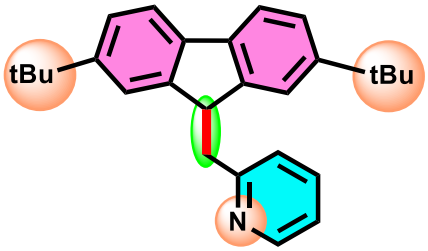

***2-((2,7-di-tert-butyl-9H-fluoren-9-yl)methyl)thiophene (11m)*:** Pale yellow solid; Eluent: Hexane/EtOAc (40:1 v/v); Yield: 281 mg, 75%. **^{1}H NMR (400 MHz, $CDCl_3$):** δ 7.66 (d, *J* = 8.1 Hz, 2H), 7.41 (d, *J* = 8.1 Hz, 2H), 7.28 (s, 2H), 7.22 (d, *J* = 6.2 Hz, 1H), 6.97 (d, *J* = 3.3 Hz, 1H), 6.80 (s, 1H), 4.21 (t, *J* = 7.4 Hz, 1H), 3.39 (d, *J* = 6.0 Hz, 2H), 1.38 (s, 18H). **^{13}C{^{1}H} NMR (101 MHz, $CDCl_3$):** δ 149.59, 146.31, 142.87, 138.42, 126.71, 126.20, 124.32, 123.91, 121.83, 119.12, 49.49, 34.95, 34.64, 31.67.

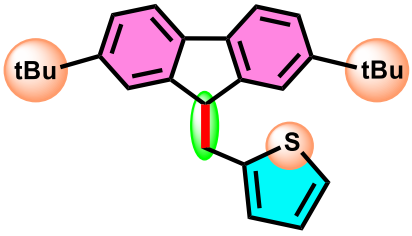

***3-((2,7-di-tert-butyl-9H-fluoren-9-yl)methyl)furan (11n)*:** Pale yellow solid; Eluent: Hexane/EtOAc (40:1 v/v); Yield: 251 mg, 70%. **^{1}H NMR (300 MHz, $CDCl_3$):** δ 7.80 (dd, *J* = 8.0, 1.2 Hz, 2H), 7.72 (d, *J* = 8.1 Hz, 3H), 7.67 (s, 1H), 7.12 (dd, *J* = 1.6, 0.9 Hz, 1H), 6.86 – 6.78 (m, 1H), 6.31 (dd, *J* = 1.8, 0.9 Hz, 1H), 4.12 (t, *J* = 7.0 Hz, 1H), 3.04 (d, *J* = 7.0 Hz, 2H), 1.40 (s, 18H). **^{13}C{^{1}H} NMR (101 MHz, $CDCl_3$):** δ 149.55, 146.83, 143.39, 139.25, 124.19, 123.91, 121.99, 121.70, 119.22, 111.76, 47.78, 37.22, 34.94, 31.77.

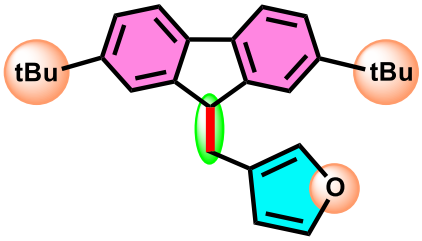

***2,7-di-tert-butyl-9-(naphthalen-1-ylmethyl)-9H-fluorene (11o)*:** White solid; Eluent: Hexane/EtOAc (40:1 v/v); Yield: 318 mg, 76%. **^{1}H NMR (400 MHz, $CDCl_3$):** δ 8.17 (d, *J* = 8.3 Hz, 2H), 8.11 (s, 1H), 7.81 (d, *J* = 7.0 Hz, 2H), 7.72 (d, *J* = 8.0 Hz, 2H), 7.68 (d, *J* = 8.0 Hz, 2H), 7.08 (s, 2H), 7.00 (s, 2H), 4.41 (t, *J* = 8.1 Hz, 1H), 3.54 (d, *J* = 8.1 Hz, 2H), 1.31 (s, 18H). **^{13}C{^{1}H} NMR (101 MHz, $CDCl_3$):** δ 147.07, 139.29, 138.25, 134.84, 133.84, 131.82, 129.13, 128.57, 127.11, 126.40, 125.47, 124.27, 123.83, 122.39, 122.24, 119.14, 48.26, 38.28, 34.60, 31.77.

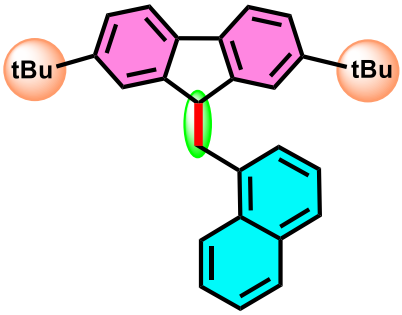

4.6.2 Copies of NMR spectra of synthesized 9-alkylated fluorenes

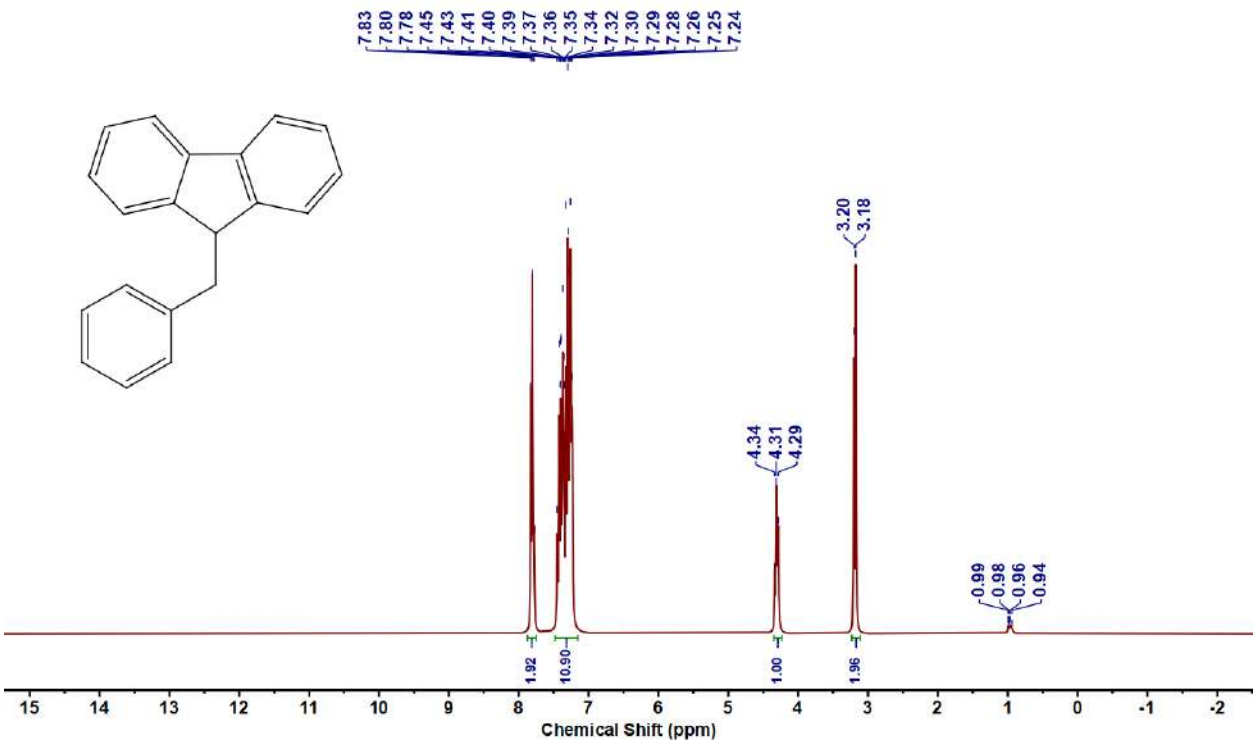

Figure 4.6.A19: ^{1}H NMR Spectrum of **8a**

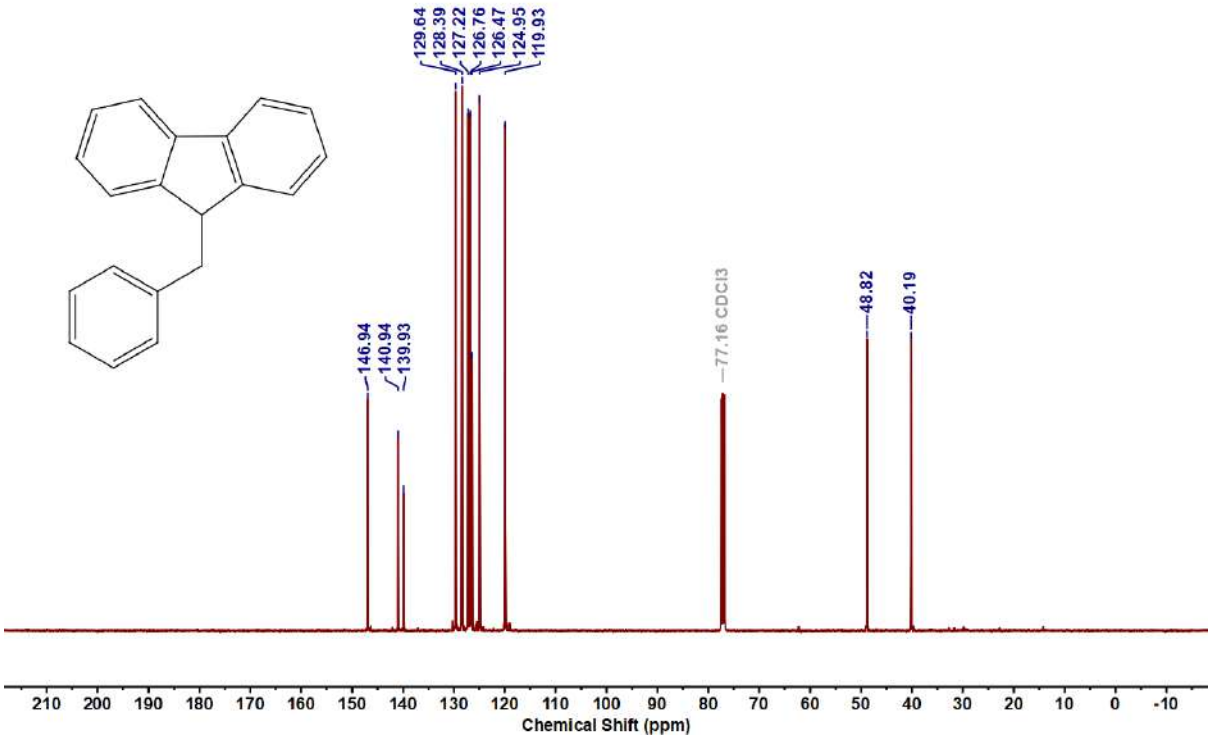

Figure 4.6.A20: ^{13}C{1H} NMR Spectrum of **8a**

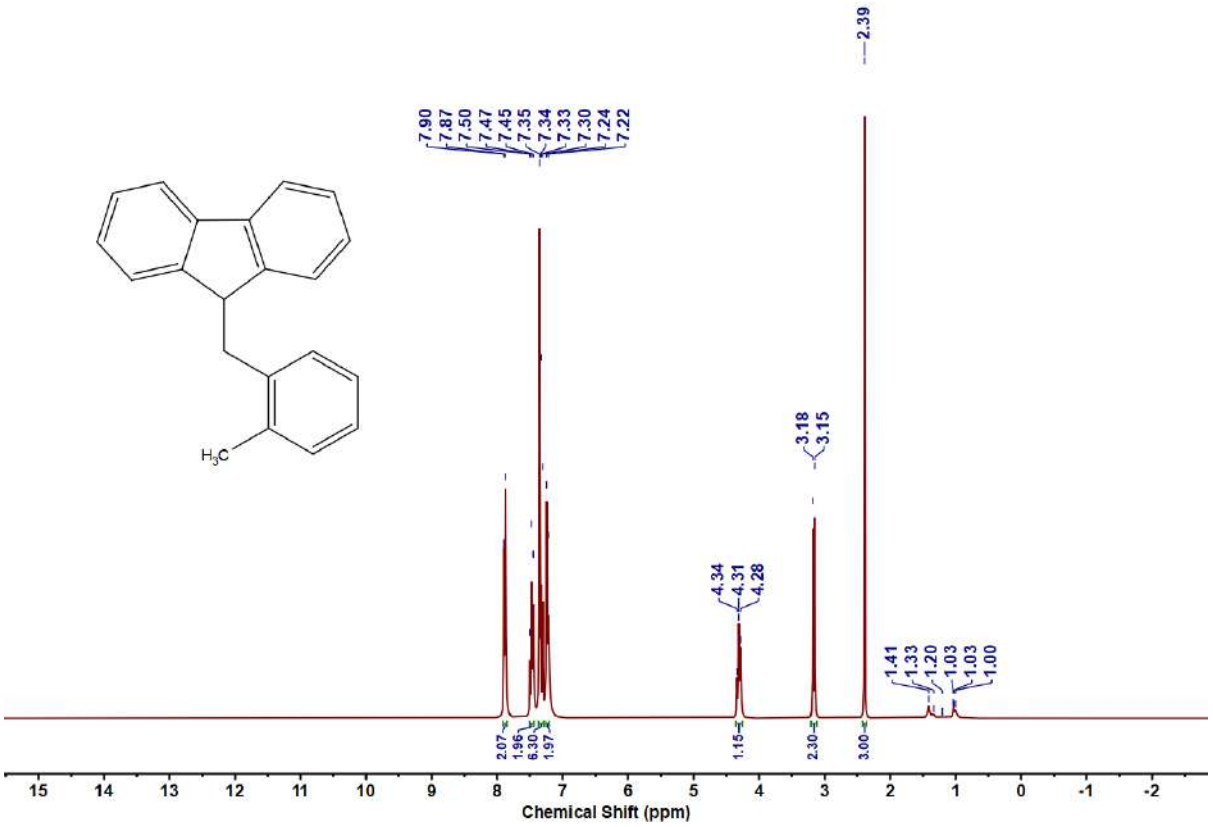

Figure 4.6.A21: ^{1}H NMR Spectrum of **8b**

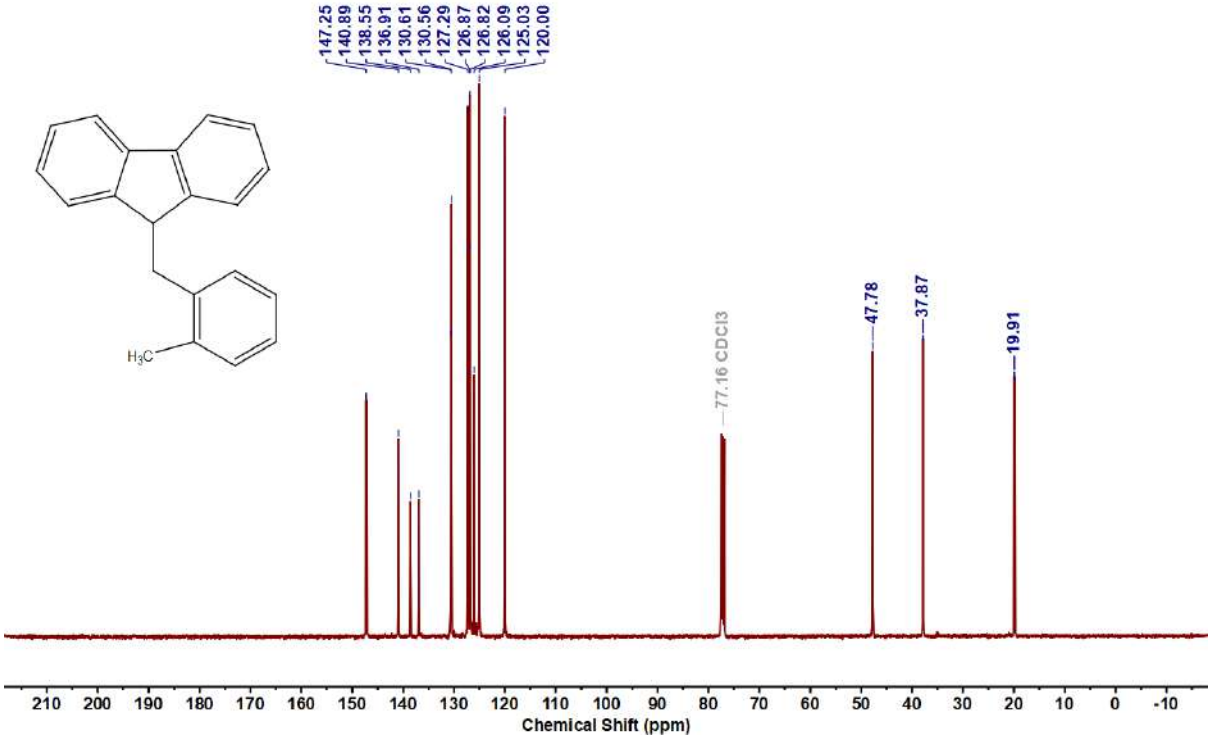

Figure 4.6.A22: ^{13}C{^{1}H} NMR Spectrum of **8b**

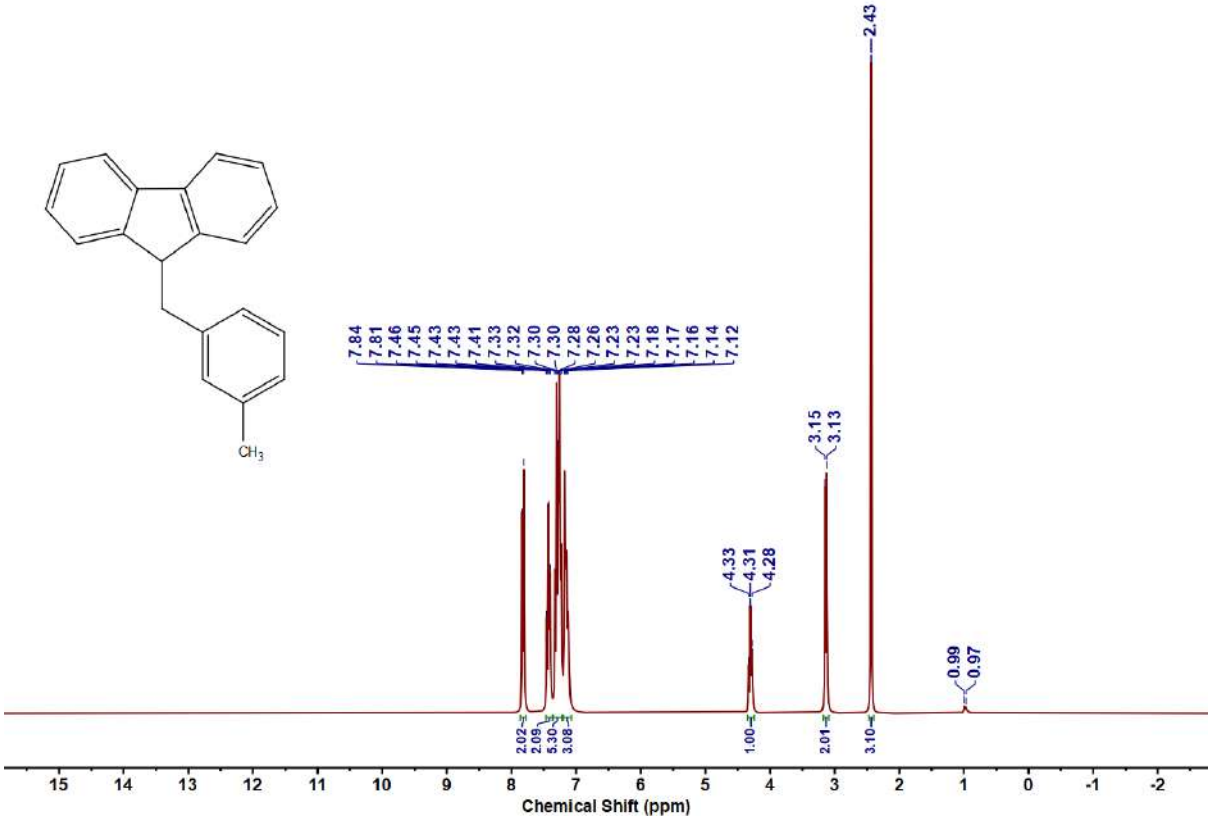

Figure 4.6.A23: ^{1}H NMR Spectrum of **8c**

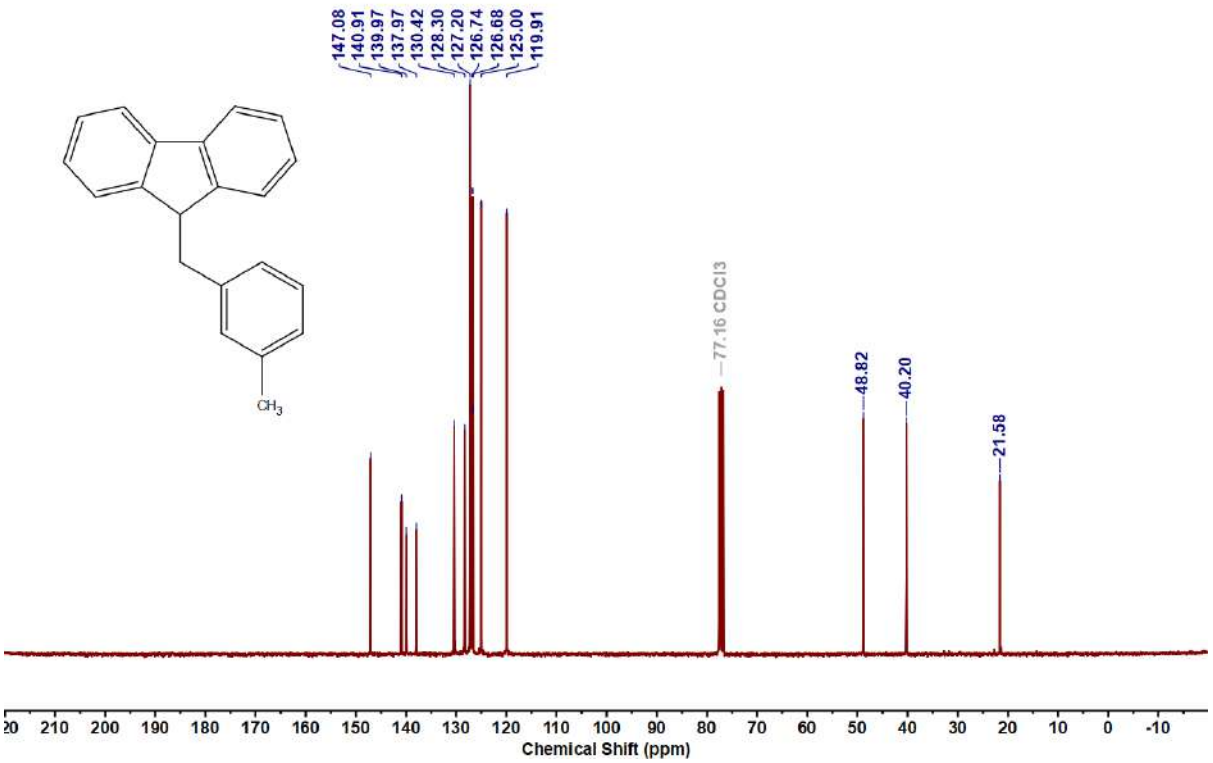

Figure 4.6.A24: ^{13}C{^{1}H} NMR Spectrum of **8c**

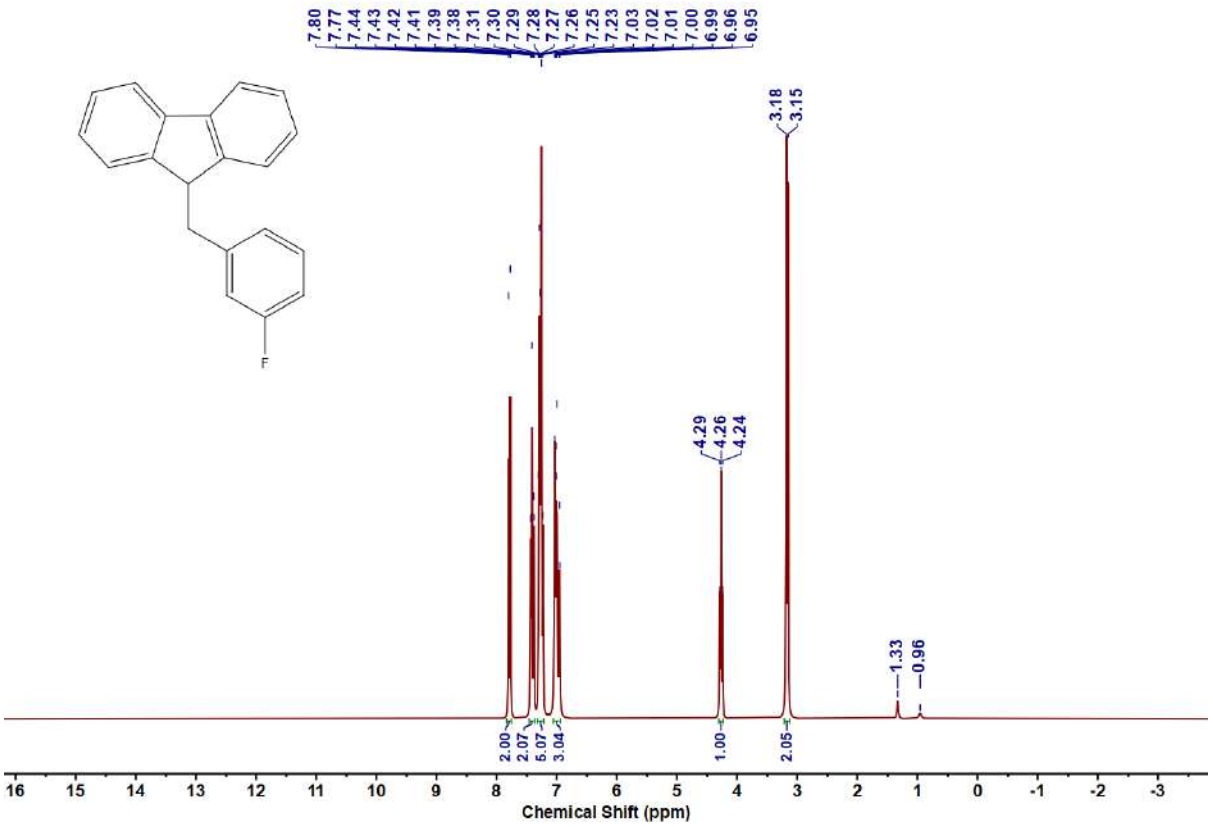

Figure 4.6.A25: ^{1}H NMR Spectrum of **8d**

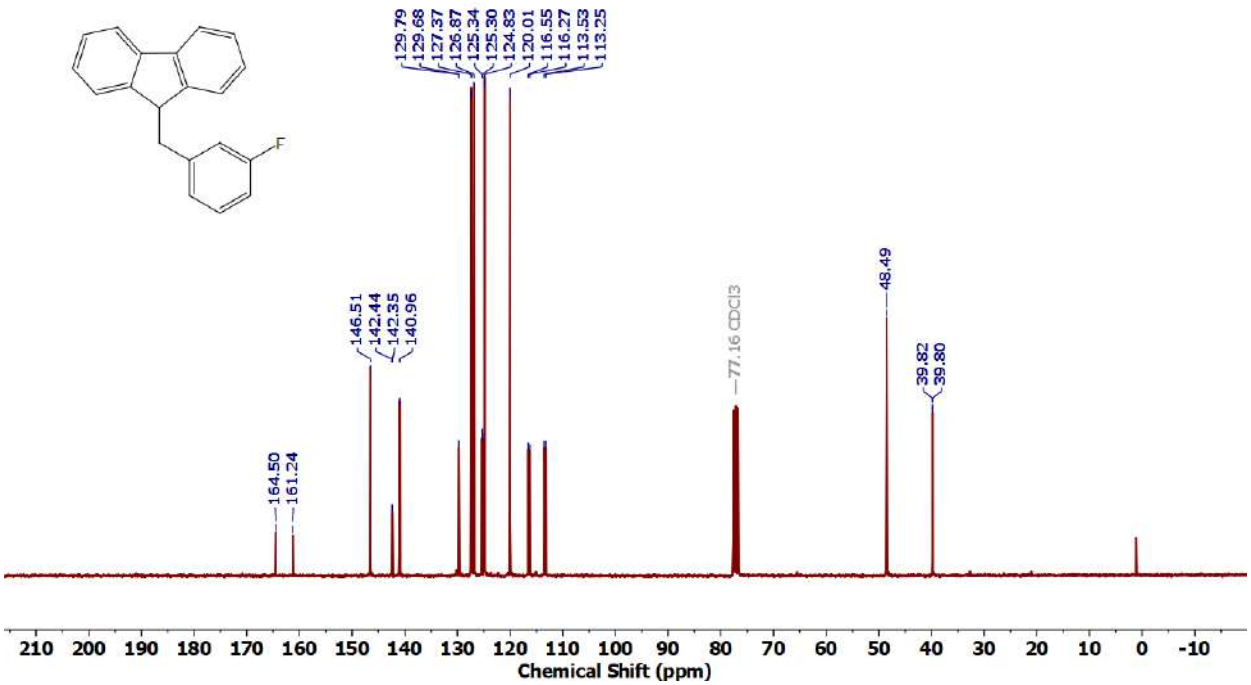

Figure 4.6.A26: ^{13}C{^{1}H} NMR Spectrum of **8d**

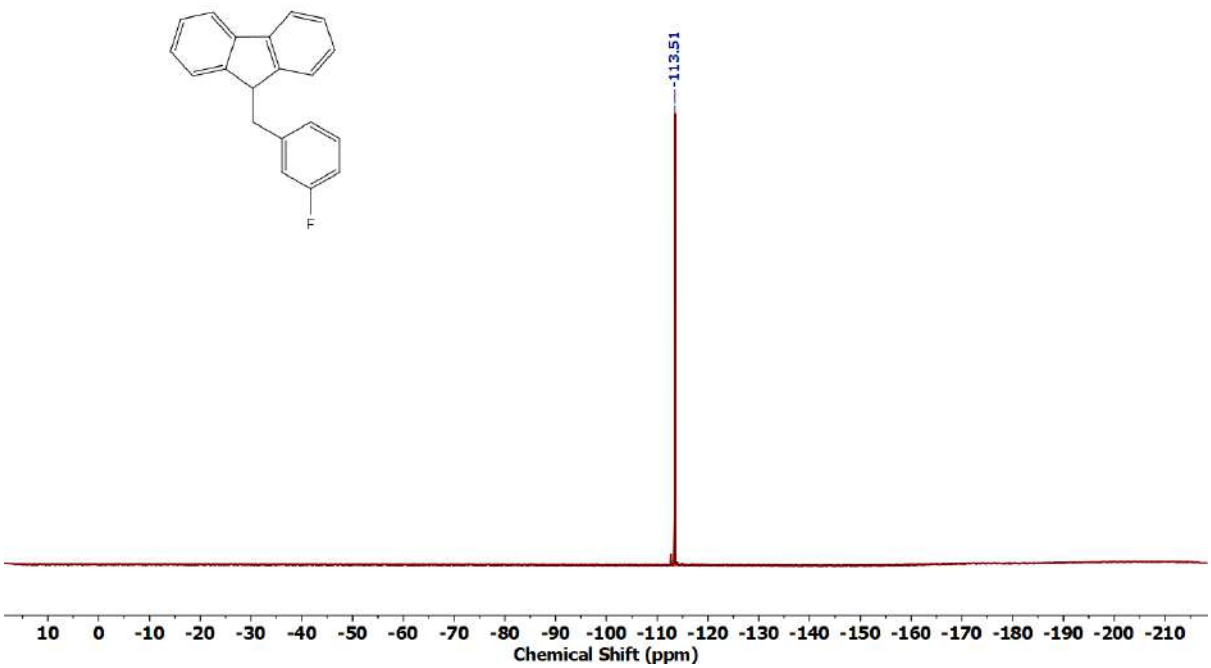

Figure 4.6.A27: ^{19}F NMR Spectrum of **8d**

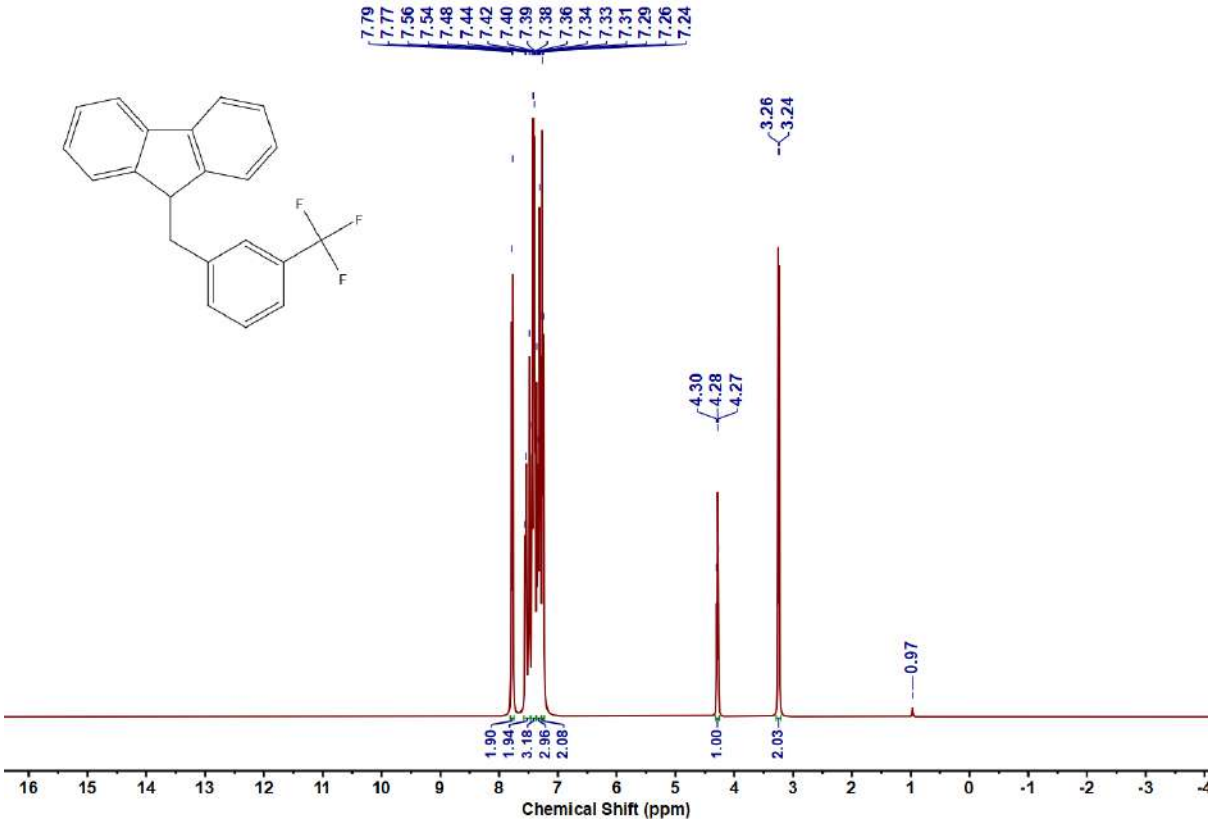

Figure 4.6.A28: ^{1}H NMR Spectrum of **8e**

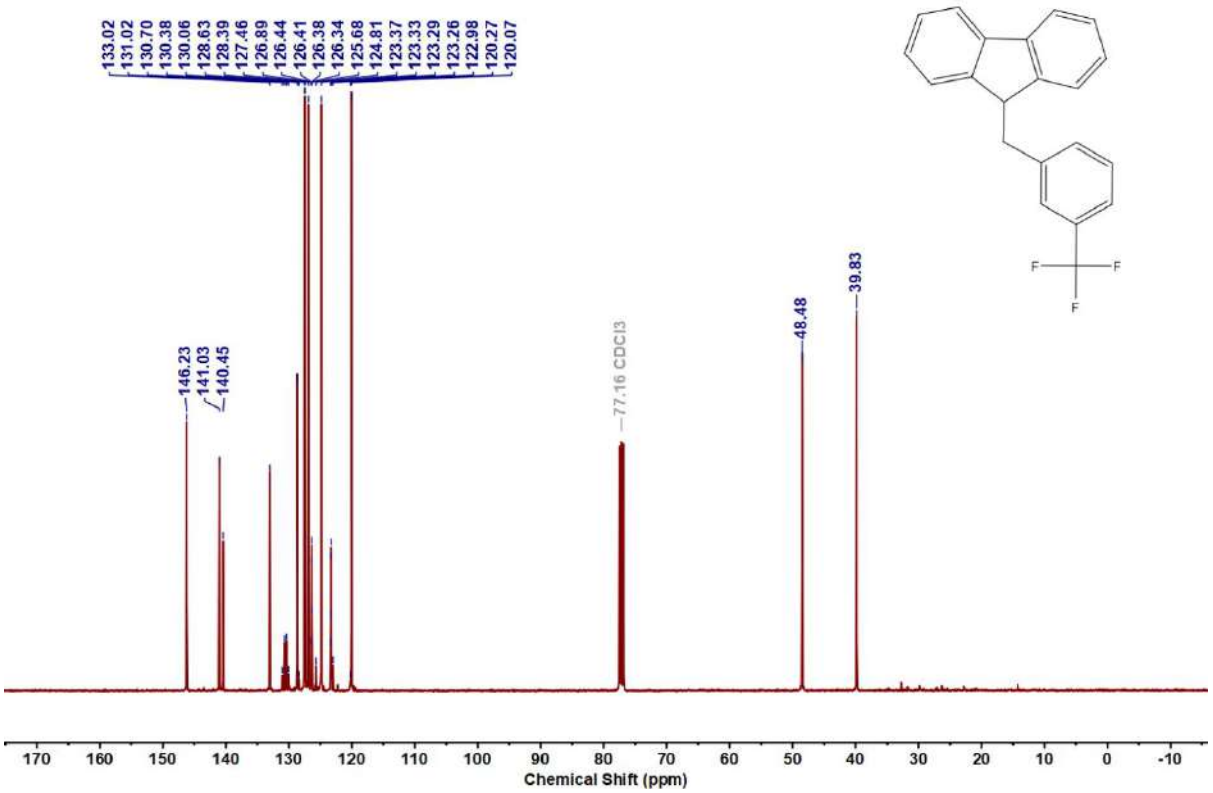

Figure 4.6.A29: $^{13}C\{^{1}H\}$ NMR Spectrum of **8e**

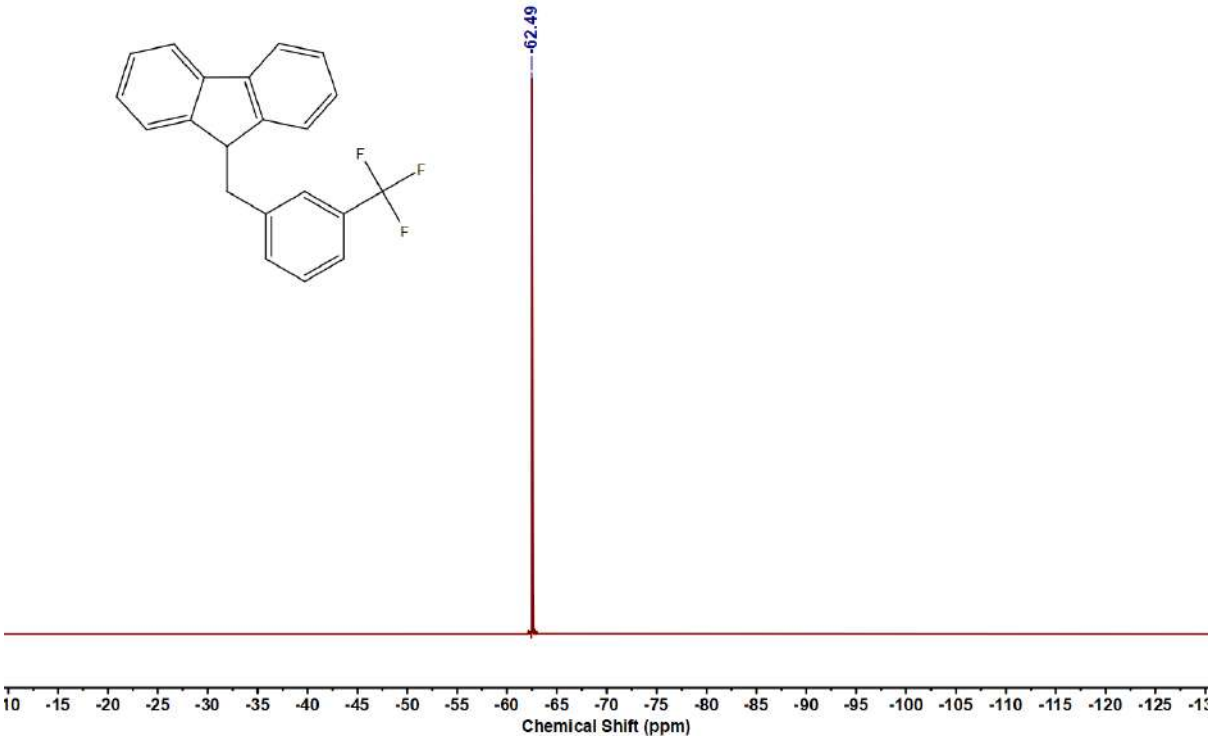

Figure 4.6.A30: ^{19}F NMR Spectrum of **8e**

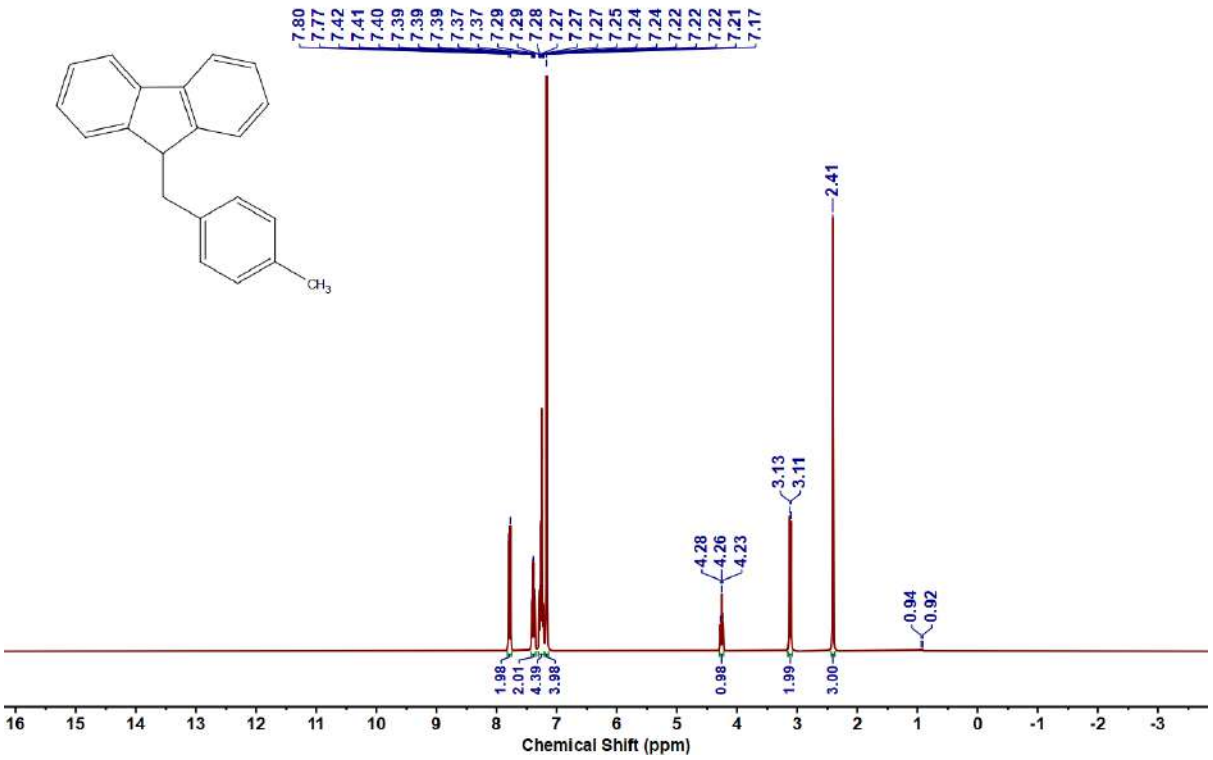

Figure 4.6.A31: ^{1}H NMR Spectrum of **8f**

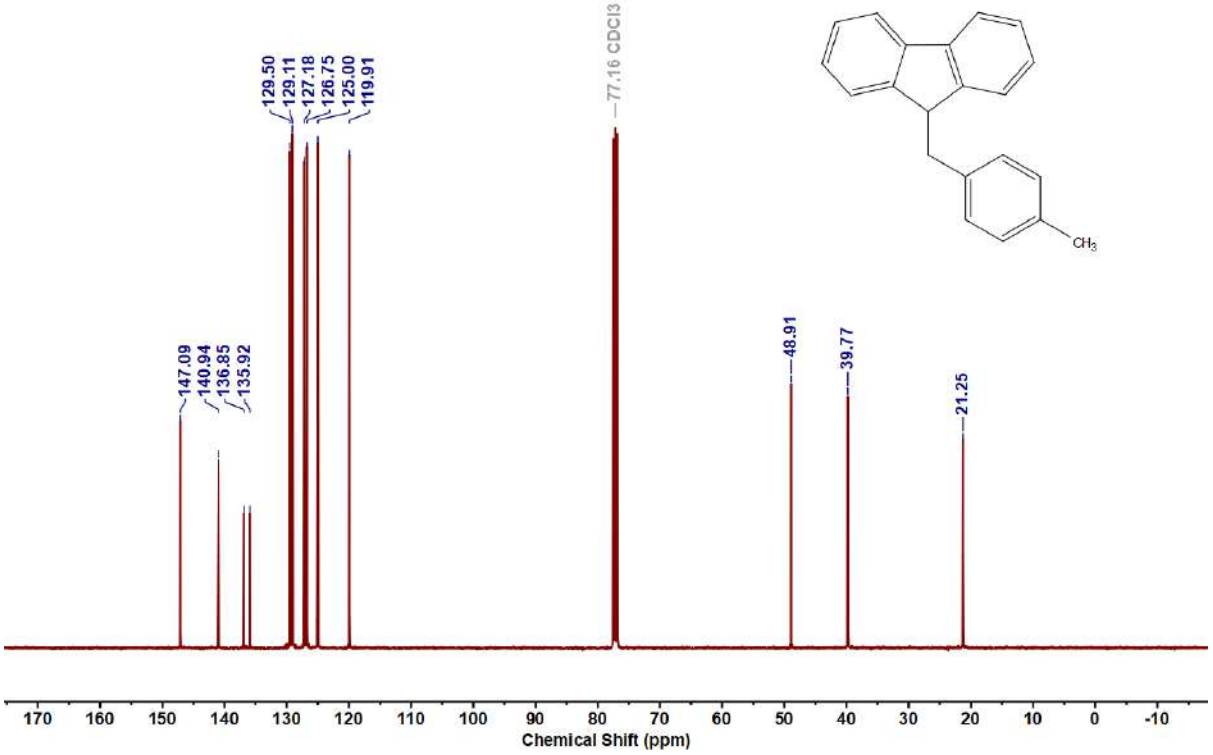

Figure 4.6.A32: ^{13}C{^{1}H} NMR Spectrum of **8f**

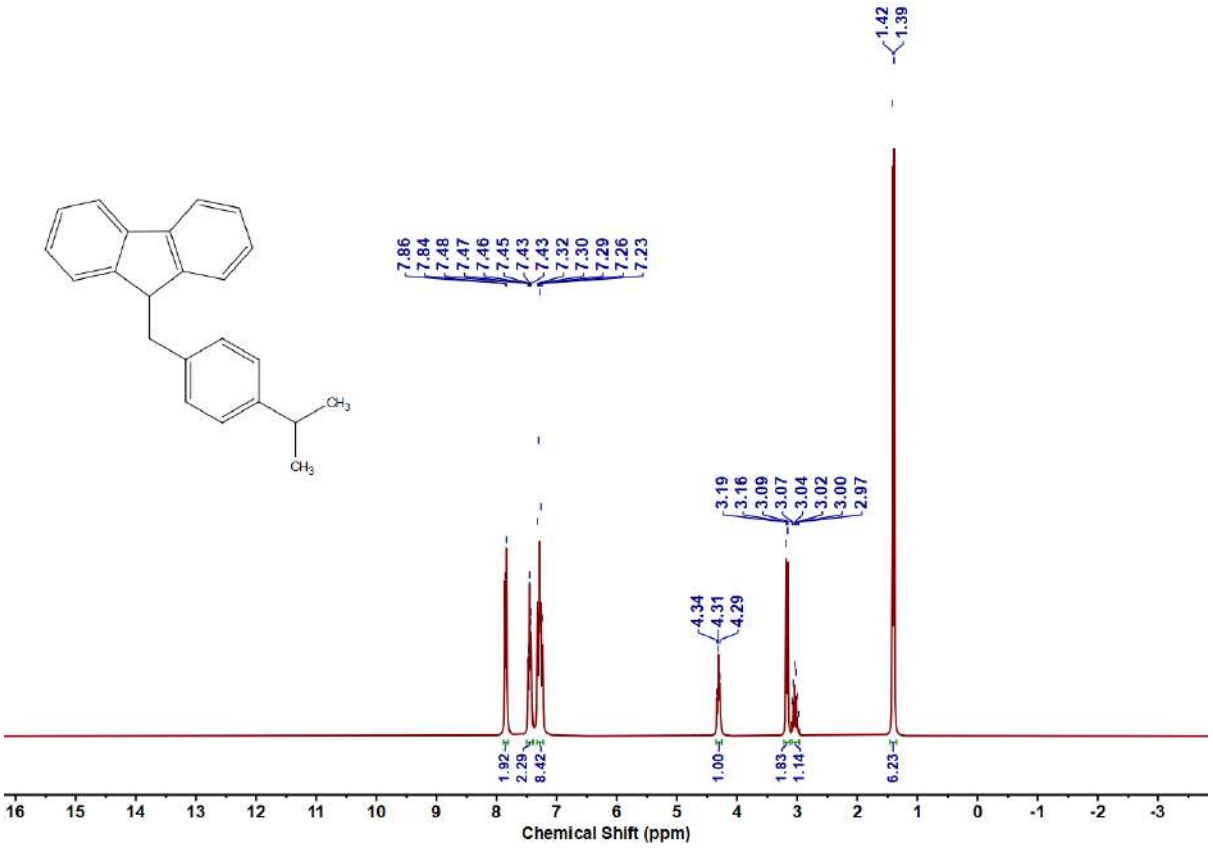

Figure 4.6.A33: ^{1}H NMR Spectrum of **8g**

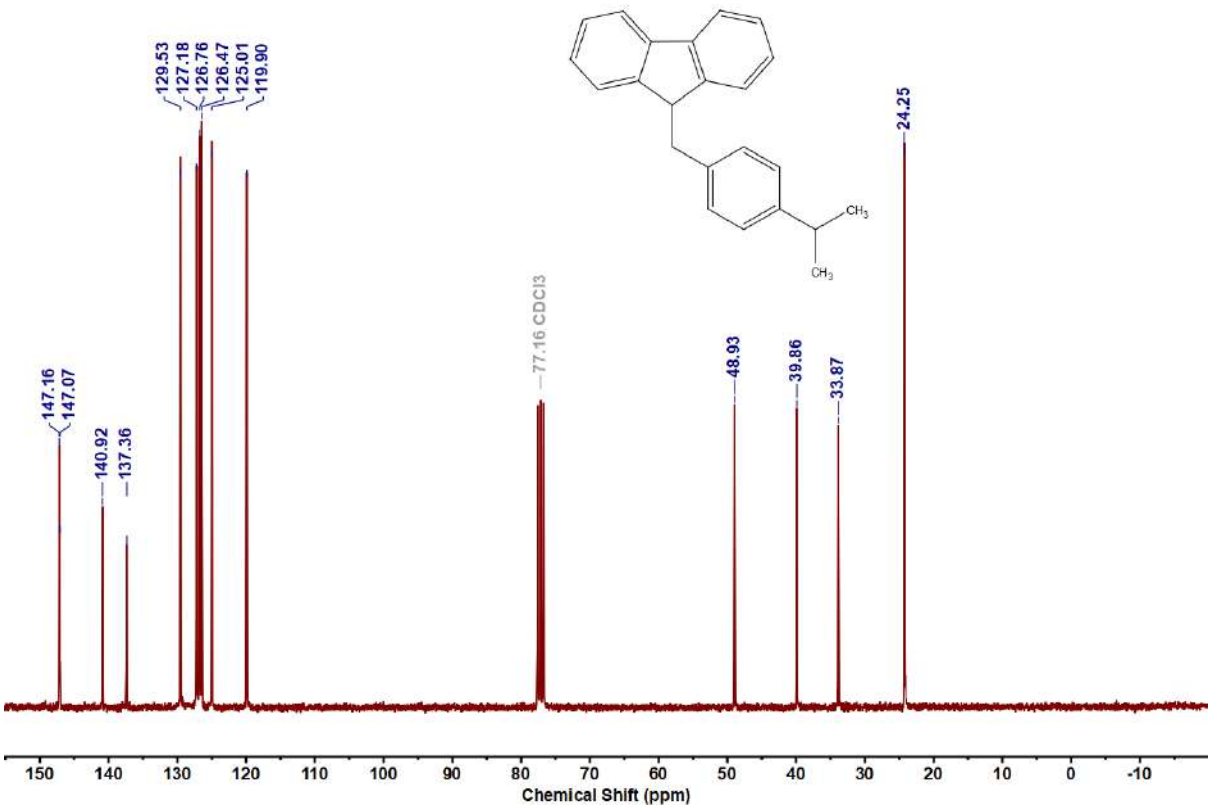

Figure 4.6.A34: ^{13}C{^{1}H} NMR Spectrum of **8g**

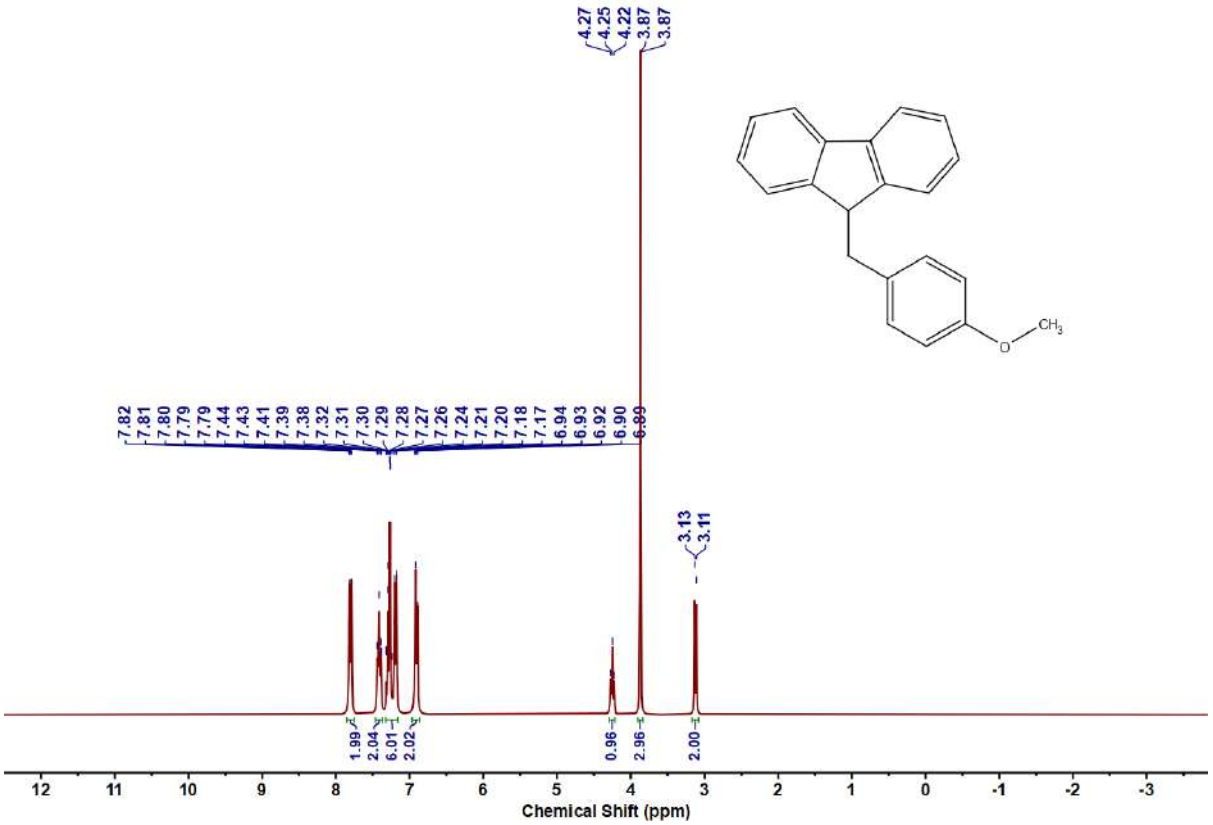

Figure 4.6.A35: ^{1}H NMR Spectrum of **8h**

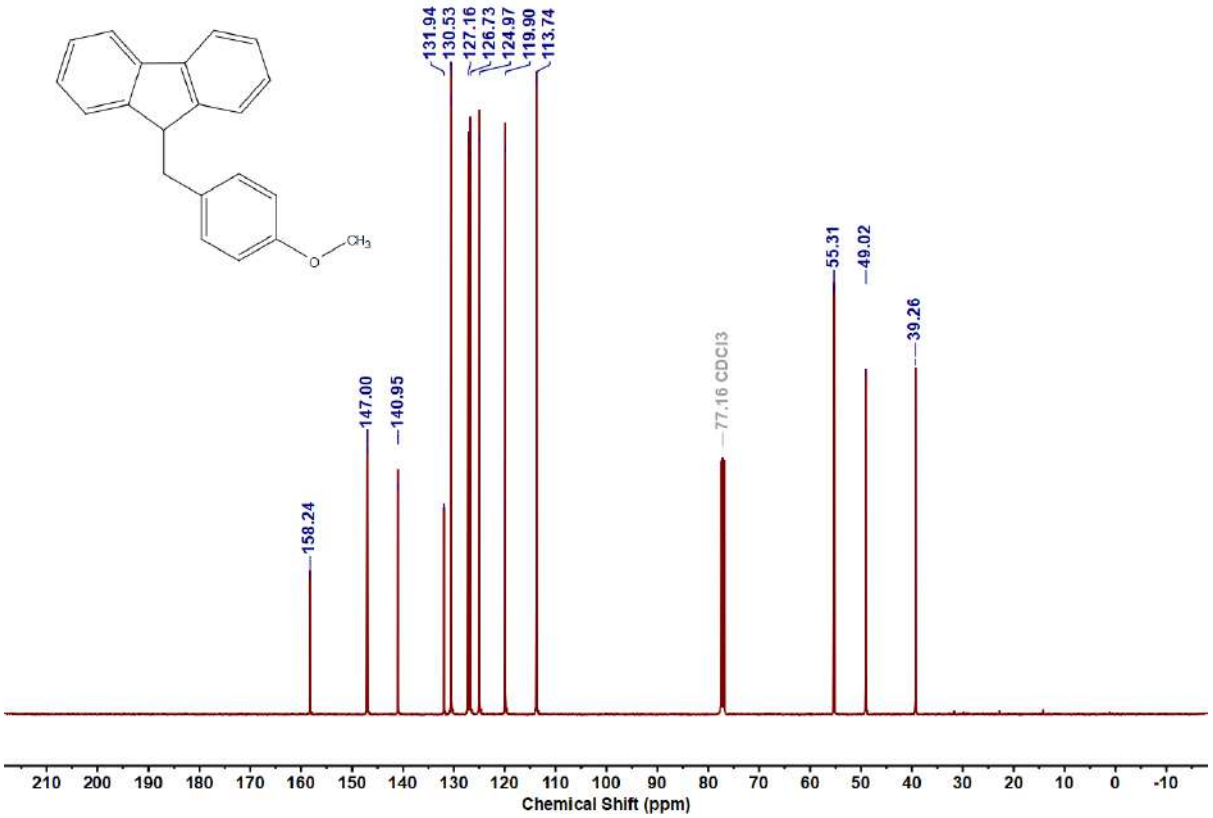

Figure 4.6.A36: ^{13}C{^{1}H} NMR Spectrum of **8h**

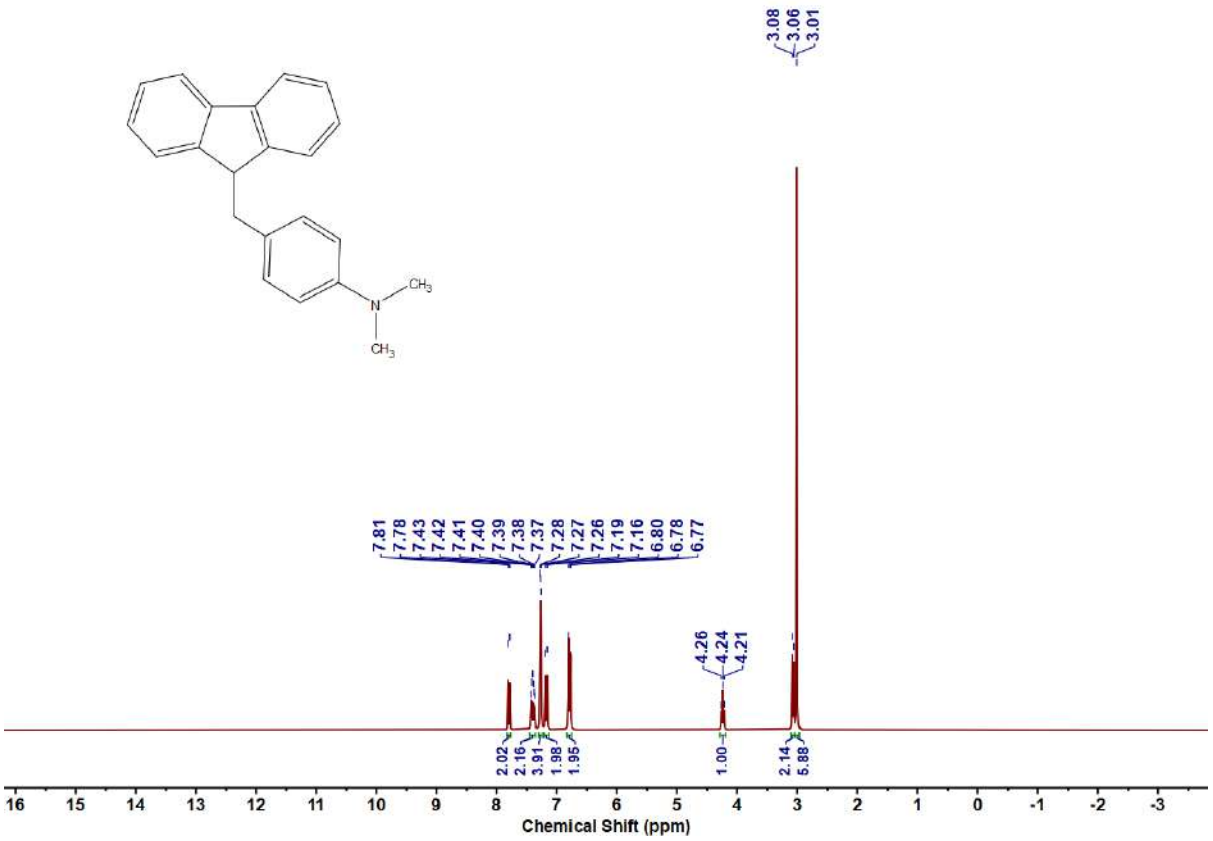

Figure 4.6.A37: ^{1}H NMR Spectrum of **8i**

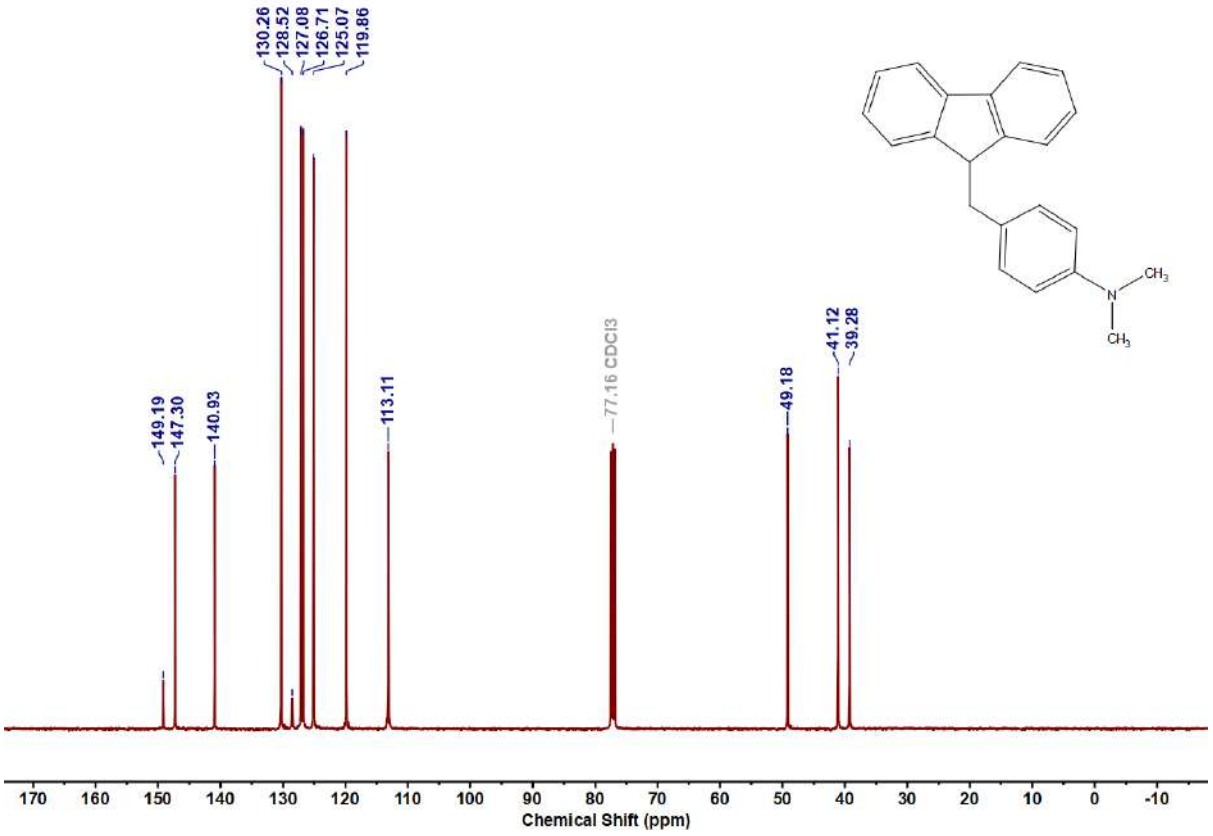

Figure 4.6.A38: $^{13}C\{^{1}H\}$ NMR Spectrum of **8i**

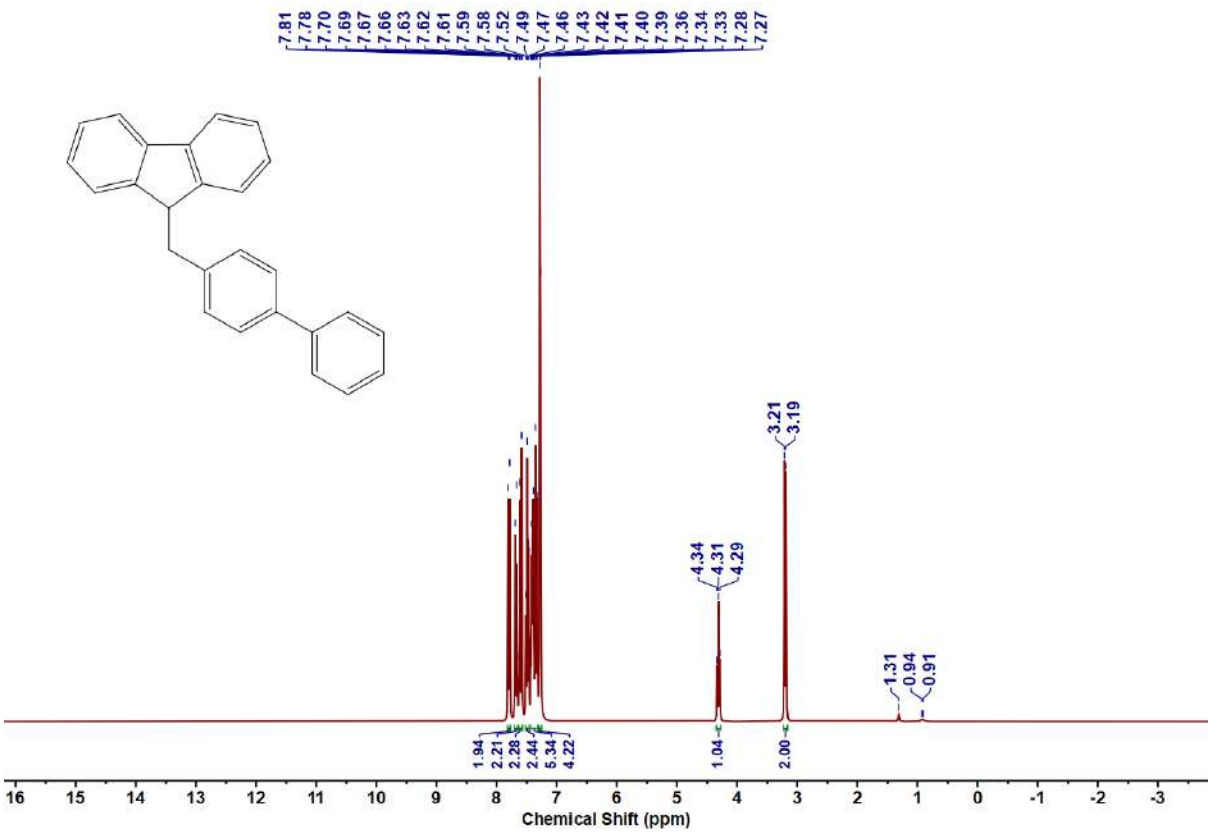

Figure 4.6.A39: ^{1}H NMR Spectrum of **8j**

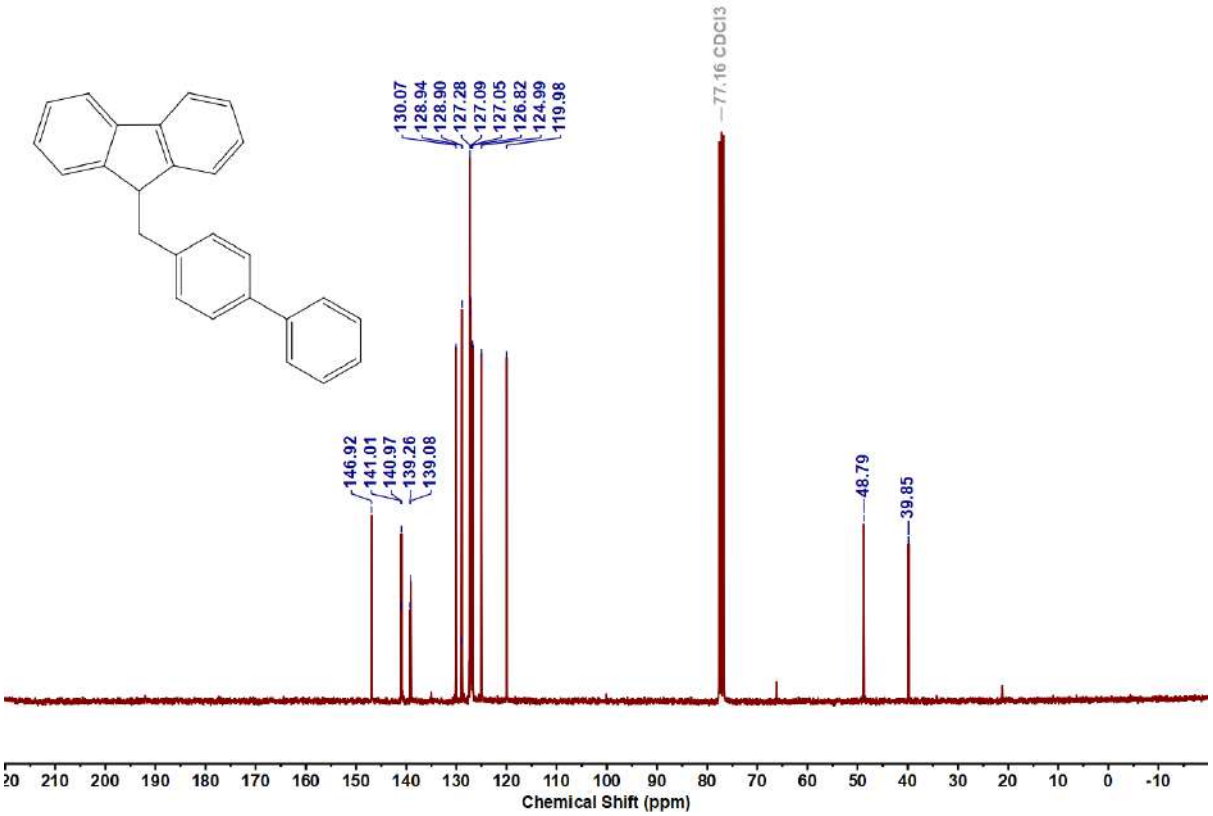

Figure 4.6.A40: $^{13}C\{^{1}H\}$ NMR Spectrum of **8j**

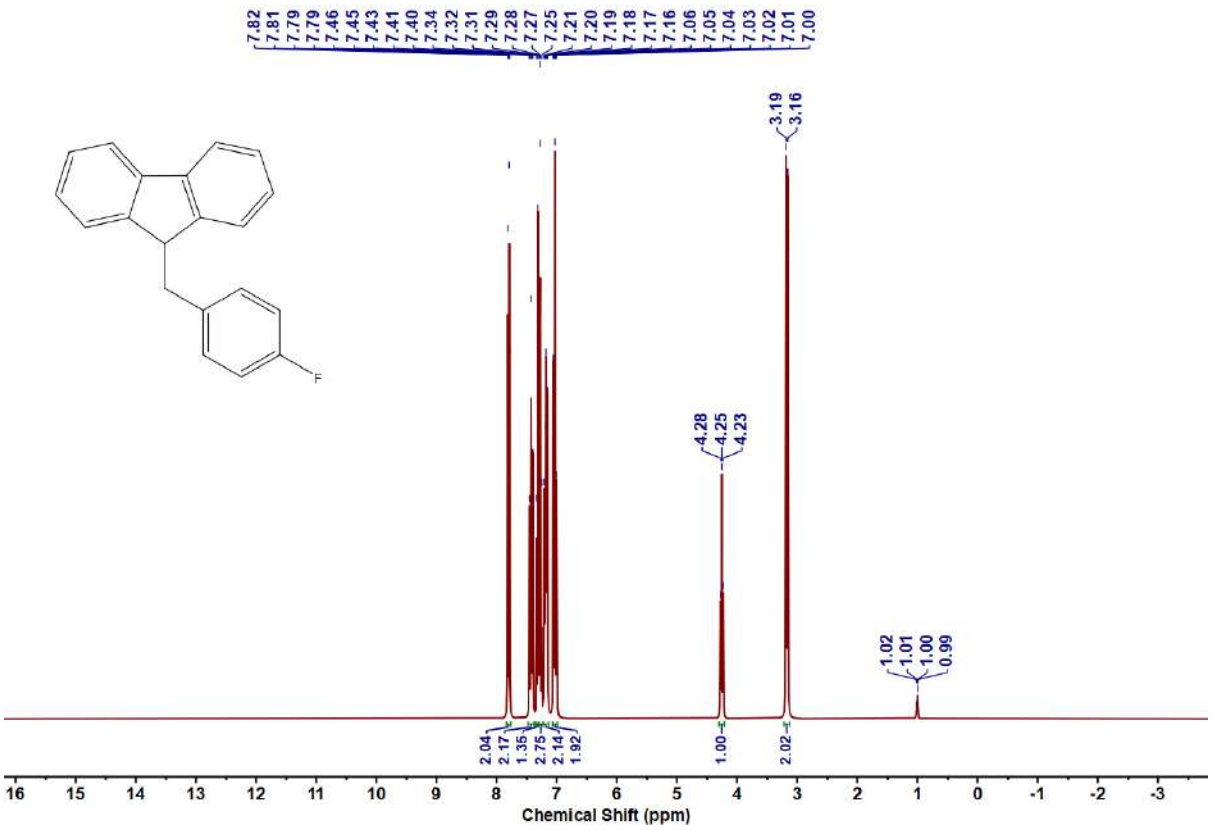

Figure 4.6.A41: ^{1}H NMR Spectrum of **8k**

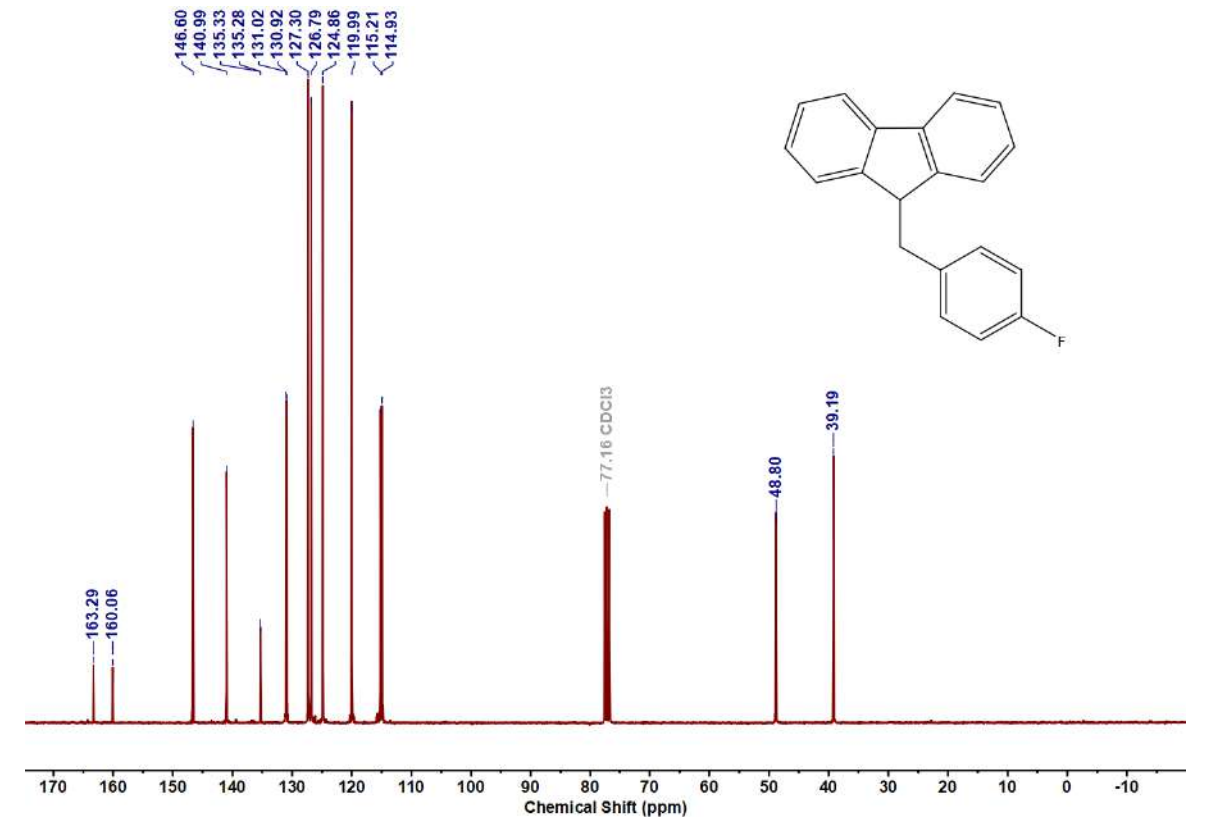

Figure 4.6.A42: $^{13}C\{^{1}H\}$ NMR Spectrum of **8k**

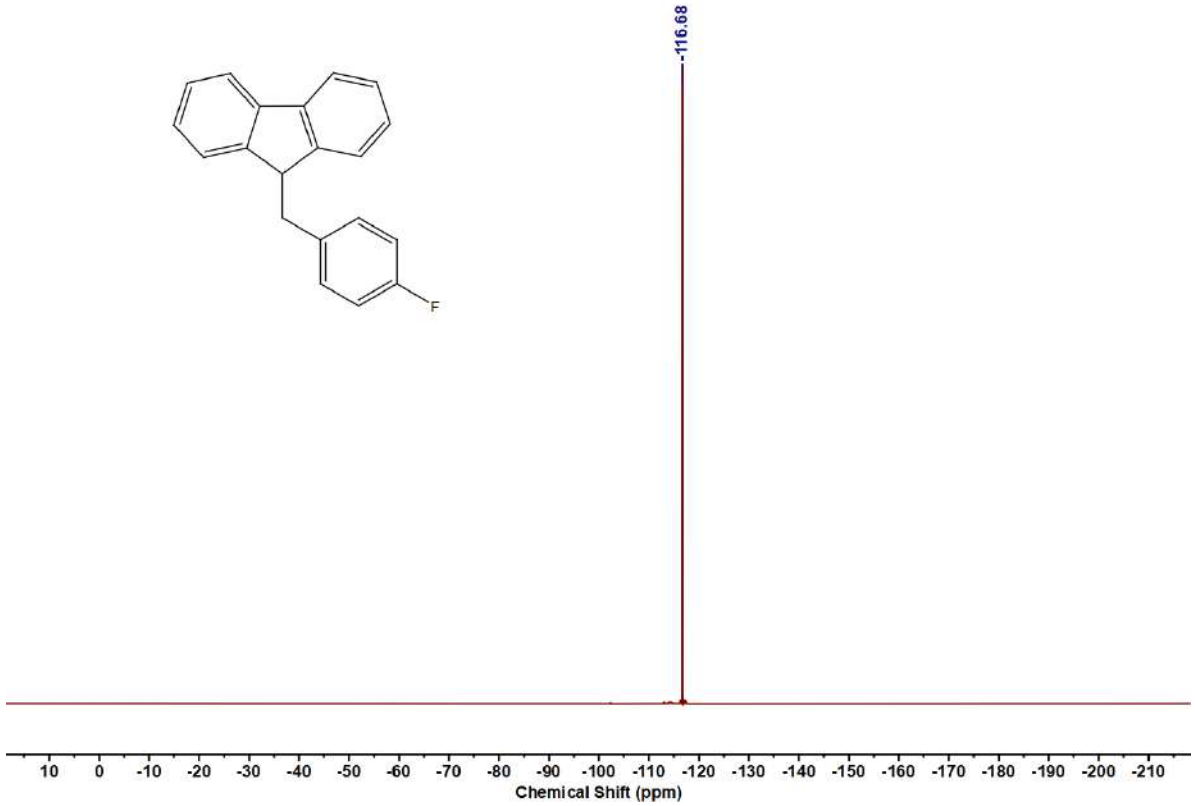

Figure 4.6.A43: ^{19}F NMR Spectrum of **8k**

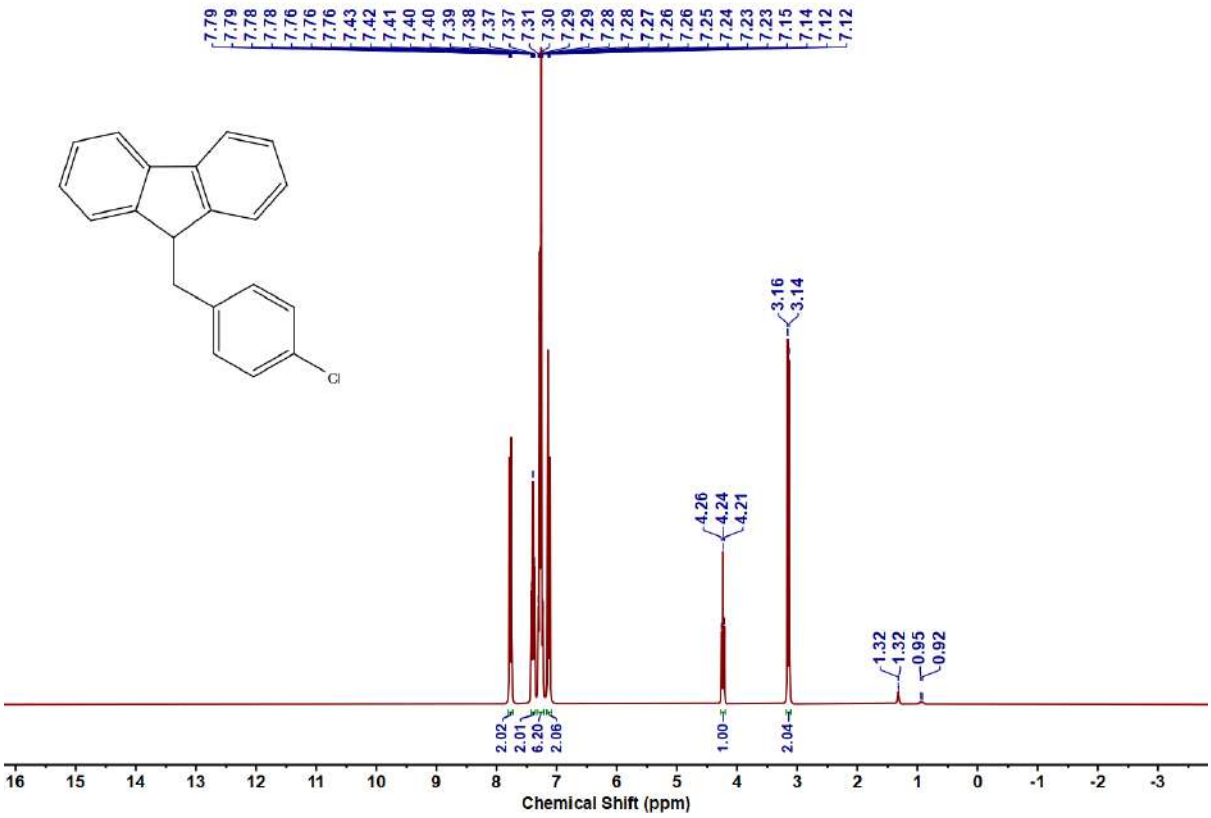

Figure 4.6.A44: ^{1}H NMR Spectrum of **8l**

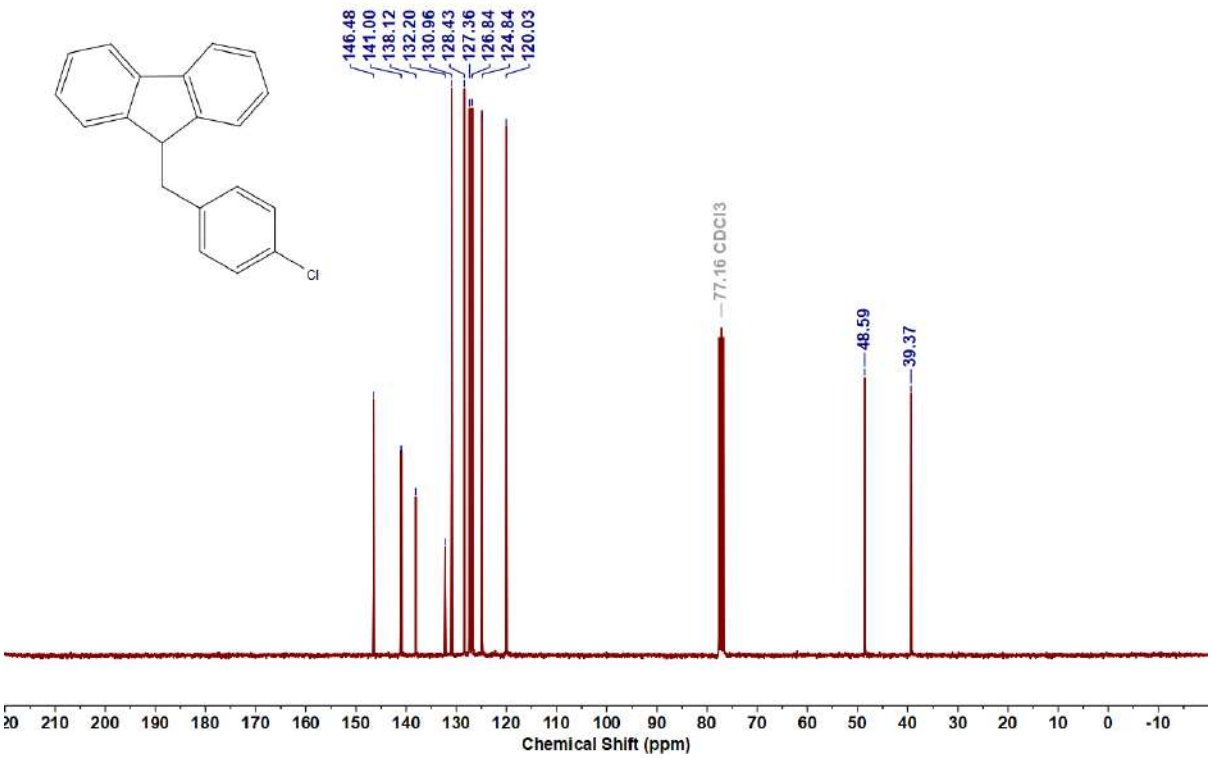

Figure 4.6.A45: $^{13}C\{^{1}H\}$ NMR Spectrum of **8l**

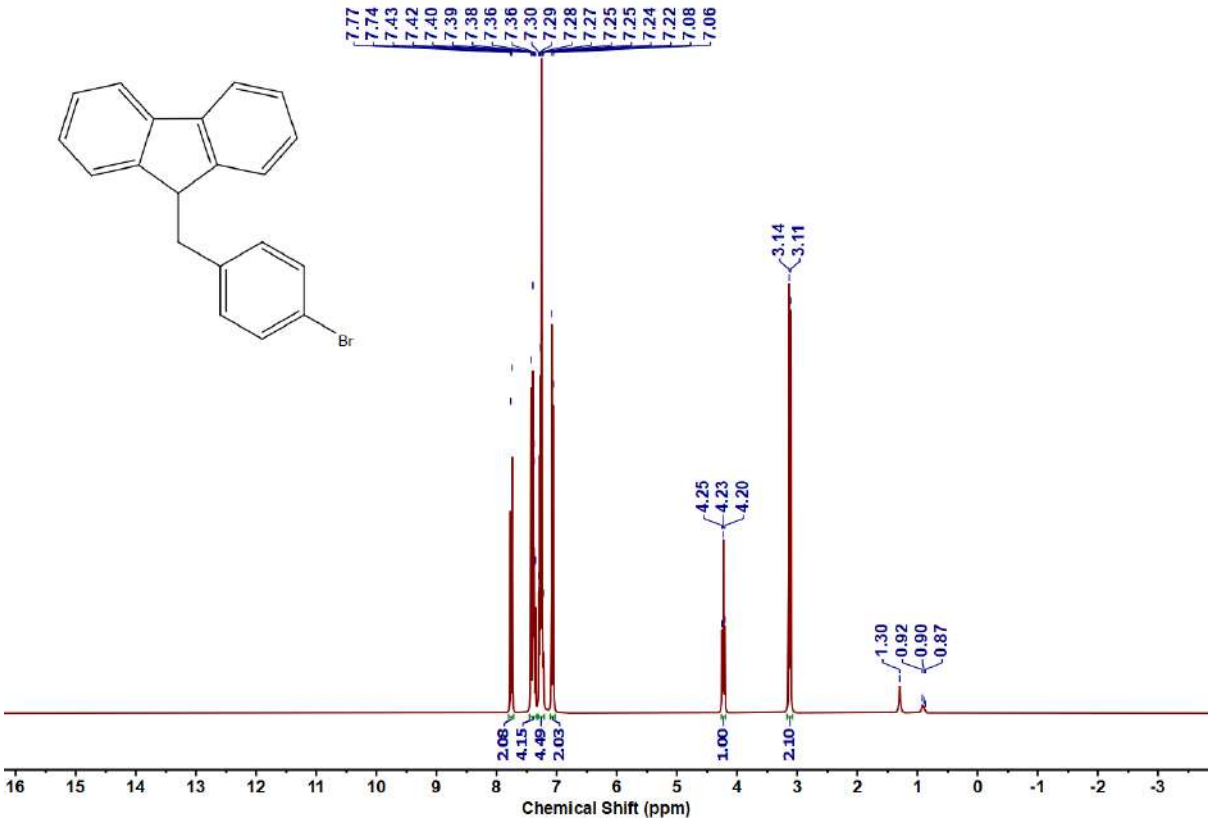

Figure 4.6.A46: ^{1}H NMR Spectrum of **8m**

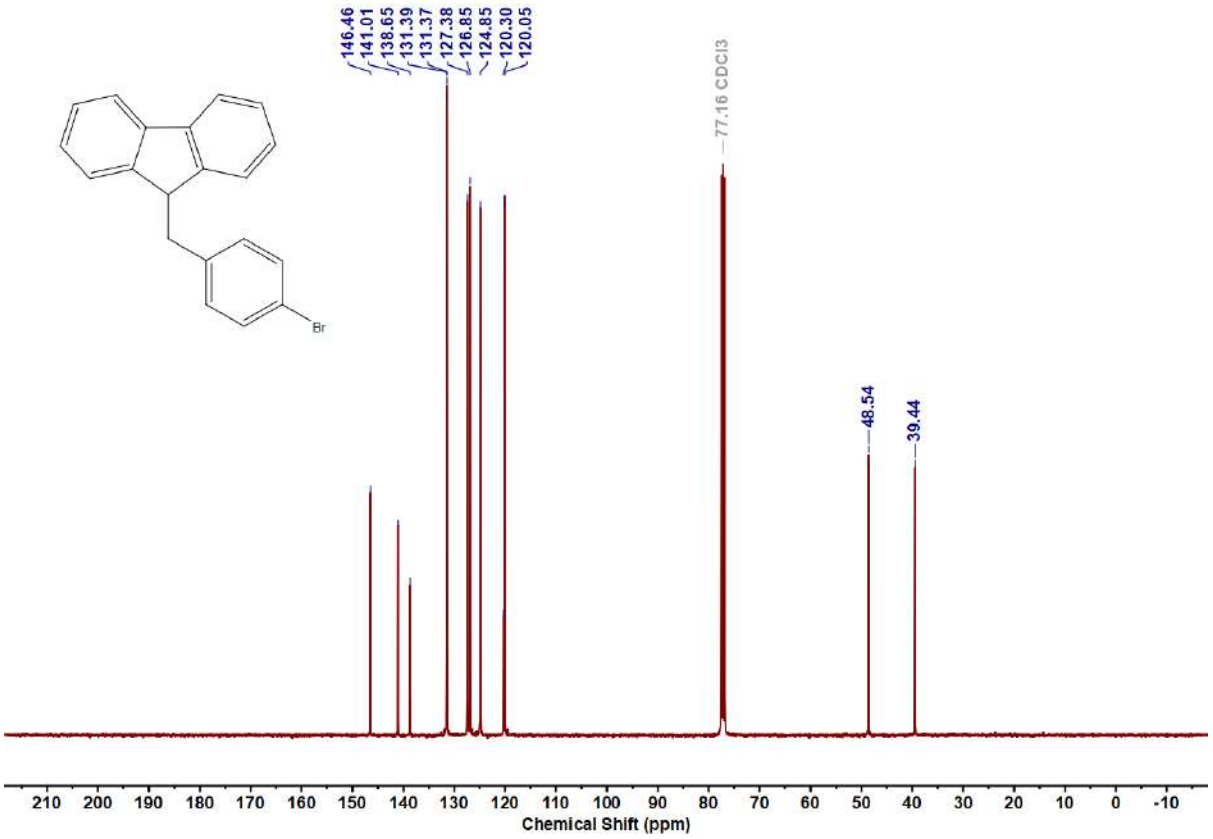

Figure 4.6.A47: $^{13}C\{^{1}H\}$ NMR Spectrum of **8m**

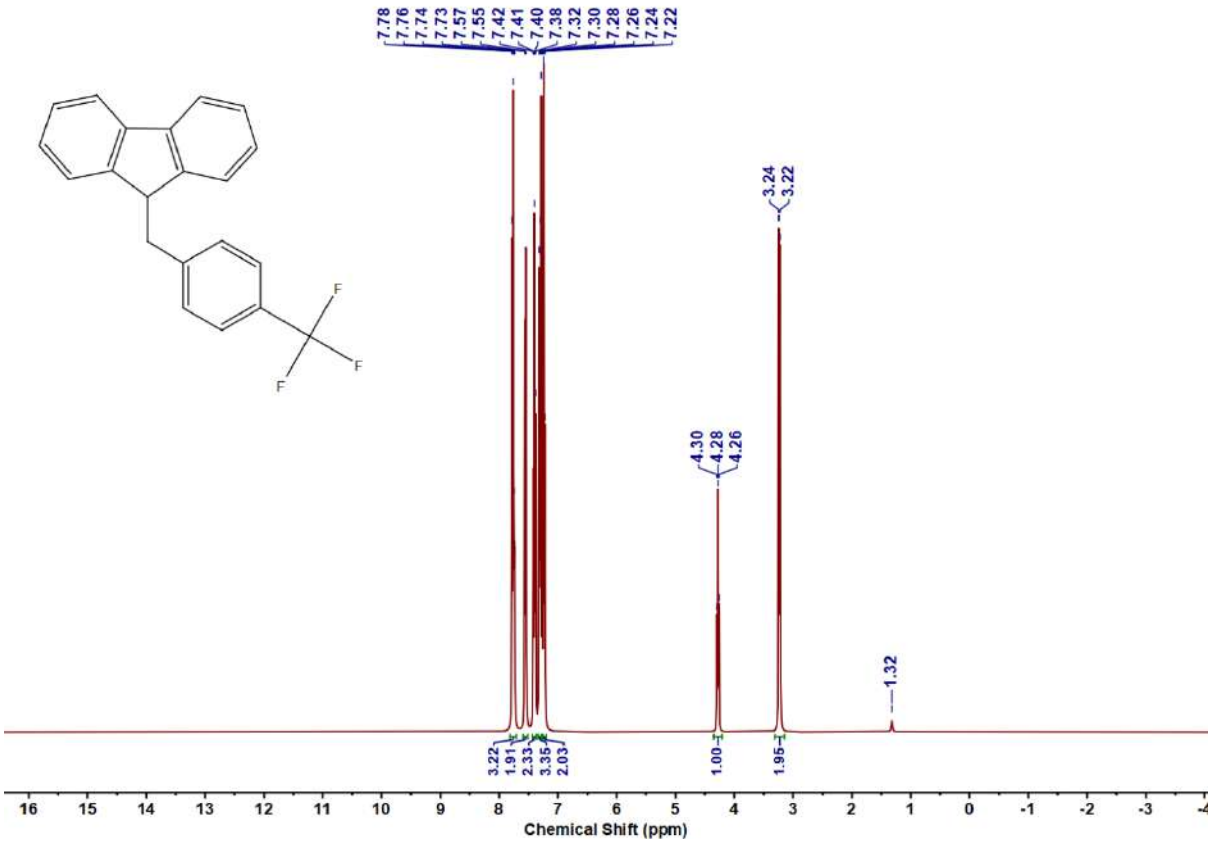

Figure 4.6.A48: ^{1}H NMR Spectrum of **8n**

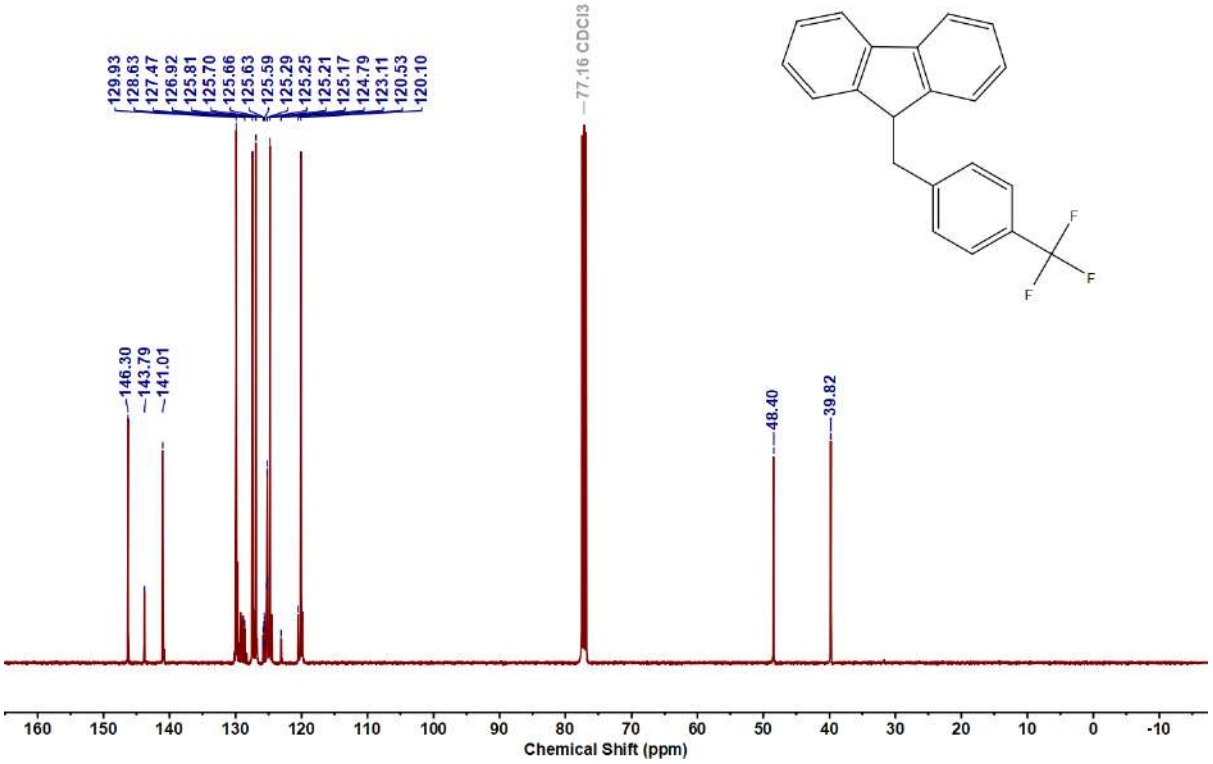

Figure 4.6.A49: $^{13}C\{^{1}H\}$ NMR Spectrum of **8n**

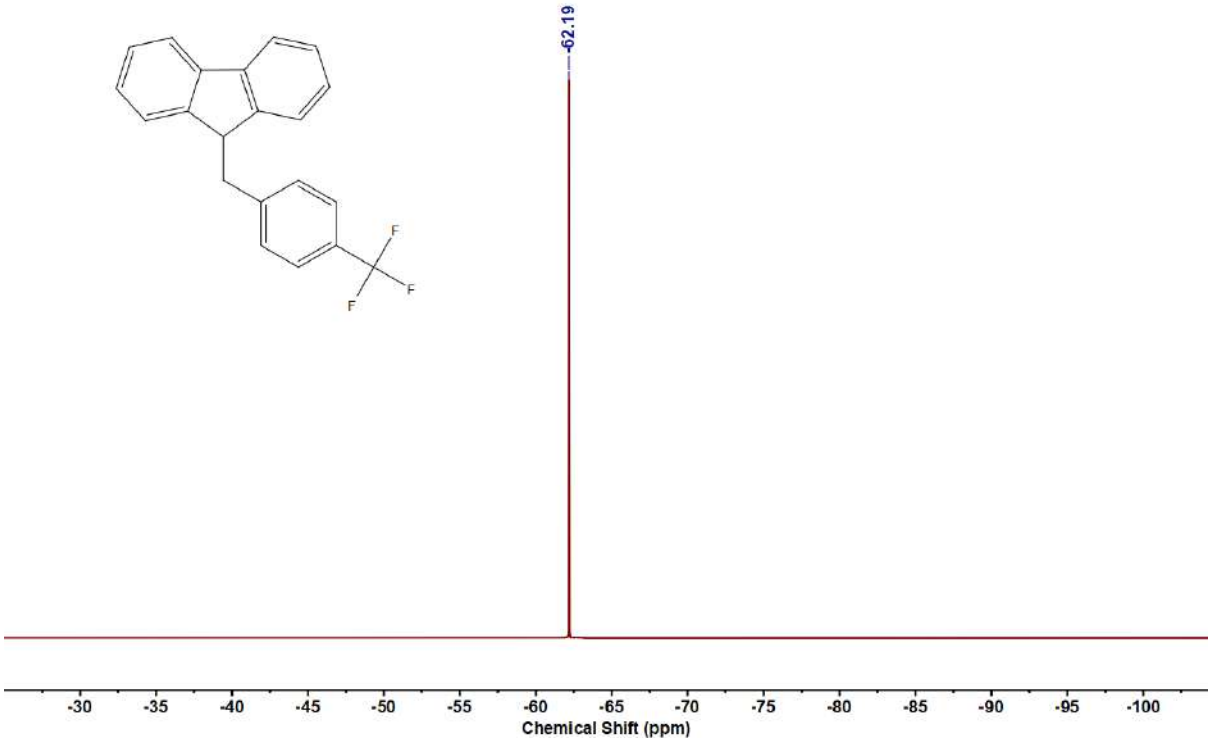

Figure 4.6.A50: ^{19}F NMR Spectrum of **8n**

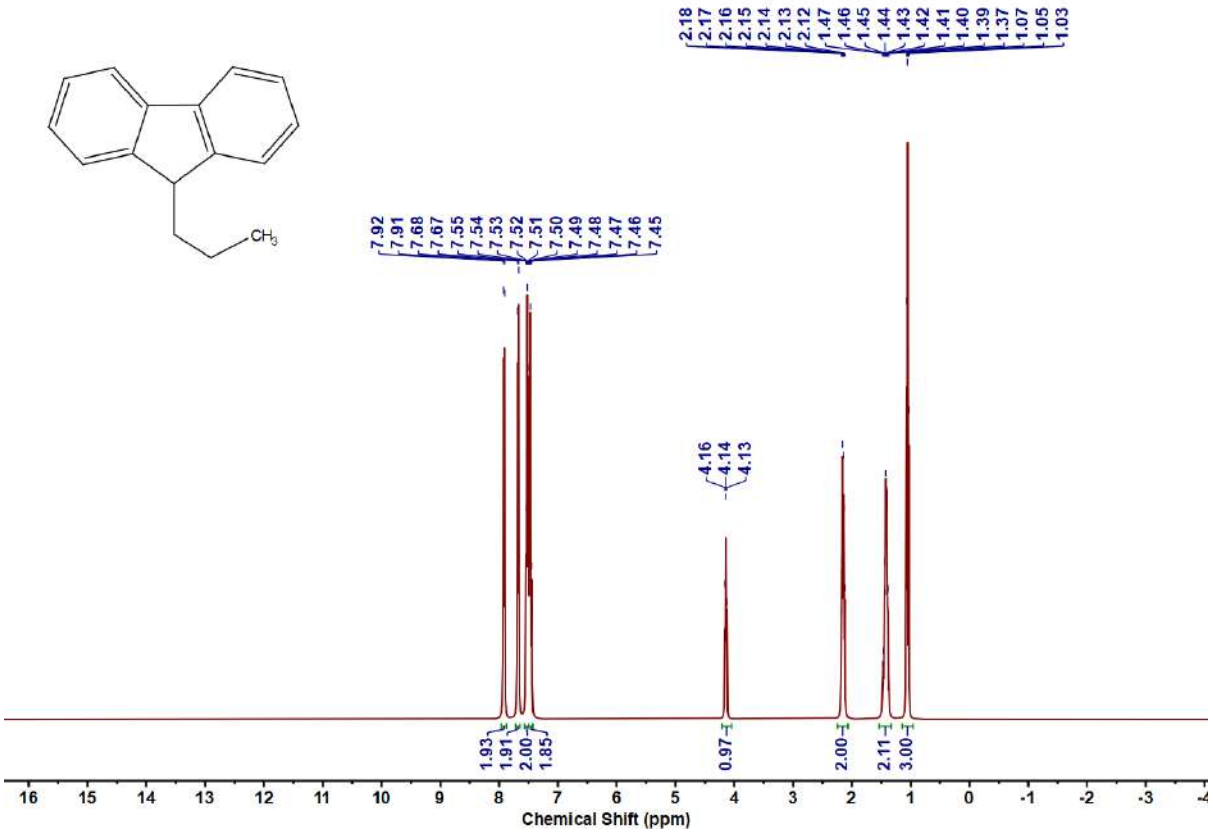

Figure 4.6.A51: ^{1}H NMR Spectrum of **8o**

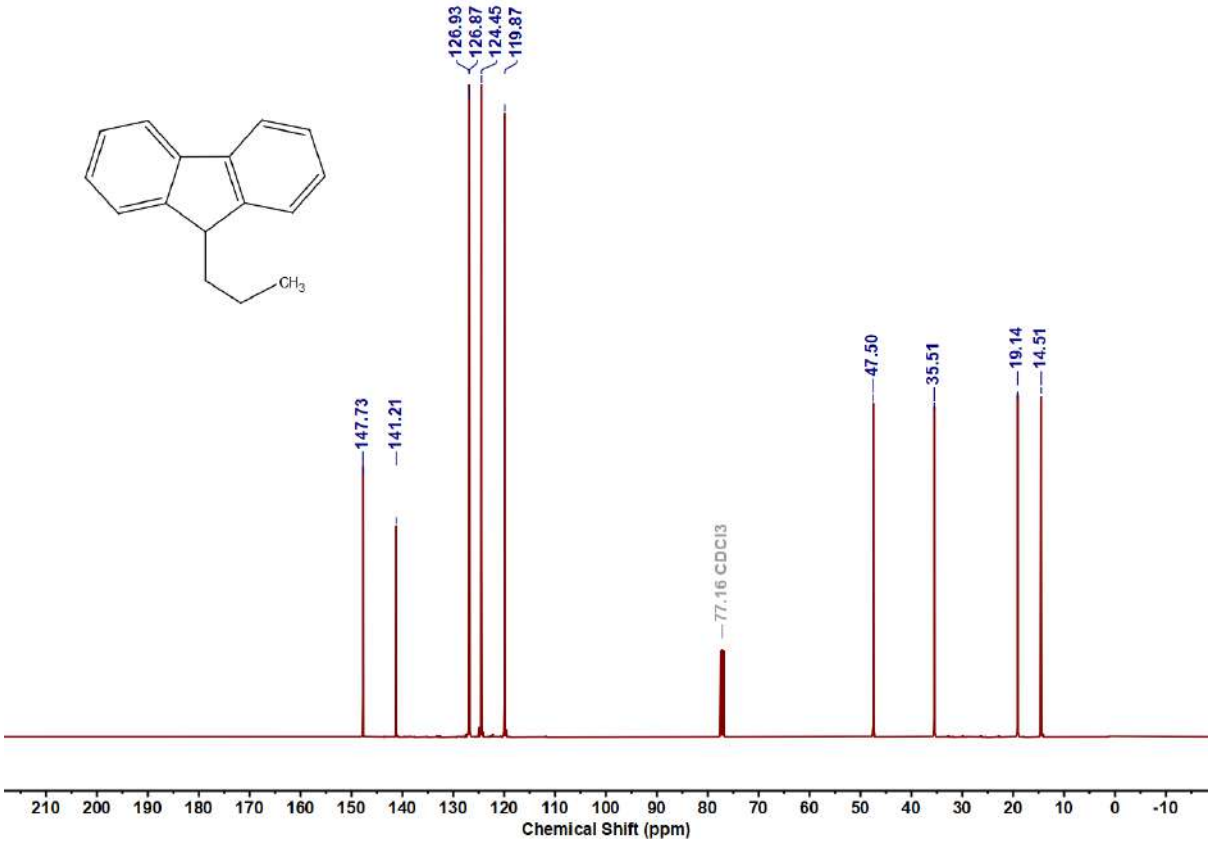

Figure 4.6.A52: ^{13}C{^{1}H} NMR Spectrum of **8o**

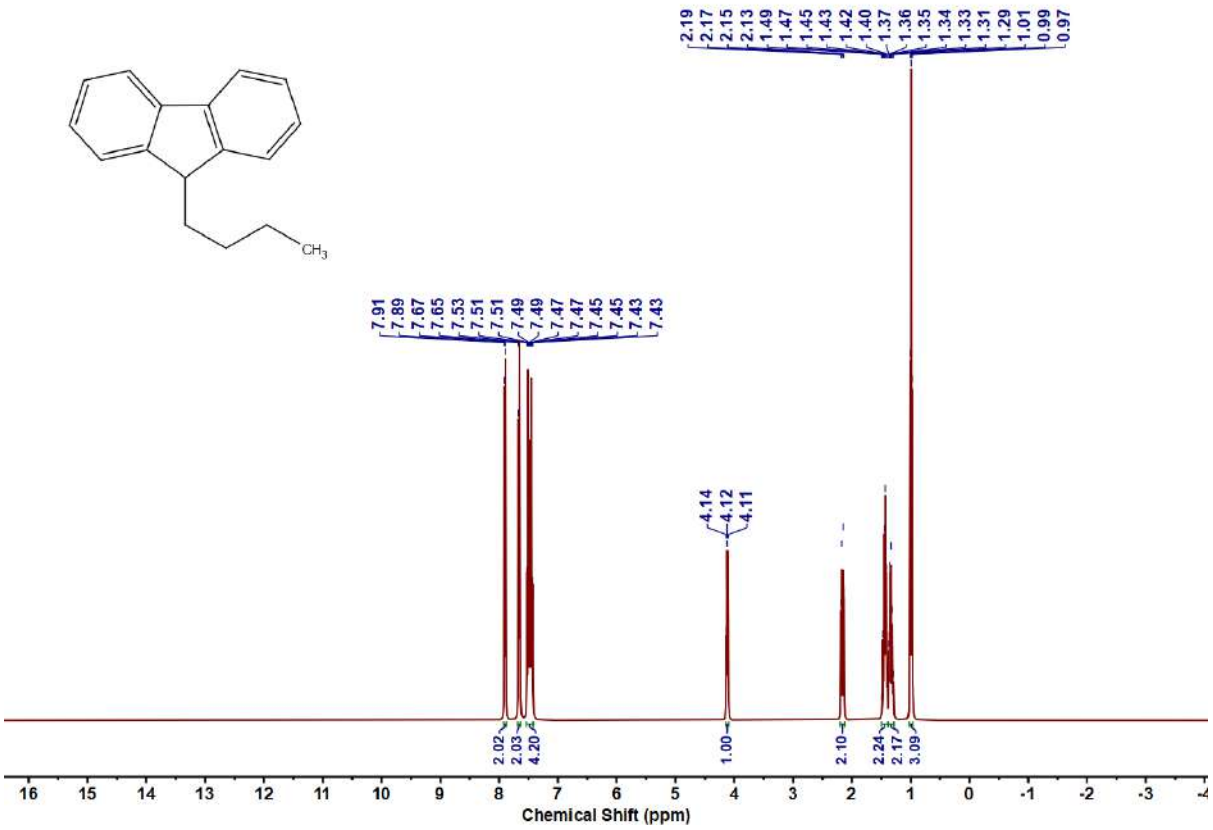

Figure 4.6.A53: ^{1}H NMR Spectrum of **8p**

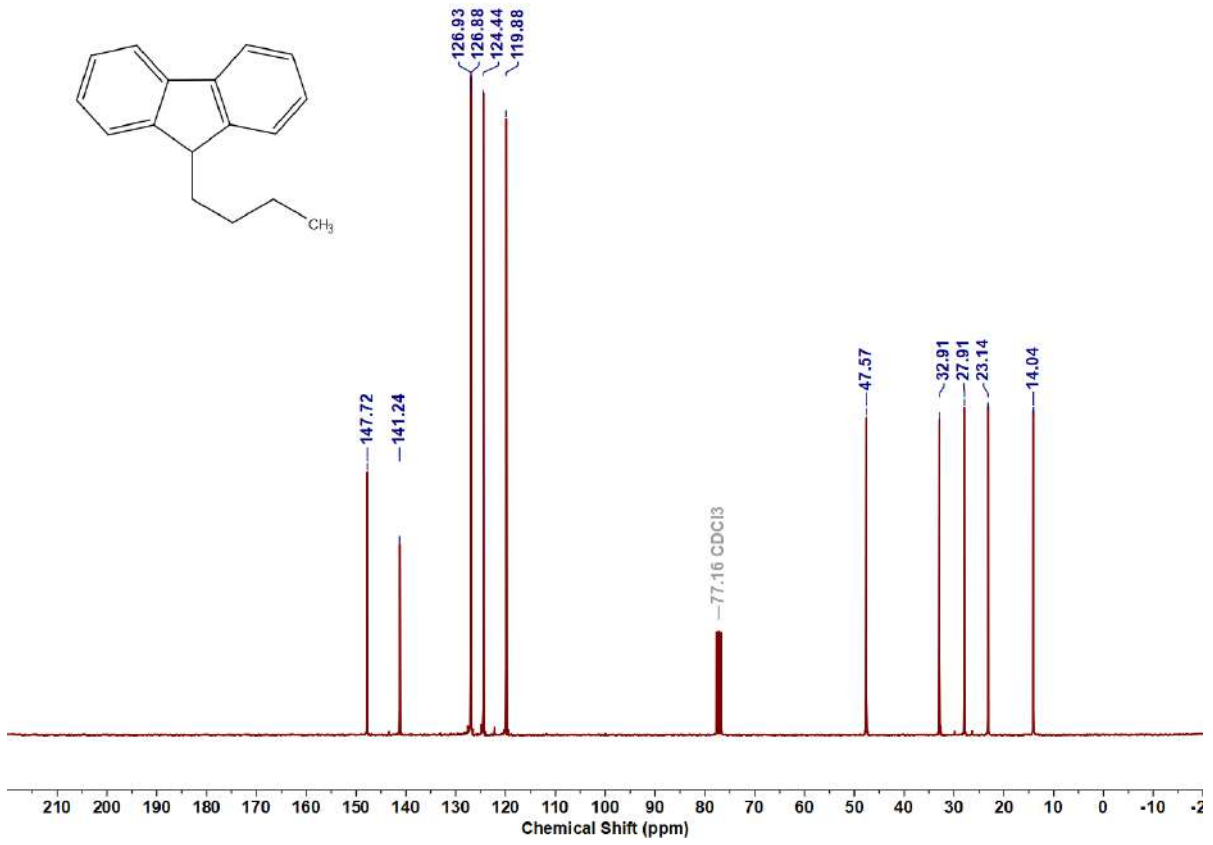

Figure 4.6.A54: ^{13}C{^{1}H} NMR Spectrum of **8p**

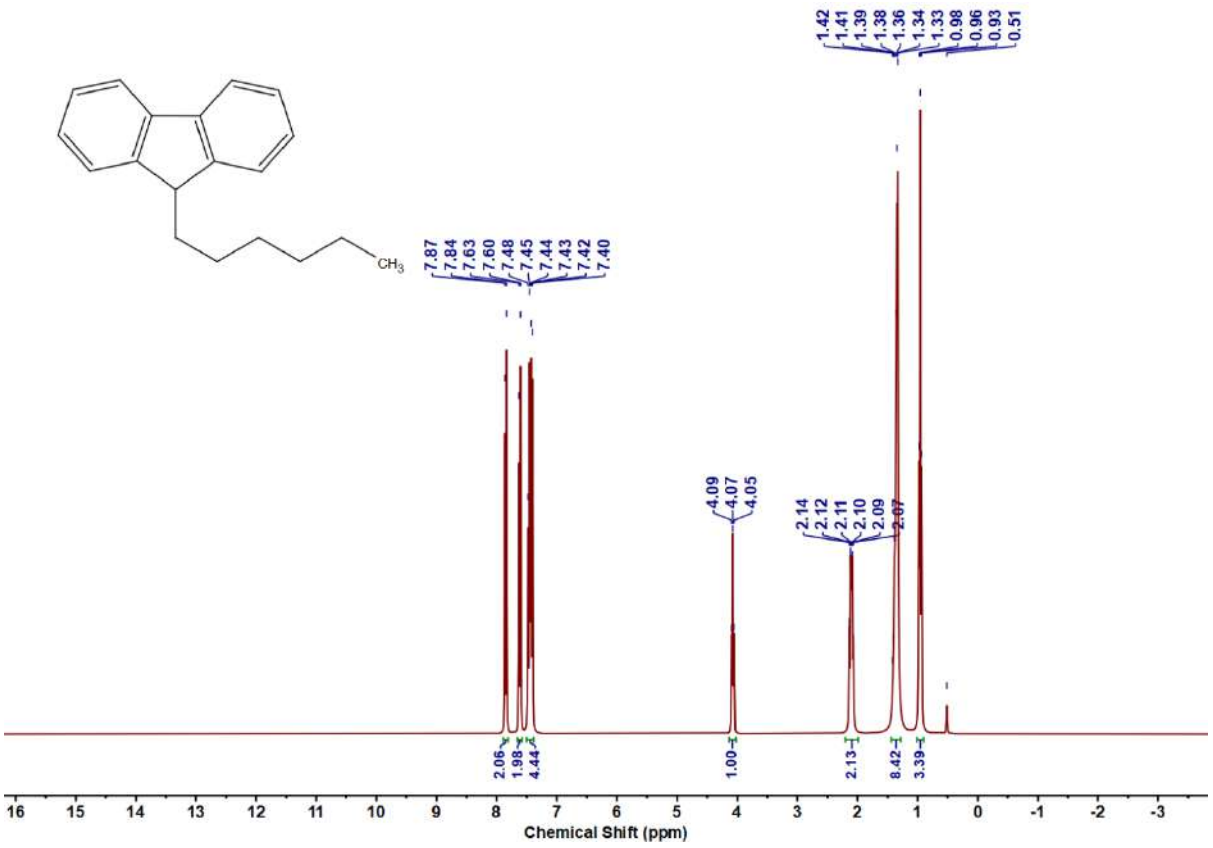

Figure 4.6.A55: ^{1}H NMR Spectrum of **8q**

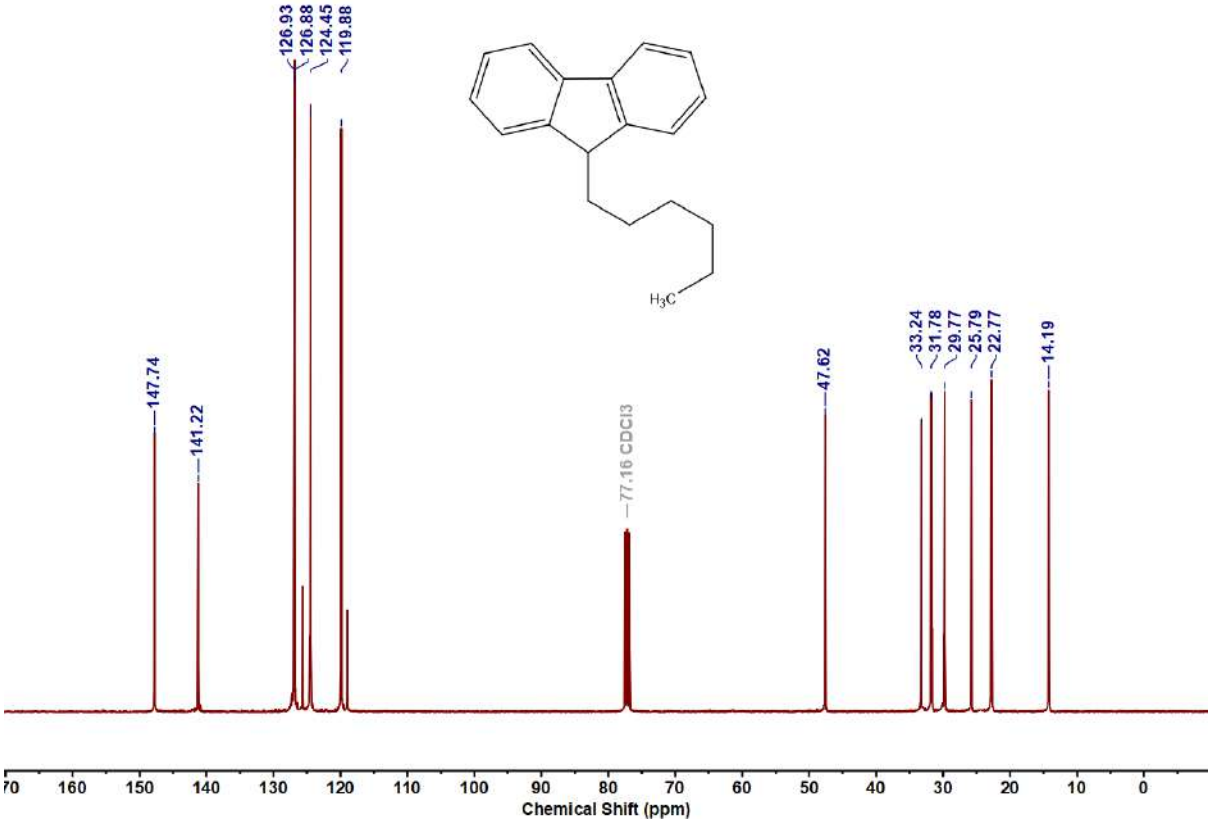

Figure 4.6.A56: $^{13}C\{^{1}H\}$ NMR Spectrum of **8q**

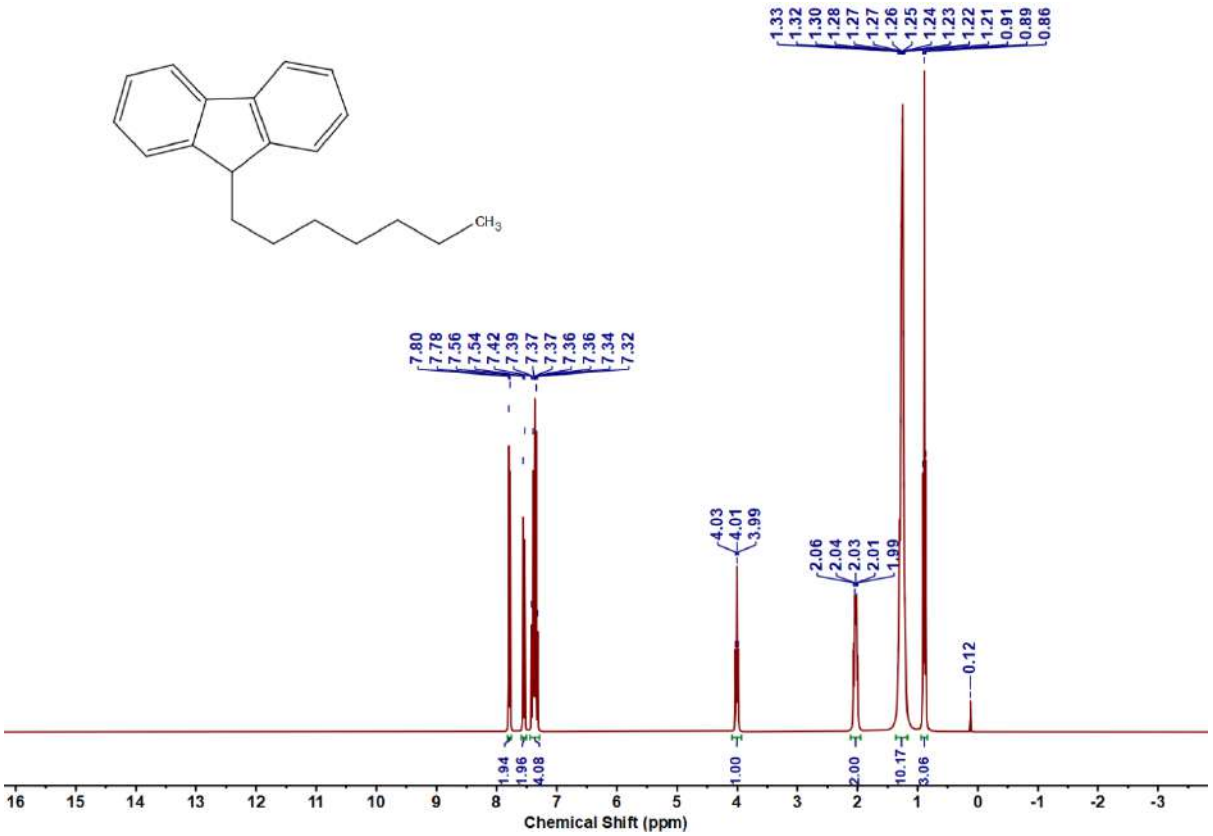

Figure 4.6.A57: ^{1}H NMR Spectrum of **8r**

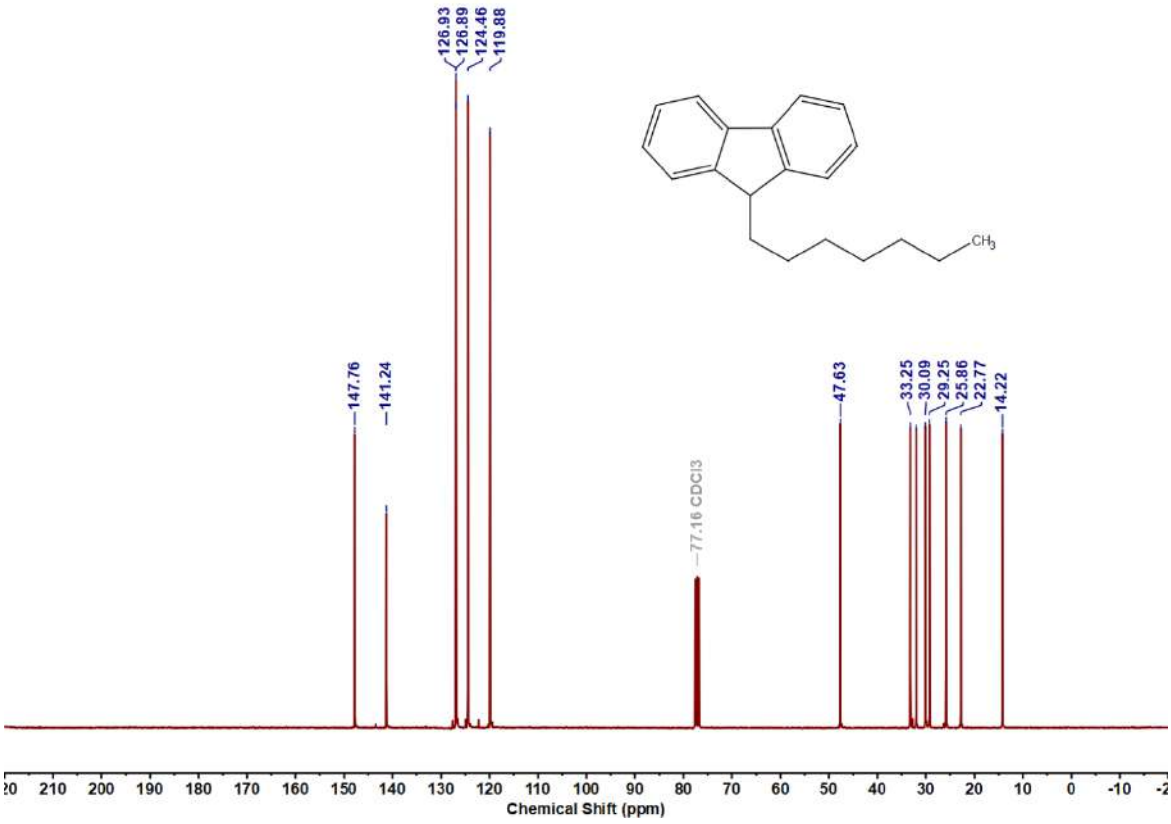

Figure 4.6.A58: ^{13}C{^{1}H} NMR Spectrum of **8r**

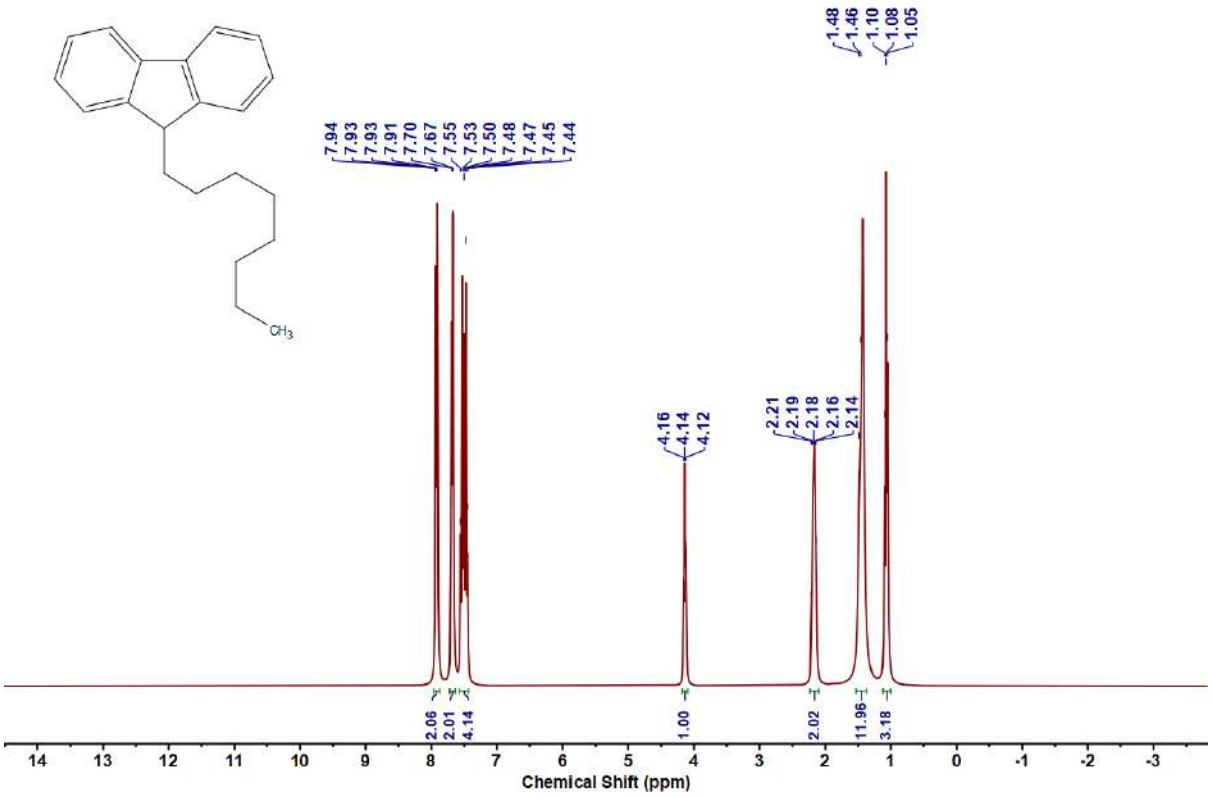

Figure 4.6.A59: ^{1}H NMR Spectrum of **8s**

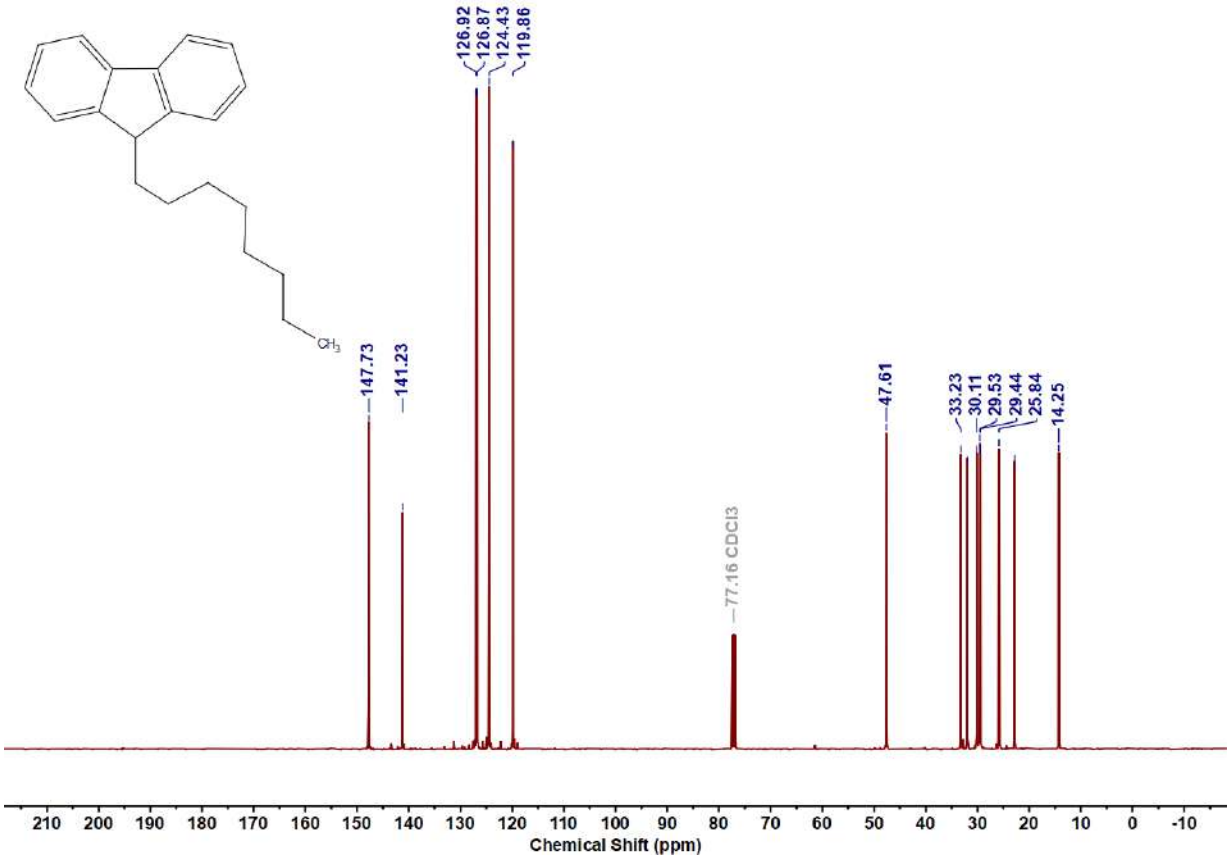

Figure 4.6.A60: ^{13}C{^{1}H} NMR Spectrum of **8s**

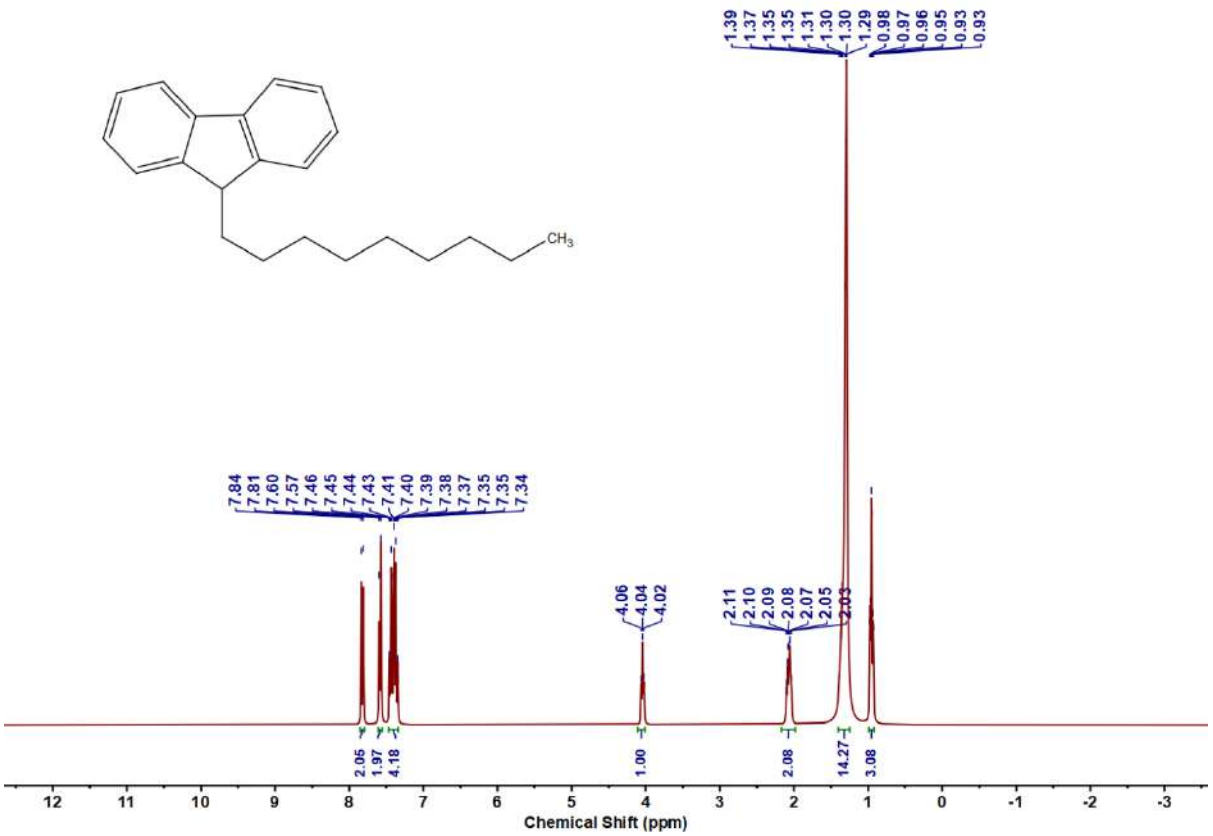

Figure 4.6.A61: ^{1}H NMR Spectrum of **8t**

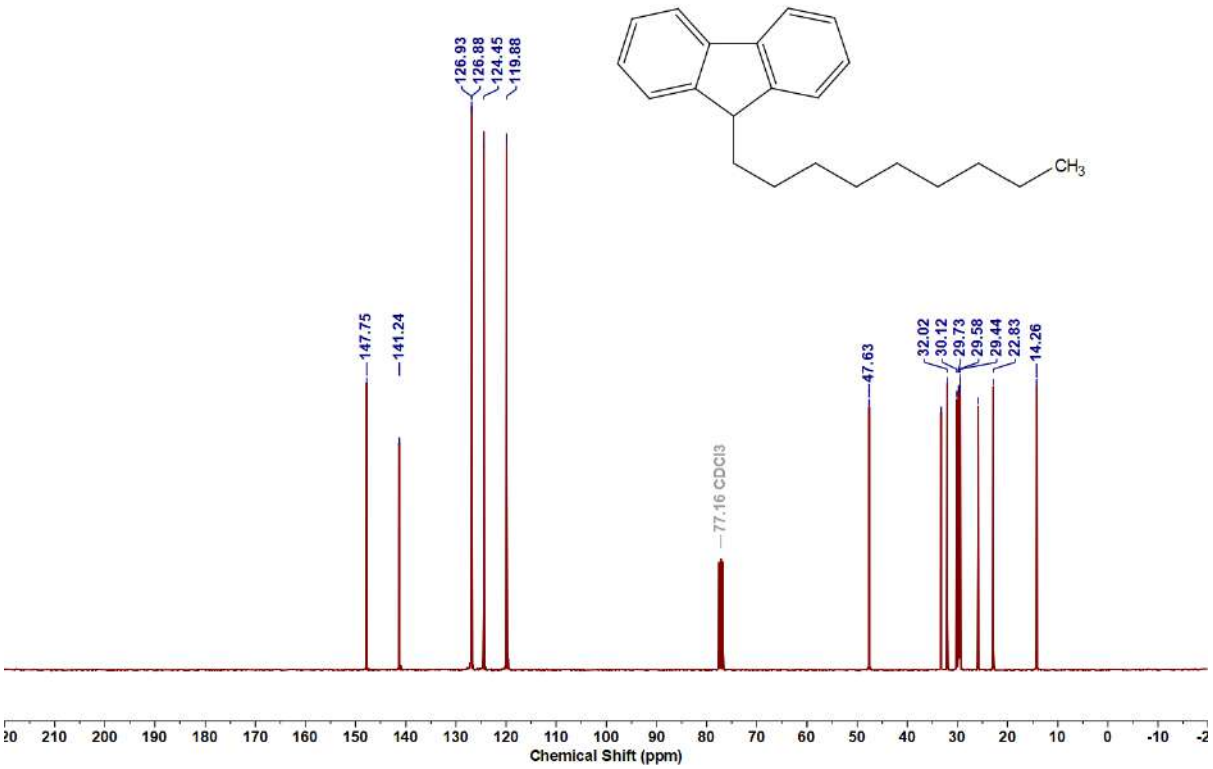

Figure 4.6.A62: ^{13}C{^{1}H} NMR Spectrum of **8t**

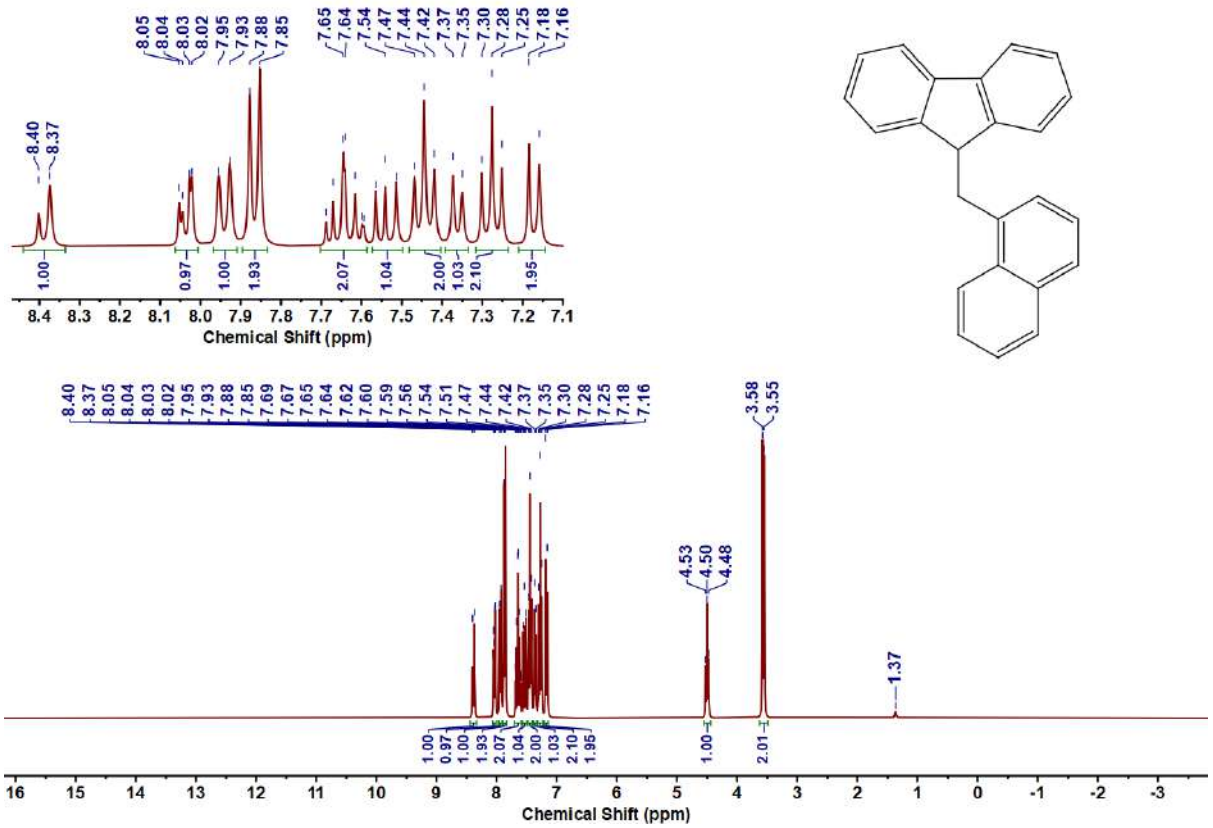

Figure 4.6.A63: ^{1}H NMR Spectrum of **8u**

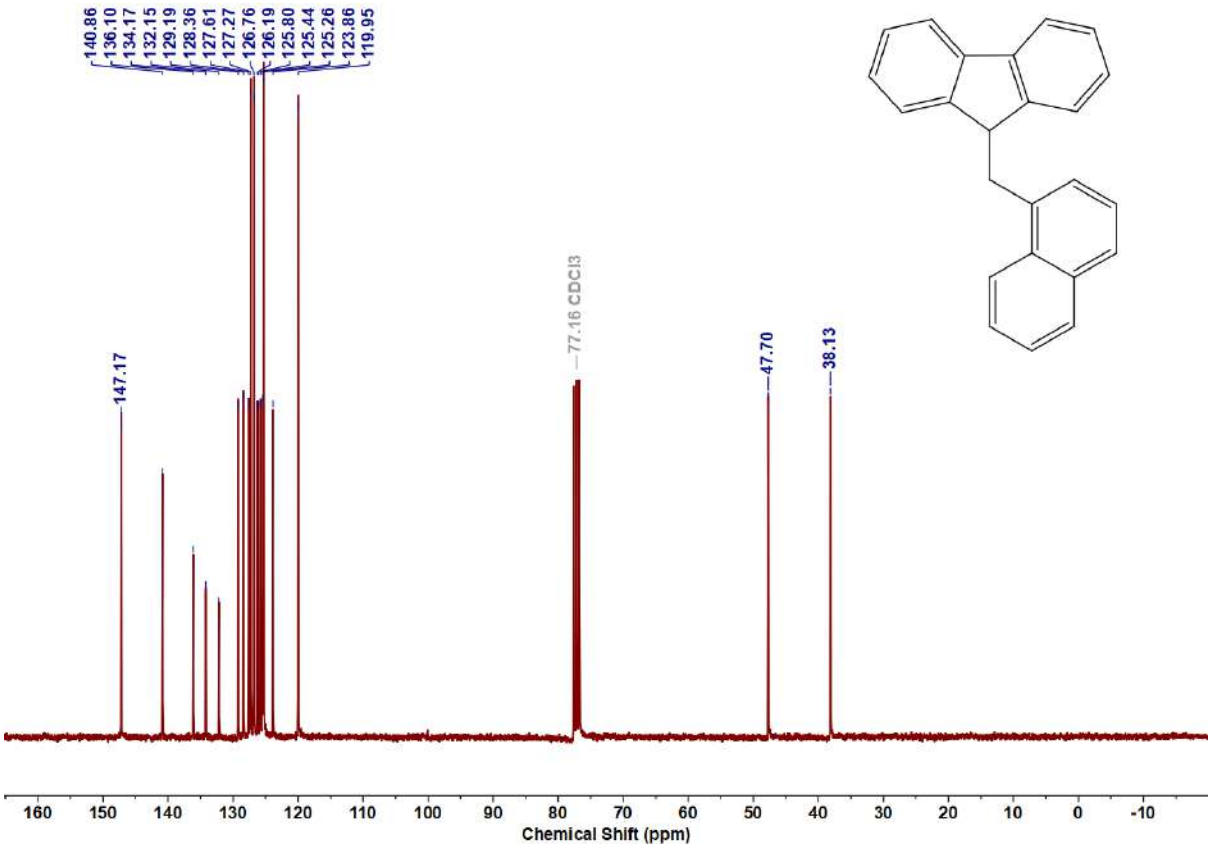

Figure 4.6.A64: ^{13}C{^{1}H} NMR Spectrum of **8u**

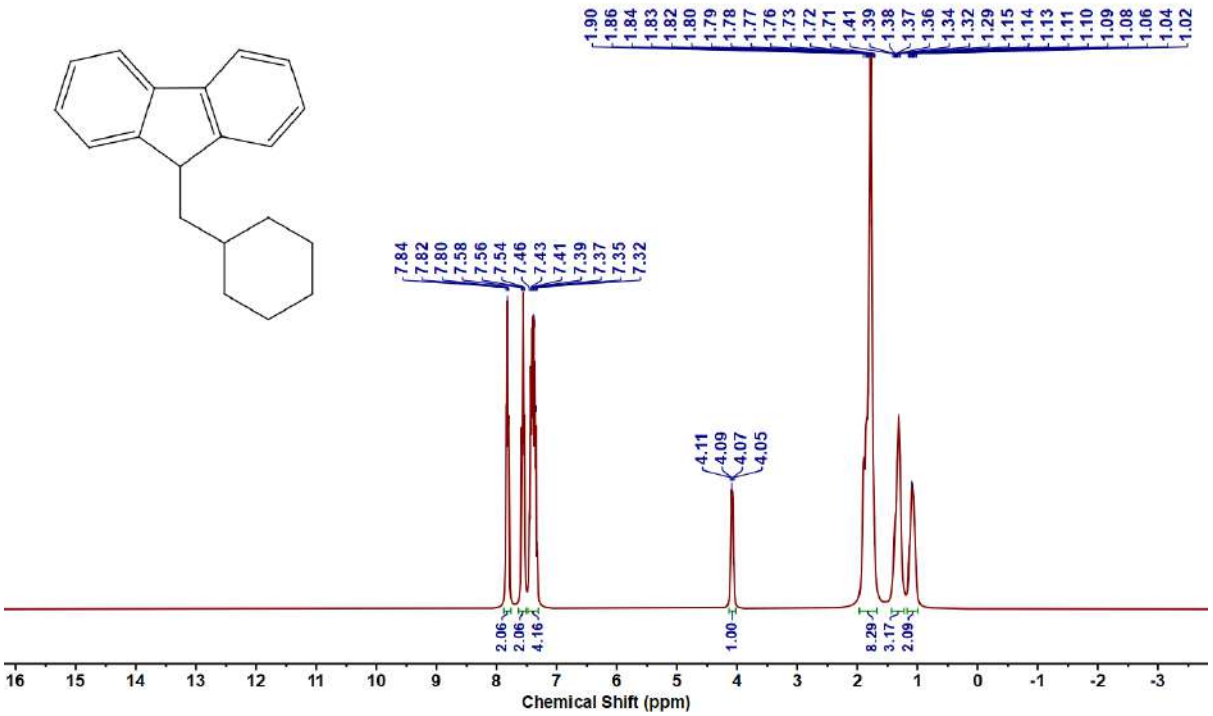

Figure 4.6.A65: ^{1}H NMR Spectrum of **8v**

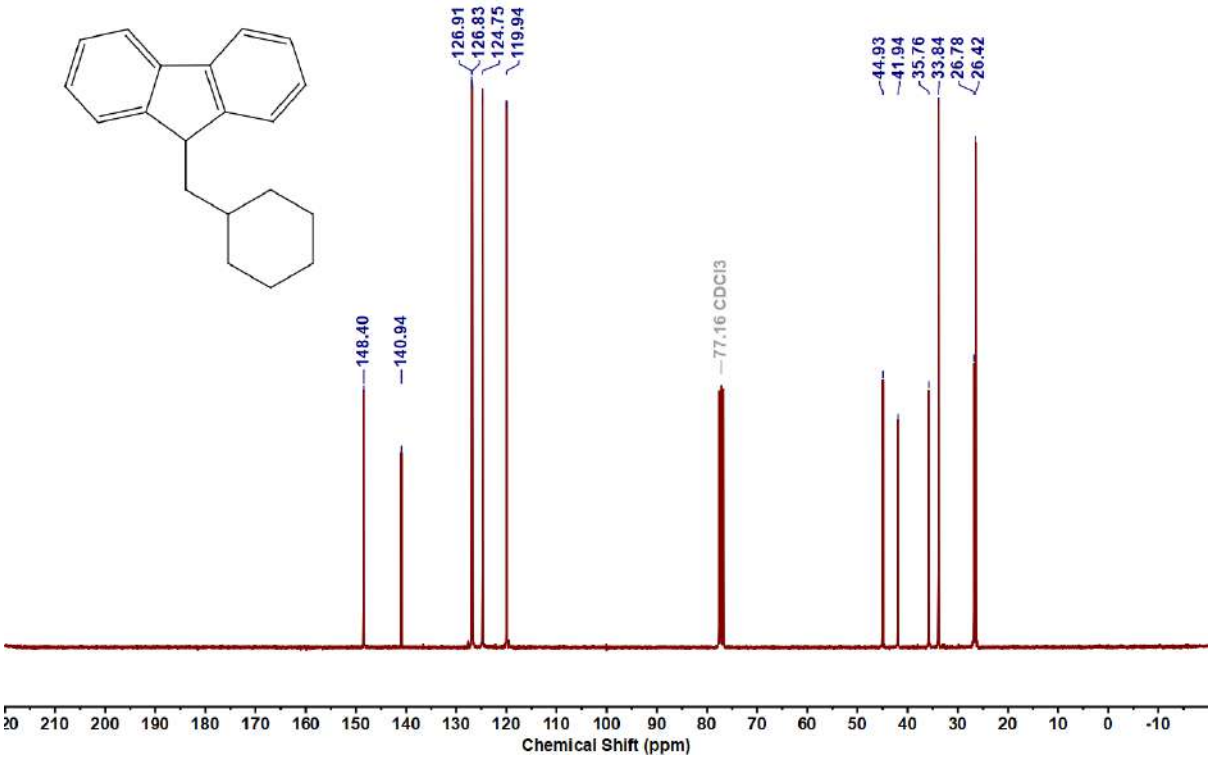

Figure 4.6.A66: ^{13}C{^{1}H} NMR Spectrum of **8v**

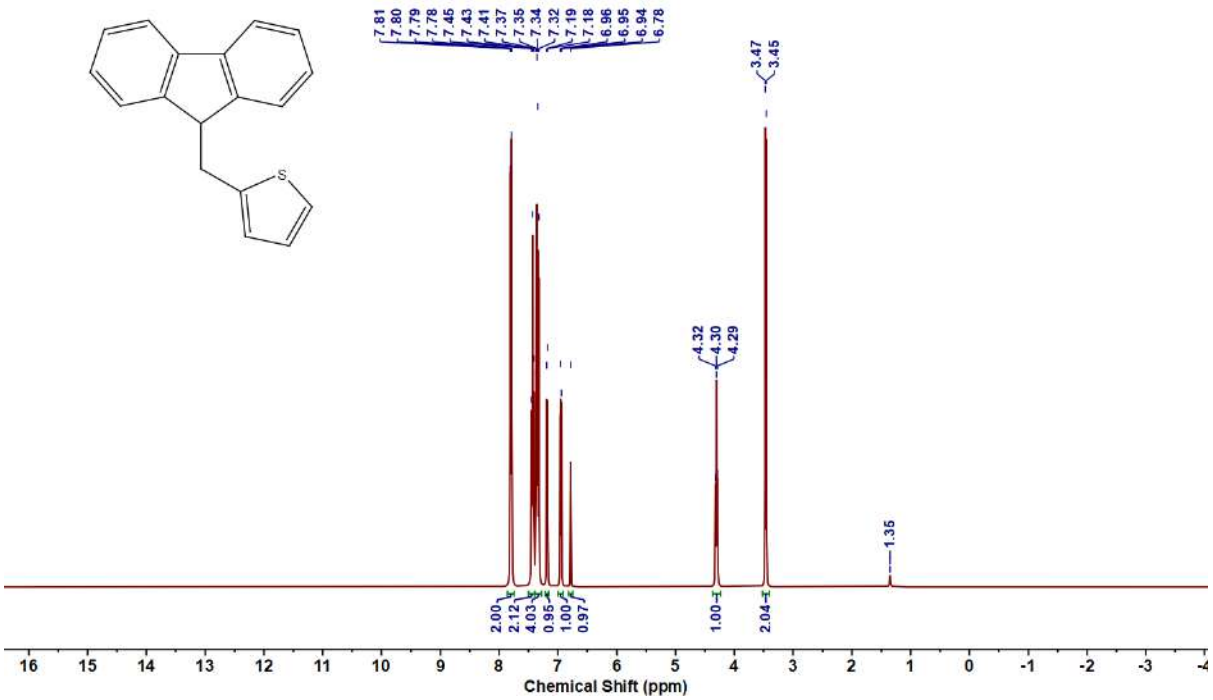

Figure 4.6.A67: ^{1}H NMR Spectrum of **8w**

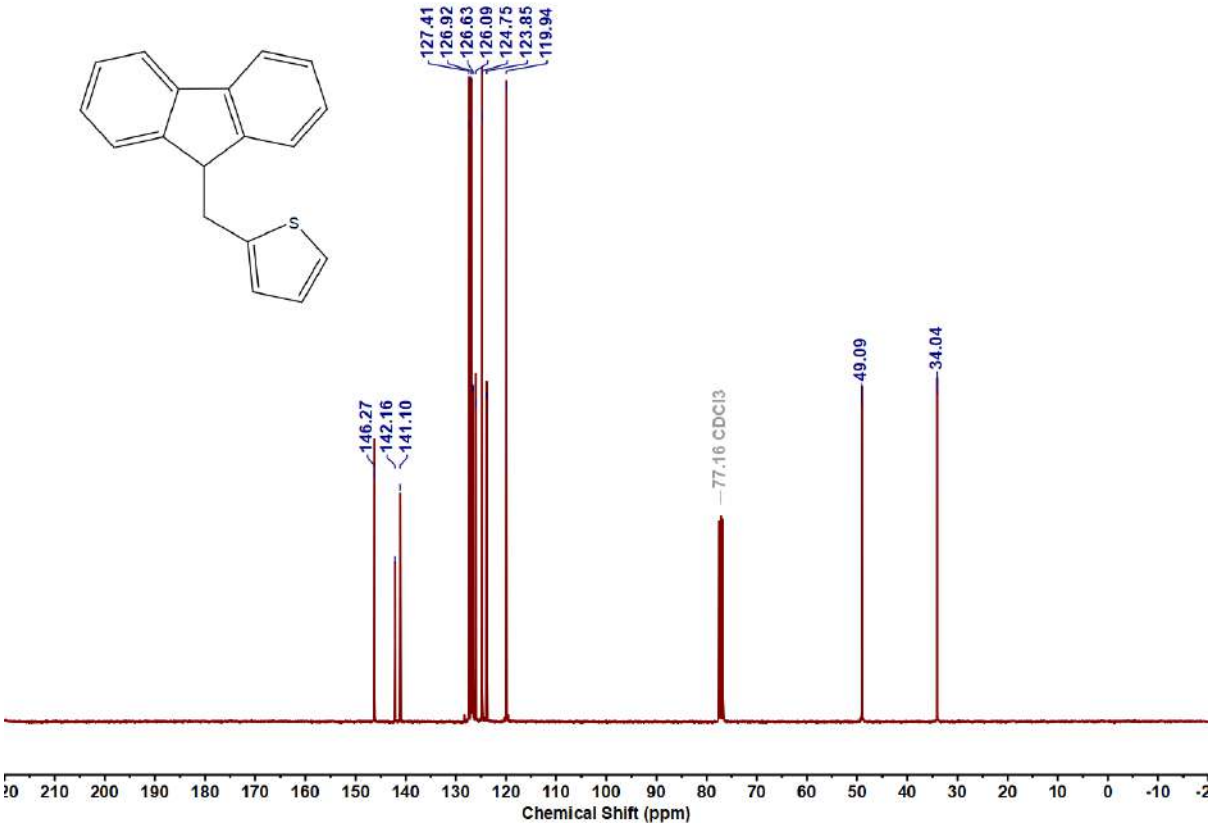

Figure 4.6.A68: ^{13}C{^{1}H} NMR Spectrum of **8w**

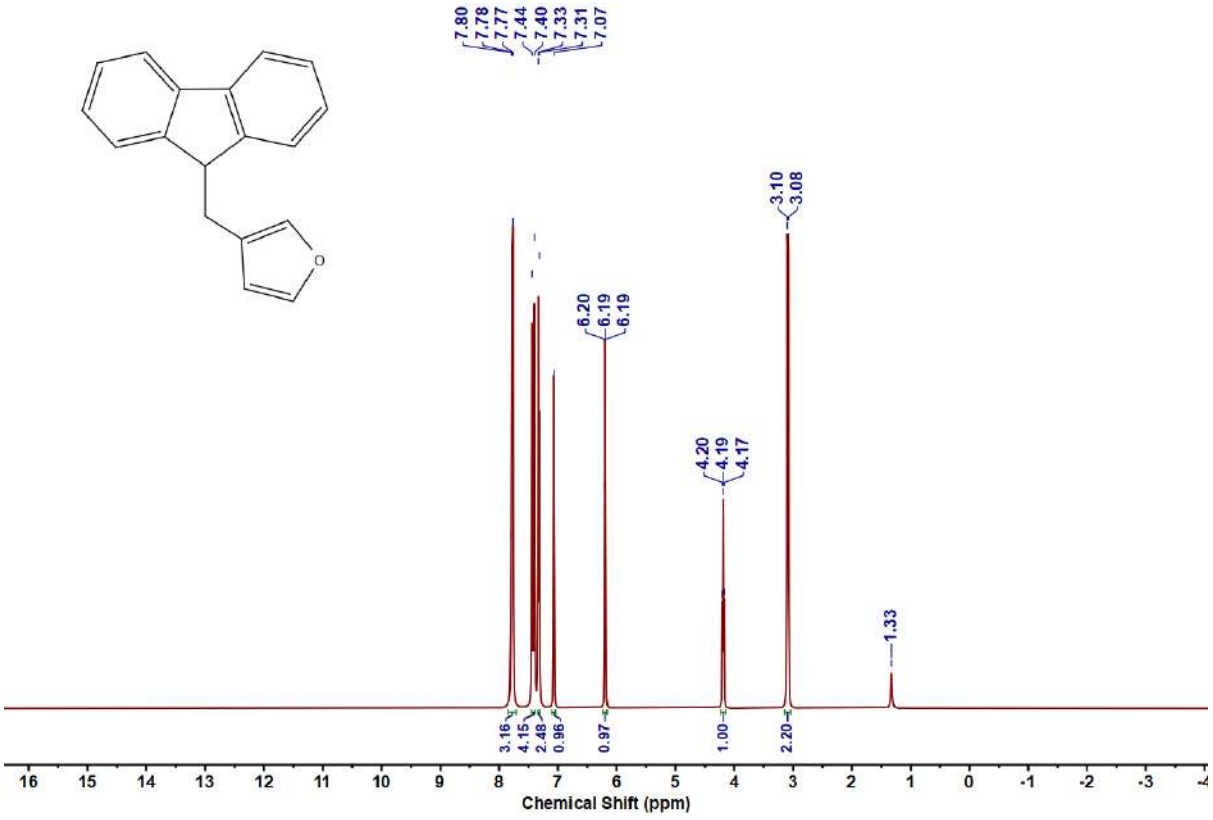

Figure 4.6.A69: ^{1}H NMR Spectrum of **8x**

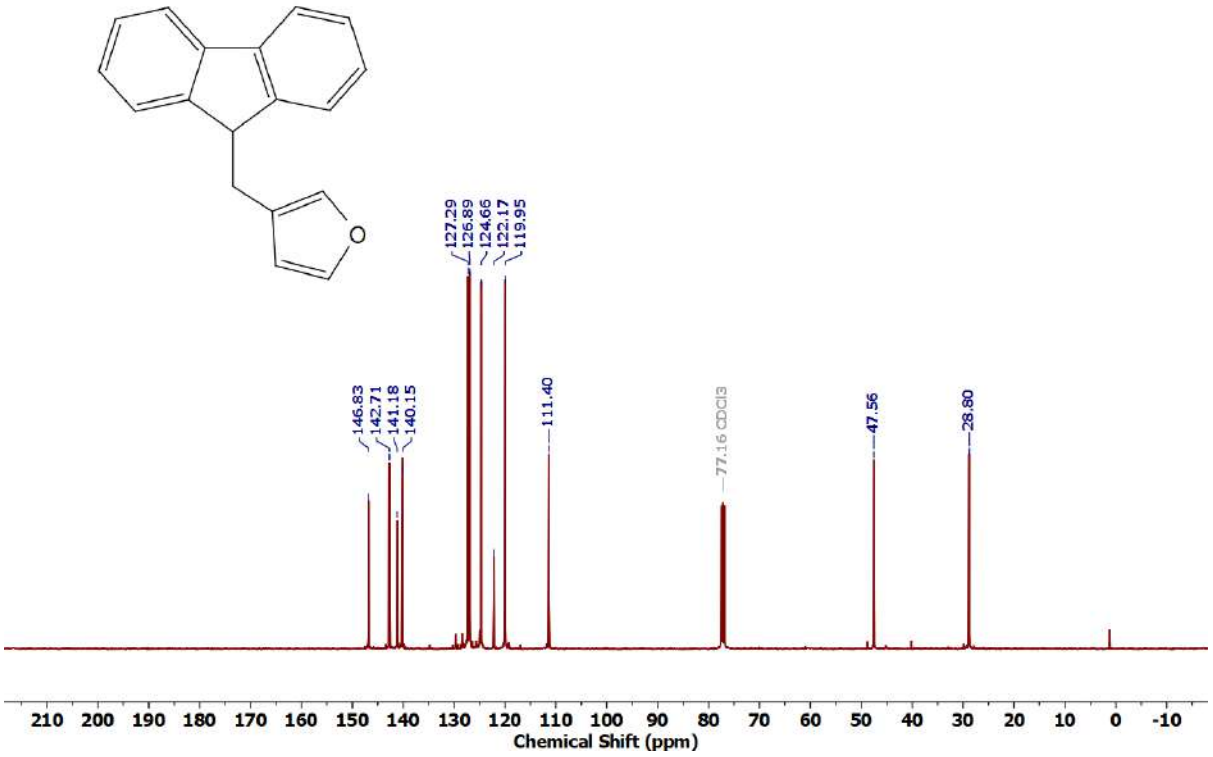

Figure 4.6.A70: $^{13}C\{^{1}H\}$ NMR Spectrum of **8x**

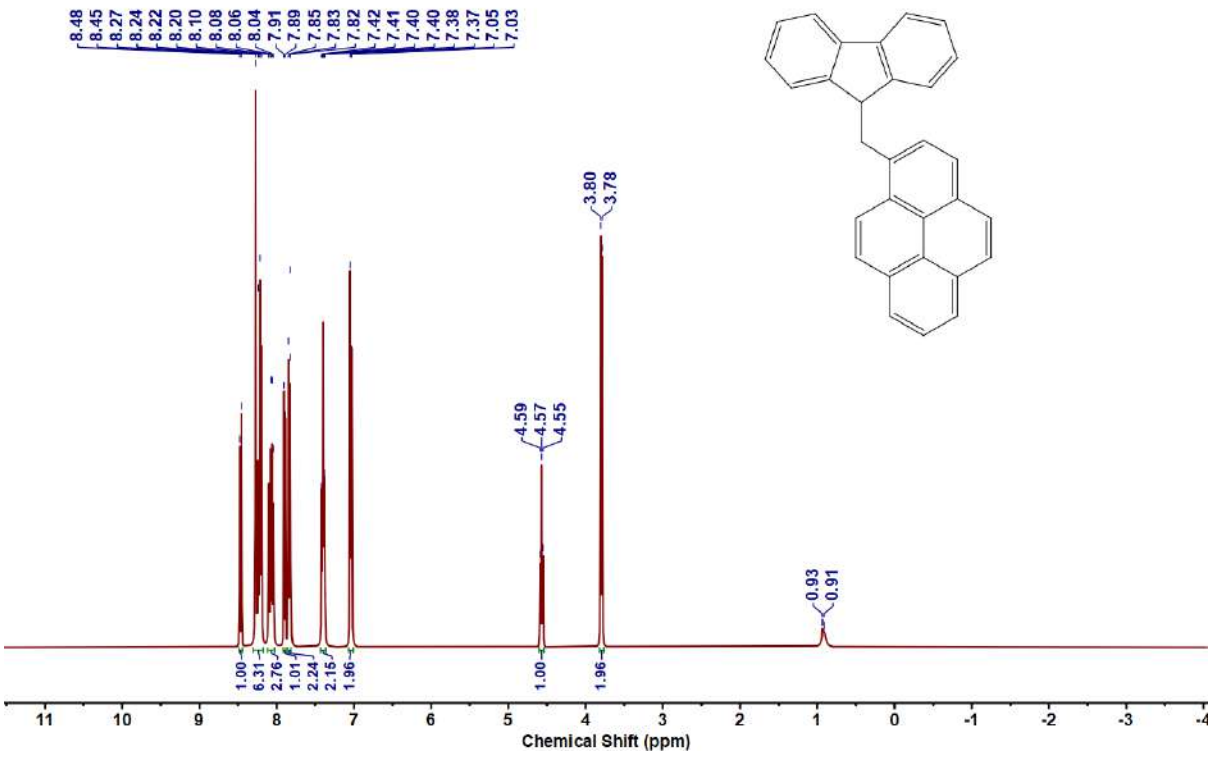

Figure 4.6.A71: ^{1}H NMR Spectrum of **8y**

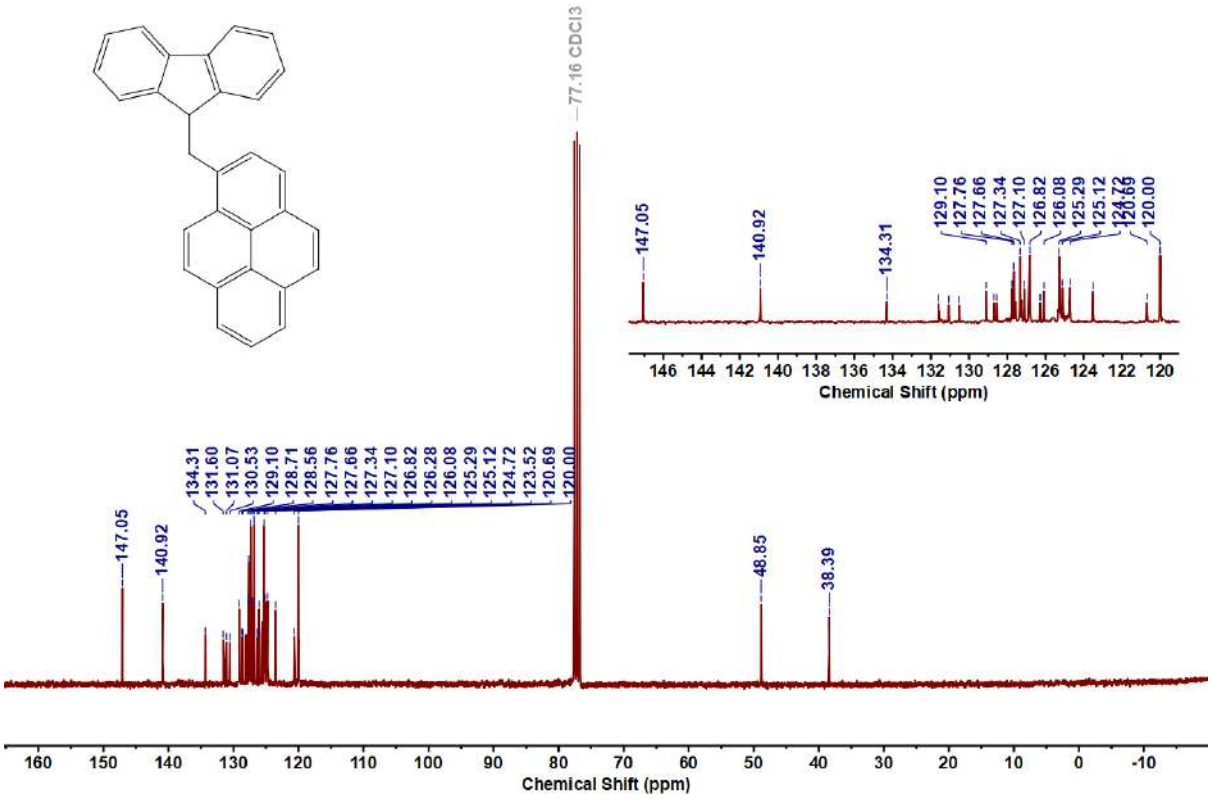

Figure 4.6.A72: ^{13}C{^{1}H} NMR Spectrum of **8y**

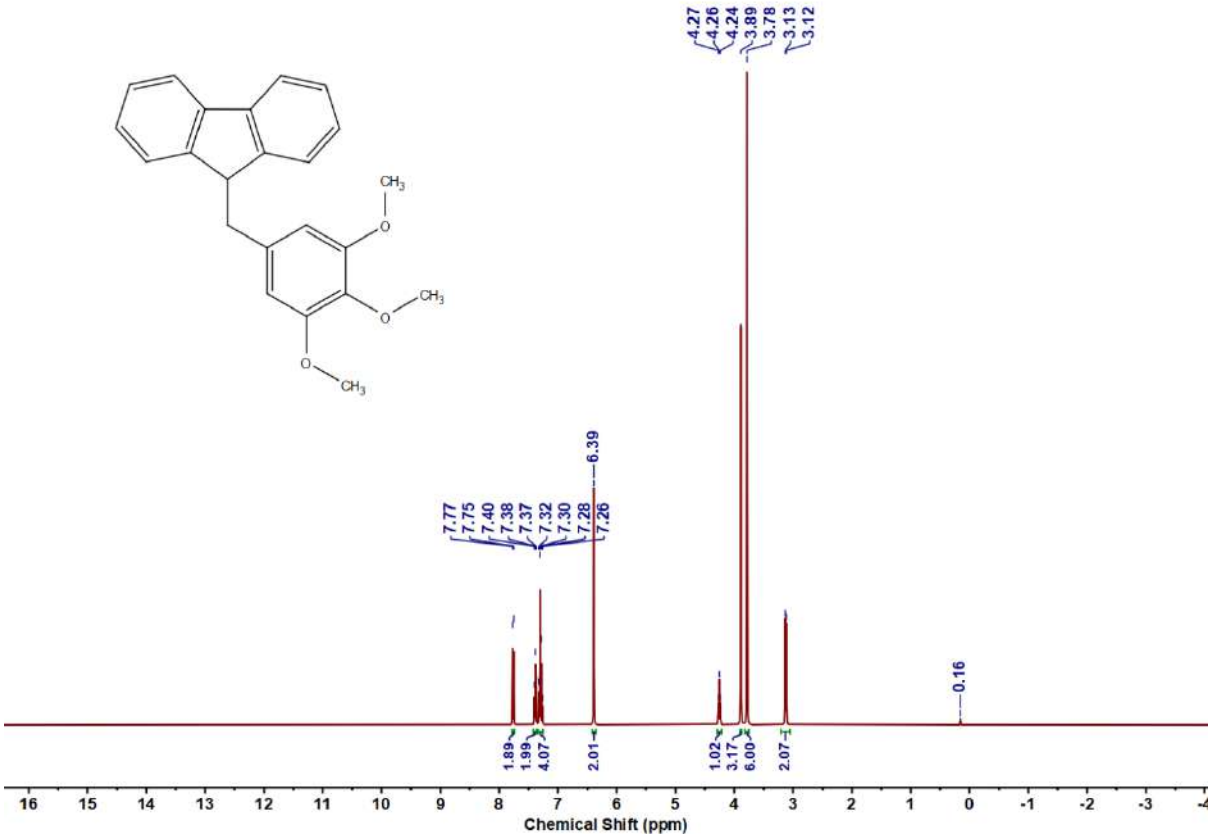

Figure 4.6.A73: ^{1}H NMR Spectrum of **8z**

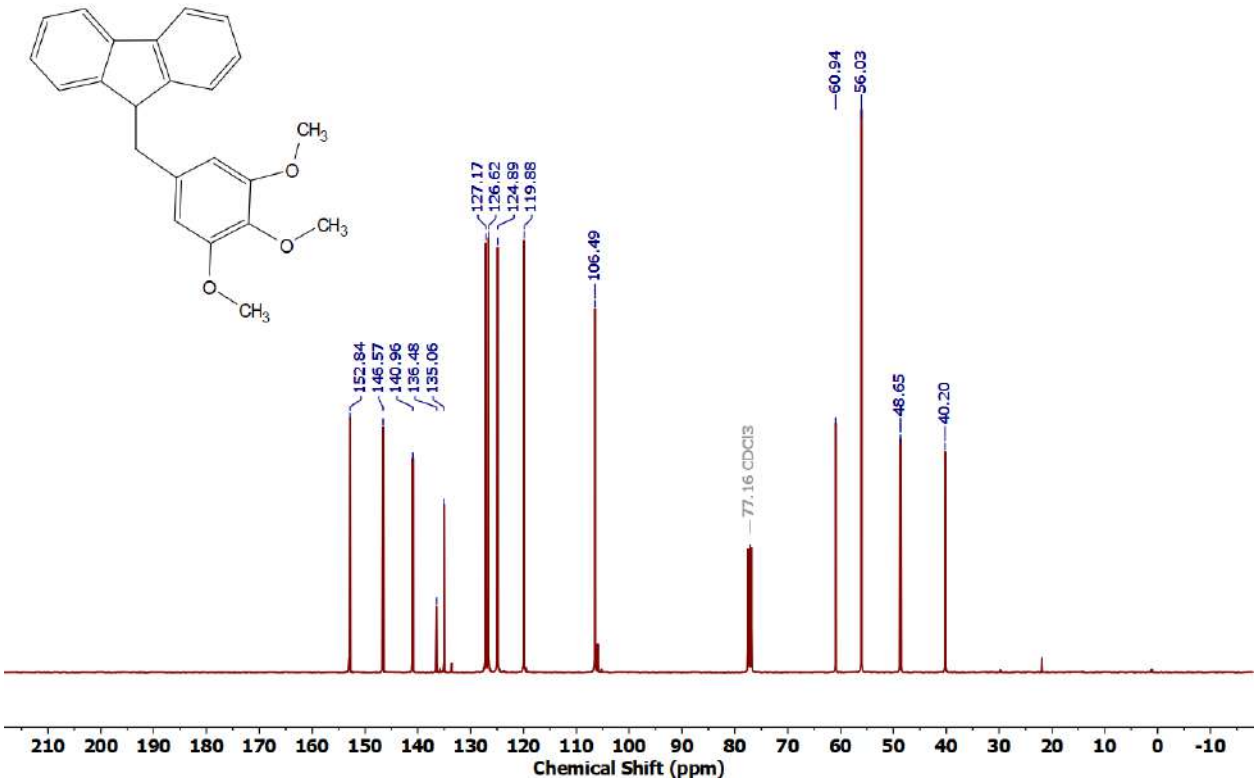

Figure 4.6.A74: ^{13}C{^{1}H} NMR Spectrum of **8z**

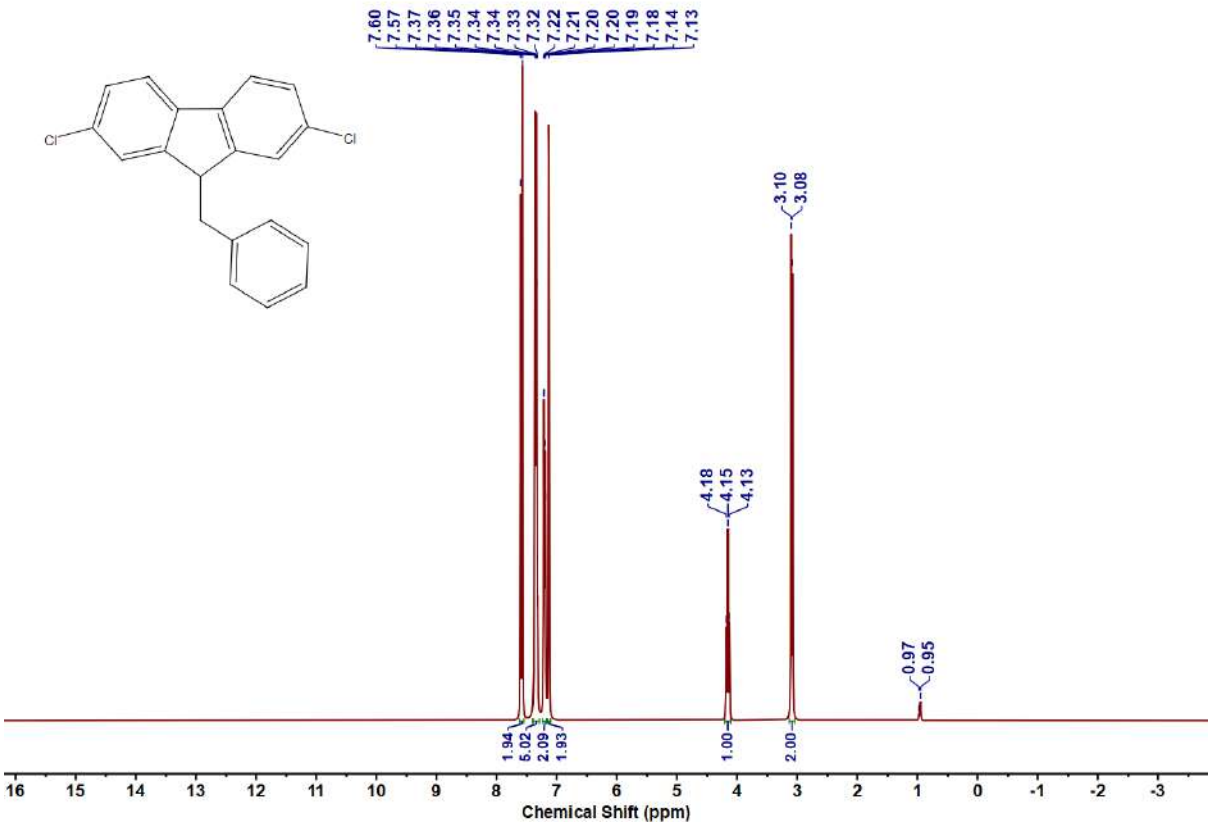

Figure 4.6.A75: ^{1}H NMR Spectrum of **9a**

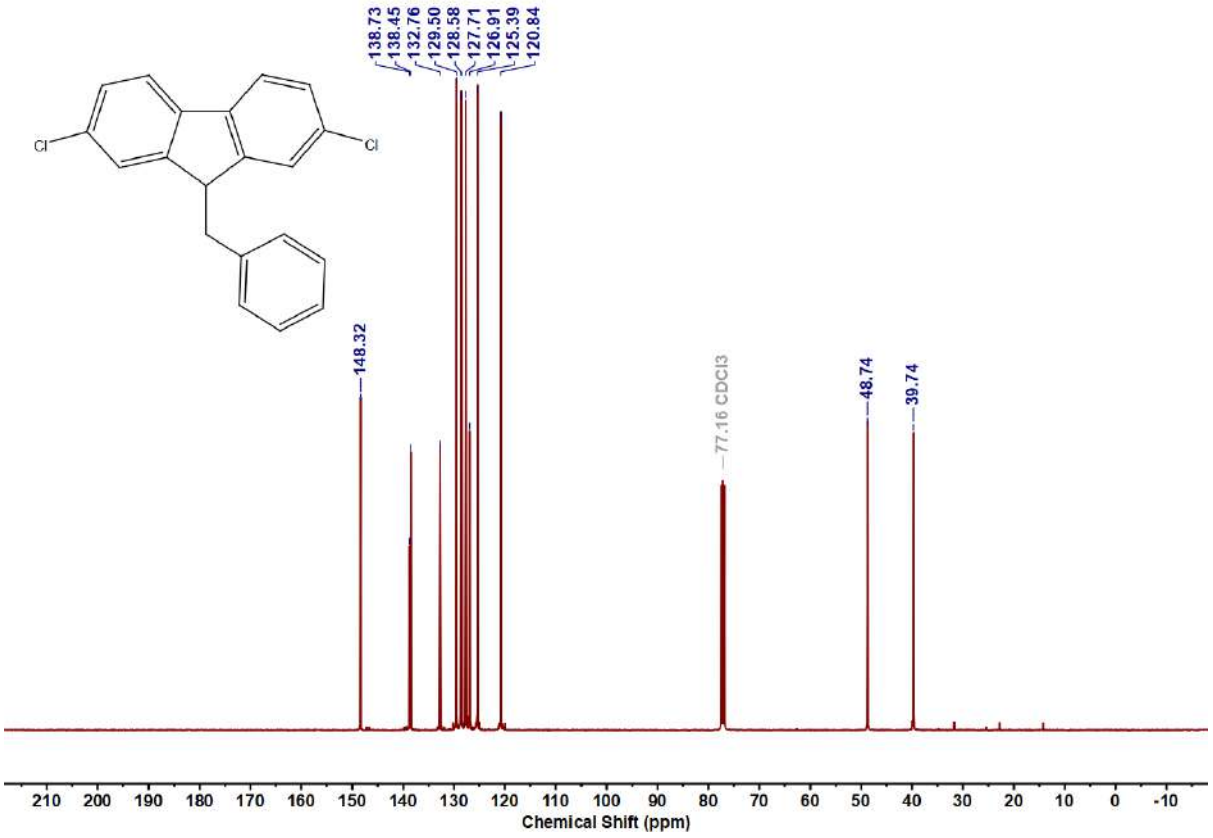

Figure 4.6.A76: ^{13}C{^{1}H} NMR Spectrum of **9a**

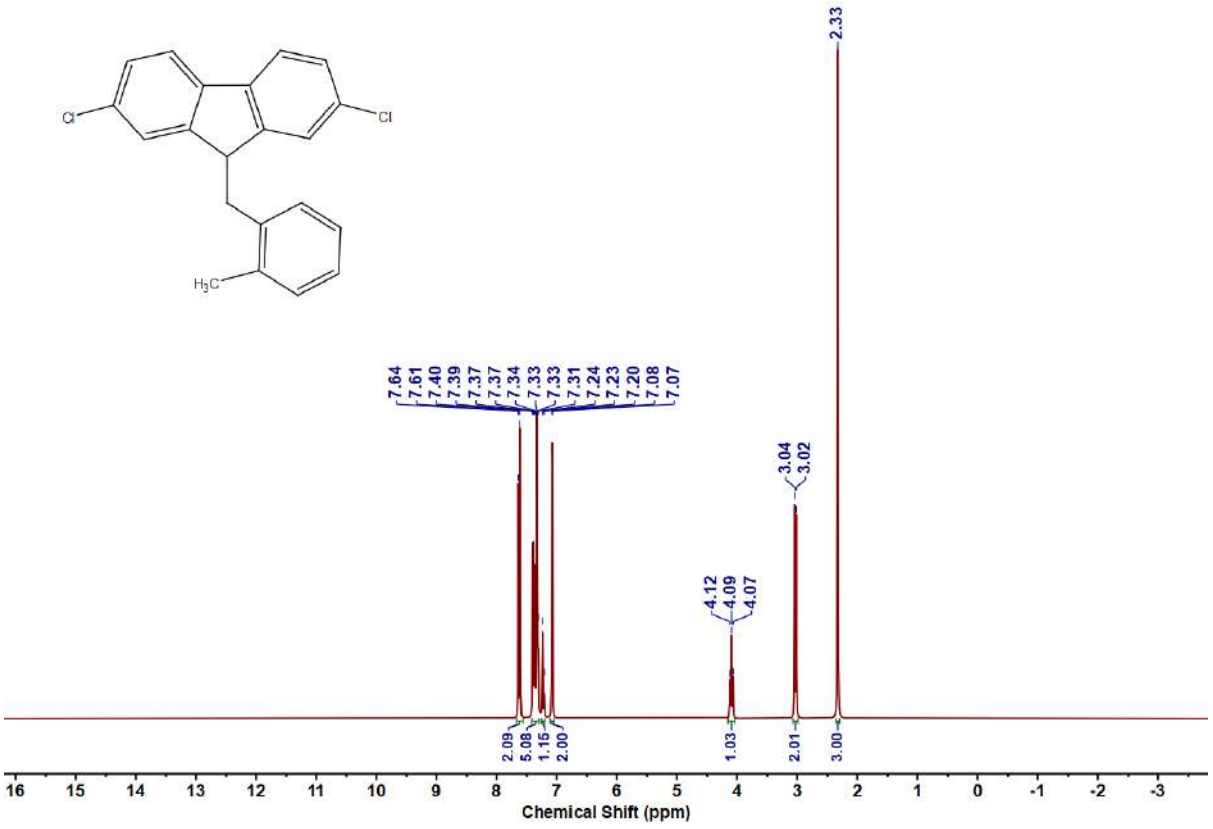

Figure 4.6.A77: ^{1}H NMR Spectrum of **9b**

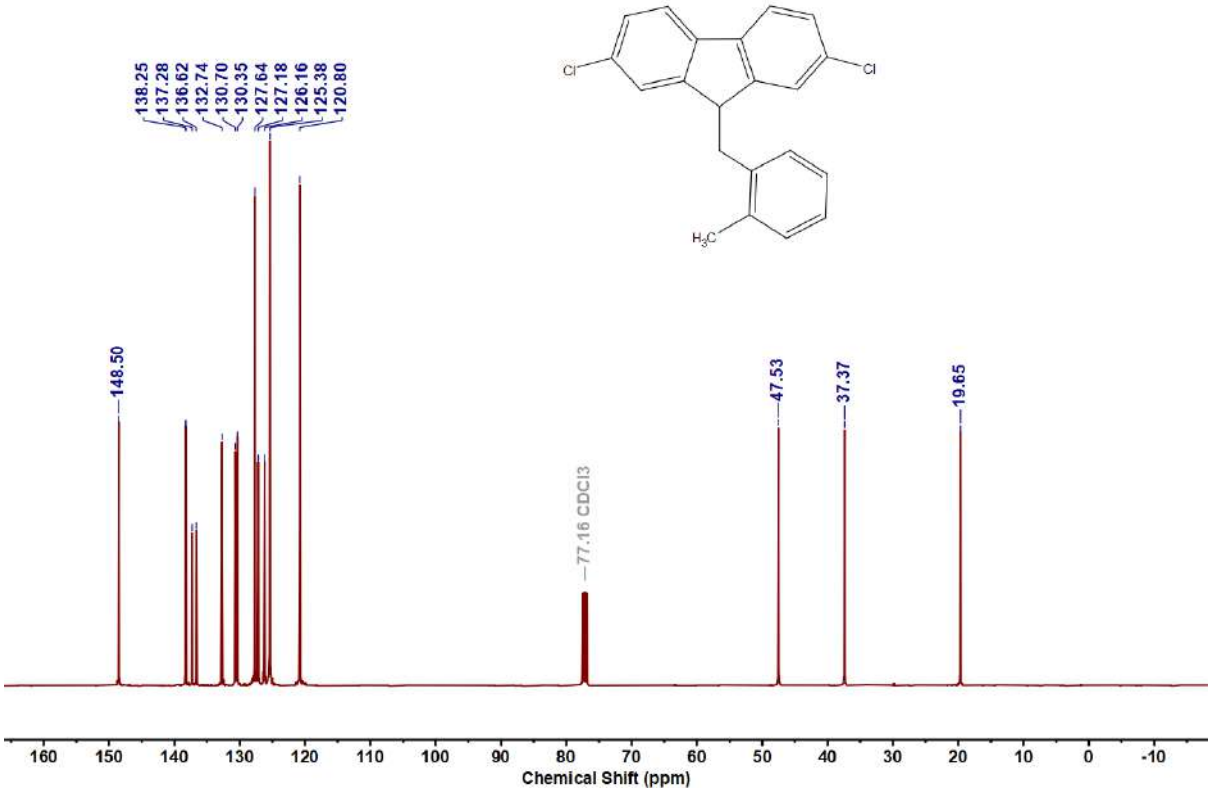

Figure 4.6.A78: ^{13}C{^{1}H} NMR Spectrum of **9b**

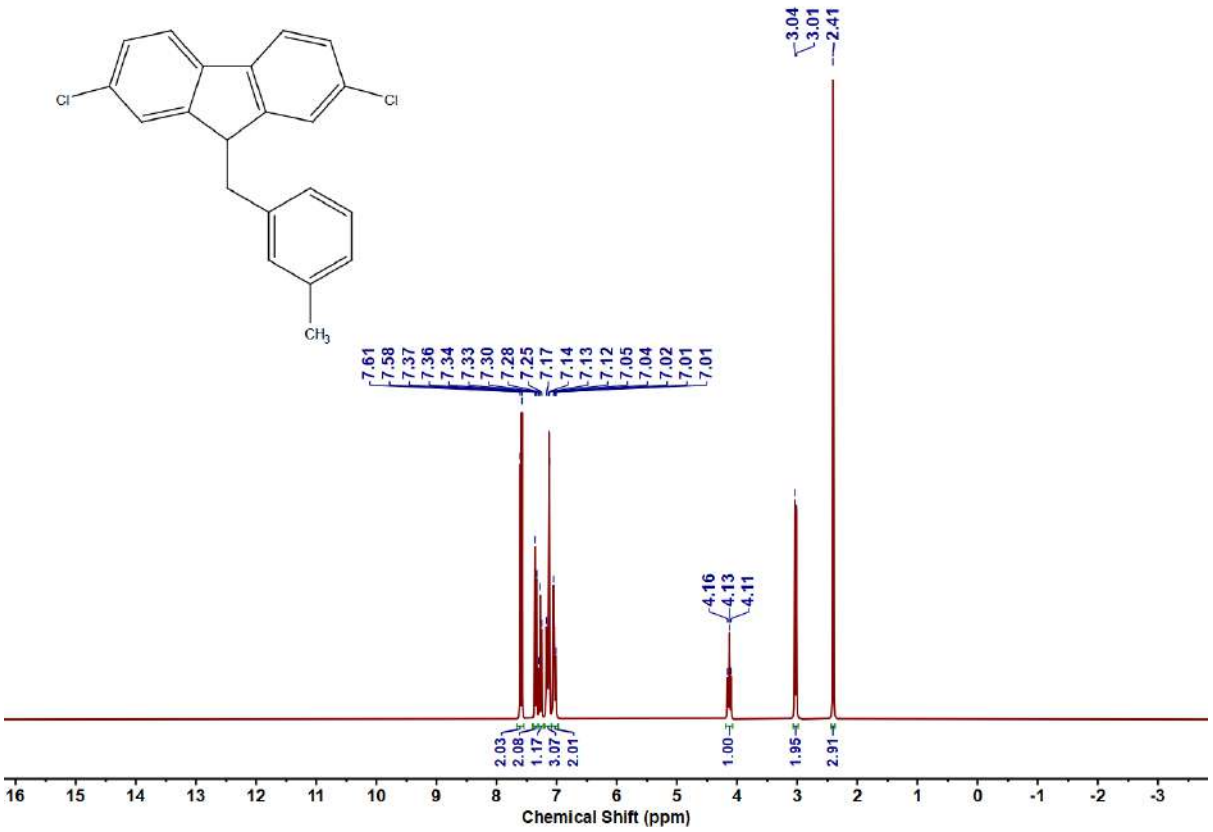

Figure 4.6.A79: ^{1}H NMR Spectrum of **9c**

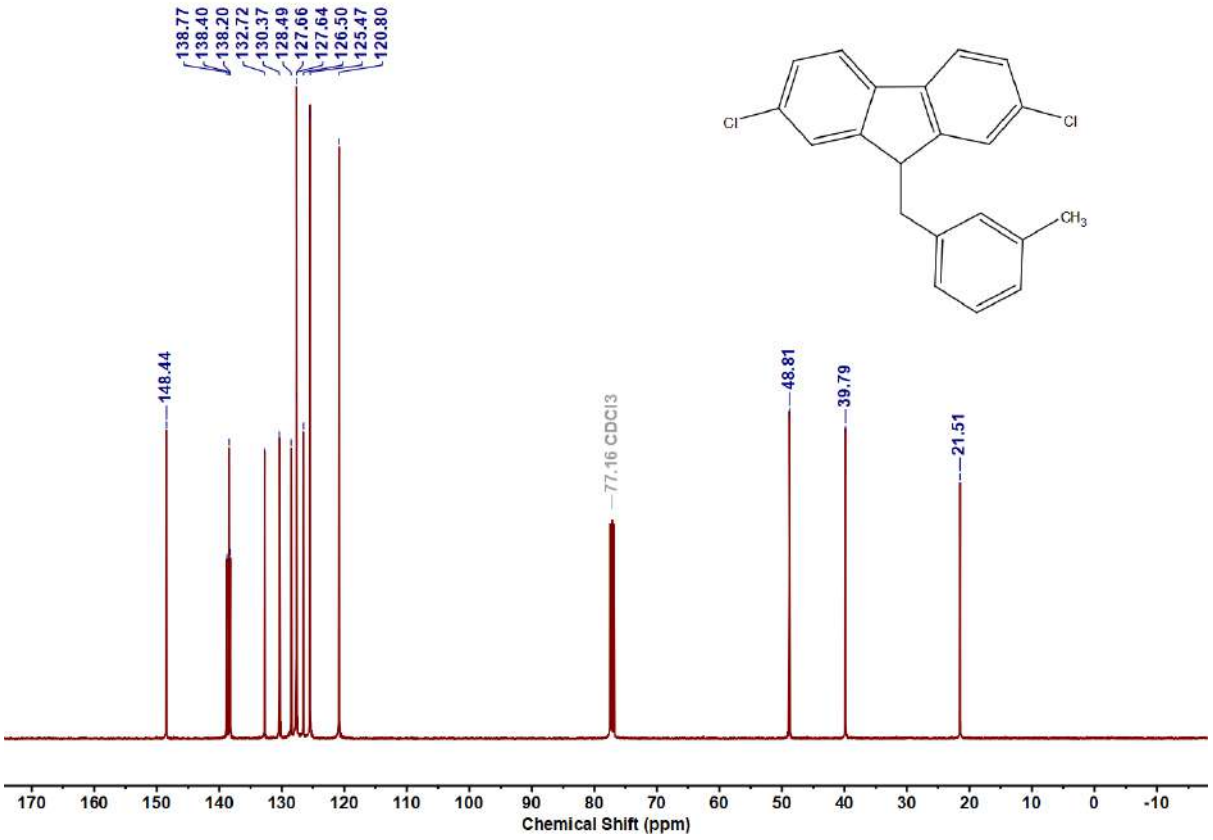

Figure 4.6.A80: ^{13}C{^{1}H} NMR Spectrum of **9c**

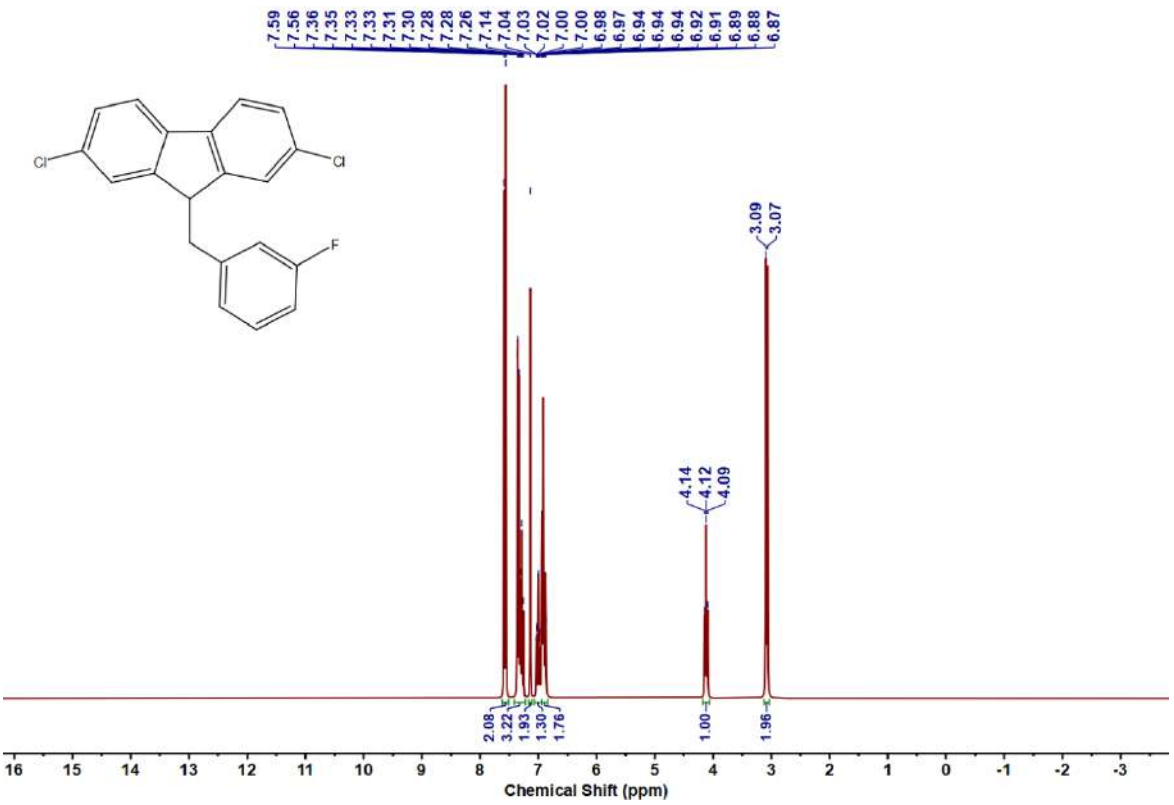

Figure 4.6.A81: ^{1}H NMR Spectrum of **9d**

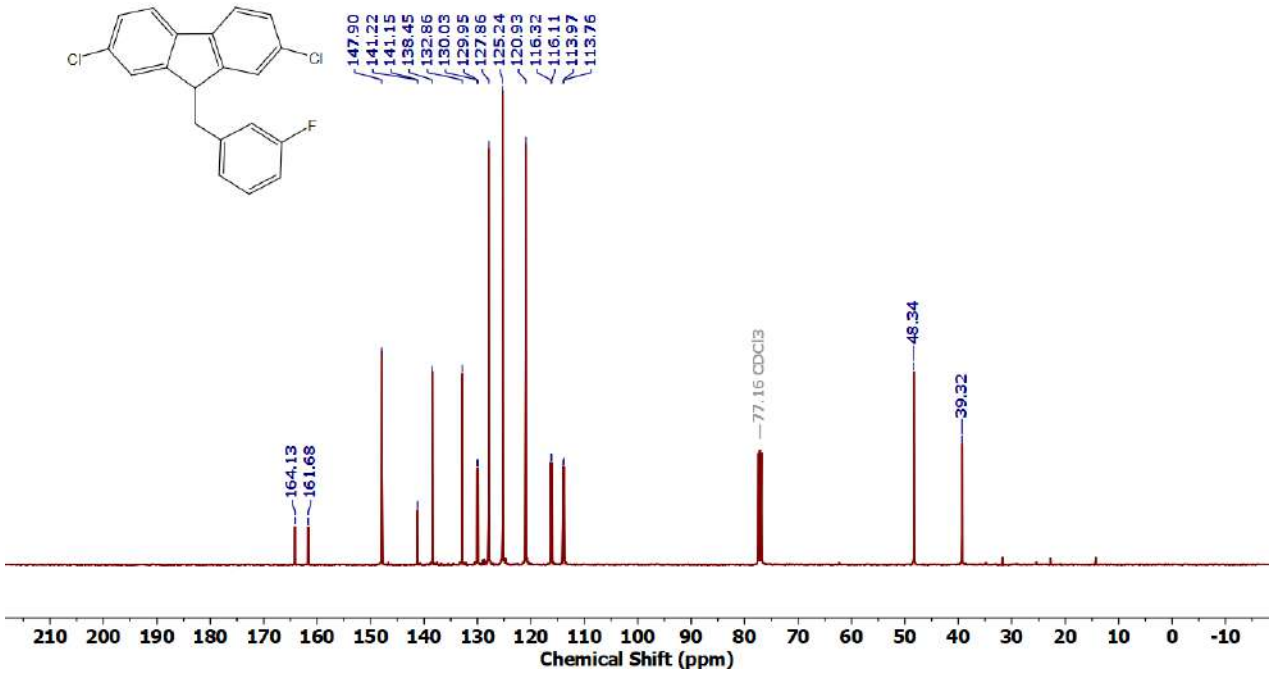

Figure 4.6.A82: ^{13}C{^{1}H} NMR Spectrum of **9d**

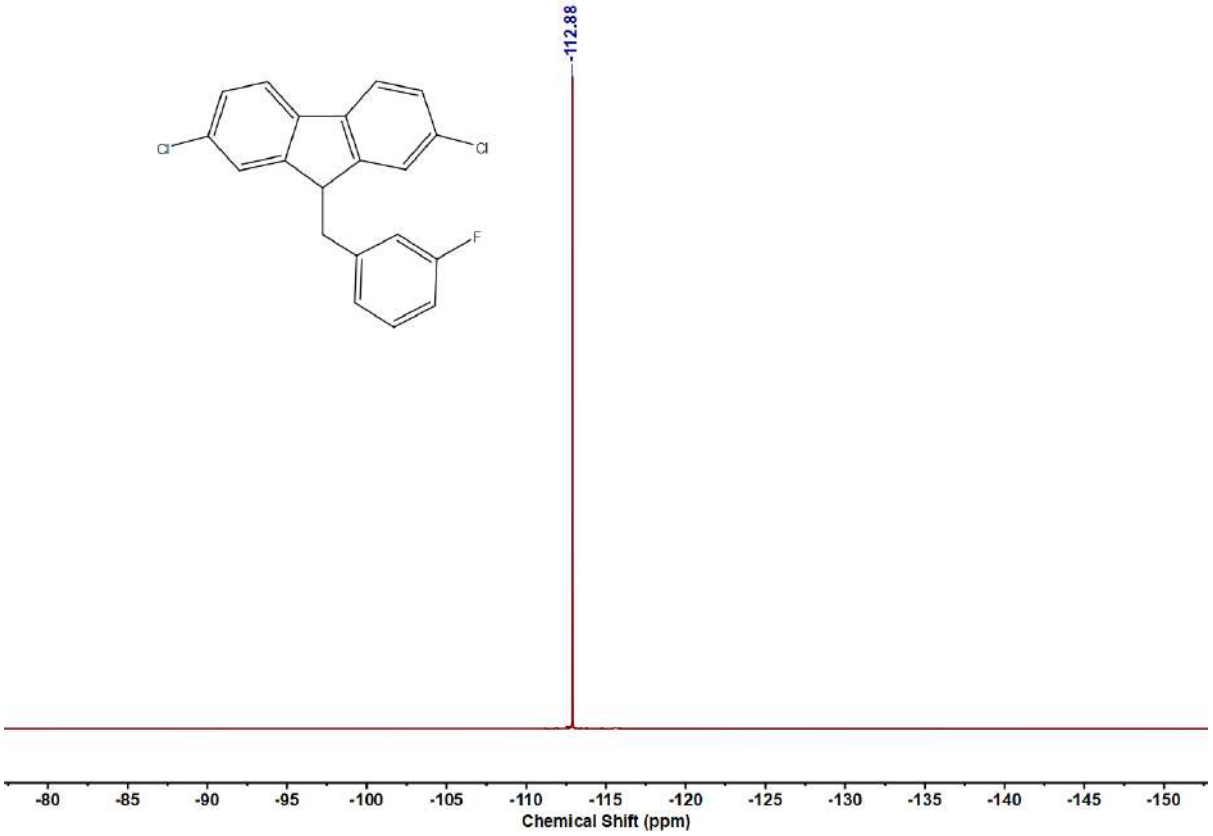

Figure 4.6.A83: ^{19}F NMR Spectrum of **9d**

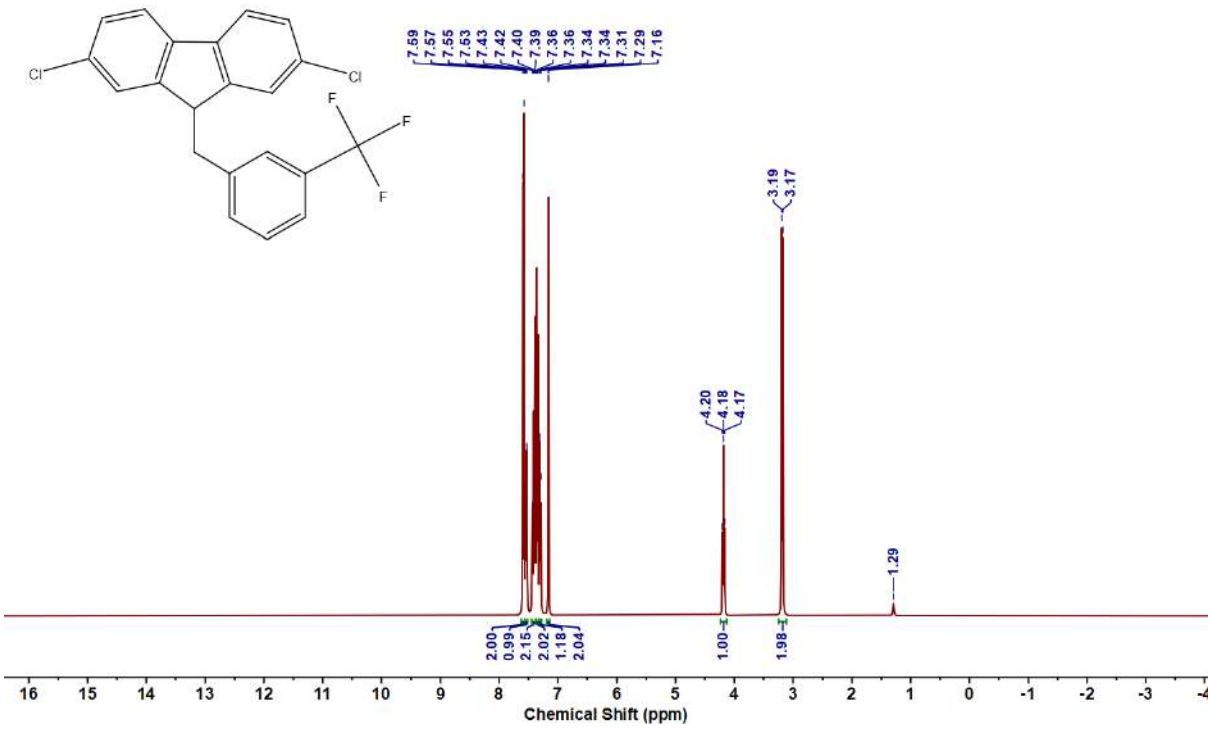

Figure 4.6.A84: ^{1}H NMR Spectrum of **9e**

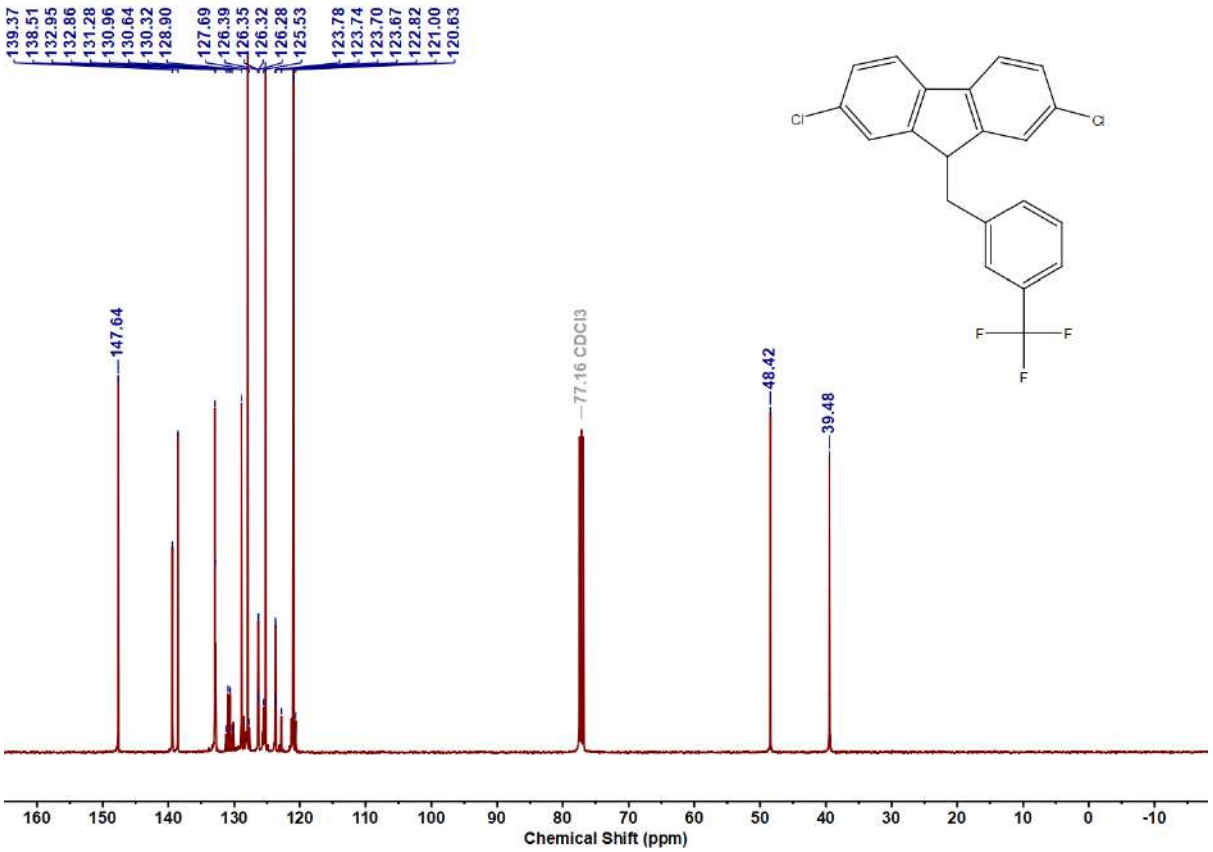

Figure 4.6.A85: $^{13}C\{^{1}H\}$ NMR Spectrum of **9e**

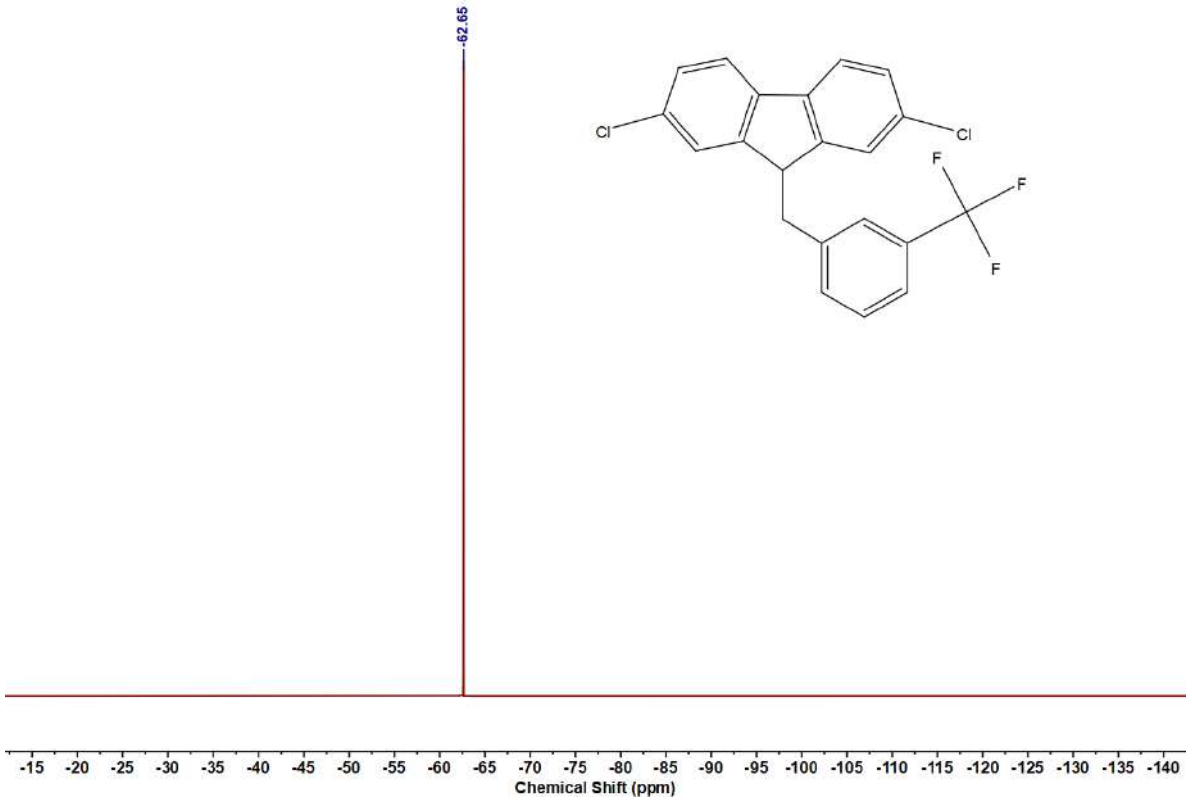

Figure 4.6.A86: ^{19}F NMR Spectrum of **9e**

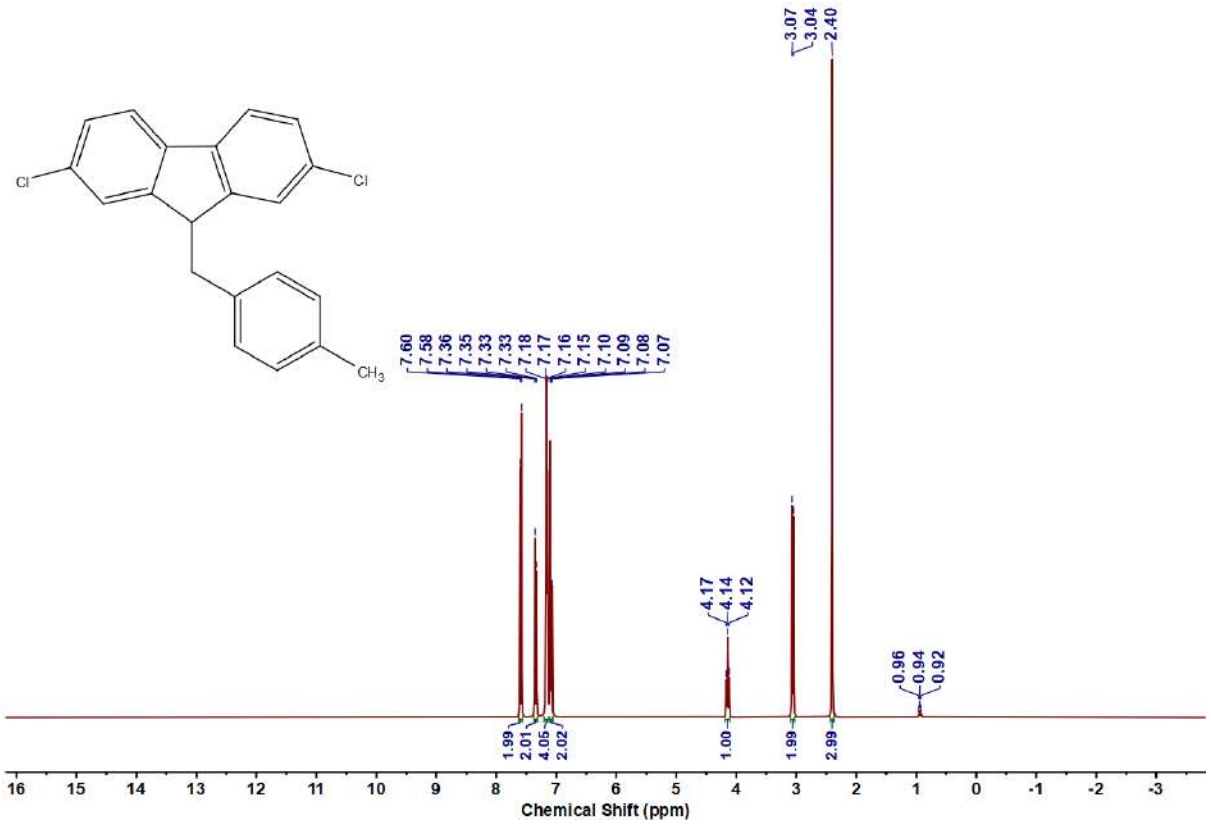

Figure 4.6.A87: ^{1}H NMR spectrum of **9f**

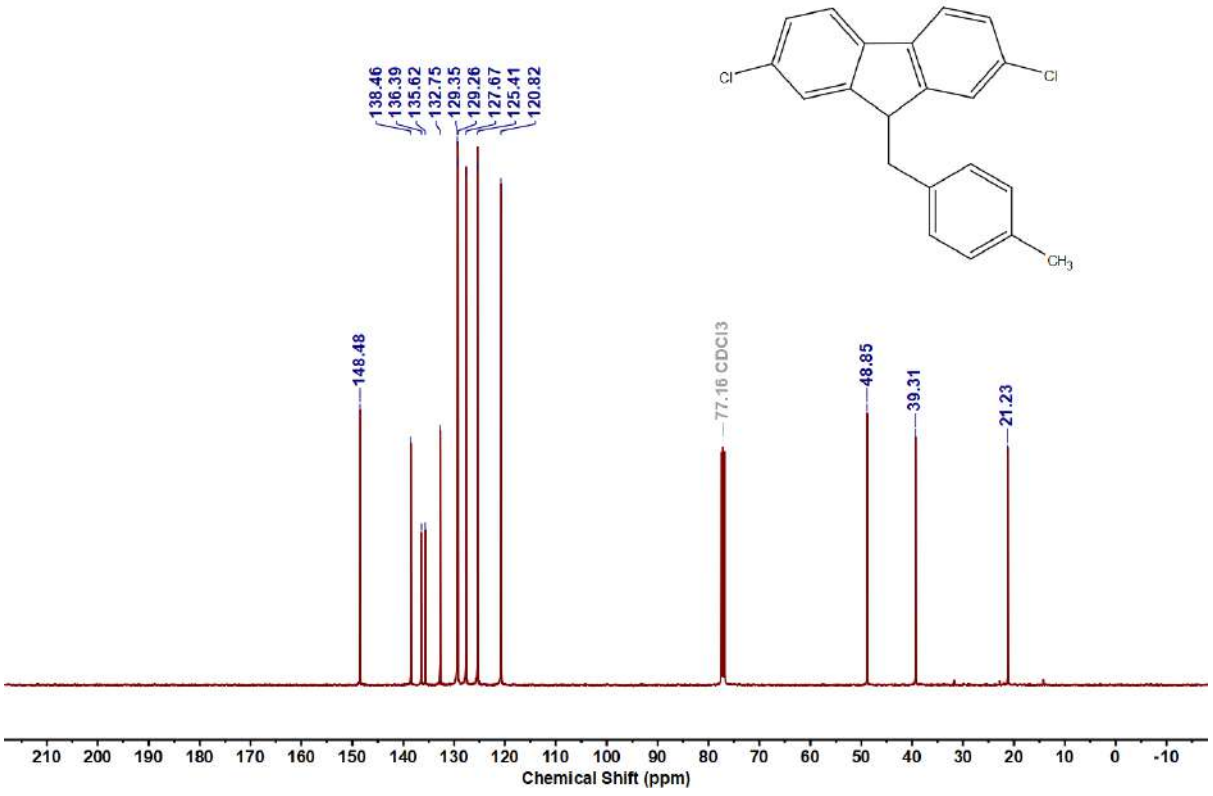

Figure 4.6.A88: ^{13}C{^{1}H} NMR Spectrum of **9f**

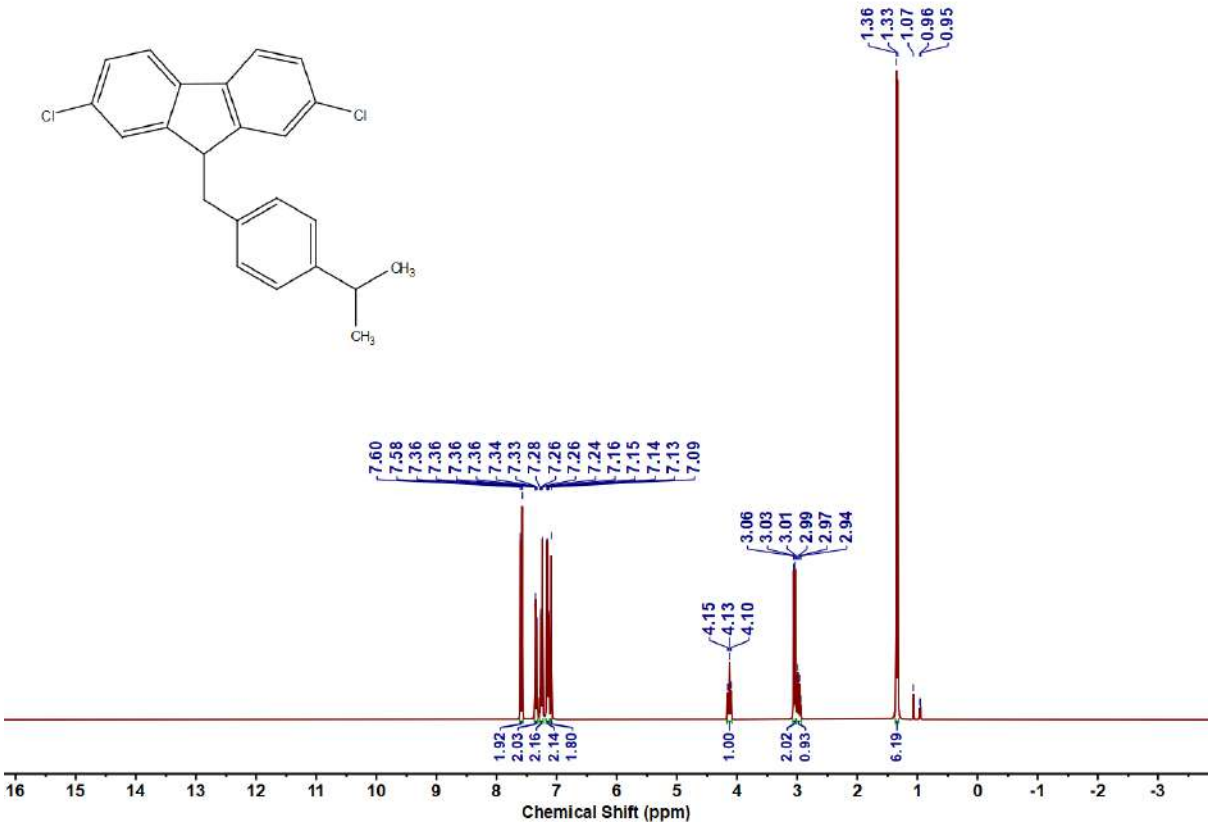

Figure 4.6.A89: ^{1}H NMR Spectrum of **9g**

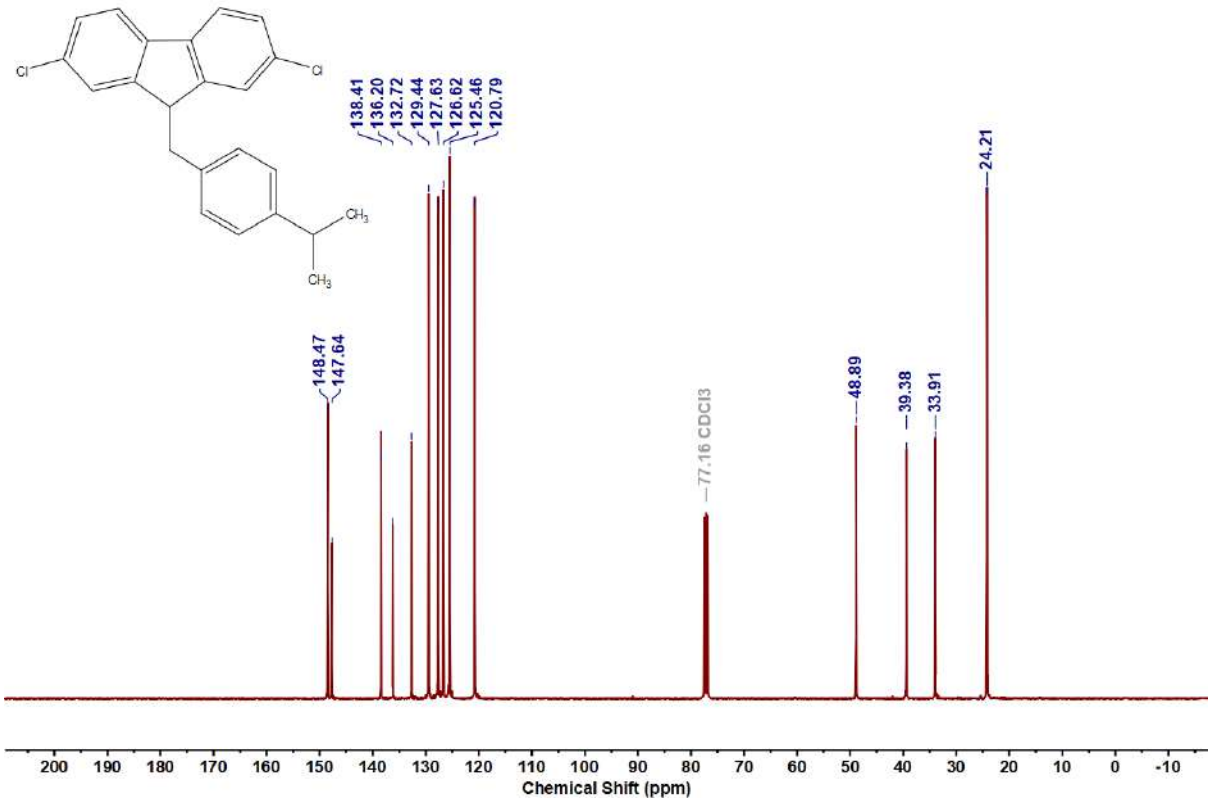

Figure 4.6.A90: ^{13}C{^{1}H} NMR Spectrum of **9g**

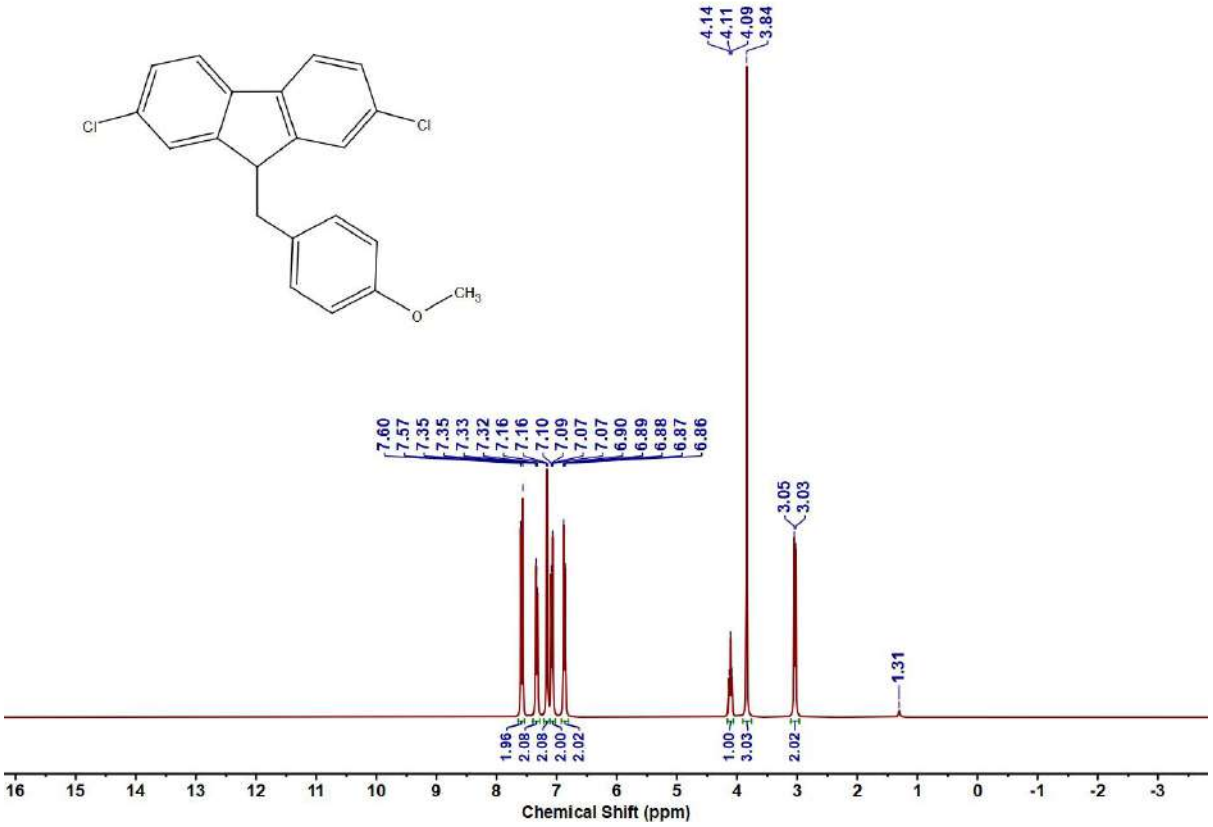

Figure 4.6.A91: ^{1}H NMR Spectrum of **9h**

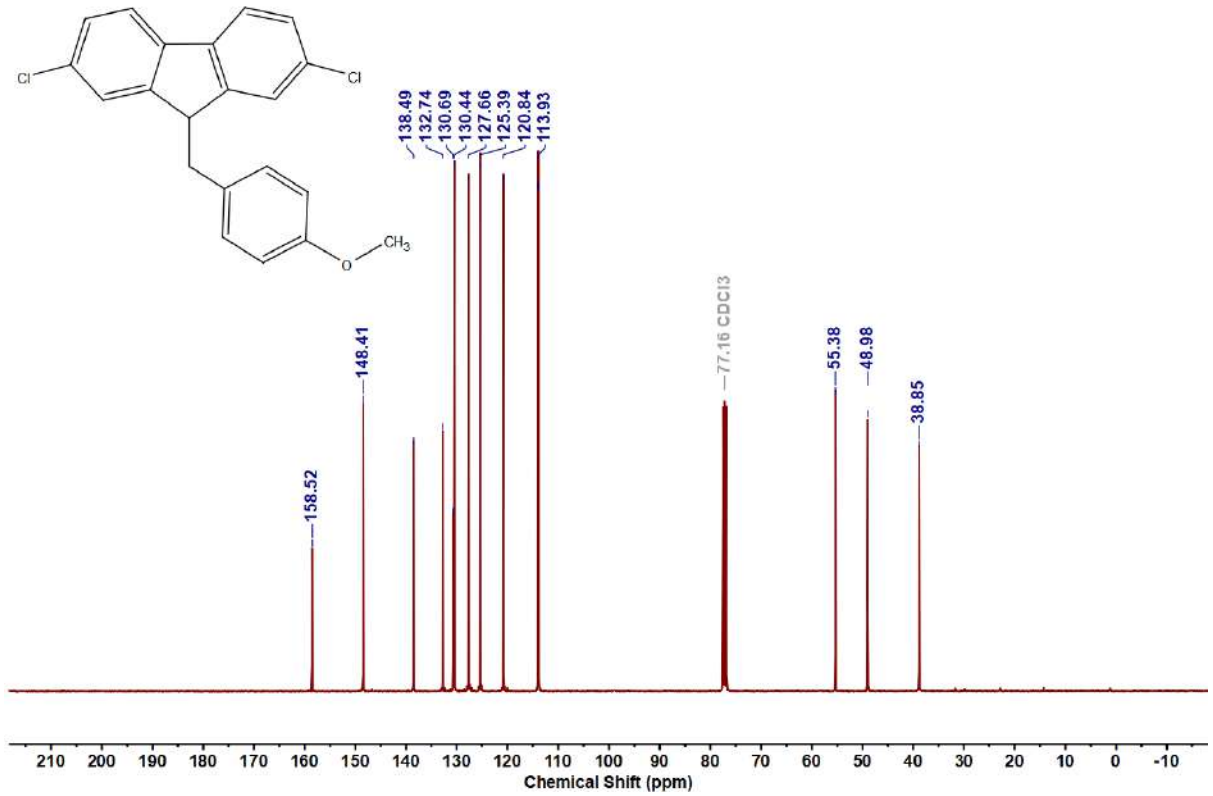

Figure 4.6.A92: ^{13}C{^{1}H} NMR Spectrum of **9h**

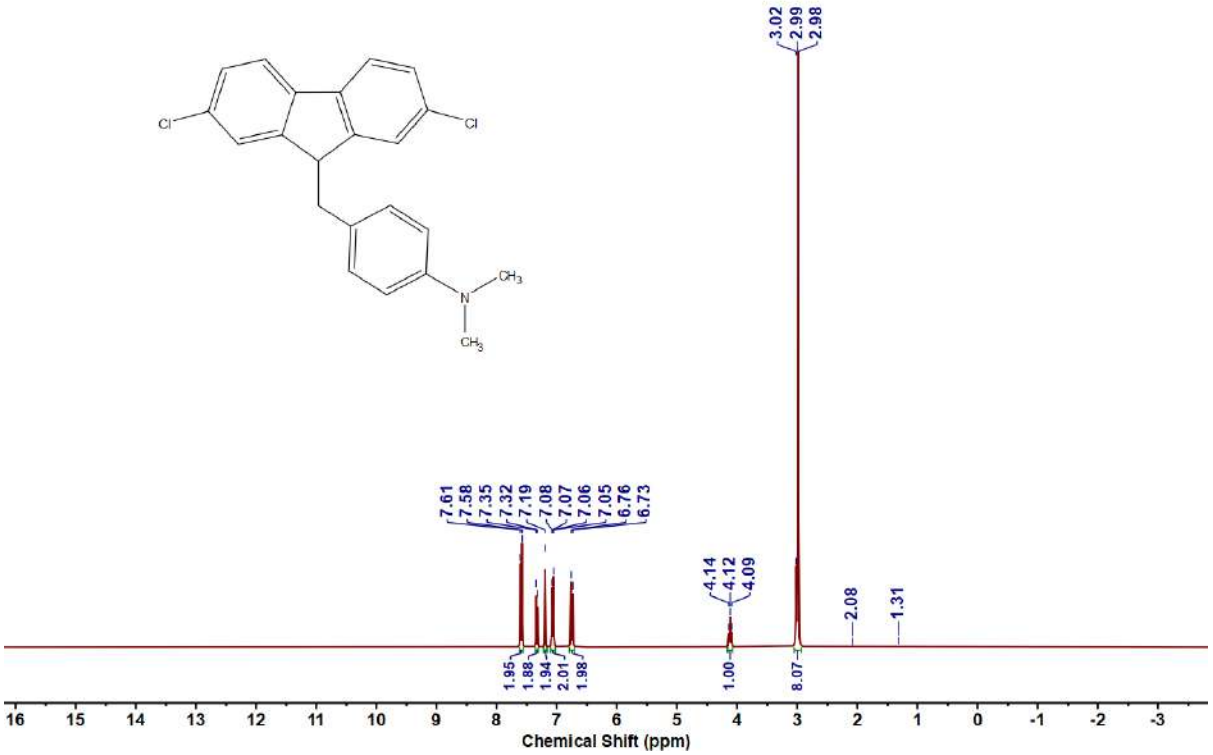

Figure 4.6.A93: ^{1}H NMR Spectrum of **9i**

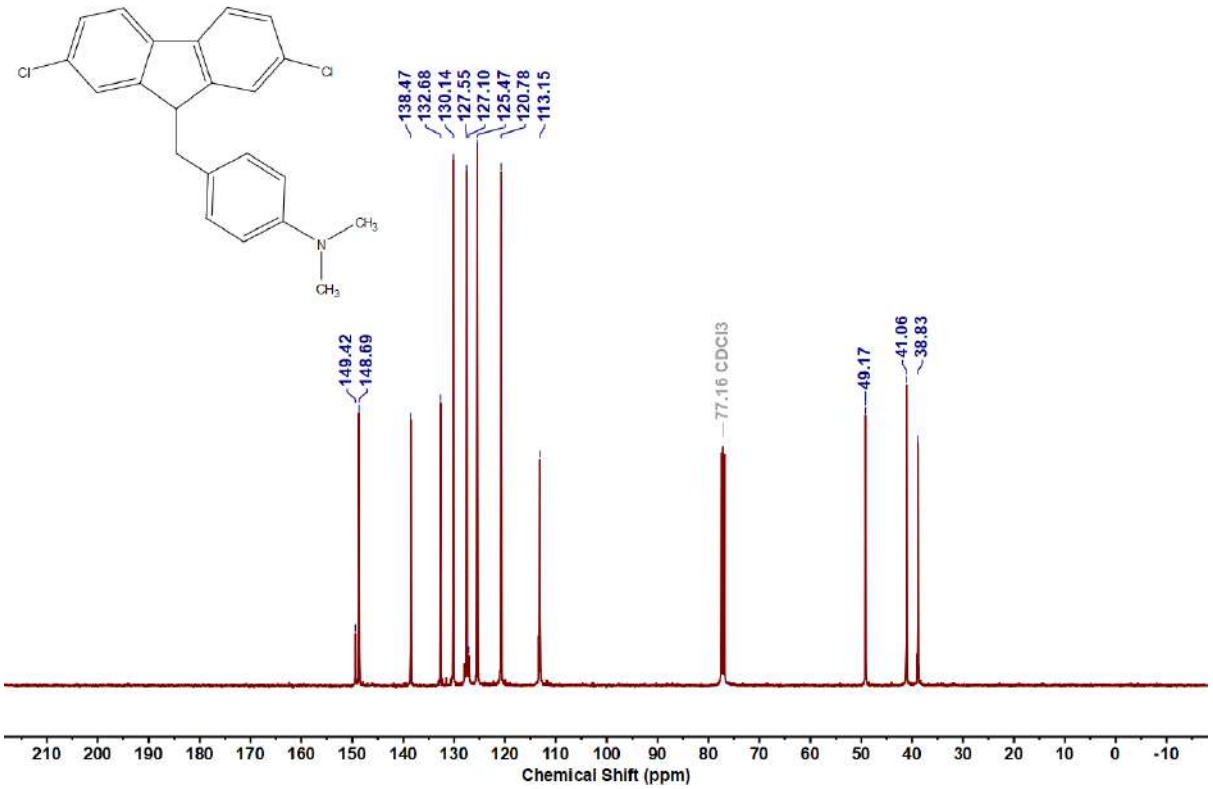

Figure 4.6.A94: ^{13}C{^{1}H} NMR Spectrum of **9i**

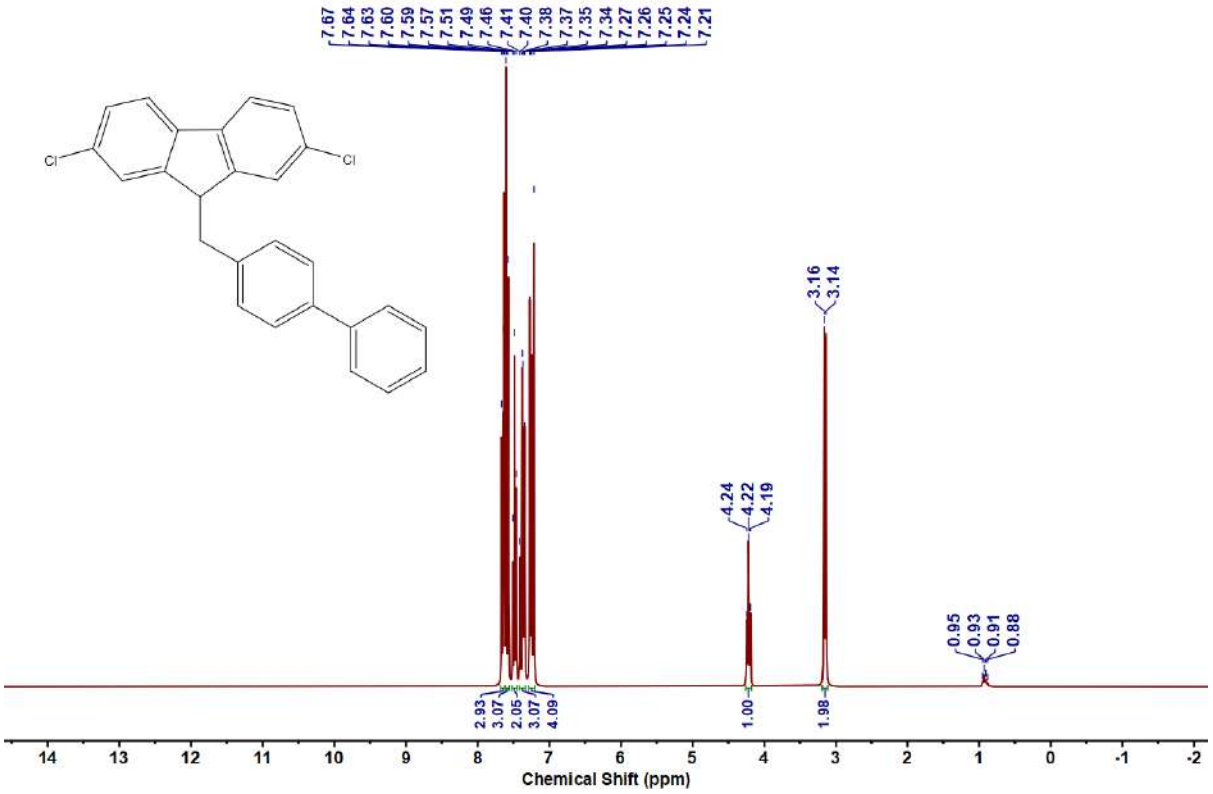

Figure 4.6.A95: ^{1}H NMR Spectrum of **9j**

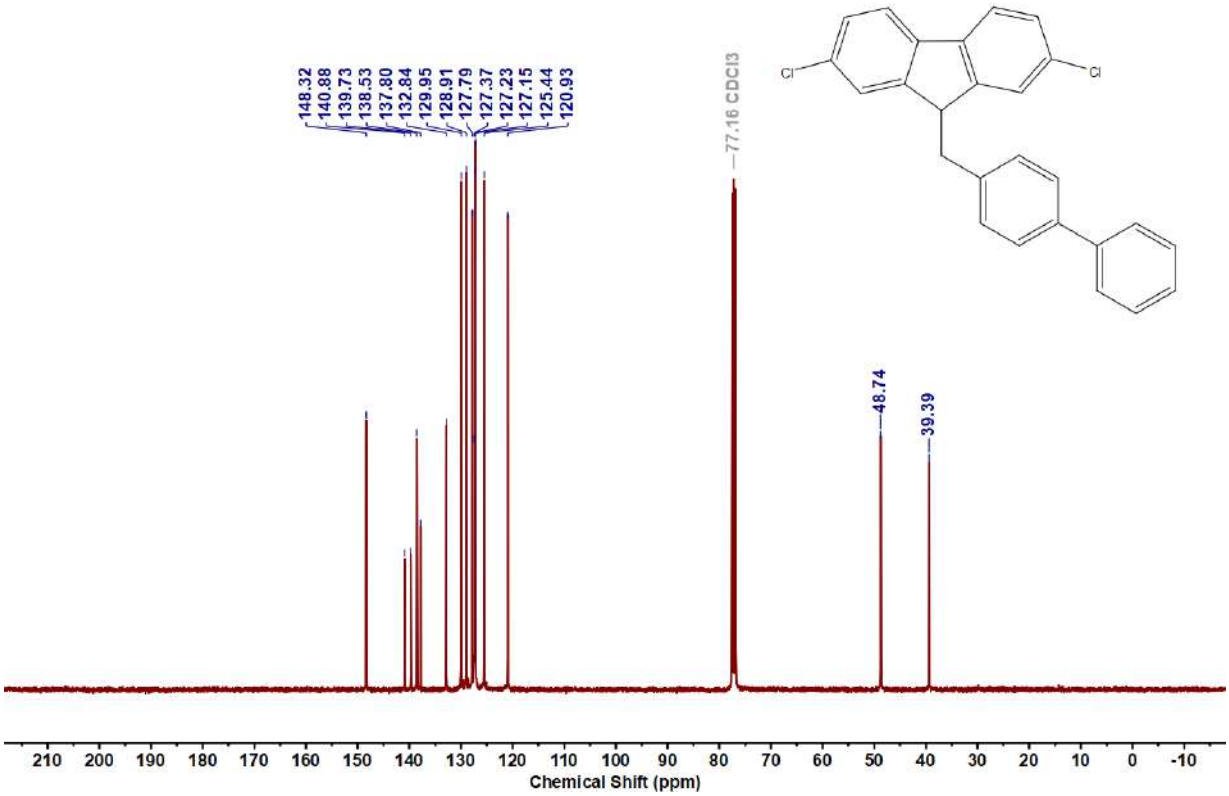

Figure 4.6.A96: $^{13}C\{^{1}H\}$ NMR Spectrum of **9j**

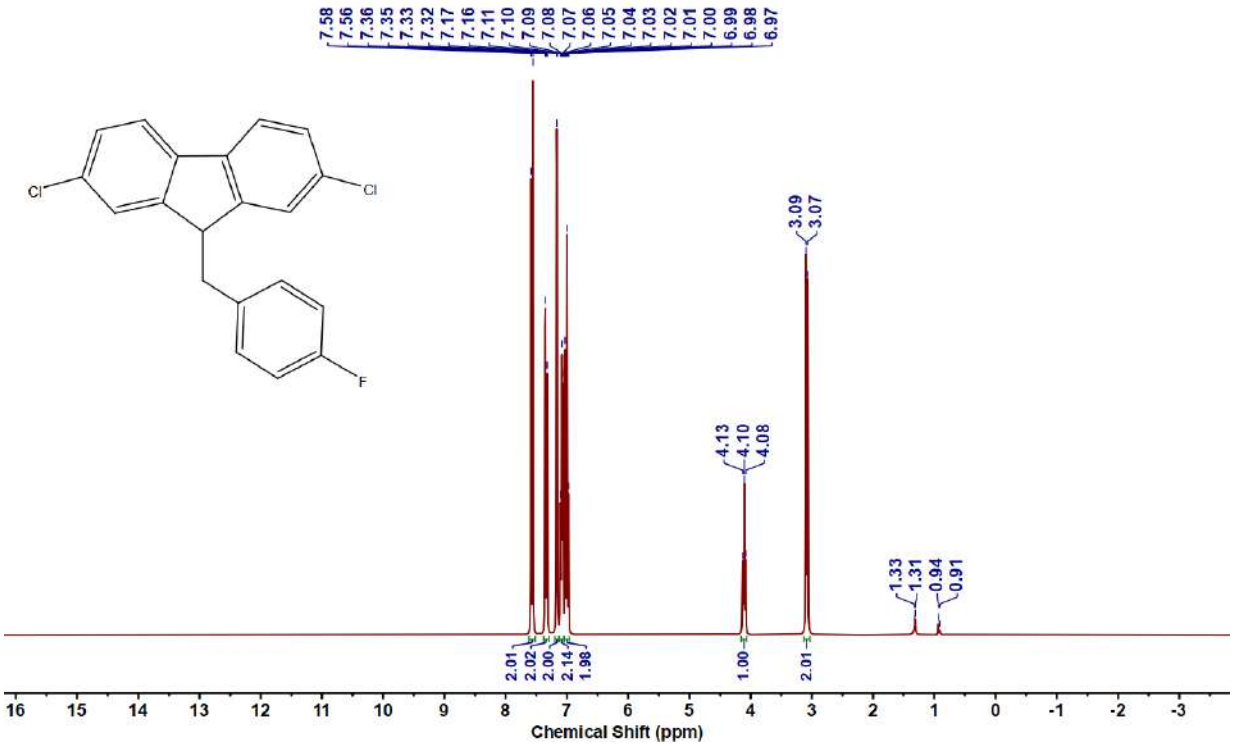

Figure 4.6.A97: ^{1}H NMR Spectrum of **9k**

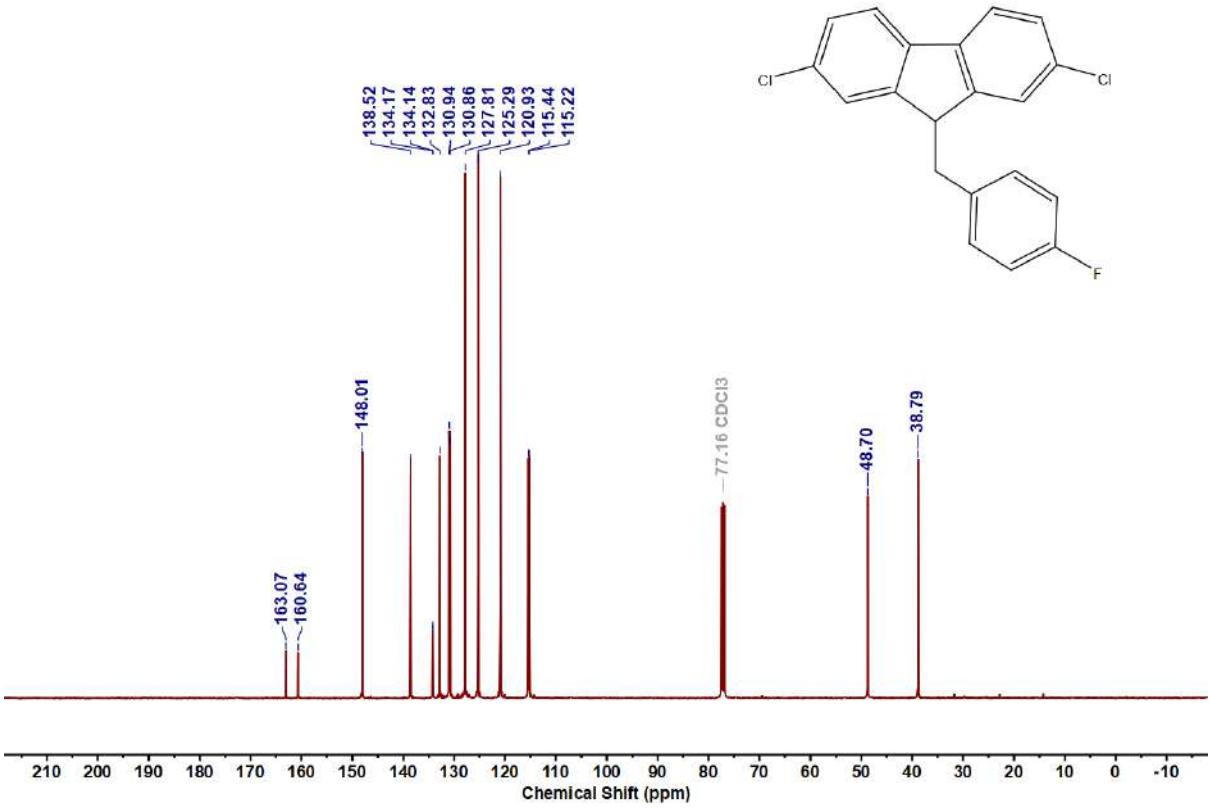

Figure 4.6.A98: ^{13}C{^{1}H} NMR Spectrum of **9k**

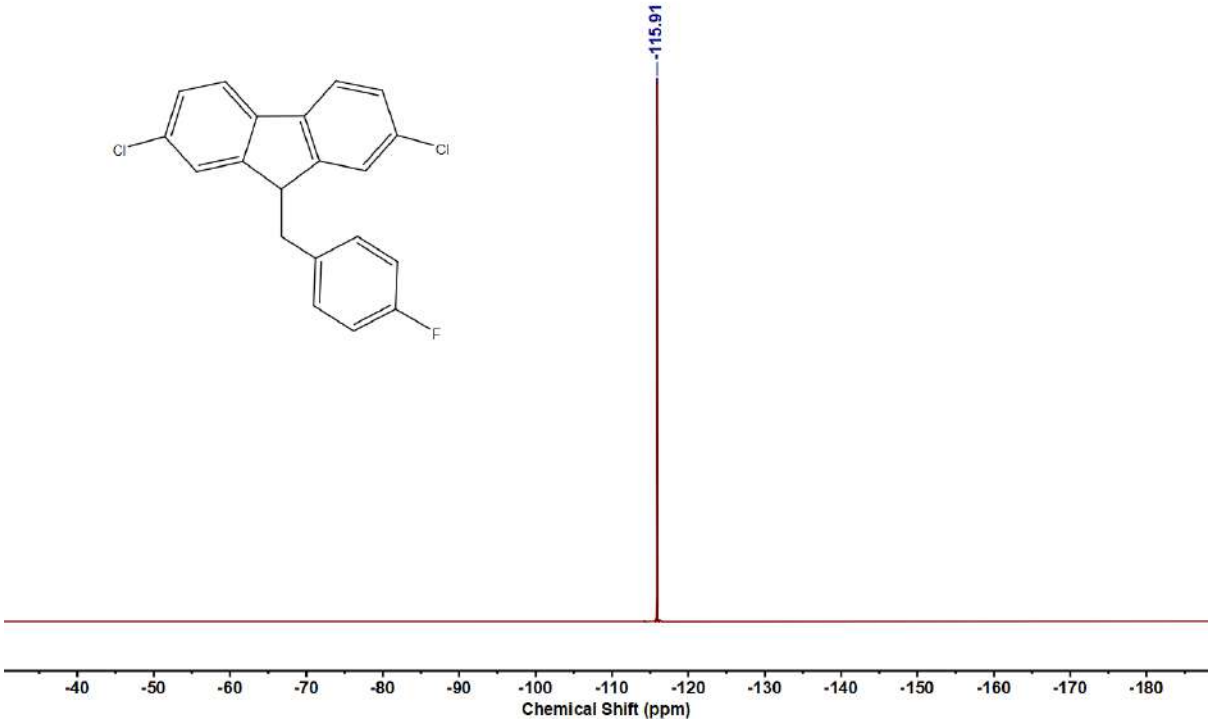

Figure 4.6.A99: ^{19}F NMR Spectrum of **9k**

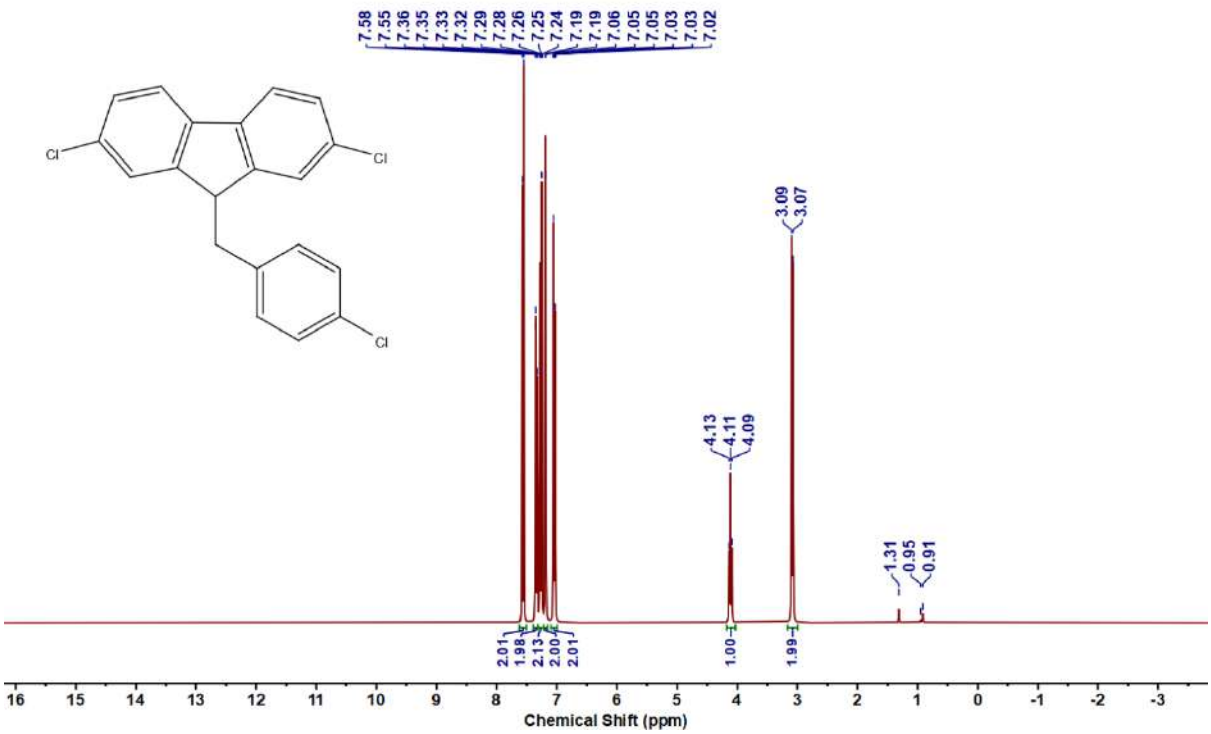

Figure 4.6.A100: ^{1}H NMR Spectrum of **9l**

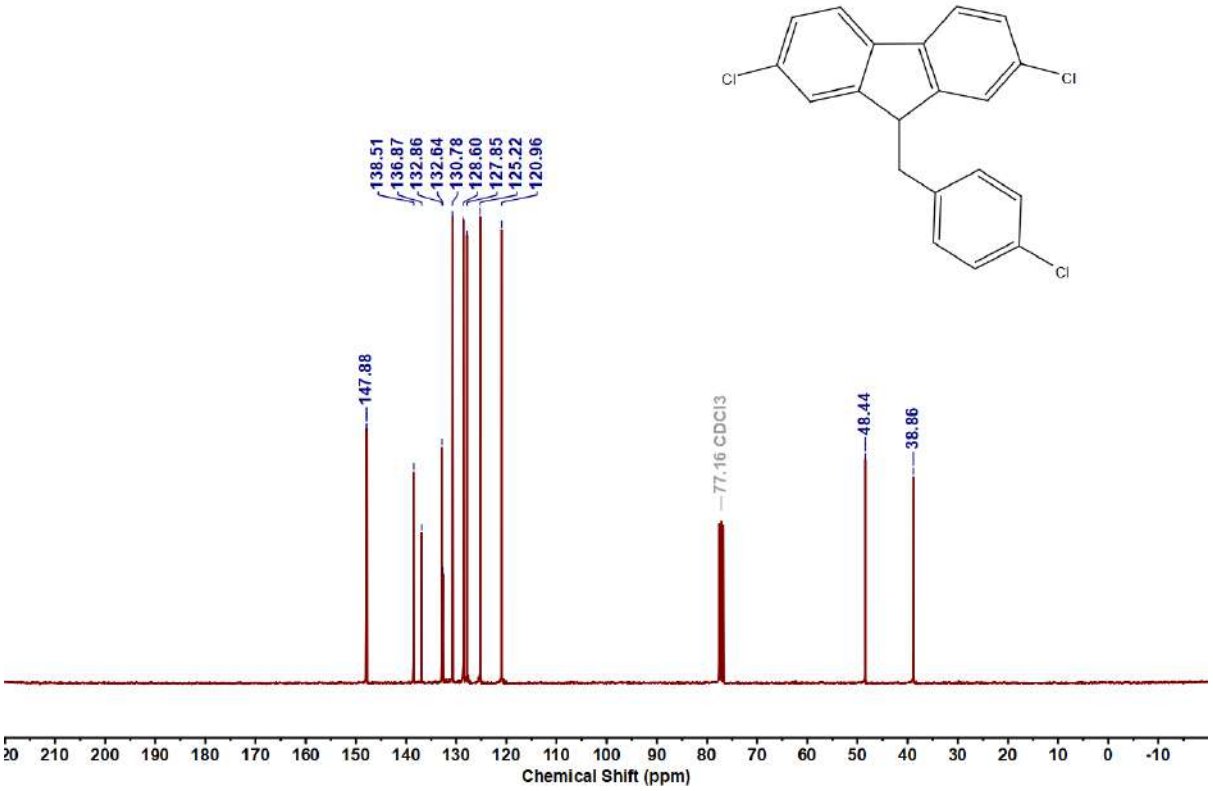

Figure 4.6.A101: $^{13}C\{^{1}H\}$ NMR Spectrum of **9l**

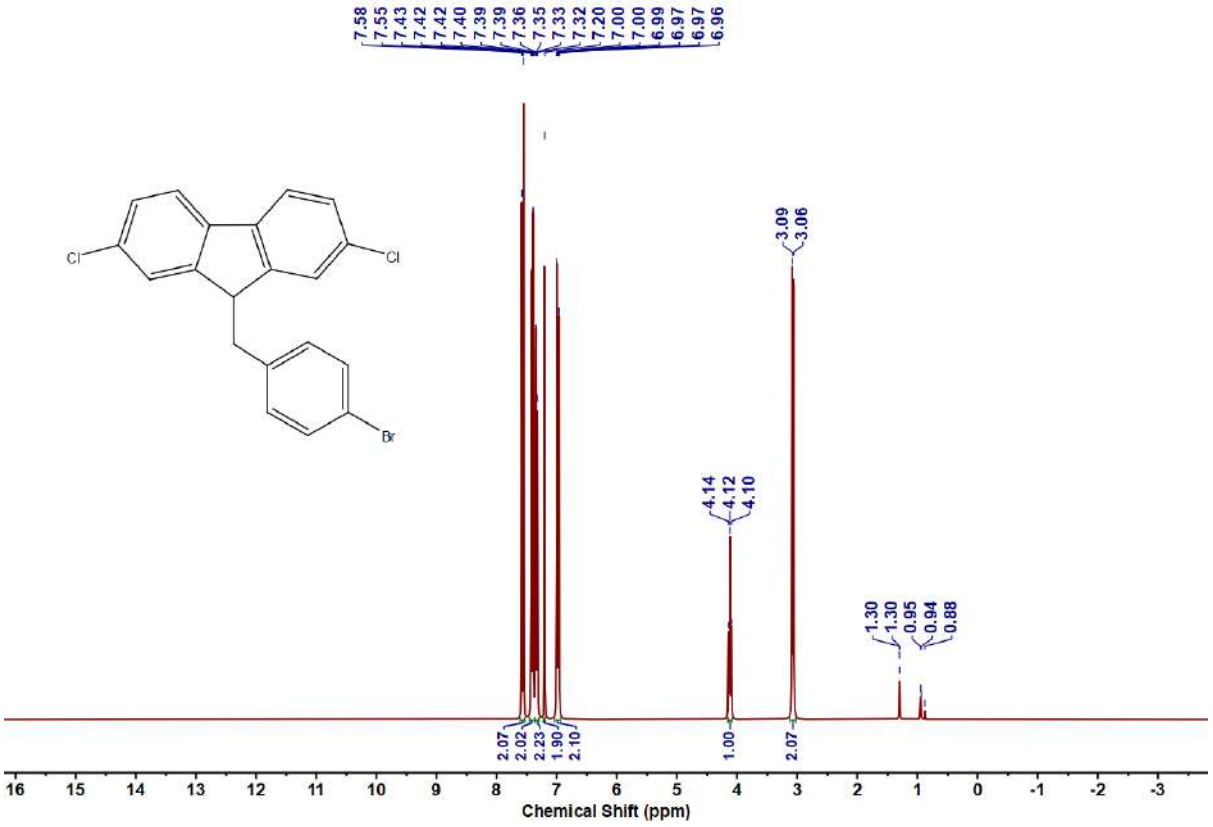

Figure 4.6.A102: ^{1}H NMR Spectrum of **9m**

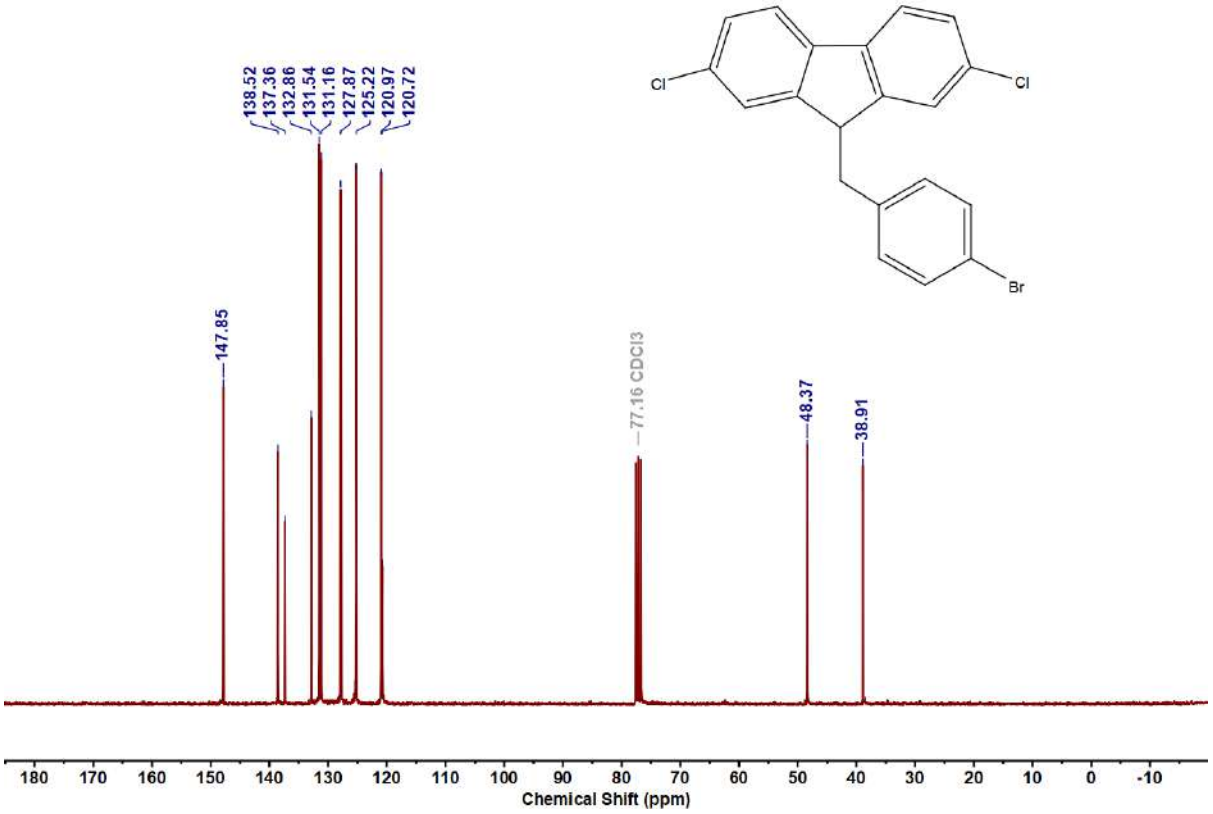

Figure 4.6.A103: $^{13}C\{^{1}H\}$ NMR Spectrum of **9m**

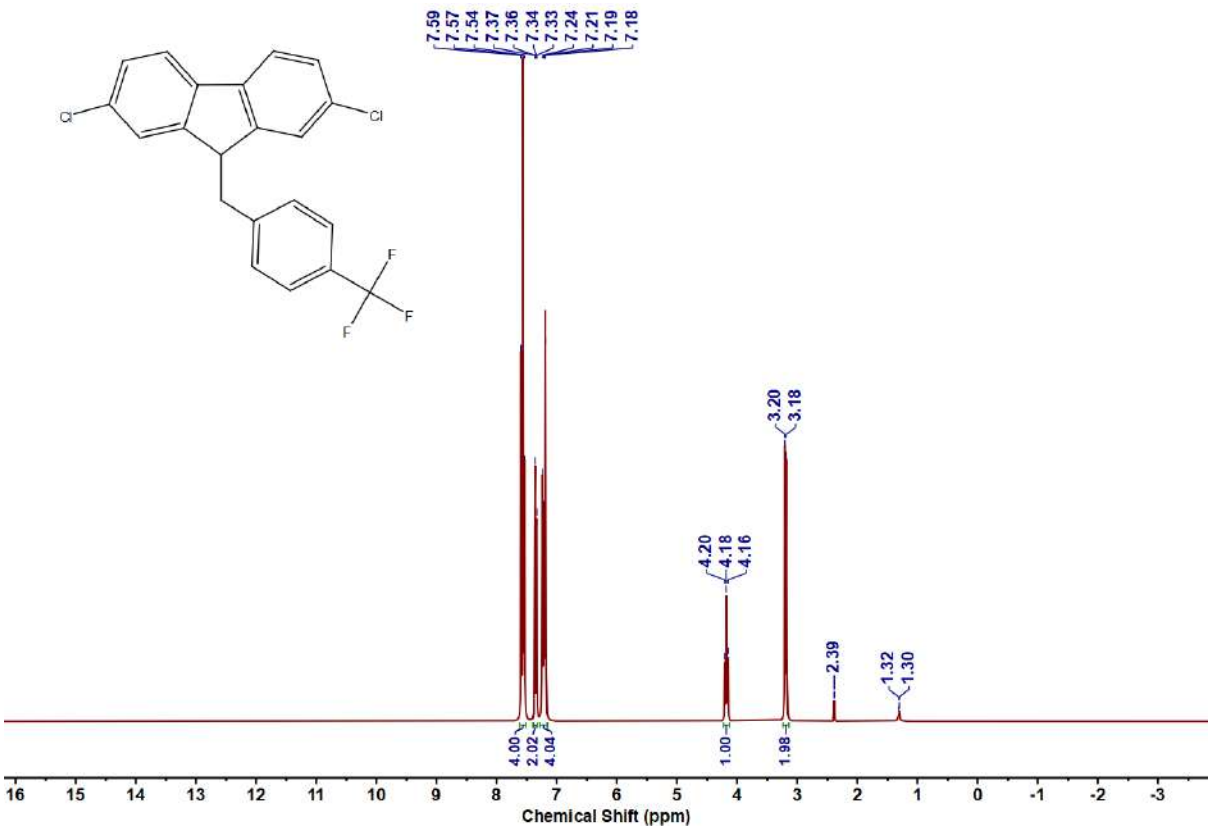

Figure 4.6.A104: ^{1}H NMR Spectrum of **9n**

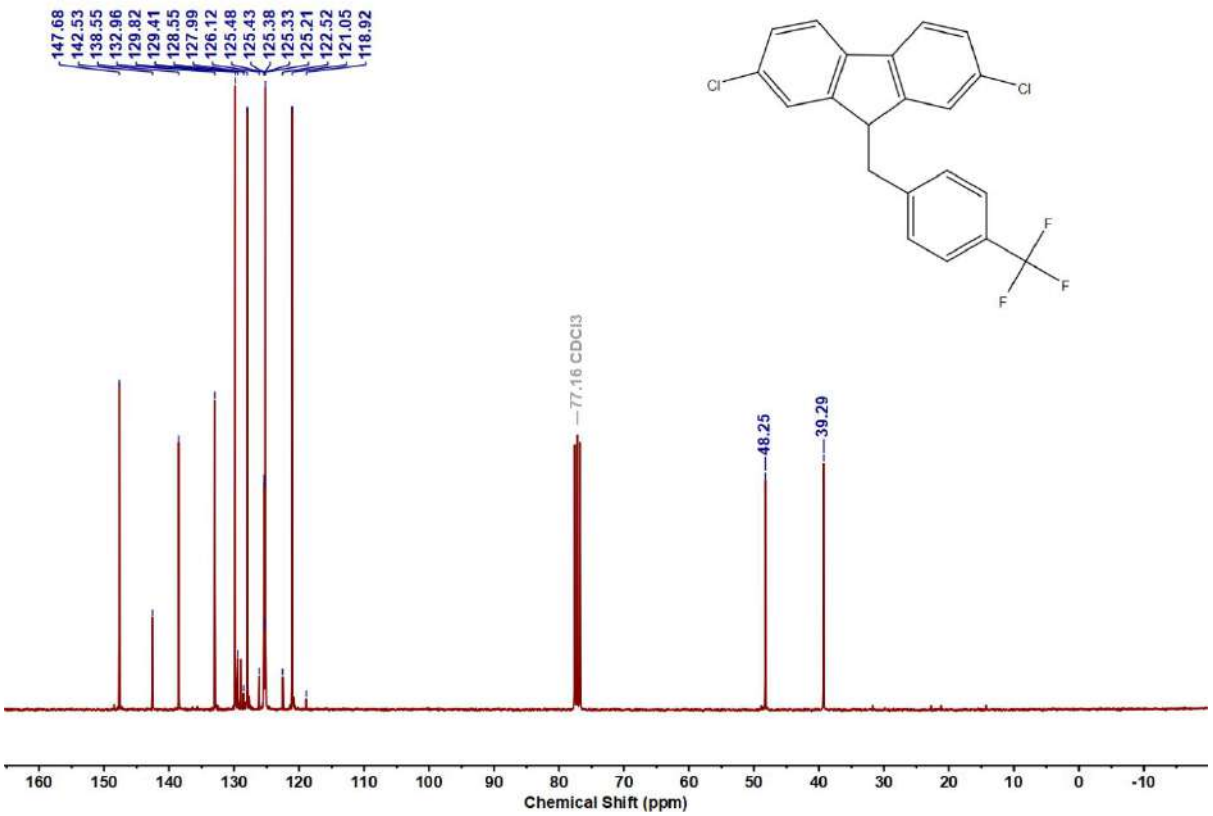

Figure 4.6.A105: $^{13}C\{^{1}H\}$ NMR Spectrum of **9n**

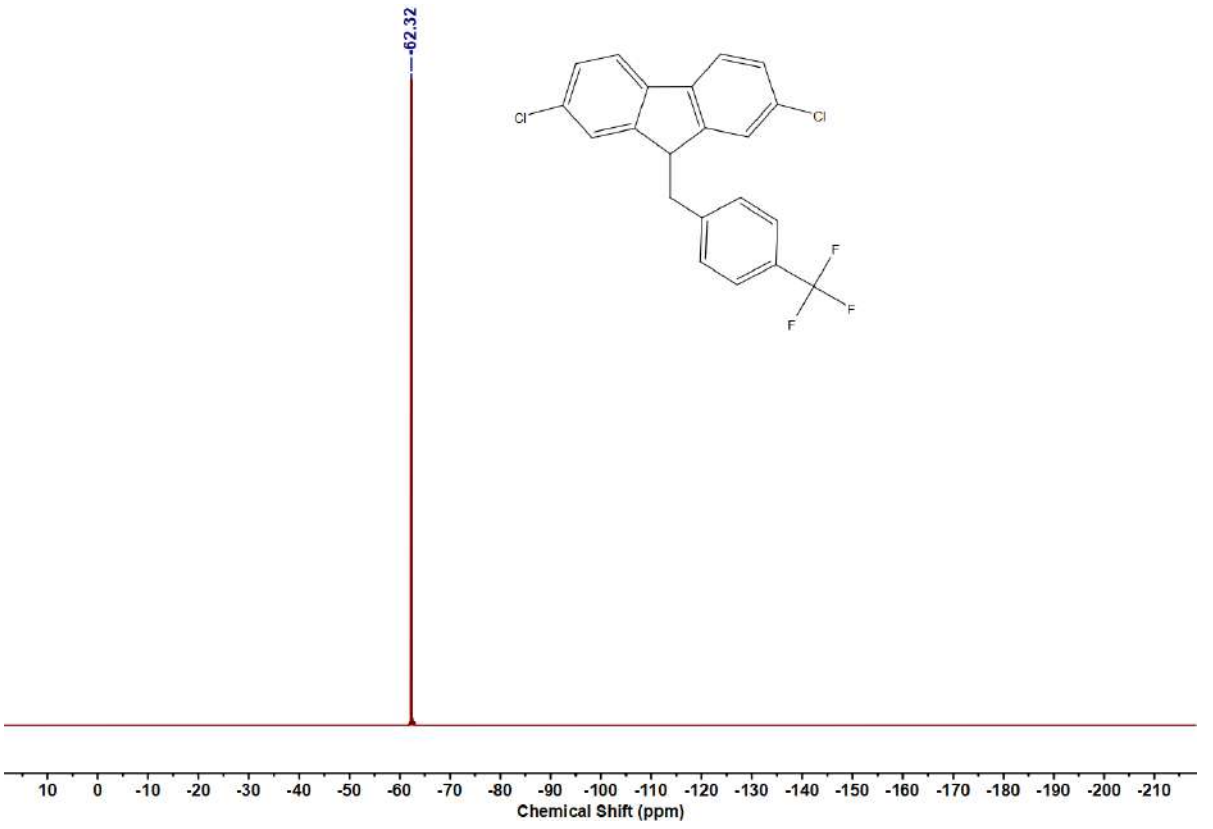

Figure 4.6.A106: ^{19}F NMR Spectrum of **9n**

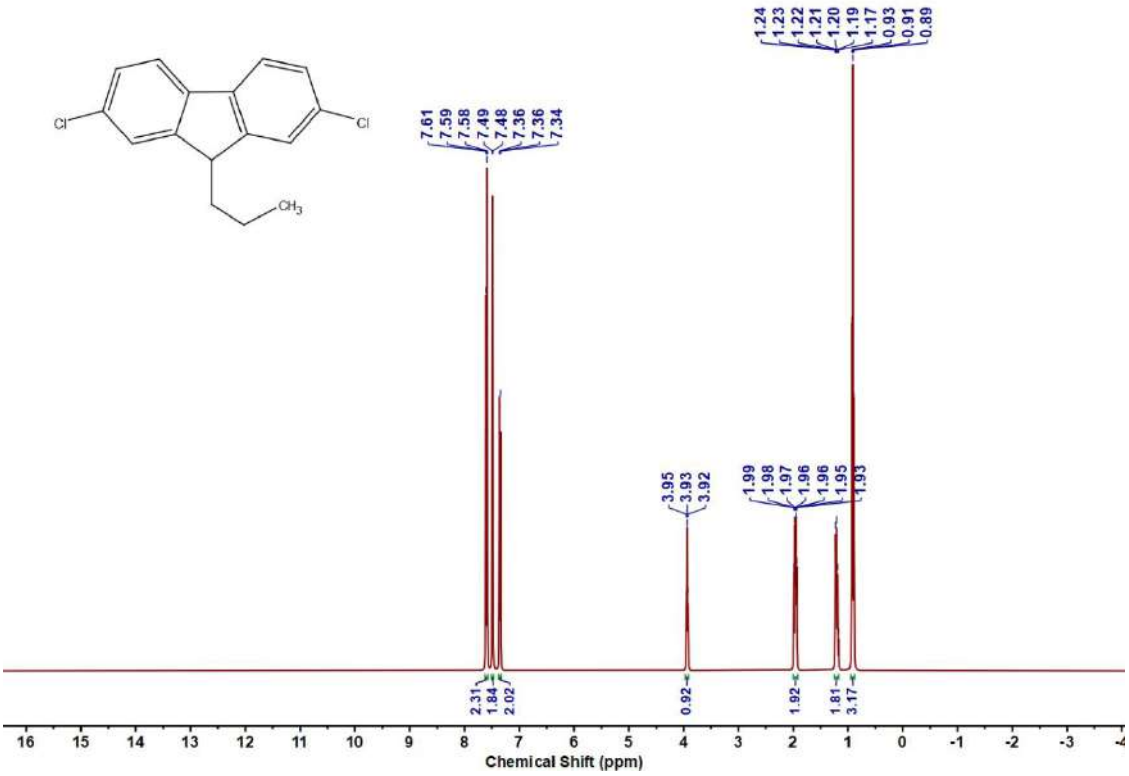

Figure 4.6.A107: ^{1}H NMR Spectrum of **9o**

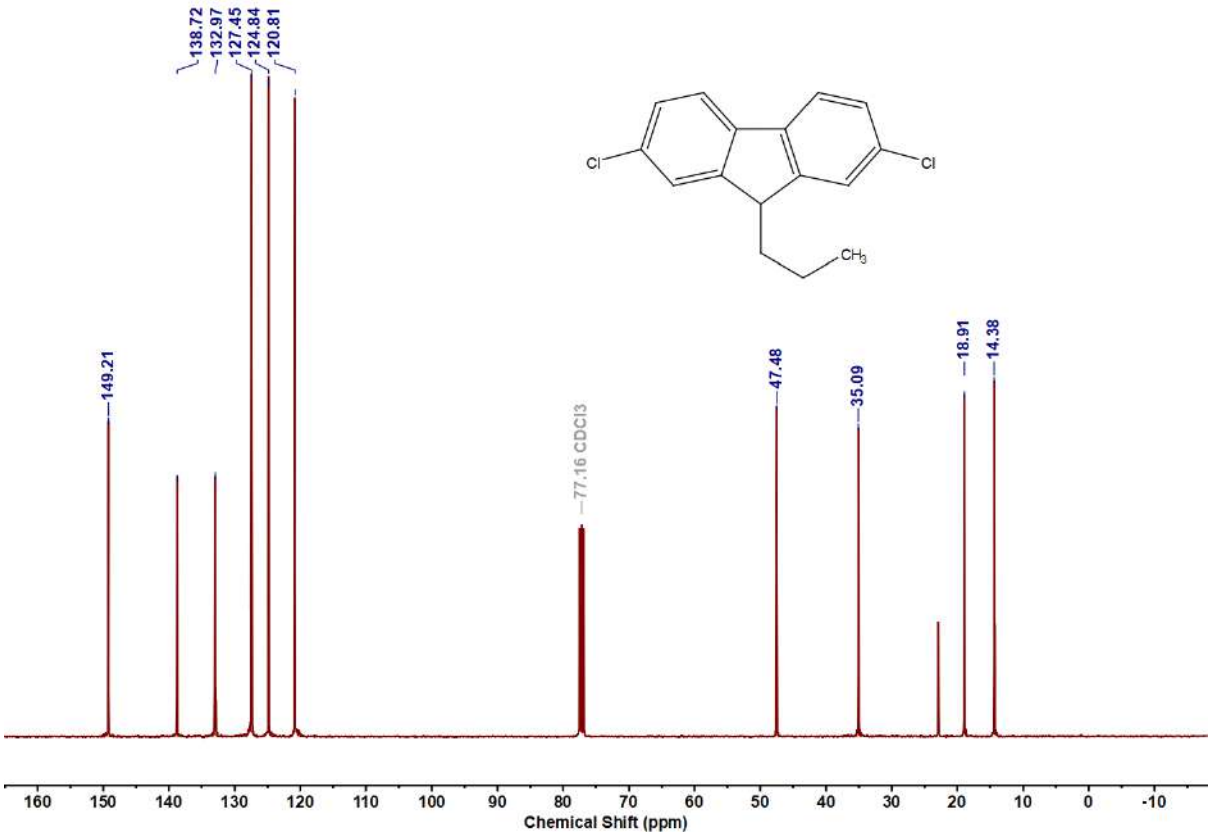

Figure 4.6.A108: $^{13}C\{^{1}H\}$ NMR Spectrum of **9o**

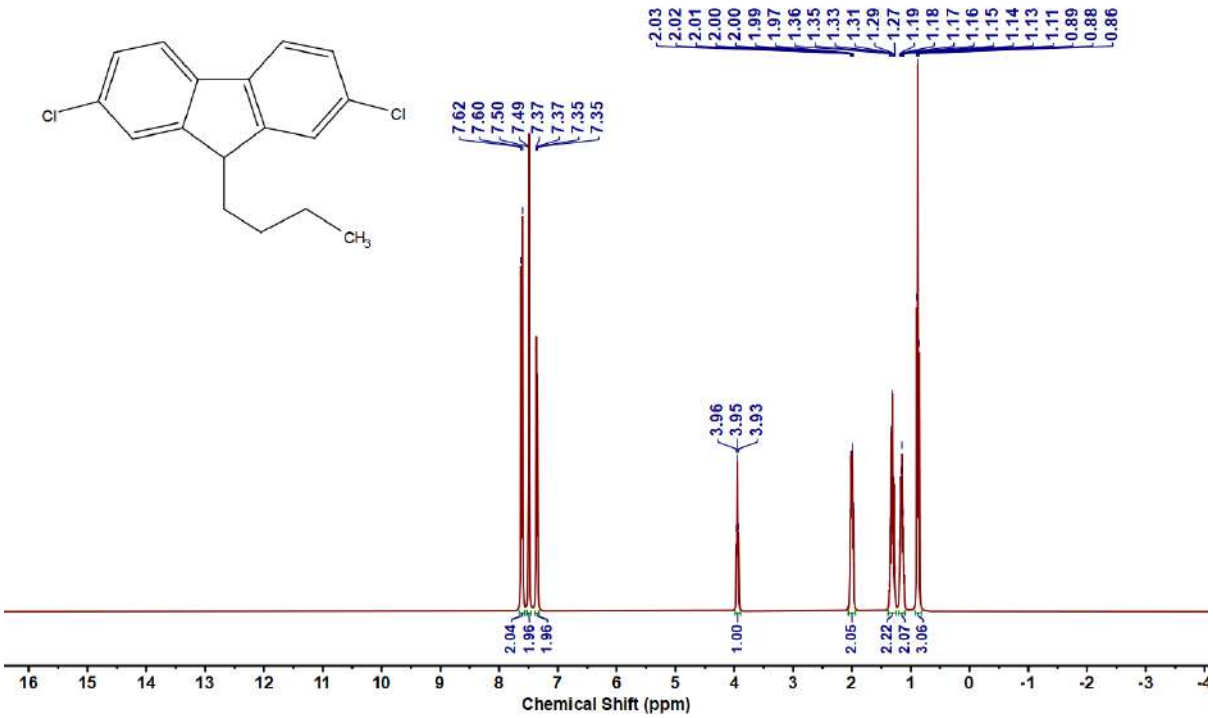

Figure 4.6.A109: ^{1}H NMR Spectrum of **9p**

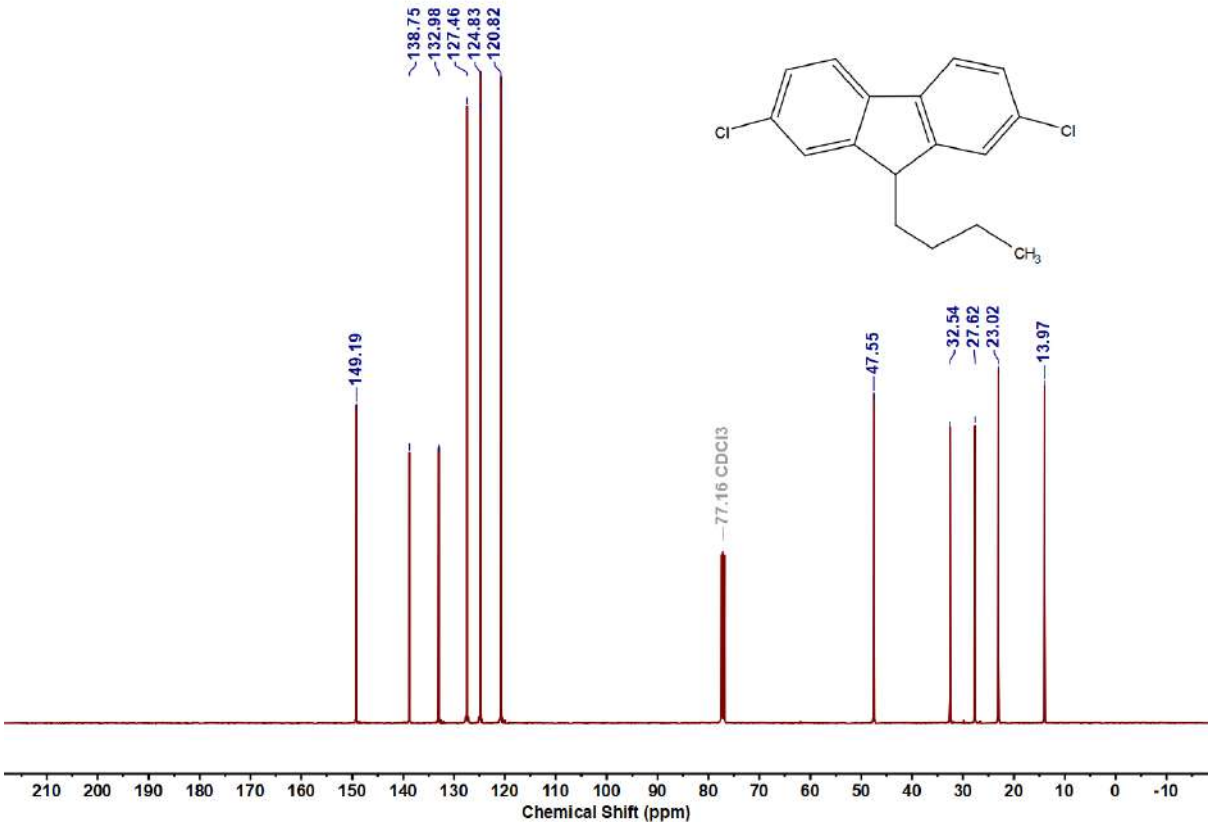

Figure 4.6.A110: $^{13}C\{^{1}H\}$ NMR Spectrum of **9p**

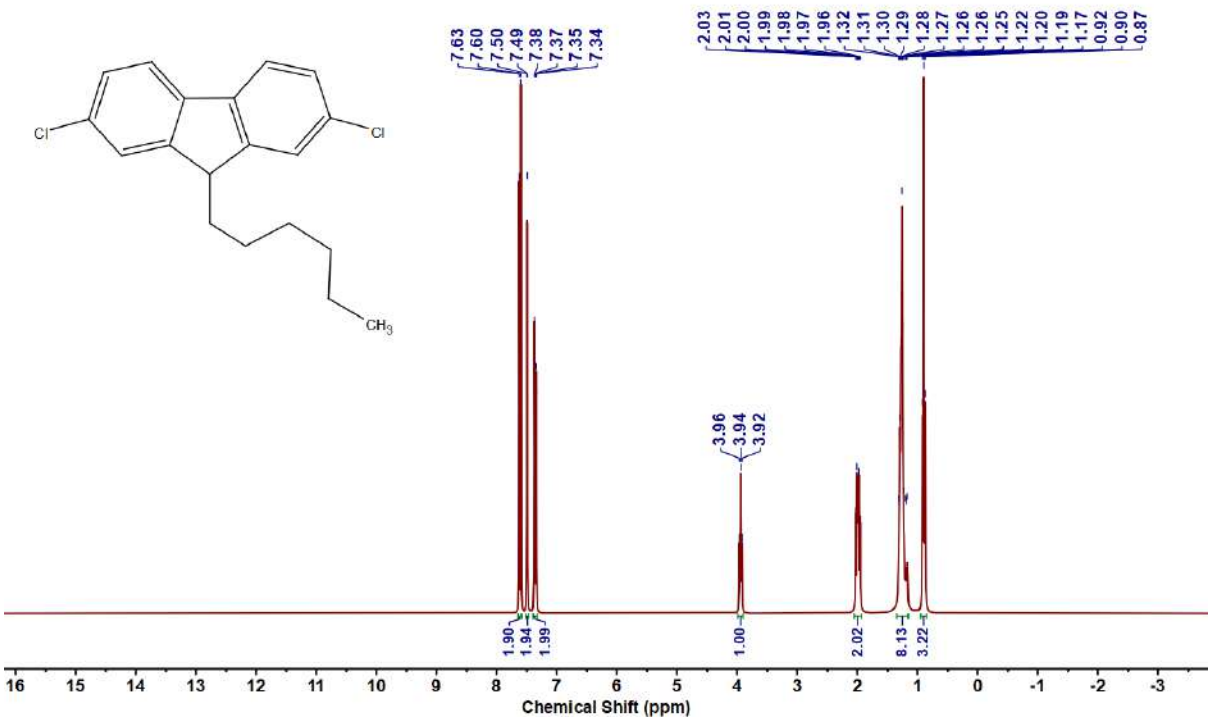

Figure 4.6.A111: ^{1}H NMR Spectrum of **9q**

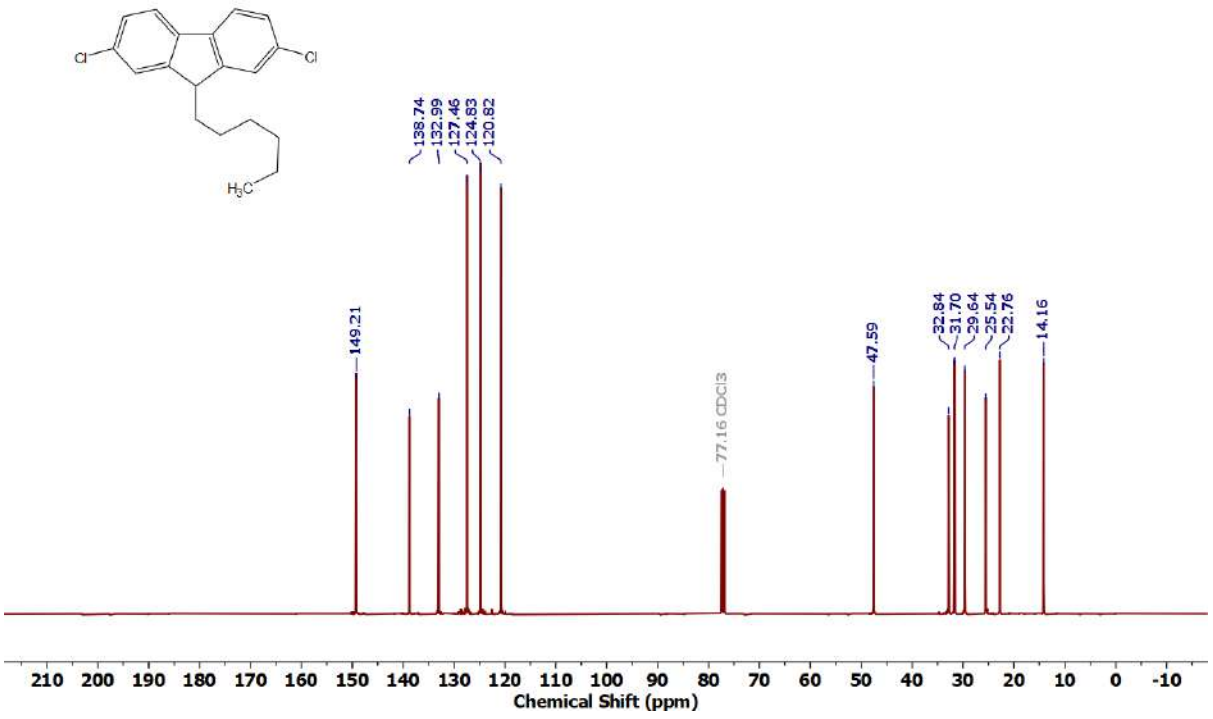

Figure 4.6.A112: ^{13}C{^{1}H} NMR Spectrum of **9q**

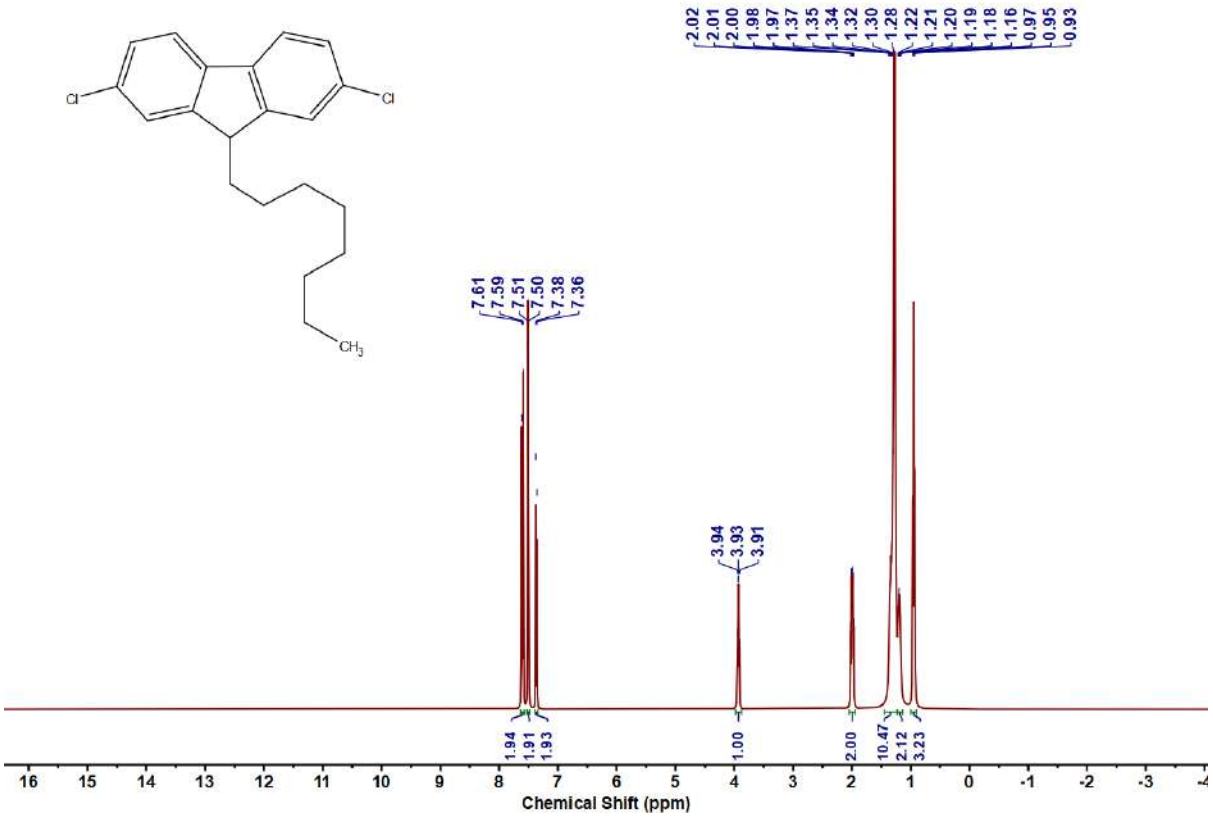

Figure 4.6.A113: ^{1}H NMR Spectrum of **9r**

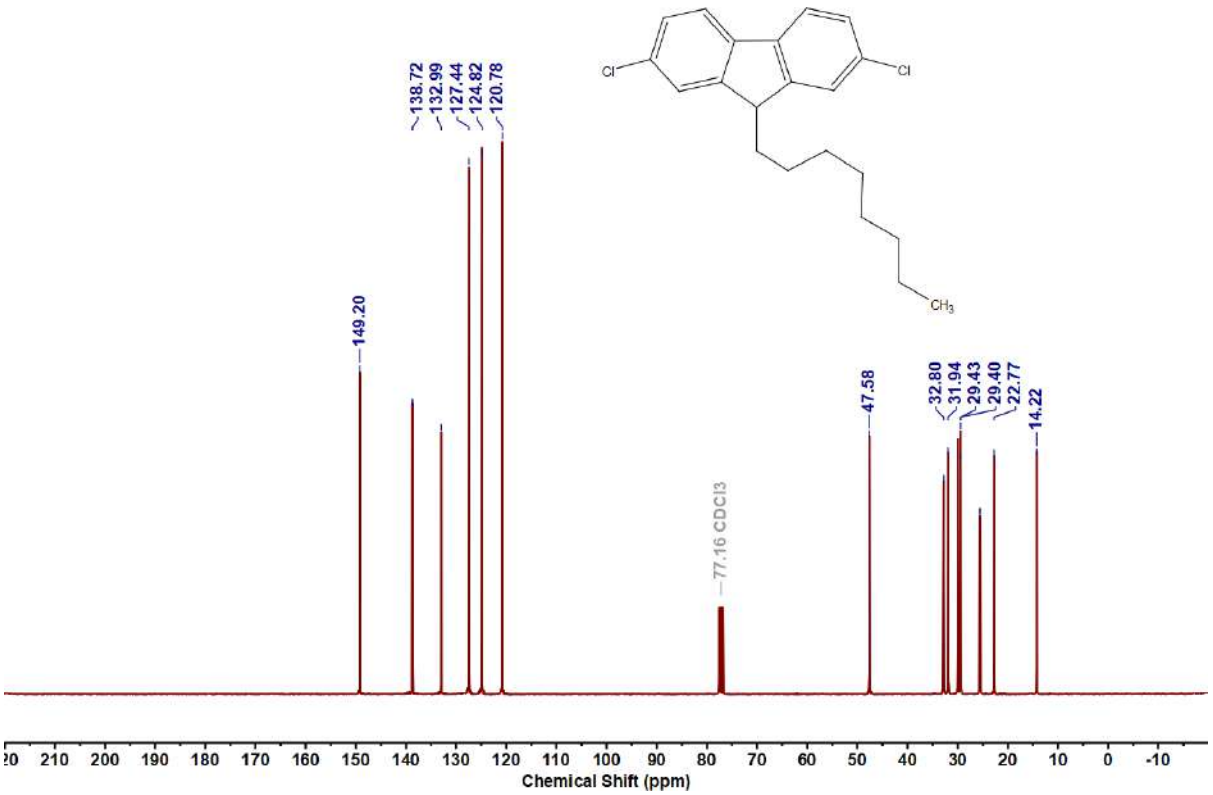

Figure 4.6.A114: $^{13}C\{^{1}H\}$ NMR Spectrum of **9r**

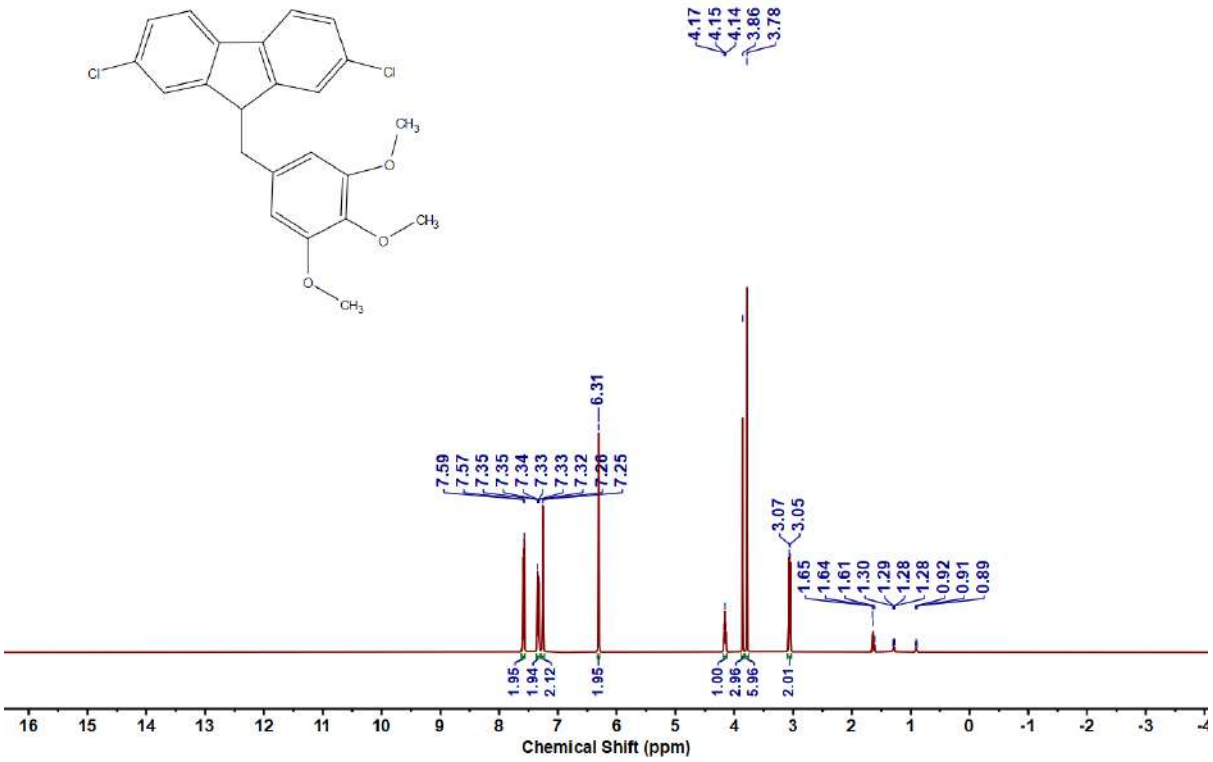

Figure 4.6.A115: ^{1}H NMR Spectrum of **9s**

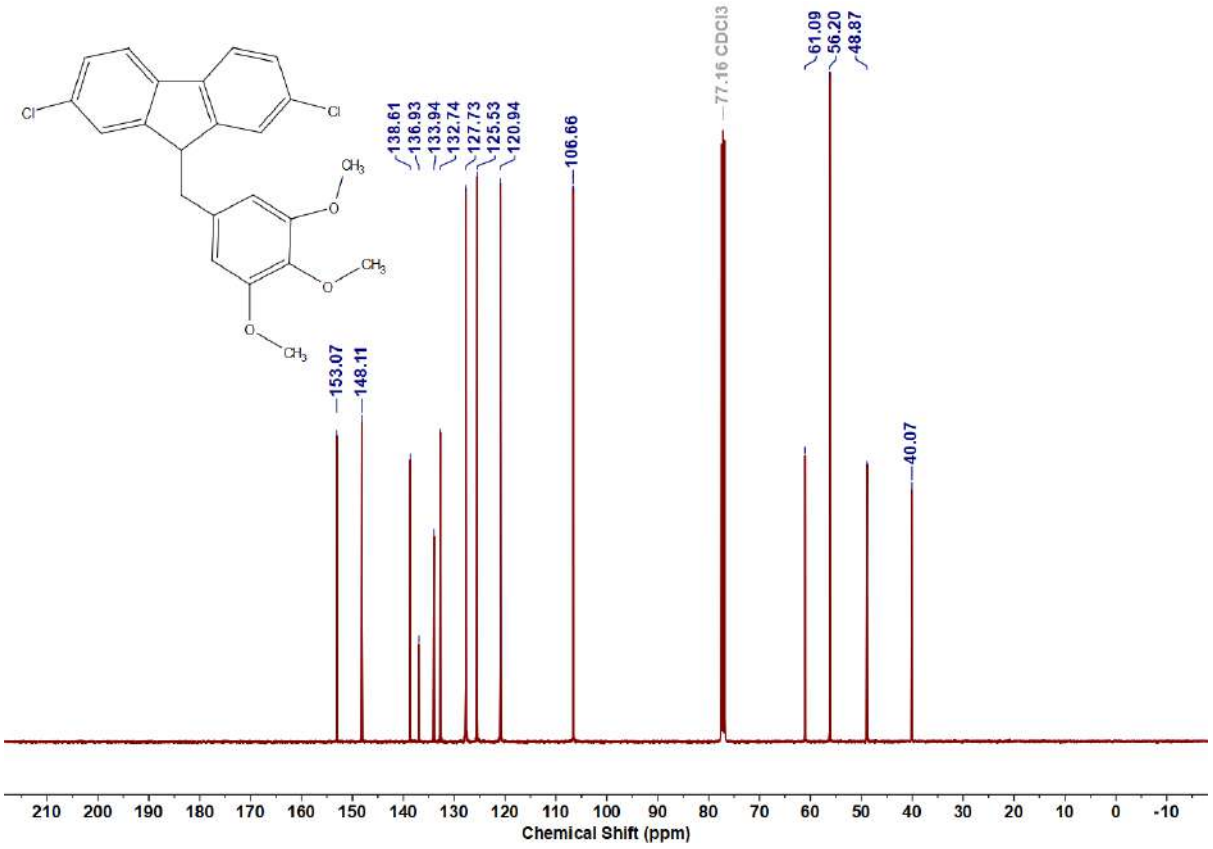

Figure 4.6.A116: ^{13}C{^{1}H} NMR Spectrum of **9s**

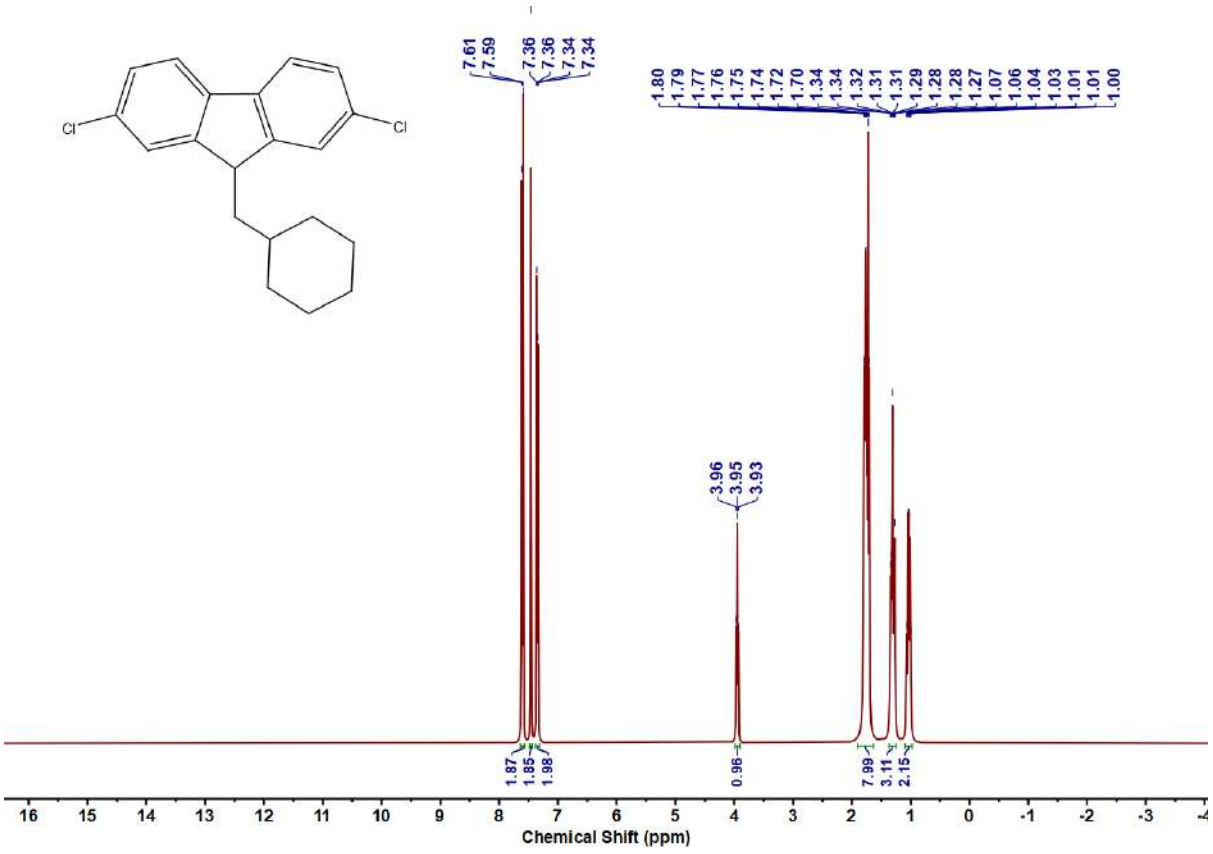

Figure 4.6.A117: ^{1}H NMR Spectrum of **9t**

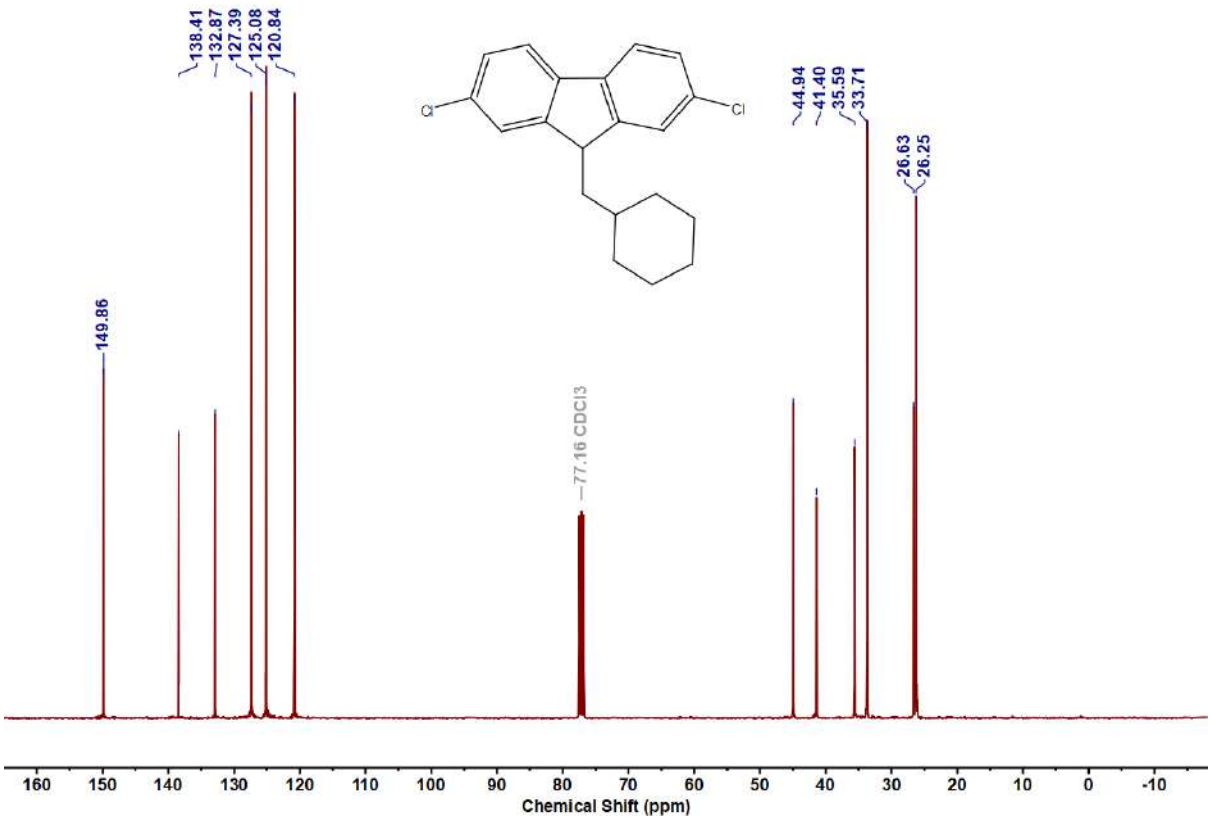

Figure 4.6.A118: ^{13}C{^{1}H} NMR Spectrum of **9t**

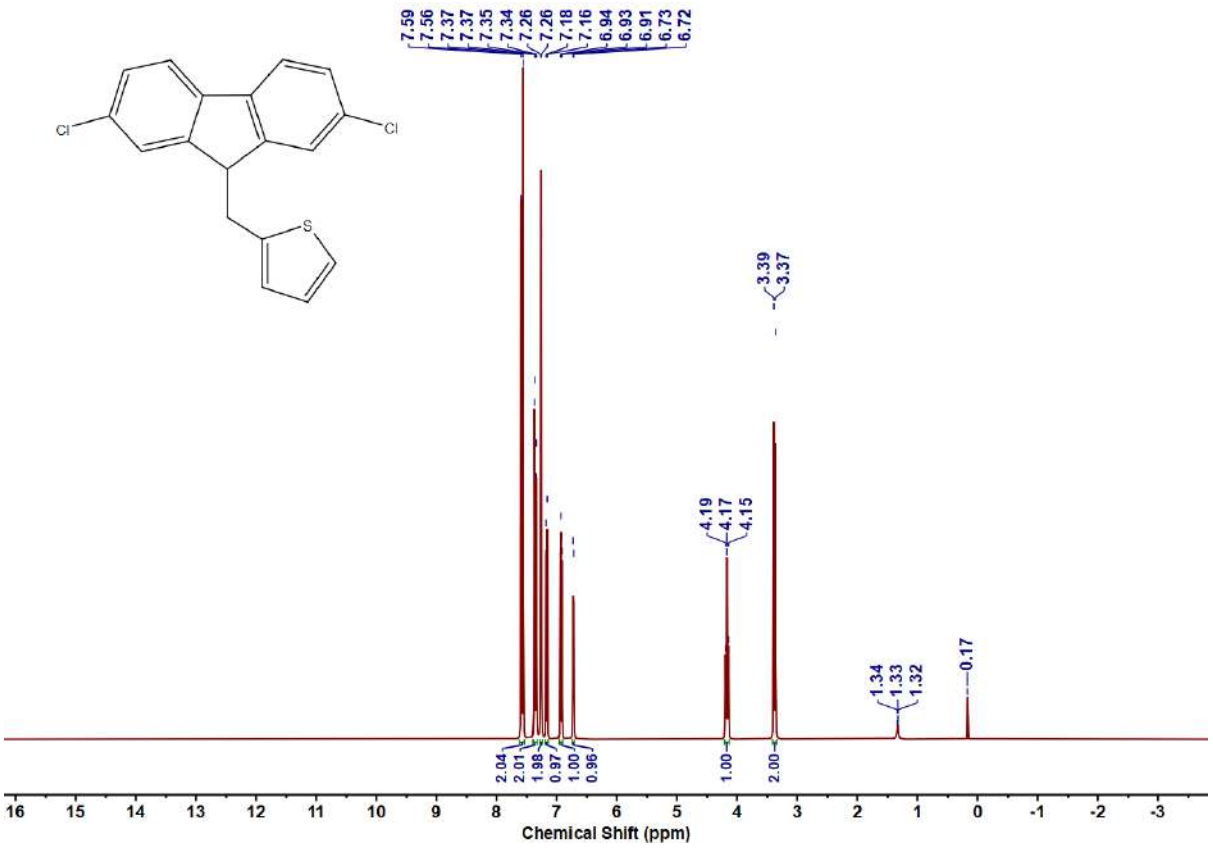

Figure 4.6.A119: ^{1}H NMR Spectrum of **9u**

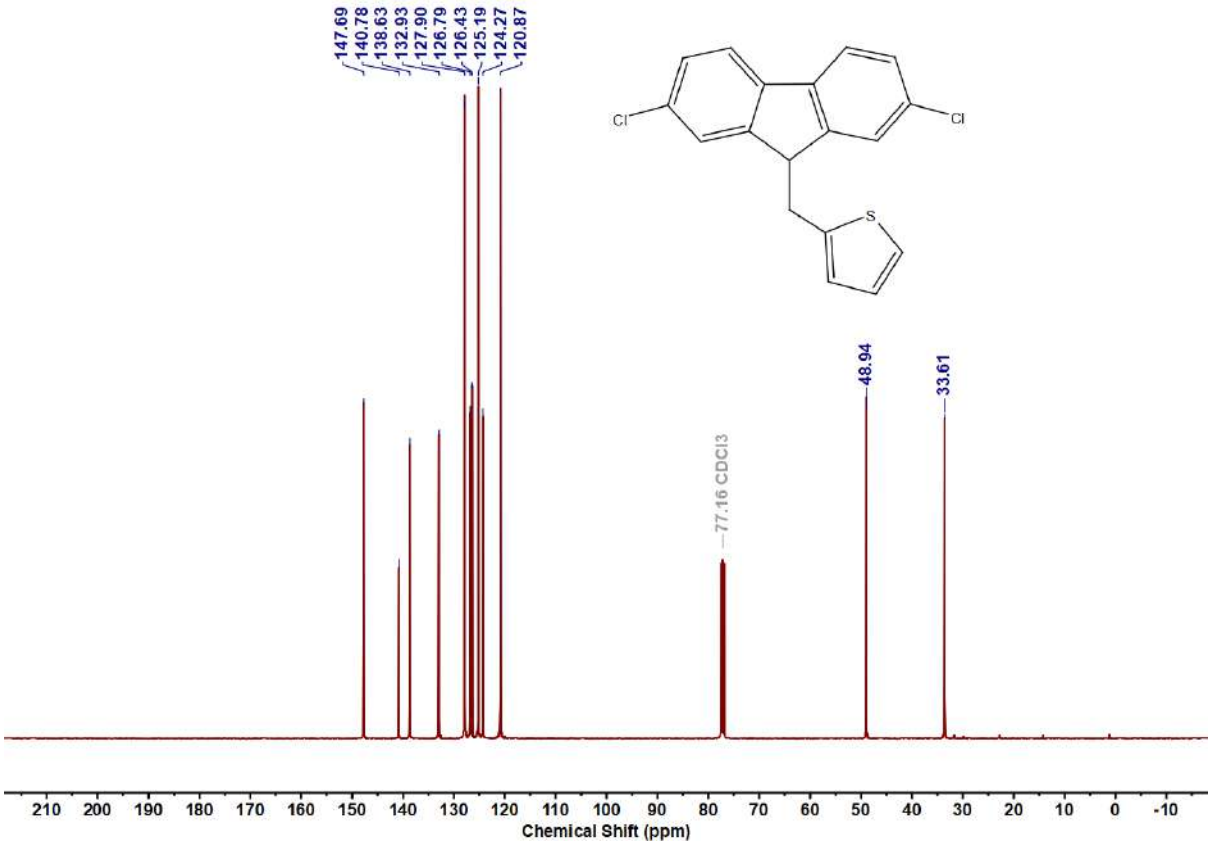

Figure 4.6.A120: ^{13}C{^{1}H} NMR Spectrum of **9u**

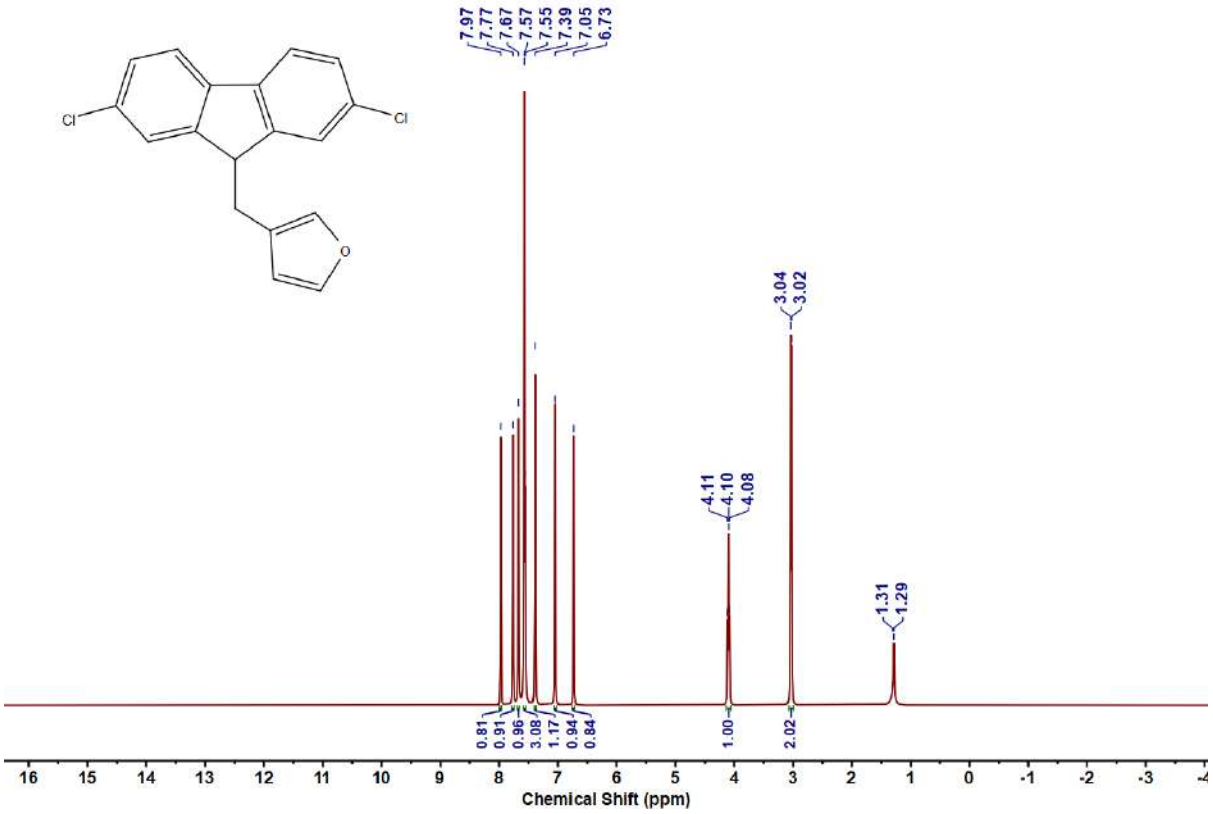

Figure 4.6.A121: ^{1}H NMR Spectrum of **9v**

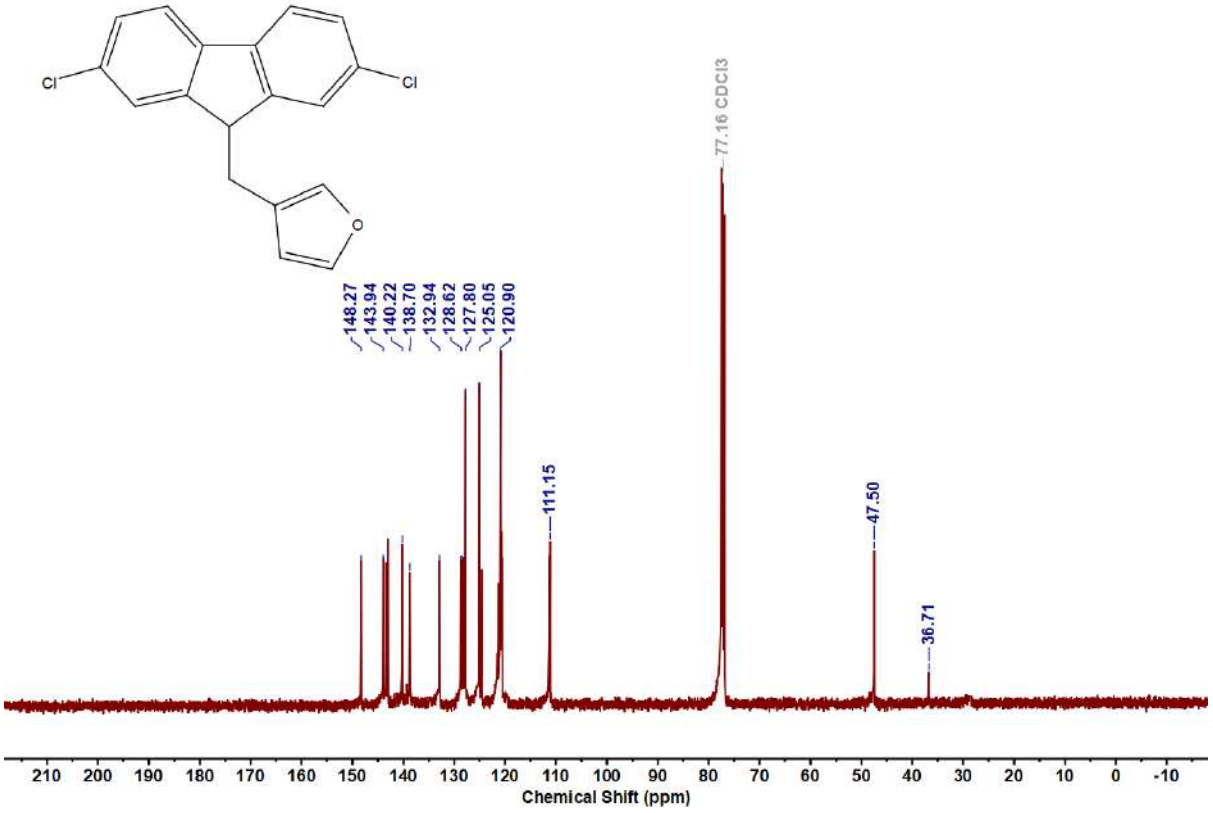

Figure 4.6.A122: ^{13}C{^{1}H} NMR Spectrum of **9v**

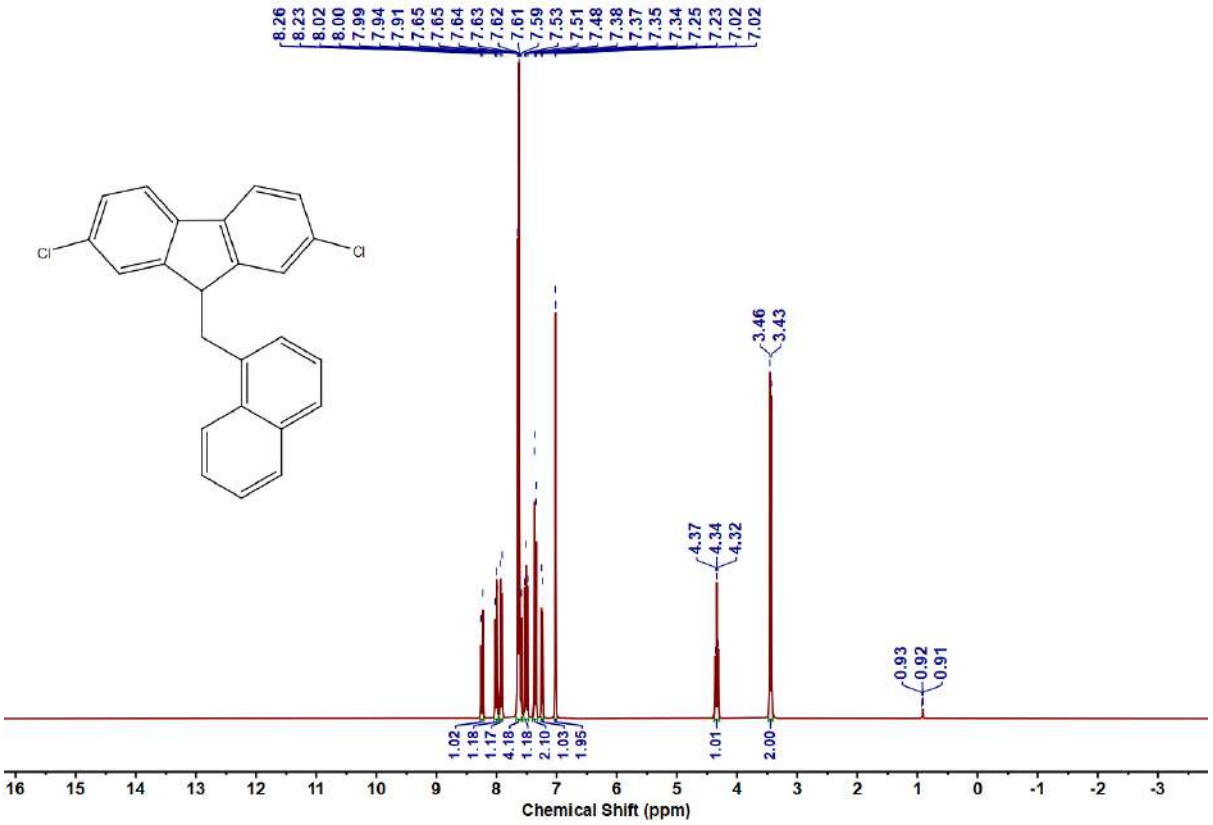

Figure 4.6.A123: ^{1}H NMR Spectrum of **9w**

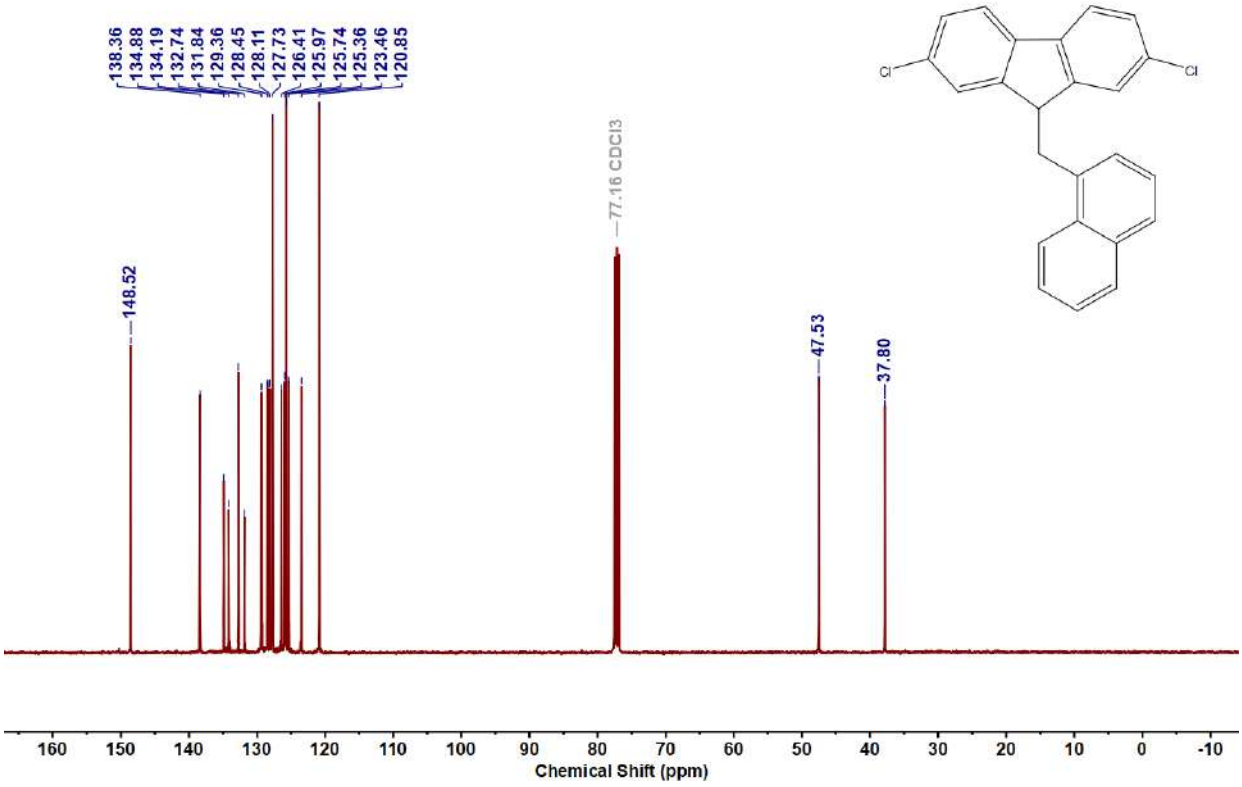

Figure 4.6.A124: ^{13}C{^{1}H} NMR Spectrum of **9w**

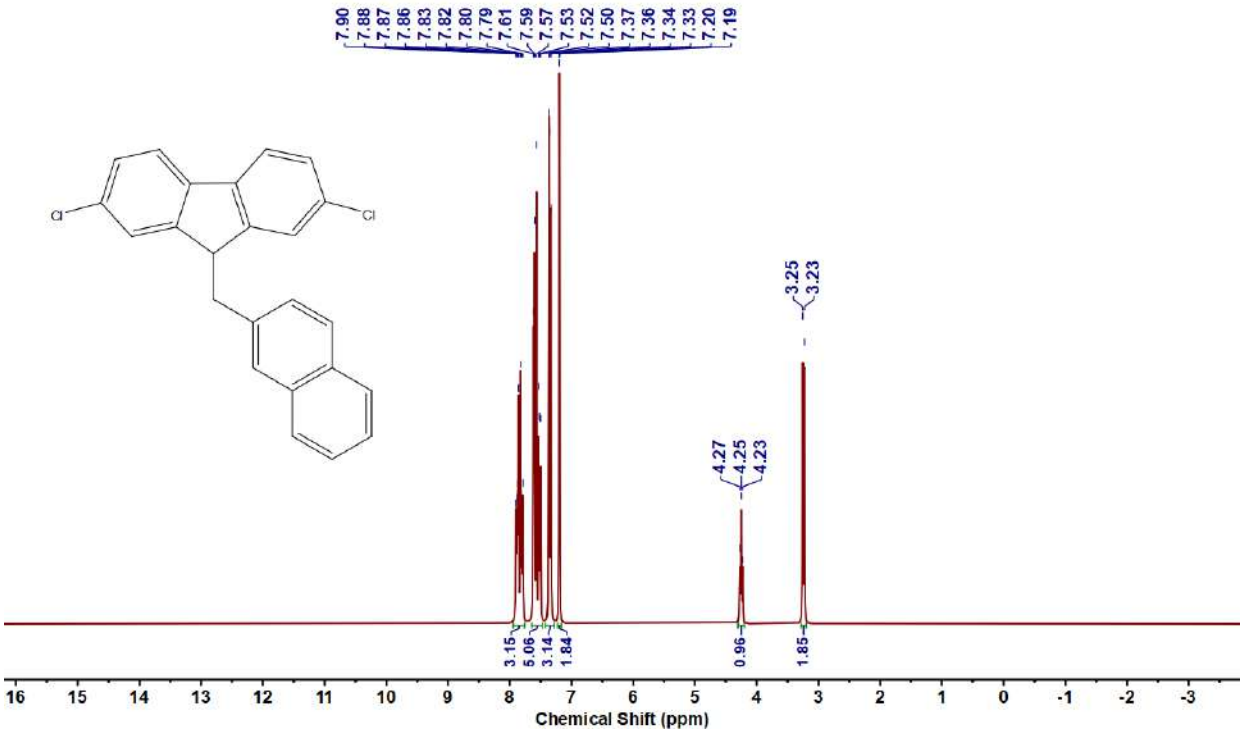

Figure 4.6.A125: ^{1}H NMR Spectrum of **9x**

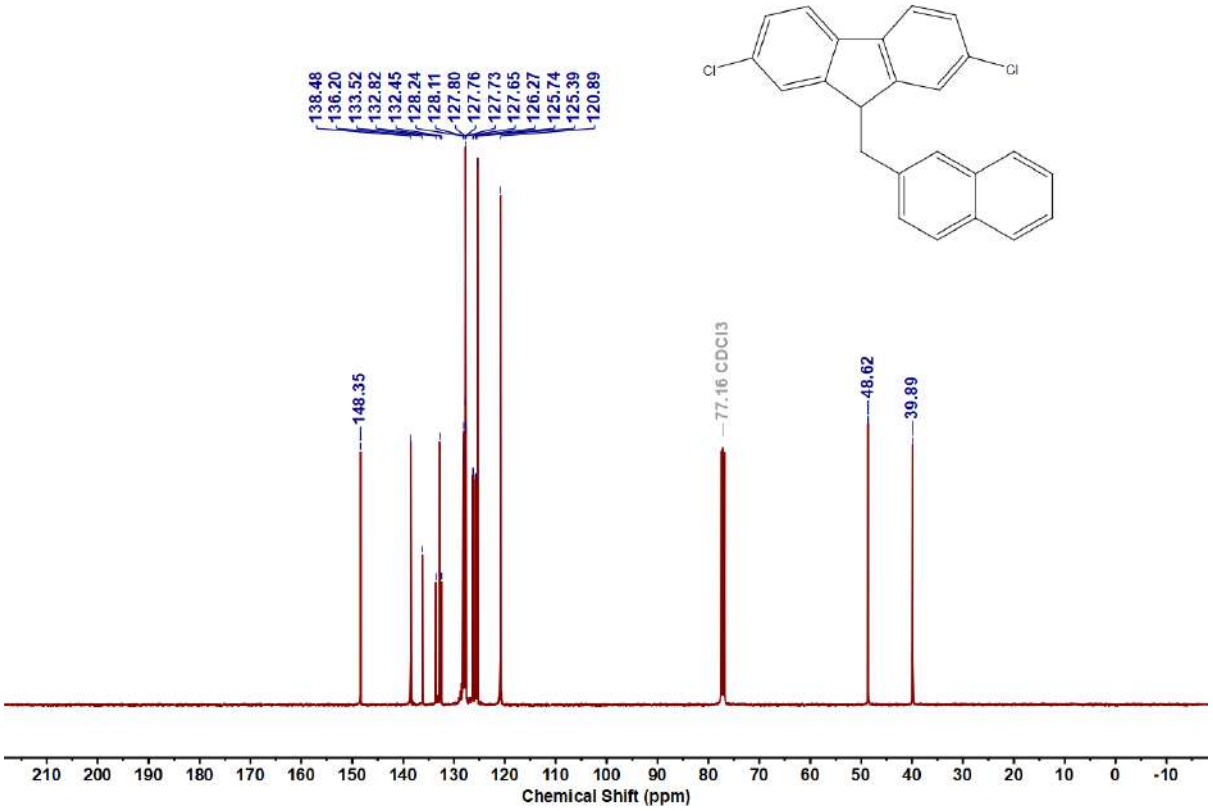

Figure 4.6.A126: $^{13}C\{^{1}H\}$ NMR Spectrum of **9x**

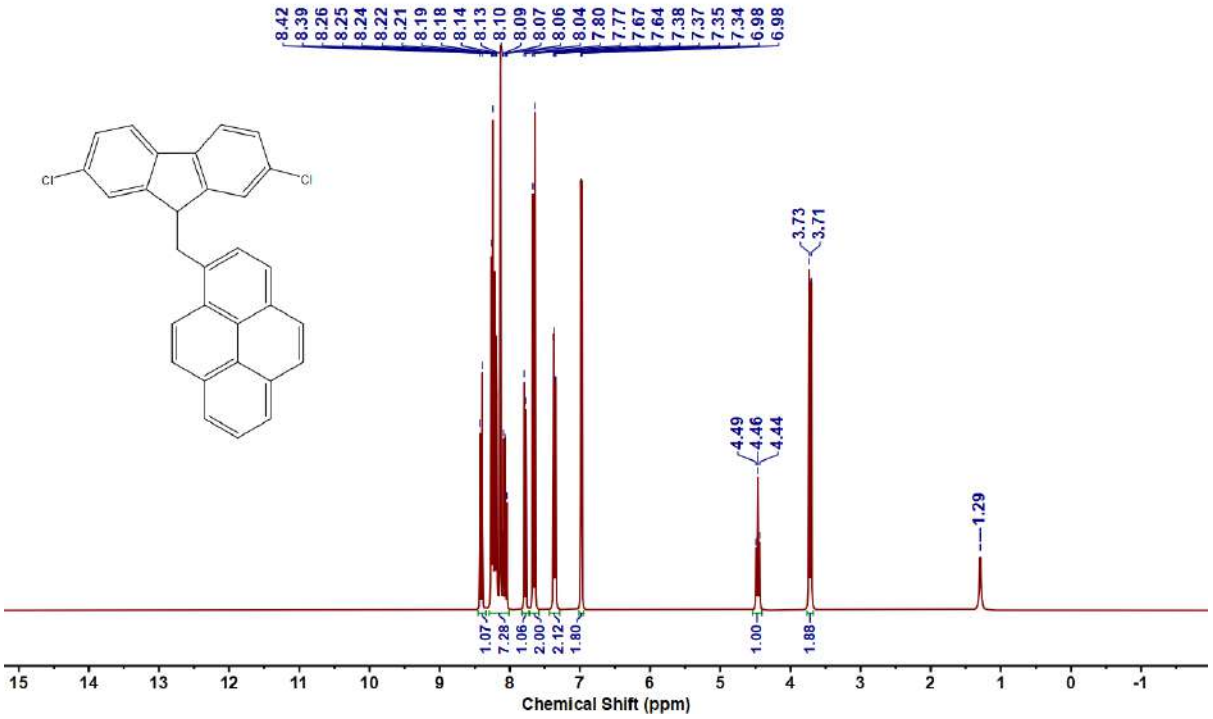

Figure 4.6.A127: ^{1}H NMR Spectrum of **9y**

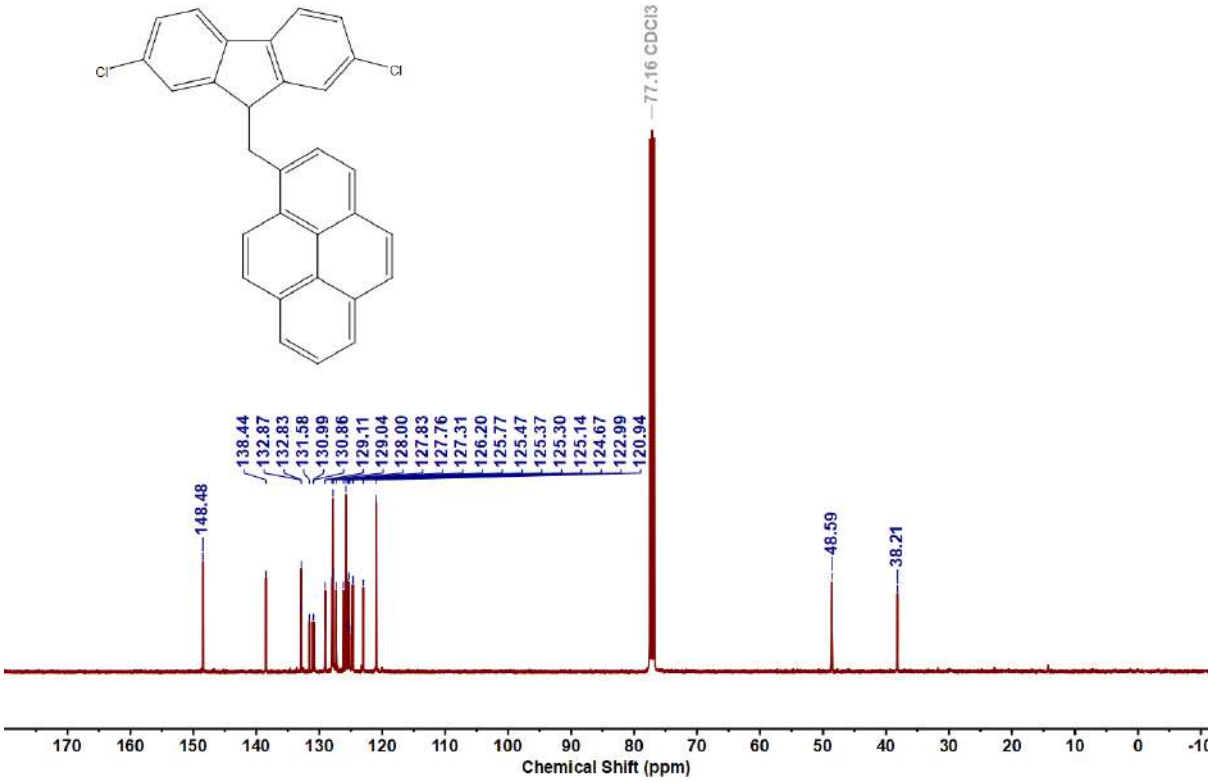

Figure 4.6.A128: ^{13}C{^{1}H} NMR Spectrum of **9y**

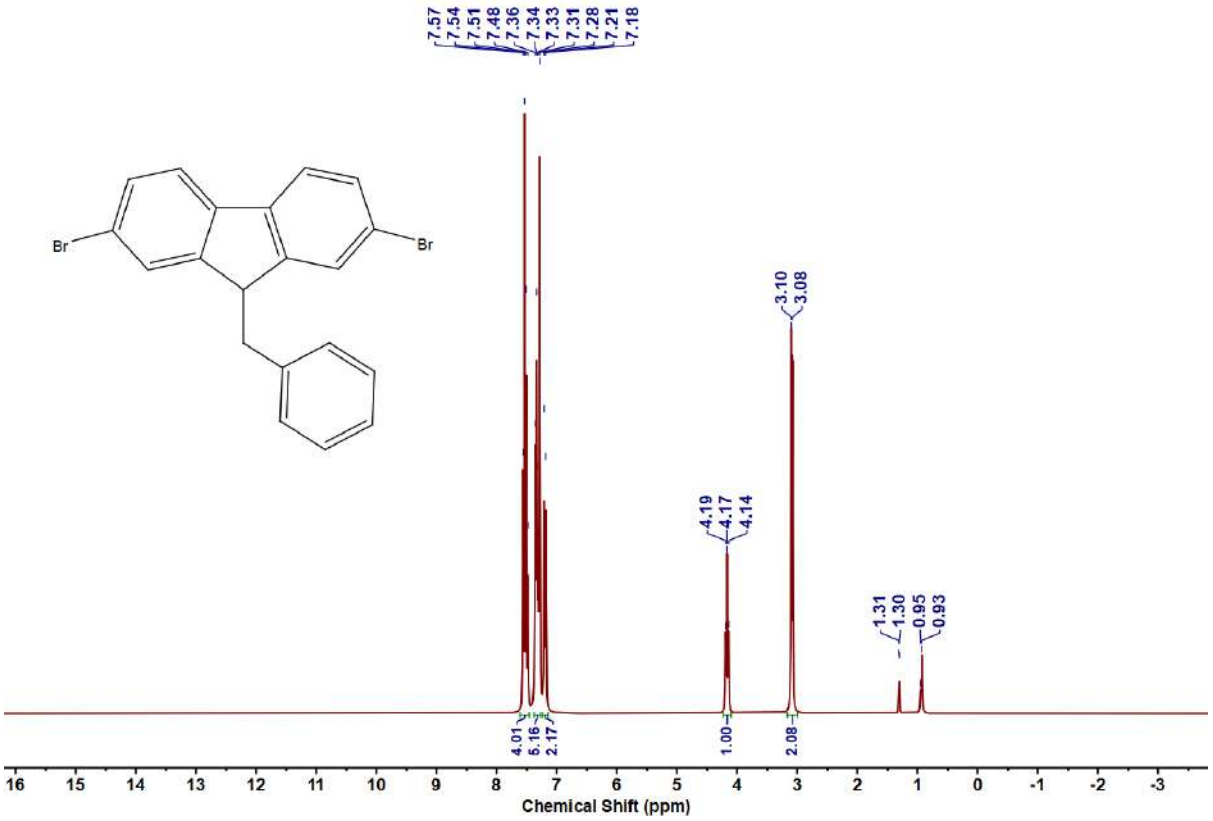

Figure 4.6.A129: ^{1}H NMR Spectrum of **10a**

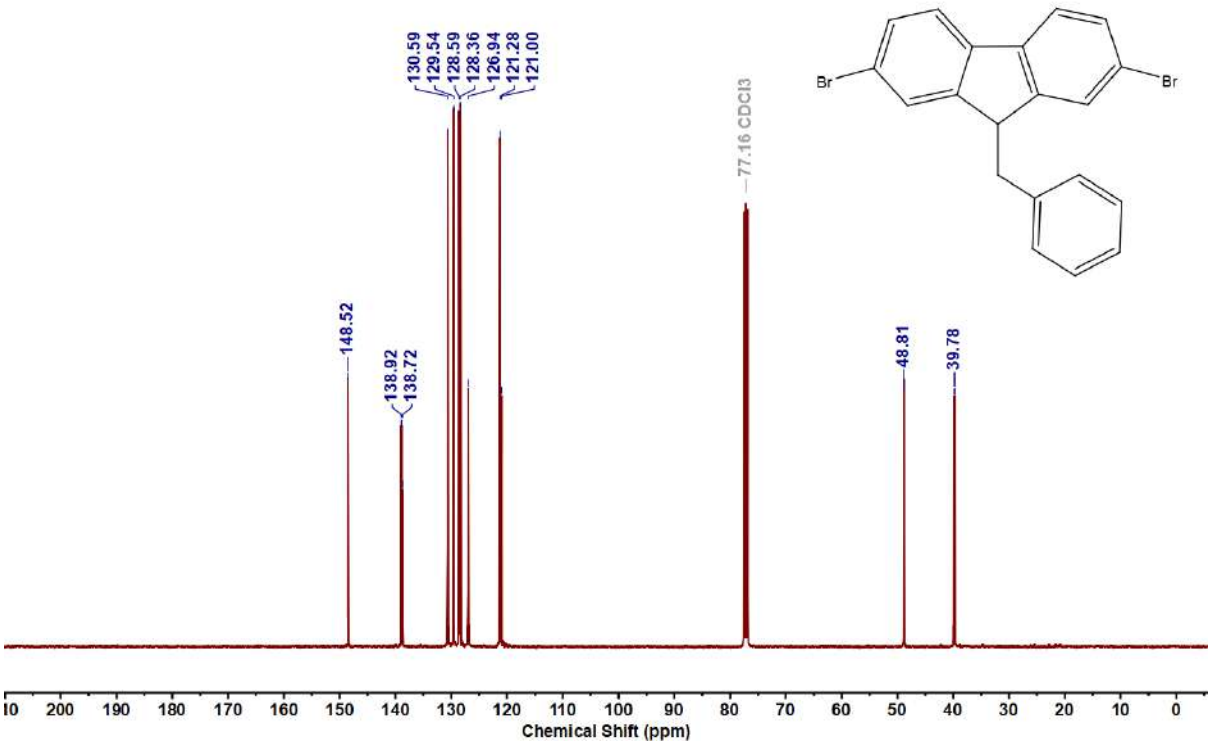

Figure 4.6.A130: ^{13}C{^{1}H} NMR Spectrum of **10a**

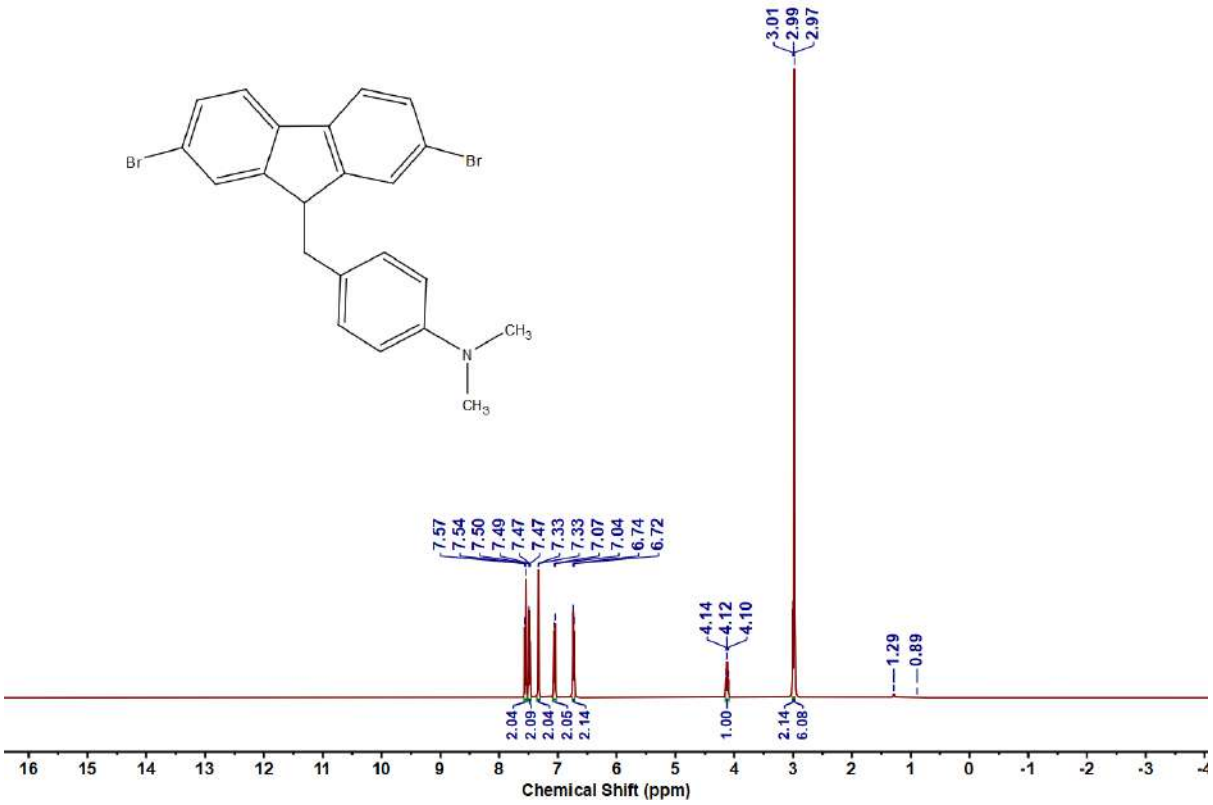

Figure 4.6.A131: ^{1}H NMR Spectrum of **10b**

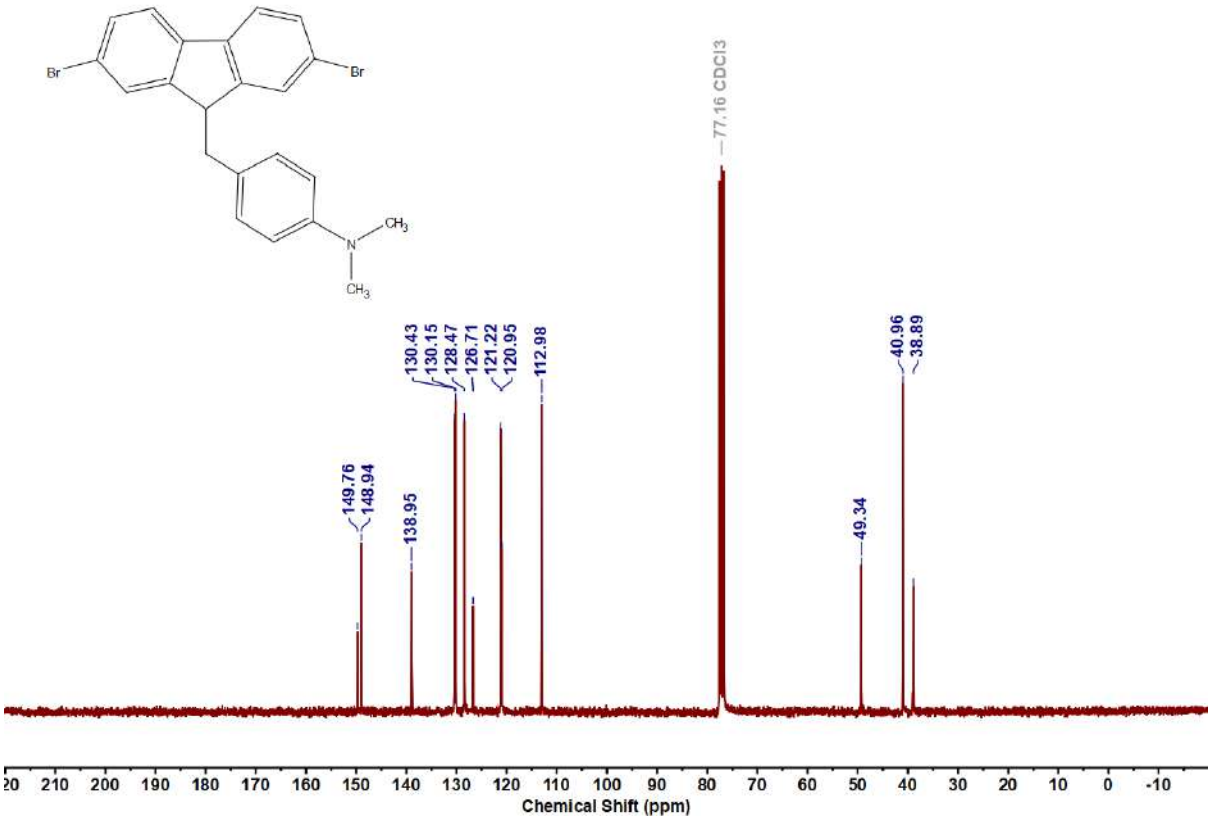

Figure 4.6.A132: ^{13}C{^{1}H} NMR Spectrum of **10b**

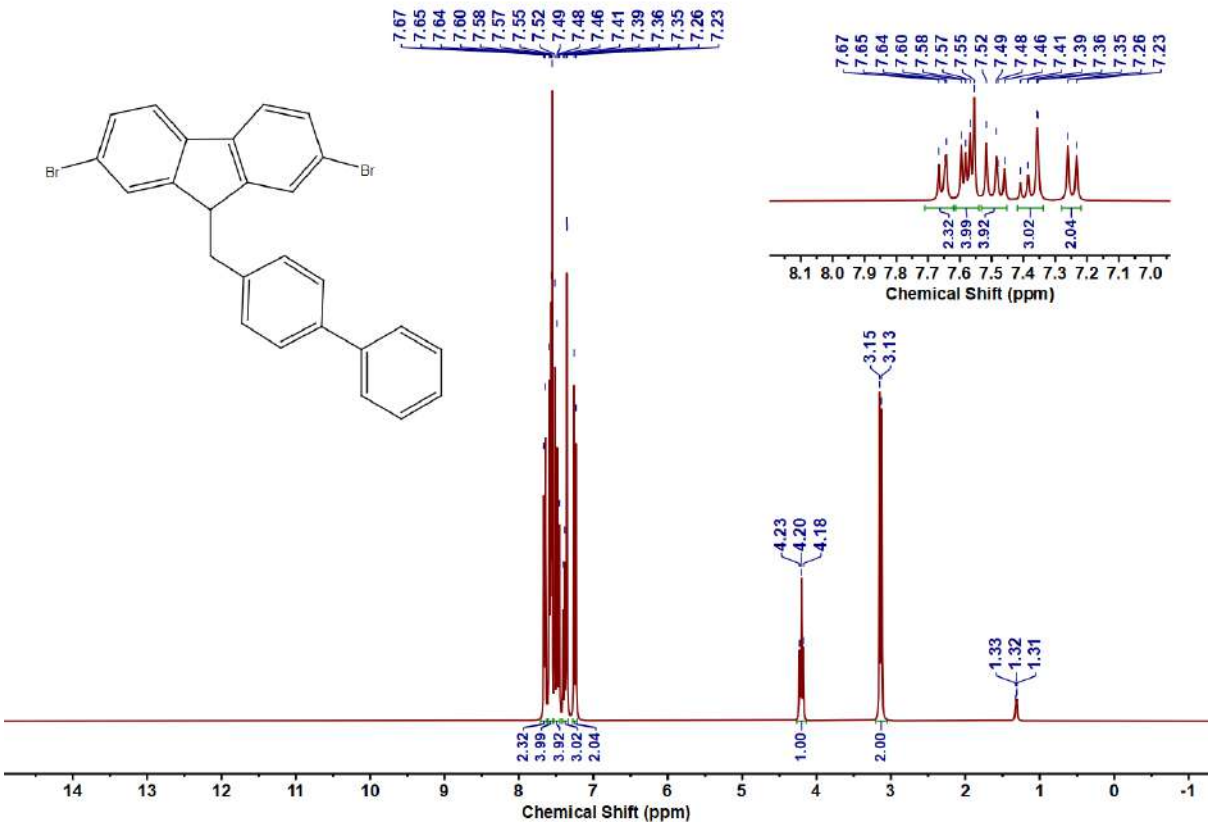

Figure 4.6.A133: ^{1}H NMR Spectrum of **10c**

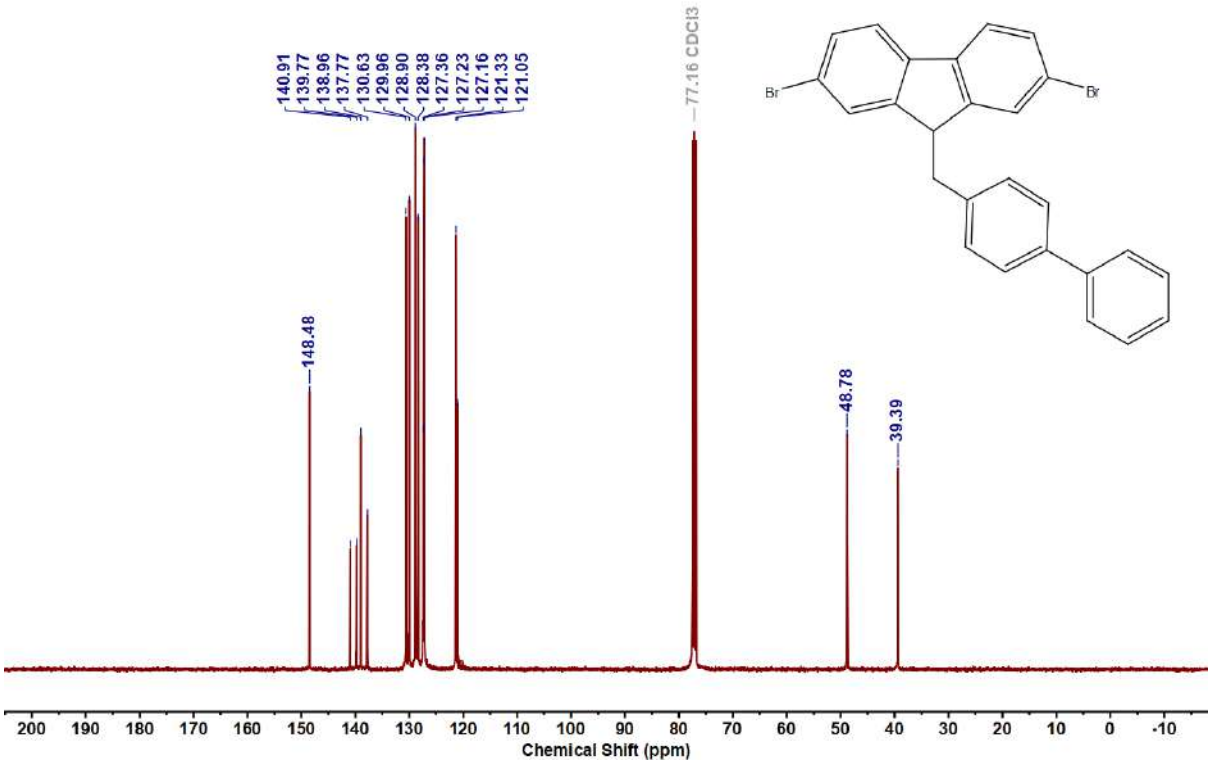

Figure 4.6.A134: ^{13}C{^{1}H} NMR Spectrum of **10c**

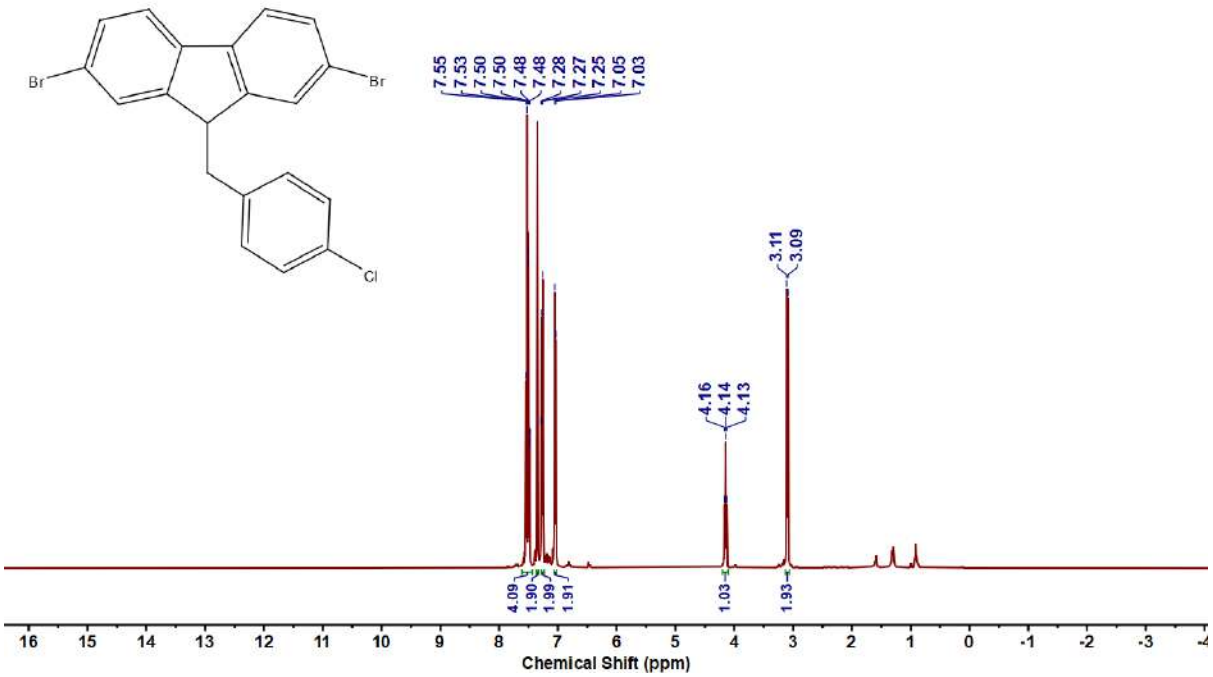

Figure 4.6.A135: ^{1}H NMR Spectrum of **10d**

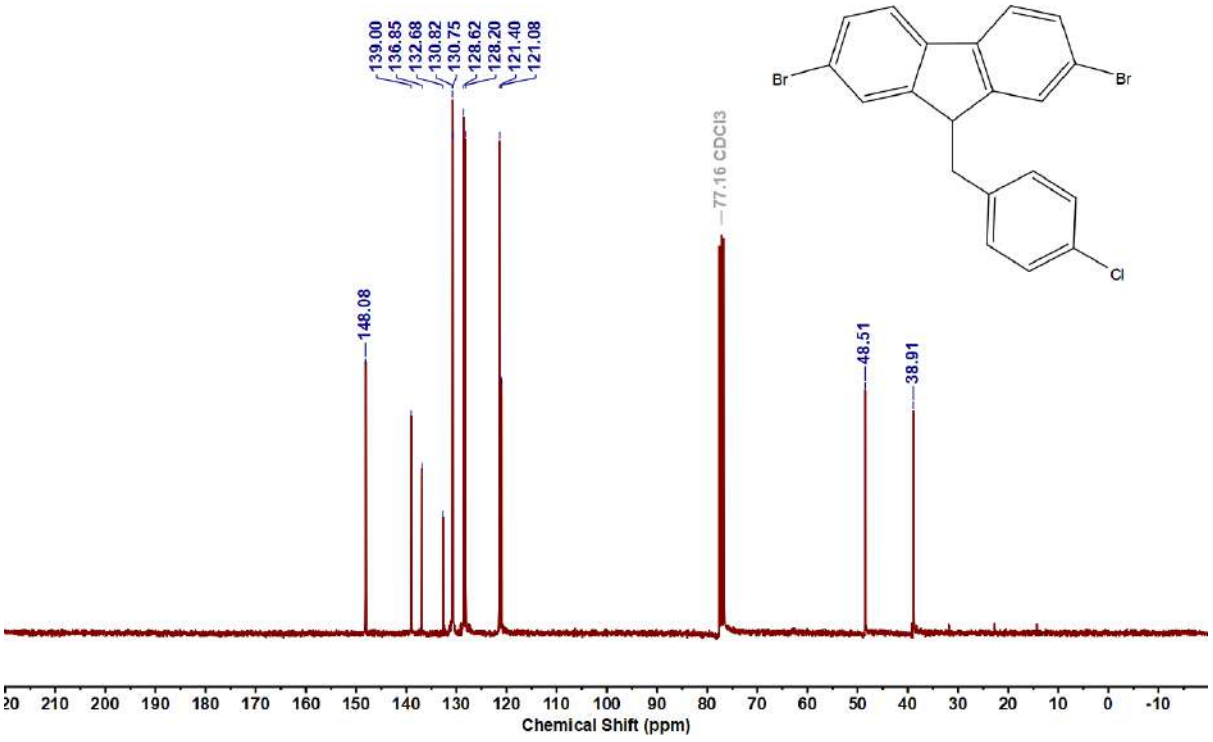

Figure 4.6.A136: ^{13}C{^{1}H} NMR Spectrum of **10d**

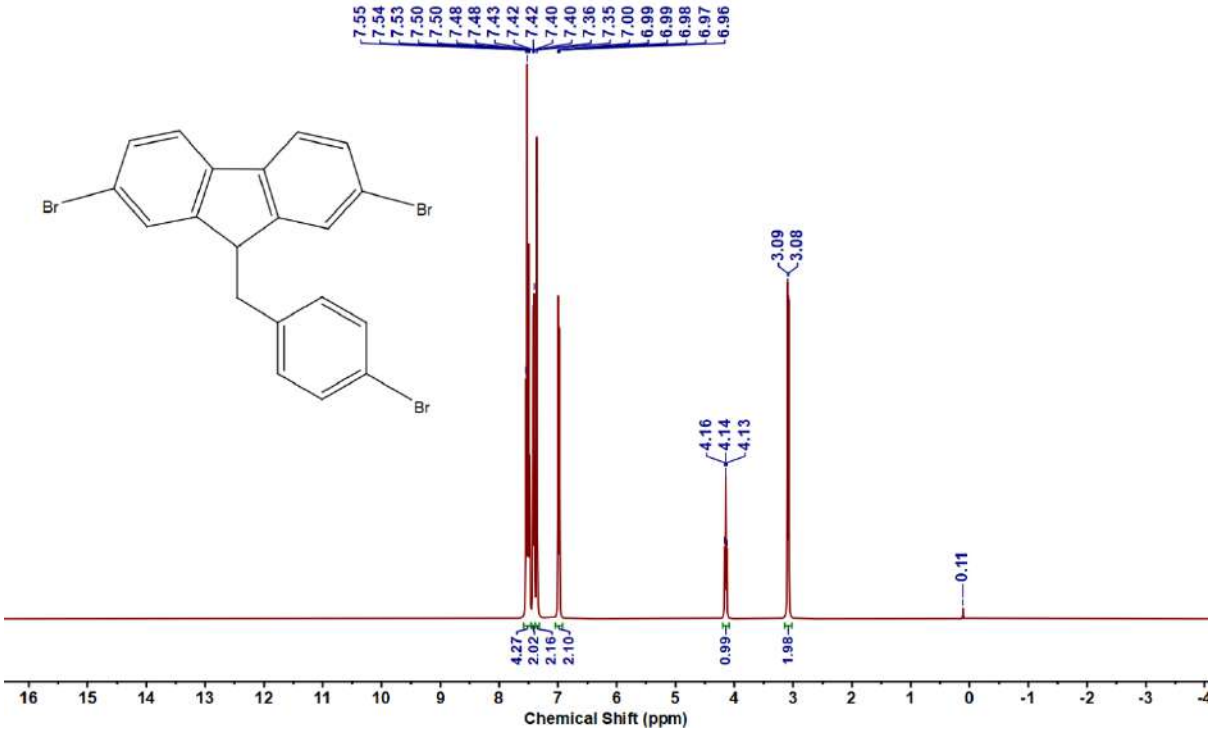

Figure 4.6.A137: ^{1}H NMR Spectrum of **10e**

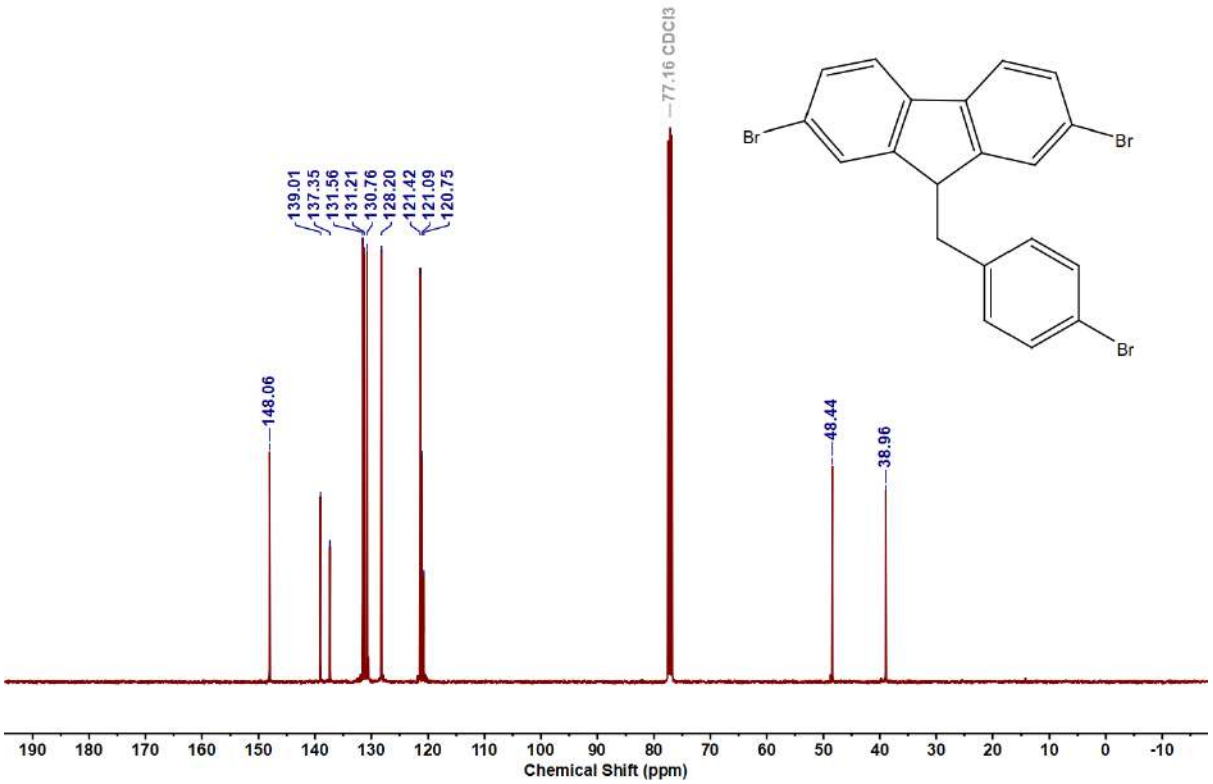

Figure 4.6.A138: ^{13}C{^{1}H} NMR Spectrum of **10e**

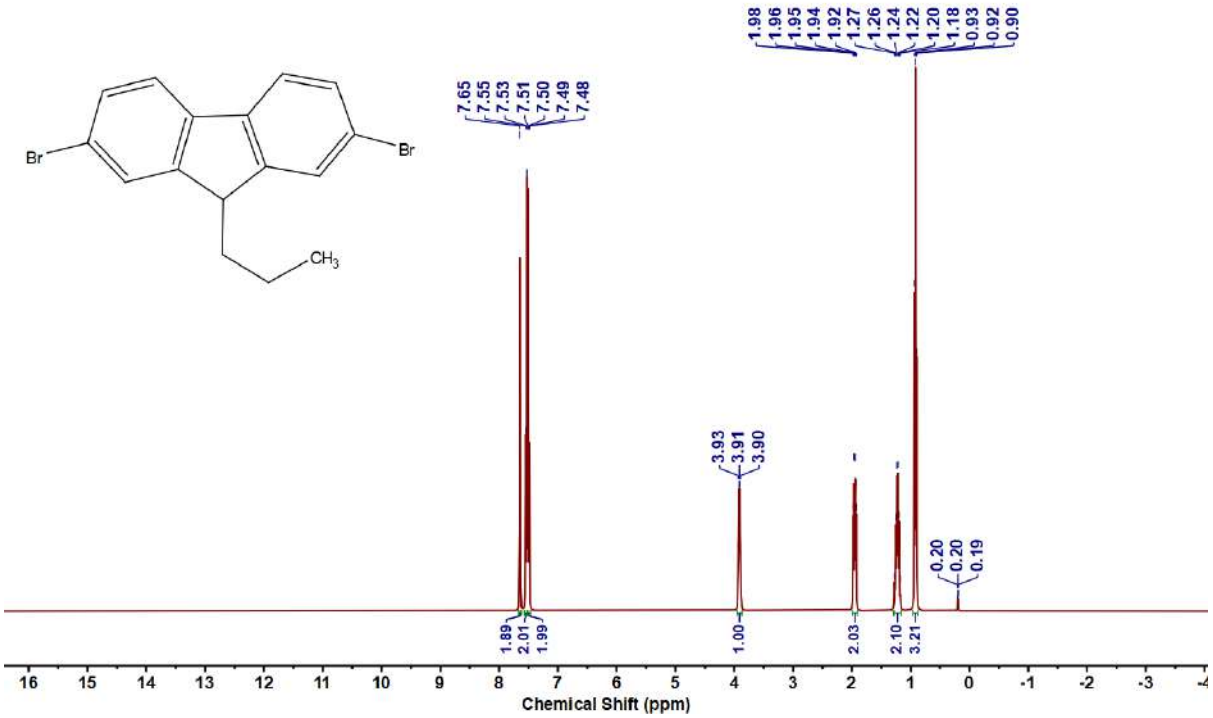

Figure 4.6.A139: ^{1}H NMR Spectrum of **10f**

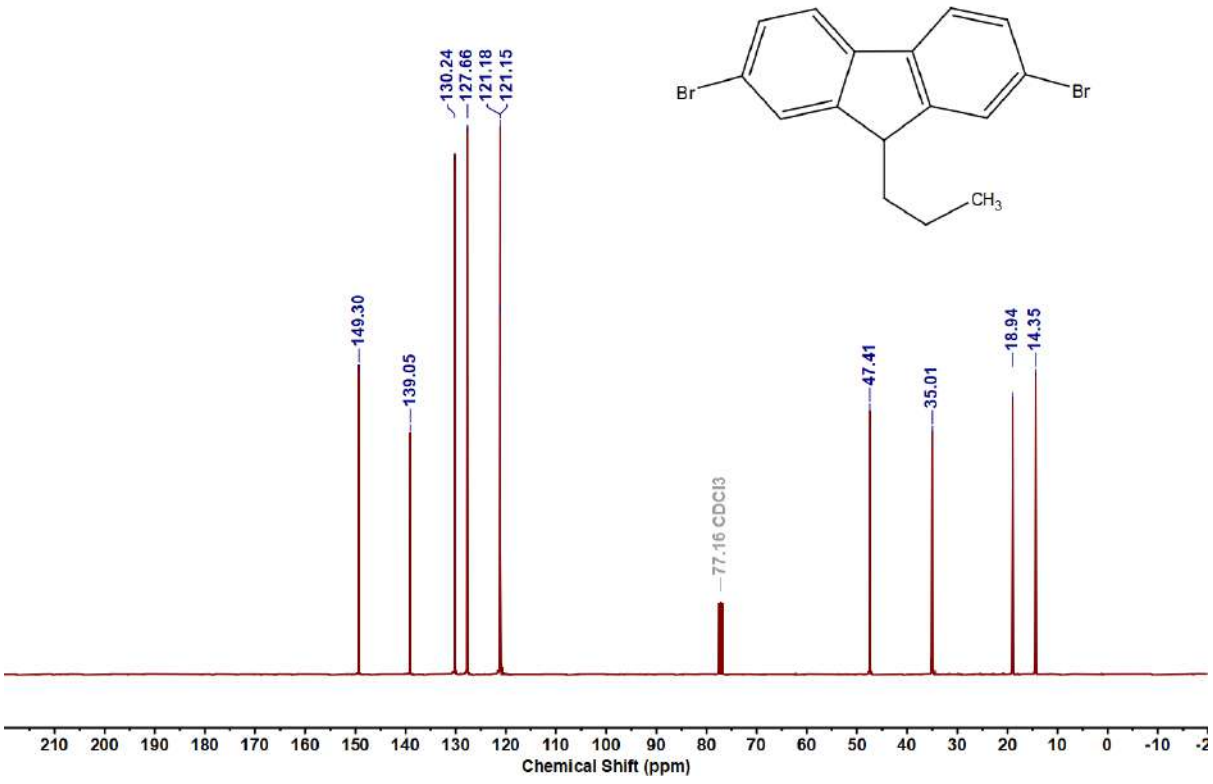

Figure 4.6.A140: $^{13}C\{^{1}H\}$ NMR Spectrum of **10f**

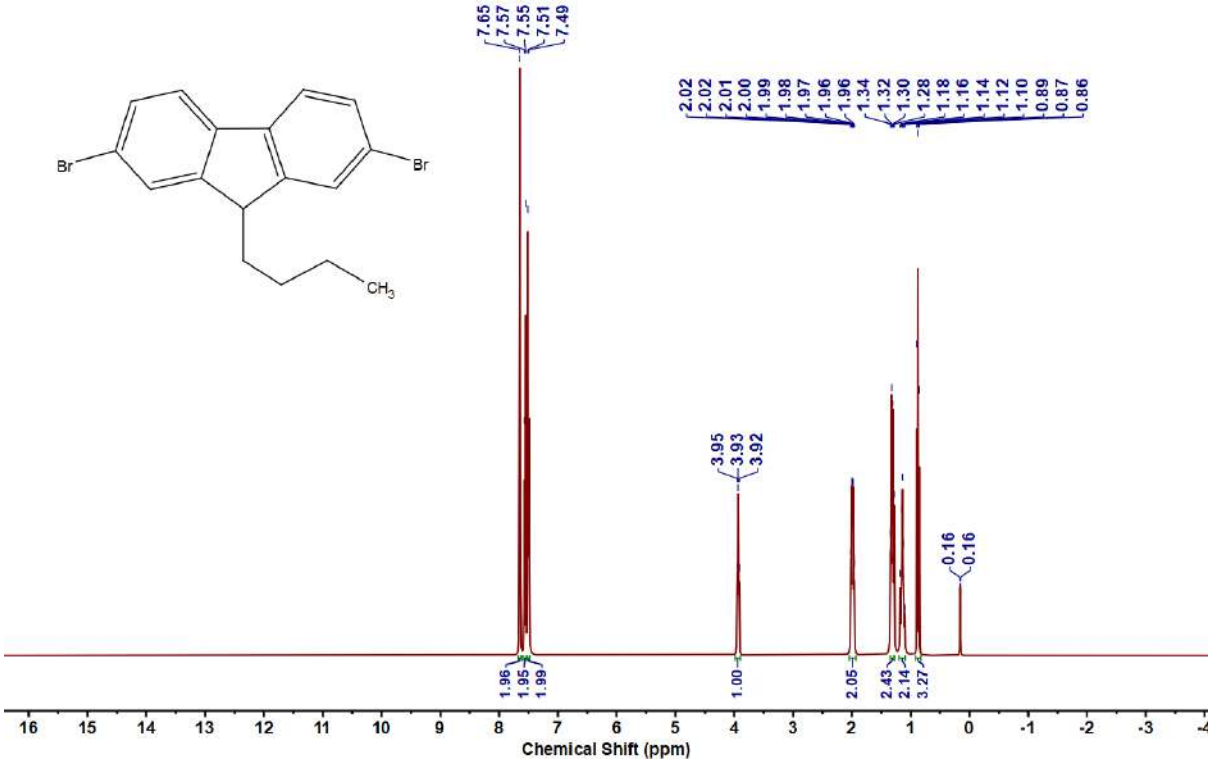

Figure 4.6.A141: ^{1}H NMR Spectrum of **10g**

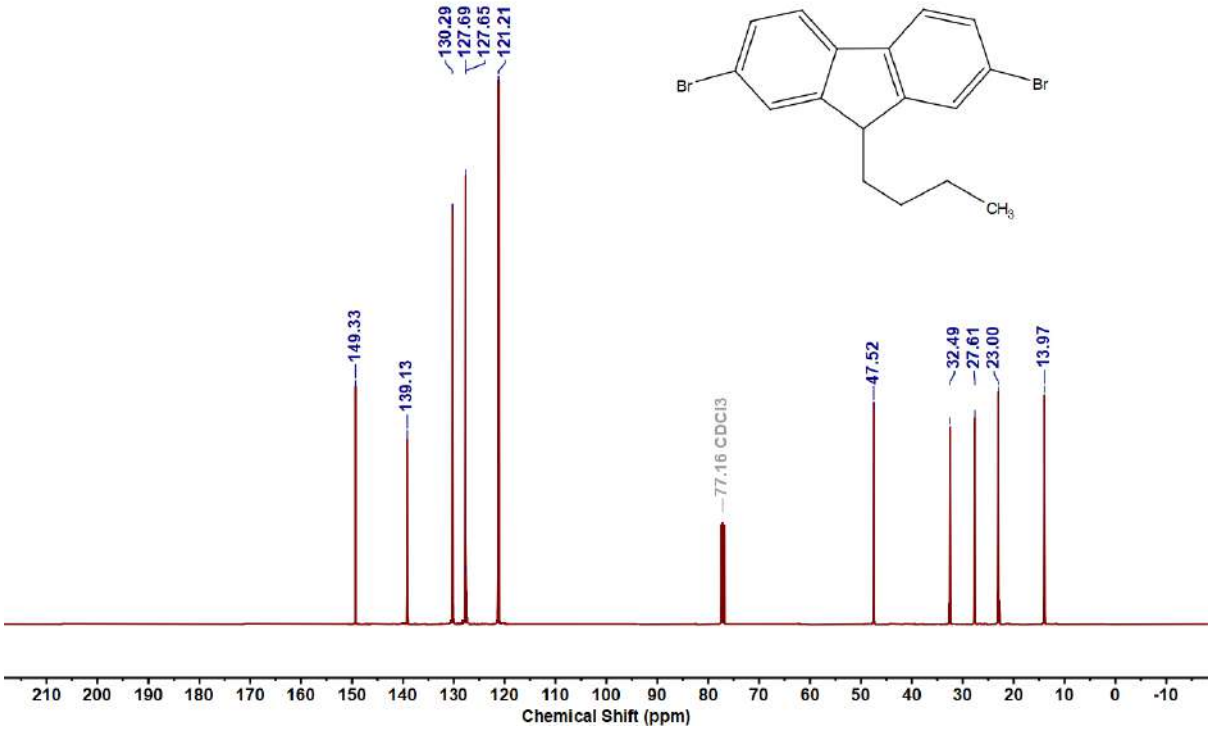

Figure 4.6.A142: ^{13}C{^{1}H} NMR Spectrum of **10g**

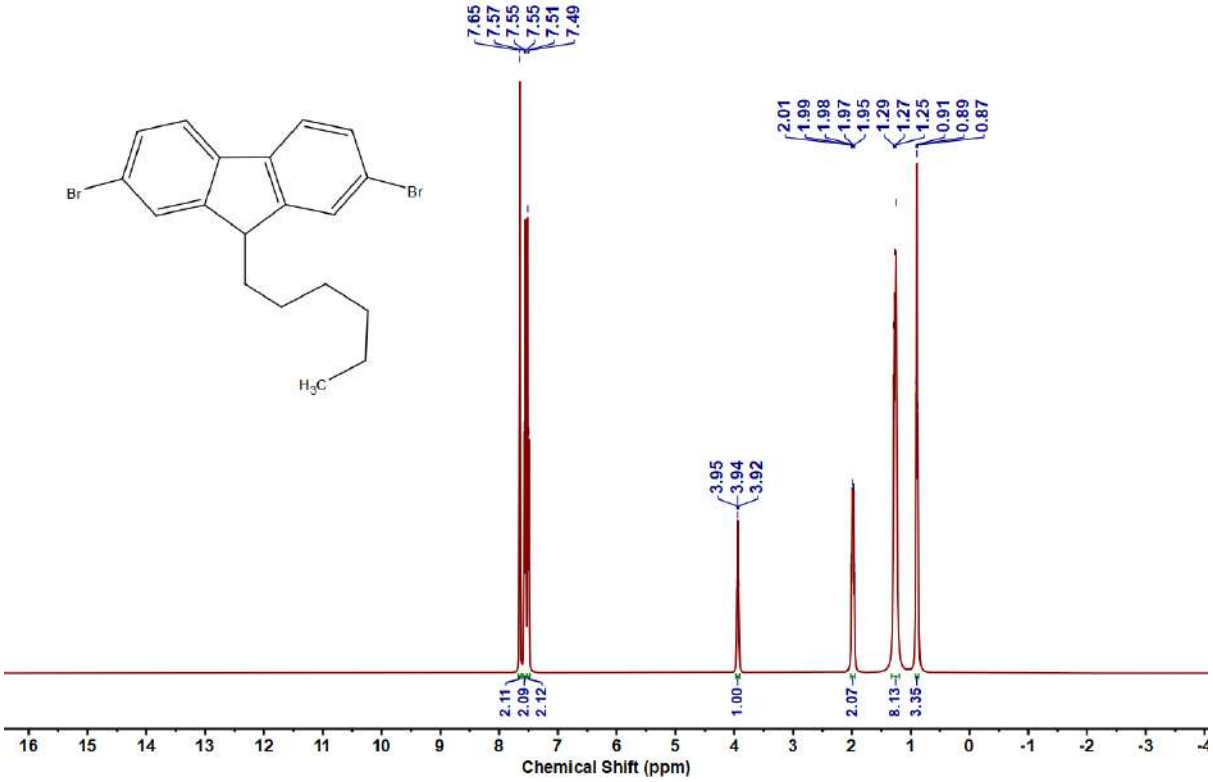

Figure 4.6.A143: ^{1}H NMR Spectrum of **10h**

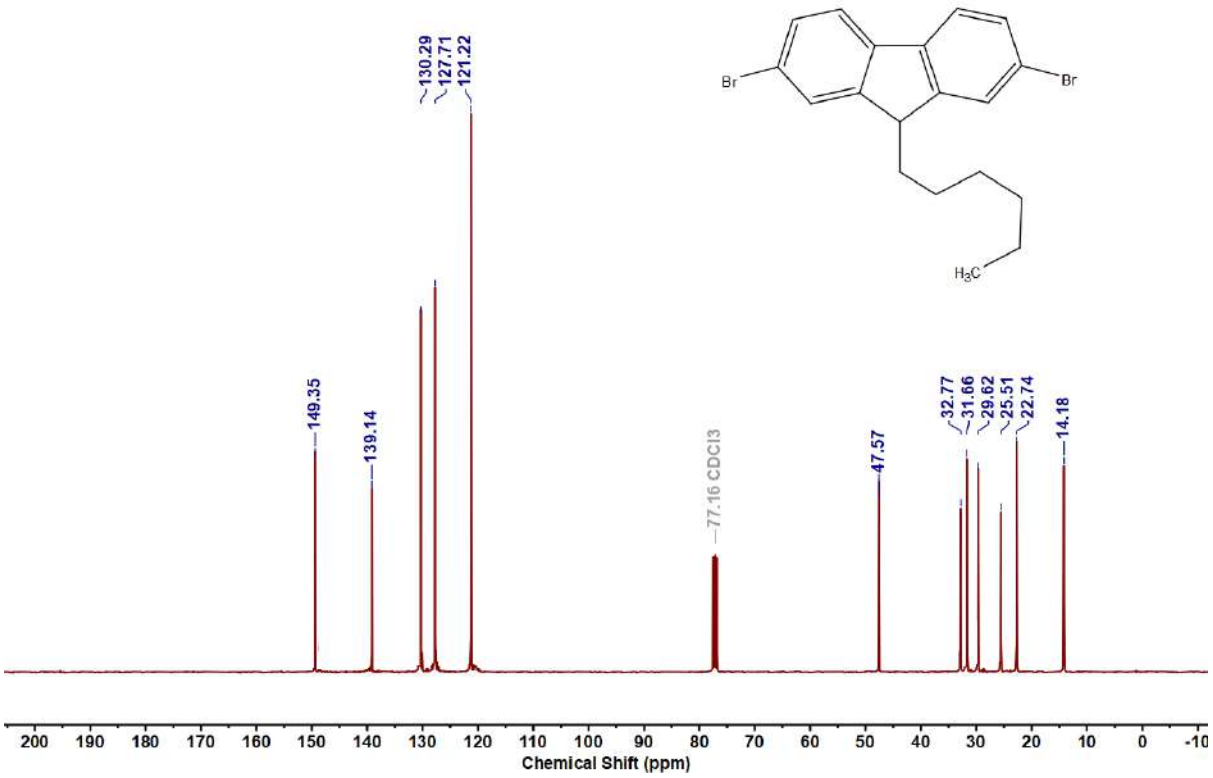

Figure 4.6.A144: ^{13}C{^{1}H} NMR Spectrum of **10h**

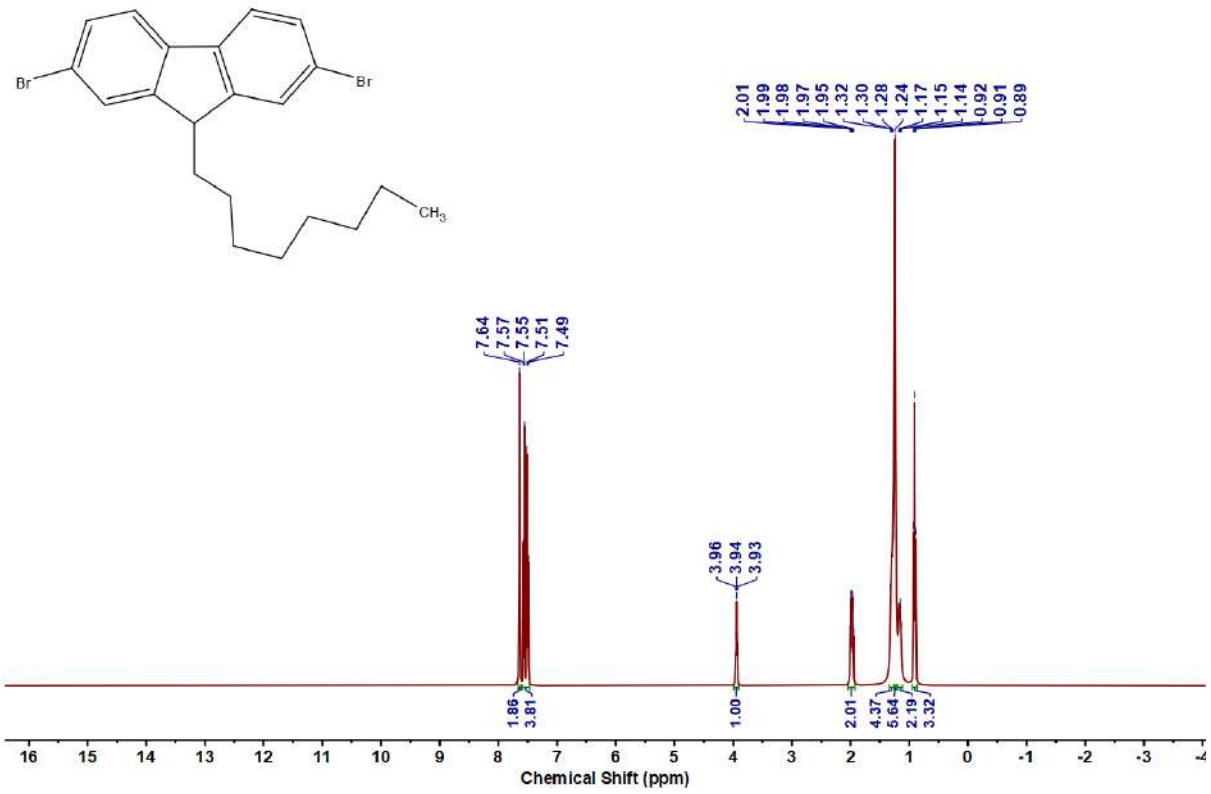

Figure 4.6.A145: ^{1}H NMR Spectrum of **10i**

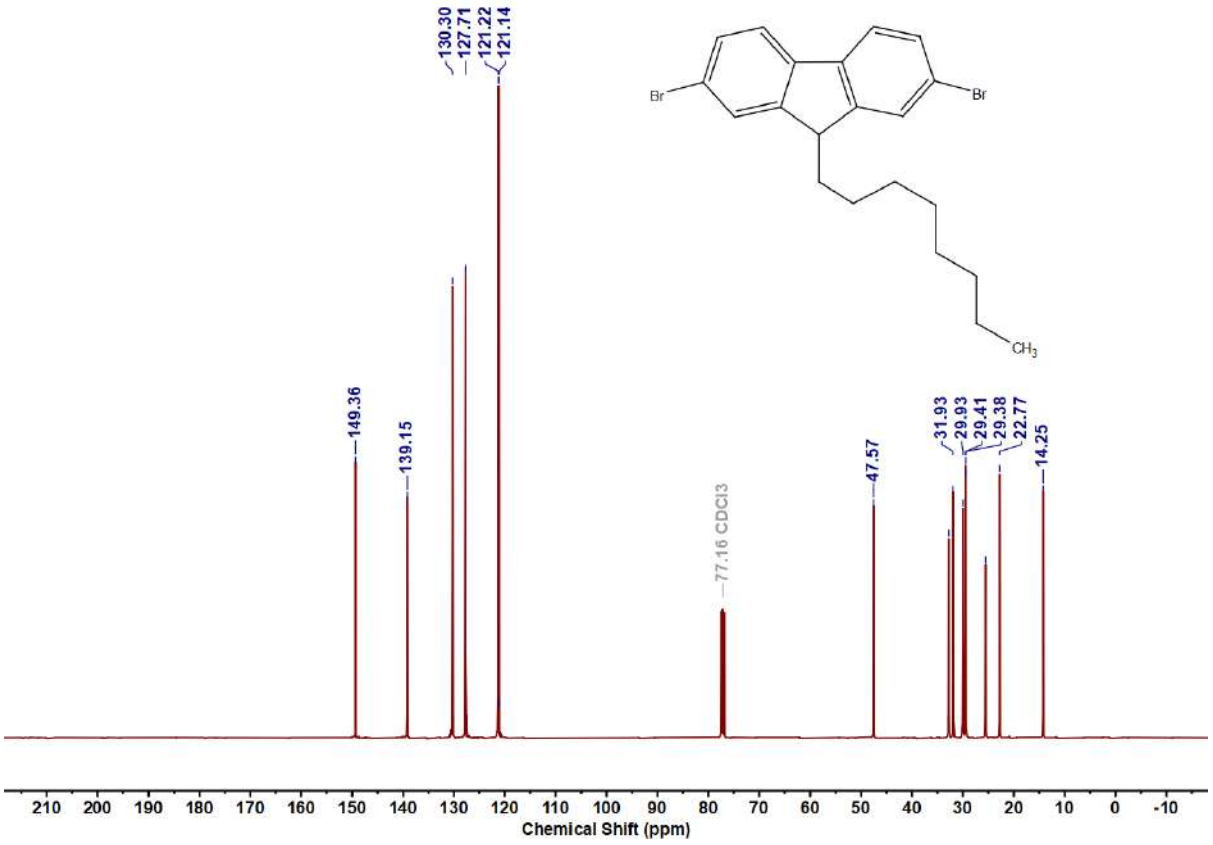

Figure 4.6.A146: ^{13}C{^{1}H} NMR Spectrum of **10i**

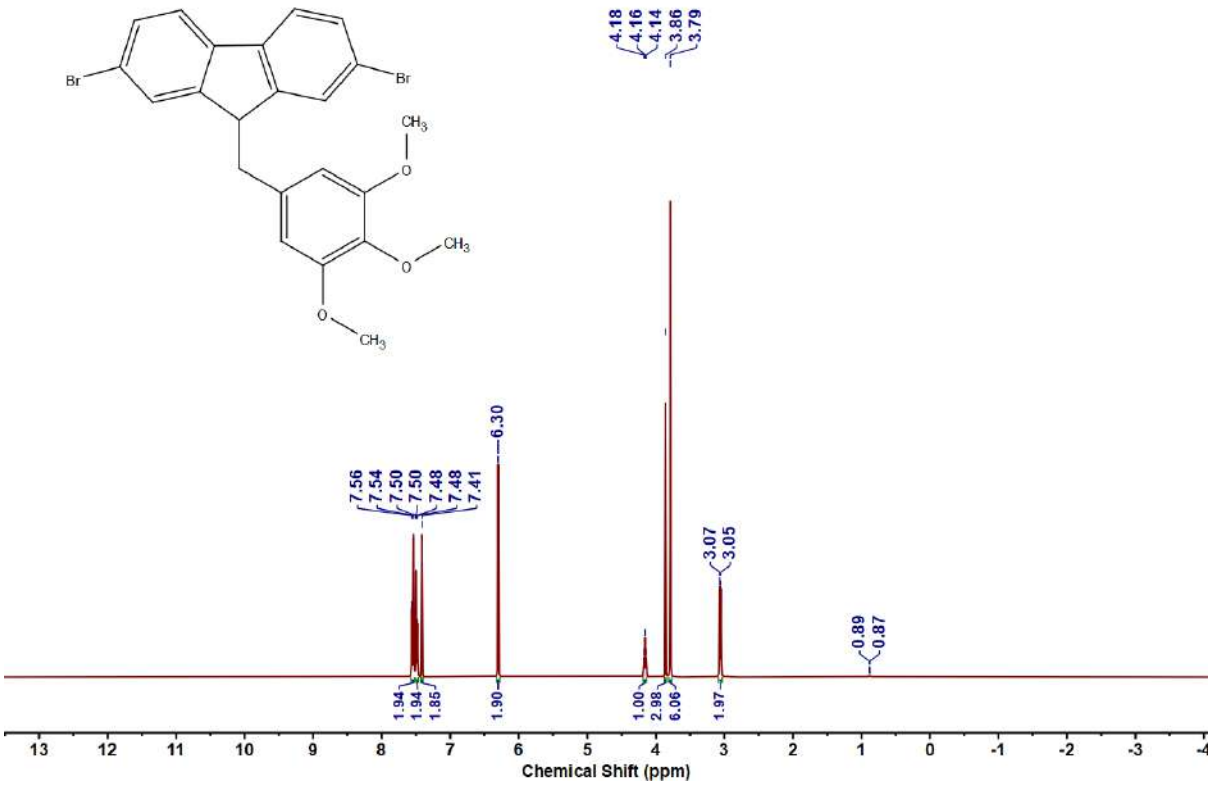

Figure 4.6.A147: ^{1}H NMR Spectrum of **10j**

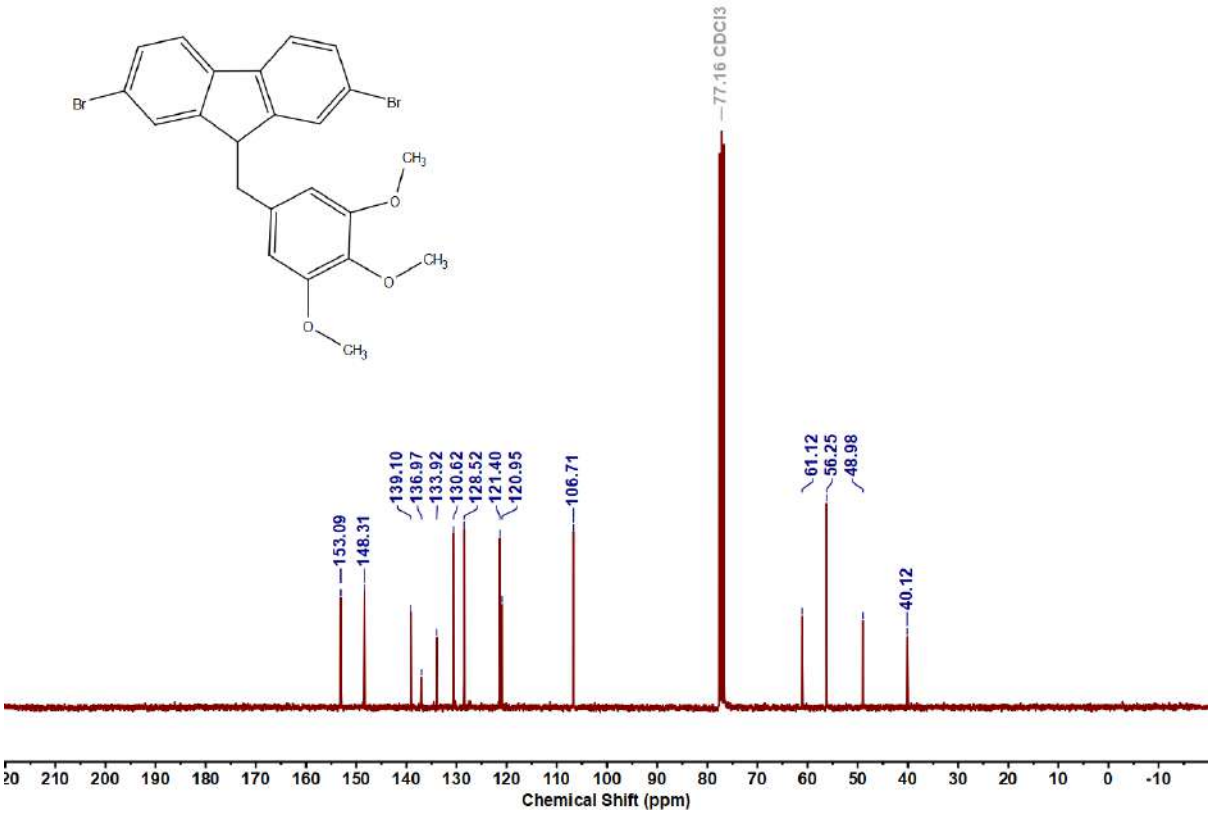

Figure 4.6.A148: ^{13}C{^{1}H} NMR Spectrum of **10j**

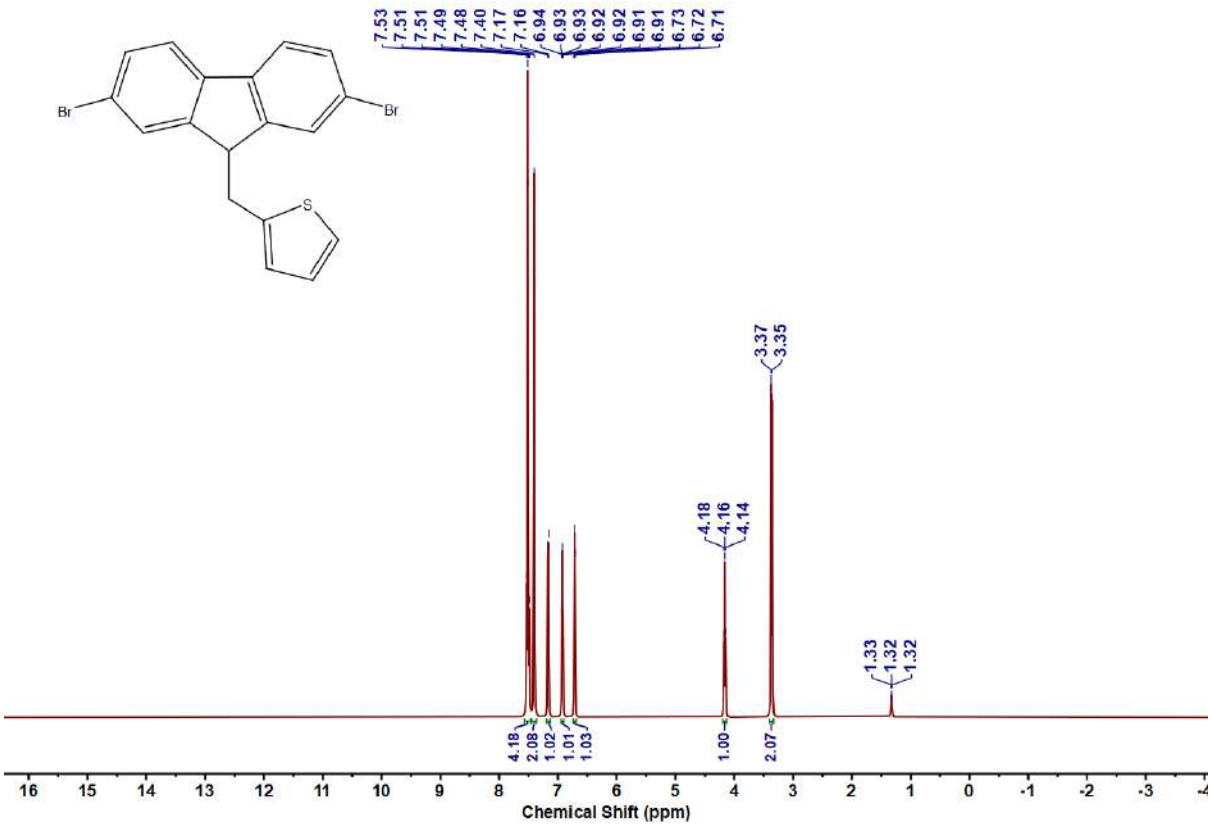

Figure 4.6.A149: ^{1}H NMR Spectrum of **10k**

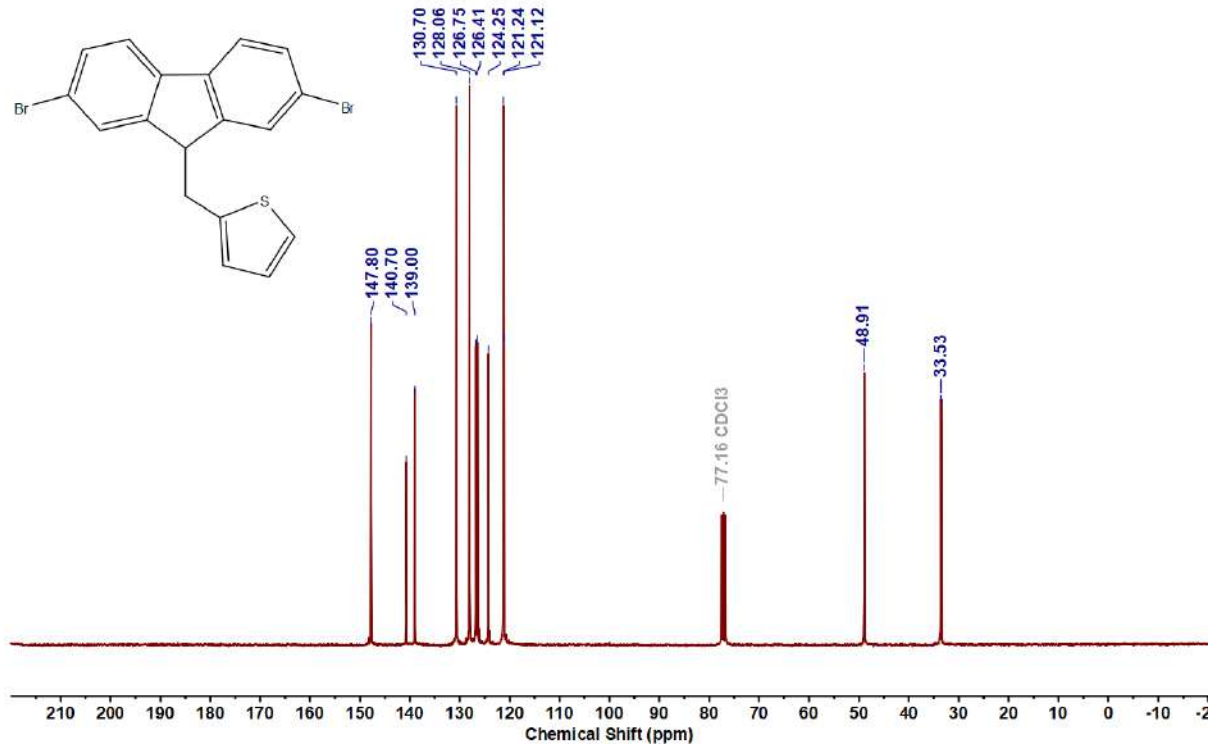

Figure 4.6.A150: ^{13}C{^{1}H} NMR Spectrum of **10k**

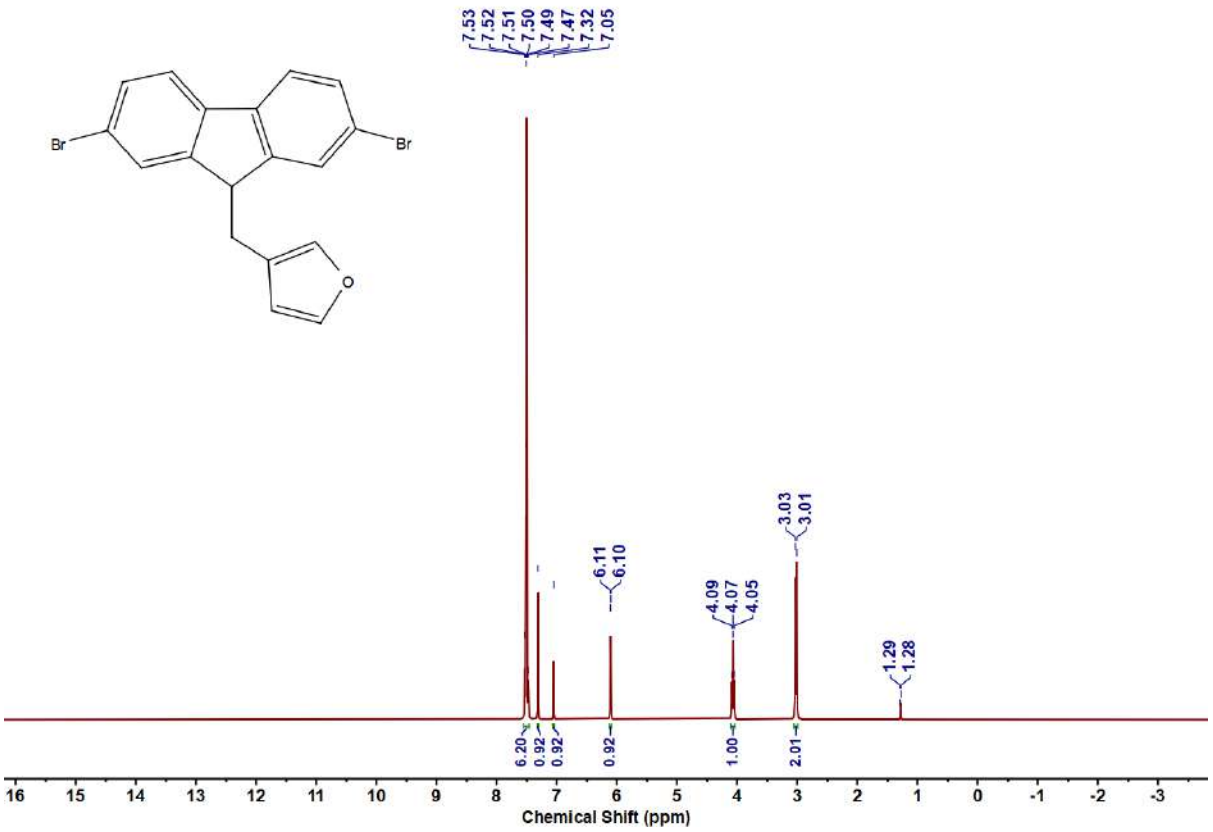

Figure 4.6.A151: ^{1}H NMR Spectrum of **10l**

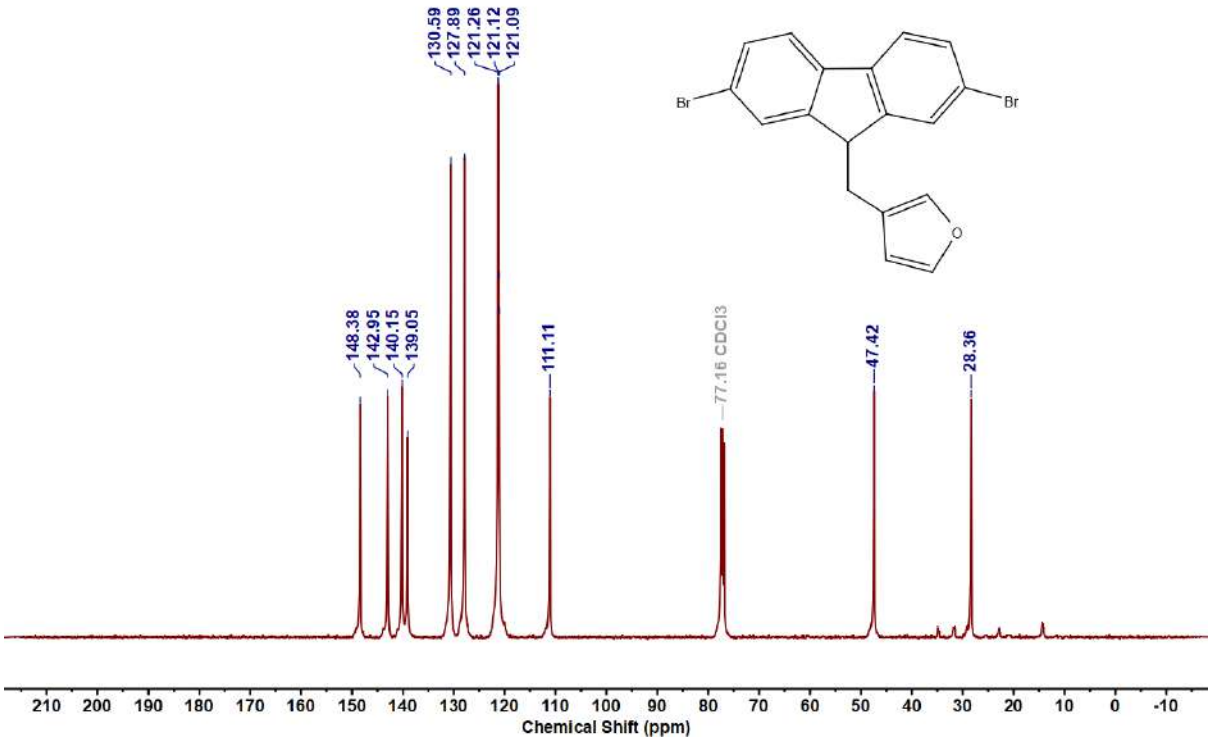

Figure 4.6.A152: ^{13}C{^{1}H} NMR Spectrum of **10l**

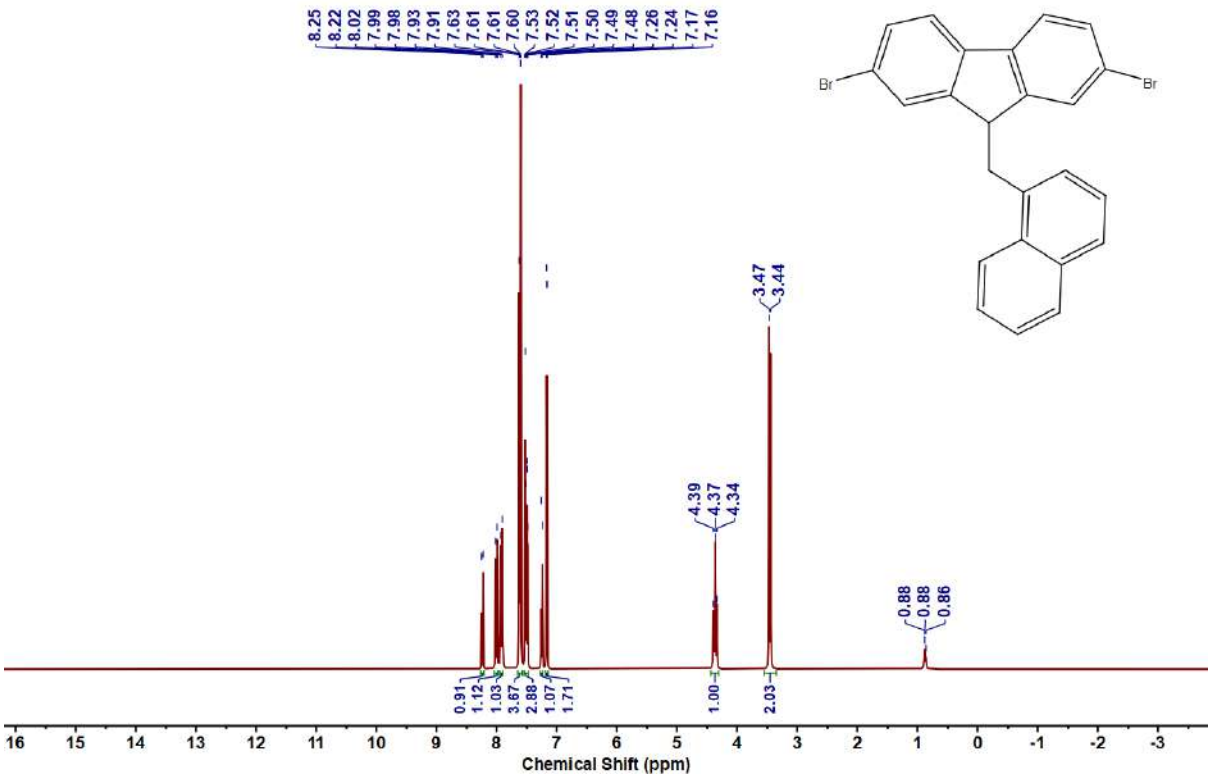

Figure 4.6.A153: ^{1}H NMR Spectrum of **10m**

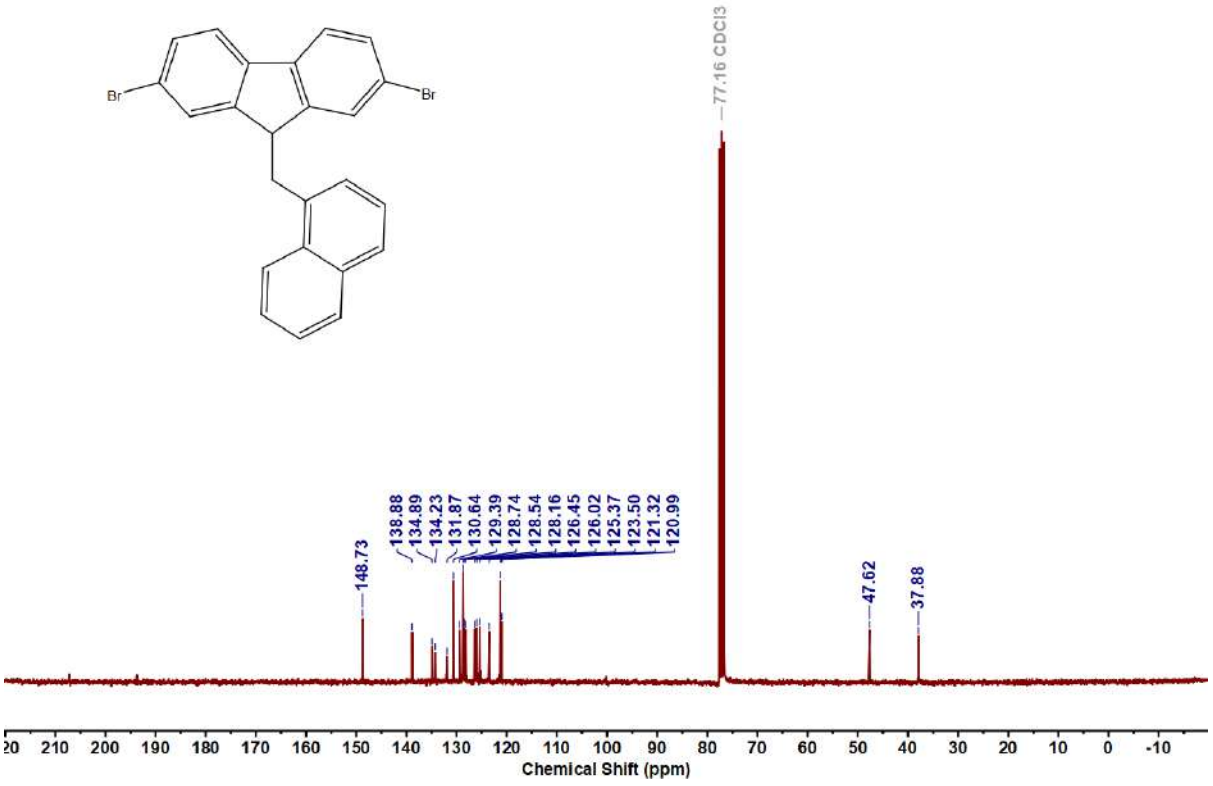

Figure 4.6.A154: ^{13}C{^{1}H} NMR Spectrum of **10m**

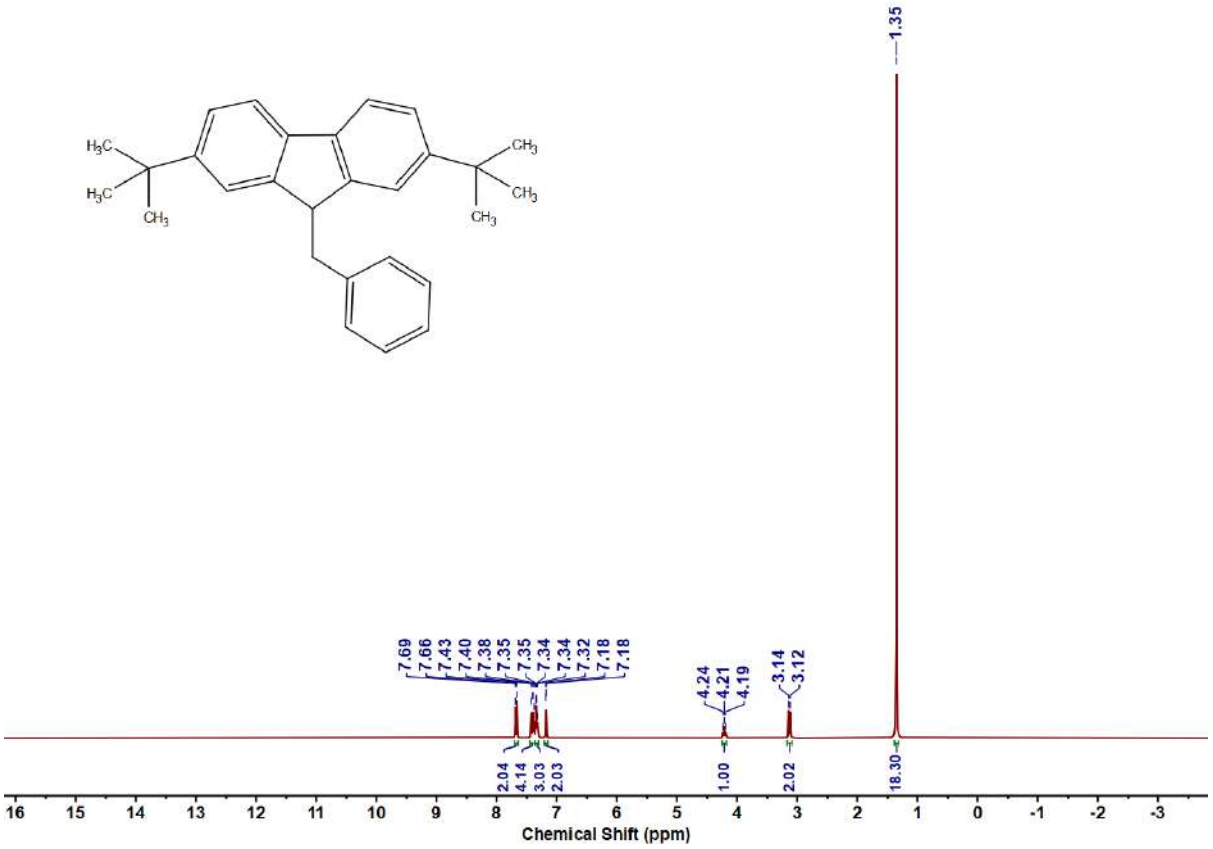

Figure 4.6.A155: ^{1}H NMR Spectrum of **11a**

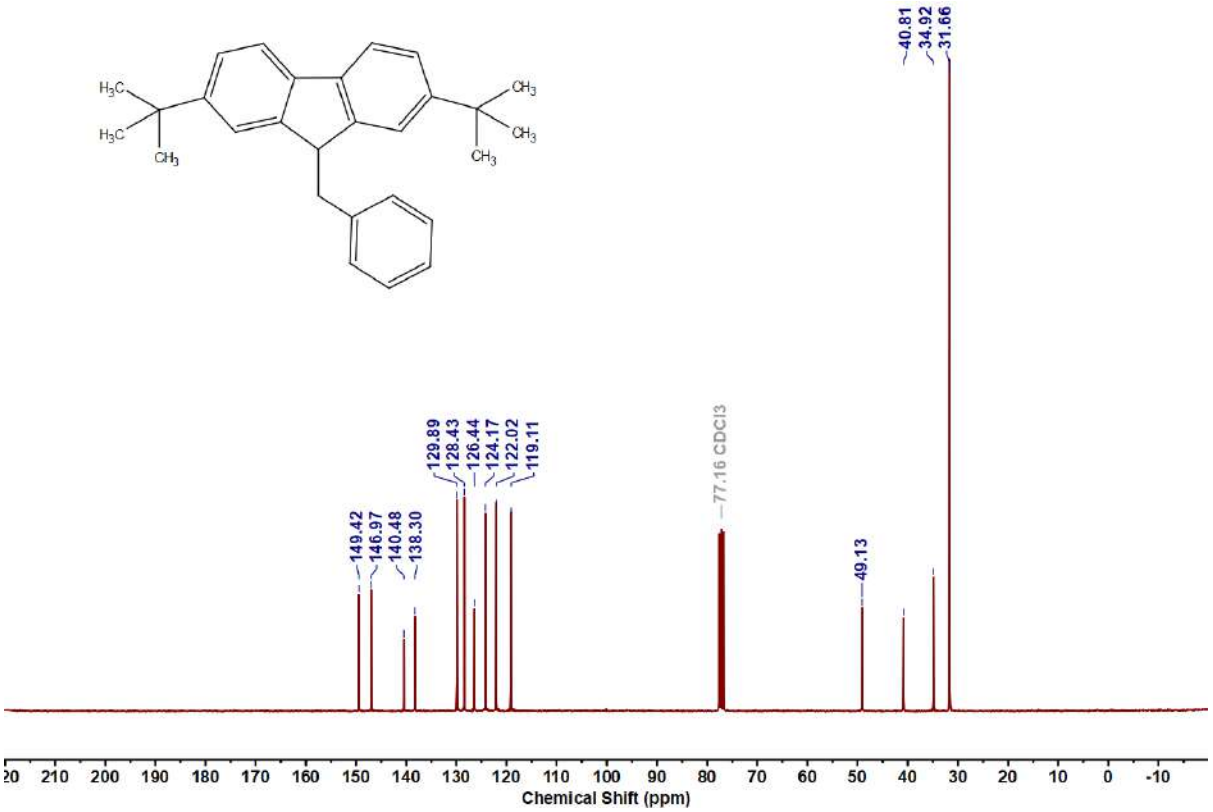

Figure 4.6.A156: ^{13}C{^{1}H} NMR Spectrum of **11a**

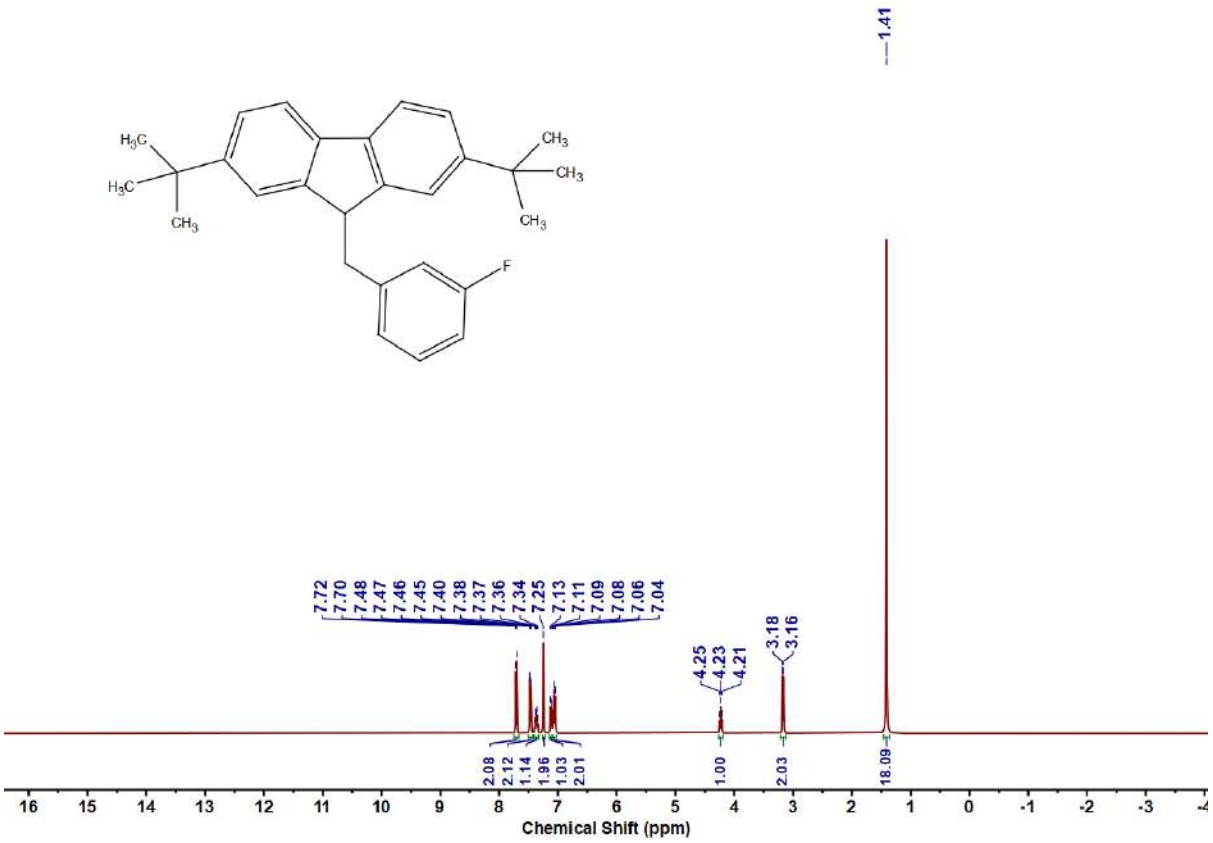

Figure 4.6.A157: ^{1}H NMR Spectrum of **11b**

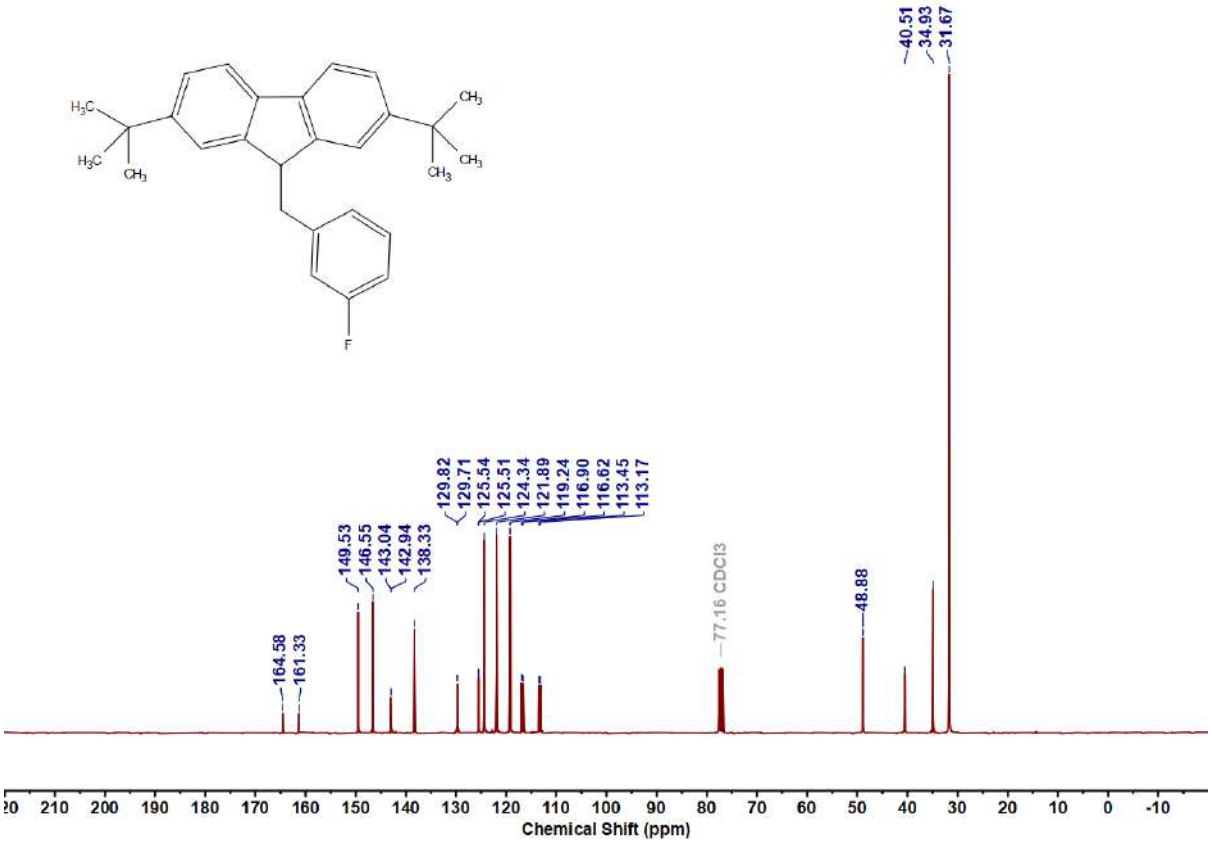

Figure 4.6.A158: ^{13}C{^{1}H} NMR Spectrum of **11b**

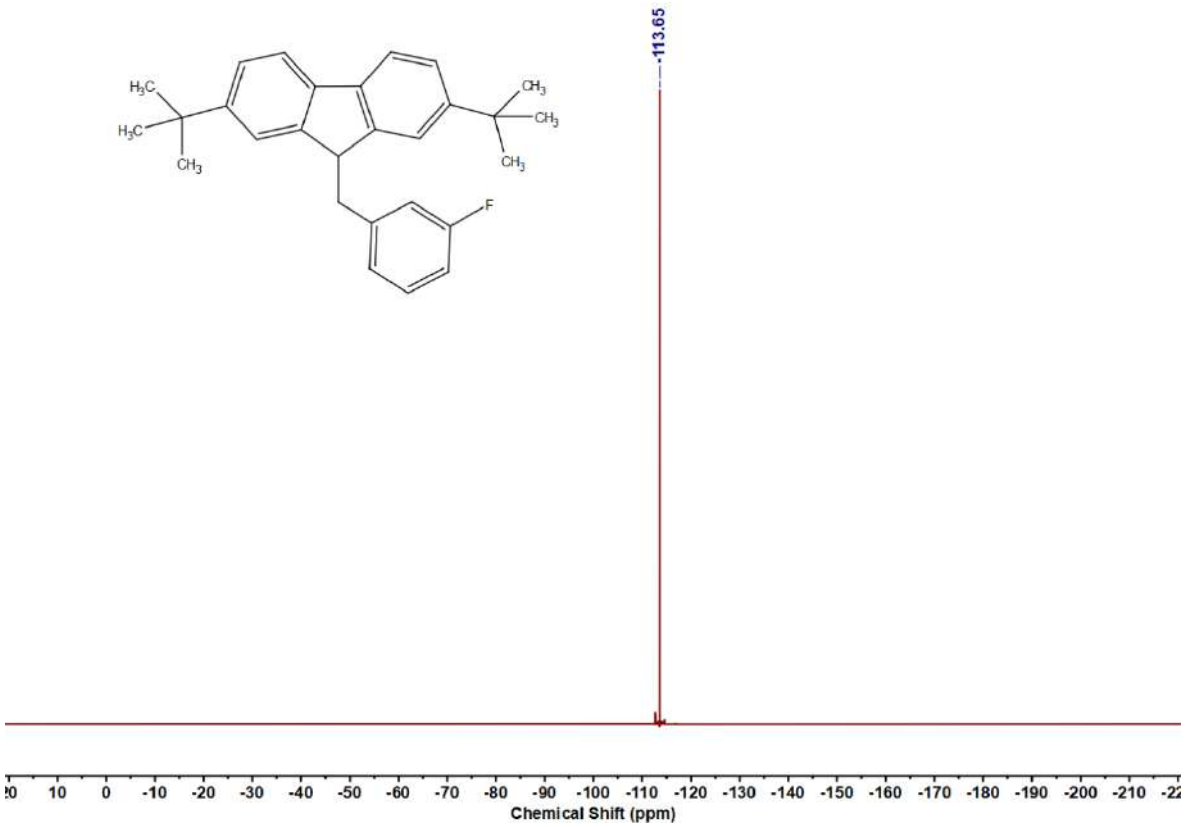

Figure 4.6.A159: ^{19}F NMR Spectrum of **11b**

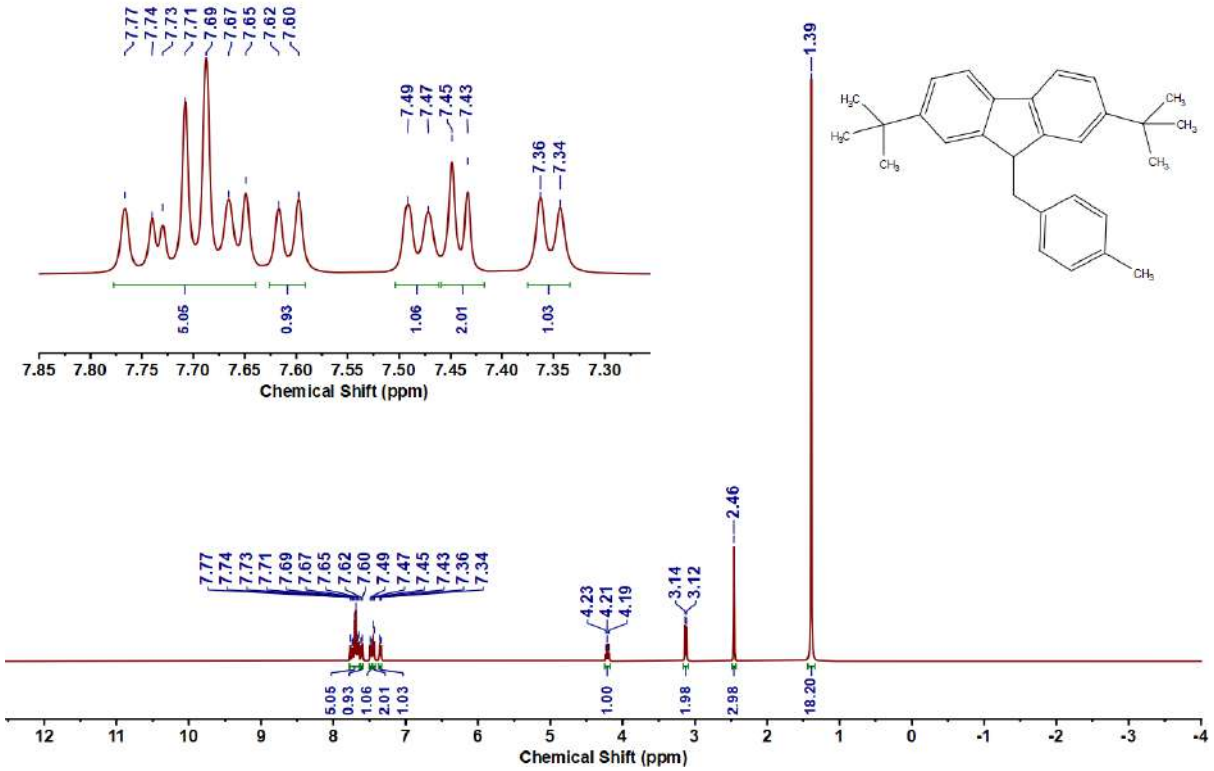

Figure 4.6.A160: ^{1}H NMR Spectrum of **11c**

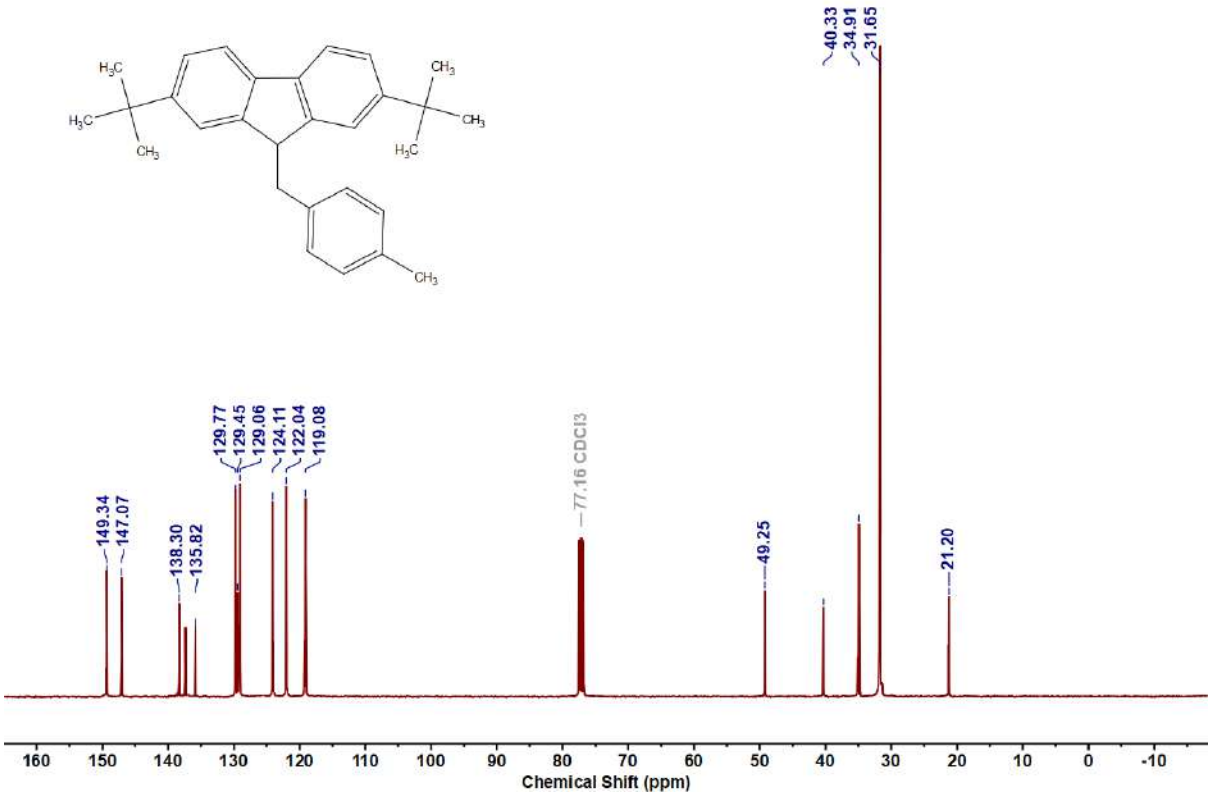

Figure 4.6.A161: $^{13}C\{^{1}H\}$ NMR Spectrum of **11c**

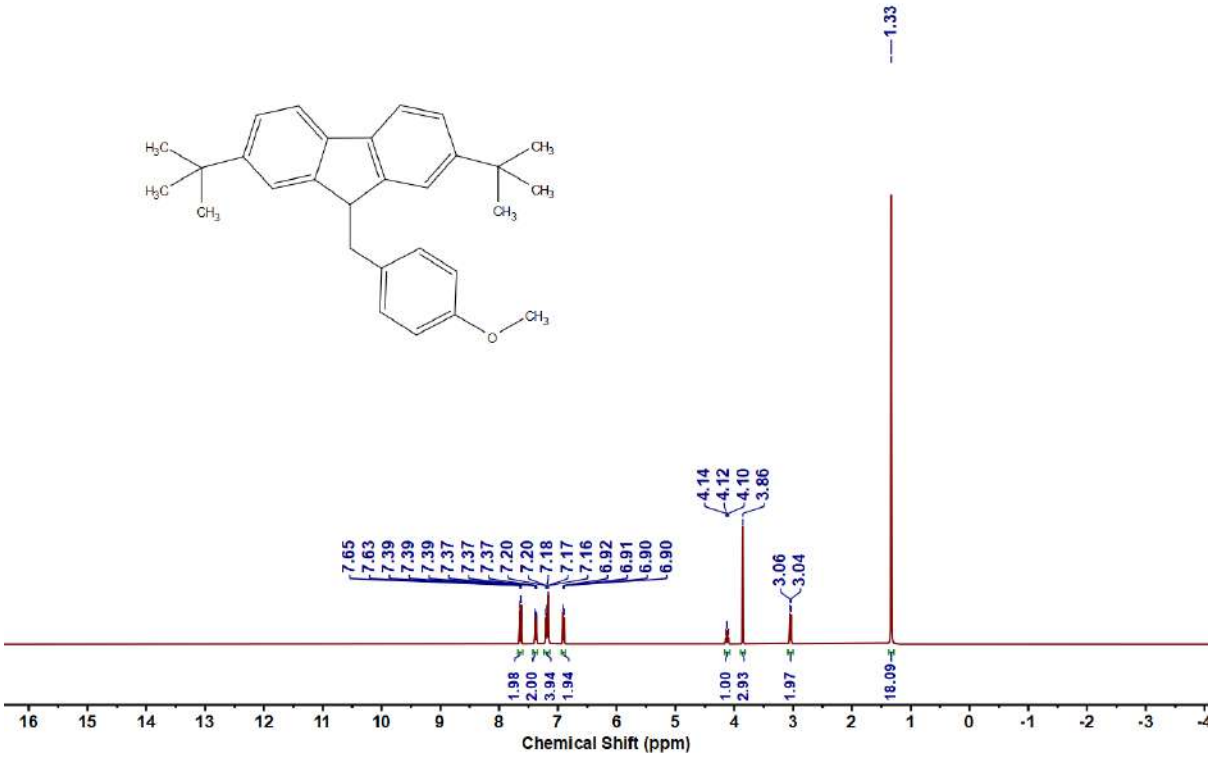

Figure 4.6.A162: ^{1}H NMR Spectrum of **11d**

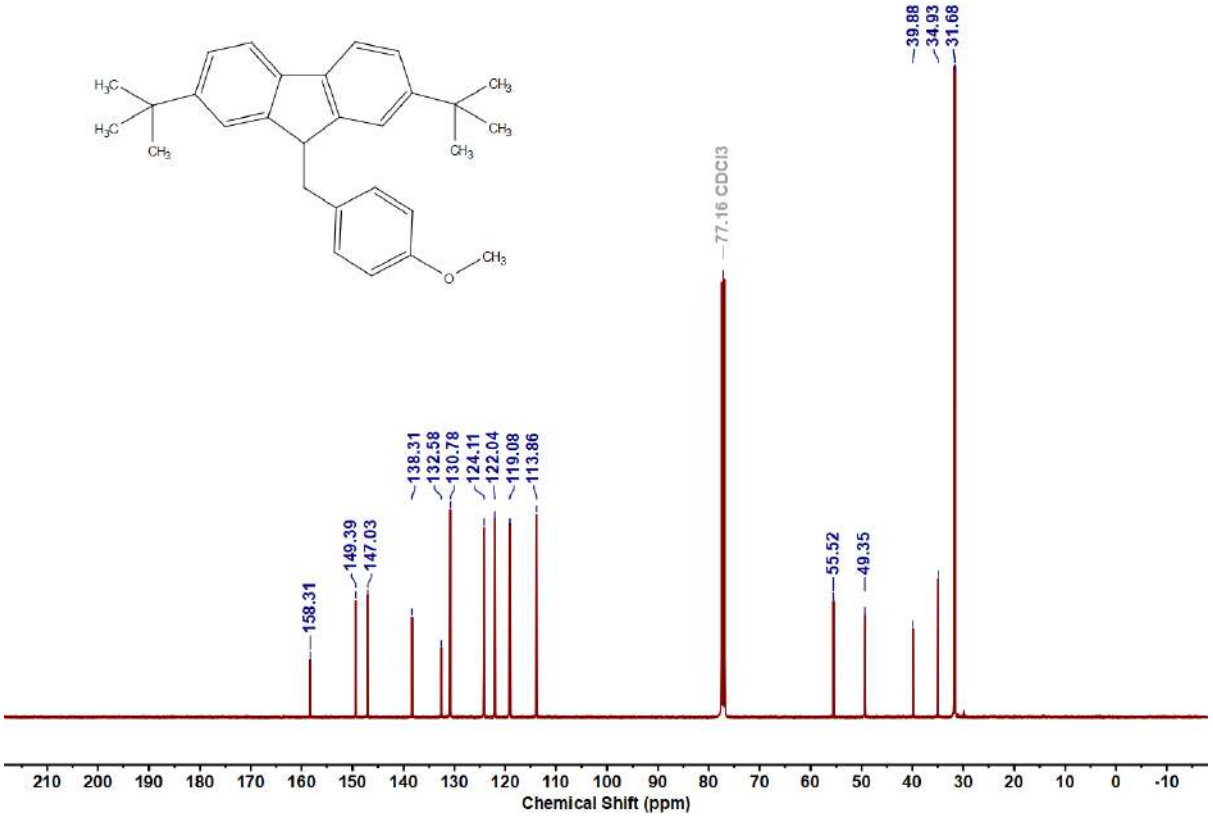

Figure 4.6.A163: $^{13}C\{^{1}H\}$ NMR Spectrum of **11d**

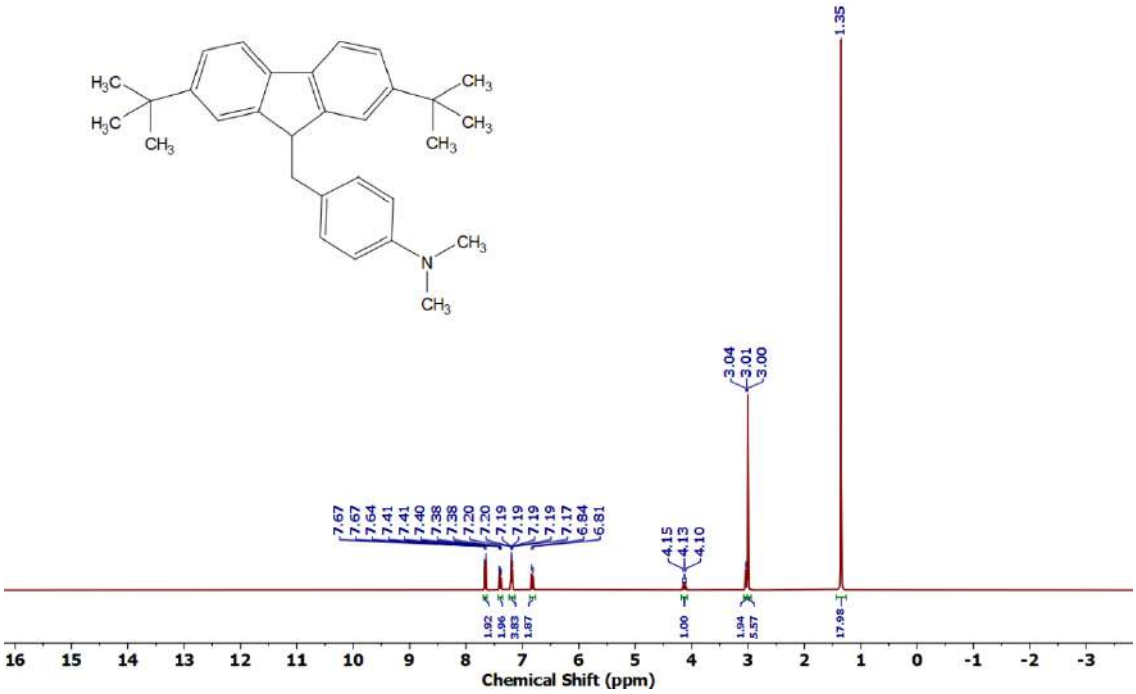

Figure 4.6.A164: ^{1}H NMR Spectrum of **11e**

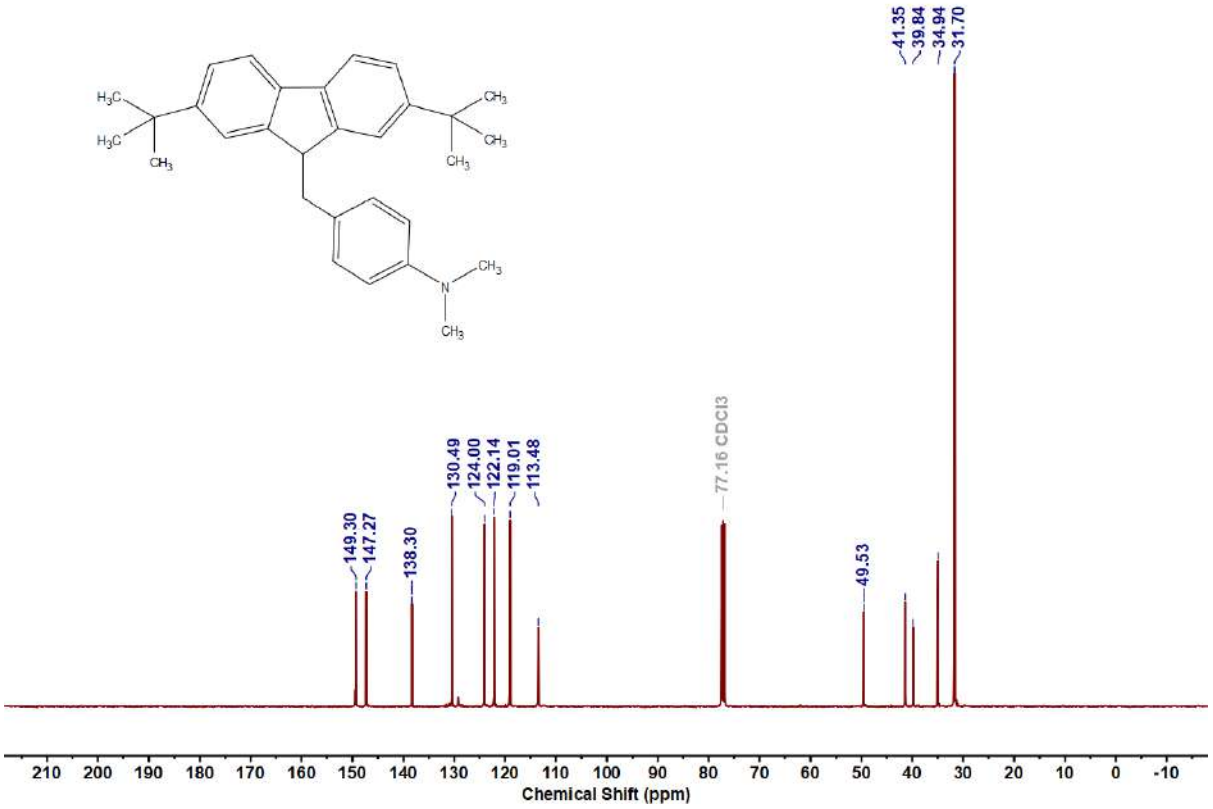

Figure 4.6.A165: $^{13}C\{^{1}H\}$ NMR Spectrum of **11e**

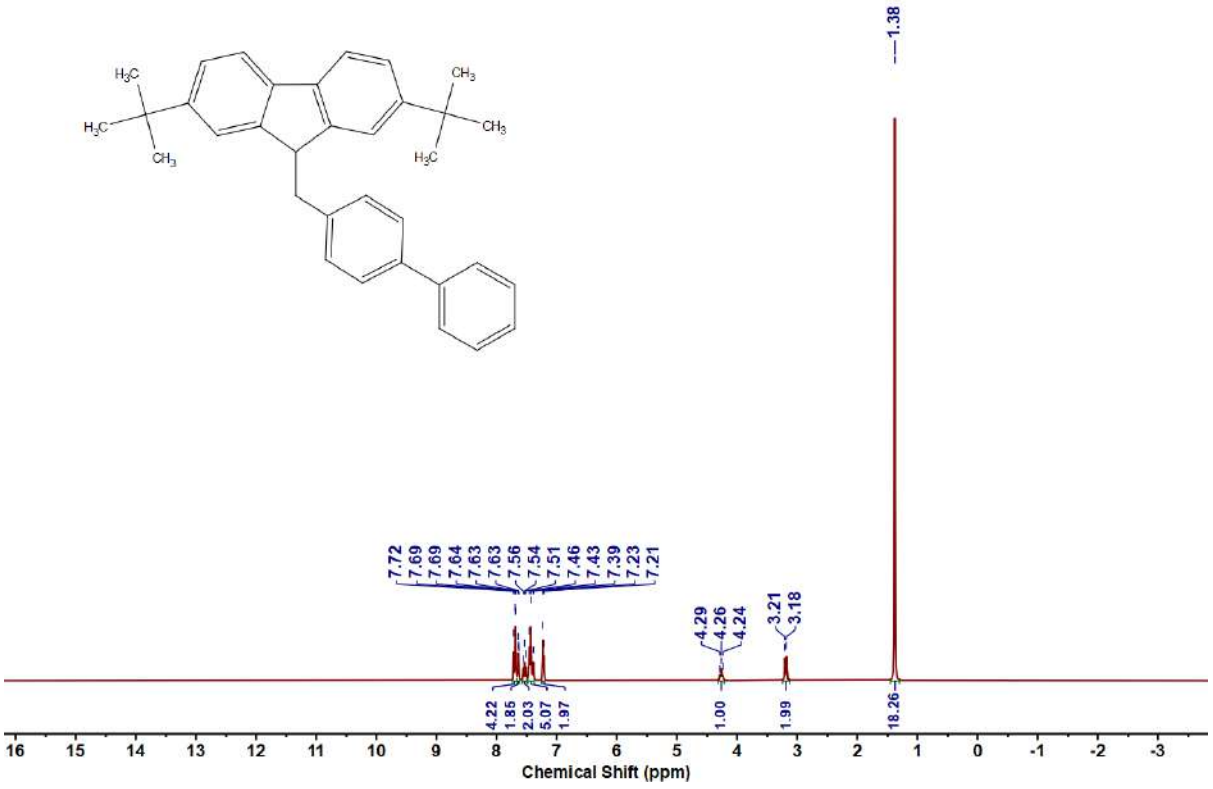

Figure 4.6.A166: ^{1}H NMR Spectrum of **11f**

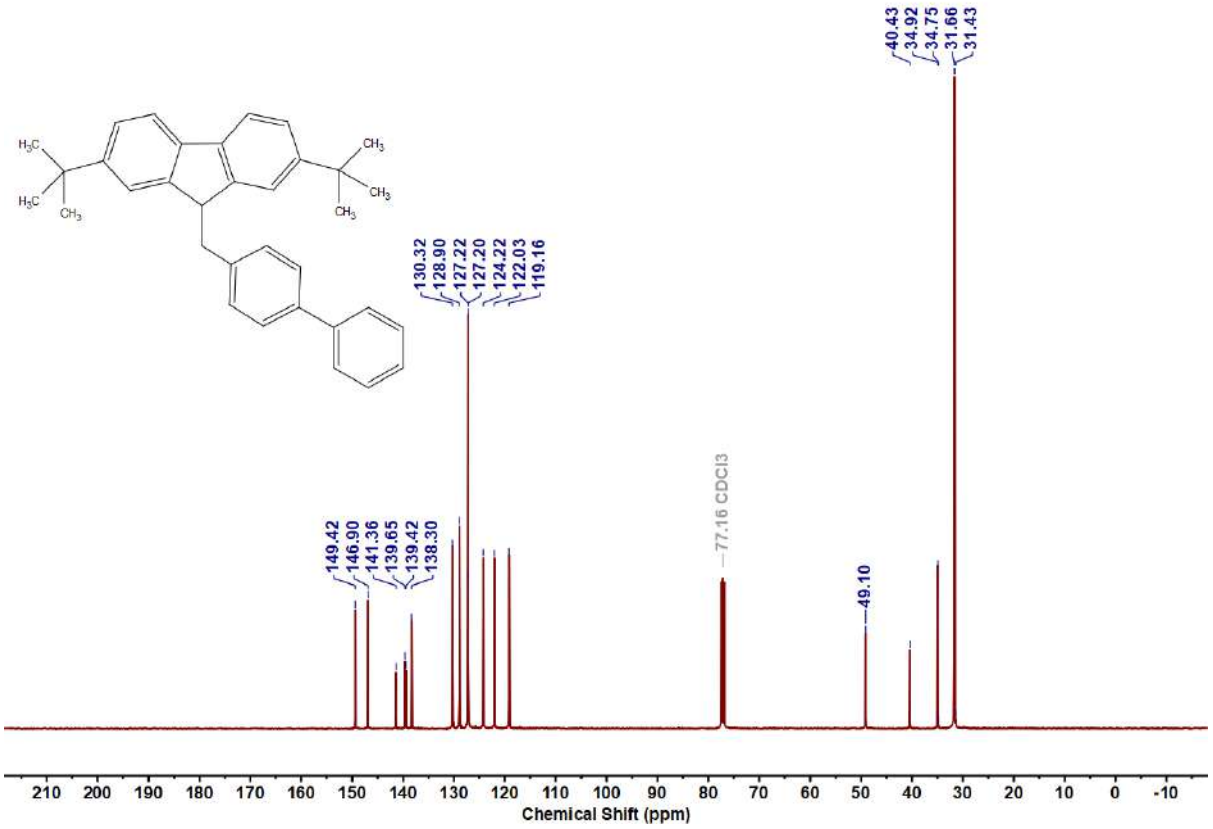

Figure 4.6.A167: $^{13}C\{^{1}H\}$ NMR Spectrum of **11f**

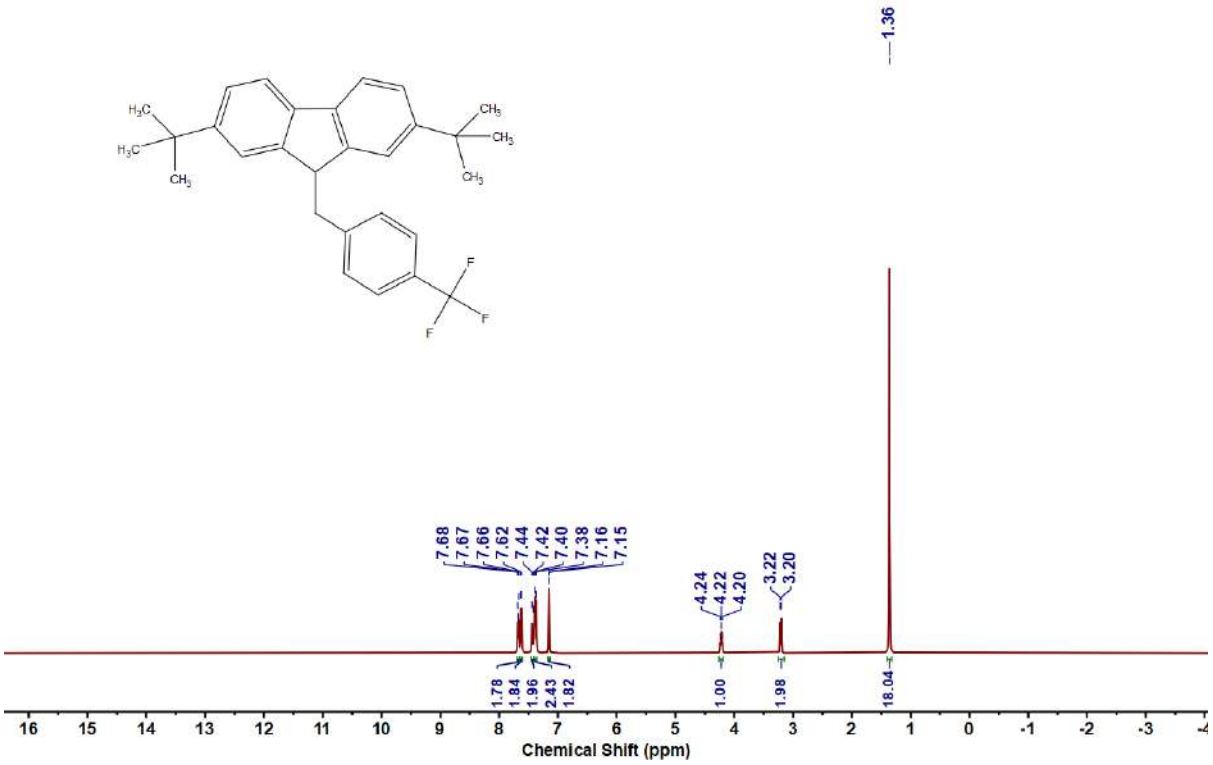

Figure 4.6.A168: ^{1}H NMR Spectrum of **11g**

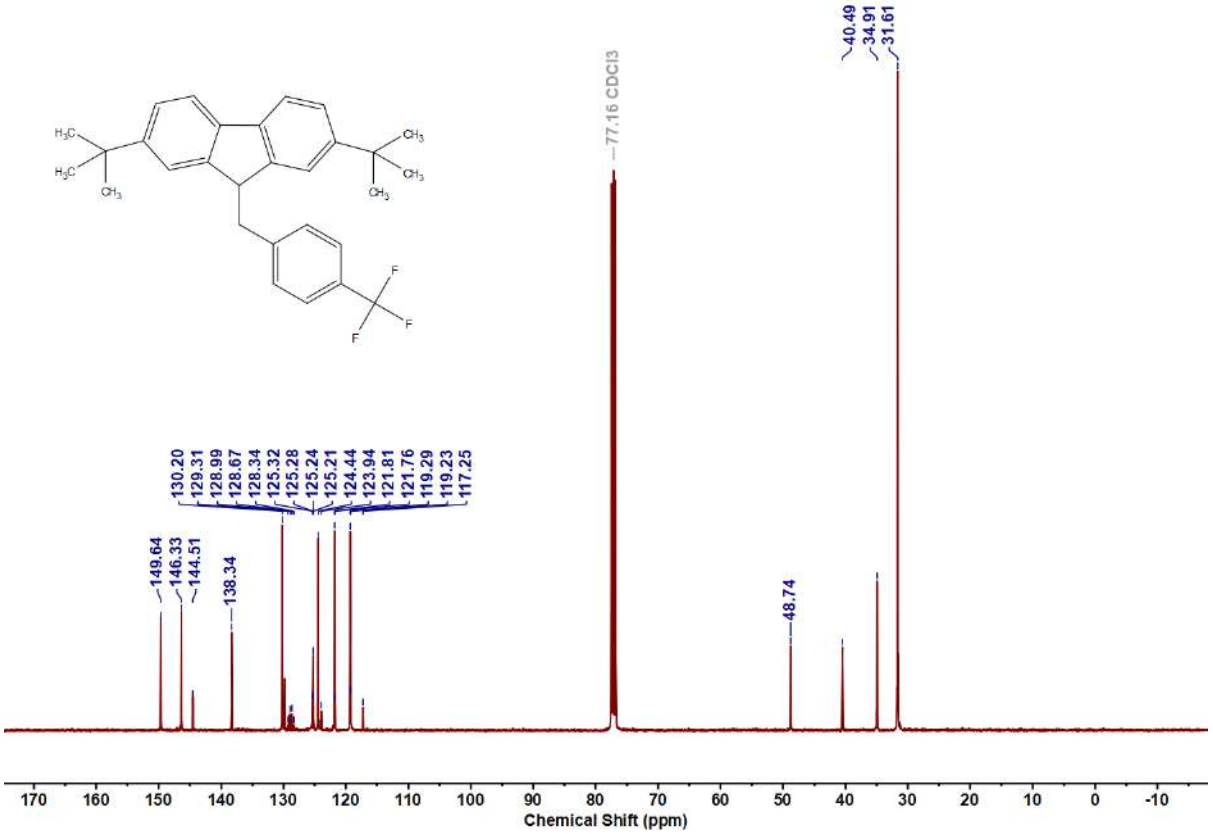

Figure 4.6.A169: $^{13}C\{^{1}H\}$ NMR Spectrum of **11g**

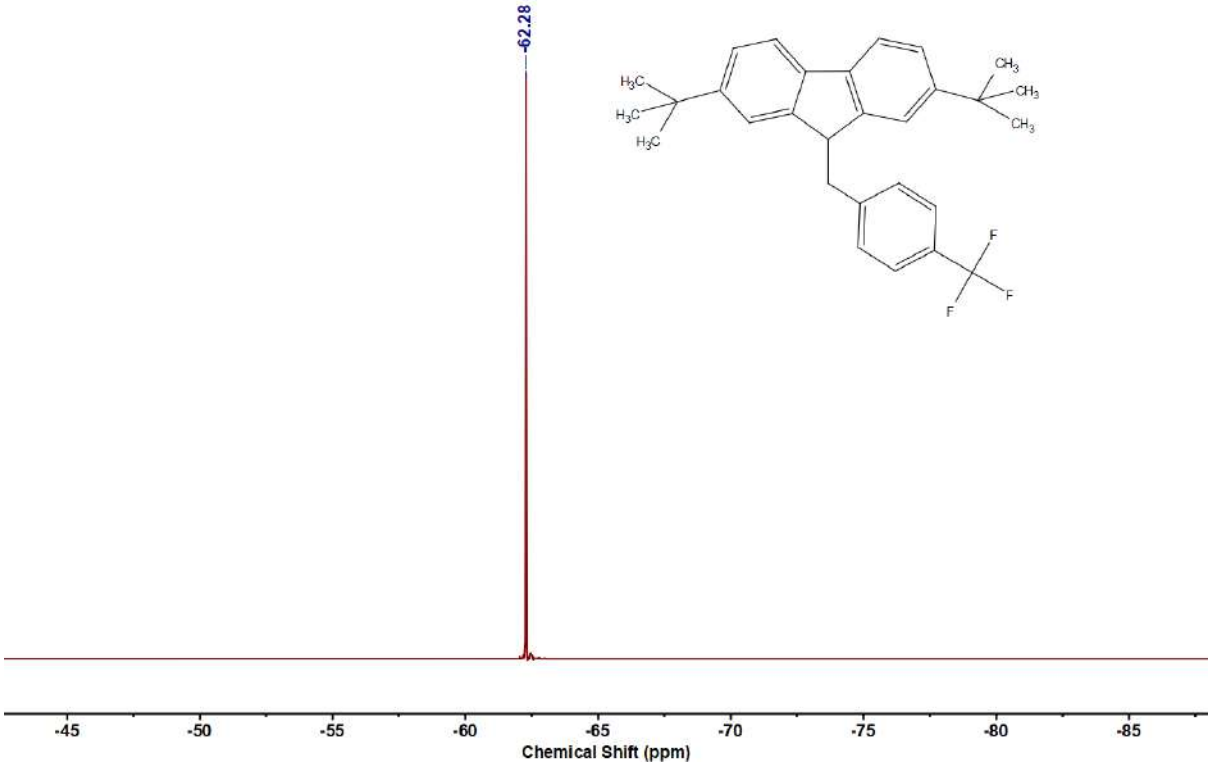

Figure 4.6.A170: ^{19}F NMR Spectrum of **11g**

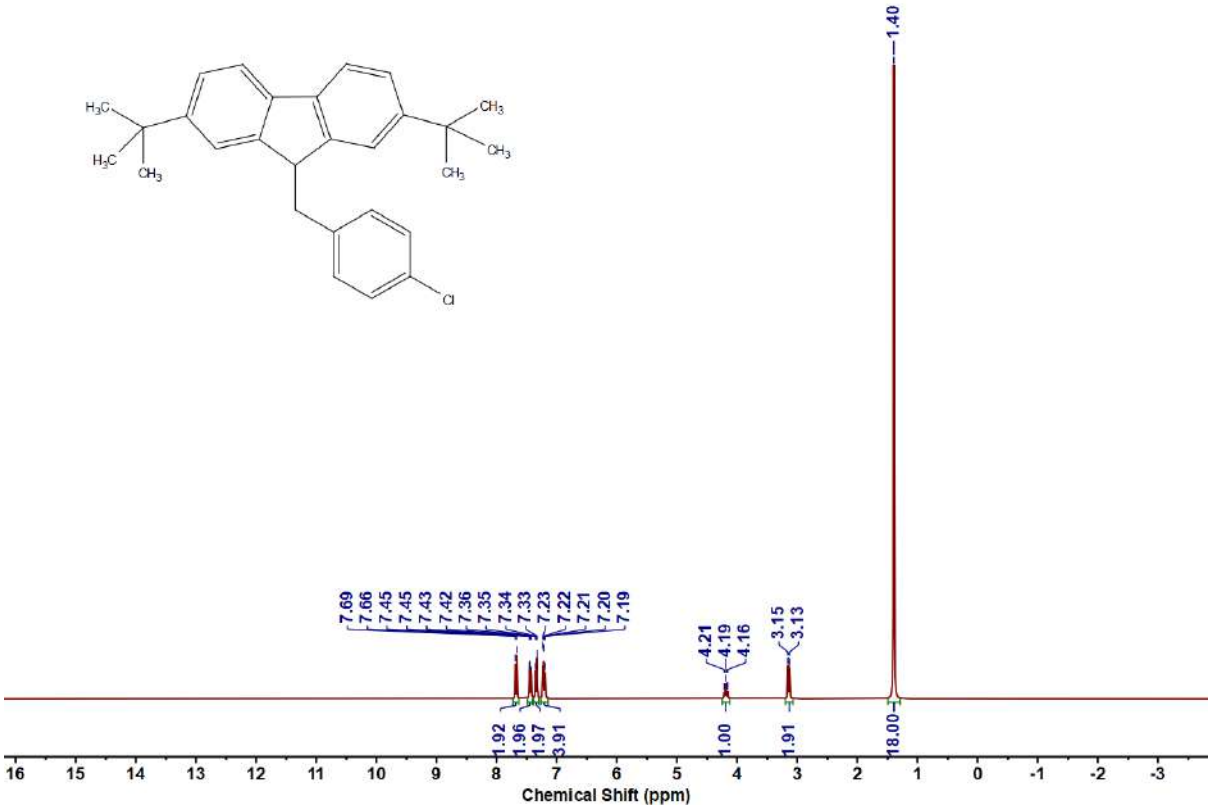

Figure 4.6.A171: ^{1}H NMR Spectrum of **11h**

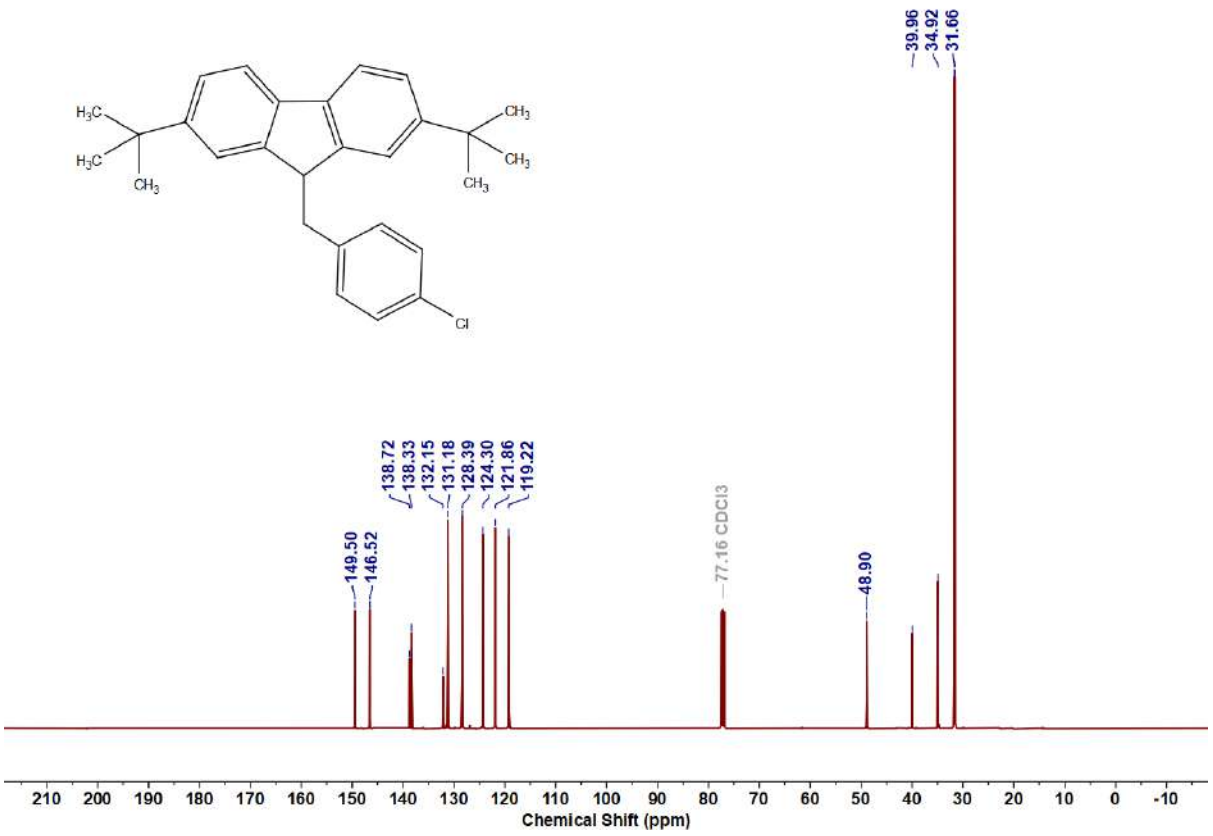

Figure 4.6.A172: ^{13}C{^{1}H} NMR Spectrum of **11h**

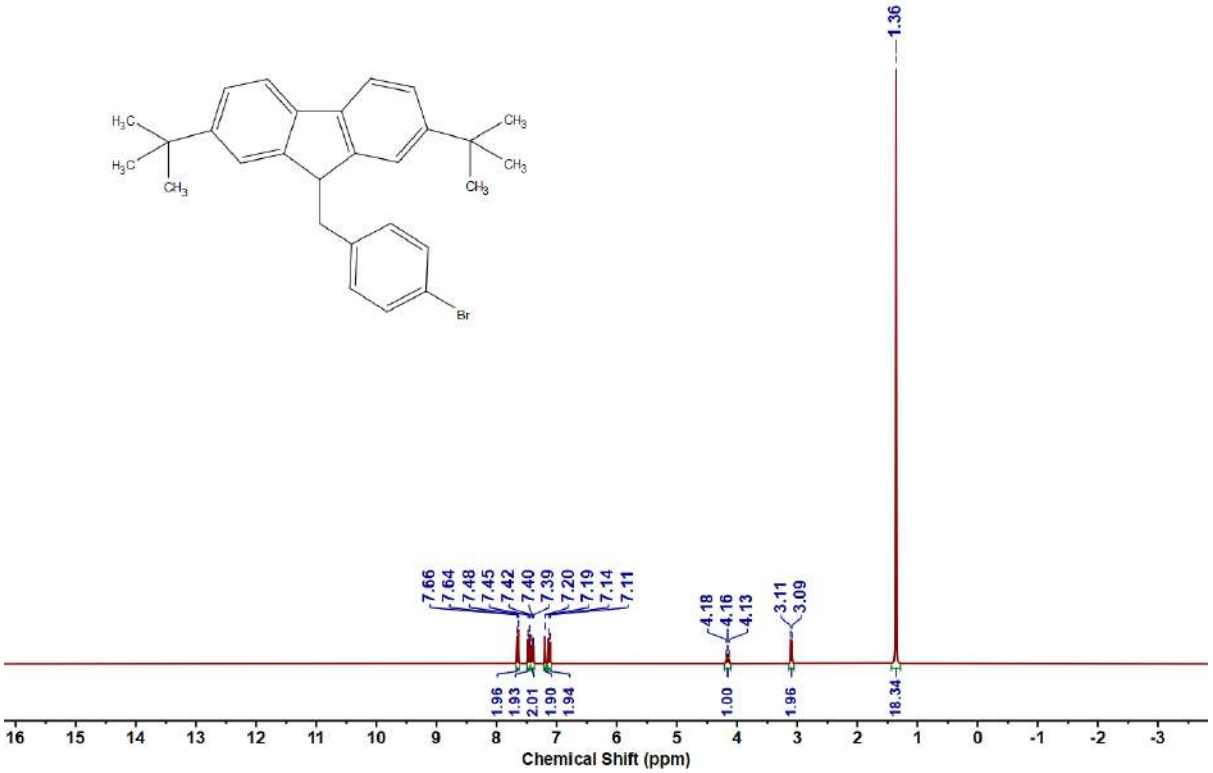

Figure 4.6.A173: ^{1}H NMR Spectrum of **11i**

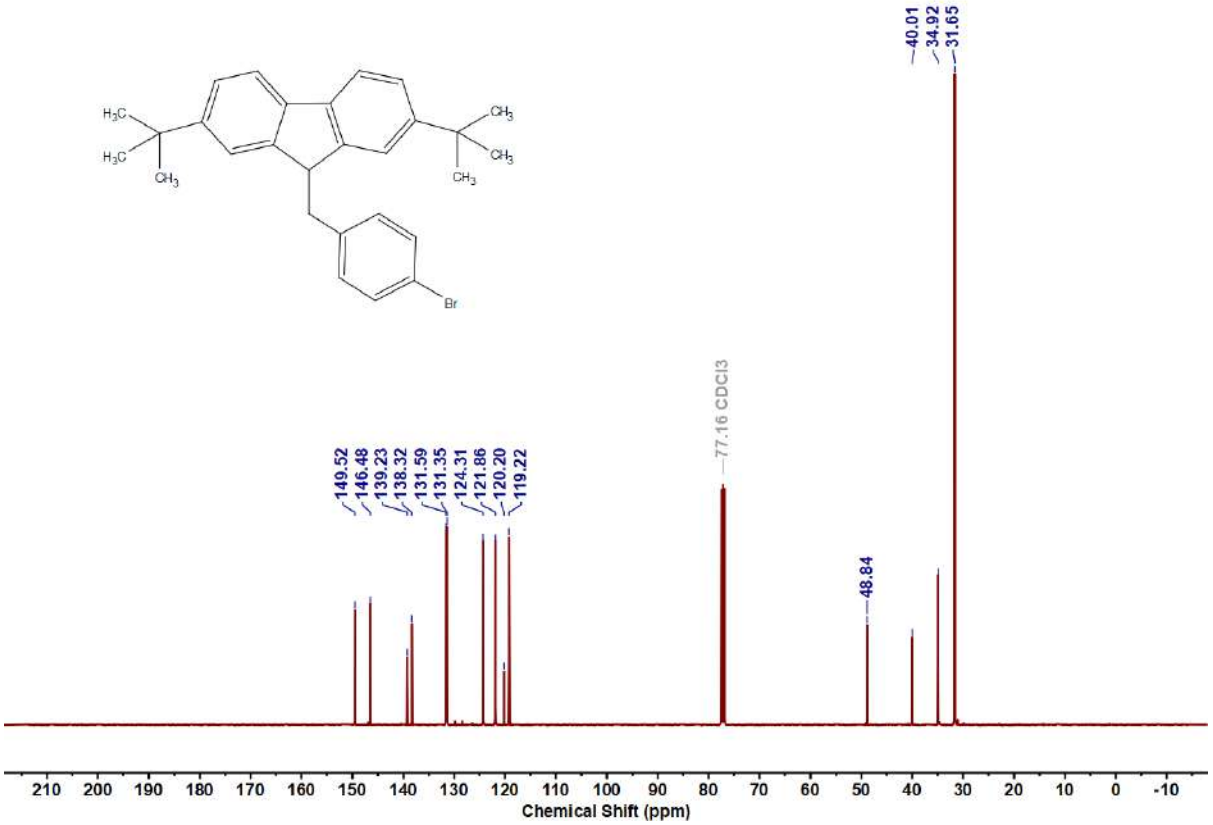

Figure 4.6.A174: ^{13}C{^{1}H} NMR Spectrum of **11i**

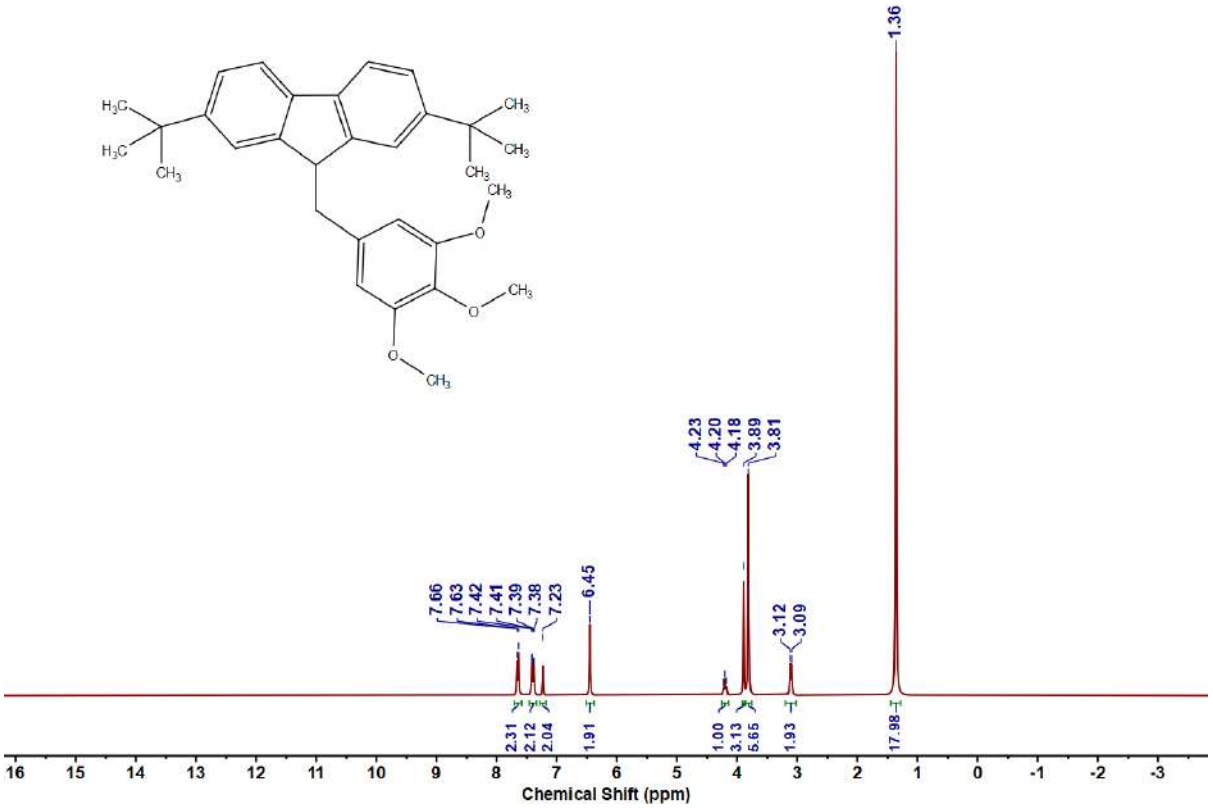

Figure 4.6.A175: ^{1}H NMR Spectrum of **11j**

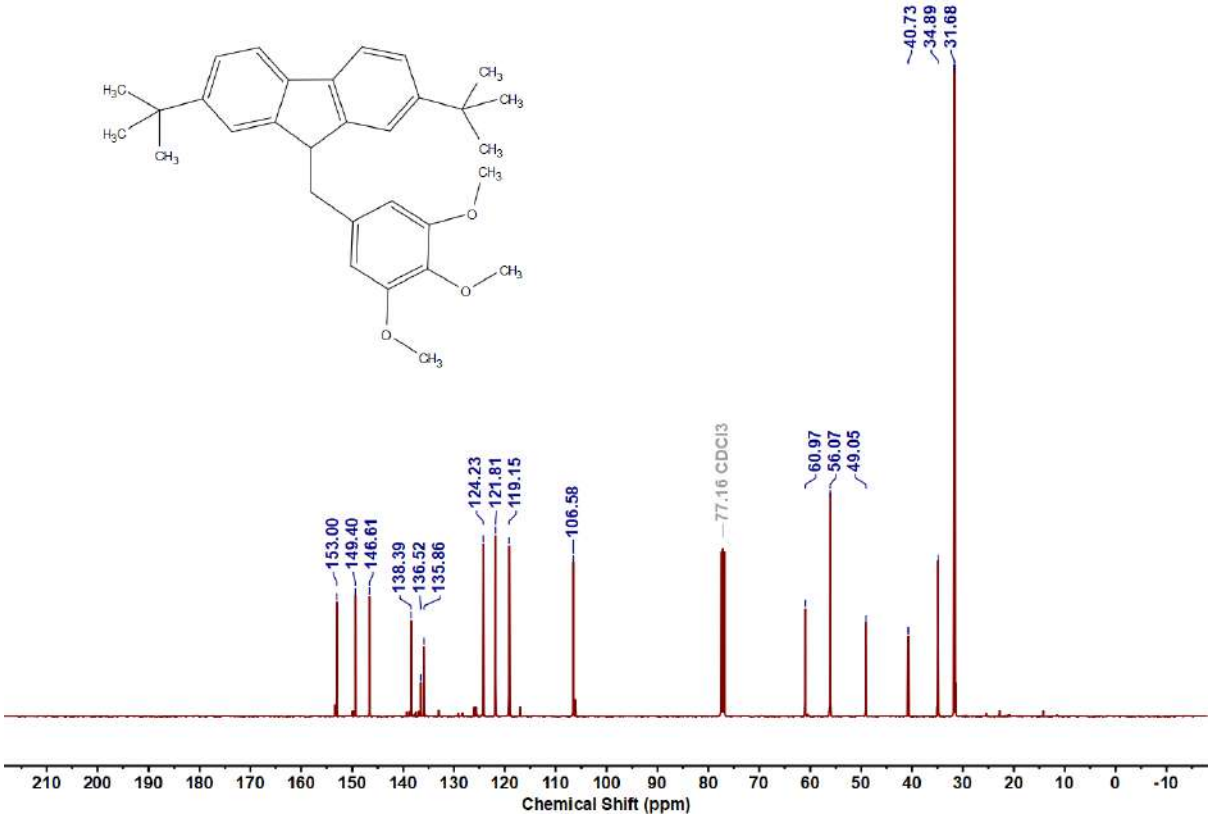

Figure 4.6.A176: ^{13}C{^{1}H} NMR Spectrum of **11j**

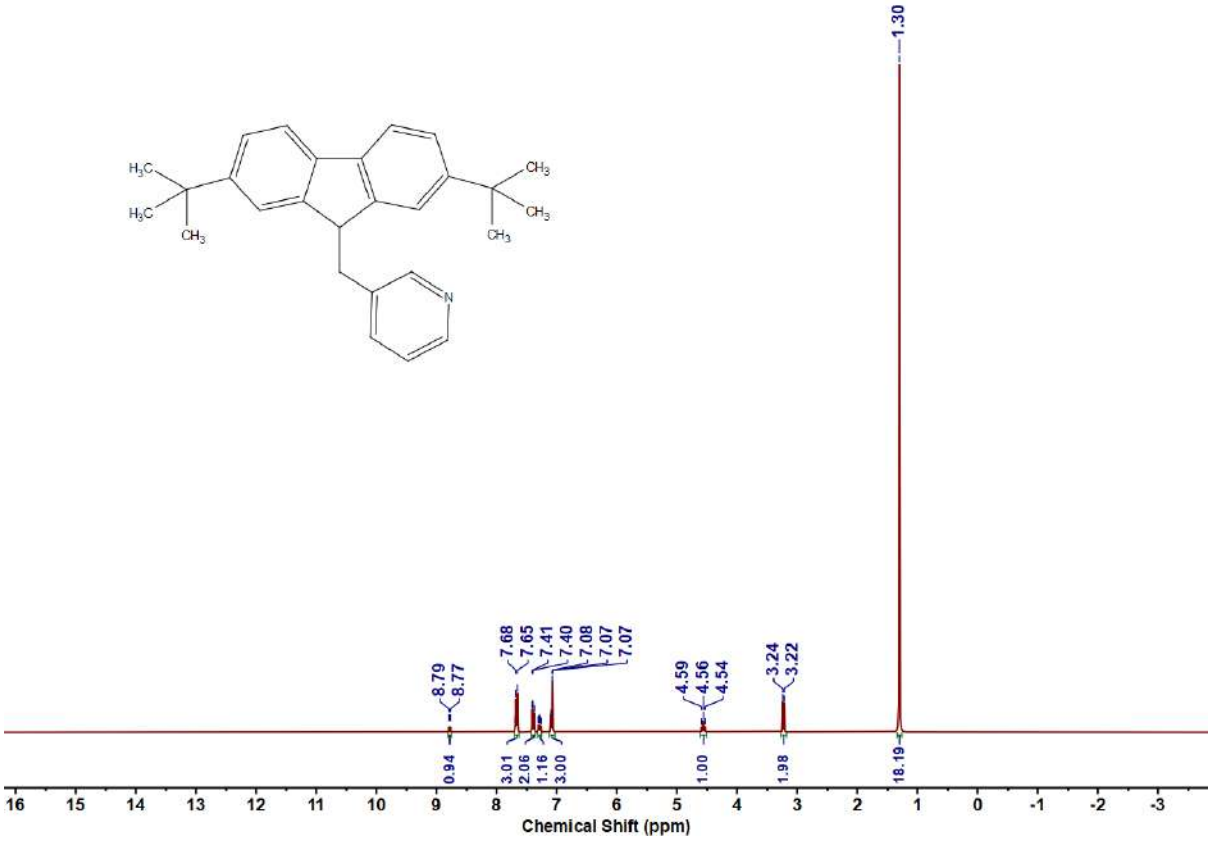

Figure 4.6.A177: ^{1}H NMR Spectrum of **11k**

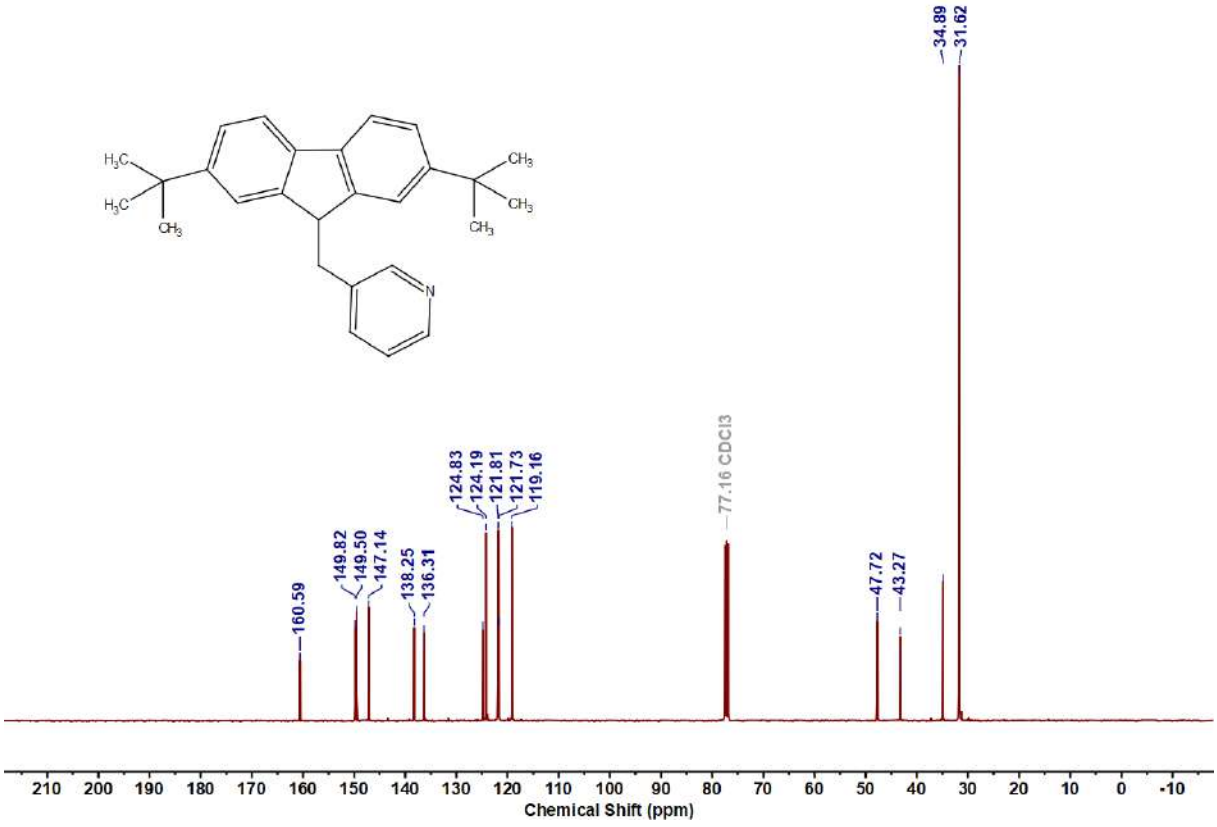

Figure 4.6.A178: ^{13}C{^{1}H} NMR Spectrum of **11k**

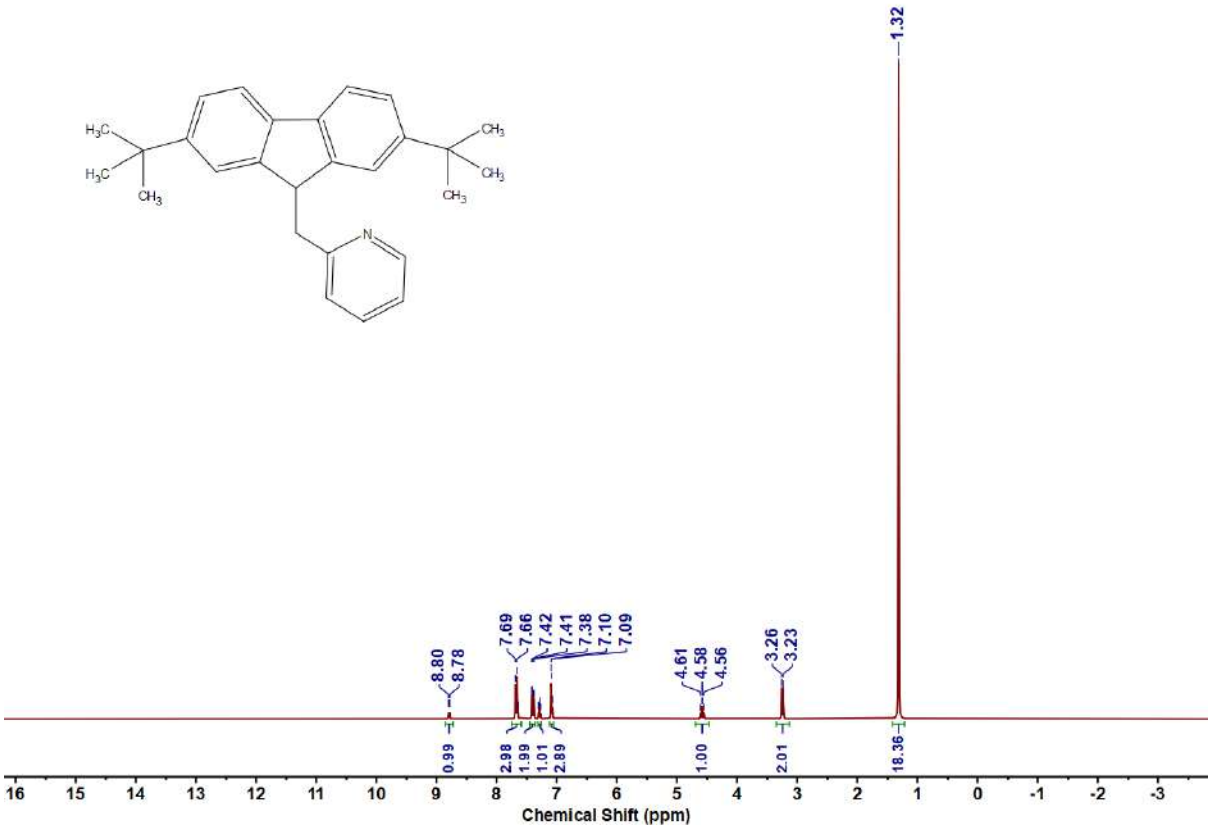

Figure 4.6.A179: ^{1}H NMR Spectrum of **11l**

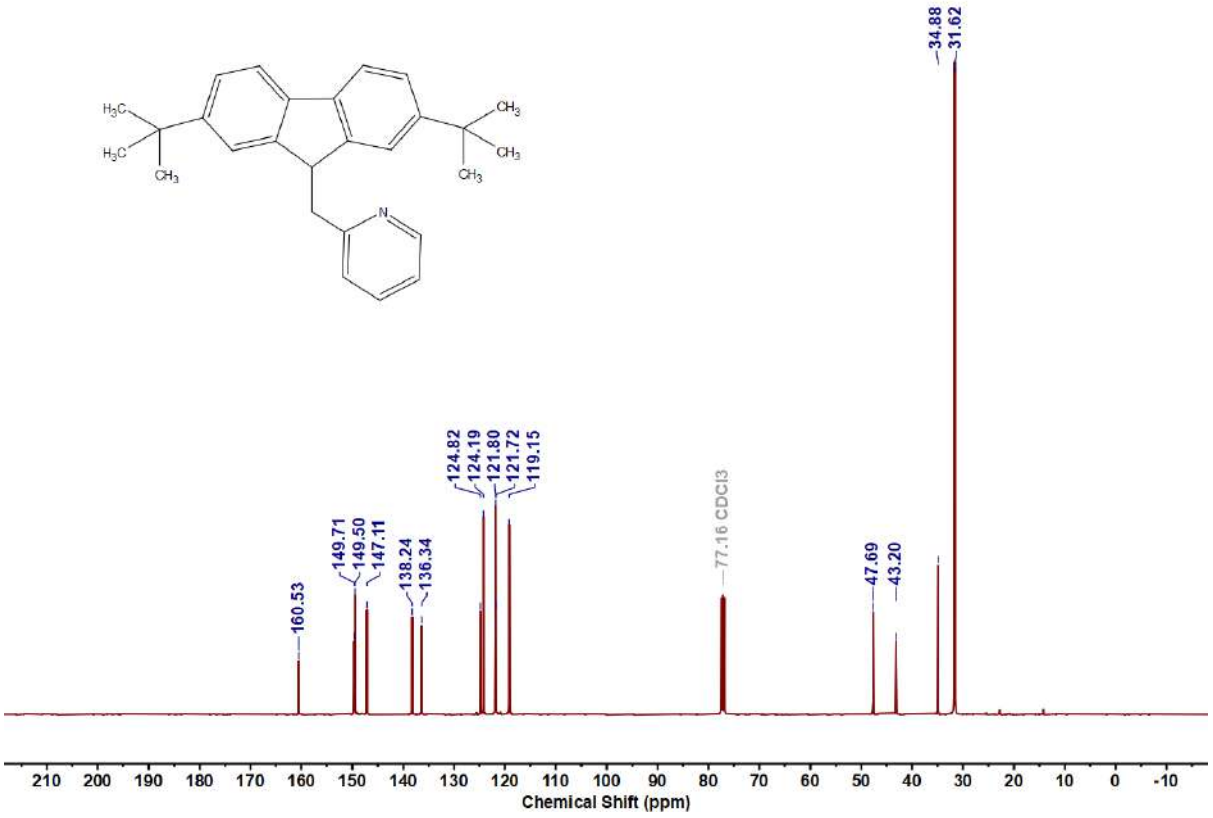

Figure 4.6.A180: ^{13}C{^{1}H} NMR Spectrum of **11l**

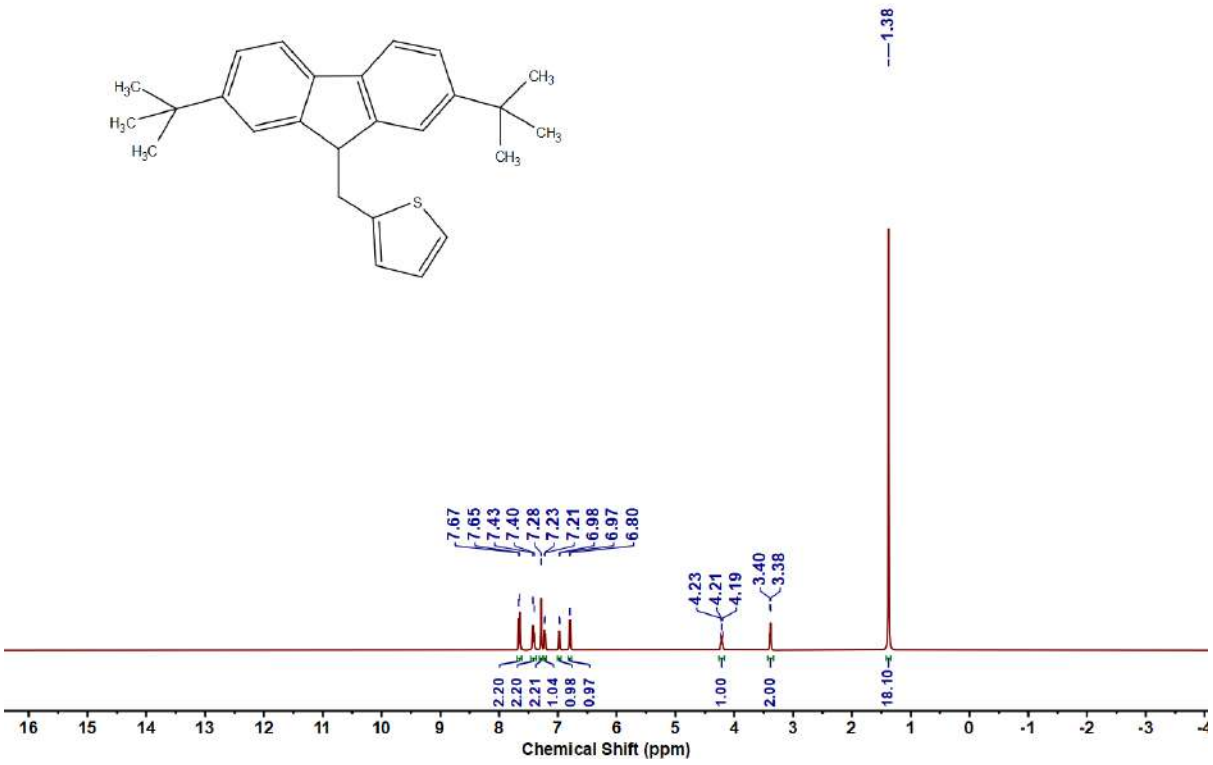

Figure 4.6.A181: ^{1}H NMR Spectrum of **11m**

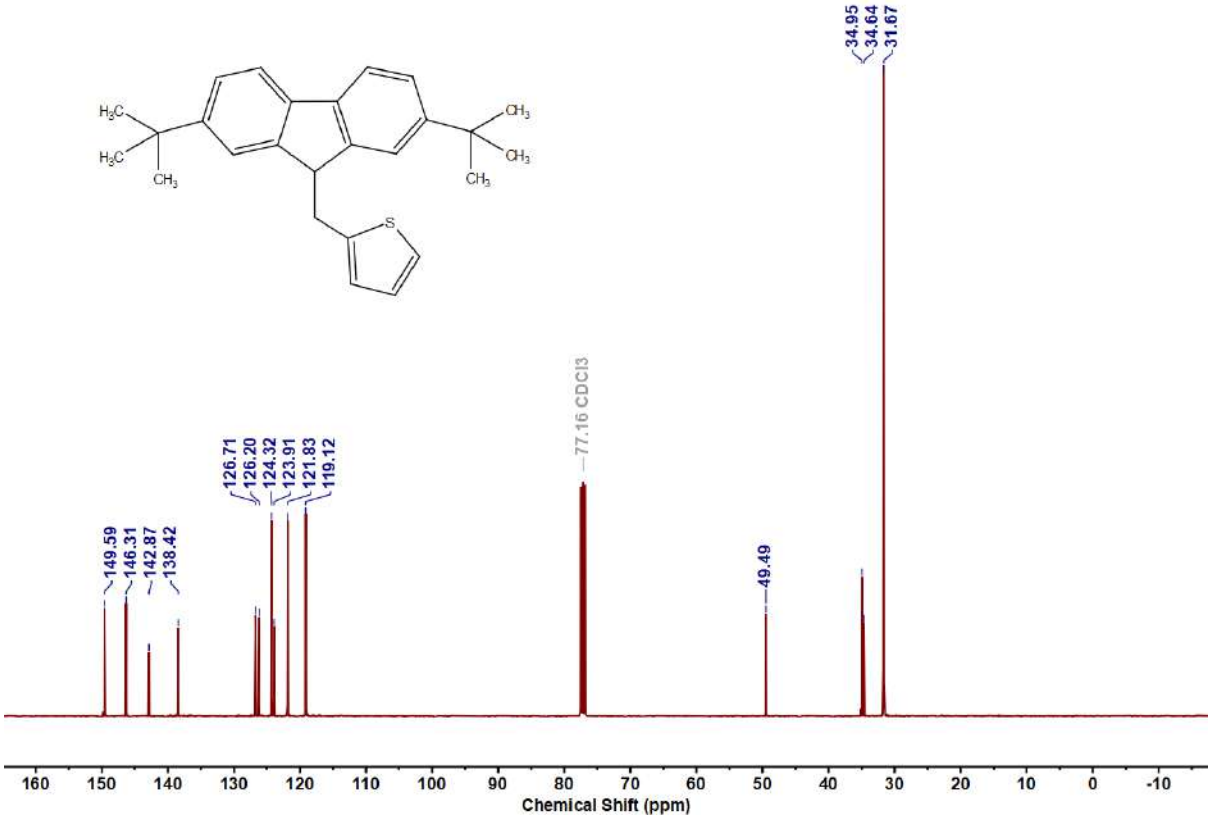

Figure 4.6.A182: ^{13}C{^{1}H} NMR Spectrum of **11m**

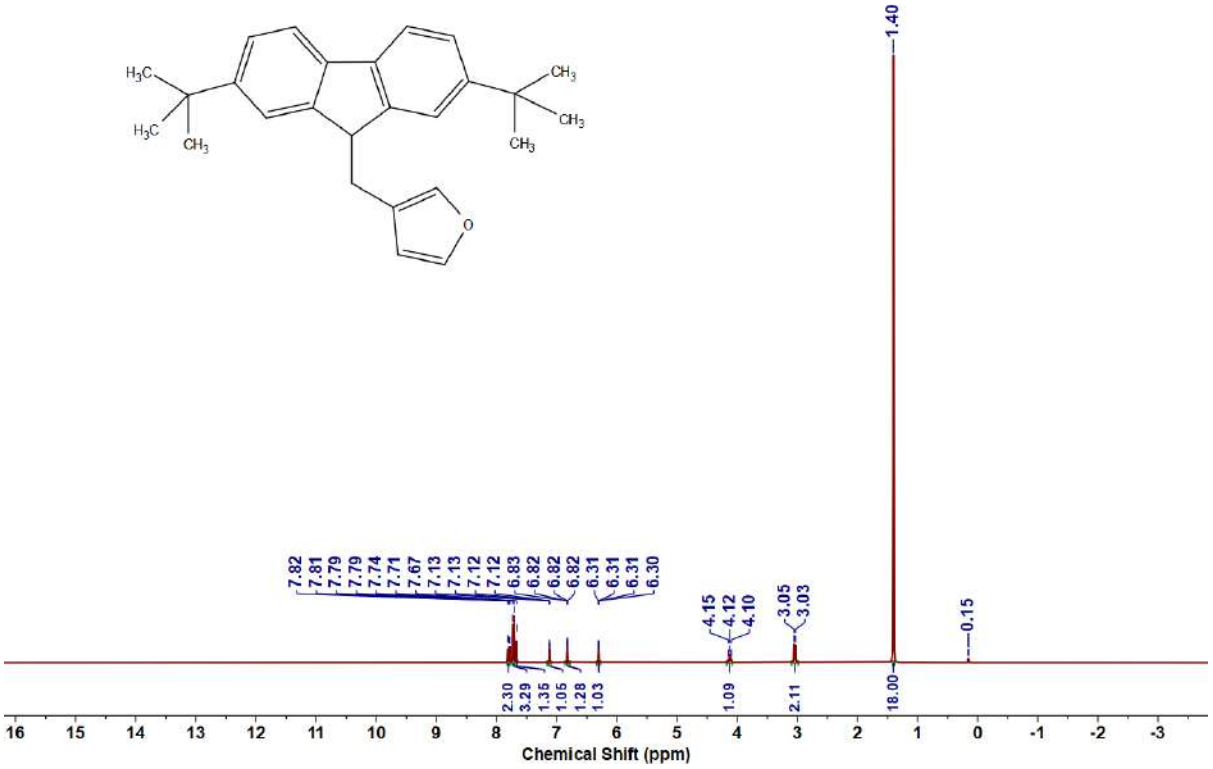

Figure 4.6.A183: ^{1}H NMR Spectrum of **11n**

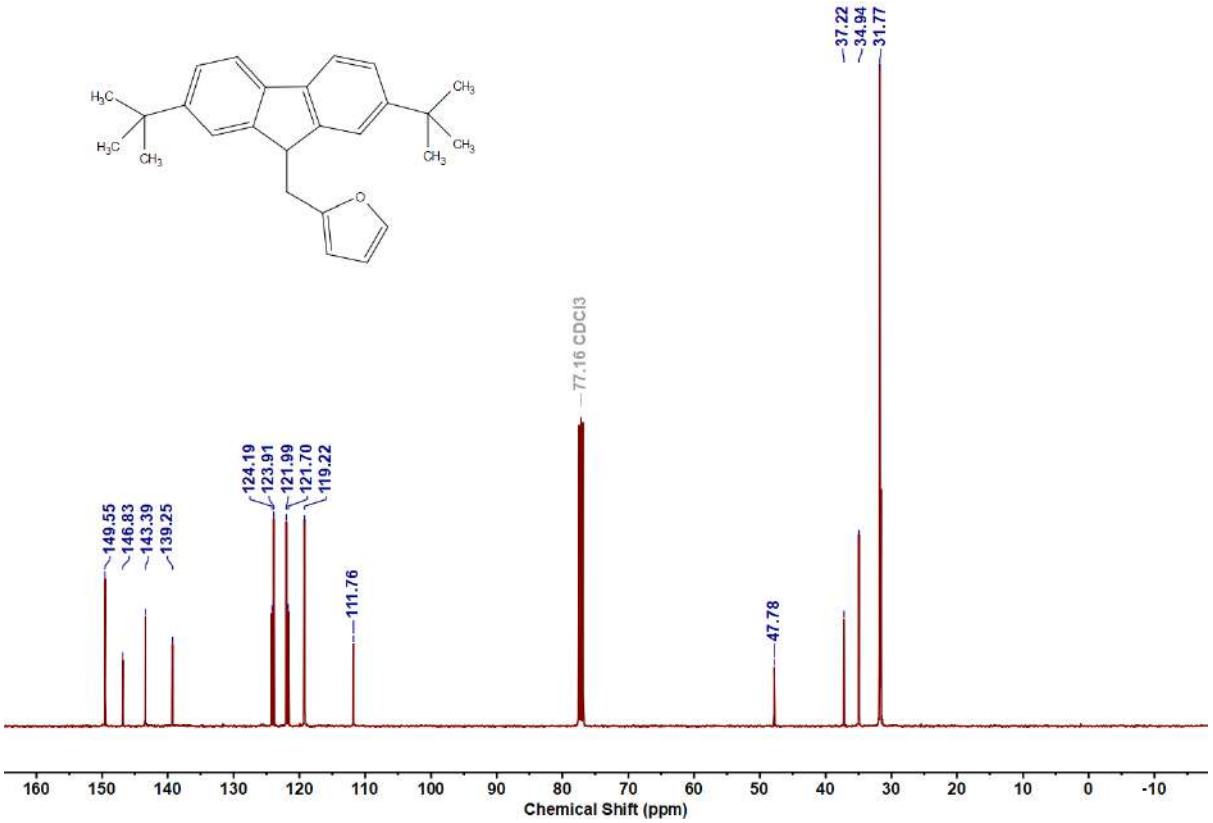

Figure 4.6.A184: ^{13}C{^{1}H} NMR Spectrum of **11n**

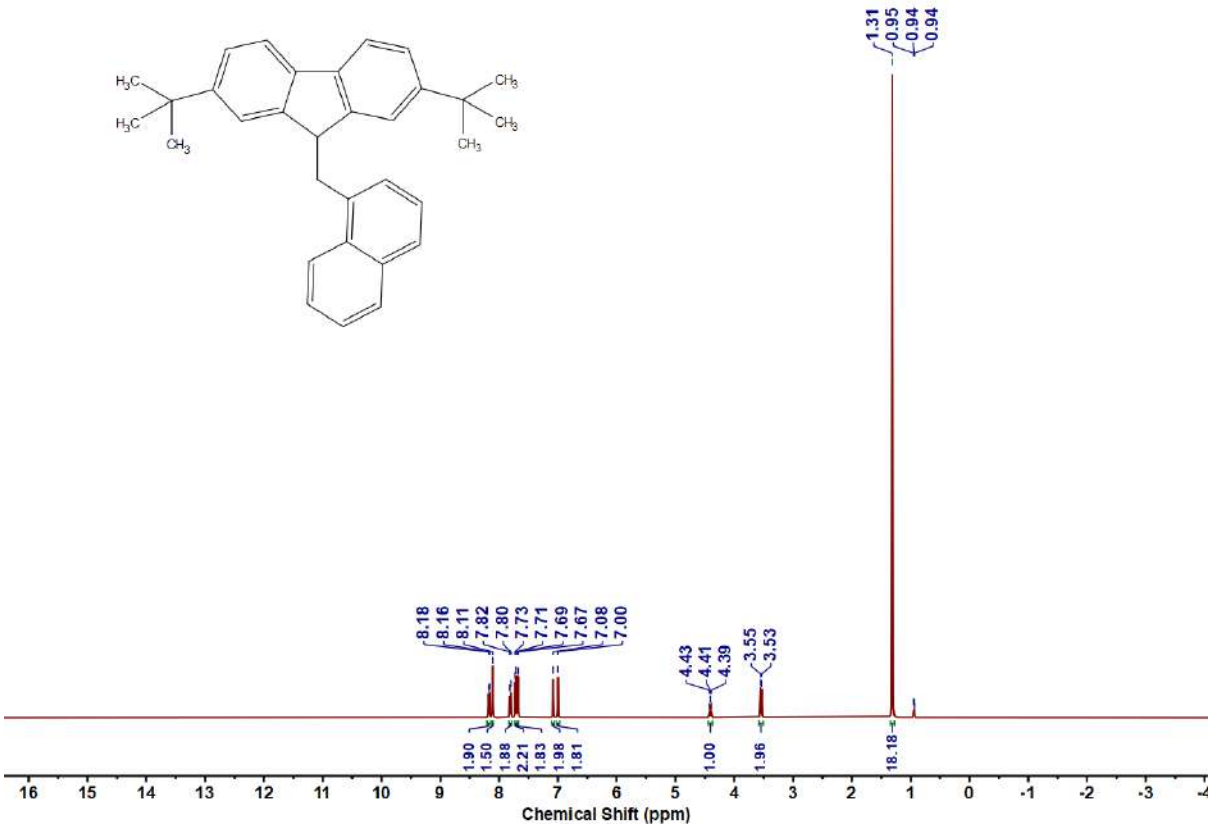

Figure 4.6.A185: ^{1}H NMR Spectrum of **11o**

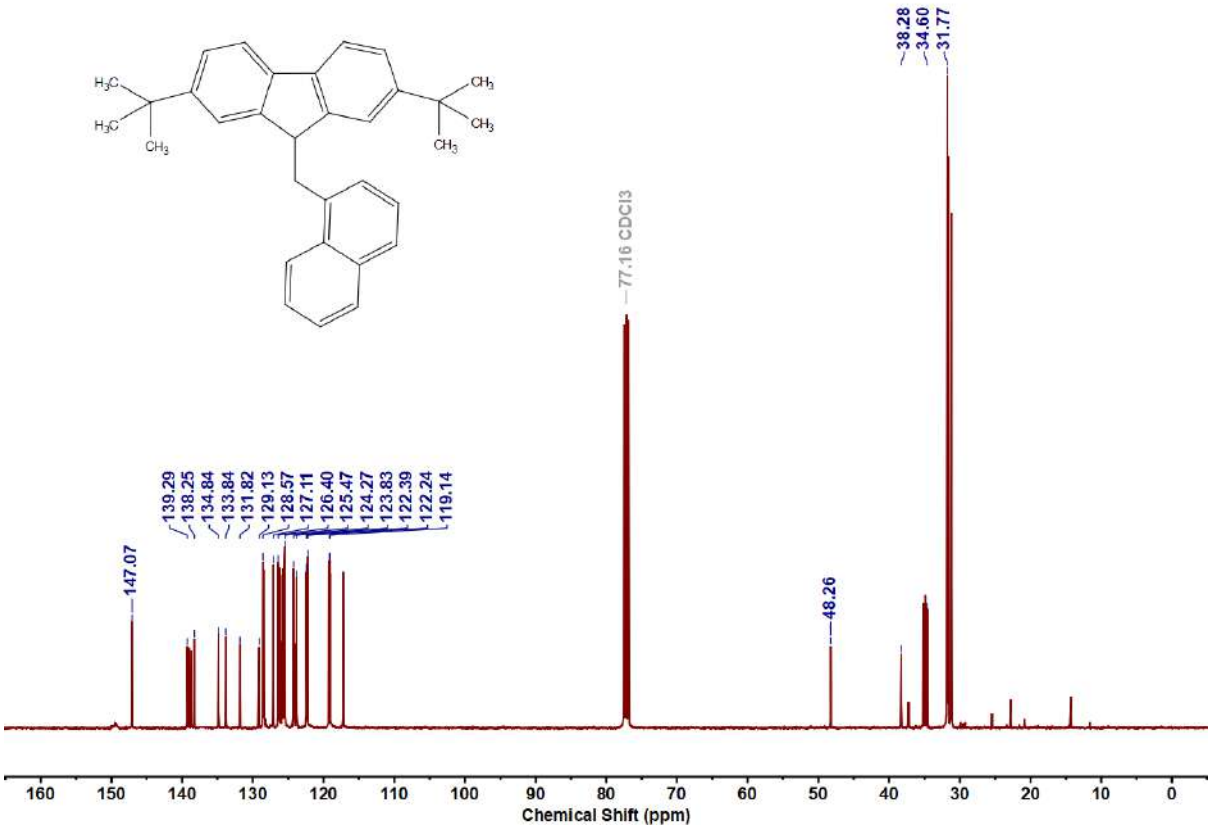

Figure 4.6.A186: ^{13}C{^{1}H} NMR Spectrum of **11o**

Chapter 5

2-(Pyridylazo)aniline Coordinated Ruthenium(II) Complex as an Efficient Catalyst for the Dehydrogenative Synthesis of Bis(indolyl)methanes from Alcohols and Indoles

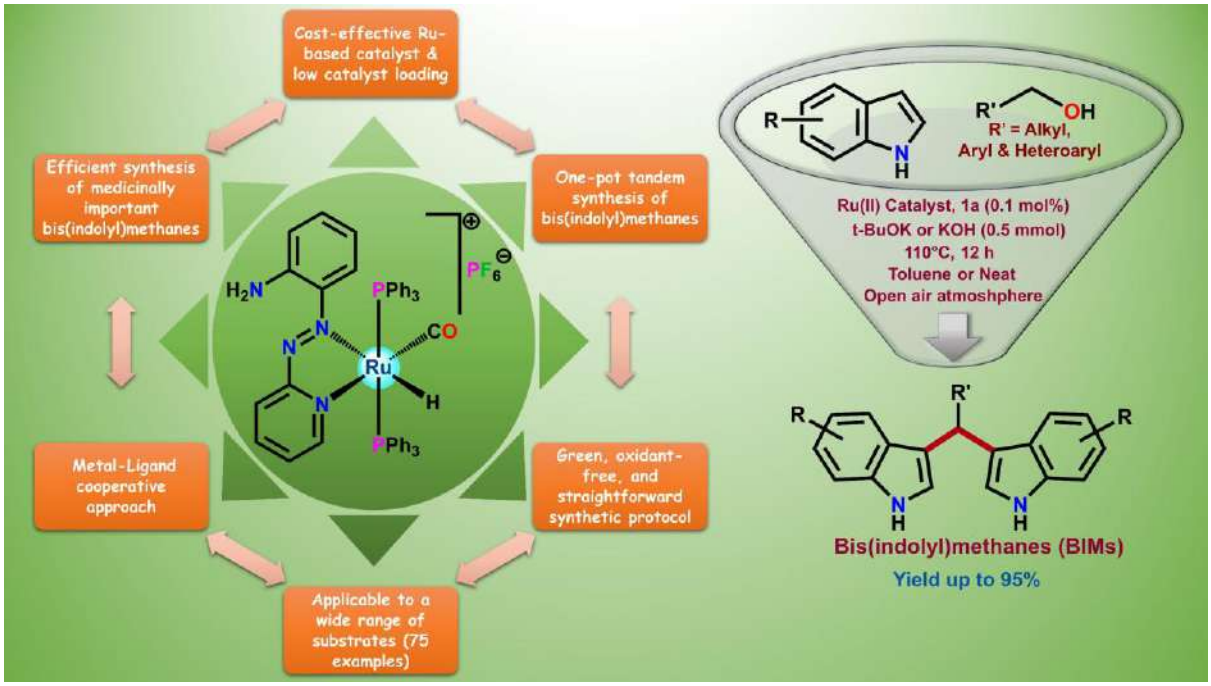

5.1 Introduction

Indole represents one of the most prevalent and versatile core structures found in a wide array of biologically active natural and synthetic compounds.[1] Functionalized indoles serve as key chemical frameworks in both medicinal and agricultural chemistry, forming the basis of many essential molecules.[2] Bis(indolyl)methanes (BIMs) has emerged as important scaffolds due to their demonstrated antibacterial,[3] antitumor,[4] and antifungal[5] properties (Scheme 5.1). Consequently, the development of efficient and selective methods for indole derivatization remains a prominent focus in synthetic organic chemistry. Traditional strategies, however, often depend on prefunctionalized starting materials and toxic reagents, typically requiring harsh reaction conditions. These limitations not only generate significant chemical waste but also compromise atom economy and sustainability, underscoring the need for greener and more practical synthetic alternatives.

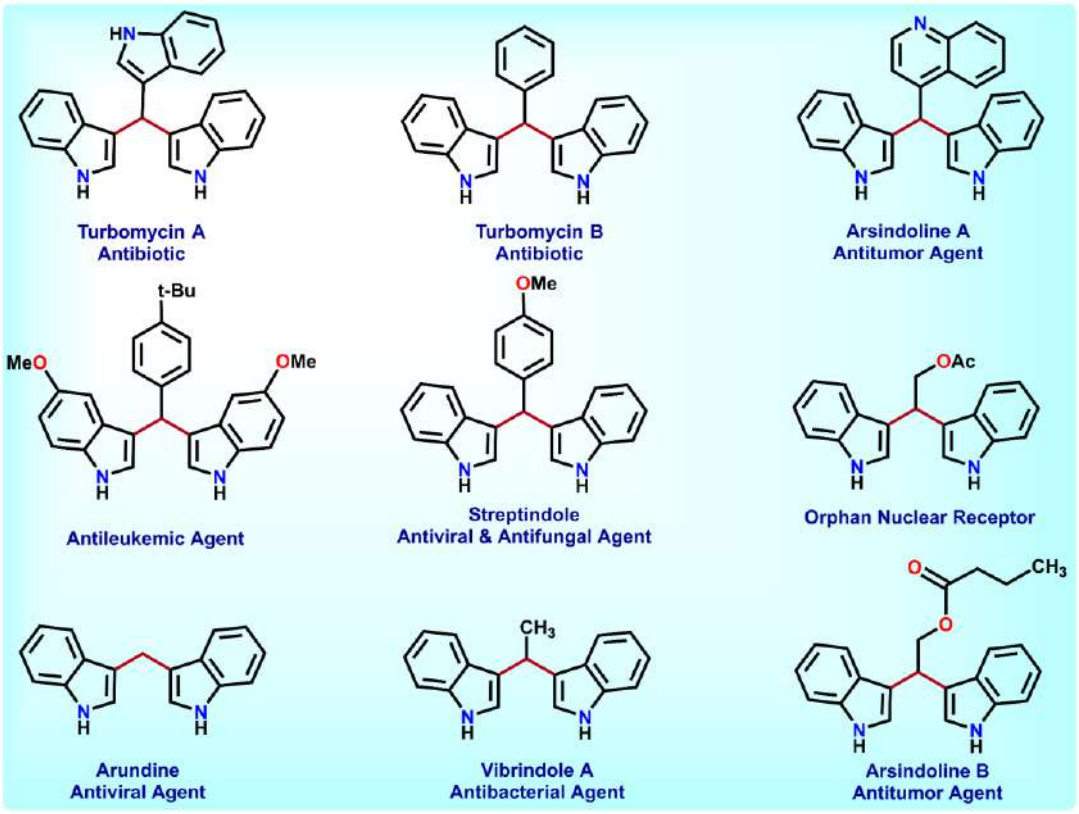

Scheme 5.1: Structural depiction of notable bis(indolyl)methane compounds with biological relevance

In 1886, Hermann Emil Fischer successfully synthesized 3,3'-BIM for the first time[6]. Traditional synthetic approaches for bis(indolyl)methanes (BIMs) have predominantly centered around the Friedel-Crafts alkylation of indoles with carbonyl-containing compounds, a reaction typically promoted by Lewis or Brønsted acids and often involving transition metal catalysts. Despite their effectiveness, these protocols are frequently associated with a number of significant limitations, including the requirement for high catalyst loadings, the use of stoichiometric amounts of strong oxidants, elevated reaction temperatures, and the dependence on relatively scarcer and sometimes toxic aldehyde substrates. These challenges not only raise concerns about the overall efficiency and cost-effectiveness of the process but also limit its alignment with the principles of green chemistry. In light of these issues, there has been a noticeable shift toward the development of more sustainable and environmentally benign methodologies. One particularly promising alternative is the dehydrogenative functionalization of alcohols. This approach has gained increasing attention due to its ability and simplicity to form diverse carbon–carbon and carbon–heteroatom (C–X, where X = C, N, S) bonds in a highly atom-economical manner (Scheme 5.2). In recent years, the development of heterocycles *via* dehydrogenative strategies particularly those employing alcohols as selective functionalizing agents has attracted significant attention.[7] This trend aligns with the growing emphasis on green, sustainable, and atom-economical approaches in modern synthetic chemistry. Alcohols represent highly attractive renewable feedstocks owing to their low cost, minimal environmental impact, and availability from lignocellulosic biomass. Their utilization reduces dependence on limited fossil carbon resources and supports efforts to reduce greenhouse gas emissions. Consequently, catalytic transformations involving alcohols have gained prominence as a green and efficient strategy for synthesizing structurally diverse and functionally complex organic molecules, including nitrogen-based heterocycles, thereby opening new avenues for eco-friendly production of high-value chemical entities.

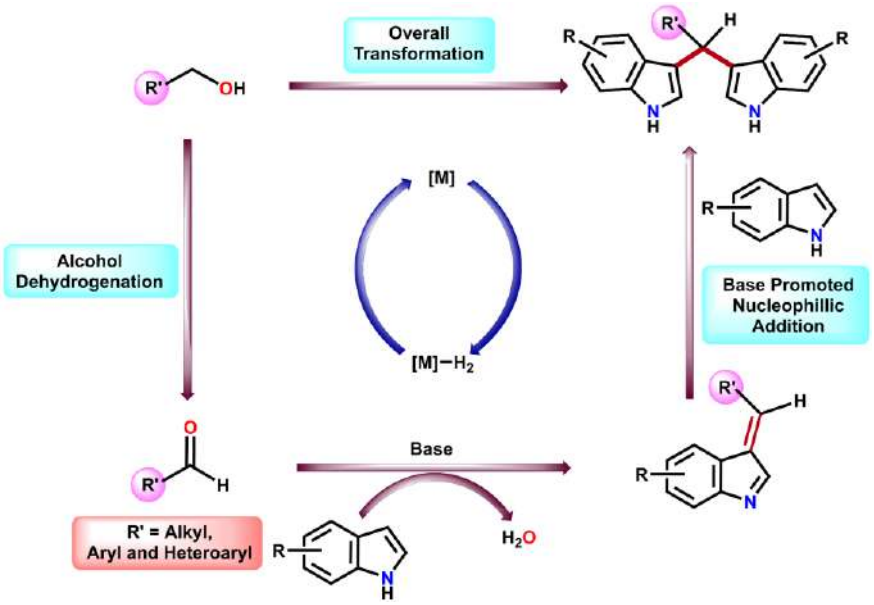

Scheme 5.2: Mechanistic overview of bis(indolyl)methane (BIM) synthesis *via* alcohol dehydrogenation–nucleophilic addition cascade

Significant strides have been made in the direct synthesis of bis(indolyl)methanes (BIMs) from indoles and alcohols, particularly through the development of catalytic systems that prioritize efficiency and sustainability. A notable contribution in this area was made by Yokoyama and Hikawa, who reported a palladium-catalyzed cascade reaction for the efficient synthesis of BIMs directly from indoles and alcohols.[8a] This pioneering work emphasized the potential of noble metal catalysis in facilitating multi-step reaction sequences under relatively mild conditions. Further advancing this area, Sekar's research group designed a domino synthetic approach employing a catalytic system based on iron(II) chloride complex with 1,1′-binaphthyl-2,2′-diamine (BINAM).[8b] This approach was particularly notable for utilizing iron, a non-toxic and earth-abundant metal as the catalytic center. However, the requirement for an expensive BINAM ligand and an excess of dicumyl peroxide (DCP) as the oxidant somewhat offsets its sustainability advantages. Langer and colleagues later expanded the scope of sustainable methodologies by developing a copper catalyzed strategy for the alkylation of indoles that utilized molecular oxygen from ambient air as the terminal oxidant using excess alcohols.[8c] In this context, Feng Li and co-workers reported the direct coupling of indoles with

methanol to afford 3,3′-BIMs in good to excellent yields using a commercially available Ir(III) complex.[9a] More recently, in 2020, Sarkar and colleagues developed an acceptorless dehydrogenative strategy for the synthesis of polyfluoroalkylated bis-indoles employing an earth-abundant Ni(II)-based catalytic system under open-air conditions.[9b] Followed by Srimani and co-workers reported the application of manganese and ruthenium based pincer complexes for the selective C3-alkylation of indoles.[9c,9e] These catalytic systems enabled the direct formation of both C3-alkylated indole derivatives and BIMs from simple, readily available alcohols, revealing the versatility and efficiency of pincer-ligated transition metal catalysts in this transformation. Complementing these developments, from research group of Mhaske[9d] and Balaraman[9h] disclosed a manganese catalyzed protocol that enabled the direct synthesis of BIMs exclusively from indoles and alcohols.[9d] Their approach further emphasized the growing potential of first-row transition metals in catalytic alkylation chemistry. More recently, the research groups of Paul[9f] Ramesh[9g] have also made important contributions by developing ruthenium- and palladium-based pincer complexes for the synthesis of BIMs, further enriching the toolbox of catalytic systems available for constructing these biologically significant molecules (Scheme 5.3).

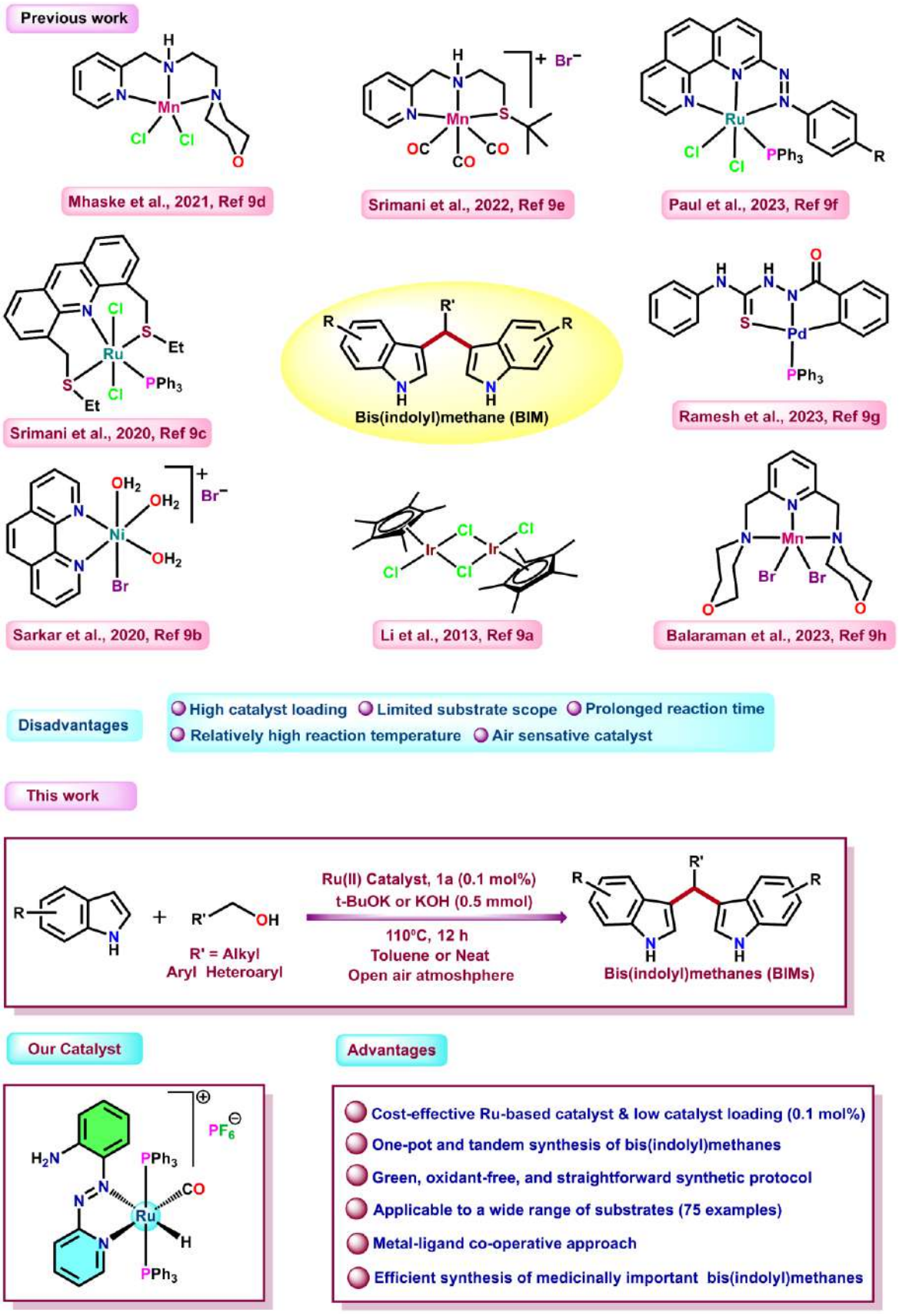

Scheme 5.3: Comparative and schematic illustration of reported studies and our current work on bis(indolyl)methanes synthesis

In this study we report a selective and efficient method for the synthesis of bis(indolyl)methanes (BIMs) through the coupling of various alcohols with indoles catalyzed by a well-defined bench-stable and easily accessible Ru(II) complex **1a** featuring a redox-active N,N-bidentate 2-(pyridylazo)aniline ligand **1**. Under aerobic conditions, the Ru(II) catalyst effectively promoted the formation of BIM derivatives. A broad range of alcohols including aromatic, heteroaromatic, and aliphatic substrates as well as structurally diverse indoles were successfully coupled to afford the corresponding BIMs with excellent efficiency at a low catalyst loading of merely 0.1 mol%. Additionally, control experiments and spectroscopic analyses were conducted to gain insights into the plausible reaction mechanism underlying BIM formation.

5.2 Results and Discussion

5.2.1 Synthesis of ligand 1 and complex 1a

In the present study, we report the synthesis and characterization of a cationic Ru(II) complex **1a**, incorporating 2-(pyridylazo)aniline ligand **1**. The ligand was synthesized following previously reported procedure,[10] involving the modified Baeyer-Mills condensation reaction of N-(2-aminophenyl)acetamide with 2-nitrosopyridine. Subsequent alkaline hydrolysis yielded the target 2-(pyridylazo)aniline ligand **1** (Scheme 5.4). Complex **1a** was prepared by reacting ligand **1** with $[RuH(CO)Cl(PPh_3)_3]$ in a 1:1 molar ratio in dry, degassed toluene at room temperature. This reaction afforded a dark bluish-green solution, from which the complex, *trans*-$[Ru^{II}(H_2L)H(CO)(PPh_3)_2]PF_6$ **1a**, was isolated in good yield *via* column chromatography (see Experimental Section).

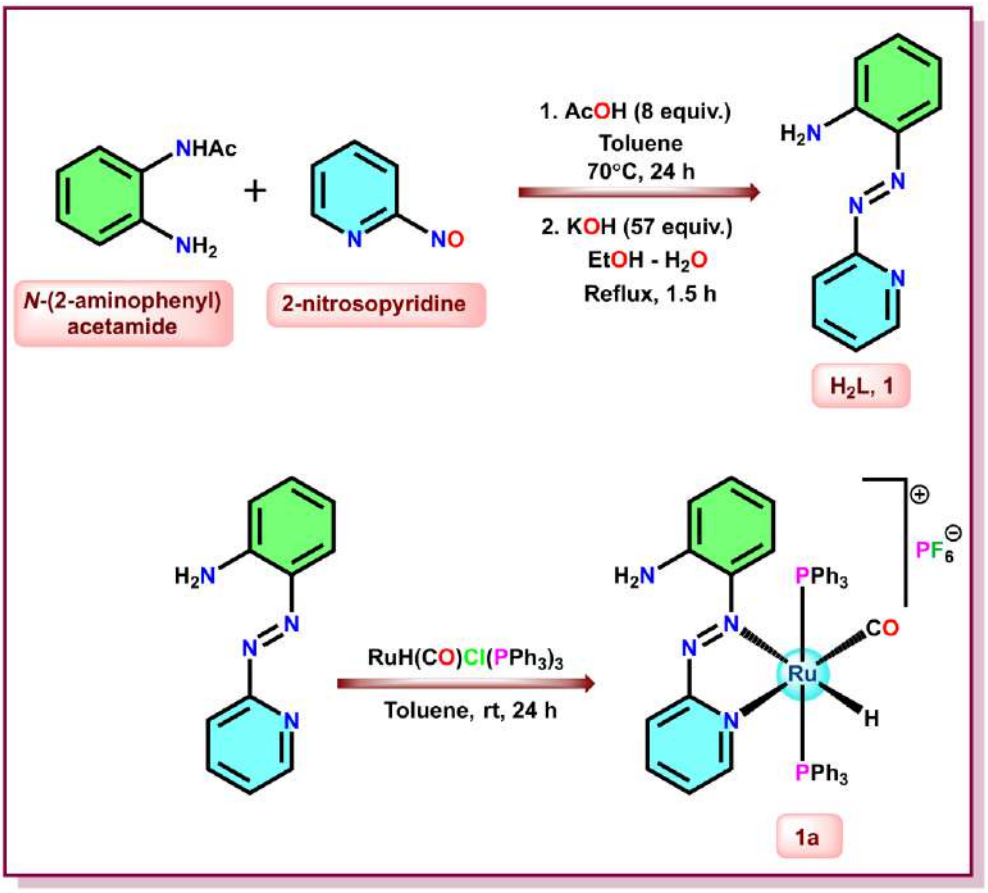

Scheme 5.4: General synthetic strategy for the preparation of the ligand and its ruthenium(II) complex

The complex was comprehensively characterized by single-crystal X-ray diffraction, various spectroscopic techniques and electrochemical study. Crystallographic analysis revealed that ligand **1** coordinates to the Ru(II) center in a bidentate fashion through the azo nitrogen (N_{azo}) and pyridyl nitrogen (N_{py}) atoms, forming a well-defined $N_{azo}N_{py}$ donor set. The hydride ligand is positioned trans to the N_{azo} atom, while the carbonyl ligand occupies the site trans to the N_{py} donor. The two triphenylphosphine (PPh_3) ligands complete the coordination sphere in a mutually trans arrangement, substantiated by the $^{31}P\{^{1}H\}$ NMR spectroscopy (Figure 5.6.A9). This coordination pattern results in a distorted octahedral geometry around the metal center. The complex crystallizes in the monoclinic $P2_1/c$ space group. The molecular structure is illustrated along with atom numbering scheme in Figure 1, and detailed crystallographic information together with selected metrical parameters (experimental and theoretical) is

summarized in Table 5.1 and Table 5.2, respectively. The ^{1}H NMR spectrum of **1a** shows three distinct types of proton signals. Resonances in the range of 6.34–8.01 ppm are attributed to aromatic protons, while a broad singlet at 6.93 ppm corresponds to the anilino protons (Ar-NH_2) (Figure 5.6.A7).

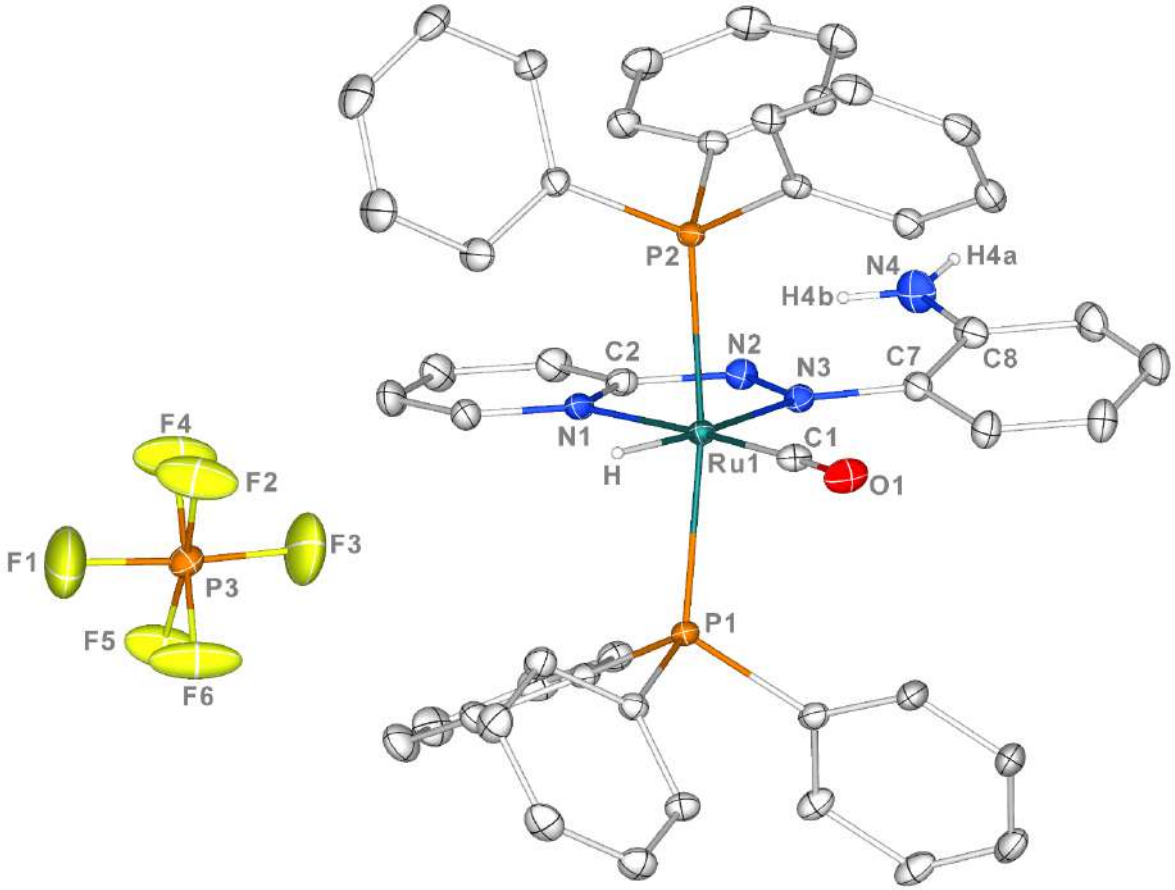

Figure 5.1: ORTEP diagram of complex **1a** with atom labelling scheme (All aromatic H atoms are excluded for clarity, Thermal ellipsoids are set at 40% probability). **CCDC No.: 2481461**; Selected bond lengths (Å) and bond angles (°): Ru1–N1 2.118(3), Ru1–N3 2.213(3), N2–N3 1.282(4), Ru1–N6 1.9912(14), Ru1–P1 2.3623(9), Ru1–P2 2.3802(9), Ru1–H 1.490(5), Ru1–C1 1.840(4), N1–Ru1–N3 73.74(12), P1–Ru1–P2 168.99(3), H–Ru1–C1 77.40(19), N3–Ru1–C1 112.57(15) and N1–Ru1–H 96.30(19)

Table 5.1: Crystallographic details of complex **1a**

Crystallographic Parameters	**1a**
Empirical formula	$C_{48}H_{41}N_4OF_6P_3Ru$
T/K	273.15
f_w	997.83
Crystal system	Monoclinic
Space Group	$P2_1/c$
a/Å	13.9972(4)
b/Å	13.8396(4)
c/Å	23.6517(7)
α/deg	90
β/deg	98.0740(10)
γ/deg	90
V/ *Å*^{3}	4536.3(2)
Z	4
D_c/Mgm^{-3}	1.461
μ/mm^{-1}	0.517
F(000)	2032
cryst size/mm^3	0.40 × 0.20 × 0.10
θ/deg	2.33 – 25.67
Measured reflns	133664
Unique reflns	8610
[a]GOF on F^2	1.094
R_1[b], wR_2[c][*I*>2*σ*(*I*)]	R_1= 0.0448, wR_2= 0.1189
R_1, wR_2	R_1= 0.0523, wR_2= 0.1265
[a]GOF = $\{\Sigma[w(F_o^2-F_c^2)^2]/(n-p)\}$ 1/2. [b]R1 = Σ $[\|F_o\|-\|F_c\|]/\Sigma\|F_o\|$. [c]wR2 = $[\Sigma[w(F_o^2-F_c^2)^2]/\Sigma[w(F_o^2)^2]]^{1/2}$ where w = $1/[\sigma^2(F_o^2)+(aP)^2+bP]$, P = $(F_o^2+2F_c^2)/3$.	

Table 5.2: Selected geometrical parameters of complex **1a**

Metrical Parameter of 1a					
Bond lengths (Å)			**Bond Angles (°)**		
	Expt.	**Theo.**		**Expt.**	**Theo.**
Ru1–N1	2.118(3)	2.155	N1–Ru1–N3	73.74(12)	72.89
Ru1–N3	2.213(3)	2.306	H–Ru1–C1	77.40(19)	84.60
Ru1– C1	1.840(4)	1.872	H–Ru1–N1	96.30(19)	91.71
Ru1– H	1.490(5)	1.597	N3–Ru1–C1	112.57(15)	110.77
Ru1–P1	2.3623(9)	2.454	N1–Ru1–P1	91.81(11)	90.97
Ru1–P2	2.3802(9)	2.472	N1–Ru1–P2	88.95(8)	88.78
N2–N3	1.282(4)	1.285	N3–Ru1–P1	98.98(8)	97.17
C1–O1	1.155(5)	1.153	N3–Ru1–P2	91.78(8)	94.80
C8–N4	1.324(6)	1.348	H–Ru1–P1	81.20(19)	82.39
C2 –N1	1.339(5)	1.353	H–Ru1–P2	87.80(19)	85.02
C2–N2	1.411(5)	1.385	C1–Ru1–P1	87.18(11)	88.30
C7–N3	1.400(5)	1.393	C1–Ru1–P2	90.86(11)	91.12
C7–C8	1.428(5)	1.444	P1–Ru1–P2	168.99(3)	167.39

In addition, a distinctive signal at -10.89 ppm corresponds to the coordinated hydride, which appears as a triplet arising from coupling with two magnetically equivalent PPh_3 ligands, with a coupling constant of 20 Hz (Figure 5.6A9). IR spectroscopy further supports this observation, revealing a characteristic Ru–H stretching band at 1977 cm^{-1}. Additionally, the spectrum confirms the presence of a coordinated Ru–CO group, evidenced by a stretching frequency at 1954 cm^{-1} (Figure 5.6A10). The proton-decoupled ^{31}P NMR spectrum reveals two different types of phosphorus environments. The signal at 43.63 ppm corresponds to the two coordinated, magnetically equivalent PPh_3 ligands, whereas the septet observed at –144.24 ppm (J = 709.06 Hz) is assigned to the hexafluorophosphate anion. The selected bond length and bond angle data provide valuable insights into the structural parameters of the complex. The Ru1–N_{azo} and Ru1–N_{py} bond lengths were measured as 2.213(3) and 2.118(3) Å, respectively. The N=N bond length of 1.282(4) Å aligns well with values expected for a coordinated azo group.

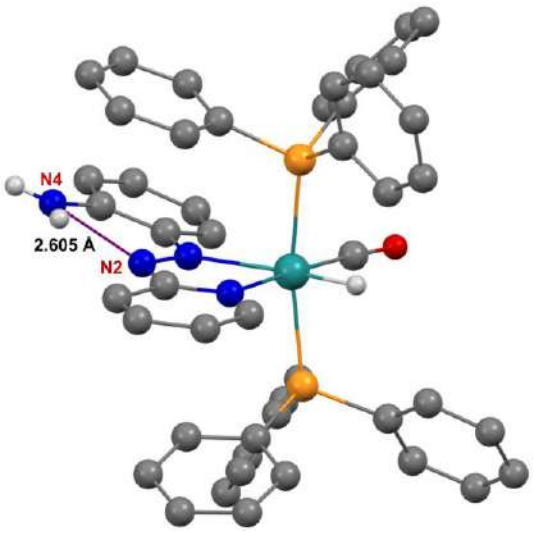

Figure 5.2: Intramolecular H-bonding in complex **1a**

Table 5.3: Intermolecular H-Bonding of complex **1a**

Donor…H	Acceptor	D…A (Å)	D–H…A (degree)
N4…H4B	N2	2.605(5)	126

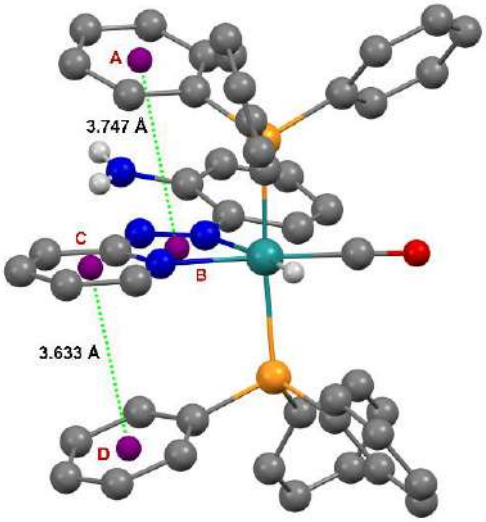

Figure 5.3: Intramolecular pi-pi stacking diagram of complex **1a**

Table 5.4: Different stacking parameters* of complex **1a**

Stacking Parameters	Ring A–B	Ring C–D
d[C_g(*I*) – C_g(*J*)] Å/α°	3.747(2)/19.39(19)	3.633(3)/20.80(2)
d[Cg(*I*) – R(*J*)] Å/β°	2.9079(13)/19.90	3.3738(18)/14.30
d[Cg(*J*) – R(*I*)] Å/γ°	3.5227(18)/39.10	3.520(2)/21.80

The hydride position was identified from the difference Fourier map and refined without any positional constraints. The Ru1–H bond length was determined as 1.490(5) Å. The P1–Ru1–P2 bond angle of 168.99(3)° shows a slight deviation from the ideal 180° geometry, which can be attributed to crystal packing effects. In addition, there is an intramolecular H-bonding present in complex **1a** between N2 and N4 with donor-acceptor distance of 2.606(5) and an angle of 126º among N4–H4b…N2 (Figure 5.2, Table 5.3). In addition to coordination bonding, the complex gains extra stabilization through intramolecular π–π stacking interactions. These occur between the phenyl rings of the triphenylphosphine ligands and the pyridyl moiety of the azo ligand. The centroid-centroid separations of the interacting rings are 3.747(2) Å and 3.633(3) Å, while the respective dihedral angles are 19.39(19)° and 20.8(2)° (Figure 5.3, Table 5.4).

5.2.2 Electrochemistry of complex 1a

The redox property the complex *trans*-$[Ru^{II}(H_2L)H(CO)(PPh_3)_2]PF_6$ **1a** was investigated by cyclic voltammetry in dry, degassed acetonitrile/dichloromethane (9:1 v/v) containing 0.2 M tetrabutylammonium hexafluorophosphate (TBAF) as the supporting electrolyte. Experiments were performed using a conventional three-electrode system comprising a platinum disk working electrode, a platinum wire auxiliary electrode, and a saturated Ag/AgCl reference electrode. The electrochemical study of the complex **1a** reveals a distinct reversible one-electron reduction process at −0.58 V, characterized by a peak-to-peak separation of 57 mV, consistent with a well-defined electron transfer event. Alongside this reduction, an irreversible oxidative wave appears at +1.47 V (Figure 5.4, Table 5.5) Theoretical calculations based on frontier molecular orbital (FMO) analysis provide further insight into the electronic nature of these processes. The reduction is found to be largely ligand-centered, with notable contributions arising from the azo fragment (36%), pyridine moiety (30%) (Table 5.6.A2). Such distribution clearly indicates the cooperative involvement of multiple donor sites within

the 2-(pyridylazo)aniline framework during electron uptake. In contrast, the oxidative events exhibit different electronic origins. The oxidation process, however, is primarily metal-centered, reflecting oxidation of the ruthenium center itself, though with partial participation of the ligand orbitals. Collectively, these findings demonstrate the inherently redox-active character of the 2-(pyridylazo)aniline scaffold and it can be inferred that the ligand plays an essential role in modulating electron-transfer behaviour. Importantly, such ligand-centered processes may be initiated through weakening or cleavage of the Ru–P bond.[11] Figure 5.5 depicts the optimized geometries of ligand 1 and its ruthenium complex 1a, together with their calculated and experimental UV–Visible absorption spectra.

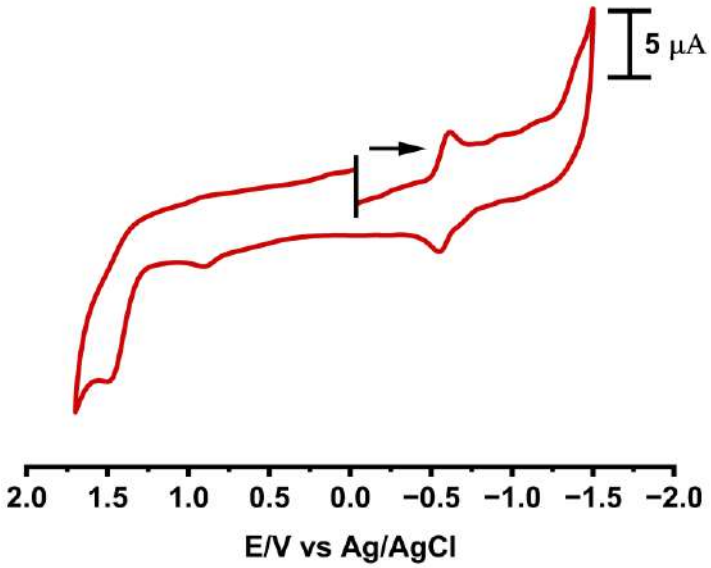

Figure 5.4: Cyclic voltammogram of complex 1a

Table 5.5: Cyclic voltametric data complex **1a** against Ag/AgCl as reference electrode

Complex	$E_{1/2}$/V (ΔE/mV)	
	Oxidation	**Reduction**
1a	+1.47	−0.58 (57)
$E_{1/2} = ½(E_{pa} + E_{pa})$, E_{pa} = anodic peak potential; E_{pc} = cathodic peak potential, ΔE = peak-to-peak separation		

5.2.3 Absorption spectra

Time-dependent density functional theory (TD-DFT) calculations were carried out at the (R)B3LYP level using the 6-311+G(d,p) basis set for non-hydrogen atoms and LANL2DZ for Ru, with the CPCM solvation model in CH_2Cl_2. For complex **1a**, the lowest 100 singlet–singlet transitions were analyzed for absorption and emission. The computed spectra showed good qualitative agreement with experiment, consistent with TD-DFT's established reliability in describing excitation energies of transition-metal complexes. To further probe the electronic character of the transitions, natural transition orbital (NTO) analysis was performed, providing a clear description of transition densities in terms of paired 'hole' and 'electron' orbitals. Vertical excitation energies were calculated at the ground-state geometry (S_0), with significant transitions ($f \geq 0.02$) spanning both low- and high-wavelength regions, successfully reproducing the major experimental spectral features (Table 5.6.A3, 5.6.A4).

In complex **1a**, the lowest-energy absorption band observed experimentally at 547 nm in the higher visible region is reproduced computationally at 514 nm (2.4094 eV, $f = 0.1882$). This band arises from two distinct electronic transitions. The first is attributed to an intraligand charge transfer (ILCT) process, characterized as [π (Azo + Ph + Amine + Py) → π* (Azo + Ph + Amine + Py)]. The second transition involves a mixed contribution of metal-to-ligand charge transfer (MLCT) and d-d excitations, corresponding to [d_{xz} → π* (Azo + Ph + Amine + Py) & (d_{xz} → d_{yz})] transitions, respectively. The next higher-energy absorption band, observed experimentally at 364 nm, is computed at 369 nm (3.3511 eV, $f = 0.2079$). This band originates from two major transitions. The first is primarily characterized by ligand-to-ligand charge transfer (LLCT), intraligand charge transfer (ILCT) and d-d excitations, assigned to [π (Azo + Ph + Py + PPh_3) → π* (Azo + Ph + Py + Amine) & (d_{xy} → d_{yz})] transitions. The second transition involves mixed LLCT, metal-to-ligand charge transfer (MLCT) and d-d character, corresponding to [d_{xy} + π (Ph + PPh_3) → π* (Azo + Ph + Py + Amine) & d_{xy} → d_{yz}]

contributions. The highest energy absorption band, observed around 232 nm, is computed at 266 nm (4.66 eV, $f = 0.271$). This transition is mainly attributed to d-d and ILCT excitations, involving $d_{xz} \rightarrow d_z^2$ and π (PPh_3) $\rightarrow \pi^*$ (PPh_3) transitions.

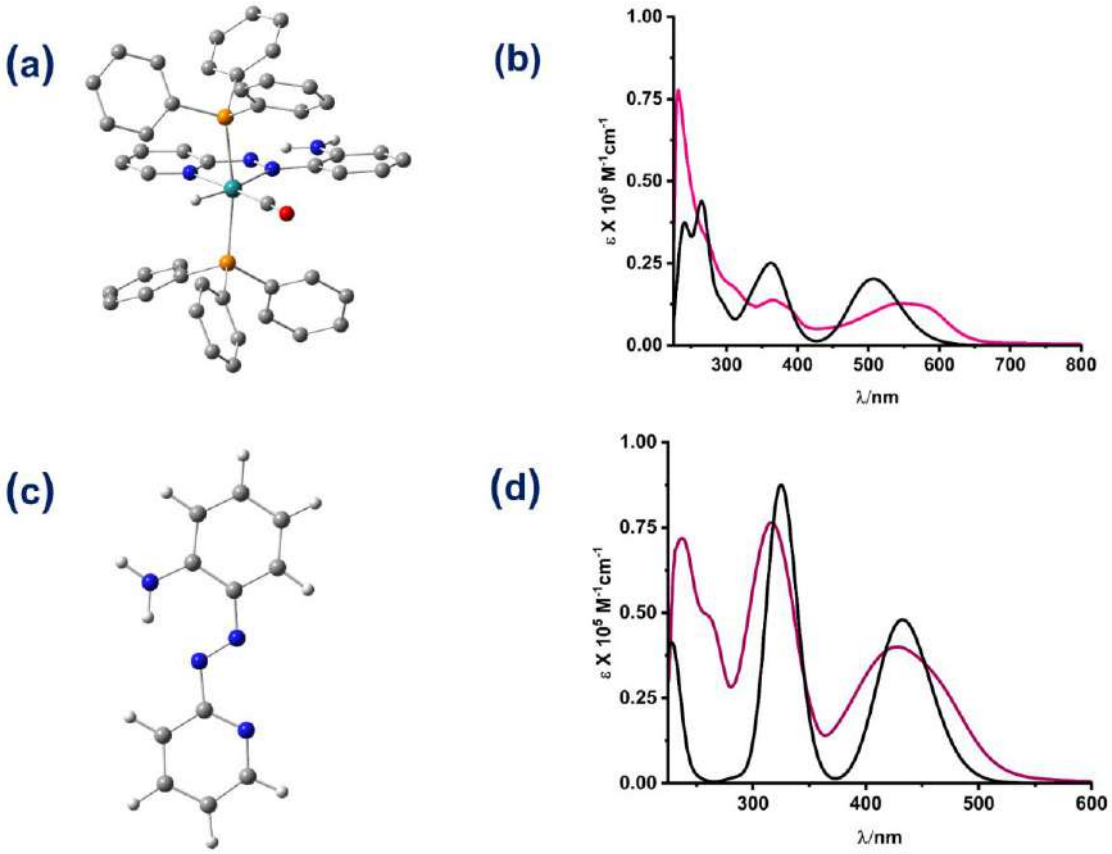

Figure 5.5: (a, c) Optimized geometries of complex **1a** and ligand **1** at the (R)B3LYP level of theory using the 6-311++G(d,p) basis set for non-hydrogen atoms and LANL2DZ for Ru. (b, d) Experimental absorption spectra of **1a** and **1** (purple and brownish-red) compared with the corresponding TD-DFT simulated spectra (black), calculated using the CPCM solvation model in dichloromethane (CH_2Cl_2)

5.2.4 Catalytic Activity

The study was initiated by optimizing the reaction parameters for the catalytic synthesis of bis(indolyl)methanes from aromatic primary alcohols. As a model reaction, indole (**2**) and benzyl alcohol (**7a**) were treated with 0.1 mol% of Ru(II) catalyst **1a** in the presence of 0.25 equiv. of NaOH, maintaining a 2:1 ratio of indole to alcohol in toluene at 110 °C for 12 h under open-air environment. This reaction afforded the desired bis(indolyl)methane **8aa** in only 20%

yield (Table 5.6, Entry 1). By changing the base loading from 0.25 to 0.5 equiv. led to only a marginal improvement in yield (Table 5.6, Entry 2). Subsequently, a series of alkali metal hydroxides and carbonates were screened as bases. However, none of these provided satisfactory results, with the highest yield of **8aa** reaching only 69% (Table 5.6, Entries 3-6). In order to evaluate a more effective base, t-BuOK (0.5 equiv.) was employed, which resulted in the formation of **8aa** with an 85% yield (Table 5.6, Entry 7). Further improvement was achieved by adjusting the indole-to-alcohol ratio to 2:1.1, producing **8aa** in 90% isolated yield (Table 5.6, Entry 8). An increase in the amount of t-BuOK (1.0 equiv.) did not lead to a significant change in yield of **8aa** (Table 5.6, Entry 9). Next, we examined the effect of different solvents on the reaction efficiency in comparison to toluene. The reaction was tested in xylene, tetrahydrofuran (THF), acetonitrile (MeCN), and N,N-dimethylformamide (DMF). Toluene was found to be the most effective solvent for this catalytic transformation, as none of the alternatives matched its efficiency. (Table 5.6, Entries 10-13). The diminished performance observed with these solvents can likely be attributed to their coordinating ability toward transition metals, which may interfere with the catalytic cycle during the reaction. We also investigated this reaction using organic amine bases such as diisopropylethylamine (i-Pr_2NEt) and triethylamine (Et_3N), but both proved completely ineffective, which can be attributed to their weaker basicity compared to the previously employed bases (Table 5.6, Entries 14-15).

Table 5.6: Evaluation of optimized conditions for aromatic primary alcohols[a,c]

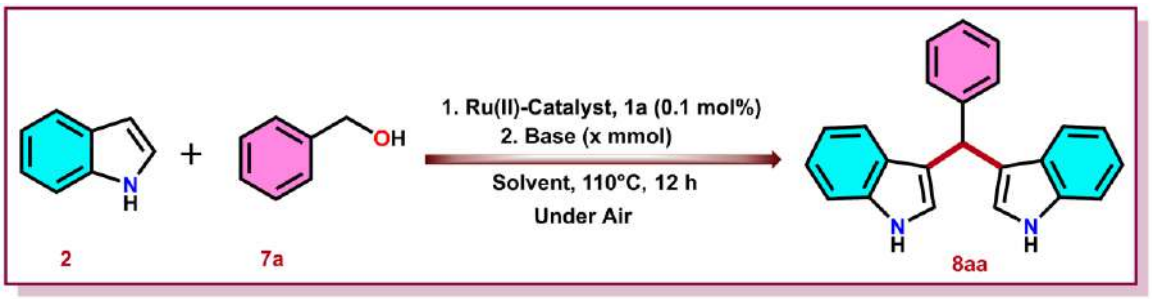

Entry	Catalyst (0.1 mol%)	Base (equiv.)	Indole: Alcohol (mmol)	Solvent	Time (h)	T°C	Yield[b] (%)
1	1a	NaOH (0.25)	2:1	Toluene	12	110	20
2	1a	NaOH (0.5)	2:1	Toluene	12	110	35
3	1a	KOH (0.25)	2:1	Toluene	12	110	58
4	1a	KOH (0.5)	2:1	Toluene	12	110	69
5	1a	K_2CO_3 (0.5)	2:1	Toluene	12	110	20
6	1a	Cs_2CO_3 (0.5)	2:1	Toluene	12	110	22
7	1a	t-BuOK (0.5)	2:1	Toluene	12	110	85
8	**1a**	**t-BuOK (0.5)**	**2:1.1**	**Toluene**	**12**	**110**	**90**
9	1a	t-BuOK (1.0)	2:1.1	Toluene	12	110	87
10	1a	t-BuOK (0.5)	2:1.1	Xylene	12	110	81
11	1a	t-BuOK (0.5)	2:1.1	THF	12	66	trace
12	1a	t-BuOK (0.5)	2:1.1	CH_3CN	12	82	trace
13	1a	t-BuOK (0.5)	2:1.1	DMF	12	110	NR
14	1a	i-Pr_2NEt (1.0)	2:1.1	Toluene	12	110	NR
15	1a	Et_3N (1.0)	2:1.1	Toluene	12	110	NR
16	1a	t-BuOK (0.5)	2:1.1	Toluene	16	110	89
17	1a	t-BuOK (0.5)	2:1.1	Toluene	20	110	83
18	1a	t-BuOK (0.5)	2:1.1	Toluene	12	120	88
19	1a	t-BuOK (0.5)	2:1.1	Toluene	12	140	81
20	1a	-	2:1.1	Toluene	12	110	NR
21	-	t-BuOK (0.5)	2:1.1	Toluene	12	110	30
22	$RuH(CO)Cl(PPh_3)_3$	^{t}BuOK (0.5)	2:1.1	Toluene	12	110	67
23	$RuCl_2(PPh_3)_3$	^{t}BuOK (0.5)	2:1.1	Toluene	12	110	62
24	$RuCl_3.xH_2O + H_2L$	^{t}BuOK (0.5)	2:1.1	Toluene	12	110	50

*[a]Reaction Conditions: Indole (**2**) (2 mmol, 1.0 equiv.), benzyl alcohol (**7a**) (1.1 mmol, 0.55 equiv.), Catalyst **1a** (0.1 mol%, 1.0 mg), base (x equiv.), solvent (3 ml), 110 [o]C (oil bath), 12 h. [b]Isolated yield after column chromatography, [c]Under air.*

With the optimal base and solvent identified, the focus was shifted to other key reaction parameters, including time and temperature. Prolonging the reaction to 16 or 20 h did not show any notable improvement in the yield of **8aa** (Table 5.6, Entries 16-17). Likewise, conducting the reaction at elevated temperatures gave comparable results, indicating that neither extended time nor higher temperature significantly enhanced the reaction outcome (Table 5.6, Entries 18-19). The absence of base completely suppressed the reaction, while exclusion of the catalyst still delivered **8aa** in 30% isolated yield. (Table 5.6, Entries 20-21). Other commercially available ruthenium complexes, such as $RuH(CO)Cl(PPh_3)_3$, $RuCl_2(PPh_3)_2$ and $RuCl_3.xH_2O$ also afforded **8aa**, though only in poor yields (Table 5.6, Entries 22-24). Based on these observations, the optimal reaction conditions for ruthenium(II) catalysed bis(indolyl)methane synthesis were established as follows: indole (2.0 mmol), primary alcohol (1.1 mmol), ruthenium(II) catalyst **1a** (0.1 mol%), toluene (3 ml), t-BuOK (0.5 equiv.) at 110 °C for 12 h.

Under the optimized conditions, indole (**2**) reacted with various aromatic and aliphatic primary alcohols. Benzyl alcohols bearing electron-donating substituents at different ring positions furnished bis(indolyl)methanes in good to excellent yields (Table 5.7, **8aa**: 90%, **8ab**: 82%, **8ac**: 85%, **8af**: 87%, **8ag**: 91%, **8ah**: 92%, **8ai**: 90%). Similarly, benzyl alcohols containing electron-withdrawing groups such as –F, –Cl, –Br, and $–CF_3$ furnished the desired products in yields ranging from 72% to 89% (Table 5.7, **8ad**: 72%, **8ae**: 76%, **8aj**: 78%, **8ak**: 80%, **8al**: 82%, **8am**: 89%). Polycyclic aromatic alcohols, exemplified by naphthalen-1-ylmethanol (**7o**), also underwent smooth transformation to give **8an** in 88% yield. In addition, a heteroaryl alcohol, thiophen-2-ylmethanol (**7p**), reacted successfully with indole to deliver the desired product **8ao** in moderate yield (67%).

Table 5.7: Substrate scope of indole and different primary alcohols

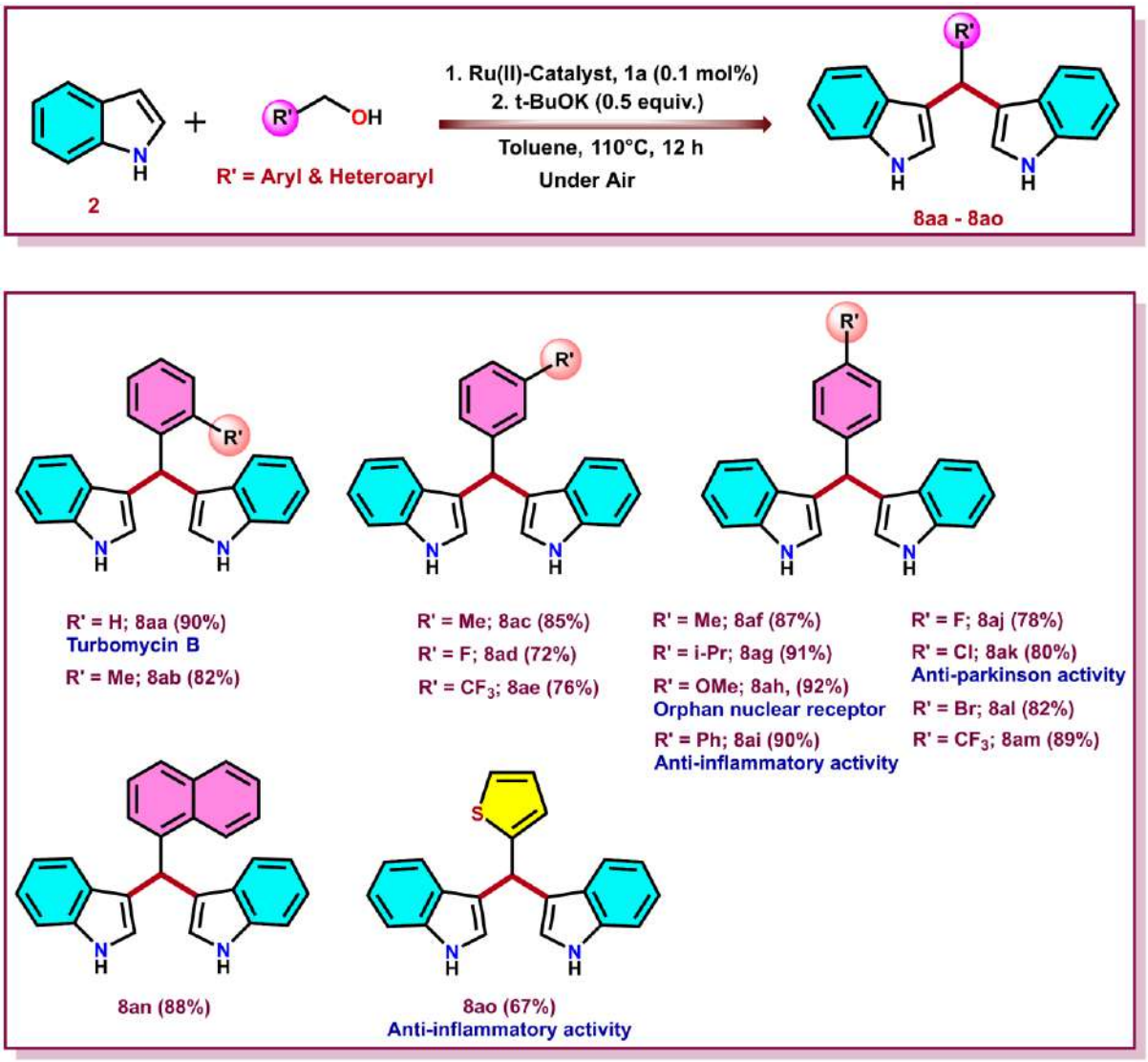

Next, we extended this protocol to other indole derivatives to evaluate its broader applicability. Indoles substituted at the 2- and 5-positions were systematically examined with a diverse set of aromatic, heteroaromatic and aliphatic primary alcohols. Indole having an electron-donating substituent, such as 5-methyl-1H-indole (**3**), reacted smoothly with aromatic primary alcohols comprising ring activating groups at the ortho, meta, and para positions, affording the corresponding bis(indolyl)methanes in excellent yields (Table 5.8: **9aa**: 87%, **9ab**: 81%, **9ac**: 87%, **9ad**: 93%, **9ae**: 95%, **9af**: 91%, **9ag**: 92%). Likewise, benzyl alcohols bearing electron-

withdrawing substituents at the para position also coupled effectively with **3**, providing the desired BIMs with respectable yields (Table 5.8: **9ah**: 82%, **9ai**: 84%, **9aj**: 87%, **9ak**: 78%).

These results highlight that both ring-activating and deactivating substituents on the alcohol component are well-suited under the optimized conditions, demonstrating the broad applicability of this protocol. Similarly, 5-methoxy-1H-indole (**4**) reacted efficiently with several benzyl alcohol derivatives. Benzyl alcohols bearing electron-donating groups at the ortho, meta, and para positions coupled effectively with 4, affording the desired bis(indolyl)methanes in excellent yields (Table 5.8: **10aa**: 88%, **10ab**: 86%, **10ac**: 90%, **10af**: 87%, **10ag**: 89%, **10ah**: 88%, **10ai**: 91%). Benzyl alcohols containing deactivating group also underwent smooth coupling with **4**, delivering the corresponding products in good yields (Table 5.8: **10ad**: 75%, **10ae**: 77%, **10aj**: 82%, **10ak**: 84%). Indole derivative **3** also underwent alkylation with heteroaryl alcohols such as pyridin-2-ylmethanol (**7r**), pyridin-3-ylmethanol (**7s**), and pyridin-4-ylmethanol (**7t**), affording the corresponding products in moderate yields (Table 5.8: **9al**: 73%, **9am**: 75%, **9an**: 78%). In addition, both indole derivatives reacted successfully with thiophen-2-ylmethanol (**7p**), furnishing the desired compounds **9ao** and **10al** in isolated yields of 70% and 60%, respectively. Similarly, both indole derivatives reacted smoothly with naphthalen-1-ylmethanol (**7o**), affording the expected bis(indolyl)methane derivatives in excellent yields (Table 5.8: **9ap**: 86%, **10am**: 89%). Electron-deficient indole (**5**) also undergoes coupling with benzyl alcohol bearing a meta–CF_3 substituent, delivering the desired product **11aa** in 69% isolated yield (Table 5.8).

Table 5.8: Substrate compatibility of indole derivatives with primary alcohols

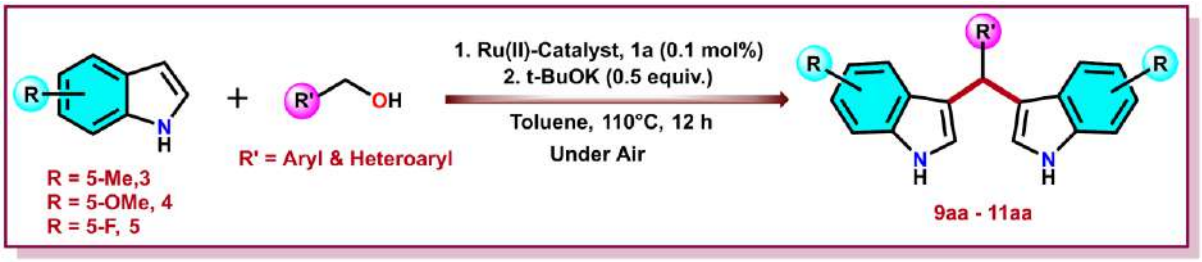

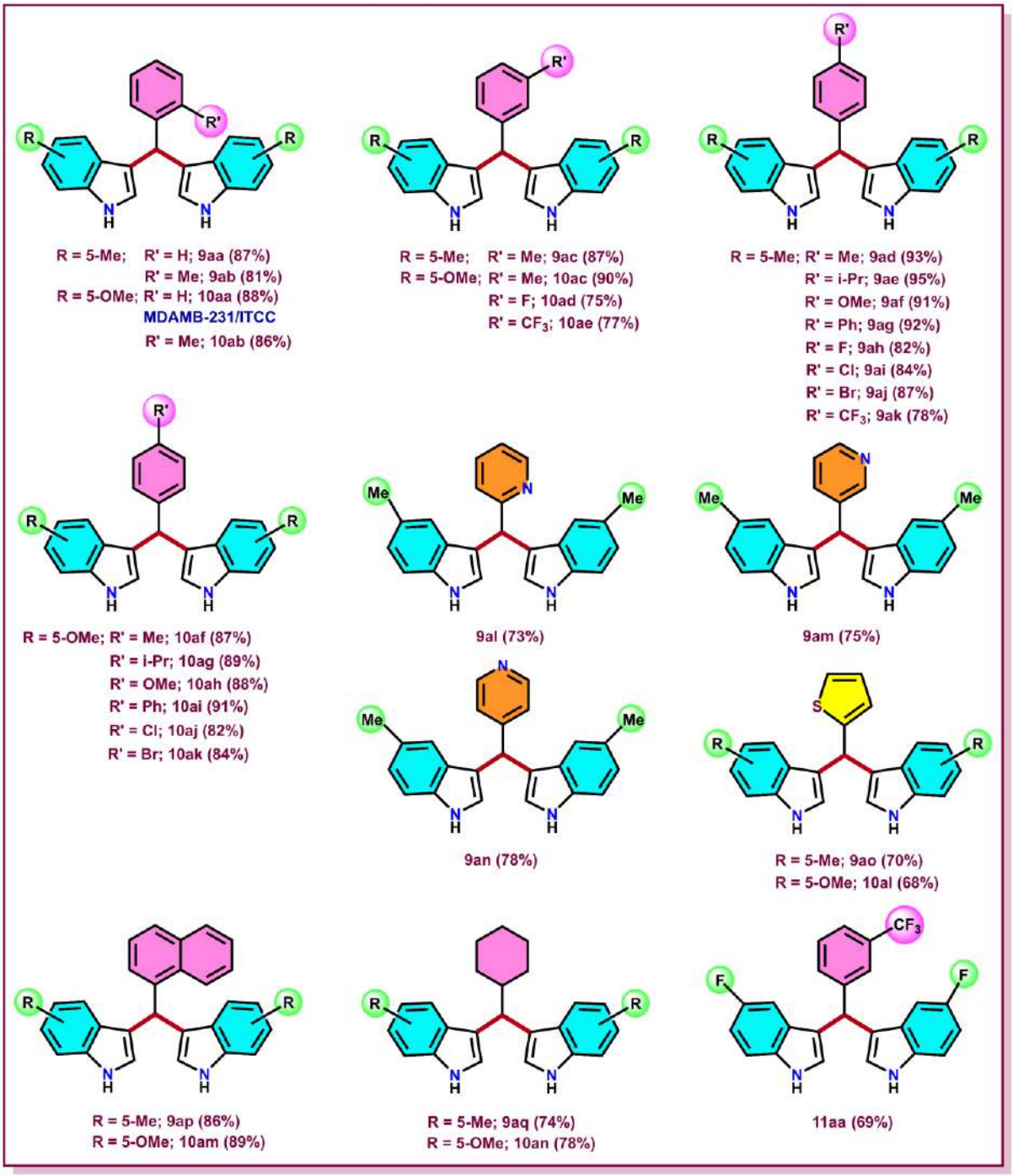

Table 5.9: Substrate scope of different indole derivatives and primary alcohols

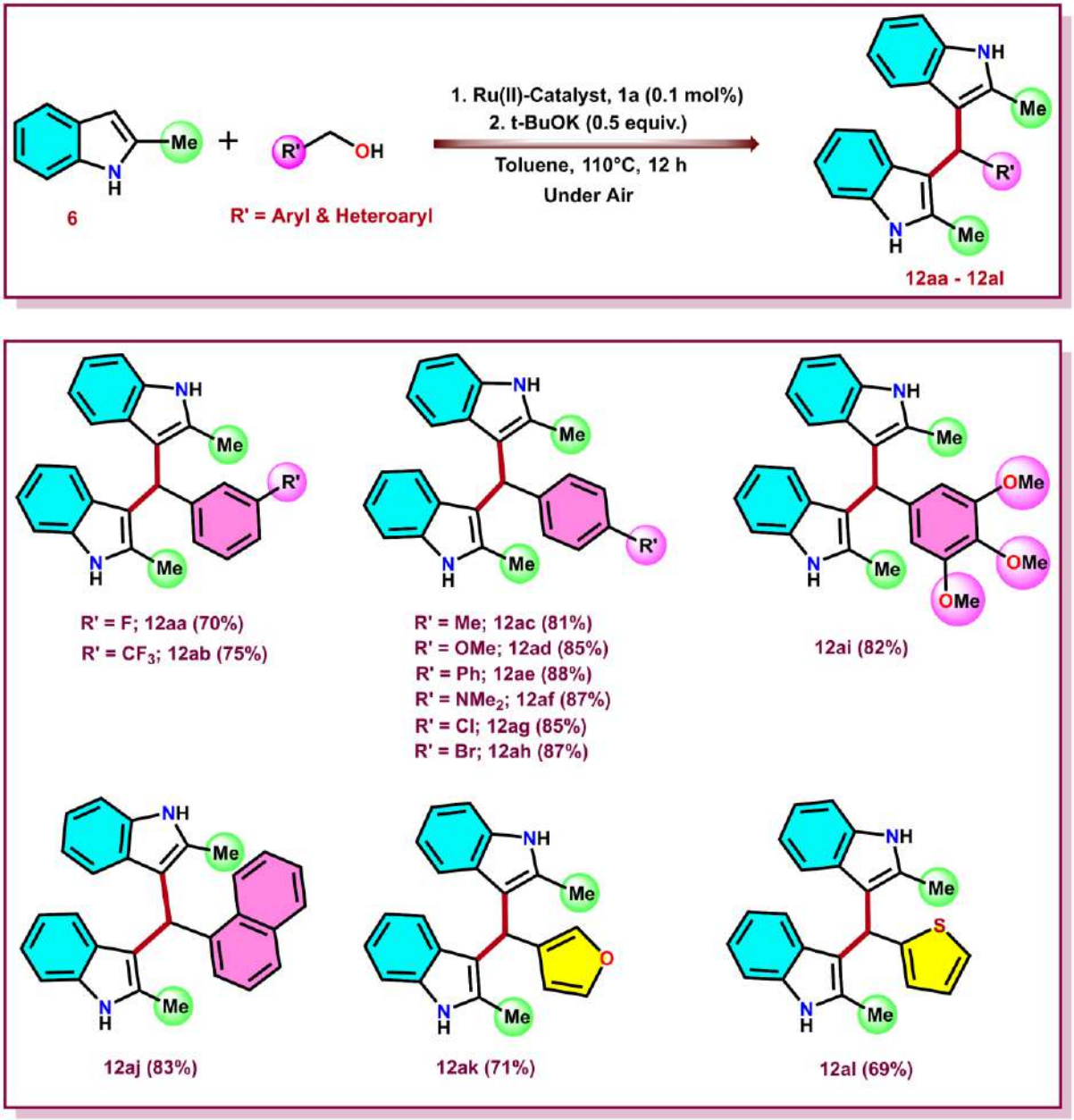

Next, we introduced sterically demanding substrate 2-methyl-1H-indole (**6**) as coupling partner. Despite the increased steric hindrance, this substrate efficiently coupled with several aromatic, heteroaromatic primary as well as polycyclic aromatic primary alcohols with good to excellent. Notably, benzyl alcohols containing electron donating substituents at para position reacted effortlessly with **6** to produce the corresponding products in excellent yields (Table 5.9, **12ac**: 81%, **12ad**: 85%, **12ae**: 88%, **12af**: 87%, **12ai**: 82%). In a comparable manner, benzyl

alcohols substituted with electron-withdrawing groups at the meta or para positions participated efficiently in the reaction, delivering the desired products in good yields. (Table 5.9, **12aa**: 70%, **12ab**: 75%, **12ag**: 85%, **12ah**: 87%).

In addition, polyaromatic primary alcohol, exemplified by naphthalen-1-ylmethanol (**7o**), as well as heteroaryl alcohols including thiophen-2- ylmethanol (**7p**) and furan-3-ylmethanol (**7q**), were also successfully coupled with indole derivative 6 to obtain the desired products in moderate to good yields (Table 5.9, **12aj**: 83%, **12ak**: 71%, **12al**: 69%).

Table 5.10: Substrate scope of pyrrolopyridine and aromatic primary alcohols

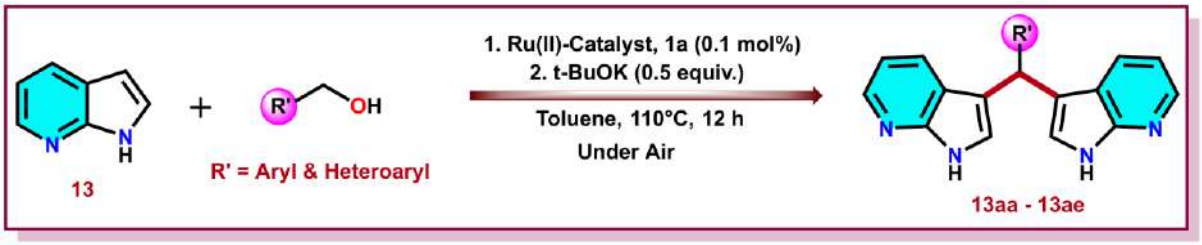

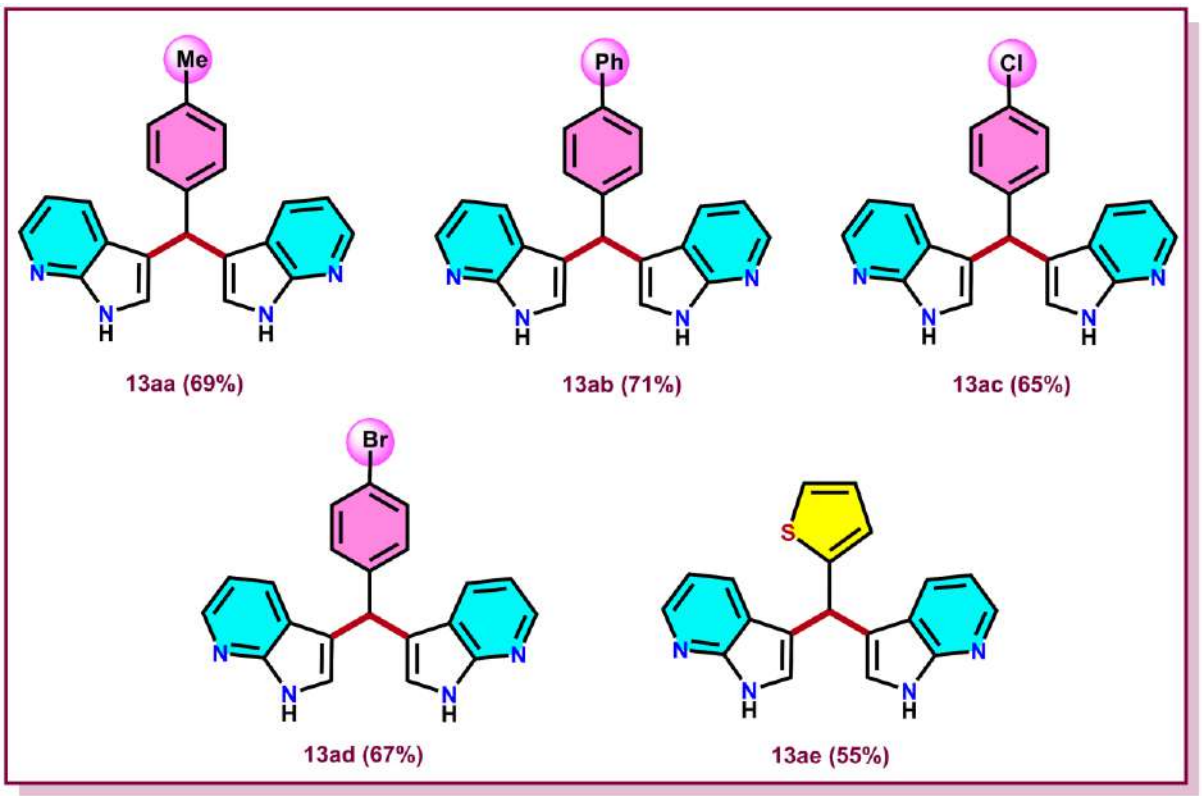

To further extend the scope of this established protocol, we introduced a more electronically demanding substrate, namely 1H-pyrrolo[2,3-b]pyridine (**13**). This electron deficient heteroaromatic framework underwent smooth alkylation with various primary alcohols, furnishing the desired products in good to moderate yields (Table 5.10, **13aa**: 69%, **13ab**: 71%, **13ac**: 65%, **13ad**: 67%, **13ae**: 55%).

After establishing the broad applicability of this catalytic protocol for C-alkylation of indole and its derivatives using aromatic, heteroaromatic, and polycyclic aromatic primary alcohols, we next turned our attention to more demanding substrates, namely aliphatic primary alcohols. Unlike aromatic alcohols, aliphatic alcohols are generally more challenging to employ as alkylating agents, mainly due to their inherently low reactivity and the relatively high enthalpic barrier associated with dehydrogenation. For instance, methanol exhibits a significantly higher dehydrogenation enthalpy ($\Delta H° = +92.4$ kJ·mol^{-1}, gas phase) compared to ethanol ($\Delta H° = +68.6$ kJ·mol^{-1}, gas phase), making the conversion of methanol into the transient active species formaldehyde *via* dehydrogenation considerably more difficult.[12] Although higher aliphatic alcohols such as 1-octanol, 1-nonanol, and 1-dodecanol could serve as coupling partners in this catalytic protocol to obtain the desired products, their overall efficiency was markedly lower compared to that of aromatic counterparts. Therefore, the reaction parameters were revised which revealed that under solvent-free conditions with potassium hydroxide (KOH) as the base, instead of t-BuOK, enabled the efficient use of aliphatic alcohols as alkylating agents for the synthesis of bis(indolyl)methanes. The details of this optimization process are given in Table 5.11.

After establishing the optimal reaction conditions for aliphatic primary alcohols, the study was next directed toward evaluating the scope and limitations of the developed protocol. (Table 5.12). As a representative case, the pharmaceutically significant molecule arundine (**14aa**) reported as a preventive agent for breast cancer, was successfully synthesized through the

coupling of methanol with indole under the established optimal conditions and the product was isolated in 68% yield. This result clearly highlighted the potential of the methodology in accessing biologically relevant scaffolds. Encouraged by this outcome, we next evaluated the reactivity of substituted indoles with methanol. Notably, 5-methoxy-1H-indole (**4**) and 2-methyl-1H-indole (**6**) underwent smooth coupling to afford the corresponding BIMs (**14ai** and **14al**) in 72% and 77% yields, respectively.

Table 5.11: Optimization of reaction condition for aromatic primary alcohols[a,c]

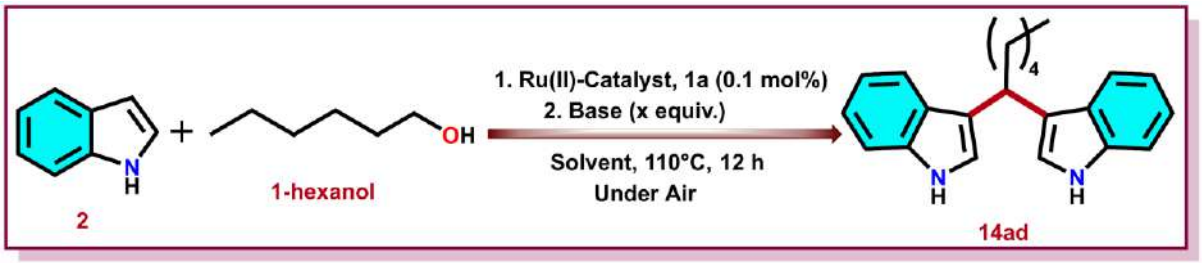

Entry	Catalyst (0.1 mol%)	Base (equiv.)	Solvent	Time (h)	T° C	Yield[b] (%)
1	1a	NaOH (0.25)	Toluene	12	110	30
2	1a	NaOH (0.5)	Toluene	12	110	33
3	1a	KOH (0.25)	Toluene	12	110	48
4	1a	KOH (0.5)	Toluene	12	110	54
5	1a	K_2CO_3 (0.5)	Toluene	12	110	12
6	1a	Cs_2CO_3 (0.5)	Toluene	12	110	15
7	1a	t-BuOK (0.5)	Toluene	12	110	51
8	**1a**	**KOH (0.5)**	**Neat**	**12**	**110**	**75**
9	1a	t-BuOK (0.5)	Neat	12	110	58
10	1a	KOH (0.5)	Xylene	12	110	55
11	1a	KOH (0.5)	THF	12	66	trace
12	1a	KOH (0.5)	CH_3CN	12	82	trace
13	1a	KOH (0.5)	DMF	12	110	NR
14	1a	i-Pr_2NEt (1.0)	Neat	12	110	NR
15	1a	Et_3N (1.0)	Neat	12	110	NR
16	1a	KOH (0.5)	Neat	20	110	71
17	1a	KOH (0.5)	Neat	12	120	72

18	1a	KOH (0.5)	Neat	12	140	68
19	1a	-	Neat	12	110	NR
20	-	KOH (0.5)	Neat	12	110	24

*[a]Reaction Conditions: Indole (**2**) (2 mmol, 1.0 equiv.), 1-hexanol (1.1 mmol, 0.55 equiv.), Catalyst **1a** (0.1 mol%, 1.0 mg), base (x equiv.), solvent (3 ml) or neat, 110 [o]C (oil bath), 12 h. [b]Isolated yield after column chromatography, [c]Under air.*

Table 5.12: Substrate scope of different indoles and aliphatic primary alcohols

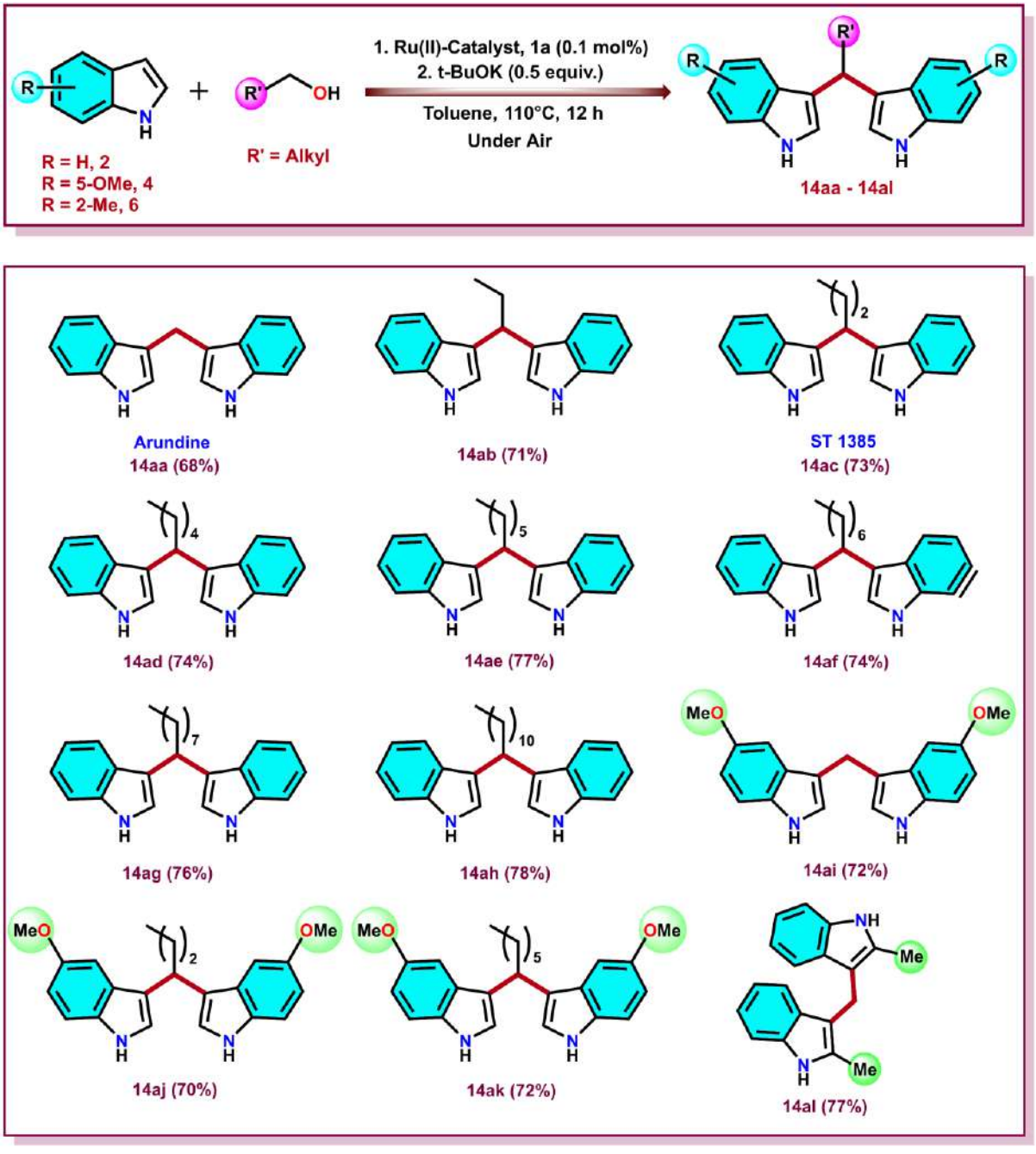

Encouraged by these findings, we explored the generality of the catalytic process with a series of aliphatic primary alcohols. Remarkably, 1-propanol, 1-butanol, 1-hexanol, 1-heptanol, 1-nonanol, and 1-dodecanol all participated efficiently in the coupling with indole, delivering the desired BIMs in good yields (Table 5.12, **14ab**: 71%, **14ac**: 73%, **14ad**: 74%, **14ae**: 77%, **14af**: 74%, **14ag**: 76%, **14ah**: 78%). Importantly, the methodology was not limited to unsubstituted indoles. For example, 5-methoxy-1H-indole (**4**) was effectively coupled with 1-butanol and 1-heptanol to delivered the desired BIMs (**14aj** and **14ak**) in 70% and 72% yields, respectively, thereby underscoring the broad applicability of the protocol to substituted indole derivatives as well.

5.2.5 Mechanistic Studies

To elucidate the underlying mechanism of the ruthenium(II)-catalyzed bis(indolyl)methane formation., a set of control experiments were designed and executed. Since the transformation proceeds under relatively high thermal conditions (110 °C), the initial investigation focused on evaluating the structural and operational stability of the catalyst. Thermal stability studies revealed that the catalyst retained its structural and operational integrity even when heated up to 130 °C in high-boiling solvents such as toluene and xylenes, demonstrating its robustness under the reaction environment. Building on literature precedents,[13] the mechanistic pathway for the formation of bis(indolyl)methanes from alcohols is generally proposed to occur *via* three sequential steps: (i) generation of carbonyl compound *via* alcohol dehydrogenation, (ii) condensation of the carbonyl intermediate with an indole to furnish 3-alkylideneindole intermediate, and (iii) base-induced nucleophilic addition of indole to this 3-alkylideneindole intermediate, leading to the bis(indolyl)methane framework. To probe the first step in this sequence, we investigated the **1a**-catalyzed dehydrogenation of (4-chlorophenyl)methanol (**7k**) under aerobic condition.

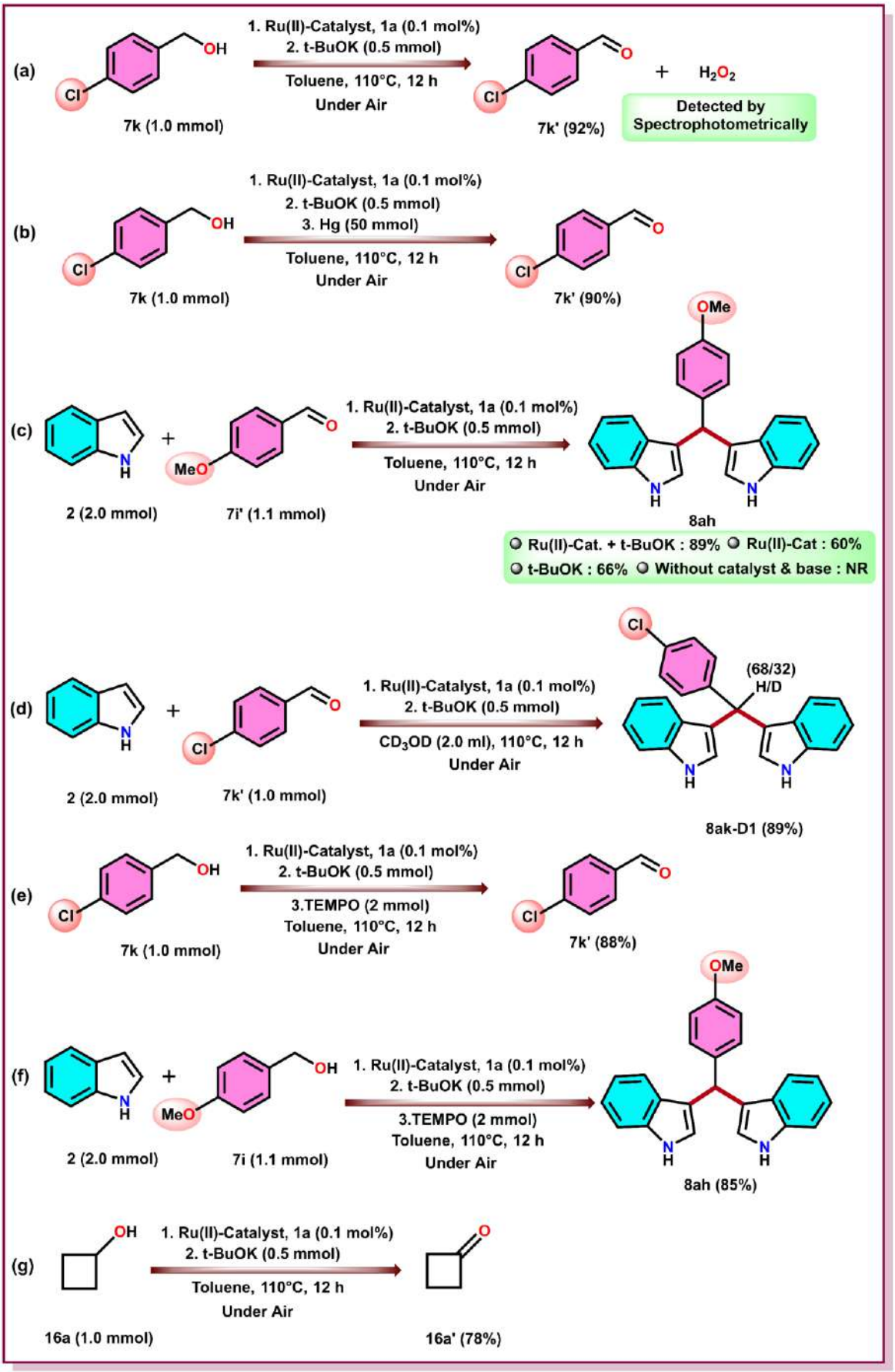

Scheme 5.5: Control Experiments

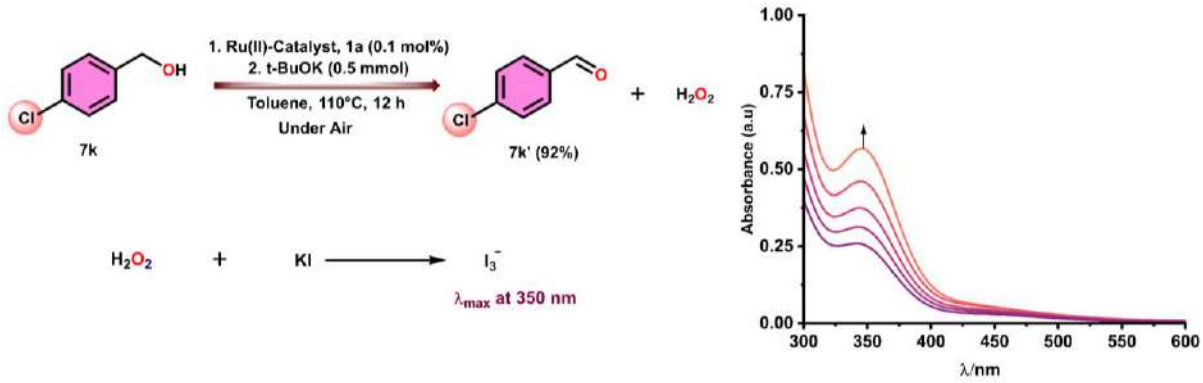

Scheme 5.6: Spectrophotometric determination of hydrogen peroxide (H_2O_2)

The transformation proceeded effectively to afford *p*-chlorobenzaldehyde (**7k′**) in 92% isolated yield, confirming the efficiency of the catalyst in mediating the dehydrogenation step (Scheme 5.5a). Notably, this transformation was accompanied by the generation of hydrogen peroxide (H_2O_2) as a by-product, which unambiguously detected by spectrophotometric analysis (Scheme 5.6). Next, we investigated the homogeneity of the ruthenium(II)-catalyzed bis(indolyl)methane synthesis (Scheme 5.5b). In order to probe the potential role of ruthenium nanoparticles in the catalytic process, the dehydrogenation of **7k** was examined under standard conditions in presence of elemental mercury, a well-established poison for heterogeneous metal nanoparticles and a diagnostic probe to differentiate homogeneous from heterogeneous catalysis. The reaction advanced without difficulty, achieving efficiency close to that of the mercury-free system. These evidences firmly suggest that the molecular complex **1a**, rather than ruthenium nanoparticles, functions as the active catalytic species. To evaluate the respective roles of the catalyst and base, the reaction between **2** and **7i′** was carried out under different conditions (Scheme 5.5c).[9e] Incorporation of the catalyst together with the base produced **8ah** in 89% yield. In contrast, omission of either component resulted in a marked decrease in efficiency, affording **8ah** in 60% and 66% yield, respectively. No reaction occurred when both the catalyst and base were omitted, highlighting their indispensable roles in this transformation. Mechanistically, deprotonation of the N–H group by the base is proposed to facilitate the condensation step, while coordination of the catalyst enhances the electrophilicity

of the aldehyde, thereby promoting the reaction. Furthermore, when **2** was reacted with **7k′** in CD_3OD, the product **8ak-D1** was obtained, showing 32% deuterium incorporation. (Scheme 5.5d). These results are consistent with the in situ generation of an alkylideneindolenine intermediate through the condensation of **2** and **7k′**, which is then intercepted by a second indole through base induced nucleophilic attack. The resulting intermediate then proceeds through a series of proton-transfer steps, with the alcohol serving as the most probable proton source. Attention was then directed toward probing the potential involvement of radical species in the bis(indolyl)methane synthesis. The dehydrogenation of **7k** and the reaction between **2** and **7i** were conducted with **TEMPO** (2,2,6,6-tetramethylpiperidin-1-yl)oxyl) as radical quencher (Scheme 5.5e and 5.5f). In both cases, the reactions proceeded efficiently under standard conditions, affording the desired products in 88% and 85% yield, respectively. The results rule out a ketyl-radical pathway involving single-electron hydrogen atom transfer (HAT) and instead point toward a two-electron hydride transfer process, in which the hydrogen source delivers a proton along with a pair of electrons in a concerted manner. To obtain more definitive evidence, we performed the dehydrogenation of cyclobutanol, a radical-clock substrate, (**16a**), under the optimized conditions (Scheme 5.5g). The exclusive formation of cyclobutanone (**16a′**) in 83% yield, without any ring-cleavage products, strongly corroborates the operation of a $2e^-$ hydride transfer pathway in the dehydrogenation of alcohol (Figure 5.6.A14).[14] Despite our several attempts, the Ru–H intermediate could not be detected by NMR spectroscopy during the catalytic process. IR analysis of the reaction mixture from the **1a**-catalyzed dehydrogenation of methanol (CH_3OH) showed corresponding N–H stretching at 2955 cm^{-1} and 3069 cm^{-1} (Figure 5.6.A15). Upon replacing CH_3OH with CD_3OD, the characteristic N–D stretching vibrations were observed at 2205 cm^{-1} and 2279 cm^{-1} (Figure 5.6.A15).[15]

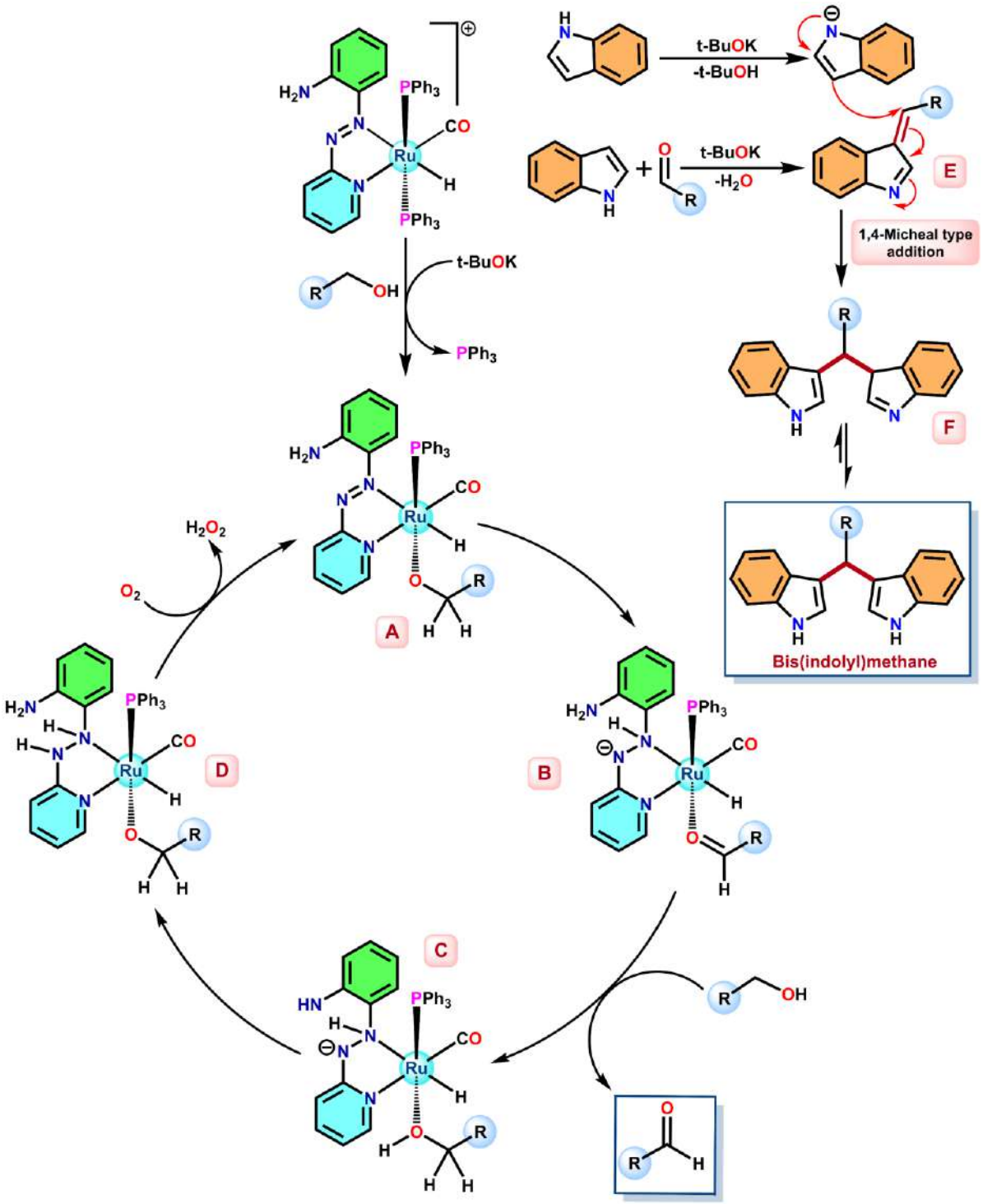

Scheme 5.7: Plausible catalytic cycle for bis(indolyl)methane synthesis

The results support the involvement of the azo/hydrazo redox couple, with the hydride on ruthenium being transferred intramolecularly to the coordinated azo group *via* a 'H-walking' pathway.

On the basis of the above experimental findings, a plausible catalytic pathway is proposed for the C–C bond formation leading to the synthesis of BIMs has been proposed, in addition to being endorsed by other literature reports,[13,15] a plausible catalytic pathway is illustrated in Scheme 5.7. In the presence of base, deprotonated alcohols coordinate to the Ru(II) center of complex **1a**, generating a Ru(II)–alkoxy intermediate (**A**) by following removal of PPh_3 which is detected as triphenylphosphine oxide ($Ph_3P{=}O$) *via* proton-decoupled ^{31}P-NMR spectroscopy (Figure 5.6.A2). Subsequent β-hydride elimination furnishes the corresponding carbonyl compound along with intermediate **B**. This transformation is proposed to proceed through the formation of a transient Ru–H species, which undergoes a rapid intramolecular "hydrogen-walking" process. The coordinated aldehyde is then released, accompanied by the coordination of another alcohol molecule to afford intermediate **C**. In the next step, proton transfer from the hydroxyl group to the azo unit generates the hydrazo intermediate **D**. This intermediate is now finally oxidised by aerial oxygen with simultaneous formation of hydrogen peroxide (H_2O_2) to generate catalytically active species **A**. The *in situ* generated carbonyl compounds, in the presence of a base, condense with indoles to yield the alkylideneindolenine intermediate **E**. Under open air atmosphere, hydrogen transfer from the hydrazo intermediate **D** to molecular oxygen is likely to occur, furnishing H_2O_2 as the terminal oxidation product. This step involves the abstraction of hydrogen from the catalytic cycle, thereby suppressing the possibility of hydrogenation of the alkylideneindolenine intermediate. As a result, the latter preferentially undergoes a base induced 1,4-Michael-type addition pathway, ultimately affording the bis(indolyl)methane (BIM) derivatives.

5.3 Conclusion

In summary, we have successfully synthesized a robust and air-stable ruthenium(II) complex, *trans*-[$Ru^{II}(H_2L)H(CO)(PPh_3)_2$]$PF_6$, derived from a redox-active 2-(pyridylazo)aniline ligand and [$RuHCl(CO)(PPh_3)_3$] precursor. Comprehensive characterization through spectroscopic, analytical, electrochemical, and SCXRD techniques established its structural and electronic features. Electrochemical studies, supported by theoretical analysis, confirmed ligand-centered redox activity, enabling efficient electron transfer processes while the ruthenium center remains a redox-inactive spectator. The complex proved to be a highly effective redox catalyst for the dehydrogenation of a wide range of aromatic and aliphatic primary alcohols and for the subsequent one-pot tandem synthesis of biologically important scaffold bis(indolyl)methanes under aerobic conditions, exhibiting excellent substrate scope (75 examples). Control experiments and mechanistic investigations revealed that the coordinated azo group plays an active role in the dehydrogenation process. Key advantages of this catalytic system include straightforward synthesis, lower catalyst loading (0.1 mol%), broad functional group tolerance, operational simplicity under relatively mild conditions and shorter reaction times.

5.4 Experimental Section

5.4.1 General Information

All reactions mentioned in this paper were carried out under aerobic conditions. Reagents and solvents were used directly without any additional purification unless otherwise specified. *o*-phenylenediamine and 2-aminopyridine were obtained from TCI Chemicals (India) Pvt. Ltd., while triphenylphosphine (PPh_3) was procured from Sigma-Aldrich. Silica gel (60-120 mesh, Merck) was employed for column chromatographic purification of products. Ruthenium trichloride hydrate ($RuCl_3 \cdot xH_2O$) was sourced from Arora-Matthey (India) Ltd. Indole and its derivatives as well as all aromatic and aliphatic primary alcohol derivatives used in this work

were purchased from BLD Pharm (India) Pvt. Ltd. $[RuH(CO)Cl(PPh_3)_3]$,[10a] 2-nitrosopyridine[10b] and N-(2-aminophenyl)acetamide[10c,10d] were prepared according to literature procedure.

5.4.2 Synthesis of ligand 1

N-(2-aminophenyl)acetamide (600 mg, 4.0 mmol) was dissolved in dry, degassed toluene (30 ml) in a 100 ml round-bottom flask equipped with a magnetic stir bar. 2-Nitrosopyridine (432 mg, 4.0 mmol) and glacial acetic acid (1.8 ml, 32.0 mmol) were added sequentially, and the mixture was heated at 70 °C under aerobic conditions for 24 h. After completion (TLC), the solvent was removed under reduced pressure, and the residue was purified by column chromatography on silica gel (100-200 mesh) using hexane/EtOAc (2:1 v/v) as eluent to afford an orange crystalline solid. The solid was dissolved in ethanol (20 ml), treated with ethanolic KOH (2.2 g, 57.0 mmol, 30 ml), and refluxed for 1.5 h. The mixture was cooled to room temperature and poured onto crushed ice (30 g), affording a dark red precipitate. The solid was extracted twice with CH_2Cl_2, and the combined extracts were concentrated under reduced pressure to yield a dark red oil, which solidified upon chilling.

5.4.3 Analytical Data of ligand 1

(E)-2-(pyridin-2-yldiazenyl)aniline **(1):** Deep red coloured solid, Yield: 625 mg (79%); **HRMS**: [M + H] m/z = 199.0985 (calcd for $[C_{11}H_{11}N_4]$ 199.0984); **FT-IR/cm^{-1}** υ = 3214 ($\upsilon_{N-H,\ strech}$), 3214 ($\upsilon_{N-H,\ strech}$), 1664 ($\upsilon_{N-H,\ bending}$), 1432 ($\upsilon_{N=N}$); **^{1}H NMR (400 MHz, $CDCl_3$):** δ 8.67 (d, *J* = 5.9 Hz, 1H), 7.92 (d, *J* = 8.1 Hz, 1H), 7.88 – 7.81 (m, 1H), 7.75 (d, *J* = 8.1 Hz, 1H), 7.35 – 7.29 (m, 1H), 7.26 – 7.19 (m, 1H), 6.85 – 6.79 (m, 1H), 6.74 (d, *J* = 8.3 Hz, 1H), 6.48 (s, 2H). **^{13}C{^{1}H} NMR (101 MHz, $CDCl_3$):** δ 163.70, 149.32, 142.82, 138.34, 136.78, 133.49, 131.42, 124.28, 117.27, 113.38, 77.36.

5.4.4 Synthesis of complex 1a

Ligand **1** (20 mg, 0.10 mmol) was dissolved in dry toluene in a 50 ml two-neck round-bottom flask equipped with a magnetic stir bar and gas inlet. The solution was degassed under a gentle stream of argon for 15 min, after which [RuH(CO)Cl(PPh_3)$_3$] (96 mg, 0.10 mmol) was added. The reaction mixture was then stirred at room temperature for 24 h under open air atmosphere. The solvent was removed under reduced pressure, and the residue was purified by column chromatography over silica gel (60-120 mesh) using acetonitrile containing NH_4PF_6 (25 mg) as the eluent to afford a dark blue crystalline solid. X-ray quality crystals were obtained by slow diffusion of n-hexane into a dichloromethane solution of the purified complex.

5.4.5 Analytical data of complex 1a

trans-[Ru^{II}(H_2L)H(CO)(PPh_3)$_2$]PF_6 **(1a):** Deep blue crystalline solid, Yield: 73 mg (71%). **HRMS**: $[M]^+$ m/z = 853.1241 (calcd for $[C_{48}H_{41}N_4OP_2Ru]^+$ 853.1799); **FT-IR/cm^{-1}** υ = 1977 (υ_{Ru-H}), 1954 ($\upsilon_{C=O}$), 1434 ($\upsilon_{N=N}$), 516 (υ_{Ru-P}); **^{1}H NMR (400 MHz, $CDCl_3$):** δ 8.03 – 7.97 (m, 1H), 7.71 (dd, *J* = 8.4, 1.4 Hz, 1H), 7.66 (d, *J* = 7.1 Hz, 1H), 7.58 – 7.53 (m, 1H), 7.35 (dq, *J* = 7.9, 3.6 Hz, 7H), 7.23 (q, *J* = 3.7 Hz, 26H), 6.93 (s, 2H), 6.67 (d, *J* = 8.5 Hz, 1H), 6.50 – 6.43 (m, 1H), 6.35 (t, *J* = 5.8 Hz, 1H), -10.89 (t, *J* = 20.0 Hz, 1H). **^{13}C{^{1}H} NMR (101 MHz, $CDCl_3$):** δ 162.34, 151.25, 143.11, 139.79, 139.00, 134.40, 133.56, 133.17, 133.11, 133.05, 131.27, 131.04, 130.81, 130.61, 129.00, 128.83, 128.79, 128.74, 128.59, 126.47, 125.27, 119.56, 116.85. **^{31}P{^{1}H} NMR (121 MHz, $CDCl_3$):** δ 43.63, -144.24 (sep, $^1J_{P-F}$ = 709.06 Hz).

5.4.6 General procedure for synthesis of bis(indolyl)methanes (8aa-13ae)

An oven-dried 35 ml ACE pressure tube equipped with a magnetic stir bar was charged with indoles (**2**-**6**) (2.0 mmol), aromatic primary alcohols (**7a-7t**) (1.1 mmol), t-BuOK (0.5 mmol), and ruthenium catalyst **1a** (0.1 mol%, 0.9 mg). Dry toluene (3 ml) was added, and the tube was sealed with a PTFE-lined cap. The reaction mixture was heated in a preheated oil bath at 110

°C for 12 h under aerobic conditions. Upon completion (monitored by TLC), the mixture was cooled to room temperature, and the solvent was removed under reduced pressure to remove volatile organic impurities. The crude residue was purified by column chromatography over silica gel (60-120 mesh or 100-200 mesh), eluting with hexane/ethyl acetate (5:1 to 3:1 v/v), to produce the desired bis(indolyl)methane products.

5.4.7 General procedure for synthesis of bis(indolyl)methanes (14ab-14aj)

An oven-dried 35 ml ACE pressure tube equipped with a magnetic stir bar was charged with indoles (**2** & **5**) (2.0 mmol), aliphatic primary alcohols (**15b-15h**) (1.1 mmol), KOH (0.5 mmol) and ruthenium catalyst **1a** (0.1 mol%, 0.9 mg). The tube was sealed with a PTFE-lined cap, and the mixture was heated in a preheated oil bath at 110 °C for 12 h under aerobic conditions. Upon completion (monitored by TLC), the reaction mixture was cooled to room temperature, and the solvent was removed under reduced pressure. The crude residue was purified by column chromatography over silica gel (60-120 mesh or 100-200 mesh) using hexane/ethyl acetate (5:1 to 3:1 v/v) as the eluent to afford the desired bis(indolyl)methane products.

5.4.8 General procedure for synthesis of bis(indolyl)methanes (14aa, 14ak, 14al)

An oven-dried 35 ml ACE pressure tube equipped with a magnetic stir bar was charged with indoles (**2**, **3**, and **5**) (2.0 mmol), methanol (**15a**) (3 ml), KOH (0.5 mmol), and ruthenium catalyst **1a** (0.1 mol%, 0.9 mg). The tube was sealed with a PTFE-lined cap, and the reaction mixture was heated in a preheated oil bath at 110 °C for 12 h under aerobic conditions. After completion (monitored by TLC), the mixture was cooled to room temperature, and the solvent was removed under reduced pressure. The crude residue was purified by column chromatography over silica gel (100-200 mesh) using hexane/ethyl acetate (3:1 v/v) as the eluent to yield the desired bis(indolyl)methane products.

5.4.9 Alcohol Dehydrogenation and Detection of H_2O_2

The dehydrogenation of (4-chlorophenyl)methanol (**7k**) in the presence of catalyst **1a** was investigated under open-air conditions, and the in situ formation of hydrogen peroxide (H_2O_2) was confirmed spectrophotometrically. The characteristic absorption band of triiodide (I_3^-) at 350 nm was monitored, showing a steady increase in intensity consistent with H_2O_2 generation. For this study, the reaction was performed in a 35 ml ACE pressure tube charged with 1 mmol of **7k**, 0.1 mol% (1.0 mg) of catalyst **1a** and 0.5 mmol (56 mg) of t-BuOK in 3 ml of dry toluene. The tube was sealed with a PTFE-lined cap and the reaction mixture was stirred at 110 °C for 12 h. After cooling, the mixture was diluted with 15 mL of water and extracted twice with CH_2Cl_2. The aqueous phase was acidified to pH 2 with dilute H_2SO_4 to avoid further oxidation. To this solution, 1 ml of 10% KI and a few drops of 3% $(NH_4)_2MoO_4$ were added. Under these conditions, H_2O_2 oxidized iodide ions (I^-) to molecular iodine (I_2), which subsequently combined with excess iodide to generate triiodide (I_3^-), according to the following reactions:

1. $H_2O_2 + 2I^- + 2H^+ \rightarrow 2H_2O + I_2$
2. $I_2(aq) + I^- \rightarrow I_3^-$

5.4.10 Mercury Poisoning Test

In a 35 ml ACE pressure tube, (4-chlorophenyl)methanol (**7k**, 142 mg, 1.0 mmol, 1 equiv.), t-BuOK (56 mg, 0.5 mmol, 0.5 equiv.) and catalyst **1a** (1.0 mg, 0.1 mol%) were combined in 3 ml of toluene in the presence of a magnetic stir bar. To this mixture, elemental mercury (738 mg, 50 equiv.) was added under an open-air atmosphere. The tube was sealed with a PTFE-lined cap, and the reaction mixture was stirred at 110 °C for 12 h. Reaction progress was monitored by TLC. After completion, the mixture was cooled to room temperature and extracted twice with dichloromethane (CH_2Cl_2). The combined organic extracts were

concentrated, and the crude product was purified by column chromatography on silica gel using hexane as the eluent, affording the desired compound (**7k′**) in 90% isolated yield.

5.4.11 Radical Scavenging Experiment

A 35 ml ACE pressure tube was charged with compound **2** (234 mg, 2.0 mmol, 2.0 equiv.), (4-methoxyphenyl)methanol (**7i**, 0.14 ml, 1.0 mmol, 1.1 equiv.), t-BuOK (56 mg, 0.5 mmol, 0.5 equiv.), catalyst **1a** (1.0 mg, 0.1 mol%), and (2,2,6,6-tetramethylpiperidin-1-yl)oxyl (**TEMPO**) (312 mg, 2.0 mmol, 2.0 equiv.) in 5 ml of toluene under an open-air atmosphere. The pressure tube was sealed with a PTFE-lined cap and the reaction mixture was stirred at 110 °C for 12 h, with progress monitored by TLC. Upon completion, the mixture was cooled to room temperature and extracted with ethyl acetate (EtOAc). The combined organic extracts were concentrated and the residue was purified by column chromatography on silica gel using hexane/EtOAc (5:1 v/v) as the eluent to afford the desired product (**8ah**) in 85% isolated yield.

5.4.12 Deuterium Labelling Experiment with Deuterated Methanol

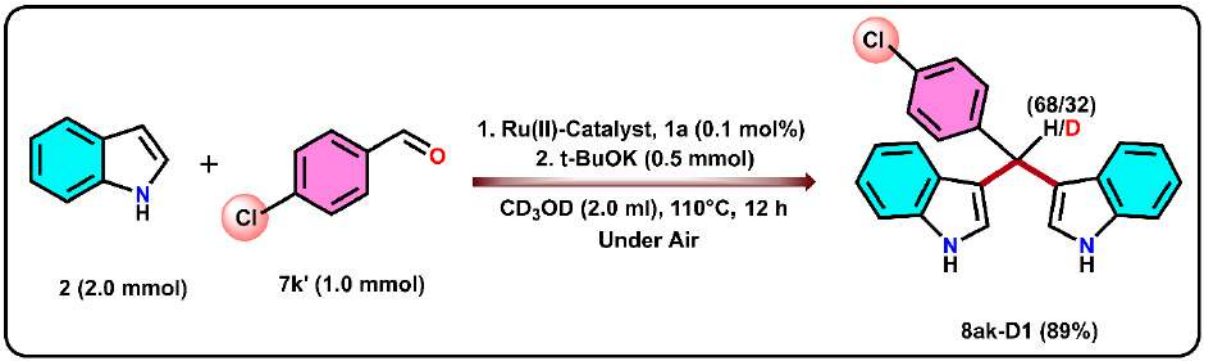

Reaction condition: *Indole (**2**) (234 mg, 2.0 mmol), 4-chlorobenzaldehyde (**7k'**) (140 mg, 1.0 mmol), Deuterated methanol (CD_3OD) (2.0 ml), **1a** (1.0 mg, 0.1 mol%), 110 ºC (oil bath), 12 h. Isolated yield after column chromatography, Under air*

	8ak-D1	**Deuterium Incorporation at α-position**
Chemical Shift (ppm)	7.95 (2H)	5.89 (1H)
Integral value	2.00	0.68
Calculated Ratio		(1–0.68)×100 = 32%

5.5 References

[1] (a) D. A. Horton, G. T. Bourne, M. L. Smythe, *Chem. Rev.,* **2003**, *103*, 893−930. (b) M. Somei, F. Yamada, *Nat. Prod. Rep.*, **2004**, *21*, 278−311. (c) M. Somei, F. Yamada, *Nat. Prod. Rep.*, **2004**, *21*, 278−311. (d) S. B. Herzon, A. G. Myers, *J. Am. Chem. Soc.*, **2005**, *127*, 5342−5344. (e) R. Tjalkens, S. Safe, *US Pat.*, 8580843, **2013**. (b) N. Netz, T. Opatz, *Mar. Drugs,* **2015**, *13*, 4814−4914. (f) T. P. Singh, O.M. Singh, *Medicinal Chemistry*, **2018**, *18*, 9−25.

[2] (a) R. Bell, S. Carmeli, N. Sar, *J. Nat. Prod.*, **1994**, *57*, 1587−1590. (b) A. Fensome, R. Bender, J. Cohen, M. A. Collins, V. A. Mackner, L. L. Miller, J. W. Ullrich, R. Winneker, J. Wrobel, P. Zhang, Z. Zhang, Y. Zhu, *Bioorg. Med. Chem. Lett.*, **2002**, *12*, 3487–3490. (c) D. E. Gillespie, S. F. Brady, A. D. Bettermann, N. P. Cianciotto, M. R. Liles, M. R. Rondon, J. Clardy, R. M. Goodman, J. Handelsman, *Appl. Environ. Microbiol.*, **2002**, *68*, 4301−4306. (d) G. R. Humphrey, J. T. Kuethe, *Chem. Rev.*, **2006**, *106*, 2875−2911. (e) S. E. Reisman, J. M. Ready, M. M. Weiss, A. Hasuoka, M. Hirata, K. Tamaki, T. V. Ovaska, C. J. Smith, J. L. Wood, *J. Am. Chem. Soc.*, **2008**, *130*, 2087–2100. (f) S. R. Walker, E. J. Carter, B. C. Huff, J. C. Morris, *Chem. Rev.*, **2009**, *109*, 3080–3098. (g) M. Shiri, M. A. Zolfigol, H. G. Kruger, Z. Tanbakouchian, *Chem. Rev.*, **2010**, *110*, 2250−2293. (h) X. -X. Sun, B. -X. Du, H. -H. Zhang, L. Ji, F. Shi, *ChemCatChem*., **2015**, *7*, 1211−1221. (i) E. M. Hussein, R. I. Alsantali, S. M. Abd El-Galil, R. J. Obaid, A. Alharbi, M. A. S. Abourehab, S. A. Ahmed, *Heliyon*, **2019**, *5*, e01982. (j) T. Yang, H. Lu, Y. Shu, Y. Ou, L. Hong, C. -T. Au, R. Qiu, *Org. Lett.*, **2020**, *22*, 827−831. (k) J. S. S. Neto, G. Zeni, *Org. Chem. Front.*, **2020**, *7*, 155–210. (l) F. A. Wati, M. Santoso, Z. Moussa, S. Fatmawati, A. Fadlan, Z. M. A. Judeh, *RSC Adv.*, **2021**, *11*, 25381–25421.

[3] (a) V. Jamsheena, G. Shilpa, J. Saranya, N. A. Harry, R. S. Lankalapalli, S. Priya, *Chem.-Biol. Interact.*, **2016**, *247*, 11−21. (b) T. Pillaiyar, M. Köse, K. Sylvester, H. Weighardt, D. Thimm, G. Borges, I. Förster, I. von Kügelgen, C. E. Müller, *J. Med. Chem.*, **2017**, *60*, 3636−3655.

[4] (a) R. Contractor, I. J. Samudio, Z. Estrov, D. Harris, J. A. McCubrey, S. H. Safe, M. Andreeff, M. Konopleva, *Cancer Res.*, **2005**, *65*, 2890−2898. (b) T. Pillaiyar, M. Köse, K. Sylvester, H. Weighardt, D. Thimm, G. Borges, I. Förster, I. von Kügelgen, C. E. Müller, *J. Med. Chem.*, **2017**, *60*, 3636−3655. (c) J. Lee, *Nutr. Cancer*, **2019**, *71*, 992−1006.

[5] G. Sivaprasad, P. T. Perumal, V. R. Prabavathy, N. Mathivanan, *Bioorg. Med. Chem. Lett.*, **2006**, *16*, 6302−6305.

[6] (a) H. E. Fischer, *Chem. Ber.*, **1886**, 19, 2988–2991. (b) H. E. Fischer, *Justus Liebigs Ann. Chem.*, **1887**, *242*, 372–383. (c) S. J. Ji, S. Y. Wang, Y. Zhang, T. P. Loh, *Tetrahedron*, **2004**, *60*, 2051–2055. (d) M. A. Pasha, V. P. Jayashankara, *J. Pharmacol. Toxicol*., **2006**, *1*, 585–590. (e) M. Bandini, A. Umani-Ronchi, Catalytic Asymmetric Friedel-Crafts Alkylations, Wiley-VCH: Weinheim, **2009**. (f) Z. H. Ma, H. B. Han, Z. B. Zhou, J. Nie, *J. Mol. Catal. A: Chem.*, **2009**, *311*, 46–53. (g) M. Rueping, B. J. Nachtsheim, *Beilstein J. Org. Chem.*, **2010**, *6*, 6. (l) F. Shirini, M. S. Langroodi, M. Abedini, *Chin. Chem. Lett.*, **2010**, *21*, 1342–1345. (h) S. R. Mendes, S. Thurow, M. P. Fortes, F. Penteado, E. J. Lenardão, D. Alves, R. G. Jacob, *Tetrahedron Lett.*, **2012**, *53*, 5402–5406. (i) M. Rekha, H. R. Manjunath, N. Nagaraju, *J. Ind. Eng. Chem.*, **2013**, *19*, 337–346. (j) G. M. Shelke, V. K. Rao, R. K. Tiwari, B. S. Chhikara, K. Parang, A. Kumar, *RSC Adv.*, **2013**, *3*, 22346–22352. (k) N. Saehlim, T. Kasemsuk, U. Sirion, R. Saeeng, *J. Org. Chem.*, **2018**, *83*, 13233–13242. (l) Y. Wu, Z. Lin, R. Fang, Y. Guo, Li Tu, Y. Yan, W. Zhang, H. Sun, Z. Gao, *Organometallics,* **2022**, *41*, 1067−1077.

[7] (a) D. Wang, D. Astruc, *Chem. Rev.*, **2015**, *115*, 6621−6686. (b) A. Mukherjee, D. Milstein, *ACS Catal.* **2018**, *8*, 11435–11469. (c) A. Corma, J. Navas, M. J. Sabater, *Chem. Rev.*, **2018**, *118*, 1410−1459. (d) G. A. Filonenko, R. V. Putten, E. J. M. Hensen, E. A. Pidko, *Chem. Soc. Rev.*, **2018**, *47*, 1459–1483. (e) J. A. Luque-Urrutia, M. Solà, D. Milstein, A. Poater, *J. Am. Chem. Soc.*, **2019**, *141*, 2398–2403. (f) L. Alig, M. Fritz, S. Schneider, *Chem. Rev.*, **2019**, *119*, 2681–2751. (g) D. Wei, C. Darcel, *Chem. Rev.*, **2019**, *119*, 2550−2610. (h) S. Waiba, B. Maji, *ChemCatChem*, **2020**, *12*, 1891–1902. (i) T. Kwok, O. Hoff, R. J. Armstrong, T. J. Donohoe, *Chem. Eur. J.*, **2020**, *26*, 12912−12926. (j) M. Maji, D. Panja, I. Borthakur, S. Kundu, *Org. Chem. Front.*, **2021**, *8*, 2673−2709. (k) A. Mondal, R. Sharma, D. Pal, D. Srimani, *Eur. J. Org. Chem.*, **2021**, *2021*, 3690−3720. (l) B. G. Reed-Berendt, D. E. Latham, M. B. Dambatta, L. C. Morrill, *ACS Cent. Sci.*, **2021**, *7*, 570−585. (m) N. Hofmann, K. C. Hultzsch, *Eur. J. Org. Chem.*, **2021**, *2021*, 6206−6223. (n) D. Jana, S. Roy, S. Naskar, S. Halder, G. Kanrar, K. Pramanik, *Org. Biomol. Chem.*, **2024**, *22*, 6393−6408 (o) D. Jana, S. Malik, G. Kanrar, S. Halder, S. Naskar, K. Pramanik, *ChemCatChem*, **2025**, 17, e202401851.

[8] (a) H. Hikawa, Y. Yokoyama, *RSC Adv.*, **2013**, *3*, 1061–1064. (b) S. Badigenchala, D. Ganapathy, A. Das, R. Singh, G. Sekar, *Synthesis*, **2014**, *46*, 101–109. (c) N. -K. Nguyen, D. L. Tran, T. Q. Hung, T. M. Le, N. T. Son, Q. T. Trinh, T. T. Dang, P. Langer, *Tetrahedron Lett.*, **2021**, *68*, 152936.

[9] (a) C. Sun, X. Zou, F. Li, *Chem. -Eur. J.*, **2013**, *19*, 14030–14033. (b) V. Arun, L. Roy, S. De Sarkar, *Chem. -Eur. J.*, **2020**, *26*, 16649–16654. (c) N. Biswas, R. Sharma, D. Srimani, *Adv.*

Synth. Catal., **2020**, *362*, 2902–2910. (d) V. Yadav, E. Balaraman, S. B. Mhaske, *Adv. Synth. Catal.*, **2021**, *363*, 4430−4439. (e) A. Mondal, R. Sharma, B. Dutta, D. Pal, D. Srimani, *J. Org. Chem.*, **2022**, *87*, 3989−4000. (f) A. K. Guin, S. Pal, S. Chakraborty, S. Chakraborty, N. D. Paul, *J. Org. Chem.*, **2023**, *88*, 16755−16772. (g) S. S. Clinton, R. Ramesh, J. G. Malecki, *Catal. Sci. Technol.*, **2023**, *13*, 3358–3365. (h) A. Mondal, R. Kumar, A. K. Suresh, M. Kumar S. E. Balaraman, *Catal. Sci. Technol.*, **2023**, *13*, 5745–5756.

[10] (a) P. S. Hallman, T. A. Stephenson, G. Wilkinson, "*Inorganic Syntheses*", 1970, Volume 12, DOI:10.1002/9780470132432.ch40. (b) E. C. Taylor, C. -P. Tseng, J. B. Rampal, *J. Org. Chem.*, **1982**, *47*, 552–555. (c) S. Bellotto, R. Reuter, C. Heinis, H. A. Wegner, *J. Org. Chem.*, **2011**, *76*, 9826–9834. (d) N. Kumari, S. Halder, S. Naskar, S. Ganguly, K. Pramanik, F. Yari, A. Dorniak, W. Schofberger, S. Roy, *Materials Today Catalysis*, **2024**, *5*,100049.

[11] M. Maji, I. Borthakur, S. Guria, S. Singha, S. Kundu, *J. Catal.*, **2021**, *402*, 37–51.

[12] (a) "Standard thermodynamic properties of chemical substances": CRC Handbook of Chemistry and Physics, Internet version 2005 (Eds.: D. R. Lide), CRC Press, Boca Raton, FL, **2005**. (b) J. Moran, A. Preetz, R. A. Mesch, M. J. Krische, *Nature Chemistry*, **2011**, *3*, 287–290. (c) G. Choi, S. H. Hong, *Angew. Chem. Int. Ed.*, **2018**, *57*, 6166 –6170.

[13] (a) D. Srimani, G. Leitus, Y. Ben-David, D. Milstein, *Angew. Chem., Int. Ed.*, **2014**, *53*, 11092−11095. (b) K. Das, A. Mondal, D. Pal, H. K. Srivastava, D. Srimani, *Organometallics*, **2019**, *38*, 1815−1825. (c) A. K. Bains, D. Dey, S. Yadav, A. Kundu, D. Adhikari, *Catal. Sci. Technol.*, **2020**, *10*, 6495−6500. (d) G. Balamurugan, R. Ramesh, *ChemCatChem*, **2022**, *14*, e202101455.

[14] (a) H. Li, M. B. Hall, *J. Am. Chem. Soc.*, **2015**, *137*, 12330−12342. (b) R. Ray, S. Chandra, D. Maiti, G. K. Lahiri, *Chem. Eur. J.*, **2016**, *22*, 8814–8822 (c) S. P. Rath, D. Sengupta, P. Ghosh, R. Bhattacharjee, M. Chakraborty, S. Samanta, A. Datta, S. Goswami, *Inorg. Chem.*, **2018**, *57*, 11995−12009. (d) S. Sinha, S. Das, R. Mondal, S. Mandal, N. D. Paul, *Dalton Trans.*, **2020**, *49*, 8448–8478. (e) B. Goswami, M. Khatua, S. Samanta, *Dalton Trans.*, **2022**, *51*, 1454–1463.

[15] (a) S. Halder, S. Naskar, D. Jana, G. Kanrar, K. Pramanik, S. Ganguly, *New J. Chem.,* **2024**, *48*, 8181−8194. (b) S. Halder, S. Naskar, D. Jana, G. Kanrar, S. C. Mandal, S. Roy, N. Bharadwaj, K. Pramanik, S. Ganguly, *Chem Asian J.*, **2025**, *20*, e202401278. (c) S. Naskar, S. Halder, A. Das, S. Malik, G. Kanrar, D. Jana, B. K. Panda, K. Pramanik, S. Ganguly, *Asian J. Org. Chem.*, **2025***, 14,* e00330.

5.6 Appendix

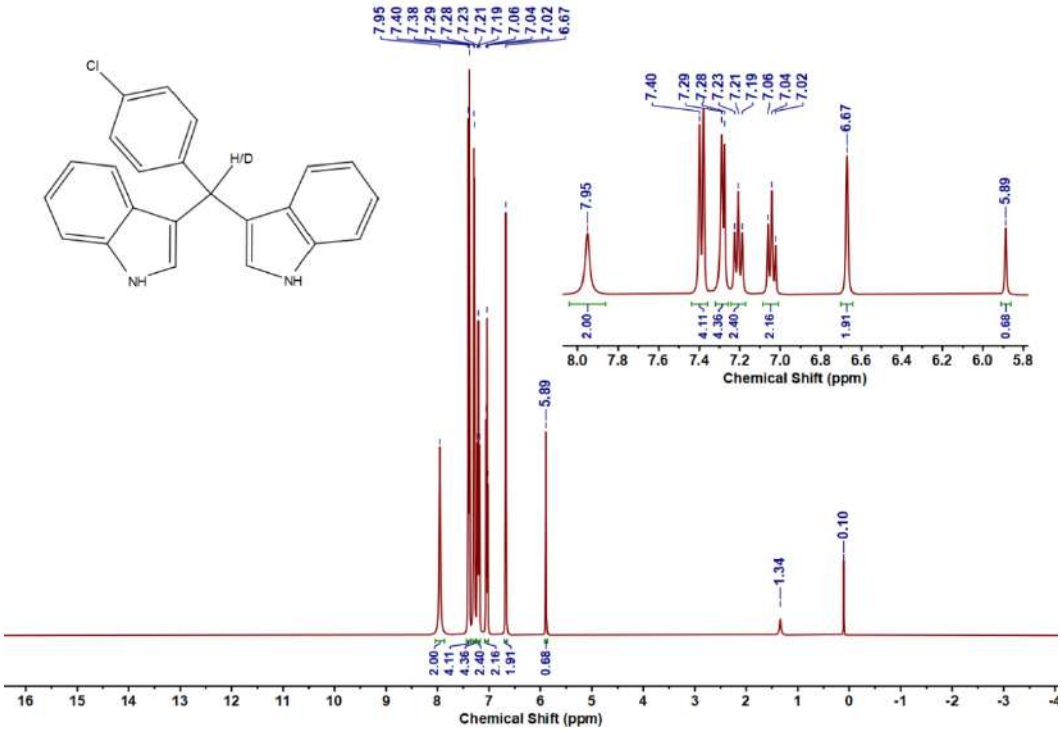

Figure 5.6.A1: ^{1}H NMR spectrum of **8ak-D1**

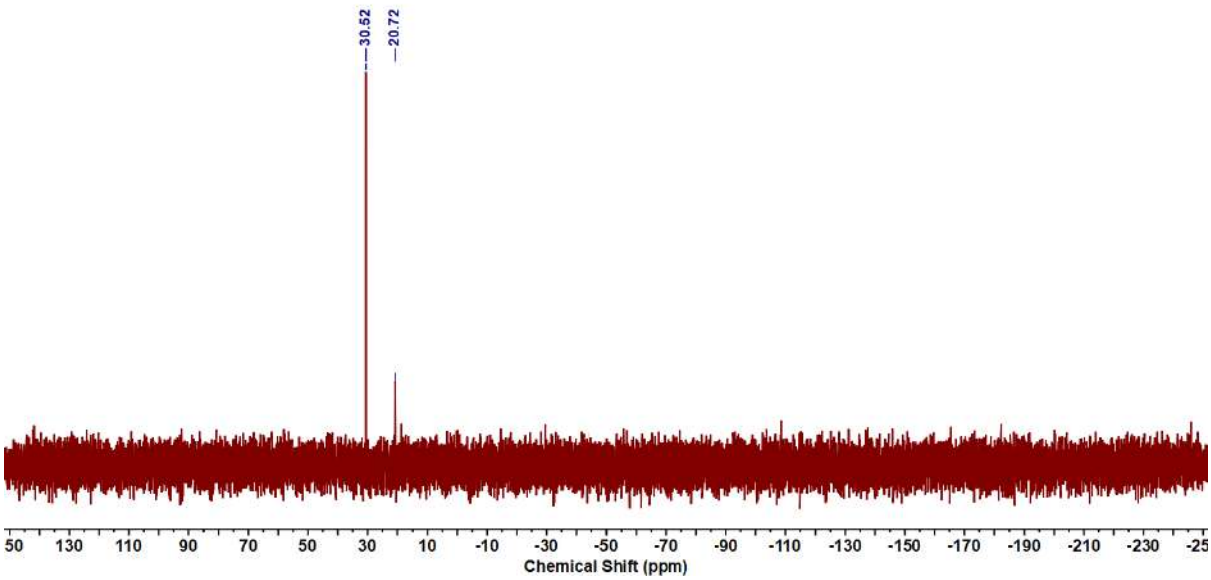

Figure 5.6.A2: ^{31}P{^{1}H} NMR spectrum of reaction mixture

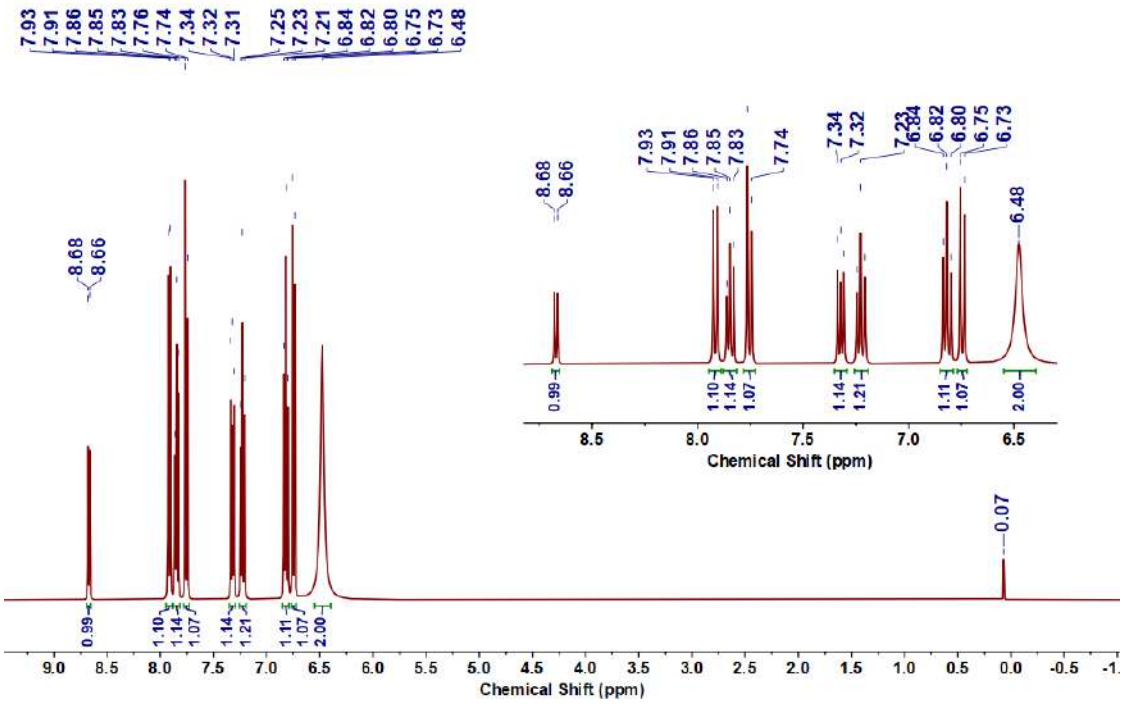

Figure 5.6.A3: ^{1}H NMR spectrum of ligand **1**

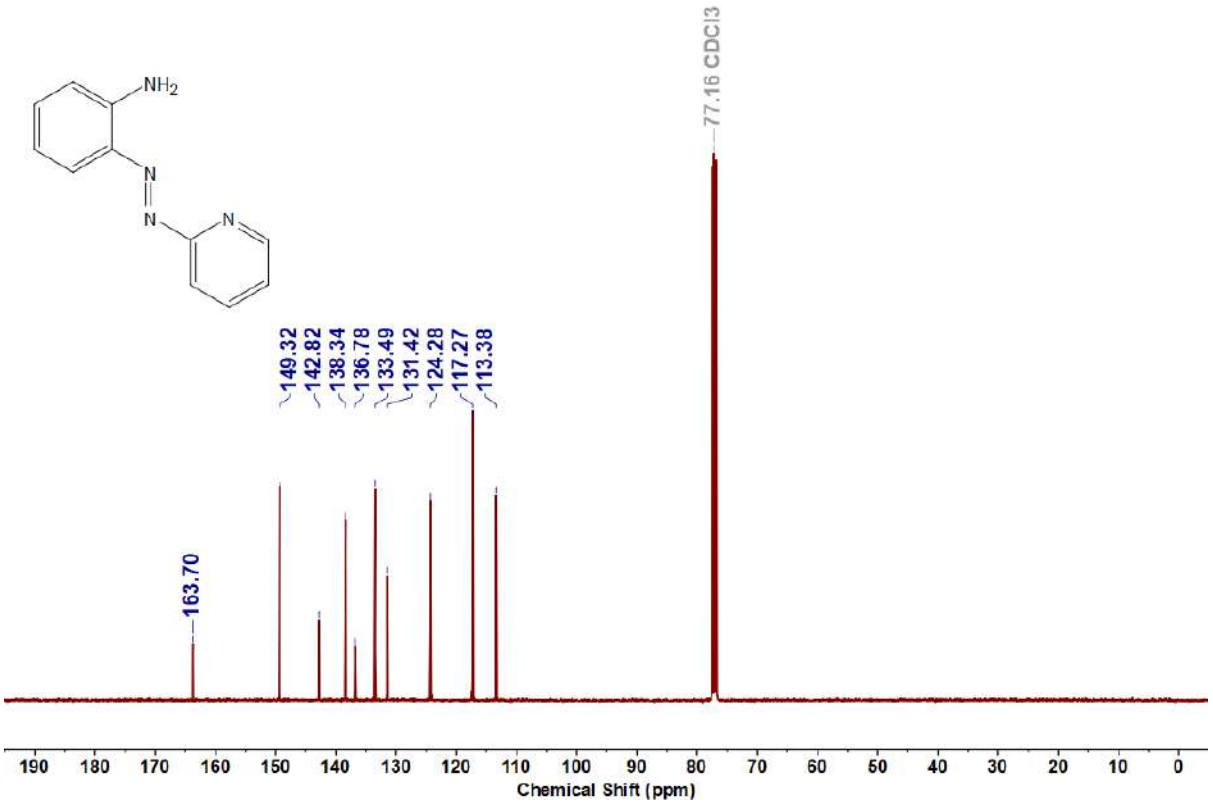

Figure 5.6.A4: $^{13}C\{^{1}H\}$ NMR spectrum of ligand **1**

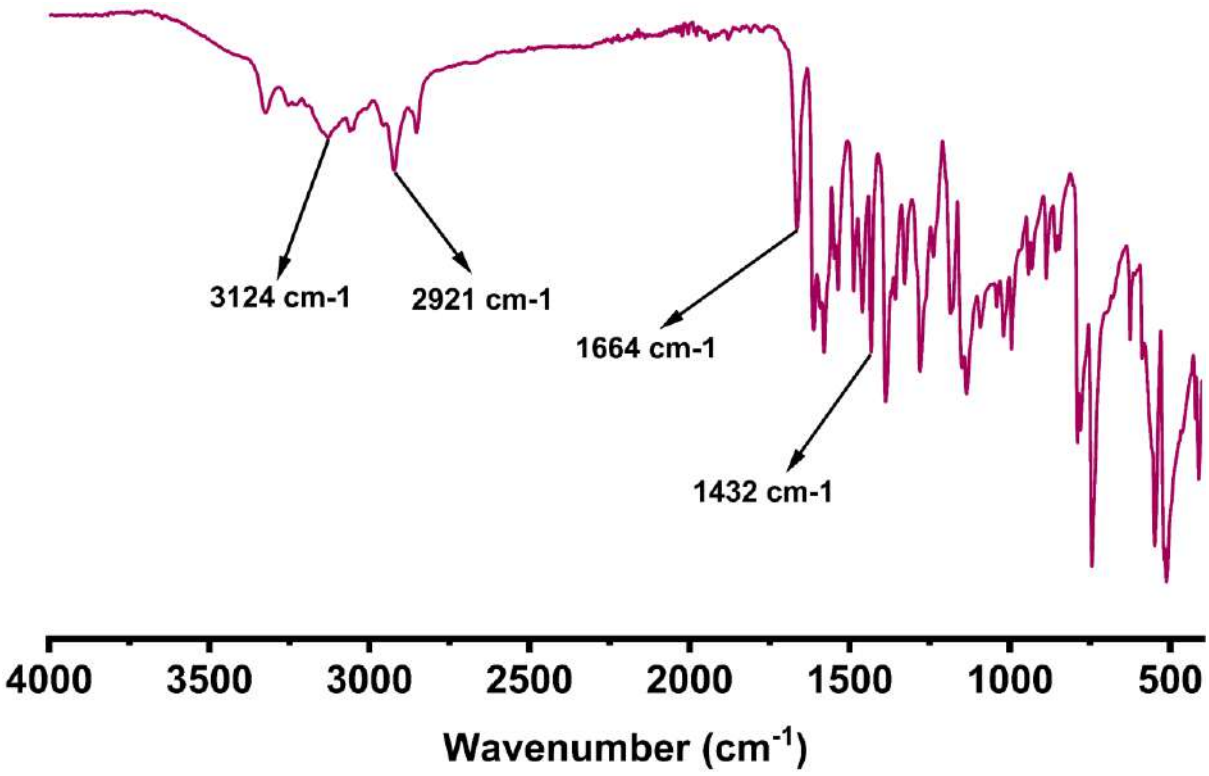

Figure 5.6.A5: IR spectrum of **1**

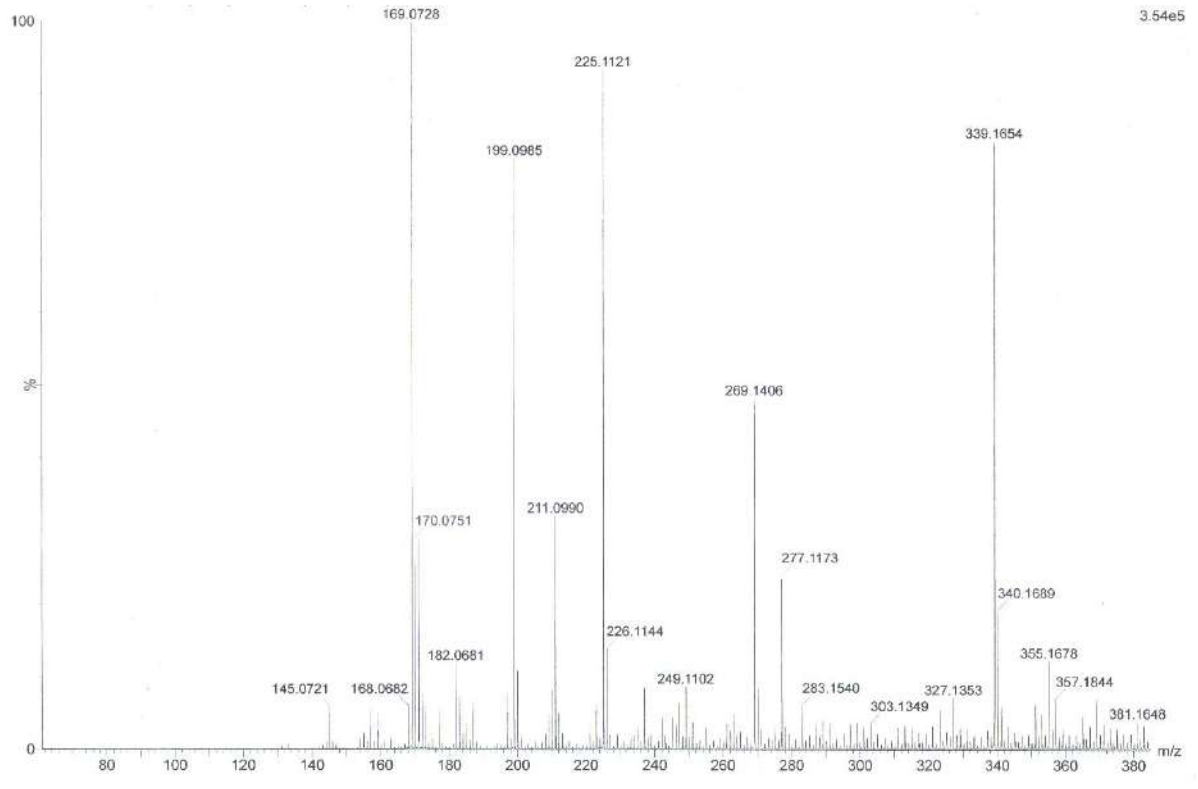

Figure 5.6.A6: HRMS spectrum of ligand **1**

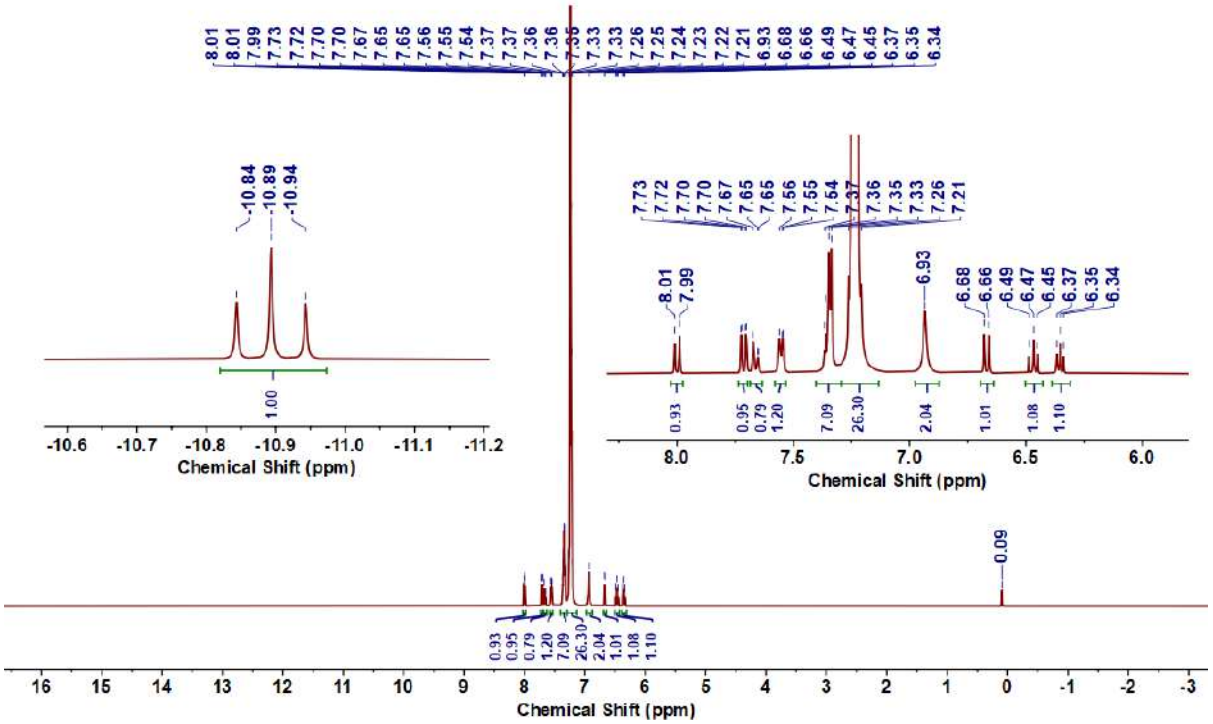

Figure 5.6.A7: ^{1}H NMR spectrum of complex **1a**

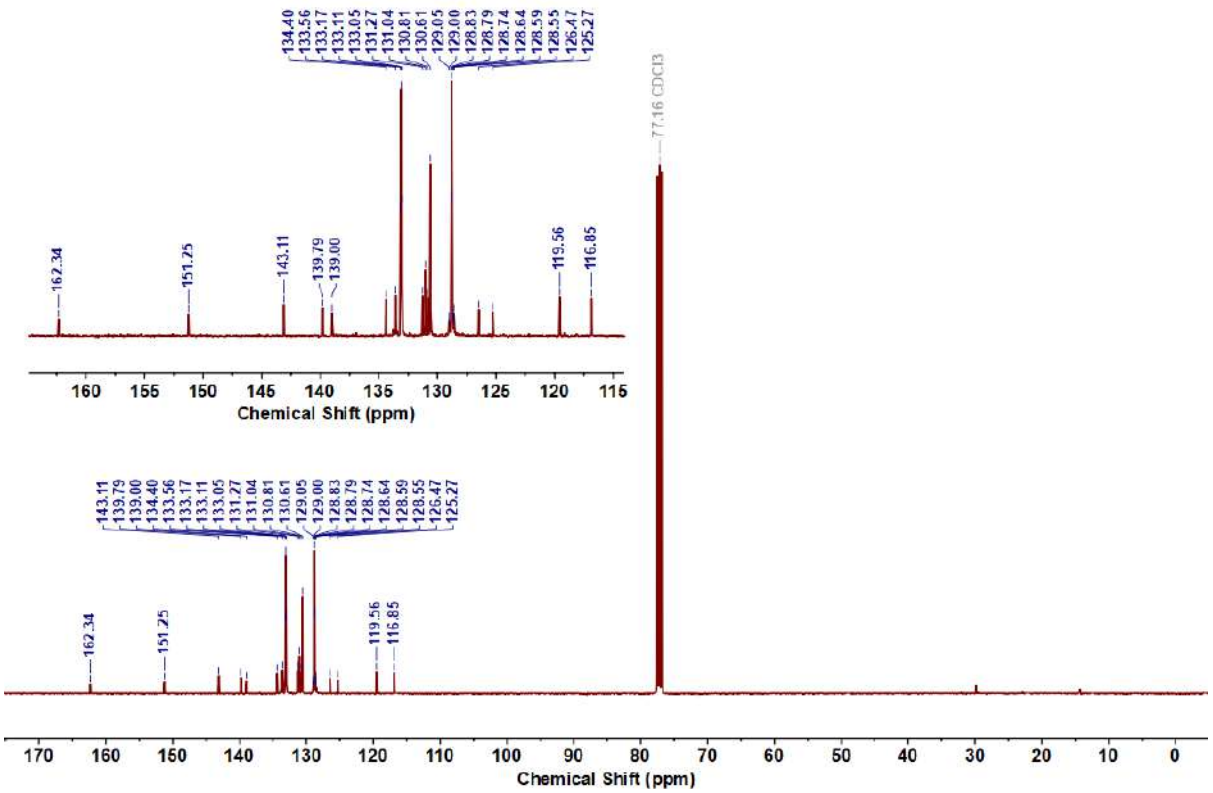

Figure 5.6.A8: $^{13}C\{^{1}H\}$ NMR spectrum of complex **1a**

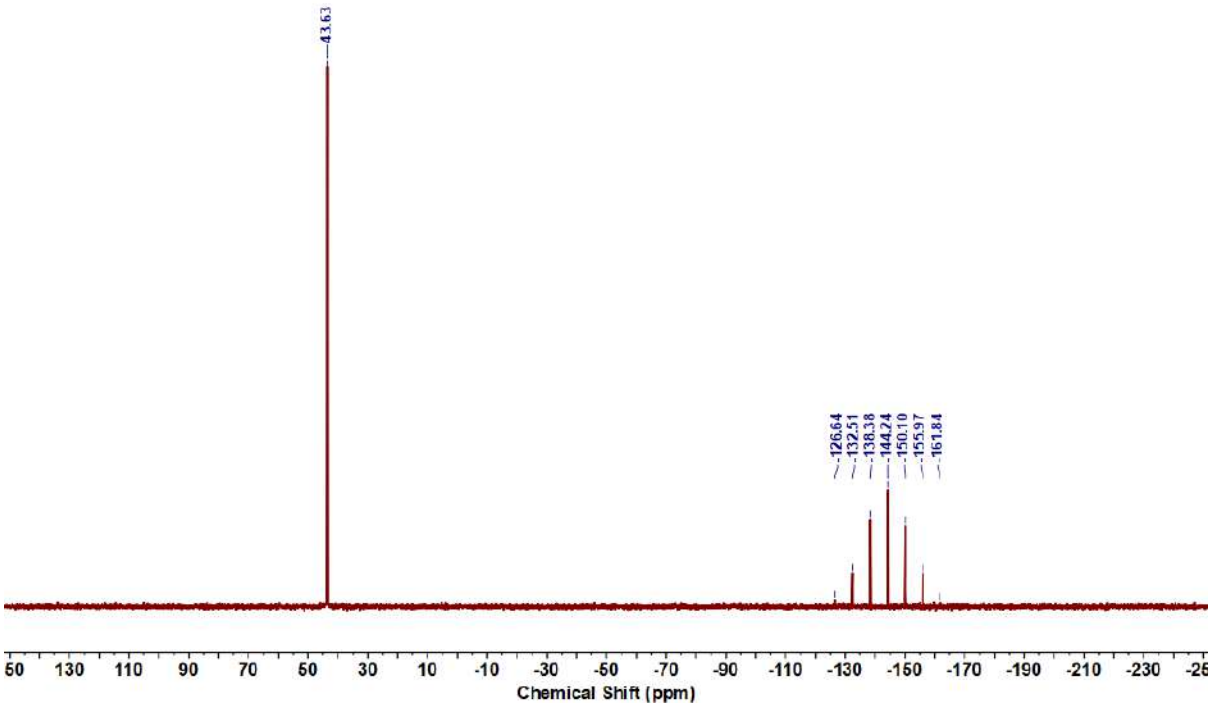

Figure 5.6.A9: $^{31}P\{^{1}H\}$ NMR spectrum of complex **1a**

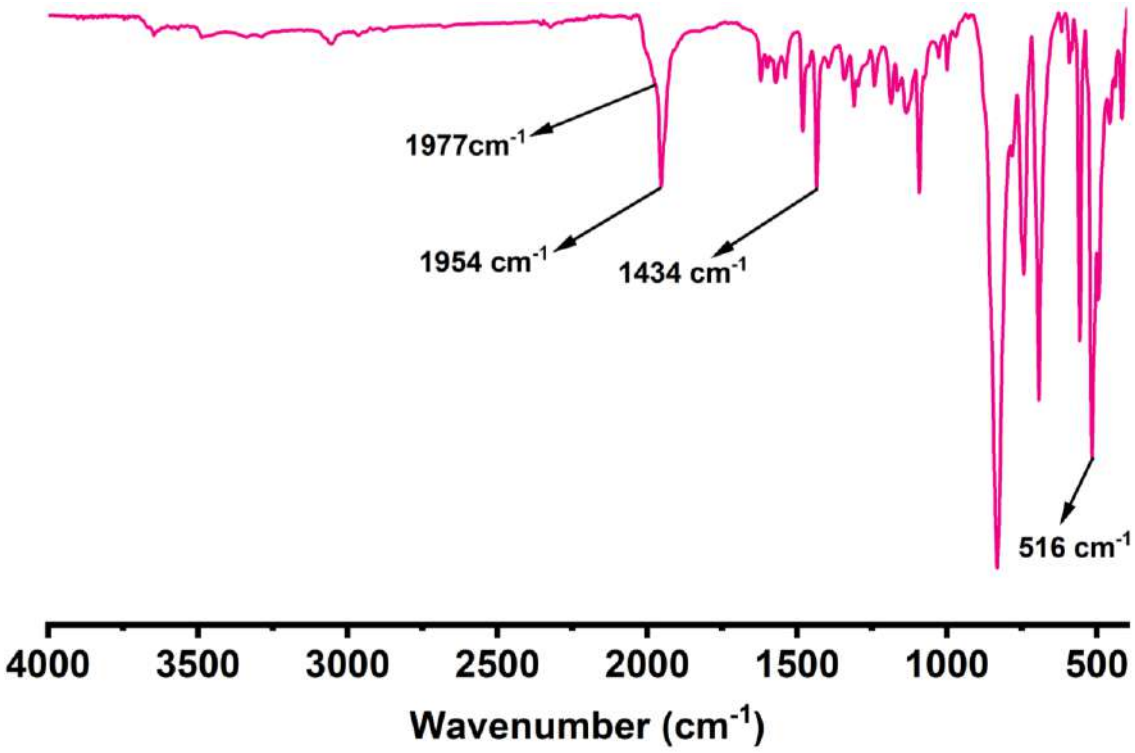

Figure 5.6.A10: IR spectrum of complex **1a**

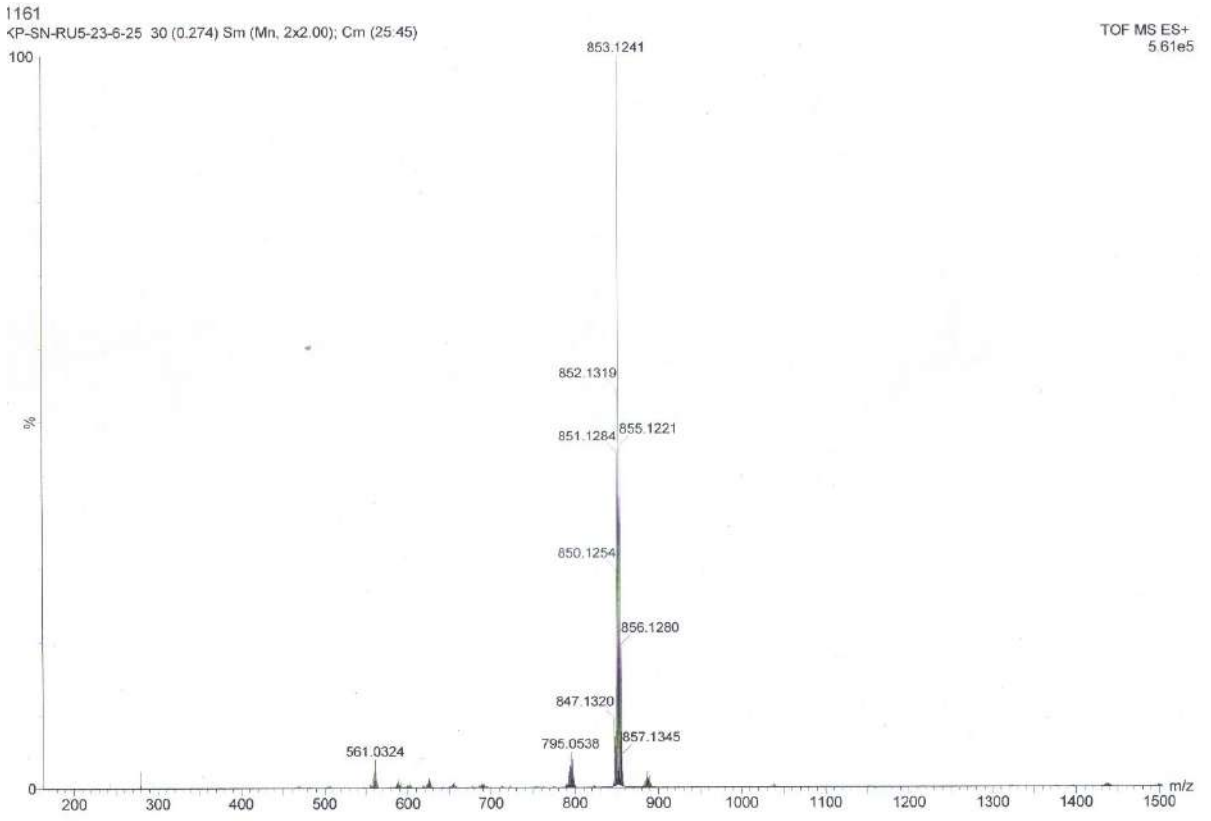

Figure 5.6.A11: HRMS spectrum of complex **1a**

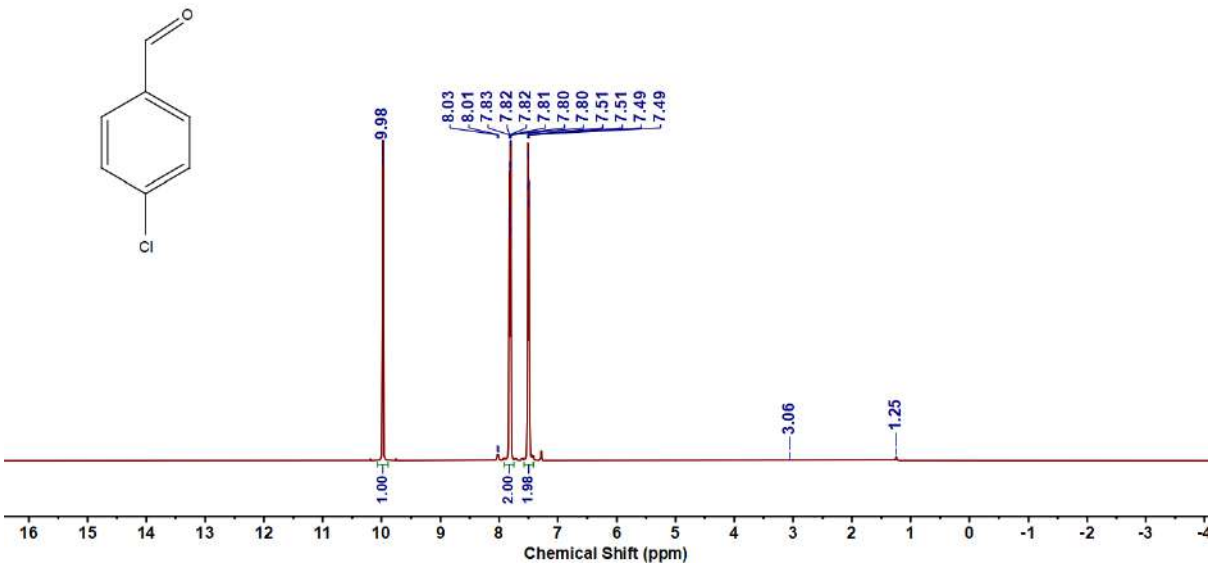

Figure 5.6.A12: ^{1}H NMR spectrum of **7k′**

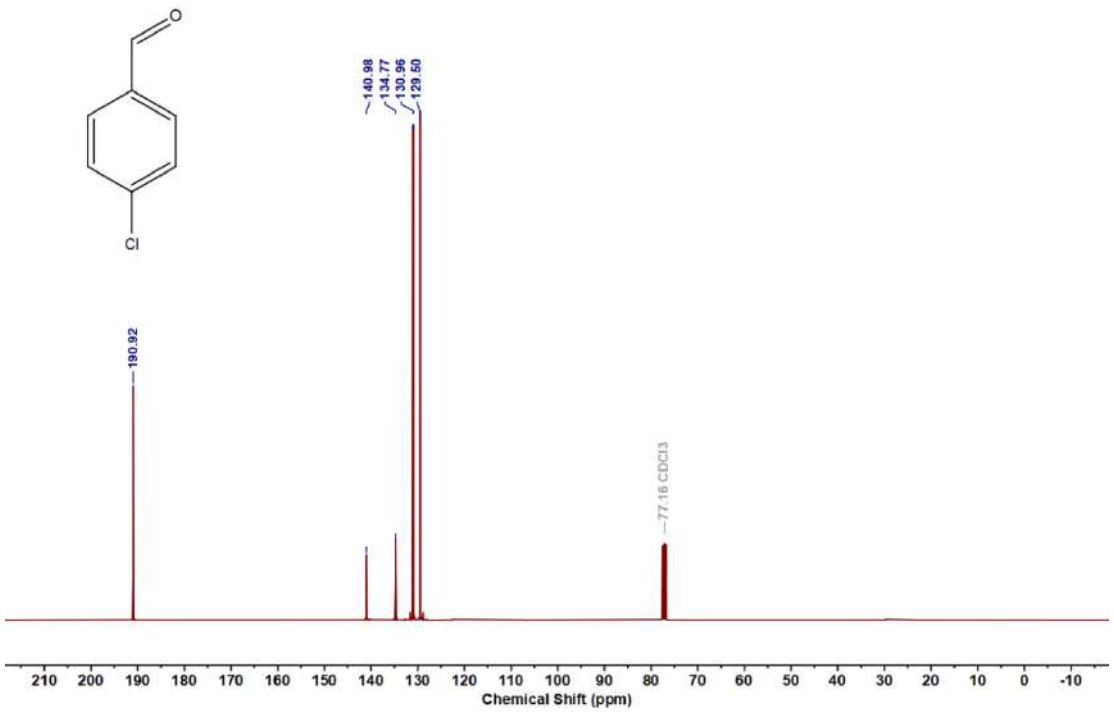

Figure 5.6.A13: $^{13}C\{^{1}H\}$ NMR spectrum of **7k′**

NMR data of 4-chlorobenzaldehyde (7k'): ^{1}H NMR (400 MHz, $CDCl_3$): δ 9.98 (s, 1H), 7.81 (dt, *J* = 8.5, 1.8 Hz, 2H), 7.50 (dd, *J* = 8.0, 2.3 Hz, 2H). **$^{13}C\{^{1}H\}$ NMR (101 MHz, $CDCl_3$):** δ 190.92, 140.98, 134.77, 130.96, 129.50.

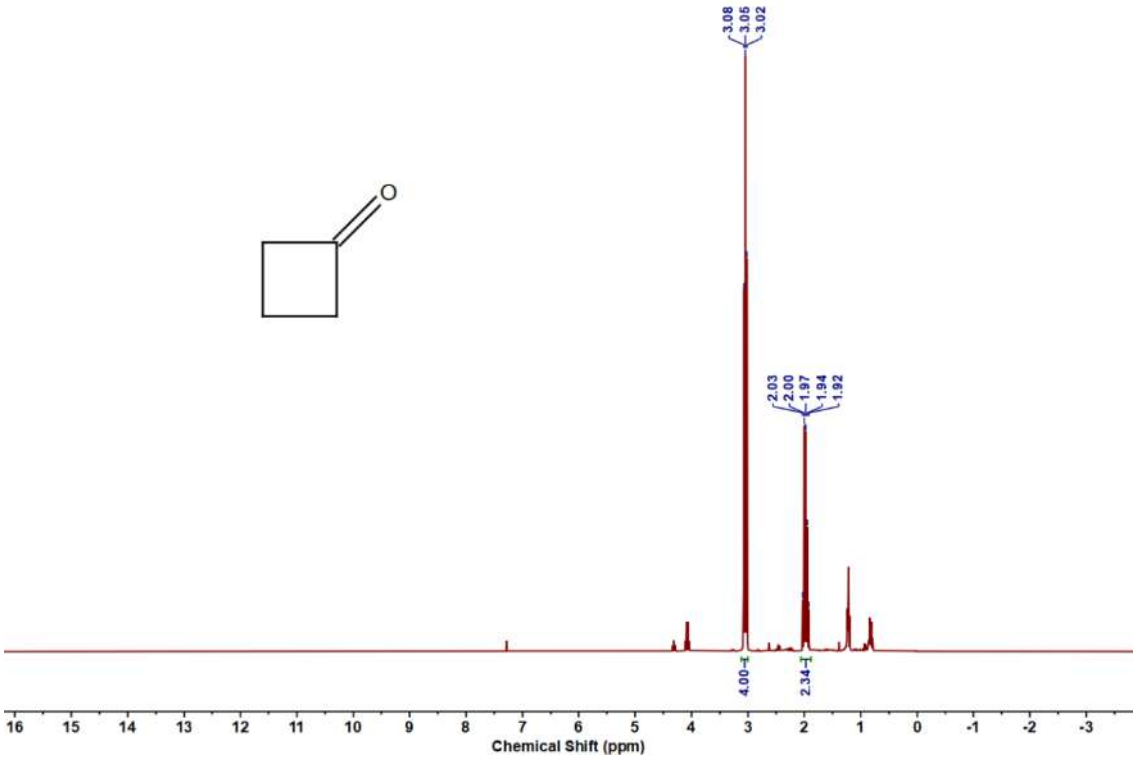

Figure 5.6.A14: ^{1}H NMR spectrum of **16a′**

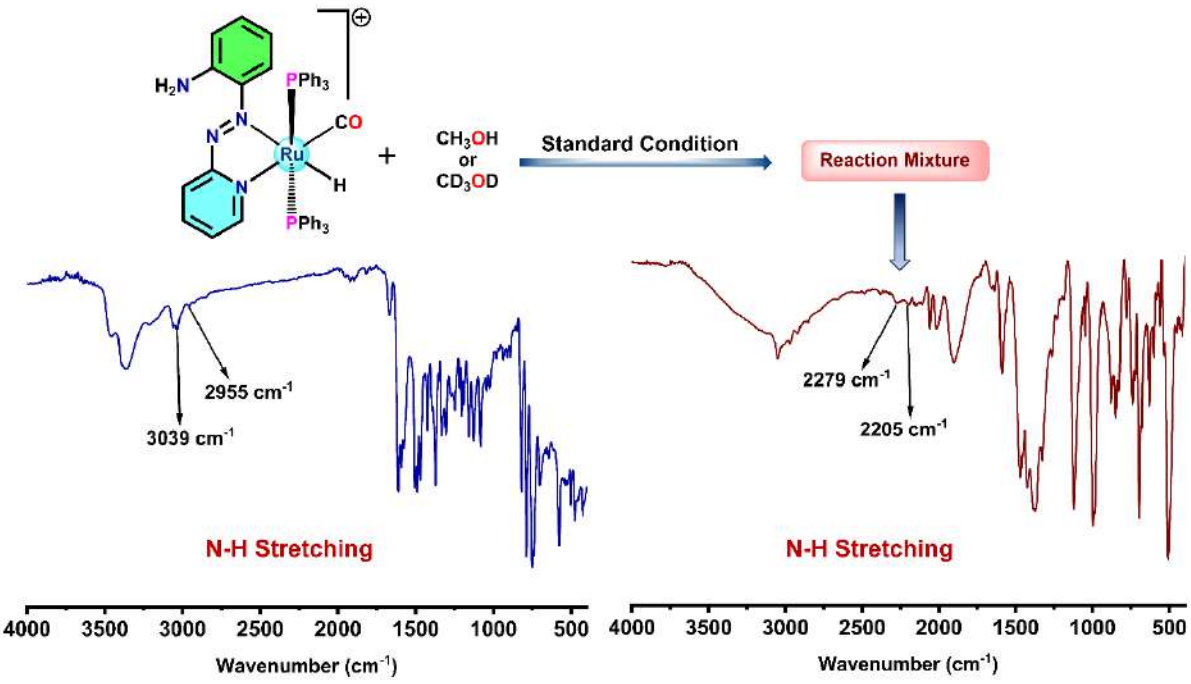

Figure 5.6.A15: IR spectra of the reaction mixture showing N-H (blue) and N-D (maroon) stretching.

Table 5.6.A1: Molecular orbital contribution table of ligand **1**

Orbital	MO	Energy (eV)	Contribution (%)			Contribution
			Azo	Py	$PhNH_2$	
58	L+5	-3.17	0	3	96	$\pi^*(PhNH_2)$
57	L+4	-3.30	31	20	48	π^*(Azo + Py + $PhNH_2$)
56	L+3	-3.32	4	21	74	π^* (Py + $PhNH_2$)
55	L+2	-3.64	3	37	60	+ π^*(Py + $PhNH_2$)
54	L+1	-3.98	0	96	3	π^* (Py)
53	LUMO	-5.55	40	29	31	π^* (Azo + Py + $PhNH_2$)
52	HOMO	-8.39	8	9	83	π ($PhNH_2$)
51	H–1	-8.56	77	9	14	π (Azo + $PhNH_2$)
50	H–2	-8.97	10	28	63	π (Py)
49	H–3	-9.06	4	96	0	π (Py + $PhNH_2$)
48	H–4	-9.12	8	62	30	π (Py)
47	H–5	-9.16	2	92	6	π (Py)

Table 5.6.A2: Molecular orbital contribution table of the complex *trans*-$[RuH(H_2L)(CO)(PPh_3)_2]PF_6$ **1a**

Orbital	MO	Energy (eV)	Contribution (%)							Contribution
			Ru	H	CO	Azo	Py	$PhNH_2$	PPh_3	
211	L+5	-3.17	6	1	3	0	1	3	86	$\pi^*(PPh_3)$
210	L+4	-3.30	10	1	1	0	5	6	77	$\pi^*(PPh_3)$
209	L+3	-3.32	1	0	0	0	3	1	96	$\pi^*(PPh_3)$
208	L+2	-3.64	21	2	5	0	2	0	71	$d_z^2 + \pi^*(PPh_3)$
207	L+1	-3.98	1	0	2	2	93	3	0	π^* (Py)
206	LUMO	-5.55	3	0	1	36	30	29	1	π^*(Azo + Py + $PhNH_2$)
205	HOMO	-8.39	7	0	0	4	5	73	11	π ($PhNH_2$ + PPh_3)
204	H–1	-8.56	30	0	1	6	6	10	48	$d_{xz} + \pi$ ($PhNH_2$ + PPh_3)
203	H–2	-8.97	50	0	1	1	2	1	45	$d_{yz} + \pi$ (PPh_3)
202	H–3	-9.06	69	1	16	6	0	5	4	$d_{x^2-y^2} + \pi$ (CO)
201	H–4	-9.12	5	0	1	1	0	1	92	π (PPh_3)
200	H–5	-9.16	21	0	3	1	3	0	73	$d_{xy} + \pi$ (PPh_3)

Table 5.6.A3: Main optical transition at the TD-DFT/(R)B3LYP using 6-311G+(d,p) level for all non-hydrogen atoms and LANL2DZ basis set for ruthenium in **1a** with composition in terms of molecular orbital contribution of the transition, computed vertical excitation energies and oscillator strength in dichloromethane (CH_2Cl_2)

Transition	CI	Composition	E(eV)	Oscillator Strength (*f*)	λ_{theo}(nm)
$S_0 \rightarrow S_1$	0.56146 0.41642	HOMO→ LUMO (63%) H–1→ LUMO (35%)	2.4094	0.1882	514.58
$S_0 \rightarrow S_7$	0.58364 0.32140	H–5→ LUMO (68%) H–4→ LUMO (21%)	3.3511	0.2079	369.98
$S_0 \rightarrow S_{36}$	0.35607	H–2→ L+2 (25%)	4.6559	0.2710	266.30

Table 5.6.A4: Natural transition orbitals (NTOs) for complex **1a** illustrating the nature of singlet excited states in the absorption bands in the range 200–800 nm. For each state, the respective number of the state, transition energy (eV), and the oscillator strength (in parentheses) are listed. Shown are only occupied (holes) and unoccupied (electrons) NTO pairs that contribute more than 20% to each excited state

Expt. λ_{max}		**Hole**	**Electron**
547 nm	S_1 w = 0.6304 2.4094 (0.1882) 514.58 nm ILCT π (Azo + Ph + Amine + Py) → π* (Azo + Ph + Amine + Py)	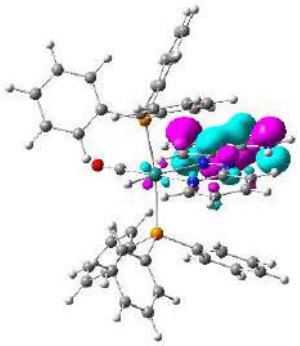	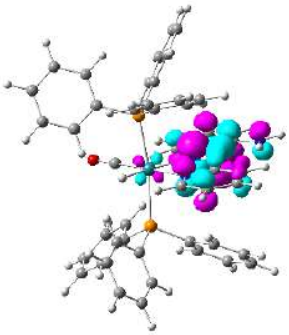
	S_5 w = 0.3468 2.4094 (0.1882) 514.58 nm MLCT & d-d d_{xz} → π* (Azo + Ph + Amine + Py) & d_{xz} → d_{yz}	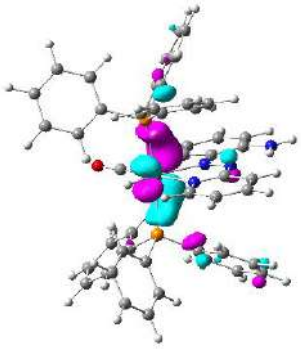	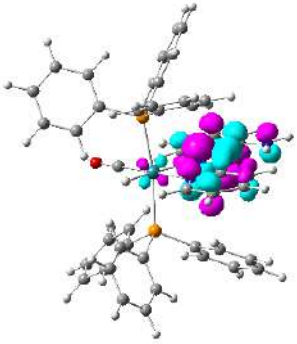
364 nm	S_7 w = 0.6812 3.3511 (0.2079) 369.98 nm LLCT, ILCT & d-d π (Azo + Ph + Py + PPh_3) → π* (Azo + Ph + Py + Amine) & d_{xy} → d_{yz}	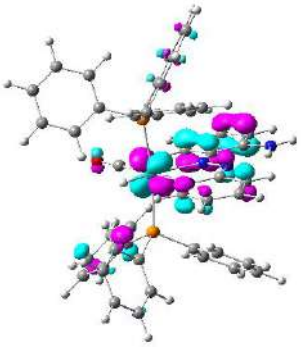	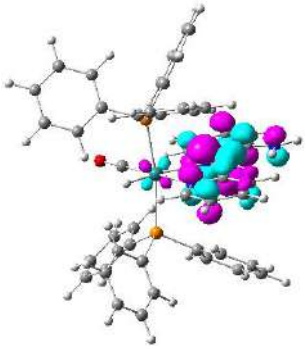

	S_7 w = 0.2065 3.3511 (0.2079) 369.98 nm LLCT, MLCT & d-d d_{xy} + π (Ph + PPh_3) → π* (Azo + Ph + Py + Amine) & d_{xy} → d_{yz}	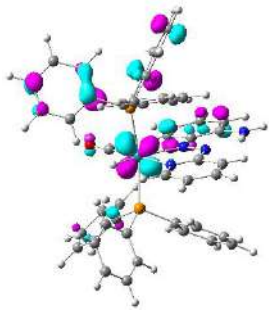	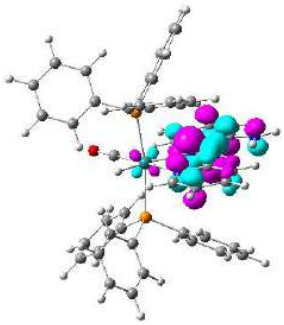
232 nm	S_{36} w = 0.2535 4.6559 (0.2710) 266.30 nm d-d & ILCT d_{xz}→ d_z^2 & π (PPh_3) → π* (PPh_3)	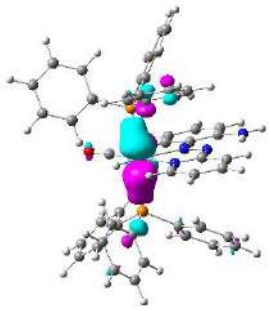	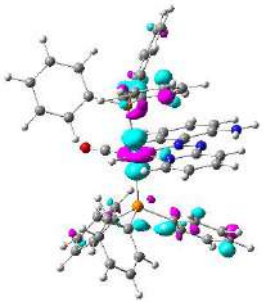

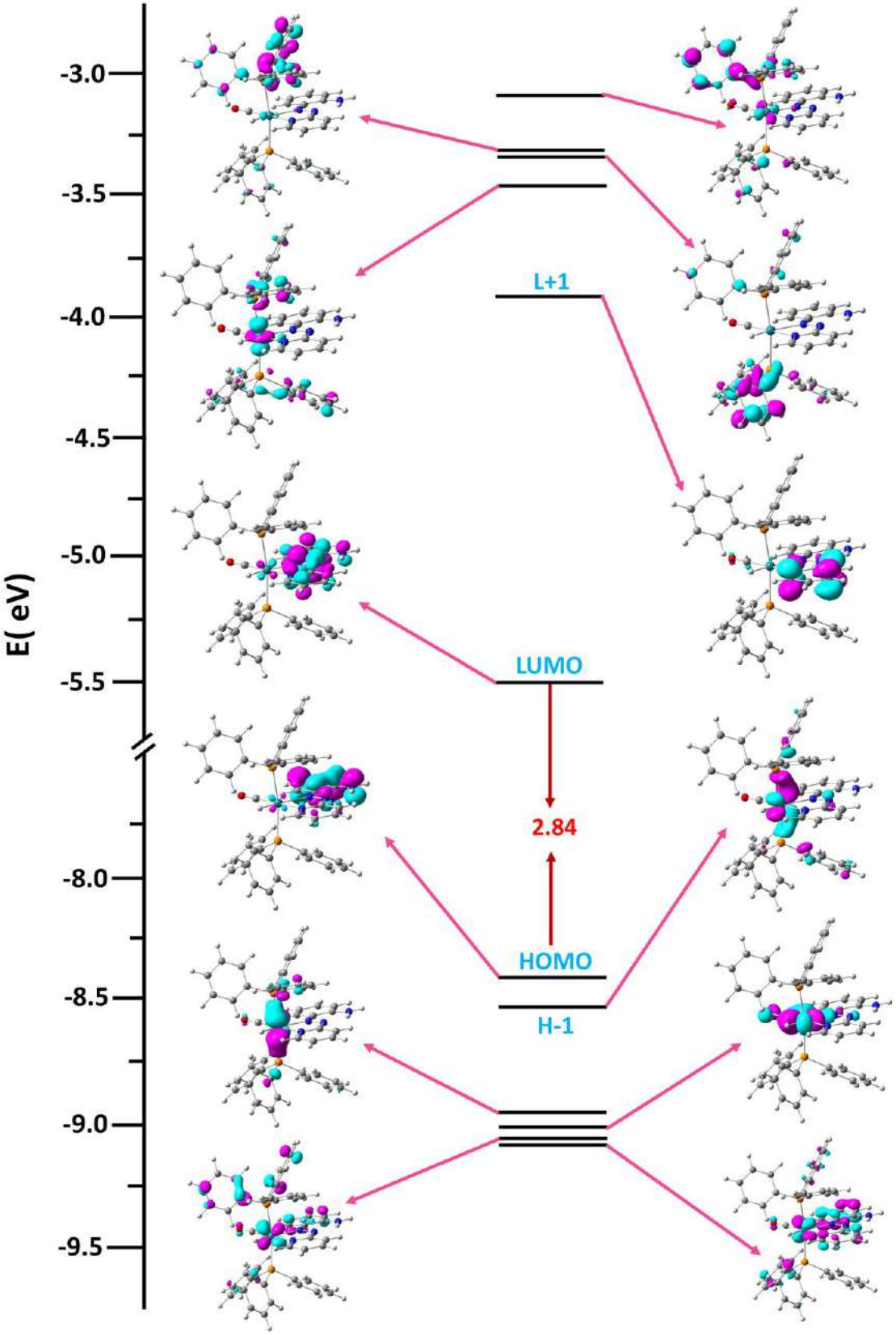

Figure 5.6.A16: Partial frontier molecular orbital energy diagram of complex **1a**

Table 5.6.A5: Coordinates of optimized geometry of **1a**

Tag	Symbol	X	Y	Z
1	C	-1.09196	9.746586	16.81459
2	C	1.612175	11.97245	15.0396
3	C	0.220039	12.1713	14.87514
4	H	-0.43844	11.45151	15.34092
5	C	-0.30446	13.2195	14.16061
6	H	-1.37988	13.33162	14.057
7	C	0.575853	14.14782	13.56878
8	H	0.181465	14.98744	13.00096
9	C	1.935961	14.00243	13.70159
10	H	2.610451	14.72149	13.24125
11	C	2.5088	12.92369	14.42557
12	C	3.688606	9.53286	16.54529
13	C	5.065309	9.281657	16.60509
14	H	5.749998	9.978067	16.13181
15	C	5.514563	8.144083	17.25541
16	H	6.577531	7.924435	17.30754
17	C	4.580132	7.288338	17.83961
18	H	4.8847	6.385292	18.35942
19	C	3.232463	7.608679	17.75619
20	H	2.475498	6.975077	18.2037
21	C	0.909253	12.26193	19.13975
22	C	1.700067	12.96841	20.05617
23	H	2.32109	12.43995	20.77232
24	C	1.691753	14.36314	20.07221
25	H	2.314242	14.89359	20.78946
26	C	0.885482	15.07258	19.18419
27	H	0.878147	16.16007	19.20055
28	C	0.084994	14.37897	18.27734
29	H	-0.55267	14.92087	17.5826
30	C	0.101138	12.98655	18.25364
31	H	-0.53166	12.4671	17.54127
32	C	-0.70358	10.09866	20.16228
33	C	-1.14341	11.05493	21.08922
34	H	-0.63822	12.01232	21.17517
35	C	-2.23769	10.79449	21.91224
36	H	-2.567	11.55125	22.62088
37	C	-2.9073	9.574613	21.82748
38	H	-3.7624	9.373743	22.46901
39	C	-2.4758	8.615959	20.91278
40	H	-2.99143	7.661259	20.83561

41	C	-1.38547	8.877409	20.08425
42	H	-1.06689	8.12327	19.37171
43	C	2.190897	9.84939	20.17786
44	C	1.986296	8.940302	21.22288
45	H	0.98792	8.576246	21.44733
46	C	3.059088	8.498594	21.99814
47	H	2.879974	7.796335	22.80937
48	C	4.348298	8.959519	21.74178
49	H	5.182651	8.620287	22.35159
50	C	4.562827	9.860577	20.69851
51	H	5.565319	10.22759	20.49007
52	C	3.495234	10.29636	19.91854
53	H	3.685603	11.00476	19.11632
54	C	-1.12968	7.789841	14.14784
55	C	-1.65181	9.007213	13.68674
56	H	-1.09638	9.930576	13.8242
57	C	-2.88444	9.055495	13.0408
58	H	-3.26752	10.00922	12.68487
59	C	-3.62552	7.888171	12.85876
60	H	-4.59138	7.925727	12.36018
61	C	-3.12246	6.675178	13.32332
62	H	-3.69395	5.759196	13.19085
63	C	-1.88229	6.623496	13.96063
64	H	-1.5101	5.665838	14.31033
65	C	1.744264	8.037381	13.63707
66	C	1.395072	8.599809	12.40324
67	H	0.363703	8.854458	12.18262
68	C	2.364674	8.825804	11.4254
69	H	2.070518	9.258674	10.47171
70	C	3.69585	8.4915	11.66231
71	H	4.449453	8.664356	10.89731
72	C	4.053439	7.923354	12.88488
73	H	5.087479	7.646681	13.07879
74	C	3.088234	7.701725	13.86347
75	H	3.388305	7.234905	14.79736
76	C	0.748211	5.972453	15.40495
77	C	0.351399	5.472516	16.65147
78	H	-0.04405	6.148095	17.40376
79	C	0.452309	4.111667	16.93805
80	H	0.138716	3.743257	17.91233
81	C	0.954937	3.229952	15.98311
82	H	1.038607	2.169039	16.20782
83	C	1.345698	3.715085	14.73541

84	H	1.732008	3.034195	13.98018
85	C	1.239677	5.07389	14.4457
86	H	1.537943	5.42777	13.4633
87	N	2.785006	8.705155	17.11939
88	N	3.271874	10.65951	15.85537
89	N	2.003878	10.85783	15.77829
90	N	3.853102	12.84846	14.50802
91	H	4.426604	13.54877	14.05685
92	H	4.277095	12.06559	14.98912
93	O	-2.22521	9.962405	16.80929
94	P	0.791891	10.41389	19.10889
95	P	0.51443	7.765541	14.99963
96	Ru	0.726446	9.311154	16.91723
97	H	0.225483	8.071991	17.79262

5.6.1 NMR data of all synthesized bis(indolyl)methanes

***3,3'-(phenylmethylene)bis(1H-indole) (8aa)*:** Eluent: Hexane / EtOAc (5:1v/v), Pinkish red coloured solid; Yield 290 mg (90%). **^{1}H NMR (400 MHz, $CDCl_3$):** δ 7.89 (s, 2H), 7.43 (d, *J* = 8.0 Hz, 2H), 7.37 (d, *J* = 7.9 Hz, 4H), 7.31 (t, *J* = 7.3 Hz, 2H), 7.20 (t, *J* = 7.7 Hz, 3H), 7.04 (t, *J* = 7.5 Hz, 2H), 6.65 (d, *J* = 2.3 Hz, 2H), 5.92 (s, 1H). **^{13}C{^{1}H} NMR (101 MHz, $CDCl_3$):** δ 144.13, 136.80, 128.85, 128.34, 127.19, 126.26, 123.75, 122.03, 120.05, 119.80, 119.34, 111.17, 40.31.

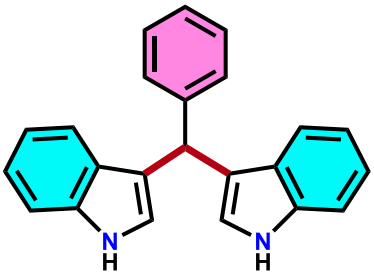

***3,3'-(o-tolylmethylene)bis(1H-indole) (8ab)*:** Eluent: Hexane / EtOAc (5:1v/v), Red coloured solid; Yield: 276 mg (82%). **^{1}H NMR (400 MHz, $CDCl_3$):** δ 7.87 (s, 2H), 7.38 (dd, *J* = 13.1, 8.0 Hz, 4H), 7.29 – 7.17 (m, 4H), 7.17 – 7.11 (m, 1H), 7.11 – 7.01 (m, 3H), 6.54 (s, 2H), 6.06 (s, 1H), 2.43 (s, 3H). **^{13}C{^{1}H} NMR (101 MHz, $CDCl_3$):** δ 142.21, 136.83, 136.17, 130.28, 128.51, 127.29, 126.17, 125.93, 124.01, 121.96, 119.87, 119.26, 119.15, 111.18, 36.30, 19.64.

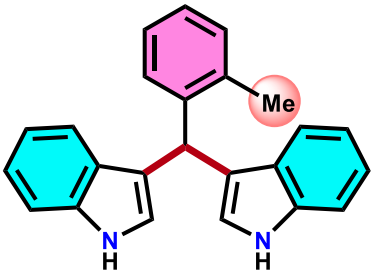

***3,3'-(m-tolylmethylene)bis(1H-indole) (8ac)*:** Eluent: Hexane / EtOAc (5:1v/v), Pink coloured solid; Yield: 286 mg (85%). **^{1}H NMR (300 MHz, $CDCl_3$):** δ 7.76 (s, 2H), 7.47 (d, *J* = 7.9 Hz, 2H), 7.35 (d, *J* = 8.1 Hz, 2H), 7.28 – 7.18 (m, 5H), 7.13 – 7.04 (m, 3H), 6.61 (s, 2H), 5.91 (s, 1H), 2.35 (s, 3H). **^{13}C{^{1}H} NMR (75 MHz, $CDCl_3$):** δ 144.07, 137.76, 136.73, 129.57, 128.18, 127.19, 127.03, 125.85, 123.73, 121.94, 120.02, 119.79, 119.27, 111.16, 40.21, 21.63.

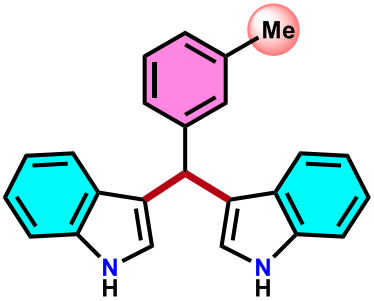

***3,3'-((3-fluorophenyl)methylene)bis(1H-indole) (8ad)*:** Eluent: Hexane / EtOAc (5:1v/v), Off-white coloured solid; Yield: 245 mg (72%). **^{1}H NMR (300 MHz, $CDCl_3$):** δ 7.94 (s, 2H), 7.40 (t, *J* = 8.6 Hz, 5H), 7.27 – 7.16 (m, 4H), 7.06 (d, *J* = 8.0 Hz, 3H), 6.68 (dd, *J* = 2.4, 1.1 Hz, 2H), 5.92 (s, 1H). **^{13}C{^{1}H} NMR (75 MHz, $CDCl_3$):** δ 163.12 (d, $^1J_{C-F}$ = 244.9 Hz), 146.92 (d, $^3J_{C-F}$ = 6.8 Hz), 136.80, 129.71 (d, $^3J_{C-F}$ = 8.2 Hz), 127.03, 124.54 (d, $^4J_{C-F}$ = 2.6 Hz), 123.71, 122.19, 119.91, 119.48, 119.17, 115.70 (d, $^2J_{C-F}$ = 21.5 Hz), 113.21 (d, $^2J_{C-F}$ = 21.3 Hz), 111.24, 40.09 (d, *J* = 1.8 Hz). **^{19}F NMR (282 MHz, $CDCl_3$):** δ -113.74.

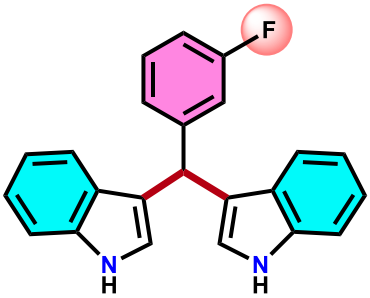

***3,3'-((3-(trifluoromethyl)phenyl)methylene)bis(1H-indole) (8ae)*:** Eluent: Hexane / EtOAc (5:1v/v), Pale pink coloured solid; Yield: 297 mg (76%). **^{1}H NMR (300 MHz, $CDCl_3$):** δ 7.69 (s, 2H), 7.53 (t, *J* = 7.5 Hz, 3H), 7.39 (d, *J* = 8.0 Hz, 4H), 7.22 (t, *J* = 7.7 Hz, 2H), 7.06 (t, *J* = 7.5 Hz, 3H), 6.63 (s, 2H), 5.98 (s, 1H). **^{13}C{^{1}H} NMR (101 MHz, $CDCl_3$):** 145.19, 136.83, 132.14, 130.61 (q, $^2J_{C-F}$ = 32.2 Hz), 128.79, 126.93, 125.59 (q, $^3J_{C-F}$ = 4.0 Hz), 124.45 (q, $^1J_{C-F}$ = 271.7 Hz), 123.26 (q, $^3J_{C-F}$ = 4.1 Hz), 123.83, 122.22, 119.79, 119.50, 118.90, 111.30, 40.21. **^{19}F NMR (282 MHz, $CDCl_3$):** δ -62.25.

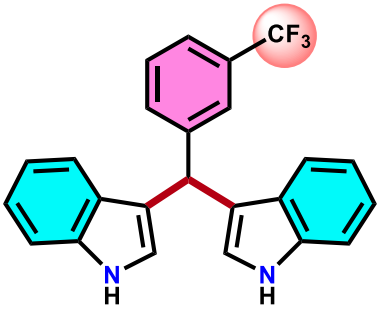

***3,3'-(p-tolylmethylene)bis(1H-indole) (8af)*:** Eluent: Hexane / EtOAc (5:1v/v), Dark red coloured solid; Yield: 293 mg (87%). **^{1}H NMR (300 MHz, $CDCl_3$):** δ 7.90 (s, 2H), 7.43 (d, *J* = 7.9 Hz, 2H), 7.37 (d, *J* = 8.1 Hz, 2H), 7.29 – 7.24 (m, 2H), 7.19 (ddd, *J* = 8.2, 6.9, 1.2 Hz, 2H), 7.11 (d, *J* = 7.8 Hz, 2H), 7.03 (td, *J* = 7.5, 1.0 Hz, 2H), 6.67 (d, *J* = 3.5 Hz, 2H), 5.88 (s, 1H), 2.35 (s, 3H). **^{13}C{^{1}H} NMR (75 MHz, $CDCl_3$):** δ 141.11, 136.82, 135.61, 129.04, 128.69, 127.23, 123.67, 122.00, 120.09, 120.03, 119.31, 111.13, 39.90, 21.21.

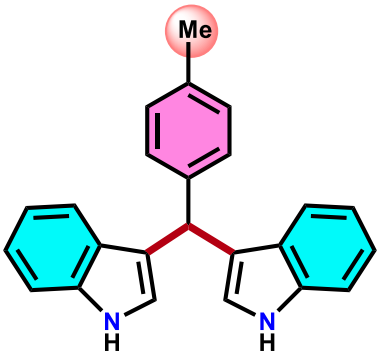

***3,3'-((4-isopropylphenyl)methylene)bis(1H-indole) (8ag)*:** Eluent: Hexane / EtOAc (5:1v/v), Light red coloured solid; Yield: 332 mg (91%). **^{1}H NMR (400 MHz, $CDCl_3$):** δ 7.85 (s, 2H), 7.45 (s, 1H), 7.36 (d, *J* = 8.1 Hz, 2H), 7.30 (d, *J* = 8.2 Hz, 3H), 7.23 – 7.14 (m, 5H), 7.04 (t, *J* = 7.5 Hz, 2H), 6.67 (d, *J* = 2.5 Hz, 2H), 5.89 (s, 1H), 2.97 – 2.87 (m, 1H), 1.27 (d, *J* = 6.9 Hz, 6H). **^{13}C{^{1}H} NMR (75 MHz, $CDCl_3$):** δ 146.59, 141.37, 136.80, 128.64, 127.27, 126.33, 123.68, 121.97, 120.12, 119.27, 111.12, 39.87, 33.78, 24.19.

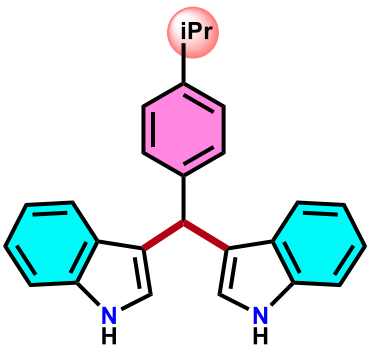

***3,3'-((4-methoxyphenyl)methylene)bis(1H-indole) (8ah)*:** Eluent: Hexane / EtOAc (3:1v/v), Pinkish red coloured solid; Yield: 324 mg (92%). **^{1}H NMR (300 MHz, $CDCl_3$):** δ 7.87 (s, 2H), 7.43 (d, *J* = 7.9 Hz, 2H), 7.36 (d, *J* = 8.1 Hz, 2H), 7.29 (d, *J* = 8.6 Hz, 2H), 7.20 (ddd, *J* = 8.1, 7.0, 1.2 Hz, 2H), 7.08 – 7.00 (m, 2H), 6.86 (d, *J* = 8.6 Hz, 2H), 6.64 (dd, *J* = 2.6, 1.3 Hz, 2H), 5.87 (s, 1H), 3.81 (s, 3H). **^{13}C{^{1}H} NMR (75 MHz, $CDCl_3$):** δ 158.01, 136.82, 136.38, 129.73, 127.18, 123.67, 121.99, 120.12, 120.09, 119.29, 113.70, 111.16, 55.34, 39.45.

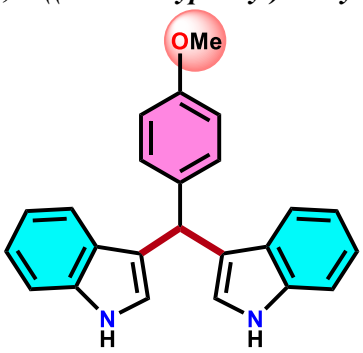

***3,3'-([1,1'-biphenyl]-4-ylmethylene)bis(1H-indole) (8ai)*:** Eluent: Hexane / EtOAc (5:1v/v), White coloured solid; Yield: 359 mg (90%). **^{1}H NMR (300 MHz, $CDCl_3$):** δ 7.95 (s, 2H), 7.61 (dd, *J* = 8.3, 1.3 Hz, 2H), 7.55 (d, *J* = 8.3 Hz, 2H), 7.48 – 7.37 (m, 9H), 7.21 (ddd, *J* = 8.2, 7.0, 1.2 Hz, 2H), 7.05 (ddd, *J* = 8.0, 7.0, 1.0 Hz, 2H), 6.74 (d, *J* = 1.4 Hz, 2H), 5.96 (s, 1H). **^{13}C{^{1}H} NMR (75 MHz, $CDCl_3$):** δ 143.30, 141.22, 139.02, 136.86, 129.25, 128.83, 127.49, 127.22, 127.11, 127.07, 123.77, 122.12, 120.11, 119.79, 119.41, 111.18, 40.01.

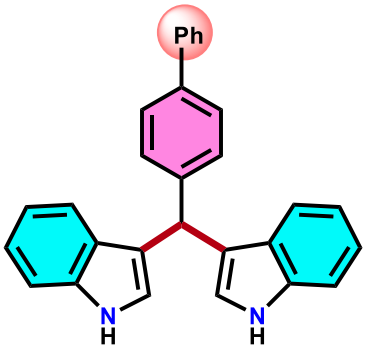

***3,3'-((4-fluorophenyl)methylene)bis(1H-indole) (8aj)*:** Eluent: Hexane / EtOAc (5:1v/v), Pale yellow coloured solid;Yield: 265 mg (78%). **^{1}H NMR (300 MHz, $CDCl_3$):** δ 7.96 (s, 2H), 7.42 – 7.39 (m, 2H), 7.38 (d, *J* = 2.5 Hz, 2H), 7.34 – 7.29 (m, 2H), 7.20 (ddd, *J* = 8.3, 7.0, 1.2 Hz, 3H), 7.08 – 7.03 (m, 2H), 7.03 – 6.98 (m, 2H), 6.66 (s, 2H), 5.90 (s, 1H). **^{13}C{^{1}H} NMR (75 MHz, $CDCl_3$):** δ 161.55 (d, $^1J_{C-F}$ = 243.8 Hz), 139.31 (d, $^4J_{C-F}$ = 3.7 Hz) 136.85, 130.21 (d, $^3J_{C-F}$ = 7.7 Hz), 127.07, 123.69, 122.18, 120.00, 119.73, 119.45, 115.10 (d, $^2J_{C-F}$ = 21.2 Hz), 111.22, 39.61. **^{19}F NMR (282 MHz, $CDCl_3$):** δ -117.41.

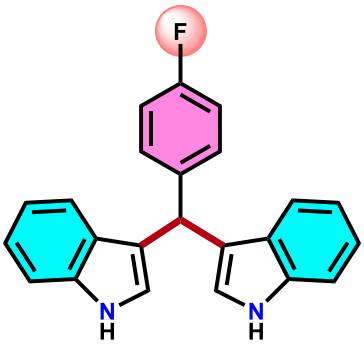

***3,3'-((4-chlorophenyl)methylene)bis(1H-indole) (8ak)*:** Eluent: Hexane / EtOAc (5:1v/v), White solid; Yield: 285 mg (80%). **^{1}H NMR (300 MHz, $CDCl_3$):** δ 7.91 (s, 2H), 7.39 (t, *J* = 8.3 Hz, 4H), 7.29 (d, *J* = 2.3 Hz, 4H), 7.22 (t, *J* = 7.6 Hz, 2H), 7.06 (t, *J* = 8.0 Hz, 2H), 6.64 (s, 2H), 5.89 (s, 1H). **^{13}C{^{1}H} NMR (101 MHz, $CDCl_3$):** δ 142.69, 136.81, 131.91, 130.20, 128.49, 127.00, 123.73, 122.20, 119.94, 119.47, 119.29, 111.25, 39.74.

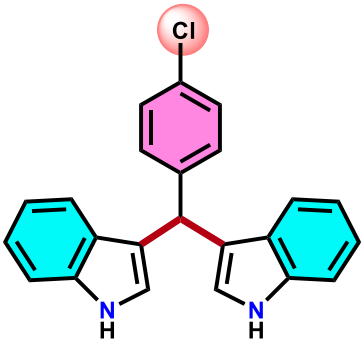

***3,3'-((4-bromophenyl)methylene)bis(1H-indole) (8al)*:** Eluent: Hexane / EtOAc (5:1v/v), Orange solid; Yield: 329 mg (84%). **^{1}H NMR (400 MHz, $CDCl_3$):** δ 7.92 (s, 2H), 7.42 (d, *J* = 8.4 Hz, 3H), 7.38 (d, *J* = 8.3 Hz, 3H), 7.31 – 7.17 (m, 5H), 7.05 (t, *J* = 7.4 Hz, 2H), 6.64 (s, 2H), 5.87 (s, 1H). **^{13}C{^{1}H} NMR (101 MHz, $CDCl_3$):** δ 143.21, 136.79, 131.44, 130.62, 126.98, 123.74, 122.20, 120.04, 119.93, 119.48, 119.19, 111.25, 39.80.

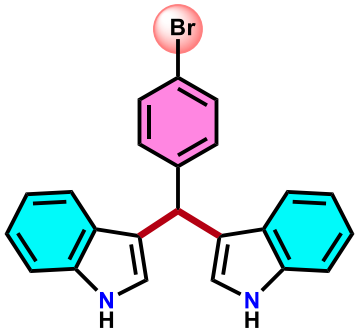

***3,3'-((4-(trifluoromethyl)phenyl)methylene)bis(1H-indole) (8am)*:** Eluent: Hexane / EtOAc (5:1v/v), Off-white solid; Yield: 347 mg (89%). **^{1}H NMR (300 MHz, $CDCl_3$):** δ 7.96 (s, 2H), 7.56 (d, *J* = 8.2 Hz, 2H), 7.51 (d, *J* = 8.8 Hz, 2H), 7.39 (d, *J* = 9.1 Hz, 5H), 7.24 (d, *J* = 8.2 Hz, 2H), 7.06 (t, *J* = 7.4 Hz, 3H), 6.65 (s, 2H), 5.98 (s, 1H). **^{13}C{^{1}H} NMR (101 MHz, $CDCl_3$):** δ 148.28, 136.82, 129.14, 128.69, 126.97, 125.49 (d, *J* = 25.4 Hz), 123.80, 122.30, 119.85, 119.56, 119.18, 118.90, 111.29, 40.22. **^{19}F NMR (282 MHz, $CDCl_3$):** δ -62.16.

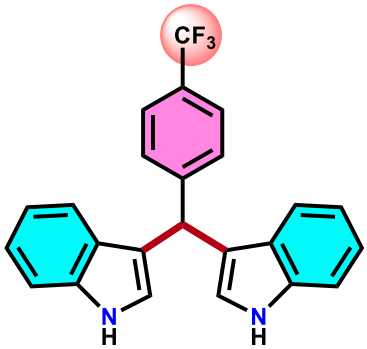

***3,3'-(naphthalen-1-ylmethylene)bis(1H-indole) (8an)*:** Eluent: Hexane / EtOAc (3:1v/v), Pale pink coloured solid; Yield: 328 mg (88%). **^{1}H NMR (400 MHz, DMSO):** δ 10.79 (s, 2H), 8.26 (d, *J* = 8.1 Hz, 1H), 7.93 (d, *J* = 7.8 Hz, 1H), 7.78 (d, *J* = 8.1 Hz, 1H), 7.45 (p, *J* = 6.9 Hz, 2H), 7.35 (d, *J* = 8.6 Hz, 3H), 7.27 (d, *J* = 7.8 Hz, 2H), 7.04 (t, *J* = 7.6 Hz, 2H), 6.85 (t, *J* = 7.5 Hz, 2H), 6.73 (d, *J* = 2.2 Hz, 2H), 6.63 (s, 1H), 5.75 (s, 1H). **^{13}C{^{1}H} NMR (101 MHz, DMSO):** δ 140.31, 136.68, 133.63, 131.35, 128.59, 126.64, 126.60, 125.85, 125.55, 125.36, 125.32, 124.28, 123.99, 120.93, 118.98, 118.30, 117.72, 111.55, 35.37.

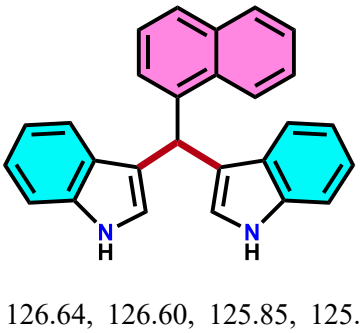

***3,3'-(thiophen-2-ylmethylene)bis(1H-indole) (8ao)*:** Eluent: Hexane / EtOAc (2:1v/v), Dark red coloured solid; Yield: 220 mg (67%). **^{1}H NMR (300 MHz, $CDCl_3$):** δ 7.91 (s, 2H), 7.50 (dq, *J* = 8.0, 0.9 Hz, 2H), 7.39 – 7.34 (m, 2H), 7.25 – 7.18 (m, 3H), 7.07 (t, *J* = 7.5 Hz, 2H), 6.98 – 6.93 (m, 2H), 6.83 (dd, *J* = 2.4, 1.0 Hz, 2H), 6.20 (s, 1H). **^{13}C{^{1}H} NMR (101 MHz, $CDCl_3$):** δ 148.78, 136.68, 126.86, 126.55, 125.26, 123.73, 123.32, 122.13, 119.88, 119.78, 119.47, 111.26, 35.43.

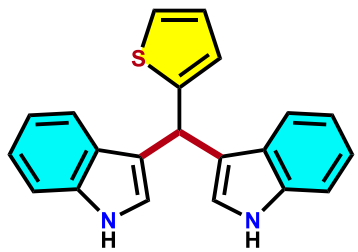

***3,3'-(phenylmethylene)bis(5-methyl-1H-indole) (9aa)*:** Eluent: Hexane / EtOAc (5:1v/v), Red coloured solid; Yield: 305 mg (87%). **^{1}H NMR (300 MHz, $CDCl_3$):** δ 7.81 (s, 2H), 7.39 – 7.35 (m, 2H), 7.32 (dd, *J* = 7.0, 1.2 Hz, 2H), 7.27 (d, *J* = 8.8 Hz, 3H), 7.24 – 7.22 (m, 2H), 7.03 (dd, *J* = 8.3, 1.7 Hz, 2H), 6.60 (dd, *J* = 2.4, 1.1 Hz, 2H), 5.86 (d, *J* = 1.2 Hz, 1H), 2.38 (s, 6H). **^{13}C{^{1}H} NMR (75 MHz, $CDCl_3$):** δ 144.31, 135.15, 128.83, 128.55, 128.30, 127.44, 126.16, 124.01, 123.66, 119.57, 119.43, 110.81, 40.14, 21.60.

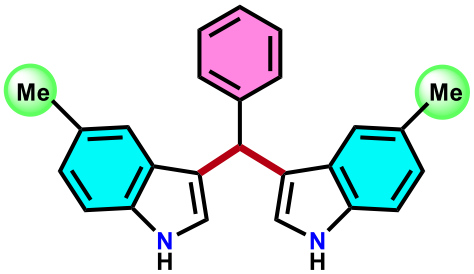

***3,3'-(o-tolylmethylene)bis(5-methyl-1H-indole) (9ab)*:** Eluent: Hexane / EtOAc (5:1v/v), Dark red coloured solid; Yield: 295 mg (81%). **^{1}H NMR (400 MHz, $CDCl_3$):** δ 7.81 (s, 2H), 7.27 (d, *J* = 8.2 Hz, 3H), 7.18 (d, *J* = 8.0 Hz, 3H), 7.12 – 7.06 (m, 2H), 7.05 – 7.01 (m, 2H), 6.51 (s, 2H), 5.99 (s, 1H), 2.41 (s, 3H), 2.39 (s, 6H). **^{13}C{^{1}H} NMR (101 MHz, $CDCl_3$):** δ 142.40, 136.22, 135.21, 130.23, 128.49, 128.40, 127.55, 126.08, 125.91, 124.23, 123.63, 119.41, 118.84, 110.81, 36.20, 21.59, 19.68.

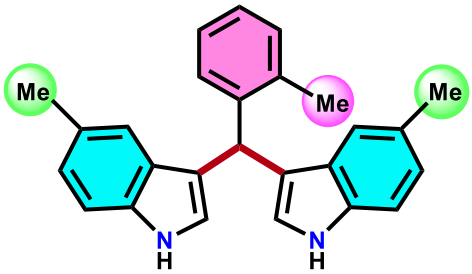

***3,3'-(m-tolylmethylene)bis(5-methyl-1H-indole) (9ac)*:** Eluent: Hexane / EtOAc (5:1v/v), Dark red coloured solid; Yield: 317 mg (87%). **^{1}H NMR (300 MHz, $CDCl_3$):** δ 7.69 – 7.65 (m, 2H), 7.30 (d, *J* = 1.6 Hz, 2H), 7.26 (d, *J* = 3.6 Hz, 2H), 7.23 (d, *J* = 2.6 Hz, 2H), 7.14 – 7.05 (m, 4H), 6.56 (dt, *J* = 2.5, 1.3 Hz, 2H), 5.87 (s, 1H), 2.44 (s, 6H), 2.37 (s, 3H). **^{13}C{^{1}H} NMR (75 MHz, $CDCl_3$):** δ 144.26, 137.68, 135.12, 129.57, 128.46, 128.14, 127.44, 126.95, 125.83, 123.99, 123.58, 119.53, 119.45, 110.80, 40.04, 21.65, 21.57.

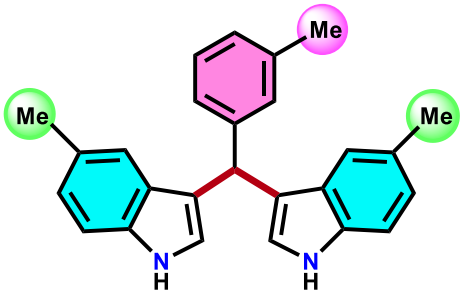

***3,3'-(p-tolylmethylene)bis(5-methyl-1H-indole) (9ad)*:** Eluent: Hexane / EtOAc (5:1v/v), Red coloured solid; Yield: 339 mg (93%). **^{1}H NMR (400 MHz, $CDCl_3$):** δ 7.78 (s, 2H), 7.27 – 7.23 (m, 6H), 7.12 (d, *J* = 7.8 Hz, 2H), 7.03 (dd, *J* = 8.3, 1.6 Hz, 2H), 6.60 (d, *J* = 2.4 Hz, 2H), 5.83 (s, 1H), 2.39 (s, 6H), 2.37 (s, 3H). **^{13}C{^{1}H} NMR (101 MHz, $CDCl_3$):** δ 141.30, 135.49, 135.16, 129.00, 128.66, 128.49, 127.46, 123.94, 123.61, 119.63, 119.58, 110.78, 39.70, 21.60, 21.21.

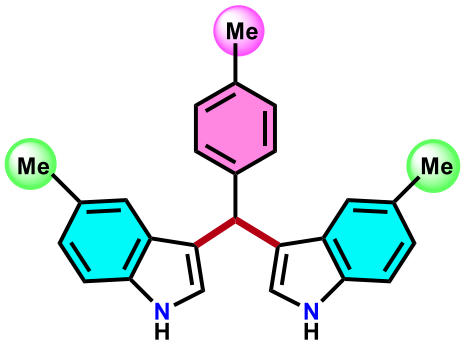

***3,3'-((4-isopropylphenyl)methylene)bis(5-methyl-1H-indole) (9ae)*:** Eluent: Hexane / EtOAc (5:1v/v),

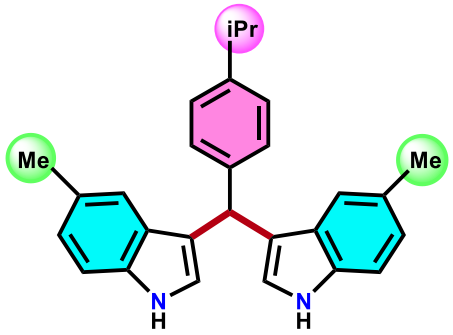

Off-white solid; Yield: 373 mg (95%). **^{1}H NMR (300 MHz, $CDCl_3$):** δ 7.82 (s, 2H), 7.28 (s, 2H), 7.25 (d, *J* = 2.3 Hz, 2H), 7.24 – 7.22 (m, 2H), 7.18 – 7.13 (m, 2H), 7.02 (dd, *J* = 8.3, 1.7 Hz, 2H), 6.63 (d, *J* = 2.4 Hz, 2H), 5.83 (s, 1H), 2.98 – 2.87 (m, 1H), 2.38 (s, 6H), 1.27 (d, *J* = 6.9 Hz, 6H). **^{13}C{^{1}H} NMR (101 MHz, $CDCl_3$):** δ 146.48, 141.57, 135.16, 128.62, 128.45, 127.51, 126.29, 123.94, 123.59, 119.73, 119.62, 110.77, 39.69, 33.79, 24.20, 21.59.

***3,3'-((4-methoxyphenyl)methylene)bis(5-methyl-1H-indole) (9af)*:** Eluent: Hexane / EtOAc (3:1v/v),

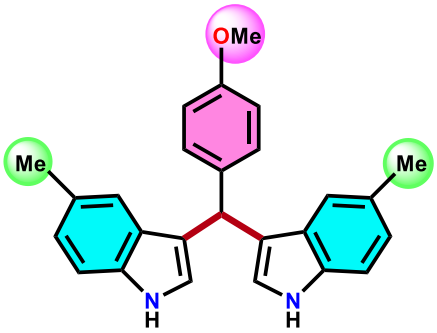

Dark red coloured solid; Yield: 346 mg (91%). **^{1}H NMR (400 MHz, $CDCl_3$):** δ 7.77 (s, 2H), 7.28 (dd, *J* = 8.3, 1.6 Hz, 6H), 7.04 (dd, *J* = 8.1, 1.8 Hz, 2H), 6.86 (dd, *J* = 9.1, 2.5 Hz, 2H), 6.57 (d, *J* = 2.4 Hz, 2H), 5.82 (s, 1H), 3.83 (s, 3H), 2.40 (s, 6H). **^{13}C{^{1}H} NMR (75 MHz, $CDCl_3$):** δ 157.92, 136.56, 135.16, 129.69, 128.46, 127.40, 123.92, 123.60, 119.69, 119.58, 113.65, 110.82, 55.31, 39.26, 21.59.

***3,3'-([1,1'-biphenyl]-4-ylmethylene)bis(5-methyl-1H-indole) (9ag)*:** Eluent: Hexane / EtOAc (5:1v/v),

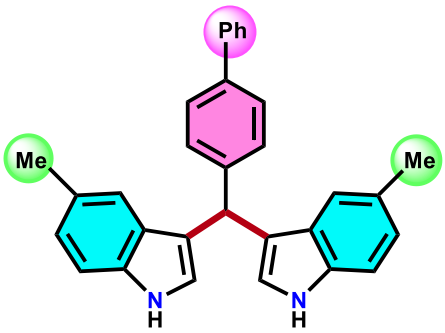

Pale pink coloured solid; Yield: 392 mg (92%). **^{1}H NMR (300 MHz, $CDCl_3$):** δ 7.85 (s, 2H), 7.65 – 7.61 (m, 2H), 7.58 – 7.52 (m, 2H), 7.45 (td, *J* = 8.2, 2.4 Hz, 4H), 7.38 – 7.31 (m, 1H), 7.30 – 7.25 (m, 4H), 7.04 (dd, *J* = 8.3, 1.7 Hz, 2H), 6.66 (dd, *J* = 2.5, 1.0 Hz, 2H), 5.90 (s, 1H), 2.39 (s, 6H). **^{13}C{^{1}H} NMR (101 MHz, $CDCl_3$):** δ 143.52, 141.26, 138.87, 135.20, 129.23, 128.83, 128.61, 127.48, 127.46, 127.09, 127.02, 124.03, 123.72, 119.60, 119.36, 110.84, 39.83, 21.61.

***3,3'-((4-fluorophenyl)methylene)bis(5-methyl-1H-indole) (9ah)*:** Eluent: Hexane / EtOAc (5:1v/v),

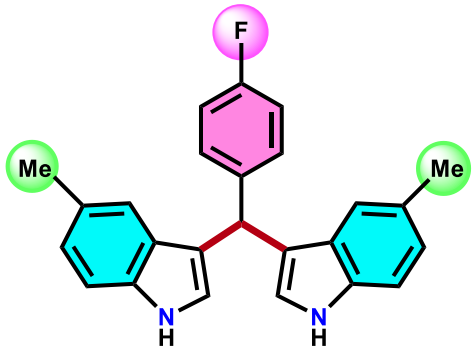

Pale pink coloured solid; Yield: 302 mg (82%). **^{1}H NMR (300 MHz, $CDCl_3$):** δ 7.84 (s, 2H), 7.32 – 7.29 (m, 1H), 7.27 – 7.19 (m, 4H), 7.06 – 6.96 (m, 4H), 6.91 (d, *J* = 8.6 Hz, 1H), 6.59 (s, 2H), 5.84 (s, 1H), 2.39 (s, 6H). **^{13}C{^{1}H} NMR (101 MHz, $CDCl_3$):** δ 162.61 (d, *J* = 246.0 Hz), 157.09, 137.03, 135.19, 130.17 (d, *J* = 7.7 Hz), 129.78, 128.66, 123.94, 119.51, 115.56 (d, *J* = 21.5 Hz), 114.61, 110.87, 39.44, 21.60. **^{19}F NMR (282 MHz, $CDCl_3$):** δ -117.57.

3,3'-((4-chlorophenyl)methylene)bis(5-methyl-1H-indole) (9ai): Eluent: Hexane / EtOAc (5:1v/v), White solid; Yield: 323 mg (84%). **^{1}H NMR (300 MHz, $CDCl_3$):** δ 7.87 (s, 2H), 7.30 – 7.26 (m, 6H), 7.19 – 7.18 (m, 2H), 7.03 (dd, *J* = 8.2, 1.7 Hz, 2H), 6.60 (s, 2H), 5.82 (s, 1H), 2.38 (s, 6H). **^{13}C{^{1}H} NMR (101 MHz, $CDCl_3$):** δ 142.89, 135.17, 131.80, 130.19, 128.73, 128.46, 127.26, 123.97, 123.83, 119.46, 118.95, 110.88, 39.59, 21.60.

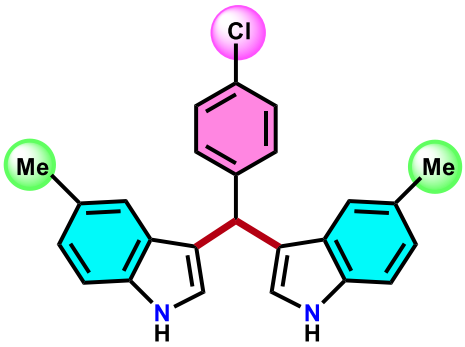

***3,3'-((4-bromophenyl)methylene)bis(5-methyl-1H-indole) ((9aj)*:** Eluent: Hexane / EtOAc (5:1v/v), Orange coloured solid; Yield: 373 mg (87%). **^{1}H NMR (300 MHz, $CDCl_3$):** δ 7.89 (s, 2H), 7.45 – 7.39 (m, 2H), 7.28 (d, *J* = 8.4 Hz, 3H), 7.24 – 7.21 (m, 2H), 7.19 – 7.18 (m, 1H), 7.03 (dd, *J* = 8.3, 1.7 Hz, 2H), 6.60 (dd, *J* = 2.4, 1.0 Hz, 2H), 5.81 (s, 1H), 2.38 (s, 6H). **^{13}C{^{1}H} NMR (101 MHz, $CDCl_3$):** δ 143.44, 135.18, 131.41, 130.62, 128.73, 127.25, 123.99, 123.83, 119.94, 119.45, 118.85, 110.89, 39.66, 21.60.

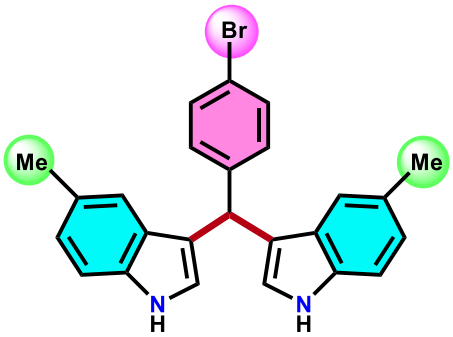

***3,3'-((4-(trifluoromethyl)phenyl)methylene)bis(5-methyl-1H-indole) (9ak)*:** Eluent: Hexane / EtOAc (5:1v/v), Pale pink solid; Yield: 364 mg (87%). **^{1}H NMR (400 MHz, $CDCl_3$):** δ 7.82 (s, 2H), 7.58 (d, *J* = 8.1 Hz, 1H), 7.47 (s, 1H), 7.28 (dd, *J* = 8.4, 3.0 Hz, 3H), 7.22 (d, *J* = 3.5 Hz, 2H), 7.07 (dt, *J* = 8.4, 2.3 Hz, 3H), 6.58 (d, *J* = 2.7 Hz, 2H), 5.93 (s, 1H), 2.42 (s, 6H). **^{13}C{^{1}H} NMR (101 MHz, $CDCl_3$):** δ 148.48, 135.13, 129.09, 128.80, 127.21 (d, *J* = 6.6 Hz), 125.63 (t, *J* = 6.0 Hz), 125.30 (q, *J* = 3.8 Hz), 124.03, 123.89, 123.82, 119.36 (d, *J* = 6.5 Hz), 118.44, 110.97, 40.02, 21.57. **^{19}F NMR (377 MHz, $CDCl_3$):** δ -62.06.

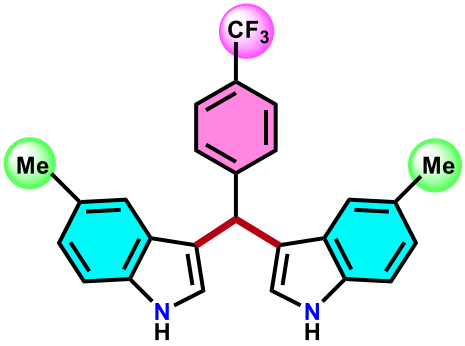

***3,3'-(pyridin-2-ylmethylene)bis(5-methyl-1H-indole) (9al)*:** Eluent: Hexane / EtOAc (1:1v/v), Off-white solid; Yield: 256 mg (73%). **^{1}H NMR (300 MHz, $CDCl_3$):** δ 8.63 (d, *J* = 5.9 Hz, 1H), 7.98 (s, 2H), 7.61 (td, *J* = 7.6, 1.8 Hz, 1H), 7.33 (d, *J* = 7.9 Hz, 1H), 7.25 (d, *J* = 8.3 Hz, 4H), 7.01 (dd, *J* = 8.3, 1.7 Hz, 3H), 6.72 (s, 2H), 6.02 (s, 1H), 2.37 (s, 6H). **^{13}C{^{1}H} NMR (101 MHz, $CDCl_3$):** δ 163.80, 149.43, 136.68, 135.16, 128.61, 127.41, 123.83, 123.71, 123.05, 121.45, 119.48, 117.97, 110.85, 43.10, 21.59.

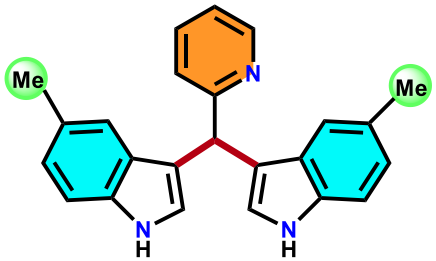

***3,3'-(pyridin-3-ylmethylene)bis(5-methyl-1H-indole) (9am)*:** Eluent: Hexane / EtOAc (1:1v/v), Off-white solid; Yield: 263 mg (75%). **^{1}H NMR (300 MHz, $CDCl_3$):** δ 8.65 (s, 1H), 8.59 – 8.46 (m, 2H), 8.03 (s, 2H), 7.85 (d, *J* = 8.0 Hz, 1H), 7.61 (d, *J* = 7.8 Hz, 1H), 7.40 (s, 1H), 7.05 (t, *J* = 6.7 Hz, 3H), 6.94 (d, *J* = 2.5 Hz, 1H), 6.61 (s, 2H), 5.88 (s, 1H), 2.38 (s, 6H). **^{13}C{^{1}H} NMR (101 MHz, $CDCl_3$):** δ 150.33, 147.44, 139.92, 136.40, 135.22, 128.82, 127.08, 124.05, 123.93, 119.33, 118.15, 110.98, 37.77, 21.58.

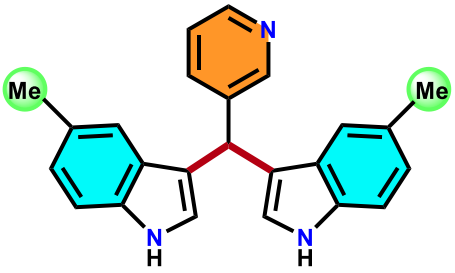

***3,3'-(pyridin-4-ylmethylene)bis(5-methyl-1H-indole) (9an)*:** Eluent: Hexane / EtOAc (1:1v/v), Off-white solid; Yield: 274 mg (78%). **^{1}H NMR (300 MHz, $CDCl_3$):** δ 8.56 (s, 2H), 8.09 (s, 2H), 7.37 – 7.29 (m, 3H), 7.15 (s, 2H), 7.05 (dd, *J* = 8.2, 1.6 Hz, 3H), 6.64 (d, *J* = 2.4 Hz, 2H), 5.86 (s, 1H), 2.38 (s, 6H). **^{13}C{^{1}H} NMR (101 MHz, $CDCl_3$):** δ 153.65, 149.73, 135.15, 128.93, 127.12, 124.05, 124.00, 119.24, 117.51, 111.01, 102.22, 39.72, 21.59.

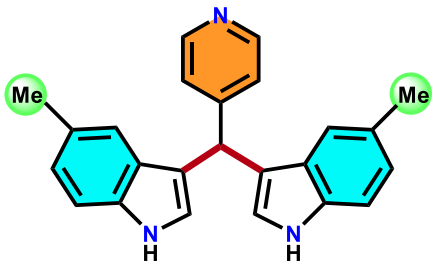

***3,3'-(thiophen-2-ylmethylene)bis(5-methyl-1H-indole) (9ao)*:** Eluent: Hexane / EtOAc (2:1v/v), Pale pink solid; Yield: 249 mg (70%). **^{1}H NMR (300 MHz, $CDCl_3$):** δ 7.84 (s, 2H), 7.29 (d, *J* = 3.2 Hz, 4H), 7.26 (s, 1H), 7.18 (dd, *J* = 5.0, 1.2 Hz, 1H), 7.04 (dd, *J* = 8.4, 1.6 Hz, 2H), 6.97 – 6.91 (m, 2H), 6.79 (h, *J* = 1.0 Hz, 2H), 6.13 (s, 1H), 2.41 (s, 6H). **^{13}C{^{1}H} NMR (101 MHz, $CDCl_3$):** δ 149.06, 135.05, 128.70, 127.13, 126.54, 125.17, 123.77, 123.62, 123.53, 119.45, 119.39, 110.90, 35.27, 21.63.

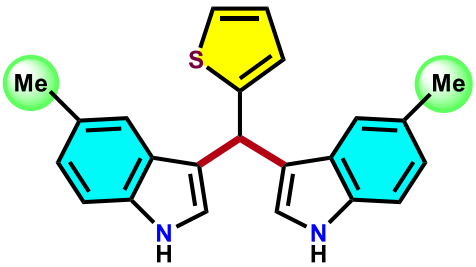

***3,3'-(naphthalen-1-ylmethylene)bis(5-methyl-1H-indole) (9ap)*:** Eluent: Hexane / EtOAc (3:1v/v), Off-white solid; Yield: 344 mg (86%). **^{1}H NMR (300 MHz, DMSO):** δ 10.66 (s, 2H), 8.20 (d, *J* = 8.1 Hz, 1H), 7.95 – 7.90 (m, 1H), 7.78 (d, *J* = 8.1 Hz, 1H), 7.50 – 7.33 (m, 4H), 7.23 (dd, *J* = 15.0, 7.7 Hz, 3H), 7.08 (s, 2H), 6.88 (dd, *J* = 8.3, 1.6 Hz, 2H), 6.61 (d, *J* = 2.3 Hz, 2H), 6.56 (s, 1H), 2.24 (s, 6H). **^{13}C{^{1}H} NMR (101 MHz, DMSO):** δ 140.49, 135.14, 133.70, 131.45, 128.65, 126.90, 126.77, 126.65, 125.92, 125.43, 125.38, 124.47, 124.10, 122.69, 118.43, 117.40, 111.39, 35.26, 21.33.

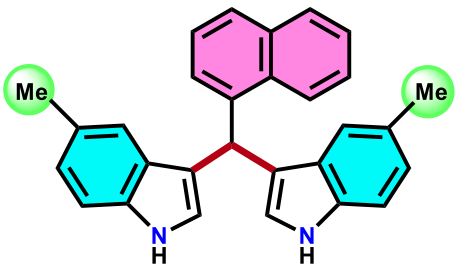

***3,3'-(cyclohexylmethylene)bis(5-methyl-1H-indole) (9aq)*:** Eluent: Hexane / EtOAc (6:1v/v), Off-white solid; Yield: 264 mg (74%). **^{1}H NMR (400 MHz, $CDCl_3$):** δ 7.52 – 7.49 (m, 2H), 7.31 (d, *J* = 8.3 Hz, 2H), 7.19 – 7.15 (m, 2H), 7.09 (dd, *J* = 8.3, 1.7 Hz, 2H), 6.53 (ddd, *J* = 3.1, 2.0, 1.0 Hz, 2H), 3.50 (d, *J* = 6.4 Hz, 1H), 2.52 (s, 6H), 1.81 (dt, *J* = 13.5, 3.2 Hz, 5H), 1.35 – 1.21 (m, 3H), 1.04 – 0.94 (m, 3H). **^{13}C{^{1}H} NMR (101 MHz, $CDCl_3$):** δ 134.22, 129.02, 128.22, 124.38, 123.64, 120.40, 110.79, 102.06, 68.86, 40.56, 29.66, 26.69, 25.93, 21.52.

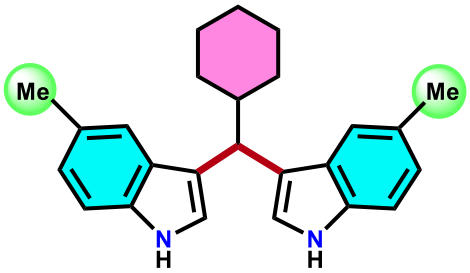

***3,3'-(phenylmethylene)bis(5-methoxy-1H-indole) (10aa)*:** Eluent: Hexane / EtOAc (5:1v/v), Red solid; Yield: 336 mg (88%). **^{1}H NMR (300 MHz, $CDCl_3$):** δ 7.85 (s, 2H), 7.42 – 7.34 (m, 2H), 7.34 – 7.30 (m, 1H), 7.28 (d, *J* = 3.9 Hz, 2H), 7.26 – 7.23 (m, 2H), 6.89 – 6.80 (m, 4H), 6.67 (t, *J* = 1.5 Hz, 2H), 5.80 (s, 1H), 3.72 (s, 6H). **^{13}C{^{1}H} NMR (101 MHz, $CDCl_3$):** δ 153.83, 144.07, 132.01, 128.86, 128.35, 127.65, 126.25, 124.58, 119.42, 112.03, 111.81, 102.12, 55.99, 40.43.

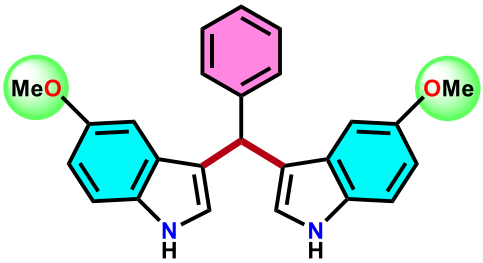

***3,3'-(o-tolylmethylene)bis(5-methoxy-1H-indole) (10ab)*:** Eluent: Hexane / EtOAc (5:1v/v), Red solid; Yield: 341 mg (86%). **^{1}H NMR (300 MHz, $CDCl_3$):** δ 7.81 (s, 2H), 7.25 (d, *J* = 8.7 Hz, 3H), 7.20 – 7.06 (m, 3H), 6.90 – 6.78 (m, 4H), 6.58 (s, 2H), 5.94 (s, 1H), 3.73 (s, 6H), 2.42 (s, 3H). **^{13}C{^{1}H} NMR (101 MHz, $CDCl_3$):** δ 153.76, 142.04, 136.14, 132.04, 130.31, 128.52, 127.75, 126.18, 125.94, 124.85, 118.78, 111.82, 102.06, 56.00, 36.48, 19.69.

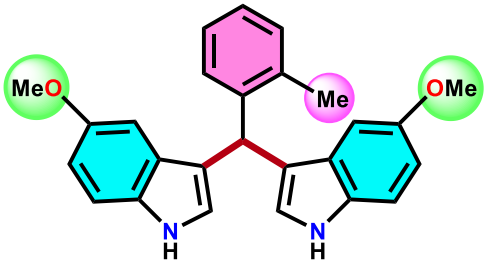

***3,3'-(m-tolylmethylene)bis(5-methoxy-1H-indole) (10ac)*:** Eluent: Hexane / EtOAc (5:1v/v), Red solid; Yield: 357 mg (90%). **^{1}H NMR (300 MHz, $CDCl_3$):** δ 7.84 (s, 2H), 7.28 (s, 2H), 7.25 (d, *J* = 2.8 Hz, 1H), 7.20 (d, *J* = 3.2 Hz, 2H), 7.17 (t, *J* = 1.5 Hz, 1H), 7.05 (dd, *J* = 5.4, 3.5 Hz, 1H), 6.87 (d, *J* = 2.5 Hz, 1H), 6.84 (d, *J* = 2.5 Hz, 3H), 6.69 (s, 2H), 5.75 (s, 1H), 3.72 (s, 6H), 2.31 (s, 3H). **^{13}C{^{1}H} NMR (75 MHz, $CDCl_3$):** δ 153.81, 143.96, 137.76, 132.00, 129.58, 128.20, 127.69, 127.04, 125.88, 124.55, 119.56, 111.97, 111.76, 102.16, 56.01, 40.36, 21.68.

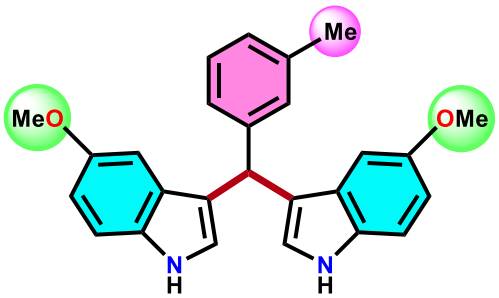

***3,3'-((3-fluorophenyl)methylene)bis(5-methoxy-1H-indole) (10ad)*:** Eluent: Hexane / EtOAc (5:1v/v), Red solid; Yield: 300 mg (75%). **^{1}H NMR (300 MHz, $CDCl_3$):** δ 7.88 (s, 2H), 7.28 (d, *J* = 9.4 Hz, 3H), 7.20 – 7.15 (m, 1H), 7.09 – 7.02 (m, 1H), 6.97 – 6.92 (m, 1H), 6.88 (d, *J* = 2.5 Hz, 1H), 6.85 (d, *J* = 2.5 Hz, 1H), 6.82 (d, *J* = 2.4 Hz, 2H), 6.69 (s, 1H), 5.80 (s, 1H), 3.73 (s, 6H). **^{13}C{^{1}H} NMR (101 MHz, $CDCl_3$):** δ 163.15 (d, $^{1}J_{C-F}$ = 244.9 Hz), 153.93, 146.88 (d, $^{3}J_{C-F}$ = 6.6 Hz), 131.99, 129.71 (d, $^{4}J_{C-F}$ = 8.2 Hz), 127.48, 124.55, 118.76, 115.70 (d, $^{3}J_{C-F}$ = 21.5 Hz), 113.20 (d, $^{2}J_{C-F}$ = 21.3 Hz), 112.03 (d, $^{2}J_{C-F}$ = 25.1 Hz), 101.96, 56.01, 40.18 (d, $^{4}J_{C-F}$ = 1.7 Hz). **^{19}F NMR (282 MHz, $CDCl_3$):** δ -113.78.

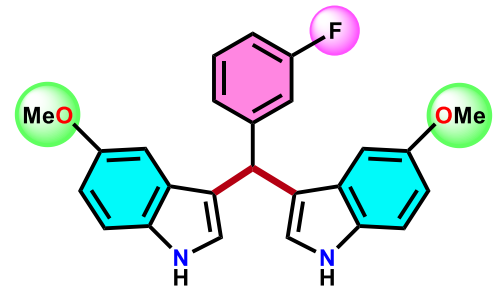

***3,3'-((3-(trifluoromethyl)phenyl)methylene)bis(5-methoxy-1H-indole) (10ae)*:** Eluent: Hexane / EtOAc (5:1v/v), White solid; Yield: 347 mg (77%). **^{1}H NMR (300 MHz, $CDCl_3$):** δ 7.90 (s, 2H), 7.68 (d, *J* = 2.1 Hz, 1H), 7.52 (dd, *J* = 8.7, 7.0 Hz, 2H), 7.41 (t, *J* = 7.7 Hz, 1H), 7.28 (d, *J* = 8.8 Hz, 2H), 6.87 (dd, *J* = 8.8, 2.5 Hz, 2H), 6.79 (d, *J* = 2.4 Hz, 2H), 6.67 (dd, *J* = 2.5, 1.0 Hz, 2H), 5.86 (s, 1H), 3.72 (s, 6H). **^{13}C{^{1}H} NMR (101 MHz, $CDCl_3$):** δ 153.97, 145.11, 132.21, 132.01, 130.62 (q, $^{2}J_{C-F}$ = 31.9 Hz), 128.83, 127.38, 125.81, 125.62 (q, $^{3}J_{C-F}$ = 3.8 Hz), 124.60, 124.45 (q, $^{1}J_{C-F}$ = 270 Hz),123.26 (q, $^{3}J_{C-F}$ = 3.8 Hz), 118.50, 112.27, 111.97, 101.85, 55.98, 40.34. **^{19}F NMR (282 MHz, $CDCl_3$):** δ -62.31.

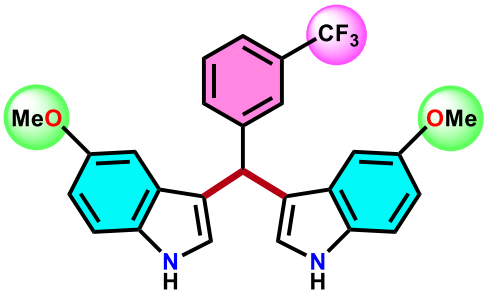

***3,3'-(p-tolylmethylene)bis(5-methoxy-1H-indole) (10af)*:** Eluent: Hexane / EtOAc (5:1v/v), Red solid; Yield: 345 mg (87%). **^{1}H NMR (400 MHz, $CDCl_3$):** δ 7.82 (s, 2H), 7.30 – 7.23 (m, 5H), 7.11 (d, *J* = 7.7 Hz, 2H), 6.85 (d, *J* = 7.5 Hz, 4H), 6.68 (s, 2H), 5.76 (s, 1H), 3.72 (s, 6H), 2.35 (s, 3H). **^{13}C{^{1}H} NMR (101 MHz, $CDCl_3$):** δ 153.79, 141.02, 135.58, 132.01, 129.04, 128.69, 127.67, 124.51, 119.65, 111.96, 111.77, 102.17, 56.00, 39.99, 21.20.

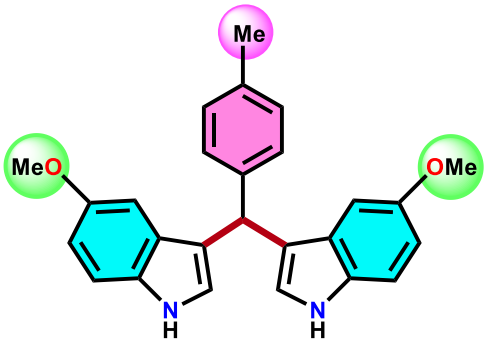

***3,3'-((4-isopropylphenyl)methylene)bis(5-methoxy-1H-indole) (10ag)*:** Eluent: Hexane / EtOAc (5:1v/v), Red solid; Yield: 378 mg (89%). **^{1}H NMR (300 MHz, $CDCl_3$)**: δ 7.82 (s, 2H), 7.32 – 7.23 (m, 5H), 7.16 (d, *J* = 8.1 Hz, 2H), 6.88 – 6.82 (m, 4H), 6.70 (dd, *J* = 2.5, 1.0 Hz, 2H), 5.77 (s, 1H), 3.71 (s, 6H), 2.96 – 2.86 (m, 1H), 1.26 (d, *J* = 6.9 Hz, 6H). **^{13}C{^{1}H} NMR (101 MHz, $CDCl_3$):** δ 153.75, 146.61, 141.36, 131.99, 128.70, 127.69, 126.33, 124.50, 119.67, 111.95, 111.78, 102.15, 55.96, 40.02, 33.82, 24.21.

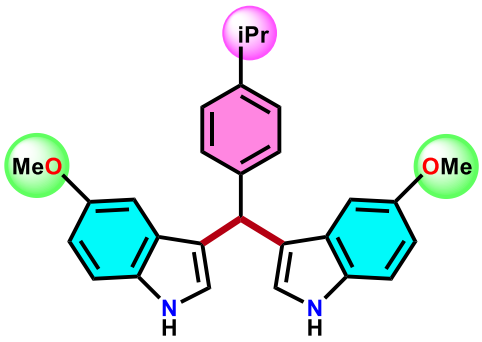

***3,3'-((4-methoxyphenyl)methylene)bis(5-methoxy-1H-indole) (10ah)*:** Eluent: Hexane / EtOAc (3:1v/v), Red solid; Yield: 363 mg (88%). **^{1}H NMR (400 MHz, $CDCl_3$):** δ 7.85 (s, 2H), 7.26 (d, *J* = 15.9 Hz, 4H), 6.85 (d, *J* = 8.6 Hz, 6H), 6.66 (d, *J* = 2.4 Hz, 2H), 5.75 (s, 1H), 3.81 (s, 3H), 3.72 (s, 6H). **^{13}C{^{1}H} NMR (101 MHz, $CDCl_3$):** δ 158.00, 153.78, 136.28, 132.03, 129.73, 127.62, 124.51, 119.74, 113.70, 111.95, 111.79, 102.17, 56.01, 55.36, 39.53.

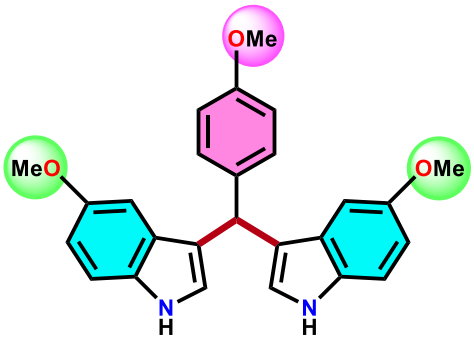

***3,3'-([1,1'-biphenyl]-4-ylmethylene)bis(5-methoxy-1H-indole) (10ai)*:** Eluent: Hexane / EtOAc (5:1v/v), Off-white solid; Yield: 417 mg (91%). **^{1}H NMR (300 MHz, $CDCl_3$):** δ 7.90 – 7.82 (m, 2H), 7.62 (d, *J* = 7.0 Hz, 2H), 7.55 (d, *J* = 8.3 Hz, 2H), 7.49 – 7.41 (m, 4H), 7.35 (t, *J* = 7.3 Hz, 1H), 7.27 (d, *J* = 9.4 Hz, 3H), 6.87 (dq, *J* = 4.5, 2.5 Hz, 4H), 6.73 (s, 2H), 5.85 (s, 1H), 3.73 (s, 6H). **^{13}C{^{1}H} NMR (75 MHz, $CDCl_3$):** δ 153.85, 143.23, 141.22, 138.99, 132.01, 129.26, 128.85, 127.63, 127.14, 127.10, 127.06, 124.61, 119.30, 112.05, 111.85, 102.12, 56.00, 40.08.

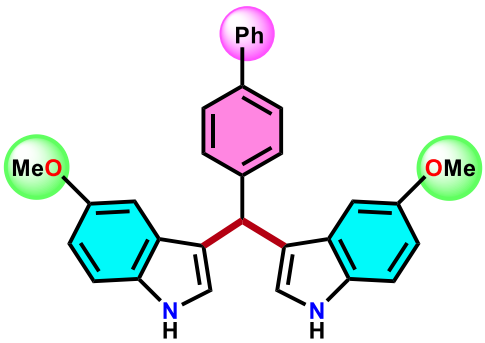

***3,3'-((4-chlorophenyl)methylene)bis(5-methoxy-1H-indole) (10aj)*:** Eluent: Hexane / EtOAc (5:1v/v), White solid; Yield: 342 mg (82%). **^{1}H NMR (400 MHz, $CDCl_3$):** δ 7.87 (s, 2H), 7.33 – 7.21 (m, 6H), 6.88 (dd, *J* = 8.8, 2.5 Hz, 2H), 6.83 (d, *J* = 2.5 Hz, 2H), 6.62 (dd, *J* = 2.5, 1.0 Hz, 2H), 5.78 (s, 1H), 3.74 (s, 6H). **^{13}C{^{1}H} NMR (101 MHz, $CDCl_3$):** δ 153.82, 142.60, 131.97, 131.84, 130.17, 128.45, 127.39, 124.59, 118.76, 112.04, 111.94, 101.98, 55.99, 39.76.

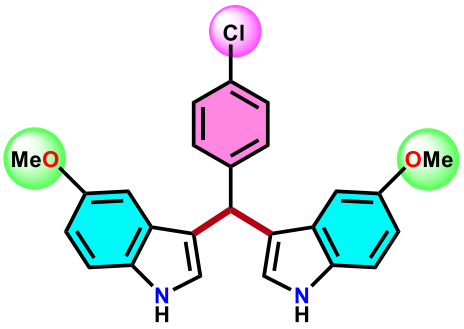

***3,3'-((4-bromophenyl)methylene)bis(5-methoxy-1H-indole) (10ak)*:** Eluent: Hexane / EtOAc (5:1v/v),

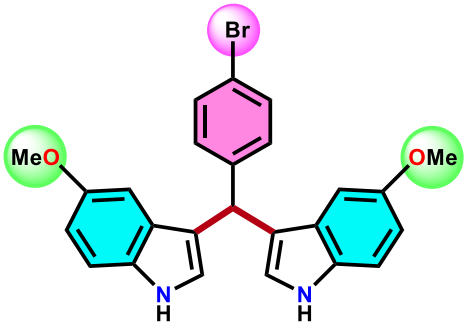

Red solid; Yield: 387 mg (84%). **^{1}H NMR (400 MHz, $CDCl_3$):** δ 7.90 – 7.86 (m, 2H), 7.43 – 7.40 (m, 2H), 7.27 (d, *J* = 8.8 Hz, 2H), 7.23 (d, *J* = 8.2 Hz, 2H), 6.87 (d, *J* = 8.8 Hz, 2H), 6.80 (s, 2H), 6.66 – 6.63 (m, 2H), 5.76 (s, 1H), 3.73 (s, 6H). **^{13}C{^{1}H} NMR (101 MHz, $CDCl_3$):** δ 153.90, 143.14, 131.99, 131.43, 130.62, 127.43, 124.59, 120.02, 118.78, 112.12, 111.92, 102.00, 56.02, 39.86.

***3,3'-(thiophen-2-ylmethylene)bis(5-methoxy-1H-indole) (10al)*:** Eluent: Hexane / EtOAc (2:1v/v),

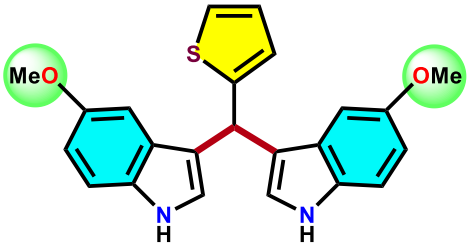

Pink solid; Yield: 264 mg (68%). **^{1}H NMR (300 MHz, $CDCl_3$):** δ 7.87 (s, 2H), 7.30 – 7.23 (m, 3H), 7.18 (dd, *J* = 4.3, 2.1 Hz, 1H), 6.96 – 6.94 (m, 2H), 6.92 (d, *J* = 2.5 Hz, 2H), 6.88 (d, *J* = 2.5 Hz, 1H), 6.85 (s, 2H), 6.08 (s, 1H), 3.75 (s, 6H). **^{13}C{^{1}H} NMR (101 MHz, $CDCl_3$):** δ 153.92, 148.71, 131.88, 127.32, 126.54, 125.28, 124.10, 123.75, 119.41, 112.14, 111.91, 101.91, 56.00, 35.54.

***3,3'-(naphthalen-1-ylmethylene)bis(5-methoxy-1H-indole) (10am)*:** Eluent: Hexane / EtOAc (5:1v/v),

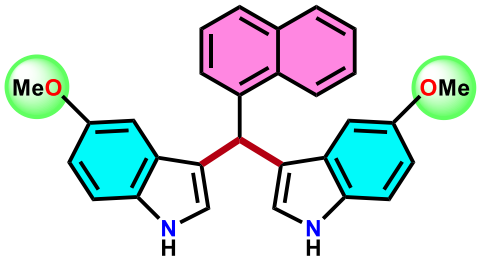

Off-white solid; Yield: 385 mg (89%). **^{1}H NMR (300 MHz, $CDCl_3$):** δ 8.18 (d, *J* = 8.3 Hz, 1H), 7.91 (d, *J* = 8.7 Hz, 1H), 7.82 (s, 2H), 7.77 (d, *J* = 7.7 Hz, 1H), 7.51 – 7.46 (m, 1H), 7.44 (dd, *J* = 5.3, 1.6 Hz, 1H), 7.39 (dd, *J* = 8.7, 1.8 Hz, 1H), 7.33 (d, *J* = 7.8 Hz, 1H), 7.27 (d, *J* = 8.8 Hz, 3H), 6.88 (d, *J* = 2.5 Hz, 1H), 6.84 (d, *J* = 3.9 Hz, 2H), 6.61 – 6.57 (m, 2H), 6.55 (s, 1H), 3.69 (s, 6H). **^{13}C{^{1}H} NMR (101 MHz, $CDCl_3$):** δ 153.92, 139.45, 134.16, 132.07, 128.77, 128.76, 127.69, 127.11, 126.28, 125.90, 125.63, 125.35, 125.27, 124.52, 119.09, 111.99, 111.84, 102.08, 56.06, 36.13.

***3,3'-(cyclohexylmethylene)bis(5-methoxy-1H-indole)(10an)*:** Eluent: Hexane / EtOAc (5:1v/v),

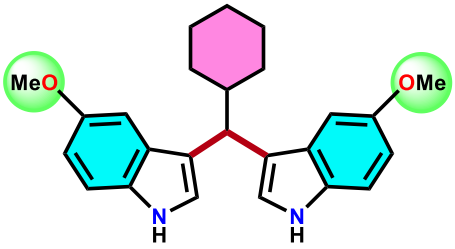

Brwon coloured solid; Yield 303 mg (78%). **^{1}H NMR (300 MHz, $CDCl_3$):** δ 7.83 (s, 2H), 7.21 (d, *J* = 8.7 Hz, 2H), 7.11 (dd, *J* = 8.5, 2.2 Hz, 4H), 6.82 (dd, *J* = 8.8, 2.5 Hz, 2H), 4.18 (d, *J* = 8.8 Hz, 1H), 3.83 (s, 6H), 2.32 – 2.20 (m, 1H), 1.87 (d, *J* = 12.7 Hz, 2H), 1.71 (d, *J* = 12.8 Hz, 3H), 1.33 – 1.19 (m, 3H), 1.15 – 1.04 (m, 2H). **^{13}C{^{1}H} NMR (75 MHz, $CDCl_3$):** δ 153.68, 131.66, 128.37, 122.55, 119.43, 111.66, 111.43, 102.28, 56.11, 42.94, 40.32, 32.47, 26.85, 26.81.

***3,3'-((3-(trifluoromethyl)phenyl)methylene)bis(5-fluoro-1H-indole) (11aa)*:** Yield: 316 mg (69%).

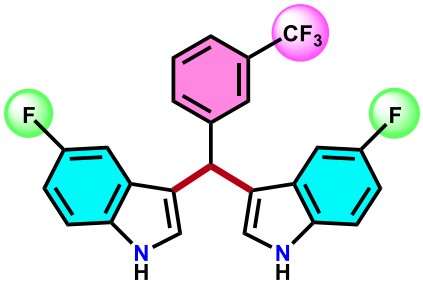

Eluent: Hexane / EtOAc (5:1v/v), Brown solid; **^{1}H NMR (300 MHz, $CDCl_3$):** δ 8.05 (s, 2H), 7.63 (s, 1H), 7.56 – 7.48 (m, 2H), 7.47 – 7.38 (m, 1H), 7.34 – 7.28 (m, 2H), 7.01 – 6.92 (m, 4H), 6.72 (s, 2H), 5.83 (s, 1H). **^{13}C{^{1}H} NMR (101 MHz, $CDCl_3$):** δ 157.76 (d, *J* = 234.7 Hz), 144.46, 133.35, 132.04, 129.00, 127.24 (d, *J* = 9.8 Hz), 125.45, 123.59 (d, *J* = 3.9 Hz), 118.74 (d, *J* = 4.7 Hz), 112.04, 111.94, 110.81 (d, *J* = 26.4 Hz), 104.80, 104.57, 40.22. **^{19}F NMR (282 MHz, $CDCl_3$):** δ -62.36, -124.19.

***3,3'-((3-fluorophenyl)methylene)bis(2-methyl-1H-indole) (12aa)*:** Eluent: Hexane / EtOAc (5:1v/v),

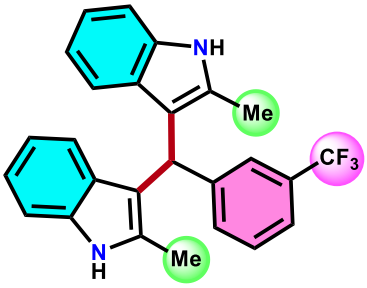

White solid; Yield: 258 mg (70%).**^{1}H NMR (300 MHz, $CDCl_3$):** δ 7.76 (s, 2H), 7.26 – 7.22 (m, 2H), 7.13 – 7.10 (m, 1H), 7.08 (d, *J* = 3.2 Hz, 1H), 7.07 – 6.99 (m, 4H), 6.98 – 6.92 (m, 2H), 6.92 – 6.87 (m, 2H), 6.02 (s, 1H), 2.07 (s, 6H). **^{13}C{^{1}H} NMR (75 MHz, $CDCl_3$):** δ 163.19 (d, $^{1}J_{C-F}$ = 244.9 Hz), 146.83 (d, $^{3}J_{C-F}$ = 6.5 Hz), 135.16, 132.04, 129.56 (d, $^{3}J_{C-F}$ = 8.2 Hz), 128.88, 124.95 (d, $^{4}J_{C-F}$ = 2.6 Hz), 120.87, 119.33, 119.29, 116.05 (d, $^{2}J_{C-F}$ = 21.6 Hz), 112.97 (d, $^{2}J_{C-F}$ = 21.1 Hz), 112.89, 110.18, 39.16, 12.53. **^{19}F NMR (282 MHz, $CDCl_3$):** δ -113.88.

3,3'-((3-(trifluoromethyl)phenyl)methylene)bis(2-methyl-1H-indole) (12ab): Eluent: Hexane / EtOAc

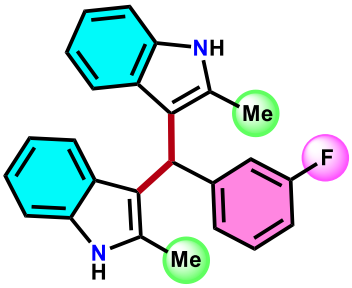

(5:1v/v), White solid; Yield: 314 mg (75%). **^{1}H NMR (400 MHz, DMSO):** δ 10.83 (s, 2H), 7.57 (s, 1H), 7.53 (d, *J* = 2.9 Hz, 1H), 7.49 (d, *J* = 7.2 Hz, 2H), 7.24 (d, *J* = 8.1 Hz, 2H), 6.91 (t, *J* = 7.5 Hz, 2H), 6.79 (d, *J* = 8.0 Hz, 2H), 6.70 (t, *J* = 7.5 Hz, 2H), 6.07 (s, 1H), 2.09 (s, 6H). **^{13}C{^{1}H} NMR (101 MHz, DMSO):** δ 146.33, 135.58, 133.23, 132.84, 129.49, 129.24 (q, $^{2}J_{C-F}$ = 31.3 Hz), 128.46, 125.50 (q, $^{3}J_{C-F}$ = 3.8 Hz), 124.87 (q, $^{1}J_{C-F}$ = 272.7 Hz) 123.07 (q, $^{3}J_{C-F}$ = 3.8 Hz), 120.18, 118.70, 118.58, 111.81, 110.96, 38.79, 12.37. **^{19}F NMR (377 MHz, DMSO):** δ -60.95.

3,3'-(p-tolylmethylene)bis(2-methyl-1H-indole) (12ac): Eluent: Hexane / EtOAc (5:1v/v), Red solid;

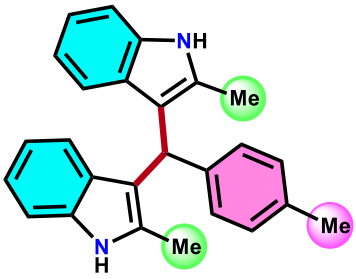

Yield: 295 mg (81%). **^{1}H NMR (300 MHz, $CDCl_3$):** δ 7.67 (s, 2H), 7.29 – 7.23 (m, 2H), 7.20 (d, *J* = 8.0 Hz, 2H), 7.10 (d, *J* = 2.7 Hz, 2H), 7.09 – 7.03 (m, 4H), 6.93 – 6.87 (m, 2H), 5.99 (s, 1H), 2.37 (s, 3H), 2.06 (s, 6H). **^{13}C{^{1}H} NMR (101 MHz, $CDCl_3$):** δ 140.71, 135.44, 135.15, 131.88, 129.11, 129.05, 128.92, 120.65, 119.52, 119.12, 113.70, 110.06, 38.94, 21.22, 12.52.

***3,3'-((4-methoxyphenyl)methylene)bis(2-methyl-1H-indole) (12ad)*:** Eluent: Hexane / EtOAc (3:1v/v), Red solid; Yield: 323 mg (85%). **^{1}H NMR (300 MHz, $CDCl_3$):** δ 7.63 (s, 2H), 7.23 (d, *J* = 8.3 Hz, 4H), 7.13 – 7.05 (m, 4H), 6.96 – 6.90 (m, 2H), 6.87 – 6.82 (m, 2H), 5.99 (s, 1H), 3.83 (s, 3H), 2.03 (s, 6H). **^{13}C{^{1}H} NMR (101 MHz, $CDCl_3$):** δ 157.89, 135.96, 135.11, 131.89, 130.03, 128.98, 120.60, 119.45, 119.09, 113.71, 113.55, 110.13, 55.31, 38.46, 12.38.

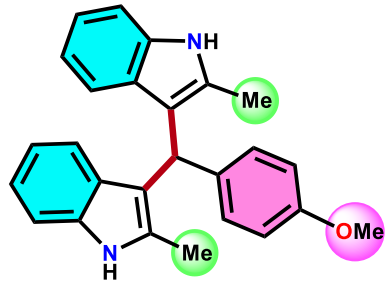

***3,3'-([1,1'-biphenyl]-4-ylmethylene)bis(2-methyl-1H-indole) (12ae)*:** Eluent: Hexane / EtOAc (5:1v/v), White solid; Yield: 375 mg (88%). **^{1}H NMR (300 MHz, $CDCl_3$):** δ 7.72 (s, 2H), 7.65 (d, *J* = 7.0 Hz, 2H), 7.54 (d, *J* = 8.3 Hz, 2H), 7.46 (t, *J* = 7.5 Hz, 3H), 7.38 (d, *J* = 8.2 Hz, 3H), 7.27 (d, *J* = 8.7 Hz, 2H), 7.10 – 7.06 (m, 3H), 6.91 (t, *J* = 7.5 Hz, 2H), 6.08 (s, 1H), 2.10 (s, 6H). **^{13}C{^{1}H} NMR (75 MHz, $CDCl_3$):** δ 143.05, 141.18, 138.75, 135.18, 131.99, 129.60, 129.05, 128.83, 127.11, 127.07, 126.86, 120.76, 119.50, 119.23, 113.41, 110.14, 39.06, 12.56.

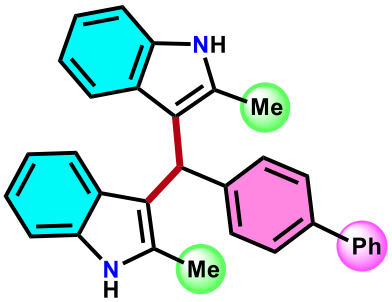

***4-(bis(2-methyl-1H-indol-3-yl)methyl)-N,N-dimethylaniline (12af)*:** Eluent: Hexane / EtOAc (5:1v/v), Red solid; Yield: 342 mg (87%). **^{1}H NMR (400 MHz, $CDCl_3$):** δ 7.69 (s, 2H), 7.24 (d, *J* = 7.9 Hz, 2H), 7.15 (d, *J* = 8.5 Hz, 2H), 7.05 (dd, *J* = 10.4, 8.0 Hz, 4H), 6.88 (td, *J* = 7.5, 1.1 Hz, 2H), 6.72 – 6.68 (m, 2H), 5.95 (s, 1H), 2.94 (s, 6H), 2.08 (s, 6H). **^{13}C{^{1}H} NMR (75 MHz, $CDCl_3$):** δ 149.14, 135.17, 132.17, 131.76, 129.72, 129.22, 120.56, 119.62, 119.07, 114.19, 112.90, 109.98, 41.06, 38.35, 12.56.

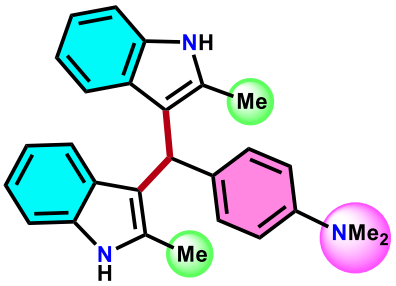

***3,3'-((4-chlorophenyl)methylene)bis(2-methyl-1H-indole) (12ag)*:** Eluent: Hexane / EtOAc (5:1v/v), Brown solid; Yield: 327 mg (85%). **^{1}H NMR (300 MHz, DMSO):** δ 10.79 (s, 2H), 7.31 (d, *J* = 8.1 Hz, 2H), 7.22 (dd, *J* = 14.1, 8.1 Hz, 4H), 6.91 (t, *J* = 7.5 Hz, 2H), 6.83 (d, *J* = 7.9 Hz, 2H), 6.71 (t, *J* = 7.5 Hz, 2H), 5.93 (s, 1H), 2.10 (s, 6H). **^{13}C{^{1}H} NMR (101 MHz, DMSO):** δ 143.45, 135.17, 132.29, 130.56, 130.32, 128.14, 127.95, 119.71, 118.45, 118.13, 111.73, 110.49, 38.11, 11.99.

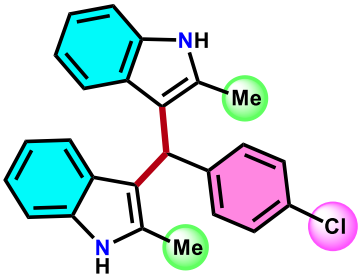

***3,3'-((4-bromophenyl)methylene)bis(2-methyl-1H-indole) (12ah)*:** Eluent: Hexane / EtOAc (5:1v/v), Red solid; Yield: 373 mg (87%). **^{1}H NMR (400 MHz, DMSO):** δ 10.81 (s, 2H), 7.45 (d, *J* = 8.2 Hz, 2H), 7.25 (d, *J* = 8.0 Hz, 2H), 7.15 (d, *J* = 8.2 Hz, 2H), 6.92 (t, *J* = 7.5 Hz, 2H), 6.85 (d, *J* = 8.0 Hz, 2H), 6.72 (t, *J* = 7.5 Hz, 2H), 5.92 (s, 1H), 2.11 (s, 6H). **^{13}C{^{1}H} NMR (101 MHz, DMSO):** δ 143.85, 135.13, 132.26, 130.95, 130.82, 128.10, 119.67, 118.73, 118.42, 118.08, 111.60, 110.44, 38.12, 11.96.

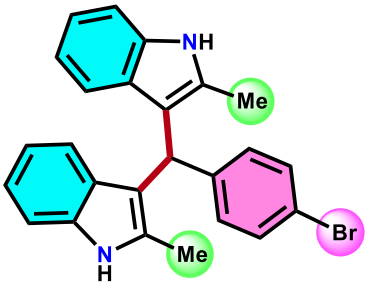

***3,3'-((3,4,5-trimethoxyphenyl)methylene)bis(2-methyl-1H-indole) (12ai)*:** Eluent: Hexane / EtOAc (1:1v/v), Orange solid; Yield: 361 mg (82%). **^{1}H NMR (400 MHz, $CDCl_3$):** δ 7.76 (s, 2H), 7.24 (d, *J* = 7.9 Hz, 2H), 7.10 – 7.04 (m, 4H), 6.90 (t, *J* = 7.5 Hz, 2H), 6.59 (s, 2H), 5.96 (s, 1H), 3.88 (s, 3H), 3.66 (s, 6H), 2.08 (s, 6H). **^{13}C{^{1}H} NMR (101 MHz, $CDCl_3$):** δ 153.08, 139.59, 136.41, 135.13, 131.84, 128.97, 120.72, 119.31, 119.18, 113.47, 110.09, 106.52, 61.09, 56.19, 39.51, 12.54.

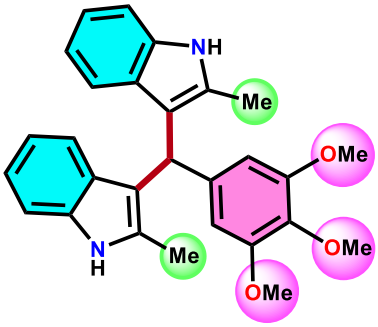

***3,3'-(naphthalen-1-ylmethylene)bis(2-methyl-1H-indole) (12aj)*:** Eluent: Hexane / EtOAc (3:1v/v), Pale pink coloured solid; Yield: 332 mg (83%). **^{1}H NMR (300 MHz, DMSO):** δ 10.75 (s, 2H), 8.00 – 7.90 (m, 2H), 7.83 (d, *J* = 8.2 Hz, 1H), 7.45 – 7.39 (m, 1H), 7.36 (d, *J* = 7.9 Hz, 2H), 7.21 (t, *J* = 6.6 Hz, 3H), 6.92 – 6.86 (m, 2H), 6.80 (d, *J* = 8.0 Hz, 2H), 6.69 – 6.62 (m, 2H), 6.52 (s, 1H), 1.97 (s, 6H). **^{13}C{^{1}H} NMR (101 MHz, DMSO):** δ 139.91, 135.05, 133.43, 132.14, 131.78, 128.50, 128.48, 126.87, 125.95, 125.81, 125.37, 125.22, 123.88, 119.61, 118.08, 118.02, 111.91, 110.39, 35.77, 11.79.

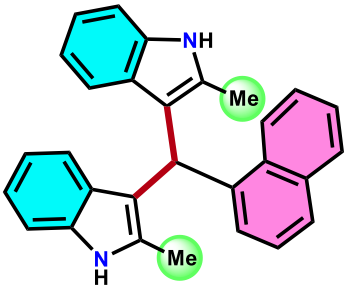

***3,3'-(furan-3-ylmethylene)bis(2-methyl-1H-indole) (12ak)*:** Eluent: Hexane / EtOAc (2:1v/v), Pink solid; Yield: 242 mg (71%). **^{1}H NMR (400 MHz, DMSO):** δ 10.73 (s, 2H), 7.61 (t, *J* = 1.6 Hz, 1H), 7.23 (d, *J* = 8.0 Hz, 2H), 7.12 (d, *J* = 8.0 Hz, 2H), 7.05 (s, 1H), 6.92 (t, *J* = 7.5 Hz, 2H), 6.76 (t, *J* = 7.5 Hz, 2H), 6.35 (d, *J* = 1.7 Hz, 1H), 5.72 (s, 1H), 2.23 (s, 6H). **^{13}C{^{1}H} NMR (101 MHz, DMSO):** δ 143.03, 139.89, 135.07, 131.56, 128.48, 127.88, 119.58, 118.56, 117.93, 112.36, 112.00, 110.35, 29.84, 12.03.

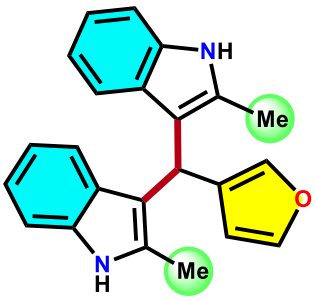

***3,3'-(thiophen-2-ylmethylene)bis(2-methyl-1H-indole) (12al)*:** Eluent: Hexane / EtOAc (2:1v/v), Red solid; Yield: 246 mg (69%). **^{1}H NMR (400 MHz, $CDCl_3$):** δ 7.76 (s, 2H), 7.29 – 7.24 (m, 3H), 7.13 (d, *J* = 8.0 Hz, 2H), 7.07 (t, *J* = 7.6 Hz, 2H), 6.93 (t, *J* = 7.4 Hz, 3H), 6.82 (d, *J* = 3.4 Hz, 1H), 6.21 (s, 1H), 2.16 (s, 6H). **^{13}C{^{1}H} NMR (101 MHz, $CDCl_3$):** δ 148.94, 135.08, 128.55, 127.03, 126.60, 125.79, 125.70, 125.65, 120.88, 119.32, 119.29, 110.15, 34.90, 12.50.

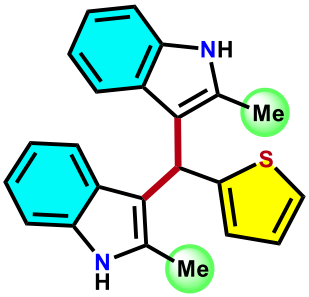

***3,3'-(p-tolylmethylene)bis(1H-pyrrolo[2,3-b]pyridine) (13aa)*:** Eluent: Hexane / EtOAc (2:1v/v), Red solid; Yield: 233 mg (69%). **^{1}H NMR (300 MHz, DMSO):** δ 11.46 (s, 2H), 8.15 (dd, *J* = 4.7, 1.6 Hz, 2H), 7.59 (dd, *J* = 7.9, 1.6 Hz, 2H), 7.23 (d, *J* = 7.7 Hz, 2H), 7.08 (d, *J* = 7.8 Hz, 2H), 6.97 – 6.93 (m, 2H), 6.93 – 6.89 (m, 2H), 5.81 (s, 1H), 2.25 (s, 3H). **^{13}C{^{1}H} NMR (75 MHz, DMSO):** δ 148.93, 142.57, 141.15, 135.19, 128.97, 128.26, 127.38, 123.96, 118.96, 116.73, 115.02, 24.12, 20.75.

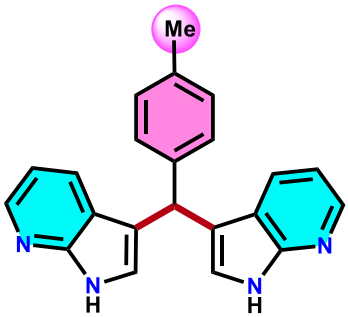

***3,3'-([1,1'-biphenyl]-4-ylmethylene)bis(1H-pyrrolo[2,3-b]pyridine) (13ab)*:** Eluent: Hexane / EtOAc (2:1v/v), White solid; Yield: 284 mg (71%). **^{1}H NMR (300 MHz, DMSO):** δ 11.51 (s, 2H), 8.17 (dd, *J* = 4.7, 1.6 Hz, 2H), 7.63 (td, *J* = 10.3, 7.8 Hz, 6H), 7.47 – 7.39 (m, 4H), 7.32 (dd, *J* = 8.3, 6.2 Hz, 1H), 7.04 (d, *J* = 2.0 Hz, 2H), 6.94 (dd, *J* = 7.9, 4.7 Hz, 2H), 5.92 (s, 1H). **^{13}C{^{1}H} NMR (75 MHz, DMSO):** δ 148.94, 143.51, 142.65, 140.04, 138.08, 129.04, 128.95, 127.38, 126.69, 126.64, 124.08, 118.96, 116.44, 115.10, 31.08.

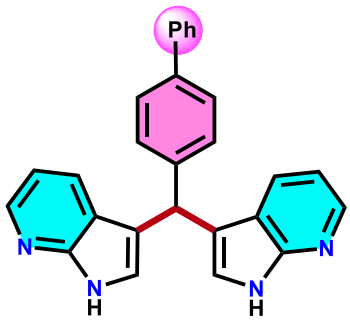

***3,3'-((4-chlorophenyl)methylene)bis(1H-pyrrolo[2,3-b]pyridine) (13ac)*:** Eluent: Hexane / EtOAc (2:1v/v), Pale pink solid; Yield: 233 mg (65%). **^{1}H NMR (300 MHz, DMSO):** δ 11.52 (s, 2H), 8.16 (dd, *J* = 4.7, 1.6 Hz, 2H), 7.61 (dd, *J* = 7.9, 1.6 Hz, 2H), 7.39 – 7.30 (m, 4H), 7.02 – 6.90 (m, 4H), 5.89 (s, 1H). **^{13}C{^{1}H} NMR (75 MHz, DMSO):** δ 148.91, 143.21, 142.70, 130.78, 130.21, 128.36, 127.30, 124.12, 118.82, 116.09, 115.13, 24.70.

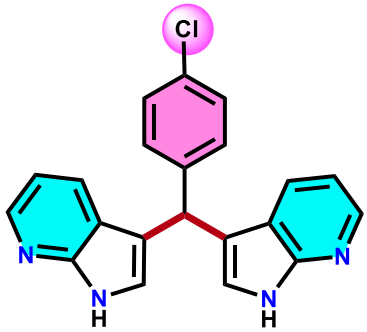

***3,3'-((4-bromophenyl)methylene)bis(1H-pyrrolo[2,3-b]pyridine) (13ad)*:** Eluent: Hexane / EtOAc (2:1v/v), Orange solid; Yield: 270 mg (67%). **^{1}H NMR (300 MHz, DMSO):** δ 11.57 (s, 2H), 8.17 (d, *J* = 3.5 Hz, 2H), 7.66 – 7.57 (m, 2H), 7.47 (d, *J* = 8.2 Hz, 2H), 7.31 (d, *J* = 8.2 Hz, 2H), 6.99 (s, 2H), 6.94 (dd, *J* = 7.9, 4.7 Hz, 2H), 5.88 (s, 1H). **^{13}C{^{1}H} NMR (75 MHz, DMSO):** δ 148.88, 143.60, 142.61, 131.19, 130.55, 127.18, 124.06, 119.19, 118.72, 115.90, 115.02, 24.59.

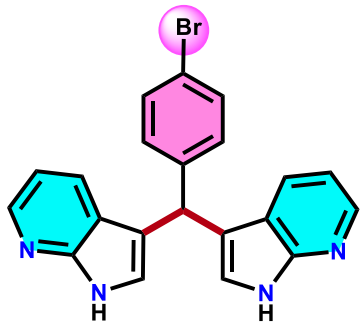

***3,3'-(thiophen-2-ylmethylene)bis(1H-pyrrolo[2,3-b]pyridine) (13ae)*:** Eluent: Hexane / EtOAc (3:1v/v), Red solid; Yield: 182 mg (55%). **^{1}H NMR (300 MHz, DMSO):** δ 11.51 (s, 2H), 8.18 (d, *J* = 3.1 Hz, 2H), 7.71 (d, *J* = 6.3 Hz, 2H), 7.36 – 7.32 (m, 1H), 7.19 (s, 2H), 6.99 – 6.92 (m, 4H), 6.19 (s, 1H). **^{13}C{^{1}H} NMR (101 MHz, DMSO):** δ 148.76, 148.39, 142.59, 127.26, 126.60, 125.01, 124.22, 123.67, 118.52, 116.51, 115.01, 35.01.

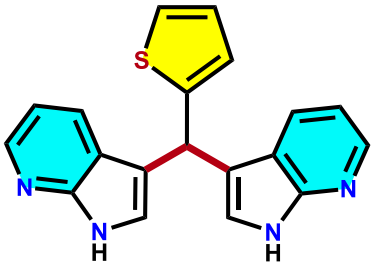

***di(1H-indol-3-yl)methane (14aa)*:** Eluent: Hexane / EtOAc (3:1v/v), Colourless crystalline solid; Yield: 167 mg (68%). **^{1}H NMR (300 MHz, CDCl$_3$):** δ 8.03 – 7.80 (m, 2H), 7.72 – 7.61 (m, 2H), 7.38 (d, *J* = 8.2 Hz, 2H), 7.26 – 7.19 (m, 2H), 7.13 (td, *J* = 7.4, 1.1 Hz, 2H), 6.95 (s, 2H), 4.28 (s, 2H). **^{13}C{^{1}H} NMR (75 MHz, CDCl$_3$):** δ 136.59, 127.70, 122.33, 122.02, 119.36, 119.31, 115.82, 111.17, 21.34.

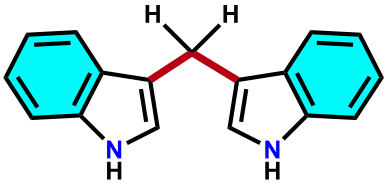

***3,3'-(propane-1,1-diyl)bis(1H-indole) (14ab)*:** Eluent: Hexane / EtOAc (5:1v/v), Light brown coloured oil; Yield: 195 mg (71%). **^{1}H NMR (300 MHz, CDCl$_3$):** δ 7.77 (s, 2H), 7.71 (d, *J* = 7.9 Hz, 2H), 7.33 (d, *J* = 8.1 Hz, 2H), 7.28 – 7.21 (m, 2H), 7.15 (dd, *J* = 8.0, 6.7 Hz, 2H), 6.92 (s, 2H), 4.46 (t, *J* = 7.4 Hz, 1H), 2.45 – 2.21 (m, 2H), 1.10 (t, *J* = 7.3 Hz, 3H). **^{13}C{^{1}H} NMR (75 MHz, CDCl$_3$):** δ 136.59, 127.24, 121.71, 121.66, 120.20, 119.72, 119.00, 111.24, 35.91, 28.82, 13.17.

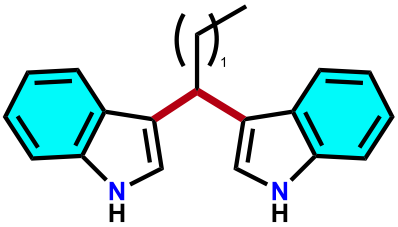

***3,3'-(butane-1,1-diyl)bis(1H-indole) (14ac)*:** Eluent: Hexane / EtOAc (5:1v/v), Brown solid; Yield: 210 mg (73%). **^{1}H NMR (300 MHz, CDCl$_3$):** δ 7.88 (s, 2H), 7.66 (d, *J* = 7.9 Hz, 2H), 7.38 – 7.30 (m, 2H), 7.23 – 7.16 (m, 2H), 7.12 – 7.06 (m, 2H), 6.99 (s, 2H), 4.54 (t, *J* = 7.5 Hz, 1H), 2.32 – 2.17 (m, 2H), 1.48 (q, *J* = 7.5 Hz, 2H), 1.01 (t, *J* = 7.4 Hz, 3H). **^{13}C{^{1}H} NMR (101 MHz, CDCl$_3$):** δ 136.57, 127.20, 121.71, 121.57, 120.42, 119.70, 119.01, 111.23, 38.24, 33.70, 21.50, 14.32.

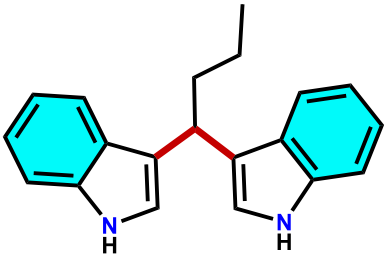

***3,3'-(hexane-1,1-diyl)bis(1H-indole) (14ad)*:** Eluent: Hexane / EtOAc (5:1v/v), Red oil; Yield: 234 mg (74%). **^{1}H NMR (400 MHz, $CDCl_3$):** δ 7.83 (s, 2H), 7.67 (d, *J* = 7.9 Hz, 2H), 7.34 (d, *J* = 8.1 Hz, 2H), 7.25 – 7.17 (m, 2H), 7.10 (t, *J* = 7.5 Hz, 2H), 6.97 (s, 2H), 4.53 (t, *J* = 7.4 Hz, 1H), 2.27 (q, *J* = 7.5 Hz, 2H), 1.56 – 1.26 (m, 8H), 0.92 (t, *J* = 7.0 Hz, 3H). **^{13}C{^{1}H} NMR (75 MHz, $CDCl_3$):** δ 136.67, 127.28, 121.78, 121.54, 120.61, 119.77, 119.06, 111.19, 35.95, 34.10, 32.14, 28.14, 22.79, 14.27.

***3,3'-(heptane-1,1-diyl)bis(1H-indole) (14ae)*:** Eluent: Hexane / EtOAc (5:1v/v), Colourless oil; Yield: 254 mg (77%). **^{1}H NMR (400 MHz, $CDCl_3$):** δ 7.72 (dd, *J* = 9.5, 4.6 Hz, 4H), 7.33 (d, *J* = 8.1 Hz, 2H), 7.29 – 7.21 (m, 2H), 7.15 (q, *J* = 6.8 Hz, 2H), 6.93 (s, 2H), 4.57 (t, *J* = 7.5 Hz, 1H), 2.31 (p, *J* = 8.1 Hz, 2H), 1.55 – 1.34 (m, 8H), 0.98 (t, *J* = 6.2 Hz, 3H). **^{13}C{^{1}H} NMR (75 MHz, $CDCl_3$):** δ 136.61, 127.23, 121.74, 121.56, 120.54, 119.73, 119.04, 111.22, 36.00, 34.06, 31.97, 29.58, 28.41, 22.82, 14.23.

***3,3'-(octane-1,1-diyl)bis(1H-indole) (14af)*:** Eluent: Hexane / EtOAc (5:1v/v), Red solid; Yield: 255 mg (74%). **^{1}H NMR (300 MHz, $CDCl_3$):** δ 7.78 (d, *J* = 7.8 Hz, 2H), 7.69 (s, 2H), 7.36 – 7.26 (m, 5H), 7.26 – 7.18 (m, 2H), 6.90 (d, *J* = 2.3 Hz, 2H), 4.62 (t, *J* = 7.4 Hz, 1H), 2.36 (q, *J* = 7.3 Hz, 2H), 1.54 – 1.36 (m, 10H), 1.05 (d, *J* = 7.0 Hz, 3H).**^{13}C{^{1}H} NMR (75 MHz, $CDCl_3$):** δ 136.57, 127.18, 121.67, 121.59, 120.41, 119.67, 118.98, 111.24, 36.01, 34.02, 32.01, 29.86, 29.39, 28.43, 22.76, 14.21.

***3,3'-(nonane-1,1-diyl)bis(1H-indole) (14ag)*:** Eluent: Hexane / EtOAc (5:1v/v), Brown coloured solid; Yield: 272 mg (76%). **^{1}H NMR (300 MHz, $CDCl_3$):** δ 7.85 – 7.62 (m, 4H), 7.33 (d, *J* = 8.0 Hz, 2H), 7.27 – 7.20 (m, 2H), 7.14 (td, *J* = 7.5, 1.2 Hz, 2H), 6.94 (s, 2H), 4.55 (t, *J* = 7.4 Hz, 1H), 2.29 (q, *J* = 7.4 Hz, 2H), 1.37 (d, *J* = 14.6 Hz, 12H), 0.98 (t, *J* = 6.7 Hz, 3H). **^{13}C{^{1}H} NMR (101 MHz, $CDCl_3$):** δ 136.66, 127.27, 121.76, 121.56, 120.59, 119.76, 119.05, 111.21, 36.00, 34.09, 32.02, 29.93, 29.72, 29.49, 28.45, 22.79, 14.24.

***3,3'-(dodecane-1,1-diyl)bis(1H-indole) (14ah)*:** Eluent: Hexane / EtOAc (5:1v/v), Yellowish brown oil; Yield: 312 mg (78%). **^{1}H NMR (300 MHz, $CDCl_3$):** δ 7.88 (s, 2H), 7.66 (d, *J* = 7.9 Hz, 2H), 7.34 (d, *J* = 8.0 Hz, 2H), 7.21 (d, *J* = 7.3 Hz, 2H), 7.10 (d, *J* = 7.5 Hz, 2H), 6.97 (s, 2H), 4.52 (t, *J* = 7.4 Hz, 1H), 2.26 (q, *J* = 7.4 Hz, 2H),1.46 – 1.34 (m, 1H), 0.95 (t, *J* = 6.9 Hz, 1H). **^{13}C{^{1}H} NMR (75 MHz, $CDCl_3$):** δ 136.71, 127.30,

121.77, 121.53, 120.66, 119.79, 119.05, 111.17, 35.99, 34.12, 32.90, 32.05, 29.83, 29.80, 29.77, 29.48, 28.47, 25.86, 22.82, 14.25.

***bis(5-methoxy-1H-indol-3-yl)methane (14ai)*:** Eluent: Hexane / EtOAc (3:1v/v), Brown solid; Yield:

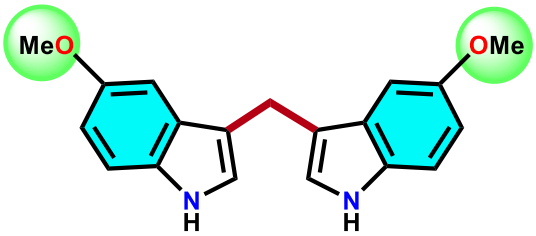

220 mg (72%). **^{1}H NMR (300 MHz, $CDCl_3$):** δ 7.85 v (s, 2H), 7.29 (s, 1H), 7.26 (s, 1H), 7.09 (d, *J* = 2.5 Hz, 2H), 6.94 (s, 2H), 6.88 (dd, *J* = 8.8, 2.5 Hz, 2H), 4.20 (s, 2H), 3.84 (s, 6H). **^{13}C{^{1}H} NMR (101 MHz, $CDCl_3$):** δ 153.99, 131.77, 128.09, 123.19, 115.45, 112.21, 111.90, 101.22, 56.08, 21.44.

***3,3'-(butane-1,1-diyl)bis(5-methoxy-1H-indole) (14aj)*:** Eluent: Hexane / EtOAc (5:1v/v), pale pink

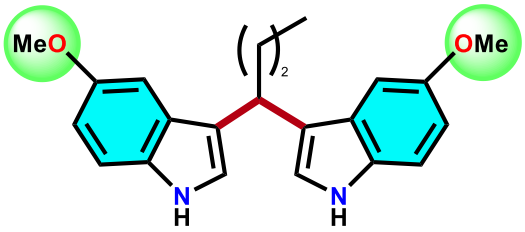

coloured oil; Yield: 244 mg (70%). **^{1}H NMR (300 MHz, $CDCl_3$):** δ 7.87 (s, 2H), 7.21 (dd, *J* = 8.8, 2.9 Hz, 2H), 7.13 (d, *J* = 2.4 Hz, 2H), 6.95 (s, 2H), 6.91 – 6.83 (m, 2H), 4.45 (t, *J* = 7.3 Hz, 1H), 3.84 (s, 6H), 2.31 – 2.18 (m, 2H), 1.58 – 1.45 (m, 2H), 1.03 (t, *J* = 7.4 Hz, 3H). **^{13}C{^{1}H} NMR (101 MHz, $CDCl_3$):** δ 153.50, 131.94, 127.66, 122.45, 120.08, 111.82, 111.47, 102.06, 56.01, 37.90, 37.70, 33.70, 21.44, 14.32.

***3,3'-(heptane-1,1-diyl)bis(5-methoxy-1H-indole) (14ak)*:** Eluent: Hexane / EtOAc (5:1v/v), Light red

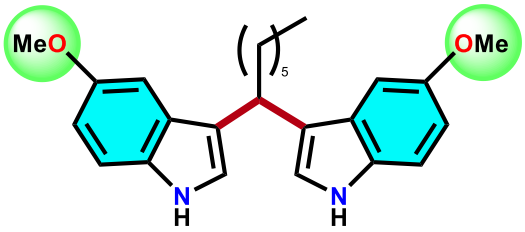

coloured oil; Eluent Yield: 281 mg (72%). **^{1}H NMR (300 MHz, $CDCl_3$):** δ 7.87 (s, 2H), 7.20 (t, *J* = 2.8 Hz, 2H), 7.07 (d, *J* = 2.5 Hz, 2H), 7.00 (d, *J* = 2.4 Hz, 2H), 6.91 (s, 2H), 4.39 (t, *J* = 7.4 Hz, 1H), 3.80 (s, 6H), 2.23 (p, *J* = 8.3 Hz, 2H), 1.42 – 1.26 (m, 8H), 0.87 (d, *J* = 7.1 Hz, 3H). **^{13}C{^{1}H} NMR (101 MHz, $CDCl_3$):** δ 153.64, 131.98, 127.74, 122.40, 120.31, 112.45, 111.64, 102.07, 56.06, 35.62, 34.11, 32.13, 28.10, 22.79, 14.27.

***bis(2-methyl-1H-indol-3-yl)methane (14al)*:** Eluent: Hexane / EtOAc (5:1v/v), Colourless oil; Yield:

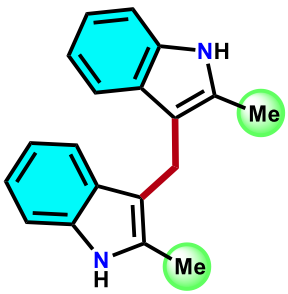

211 mg (77%). **^{1}H NMR (400 MHz, DMSO):** δ 10.63 (s, 2H), 7.21 (dd, *J* = 20.1, 8.4 Hz, 4H), 6.84 (dt, *J* = 42.9, 7.4 Hz, 4H), 3.97 (s, 2H), 2.36 (s, 6H). **^{13}C{^{1}H} NMR (101 MHz, DMSO):** δ 135.13, 131.14, 128.47, 119.64, 117.81, 117.71, 110.19, 109.69, 18.84, 11.57.

5.6.2 Copies of NMR spectra (^{1}H, ^{13}C and ^{19}F) of all synthesized bis(indolyl)methanes

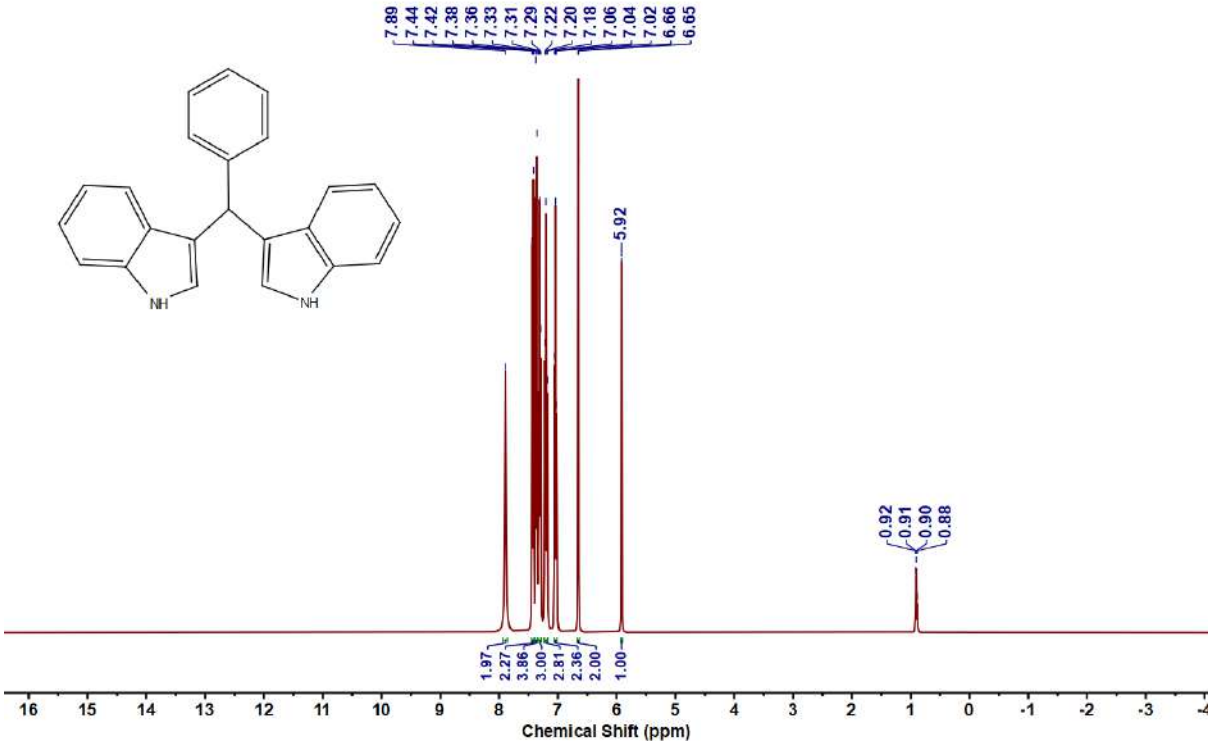

Figure 5.6.A17: ^{1}H NMR spectrum of **8aa**

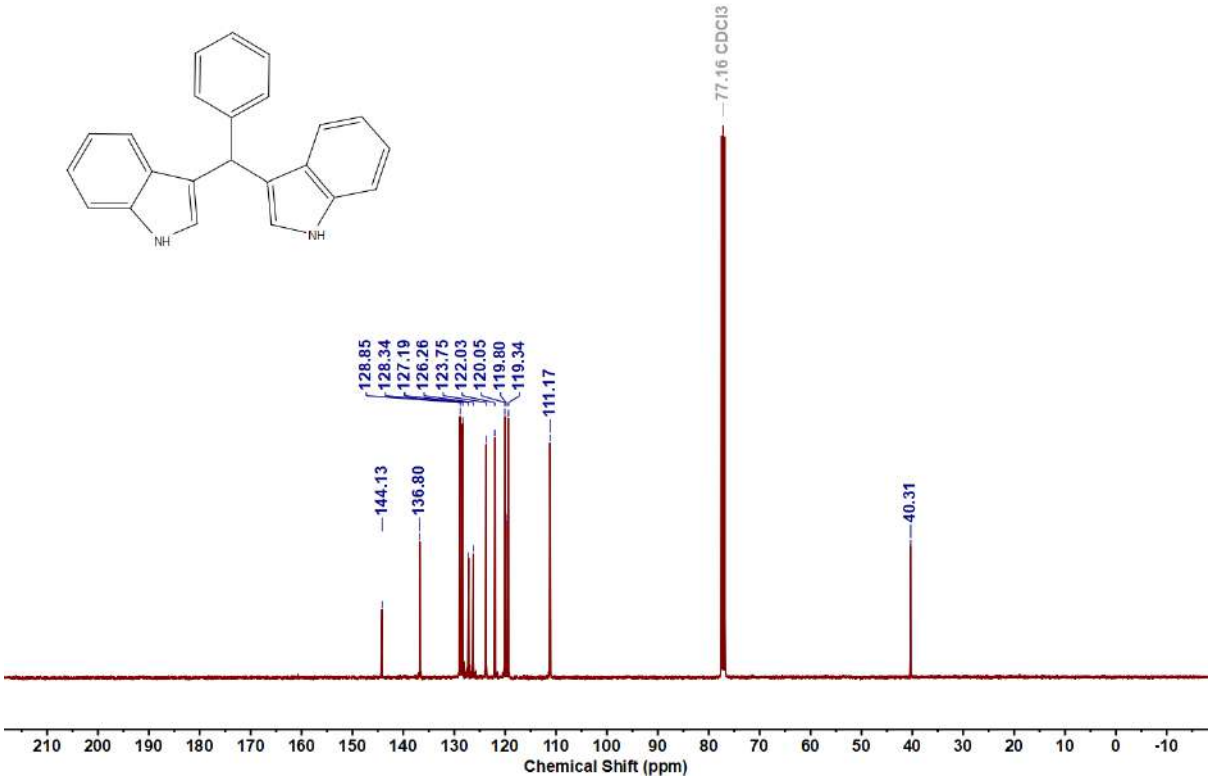

Figure 5.6.A18: $^{13}C\{^{1}H\}$ NMR spectrum of **8aa**

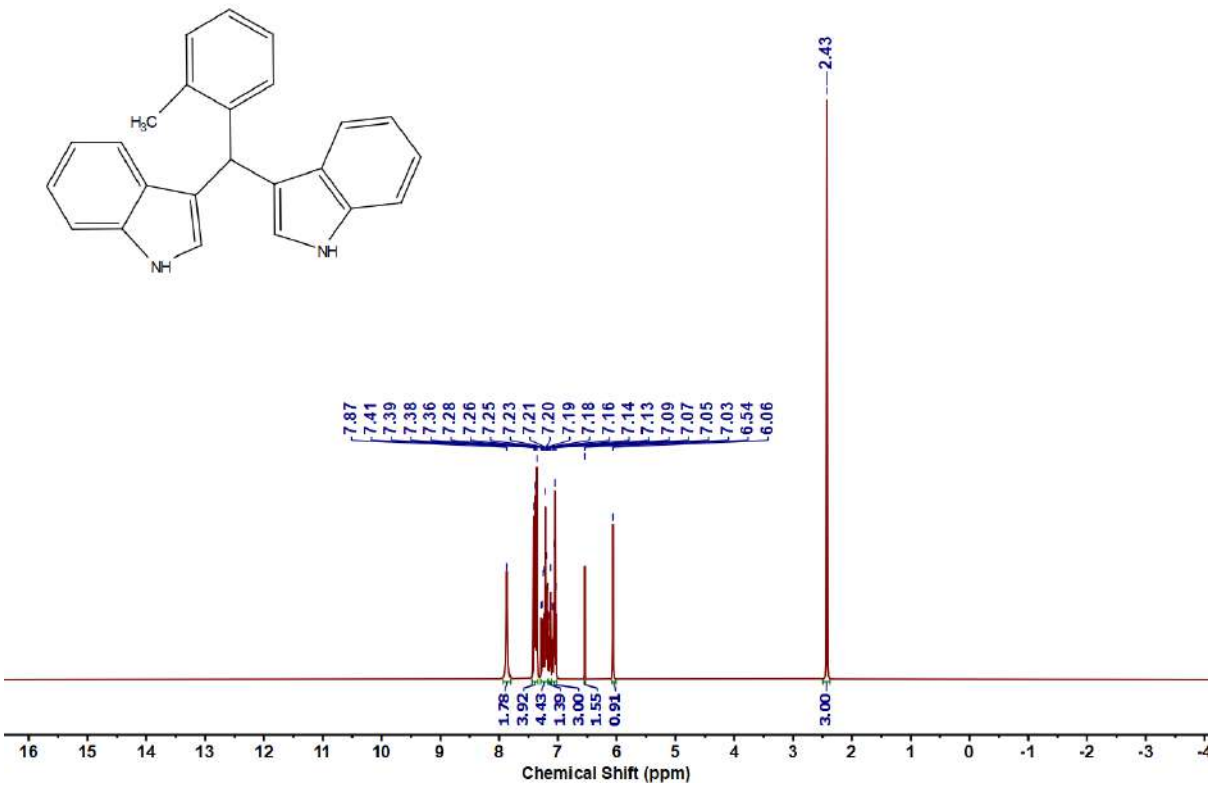

Figure 5.6.A19: ^{1}H NMR spectrum of **8ab**

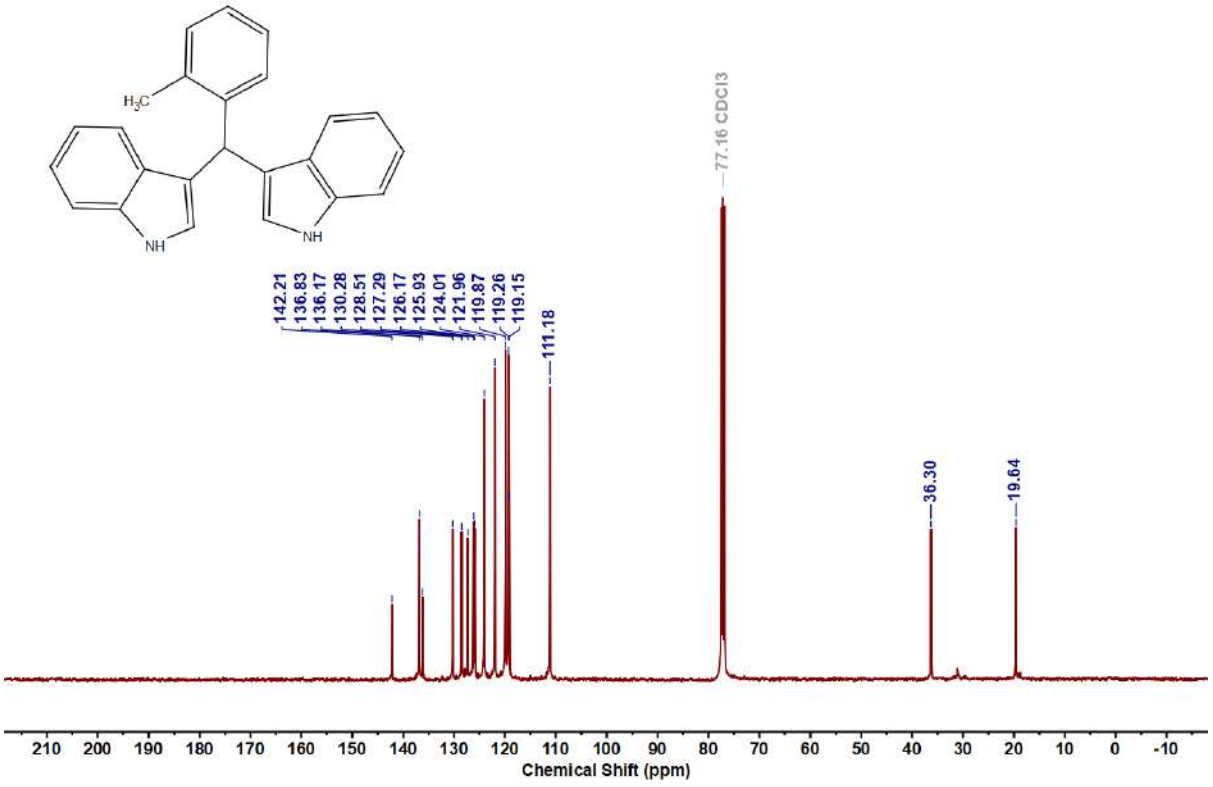

Figure 5.6.A20: ^{13}C{^{1}H} NMR spectrum of **8ab**

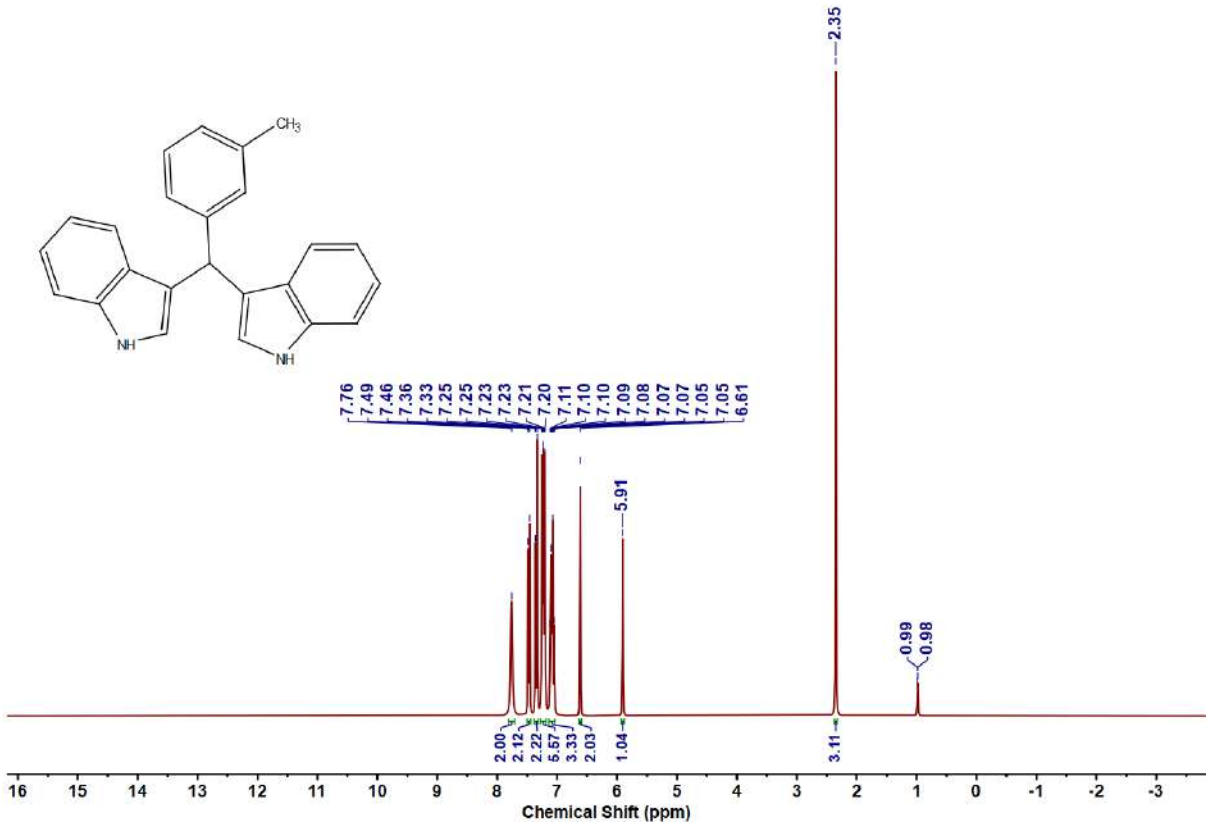

Figure 5.6.A21: ^{1}H NMR spectrum of **8ac**

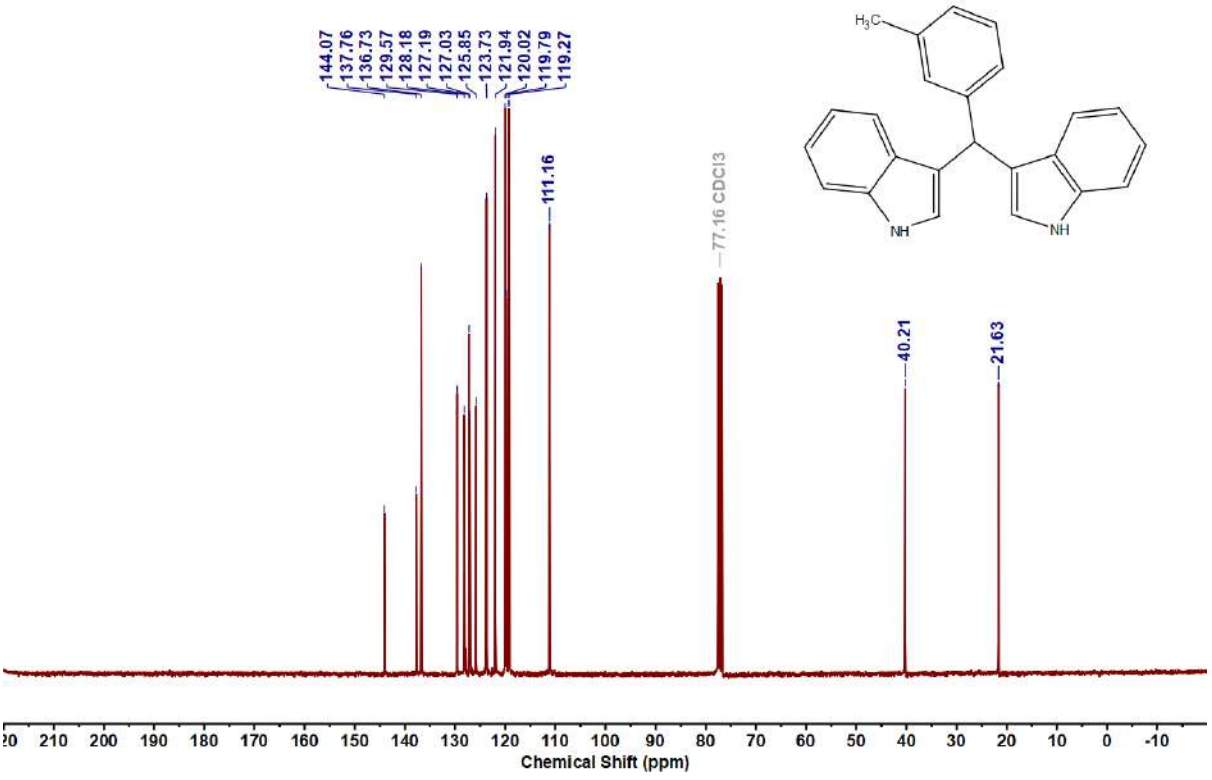

Figure 5.6.A22: ^{13}C{^{1}H} NMR spectrum of **8ac**

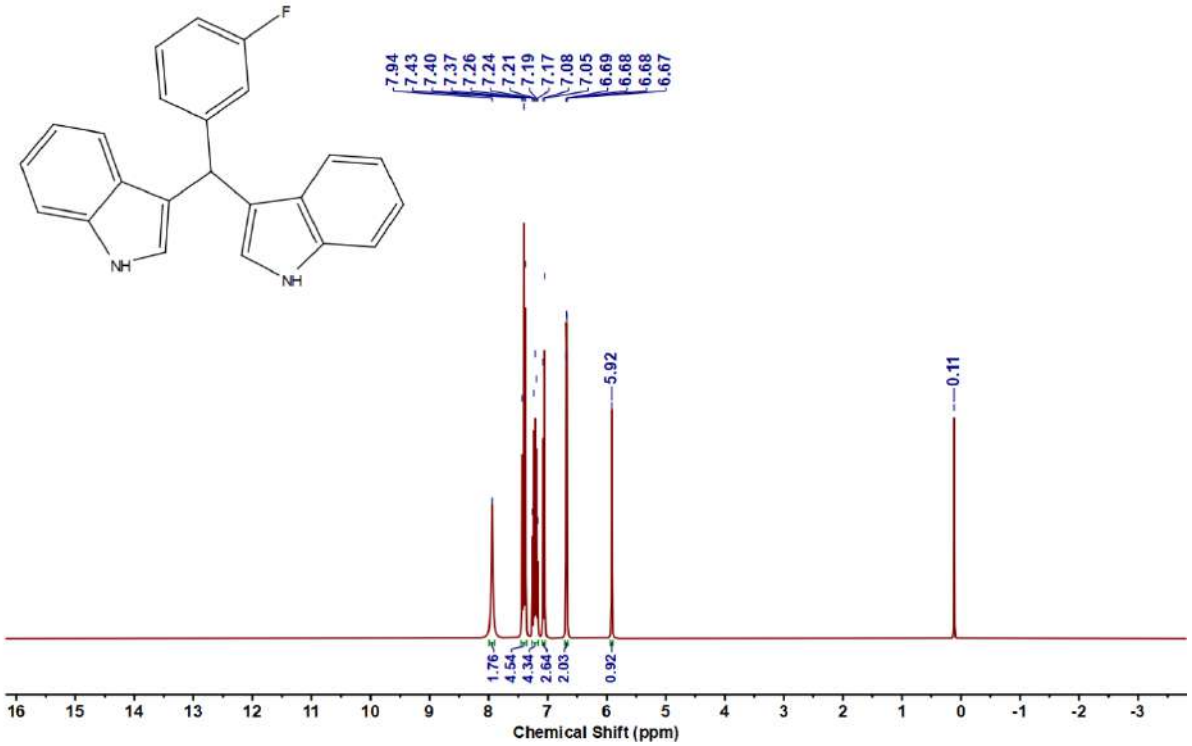

Figure 5.6.A23: ^{1}H NMR spectrum of **8ad**

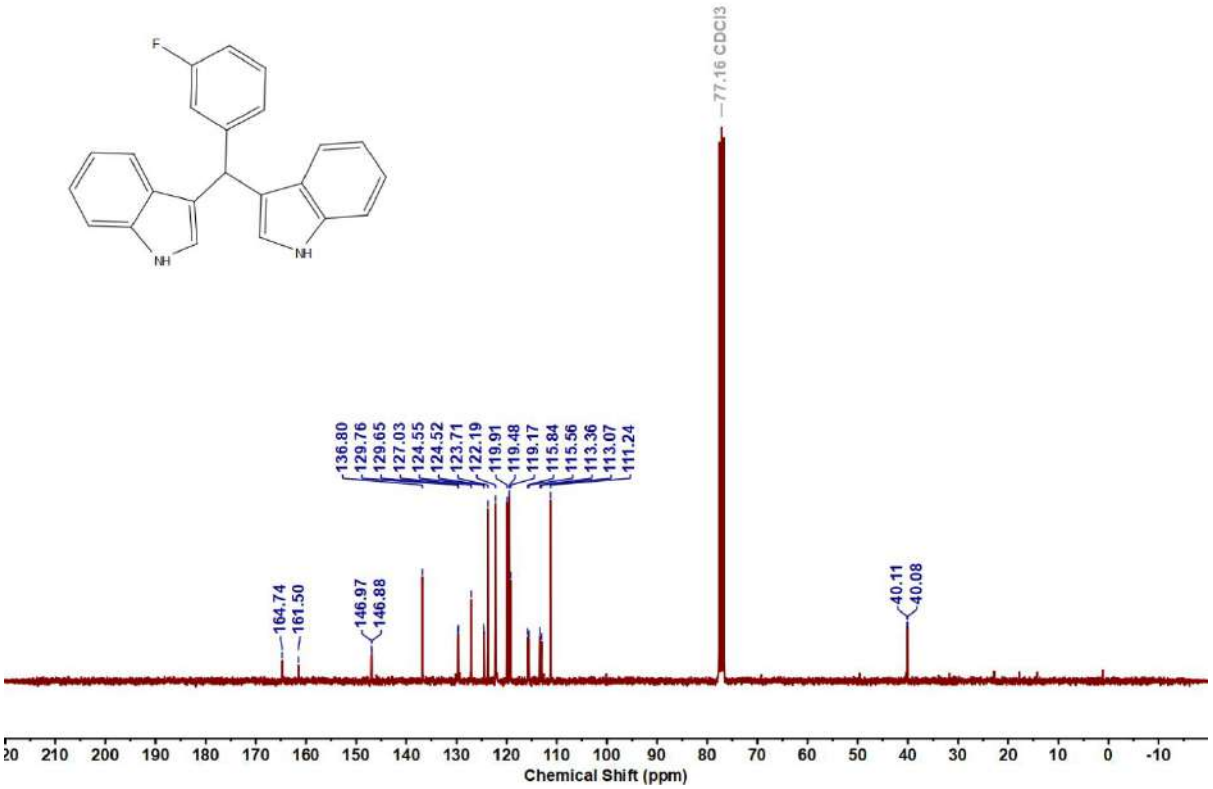

Figure 5.6.A24: $^{13}C\{^{1}H\}$ NMR spectrum of **8ad**

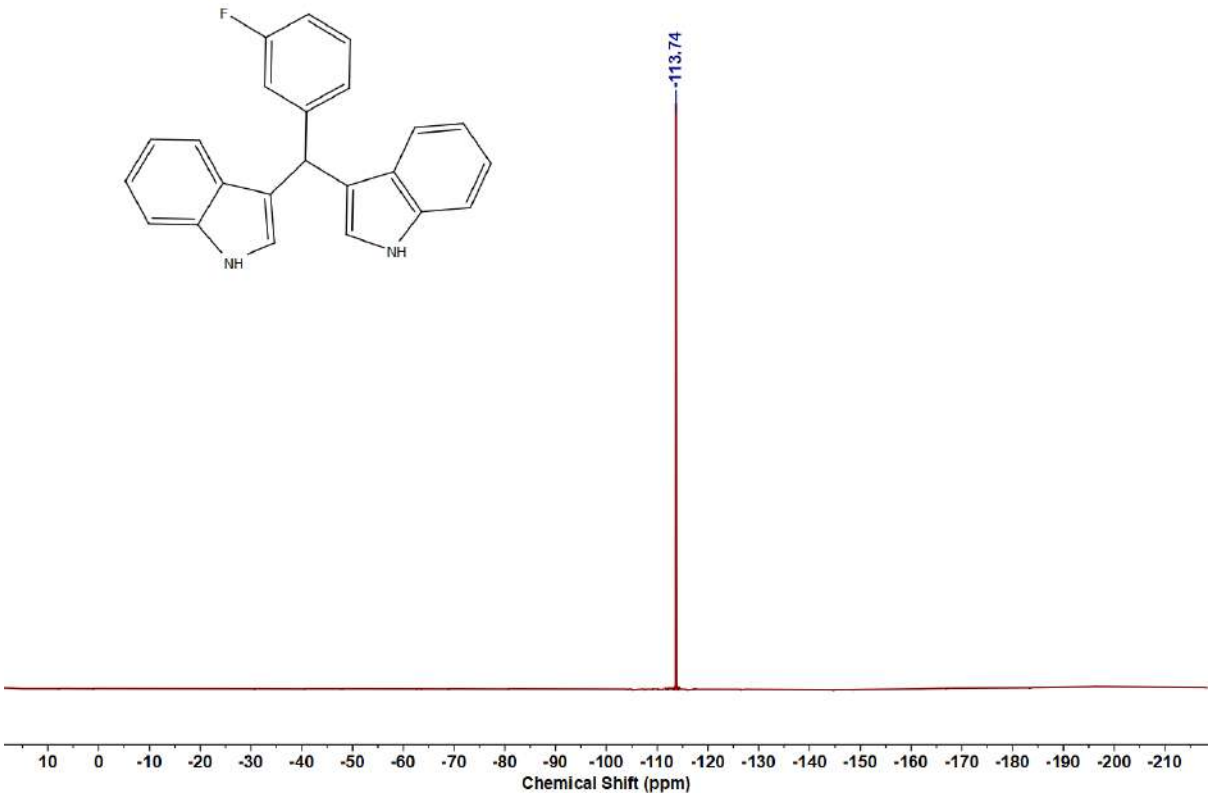

Figure 5.6.A25: ^{19}F NMR spectrum of **8ad**

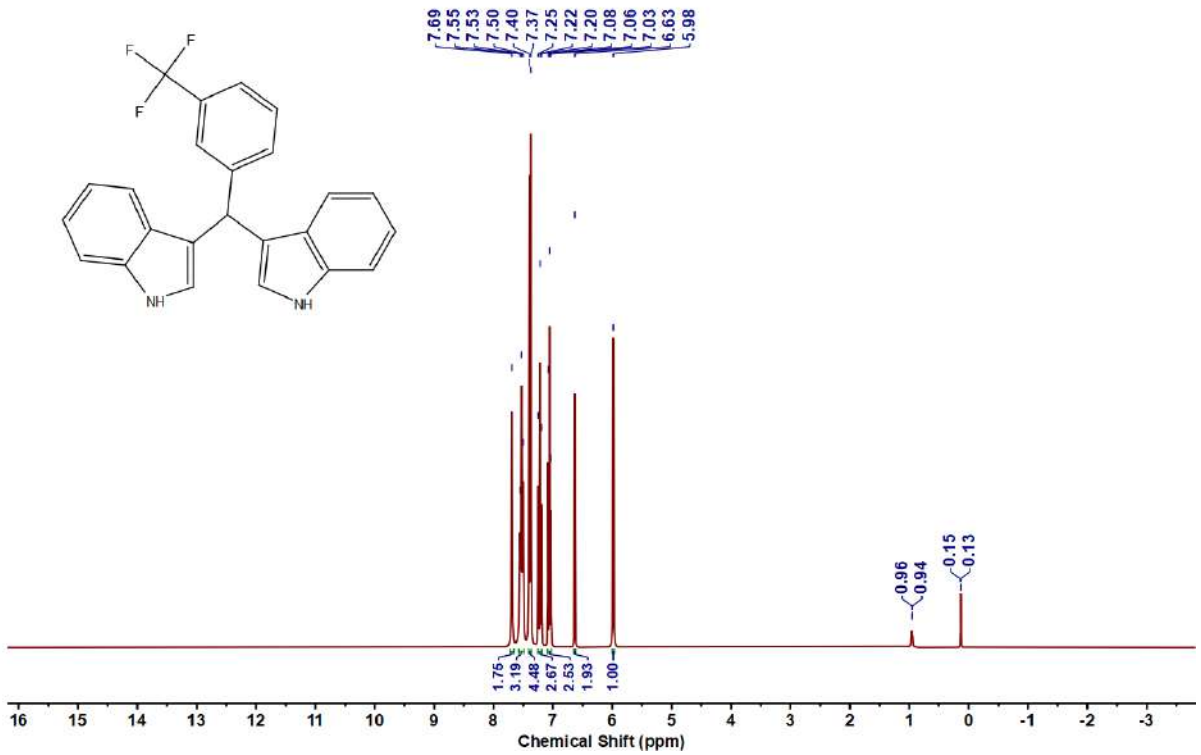

Figure 5.6.A26: ^{1}H NMR spectrum of **8ae**

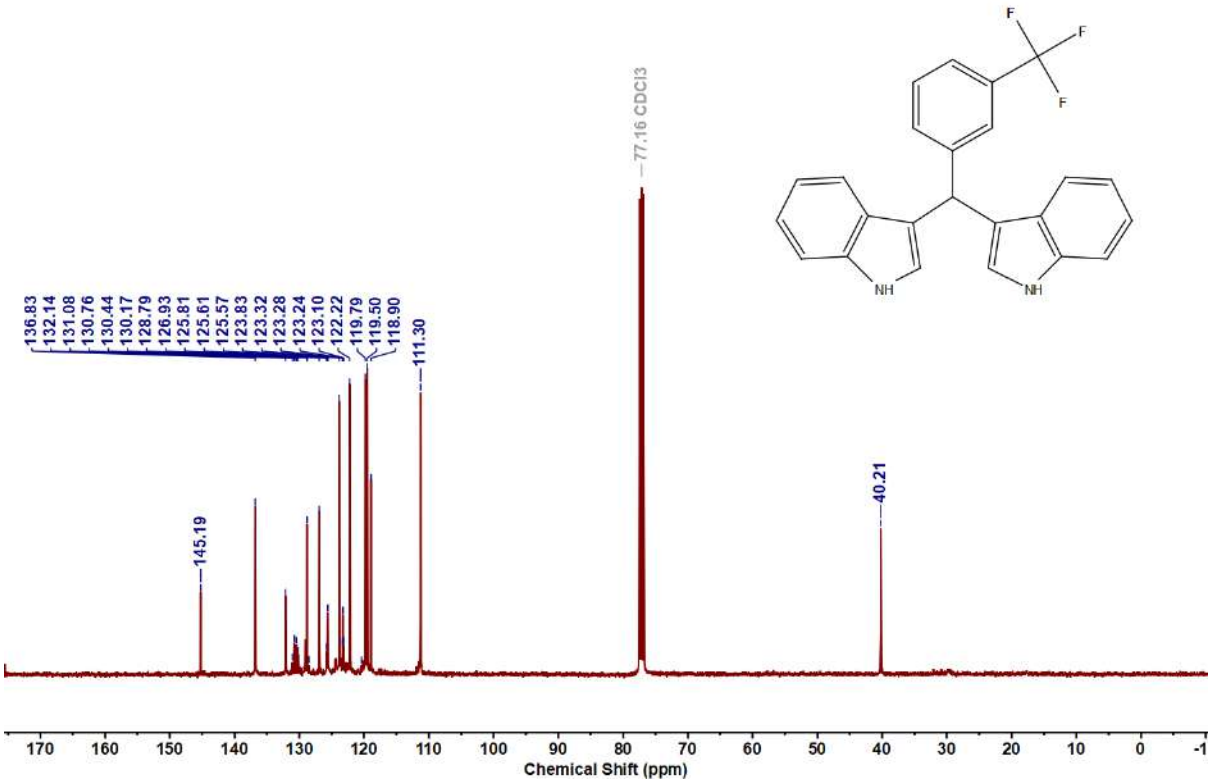

Figure 5.6.A27: $^{13}C\{^{1}H\}$ NMR spectrum of **8ae**

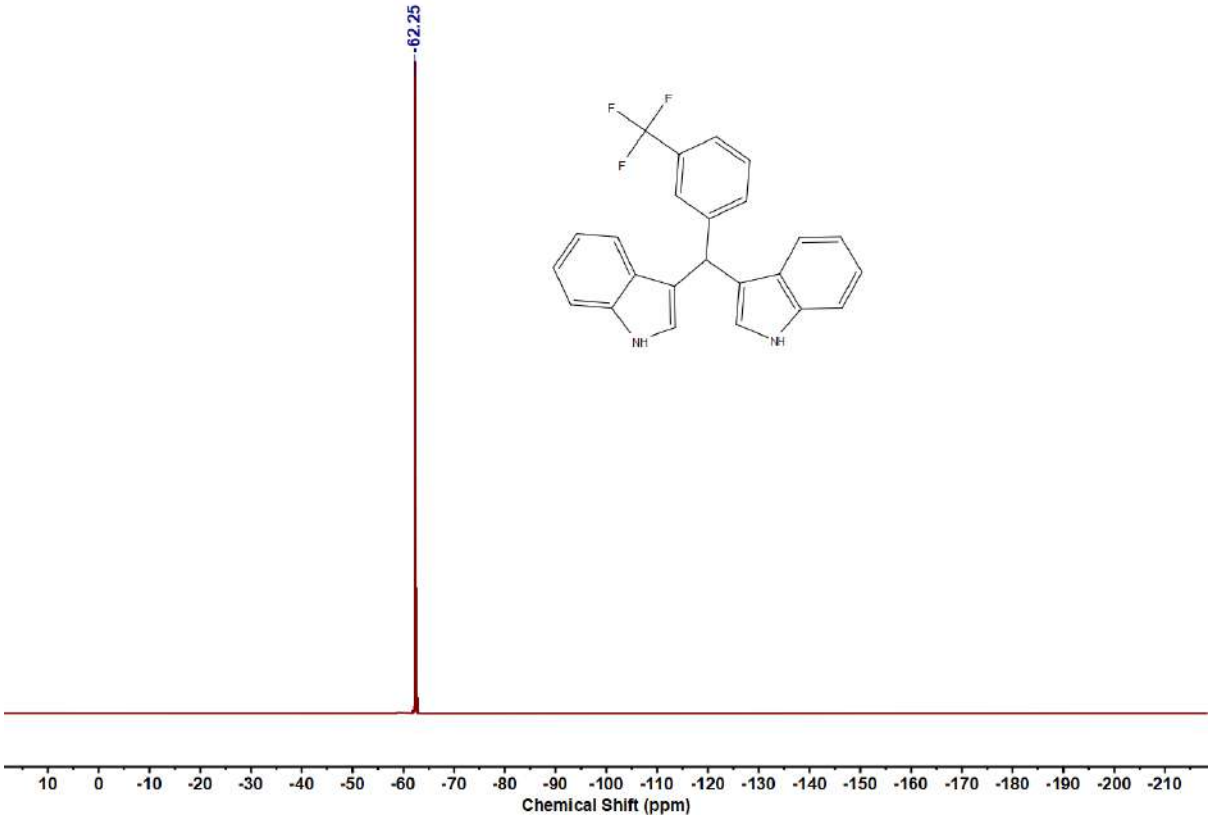

Figure 5.6.A28: ^{19}F NMR spectrum of **8ad**

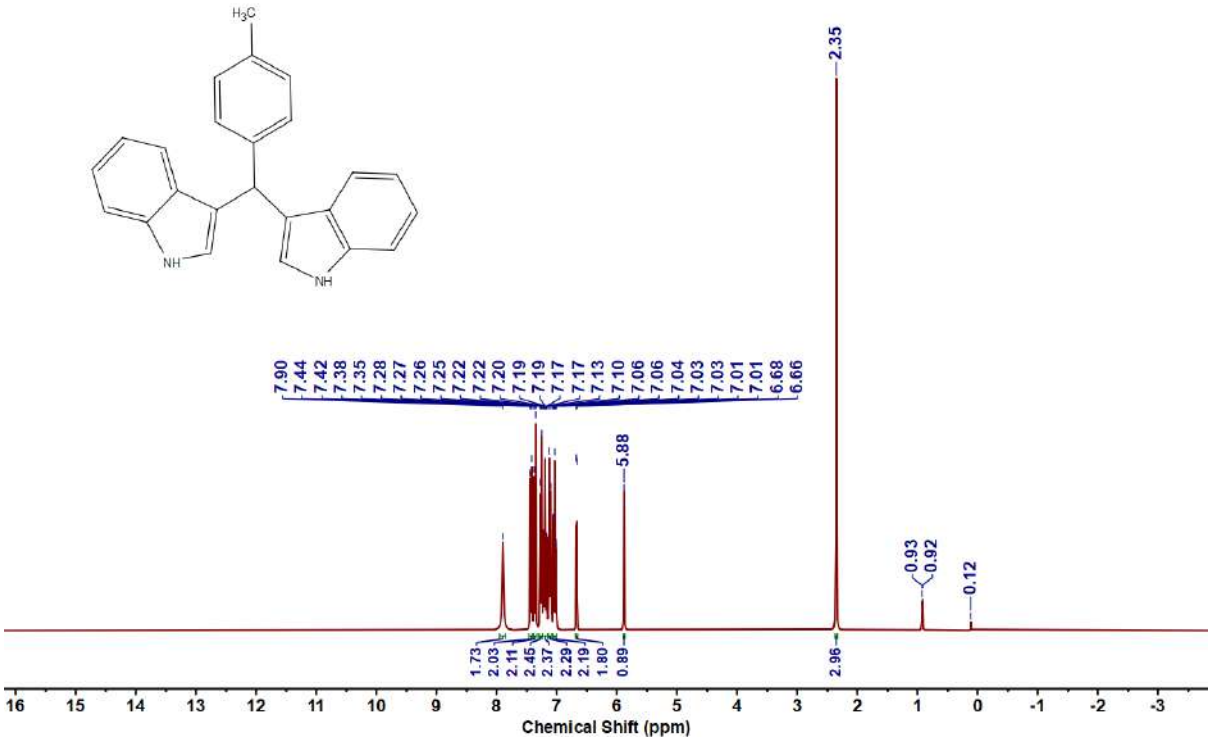

Figure 5.6.A29: ^{1}H NMR spectrum of **8af**

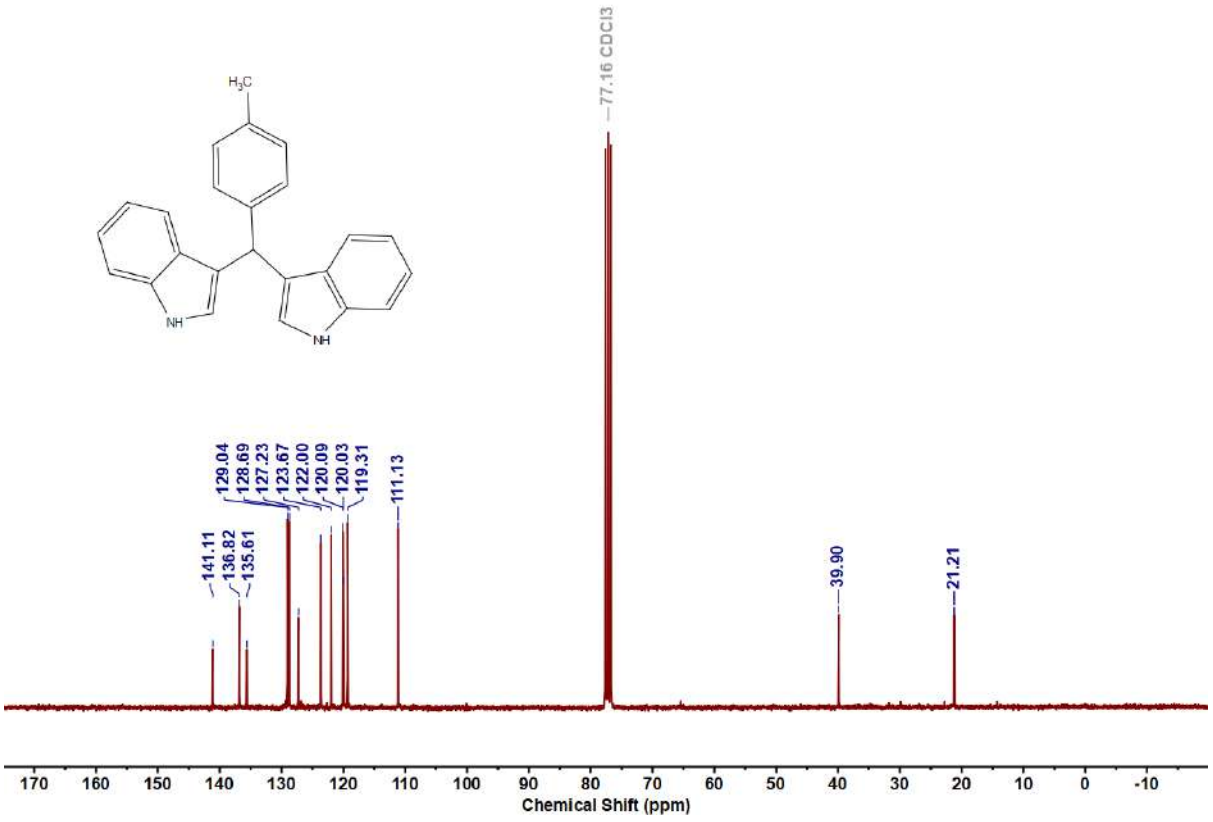

Figure 5.6.A30: ^{13}C{^{1}H} NMR spectrum of **8af**

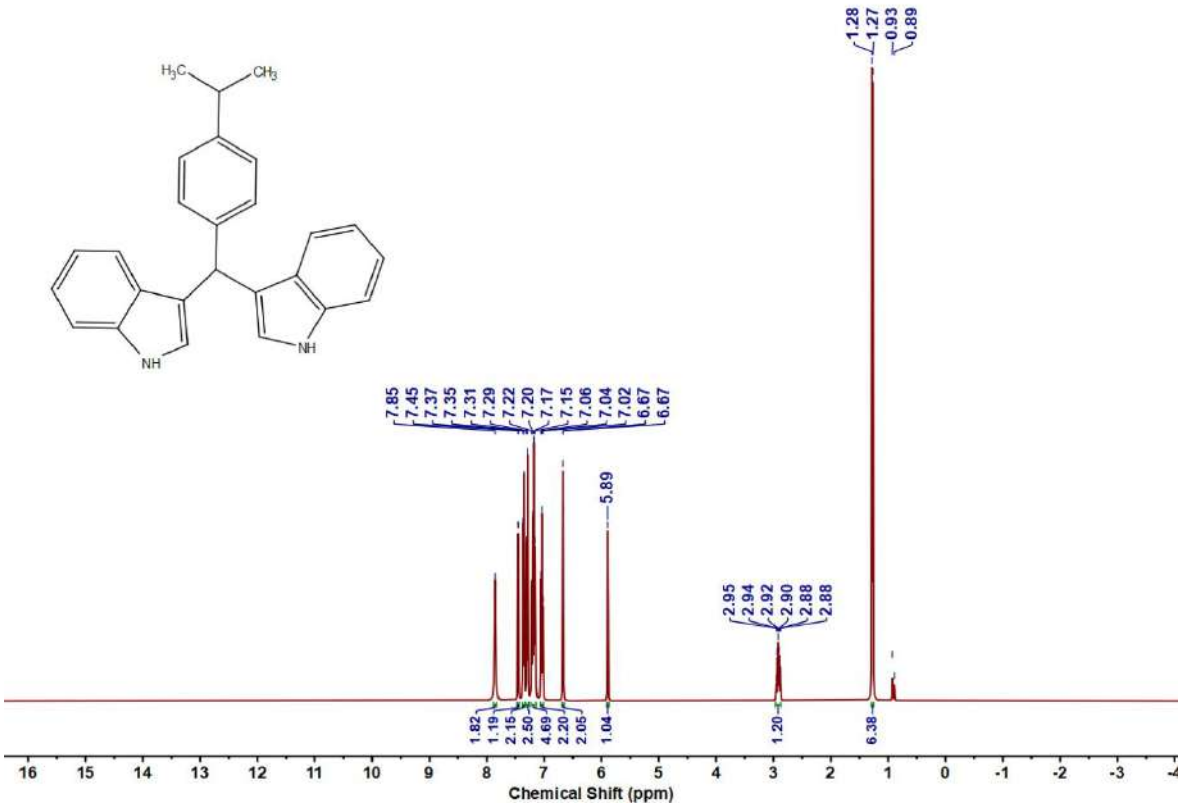

Figure 5.6.A31: ^{1}H NMR spectrum of **8ag**

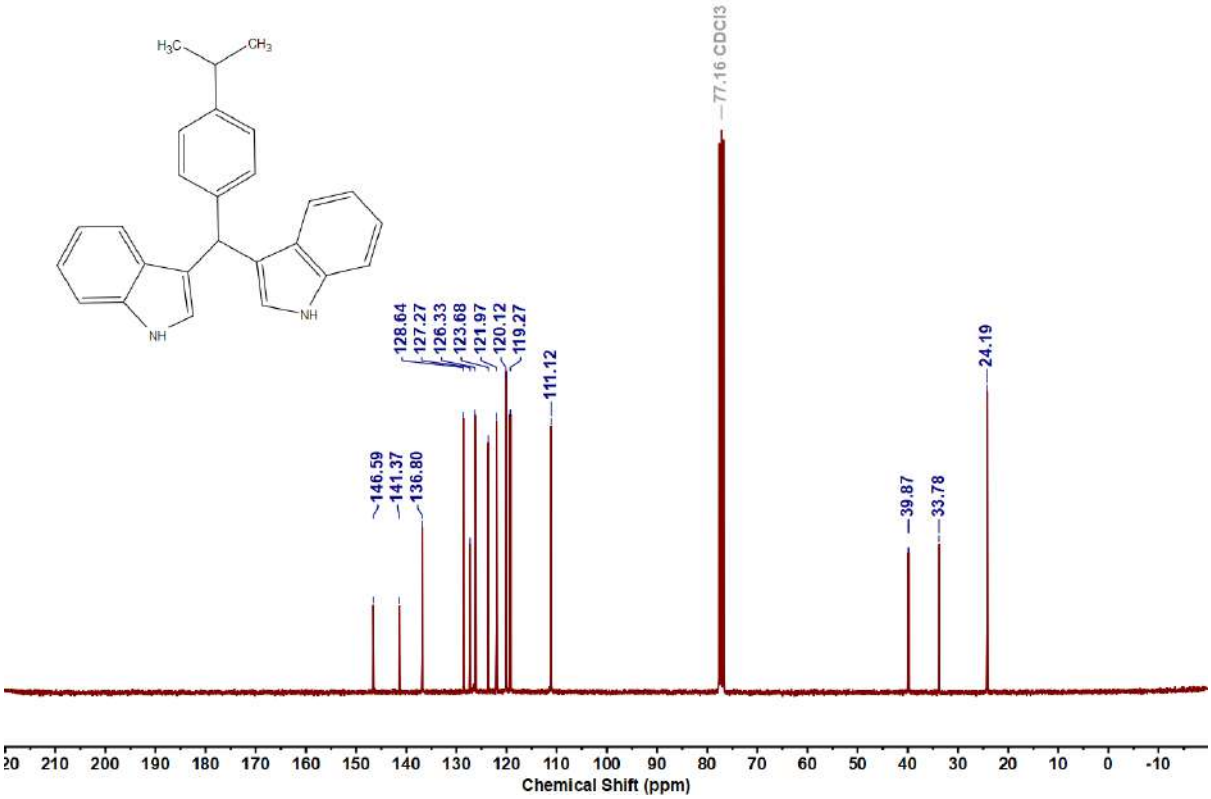

Figure 5.6.A32: ^{13}C{^{1}H} NMR spectrum of **8ag**

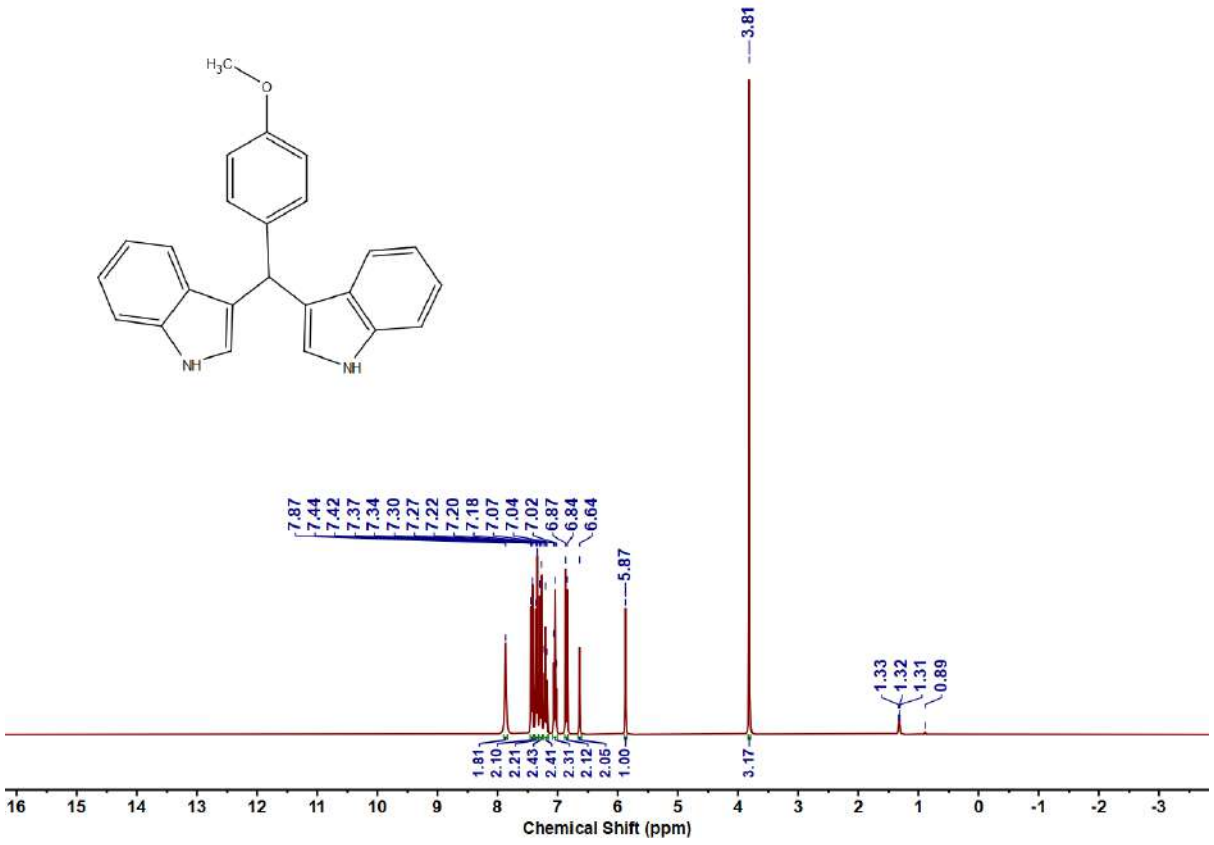

Figure 5.6.A33: ^{1}H NMR spectrum of **8ah**

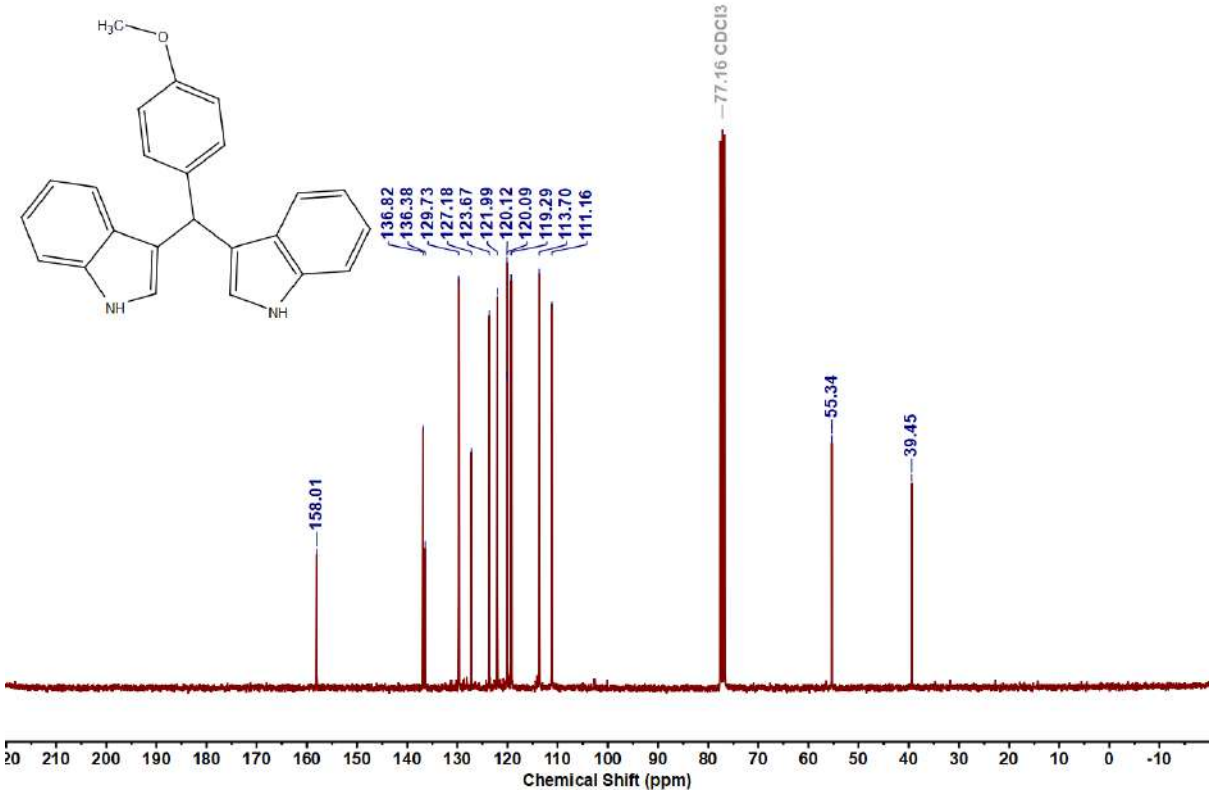

Figure 5.6.A34: ^{13}C{^{1}H} NMR spectrum of **8ah**

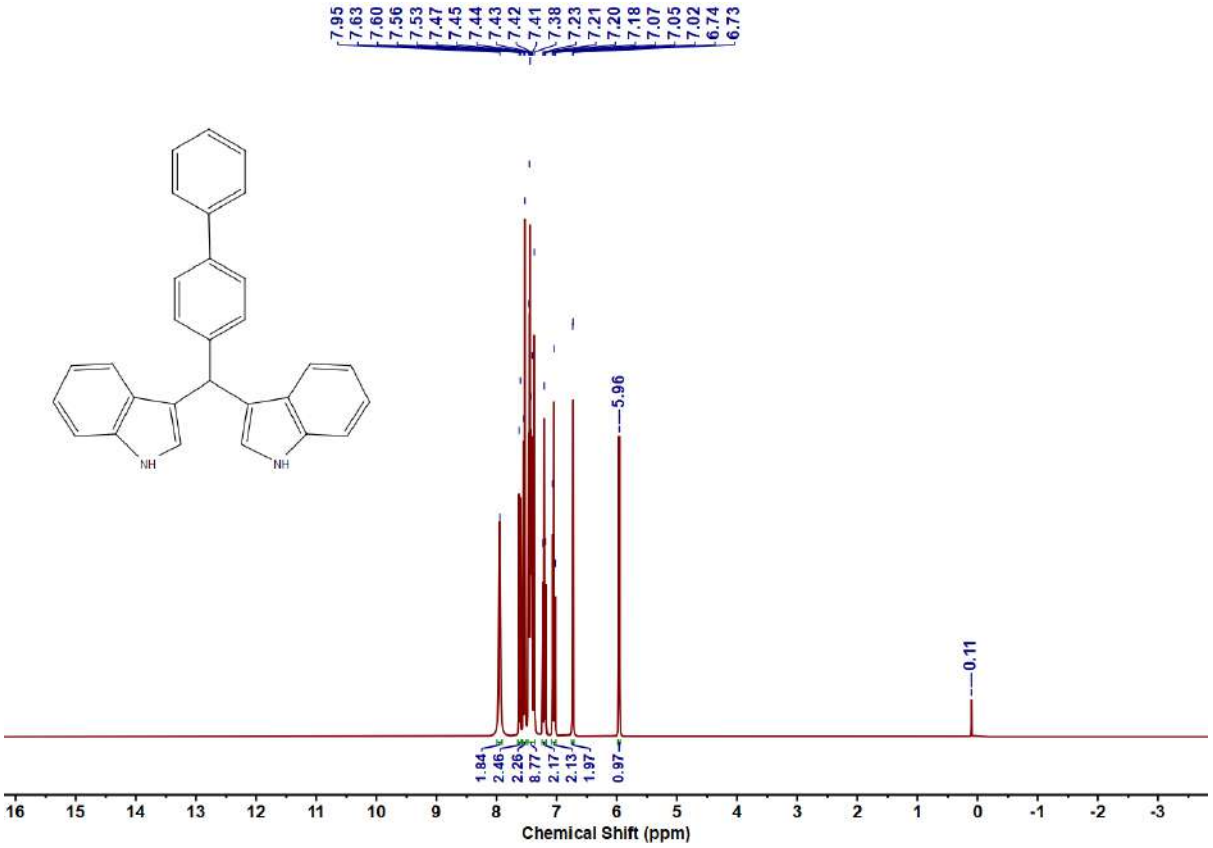

Figure 5.6.A35: ^{1}H NMR spectrum of **8ai**

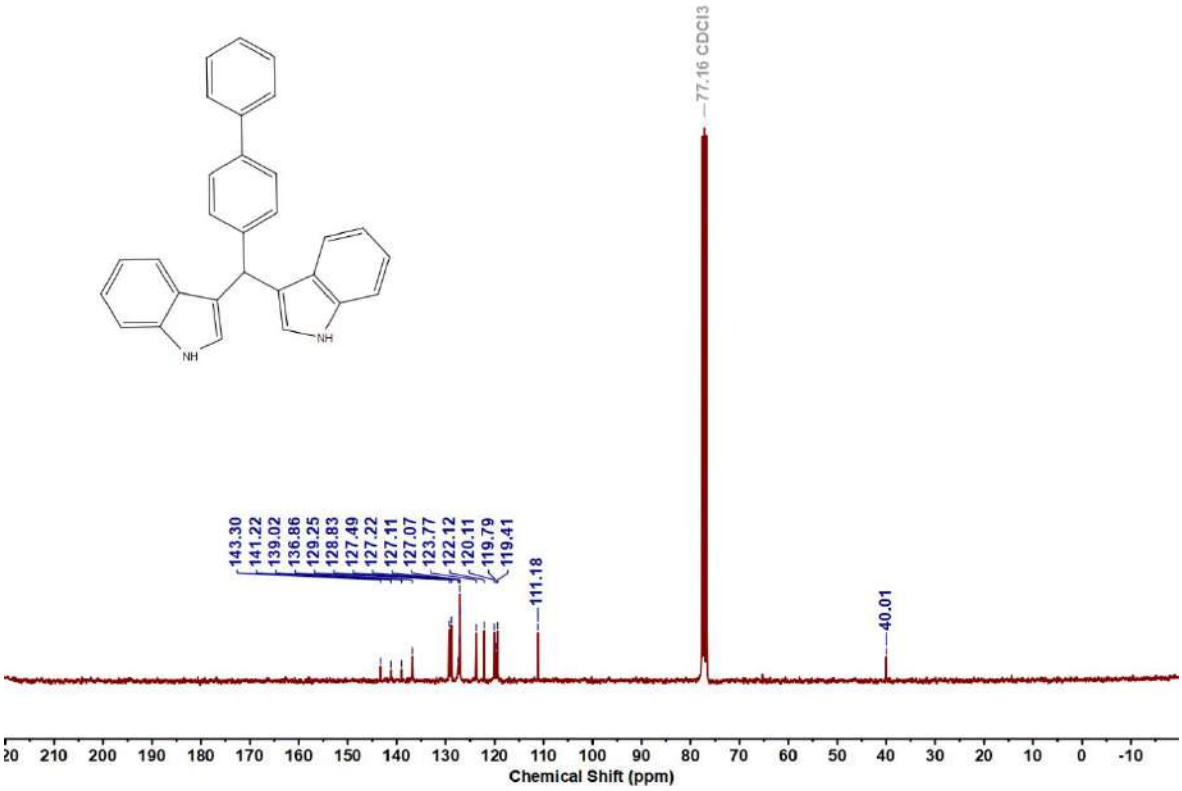

Figure 5.6.A36: $^{13}C\{^{1}H\}$ NMR spectrum of **8ai**

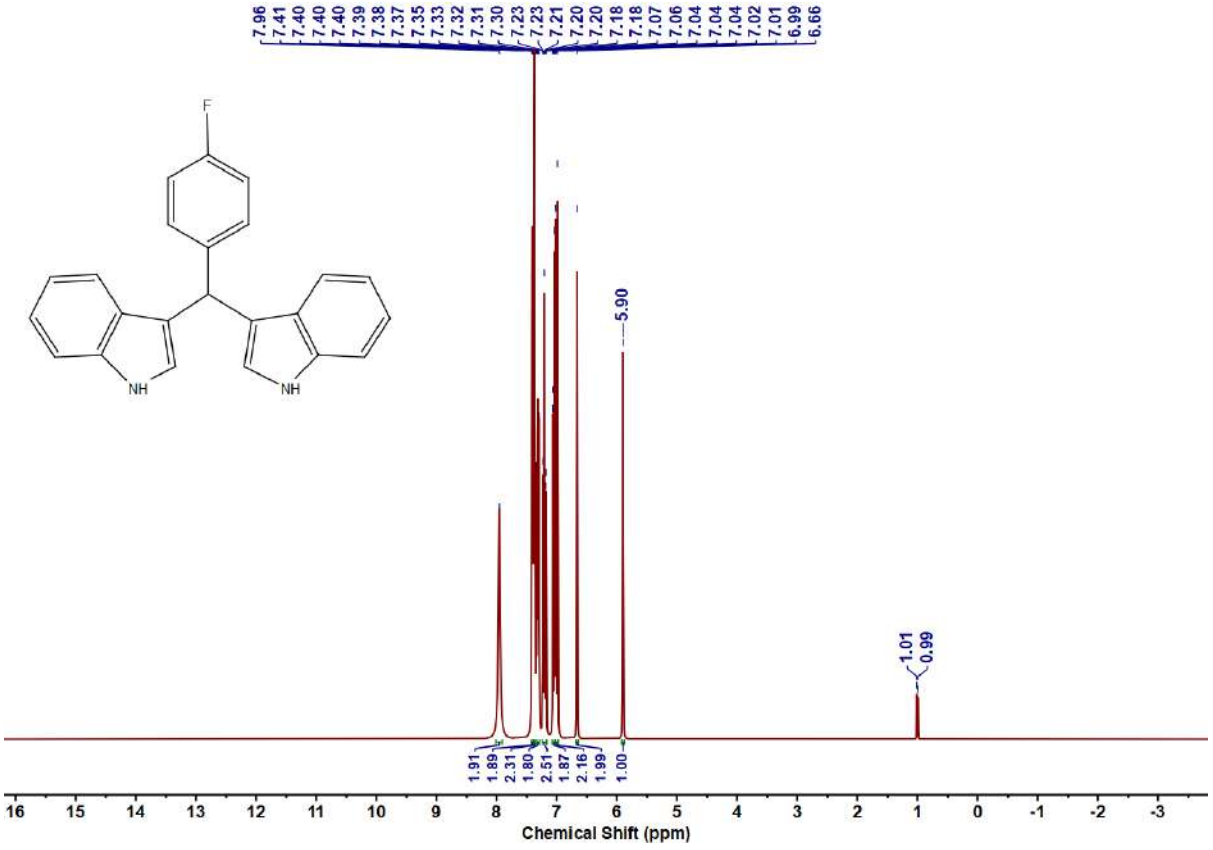

Figure 5.6.A37: ^{1}H NMR spectrum of **8aj**

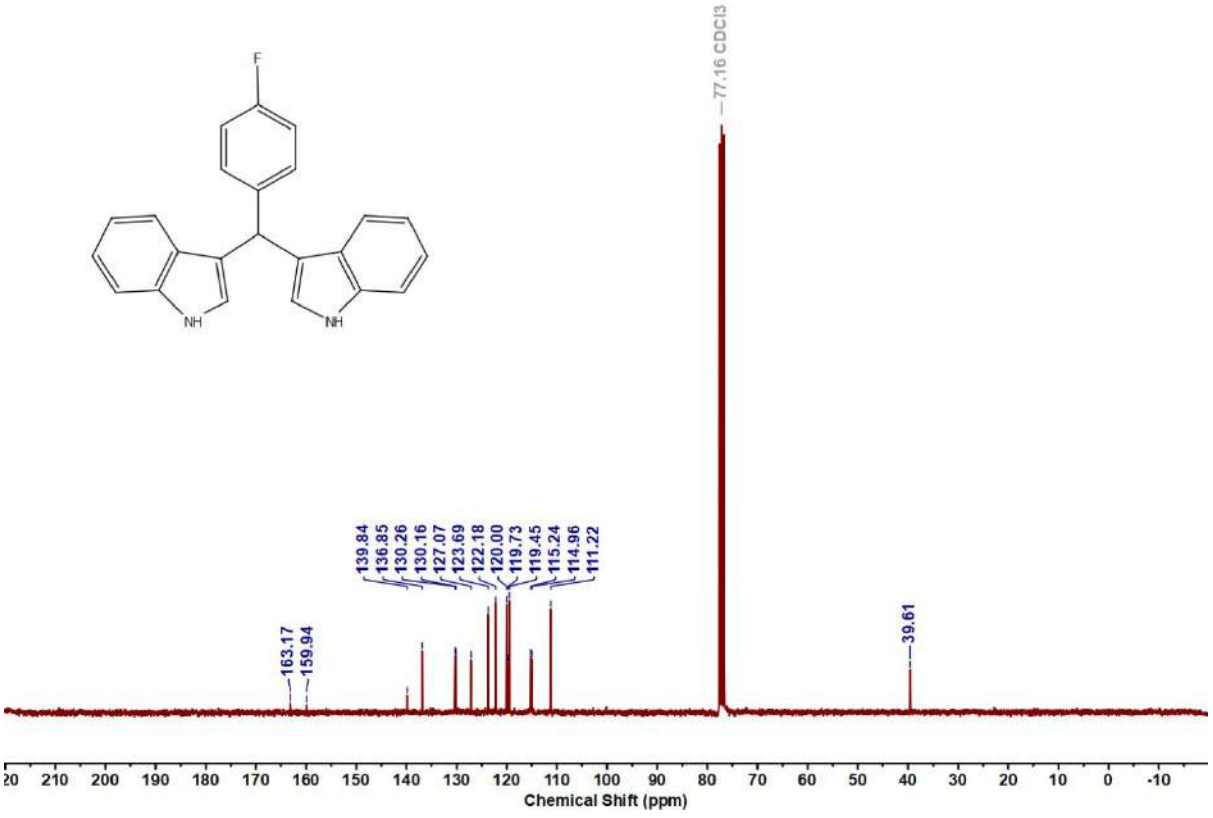

Figure 5.6.A38: ^{13}C{^{1}H} NMR spectrum of **8aj**

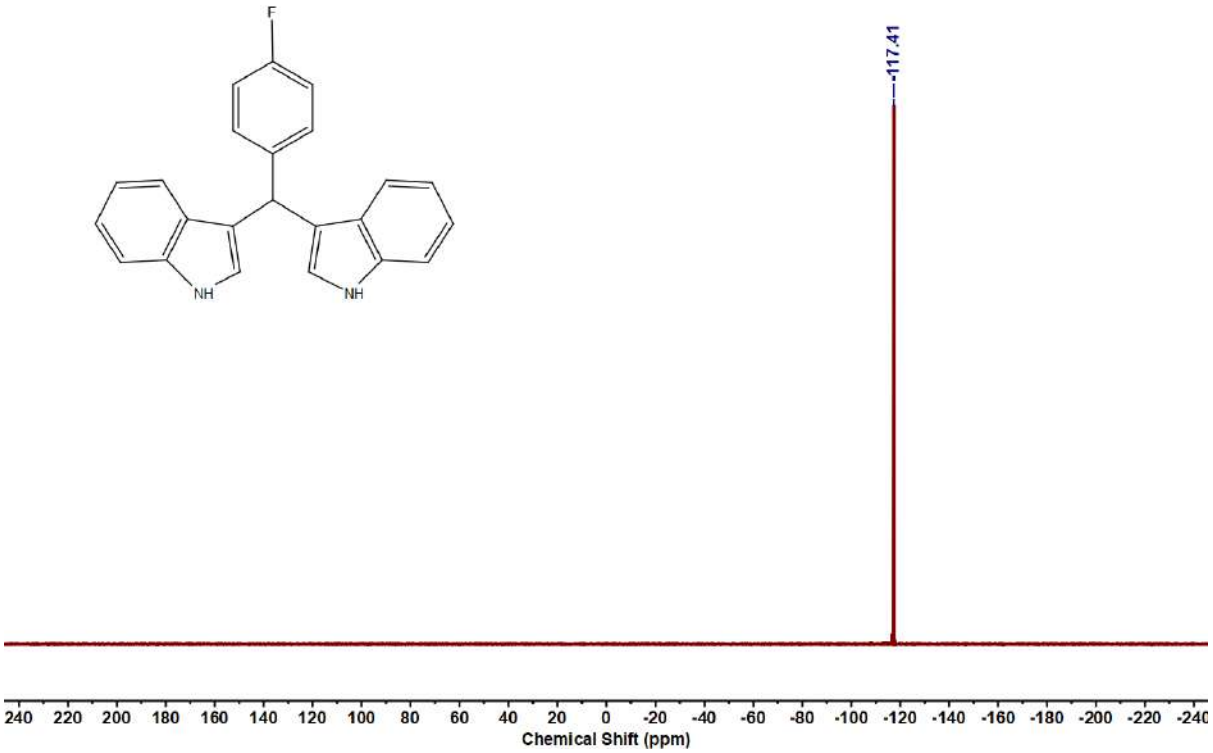

Figure 5.6.A39: ^{19}F NMR spectrum of **8aj**

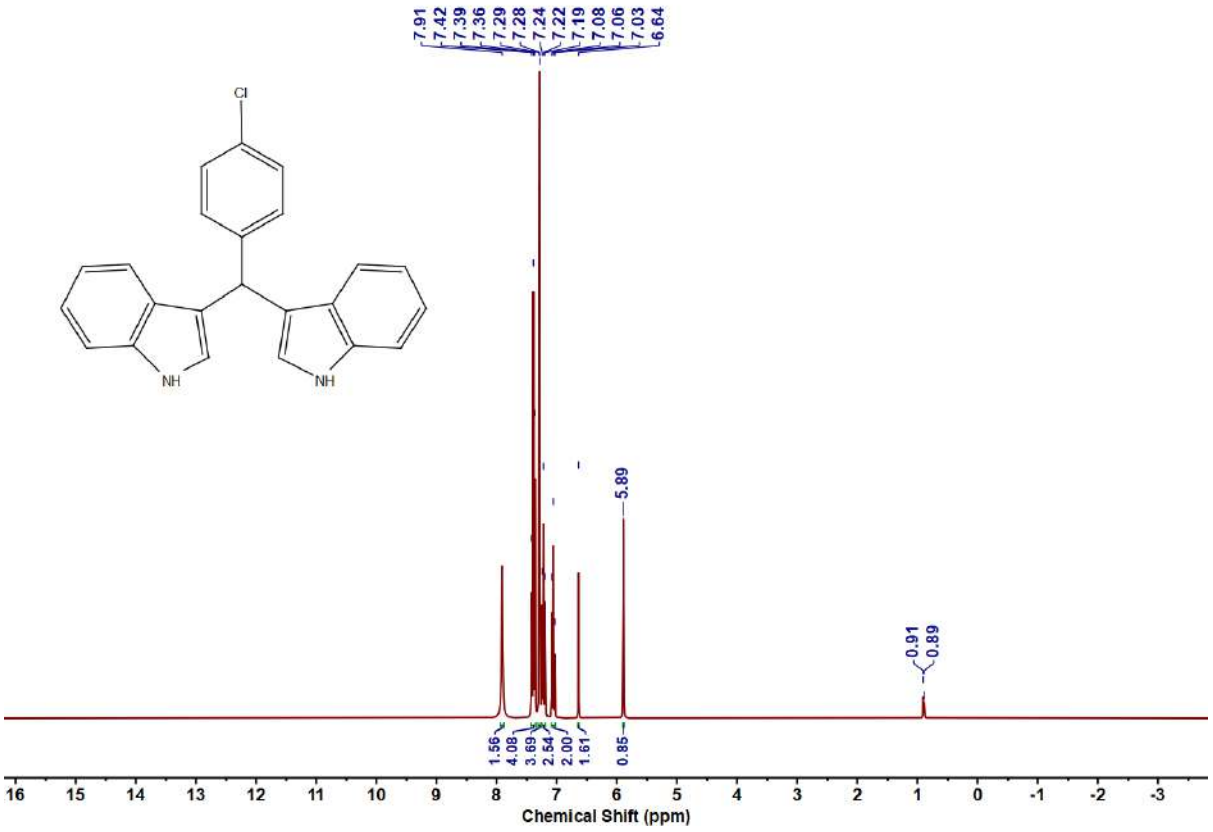

Figure 5.6.A40: ^{1}H NMR spectrum of **8ak**

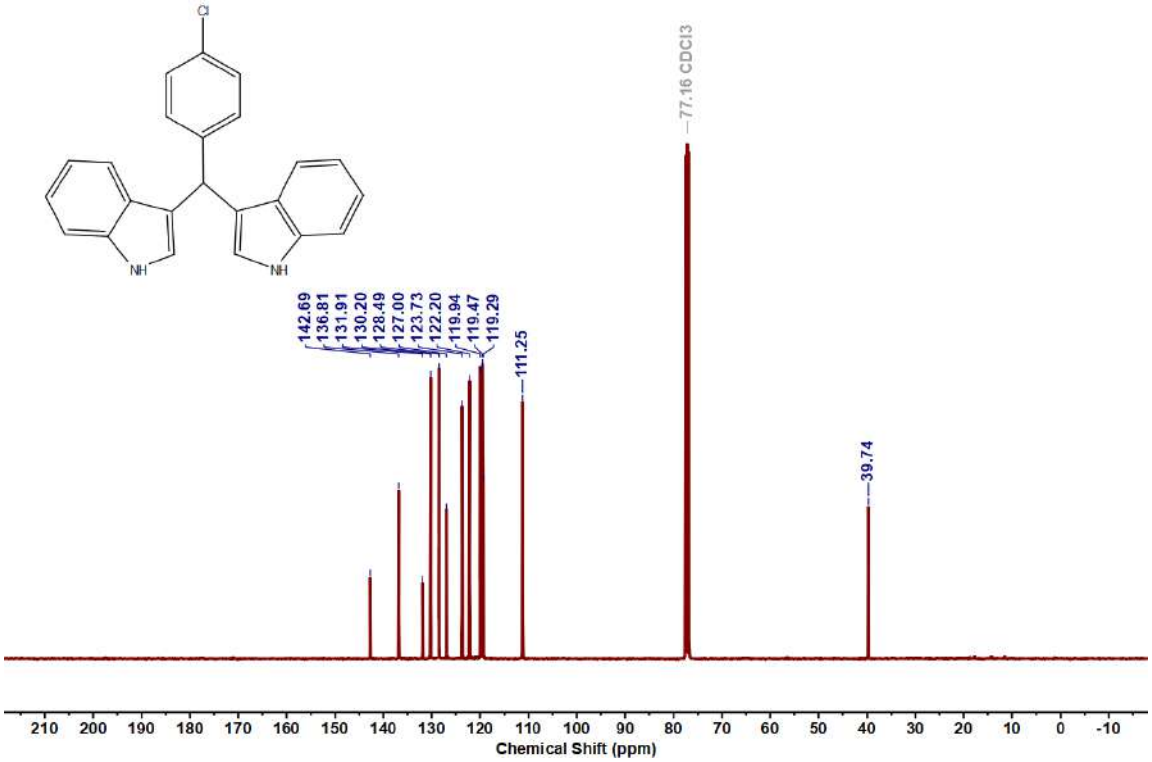

Figure 5.6.A41: $^{13}C\{^{1}H\}$ NMR spectrum of **8ak**

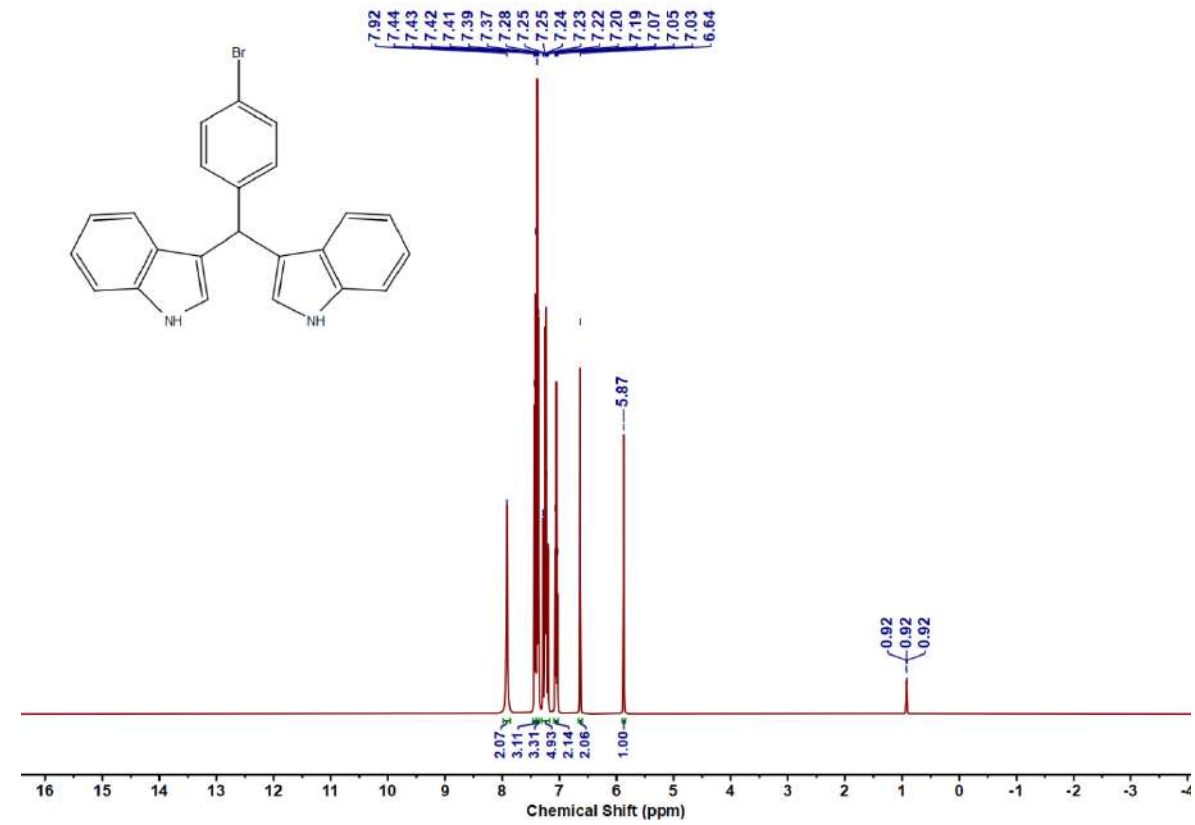

Figure 5.6.A42: ^{1}H NMR spectrum of **8al**

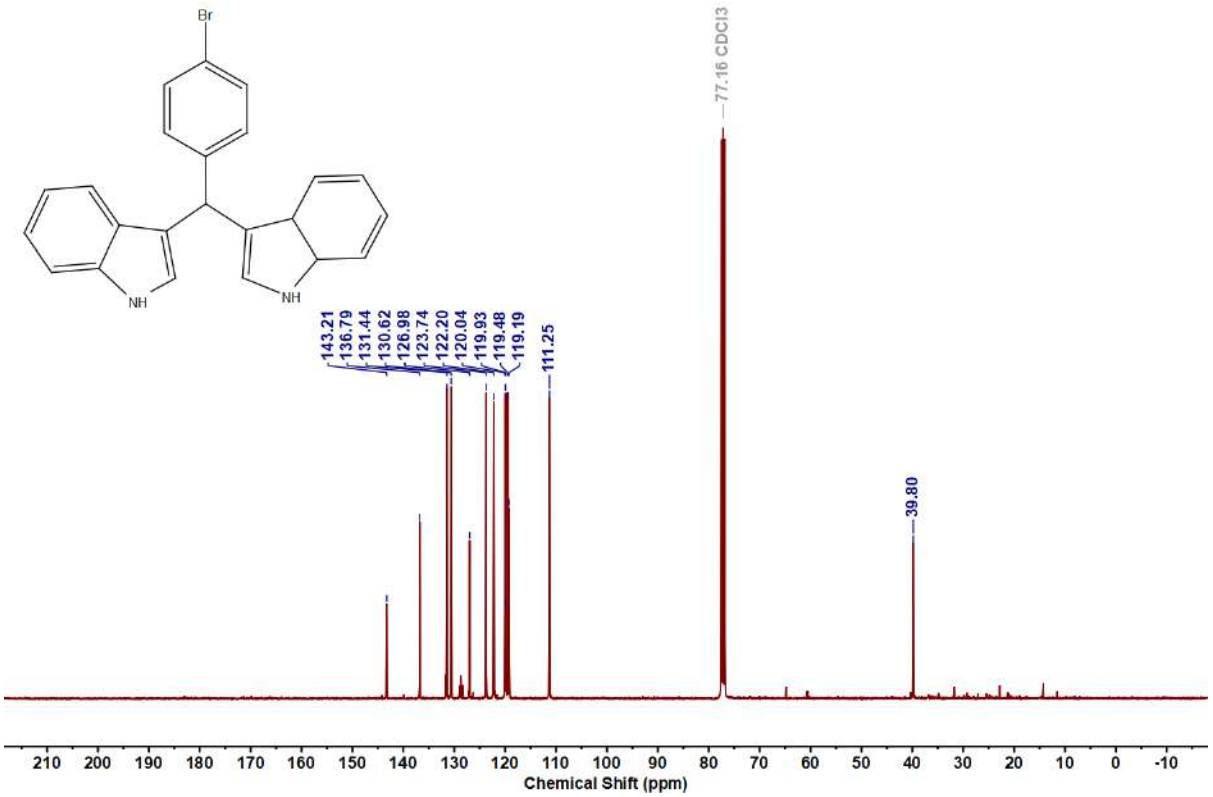

Figure 5.6.A43: $^{13}C\{^{1}H\}$ NMR spectrum of **8al**

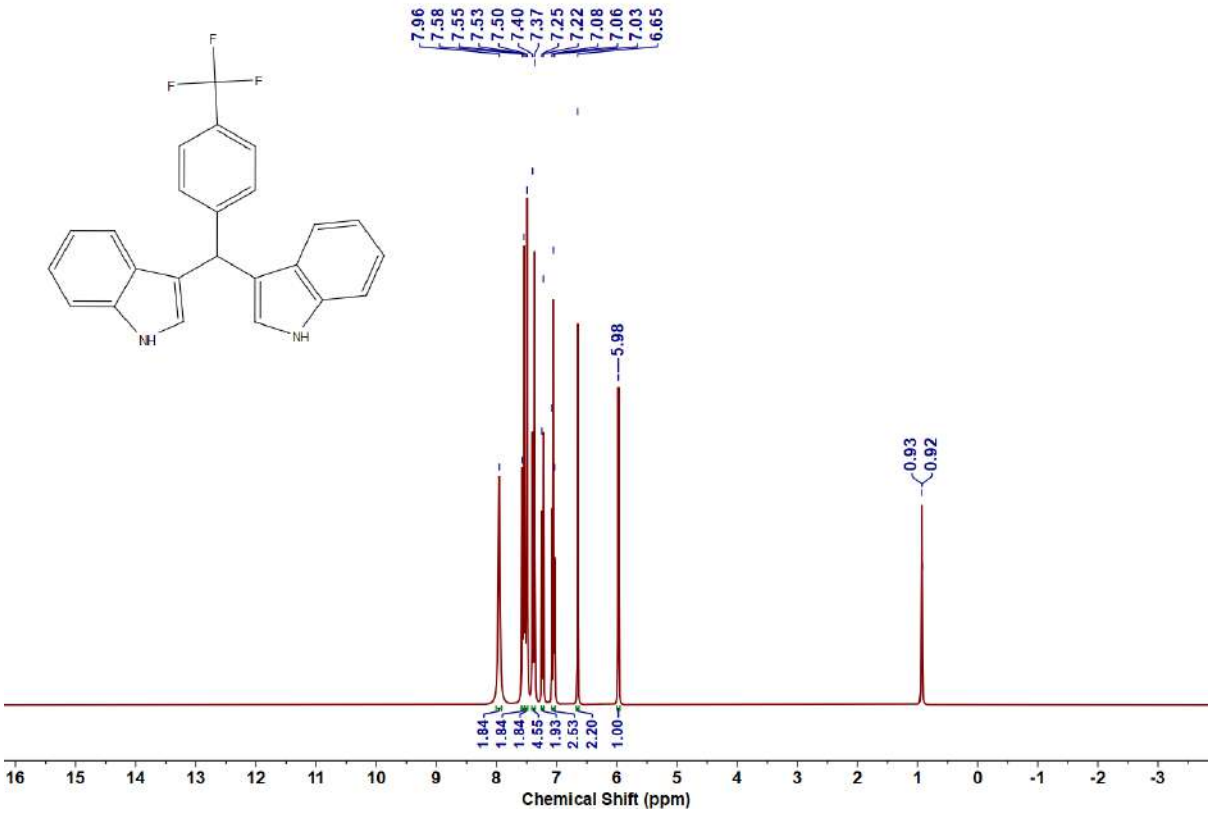

Figure 5.6.A44: ^{1}H NMR spectrum of **8am**

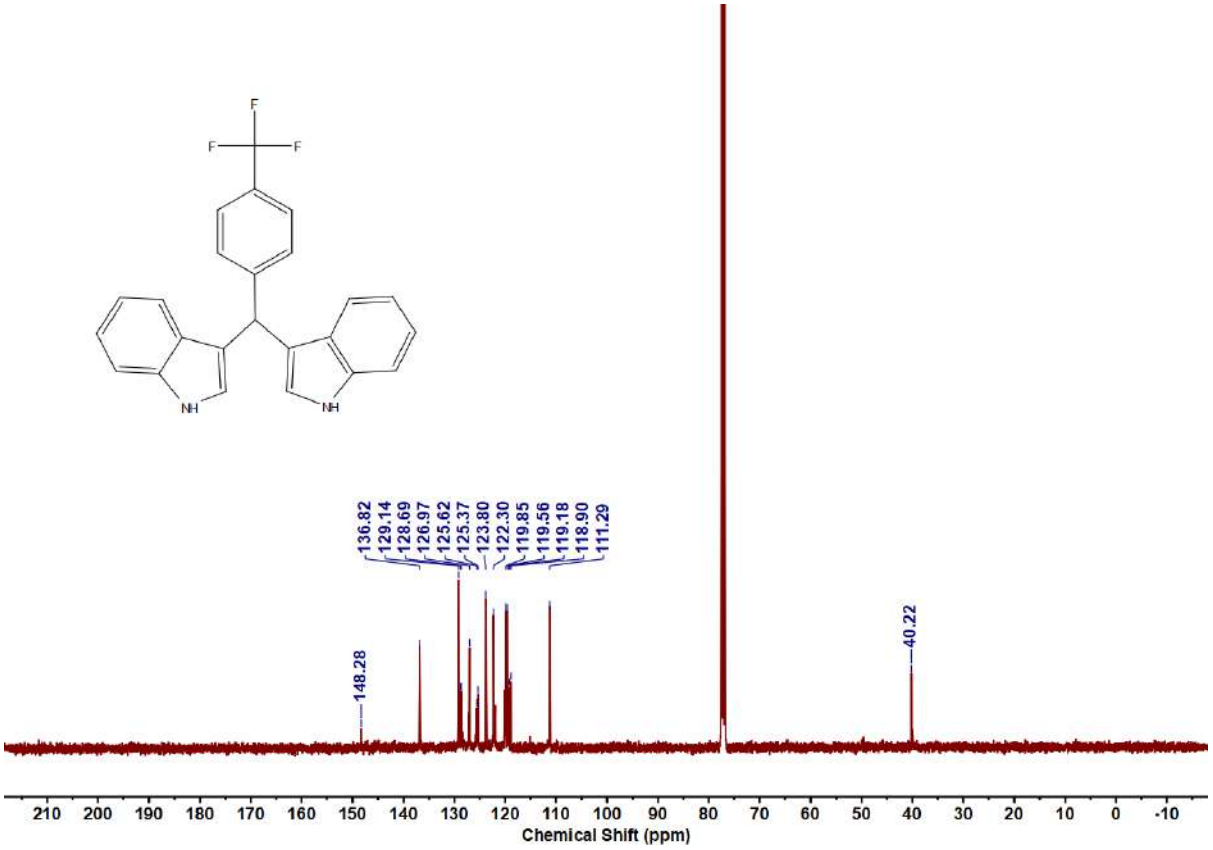

Figure 5.6.A45: $^{13}C\{^{1}H\}$ NMR spectrum of **8am**

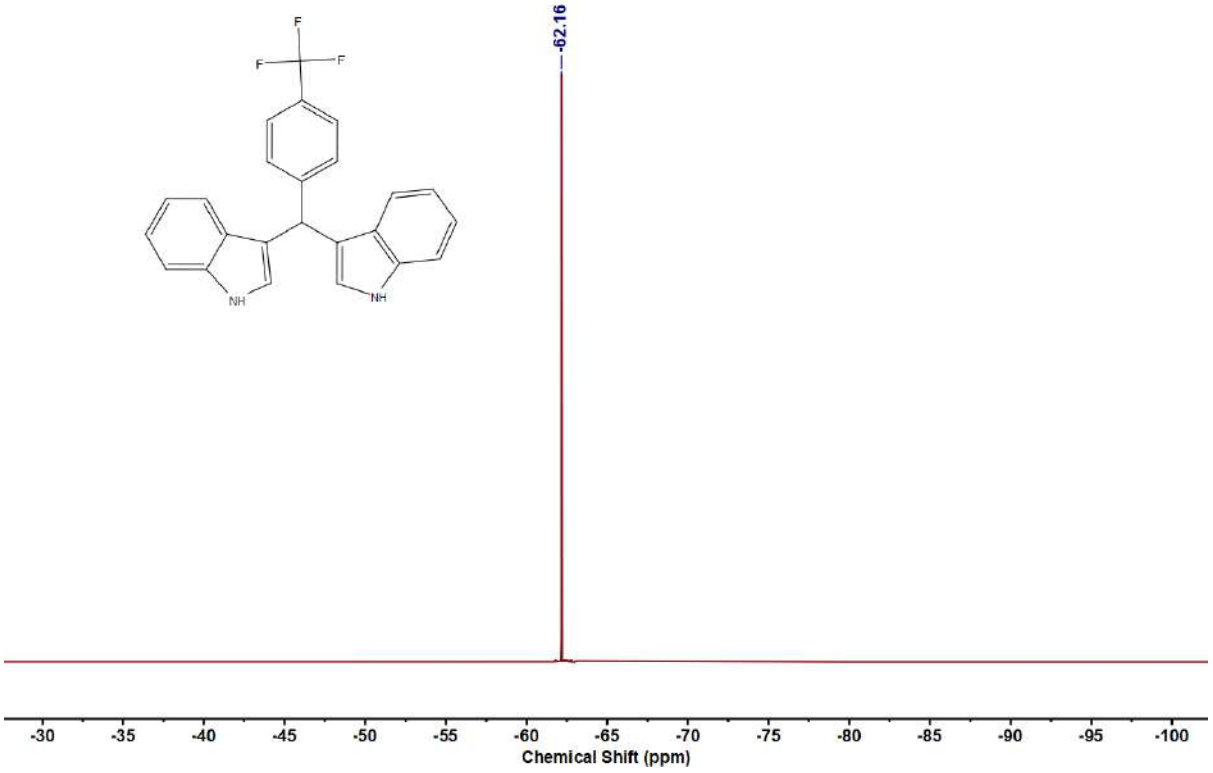

Figure 5.6.A46: ^{19}F NMR spectrum of **8am**

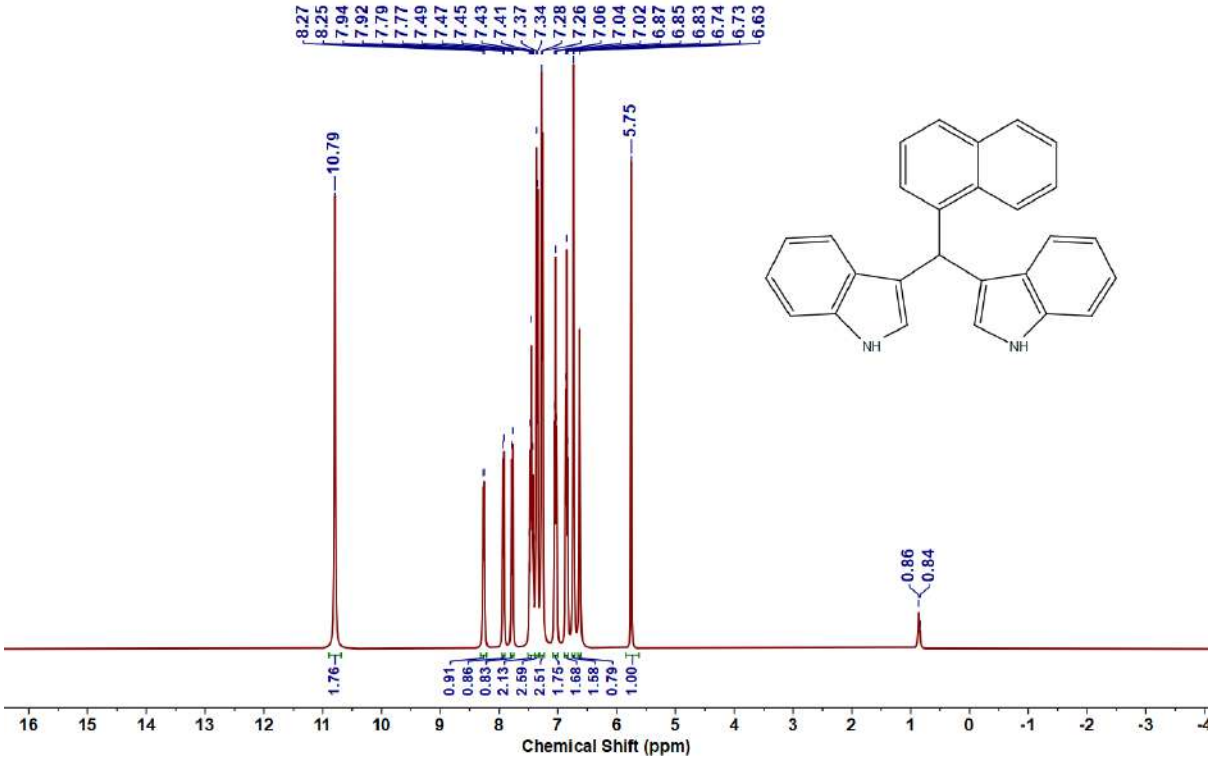

Figure 5.6.A47: ^{1}H NMR spectrum of **8an**

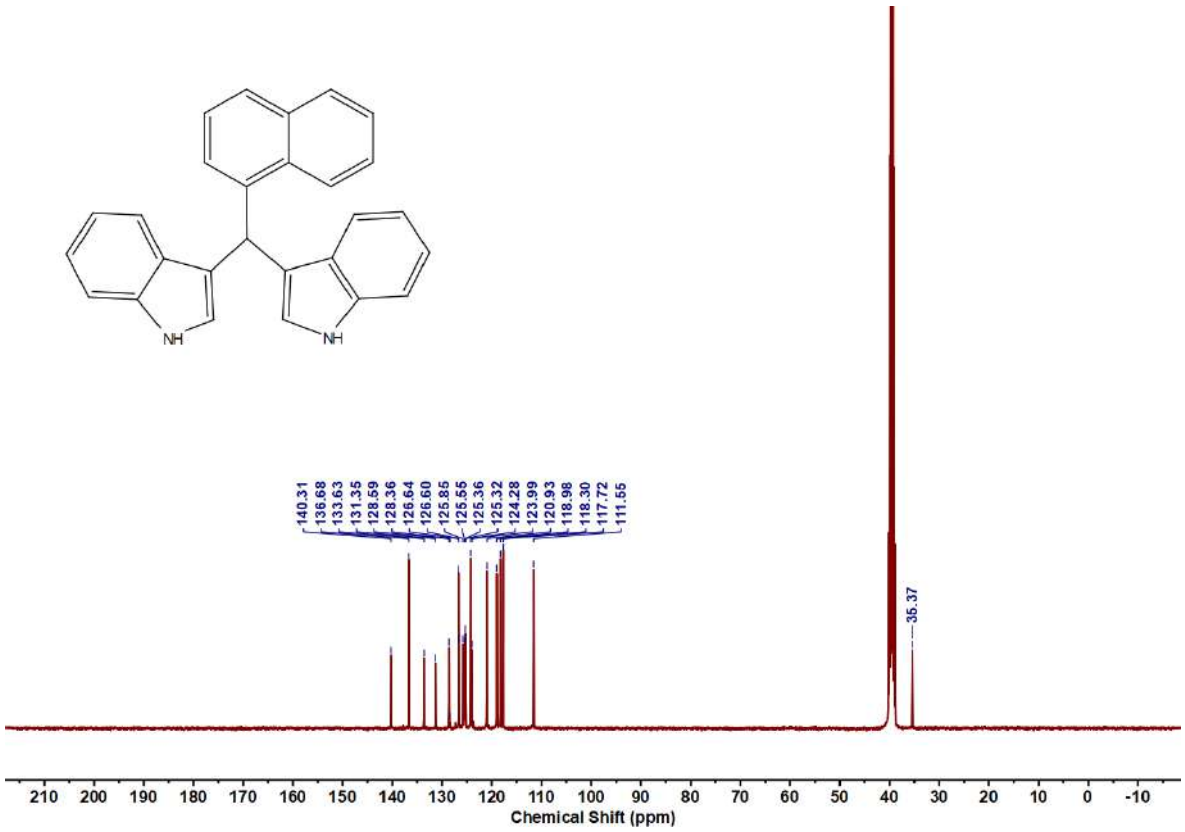

Figure 5.6.A48: ^{13}C{^{1}H} NMR spectrum of **8an**

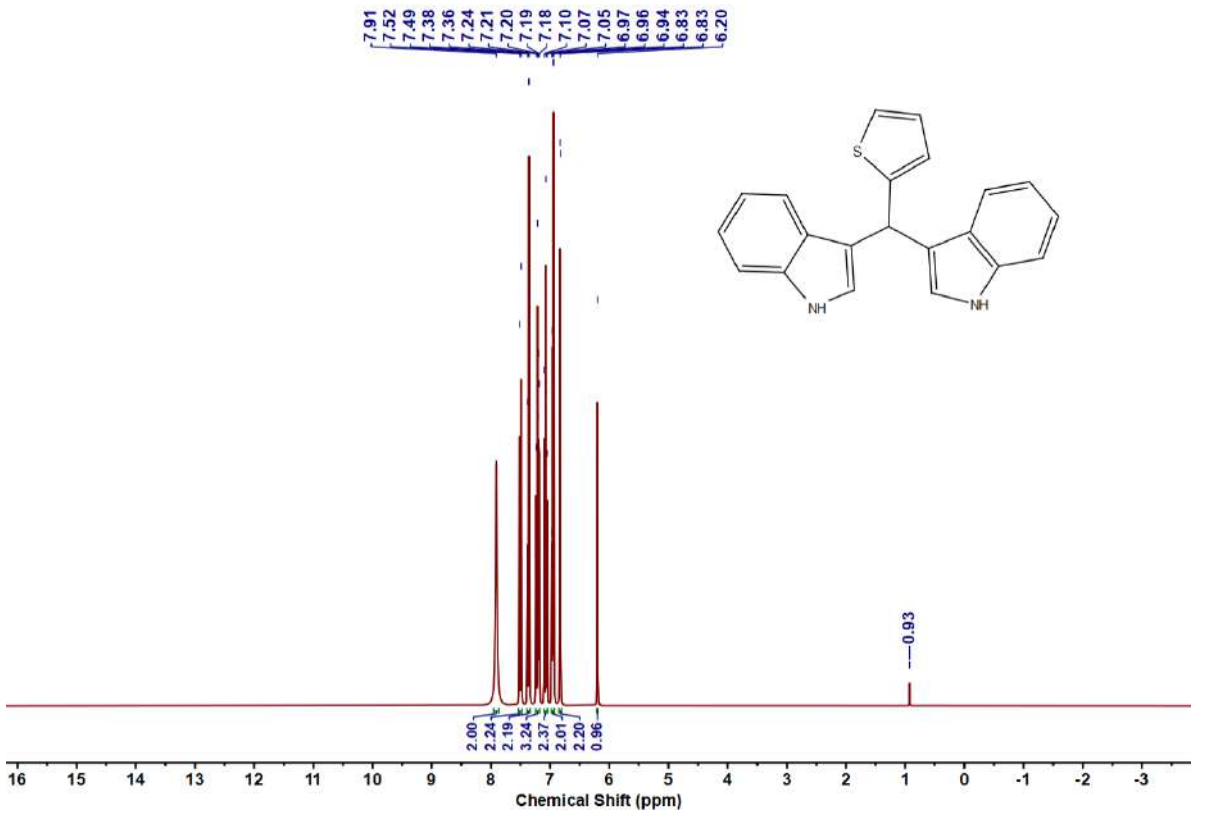

Figure 5.6.A49: ^{1}H NMR spectrum of **8ao**

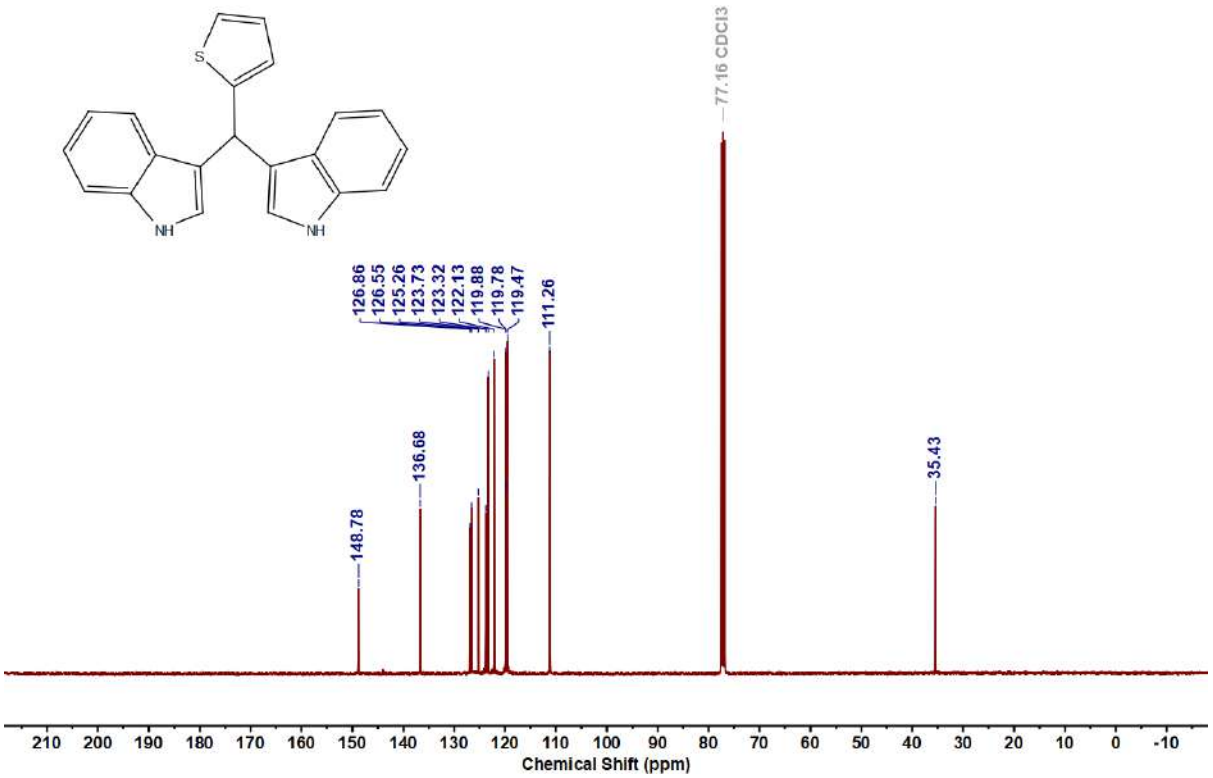

Figure 5.6.A50: $^{13}C\{^{1}H\}$ NMR spectrum of **8ao**

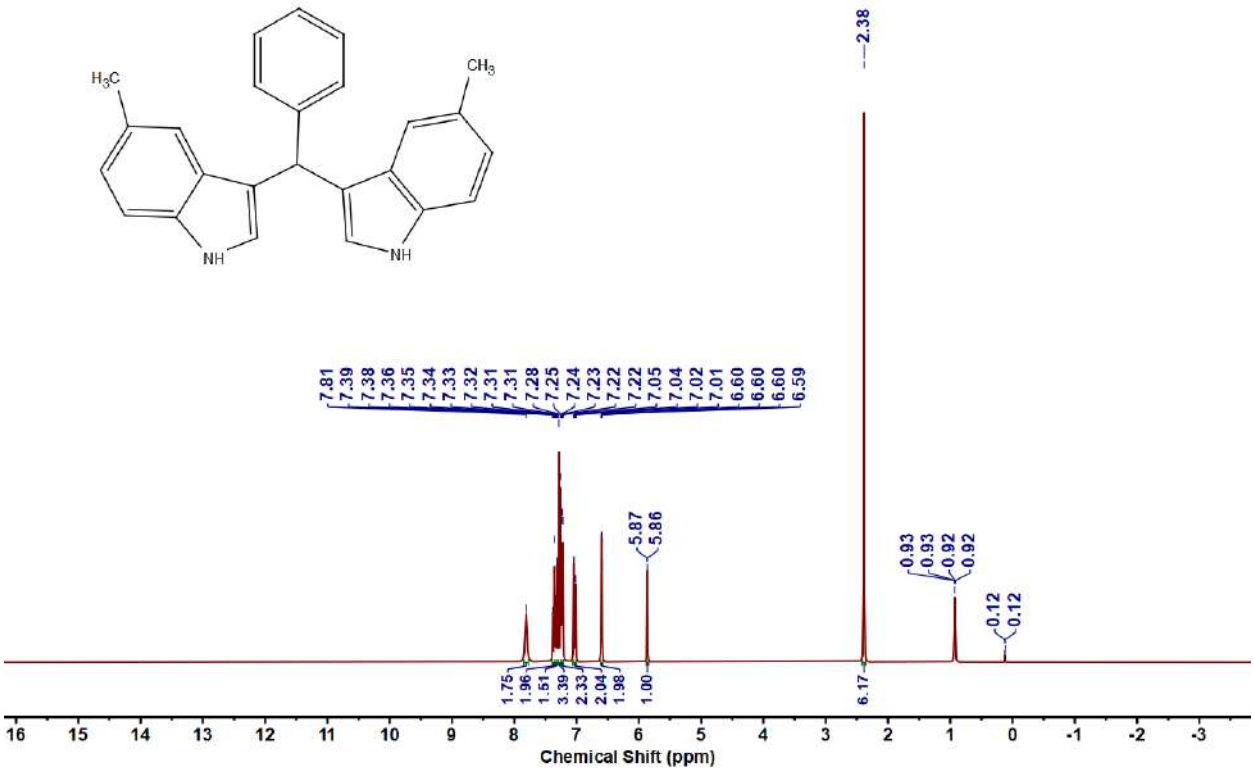

Figure 5.6.A51: ^{1}H NMR spectrum of **9aa**

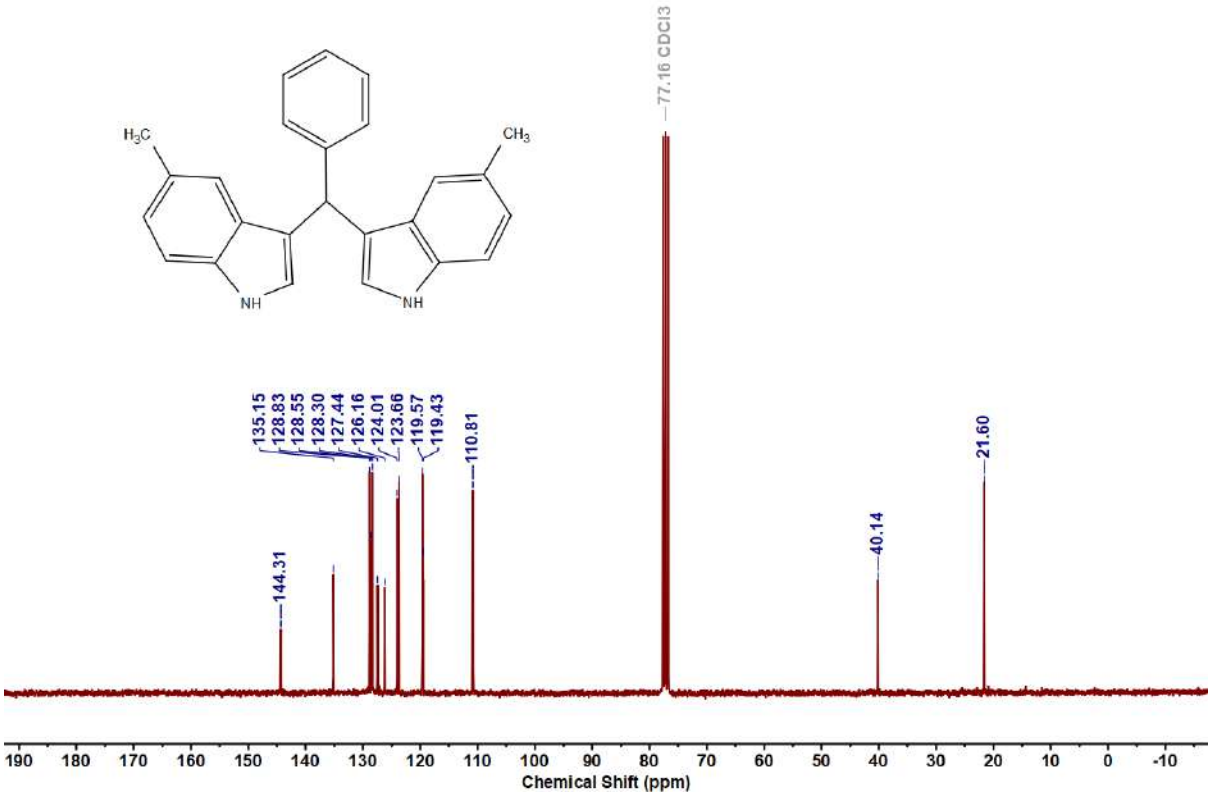

Figure 5.6.A52: ^{13}C{^{1}H} NMR spectrum of **9aa**

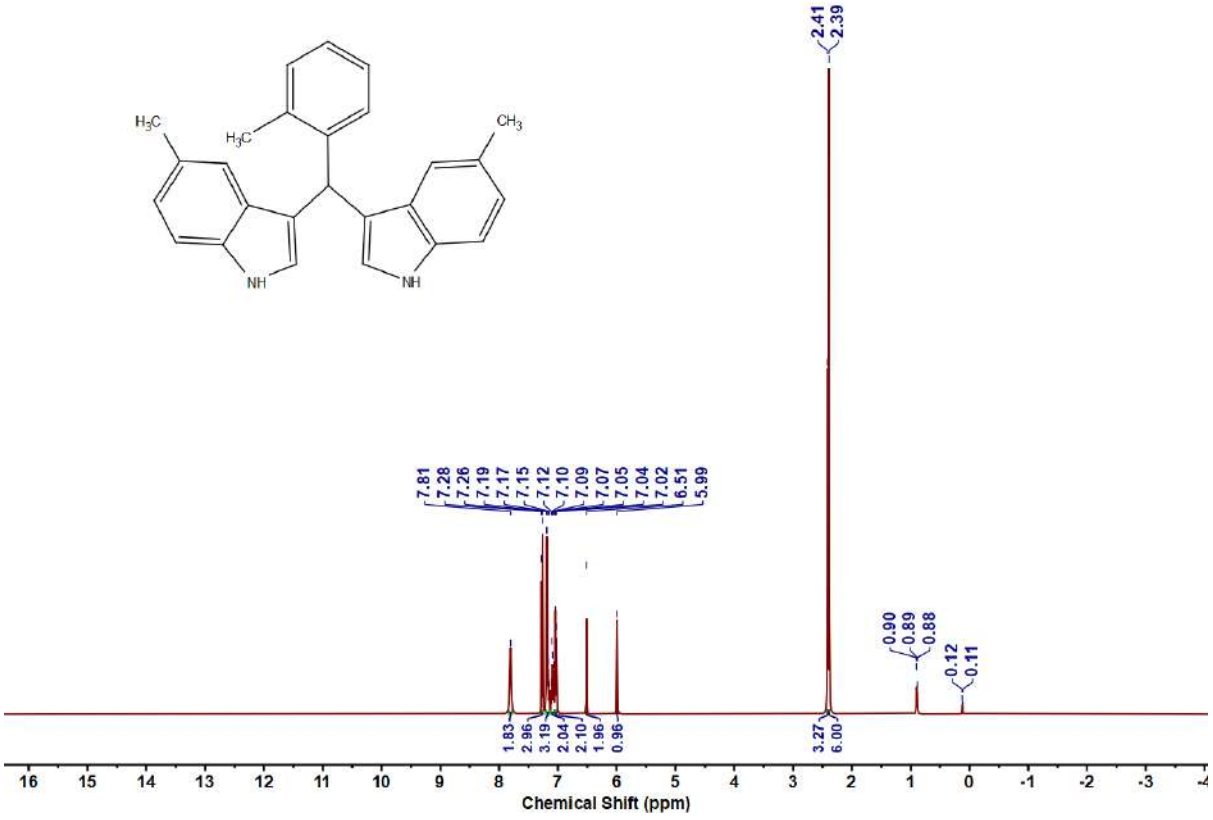

Figure 5.6.A53: ^{1}H NMR spectrum of **9ab**

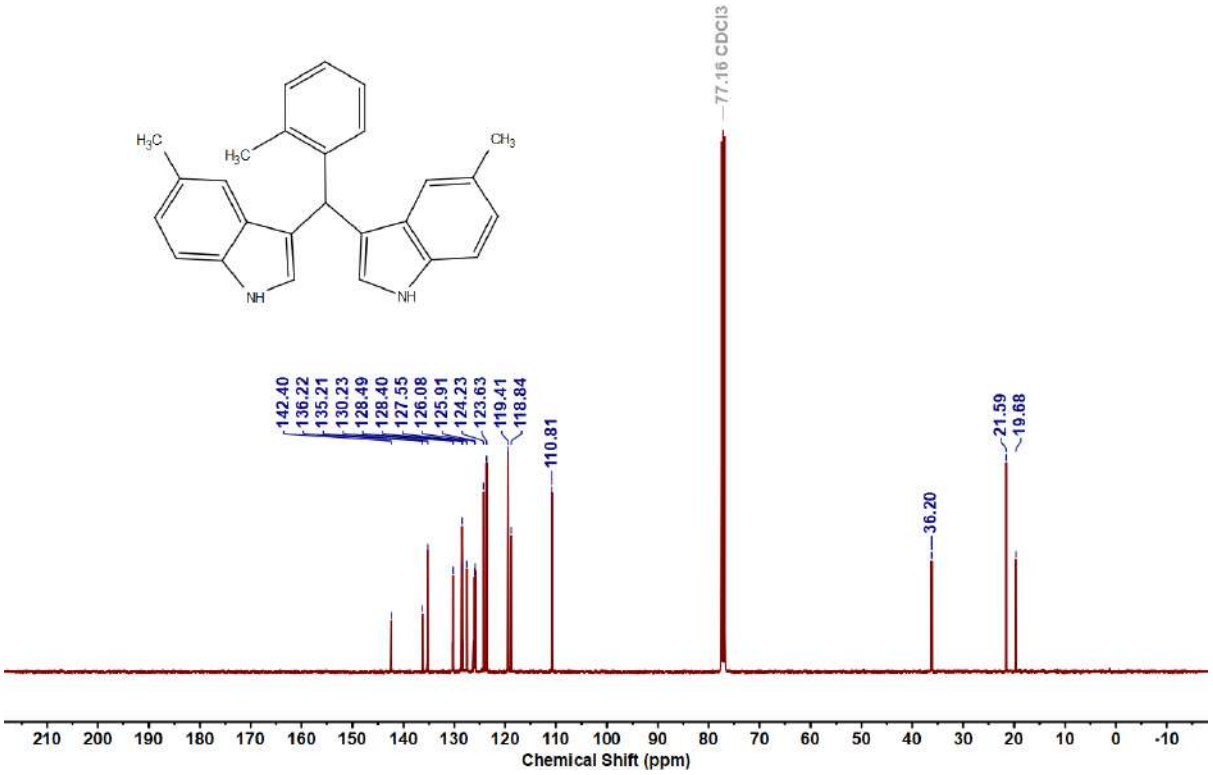

Figure 5.6.A54: ^{13}C{^{1}H} NMR spectrum of **9ab**

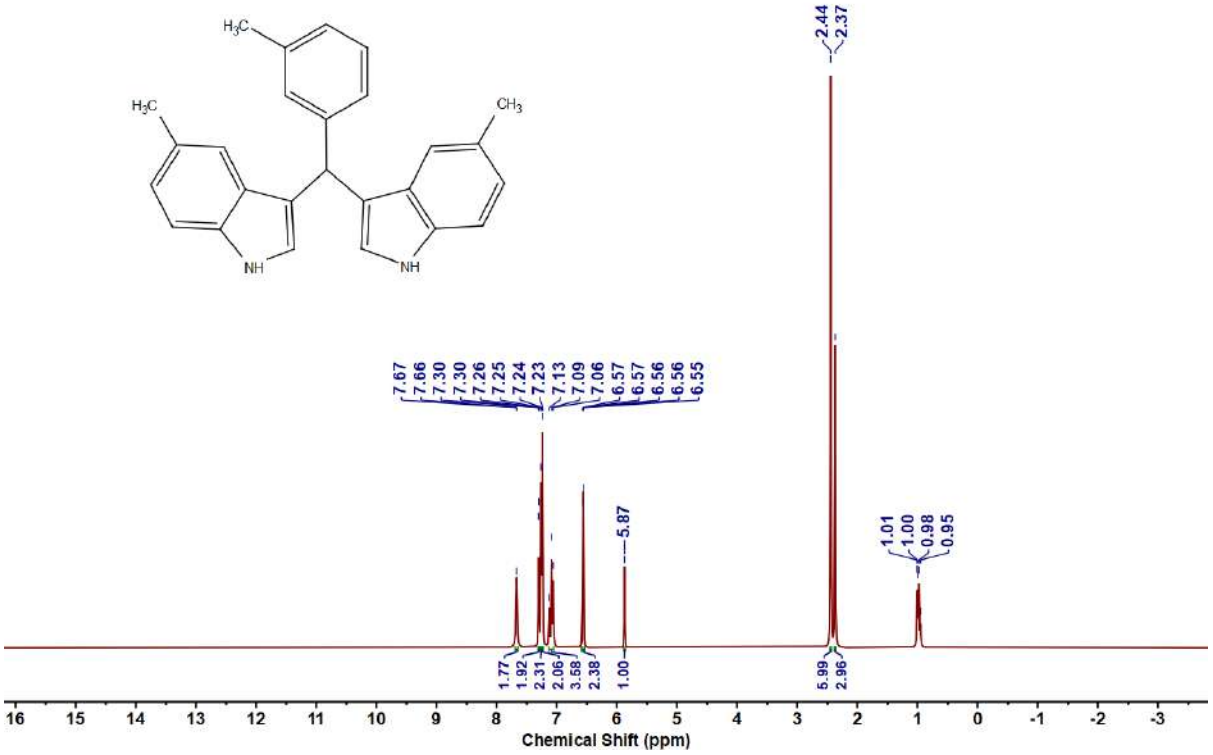

Figure 5.6.A55: ^{1}H NMR spectrum of **9ac**

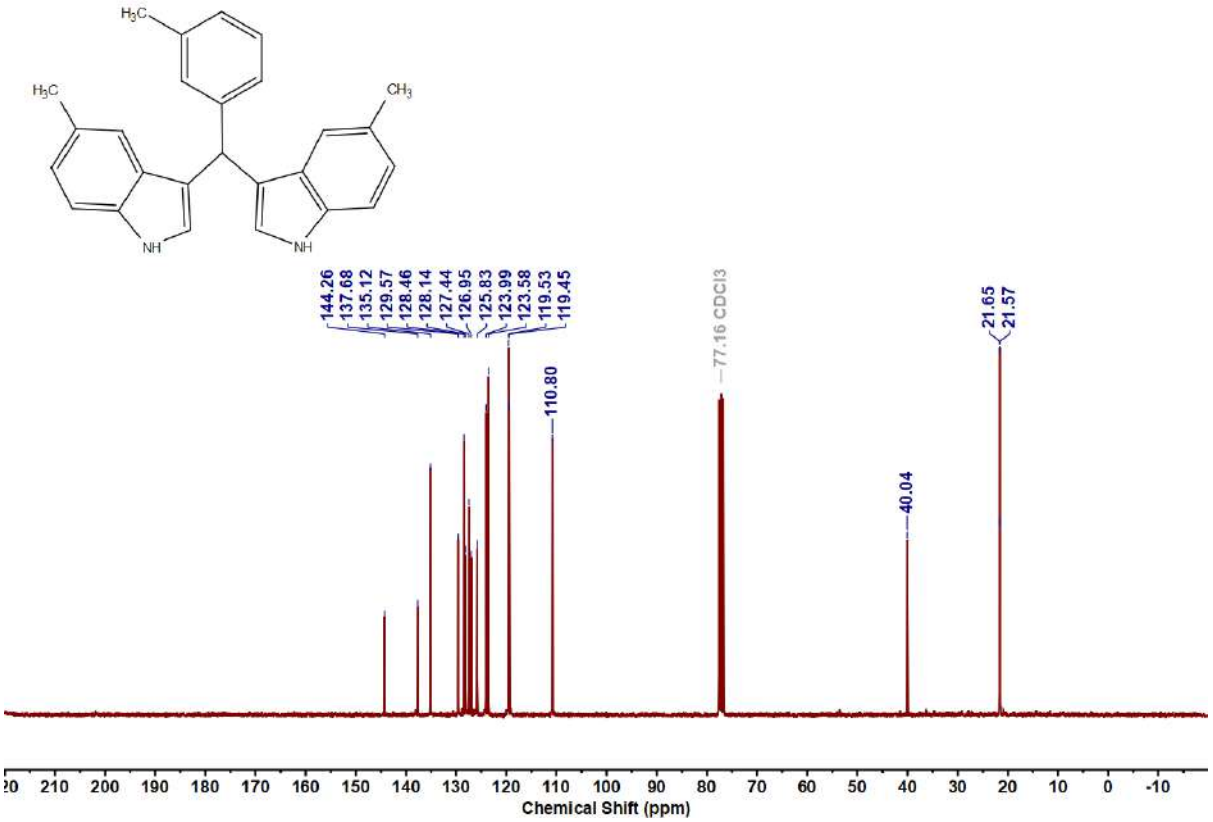

Figure 5.6.A56: ^{13}C{^{1}H} NMR spectrum of **9ac**

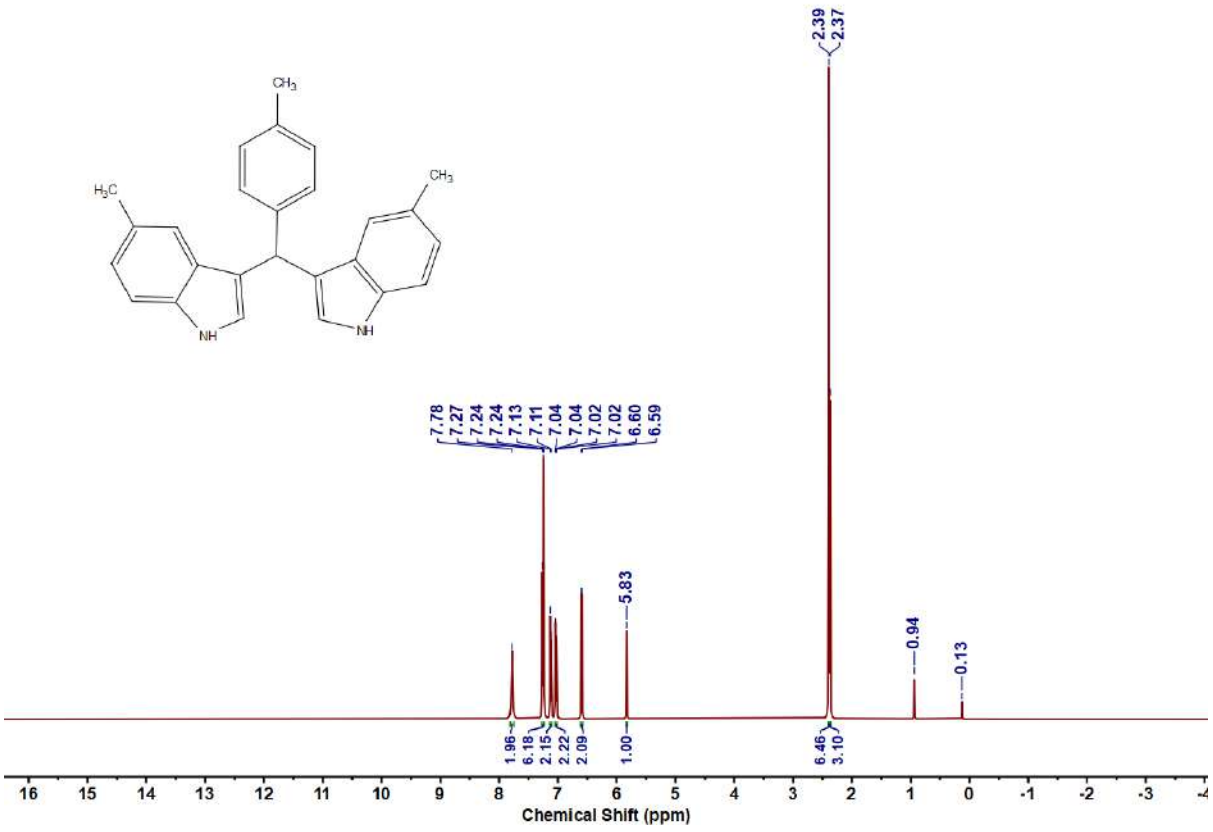

Figure 5.6.A57: ^{1}H NMR spectrum of **9ad**

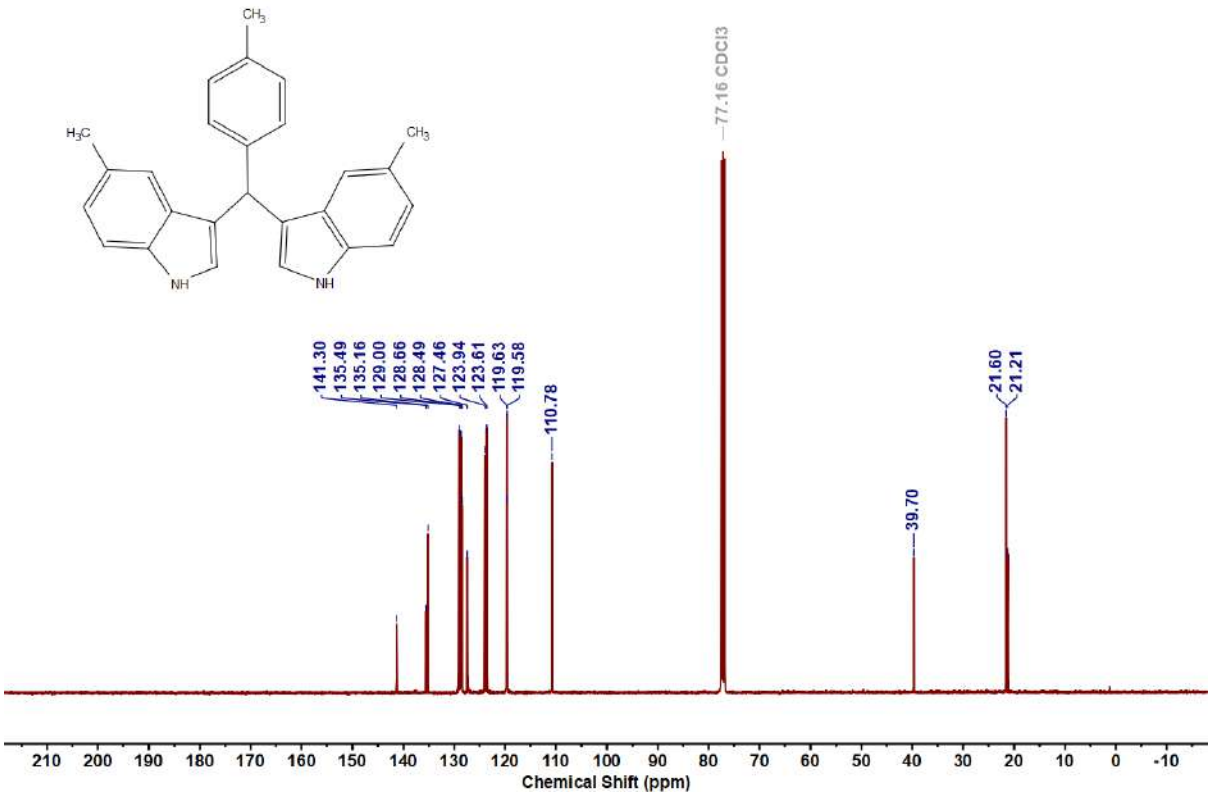

Figure 5.6.A58: ^{13}C{^{1}H} NMR spectrum of **9ad**

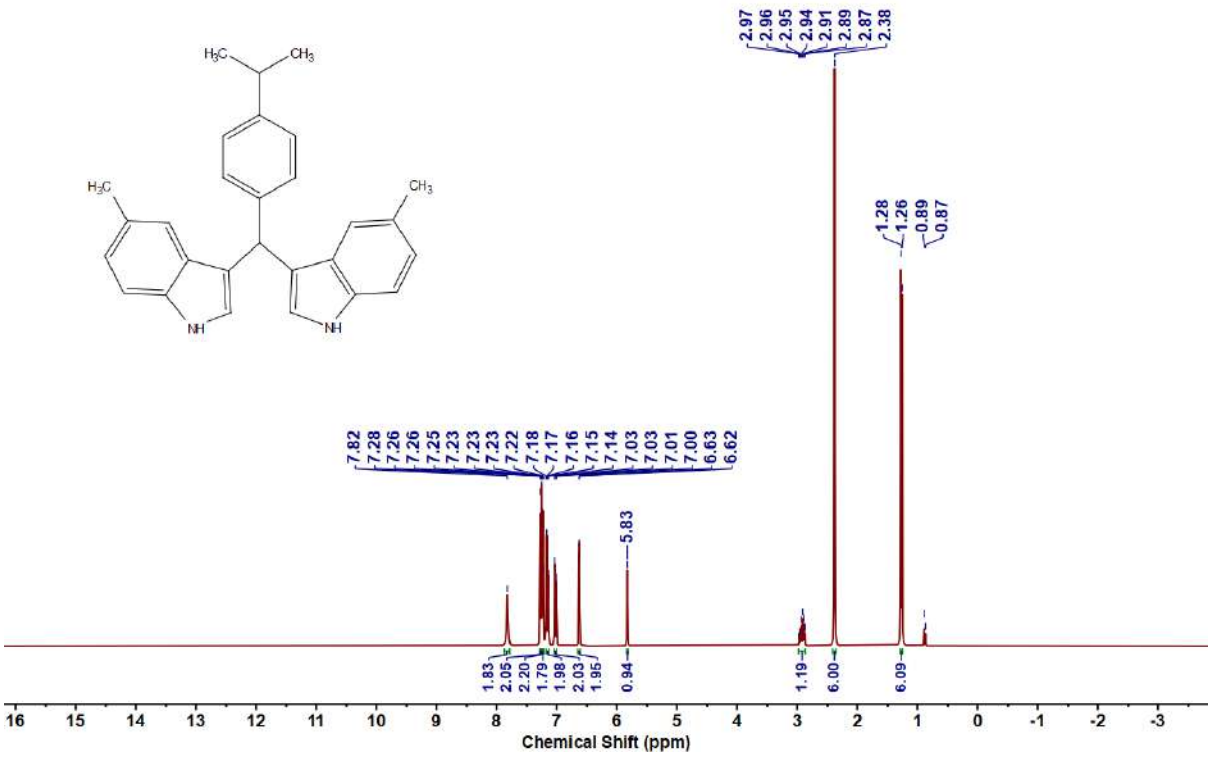

Figure 5.6.A59: ^{1}H NMR spectrum of **9ae**

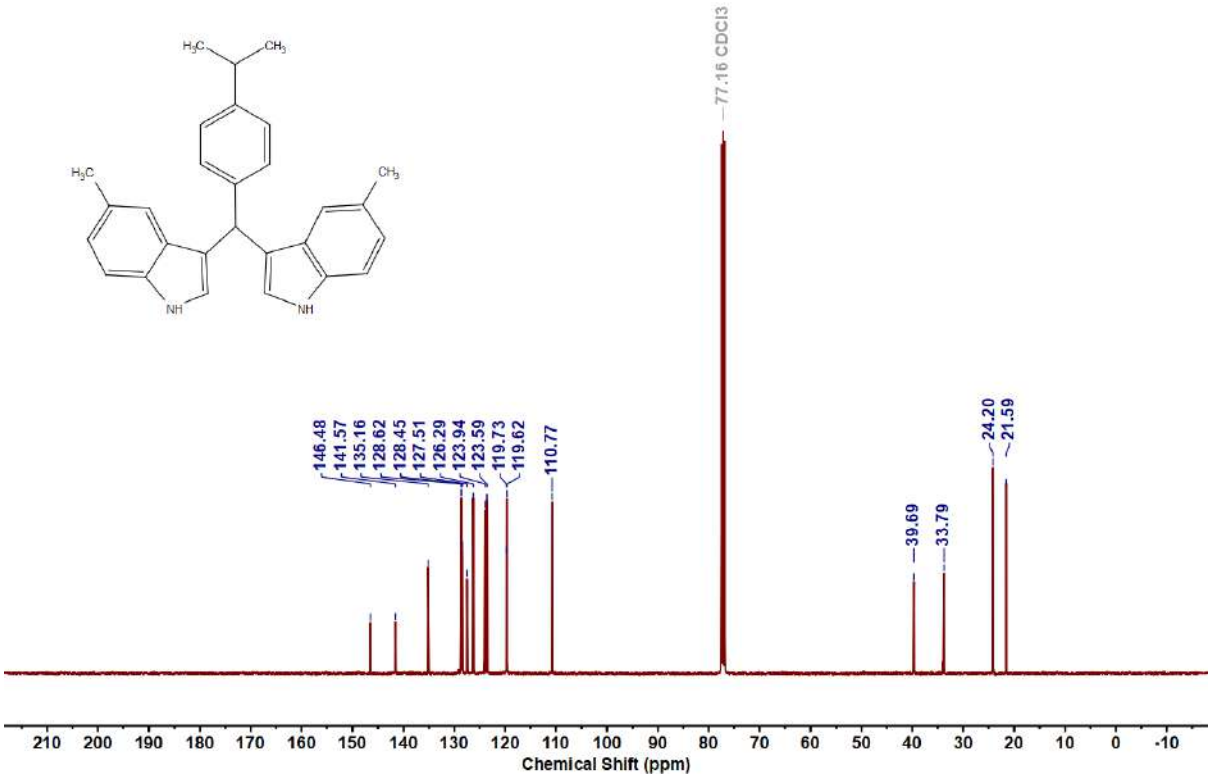

Figure 5.6.A60: ^{13}C{^{1}H} NMR spectrum of **9ae**

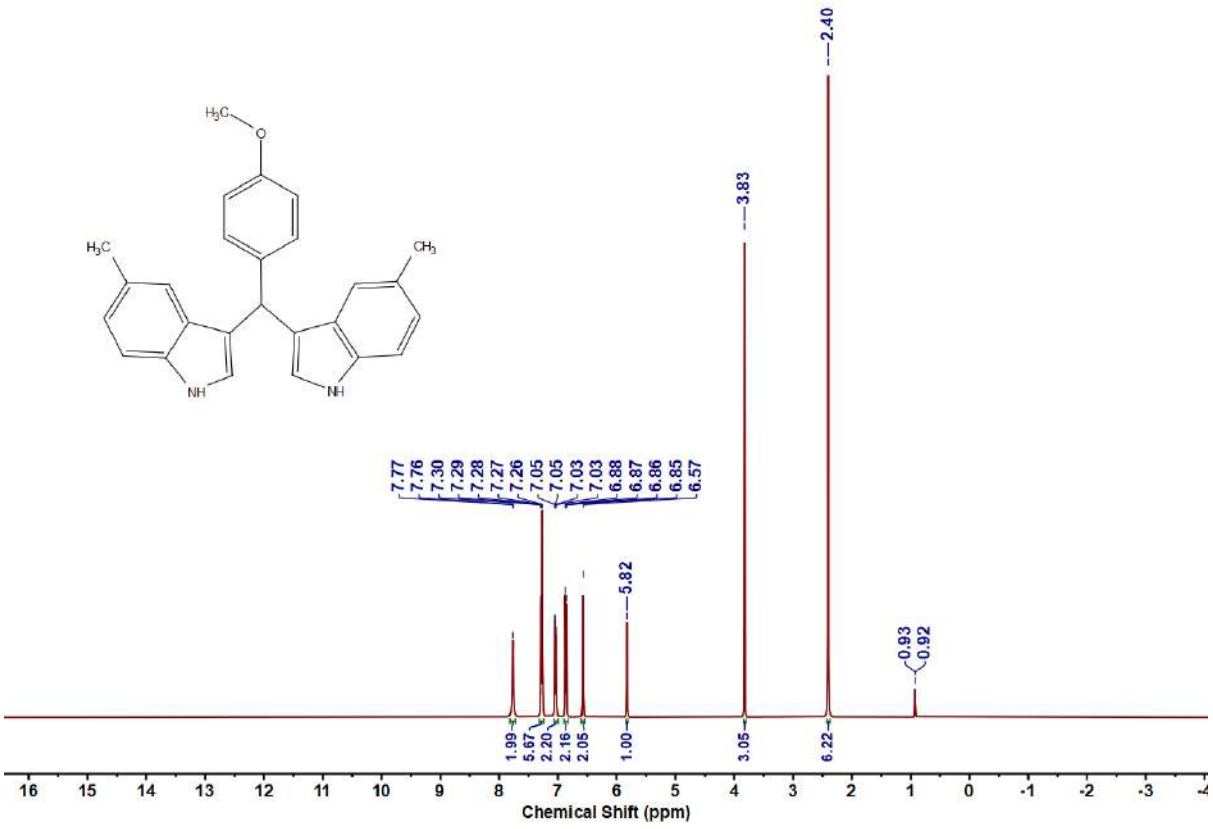

Figure 5.6.A61: ^{1}H NMR spectrum of **9af**

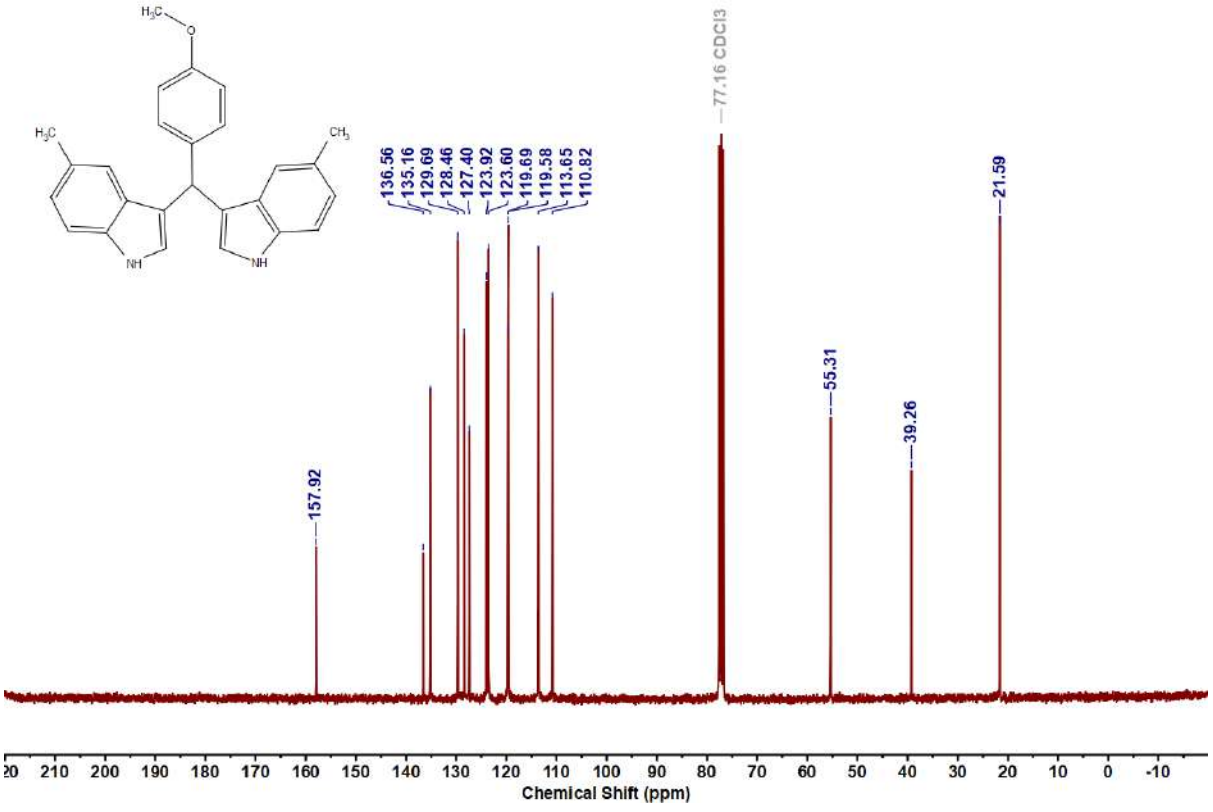

Figure 5.6.A62: ^{13}C{^{1}H} NMR spectrum of **9af**

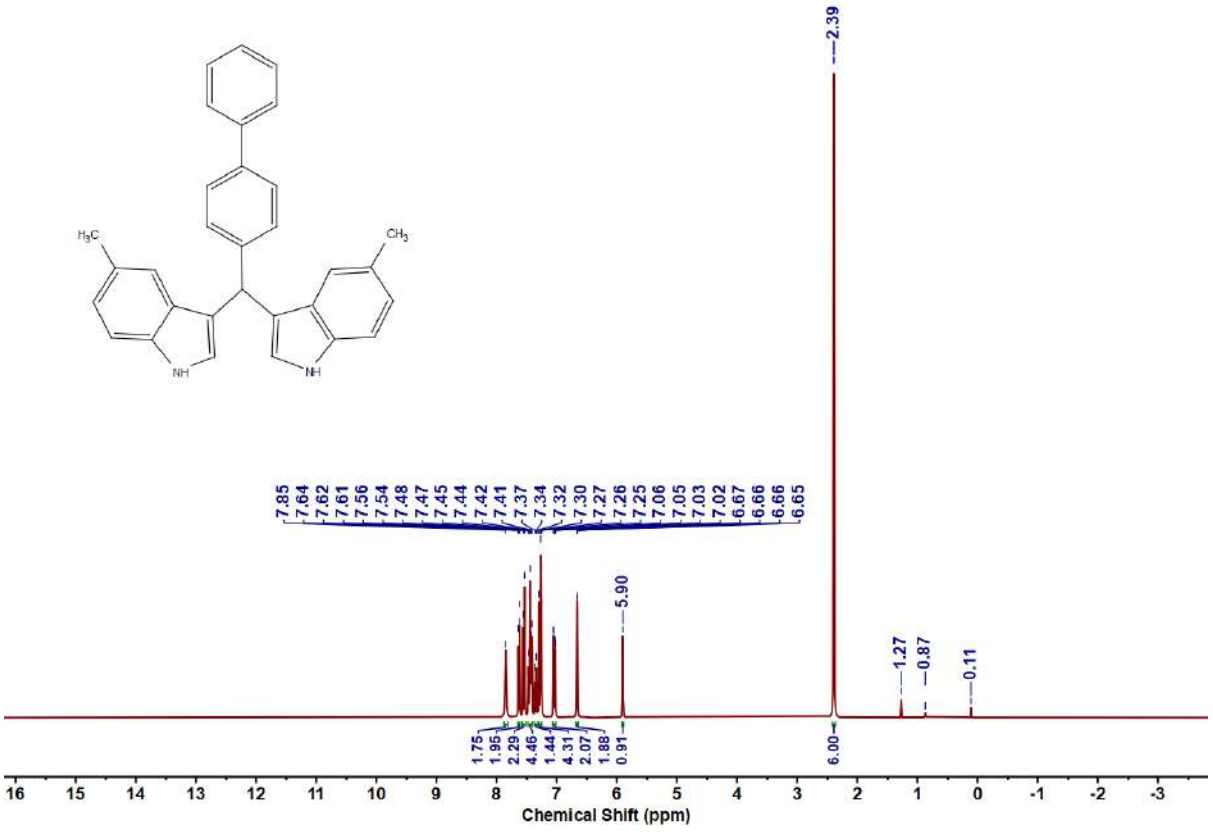

Figure 5.6.A63: ^{1}H NMR spectrum of **9ag**

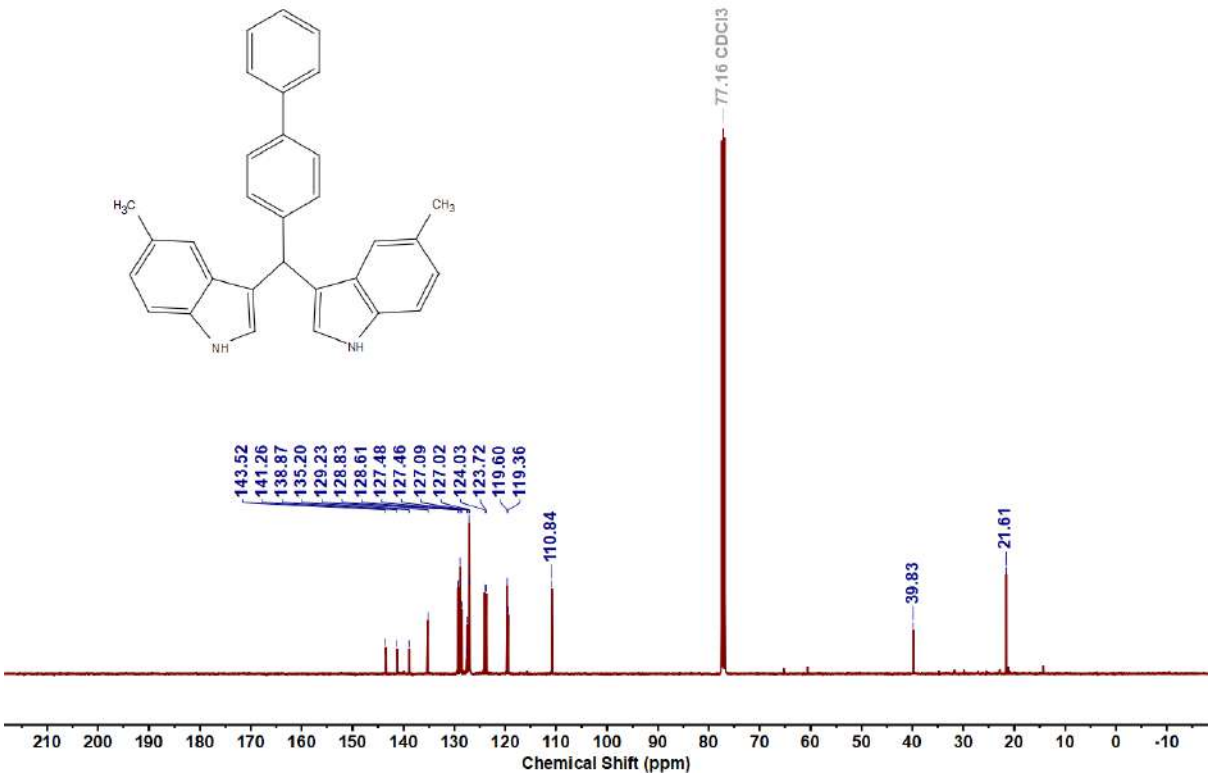

Figure 5.6.A64: $^{13}C\{^{1}H\}$ NMR spectrum of **9ag**

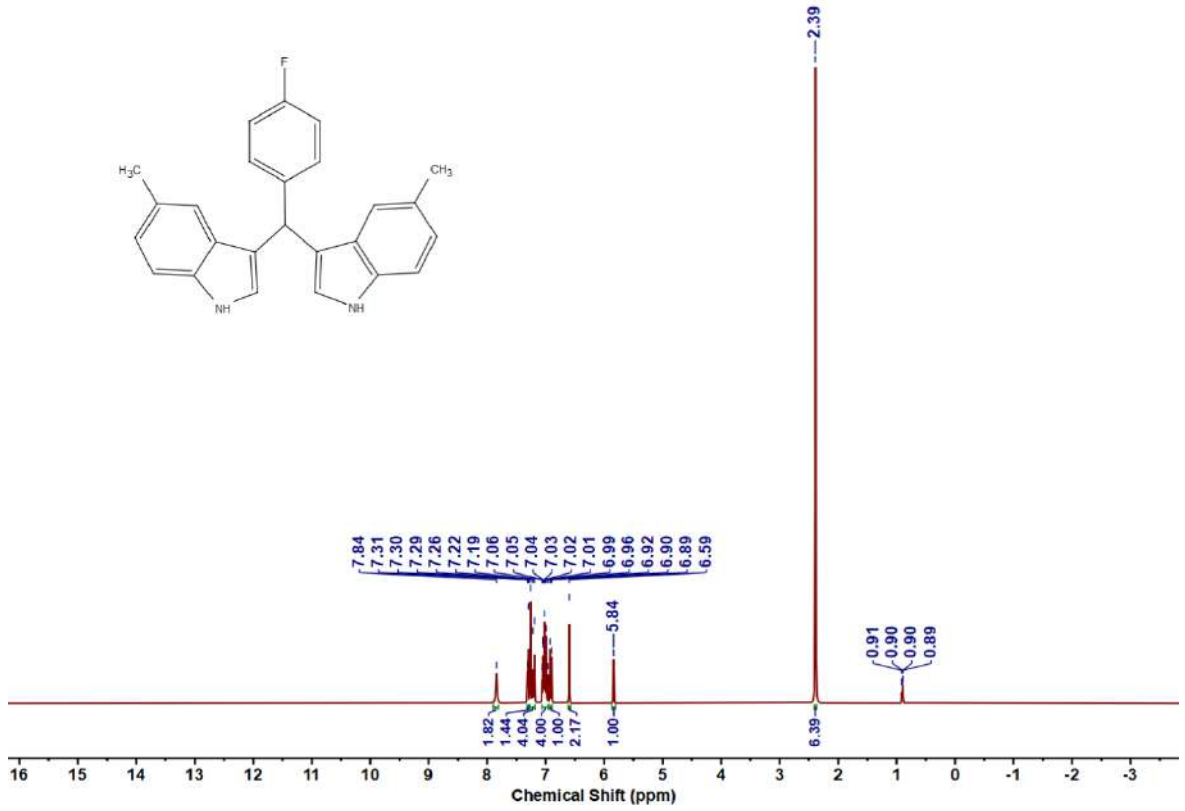

Figure 5.6.A65: ^{1}H NMR spectrum of **9ah**

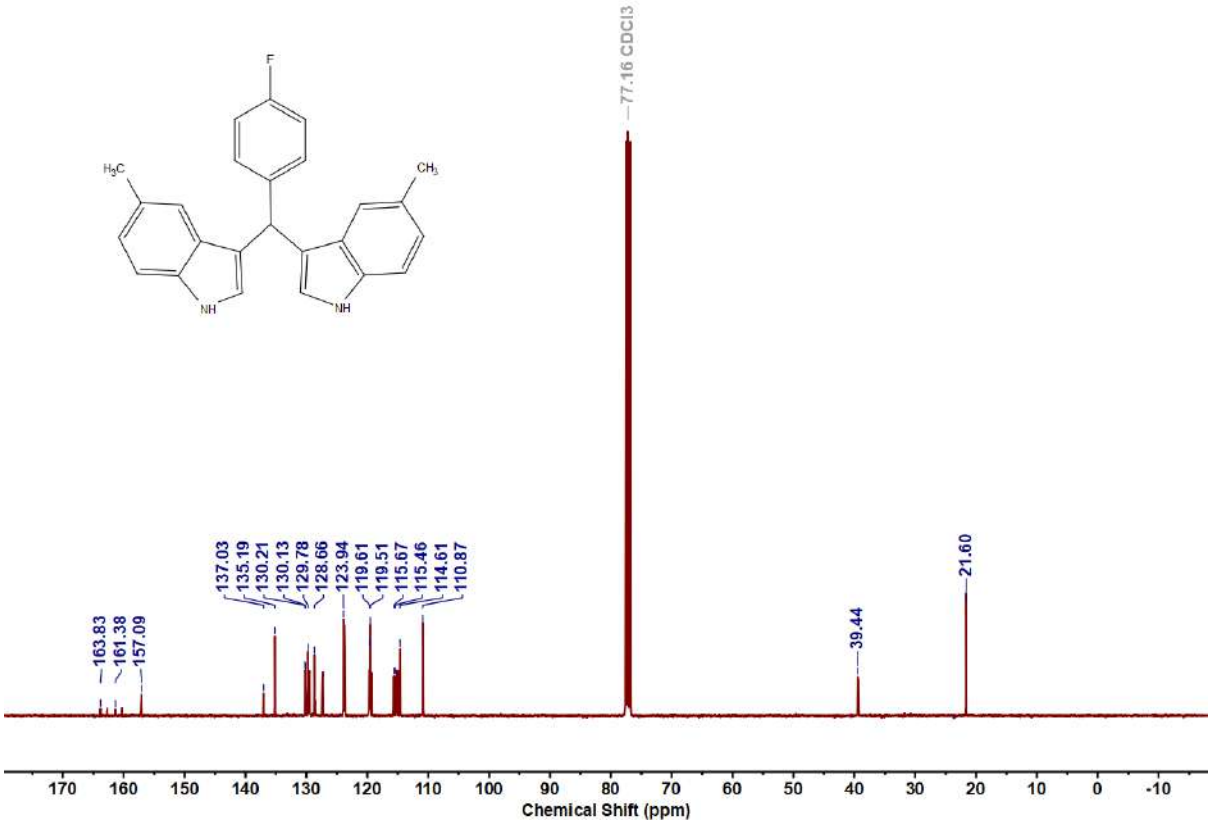

Figure 5.6.A66: ^{13}C{^{1}H} NMR spectrum of **9ah**

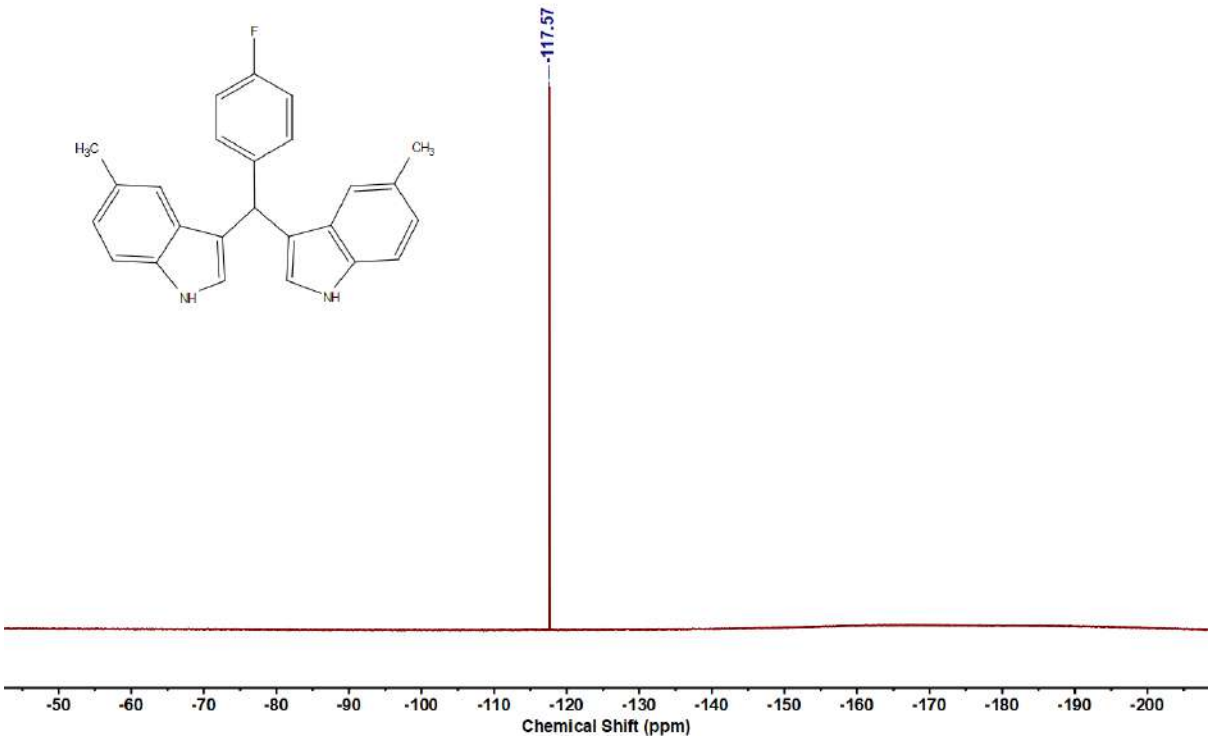

Figure 5.6.A67: ^{19}F NMR spectrum of **9ah**

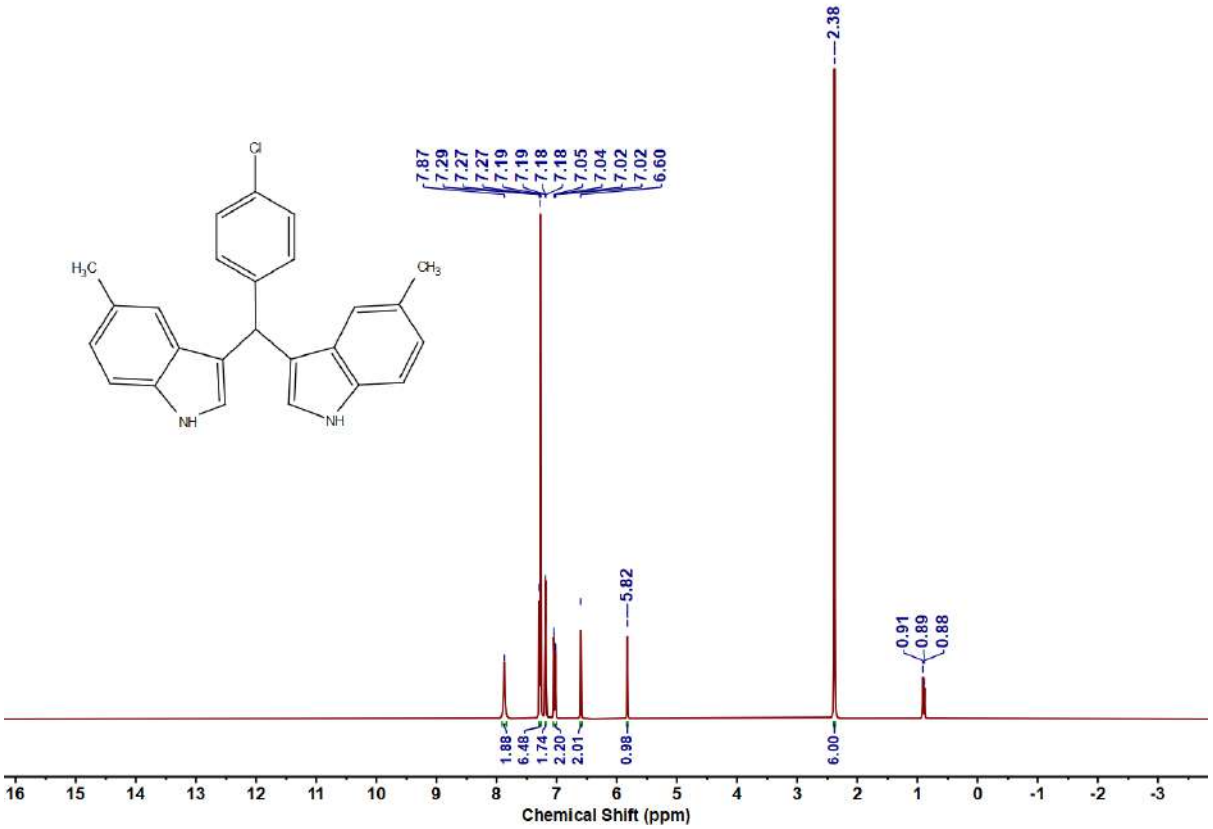

Figure 5.6.A68: ^{1}H NMR spectrum of **9ai**

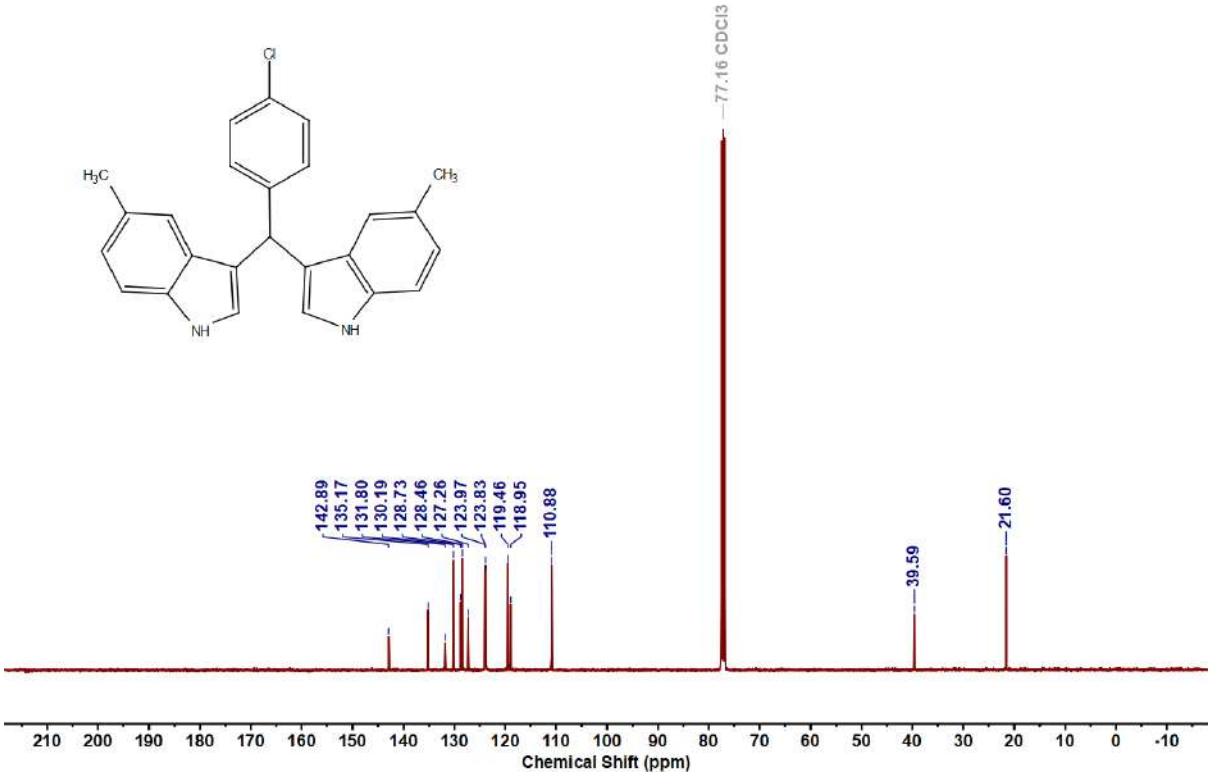

Figure 5.6.A69: $^{13}C\{^{1}H\}$ NMR spectrum of **9ai**

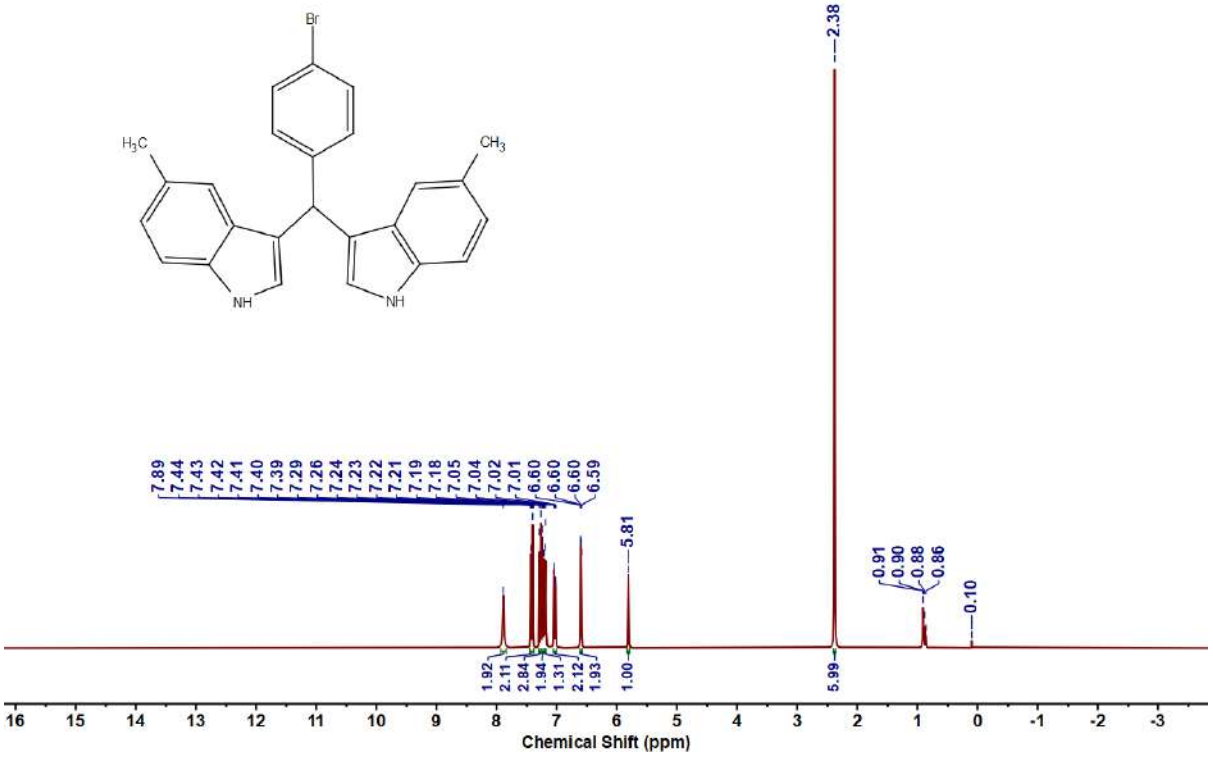

Figure 5.6.A70: ^{1}H NMR spectrum of **9aj**

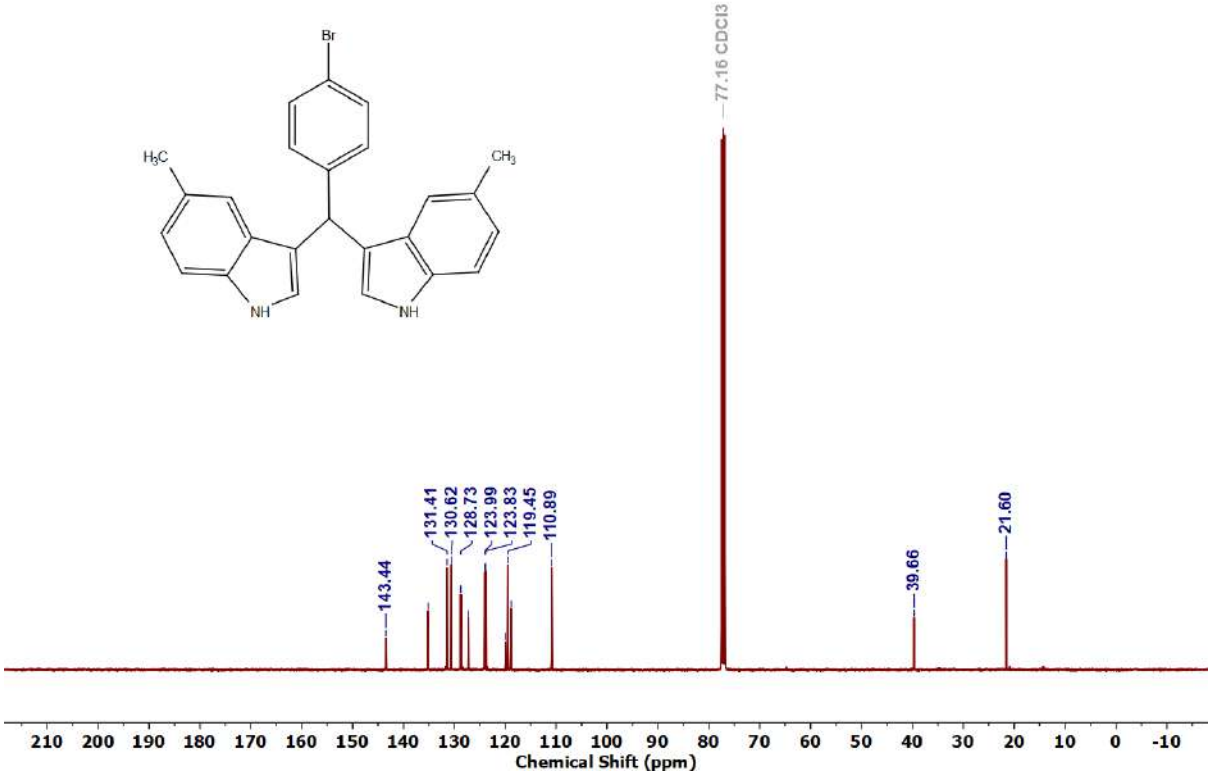

Figure 5.6.A71: $^{13}C\{^{1}H\}$ NMR spectrum of **9aj**

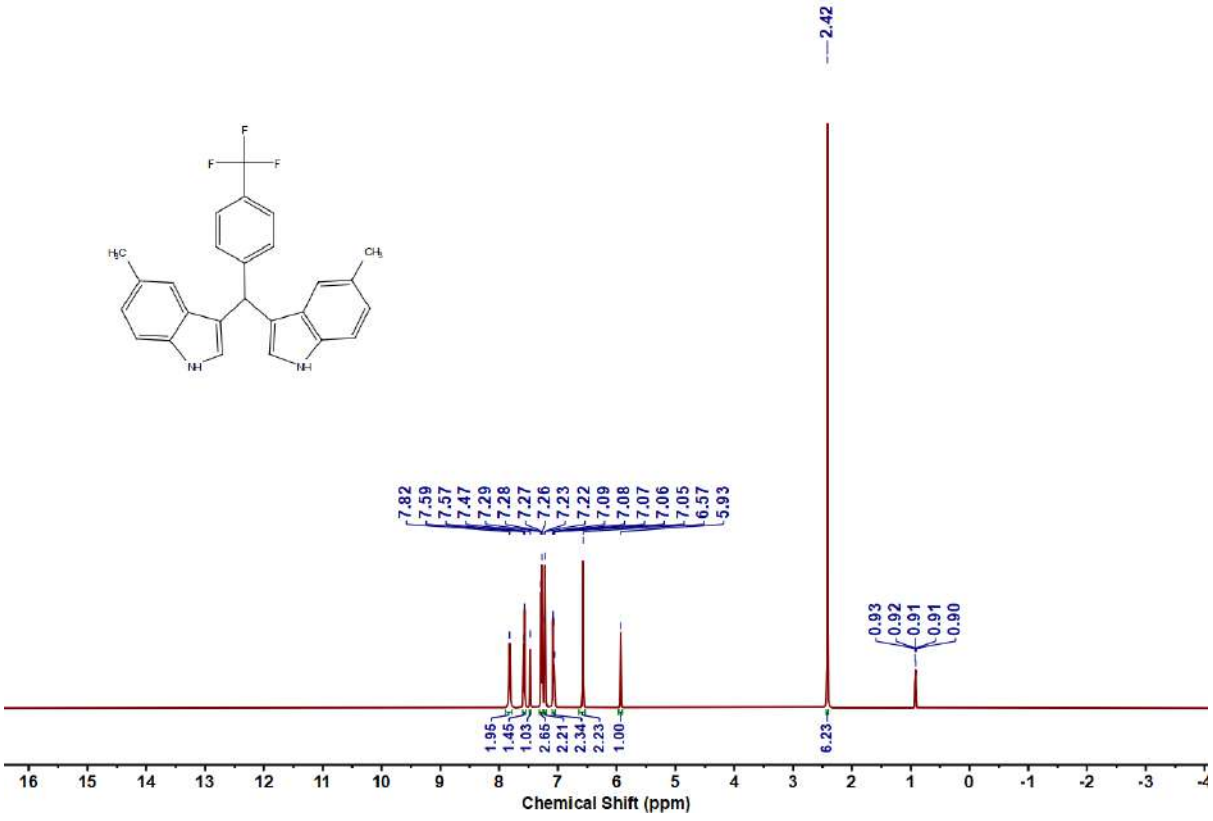

Figure 5.6.A72: ^{1}H NMR spectrum of **9ak**

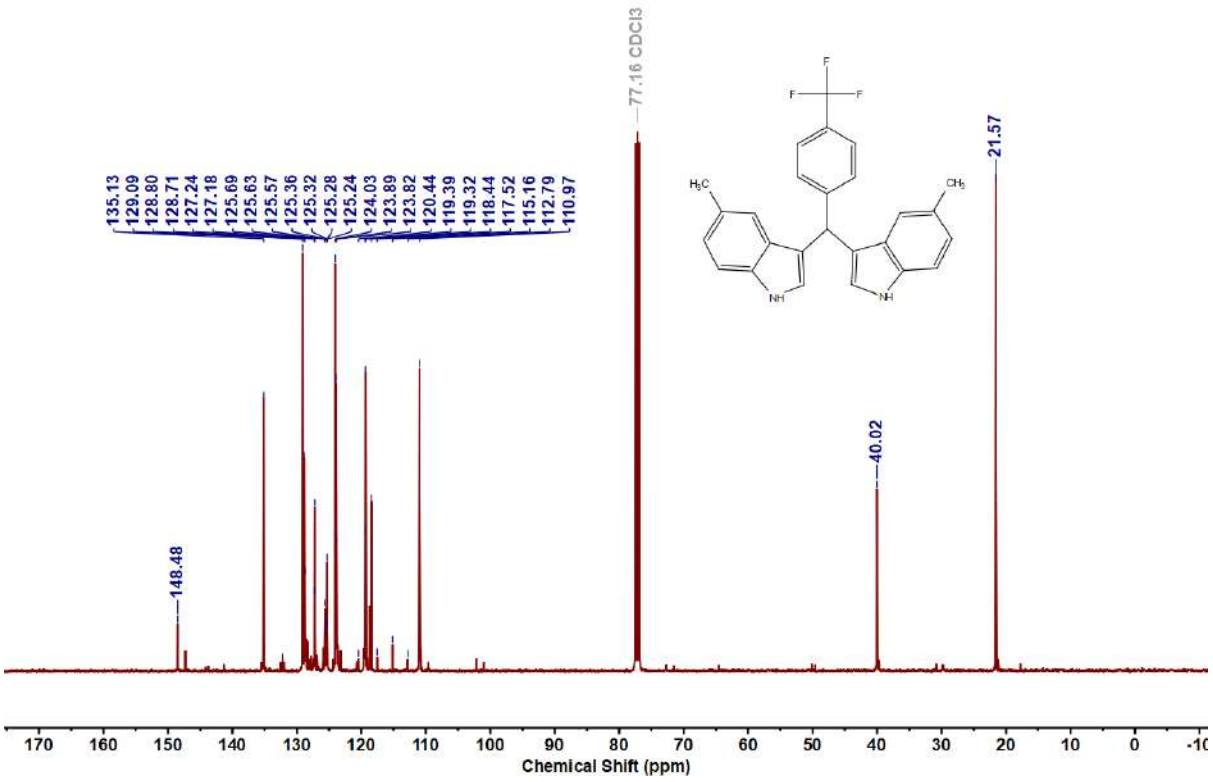

Figure 5.6.A73: $^{13}C\{^{1}H\}$ NMR spectrum of **9ak**

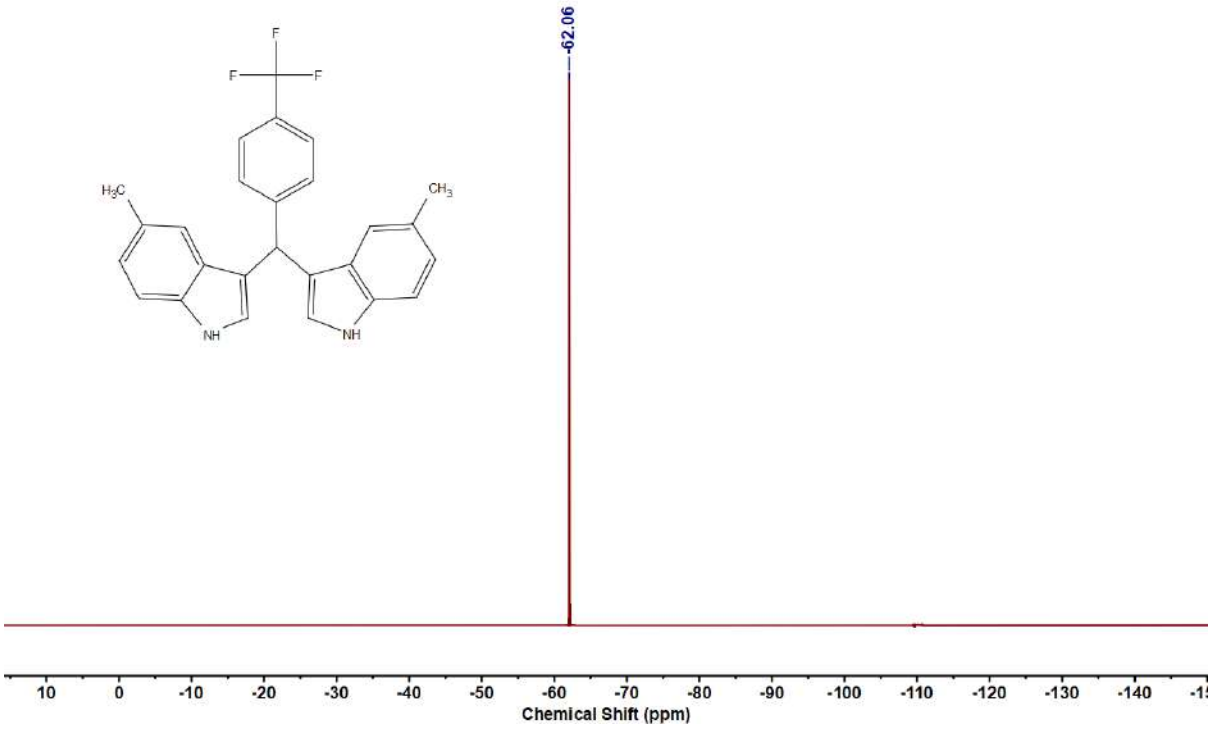

Figure 5.6.A74: ^{19}F NMR spectrum of **9ak**

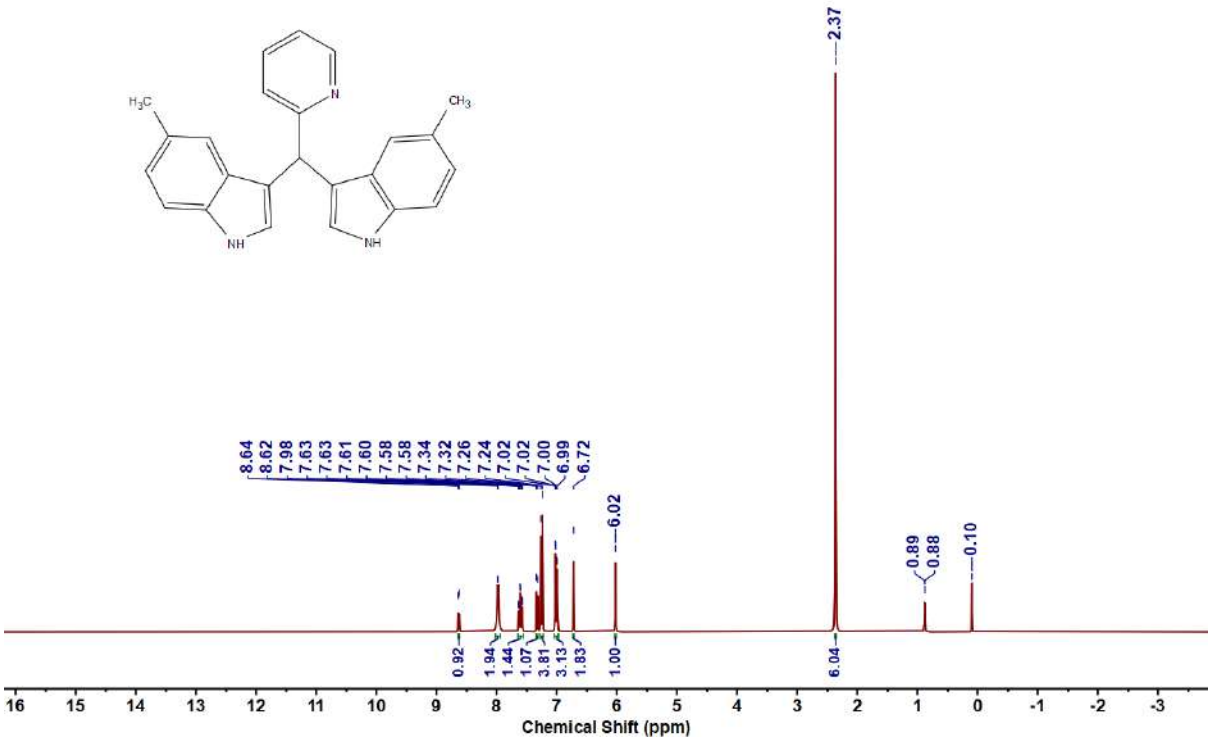

Figure 5.6.A75: ^{1}H NMR spectrum of **9al**

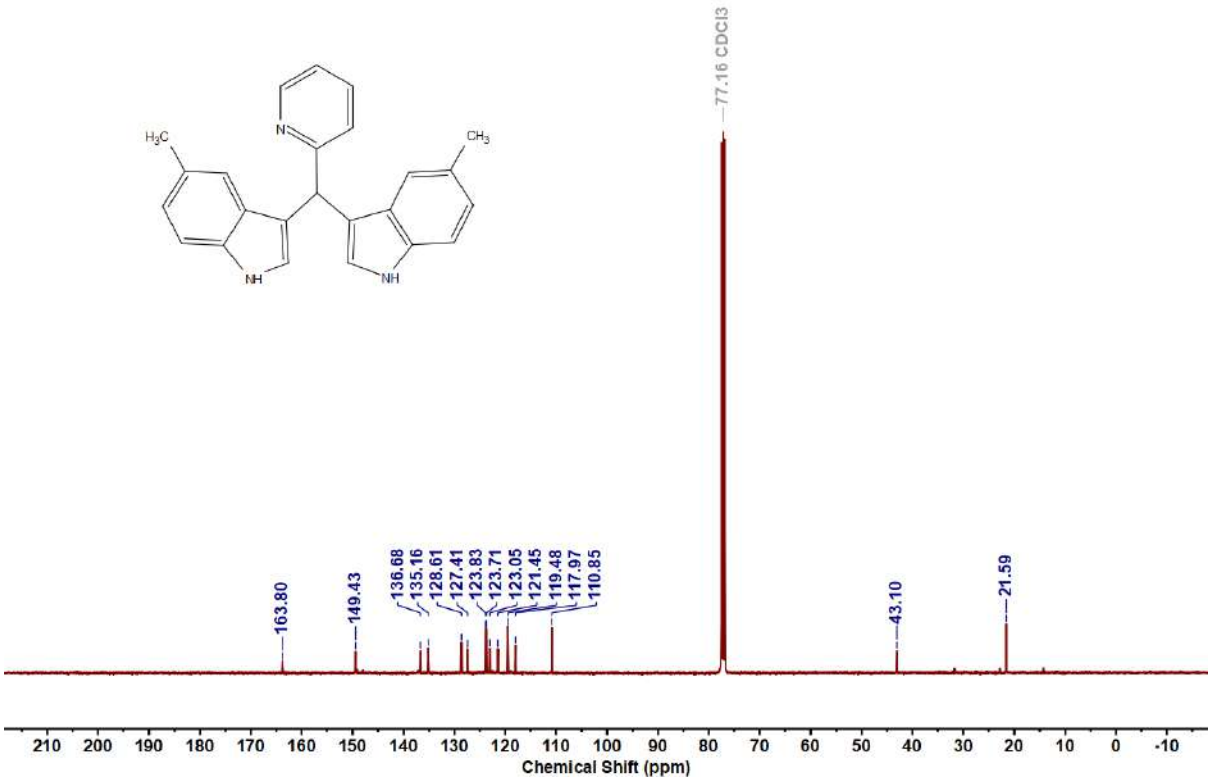

Figure 5.6.A76: ^{13}C{^{1}H} NMR spectrum of **9al**

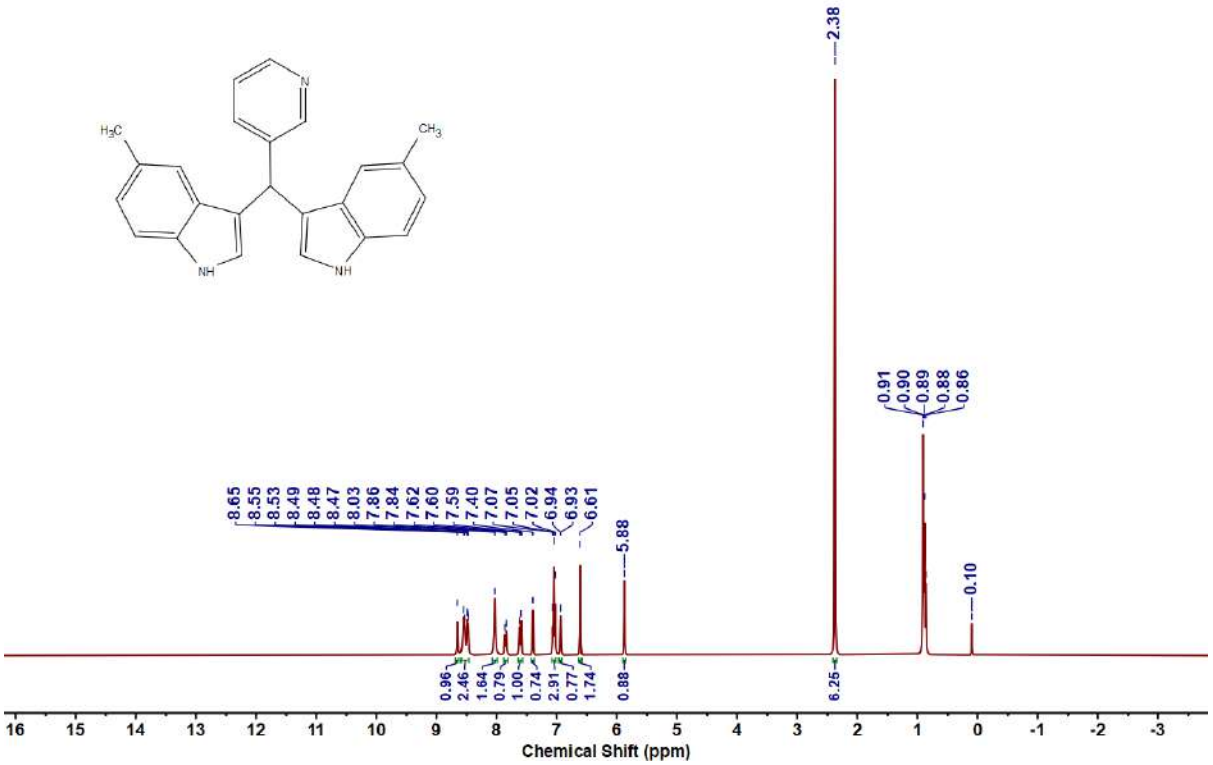

Figure 5.6.A77: ^{1}H NMR spectrum of **9am**

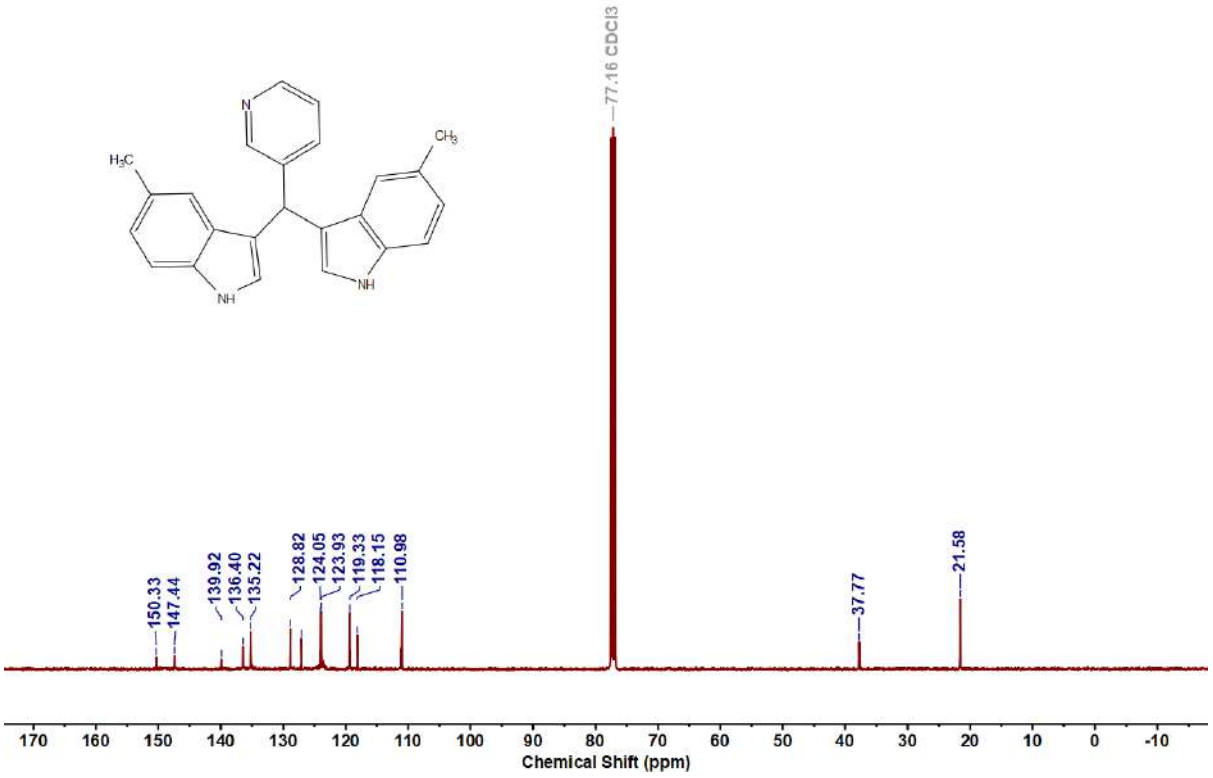

Figure 5.6.A78: ^{13}C{^{1}H} NMR spectrum of **9am**

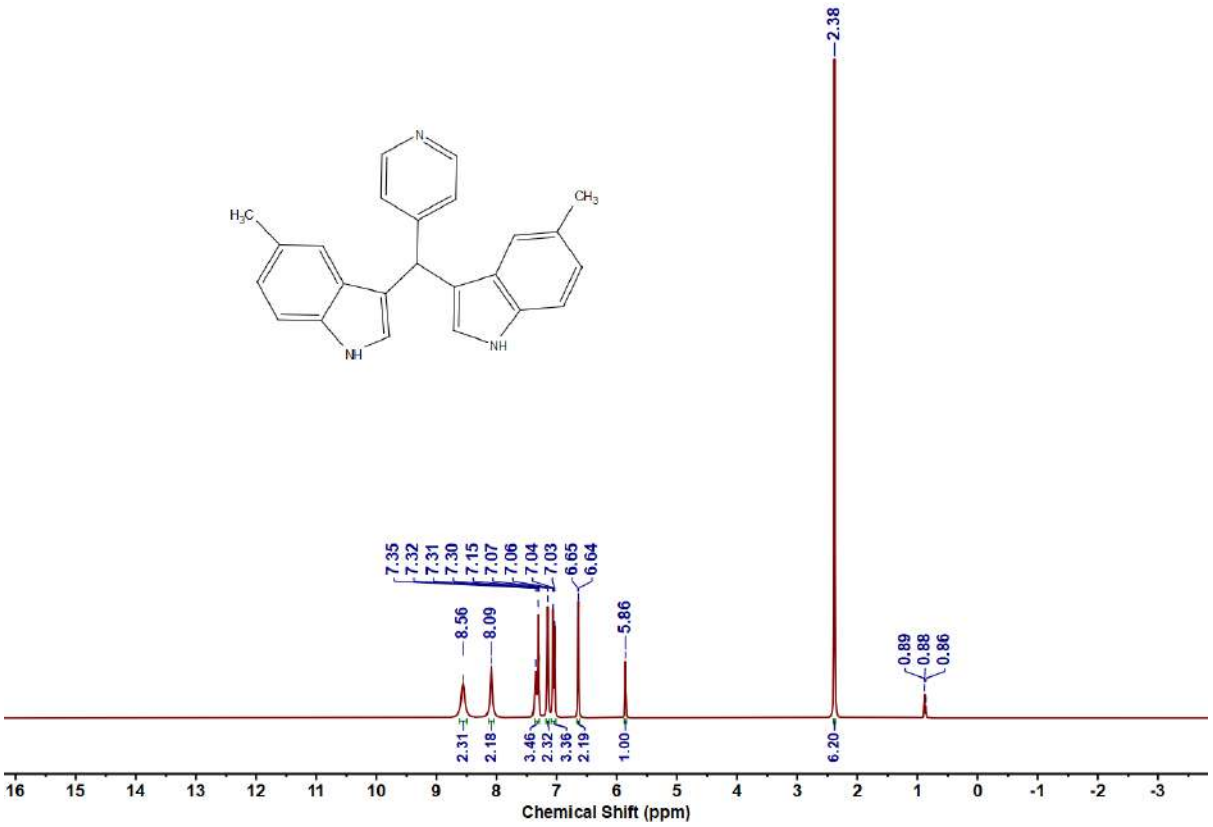

Figure 5.6.A79: ^{1}H NMR spectrum of **9an**

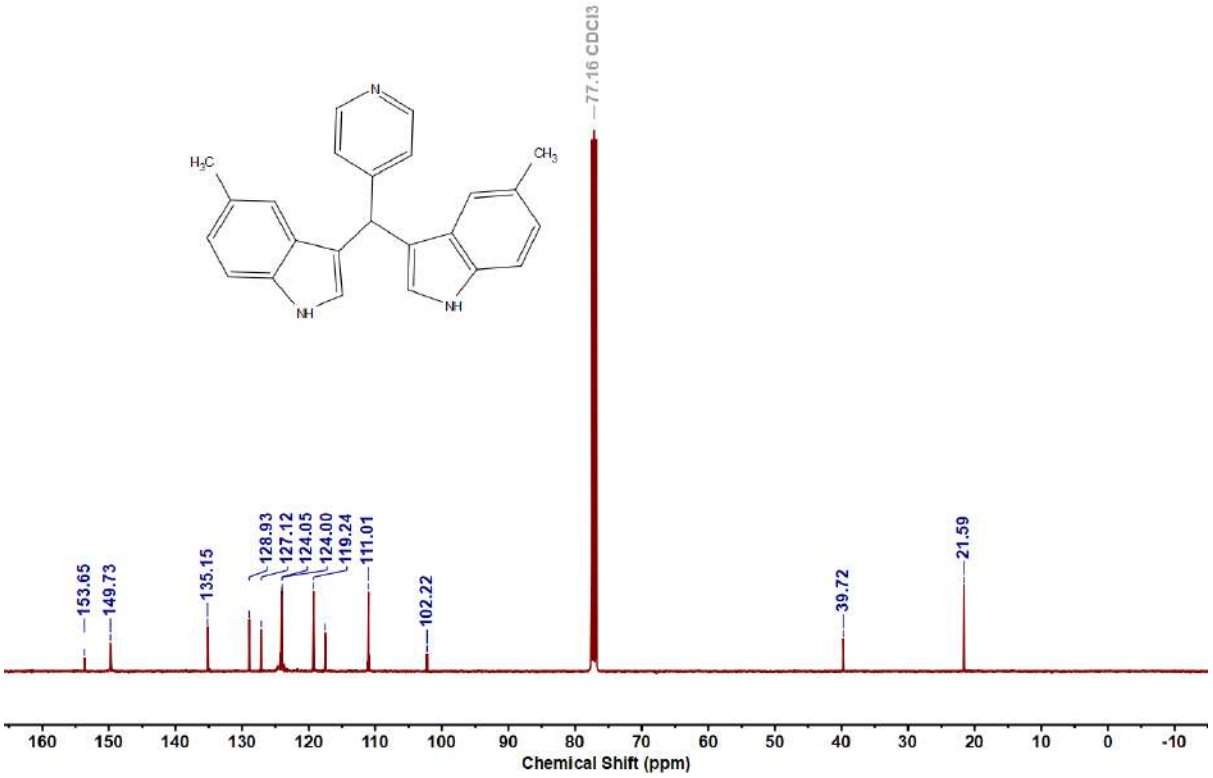

Figure 5.6.A80: ^{13}C{^{1}H} NMR spectrum of **9an**

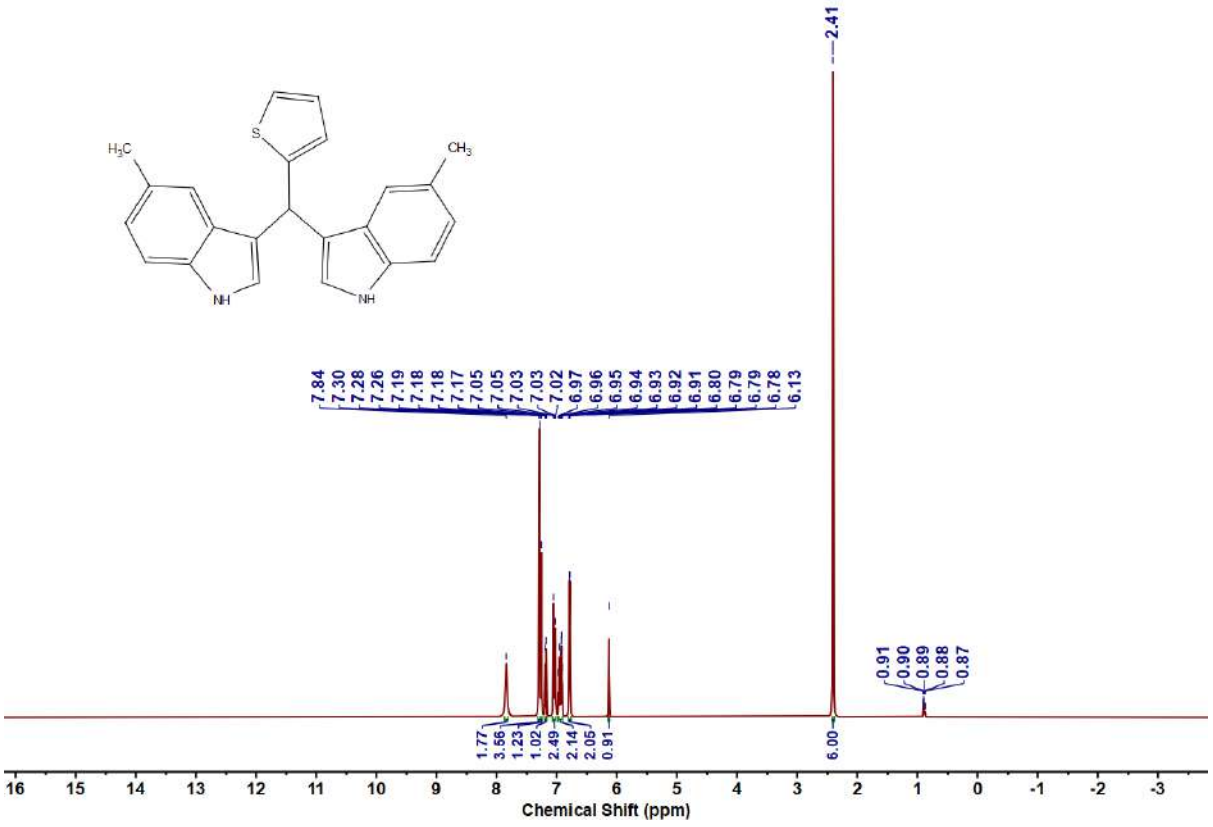

Figure 5.6.A81: ^{1}H NMR spectrum of **9ao**

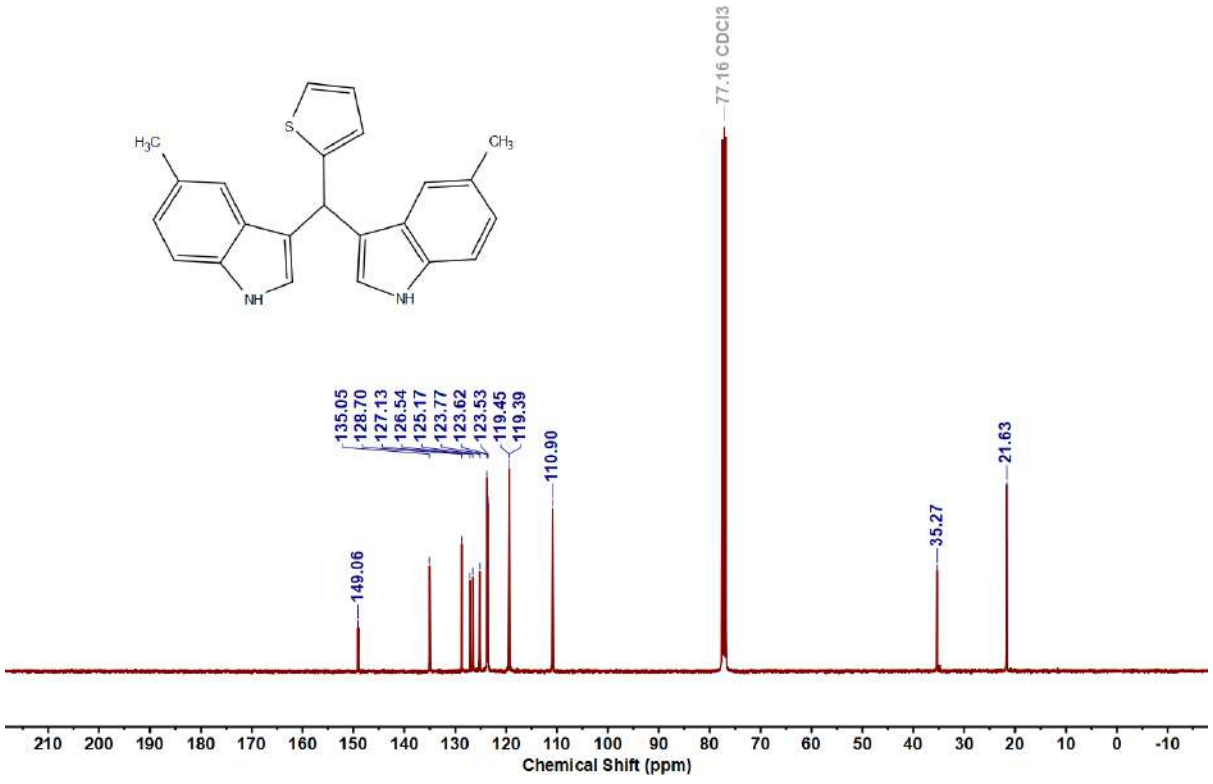

Figure 5.6.A82: ^{13}C{^{1}H} NMR spectrum of **9ao**

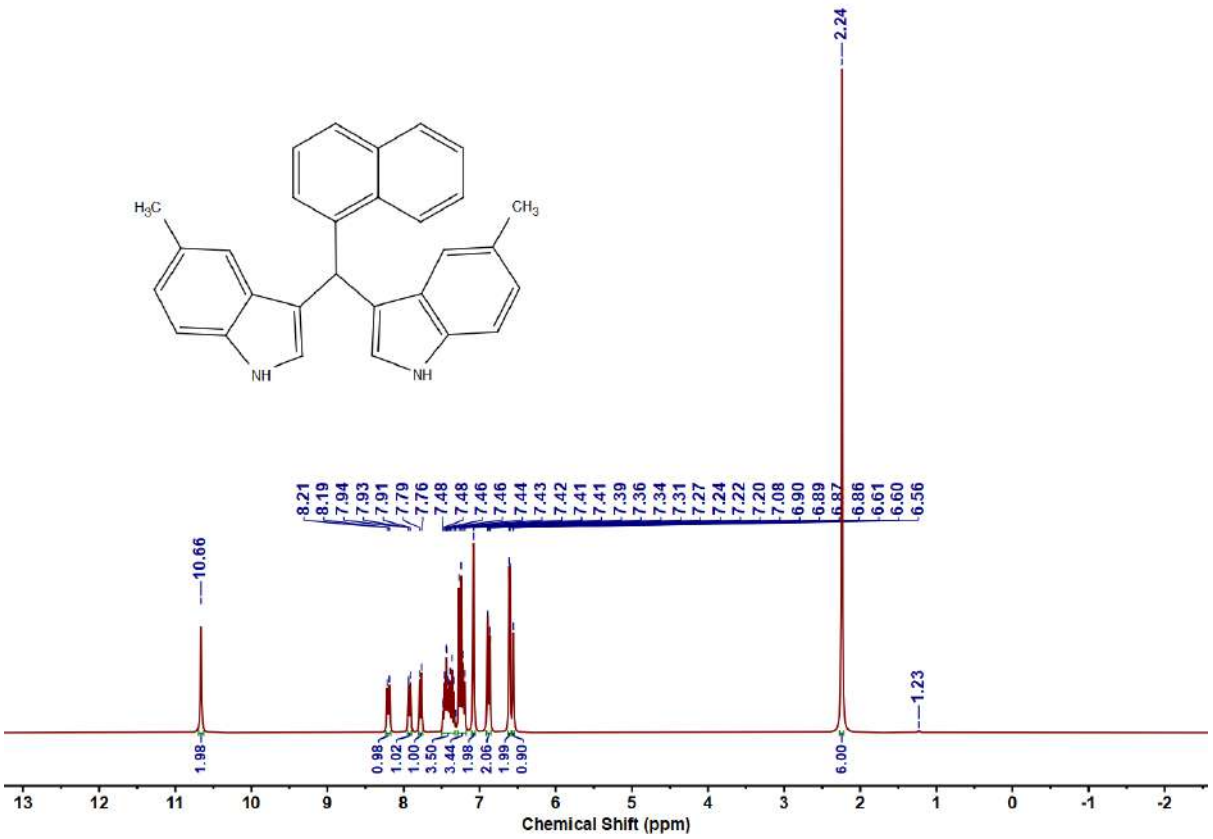

Figure 5.6.A83: ^{1}H NMR spectrum of **9ap**

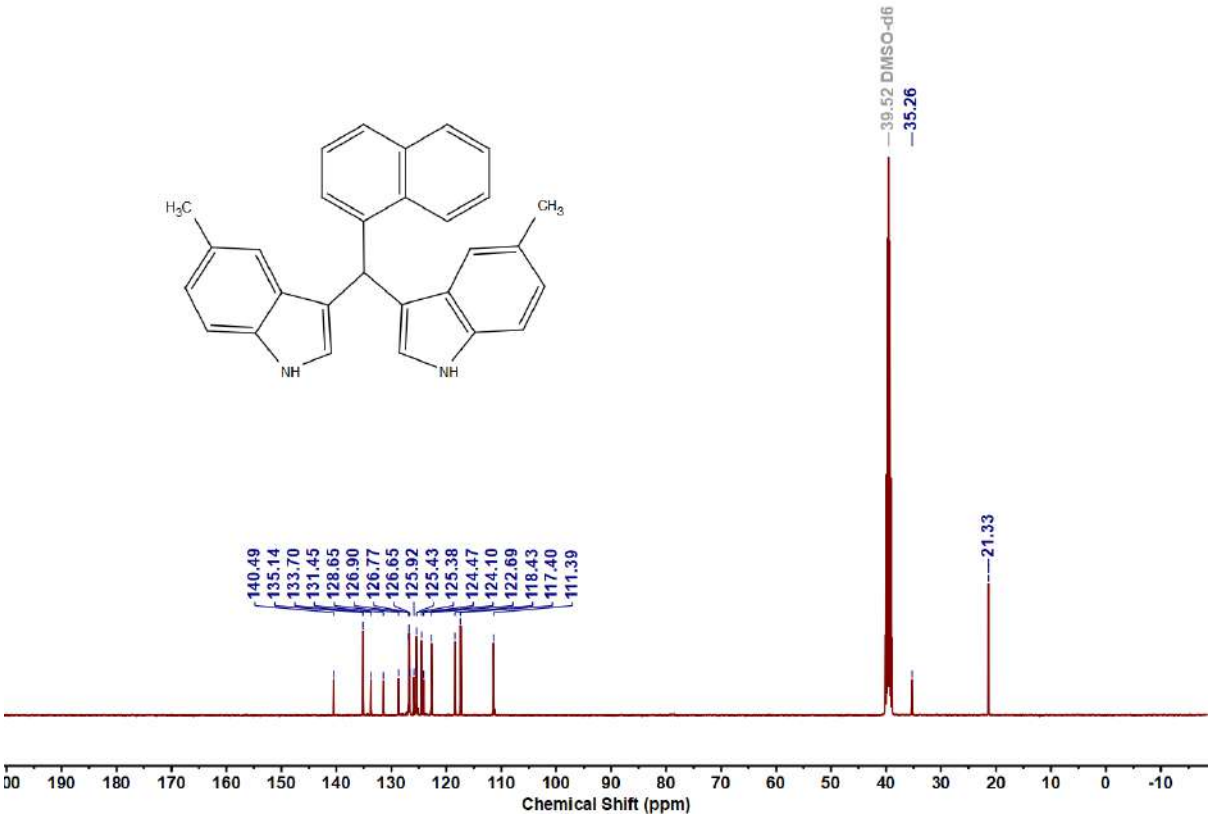

Figure 5.6.A84: ^{13}C{^{1}H} NMR spectrum of **9ap**

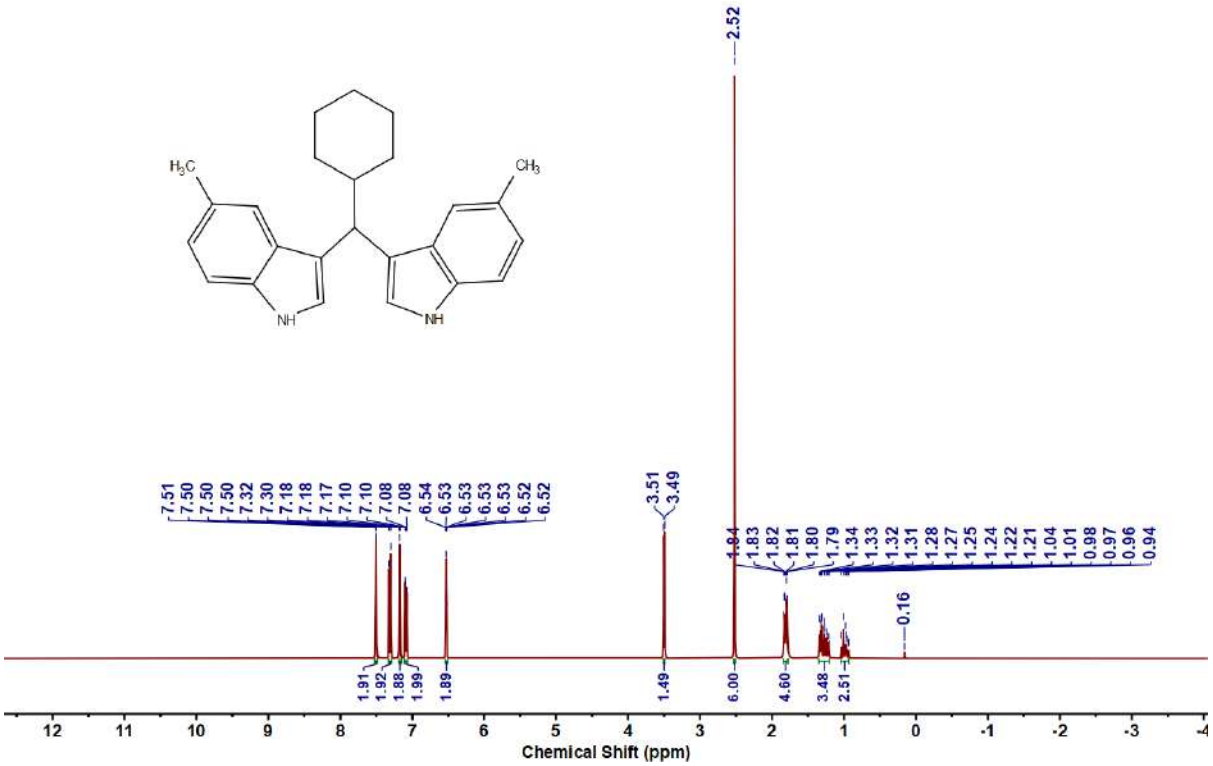

Figure 5.6.A85: ^{1}H NMR spectrum of **9aq**

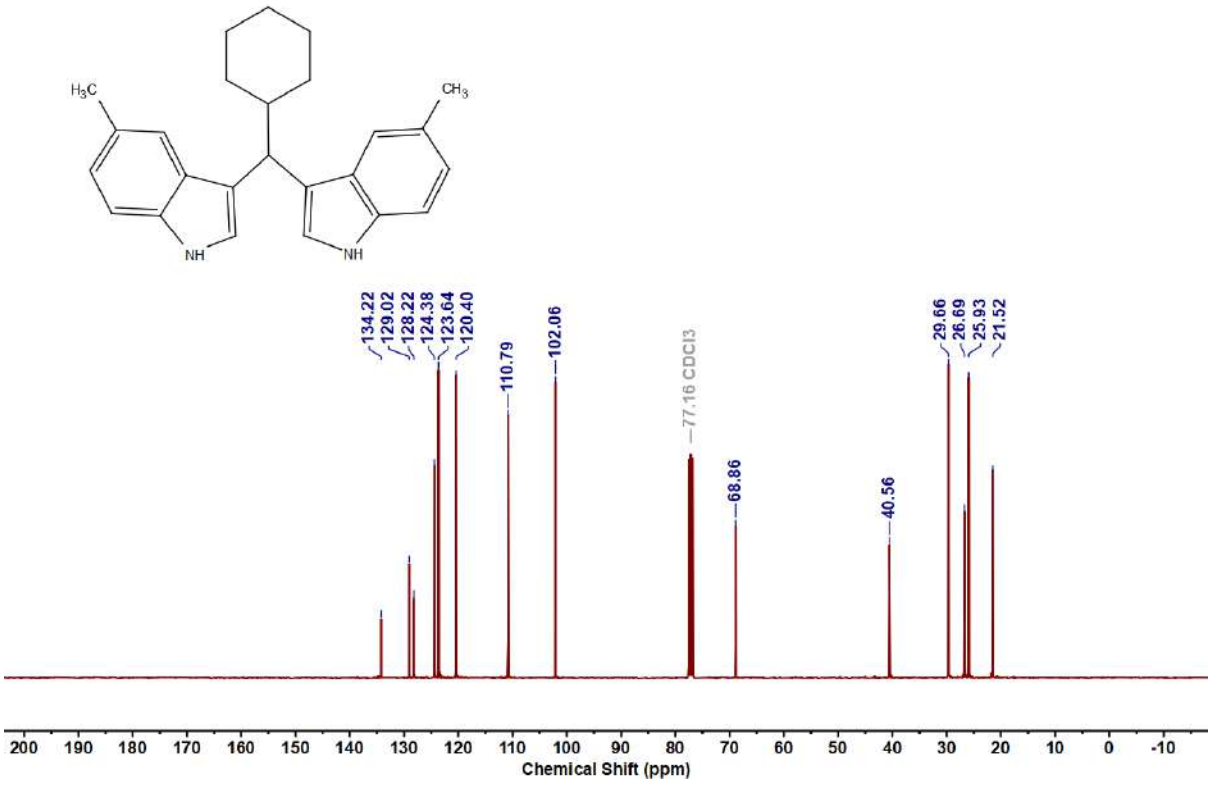

Figure 5.6.A86: ^{13}C{^{1}H} NMR spectrum of **9aq**

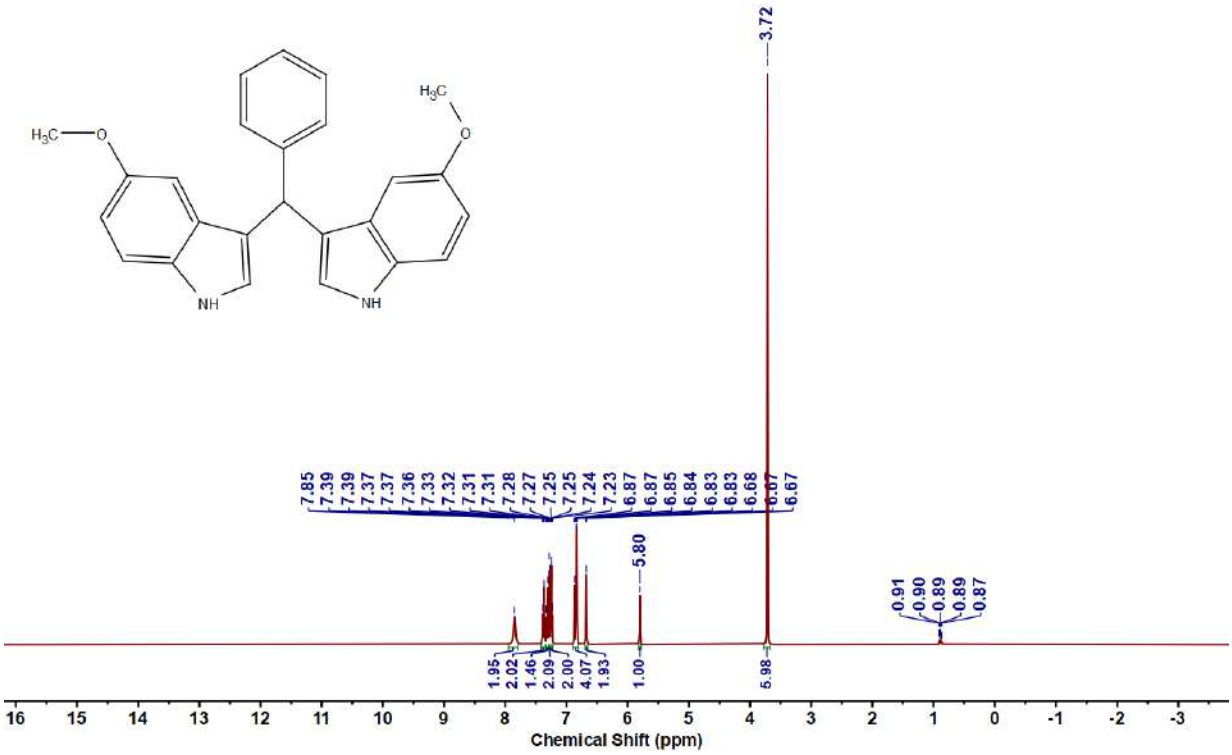

Figure 5.6.A87: ^{1}H NMR spectrum of **10aa**

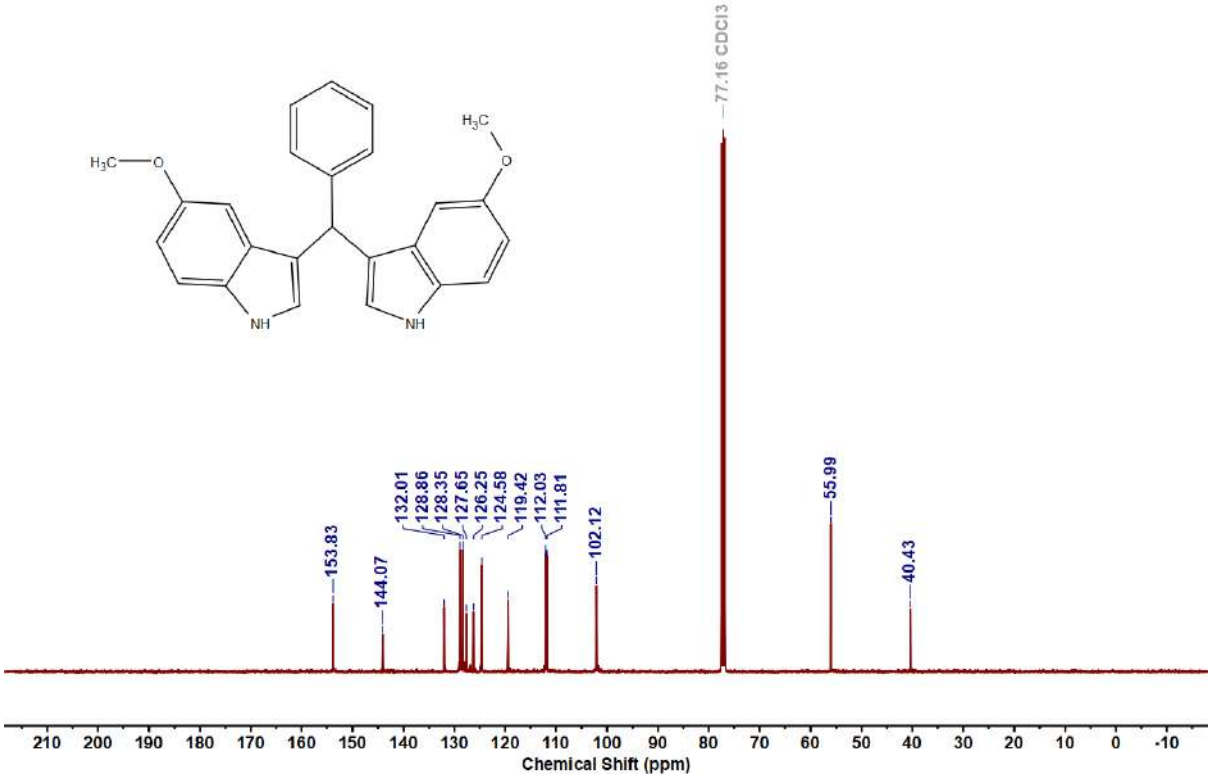

Figure 5.6.A88: ^{13}C{^{1}H} NMR spectrum of **10aa**

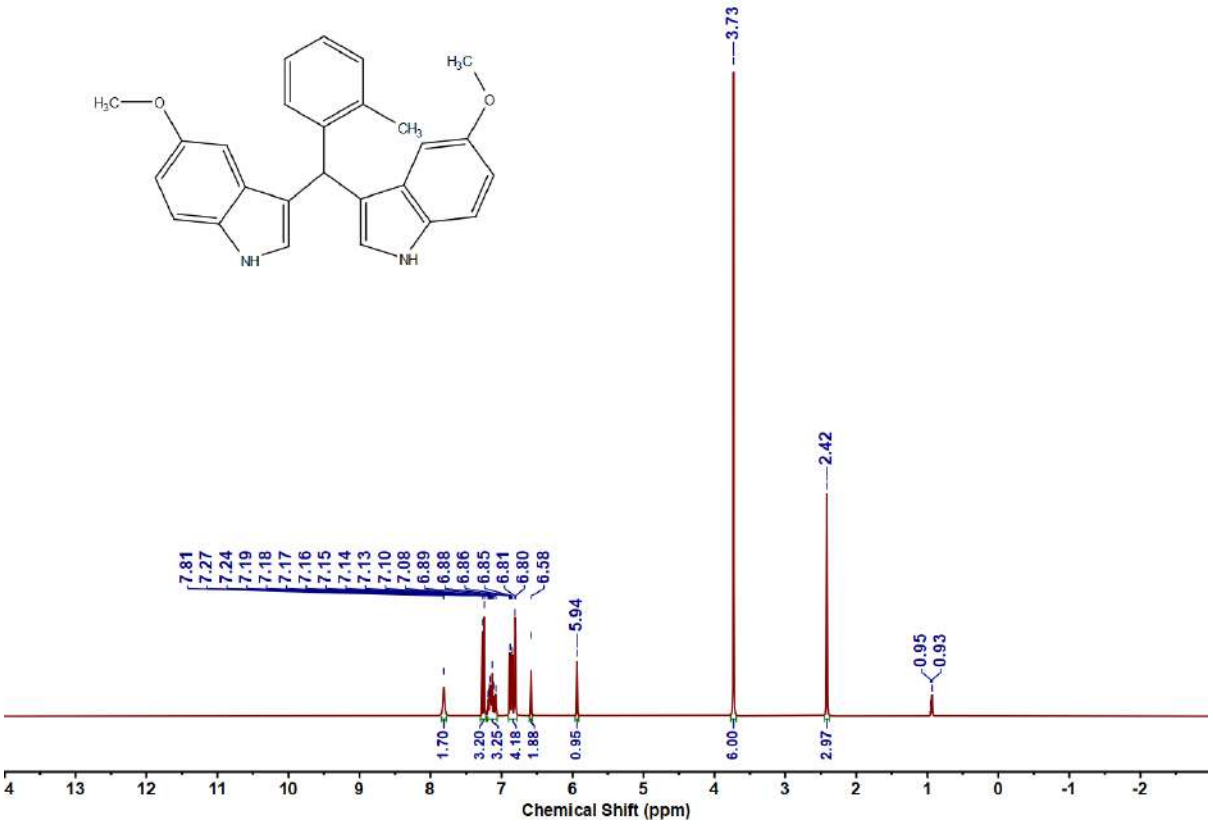

Figure 5.6.A89: ^{1}H NMR spectrum of **10ab**

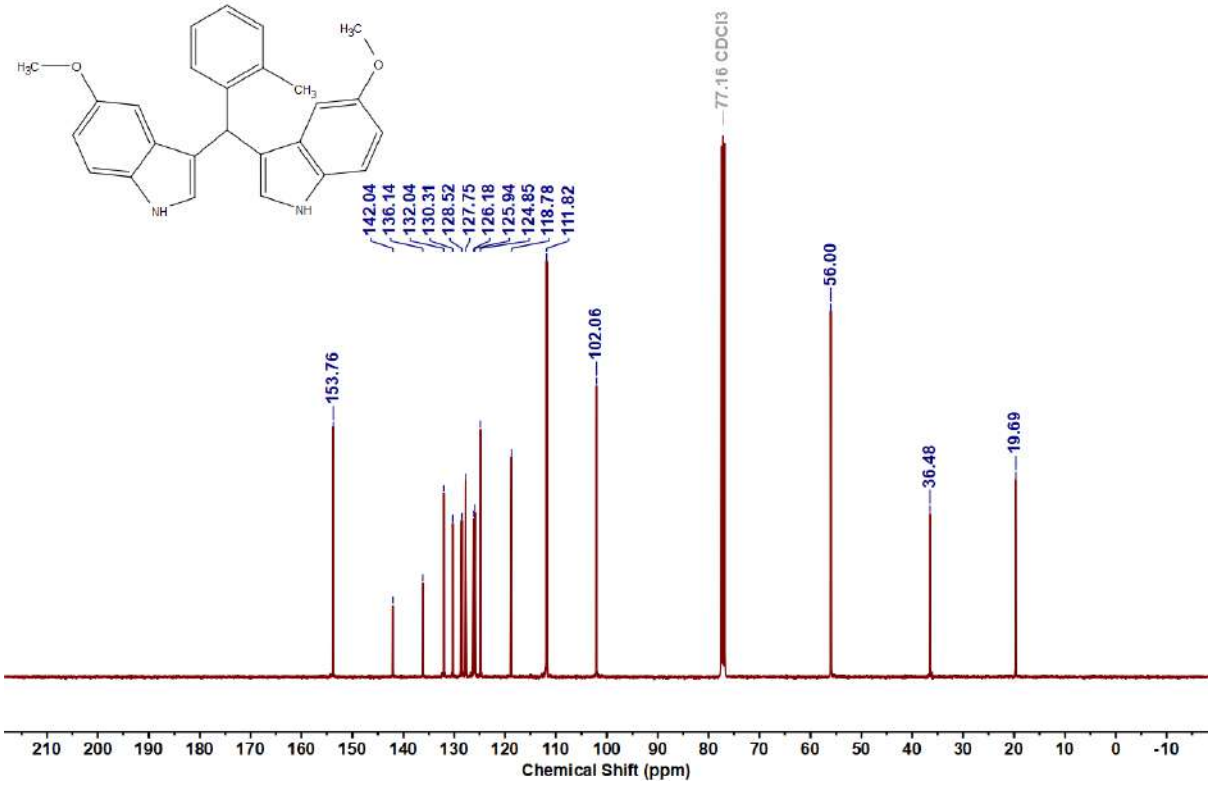

Figure 5.6.A90: ^{13}C{^{1}H} NMR spectrum of **10ab**

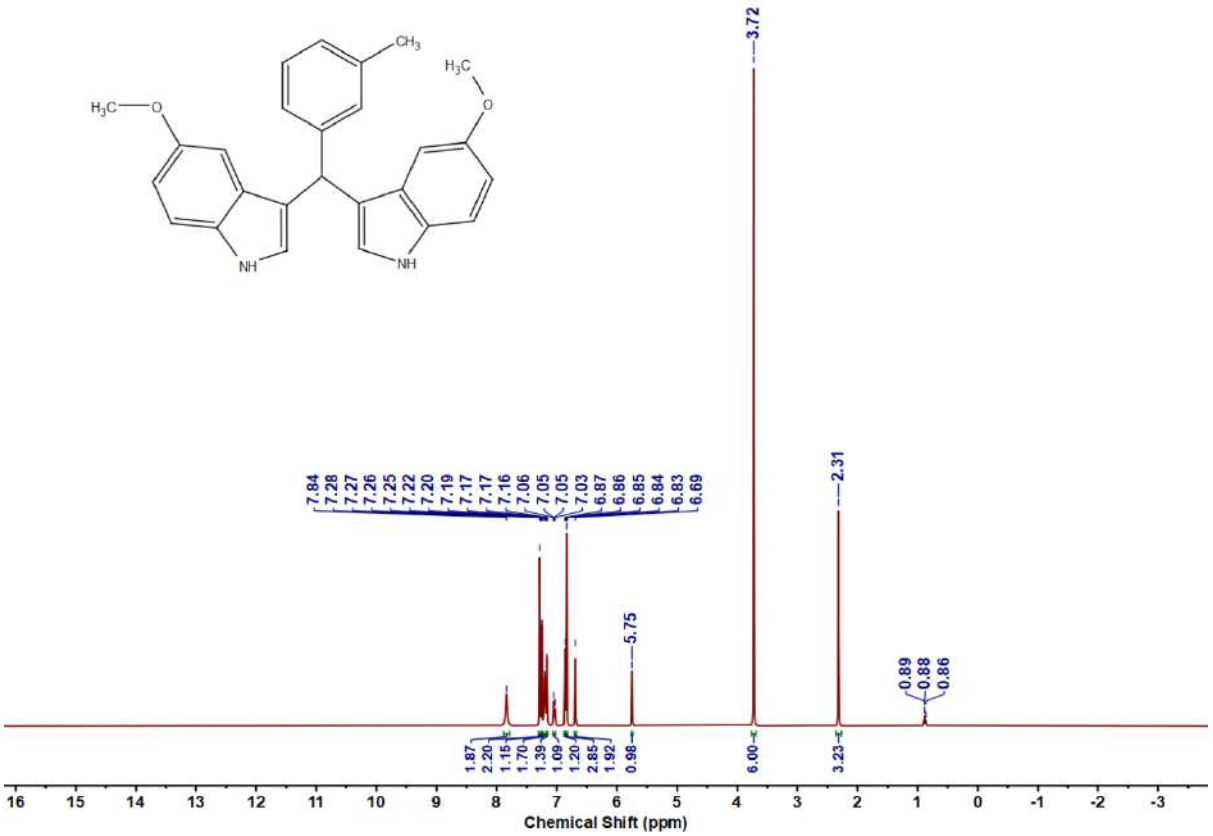

Figure 5.6.A91: ^{1}H NMR spectrum of **10ac**

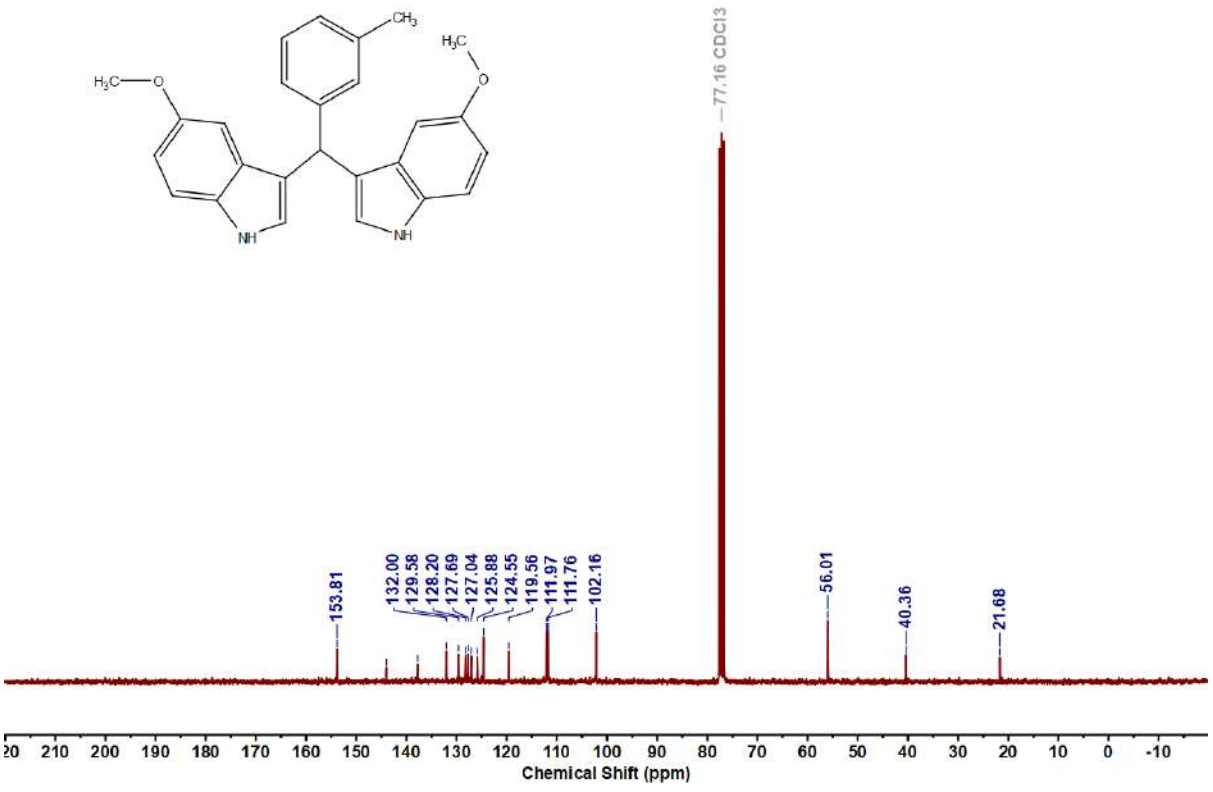

Figure 5.6.A92: ^{13}C{^{1}H} NMR spectrum of **10ac**

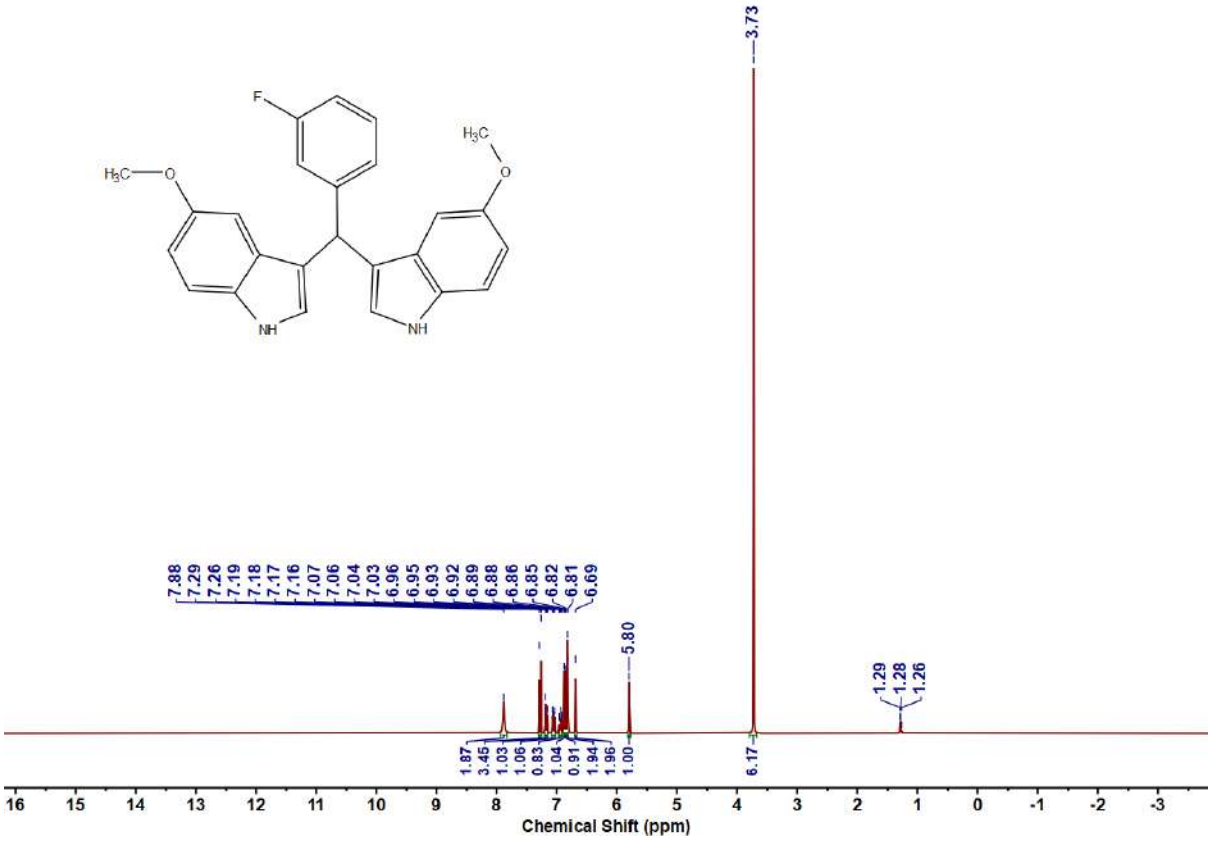

Figure 5.6.A93: ^{1}H NMR spectrum of **10ad**

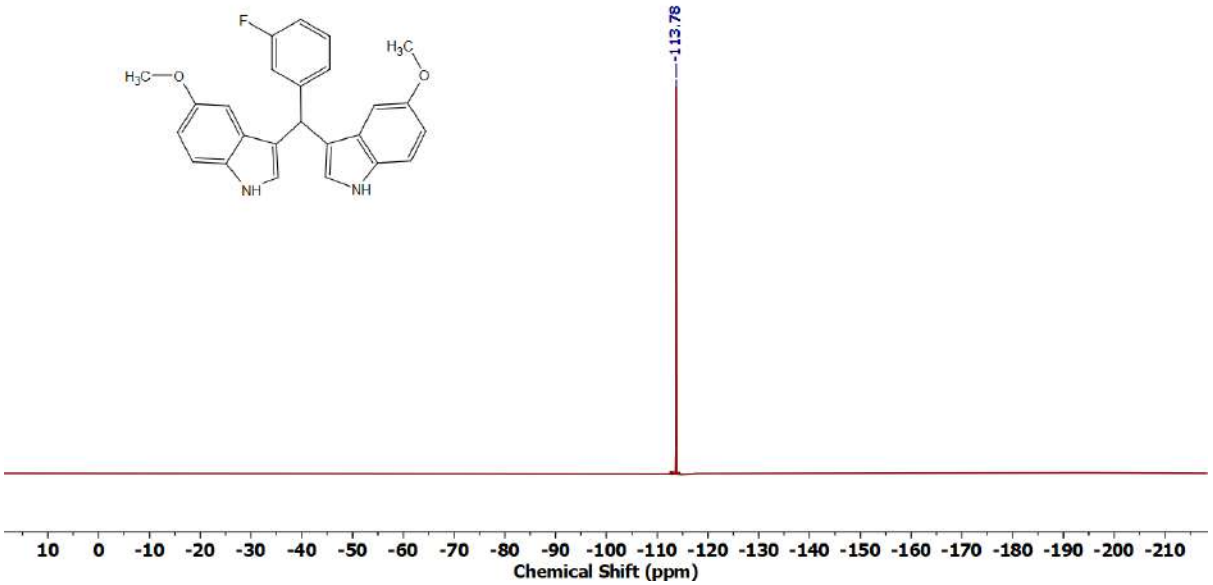

Figure 5.6.A94: ^{19}F NMR spectrum of **10ad**

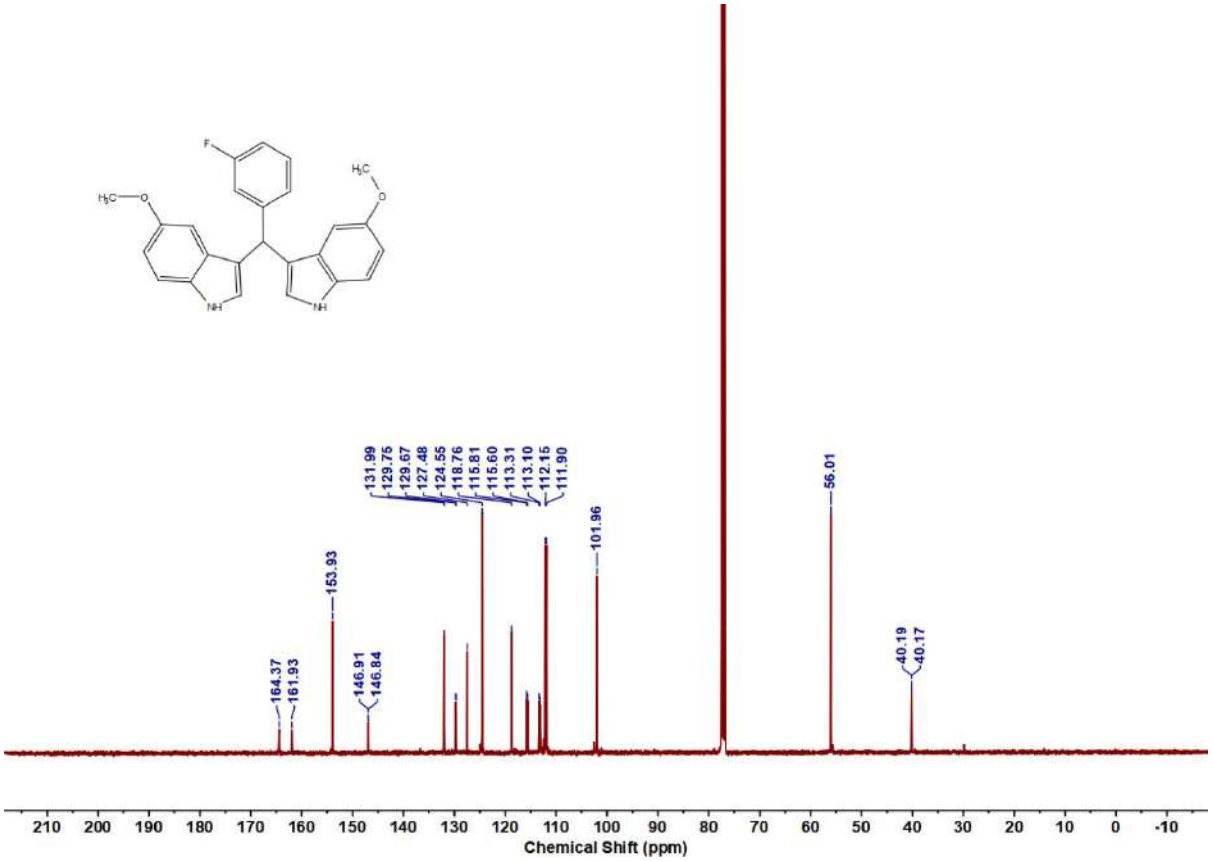

Figure 5.6.A95: $^{13}C\{^{1}H\}$ NMR spectrum of **10ad**

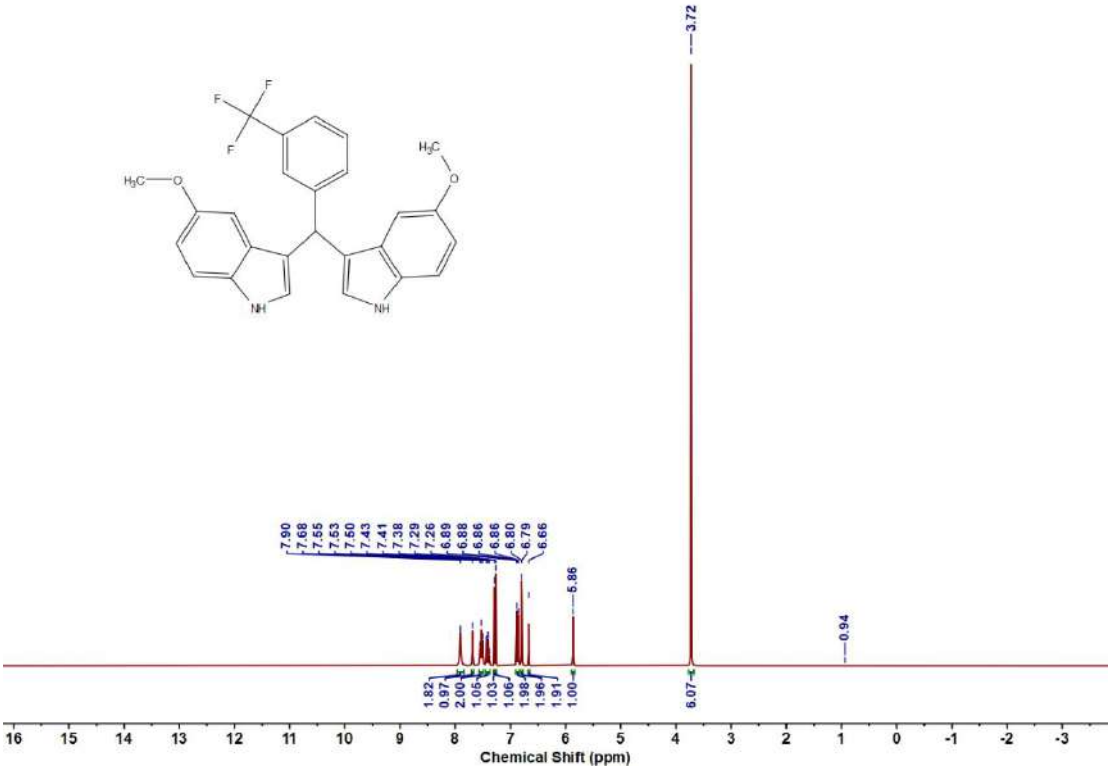

Figure 5.6.A96: ^{1}H NMR spectrum of **10ae**

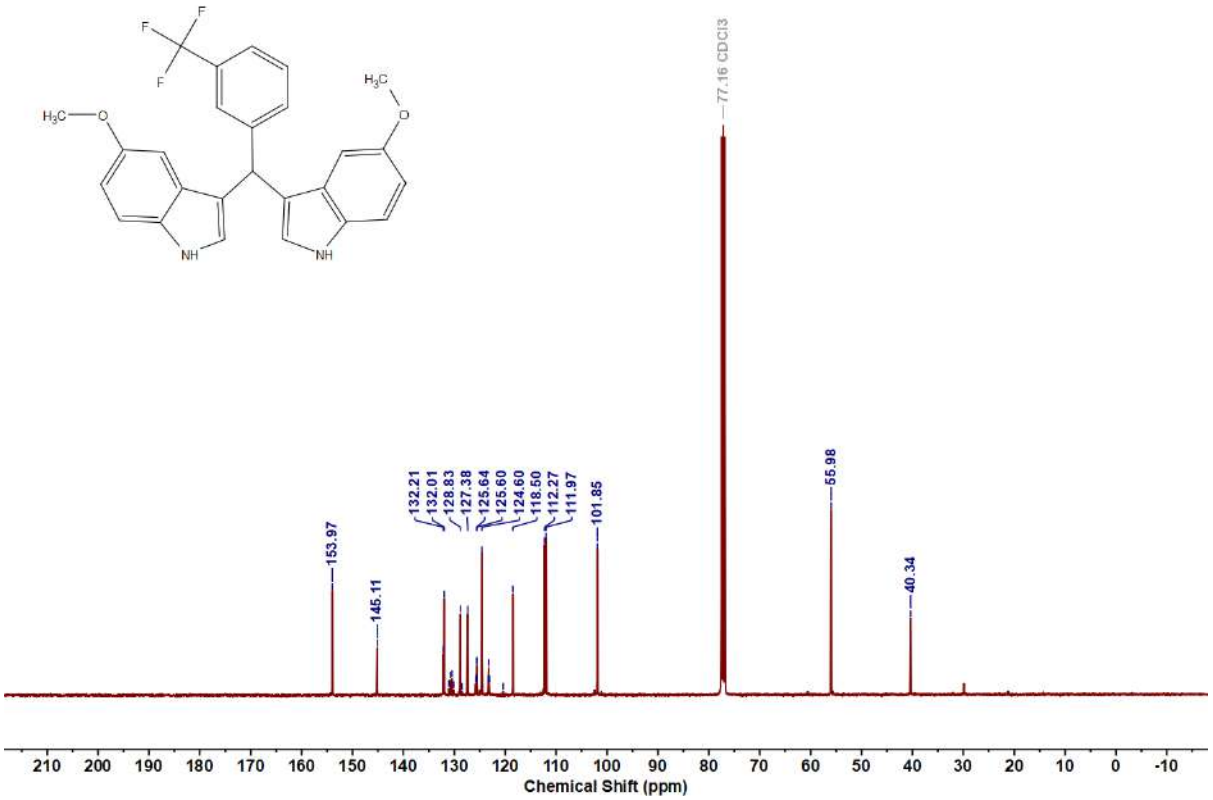

Figure 5.6.A97: $^{13}C\{^{1}H\}$ NMR spectrum of **10ae**

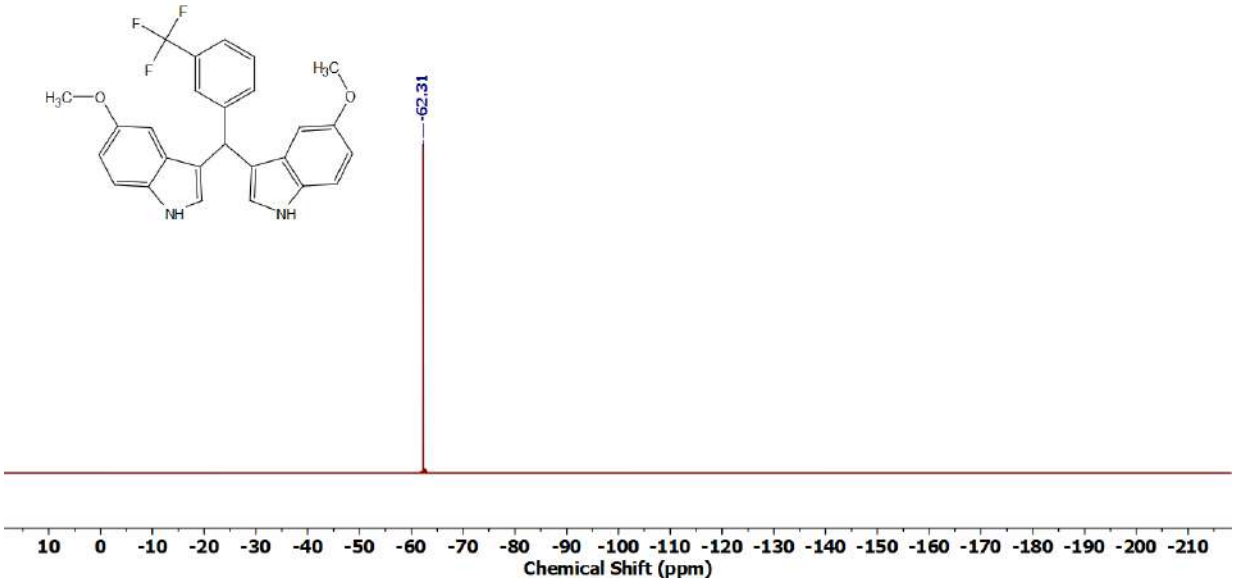

Figure 5.6.A98: ^{19}F NMR spectrum of **10ae**

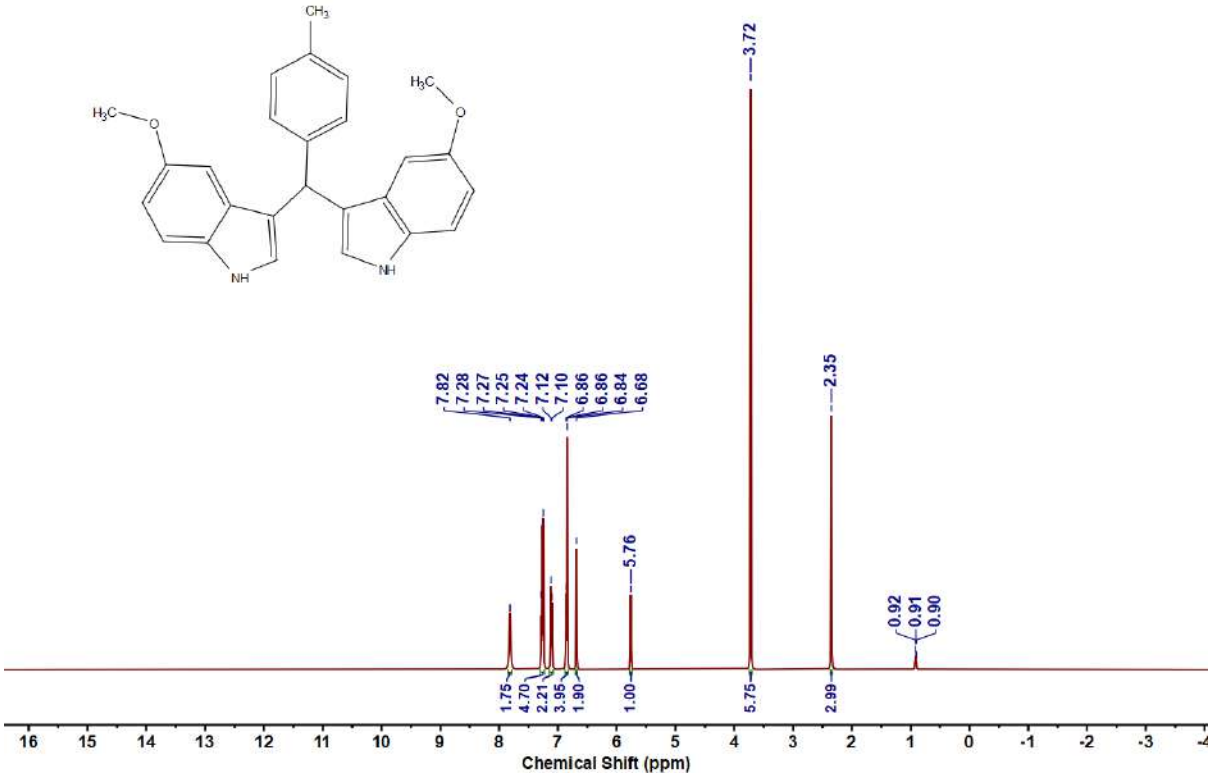

Figure 5.6.A99: ^{1}H NMR spectrum of **10af**

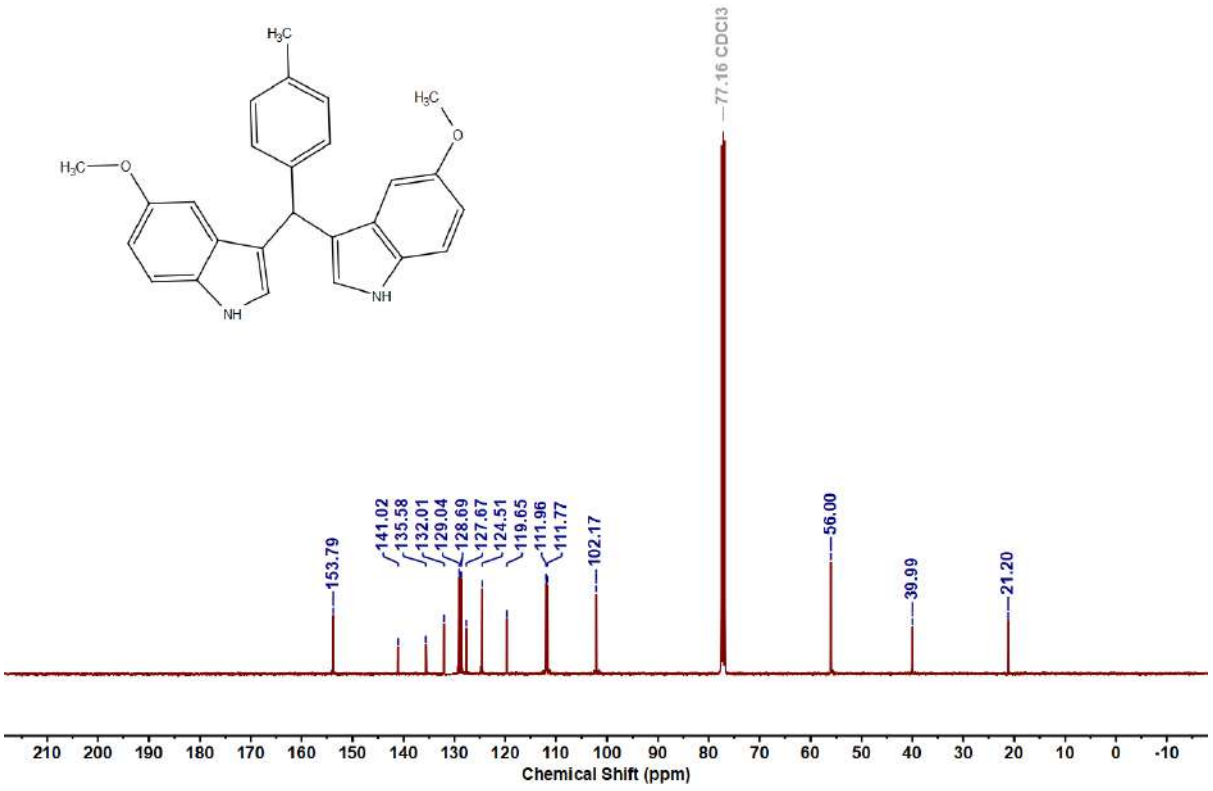

Figure 5.6.A100: ^{13}C{^{1}H} NMR spectrum of **10af**

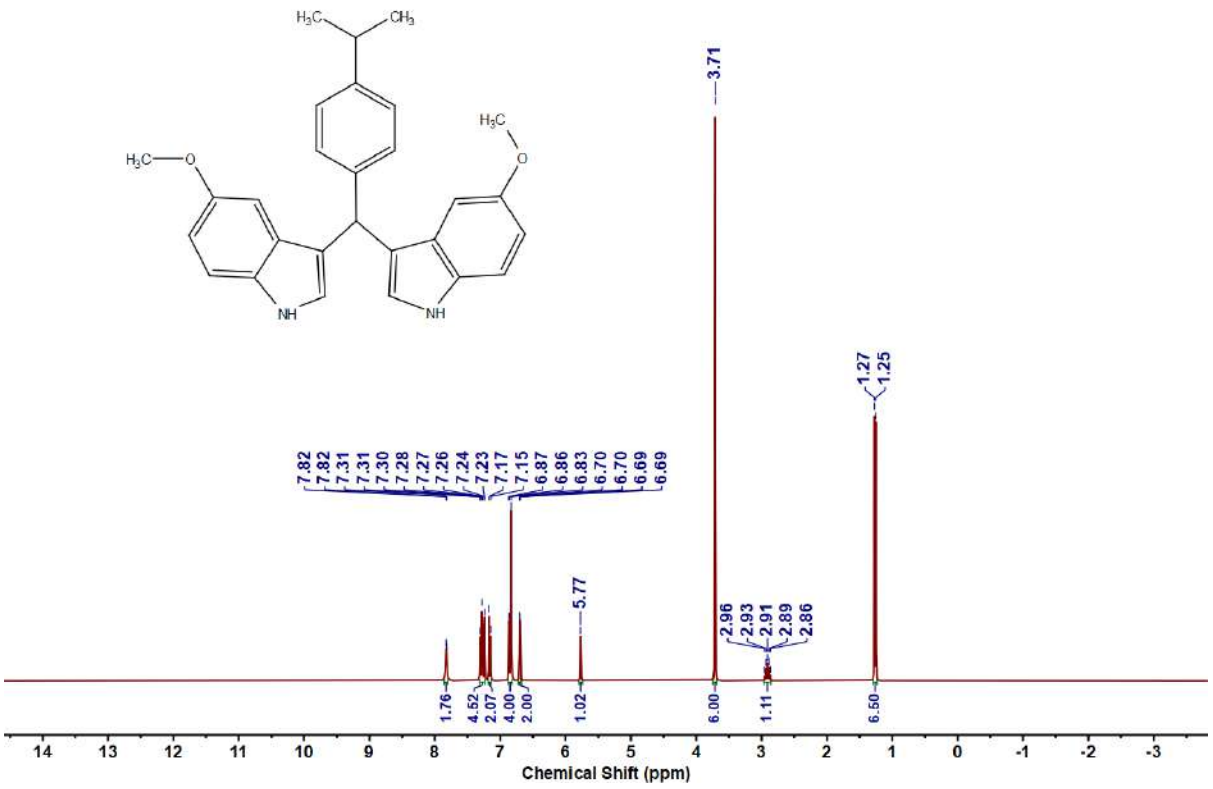

Figure 5.6.A101: ^{1}H NMR spectrum of **10ag**

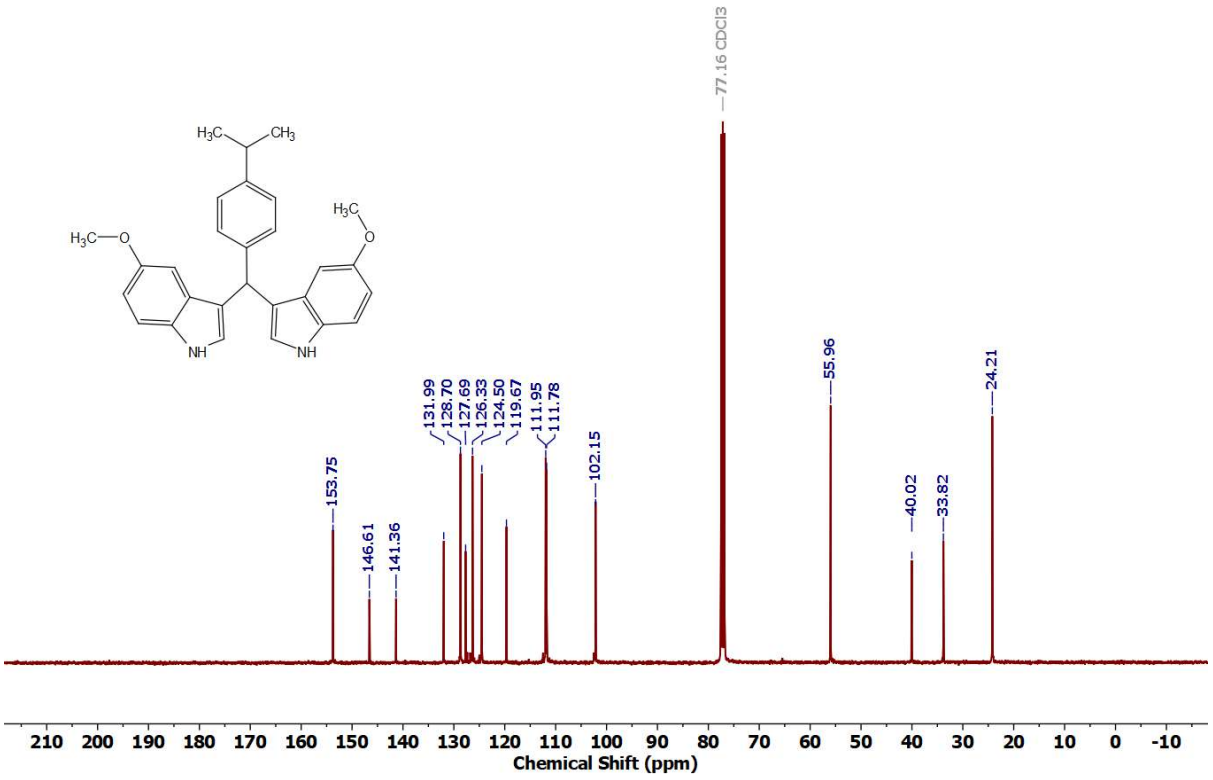

Figure 5.6.A102: ^{13}C{^{1}H} NMR spectrum of **10ag**

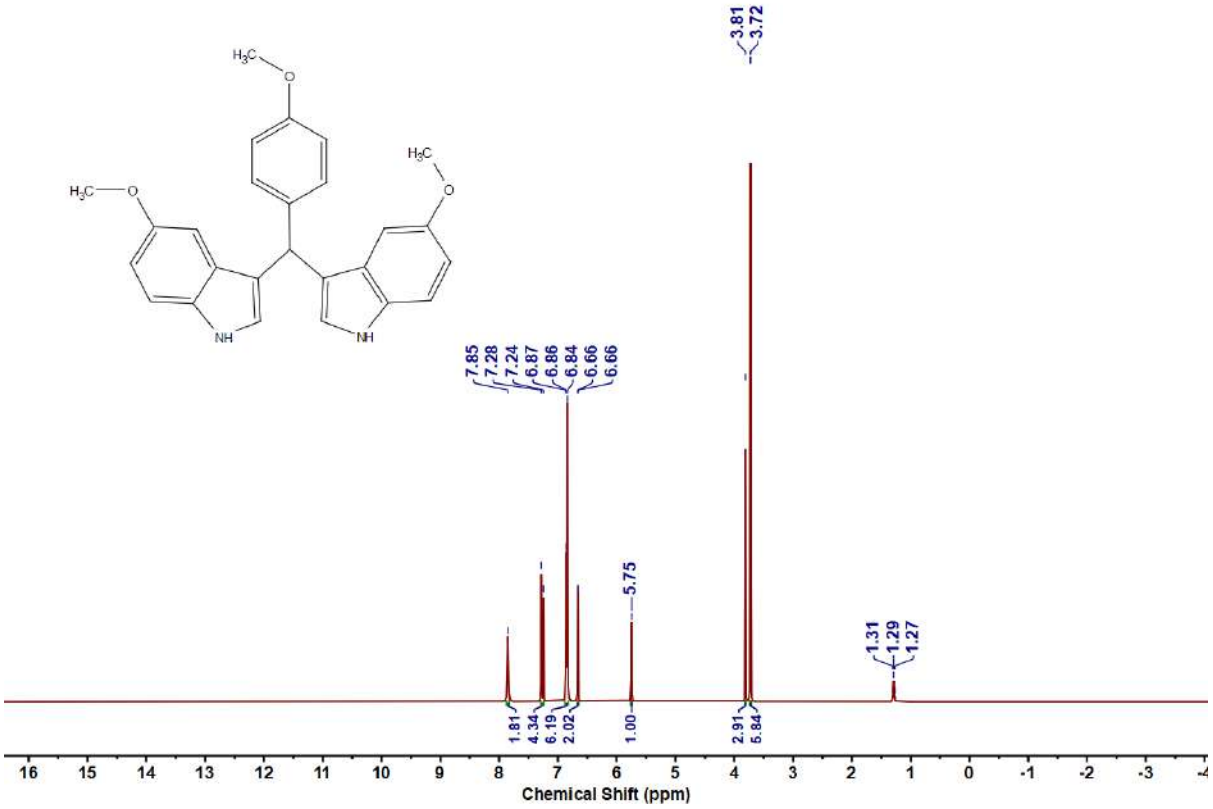

Figure 5.6.A103: ^{1}H NMR spectrum of **10ah**

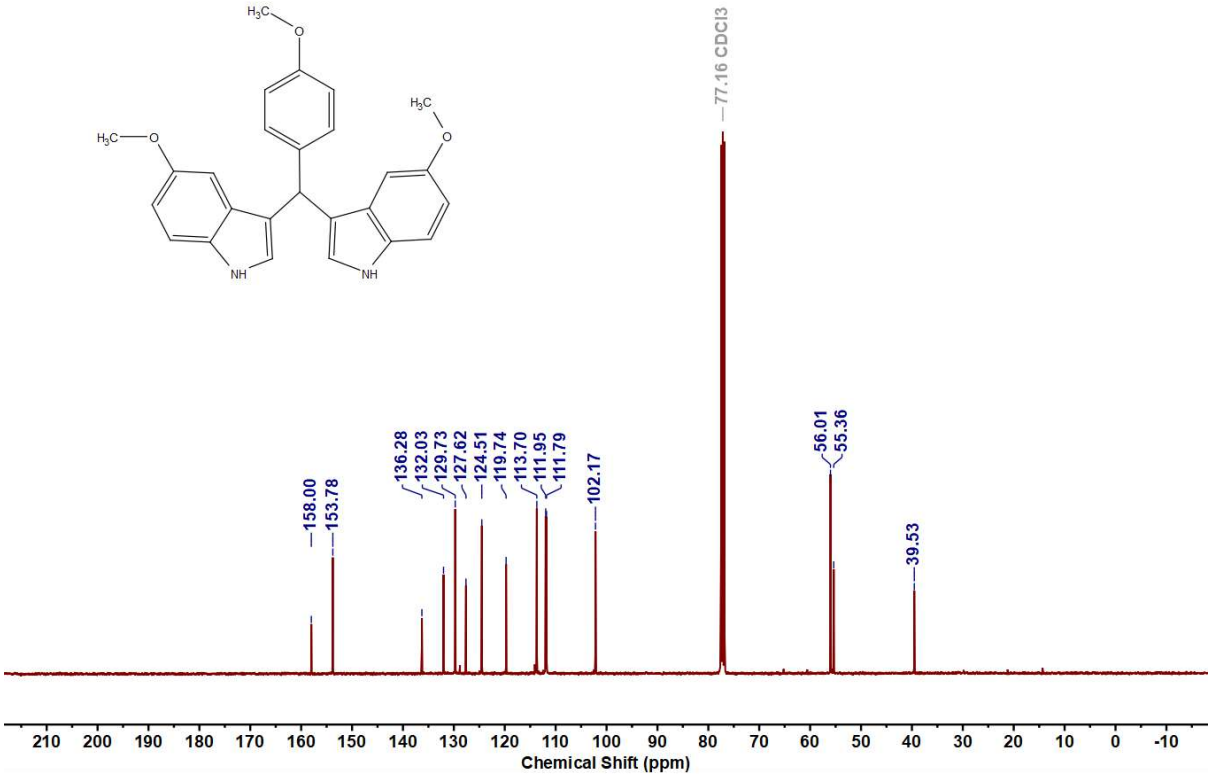

Figure 5.6.A104: ^{13}C{^{1}H} NMR spectrum of **10ah**

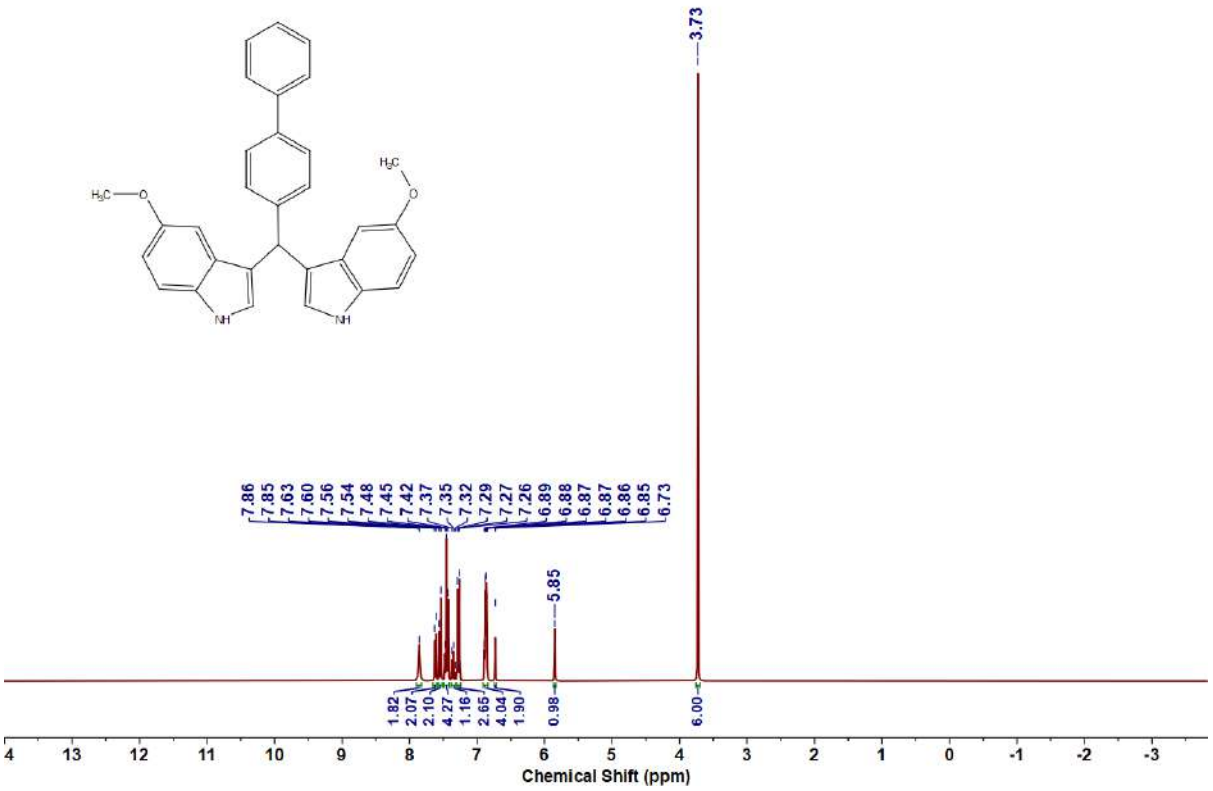

Figure 5.6.A105: ^{1}H NMR spectrum of **10ai**

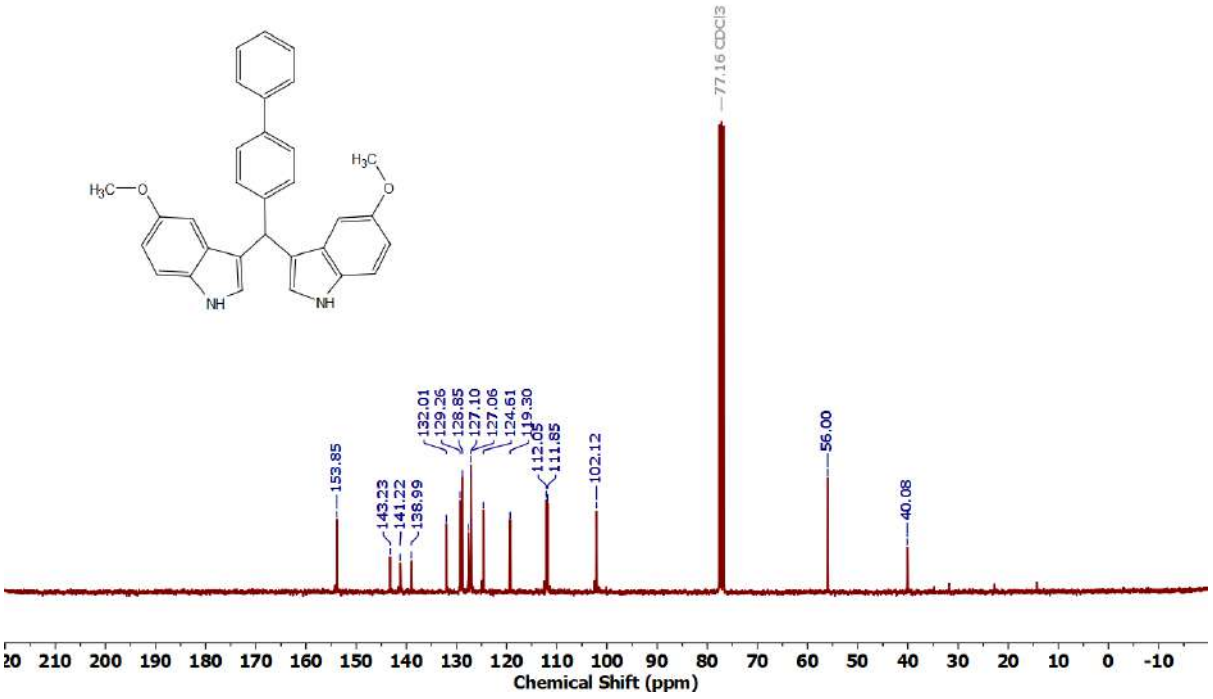

Figure 5.6.A106: ^{13}C{^{1}H} NMR spectrum of **10ai**

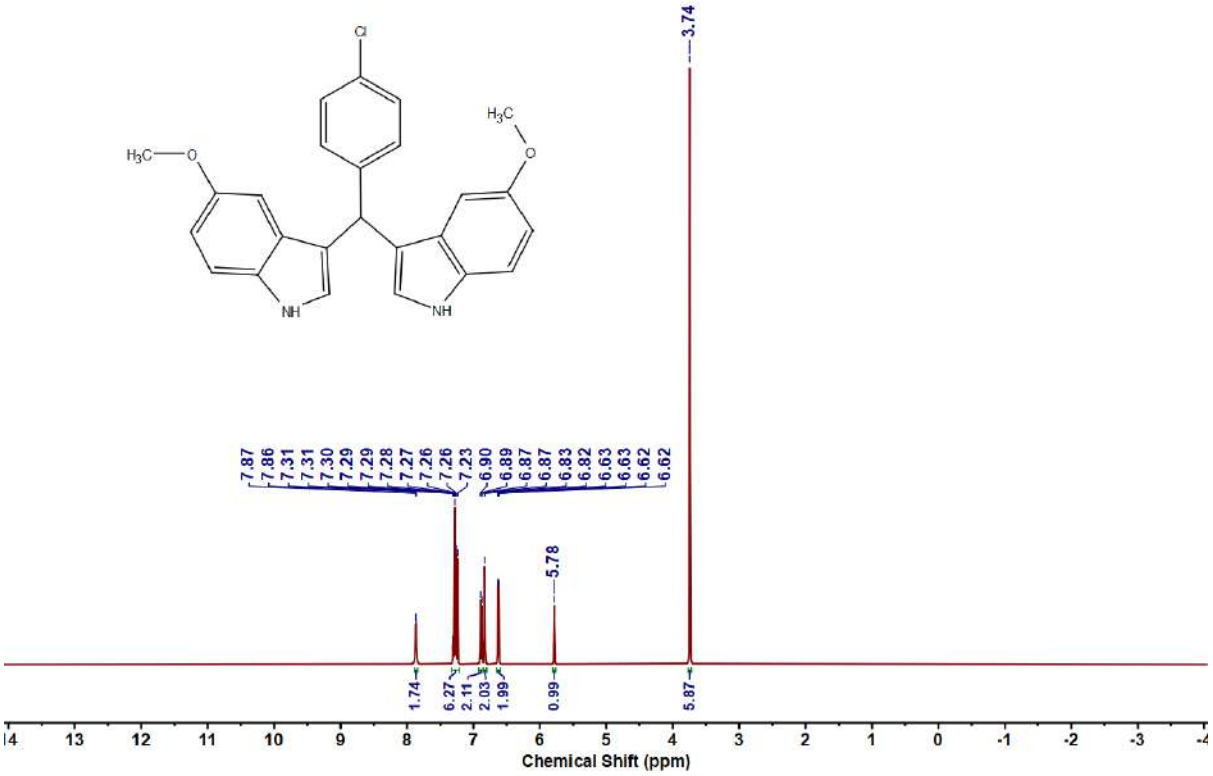

Figure 5.6.A107: ^{1}H NMR spectrum of **10aj**

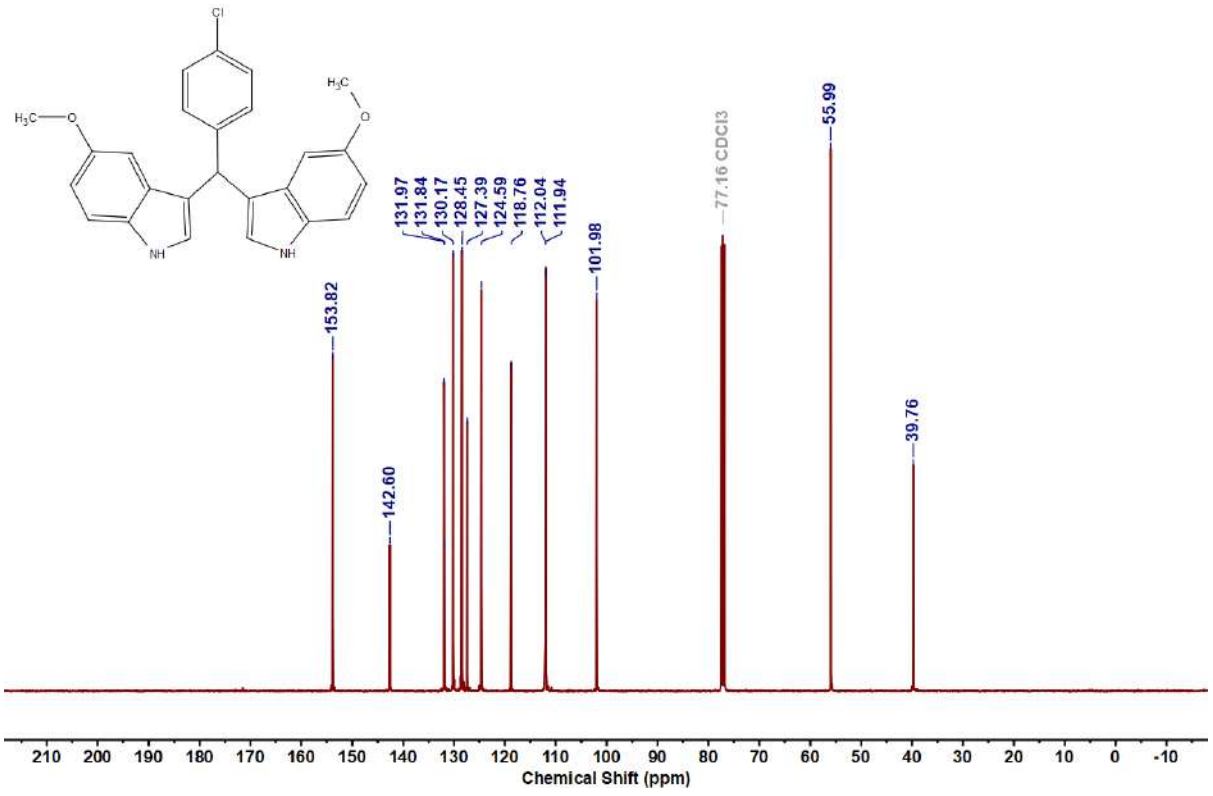

Figure 5.6.A108: ^{13}C{^{1}H} NMR spectrum of **10aj**

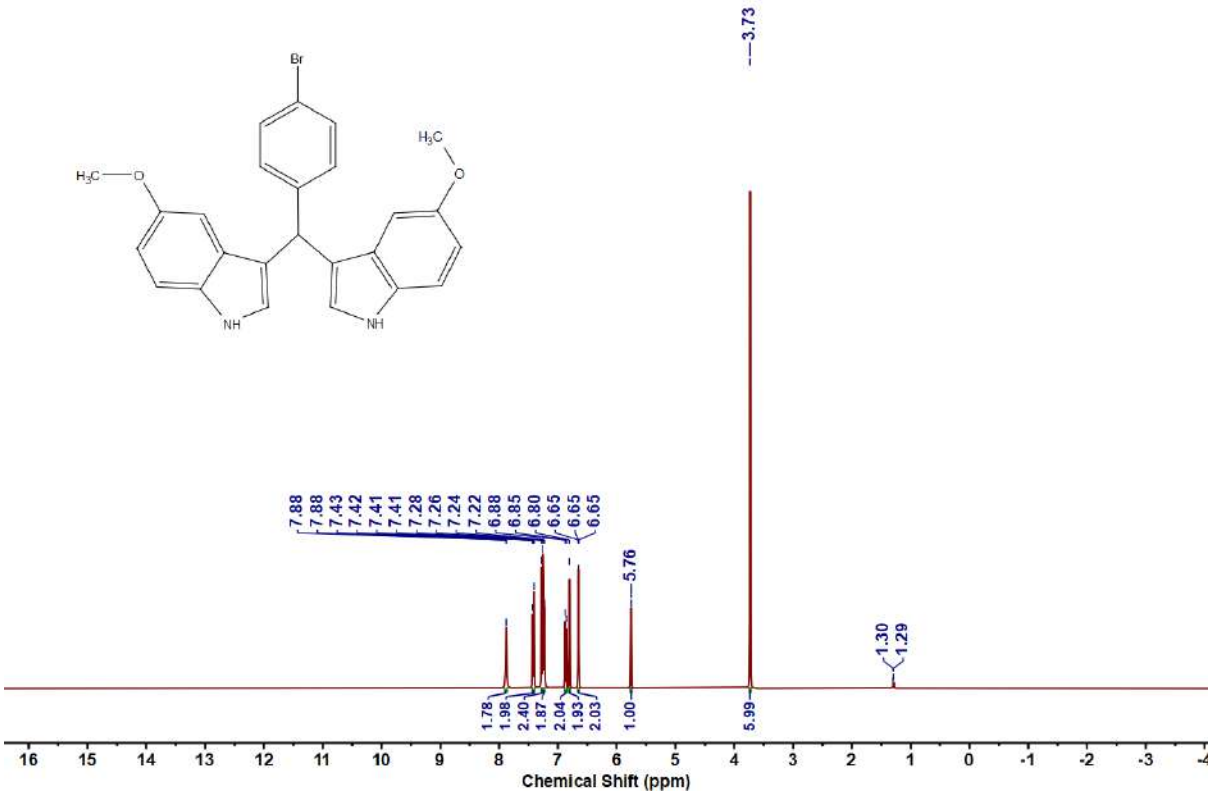

Figure 5.6.A109: ^{1}H NMR spectrum of **10ak**

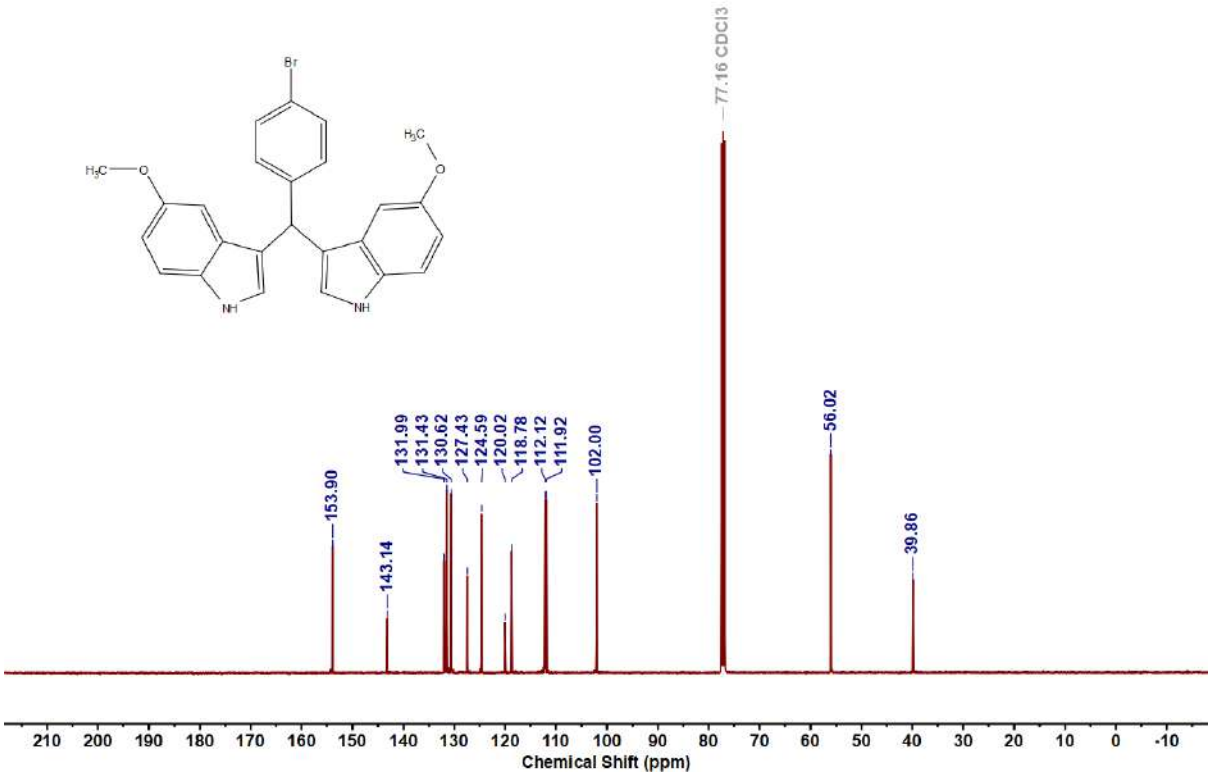

Figure 5.6.A110: ^{13}C{^{1}H} NMR spectrum of **10ak**

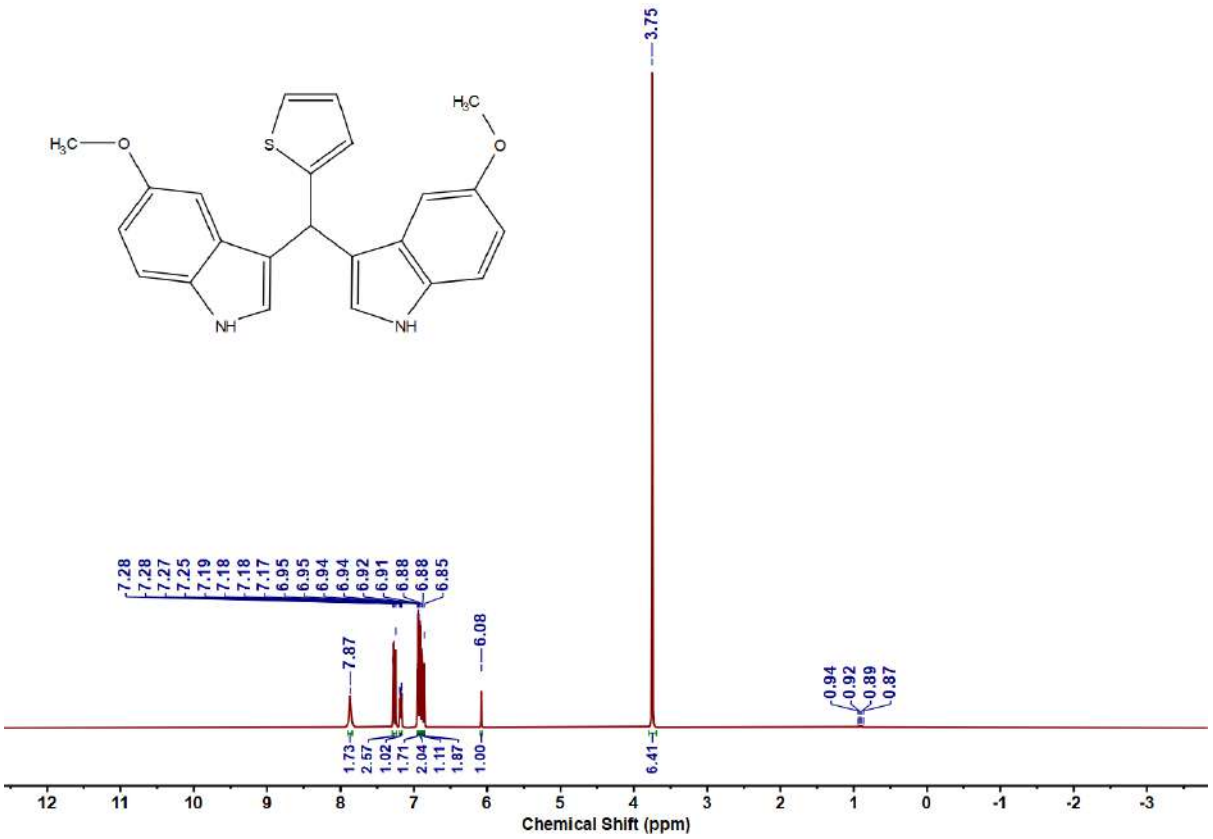

Figure 5.6.A111: ^{1}H NMR spectrum of **10al**

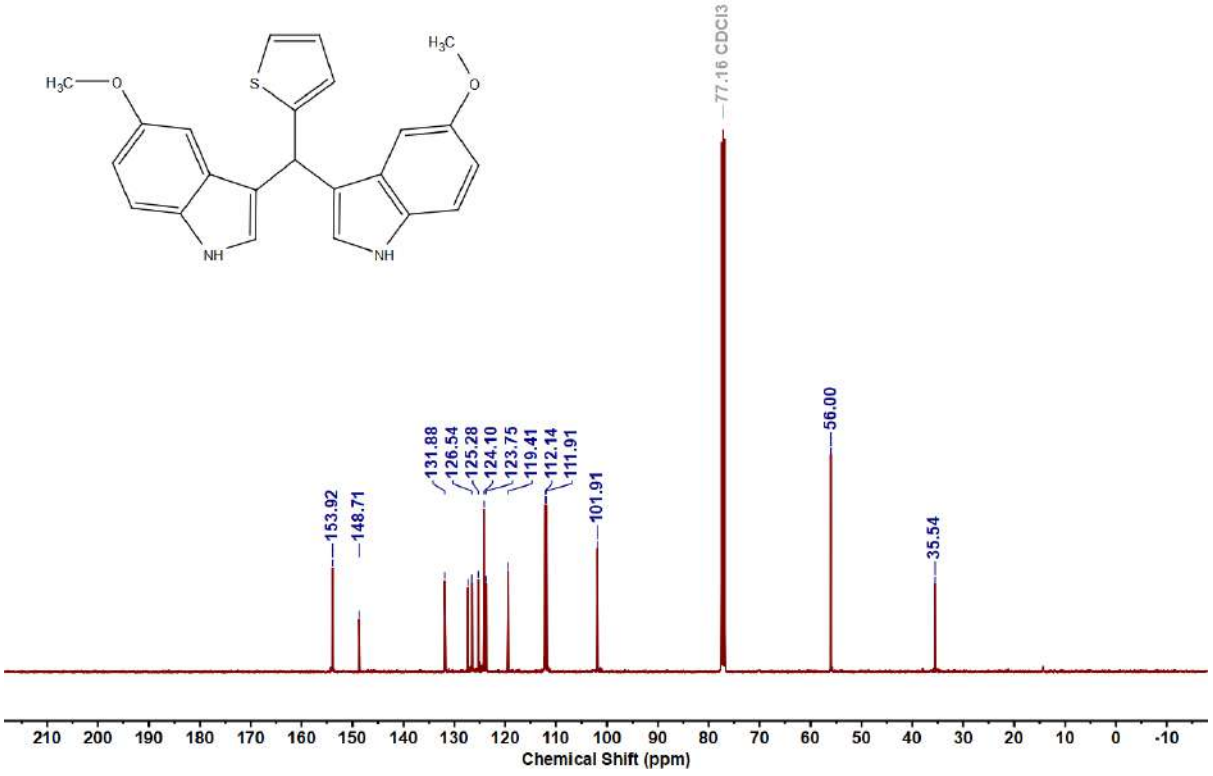

Figure 5.6.A112: $^{13}C\{^{1}H\}$ NMR spectrum of **10al**

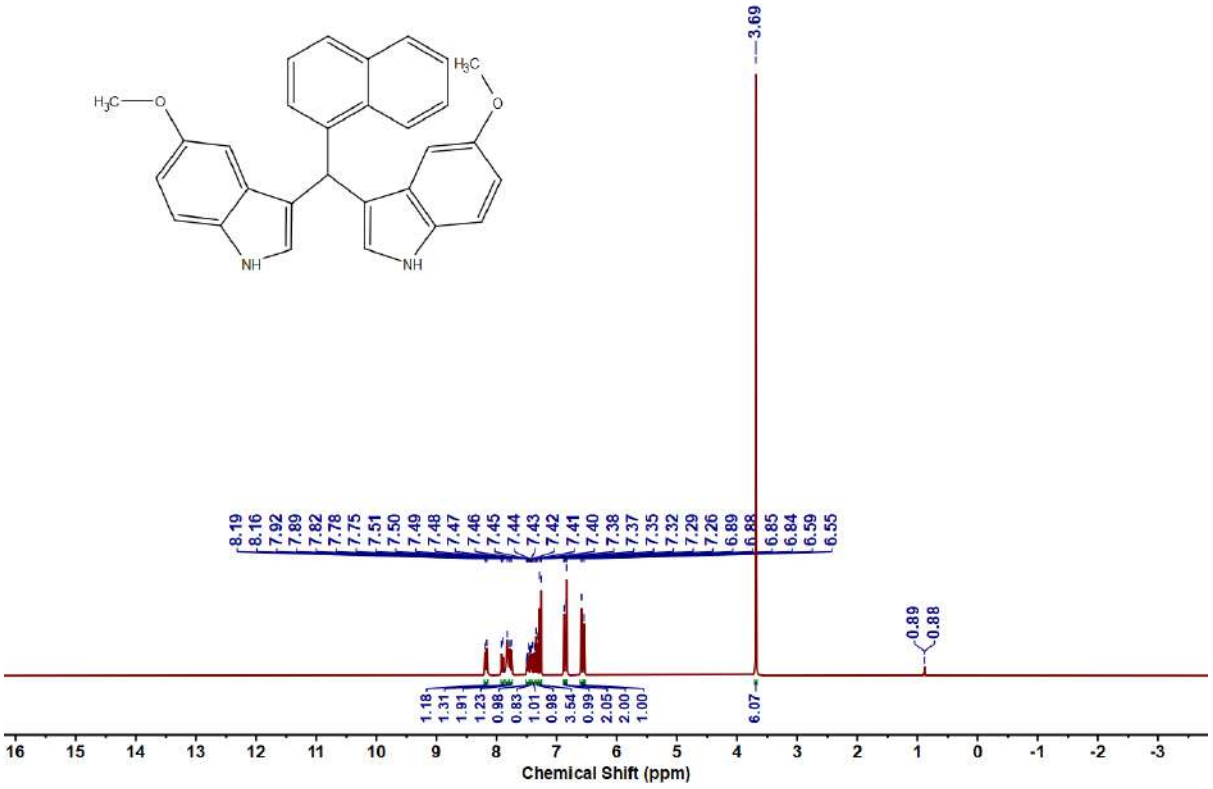

Figure 5.6.A113: ^{1}H NMR spectrum of **10am**

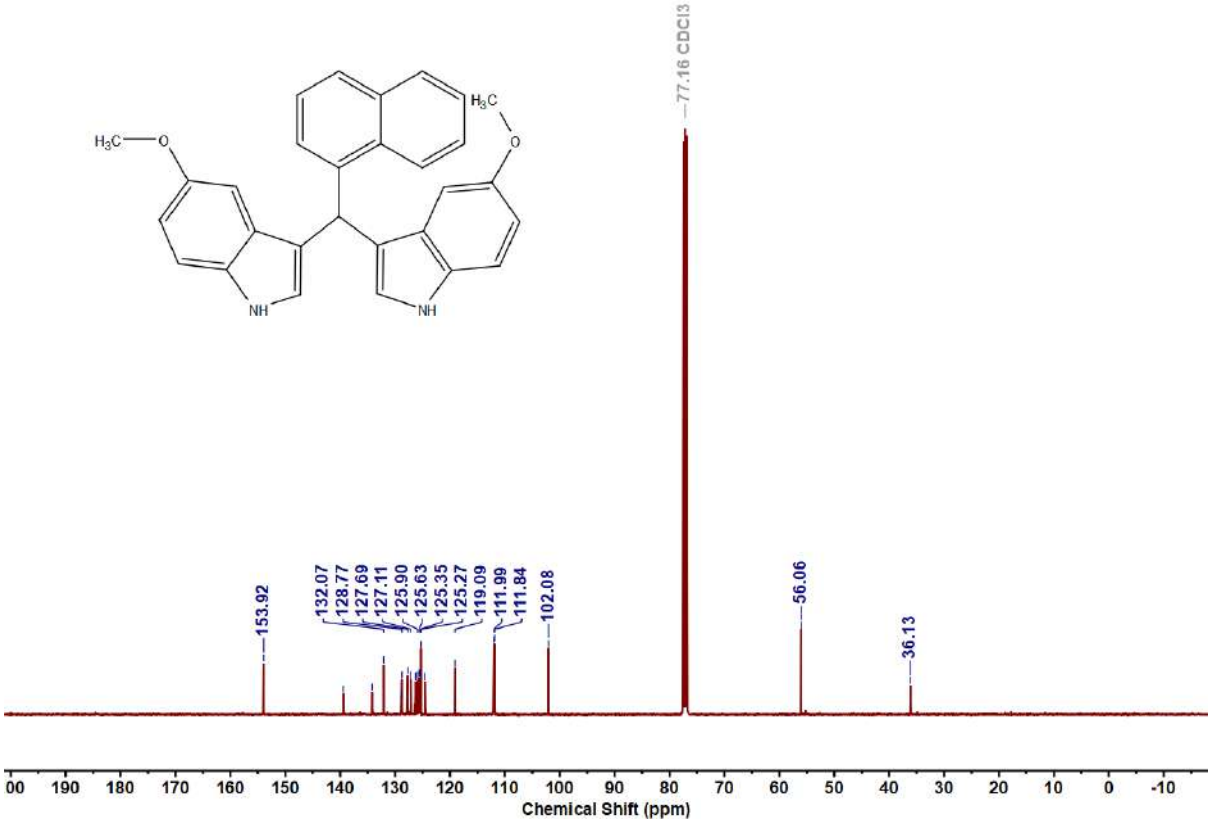

Figure 5.6.A114: $^{13}C\{^{1}H\}$ NMR spectrum of **10am**

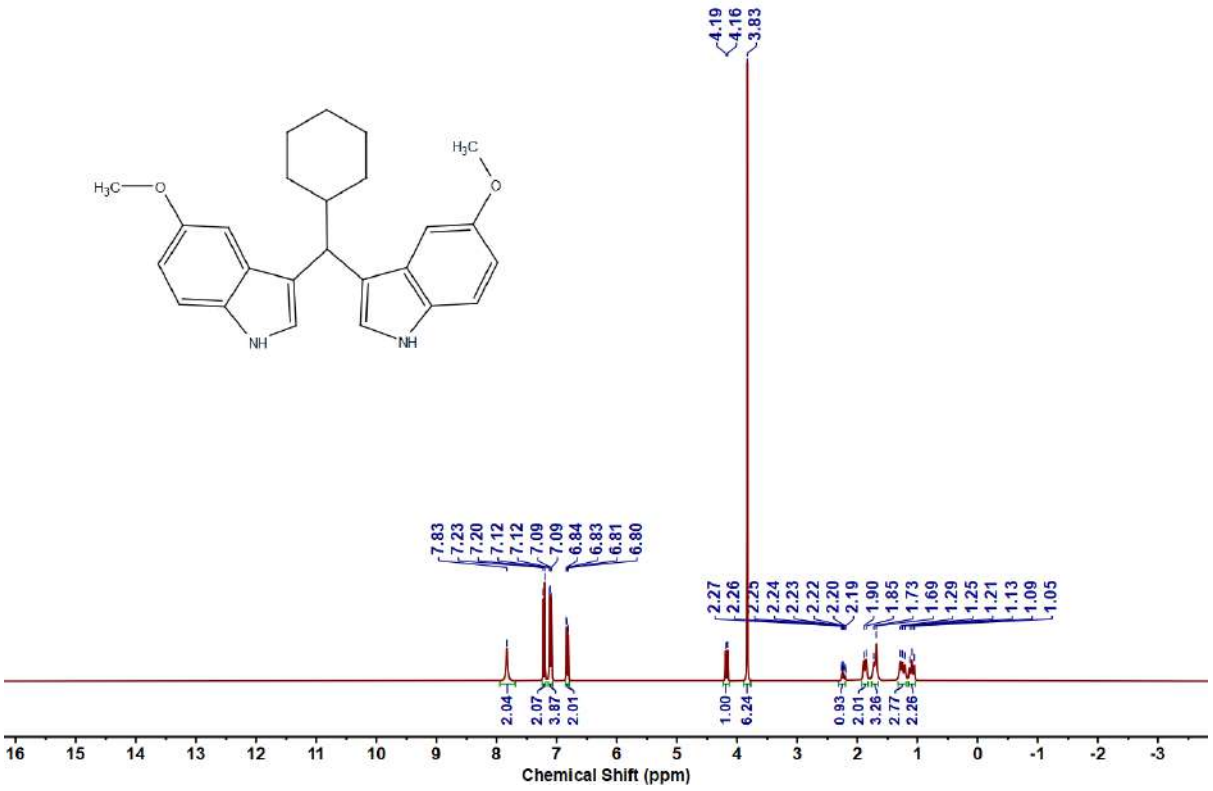

Figure 5.6.A115: ^{1}H NMR spectrum of **10an**

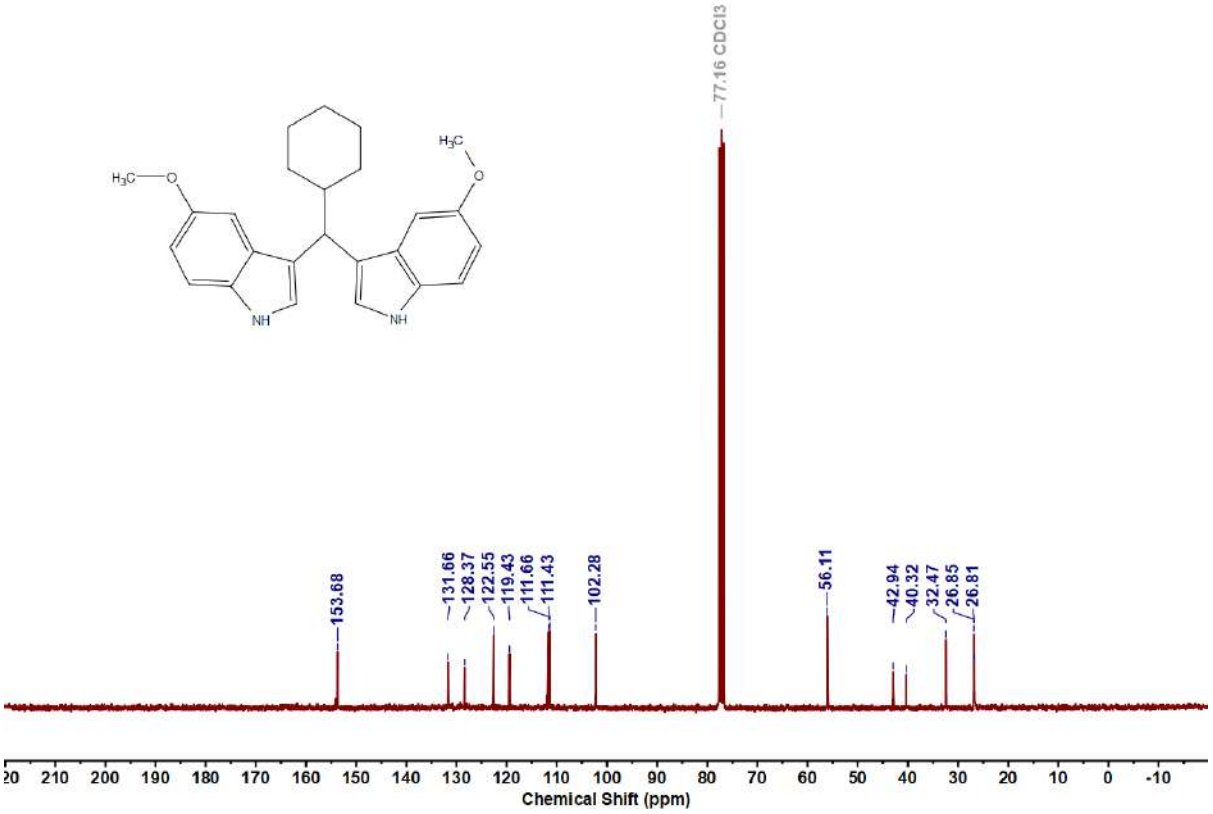

Figure 5.6.A116: ^{13}C{^{1}H} NMR spectrum of **10an**

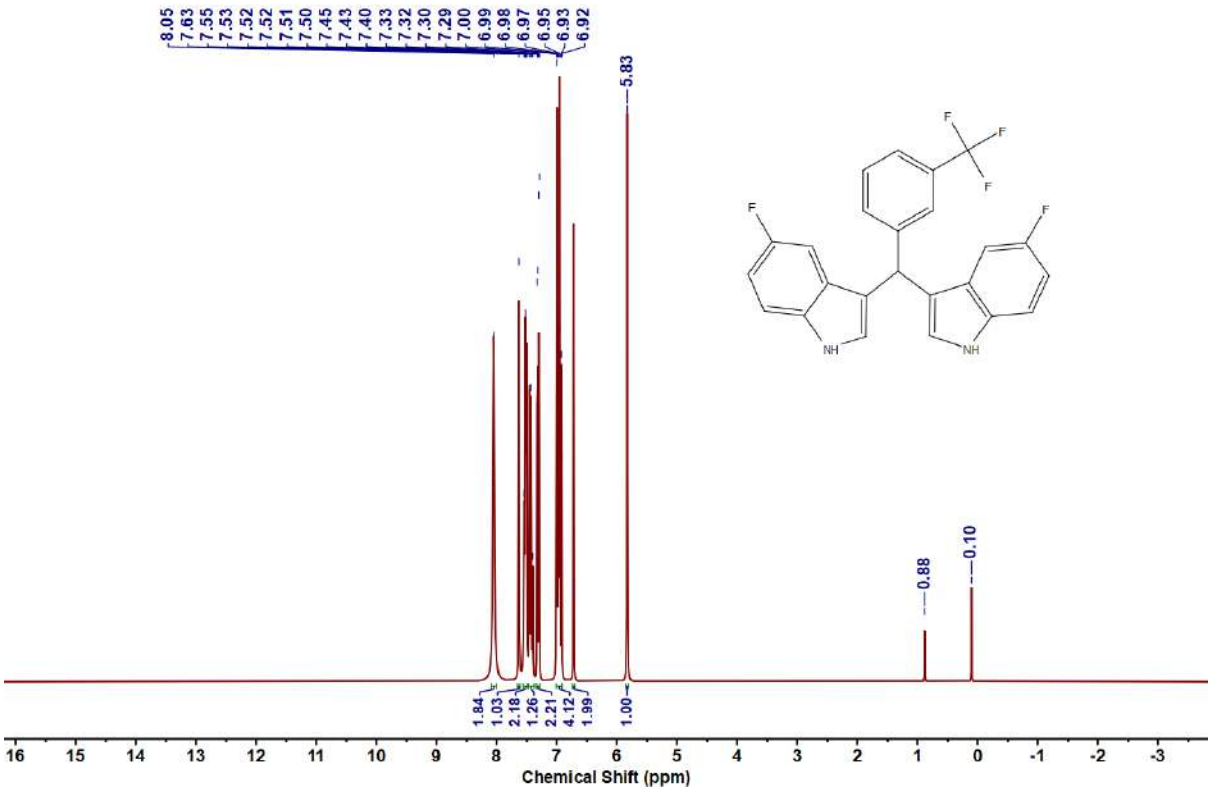

Figure 5.6.A117: ^{1}H NMR spectrum of **11aa**

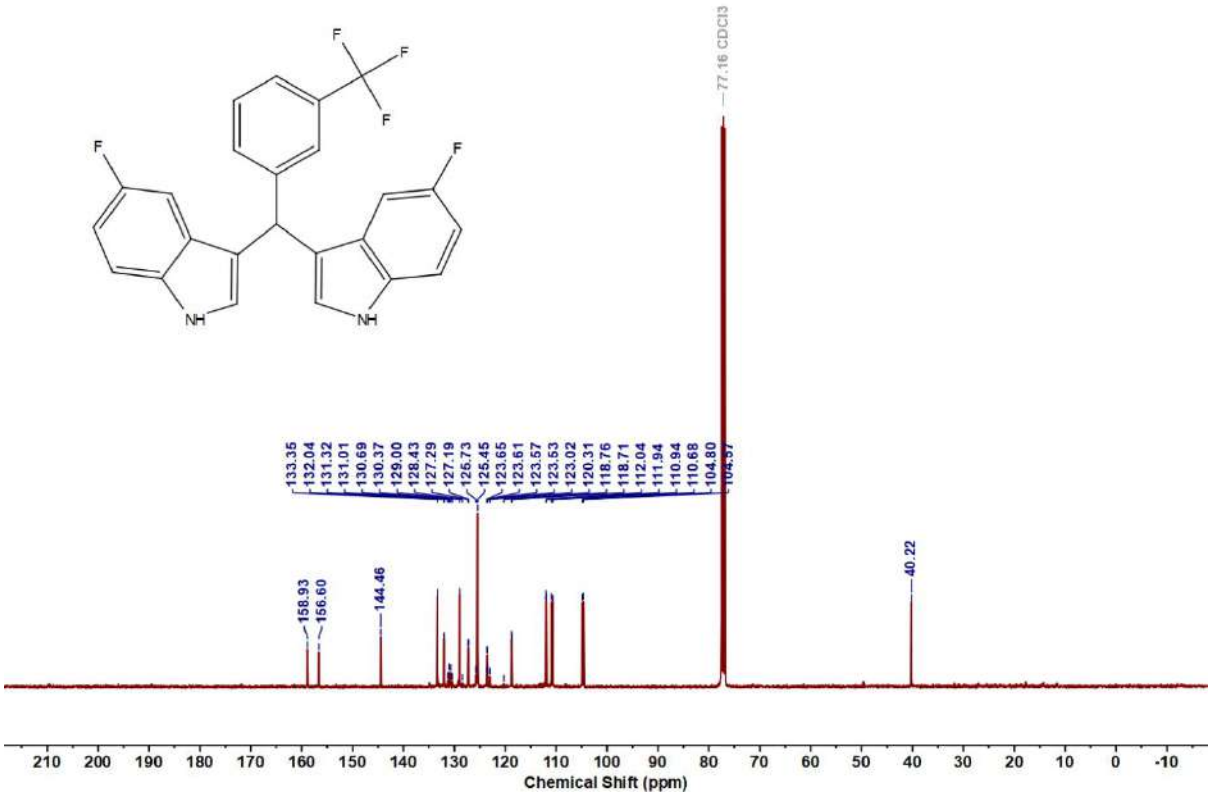

Figure 5.6.A118: $^{13}C\{^{1}H\}$ NMR spectrum of **11aa**

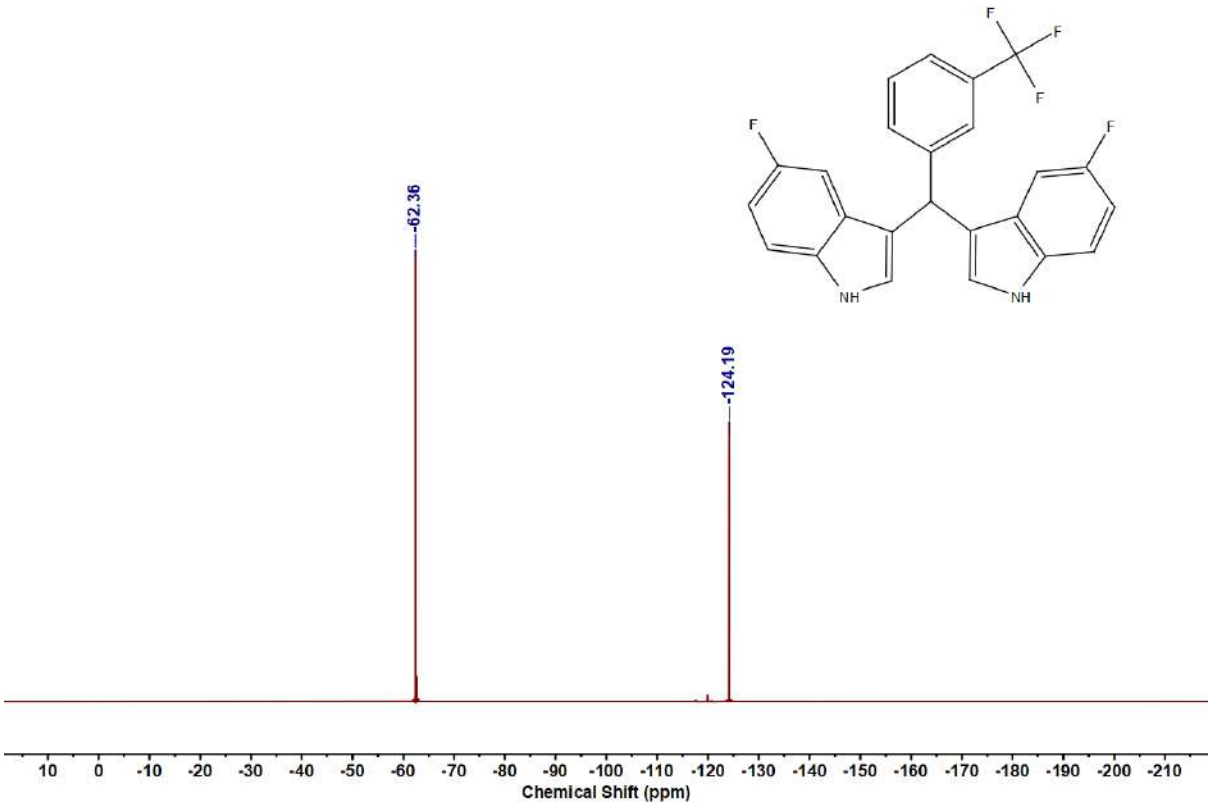

Figure 5.6.A119: ^{19}F NMR spectrum of **11aa**

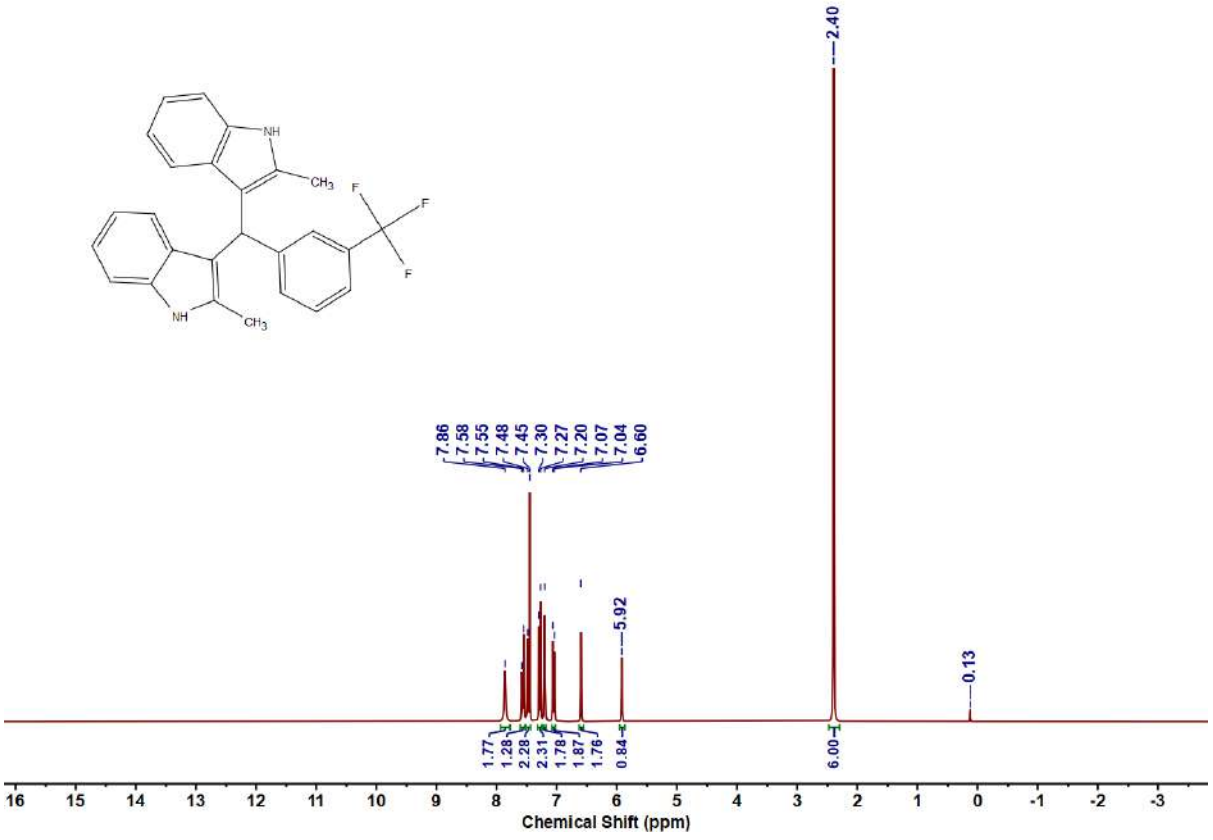

Figure 5.6.A120: ^{1}H NMR spectrum of **12ab**

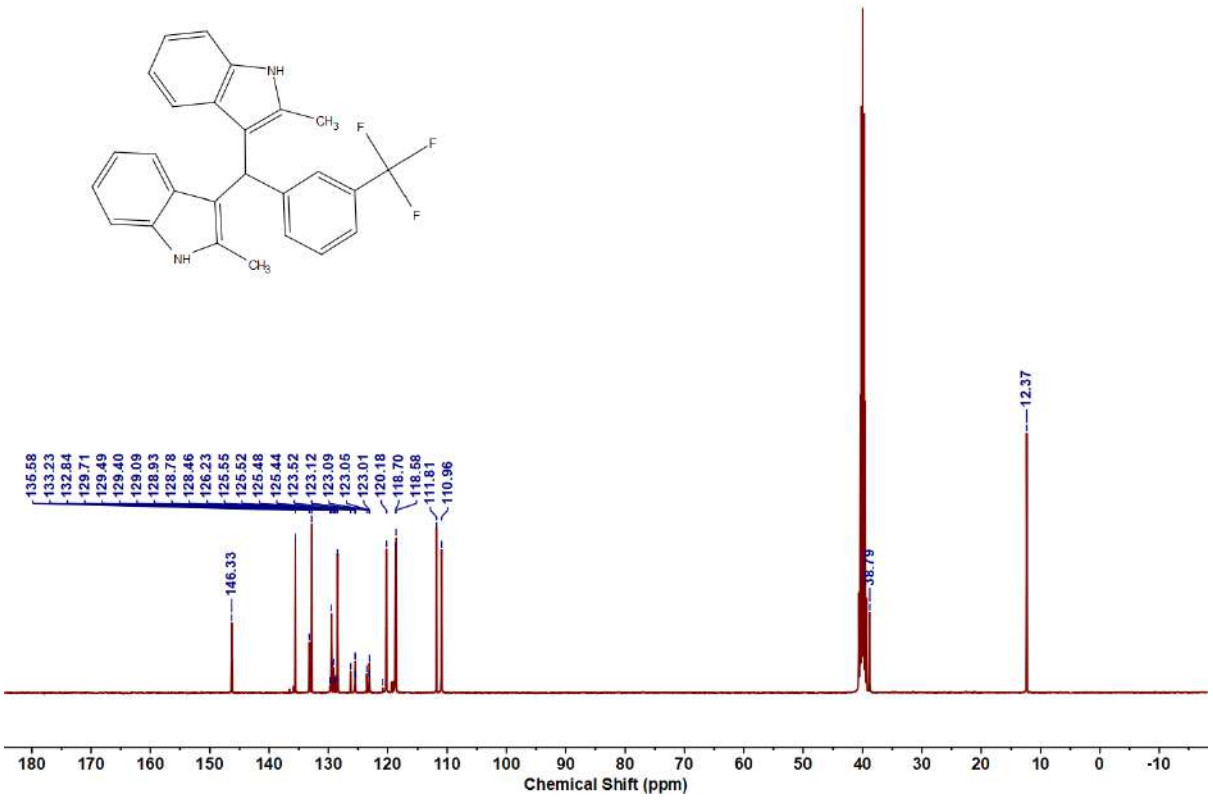

Figure 5.6.A121: $^{13}C\{^{1}H\}$ NMR spectrum of **12ab**

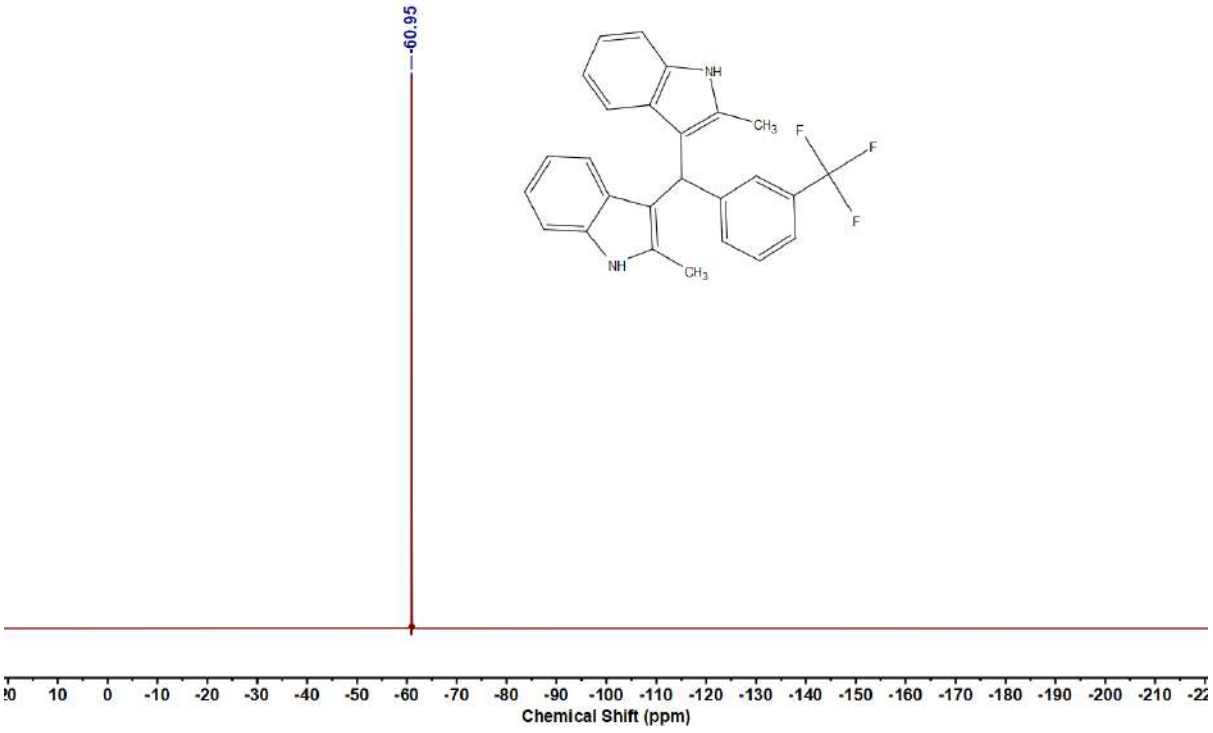

Figure 5.6.A122: ^{19}F NMR spectrum of **12ab**

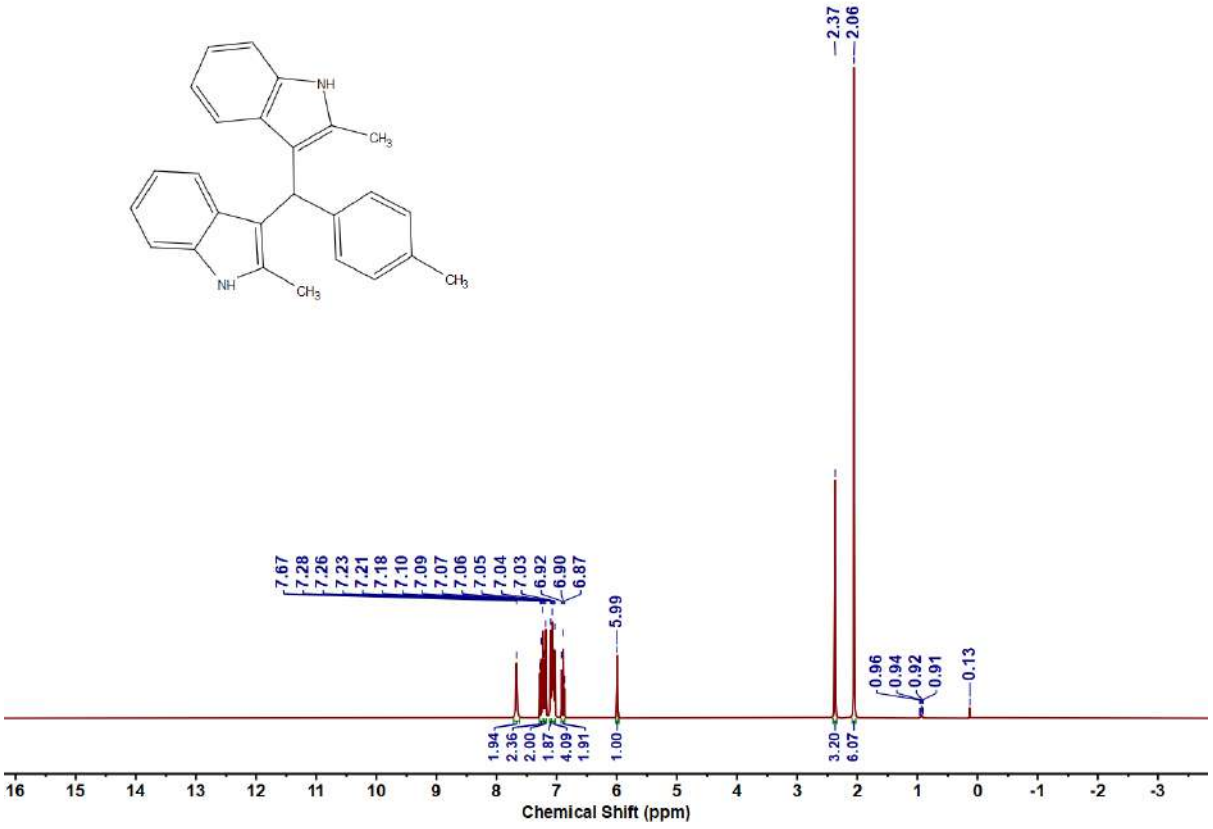

Figure 5.6.A123: ^{1}H NMR spectrum of **12ac**

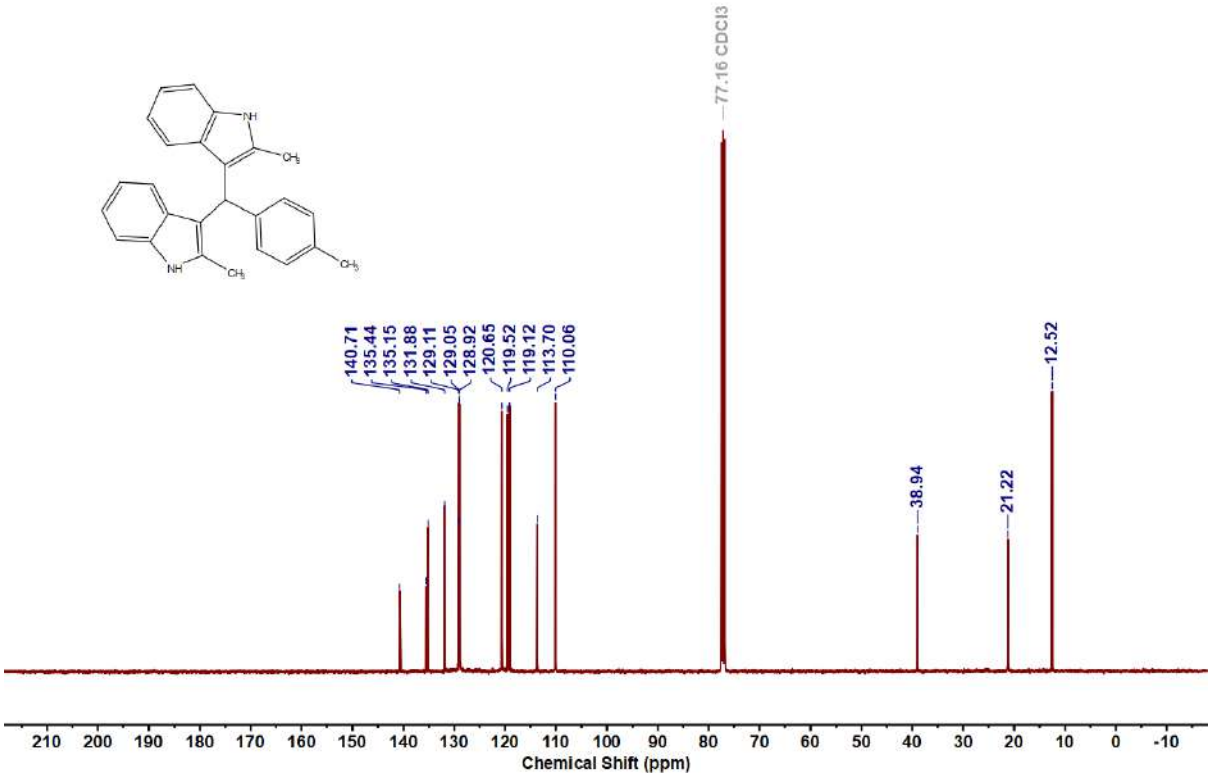

Figure 5.6.A124: $^{13}C\{^{1}H\}$ NMR spectrum of **12ac**

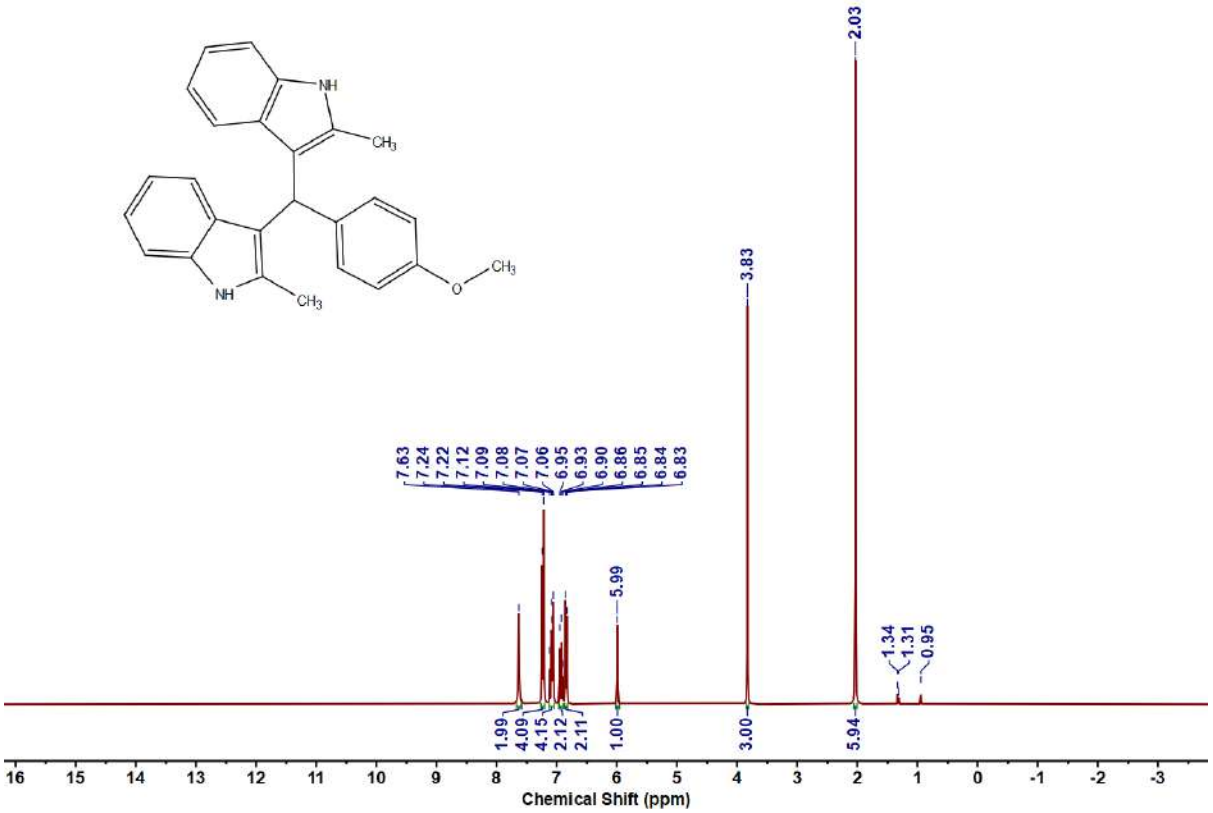

Figure 5.6.A125: ^{1}H NMR spectrum of **12ad**

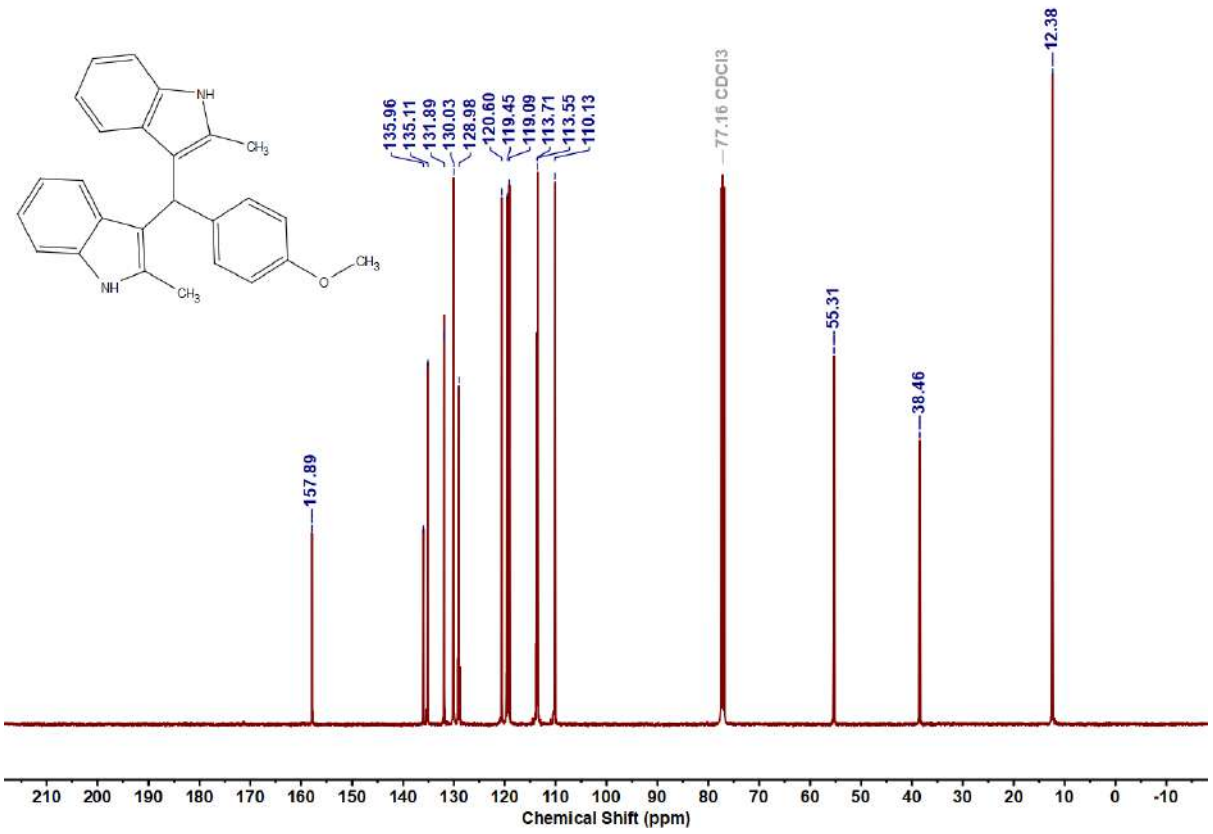

Figure 5.6.A126: $^{13}C\{^{1}H\}$ NMR spectrum of **12ad**

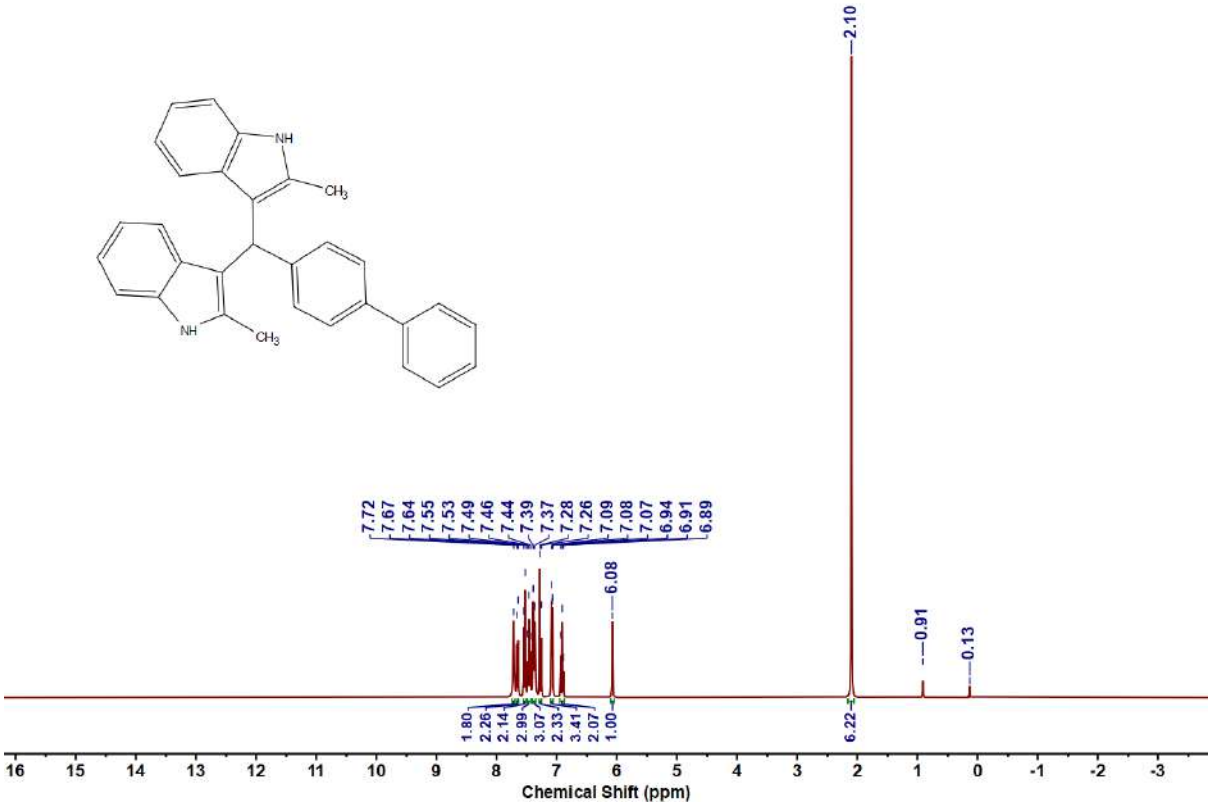

Figure 5.6.A127: ^{1}H NMR spectrum of **12ae**

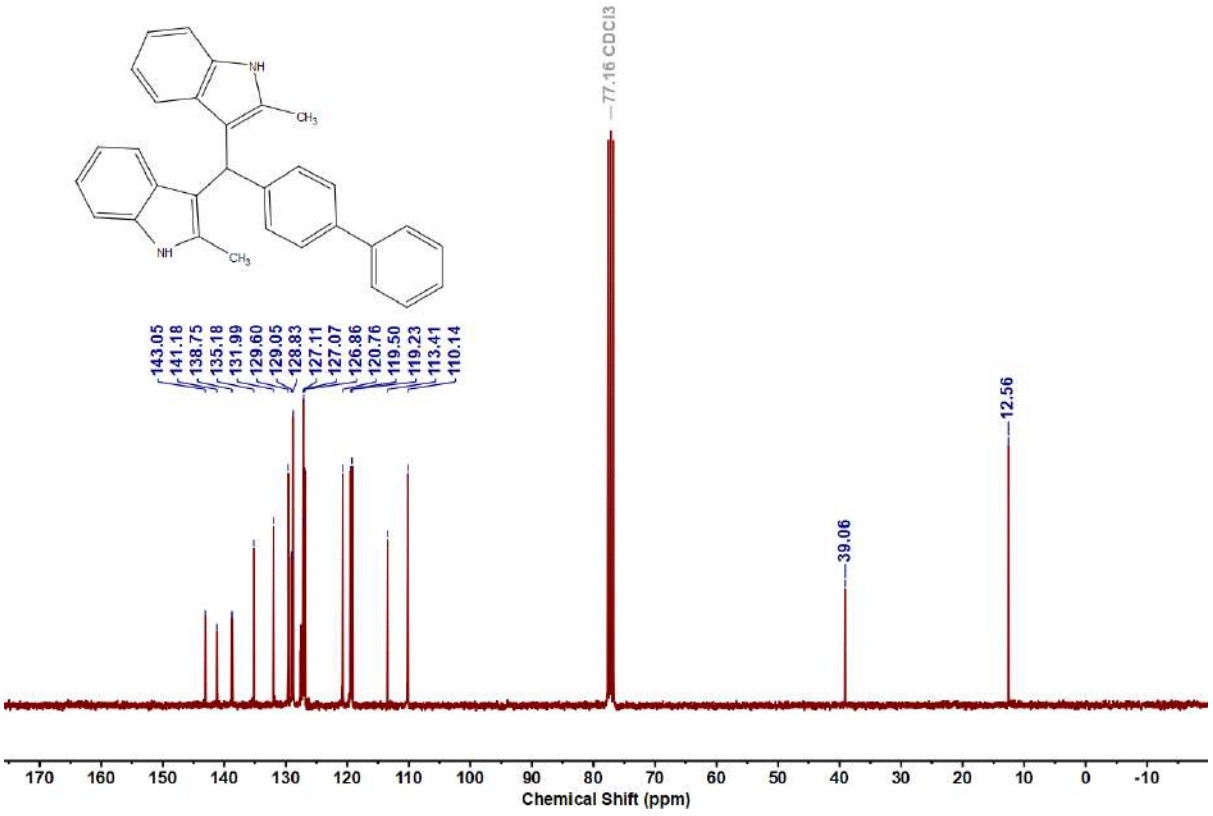

Figure 5.6.A128: ^{13}C{^{1}H} NMR spectrum of **12ae**

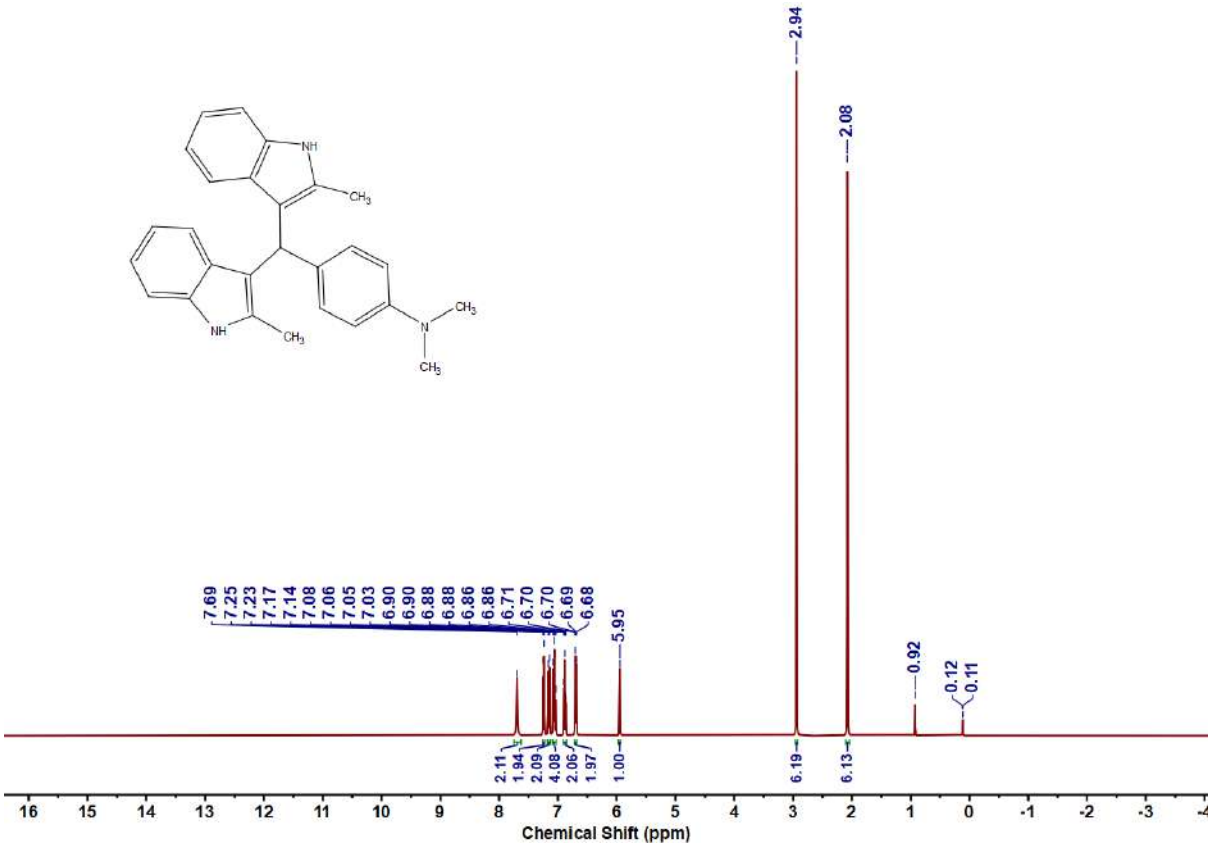

Figure 5.6.A129: ^{1}H NMR spectrum of **12af**

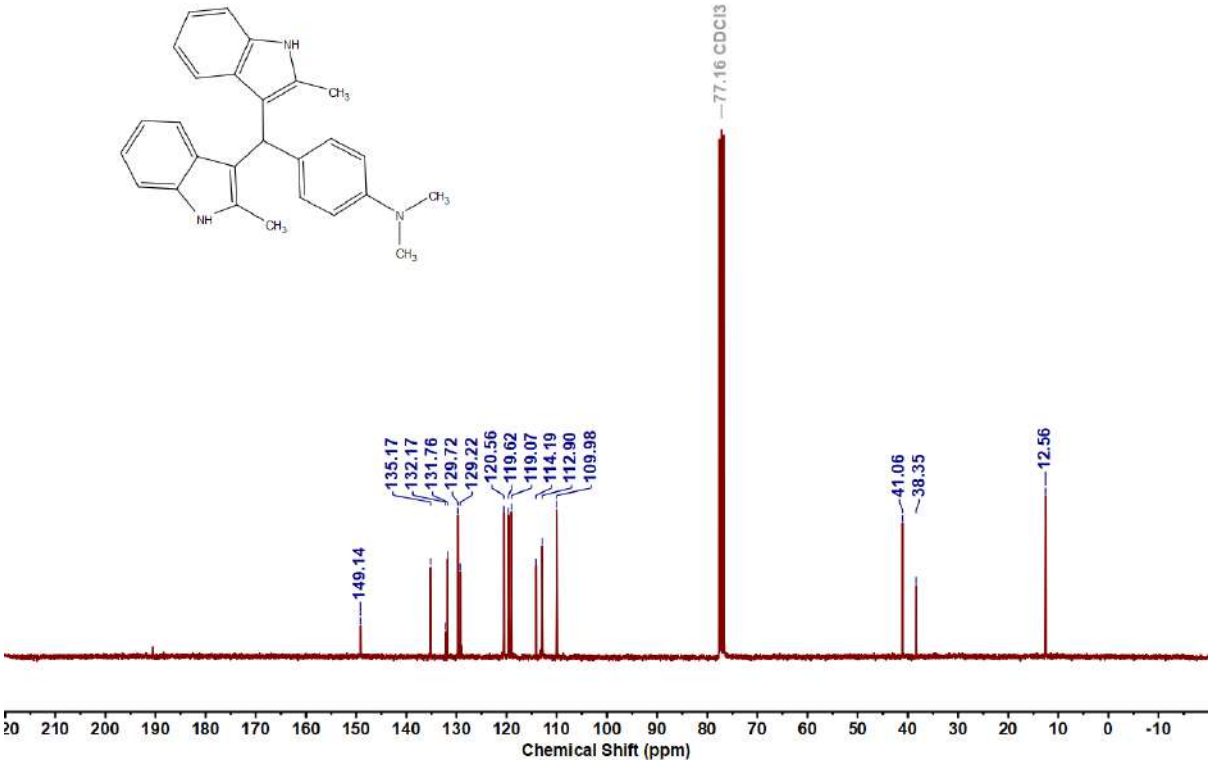

Figure 5.6.A130: ^{13}C{^{1}H} NMR spectrum of **12af**

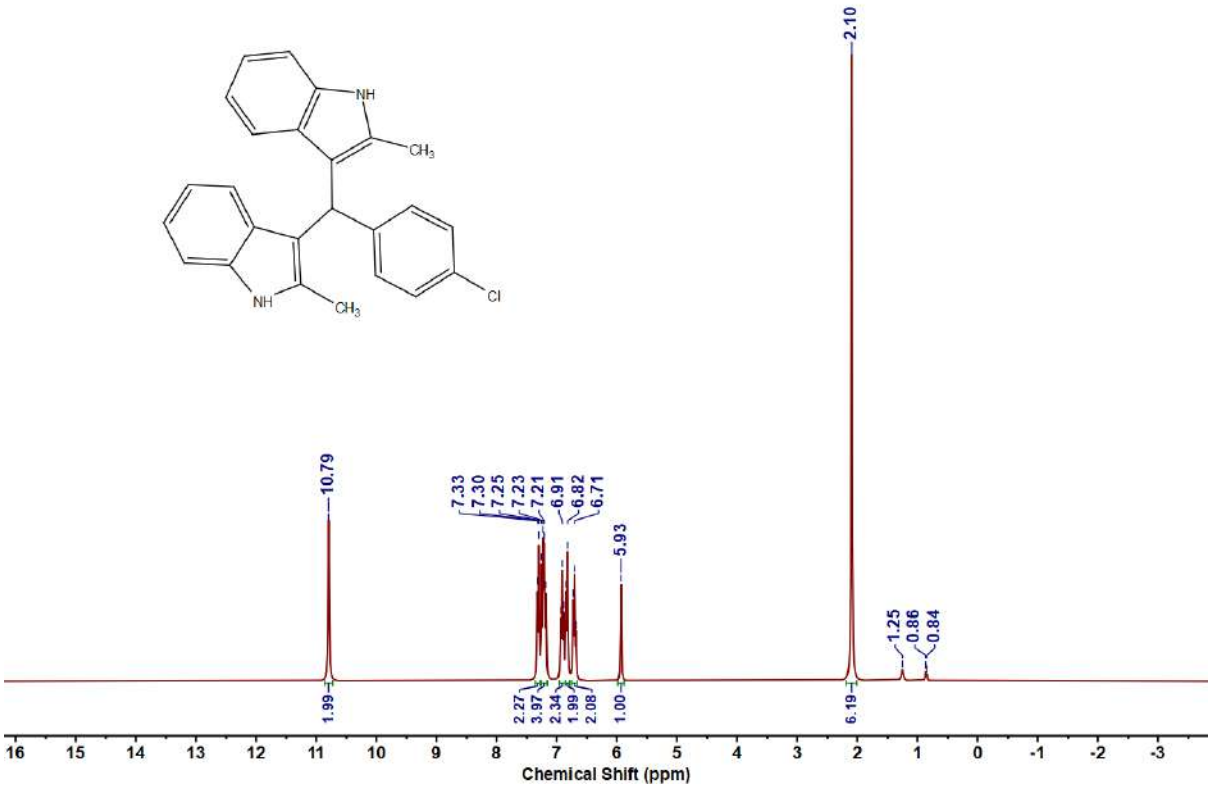

Figure 5.6.A131: ^{1}H NMR spectrum of **12ag**

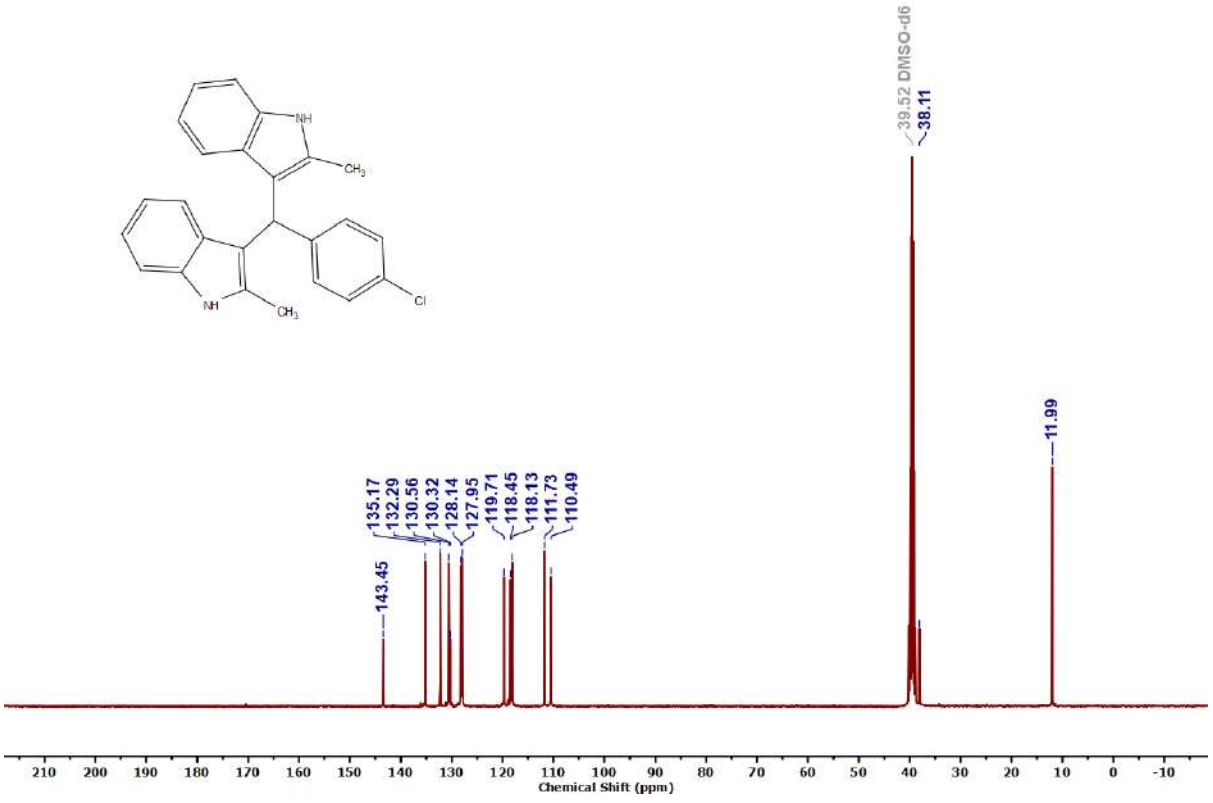

Figure 5.6.A132: ^{13}C{^{1}H} NMR spectrum of **12ag**

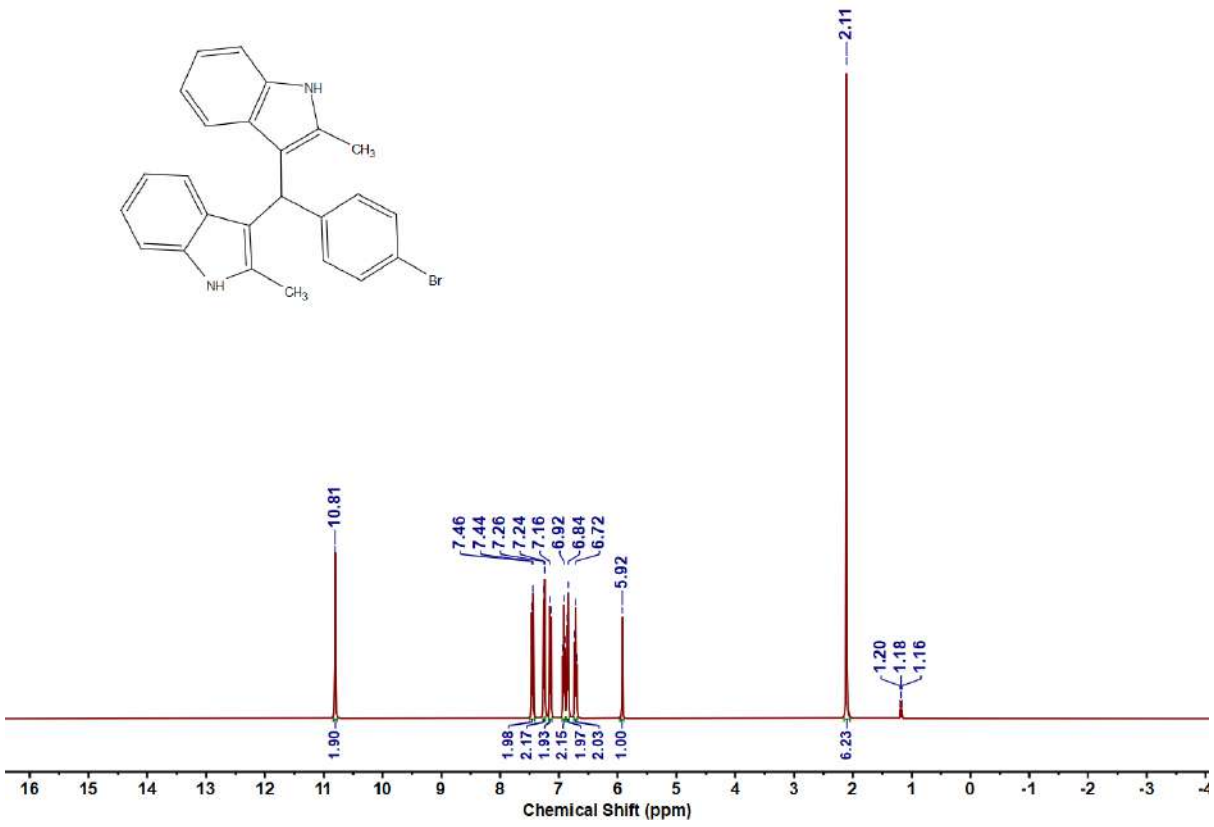

Figure 5.6.A133: ^{1}H NMR spectrum of **12ah**

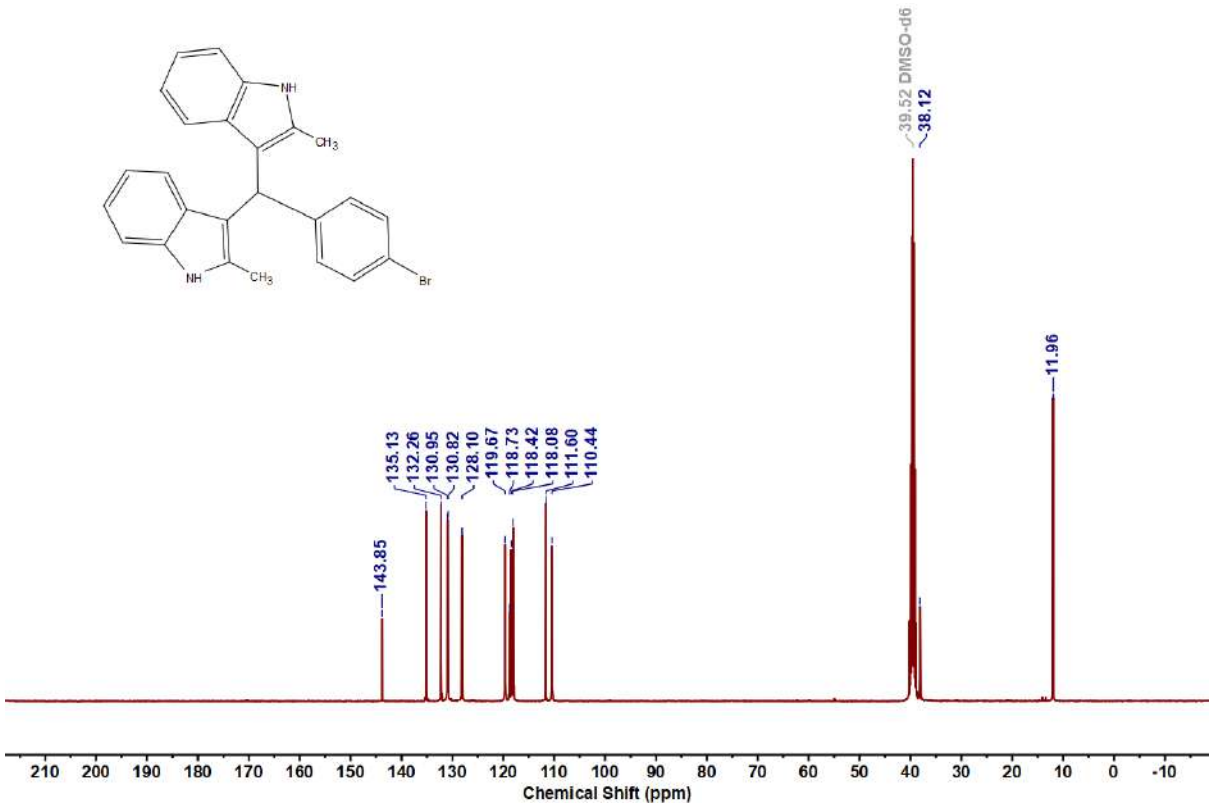

Figure 5.6.A134: ^{13}C{^{1}H} NMR spectrum of **12ah**

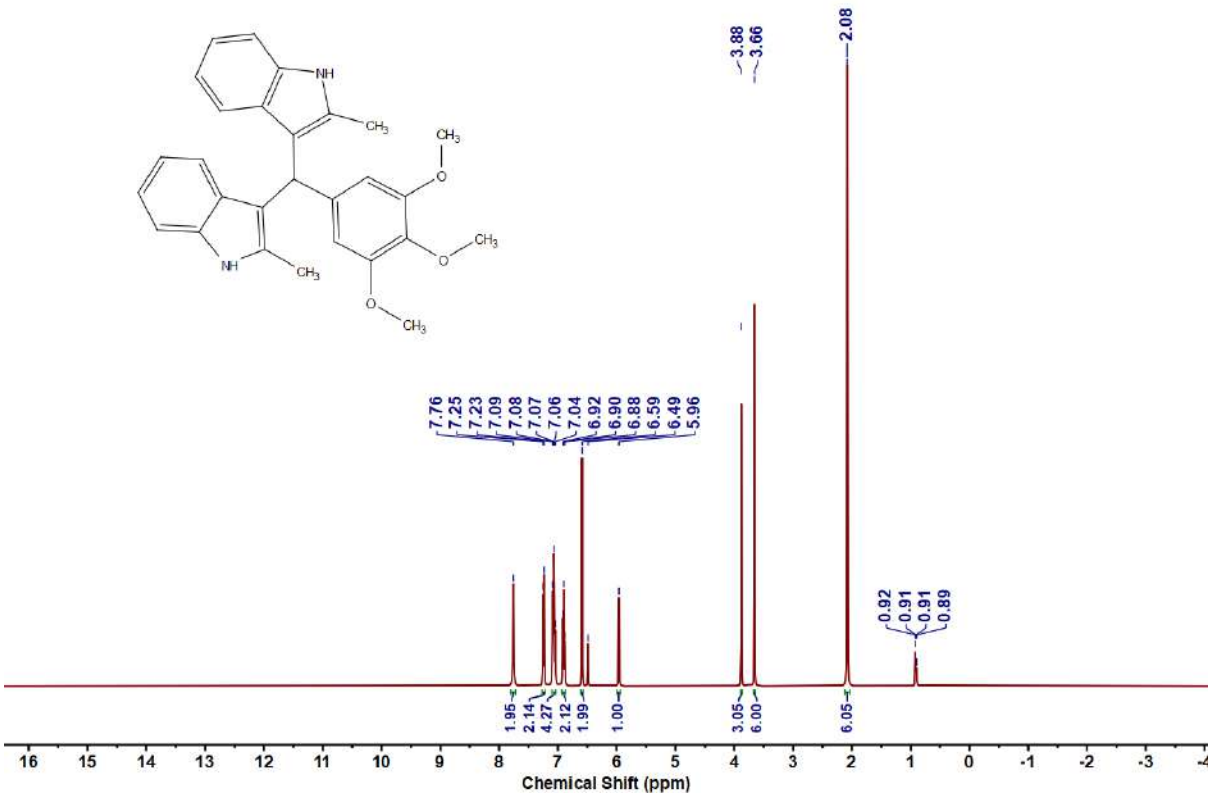

Figure 5.6.A135: ^{1}H NMR spectrum of **12ai**

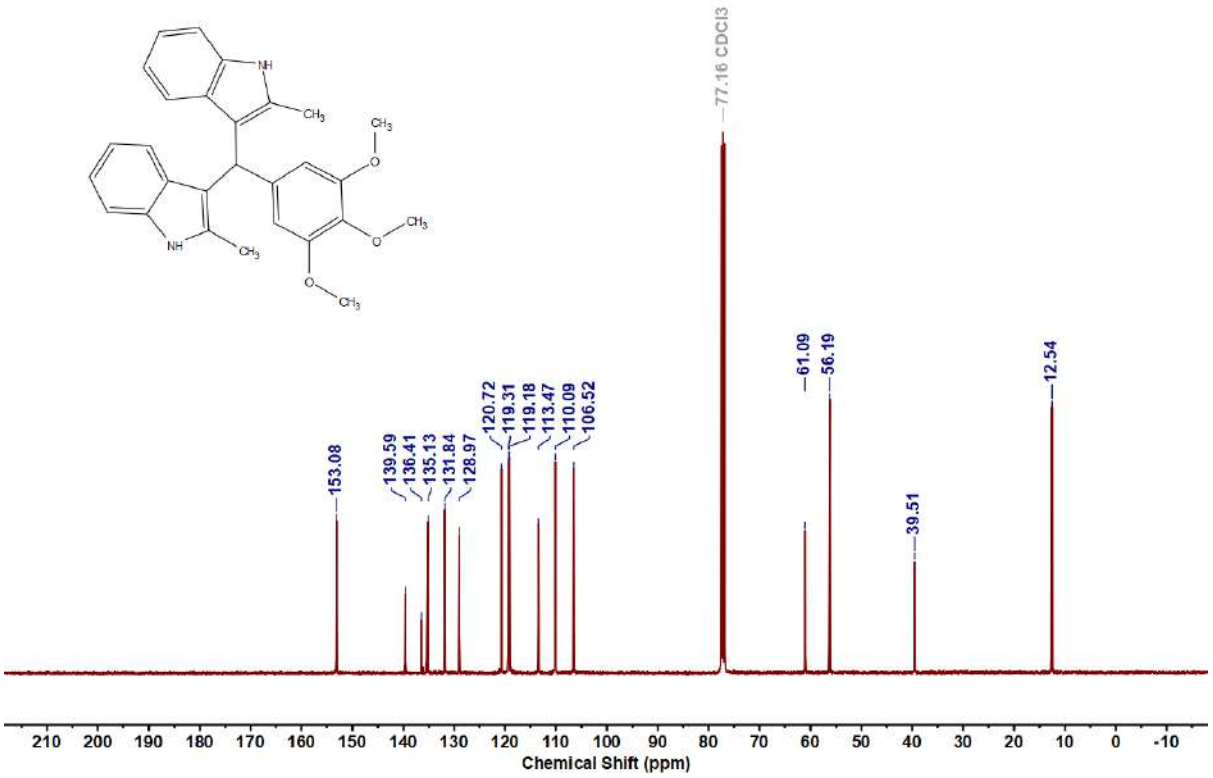

Figure 5.6.A136: $^{13}C\{^{1}H\}$ NMR spectrum of **12ai**

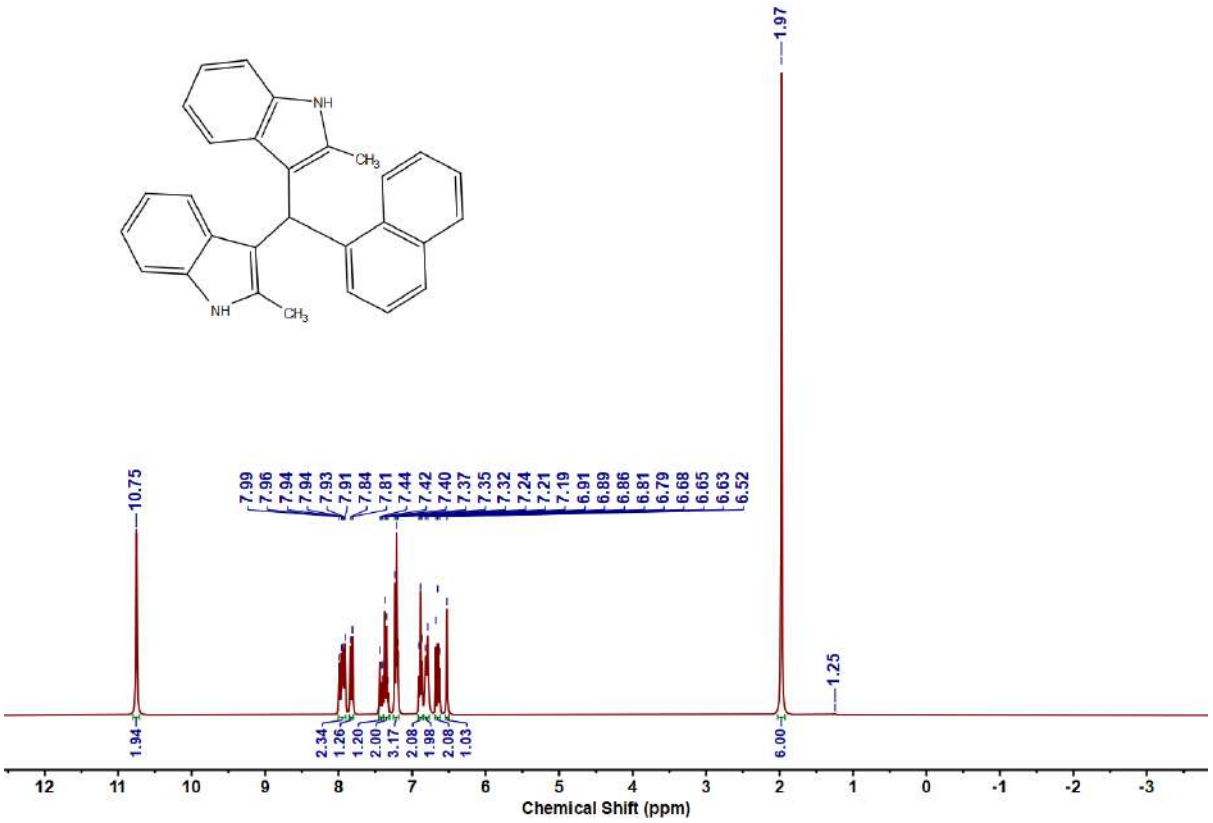

Figure 5.6.A137: ^{1}H NMR spectrum of **12aj**

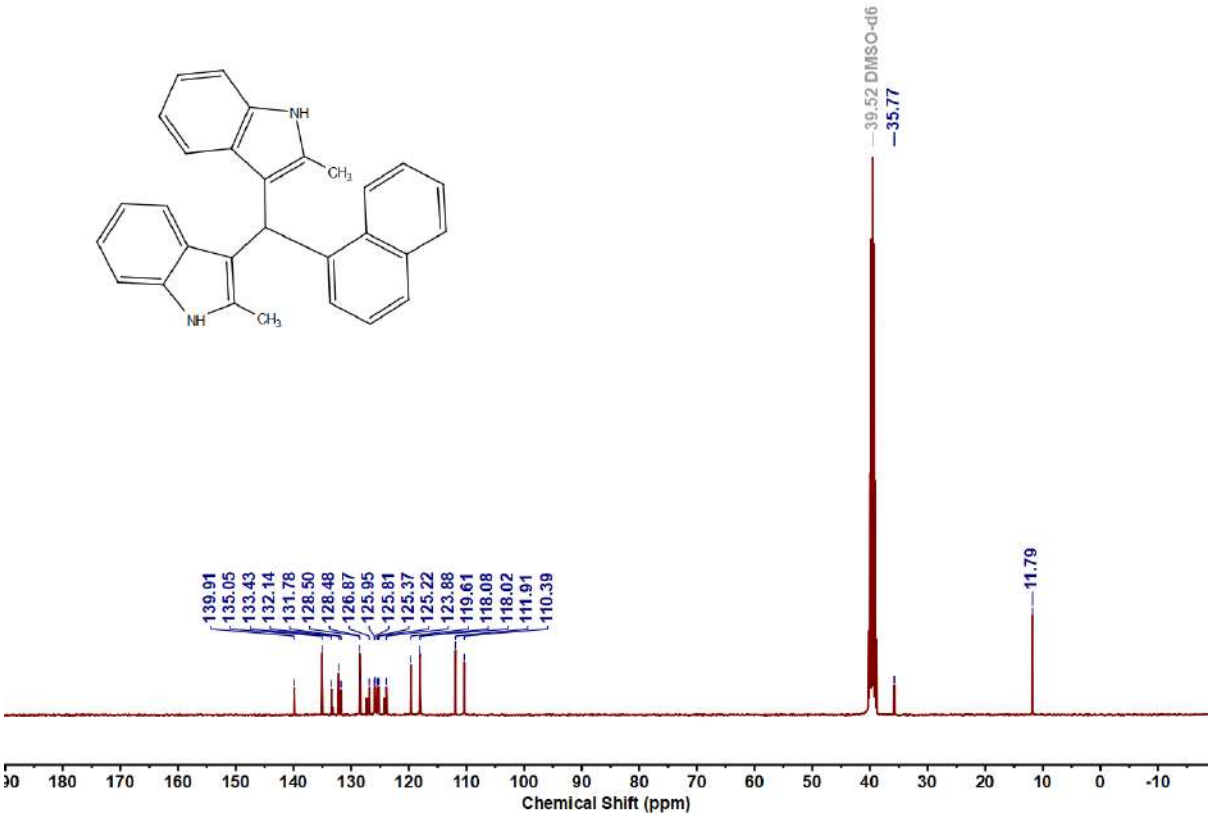

Figure 5.6.A138: $^{13}C\{^{1}H\}$ NMR spectrum of **12aj**

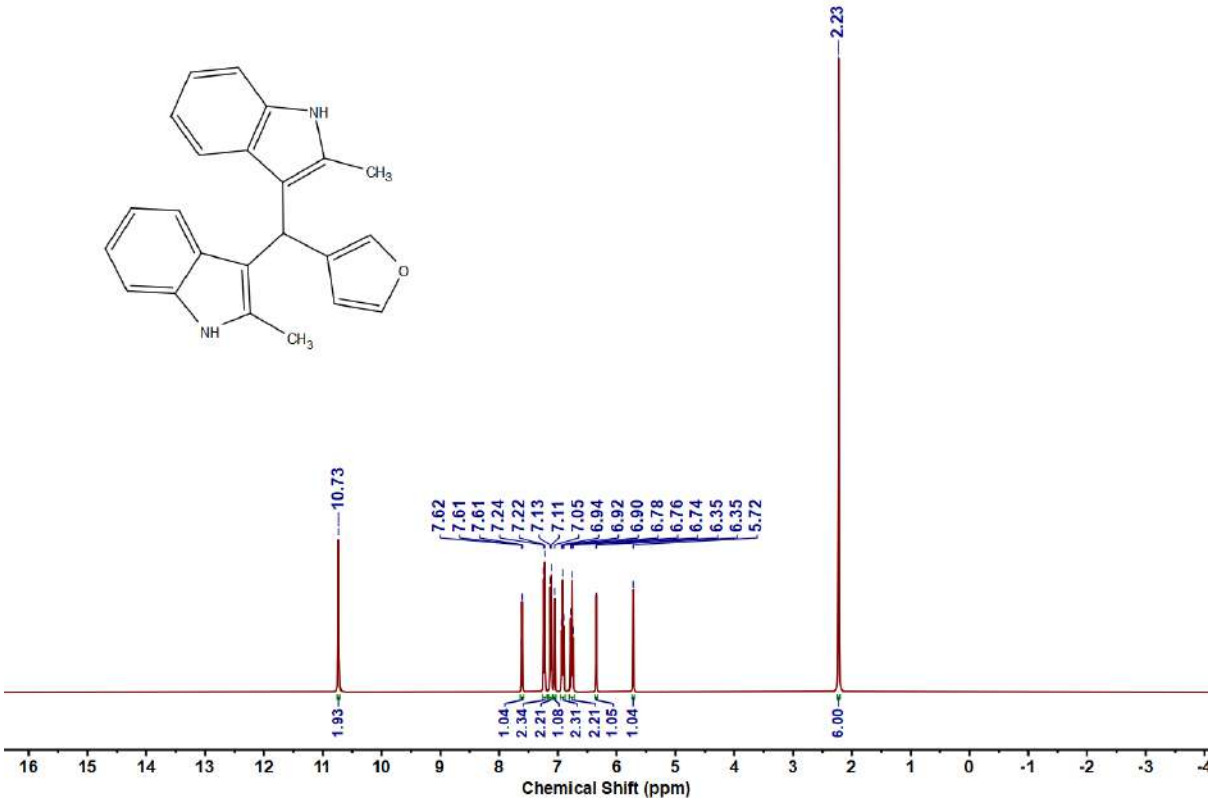

Figure 5.6.A139: ^{1}H NMR spectrum of **12ak**

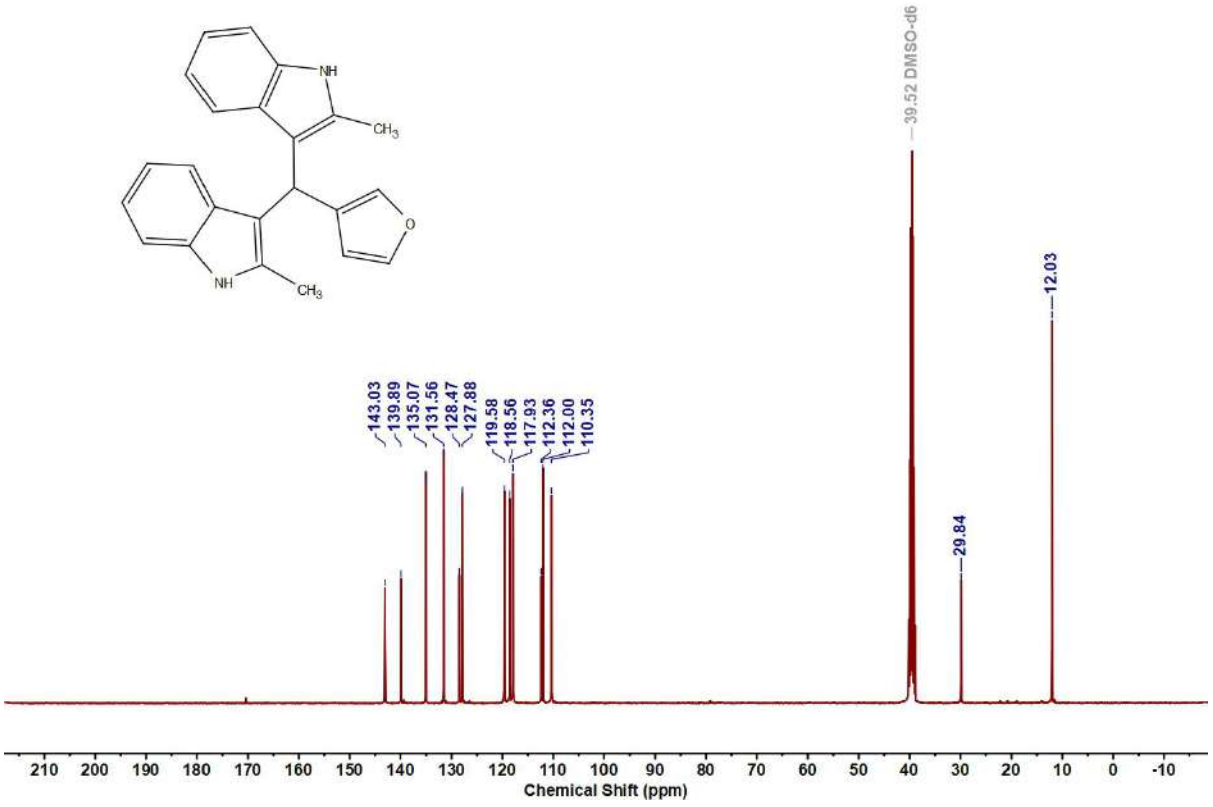

Figure 5.6.A140: ^{13}C{^{1}H} NMR spectrum of **12ak**

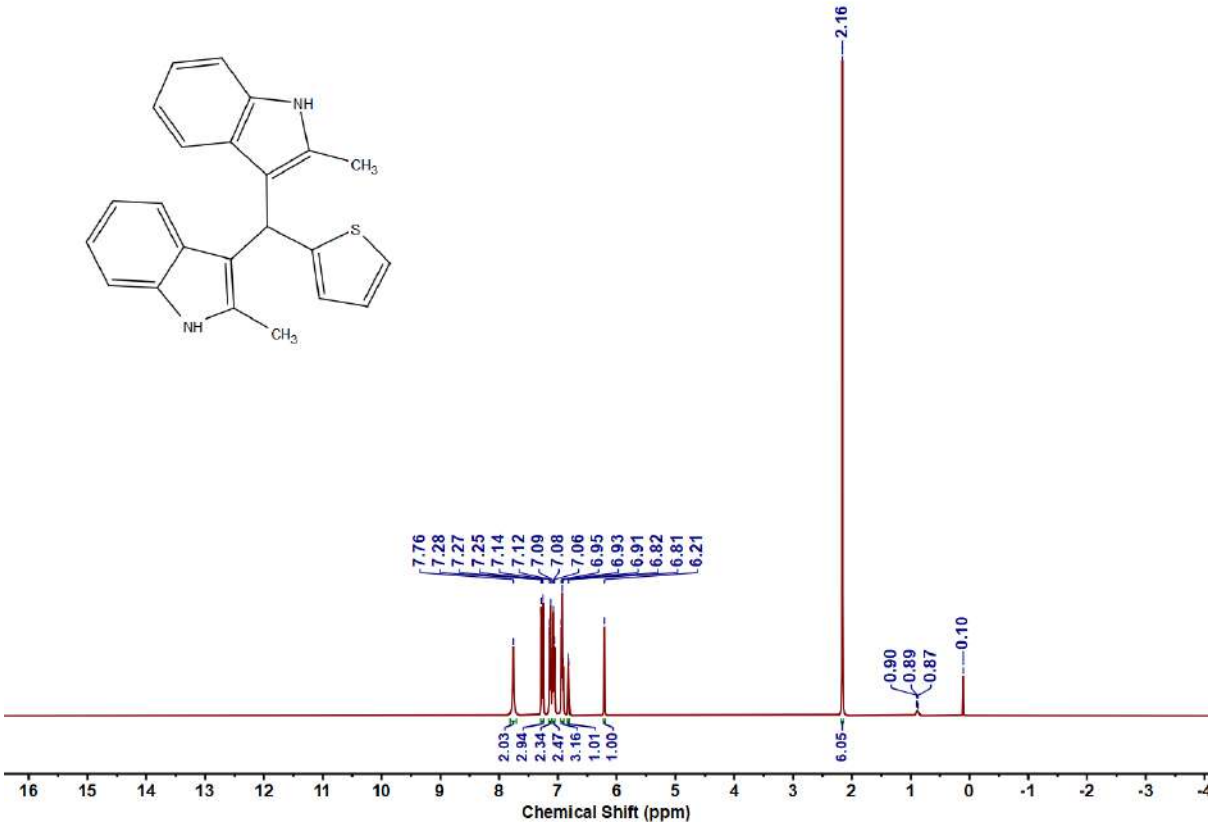

Figure 5.6.A141: ^{1}H NMR spectrum of **12al**

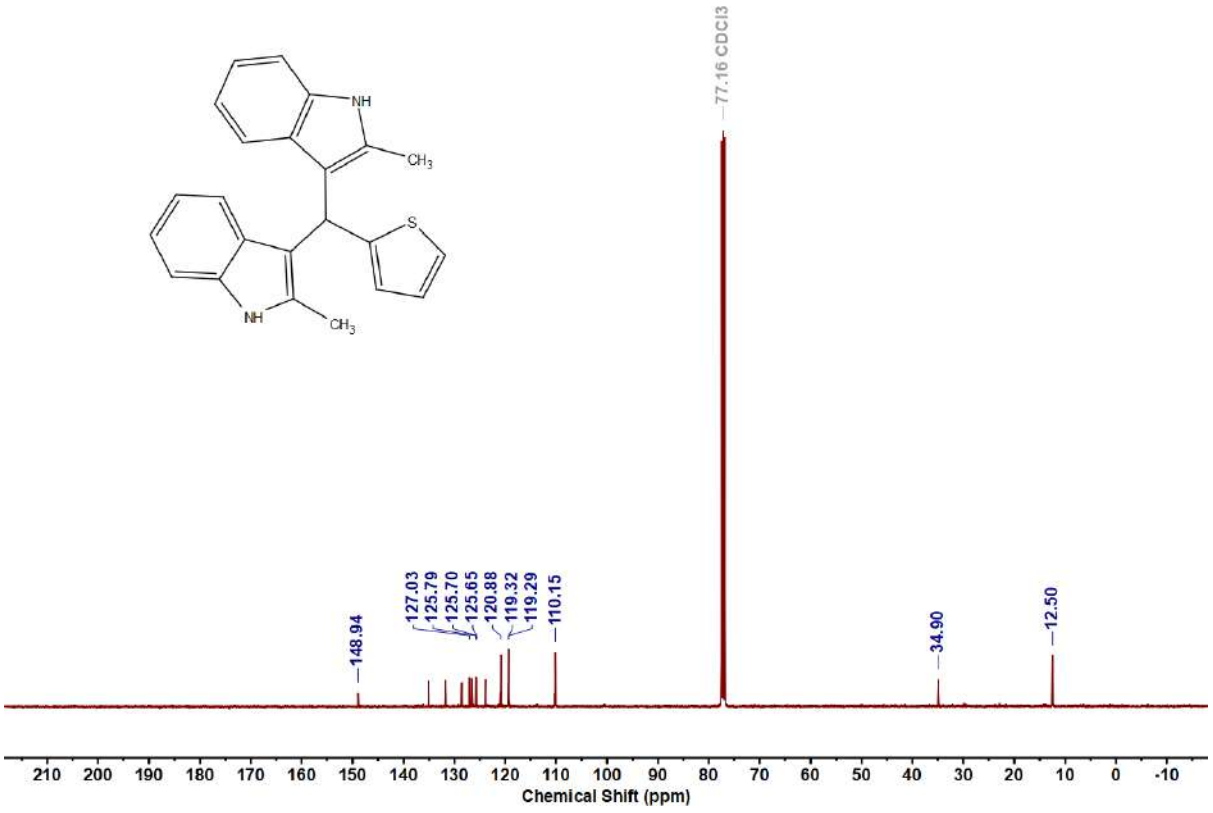

Figure 5.6.A142: ^{13}C{^{1}H} NMR spectrum of **12al**

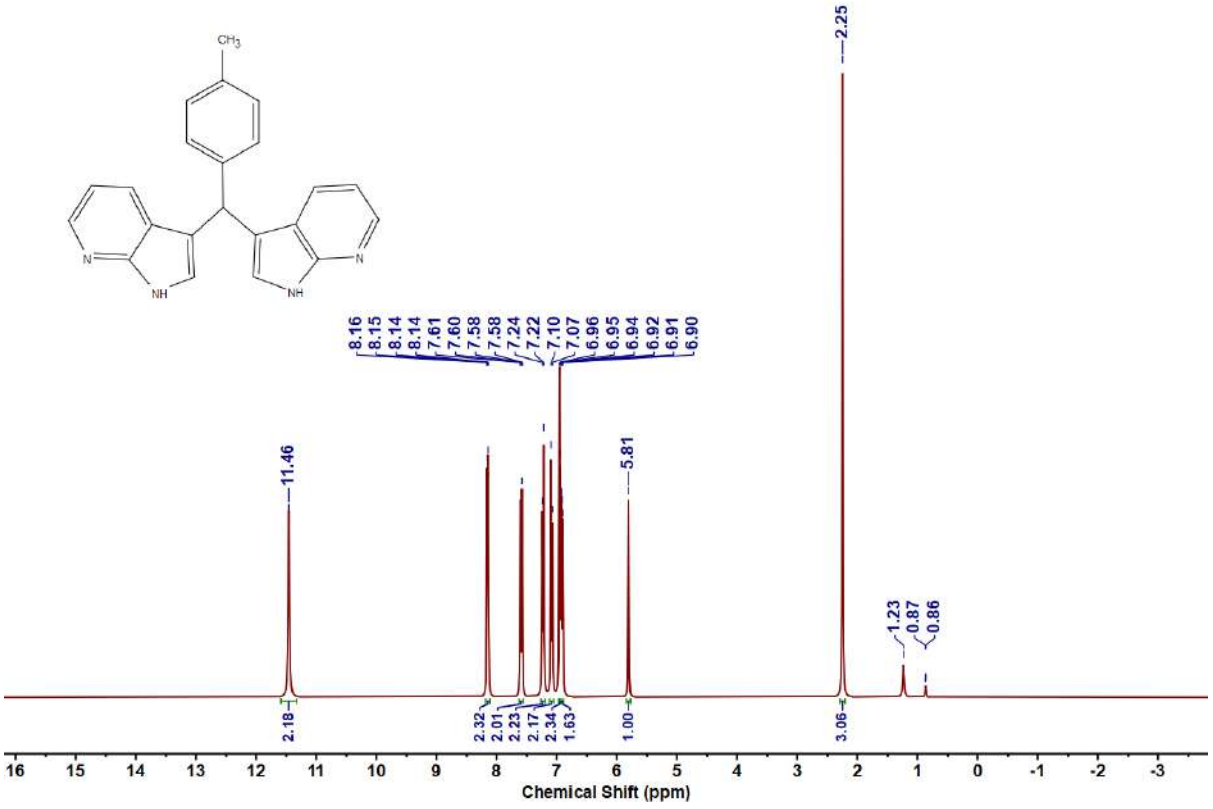

Figure 5.6.A143: ^{1}H NMR spectrum of **13aa**

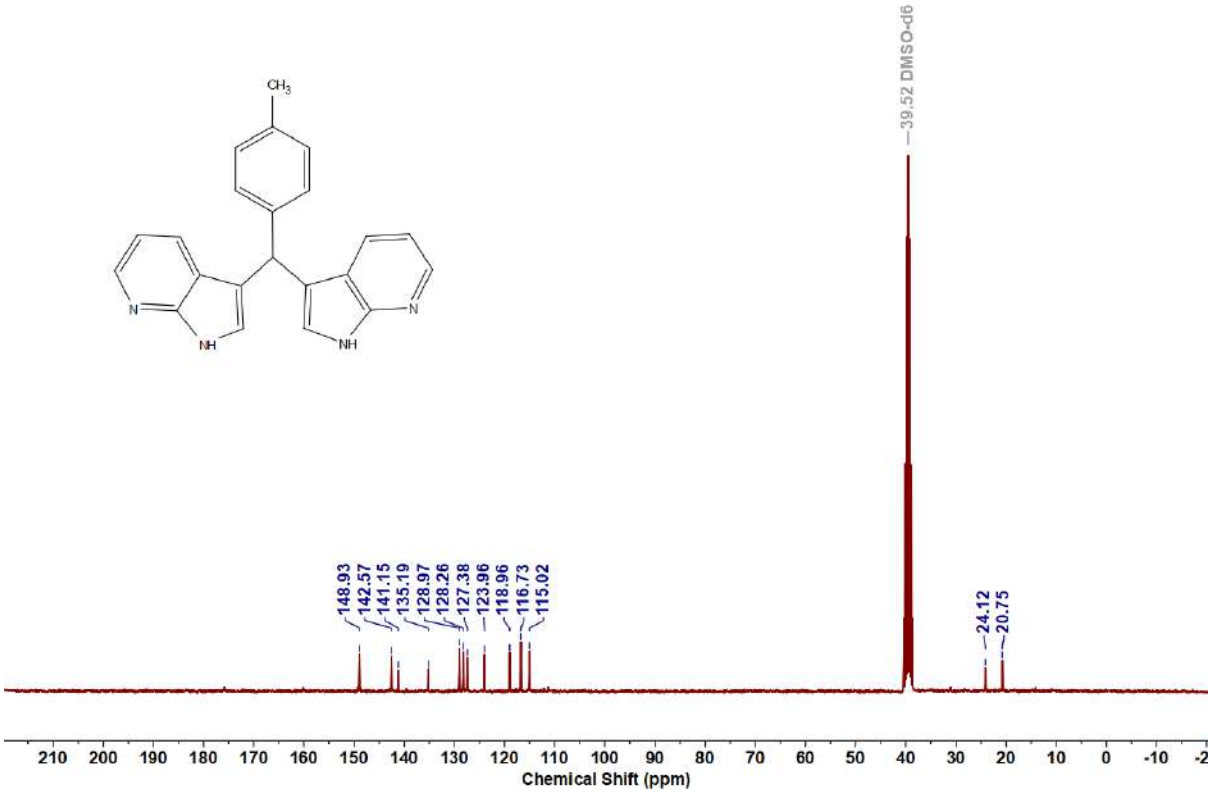

Figure 5.6.A144: $^{13}C\{^{1}H\}$ NMR spectrum of **13aa**

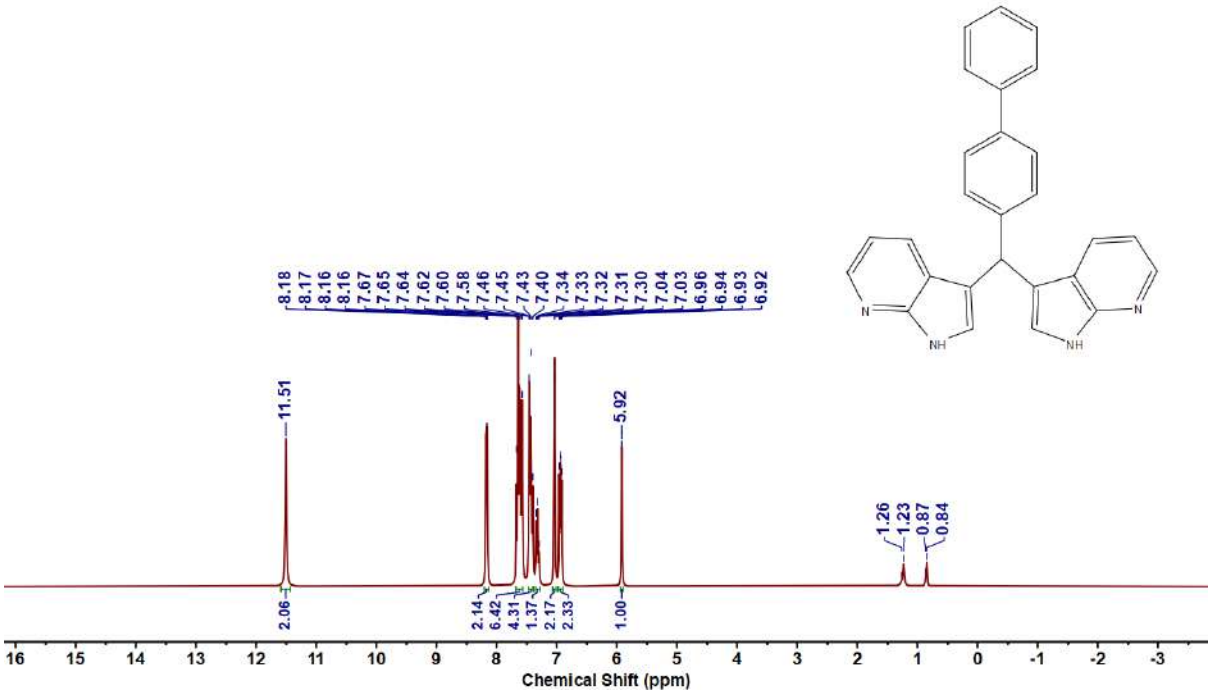

Figure 5.6.A145: ^{1}H NMR spectrum of **13ab**

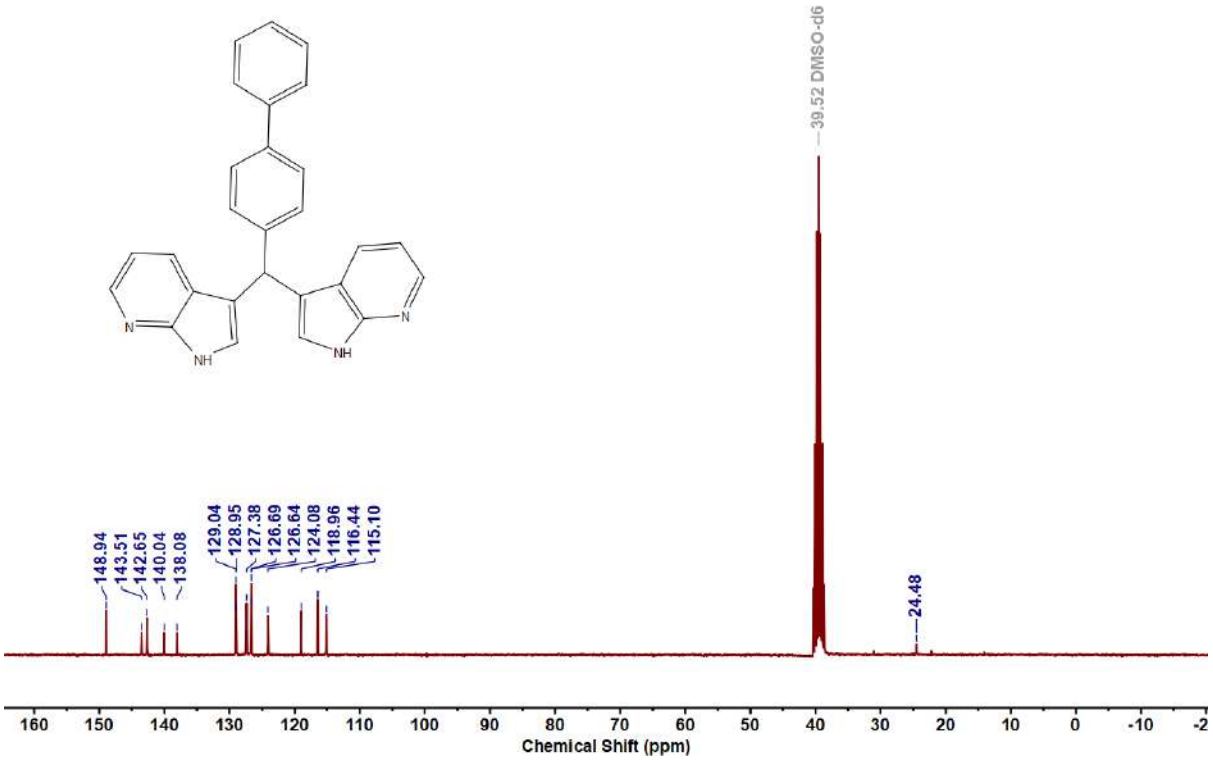

Figure 5.6.A146: $^{13}C\{^{1}H\}$ NMR spectrum of **13ab**

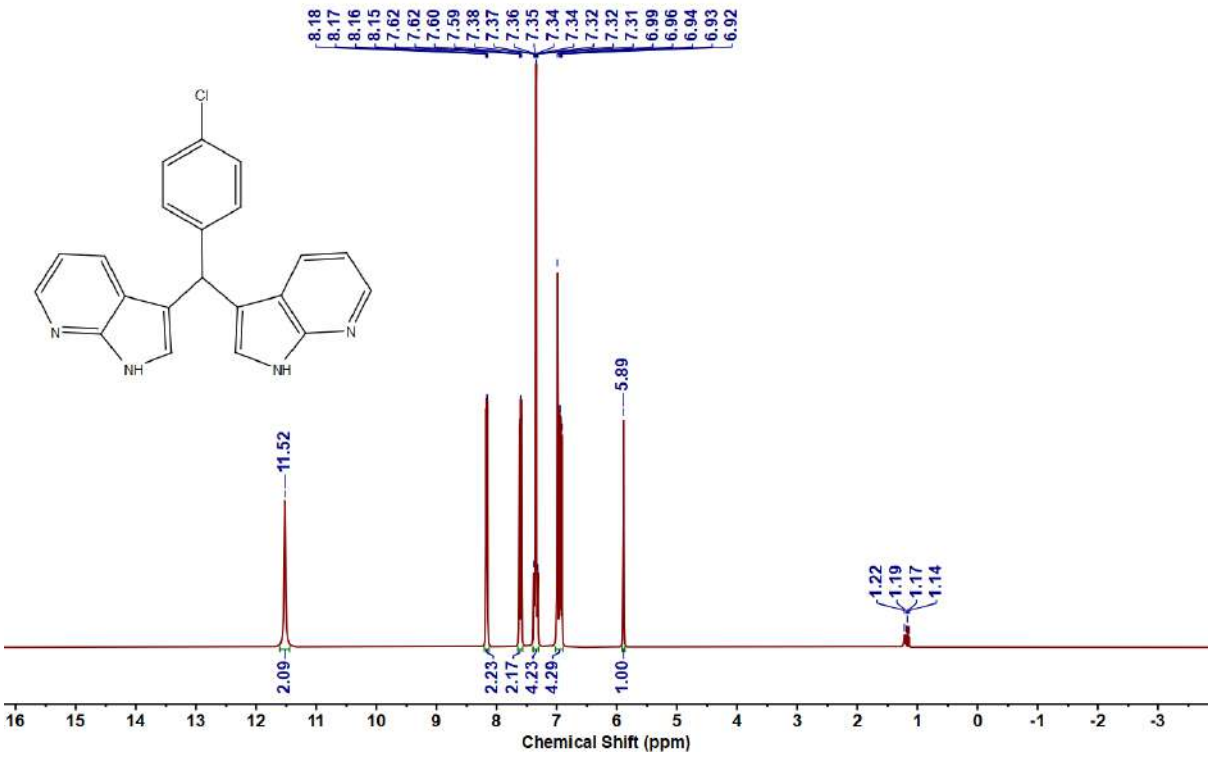

Figure 5.6.A147: ^{1}H NMR spectrum of **13ac**

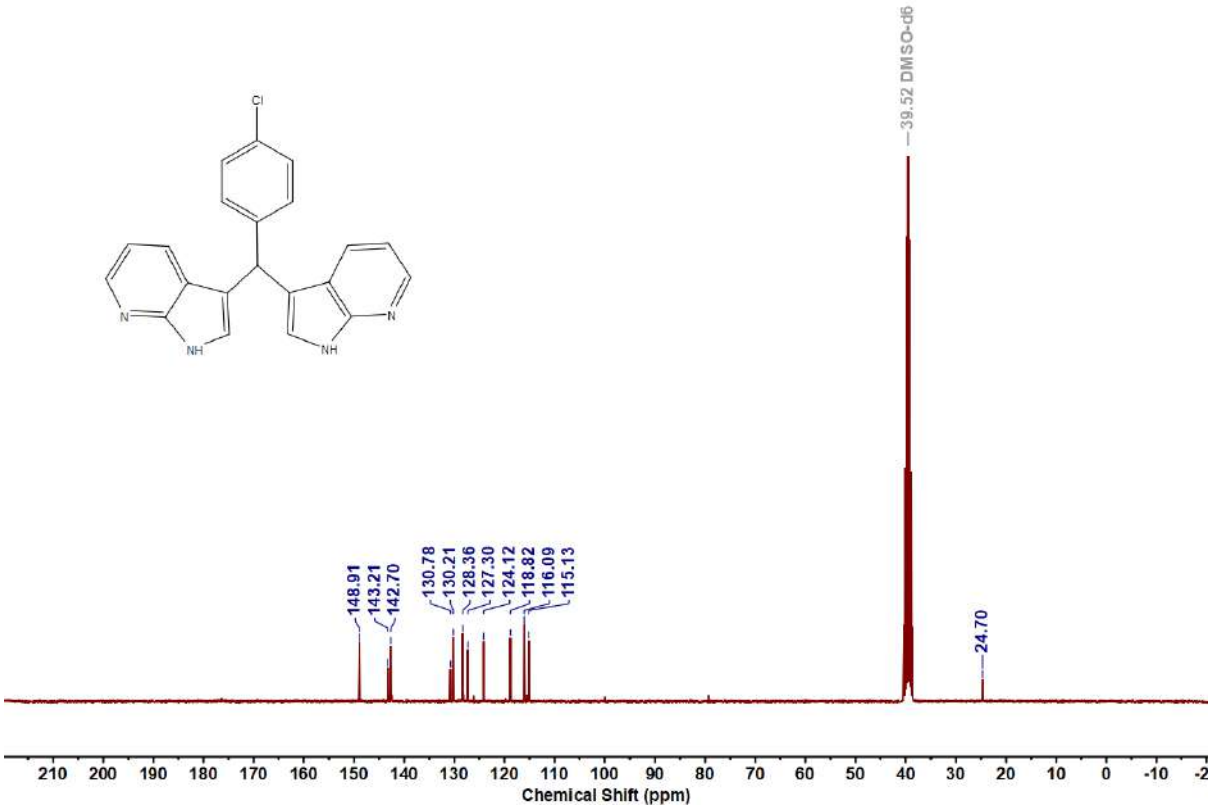

Figure 5.6.A148: ^{13}C{^{1}H} NMR spectrum of **13ac**

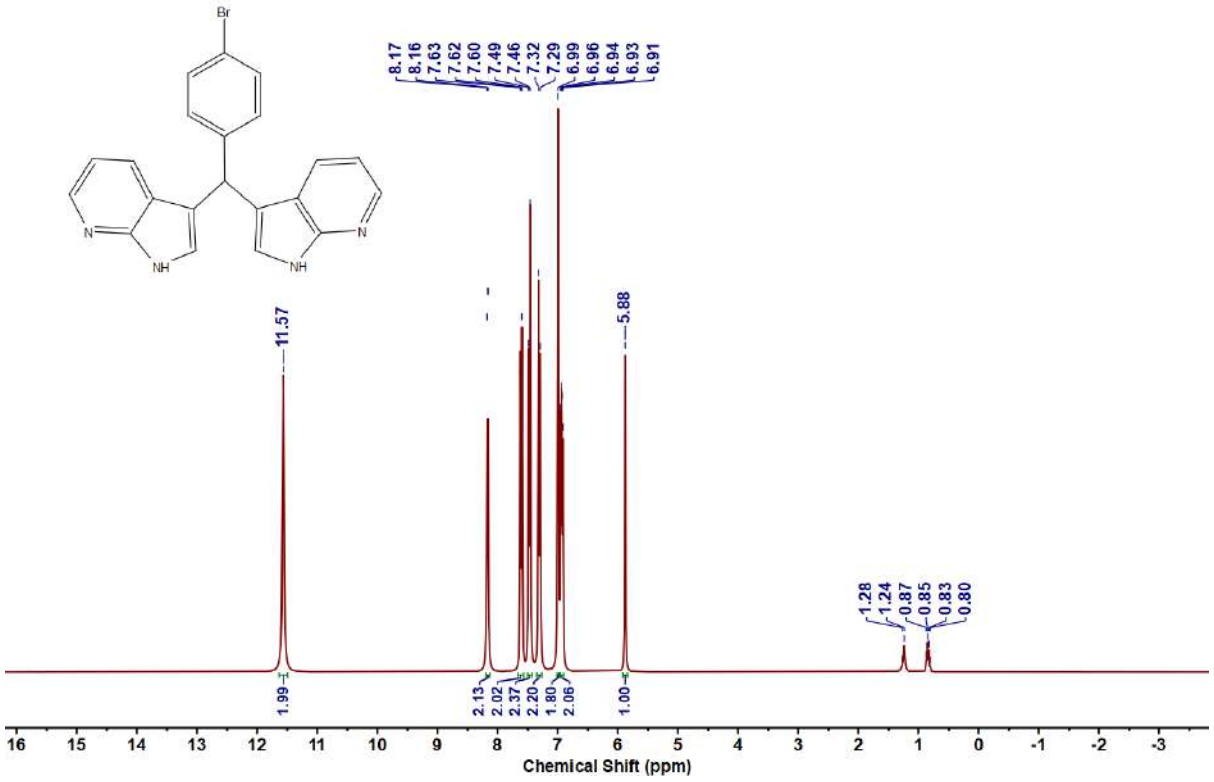

Figure 5.6.A149: ^{1}H NMR spectrum of **13ad**

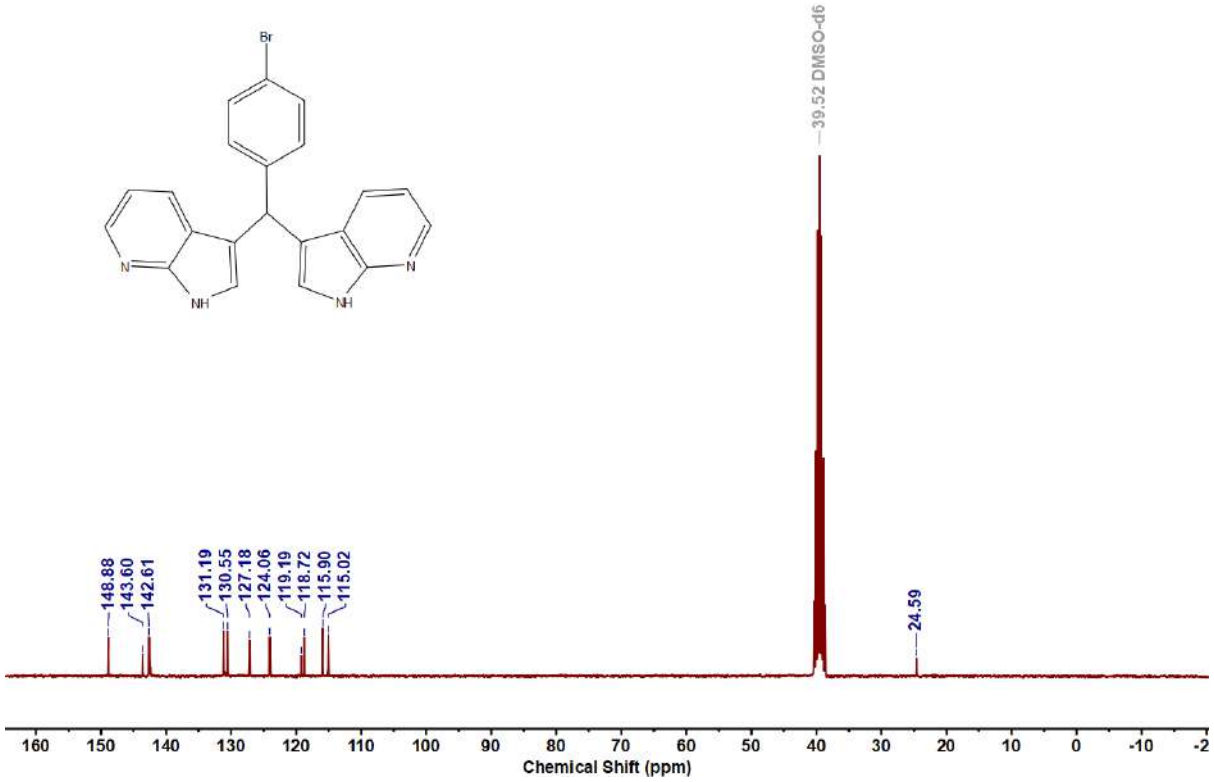

Figure 5.6.A150: $^{13}C\{^{1}H\}$ NMR spectrum of **13ad**

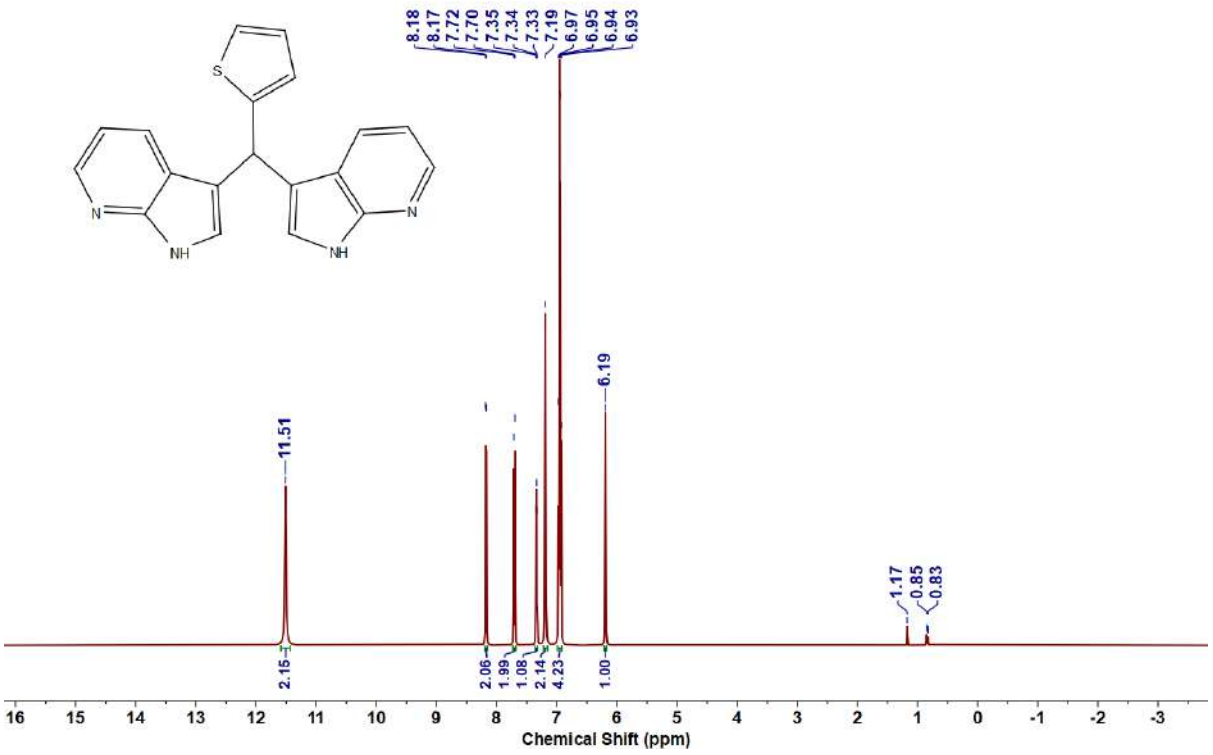

Figure 5.6.A151: ^{1}H NMR spectrum of **13ae**

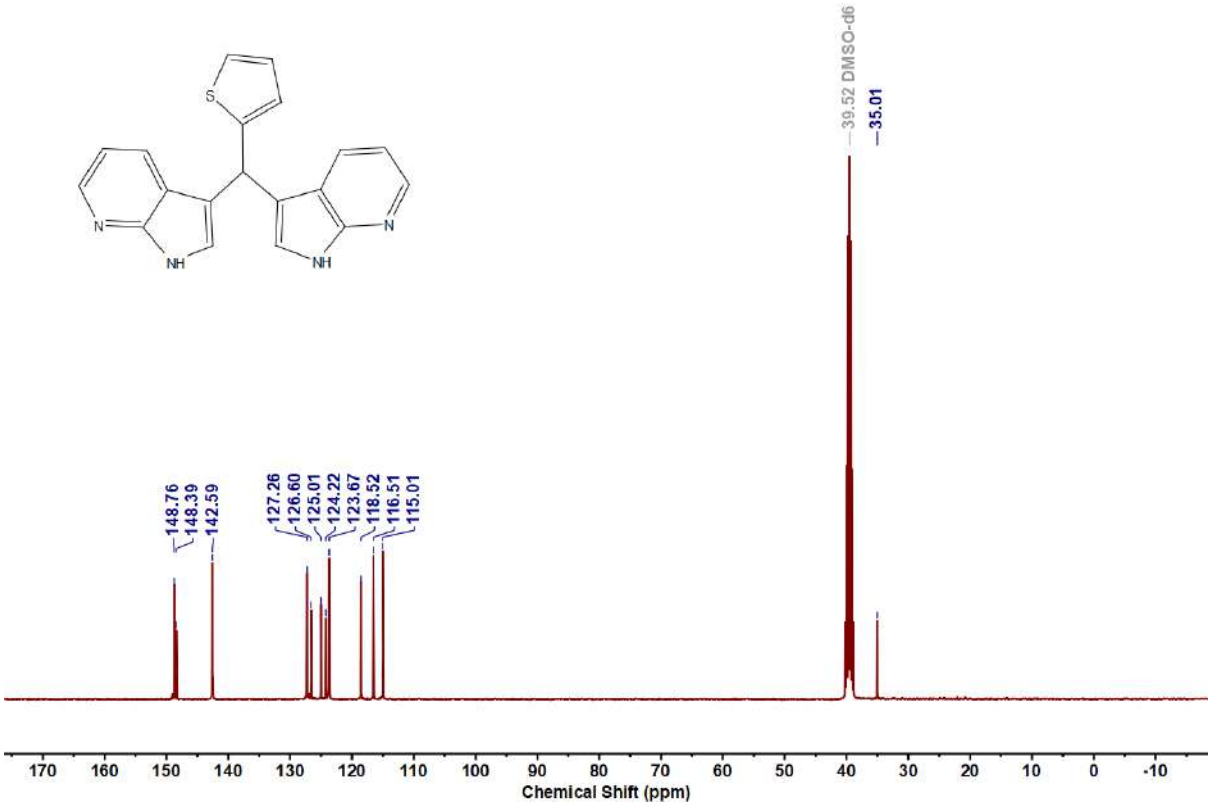

Figure 5.6.A152: $^{13}C\{^{1}H\}$ NMR spectrum of **13ae**

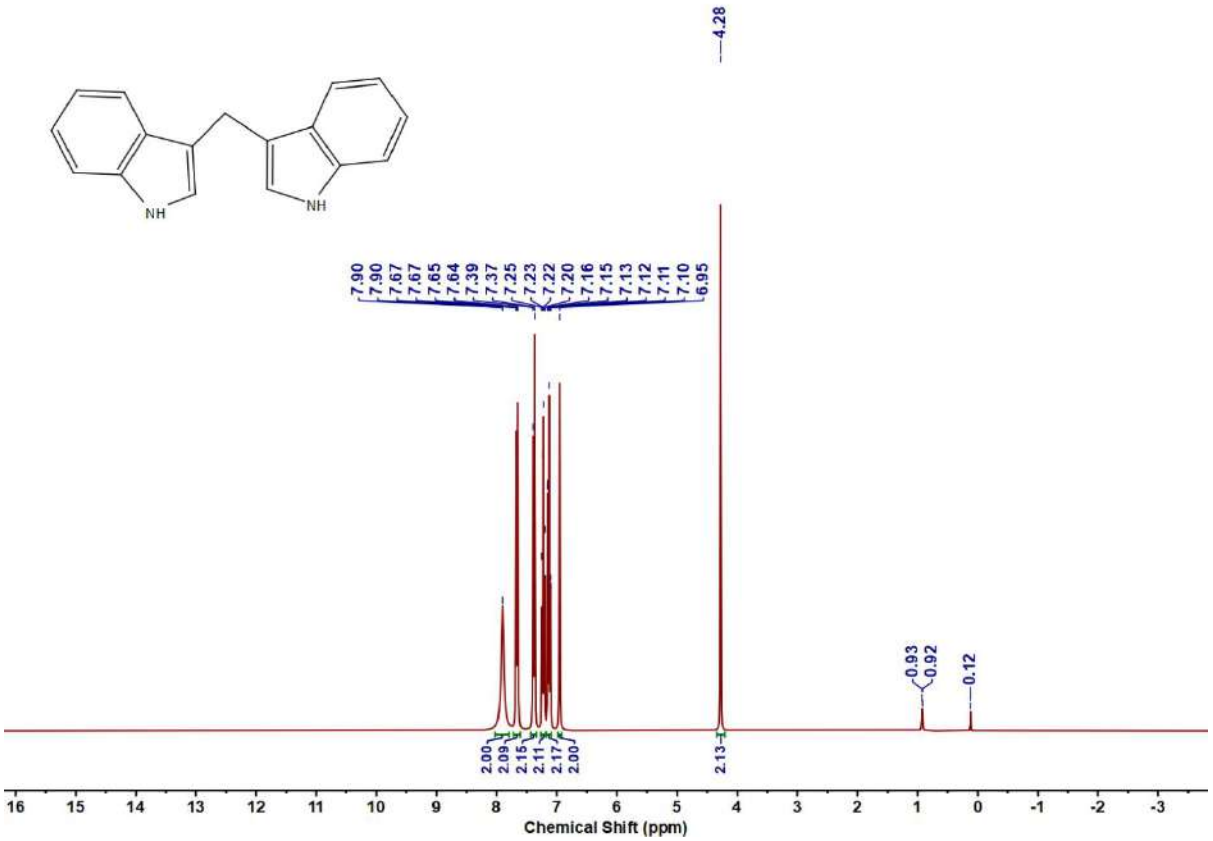

Figure 5.6.A153: ^{1}H NMR spectrum of **14aa**

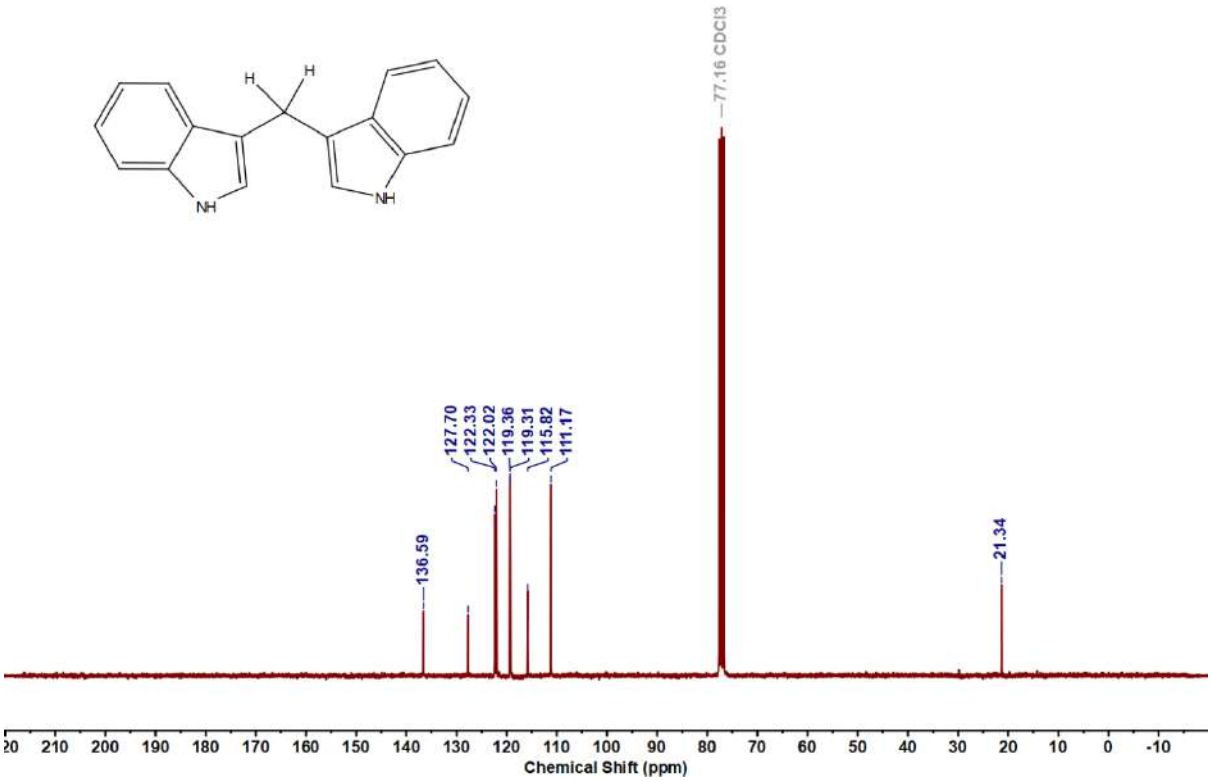

Figure 5.6.A154: ^{13}C{^{1}H} NMR spectrum of **14aa**

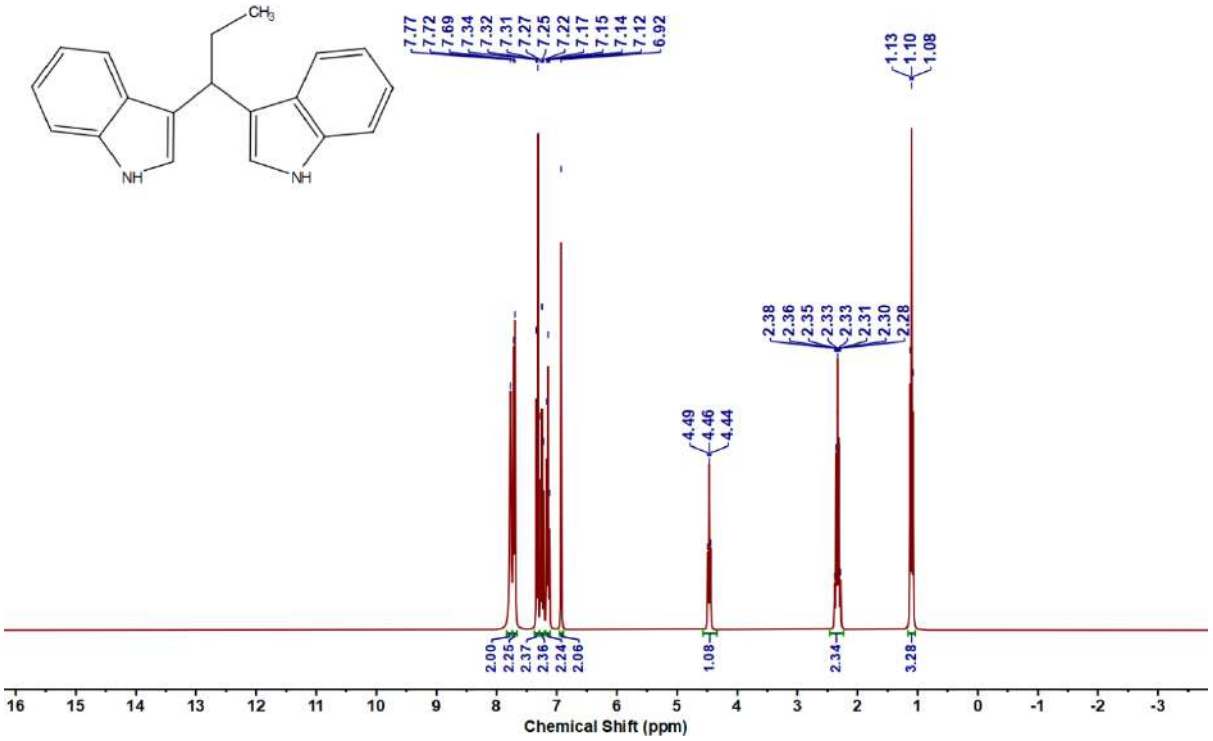

Figure 5.6.A155: ^{1}H NMR spectrum of **14ab**

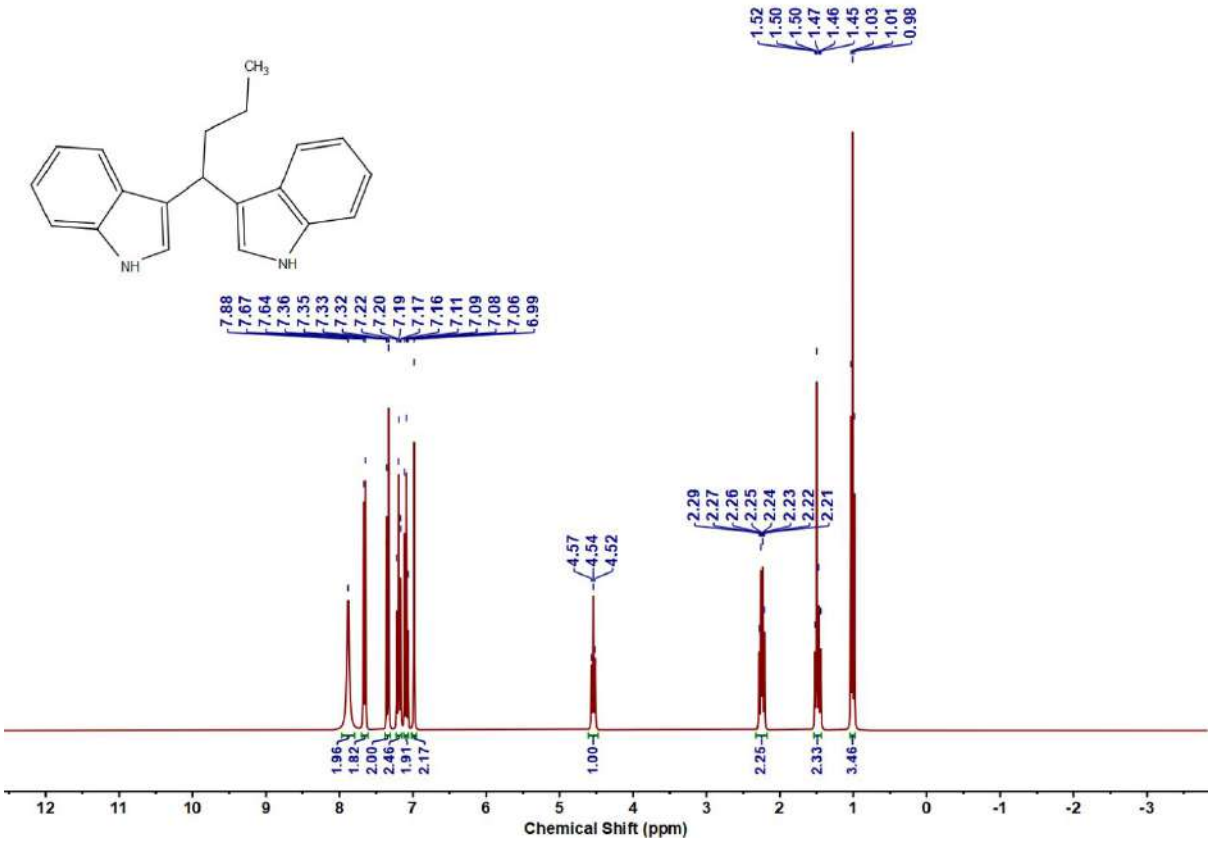

Figure 5.6.A156: ^{1}H NMR spectrum of **14ac**

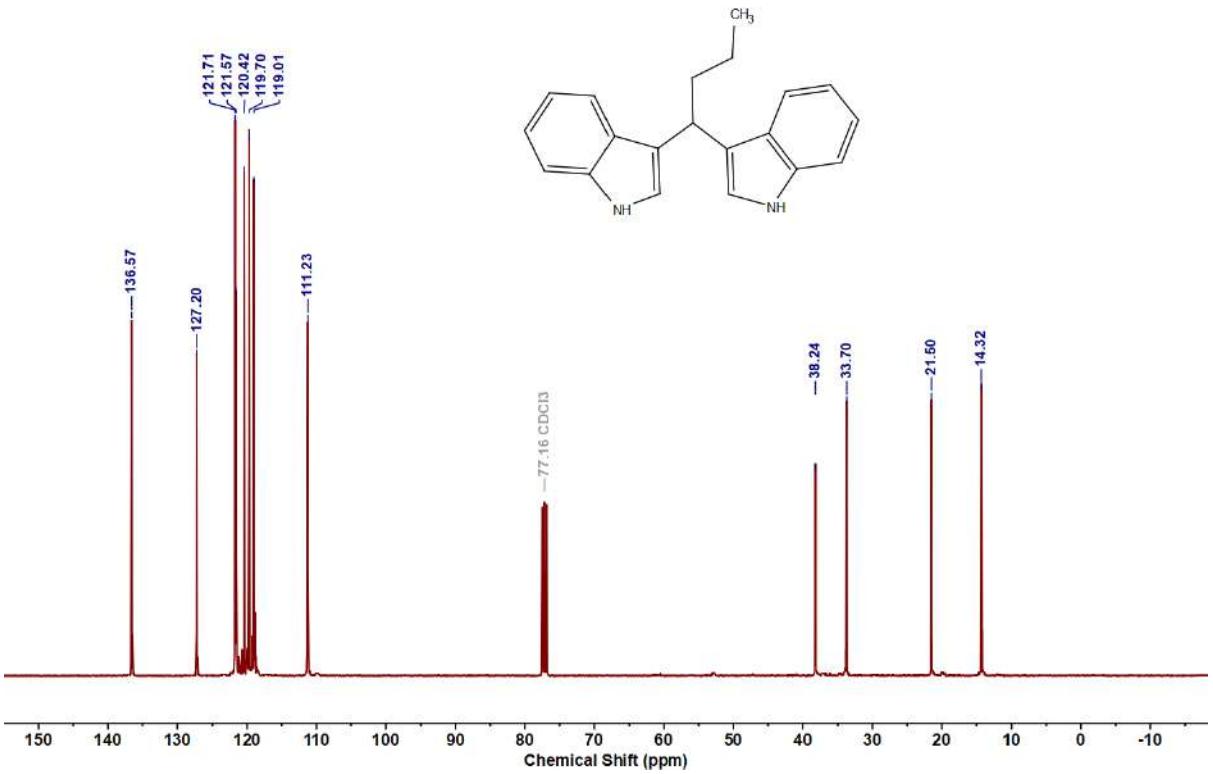

Figure 5.6.A157: $^{13}C\{^{1}H\}$ NMR spectrum of **14ac**

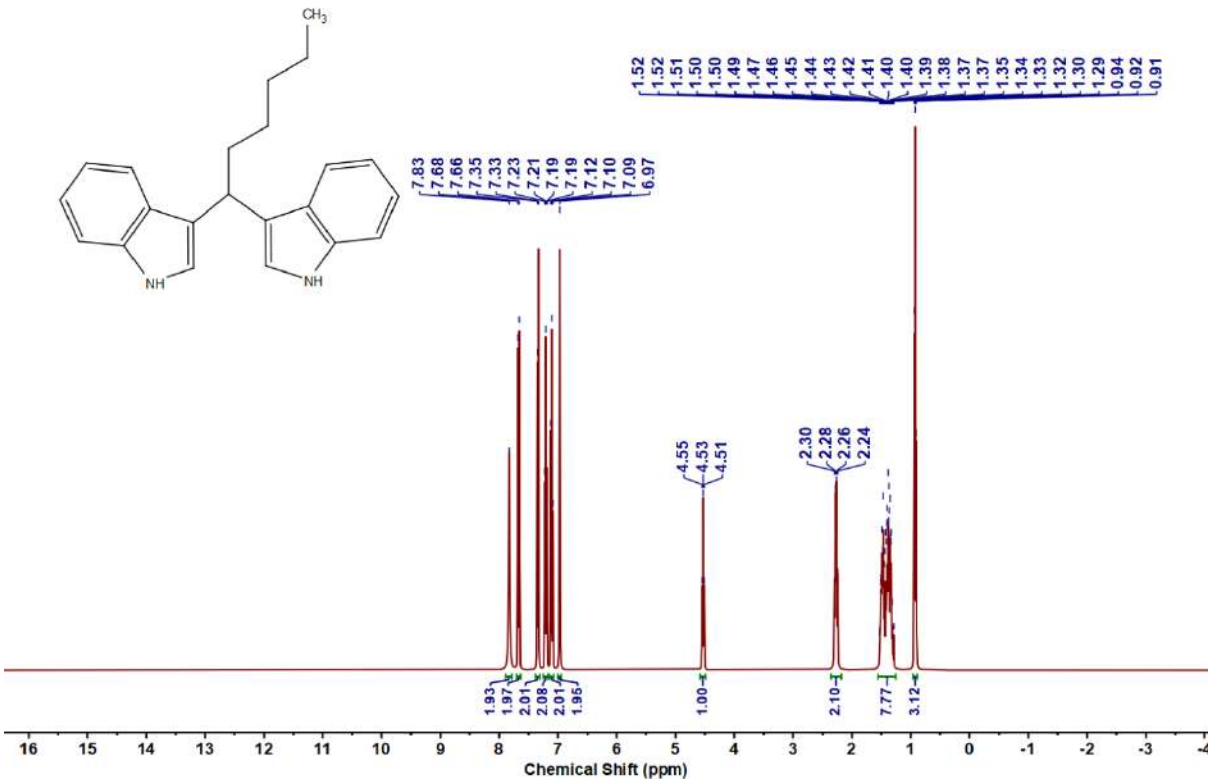

Figure 5.6.A158: ^{1}H NMR spectrum of **14ad**

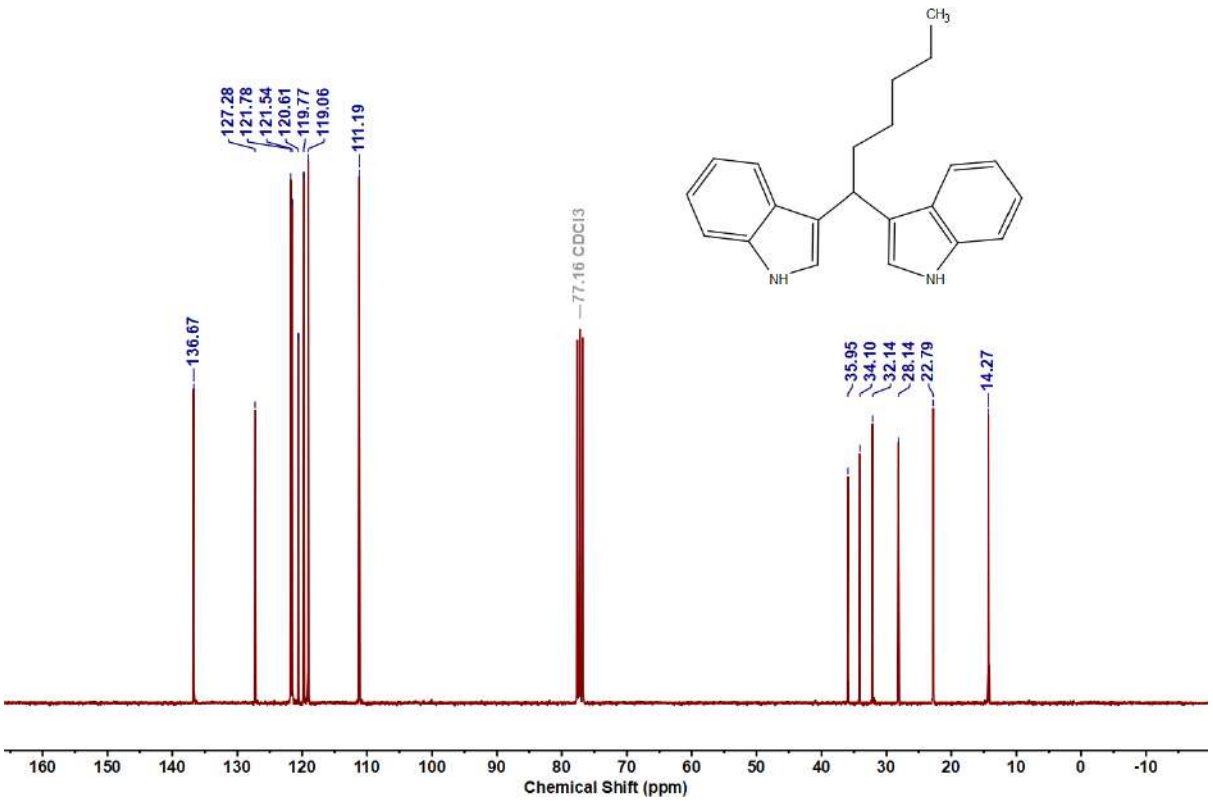

Figure 5.6.A159: $^{13}C\{^{1}H\}$ NMR spectrum of **14ad**

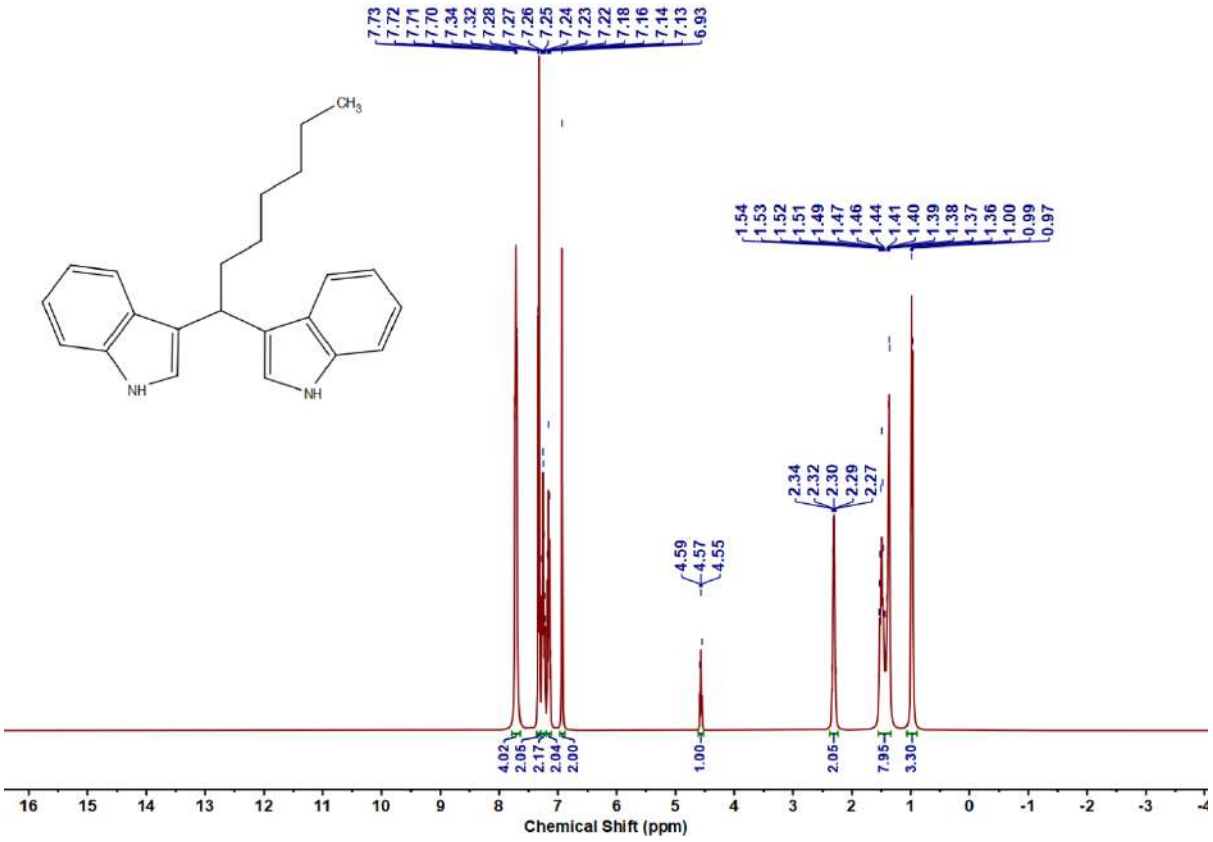

Figure 5.6.A160: ^{1}H NMR spectrum of **14ae**

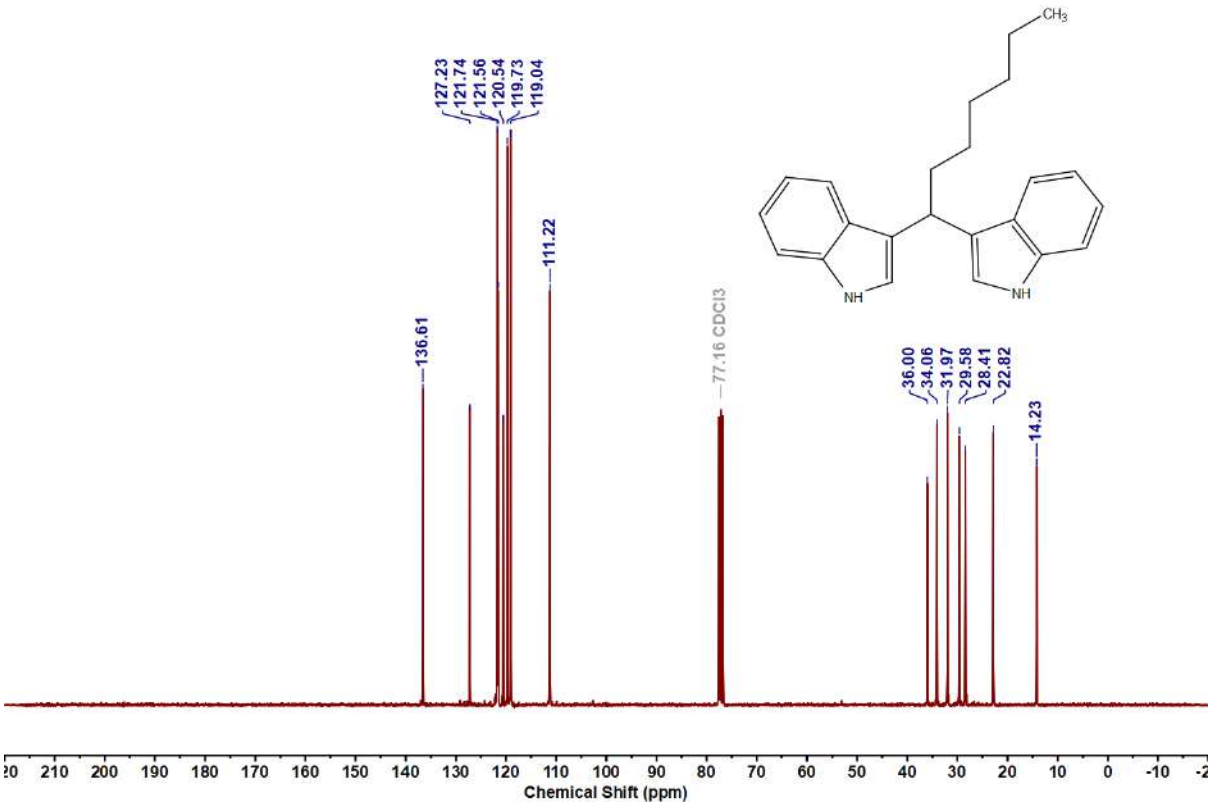

Figure 5.6.A161: $^{13}C\{^{1}H\}$ NMR spectrum of **14ae**

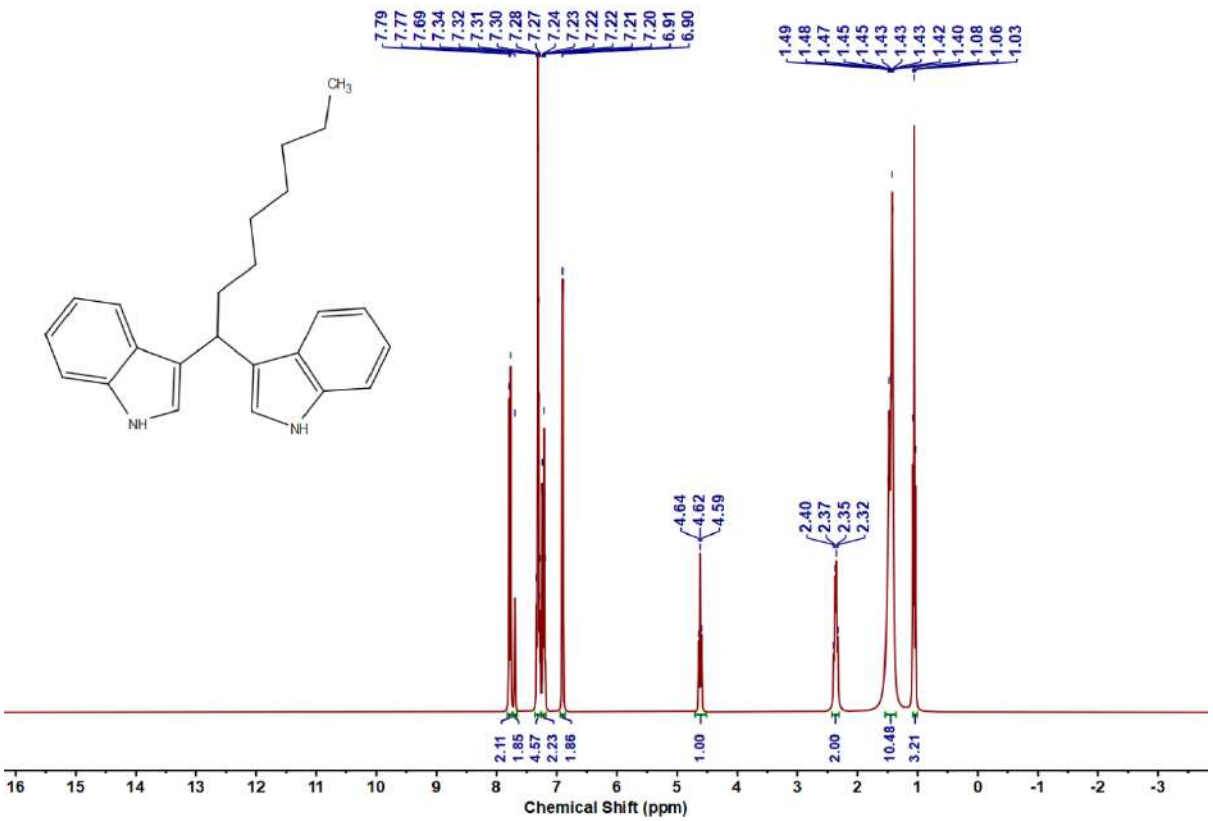

Figure 5.6.A162: ^{1}H NMR spectrum of **14af**

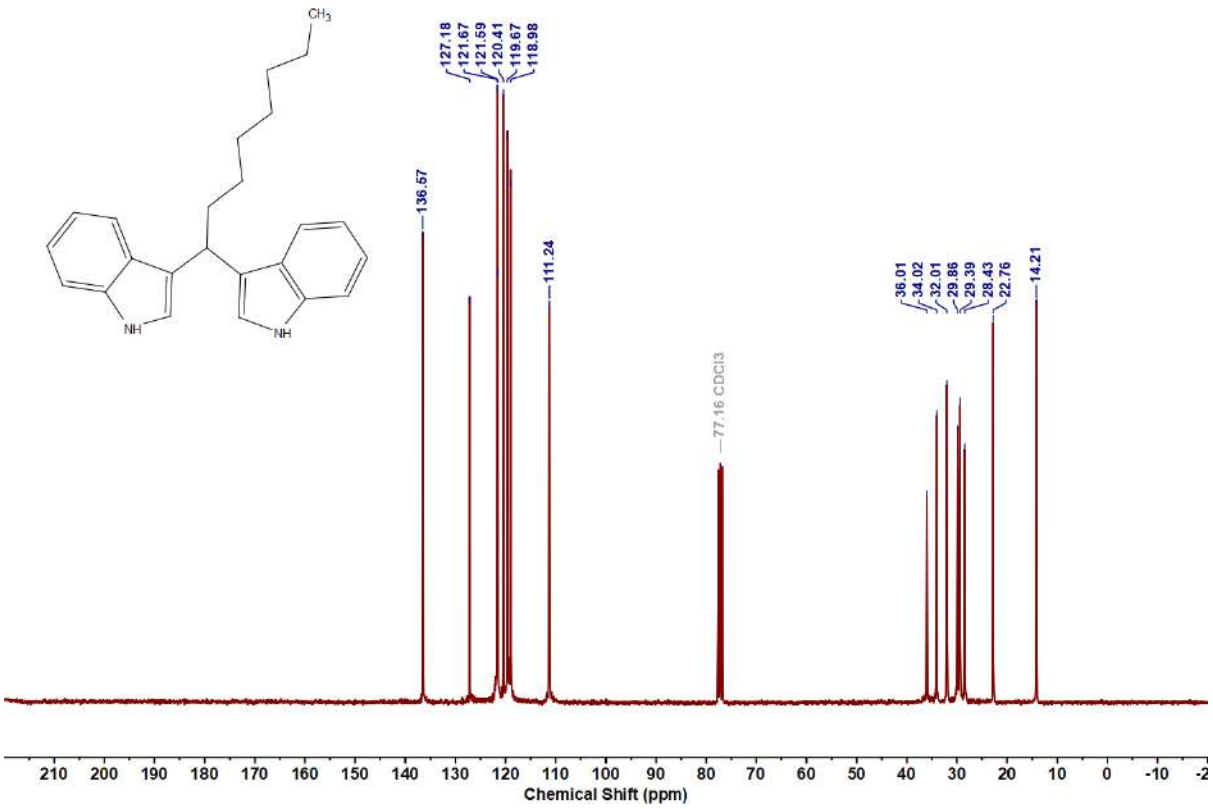

Figure 5.6.A163: $^{13}C\{^{1}H\}$ NMR spectrum of **14af**

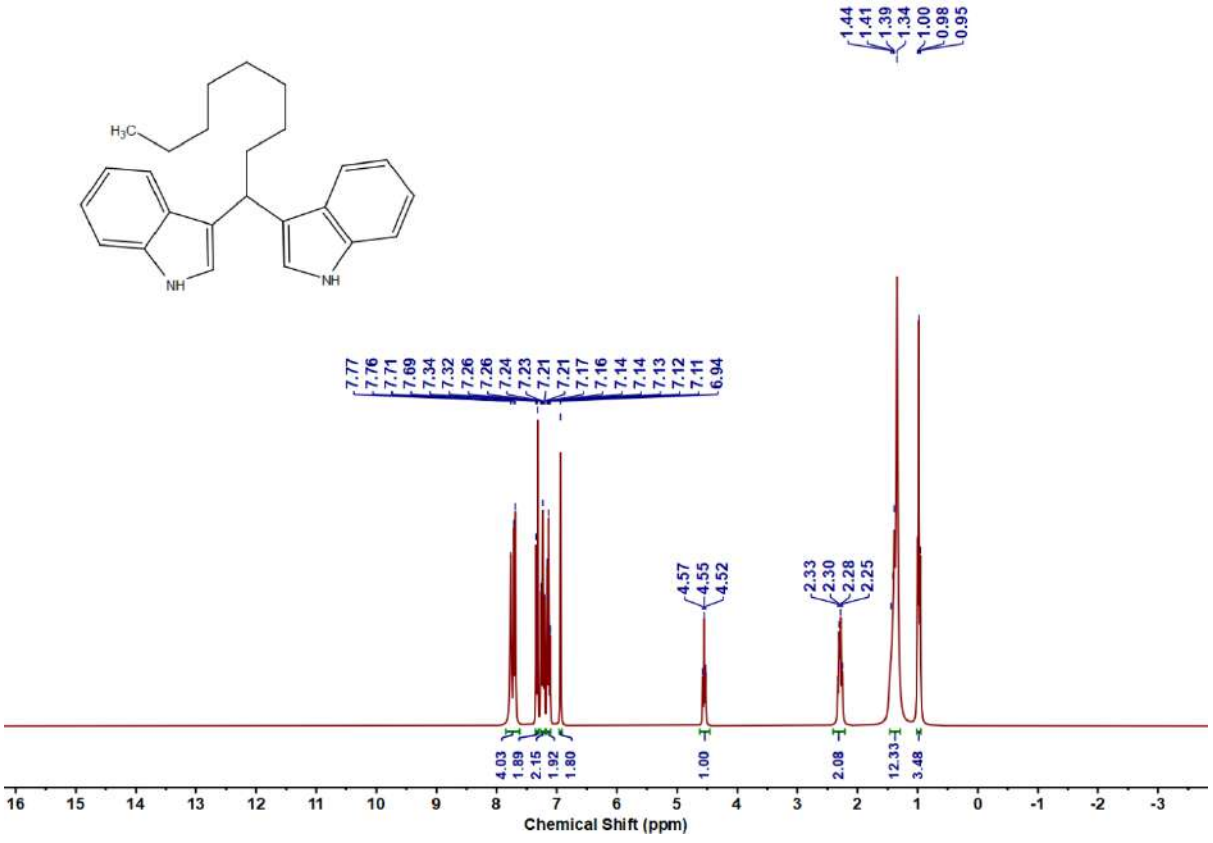

Figure 5.6.A164: ^{1}H NMR spectrum of **14ag**

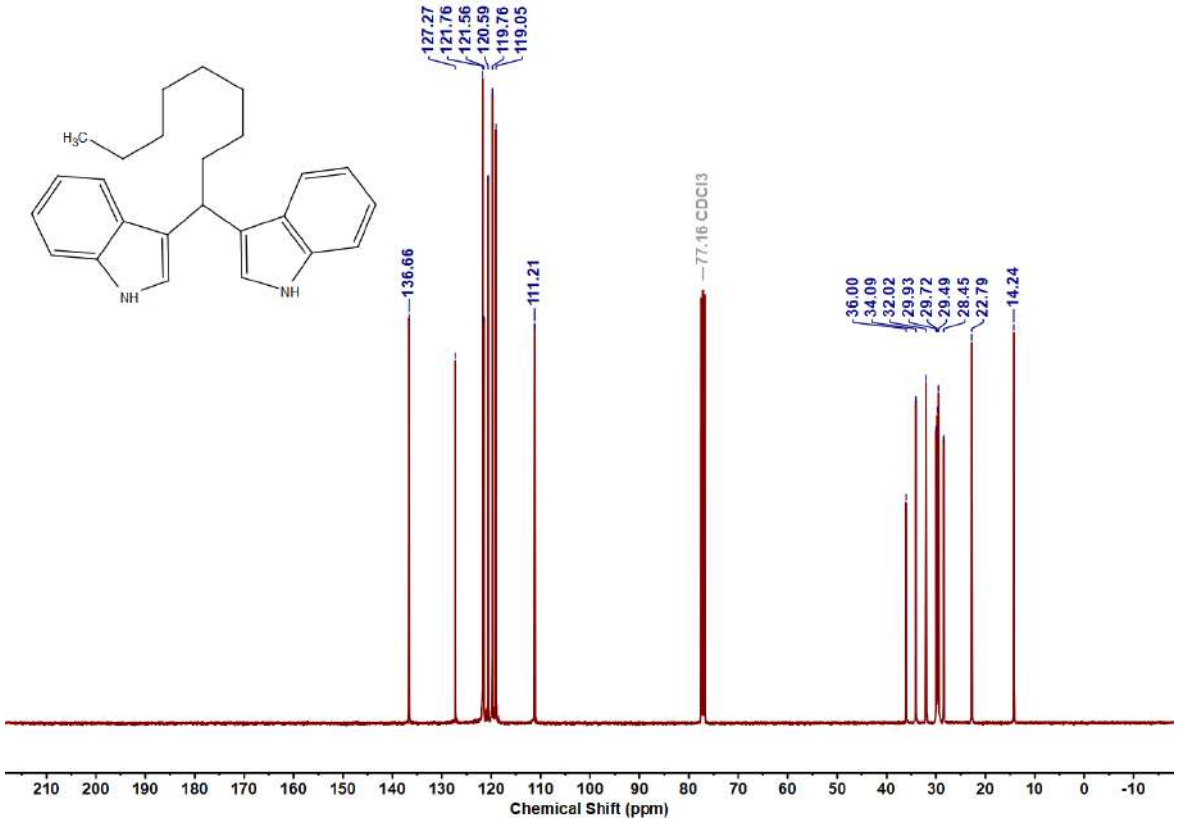

Figure 5.6.A165: $^{13}C\{^{1}H\}$ NMR spectrum of **14ag**

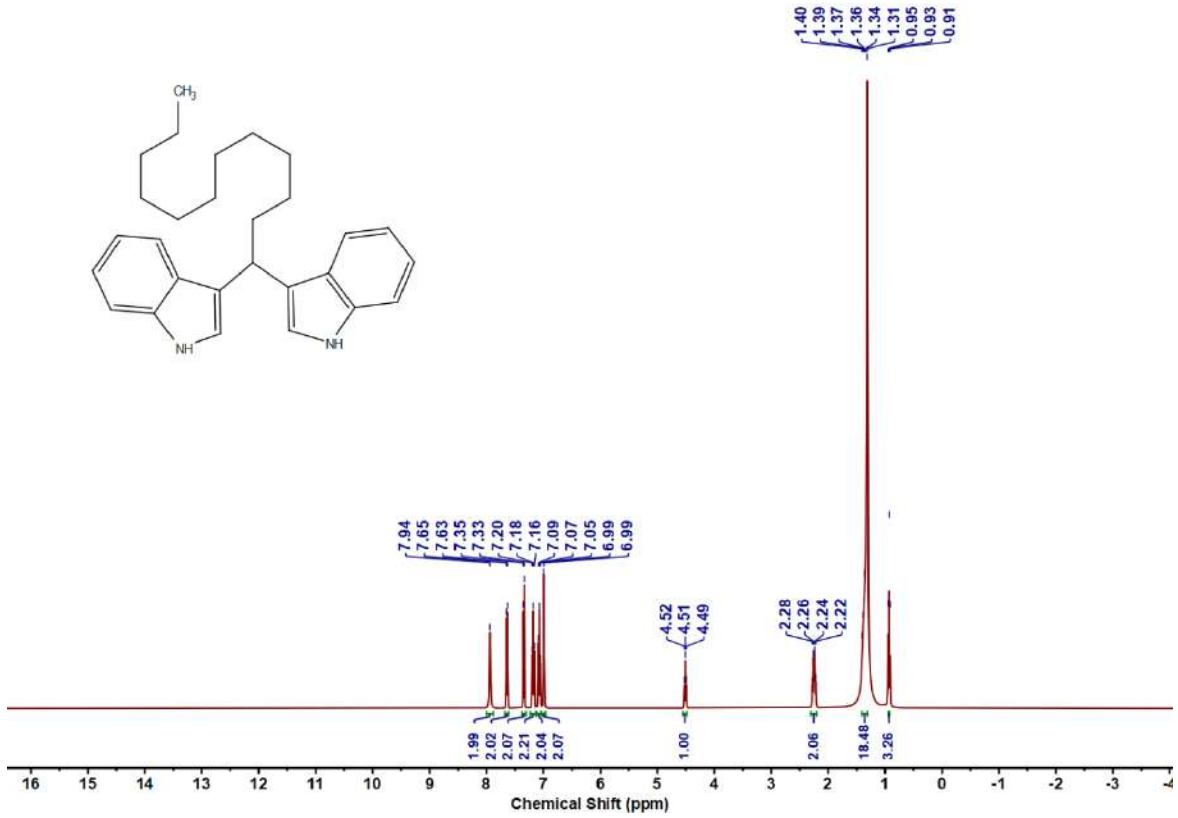

Figure 5.6.A166: ^{1}H NMR spectrum of **14ah**

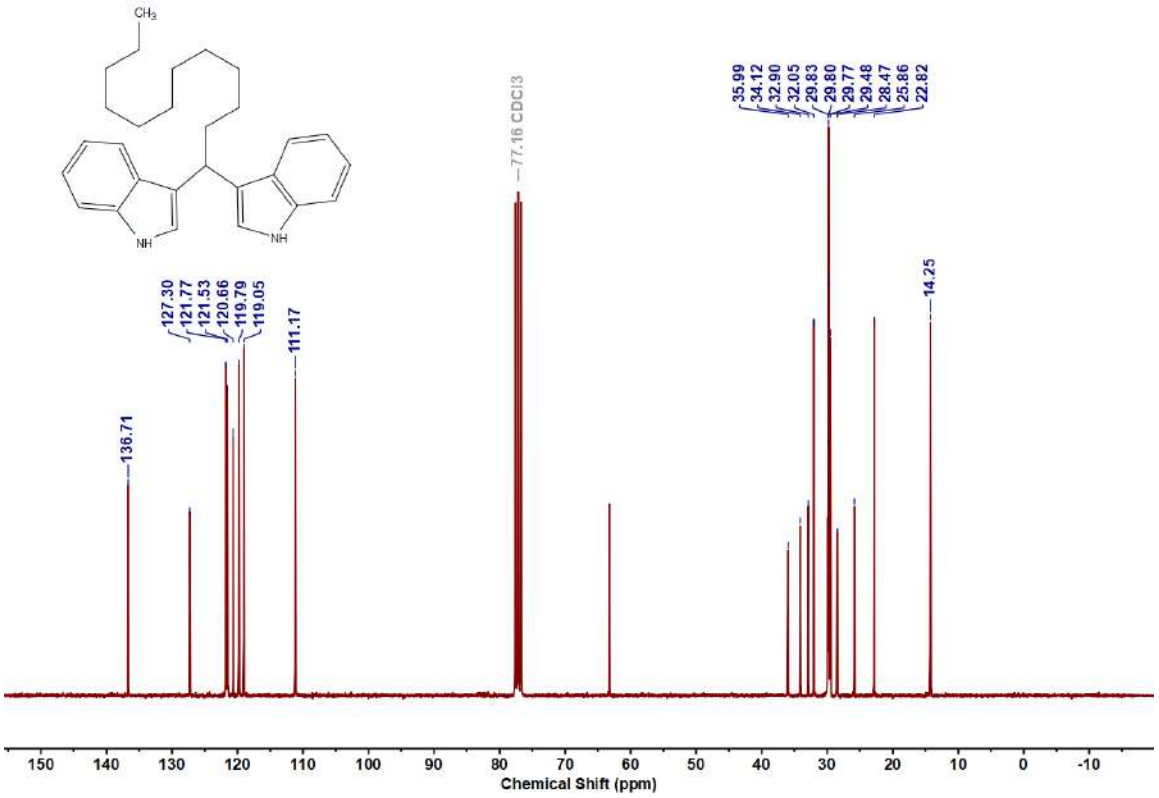

Figure 5.6.A167: $^{13}C\{^{1}H\}$ NMR spectrum of **14ah**

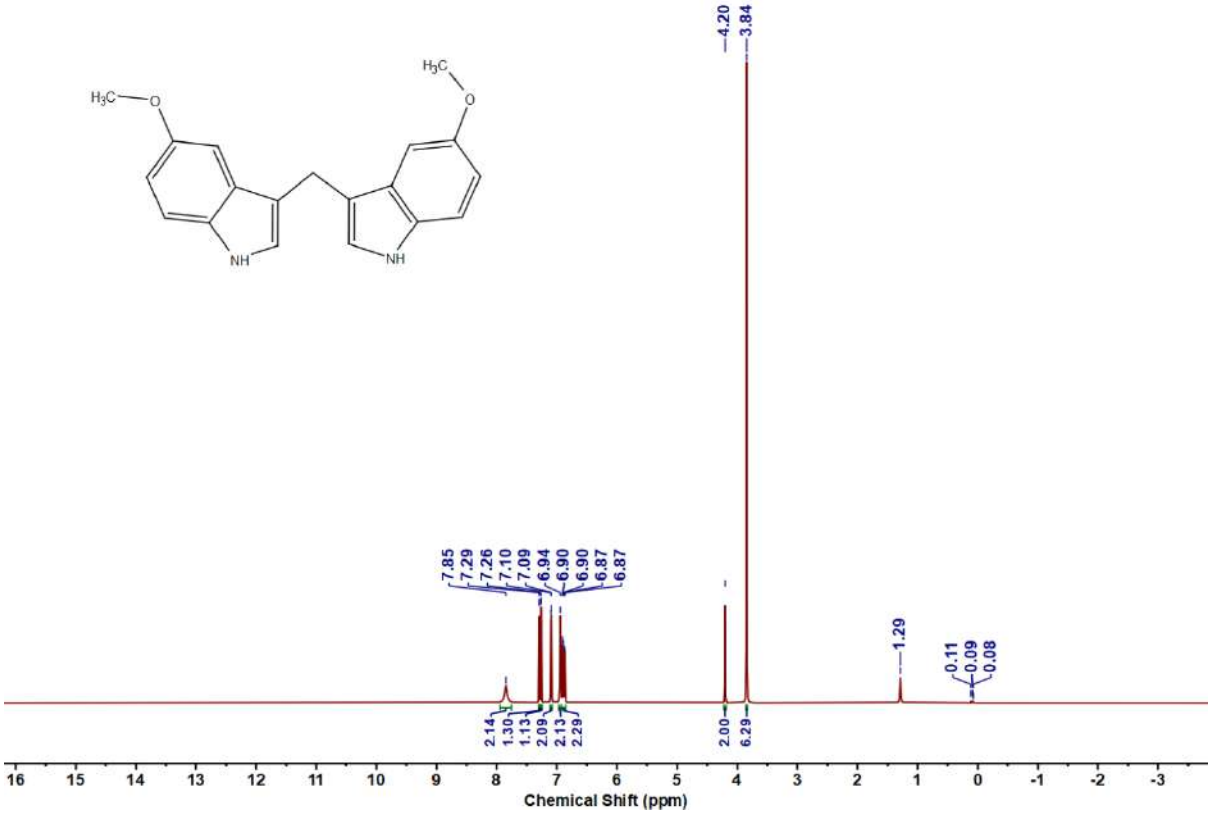

Figure 5.6.A168: ^{1}H NMR spectrum of **14ai**

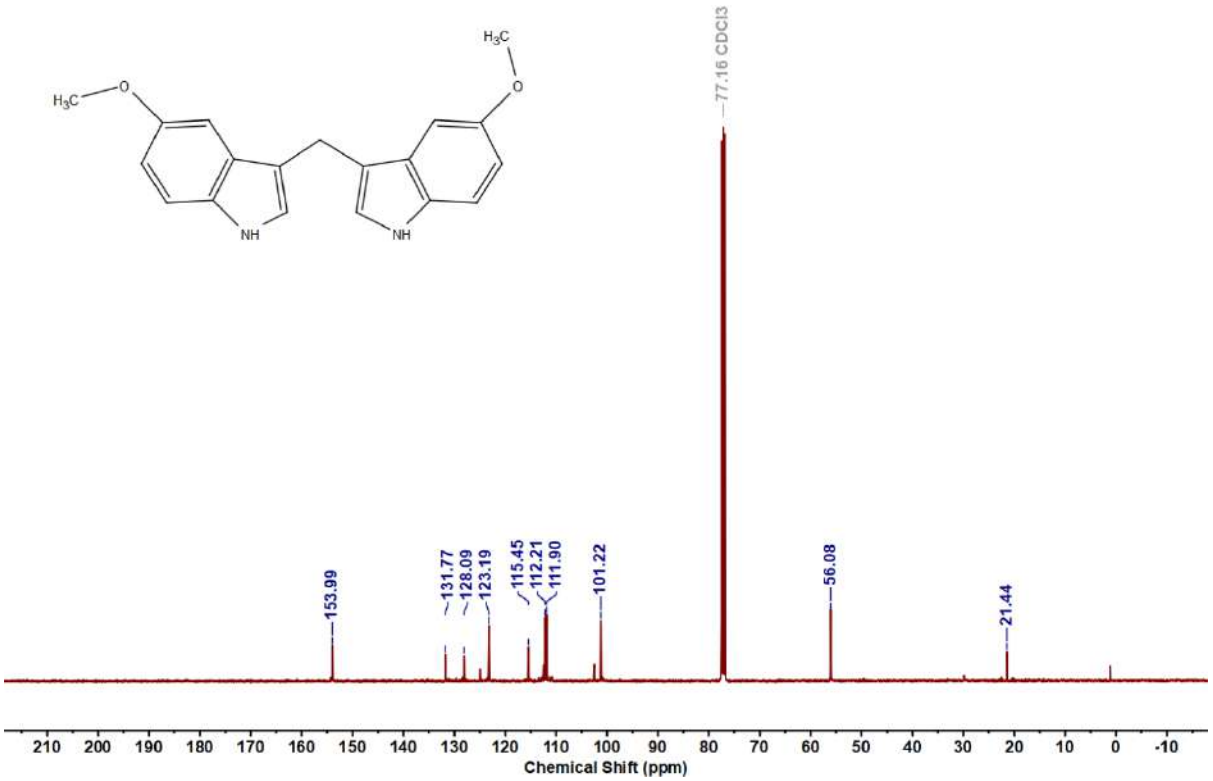

Figure 5.6.A169: $^{13}C\{^{1}H\}$ NMR spectrum of **14ai**

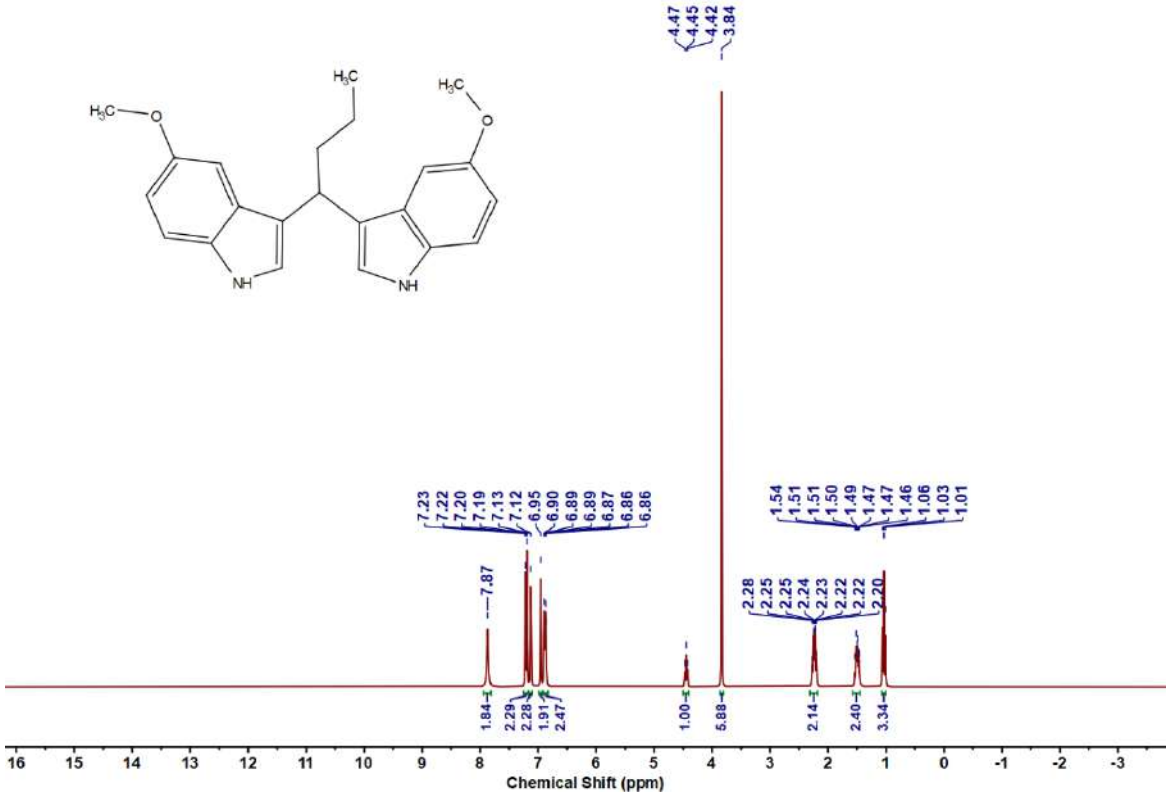

Figure 5.6.A170: ^{1}H NMR spectrum of **14aj**

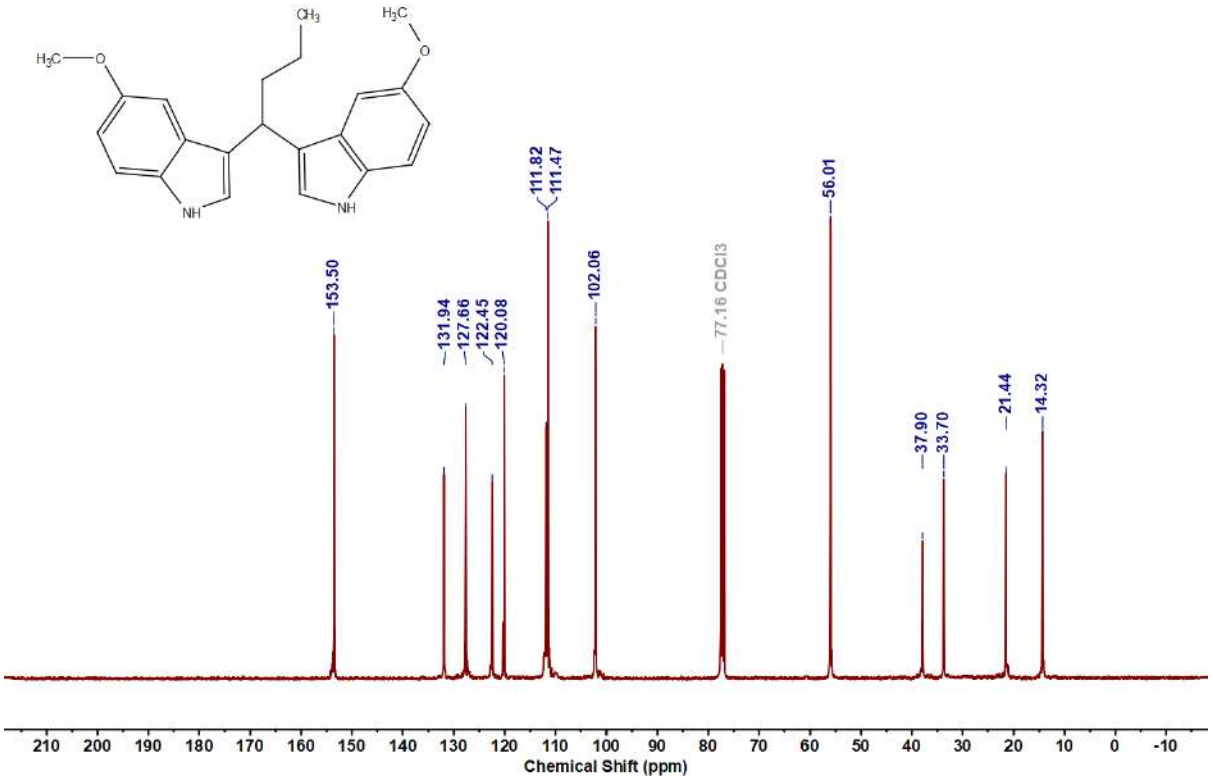

Figure 5.6.A171: $^{13}C\{^{1}H\}$ NMR spectrum of **14aj**

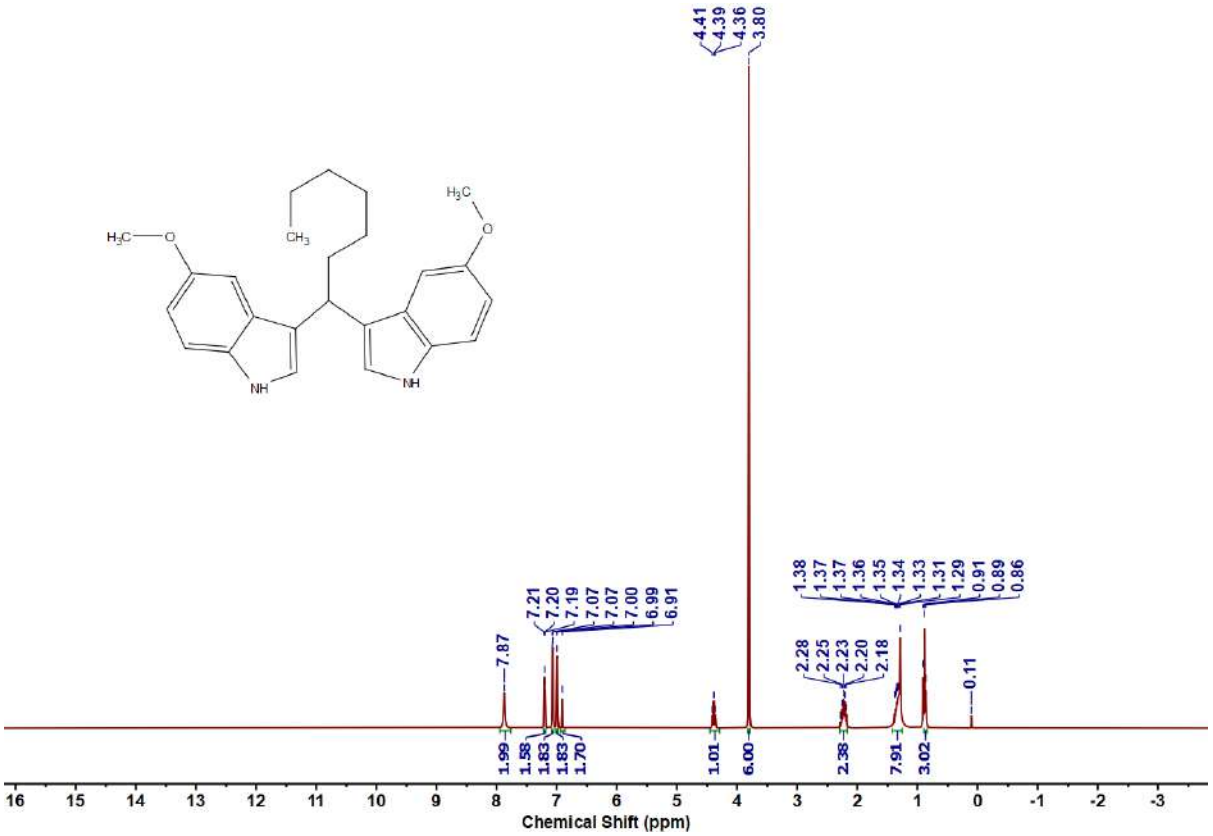

Figure 5.6.A172: ^{1}H NMR spectrum of **14ak**

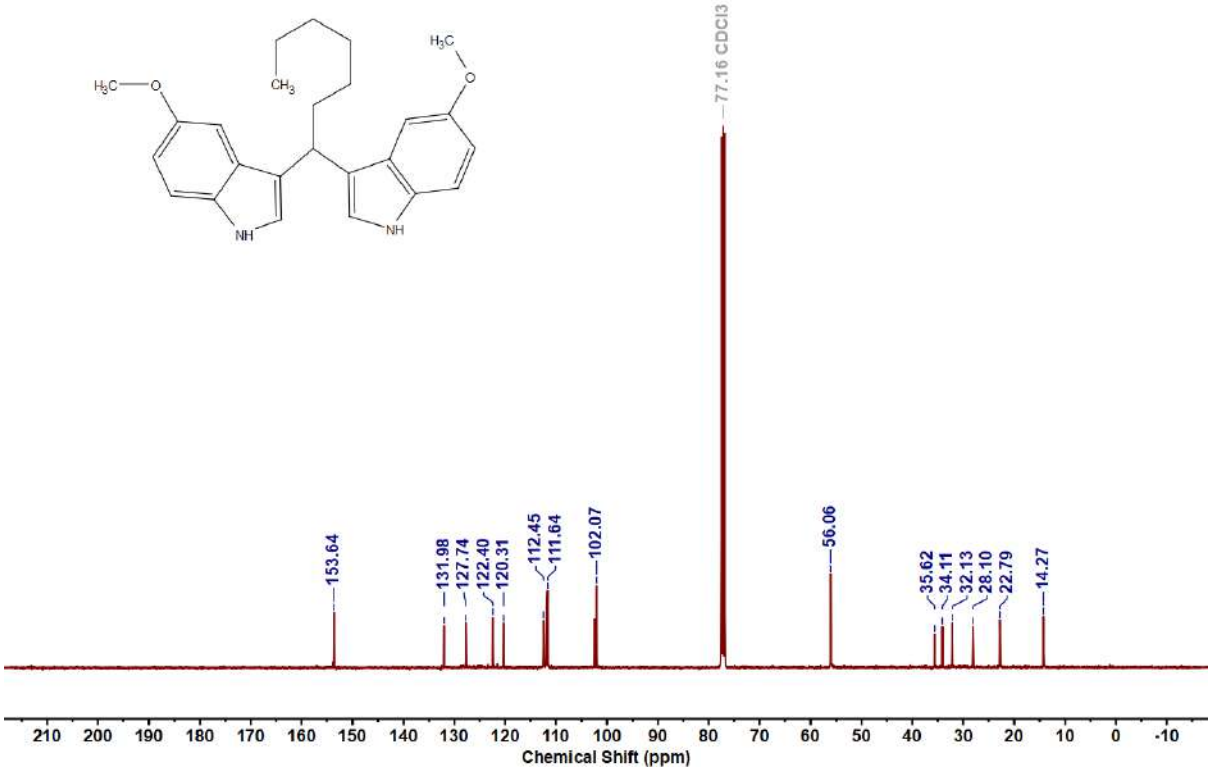

Figure 5.6.A173: $^{13}C\{^{1}H\}$ NMR spectrum of **14ak**

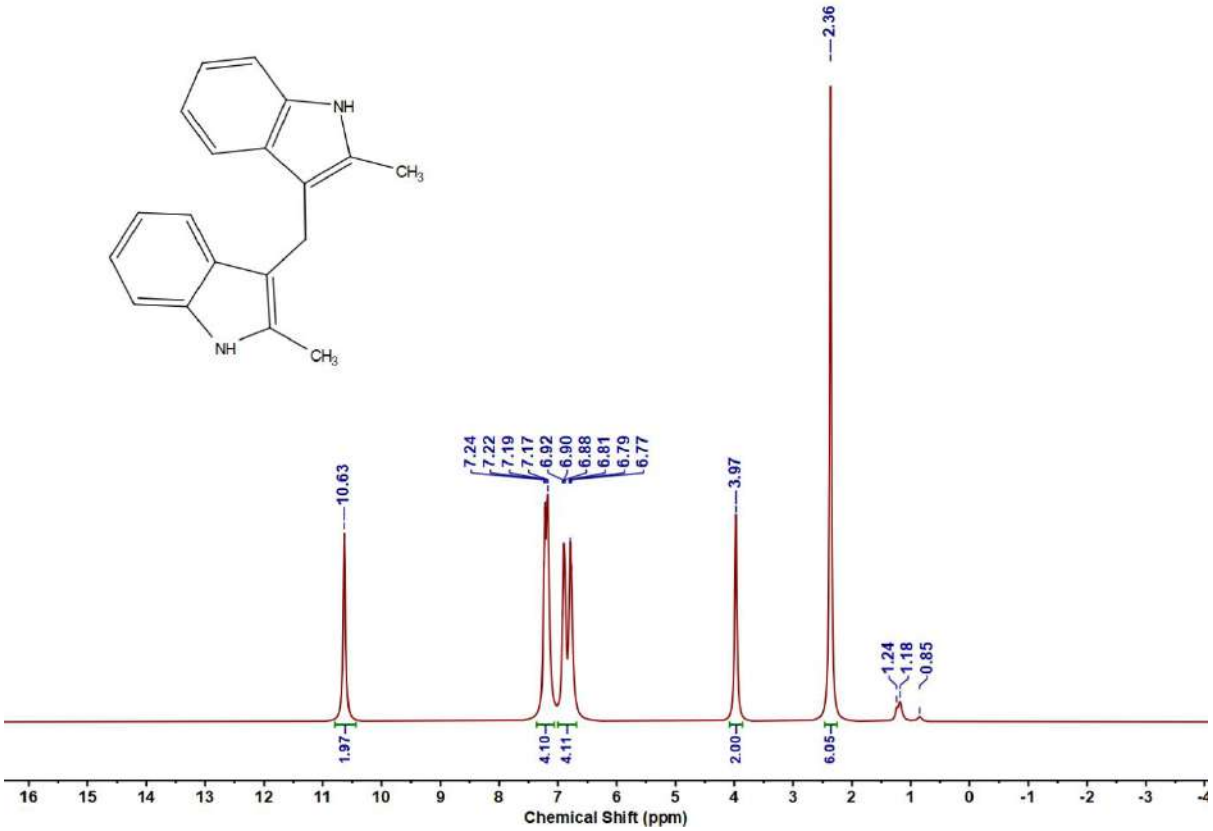

Figure 5.6.A174: ^{1}H NMR spectrum of **14al**

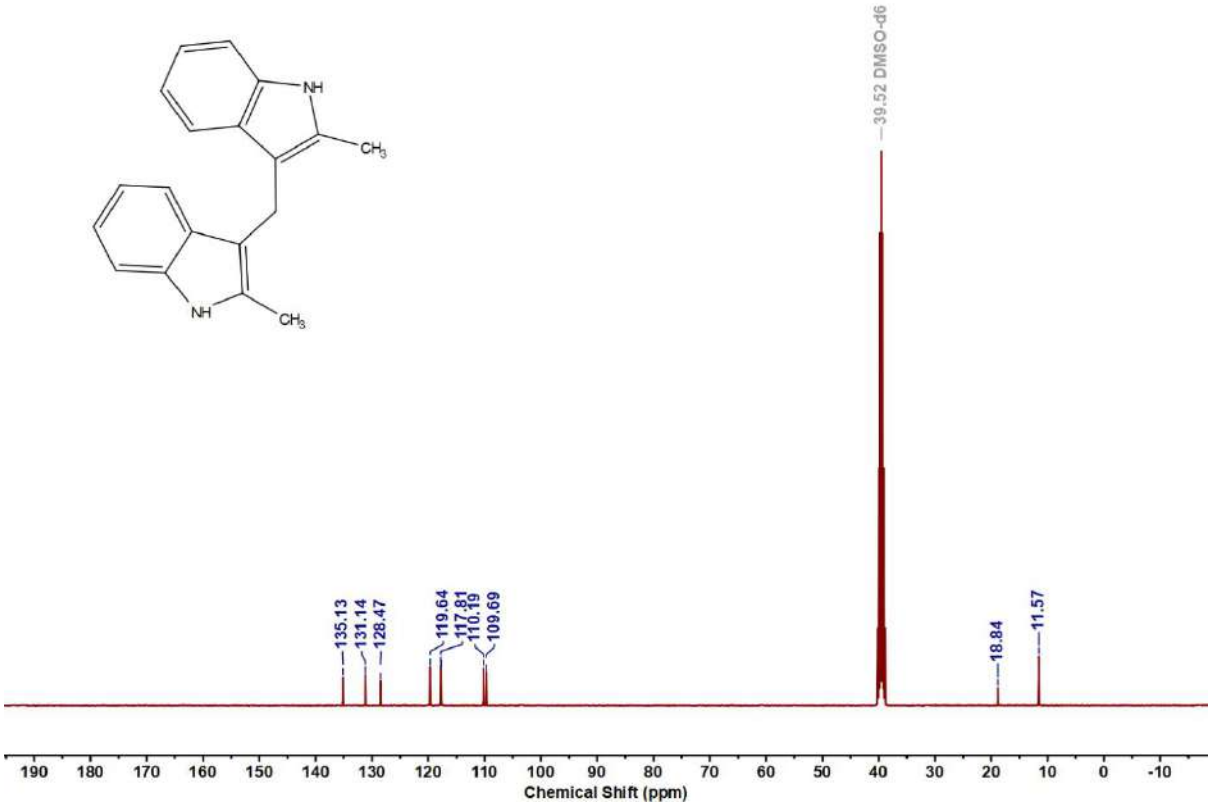

Figure 5.6.A175: $^{13}C\{^{1}H\}$ NMR spectrum of **14al**

Summary

Chapter 1

The first chapter provides a conceptual foundation for the thesis and introduces three distinct types of azo-based redox-active ligand, namely diaryl-azo-oxime, amino-azo-quinoline and pyridyl-azo-amine. It establishes the importance of azo scaffolds in modulating redox processes and highlights their coordination chemistry with transition metals. The chapter further outlines the research objectives, experimental methodologies and computational techniques employed, while also detailing the instrumentation used for structural and electronic characterization.

Chapter 2

This chapter investigates the redox behaviour of phenyl-azo-oxime ligands (HL) coordinated to Rh(III). The spatial orientation of azo-oxime groups in bis-complexes was shown to strongly influence redox non-innocence. Two structural isomers, *cis*-[$RhL_2Cl(PPh_3)$] and *trans*-[$RhL_2Cl(PPh_3)$], were synthesized and structurally characterized by SCXRD. The *trans*-isomer displayed enhanced π–π stacking interactions and superior electron-accepting capacity. Upon $NaBH_4$ reduction, the *trans*-isomer generated a ligand-centered azo-anion radical complex *via* proton-coupled electron transfer (PCET), stabilized by intramolecular hydrogen bonding. DFT and TD-DFT validated the experimental findings.

Chapter 3

This chapter focuses on a novel ligand (H_2L) featuring an electron-poor azo group and a quinoline moiety and its Ni(II) complexes [Ni(HL)(OAc)]·H_2O and [Ni(HL)Cl]. SCXRD revealed extensive hydrogen bonding and π–π stacking stabilizing the lattices. Electrochemical studies showed that reduction is ligand-centered while oxidation involves both the ligand and

metal. Both ligand and complexes demonstrated significant anti-cancer activity, with stronger efficacy observed for the rigid square-planar complexes. Molecular docking with B-DNA confirmed stronger interactions for the complexes compared to the free ligand.

Chapter 4

This chapter presents the synthesis and characterization of *trans*-[Ru(*p*-Cl-aaO)(PPh_3)$_2$Cl(CO)] derived from a *p*-chloro-aryl-azo-oxime ligand. The complex displayed high stability under air and moisture. Electrochemical, spectroscopic, SCXRD and computational analyses revealed its efficacy as a redox catalyst for alcohol dehydrogenation followed by sp^3 C–H functionalization of fluorene under aerobic conditions. Mechanistic insights confirmed that the azo-oxime unit within the ligand framework functions as the active redox site, while the Ru(II) center served as a spectator. The system offered key advantages of low catalyst loading, mild reaction conditions, broad substrate scope, shorter reaction time as well as lower reaction temperature.

Chapter 5

The final chapter reports a Ru(II)-hydride complex featuring a 2-(pyridylazo)aniline ligand, applied in the direct dehydrogenative synthesis of bis(indolyl)methanes (BIMs). Using primary alcohols as substrates, the catalyst enabled $2e^-$ hydride transfer mechanism from alcohols to the azo group, followed by aldehyde condensation with indoles and base promoted nucleophilic addition. This sustainable ligand-driven process delivered biologically potent BIM derivatives efficiently under relatively mild conditions.

Overall Outlook

This thesis establishes azo-based ligands as powerful platforms for controlling redox non-innocence, ligand-centered radical stability, catalytic activity and biological function. Across Rh, Ni and Ru systems, the studies highlight the unique ability of azo groups to dictate electron transfer and bond activation. Moving forward, integration of these ligands in multifunctional catalytic systems, coupling with green chemistry principles and exploration of bioactivity in medicinal contexts can pave the way for new frontiers in redox chemistry, catalysis and metallodrug development.

List of Publications

1. Role of ligand Disposition and Oxime…Oximato Hydrogen Bonding upon Redox Non-innocent Character of Rhodium(III) Phenylazooximates

   Srijita Naskar, Supriyo Halder, Gopal Kanrar, Debashis Jana, Soumitra Dinda, Kausikisankar Pramanik,* Sanjib Ganguly,* *Polyhedron*, **2023**, *235*,116342.

2. Designed Synthesis of Amino-Azo-Quinoline and Their Nickel(II) Complexes: Molecular Structure, Electrochemistry and an Insight Into Their In Vitro Anti-Cancer Activities

   Srijita Naskar,‡ Koushik Sarkar,‡ Supriyo Halder, Bidisha Chatterjee, Debjeet Chakraborty, Arka Laha, Rahul Sharma, Arup Kumar Mitra, Kausikisankar Pramanik,* Sanjib Ganguly,* *Chemistry & Biodiversity*, **2025**, *22*, e202402436.

3. Alcohol Dehydrogenation Catalyzed by Azo-Oxime Coordinated Ruthenium(II): A Strategic and Sustainable Route towards Site-Selective C(sp^3)–H Functionalization of 9H-Fluorene

   Srijita Naskar,‡ Supriyo Halder,‡ Aritra Das, Sampad Malik, Gopal Kanrar, Debashis Jana, Bikash Kumar Panda, Kausikisankar Pramanik,* Sanjib Ganguly,* *Asian J. Org. Chem.*, **2025**, *14*, e00330.

4. 2-(Pyridylazo)aniline Coordinated Ruthenium(II) Complex as an Efficient Catalyst for the Dehydrogenative Synthesis of Bis(indolyl)methanes from Alcohols and Indoles

   Srijita Naskar,‡ Supriyo Halder,‡ Sampad Malik, Kausikisankar Pramanik*

   (*Manuscript under revision*)

Other publications

5. An insight into the coordination specificity of polyaromatic hydrocarbons (PAHs) grafted hydrazones towards rhodium(III)

   Soumitra Dinda, **Srijita Naskar**, Subhadip Roy, Kausikisankar Pramanik,* Sanjib Ganguly*, *Polyhedron*, **2021**, *205*, 115318.

6. Coordinatively fluxional diazo-based organo-electrocatalyst for conversion of CO_2 to C_2 and C_3 products

   Nidhi Kumari,‡ Supriyo Halder,‡ **Srijita Naskar**, Sanjib Ganguly,* Kausikisankar Pramanik,* Farzaneh Yari, Adrian Dorniak, Wolfgang Schöfberger,* Soumyajit Roy,* *Materials Today Catalysis*, **2024**, *5*, 100049.

7. Ruthenium complexes of redox non-innocent aryl-azo-oximes for catalytic α-alkylation of ketones and synthesis of 2-substituted quinolines

   Supriyo Halder,‡ **Srijita Naskar**,‡ Debashis Jana, Gopal Kanrar, Kausikisankar Pramanik,* Sanjib Ganguly,* *New J. Chem.*, **2024**, *48*, 8181–8194.

8. Dehydrogenative Coupling for Synthesis of Quinazolin-4(3H)-ones *via* Tandem Reaction using Ruthenium(II)-Phenyl-Azo-Naphthaldoxime: An Experimental and Theoretical Investigation

   Supriyo Halder,‡ **Srijita Naskar**, ‡ Debashis Jana, Gopal Kanrar, Shyama Charan Mandal, Subhadip Roy, Nishchal Bharadwaj, Kausikisankar Pramanik,* Sanjib Ganguly,* *Chem Asian J.*, **2025**, *20*, e202401278.

9. Synthesis of N-Alkylated Amines *via* Alcohol Dehydrogenation Catalyzed by a Bis-Azo-Diamido Coordinated Ruthenium(III) Complex

   Supriyo Halder,‡ **Srijita Naskar**,‡ Sampad Malik, Dipika Roy, Kausikisankar Pramanik*, *Dalton Trans.*, **2025**, Accepted Manuscript, https://doi.org/10.1039/D5DT01716E.

10. N–N hydrazonyl bond cleavage in benzothiazolyl-hydrazino-phenathrenequinone mediated by ruthenium(II) *via* an anion radical intermediate

Gopal Kanrar, Supriyo Halder, **Srijita Naskar**, Debashis Jana, Arup Sarkar, Bikash Kumar Panda, Soumitra Dinda, Kausikisankar Pramanik,* Sanjib Ganguly,* *Journal of Molecular Structure*, **2024**, *1314*, 138720.

11. Potent pincer-zinc catalyzed homogeneous α-alkylation and Friedländer quinoline synthesis reaction of secondary alcohols/ketones with primary alcohols

Debashis Jana, Sima Roy, **Srijita Naskar**, Supriyo Halder, Gopal Kanrar, Kausikisankar Pramanik,* *Org. Biomol. Chem.*, **2024**, *22*, 6393–6408.

12. One-Pot Cascade [3+2+1] Annulation: Synthesis and Mechanistic Insight of *s*-Triazines and Pyrimidines Using Azo-Supported Metalloradical Nickel Catalyst

Debashis Jana, Sampad Malik, Gopal Kanrar, Supriyo Halder, **Srijita Naskar**, Kausikisankar Pramanik,* *ChemCatChem*, **2025**, *17*, e202401851.

Polyhedron 235 (2023) 116342

Contents lists available at ScienceDirect

Polyhedron

journal homepage: www.elsevier.com/locate/poly

Role of ligand disposition and oxime…oximato hydrogen bonding upon redox non-innocent character of rhodium(III) phenylazooximates

Srijita Naskar [a], Supriyo Halder [a], Gopal Kanrar [b], Debashis Jana [a], Soumitra Dinda [b], Kausikisankar Pramanik [a,*], Sanjib Ganguly [b,*]

[a] Department of Chemistry, Jadavpur University, Kolkata 700032, India
[b] Department of Chemistry, St. Xavier's College (Autonomous), Kolkata 700016, India

A B S T R A C T

The diaryl-azo-oxime ligands HL, **1** undergoes oxidative coordination reaction with Wilkinson's catalyst to form two isomeric complexes of type *cis*-[$Rh^{III}L_2Cl(PPh_3)$], **2a** (Cl and PPh_3 are *cis*) and *trans*-[$Rh^{III}L_2Cl(PPh_3)$], **2b** where they are *trans* with respect to each other. Unlike the case of **2a**, the complex **2b** upon treatment with sodium borohydride, can be transformed to *trans*-[$Rh^{III}(HL^{\bullet})(L^{-})Cl(PPh_3)$], **3** and the reaction appears to progress *via* PCET. The disposition of ligand frameworks as well as the formation of oxime…oximato hydrogen bond appears to have a significant function for phenylazooxime to exhibit redox non-innocent behaviour in presence of rhodium(III). The compounds were characterized by electrochemical analysis, different spectral methods, single crystal XRD and optoelectronic properties, particularly the nature of transitions in the chelates were scrutinized by TD-DFT.

1. Introduction:

Redox non-innocent ligands are interesting owing to their inherent capacity to exhibit various ligand redox levels upon coordination [1–23] and such systems have the aptitude to embrace and reject electron(s) during the course of catalytic processes [24–30], in chemical and biochemical reactions [31–33]. Coordinated azo-aromatic systems have been found to act as apposite precursors for stabilizing ligand centered anion radical complexes since they possess low-lying azo-π* orbital [34–47]. It has been well understood that structure of the ligand skeleton and redox character of the metal centre has a significant role for controlling the stabilisation of these type of complexes and ligand–metal π-interaction can further adjust the electronic structural features for maximum stabilization [48–50]. Moreover, ligand environment around the metal centre may also influence the aptitude of these chelated azo-ligands in conjunction with other moieties to receive or donate odd electron(s) and this may be attributed to electronic or steric factors. The impact of electronic environment of auxiliary ligands in supporting extra electron(s) within π* LUMO of these ligands have been much less reported [48,51]. As a continuation of our study on stabilization of odd electron in coordinated azooximes [51–53], we have tried to investigate the competence of these ligand to retain an unpaired electron over azo-oxime framework in presence of rhodium(III) and to stabilize the corresponding open shell complexes. In this regard, we have started with the diaryl-azo-oxime HL, **1** which possesses low lying π* LUMO, thereby having the aptitude to perform as an electron-sink upon ligation, and have successfully isolated two isomeric complexes of type *cis*-[$Rh^{III}L_2Cl(PPh_3)$] (**2a**), where Cl and PPh_3 are in *cis* positions and *trans*-[$Rh^{III}L_2Cl(PPh_3)$] (**2b**), where they are *trans* with respect to each other. The complex **2b** can be reduced to the azo-oxime radical anion complex of type *trans*-[$Rh^{III}(HL^{\bullet})(L^{-})Cl(PPh_3)$] (**3**) and the reaction appears to progress *via* PCET but the corresponding anion radical analog of the *cis* isomer could not be isolated. Thus, the *trans* isomer behaves as a superior electron carrier and this has been attributed to stereochemical control around the rhodium centre. In fact, in the *trans* isomer **2b**, there is scope for unpaired electron to be delocalized on both the ligands much more efficiently since they are practically coplanar. Furthermore, the stabilization of **3** may also be attributed to formation of oxime…oximato intramolecular hydrogen bonding during the course of electron acceptance in presence of protons and this is also consistent with theoretical scrutiny. (see Scheme 1.)

2. Experimental details

2.1. General information

Drying and purification of solvents were performed using literature procedure and distilled out before using as required. The required chemicals were purchased from following sources: Phenyl hydrazine and Benzaldehyde from TCI Chemical (India) Pvt. ltd. Wilkinson's

* Corresponding authors.
E-mail address: icsg@sxccal.edu (S. Ganguly).

https://doi.org/10.1016/j.poly.2023.116342
Received 21 December 2022; Accepted 14 February 2023
Available online 19 February 2023

Chemistry & Biodiversity

WILEY-VCH

CHEMISTRY & BIODIVERSITY

RESEARCH ARTICLE

Designed Synthesis of Amino-Azo-Quinoline and Their Nickel(II) Complexes: Molecular Structure, Electrochemistry and an Insight Into Their In Vitro Anti-Cancer Activities

Srijita Naskar[1] | Koushik Sarkar[2] | Supriyo Halder[1] | Bidisha Chatterjee[3] | Debjeet Chakraborty[3] | Arka Laha[3] | Rahul Sharma[2] | Arup Kumar Mitra[3] | Kausikisankar Pramanik[1] | Sanjib Ganguly[2]

[1]Department of Chemistry, Jadavpur University, Kolkata, India | [2]Department of Chemistry, St. Xavier's College (Autonomous), Kolkata, India | [3]Department of Microbiology, St. Xavier's College (Autonomous), Kolkata, India

Correspondence: Kausikisankar Pramanik (kpramanik@hotmail.com) | Sanjib Ganguly (icsgxav@gmail.com; icsg@sxccal.edu)

Received: 26 September 2024 | **Revised:** 20 January 2025 | **Accepted:** 21 January 2025

Funding: We would like to express our sincere gratitude to the CAS-II and RUSA 2.0 programs available in the Department of Chemistry, at Jadavpur University. Sanjib Ganguly is grateful to the Intramural Grant (Sanction No. IMSXC2022-23/001) and Koushik Sarkar for Intramural Grant (Sanction No. IMSXC2022-23/011) from St. Xavier's College (Autonomous), Kolkata. Srijita Naskar and Supriyo Halder thank SVMCM, Department of Higher Education, Govt. of West Bengal, and UGC (ref. No. 210/CSIR-UGC NET DEC.2017) New Delhi India, respectively, for the research fellowship. Arup Kumar Mitra is thankful to DBT, New Delhi, for the Grant (Sanction No. BT/INF/22/SP41296/2020, Dated: March 25, 2021).

Keywords: anti-cancer activity | coordination chemistry | DFT study | Molecular Docking study | X-ray crystallography

ABSTRACT

Amino-quinolines are potential candidates that may provide some insight into the current chemotherapeutic research due to their demonstrated anti-cancer activity. This led us to synthesize and explore a new amino-azo-quinoline ligand H_2L **1** and its square planar nickel(II) complexes [Ni(HL) (OAc)], **2** and [Ni(HL)Cl], **3** and the structures were determined by Single Crystal X-Ray Diffraction. Theoretical investigation of redox orbitals of the complexes discloses that the reduction process is due to ligand reduction whereas both metal and ligand are contributing towards oxidation. The anti-cancer properties of the ligand and one of the nickel(II) complexes have been assessed by 3-[4,5-dimethylthiazol-2-yl]-2,5-diphenyltetrazolium bromide assay, cell migration along with the generation of reactive oxygen species using human epithelial cancer cell line cells. The ligand **1** and complex **3** have been found to show effective anti-cancer activity and for the latter, it is more promising. This may be ascribed to the rigid and robust nature of square planar complex **3**, which supports stronger binding with DNA than that of free ligands, possibly due to the flexible nature of the latter. This result has also been validated by molecular docking using nine conformers of the ligand and complex **3** via interaction with B-DNA (PDB ID: 1BNA) where the binding affinity with the complex has been found to be stronger.

1 | Introduction

The fabrication of *cis*-platin as a chemotherapeutic for a wide range of cancer treatments including solid cancers such as bladder, cervical, head and neck, lung cancer, testicular, ovarian, gastric cancer etc. [1–4], has triggered the research on the anti-blastoma activity of several other platinum complexes [5, 6]. Over the years, combination chemotherapy with *cis*-DDP has

Srijita Naskar and Koushik Sarkar contributed equally to this study.

ACES Asian Chemical Editorial Society

doi.org/10.1002/ajoc.202500330

ASIAN JOURNAL OF ORGANIC CHEMISTRY
Research Article

www.asianjoc.org

Alcohol Dehydrogenation Catalyzed by Azo-Oxime Coordinated Ruthenium(II): A Strategic and Sustainable Route towards Site-Selective C(sp^3)–H Functionalization of 9H-Fluorene

Srijita Naskar,[a] Supriyo Halder,[a] Aritra Das,[b] Sampad Malik,[a] Gopal Kanrar,[b] Debashis Jana,[a] Bikash Kumar Panda,[c] Kausikisankar Pramanik,*[a] and Sanjib Ganguly*[b]

The bidentate redox non-innocent azo-oxime ligand *p*-chloro-aryl-azo-oxime (*p*-Cl-aaOH) has been used to synthesize a robust as well as air- and moisture-stable complex *trans*-[Ru(*p*-Cl-aaO)Cl(CO)(PPh_3)$_2$]. It has been thoroughly characterized by various analytical, spectroscopic and Single-Crystal X-Ray Diffraction (SCXRD) analysis. Its electrochemical property has also been investigated and supported by theoretical studies. The complex has functioned as an effective ligand-based catalyst for dehydrogenation of diverse aromatic and aliphatic primary alcohols followed by selective C(sp^3)–H activation of 9H-Fluorene under aerobic conditions through a tandem process. A probable catalytic cycle has been projected from relevant experiments, where the azo group of coordinated ligand plays a key role in both dehydrogenation and borrowing hydrogenation processes, while the ruthenium(II) centre behaves as a passive spectator throughout the reaction. The main advantages of this ruthenium catalyst include its simple synthetic methodology, low catalyst loading, wide substrate scope, shorter reaction times, and the ability to perform catalytic transformations at relatively lower temperatures.

1. Introduction

Fluorene and its derivatives are important group of compounds having a biphenyl skeleton along with a rigid plane, thereby facilitating π-cloud delocalization.[1] These remarkable structural features accounts for their varied properties and they can be further modulated via introducing suitable functional groups into the fluorene ring.[2] The sustainable synthetic strategies of fluorene derivatives is gaining importance in current research owing to their potential applications in electronic and photochromic materials, particularly OLED [3] and solar cells.[4] This is majorly attributed to the rich photophysical and photoelectric properties of fluorene.[5] These features have also been smartly exploited over the years to formulate and synthesize a wide range of polymers[6] and dyes.[7] This polyaromatic hydrocarbon (PAH) framework has been found to exhibit anticancer and antimicrobial properties.[8] It also finds utility for exploration of two-photon fluorescence bioimaging[9] (Scheme 1). As a crucial component of coal tar, this PAH framework enables the C—H functionalization of fluorene derivatives at the 9-position, offering a transformative strategy for advancing environmental sustainability and converting coal tar into valuable, high impact products.

Conventional approaches for 9-alkylation of fluorene involve condensation of aldehydes with fluorene, followed by hydrogenation or an S_N2 reaction of fluorenes with excess alkylating agents like haloalkanes in presence of strong and highly reactive bases, *for example* KOH or t-BuLi. The earliest report published in 1955 by Becker and co-workers defined the base-promoted alkylation of fluorene using several aliphatic alcohols conducted under rigorous conditions that involved the use of excess base and elevated temperatures ranging from 210 to 220 °C. In 1965, Atkin's group at Union Carbide Corporation revealed a method for base-catalysed alkylation of fluorene and indene with aliphatic alcohols.[10] The process, however, demanded excessive amount of base and harsh reaction conditions such as high temperature (250 °C) and pressure (500 psi). The major shortcoming of these strategies is formation of certain undesirable byproducts and poly-alkylated compounds.[11] These methods lack sufficient control, often leading to a higher degree of dialkylation rather than selective monoalkylation. A greener and more selective approach for synthesis is the dehydrogenation of alcohols using appropriate transition metal complexes as catalyst via dehydrogenation and borrowing hydrogenation (BH) or hydrogen auto transfer (HAT).[12] Owing to its operational

[a] S. Naskar, S. Halder, S. Malik, D. Jana, K. Pramanik
Department of Chemistry, Jadavpur University, Kolkata 700032, India
E-mail: kpramanik@hotmail.com
kausikis.pramanik@jadavpuruniversity.in

[b] A. Das, G. Kanrar, S. Ganguly
Department of Chemistry, St. Xavier's College (Autonomous), Kolkata 700016, India
E-mail: icsg@sxccal.edu

[c] B. K. Panda
Department of Chemistry, Jangipur College, Jangipur, Murshidabad, West Bengal 742213, India

Srijita Naskar and Supriyo Halder contributed equally to this work

Supporting information for this article is available on the WWW under https://doi.org/10.1002/ajoc.202500330

Polyhedron 205 (2021) 115318

Contents lists available at ScienceDirect

Polyhedron

journal homepage: www.elsevier.com/locate/poly

An insight into the coordination specificity of polyaromatic hydrocarbons (PAHs) grafted hydrazones towards rhodium(III)

Soumitra Dinda [a], Srijita Naskar [b], Subhadip Roy [c], Kausikisankar Pramanik [b,*], Sanjib Ganguly [a,*]

[a] Department of Chemistry, St. Xavier's College (Autonomous), Kolkata 700016, India
[b] Department of Chemistry, Jadavpur University, Kolkata 700032, India
[c] Department of Chemistry, The ICFAI University Tripura, Kamalghat, Mohanpur, Agartala Pin 799210, Tripura, India

ARTICLE INFO

Keywords:
Hydrazone
Polyaromatic hydrocarbon
Intra-molecular π-π stacking interaction
Flexidentate behaviour
Electrochemistry

ABSTRACT

Upon treatment of the polyaromatic hydrocarbon (PAH) grafted hydrazones HL (**1**) with $[RhCl(PPh_3)_3]$, complexes of type $[Rh(L)Cl_2(PPh_3)_2]$ (**2**) have been isolated. The X-ray diffraction technique has been used to elucidate the structures of three complexes. The rich spectral features of the complexes in the UV–vis region have been explained by TD-DFT and their redox active nature has been validated from the well-defined responses at mild potentials as well as from a theoretical investigation of the redox orbitals. Intra-molecular π–π stacking interactions coupled with the electron withdrawing ability of the pendant PAH moiety within the ligand framework play a significant role in altering the mode of coordination (flexidentate behaviour of HL) as well as the metal–ligand bond parameters.

1. Introduction

Hydrazones are triatomic linkage (>C═N–N<) that have frequently enraptured chemists owing to the flexibility in their mode of coordination during the course of chelation. This is attributed to the diversity of the donor atoms, *viz.* nucleophilic imine (>C═*N*–) and amine (═N–*N*HAr) nitrogen atoms. Additionally, the >C═N– moiety has the ability to exhibit configurational isomerism and the presence of an acidic amine N—*H* proton is also instrumental for their aptitude to display a variety of metal-hydrazone bonding interactions [1,2]. The coordination diversity of hydrazones have been extensively explored and further deliberations are still in progress [3–6]. Current reports reveal that hydrazones, upon coordination to rhodium, have the propensity to exhibit promising biological activities [7–10] and they can also behave as a robust directing group (DG) to bring about C—H bond activation as well as functionalization [11–20]. Consequently, appropriate insight into the molecular and electronic structures of novel rhodium(III) hydrazones is imperative for the proper apprehension of electron transfer and optoelectronic properties within the metal–organic composites, especially for metal centers with a diamagnetic closed shell d^6 configuration.

In continuation of our pursuit in the exploration of pertinent hydrazone complexes of rhodium [20–22], we report the synthesis of three rhodium(III) complexes of the type $[Rh(L)Cl_2(PPh_3)_2]$ (**2**) with polyaromatic hydrocarbons (PAHs) grafted hydrazones of the type HL (**1**), (Scheme 1). The single crystal X-ray diffraction study of **2** reveals the formation of a five-membered metallacycle with the rhodium(III) ion, unlike the case of the ruthenium(II) analogues where four-membered rings are formed [23], signifying the flexidentate behavior of the hydrazones, **1** (Scheme 2). The electrochemical behavior of these compounds in solution discloses the feasibility of electron transfer processes within the rhodium(III)-hydrazone composites. Notably, the redox-active nature of the PAH-derivatized hydrazone backbone in **2** has been validated from the well-defined responses at mild-to-moderate potentials and the origin of these responses has been analyzed by theoretical analysis. The complexes exhibit rich spectral features in the UV–vis region, which have been scrutinized theoretically by TD-DFT. Furthermore, and most significantly, it has been found that the pendant polyaromatic hydrocarbons in the complexes, along with their associated intra-molecular π–π stacking interactions, play a decisive role in altering the coordination mode as well as the metal–ligand bond parameters.

* Corresponding authors.
E-mail addresses: kpramanik@hotmail.com (K. Pramanik), icsgxav@gmail.com (S. Ganguly).

https://doi.org/10.1016/j.poly.2021.115318
Received 18 March 2021; Accepted 24 May 2021
Available online 9 June 2021

Materials Today Catalysis 5 (2024) 100049

Contents lists available at ScienceDirect

Materials Today Catalysis

journal homepage: www.journals.elsevier.com/materials-today-catalysis

Coordinatively fluxional diazo-based organo-electrocatalyst for conversion of CO_2 to C_2 and C_3 products

Nidhi Kumari [a,1], Supriyo Halder [b,1], Srijita Naskar [b], Sanjib Ganguly [c,*], Kausikisankar Pramanik [b,*], Farzaneh Yari [d], Adrian Dorniak [d], Wolfgang Schöfberger [d,*], Soumyajit Roy [a,*]

[a] Eco-Friendly Applied Materials Laboratory, Department of Chemical Sciences, Materials Science Centre, Indian Institute of Science Education and Research, Kolkata, West Bengal 741246, India
[b] Department of Chemistry, Jadavpur University, Kolkata, West Bengal 700032, India
[c] Department of Chemistry, St. Xavier's College, Kolkata, West Bengal 700016, India
[d] Institute of Organic Chemistry, Laboratory for Sustainable Chemistry and Catalysis (LSusCat), Johannes Kepler University Linz, Altenberger Straße 69, Linz 4040, Austria

ARTICLE INFO

Keywords:
Metal free
Diazo-based ligand
Catalyst
CO_2 electroreduction
C_2 and C_3 products

ABSTRACT

The conversion of carbon dioxide (CO_2) into valuable chemicals, specifically C_2 and C_3, through metal-free electrocatalysis remains a formidable challenge. Breaking away from traditional transition metal complexes, the focus is on designing and selecting efficient organic catalysts. In this pursuit, a diazo-based organic bulky ligand emerges as a promising candidate, offering a solution that is both sustainable and renewable. The key feature of this ligand is its low-lying π* (LUMO), enabling it to readily accept an electron in an electrochemical environment when a potential is applied. The synthesized Diazo-based ligands have been meticulously characterized using various techniques, including ^{1}H NMR, ^{13}C NMR, UV-Vis, and IR spectroscopy. This diazo-based ligand serves as an electrocatalyst, undergoing reduction to a triplet diradical that acts as a nucleophile. In an aqueous medium, it forms an adduct with CO_2, leading to the generation of a formyl radical. This radical further couples to produce acetic acid and acetone with efficiencies of 19.6% and 24.2%, respectively, at pH 5.5. To provide a deeper understanding, we present a proposed mechanism pathway supported by *in-situ* UV-Vis spectroscopy and a comprehensive Density Functional Theory (DFT) study. These findings mark a significant step forward in the field of metal-free electrocatalysis, offering a sustainable approach to the conversion of CO_2 into valuable chemicals, contributing to the development of renewable and environmentally friendly systems.

1. Introduction

Today's climate change demands the immediate implementation of innovative sustainable technologies [1]. Among these technologies, the electrocatalytic conversion of carbon dioxide (CO_2) into valuable products is of utmost importance due to its dual potential for atmospheric CO_2 reduction and generation of renewable energy. Despite notable progress in this area, the synthesis of three-carbon (C_3) [2] products from CO_2 electro-reduction remains a less explored yet promising frontier [3]. In this article, we address this issue. The present published research paradigm predominantly focuses on the generation of one-carbon (C_1) products such as formaldehyde or formate [4] or two-carbon (C_2) products like ethanol [5] and ethanoic acid [6]. These transformations, although valuable, are stepping stones specifically for higher-carbon products (C_3), that hold considerable potential in the realms of renewable fuels and chemicals [7]. Synthesizing C_3 products from CO_2 electro-reduction represents an essential step towards the direct utilization of CO_2 in chemical synthesis, a goal of paramount practical importance in the context of a circular carbon economy. However, the intricate interplay of mechanistic, thermodynamic, and kinetic factors [8] in the C_3 production pathway present a complex landscape, posing unique challenges for such developments [9].

* Corresponding authors.
E-mail addresses: icsgxav@gmail.com (S. Ganguly), kpramanik@hotmail.com (K. Pramanik), wolfgang.schoefberger@jku.at (W. Schöfberger), s.roy@iiserkol.ac.in (S. Roy).
[1] These authors contributed equally.

https://doi.org/10.1016/j.mtcata.2024.100049
Received 6 February 2024; Received in revised form 5 March 2024; Accepted 8 March 2024
Available online 10 March 2024

NJC

ROYAL SOCIETY OF CHEMISTRY

PAPER

View Article Online
View Journal | View Issue

Cite this: *New J. Chem.*, 2024, **48**, 8181

Ruthenium complexes of redox non-innocent aryl-azo-oximes for catalytic α-alkylation of ketones and synthesis of 2-substituted quinolines†

Supriyo Halder,‡[a] Srijita Naskar,‡[a] Debashis Jana,[a] Gopal Kanrar,[b] Kausikisankar Pramanik *[a] and Sanjib Ganguly *[b]

Received 24th January 2024,
Accepted 3rd April 2024

DOI: 10.1039/d4nj00391h

rsc.li/njc

Ruthenium(II) complexes [RuL(CO)Cl(PPh$_3$)$_2$], **1a**–**4a**, have been synthesized using ligands PhN=NC(Ar)NOH, HL **1**–**4**, respectively, by varying the pendant aryl (Ar) groups. The single crystal X-ray diffraction studies of complexes reveal that there are certain changes in Ru–N$_{azo}$ and Ru–N$_{oxime}$ bond lengths that may be explained primarily on the basis of electronic effects of pendant aryl groups. In **4a**, all Ru–N bond lengths are longer and this is attributed to oximato–O···O (hydroxyphenyl) interactions. Furthermore, there are weak intramolecular F···π interactions in **3a**. The complexes display multiple reductive responses ascribable to electron acceptance within the azo-oxime framework of the coordinated ligand and the corresponding one-electron reduced metastable anion radical complexes of type [Ru(L$^{\bullet-}$)(CO)Cl(PPh$_3$)$_2$]$^-$ **[1]$^{\bullet-}$** have been generated. This property of the complexes has been exploited in electron transfer catalysis *via* trapping of electrons in the azo-oxime skeleton in two types of reactions: (1) α-alkylation of ketones with primary alcohols and (ii) synthesis of 2-substituted quinoline derivatives from 2-aminobenzyl alcohols and substituted acetophenones/alkyl methyl ketones. The scope of catalysis has been studied and the probable catalytic pathway has been established from experimental results. The catalytic pathway is ligand-centric and redox-driven for the dehydrogenation process and the initial step involves formation of a coordinated anion radical. This leads to conversion of the starting 1° alcohol to the corresponding carbonyl *via* the HAT pathway, with the ruthenium(II) centre practically behaving as a template and remaining redox inactive. The catalytic reactions have been proven to be affected by the nature of pendant aryl (Ar) groups within the coordinated ligand.

Introduction

The redox non-innocence[1] of coordinated ligands is gaining profound importance in the field of electron transfer catalysis since the metal center and the ligand skeleton have the ability to stimulate a process in a collaborative manner, with the catalyst switching from one spin isomeric state to another.[2–16] Such reactions may proceed *via* formation of a meta-stable ligand-centric coordinated radical and it is usually accompanied by proton coupled electron transfer (PCET)[17–22] or hydrogen atom transfer (HAT).[23–29] The chemistry of redox non-innocent ligands containing azo functions has developed over the past two and a half decades[30–43] and at present the catalytic role of their complexes is under intense investigation.[44–62] In the majority of the cases, ligands are of tridentate azo pincer type, where the ligated azo moieties have the ability to behave as electron pockets to store electron/s in the form of an azo anion-radical. In addition, the reserved electron/s may be transferred to suitable centres to bring about catalytic reduction and this concept has been widely employed to synthesize several value-added chemicals of pharmaceutical and industrial importance, in a cost effective and atom efficient manner.

We have been striving to explore and figure out the electron extracting ability of coordinated diaryl-azo-oximes in order to effectuate certain unusual redox transformations.[63–67] We are further motivated to synthesize suitable complexes of azo-oximes where the ligand skeleton may become redox active in the presence of ruthenium(II) and they may be skillfully employed to bring about electron-transfer catalysis for synthesis of useful organic compounds in an atom efficient manner. It is worth mentioning that there has been no report on

[a] *Department of Chemistry, Jadavpur University, Kolkata–700032, India. E-mail: kpramanik@hotmail.com; Tel: +91 33 2457 2781*
[b] *Department of Chemistry, St. Xavier's College (Autonomous), Kolkata–700016, India. E-mail: icsgxav@gmail.com, icsg@sxccal.edu; Tel: +91 33 2255 1266*

† Electronic supplementary information (ESI) available. CCDC 2303589, 2303590, 2303602, 2303603, 2303607 and 2303608. For ESI and crystallographic data in CIF or other electronic format see DOI: https://doi.org/10.1039/d4nj00391h

‡ Authors contributed equally to this work.

ACES Asian Chemical Editorial Society

doi.org/10.1002/asia.202401278

CHEMISTRY
AN ASIAN JOURNAL
Research Article

www.chemasianj.org

Dehydrogenative Coupling for Synthesis of Quinazolin-4(3H)-ones *via* Tandem Reaction using Ruthenium(II)-Phenyl-Azo-Naphthaldoxime: An Experimental and Theoretical Investigation

Supriyo Halder[+],[a] Srijita Naskar[+],[a] Debashis Jana,[a] Gopal Kanrar,[b] Shyama Charan Mandal,[c] Subhadip Roy,[d] Nishchal Bharadwaj,[e] Kausikisankar Pramanik,*[a] and Sanjib Ganguly*[b]

The bidentate N, N, donor phenyl-azo-naphthaldoxime NpLH, **1** was used to synthesize the ruthenium(II) complex trans-[Ru(NpL)(CO)Cl(PPh$_3$)$_2$], **2**. It has been characterized by SCXRD, electrochemical and spectral studies. Computational analysis indicates that the low-lying π*-LUMO of the complex has substantial azo-character of coordinated ligand. This property has been exploited to form an efficient electron transfer pre-catalyst to effectuate dehydrogenative functionalization of a large number of benzyl alcohols to quinazolin-4(3H)-ones via condensation with diverse o-amino benzamides as well as N-substituted benzamides under aerobic conditions (57 entries). A reaction mechanism has been projected via isolation of intermediates and certain control experiments. Furthermore, it has been substantiated by theoretical scrutiny using density functional theory (DFT) calculation. The catalytic cycle involves stepwise hydrogen atom transfer (HAT) from benzyl alcohols to the N_{azo} atoms of the coordinated ligand with subsequent removal of the H-atoms from the N_{azo} atoms to regenerate the active catalyst.

Introduction

N-heterocycles have been found to be in plenitude in natural products due to their intimate biological relevance. This leads to extensive research towards the development of innovative, sustainable and greener methods for synthesis of aza-heterocycles.[1] The quinazolinone moiety is present as a building block in a wide range of naturally occurring alkaloids that have been sequestered from natural resources like micro-organisms, plants, and animals.[2,3] Quinazolin-4(3H)-ones and their substituted analogues have gained significant attention owing to various pharmacological activities, such as anti-inflammatory,[4] antimicrobial,[5] anticancer,[6,7] antihypertensive,[8] dihydrofolate reductase inhibition,[9] and Tyrosine Kinase inhibition.[10] Despite significant progress in this area, it has been found that in most cases multi-step synthesis is required. This creates unwanted byproducts and often needed hazardous chemicals for catalytic transformation. Furthermore, the precursor molecules are often expensive and less available.[11,12] Accordingly, it is always challenging to develop cost-effective and atom efficient production of substituted quinazolin-4(3H)-ones. There have been some reports of transition metal catalysed synthesis of substituted quinazolin-4(3H)-ones via dehydrogenative functionalization of aliphatic and aromatic alcohols and this strategy is quite promising since it is a single-step, economical, environment friendly synthesis starting from readily available precursors and generates hydrogen or water as the only byproducts (Scheme 1).[13–15]

We were inquisitive regarding the electron trapping aptitude of coordinated azooximes[16] for the past few years and this led us to explore their ability to bring about dehydrogenative functionalization of aliphatic and aromatic alcohols to form value added products.[17–19] As a continuation of our previous work, in this paper we have utilized phenyl-azo-naphthaldoxime NpLH, **1** to synthesize a ruthenium(II) complex trans-[Ru(NpL)(CO)Cl(PPh$_3$)$_2$], **2** (Scheme 2). The structural, electrochemical, and theoretical studies of **2** have been performed in order to have a comprehension of their competence to bring about electron transfer catalysis. The ruthenium(II) complex

[a] S. Halder,[+] S. Naskar,[+] D. Jana, K. Pramanik
Department of Chemistry, Jadavpur University, Kolkata 700032, India
Tel: +91 33 2457 2781
E-mail: kpramanik@hotmail.com

[b] G. Kanrar, S. Ganguly
Department of Chemistry, St. Xavier's College (Autonomous), Kolkata – 700016, India
Tel: +91 33 2255 1266
E-mail: icsgxav@gmail.com
icsg@sxccal.edu

[c] S. C. Mandal
SUNCAT Center for Interface Science and Catalysis, SLAC National Accelerator Laboratory
2575 Sand Hill Road, Menlo Park, CA 94025 (USA)

[d] S. Roy
Department of Chemistry, The ICFAI University Tripura, Agartala, Tripura 799210, India

[e] N. Bharadwaj
Department of Chemistry, Indian Institute of Technology (IIT) Indore, Indore, Madhya Pradesh 453552

[+] Authors contributed equally to this work

Supporting information for this article is available on the WWW under https://doi.org/10.1002/asia.202401278

Journal of Molecular Structure 1314 (2024) 138720

Contents lists available at ScienceDirect

Journal of Molecular Structure

journal homepage: www.elsevier.com/locate/molstr

N–N hydrazonyl bond cleavage in benzothiazolyl-hydrazino-phenathrenequinone mediated by ruthenium(II) via an anion radical intermediate

Gopal Kanrar [a], Supriyo Halder [b], Srijita Naskar [b], Debashis Jana [b], Arup Sarkar [a], Bikash Kumar Panda [c], Soumitra Dinda [a], Kausikisankar Pramanik [b,*], Sanjib Ganguly [a,*]

[a] Department of Chemistry, St. Xavier's College (Autonomous), Kolkata 700016, India
[b] Department of Chemistry, Jadavpur University, Kolkata 700032, India
[c] Department of Chemistry, Jangipur College, Jangipur, Murshidabad, West Bengal 742213, India

ARTICLE INFO

Keywords:
Redox non-innocent ligand
Crystallography
DFT
NMR
Cyclic voltammetry

ABSTRACT

The complexes [Ru(L^{Benz})H(CO)(PPh_3)$_2$] **2**, [Ru(L^{Benz})Cl(CO)(PPh_3)$_2$] **3**, (ligand behaving as bidentate monoanionic) and [Ru(L^{Benz})Cl(CO)(PPh_3)] **4**, (ligand is tridentate monoanionic) have been synthesized starting from benzothiazolyl-hydrazino-phenathrenequinone (HL) **1** and [RuH(CO)Cl(PPh_3)$_3$]. These are characterized by electrochemical and spectral methods as well as single crystal X-ray diffractometry (SCXRD). Upon treating with $NaBH_4$, **3** accepts an electron within the coordinated ligand framework and the anionic hydrazonyl-*N* takes up a proton to be transformed to meta-stable hydrazinoquinone anion radical complex of ruthenium(II) [Ru($HL^{Benz\bullet-}$)Cl(CO)(PPh_3)$_2$] **5**, possibly *via* concerted proton electron transfer process (CPET). Thus, the redox non-innocent character of the ligand upon complexation with ruthenium(II), has been disclosed and it is attributed to presence of low lying π* orbitals of almost entirely of phenanthraquinone and hydrazone character. In **5**, the π–acceptor ability of the ligand donor centres are reduced due to the existence of an odd electron in SOMO and hence the M-L distances around the coordination sphere are altered. The N–N (hydrazonyl bond length increases from 1.296 (6) Å in **3** to 1.429 Å in **5**, leading to lesser thermodynamic stability of the latter and upon standing, the N–N bond is cleaved to be transformed to $\mathbf{6}^+$, possibly *via* the formation of iminoquinone anion radical complex, [6] (reported elsewhere). Also, it is *via* the dissociation of N–N (hydrazonyl) bond, the biologically important molecule 2-aminobenzothiazole is formed along with $\mathbf{6}^+$, so as to provide a novel route for its synthesis.

1. Introduction

It has been well understood that concerted proton-electron transfer (CPET) has consequential roles in a diverse field of biological processes as well as in efficient energy conversions. [1–7] The most demanding and challenging illustration is the biological nitrogen fixation, which comprises of successive transfer and swapping of protons as well as electrons to coordinated nitrogen, [8–12] although the exact reaction pathway is still a matter of conjecture. In this regard, well-defined complexes having N–N bonds are good candidates to provide some illustrative clarification with respect to reduction sequences since they may be suitably engineered to comprehend the redox transformations accompanying the cleavage of N–N bonds. [13–24] Moreover, it has also been reported that metal–ligand synergy [25–27] is one of the significant aspects that regulate the activity of several redox metalloenzymes like cytochrome P450, galactose oxidase and hydrogenases etc. [28–30] In these cases, both ligands (of the prosthetic group) and metal centres contribute to the redox events as well as in bond cleavage or activation. In fact, these types of ligands are often referred to as redox non-innocent [31–44] and they have the distinctive aptitude to confer unprecedented reactivity to the metal complexes by regulating loss or gain of electrons and protons.

We have been working with redox non-innocent ligands [45–56] and their roles in metal mediated redox transformations for a considerable period of time [57–61] and as an extension of our work in this field, we were motivated towards exploration of cooperative effect of metal along with redox active ligand comprising of hydrazone and iminoquinone moieties, to foster the cleavage of N–N bonds. [62–64] In the present

* Corresponding authors.
E-mail addresses: icsgxav@gmail.com, icsg@sxccal.edu (S. Ganguly).

https://doi.org/10.1016/j.molstruc.2024.138720
Received 19 March 2024; Received in revised form 17 May 2024; Accepted 21 May 2024
Available online 22 May 2024

Organic & Biomolecular Chemistry

ROYAL SOCIETY OF CHEMISTRY

PAPER

View Article Online
View Journal | View Issue

Cite this: *Org. Biomol. Chem.*, 2024, **22**, 6393

Potent pincer-zinc catalyzed homogeneous α-alkylation and Friedländer quinoline synthesis reaction of secondary alcohols/ketones with primary alcohols†

Debashis Jana, [a] Sima Roy, [a] Srijita Naskar,[a] Supriyo Halder,[a] Gopal Kanrar[b] and Kausikisankar Pramanik *[a]

Received 12th June 2024,
Accepted 10th July 2024

DOI: 10.1039/d4ob00988f

rsc.li/obc

Herein, we describe an air- and moisture-stable, homogeneous zinc catalyst stabilised using an electron deficient N^N^N pincer-type ligand. This ternary, penta-coordinated neutral molecular catalyst [Zn(N^N^N)Cl_2] selectively produces α-alkylated ketone derivatives (14 examples) through a one-pot acceptorless dehydrogenative coupling (ADC) reaction between secondary and primary alcohols using the borrowing hydrogen (BH) approach in good to excellent isolated yields (up to 93%). It is worth noting that this catalyst also provides an eco-friendly route for the synthesis of quinoline derivatives (30 examples) using 2-aminobenzyl alcohols as alkylating agents *via* successive dehydrogenative coupling and N-annulation reactions. This cost effective, easy to synthesize and environmentally benign catalyst shows excellent stability in catalytic cycles under open-air conditions, as evident from its high turnover number (~10^4), and is activated by using a catalytic amount of base under milder conditions.

Introduction

The construction of molecules with diverse functional groups from commonly available small molecules/building blocks by C–C and C–heteroatom bond activation is one of the fundamental aspects of chemical and biochemical syntheses.[1] In reality, the majority of classical methods require expensive and environmentally toxic reagents and discharge hazardous waste even in (over)stoichiometric amounts.[2] Thus, the development of an efficient approach is desirable for selective C–C and C–heteroatom formation reactions. Accordingly, beneficial organic compounds with potential applications in the medical, agrochemical and pharmaceutical industries may be synthesized.[3] In this context, conversion of alcohols to C-alkylated derivatives and N-heterocycles *via* acceptorless dehydrogenation coupling (ADC) and borrowed hydrogen (BH)/N-annulation methodologies using homogeneous catalysts has received considerable attention in recent years.[4] Although such transformation reactions can be accomplished with 0.5–5 mol% platinum-group-metal catalysts (*e.g.*, Ru, Rh, Ir, Pd and Pt) in satisfactory yields.[5–9] In general, catalysis using non-precious first-row transition metals with good turnover numbers (TONs) under open-air conditions for α-alkylation and Friedländer annulation reactions remains challenging for gram-scale production of high-value bio-active molecules.[10] Nonetheless, continuous effort has been made with 3d metal catalysts (Mn, Fe, Co, Ni and Cu) with comparable catalyst loading (0.5–5 mol%), since they provide a more economically viable solution (Schemes 1 and 2).[11–15] A few examples have recently been reported where analogous reactions can be accomplished with 0.05% or less catalyst loading with Ni(II) and Mn(I), respectively.[16]

It is worth noting that the use of zinc(II) is less cited for homogeneous catalysis than other 3d metals plausibly due to its closed-shell, electron-rich, redox innocent nature. Only very recently molecular zinc-catalyzed dehydrogenation reactions of secondary alcohols have been documented.[17] Here, dehydrogenation of an alcohol occurs first to produce an aldehyde or ketone that undergoes an *in situ* condensation reaction with an enolate or amine to form an α,β-unsaturated ketone or imine, where the former is finally reduced to form a new C–C bond (Scheme 3) or the subsequent cyclization of aniline derivatives leads to quinolines because of the aromatization in the case of the C–N annulation reaction (Scheme 4).

In general, the catalytic performance of homogeneous catalysts is superior to that of heterogeneous catalysts.[18] Nonetheless, the disadvantage in the use of homogeneous cat-

[a]*Department of Chemistry, Jadavpur University, Kolkata 700032, India. E-mail: kpramanik@hotmail.com; Tel: +91 94333 66013*

[b]*Department of Chemistry, St. Xavier's College (Autonomous), Kolkata–700016, India*

† Electronic supplementary information (ESI) available. CCDC 2348683, 2348684, 2349095 and 2349099. For ESI and crystallographic data in CIF or other electronic format see DOI: https://doi.org/10.1039/d4ob00988f

ChemCatChem

Research Article
doi.org/10.1002/cctc.202401851

Chemistry Europe
European Chemical Societies Publishing

www.chemcatchem.org

One-Pot Cascade [3 + 2 + 1] Annulation: Synthesis and Mechanistic Insight of *s*-Triazines and Pyrimidines Using Azo-Supported Metalloradical Nickel Catalyst

Debashis Jana,[a] Sampad Malik,[a] Gopal Kanrar,[b] Supriyo Halder,[a] Srijita Naskar,[a] and Kausikisankar Pramanik*[a]

Highly efficient Ni-catalyzed C—N/C—C bond formation from amidines during the [3 + 2 + 1] annulation by primary alcohols alone or by primary alcohols with secondary alcohols/phenyl acetylenes has been successfully accomplished toward scaled synthesis of *s*-triazine and pyrimidines, respectively. A strongly π-acidic *bis*-azo NNN-pincer scaffold was successfully introduced for dual functionalization such as augmenting the sustainability of the molecular catalyst by enhancing the metal–ligand integrity and interposing a potent electron-sink chromophore. The high yield synthesis (up to 94%) of *poly*-azaheterocycles with merely 0.001 mol% catalyst loading demonstrates the potency of azo-anion radical assisted catalysis. A diverse range of primary and secondary alcohols are successfully used as substrates. Furthermore, use of methanol/ethanol as C1/C2 synthon (alkylating agents) enables the formation of challenging imine intermediates from amidines through dehydrogenation under mild conditions. This facilitates the synthesis of wide varieties of *s*-triazines, and pyrimidines driven by the auto-tandem catalyst. Mechanistic investigations reveal that the formation of C—C and C—N bonds proceed through a metalloradical catalysis (MRC) pathway instead of borrowing hydrogen (BH) method and thereby addresses the challenge of controlling stereoselection. This process is initiated by Ni-catalyzed acceptorless dehydrogenation (AD) of the alcohol substrate, followed by a series of sequential steps, including condensation, aza-Michael addition, cyclization, and subsequent dehydrogenation. The well-defined one-electron reductive response at −0.34 V (versus Fc^+/Fc) is indicative of the involvement of azo anion radical during catalytic annulation. The formation of the ligand radical intermediate was further substantiated by an electron paramagnetic resonance (EPR) study conducted both in the presence and absence of radical scavengers, specifically 2,2,6,6-tetramethyl-1-piperidinyloxy (TEMPO), and butylated hydroxytoluene (BHT).

1. Introduction

Metal-organic catalysts have played an important role in achieving numerous synthetically valuable organic and biomolecules that are otherwise challenging to achieve in realism. Remarkably, palladium continues to rule the field in fine organic synthesis when compared to other metals because it validates reliability and uniformity in metal-mediated catalysis and exhibits a wide substrate tolerance.[1] However, the substantial expense associated with palladium has limited its commercial adequacy, thereby motivating the exploration of catalysts based on earth-abundant, low-cost metals. Being the sibling, cost-effective nickel is the most viable option. Furthermore, they show striking resemblance in a number of organic catalytic transformation.[2] Nevertheless, they differ in many instances as well due to their innate physicochemical aspects. The recent development of homogeneous catalysis using 3d metals in organic synthesis is highly promising as it has only lately begun to challenge the abiding supremacy of late and mostly noble metals in this field and they hold the potency of being able to encompass large-scale synthesis with substantially high turnover number (TON).[3]

The synthesis of bio-active *poly*-azaheterocycles such as pyrroles, pyridines, imidazoles, pyrimidines, and triazines procured from common alcohols is a rapidly expanding area of interest for green sustainable chemistry.[4] Among these *N*-heterocycles, the pyrimidine and *s*-triazine are found in a wide range of bio-relevant molecules and are crucial structural motifs found in many pharmacological, enzyme inhibitor, antifungal, anticancer, antitubercular activity, argochemicals.[5,6] In fact, a variety of synthetic procedures have been cited in the literature depending on the substrates, reagents and reaction conditions; where metal-mediated homogeneous catalysis emerging as a versatile and valuable synthetic protocol due to their gradual improvising catalytic efficiency, sustainability and atom-economy (Scheme 1).[7] Nevertheless, such methods in general suffer from the complications of physical separation of product(s), formation of hazardous by-products, use of stoichiometric or high amounts of base and low TON, i.e., high catalyst loading. The primary drawback of homogeneous catalysts is that they cannot be efficiently reinstated after the reaction cycle, which makes cost reduction challenging in industrial

[a] D. Jana, S. Malik, S. Halder, S. Naskar, K. Pramanik
Department of Chemistry, Jadavpur University, Kolkata 700032, India
E-mail: kausikis.pramanik@jadavpuruniversity.in

[b] G. Kanrar
Department of Chemistry, St. Xavier's College (Autonomous), Kolkata 700016, India

Supporting information for this article is available on the WWW under https://doi.org/10.1002/cctc.202401851